nature

THE INTERNATIONAL WEEKLY JOURNAL OF SCIENCE

Coral reef bright spots show the way for conservation

PAGES 361 & 416

AGAINST THE ODDS

BICYCLE DYNAMICS

TWO WHEELS GOOD

The mysterious physics that keeps bikes upright

PAGE 338

BIOMEDICAL DATA

UNHEALTHY DEVELOPMENT

A downside to the tech giants' move into health

PAGE 345

AGEING RESEARCH

A LIFESPAN IN THE FAST LANE

Turquois killifish are making waves as a lab model

PAGE 453

NATURE.COM/NATURE
21 July 2016 £10
Vol. 535, No. 7612

THIS WEEK

EDITORIALS

BIKE RACE Science and innovation on two wheels **p.324**

WORLD VIEW Meet the new breed of dry cell biologists **p.325**

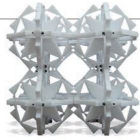

MATERIALS Hinges offer new stability for Teflon towers **p.327**

Forgotten foot soldiers of science

The story of CRISPR–Cas9 gene editing has tended to focus on a few key players. But, as with any area of basic research, it takes a small army of talented researchers to make a discovery.

"It is amazing what you can accomplish if you do not care who gets the credit." Harry Truman supposedly said that, and as the US president who dropped the atomic bomb, he had more reason than most to be amazed.

Science is a collective effort, but human nature — including that of people who sit on grant committees and decide prizes — tends to select and reward individuals. Hence the popular parlour game among scientists: speculating on who will get the Nobel prize for impressive discoveries.

They don't come much more impressive than a molecular-biology technique that has swept through laboratories in the past few years, accelerating genetic research and tantalizing the public with its potential to change how genetic diseases are treated. As a result, the scientists who helped establish the technique — which rewrites DNA using a bacterial immune system called CRISPR–Cas9 — have received accolades and awards, and ample coverage in the media.

But the researchers who did much of the work — the graduate students and postdocs who carried out the experiments — are rarely mentioned. In this week's *Nature*, we take a look at a small sample of those researchers and how their experience with CRISPR has affected their careers (see page 342).

Our article is an attempt to grant these junior investigators a little of the limelight, but it also shows how difficult it is to do so: owing to space limitations, many young scientists who made important contributions to the field were left out of the article. (It is a decision that journalists face all the time, but it was made all the more painful in this case.)

The fairest approach would perhaps have been to replace the article with a simple two-page list, in fine print, of key researchers. Even then, there would be missing entries. The development of CRISPR gene editing is basic research at its finest: a handful of researchers initially noticed an oddity in bacterial genomes and decided to investigate, and this small squad swelled into a global army of scientists investigating every aspect of the system and how it can best be applied to treat diseases and engineer transgenic plants and animals. It is impossible to adequately assign credit in any one article or documentary — or on one awards podium. And that means postdoctoral researchers and graduate students are largely left unrecognized.

The focus on senior figures is rational. They are more likely to have spent many years pioneering a field, and principal investigators set the tone and direction of their laboratories.

There are also benefits to staying out of the public eye, particularly for young investigators. The barrage of interview and speaking requests takes time away from the focus needed to launch a laboratory. And becoming famous for a particular advance, particularly a technological one, can pigeonhole a young investigator at a time when they would rather spread their wings and visit new fields.

But there is also a price. Aside from the ego boost, awards — particularly in the form of grants — bolster a career. Scientific fame that spreads outside one specific community has a greater chance of influencing review panels. This is particularly important for young investigators who are starting their careers in what suddenly becomes a highly competitive area. Senior investigators must ensure that they promote their best and brightest junior colleagues both inside and outside their field.

"Postdoctoral researchers and graduate students are largely left unrecognized."

The mentors featured in our article show that this can be done. They work hard to foster an atmosphere of independence and fearless exploration in their laboratories. They credit their graduate students and postdocs during talks, offer them opportunities to present at major conferences, and actively promote their careers — even long after their junior colleagues have moved on to other labs.

To achieve notoriety beyond scientific circles is a greater challenge, but still possible. Reporters often seek comment from celebrity scientists: the better known and more established, the better. In this case, reputation serves as a proxy for quality: given limited space, journalists seek to get the most credible comment that they can squeeze in. But good reporters sprinkle their articles with comments from younger investigators as well. Senior researchers can encourage this practice, and point journalists in the right direction.

Assigning scientific credit will never be entirely fair. But with consideration and support, wouldn't it be amazing if young investigators got a taste of the attention — and the career boost — they deserve? ■

Virtual taxonomy

People everywhere are catching Pokémon. Can they also catch real new species?

Millions of people have spent the past week walking around. Ostensibly, they are playing the online game *Pokémon Go* and hunting for critters in an 'augmented reality' world. But as gamers wander with their smartphones — through parks and neighbourhoods, and onto the occasional high-speed railway line — they are spotting other wildlife, too.

Scientists and conservationists have been quick to capitalize on the rare potential to reach a portion of the public usually hunched over consoles in darkened rooms, and have been encouraging Pokémon hunters to snap and share online images of the real-life creatures they find. The question has even been asked: how long

before the game prompts the discovery of a new species?

It's not out of the question: success is 90% perspiration after all, and millions of gamers peering around corners and under bushes across the world can create a very sweaty exercise indeed. By definition, each Pokémon hunter almost certainly holds a high-definition camera in their hands. And there is a precedent: earlier this year, scientists reported *Arulenus miae*, a new species of pygmy devil grasshopper, identified in the Philippines after a researcher saw an unfamiliar insect in a photo on Facebook (J. Skejo and J. H. S. Caballero *Zootaxa* **4067,** 383–393; 2016).

But *Pokémon Go* players beware. It is one thing to conquer a world of imaginary magical creatures with names like Eevee and Pidgey, and quite another to tangle with the historical complexity of the International Code of Zoological Nomenclature. So, say you do manage to snap a picture of something previously unknown to science — what then? Let *Nature* be your guide.

First, the good news — the Code (we'll call it that from now on to save on Twitter characters) is now officially with the times, and no longer reliant on the dead trees that were so popular before you were born. Despite grumbles from traditionalists, in 2012 the International Commission on Zoological Nomenclature, which hosts the Code, agreed to embrace online-only media. In doing so, it relaxed its rule that species could be officially named only in printed academic journals.

Now, the bad news — if your picture of an unusual butterfly or bird or hippopotamus does look to a friendly online biologist like a new species, then you'll probably have to go back and catch the beast. (Whisper it, but you might even have to kill it.)

If you think that sounds too difficult, then some (but not many) zoologists agree with you. What's in a name? To most biologists, it's still a fresh corpse — as two scientists discovered last year when they tried to identify and name a new species of bombyliid (bee fly) that they had caught and photographed in South Africa. Convention demands a reference sample called a holotype in exchange for a formal taxonomic listing, but — disaster! — the fly escaped before it could be killed and immortalized. Unwilling to chase it down again, the cheeky duo chanced their arm and showed the photographs alone as evidence, in the stead of their long-flown bee fly (S. A. Marshall and N. L. Evenhuis *ZooKeys* **525,** 117–127; 2015).

"Digital collectors" are fast outnumbering specimen collectors, the scientists warned, and new conservation rules are making it harder to collect and transport real species samples. The biodiversity community is going to have to move with the times, they said, and "adapt to growing numbers of new taxa recognized without benefit of dead, preserved type specimens". High-resolution photos, they added, rather unconvincingly, "can often provide enough information for a proper description".

"What's in a name? To most biologists, it's still a fresh corpse."

But rules is rules — and sometimes they are in place for a good reason. This month, zoologists from around the world came down on the idea like a tonne of pavement ants. A photo can't be prodded and turned over. It can't be dug out of storage and have its back legs gently stretched. It can't have its genitals re-examined. In other words, it can't have science done with it — not proper, verifiable, reproducible and falsifiable science. "The spirit of the International Code of Zoological Nomenclature is willfully violated by a description based only on a photograph," their report concluded (D. S. Amorim *et al.* *Zootaxa* **4137,** 121–128; 2016)

Still, hippos don't run that fast and can't be that hard to catch. Let's say our brave *Pokémon Go* player really does have a new species on their hands, and not just a high-resolution photo. What they want to know, of course, is can they name it after their mum? Here, the zoologists are remarkably relaxed. Unlike planets, chemical elements and human diseases, almost anything goes with wildlife. (Hence Dick Cheney, George W. Bush and Donald Rumsfeld each share their name with a slime-mould beetle.) Be prudent, though — your idol or hero may not appreciate the attention.

The ecologist Cheng-Bin Wang last month poetically named a new beetle after Chinese President Xi Jin-Ping to honour "his leadership making our motherland stronger and stronger" (C.-B. Wang *Zootaxa* **4126,** 287–294; 2016). Chinese censors responded with some augmented reality of their own, attempting to scrub all mentions of the beetle from the Internet. ■

Two wheels good

As cycling enjoys a popularity surge, science can help riders to get faster and stay safer.

As the Tour de France enters Paris this weekend, an increasing number of amateur cyclists are stretching their legs on two wheels, and stretching their Lycra as they do so. The resurgence in the popularity of cycling in many countries is a twenty-first-century success story, and one that offers some hope as the world searches for sustainable cities and transport systems.

Still, as we discuss in a News Feature on page 338, despite advances in materials and technology (and an obsession with shedding weight), the geometry of a bicycle frame this year looks, to a physicist at least, pretty much the same as last year, and as it almost always has.

Where is the innovation? The Ford Motor Company has patented an inflatable bicycle frame, although (not surprisingly) the invention tries more to tackle the problem of how a bicycle can be transported, say in the boot of a car, than how it can be ridden.

For raw speed, enthusiasts should head not to the peaks of France, but to Battle Mountain, Nevada, this September. On a 200-metre run of State Route 305 (closed to traffic), cyclists will compete to break the human-powered land-speed record. The annual event draws engineers and riders from across the globe, to roll machines that look from a distance like eggs along one of the world's straightest, flattest and smoothest roads. The current record is just under 135 kilometres per hour.

The frames of these speed machines do look different from your standard racer. For better aerodynamics, they are recumbent bicycles (prone bikes, on which the rider lies chest down, have also been built). And this is where the physics of cycling does have an important role — some teams are experimenting with rear-wheel steering, which offers a shorter, and so more efficient, chain.

Rear-wheel steering is less stable than front-wheel. Yet, as most people who have got upright on two wheels will recognize, bicycles in general are more stable than they look to non-riders and learners. Given a push, most will even stay upright without a rider. Sometimes, it takes a person trying to control a bike to make it fall over.

The majority of times that a rider and bike do fall over and cause injury, there is no one else involved. And often the problems come at the start or end of the journey, or when a rider is forced to stop en route — especially for older people. A paper this year in *Safety Science* found that 20% of injuries to older cyclists come when the riders are trying to get on or off (R. Dubbeldam *et al.* *Safety Sci.* http://doi.org/bmqf; 2016). This is where science can help. The study analysed the mounting and dismounting strategies of cyclists young and old, and saw that older people — perhaps because of how they were taught — tend to begin and brake with one foot hopping along the ground as the wheels turn, which is less stable than starting or stopping with both feet on the pedals. You never forget how to ride a bike. But some people need a refresher. ■

Cell biologists should specialize, not hybridize

Dry cell biologists, who bridge computer science and cell biology, should have a pivotal role in driving effective team science, says **Assaf Zaritsky**.

Cell biologists have come a long way since Robert Hooke first observed plants through his microscope some 350 years ago. They have adapted and adopted new technologies in molecular biology, chemistry and microscopy. But unlike researchers in genomics and other branches of biology, they have yet to fully embrace computer science.

The days of staring at microscope images to explain cell processes, as Hooke did, are over. Microscope data today are diverse and highly variable, and contain complex cellular patterns that are often invisible to the human observer. Only computers and digital vision can find them, and so identify cell and molecular dynamics. Computer vision can help, for example, to map spatial organization of subcellular components and understand how they work together to generate cell behaviour.

Digital tools already help cell biologists to carry out routine tasks: measuring cell shape or detecting and tracking intracellular components. More complex analysis should be a full-time speciality, but cell biologists do not treat it as such. Rather than embrace a truly interdisciplinary approach, with experts with different skills working together, cell biology has opted for hybridization. Academic departments and principal investigators seek individuals who can do both the biology and the computer analysis, and so encourage students and postdocs to train in both fields. For young scientists, this comes at a cost. Doing top-notch biology or computer science requires long training, expertise and attention. Either is a full-time job — aiming to train experts in both produces Jacks of all trades, masters of none.

My postdoctoral research is in computational cell dynamics, and I would like to continue in this field as an independent investigator. I recently discussed my academic future with several established principal investigators and department chairs from computer science, engineering and biomedical sciences: they were concerned about my inherent dependence on experimental partners to produce data, and warned it would undermine my ability to secure grants. To make myself more attractive to employers and funders, they suggested, I should learn to perform simple cell-biology experiments.

A colleague faced a similar reaction when she proposed to apply computer vision to study cell migration in 3D environments. One reviewer commented that analysis of other people's data was a weakness. My colleague decided to heed the advice and follow the hybrid path. What a waste! Instead of using her unique expertise, she now spends valuable time learning basic bench science that repeats what others already do and will yield only standard data.

Funders laud the importance of team science, but for cell biology it seems those teams must be made up of otherwise independent scientists. True collaborative science should follow industry by including specialists who simply can't do science without the team.

When computer scientists work on collaborative projects, too often we are expected only to provide a service: to develop custom tools and crunch data collected by the experimentalists. In this mode, the computational collaborator is required only to solve a given technical challenge. Accordingly, the emerging field of bioimage informatics develops algorithms and tools to analyse biological images at high volumes and throughput, but its main motivation is to outperform other algorithms on common problems such as registration, detection and segmentation. It demands no deep understanding of the underlying biological aspects, which limits what it can achieve.

The role of a quantitative collaborator can go further. Discovery of complex dynamic patterns requires knowledge of the biological process, the experimental possibilities and the type of information that can be extracted from data. Such insight into where to look, what to look for and how to look for it leads to more productive collaboration, in which quantitative scientists also drive biological inquiry. They adopt the motivation, terminology and intellectual framework of biology. This gives the research a more solid quantitative basis — just as genomics and computer science have combined to develop bioinformatics.

> COLLABORATIVE SCIENCE SHOULD **INCLUDE SPECIALISTS** WHO CAN'T DO SCIENCE WITHOUT **THE TEAM.**

This type of partnership has also produced major innovations in evolutionary biology and proteomics. It will not happen in cell biology while we insist on retraining computer scientists to do undergraduate biology.

To promote better collaboration, we need to nurture quantitative scientists with scientific motivations in cell biology. We can call them dry cell biologists. These scientists work at the boundaries of quantitative disciplines and cell biology. They identify scientific problems, steer (but do not perform) experiments, import, adapt and apply quantitative tools, and interpret the data to conceive testable numerical predictions.

Importantly, dry cell biology is different from theory or *in silico* biology. Theoreticians build mathematical models and simulations to explain an observation. Dry cell biologists, by contrast, extract information from data to learn about biological processes.

There are considerably more biologists who can generate visual data than can process and interpret it effectively. Thus, dry cell biologists will fill in a necessary piece of this puzzle, working hand in hand with conventional cell biologists to drive the subject forward.

In some disciplines, such as structural biology, the value of dry research is taken for granted. It is time for cell biology to embrace us. ■

Assaf Zaritsky *is a postdoc investigating computational cell dynamics at the University of Texas Southwestern Medical Center, Dallas.*
e-mail: assafzar@gmail.com

RESEARCH HIGHLIGHTS

Selections from the scientific literature

NUCLEAR FORENSICS

Reconstruction of 1945 nuclear test

By measuring concentrations of stable isotopes in bomb debris, researchers have worked out the details of a nuclear test performed 70 years ago.

Scientists have long debated the efficiency and yield of the first atomic bomb, called Trinity, which was detonated in 1945 in New Mexico. Susan Hanson and her colleagues at the Los Alamos National Laboratory in New Mexico analysed bomb debris and measured changes in both the isotope ratios and the total levels of molybdenum — a stable decay product of zirconium isotopes, which form as a result of nuclear detonation and are short-lived. The team then calculated the original concentrations of the zirconium isotopes and came up with a yield for the Trinity detonation that was in line with that officially reported.

This approach could prove useful in ongoing nuclear non-proliferation and verification efforts, the authors say.

Proc. Natl Acad. Sci. USA
http://doi.org/bmjk (2016)

THOMAS P. PESCHAK/NATL GEOGR./GETTY

MARINE SCIENCE

Shark-tracking study shapes marine park

Monitoring the movements of sharks can help researchers to advise on the areas best served by marine reserves.

In the Seychelles in the Indian Ocean, a proposed marine protected area has been designed to safeguard mainly turtles and coral reefs. To see how well it might protect sharks, James Lea at the Marine Biological Association of the United Kingdom in Plymouth and his colleagues used acoustic transmitters to track 116 sharks (five species, including *Carcharhinus melanopterus*; pictured) over a three-and-a-half-year period in and around an area earmarked for a reserve in the Seychelles. They also tracked 25 turtles. When they compared the areas that these animals favoured with two proposed reserve sizes, they found that the larger reserve covered about 34% more of the animals' movements than the smaller one.

In response to the research, the Seychelles government agreed to use the larger protected area.

Proc. R. Soc. B 283, **20160717 (2016)**

NEUROSCIENCE

Brain can retrieve baby memories

'Lost' infant memories can be reinstated later in life, thanks to specific mechanisms in the hippocampus, the brain's memory centre.

Humans and other animals are often unable to recall early-life events, but these experiences can still affect the brain and behaviour later in life. To figure out how, Cristina Alberini at New York University in New York City and her colleagues administered electric shocks to the feet of infant rats and showed that the animals seemed to lose this memory within 24 hours. However, when presented with contextual reminders and another footshock several days later, the rats behaved as if they remembered the initial shock. The researchers pinpointed specific mechanisms in the hippocampus — including a shift in the relative levels of two forms of a receptor for a molecule called NMDA — that are involved in the formation and storage of early-life memories.

The results suggest that the hippocampus goes through a critical period of rapid development during infancy.

Nature Neurosci. **http://dx.doi.org/10.1038/nn.4348 (2016)**

GENOMICS

Mitochondrial mismatch in mice

Mouse embryos containing DNA from three animals may not survive gestation, and those that do could go on to develop reproductive problems — a finding with potential implications for a proposed human therapy.

Energy-producing cell organelles called mitochondria carry their own DNA, which when mutated can cause disease. Mitochondrial-replacement therapy is being developed to prevent the inheritance of such diseases and involves the replacement of the organelles with donor ones, resulting in embryos with DNA from three people. To look for potential incompatibilities between the mitochondrial and nuclear genomes, a team led by Shoukhrat Mitalipov at the Oregon Health and Science University in Portland replaced the mitochondria

L: EMILY L. A. KELLY/R: ANDREW MULLEN

in fertilized eggs from one subspecies of mouse with those from another subspecies.

Embryos containing nuclear DNA from *Mus mus domesticus* and mitochondrial DNA (mtDNA) from *Mus mus musculus* produced healthy female progeny and males with reduced fertility. However, most of the embryos containing nuclear DNA from *M. m. musculus* and mtDNA from *M. m. domesticus* were aborted or stillborn.

Should mitochondrial-replacement therapy reach the clinic, the authors recommend selecting donors with similar mtDNA to recipients.

Cell Metab. **http://doi.org/bmn5 (2016)**

MATERIALS

Shape-shifters made with a snap

Materials that include a modular system of hinges have been used to build shape-shifting structures.

Current methods can make reconfigurable structures with only a limited number of stable forms. To make such materials more versatile, Lorenzo Valdevit of the University of California, Irvine, and his colleagues created a triangular Teflon structure several centimetres across, with hinges that allow it to snap into an open or closed configuration. By linking these subunits together, the team built 3D structures with multiple stable positions (**pictured**).

The approach could be used with a wide range of materials to make tools that have different forms and functions, the authors say.

Adv. Mater. **http://doi.org/f3qmr2 (2016)**

B. HAGHPANAH *ET AL*./*ADV. MATER.*

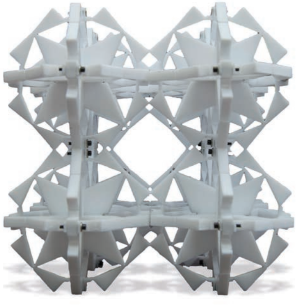

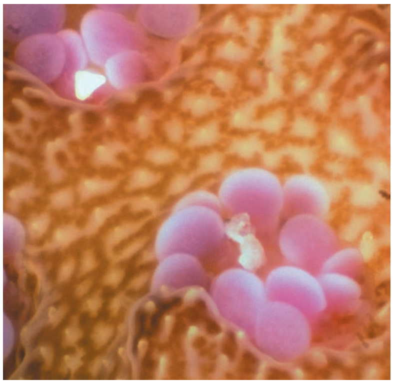

OCEAN SCIENCE

Microscope can see under the sea

An underwater microscope allows researchers to capture behaviours of corals and other marine organisms in their native habitats.

Andrew Mullen at the Scripps Institution of Oceanography in La Jolla, California, and his colleagues designed a system (**pictured** left) that divers can use to take almost micrometre-resolution images (*Stylophora* coral pictured right) at depths of up to 30 metres. It lets marine biologists observe biological processes on the sea floor that cannot be easily replicated in a lab.

The authors used their instrument to study millimetre-sized coral polyps off the coast of Maui, Hawaii, in 2015, during the first mass coral-bleaching event recorded for the main Hawaiian islands. They found that algae colonized bleaching corals in specific patterns. Near Eilat in Israel, they discovered that coral polyps connect to each other through their openings, probably to share chemicals.

Nature Commun. 7, **12093 (2016)**

NANOTECHNOLOGY

Chlorine atom arrays store data

A device that uses arrangements of atoms to encode and store information has orders of magnitude more capacity than current hard drives.

Sander Otte at Delft University of Technology in the Netherlands and his colleagues assembled arrays of chlorine atoms on a nanometre-sized copper surface. They used a scanning tunnelling microscope to manipulate the atoms and vacant spaces on the surface, creating many different arrangements that encode information. The researchers used these arrays to build a 1-kilobyte rewritable data-storage device with an information density as high as 78 terabits per square centimetre.

If the device were scaled up, it could store the entire US Library of Congress in a cube just 100 micrometres wide, according to the authors.

Nature Nanotech. **http://dx.doi.org/10.1038/nnano.2016.131 (2016)**

BEHAVIOURAL ECOLOGY

Bees like their pollen sweet

Bees can taste the pollen they collect, and favour the sweet kind.

Felicity Muth and her colleagues at the University of Nevada in Reno offered bumblebees (*Bombus impatiens*) an artificial flower containing one of three types of pollen — sweet, bitter or unflavoured. Bees presented with the sweet flower spent longer collecting pollen than did those offered the other types. When the bees were presented with two more flowers, one of which was the same colour as the first, few bees opted to change colour if their first flower had been sweet or unflavoured.

Many plants rely on bees for widespread pollination, so plants may have evolved pollen just sweet enough to keep bees coming back for more, but not so sweet that one bee takes it all, the authors say.

Biol. Lett. 12, **20160356 (2016)**

NEURODEGENERATION

ALS gene linked to autoimmunity

A gene that is often mutated in people with a neurodegenerative disease may help to keep immune responses in check.

Mutations in the *C9ORF72* gene are commonly found in people with motor neuron disease, also known as amyotrophic lateral sclerosis (ALS), as well as in people with a form of dementia. To determine the function of the C9ORF72 protein, Kevin Eggan at Harvard University in Cambridge, Massachusetts, and his colleagues introduced mutations that diminished or eliminated the function of the equivalent protein in mice. The mutant mice had autoimmune disease, over-produced inflammatory molecules and died prematurely.

The authors conclude that C9ORF72 has an important role in controlling inflammation and autoimmunity.

Sci. Transl. Med. 8, **347ra93 (2016)**

NATURE.COM
For the latest research published by *Nature* visit:
www.nature.com/latestresearch

SEVEN DAYS *The news in brief*

EVENTS

New UK government

Theresa May became UK prime minister on 13 July in the wake of the country's Brexit referendum, and quickly proceeded to appoint a new government. A newly created Department for Business, Energy and Industrial Strategy (BEIS), led by former science minister Greg Clark, will take on responsibilities that include science and energy policy; the Department of Energy and Climate Change will be disbanded. Jo Johnson stays on as universities and science minister, with his brief split between the Department of Education and BEIS. See page 331 for more.

CHRIS MCGRATH/GETTY

Turkey turmoil prompts academic purge

In the wake of the failed coup in Turkey on 15 July, the Turkish Council of Higher Education (YÖK) has told university rectors to identify academics and administrators with connections to the Gülen movement — which Turkey's President Recep Tayyip Erdoğan considers to be behind the coup — and take steps to expel them. YÖK made the statement during an emergency meeting of 165 university rectors on 18 July in Ankara. The council did not invite a further 28 rectors to the meeting, saying that their universities are suspected of being pro-Gülenist. Some of these institutions will be taken over by the state, YÖK said. The council also ordered all 1,577 university deans to resign. Separately, the international Committee on Space Research cancelled its biennial conference, due to start on 30 July in Istanbul, on security grounds.

FACILITIES

African institute

The Wellcome Trust and the Howard Hughes Medical Institute (HHMI) announced on 18 July that they will merge their South African medical research institutes. The HHMI-backed KwaZulu-Natal Research Institute for TB-HIV (K-RITH) in Durban will join the Africa Centre for Population Health in Mtubatuba, backed by Wellcome, to create the Africa Health Research Institute. Supported by a US$83-million grant from both funders, the institute will link K-RITH's laboratory facilities with the Africa Centre's detailed longitudinal population-health data to combat the epidemics of HIV and tuberculosis.

Romania joins CERN

On 17 July, Romania became a member of CERN, Europe's particle-physics laboratory near Geneva, Switzerland. The former socialist republic became a fee-paying candidate member state of the organization in 2010, following a government decision to participate in large European infrastructures and projects as a way of increasing its own scientific strength. Romania is CERN's 22nd member state.

POLICY

GM food labels

The US House of Representatives has passed a bill that would create a national labelling requirement for many foods that contain genetically modified (GM) ingredients. The bill, passed by the House on 14 July and by the Senate on 7 July, will now go to President Barack Obama, who is expected to sign it into law. The requirement allows the labels to include links to websites that contain the required information; foods that are genetically altered in ways that could be found in nature will not need to be labelled.

Navy sonar ruling

An authorization that allowed the US Navy to use a type of sonar that might be harmful to marine mammals was in violation of the Marine Mammal Protection Act, a federal court ruled on 15 July. A 2012 decision had allowed the navy to use low-frequency active sonar for training, testing and routine operations — despite protests by environmental groups that it disrupts feeding and mating patterns in certain marine animals, including whales and dolphins. The navy uses the sonar to detect submarines.

BUSINESS

Chipmaker buyout

Japanese technology company SoftBank will buy ARM Holdings, a major UK computer-chip maker based in Cambridge, for US$32 billion, the company announced on 18 July. Some industry experts

have voiced concerns over the takeover, citing ARM's role as a pillar of the British tech industry. But members of the new UK government said the deal showed that Britain was still attractive to international investors after the country's vote to leave the European Union. ARM designs the chips used in most smartphones.

PEOPLE

Trump picks Pence

Donald Trump, the Republican party's presumptive nominee for US president, selected Indiana governor and former congressman Mike Pence as his vice-presidential running mate on 15 July. A religious conservative who could help Trump to shore up support in the Republican party, Pence has spoken out against embryonic-stem-cell research and prevaricated when asked whether he believes in evolution. He has also called the science underlying global warming "very mixed" and has a 4% rating with the League of Conservation Voters, an advocacy group that tracks politicians' votes on environmental issues.

Cancer pioneer dies

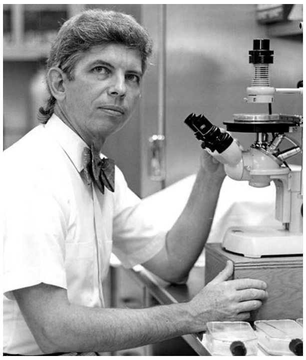

COURTESY OF UT GRADUATE SCHOOL OF BIOMEDICAL SCIENCES AT HOUSTON

Alfred Knudson (**pictured**), who proposed that cancers can be driven by accumulated mutations, died on 10 July, aged 93. In a seminal 1971 paper on the epidemiology of retinoblastoma (a tumour of the retina), he found that people typically develop the tumour either as children or much later in life. He surmised that children with the condition inherit a defective copy of a cancer-causing gene and develop the cancer after a mutation arises in the second copy of the gene. However, in the adult form, the cancer develops only after non-inherited mutations occur in both copies.

Australian cabinet

Australia's freshly re-elected prime minister, Malcolm Turnbull, announced a new minister for science on 18 July, one of several appointments to his government. Former environment minister Greg Hunt, the architect of the government's climate policy, will now be in charge of innovation, industry and science. Turnbull, whose conservative coalition was re-elected with a narrow majority earlier this month, unveiled Josh Frydenberg as the next environment minister, who will also take responsibility for energy. Some climate analysts think that combining the portfolios could help to reduce the country's reliance on fossil fuels.

FUNDING

Columbia costs

Columbia University in New York City has agreed to pay US$9.5 million in a settlement for seeking "excessive cost recoveries" from the US National Institutes of Health (NIH) in connection with hundreds of research grants, the US justice department announced on 14 July. Columbia is alleged to have repeatedly billed the NIH at a higher 'on-campus' rate, rather than a cheaper 'off-campus' rate, for research that was mainly done off campus, the settlement said.

RESEARCH

Dengue dip

The introduction of mosquitoes carrying a gene that kills their offspring has apparently reduced the number of new cases of dengue fever in a small trial in Brazil. The incidence of dengue, which is caused by a virus transmitted by the *Aedes aegypti* mosquito, fell by 91% (to 12 new cases, from 133 the previous year) in a district of the southern city of Piracicaba. Genetically modified *A. aegypti* were released in the district in April 2015. By comparison, incidence dropped by just 52% in the rest of the municipality. Oxitec, the biotechnology company in Oxford, UK, that developed the mosquito, announced the results on 14 July. Philip McCall, an entomologist at the Liverpool School for Tropical Medicine, UK, says that it is possible that other control efforts were responsible for the reductions, but calls the trial a "step in the right direction".

Greenland ice loss

Greenland lost around 1 trillion tonnes of ice between 2011 and 2014, the European Space Agency (ESA) revealed on 12 July. The loss corresponds to an annual sea-level rise that is about twice the average rate in the previous two decades. An analysis of data from ESA's CryoSat satellite shows that five thinning glaciers, which cover less than 1% of the area of Greenland, were responsible for more than 12% of the total loss (M. McMillan *et al. Geophys. Res. Lett.* http://doi.org/bmns; 2016).

TREND WATCH

Electronic cigarettes were thought by many to have simply replaced cigarettes among smokers, but an analysis of 5,490 schoolchildren in California reveals that a growing number of potential non-smokers are taking up 'vaping' — indicating a rise in nicotine use among teenagers (J. Barrington-Trimis *et al. Pediatrics* http://doi.org/bmnv; 2016). The study, published on 11 July, shows that in 2004, 9% of 17–18-year-olds smoked (conventional cigarettes), but by 2014, 14% were smoking or vaping.

E-CIGARETTES BOOST NICOTINE USE

Fewer Californian teens smoke cigarettes than they did 20 years ago — but with the emergence of e-cigarettes, nicotine use is on the rise.

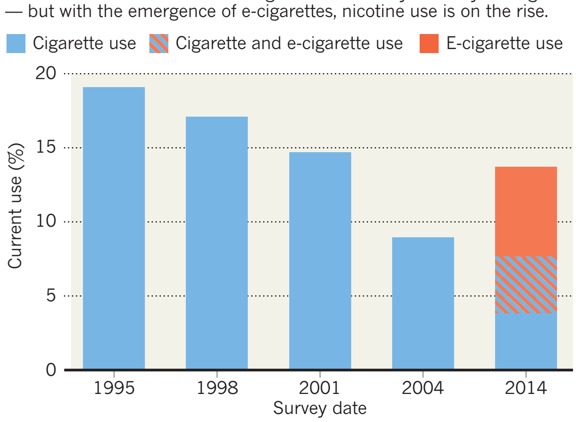

Based on data for 17–18-year-old children in Southern California Children's Health Study.

SOURCE: J. BARRINGTON-TRIMIS *ET AL.* (2016)

COMING UP

18–22 JULY
The 21st International AIDS Conference takes place in Durban, South Africa.
www.aids2016.org

25–27 JULY
The University of Aveiro in Portugal hosts the 7th International Conference on Advanced Nanomaterials.
www.anm2016.com

NATURE.COM
For daily news updates see:
www.nature.com/news

NEWS IN FOCUS

NICK OBANK, WPA POOL/GETTY

UK prime minister Theresa May meets astronaut Tim Peake, days after taking up her new post.

POLITICS

New Brexit government spells shake-up for science

Theresa May promotes a former science minister and abolishes climate-change department.

BY DAVIDE CASTELVECCHI

Three weeks after UK voters chose to leave the European Union, the country has a new prime minister, Theresa May — and a revamped administration that is poised to change science's place in government.

An overall atmosphere of chaos has reigned since the referendum, and May's ascendance has brought a measure of stability. Notably for researchers, she announced on 16 July that the universities and science minister Jo Johnson would continue in his role.

But since she took charge, May has also shaken up the government in ways that affect researchers. On 15 July, she created a new department by merging two existing ones — the Department for Business, Innovation and Skills (BIS), which had overseen the United Kingdom's annual £4.7-billion (US$6.3-billion) research budget, and the Department of Energy and Climate Change (DECC). And she appointed Greg Clark, a former science minister, to lead the new Department for Business, Energy and Industrial Strategy (BEIS) .

Science-policy experts welcome the appointment of Clark. "People will be happy that he has played that role in the past and understands the importance of science and of the research system," says Kieron Flanagan, ▶

▶ a science-policy researcher at the Alliance Manchester Business School.

It is less clear what the abolition of DECC will mean for climate research and policy, and some fear it will weaken the United Kingdom's responsibilities on climate change. "DECC's disappearance raises urgent questions," said Angus MacNeil, who leads the cross-parliamentary Energy and Climate Change Committee.

Bob Ward, a climate-change policy expert at the London School of Economics and Political Science, warns against jumping to the conclusion that May will be timid on climate action. "From what we know of her statements on climate change, she understands the importance of it," he says. "I don't think the fact that there is no climate change in the title necessarily means a reduction in commitment."

NEIL HALL/REUTERS

Former science minister Greg Clark leads a newly created department.

A more consequential change will come if some of the civil servants who are experts on climate change are lost in the transition. DECC's staff understood not only climate science but also its effects on regional weather and the need for UK infrastructure to adapt, says Corinne Le Quéré, director of the Tyndall Centre for Climate Change Research at the University of East Anglia in Norwich.

May's own recent rival for the prime minister position, Andrea Leadsom, is the new environment secretary, and May has moved responsibilities for higher education from BIS to the education department, which is now under Justine Greening.

As a result, Johnson's brief will now be split between the education department and BEIS. Universities and schools are very different, notes Nick Hillman, director of the Higher Education Policy Institute in Oxford. But, he adds, the reorganization could work provided Johnson has "considerable autonomy" within the education department. Importantly, Johnson's reappointment signals that May plans to push on with reforms of higher education and of research funding begun by her predecessor, David Cameron.

STABILITY, FOR NOW

May's appointment of Philip Hammond as Chancellor of the Exchequer, a job that includes overseeing the state's budget including allocations to research, is expected to provide stability, too. "He is seen as being a person who doesn't make headline decisions, so we might have some hope of status quo at the very least with regard to research funding," says Jenny Rohn, who chairs the UK lobby group Science is Vital.

But the country still faces the uncertainty of Brexit. May, who became the United Kingdom's second female prime minister on 13 July, had opposed leaving the EU, like Cameron. But she has made it clear that under her watch, the United Kingdom will leave the EU, and has sought to differentiate herself from Cameron's government. She has sacked some of its key members, and filled some posts with pro-Brexit politicians, putting Boris Johnson, the pro-Leave former mayor of London, in charge of the Foreign Office, for example. She has also created a post for leading the negotiations that will determine the United Kingdom's new relations with the EU.

Scientists are still in the dark about how May herself views science. She ran virtually no formal campaign for prime minister and has given little indication of what her policy priorities on research would be. In a speech in Birmingham on 11 July, she called for "a better research and development policy that helps firms to make the right investment decisions" and "an energy policy that emphasizes the reliability of supply and lower costs for users", but did not go into further detail.

➲ NATURE.COM
For the latest on Brexit and science, see:
go.nature.com/29x6w7d

PRAGMATIC OPERATOR

In her former role as home secretary, May's push to reduce immigration and tighten up visa requirements sometimes put her at odds with university administrators. She also helped to push through a bill that enacted a blanket prohibition on so-called designer drugs. But she has shown pragmatism and a willingness to change her mind when presented with compelling evidence, says Paul Nightingale, deputy director of the Science Policy Research Unit at the University of Sussex.

"She has been an example of good practice in gathering evidence, and also of explaining her decisions when they have not gone with the scientific advice," says Sarah Main, director of the London-based Campaign for Science and Engineering.

May's past decisions do not necessarily give a good indication of how she will act as prime minister, Flanagan says. As a home secretary positioning herself to be the next prime minister, May had to seem tough on issues such as immigration and security, he says.

Central to scientists' concerns are the terms of the Brexit negotiation. In particular, they want reassurance that they will still be able to access EU science funding and to easily hire people from throughout the bloc. "We need to make sure people understand that, perhaps unintentionally, the UK research community does have a lot to lose," says Main.

The community is anxious for the government to commit to shielding them from the possible impacts of Brexit. "The challenge would be for the new government and the new prime minister to set out clearly what is their ambition for science and research to play a part in the UK future," Main says. "We would like to see that clearly stated." ■

Additional reporting by Richard Van Noorden and Elizabeth Gibney.

MORE ONLINE

TOP NEWS

ALEX WONG/GETTY

Atom wranglers create rewritable memory go.nature.com/2a4uqhp

MORE NEWS

- Human eye can detect single photons go.nature.com/29lq5nd
- Bright light accelerates ageing in mice go.nature.com/29rdwdm
- Scientists fume over new pick to lead French agriculture agency go.nature.com/29qof81

NATURE PODCAST

The science of what sounds good; tumour-fighting bacteria; and tech in health nature.com/nature/podcast

FUNDING

First Greek science agency is rare source of joy

European Investment Bank provides surprise loan to halt startling brain drain.

BY ALISON ABBOTT

YORGOS KARAHALIS/REUTERS

Blue-skies research in Greece gets a boost after six years of economic strain.

A massive loan from the European Union's investment bank gives Greek researchers their first ray of hope since the debt crisis hit six years ago: a government-backed plan to create a Greek research agency.

Dubbed the Hellenic Foundation for Research and Innovation (HFRI), it will issue regular calls for basic research proposals, fill requests for research equipment and award fellowships for young scientists.

Its funder, the European Investment Bank (EIB) in Luxembourg, generally finances projects that contribute to growth and employment, including many green-energy and water-security programmes. So the decision to support Greek research came as a surprise to some. "At first we hadn't believed that the EIB would pay for blue-skies research," says Greek research minister Costas Fotakis, a former laser physicist.

The EIB says that the HFRI is crucial to halting Greece's startling brain drain: graduates and postgraduates have left Greece in droves since the crisis began.

On 15 July, the bank approved the €180-million (US$200-million) loan, which the Greek government will top up with €60 million. The total will support the HFRI during its first two-and-a-half years. The EIB rarely loans more than 50% of the cost of a project, but the 28 EU member states voted unanimously to make an exception, says EIB spokesman Richard Willis.

"Given the key issues around fundamental research in Greece, 75% was seen as justified," he says. "It is about competitiveness, forward-thinking and the future."

The EIB does not make the detailed conditions of its loans public, but Willis says that the terms for the HFRI are very attractive and that Greece has a full 15 years to repay the money. If the HFRI is successful, the bank will consider additional loans in the future, he adds.

A parliamentary bill to establish the agency is currently being discussed. It proposes that the HFRI operate along the lines of the US National Science Foundation and the DFG, Germany's main funding agency — and without direct political influence.

"For the first time we'll have some regularity in research funding in Greece," says Nektarios Tavernarakis, director of the FORTH Institute of Molecular Biology and Biotechnology (IMBB) in Heraklion, Crete. "It will definitely help make Greece a more attractive place to do research."

Tavernarakis, who in April won his second grant from the prestigious European Research Council, knows from bitter experience how hard it is to persuade ambitious young scientists to join even a high-performing research institute like his own. When the debt crisis hit a peak last July, triggering bank closures, the resulting controls on the flow of capital out of the country frightened off candidates who had previously been prepared to work at the IMBB, he says. "And that was quite understandable."

Fotakis says that the HFRI is a key part of government strategy to increase the country's potential. He blames the brain drain on the austerity measures imposed by the European Commission, the European Central Bank and the International Monetary Fund in exchange for keeping the country from bankruptcy. "They have lowered wages and pensions, and made all aspects of research difficult," he says.

Because parliament is unlikely to pass the HFRI bill before September, Fotakis plans to launch calls for some PhD and postdoctoral grants immediately. Even before the crisis, Greece has been one of the lowest investors in research in the EU. But once the crisis began, calls for research proposals, which were always modest and irregular, nearly disappeared. Scientists had to survive on international funding sources, particularly those from the EU.

The country still manages to host several internationally competitive research centres, but Fotakis says that even this is not sustainable. "Scientific output is obviously not going to be sustained for ever when the brain drain is so intense."

The initial total of €240 million earmarked for the agency will support fundamental research, but the HFRI will eventually support a second stream for translational research. Beyond 2018, Fotakis expects the government to support the fundamental research stream with an annual €20 million. "And now that the EIB has demonstrated its confidence in Greek science with this loan, it'll be much easier to attract other sources of financing to the HFRI," he says.

Greece fixed a few more bugbears when it passed a general law on research in May — for example, researchers will now be able to top up salaries for themselves and their groups if they bring in outside grants.

No one imagines that the problems of Greek science are now solved. "Still," says Tavernarakis, "these measures show things are at least going in the right direction." ■

ERIK DE CASTRO/REUTERS

A Filipino ship and a Chinese coast-guard vessel pass each other in the South China Sea.

CONSERVATION

Ecosystem fear in South China Sea

Court decision escalates tensions in ecologically sensitive region, but may also push nations to cooperate.

BY DAVID CYRANOSKI

An international tribunal has ruled against China's territorial claims in the South China Sea — and ecologists are worried. They warn that the decision, which China has vowed to ignore, could escalate tensions between China and its neighbours, leading to increased competition for fish and a subsequent collapse in stocks.

"Now catastrophe looks much closer than before," says John McManus, a marine ecologist at the University of Miami in Florida. "The Hague decision stirred the pot."

But McManus and others also note that the ruling, by the Permanent Court of Arbitration in The Hague, may nudge China to cooperate more with regional rivals on scientific and environmental issues.

The Philippines brought the case in 2013 following China's occupation of a reef, called Scarborough Shoal, that both countries claim. On 12 July, the court upheld Philippine allegations that China had unlawfully restricted access to its fisherman there. And it rebuked China for its broader territorial claims within the 'nine-dash line' that envelops most of the South China Sea (see 'Disputed waters').

China argues that certain geological fixtures in the sea are islands that belong to its sovereign land and that the waters that surround them are within its 'exclusive economic zone'. The court found that the fixtures are merely rocks or "low-tide elevations".

The tribunal also said that China had violated the United Nations Convention on the Law of the Sea by constructing artificial islands that damaged coral reefs, and by failing to stop its fishers from snatching protected species.

The judgement is legally binding, but China, which views the South China Sea as increasingly important strategically, looks likely to ignore it. "China neither accepts nor recognizes it," says a statement from the foreign affairs ministry. The region contains more than 1 billion tonnes of oil reserves and is an important nexus connecting the Pacific and Indian oceans. "No one will force China from those islands if they don't want to go," says Tim Johnston, Asia program director for the Brussels-based International Crisis Group. Days after the ruling, China cordoned off a swathe of the area for military exercises.

Military escalation could follow. For instance, the tribunal found that Mischief Reef is within the Philippines' exclusive economic zone but China has built a military base there, and, since the ruling, landed an aircraft there.

Ecologists will be watching out for an escalation in fishing, in particular at the Scarborough Shoal. Fish densities and catch rates in the South China Sea have plummeted in past decades. McManus's research suggests that the reef sits at the centre of a crucial region from which many coastal fishing stocks are replenished. He fears that the ruling — which found that China and the Philippines share fishing rights there — will lead both to increase their fishing activity. "One will try to get there before the other one," says McManus. "When we have a present fisheries crisis and a looming fisheries catastrophe, you shouldn't go to one of the most important places for fisheries and destroy it." Such a rush could affect hundreds of species, he says, and permanently reduce the numbers of some, including sea turtles, sharks and giant clams.

Another problem for conservationists is the destruction of coral reefs. McManus estimates that 162 square kilometres of reef has been destroyed, almost all of it by the Chinese in the past few decades. His calculations, which he presented at the South China Sea Conference on 12 July, suggest that Chinese cutter boats that hunt endangered giant clams account for 104 km^2 of the damage, with 55 km^2 a result of island building by dredging sediment from the ocean floor and dumping it on the reefs.

A statement by China's ministry of foreign affairs says that island building is carried out "based on thorough studies and scientific proof" and that "the impact on the ecological system of coral reefs is limited". But scientists have long said that the island building has to stop. Kwang-Tsao Shao, a marine-biodiversity expert at Taiwan's Academia Sinica in Taipei,

DISPUTED WATERS

An international tribunal has ruled that China's territorial claims based on the 'nine-dash line' in the South China Sea are invalid.

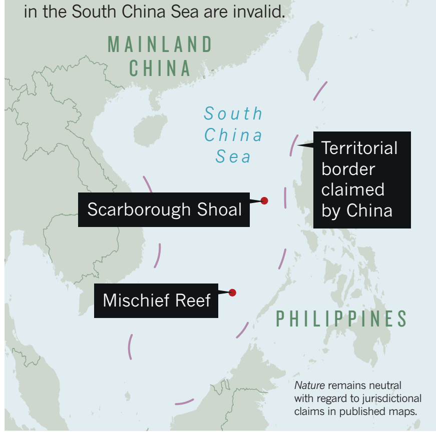

says that at meetings that include his mainland peers, there is consensus from ecologists on both sides of the strait that the region should be set aside as a marine protected area.

Scientists in the region do already collaborate: Zhifei Liu at Tongji University in Shanghai, China, leads a UNESCO research project which brings together scientists from China, the Philippines and other countries to study how sediment is deposited and transported in the South China Sea. Liu says that this and other China-funded projects will be unaffected by the ruling, although he worries that Philippine collaborators might now drop out.

But scientific interest and environmental objectives in the area could strengthen diplomacy, by giving adversaries a reason to sit down and iron out priorities of mutual interest. The tribunal ruling may be what is needed to spark such dialogue, says Johnston. China — although bullish in its responses so far and unlikely to give up its claims — will want to at least look as though it is acting fairly and for the common good. "We are hoping this may tip the balance and persuade China that constructive negotiation is the way forward," he says.

Since the 1990s, McManus has advocated for a jointly run marine 'peace park' in the region. "It's the only way to avert a fisheries collapse. It will have a good effect on efforts to avert military action," he says. The tribunal decision makes him slightly more optimistic. He now gives the park a 1 in 10 chance of happening rather than 1 in 100. "If China can just sit there thinking 'this is all ours', we won't get anywhere," he says. ■

EPIDEMIOLOGY

Social cycle aids HIV spread

Genetics study shows older men and young women drive South Africa's epidemic.

BY AMY MAXMEN

Sex between young women and older men is no secret in South Africa. The name 'blesser' is commonly used to describe a man who may at first pay for a teenager's bus fare to high school, then buy school supplies she cannot afford, and perhaps lunch at a decent café. Over time, the adolescent sleeps with her provider.

A genetic analysis now suggests how this social phenomenon plays into the cycle of HIV transmission in the country, which has the world's largest HIV epidemic. By analysing the similarity of viral genetic sequences from nearly 1,600 people with HIV in one community in KwaZulu-Natal, the study shows that adolescent girls and women in their early 20s tend to pick up the virus from men aged around 30. When the women grow older, they go on to infect their long-term partners, who in turn may pass the virus on through affairs with younger women.

"This is the engine driving high rates of HIV," says epidemiologist Salim Abdool Karim, senior author of the unpublished study and director of the Centre for the AIDS Program of Research in South Africa (CAPRISA). He presents the work this week at the International AIDS Conference in Durban.

Karim thinks that the study adds to growing evidence that HIV-free young women in regions with very high rates of HIV should be encouraged to take antiretroviral medications regularly to prevent infection. The World Health Organization also recommends that people at substantial risk of HIV be offered what is known as PrEP (pre-exposure prophylaxis). But, owing in part to disappointing results in clinical trials, the South African government has not yet recommended PrEP for young women.

Karim's study also shows the importance of making broader social changes, adds Michel Sidibé, executive director of the Joint United Nations Programme on HIV/AIDS (UNAIDS). In parts of South Africa, 8 times as many teenage girls have HIV as do teenage boys, and in some communities in KwaZulu-Natal, a 15-year-old girl has an 80% risk of getting HIV in her lifetime. "Something that underlies the study is how common it is for older men to have sex with young girls. Pills are useful, but how can we break this silence around the lack of enforcement of laws that protect young women? How can we invest in the capacity of people to claim their rights and reduce this kind of violence?"

"This is the engine driving high rates of HIV."

VICIOUS CYCLE

Researchers have long known of the high burden of HIV infections in young South African women, and that they get infected by older men, says Thomas Quinn, an epidemiologist at Johns Hopkins Bloomberg School of Public Health in Baltimore, Maryland, who was not involved in the study. But, he says, "it is very exciting to use molecular genetic information to actually show how the virus spreads among people" — and to pinpoint the ages of women and men at key points in the cycle of HIV transmission.

Karim has tracked HIV genetic data for the past couple of years, and his work has already affected how governments and international organizations tackle the virus. He has been sharing results regularly with Deborah Birx, the US Global AIDS Coordinator who oversees the US President's Emergency Plan for AIDS Relief (PEPFAR), the largest federal funder of HIV-prevention research.

In 2014, PEPFAR launched an initiative called DREAMS to protect young women from HIV, in response to the finding that more than 1,000 women aged 16–24 become infected every day in southern and eastern Africa. When Birx heard details of Karim's results last year, she convinced PEPFAR to target particular demographic groups. For example, she says, half of the recipients of the US$85-million DREAMS Innovation Challenge, announced on 18 July, are 15- to 19-year-old girls.

Despite the results, health officials remain reluctant to recommend PrEP for adolescent girls and young women. In June, the South African government endorsed PrEP for sex workers — but not for other high-risk groups, such as gay men and young women. One reason for its hesitancy is that the treatments have not proved effective in clinical trials, and blood tests have suggested that is because women in these trials did not consistently take their medications (either daily pills or a vaginal gel).

But at the conference, the CAPRISA team announced another as-yet-unpublished finding that suggests a woman's vaginal microbiome may be in part responsible for the inefficacy of PrEP. A study of women who used the gel tenofovir to prevent HIV infection suggests that it was less effective in those who had *Gardnerella vaginalis* bacteria in their vaginal lining. The researchers found that *G. vaginalis* absorbed the PrEP drugs, reducing the amount of medication in the blood.

This hints that more women may actually have taken their medications than the disappointing blood tests from earlier trials suggested, Karim says — and also that treatment for an imbalance in vaginal bacteria might help PrEP to work better in some young women. ■

CLIMATE CHANGE

Algae speed up Greenland ice melt

Project probes how microbes affect ice sheets.

BY ALEXANDRA WITZE

Researchers are fanning out across the Greenland ice sheet this month to explore a crucial, but overlooked, influence on its future: red, green and brown algal blooms. These darken the ice, causing it to absorb more sunlight and melt faster.

The £3-million (US$4-million) Black and Bloom project is the first to systematically measure how algae are changing the amount of sunlight that Greenland's ice sheet bounces back into space. "We want to know how much of the darkness is due to microbes and how much to other factors" such as soot or mineral dust, says principal investigator Martyn Tranter, a biogeochemist at the University of Bristol, UK.

The heart of the study is a region measuring half a kilometre long on each side, near Kangerlussuaq, Greenland. The researchers will spend six weeks collecting samples of black carbon and microorganisms while measuring incoming sunlight and reflectivity. The project will continue for two more summers, exploring different parts of the ice sheet.

"They're extremely lazy algae — they sleep for nine months and then wake up and have a party," says team member Liane Benning, a biogeochemist at both the University of Leeds, UK, and the German Research Centre for Geosciences in Potsdam. The blooms create vast, colourful fields of 'watermelon snow'.

Last month, Benning and her team reported that algal blooms across the Arctic could reduce reflectivity by 13% over the melting season (S. Lutz *et al. Nature Commun.* **7,** 11968; 2016). Their results should enable climate modellers to improve estimates of how the ice sheet — which holds enough water to raise sea levels by 7 metres — is likely to melt in coming decades. The past several years have seen record temperatures and melting across Greenland.

Black and Bloom will provide "a one-of-a-kind data set" to help researchers understand Greenland's future, says Marco Tedesco, a geophysicist at the Lamont–Doherty Earth Observatory in Palisades, New York. ■

People line up to buy groceries outside a supermarket in Caracas.

Q&A Claudio Bifano

Venezuelan science under siege

The political and economic crisis in Venezuela continues to worsen. As the price of oil — the country's major export — has fallen, Venezuela has struggled to pay for imported goods while maintaining socialist economic policies put in place by former president Hugo Chávez. Claudio Bifano, a chemist at the Central University of Venezuela in Caracas, continues to teach despite rolling blackouts, food lines and increasing violence. "This is not a good time for the country, but we have to keep working," he says. "We have to keep living." Bifano, who is also the president of the Latin American Academy of Sciences, spoke to Nature *about how Venezuelan scientists are coping with the turmoil.*

What is daily life like for Venezuelans?
There is a serious scarcity of food and medicines, and there is high inflation, so the little that people can buy is extremely expensive. We depend on what the government imports, and as the credit that the government uses for imports is shrinking, it is more difficult to import. This is an economic model that has proven absolutely inefficient.

How are the food shortages affecting society?
We're already seeing a malnutrition problem. Many schools can no longer serve lunches, and the schools that still provide lunch, in a couple of states, as far as I know, serve 40% of what they used to provide. In a few years, we'll see the consequences of children and youth who were malnourished and had poor health care. Those problems will affect the country's development.

How are universities weathering the crisis?
Universities are becoming degraded because of incomprehensible policies. Of the budget that autonomous universities receive from the state, 95% goes to pay personnel and only 5% is left for infrastructure, graduate programmes, research, outreach and everything else that

FEDERICO PARRA/AFP/GETTY

universities should do. And the salaries are ridiculous.

I am a tenured professor and have been working at the university for 50 years. I have a PhD from the University of California [San Diego]. I'm as high on the scale as I can go. My salary is 40,000 bolívares a month. At the real exchange rate, the rate at which I have to buy things in stores, I earn $40.

As a result, 700 professors, of a total of about 3,000, have left the Central University. Four hundred have left Simón Bolívar University [in Sartenejas], which is a relatively small university. And although the Metropolitan University [in Caracas] is a private university, about 10% of its personnel have left. Why? Simply because you can't live on the salary that the university pays.

Where are these people going?

In the area of science and technology, many go to the United States, others to European countries. A person with good academic training, a researcher or experienced professor, can get a job at an Ecuadorian university or go to Brazil, which has a policy to attract outside researchers to strengthen some of its universities.

Do research opportunities still exist in Venezuela?

Fewer and fewer. With the degrading of the universities, laboratories are eliminated, resources are lost. Libraries don't have current journals. Laboratories can't buy the reagents they need, because it's expensive to do research that's competitive internationally.

The government says there are 16,000 researchers here, and that it invests 2.6% of gross domestic product in science and technology, but the number of publications has decreased in recent years by practically 40%, and the flight of young, well-trained people from Venezuela is huge. In science and technology, it's estimated that 1,500 researchers have left the country.

"The flight of young, well-trained people from Venezuela is huge."

What future do you foresee?

Something has to change. There are endless lines of people at markets, trying to buy food. The government controls the prices of some items and you can only buy them at certain stores. So when they say there are baby nappies or milk, for example, the lines are unending.

There has also been an increase in violence. Around 6 p.m., when it starts to get dark, I go home, because I don't feel safe on campus. About a month ago, there was a lynching in the Central University. A boy tried to snatch a girl's purse, a friend came to her aid and there was a fight. The assailant pulled out a pistol and shot the other boy, but fortunately only grazed his head. Then the assailant hid in the university, but other kids saw him, grabbed him and beat him to death, inside the university.

How are students dealing with the crisis?

They go to class, and I tell them, "Try to learn everything you can from your professors. Get as much education as you can." But when you ask, "How many of you want to practise your profession here in the country?" out of 10, two raise their hands. They're more material for export.

It will take a long time to recover from this — at least two generations. I don't think I'll see it. ■

INTERVIEW BY BARBARA FRASER

This interview has been edited for length and clarity.

CORRECTION

The article 'Interference puts satellite data at risk' (*Nature* **535,** 208–209; 2016) wrongly stated that William Mahoney would lead a panel on spectrum-sharing at an American Meteorological Society meeting later this month. Jonathan Porter is the panel chairman. The story also did not make it clear that Ligado Networks is a satellite-communications company.

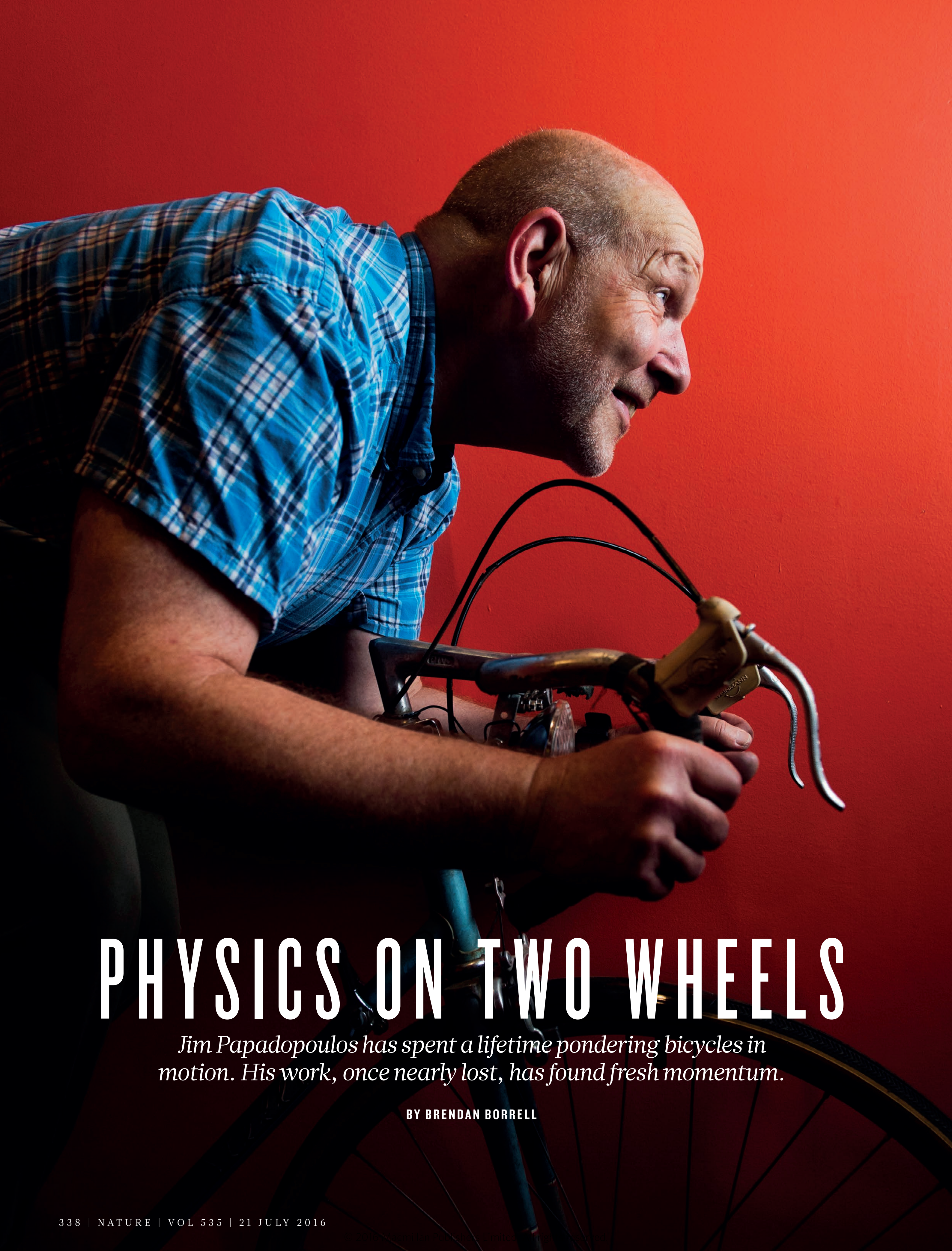

PHYSICS ON TWO WHEELS

Jim Papadopoulos has spent a lifetime pondering bicycles in motion. His work, once nearly lost, has found fresh momentum.

BY BRENDAN BORRELL

Seven bikes lean against the wall of Jim Papadopoulos's basement in Boston, Massachusetts. Their paint is scratched, their tyres flat. The handmade frame that he got as a wedding present is coated in fine dust. "I got rid of most of my research bikes when I moved," he says. The bicycles that he kept are those that mean something to him. "These are the ones I rode."

Papadopoulos, who is 62, has spent much of his life fascinated by bikes, often to the exclusion of everything else. He competed in amateur races while a teenager and at university, but his obsession ran deeper. He could never ride a bike without pondering the mathematical mysteries that it contained. Chief among them: What unseen forces allow a rider to balance while pedalling? Why must one initially steer right in order to lean and turn left? And how does a bike stabilize itself when propelled without a rider?

He studied these questions intensely as a young engineer at Cornell University in Ithaca, New York. But he failed to publish most of his ideas — and eventually drifted out of academia. By the late 1990s, he was working for a company that makes the machines that manufacture toilet paper. "In the end, if no one ever finds your work, then it was pointless," he says.

But then someone did find his work. In 2003, his old friend and collaborator from Cornell, engineer Andy Ruina, called him up. A scientist from the Netherlands, Arend Schwab, had come to his lab to resurrect the team's research on bicycle stability.

"Jim, you need to be a part of this," Ruina told him.

TWO WHEELS GOOD

Together, the researchers went on to crack a century-old debate about what allows a bicycle without a rider to balance itself, publishing in *Proceedings of the Royal Society*[1] and *Science*[2]. They have sought to inject a new level of science into the US$50-billion global cycling industry, one that has relied more on intuition and experience than on hard mathematics. Their findings could spur some much needed innovation — perhaps helping designers to create a new generation of pedal and electric bikes that are more stable and safer to ride. Insights from bicycles also have the potential to transfer to other fields, such as prosthetics and robotics.

"Everybody knows how to ride a bike, but nobody knows how we ride bikes," says Mont Hubbard, an engineer who studies sports mechanics at the University of California, Davis. "The study of bicycles is interesting from a purely intellectual point of view, but it also has practical implications because of their ability to get people around."

For a mechanician — that fusty breed of engineer whose subject is defined by Newton's three laws of motion — the conundrums of the bicycle hold a special allure. "We are all stuck in the nineteenth century, when there wasn't such a difference between math and physics and engineering," says Ruina. Bicycles, he says, are "a math problem that happens to relate to something you can see".

The first patents for the velocipede, a two-wheeled precursor to the bike, date to 1818. Bikes evolved by trial and error, and by the early twentieth century they looked much as they do today. But very few people had thought about how — and why — they work. William Rankine, a Scottish engineer who had analysed the steam engine, was the first to remark, in 1869, on the phenomenon of 'countersteering', whereby the rider can steer to the left only by first briefly torquing the handlebars to the right, allowing the bike to fall into a leftward lean.

The link between leaning and steering gives rise to the bicycle's most curious feature: the way that it can balance while coasting on its own. Give a riderless bike a shove and it may wend and wobble, but it will usually recover its forward trajectory. In 1899, English mathematician Francis Whipple derived one of the earliest and most enduring mathematical models of a bicycle, which could be used to explore this self-stability. Whipple modelled the bicycle as four rigid objects — two wheels, a frame with the rider and the front fork with handlebars — all connected by two axles and a hinge that are acted upon by gravity.

Plugging the measurements of a particular bicycle into the model revealed its path during motion, like a frame-by-frame animation. An engineer could then use a technique called eigenvalue analysis to investigate the stability of the bicycle as one might do with an aeroplane design. In 1910, relying on such an analysis, the mathematicians Felix Klein and Fritz Noether along with the theoretical physicist Arnold Sommerfeld focused on the contribution of the gyroscopic effect — the tendency of a spinning wheel to resist tilting. Push a bicycle over to the left and the rapidly spinning front wheel will turn left, potentially keeping the bicycle upright.

In April 1970, chemist and popular-science writer David Jones demolished this theory in an article for *Physics Today*[3] in which he described riding a series of theoretically unrideable bikes. One bike that Jones built had a counter-rotating wheel on its front end that would effectively cancel out the gyroscopic effect. But he had little problem riding it hands-free.

This discovery sent him hunting for another force that could be at play. He compared a bike's front wheel to the casters on a shopping trolley, which turn to follow the direction of motion. A bicycle's front wheel can act as a caster because the point at which the wheel contacts the ground typically sits anywhere from 5 centimetres to 10 centimetres behind the steering axis (see 'What keeps a riderless bike upright?'). This distance is known as the trail. Jones discovered that a bike with too much trail was so stable that it was awkward to ride, whereas one with negative trail was a death trap and would send you tumbling the moment you released the handlebars.

When a bicycle starts to topple, he concluded, the caster effect steers the front end back under the falling weight, keeping the bicycle upright. To Jones, the caster trail was the sole explanation for a bike's self-stability. In his memoir, published 40 years later, he counted the observation as one of his great accomplishments. "I am now hailed as the father of modern bicycle theory," he declared.

"EVERYBODY KNOWS HOW TO RIDE A BIKE, BUT NO ONE KNOWS HOW WE RIDE BIKES."

GEARING UP

That article would make an impression on Jim Papadopoulos, then a teenager in Corvallis, Oregon, with a gift for numbers and a home life in tatters. In 1967, his father Michael, an applied mathematician, had moved his wife and four children from England to the United States to start a job at Oregon State University. But Michael Papadopoulos was denied tenure after protesting against the Vietnam War, setting off a decade-long legal battle with the university that left him out of a job and the family scouring rubbish bins for scraps. Jim's mother killed herself in the early 1970s. "Just as I was opening my eyes to the world and deciding who I was," Papadopoulos says, "my family was falling apart."

He found solace in bikes. He pedalled his Peugeot AO8 around town and grew his hair to his shoulders. He stopped going to classes, and his grades took a tumble. At 17, he dropped out of school and left home. But before he abandoned his studies, a teacher gave him the Jones article.

Papadopoulos found it captivating but confusing. "I've got to learn this stuff," he thought. He spent the summer bumming around Berkeley, California, reading George Arfken's textbook *Mathematical Methods for Physicists* in his spare time. Then, he worked at a plywood mill in Eugene, Oregon, earning enough money to buy the legendary Schwinn Paramount that he raced every weekend. In 1973, he worked for the frame builder Harry Quinn in Liverpool, UK, but he was terrible at it and Quinn asked him to leave.

Papadopoulos returned to Oregon, took a

ADAM GLANZMAN FOR *NATURE*

Jim Papadopoulos sees a future with radically new bicycle designs.

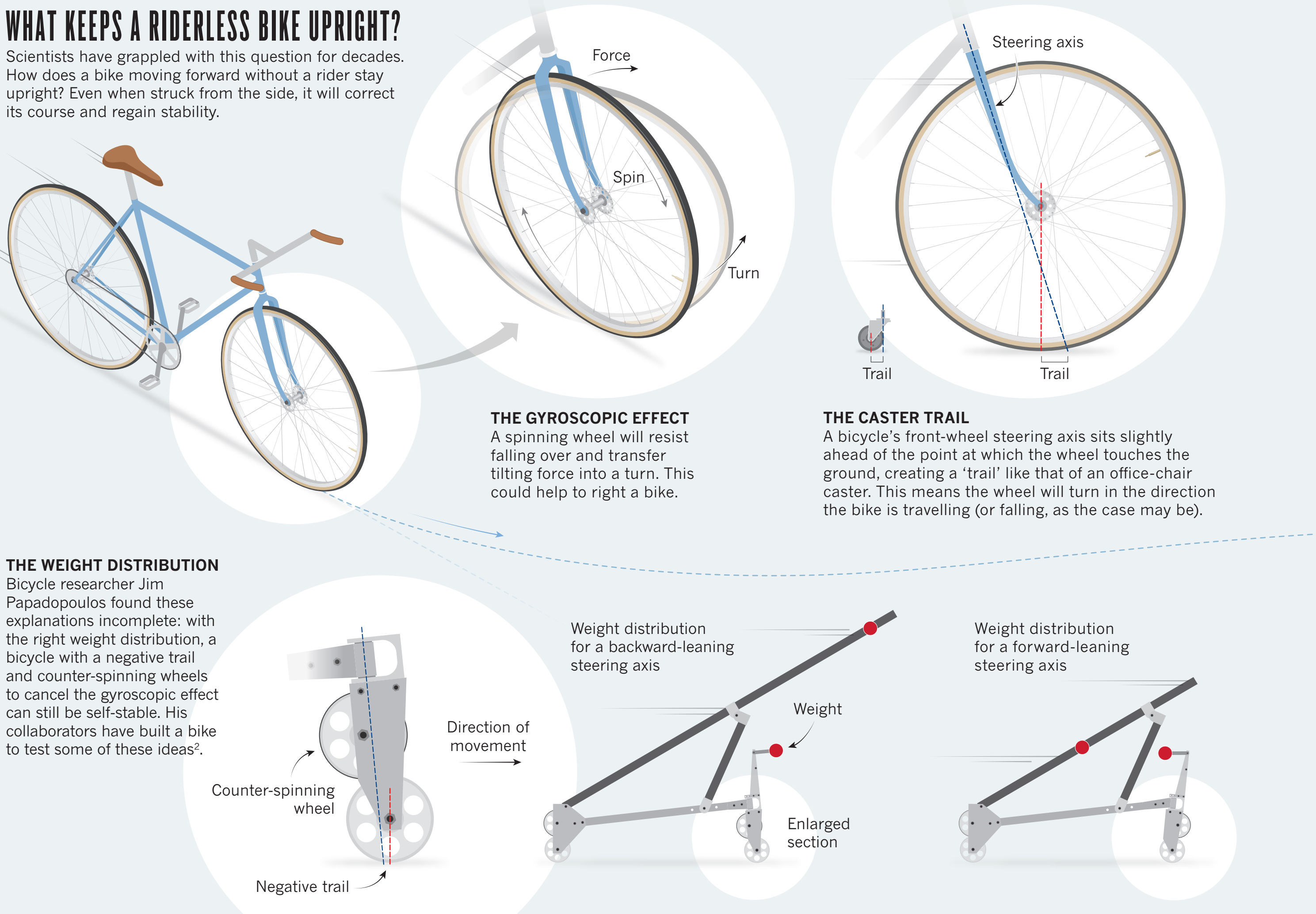

JASIEK KRZYSZTOFIAK/NATURE

few college classes and, in 1975, started undergraduate studies in mechanical engineering at the Massachusetts Institute of Technology (MIT) in Cambridge. He did well. Oil company Exxon later supported him as he studied for a PhD in fracture mechanics. Papadopoulos's adviser, Michael Cleary, was optimistic about his prospects as an academic. "I think Jim will become a university professor — and we certainly hope it's going to be here at MIT," he told a writer from Exxon's in-house magazine.

Papadopoulos had other ideas. He had been studying Whipple's model and Jones's article, and wrote to bike companies offering his services as an engineer. He didn't receive a single response. Instead, Cleary helped him to get a position at the US Geological Survey in Menlo Park, California, where he first met Andy Ruina.

The two became fast friends. When Ruina got a job at Cornell, he hired Papadopoulos as a postdoc. "We talked about bikes all the time, but I didn't realize he wanted to make a serious thing about it," Ruina says.

Papadopoulos convinced Ruina that bicycle companies — like oil companies — might be interested in supporting academic research. So he started fund-raising, reaching out to bike makers. For $5,000, they could be benefactors of the Cornell Bicycle Research Project, an ambitious effort that would investigate everything from the strength of wheels to brake failure in the rain.

Papadopoulos's first goal was to finally understand what makes one bicycle more stable than another. He sat in his office and scrutinized 30 published attempts at writing the equations of motion for a bicycle. He was appalled by the "bad science", he says. The equations were the first step towards connecting the geometry of a bicycle frame with how it handled, but each new model made little or no reference to earlier work, many were riddled with errors and they were difficult to compare. He needed to start from scratch.

After a year of work, he had what he believed to be the definitive set of equations in hand. Now it was time for them to talk back to him. "I was sitting for hours at a time, staring at the equations and trying to figure out what they implied," he says.

He first rewrote the bicycle equations in terms of the caster trail, the crucial variable that Jones had championed. He expected to find that if the trail was negative, the bicycle would be unstable, but his calculations suggested otherwise. In a report that he prepared at the time, he sketched a bizarre bicycle with a weight jutting out in front of the handlebars. "A sufficiently forward [centre of mass] can compensate for a slightly negative trail," he wrote. No single variable, it seemed, could account for self-stability.

This discovery meant that there was no simple rule-of-thumb that could guarantee that a bike is easy to ride. Trail could be useful. Gyroscopic effects could be useful. Centre of mass could be useful. For Papadopoulos, this was revelatory. The earliest frame builders had simply stumbled on a design that felt OK, and had been riding around in circles in that nook of the bicycle universe. There were untested geometries out there that could transform bike design.

THE CRASH

After two years, Ruina could no longer support Papadopoulos. Apart from the bike manufacturer Murray, the only industry donations the two ever got were from Dahon and Moulton, makers of small-wheeled bicycles — perhaps because the bikes' unconventional designs could make them tricky to ride. Ruina joked that he should change the name to the "Folding Bicycle

Research Project". It was gallows humour.

And although Papadopoulos was making progress in the mathematics of bikes, the only article that he ever published as the first author was a book chapter[4]. "I find much more joy discovering the new and working out the details and, of course, it's boring to write it up," he says. Without money or publications, his time in bicycle research wound down. In 1989, he put his bikes into a moving van and drove west to Illinois, where his then-wife had a job. He endured a succession of teaching and industry jobs that he hated. In his spare time, he moderated the Bicycle Science e-mail list for bicycle-science nerds and helped to build a car that fitted into a few suitcases for the reality television show *Junkyard Wars*.

In 2001, David Wilson, an MIT engineer and inventor of one of the first modern recumbent bicycles, invited Papadopoulos to co-author the third edition of the book *Bicycling Science*. Papadopoulos was overwhelmed by monetary debts and responsibilities. He failed to send Wilson the first chapter, and then stopped responding to e-mails altogether. Wilson felt betrayed. "He is a rather brilliant guy," Wilson says, but "he always had problems finishing anything".

BACK TO THE BIKE

At Cornell, Ruina moved on. He applied the team's insights about bicycles to a new arena: robots. If bicycles could demonstrate such elegant stability without a control system, he reasoned, it might be possible to design a stripped-down walking machine that achieves the same thing. In 1998, he worked with Martijn Wisse, a graduate student of Schwab's at the Delft University of Technology in the Netherlands, to build a bipedal machine that could walk down a slight incline with no motor at all, storing energy in its swinging arms. Adding a few electronic motors generated an energy-efficient robot that could walk on level ground.

In 2002, Schwab decided to spend his sabbatical with Ruina, and they started discussing the old bicycle work. It was then that Ruina called Papadopoulos and paid for him to visit. "That was the first time I met the genius," says Schwab.

With more bicycles on the road than ever before, Schwab found it inconceivable that no one had published the correct set of bike equations, or applied it to bicycle design challenges. Within a year, he and Jaap Meijaard, an engineer now at the University of Twente in the Netherlands, independently derived their own equations and found complete concordance with Papadopoulos's. They presented the definitive bicycle equations at an engineering conference in South Korea, and the four collaborators published them jointly[1].

The challenge now was to prove that it was more than just a mathematical finding. Schwab and a student spent a year building a self-stable bike with a very small negative trail. Looking like the offspring of a razor scooter and a see-saw, it had a weight angled out in front of the front wheel and a counter-turning wheel to cancel out gyroscopic effects. In a video of it coasting, you can see it lean and veer to the right, but then recover on its own[2]. The experiment proved that Papadopoulos had been right about the complex interplay of factors that make a bicycle stable or unstable.

Yet, after waiting for three decades for his discoveries to reach a wider audience, Papadopoulos can't help but feel deflated. "It did not change everything in the way that we imagined," he says. This year's bike frames look much like last year's. "Everyone is still in the box," he says. Nevertheless, other researchers have since been pulled into the group's orbit, creating enough momentum to launch a Bicycle and Motorcycle Dynamics conference in 2010. It gathers together tinkerers from all over the world, some of whom have also built weird experimental bicycles to test design principles.

One of the organizers of this year's conference, engineer Jason Moore of the University of California, Davis, has sought to probe the link between a bicycle frame's geometry and an objective measure of handling — its ease of control[5]. The work was inspired by extensive military research on aircraft pilots. Moore created a model of human control by performing various manoeuvres on bikes kitted out with sensors to monitor his steering, lean and speed. To force himself to balance and ride using steering movements alone (rather than shifting his weight), he had to don a rigid upper-body harness that bound him to the bike. The research confirmed the long-standing assumption that more stable bikes handle better, and potentially gives frame builders a tool to optimize their designs.

It also introduced a puzzle: the steering torque required was two or three times that predicted by the Whipple bicycle model[6]. This might have been caused by friction and flexing of the tyres, which are not part of the model, but no one is certain. For further tests, Moore and his colleagues have built a robotic bike that can balance itself. "Once you have a robot bicycle, you can do a lot of crazy experiments without having to put a human in danger," he says. (One of his earlier handling experiments had him regaining his balance after a sideways blow from a wooden stick.) Unlike many other riderless-bike robots, it does not use internal gyroscopes to stay upright, but depends on steering alone. Moore has shipped it to Schwab for further study.

"ONCE YOU HAVE A ROBOT BICYCLE, YOU CAN DO A LOT OF CRAZY EXPERIMENTS."

Today, Schwab has the kind of laboratory that Papadopoulos always dreamed of, and Papadopoulos is grateful to be able to collaborate. "It's the most beautiful thing you can imagine," he says. Schwab's other projects include a 'steer by wire' bike, which allows him to separate steering movements from balancing ones, and a 'steer assist' bicycle, which stabilizes itself at slow speeds. He has also identified a rear-steered recumbent bike that shows self-stability, in part owing to an enlarged front wheel that boosts gyroscopic effects. The chief advantage of a rear-steered recumbent is that it would have a shorter chain than standard recumbents, which should lead to better energy transfer. "People have tried to build them before, but they were unrideable," Schwab says.

Papadopoulos, who now has a teaching position at Northeastern University in Boston, is trying to get comfortable with academia once again. He's establishing collaborations, and testing out long-dormant ideas about why some bicycles wobble at high speed[7]. He believes he can eliminate speed wobble with a damper to soak up vibrations in the seat post. With his new colleagues and students, he is branching out into other types of question, not all them bike-related.

Down in his basement, Papadopoulos opens the drawer of a tan filing cabinet and starts flipping through crinkled manila folders marked with labels such as 'tire pressure', 'biomechanics' and 'Cornell'. He pulls out a textbook. "Exercise physiology? I never really got into that one," he says, tossing it aside. In the back of the drawer, he finds a thick folder of bicycle research ideas, marked 'Unfinished'.

Papadopoulos thinks for a second and then offers a correction: "Mostly unfinished." ■

Brendan Borrell *is a journalist in New York City.*

1. Meijaard, J. P., Papadopoulos, J. M., Ruina, A. & Schwab, A. L. *Proc. R. Soc. A* **463**, 1955–1982 (2007).
2. Kooijman, J. D., G. Meijaard, J. P., Papadopoulos, J. M., Ruina, A. & Schwab, A. L. *Science* **332**, 339–342 (2011).
3. Jones, D. E. H. *Phys. Today* **23**(4), 34–40 (1970).
4. Papadopoulos, J. in *Biomechanics in Sport: A 1987 Update* (eds Rekow, R., Thacker, V. G. & Erdman, A. G.) 83–92 (Am. Soc. Mech. Eng., 1987).
5. Hess, R., Moore, J. K. & Hubbard, M. *IEEE Trans. Syst. Man Cy. A* **42**, 545–557 (2012).
6. Schwab, A. L., de Lange, P. D. L., Happee, R. & Moore, J. K. *Proc. Inst. Mech. Eng. K* **227**, 390–406 (2013).
7. Magnani, G., Ceriani, N. M. & Papadopoulos, J. *2013 IEEE Internatl Conf. Mechatronics* 400–405 (2013).

THE UNSUNG HEROES OF CRISPR

The soaring popularity of gene editing has made celebrities of the principal investigators who pioneered the field — but their graduate students and postdocs are often overlooked.

BY HEIDI LEDFORD

When Blake Wiedenheft started studying microbes, his work was both remote and obscure.

He spent his PhD sampling hot springs in Yellowstone National Park, then created artificial versions in the laboratory to study the microorganisms that lived in the inhospitable water. "We wanted to understand how life could survive in boiling acid," he says.

Over time, Wiedenheft became more interested in how microbes fend off viruses. He read around, and came across a peculiar bacterial immune system called CRISPR. In 2007, he approached Jennifer Doudna, a molecular biologist at the University of California, Berkeley, and found that she shared his interest. Join the lab, she said — and he did. Over the next five years, he studied the structure and biochemistry of CRISPR systems, landing a first-author publication in *Nature*[1].

Today, CRISPR is a household name for molecular biologists around the world. Researchers have eagerly co-opted the system to insert or delete DNA sequences in genomes across all kingdoms of life. CRISPR is being used to generate a new breed of genetically modified crops and may one day treat human genetic diseases. Doudna and other principal investigators involved in the seminal work have become scientific celebrities: they are profiled in major newspapers, star in documentaries and are rumoured to be contenders for a Nobel prize. "When I came to the lab, I was the only person studying CRISPR," Wiedenheft says. "When I left the lab, almost everyone was studying it."

Wiedenheft, however, has hardly achieved the same fame as his mentor — and nor have the other students and postdocs who toiled at the bench to make CRISPR genome editing a reality. They certainly reap benefits from their work: support and reflected glory from their supervisors, as well as expertise in a coveted technique. But some also face a difficult transition to becoming independent scientists as they try to establish themselves in a hypercompetitive field.

For Wiedenheft, the key to survival has been seclusion. When he struck out from Doudna's lab, he opted for a return to Montana State University in Bozeman, where he did his PhD, over an offer from a larger, better-known institution. "At the end of the day, the opportunities for solitude and being outdoors make me more creative and a better scientist," he says. But like other young scientists who graduate from powerhouse labs, he can't help but wonder how different life might have been if accolades in biomedical science were given to the first authors on a paper, rather than the last. Now and then, he admits, he doesn't feel quite appreciated enough. "Some days it matters, some days it doesn't."

AN EDITED HISTORY

The history of CRISPR–Cas9 gene editing has become a subject of fierce debate and a bitter, high-stakes patent battle. Researchers and institutes have been jostling aggressively to make sure that they are credited for their share of the work in everything from academic papers to news stories. "I get a lot of phone calls from lawyers about what I did and when," Wiedenheft says.

In January, Eric Lander, president of the Broad Institute of MIT and Harvard in Cambridge, Massachusetts, tossed into this minefield a historical portrait called 'The Heroes of CRISPR'[2]. It was instantly controversial. Some said that it marginalized the contributions of certain researchers, and they questioned the decision to publish the article without a conflict-of-interest statement noting that the Broad Institute is embroiled in a patent dispute that hinges on determining who invented CRISPR–Cas9 gene editing.

But for George Church, a geneticist at Harvard Medical School in Boston, Massachusetts, who is also a pioneer in the field, it was particularly painful to see statements attributing key discoveries to him rather than his postdocs and graduate students. "Eric said my name too many times," Church says.

Lander says that there was no intended slight in the 'Heroes' story. He was mindful that there were dozens of other co-authors on the key papers, "But I couldn't figure out how to collect and tell their stories within a nine-page article." If anything, he adds, the article widened the CRISPR spotlight: most discussion up to that point had focused on 3 major contributors to the field, whereas his piece featured 17 major players and acknowledged that there were many others.

Any lack of attention to CRISPR's junior discoverers comes despite fervent advocacy on the part of their advisers. Junior investigators in the Church lab praise their leader's unwavering support, along with the unique intellectual environment he has fostered in the lab. Doudna is a fierce champion of the scientists she has mentored. "It's really important for junior investigators to get the credit they deserve," she says. "They really drive the scientific enterprise." What is more, academic papers often set out each author's contribution to the work.

But those details often get lost simply because, broadly speaking, credit in science goes to the leader of the lab, as do any prizes that follow. "That's just how the system works, and I accept my role in this system," says Martin Jinek, another Doudna lab alumnus. "But yeah, it's something you can't help but think about." ▶

ILLUSTRATION BY VASAVA

Sometimes people may take note of the first author, but not in a meaningful way, says Rachel Haurwitz, a former Doudna graduate student and now president of Caribou Biosciences in Berkeley, California. "They'll say 'the 2012 Jinek paper' but most people have no idea who Martin Jinek is," she says.

Jinek was co-first author on a seminal paper[3] showing that the enzyme Cas9 can be programmed to target specific sequences of DNA using only a short strand of RNA — and he found that his life became defined by CRISPR. When he entered the job market, he couldn't even discuss the work in interviews because the patent had not been filed. Even so, he got an attractive offer from the University of Zurich in Switzerland, and has since built a lab there that focuses on the basic biology of CRISPR more than its applications.

As interest in CRISPR–Cas9 gene editing grew, his schedule became packed: he now travels to talks two to three times a month. Although he appreciates the professional boost that the CRISPR frenzy has given him, he also struggles to find a balance between running his lab and other obligations.

Haurwitz has faced obstacles, too. She spent her PhD characterizing the CRISPR-based microbial immune system and the structure of a CRISPR-associated enzyme called Cys4 (ref. 4). In 2011, she co-founded Caribou along with Doudna and others to commercialize research tools based on CRISPR. The early days were tough, but Caribou has since formed partnerships with major industry players, and the company announced in May that its latest round of fundraising had brought in US$30 million. Yet as the firm has grown, some investors have pushed to replace Haurwitz with a more seasoned leader. Doudna has quashed the idea. "There's no reason to replace her," says Doudna. "She keeps showing that she has the talent to be successful."

RIDING THE WAVE

For many early career scientists, working in such a hot field has clear advantages. As a postdoc, bioengineer Prashant Mali helped to launch the CRISPR project in Church's lab. He was a co-first author on the lab's 2013 paper[5] demonstrating that CRISPR–Cas9 could be used to edit the genome in human induced pluripotent stem cells.

The discovery sent CRISPR excitement to fever pitch — a wave of enthusiasm that Mali rode into the job market later that year. "I definitely got a lot of endorsements," he says. (There is, however, no mention of him in 'Heroes of CRISPR' — a sore point with Church.) Eventually settling at the University of California, San Diego, Mali continues to study stem-cell development and develop CRISPR-based tools. He accepts the intensity of the field as a small price to pay. His lab is just 18 months old — too young to have been scooped yet, he says — but competition is inevitable. "There will obviously be a lot of overlap of good ideas."

CRISPR threw open doors for Luhan Yang, the other first author on the 2013 *Science* paper from Church's lab. Soon after the paper was published, the lab was contacted by several researchers who study organ transplantation. They wanted to know whether genome editing could now be used to engineer pig organs so that they would be less likely to provoke an immune response in humans. Yang seized the idea with gusto, says Church.

"The idea that scientific discovery involves just one, two or three people is so nineteenth-century."

The pig genome is home to retroviral DNA, and concern that those retroviruses might become reactivated in a human host led many researchers to flee the field in the late 1990s. Yang reasoned that the retroviral sequences are so similar to one another that a single CRISPR–Cas9 experiment might knock out many of them at once. She and her three co-first authors now hold the world record[6] for the largest number of sequences targeted in a single CRISPR–Cas9 experiment: 62. And Yang is raising money to launch a company with Church called eGenesis, to further the work. "George always gave me the opportunity to establish my leadership," she says.

Across the Charles River from the Church lab, graduate student Le Cong worked side-by-side, late into the night with his mentor, bioengineer Feng Zhang at the Broad Institute, to develop CRISPR gene editing in mammalian cells. Zhang was himself a young investigator just launching a lab when Cong joined; Cong remembers opening the box containing the lab's first centrifuge and sitting with Zhang at a computer googling 'DNA-binding protein' to look for new ways to edit genomes. The two became a tightly knit team.

When they embarked on the CRISPR project, it seemed like a long shot as Cong screened enzymes and reaction conditions, trying to find those that would work in human cells.

But Cong was willing to take the risk. He and Zhang had previously pioneered the use of a different gene-editing system, called TALENs, in mammalian cells, and he reasoned that this early success would be enough to allow him to graduate if the CRISPR project failed. He never had to test that hypothesis: in 2013, Cong and his fellow graduate student Fei Ann Ran co-first authored a *Science* paper[7] showing that the system works in mammalian cells — the paper was published simultaneously with that of Mali, Church and their team.

At that point, Cong was advised that he could skip the postdoc and go straight to a faculty position. But he worried that doing so would limit him: he could be pigeonholed as 'the CRISPR guy'. "I felt uncomfortable about that," he says. "I was not only looking to develop technology." Instead, Cong opted for another postdoc; he is now embarking on a faculty job search, and plans to use his lab to study allergies and autoimmune disorders.

Cong says that he feels no resentment at being largely excluded from the CRISPR media frenzy and attention centred on Zhang. "I do think I've been recognized," he says; Zhang has been generous in giving him credit within the scientific community, and has encouraged Cong to give talks in his stead.

And Cong, like others interviewed for this story, is himself insistent about giving credit to others in the field. He sprinkles in references to work done in other labs, including some of the earliest microbiology work characterizing the CRISPR system. Wiedenheft says that's characteristic of the CRISPR community. "It's competitive, but it's friendly."

Outside that community, however, the accolades continue to be heaped on senior investigators. "We need to invent ways to expand the medals podium," says Lander. "The idea that scientific discovery involves just one, two or three people is so nineteenth-century."

There are many more unsung heroes of CRISPR than this article could do justice to. One often overlooked group is headed by Virginijus Siksnys at Vilnius University in Lithuania — where Giedrius Gasiunas began his PhD in 2007. He plugged away for years, tackling the biochemistry of CRISPR–Cas9 and, like Jinek, eventually came to the conclusion that the Cas9 enzyme could be programmed to cut isolated DNA at specific sites.

In 2012, the lab sent a paper to *Cell*, where it was rejected without review. Gasiunas then submitted the paper to the *Proceedings of the National Academy of Sciences* and waited. A few months later, while his paper was still under review, the now-legendary Jinek paper appeared in *Science*. The two papers had key differences, but reached similar conclusions. Gasiunas had been scooped[8].

Seeing other scientists collect awards for CRISPR gene editing sometimes irks Gasiunas, now a postdoc in Siksnys's lab. But the experience has not entirely soured him on the subject. Although he has since been scooped again, he finds it no longer stings as much as it did. "It's a risky field," he says. "But I think if you want to achieve something great, you need to take risks." ■

Heidi Ledford *is a senior reporter for* Nature *based in London.*

1. Wiedenheft, B. *et al. Nature* **477,** 486–489 (2011).
2. Lander, E. S. *Cell* **164,** 18–28 (2016).
3. Jinek, M. *et al. Science* **337,** 816–821 (2012).
4. Haurwitz, R. E., Jinek, M., Wiedenheft, B., Zhou, K. & Doudna, J. A. *Science* **329,** 1355–1358 (2010).
5. Mali, P. *et al. Science* **339,** 823–826 (2013).
6. Yang, L. *et al. Science* **350,** 1101–1104 (2015).
7. Cong, L. *et al. Science* **339,** 819–823 (2013).
8. Gasiunas, G., Barrangou, R., Horvath, P. & Siksnys, V. *Proc. Natl Acad. Sci. USA* **109,** E2579–E2586 (2012).

COMMENT

ENVIRONMENT Will climate change mean more vast algal blooms? **p.349**

BIOTECHNOLOGY Lots of ways to alter life but not enough bioethics **p.352**

TECHNOLOGY Biography of Marconi explores global communications **p.354**

CHEMISTRY Goals change the breath composition of spectators **p.355**

STEPHEN LAM/GETTY

Wearable devices that track fitness are a rich source of real-time health data.

Stop the privatization of health data

Tech giants moving into health may widen inequalities and harm research, unless people can access and share their data, warn **John T. Wilbanks** and **Eric J. Topol**.

Over the past year, technology titans including Google, Apple, Microsoft and IBM have been hiring leaders in biomedical research to bolster their efforts to change medicine.

In September 2015, Tom Insel announced that he would quit his position as head of the US National Institute of Mental Health to join Google Life Sciences (now Verily). Three months later, Michael McConnell took a leave of absence from directing major cardiovascular research programmes at California's Stanford University to join him. And last month, Stephen Friend took a senior position with Apple. He is co-founder and former president of Sage Bionetworks, a non-profit organization that promotes open science and patient engagement in research (where one of us, J.T.W, works).

In many ways, the migration of clinical scientists into technology corporations ▶

that are focused on gathering, analysing and storing information is long overdue. Because of the costs and difficulties of obtaining data about health and disease, scientists conducting clinical or population studies have rarely been able to track sufficient numbers of patients closely enough to make anything other than coarse predictions. Given such limitations, who wouldn't want access to Internet-scale, multidimensional health data; teams of engineers who can build sensors for data collection and algorithms for analysis; and the resources to conduct projects at scales and speeds unthinkable in the public sector?

Yet there is a major downside to monoliths such as Google or smaller companies such as consumer-genetics firm 23andMe owning health data — or indeed, controlling the tools and methods used to match people's digital health profiles to specific services.

Digital profiling in other contexts is already creating what has been termed a 'black box' society. Online adverts are tailored to people's age, location, spending and browsing habits. Certain retail services have preferentially been made available only to particular groups of people. And law enforcers are being given tools to help them make sentencing decisions that cannot be openly assessed (see go.nature.com/29umpu1). This is all thanks to the deliberately hidden collection and manipulation of personal data.

If undisclosed algorithmic decision-making starts to incorporate health data, the ability of black-box calculations to accentuate pre-existing biases in society could greatly increase. Crucially, if the citizens being profiled are not given their data and allowed to share the information with others, they will not know about incorrect or discriminatory health actions — much less be able to challenge them. And most researchers won't have access to such health data either, or to the insights gleaned from them.

THE DIGITAL HEALTH RUSH

Analysts predict that worldwide, the value of Internet-enabled devices used to collect, analyse and distribute health and fitness data will exceed US$163 billion within 4 years.

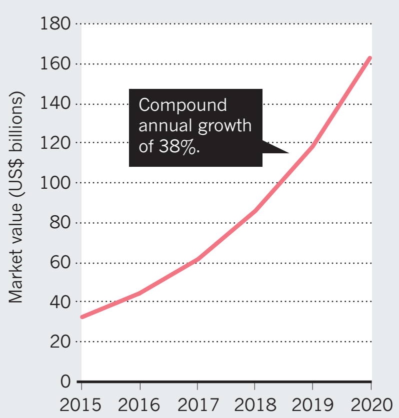

SOURCE: EMARKETER

INFORMATION FLOW

We believe that the influx of health experts into Silicon Valley could foreshadow a fundamental shift in biomedical research and health care.

In various countries, including the United Kingdom, Sweden, Norway and Estonia, sustained pushes by governments and civil society have made standardized electronic health records the norm. And in the United States, hopes are high that truly useful electronic health records (that can be called up no matter which provider a patient goes to) will be rolled out within the next five years. Meanwhile, advances are being made in machine learning, and there is increased availability of digital health data outside the medical system. This type of information is much more amenable to machine-learning approaches than are conventional clinical observations. Furthermore, some of the technology corporations entering health have hundreds of billions of dollars in cash reserves. These factors combined could enable the new players to eclipse, not just join, the old ones.

Until now, obtaining health data has generally depended on highly skilled professionals who record perhaps tens to hundreds of observations in a clinic or hospital ward once or twice a year, and on researchers who painstakingly extract the relevant information from hard-to-obtain, non-standardized medical records. Now, thanks to smartphone apps — such as those created using Apple's software framework ResearchKit, launched last year — and wearable sensors that can detect gait, location, heart rate and even brain activity, analysts can draw on tens of thousands of real-time observations collected from tens of thousands of people every day, even every minute.

People's search behaviour contains health information too. In February 2015, Google partnered with the Mayo Clinic, a non-profit medical practice and research group based in Rochester, Minnesota, to curate health-related facts, such as the most common causes of low back pain. Google's teams are plugging curated and verified health information into the search engine's smart search algorithm, Knowledge Graph, so that users obtain information that is more relevant and supposedly more accurate whenever they type in their symptoms or condition. The service (which for many ailments may replace visits to the doctor) will only enhance Google's — and only Google's — ability to conduct an unprecedented level of information retrieval for health. By the tech

giant's own calculations, of the 40,000 or so searches that are made every second, 2,000 are health-related.

Meanwhile, machine learning is enabling researchers to mine petabytes of data for patterns and associations. The IBM Watson technology platform, for example, sifts through unstructured data using natural language processing and machine learning. Since April last year, IBM has been building 'knowledge experts' for health using the Watson Health cloud platform: customers who store their data in the cloud are given access to algorithms that can help them to make sense of the data. IBM is already using Watson to tackle complex disease problems in collaboration with the University of Texas MD Anderson Cancer Center in Houston — specifically, how to use genomic information from cancer cells to provide individuals with targeted treatments.

Even the rudimentary measurements already flowing from smartphones and wearable sensors can drive better outcomes than decades of medical-device development have been able to provide. For instance, in 2014, a woman with type 1 diabetes wired together a tiny processor, an insulin pump and a continuous glucose monitor to automate the regulation of her blood sugar levels. For a small community of patients, the collective use of such 'homemade' systems has resulted in improvements that are well ahead of those provided

THOMAS PETER/REUTERS

A 2011 protest in Berlin called for the right to keep personal digital data private.

by devices and interventions emerging from conventional markets[1].

In short, actors big and small are waking up to the enormous profits that could be made from inexpensive consumer health data. Around ten years ago, a scattering of start-ups were obtaining people's genomic information and other health data at low cost and making them available to pharmaceutical partners or other customers. In 2016, every major player in tech — Apple, Google, IBM, Facebook, even Uber — has signalled plans to enter this 'digital health' market.

A CLOSED LOOP

To be fair, harnessing advances in technology and analytics to radically improve health care is a principal motivator for many corporations. But it is telling that the early players in the game have sequestered information in 'closed loop' systems.

Take the wearable device Enlite, which was made available by the Dublin-based firm Medtronic to people with diabetes in 2013. This sends insulin into the wearer's blood when a sensor detects a drop in glucose levels. Although patients can monitor their glucose levels at any instant, their aggregate records are not made accessible to them. And there is no mechanism by which patients or researchers outside the company can gain access to Medtronic's tens of thousands of measurements. The same is true for other wearable devices produced by the same firm. In fact, the company has refused requests for patients' own heart data (see go.nature.com/29tdzud).

Even when corporations do give customers access to their own aggregate data, built-in blocks on sharing make it hard for users to donate them to science. 23andMe, holder of the largest repository of human genomic data in the world, allows users to view and download their own single-letter DNA variants and share their data with certain listed institutions. But for such data to truly empower patients, customers must be able to easily send the information to their health provider, genetic counsellor or any analyst they want.

"Of the 40,000 or so searches that are made every second, 2,000 are health-related."

Pharmaceutical firms have long sequestered limited types of hard-to-obtain data, for instance on how specific chemicals affect certain blood measurements in clinical trials. But they generally lack longitudinal health data about individuals outside the studies that they run, and often cannot connect a participant in one trial to the same participant in another. Many of the new entrants to health, unbound by fragmented electronic health-record platforms, are poised to amass war chests of data and enter them into systems that are already optimized (primarily for advertising) to make predictions about individuals.

The companies jostling to get into health face some major obstacles, not least the difficulties of gaining regulatory approval for returning actionable information to patients. Yet the market value of Internet-enabled devices that collect and analyse health and fitness data, connect medical devices and streamline patient care and medical research is estimated to exceed US$163 billion by 2020, as a January report from eMarketer notes (see 'The digital health rush' and go.nature.com/29fbvch). Such a tsunami of growth does not lend itself to ethically minded decision-making focused on maximizing the long-term benefits to citizens.

It is already clear that proprietary algorithms can replicate and exacerbate societal biases and structural problems. Despite the best efforts of Google's coders, the job postings that its advertising algorithm serves to female users are less well-paying than are those displayed to male users[2]. A ProPublica investigation in May demonstrated that algorithms being used by US law-enforcement agencies are likely to wrongly predict that black defendants will commit a crime (see go.nature.com/29aznyw). And thanks to 'demographically blind' algorithms, in several US cities, black people are about half as likely as white people to live in neighbourhoods that have access to Amazon's one-day delivery service (see go.nature.com/29kskg3).

We believe that closed-data and closed-algorithm business models in health — at scale — will hamper scientific progress by blocking the discovery of diverse ways to examine and interpret health data. Longer term, they could increase rather than reduce inequalities and injustices. It is not hard to picture a future in which companies are able to trade people's disease profiles, unbeknown to the patients. Or one in which health decisions are abstruse and difficult to challenge, and advances in understanding are used to aggressively market health-related services to people — regardless of whether those services actually benefit their health.

FOR BETTER, NOT WORSE

It is not our intention to demonize technology companies. Closed systems have some innate short-term advantages over open ones. For instance, they can achieve coherence and scale faster than open systems can because their chief executives can dictate formats, standards and norms. But private capital will better serve public interests if at least some layers of the emerging health-research infrastructure are open (the raw data being one layer, the tools for analysis

another and the development of treatments and services for patients a third).

In our view, sensor and other data and the methods for converting those data into clinically usable information should be a public good. The technical and business services that translate insights into value for individual citizens could well be closed. This would be analogous to Google, Apple Maps and Waze providing maps on the back of government-funded geospatial data. Under this scenario, private capital would fund the creation of meaningful patient experiences, not the creation of trade secrets about health.

In theory, hard government regulation could prevent the collection and analysis of digital health data from becoming a high-profit business. The European Union has already passed sweeping directives to protect people's digital information from being exploited for commercial or other purposes. But in the United States at least, the odds are slim that well-constructed digital civil-rights laws will be passed in the next 2–3 years.

Many of the largest tech corporations have come to resemble small nations in their own right: they have enormous 'natural resources' (data and computing power) and global interests to pursue and protect. Just five US-based tech firms — Apple, Microsoft, Alphabet (Google's parent company), Cisco Systems and Oracle — had combined cash reserves of $504 billion in late 2015, much of which is held offshore to avoid taxation and regulation (see go.nature.com/29ep3zx). Even if the US government wanted to intervene, technologies and their accompanying business models are evolving faster than it can keep up.

In our view, the creation of credible competitors that are open source is the most promising way to regulate closed business models. During the late 1990s, IBM, then one of the biggest players in the software market, abandoned its proprietary web server software in favour of selling services around open-source software. Once users realized that the open-source Apache web server and Linux operating system offered a viable alternative to commercial packages, IBM started selling them its support and configuration services. At around the same time, the release of Netscape's browser source code rapidly fuelled innovation in the browser market and prevented Microsoft from creating a monopoly with Internet Explorer. In both cases, communities of hundreds, or at most a few thousand, transformed the landscape for the world's largest corporations.

The creation of public resources through government funding has a role in this. Soon after the publicly funded Human Genome Project announced in 2000 that a draft was complete, the private sequencing company Celera stopped charging researchers for access to its data, deposited those data into the public database GenBank and focused instead on trying to develop treatments for disease. Yet the sums of money being directed towards public projects today — such as the Obama administration's Precision Medicine Initiative, which aims to match treatments to patients' genetic and physiological data — pale in comparison to the investment that many companies can bring. (23andMe's latest fundraising round of $150 million represents 70% of the entire federal investment allotted to the Precision Medicine Initiative.)

What is needed are networks of open projects, combined with sufficient numbers of patients and citizens who are motivated to feed such projects with their health data.

CASE STUDY

At Sage Bionetworks, we are conducting four ongoing clinical studies on various diseases including Parkinson's. We are also providing the online interfaces for patients to upload their information, and portals to enable data sharing for a further three studies (on diabetes, asthma and cardiac health). Across these seven studies, we have enrolled more than 90,000 participants since March 2015 (see go.nature.com/29qqk57). Participants have the automatic right to access and download complete copies of their own data. They also have the right to donate their data for broad reuse by 'qualified researchers', meaning those that have validated their identity, passed a short test and signed a code of ethical practice.

"When it comes to control over our own data, health data must be where we draw the line."

In our studies, more than 75% of participants elect to share their data — presumably to maximize the chances of investigators finding a way to help them and others like them. Our numbers are biased by the fact that we are surveying people who are already enrolled in clinical studies. But in a 2015 survey of a more generic US population by National Public Radio, 53% of those polled said that they would be willing to share their data anonymously with health-care professionals (see go.nature.com/29qr0b7). It could be transformative if even just 5% of the US population donated a copy of their health data to science. After all, it took only a small community of open-source software programmers worldwide to drive major shifts in the computing industry.

In short, a movement not dissimilar to the environmental one is needed to break open how people's data are being used, and to illuminate how they could be used in the future. In the United States, it was the unified lobbying of small groups of activists in the 1960s and 1970s — each with different reasons for being concerned — that led to a series of groundbreaking federal initiatives, such as the Clean Air Act and the creation of the Environmental Protection Agency. Likewise, at first, data donors may predominantly include those with personal incentives, or those who are philosophically driven to share their health data, for instance through being part of the Quantified Self community, which aims to use technology to measure all aspects of our daily lives. Such early advocates for sharing could help to change norms by pushing for clearer messaging around consent and by raising awareness about what is at stake.

Openness is not an easy goal. Numerous interlocking systems need to be designed, including those to protect privacy, to mitigate harm caused by certain insights becoming public knowledge, and to enable people who do not wish to be phenotyped to opt out. But if the new era of digital health is accompanied by citizen-led pushes for more openness, it may not just be health care that is transformed.

Citizens worldwide have too long a history of being passive players in health care — blindly following instructions from providers. And studies that have tracked reactions to revelations about global surveillance programmes suggest that most people are resigned to the idea that ownership and control of personal information is incompatible with the Internet age[3].

Yet just as social networking has rocketed around the world in a decade, a worldwide knowledge resource could soon be used to identify the best course of treatment for an individual on the basis of the experiences of millions. This resource will never be built unless each of us takes responsibility for our own health and disease, and for the information that we can generate about ourselves. When it comes to control over our own data, health data must be where we draw the line. ■

John T. Wilbanks *is chief commons officer at Sage Bionetworks in Seattle, Washington, USA.* **Eric J. Topol** *is professor of genomics at the Scripps Research Institute in La Jolla, California, USA.*
e-mails: wilbanks@gmail.com; etopol@scripps.edu

1. Lewis, D. M. & Leibrand, S. M. Real-World Use of Open Source Artificial Pancreas Systems. *Am. Diabetes Assoc. 76th Sci. Sessions* (2016); available at http://go.nature.com/29kiyne
2. Datta, A., Tschantz, M. C. & Datta, A. *Proc. Priv. Enhancing Technol.* **2015,** 92–112 (2015).
3. Turow, J., Hennessy, M. & Draper, N. *The Tradeoff Fallacy: How Marketers Are Misrepresenting American Consumers and Opening Them Up to Exploitation* (Univ. Pennsylvania, 2015); available at http://go.nature.com/29khjju

GREG LOVETT/PALM BEACH POST VIA ZUMA WIRE

An algal bloom in Stuart, Florida, in June led to a state of emergency.

Study role of climate change in extreme threats to water quality

Record-breaking harmful algal blooms and other severe impacts are becoming more frequent. We need to understand why, says **Anna M. Michalak**.

With concerns about climate 'extremes' growing[1], water is often the focus — either too much or too little. That is no coincidence: climate and the hydrological cycle are tightly coupled, and water is essential to ecosystems and societies. But it is not just the quantity of water that matters. So does its quality.

Last year, Lake Erie, one of the US Great Lakes (which contain one-fifth of the world's fresh surface water), experienced its biggest recorded harmful algal bloom. At its peak, the bloom spread some 200 kilometres across most of the lake[2]. Meanwhile, off the continent's west coast, another record harmful bloom stretched from Baja California in Mexico up to Alaska, probably triggered by unusually warm water in the Pacific Ocean[3]. Both blooms were dominated by species of phytoplankton that produce powerful toxins.

Such episodes can wreak havoc. During a previous bloom, in 2014, 500,000 people living near Lake Erie were ordered not to drink tap water, because it contained levels of hepatotoxins produced by the cyanobacterium *Microcystis* that were 2.5 times higher[4] than the World Health Organization's safe standard. The 2015 west-coast bloom of the diatom algae *Pseudo-nitzschia* shut down fisheries. The Dungeness crab fishery, one of the most valuable on the west coast, opened four months late owing to toxic levels of the neurotoxin domoic acid in the crabs. Brain damage in sea lions has also been documented as a result of exposure to this toxin[5].

Impaired water quality is a global and growing problem, limiting resources for drinking, domestic use, food production and recreation, as well as harming ecosystems. The types and causes range from excess nutrients feeding harmful algal blooms and hypoxic 'dead zones', to bacterial, viral and chemical contamination, to pollution by personal-care products and pharmaceuticals. Cases of extreme impairment often lead to disproportionate human and ecosystem impacts. The costs can be huge. More than US$4 billion are lost each year in the United States alone as a result of harmful algal blooms[6].

Because the most severe water-quality impacts are exacerbated by weather, climate plays a part. Runoff of nutrients from farmland spikes after heavy rains; warm temperatures accelerate the growth of bacteria and phytoplankton. As climate change alters weather patterns and variability, conditions conducive to severe water impairment are likely to become more frequent.

Yet there has been scant study of how climate will affect the occurrence of the extreme events that relate to water quality rather than quantity. We do not know how to relate water-quality extremes, their causes, their severity or their occurrence directly to changes in climate. It is time to plug this knowledge gap.

COMPLEX CHAIN

Scientific understanding of extreme storms, droughts and rising sea levels has improved markedly over the past decade. The impacts of extreme weather events are integral to discussions about climate-change mitigation and adaptation. The expected rise in the frequency and severity of such events is well established, and even individual episodes have been linked probabilistically to climate change[1].

Not so for water quality. Researchers have explored trends in water quality with climate, but the science of projecting and attributing the occurrence of extremes is in its infancy. This is despite evidence of strong links with climate.

Regional studies reveal how multiple factors often conspire to create conditions ripe for dire water quality. For example, summer toxic blooms in Lake Taihu, the third-largest freshwater lake in China, are more intense after tropical cyclones, because the associated rains wash more nutrients into the lake, and the subsequent warmer temperatures and lower wind speeds further encourage the growth of blooms[7]. In 1999, a series of hurricanes triggered severe hypoxia in Pamlico Sound, North Carolina (part of the United States' second-largest estuarine system) by delivering huge amounts of nutrients, organic carbon and fresh water to the estuary[8]. In North American regions as diverse as the Great Lakes, the east coast's Chesapeake Bay

and the Gulf of Mexico, the severity of summer hypoxia has been linked to the effects of weather on nutrient loading, water-column structure and water circulation. Although these examples all relate to harmful algal blooms and hypoxia, other types of water pollution are also affected by weather conditions, which are altered by climate change.

THE CHALLENGE

Several factors explain the paucity of research. First, the role of climate is difficult to pinpoint, because changes in water quality result from a delicate and complex interplay of human activities across local, regional and global scales. Complex chains of causative steps must be understood. These start with how climate change affects factors such as precipitation, temperatures and wind patterns for given regions and watersheds. Next, we must understand how these conditions alter the flow of water, nutrients, contaminants and other constituents to water bodies. Finally, we need to assess how these inputs, combined with meteorological conditions that influence freshwater and coastal systems directly, will change water quality. We do not yet know how to put the pieces of this puzzle together.

For example, the harmful algal blooms in Lake Erie are driven by excess phosphorus from changing farming and land-management practices in the region, but a summer 2011 bloom shattered previous records. A forensic analysis[9] revealed that a series of intense rainstorms led to record springtime discharge from rivers, which flooded the lake with a record amount of nutrients flushed from fields. Warmer-than-average summer temperatures and low winds then accelerated the growth of buoyant *Microcystis* cyanobacteria. Unusually weak water circulation during the summer kept nutrients in the lake for longer, further feeding the bloom. How climate change influences the occurrence of all these factors, individually and together, needs to be elucidated to predict the likelihood of similar events happening more frequently in the future.

Second, water-quality and climate scientists work in disciplinary silos, and each tends to have a different scale of focus. Whereas much of climate science is global or concerned with large regions, most hydrologists and limnologists study processes in individual streams, lakes, watersheds or estuaries. Similarly, water-quality impacts have been treated mostly as local or regional issues, resulting from human activities in a particular basin or watershed. Little attention has been given to the local impacts of human action at global scales. For example, strategies for preventing harmful blooms and hypoxia often rightly focus on limiting nutrient loads through land management, but should also consider how a shifting climate will alter local meteorology, and thus nutrient loads.

A clear understanding of the interplay between climate and severe water-quality impairment events is predicated on tracking cause and effect across a cascading range of scales, from the globe to individual watersheds and from decades to days.

Third, observational evidence to underpin a global view of this interplay is lacking. Unlike for weather variables such as temperature and precipitation, no global network tracks water quality. Existing monitoring of water quality is sparse in space and time, and site-specific. Satellite-based observations could expand coverage, but there are no widely accepted approaches for doing so. There is even disagreement about which variables best capture water quality. For example, is the severity of a harmful algal bloom best represented by its area, the total mass of phytoplankton it contains, the amount of toxins that it produces or the ecosystem and human impacts that it engenders? Each brings a different observational challenge.

> ***"There is disagreement about which variables best capture water quality."***

NEXT STEPS

Researchers need to assess which meteorological conditions, in what combination, make extreme water-quality impairments most likely. In doing so, they must also consider land use, land management, population distributions and other regional factors that compound the effects of weather. An initiative such as Future Earth, which provides a research platform for global sustainability science, would be a good umbrella for developing and integrating such knowledge globally.

The first step should be a retrospective analysis of past extreme events, to understand commonalities and differences across types of systems and impacts. The resulting conceptual model will differ depending on the type of problem — hypoxic dead zones and microbial outbreaks in recreational waters will not link to climate in the same ways. The water-quality and climate research communities will have to work together to identify key mechanisms and feedbacks.

Understanding meteorological drivers would allow researchers to assess whether climate models can accurately represent the occurrence of key specific conditions (such as high precipitation or warm temperatures), as well as their joint or sequential occurrence (such as high precipitation followed by low winds and high temperatures). This could be explored, for example, in the context of the Coupled Model Intercomparison Project Phase 6 (CMIP6), and effort to compare climate projections under different scenarios that is under way in anticipation of the next Intergovernmental Panel for Climate Change assessment.

A clear conceptual model would also inform observational needs. Observations must capture the severity of extreme events, their impacts and key variables for assessing the links to climate change. There will be trade-offs between specificity and coverage. For example, whereas satellites might monitor some water-quality parameters and impacts globally, other key indicators such as toxin concentrations can be tracked only *in situ*. The GEO (Group on Earth Observations) AquaWatch initiative would be a natural forum for exploring these challenges[10].

As the science improves, its implications must inform broader global discussions around water, such as the strategy for meeting the United Nations' Sustainable Development Goal of ensuring 'availability and sustainable management of water and sanitation for all', one of 17 such goals adopted last year.

The scientific community has made remarkable progress in understanding the role of climate in the occurrence and intensity of droughts, storms and other extreme events relating to water quantity. It is time for a similar examination of extremes in water quality. ■

Anna M. Michalak *is a faculty member in the Department of Global Ecology, Carnegie Institution for Science, Stanford, California, USA.*
e-mail: michalak@stanford.edu

1. IPCC. *Managing the Risks of Extreme Events and Disasters to Advance Climate Change Adaptation. A Special Report of Working Groups I and II of the Intergovernmental Panel on Climate Change.* (Cambridge Univ. Press, 2012).
2. Stumpf, R. & Wynne, T. *Experimental Lake Erie Harmful Algal Bloom Bulletin* Bulletin 27 (NOAA, 2015).
3. Di Liberto, T. 'This summer's West Coast algal bloom was unusual. What would usual look like?' *ClimateWatch Magazine* (30 September 2015).
4. Wilson, E. K. *Chem. Eng. News* **92,** 9 (2014).
5. Cook, P. F. *et al. Science* **350,** 1545–1547 (2015).
6. Kudela, R. M. *et al. Harmful Algal Blooms. A Scientific Summary for Policy Makers* (IOC/UNESCO, 2015).
7. Zhu, M. *et al. Harmful Algae* **39,** 310–321 (2014).
8. Paerl, H. W. *et al. Proc. Natl Acad. Sci. USA* **98,** 5655–5660 (2001).
9. Michalak, A. M. *et al. Proc. Natl Acad. Sci. USA* **110,** 6448–6452 (2013).
10. Group on Earth Observations/AquaWatch. *AquaWatch 2016 Work Plan and Structure* (2016); available at http://go.nature.com/29ye4ul

CORRECTION

The Comment 'No wild east' (D. Sipp and D. Pei *Nature* **534,** 465–467; 2016) incorrectly cited (in ref. 4) and referred to the 2001 Chinese national guidelines on assisted reproduction when discussing the implantation of modified human embryos for reproductive purposes.

IMAGINECHINA

Genetically modified pet pigs: is tinkering with an animal's genome to stunt its growth more ethically dubious than conventional breeding for small size?

GENE EDITING

Running with scissors

John Harris probes a study on the science and ethics of genome editing.

In *Redesigning Life*, molecular pharmacologist John Parrington has produced a veritable compendium of games that scientists like him can play with life itself. He invites us to imagine the potential of life forms "whose very genetic recipe was manufactured in a chemistry lab using new components never seen before on Earth". What larks!

What follows is a thorough and comprehensive account of the methodologies for altering life that have been or are being developed, and the directions that they may take in future. Those methodologies include the insertion or deletion of genes, the engineering of synthetic genes and the design of creatures unprecedented in nature. As Parrington shows, many of the technologies are familiar: for example, designing immunity to disease through vaccination, or animal and plant breeding. He ends with the concept of a "redesigned planet", replete with new types of people, as well as designer babies, pets, plants and drugs. Invoking the catchphrase of comic-book superhero Spiderman, "with great power comes great responsibility", he touches on the challenges that such a possibility would entail.

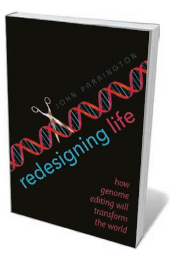

Redesigning Life: How Genome Editing Will Transform the World
JOHN PARRINGTON
Oxford University Press: 2016.

However, Parrington's way of dealing with the ethical issues raised by the technologies that he so gleefully explores is rather limited. Three examples give a sense of the nature of this problem.

Early on, he notes that in agriculture, it is important to ensure that genome editing benefits the majority of humanity rather than stuffing the coffers of vast corporations. But he fails to say how this might be achieved. Given that we cannot ensure this for any product or service in any field, I wonder what this criticism amounts to? Attempting global distributive justice is a major political problem of moral significance, but really, only governments can approach such utopian ideals. Demanding the impossible can never be rational ethics.

Later, Parrington worries about designer babies engineered for looks, intelligence or extraordinary talent (opining, "Such fears run deep among scientists"). But he offers not a word about the cogency of the fears, or about the moral basis — or lack of it — for how people see things. Parrington also questions the use of stem-cell technology in helping older women to have children: "Would this be seen as liberating or an irresponsible extension

➲ NATURE.COM
For more on science in culture see:
nature.com/booksandarts

of a woman's reproductive age?" However, how it would be seen is a sociological question. The ethical responsibility involves showing how it should be seen, and why.

If Parrington is serious about the need to address ethical issues when tinkering with genes, more explanation is needed of just what the ethical issues are and how they might be resolved. Such an attempt involves, at the very minimum, an analysis of the types of design involved in, for example, producing designer babies; it also involves giving reasons to morally prefer some sorts of design or ways of designing to others, as I explain in my book *How to be Good* (Oxford University Press, 2016). Why might it be better to aim to increase cognitive powers and perhaps even intelligence by education, diet or exercise than through gene editing or drugs? One would also need to identify elements that would clearly be unethical to design into a person, such as an increased propensity to disease or premature death.

> ***"Why might it be better to increase intelligence by education, diet or exercise than through gene editing?"***

Most importantly, one would need to consider why attempts at design are morally worse (if they are) than simply leaving things to the genetic lottery of sexual reproduction. There is a story that in the early twentieth century, the pioneering modern dancer Isadora Duncan suggested to writer George Bernard Shaw that they should have a child, surmising that with her looks and his brains any progeny would have huge advantages. The ever-rational Shaw responded, "But what if it had your brains and my looks?" Was Duncan's proposal unethical or just misconceived? What would or should have made such a proposal ethically problematic? And if it was not ethically problematic, why might more 'techie' attempts become unethical?

Gene editing is now the stuff of do-it-yourself 'garage research', opening up nightmares for regulation and oversight. Our best hope is to clarify what it is morally permissible to do behind closed doors. I have no quarrel with the idea of redesigning our planet, or indeed ourselves, if the elements of design promote life, liberty and the pursuit of happiness for those creatures to whom such things matter. These objectives are not only ethical, but mandatory if intelligent life forms are to survive into the far future. The best way of ensuring that this is allowed to happen is to be clear about which are and which are not morally permissible means to this clearly desired and desirable end. ■

John Harris *is professor emeritus in the ethics of science and technology at the University of Manchester, UK.*
e-mail: john.harris@manchester.ac.uk

Books in brief

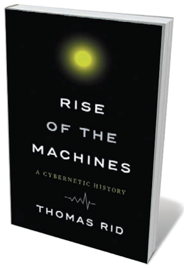

Rise of the Machines: A Cybernetic History
Thomas Rid W. W. NORTON *(2016)*
Cybernetics, the science of communication and control in machines and organisms, has had a tangled history. Here, professor of war studies Thomas Rid unravels seven strands of it, starting with mathematician Norbert Wiener's book *Cybernetics* (1948). Wiener's big idea first gained traction in post-war research on ballistic calculations in airborne warfare. It then popped up in 1950s dreams of automated utopias, the concept of benevolent machines serving humanity in the 1970s and, from the 1980s, applications such as virtual reality, public-key cryptography and, ominously, cyberwar.

Margherita Sarrocchi's Letters to Galileo
Meredith K. Ray PALGRAVE *(2016)*
When astronomer Galileo Galilei was a rising star, he corresponded with the formidable Margherita Sarrocchi — a salon host, epic poet and polymath versed in geometry, natural philosophy and logic (J. Rampling *Nature* **520,** 154–155; 2015). In this rich analysis of the exchange, Meredith Ray shows how the pair found common ground in assessing each other's work, whether the discovery of Jupiter's satellites or the crafting of poetic nuance. An illuminating explication of the dynamics in early-modern arts and sciences, complemented by the first full English translation of the letters.

Fighting Fit: The Wartime Battle for Britain's Health
Laura Dawes WEIDENFELD & NICOLSON *(2016)*
Historian Laura Dawes digs into that other victory of the Second World War: public health in Britain. There had been dire predictions, such as epidemics incubated in air-raid shelters. But by war's end, UK rates of almost all infectious diseases had dropped, thanks to the Medical Research Council, Nobel laureates such as physiologist Andrew Huxley, hordes of researchers and a willing public. Dawes' sparky account demonstrates how that rare teamwork advanced emergency care, preventive medicine, the treatment of insect-borne disease and, ultimately, the formation of the National Health Service.

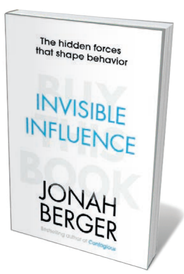

Invisible Influence: The Hidden Forces that Shape Behavior
Jonah Berger SIMON & SCHUSTER *(2016)*
In his best-seller *Contagious* (Simon & Schuster, 2013), marketing scholar Jonah Berger explored influence through word of mouth — a territory much probed by social psychologist Robert Cialdini (T. Dietz *Nature* **479,** 176; 2011). Here, Berger turns the tables, examining the hidden social influences that nudge us into choosing everything from jobs to desserts. Neatly compressing findings in ethology, economics and more, he looks at imitation, differentiation, motivation and the see-saw between novelty and familiarity. Crowded with insights — not least, for wary voters.

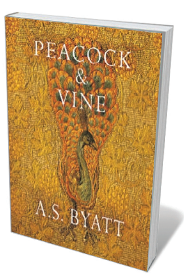

Peacock and Vine: Fortuny and Morris in Life and at Work
A. S. Byatt CHATTO & WINDUS *(2016)*
In this faceted gem of a book, novelist A. S. Byatt muses on design revolutionaries Mariano Fortuny and William Morris. Fortuny, galvanized by ancient Minoan fabrics, printed scarves with patterns of murex shells and trilobite fossils, and devised intricate, permanent pleating for his sinuous 'Delphos' gowns. Morris recorded the "geometry of branches and petals and fruits", bringing hedgerow and copse indoors with motifs and natural dyes that transformed typography, wallpaper and textiles. An ingenious comparison. **Barbara Kiser**

Correspondence

Goals change crowd air chemistry

During live public screenings of the 2016 UEFA European Championships, the emission rates of particular chemicals in the audience's breath vary sharply — apparently in response to events on the football pitch.

Football matches induce fans to roar in jubilation, hold their breath in suspense and sigh with disappointment. On 26 June, we tracked reactions from a cinema audience during the Germany–Slovakia game by monitoring changes in air composition resulting from their exhalations (for methodology, see J. Williams *et al. Sci. Rep.* **6,** 25464; 2016).

In moments of high excitement, exhaled carbon dioxide seems to spike as people's heartbeats and breathing accelerate (see 'Breath chemistry of football fans'). So do emission rates of isoprene, which is released from muscles as fans spring from their seats when a goal is scored. Breath chemistry therefore appears to ride the same emotional roller coaster as the live broadcast.

Christof Stönner, Jonathan Williams *Max Planck Institute for Chemistry, Mainz, Germany.*
jonathan.williams@mpic.de

BREATH CHEMISTRY OF FOOTBALL FANS

People exhale bursts of carbon dioxide and isoprene whenever a goal is scored.

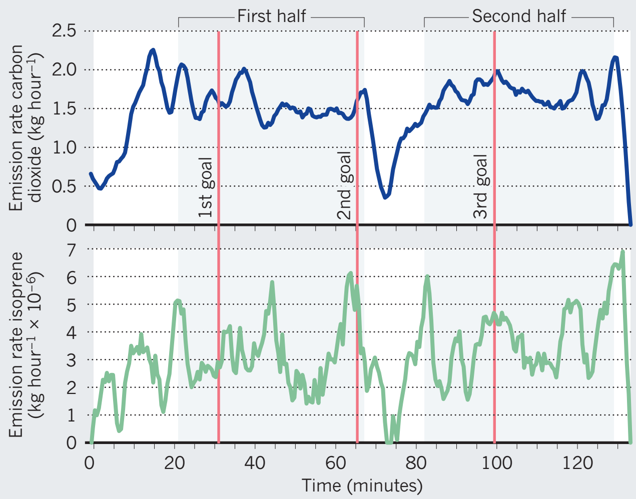

SOURCE: C. STÖNNER & J. WILLIAMS/MPI

Journals should drive data reproducibility

Peer-reviewed journals — as well as researchers and their funders — must take responsibility for improving the reproducibility of published results (see *Nature* **533,** 452–454; 2016).

I suggest that journals should be required to sign a global statement indicating that, to the best of their knowledge, the data that they publish are reproducible. This statement would be collaboratively formulated by the editors-in-chief in accordance with recommendations from the International Committee of Medical Journal Editors and guidelines proposed by the US National Institutes of Health, *Nature* and *Science* (see *Nature* **515,** 7; 2014 and go.nature.com/29bxphv).

Journals would then publish only papers that are accompanied online by full experimental protocols, raw data and source code, as in the Protocol Exchange repository (www.nature.com/protocolexchange). For manuscripts containing statistical analyses, journals should peer review only those papers that use statistics environments based on source code, enforcing the ban on 'point-and-click' statistical software (see go.nature.com/29pdpcl).

Gregorio Santori *University of Genoa, Italy.*
gregorio.santori@unige.it

Don't mar legislation with pseudoscience

We are concerned that some of the European Union's processes for setting safety regulations for chemicals are being influenced by media and pseudoscience scaremongering. Pseudoscience has no place in such decisions, which should be based purely on well-defined and transparent evidence.

For example, endocrine disruptors are being blamed for obesity and type 2 diabetes (J. Legler *et al. J. Clin. Endocrinol. Metab.* **100,** 1278–1288; 2015) despite the absence of supporting evidence for this, and despite food and sugar over-consumption being established as a proven cause. As a consequence, the European Commission's criteria for regulating endocrine-disrupting compounds as a threat to human health are based on correlational, not causal, studies (see go.nature.com/29rjlik).

Conflicts of interest can contribute to the problem, beyond the commercial motivation of industry. Some non-governmental organizations might need to maintain public concerns to boost charitable donations. Decision-makers might prefer to disregard evidence-based data that contradict a precautionary viewpoint. And some scientists put securing research funds above objective appraisal of the evidence.

Acting on hazard identification alone relieves the scaremongering party of the burden of proof, when harm is simply assumed. As a result, regulations can become unnecessarily restrictive. They may even be damaging, for example if an agricultural ban were to be imposed on triazole fungicides because of their endocrine-disrupting potential. The risk to humans at such levels of exposure would be negligible (J. E. Chambers *et al. Crit. Rev. Toxicol.* **44,** 176–210; 2014). It makes no sense to override such evidence with a blanket ban on potentially hazardous chemicals that ignores the public's demonstrable low level of exposure.

Daniel R. Dietrich* *University of Konstanz, Germany.*
daniel.dietrich@uni-konstanz.de
**On behalf of 8 correspondents (see go.nature.com/29kbyqb for full list).*

Drug repositioning needs a rethink

Repurposing drugs to treat illnesses for which they were not originally intended can be faster and cheaper than developing new ones (see *Nature* **534,** 314–316; 2016). I suggest that greater improvements would come from testing different drug combinations, rather than relying only on high-throughput screening of generic or failed drugs.

Disease is often an integration of multiple pathologies (see, for example, J. N. Weinstein *et al. Nature* **507,** 315–322; 2014), so these are potentially treatable with different drug combinations that act in synergy. Such combinations often show better efficacy than single treatments, have fewer side effects and are less likely to result in drug resistance (see *Nature* **492,** 118–122; 2012).

For commercial reasons, pharmaceutical firms tend to dismiss reposition testing of drugs that are off patent. I therefore suggest that governments step in to fund the repurposing of established drugs to broaden the search.

Xianting Ding *Shanghai Jiao Tong University, Shanghai, China.*
dingxianting@sjtu.edu.cn

Robert Treat Paine

(1933–2016)

Ecologist who established concept of keystone species.

BENJAMIN DRUMMOND

In the 1960s, ecology was dominated by descriptions of patterns in nature and assertions that these patterns were determined by physiological tolerances, energy flows through ecosystems or competition among similar species.

Robert Treat Paine changed the field's course with a simple experiment. He removed ochre starfish (*Pisaster ochraceus*) from a seashore in Washington state, revealing that a single predator could control the abundance, diversity and distribution of other organisms sharing its ecosystem. Thus was born Paine's concept of a 'keystone species' — one that influences most of the other species in its community, just as the wedge-shaped stone at the top of an arch holds the structure in place.

Paine, who died on 13 June, was born in Cambridge, Massachusetts, in 1933; his mother was a photographer and writer, his father an art historian. As a boy, he spent hours exploring the woods, acquiring a feel for the rhythms of nature and honing his powers of observation.

Paine developed a passion for palaeontology as an undergraduate at Harvard University in Cambridge. But his plan to study fossils as a graduate — at the University of Michigan in Ann Arbor — was derailed after he started attending classes taught by ecologist Frederick E. Smith. Smith was unafraid to ask provocative questions about patterns in nature. Switching to ecology, Paine studied a living fossil: a species of lamp shell, or brachiopod, for his 1961 PhD.

Following a postdoctoral fellowship at the Scripps Institution of Oceanography in La Jolla, California, in 1962, Paine joined the zoology faculty at the University of Washington in Seattle. There he conducted his now-classic starfish experiments, developed other transformative ideas and established a dynasty of experimental ecologists up to and beyond his official retirement 36 years later.

Paine's studies at Michigan coincided with the development of an avant garde idea in ecology. Challenging conventional wisdom that the availability of prey regulated predators, the zoology faculty troika of Smith and his colleagues Nelson Hairston and Lawrence Slobodkin proposed in 1960 the 'green world hypothesis'. In their view, the world was green because herbivores, who could otherwise consume all plant (green) matter, were regulated by their predators (N. G. Hairston *et al. Am. Nat.* **94,** 421–425; 1960). The paper attracted considerable attention, but like all conceptual and most field ecology at the time, lacked solid field evidence.

Enter Paine's starfish. Paine demonstrated conclusively that, at least on one rocky shore, the top predator both controlled its prey and affected most of the other species in the community (R. T. Paine *Am. Nat.* **100,** 65–75; 1966). The ochre starfish is a generalist predator, consuming barnacles, snails, limpets and more. Its favourite food is the California mussel — the dominant competitor for space on the rocks. By controlling mussel numbers, starfish enable a wide diversity of species to co-exist, including other prey species, and an array of seaweeds, sponges and anemones that the starfish do not consume. When Paine removed the stars from the system, mussels quickly crowded out other species. Comparable dynamics were later demonstrated for keystone species in other marine, terrestrial and freshwater ecosystems.

Paine expanded these ideas to include the concept of 'trophic cascades' — the rippling through a community of strong, top-down effects that affect multiple ecosystem levels and species. These ideas upended established theories about the dominance of 'bottom-up' effects, such as those mediated by changes in rainfall or nutrients. Experimental evidence is hard to argue against, and it was clear from Paine's experiments that single species could matter.

His findings had a major effect on conservation. Sharks, for example, are now understood to have key roles in controlling the distribution, abundance and diversity of many species in ocean ecosystems.

Paine delighted in romping around the rocky intertidal zone, especially at his long-term study site on Tatoosh Island off the Olympic peninsula of Washington. He was in his element in the field — steering his outboard motor boat through swells, navigating his two-metre frame over slippery algae, hauling supplies up steep cliff faces, peppering everyone with observations, and generally outpacing students decades younger than him. He also took intense pleasure in devising ways to adapt hardware supplies to manipulate the abundance of species with different characteristics. A home-made fence or cage had to achieve its intended ecological purpose as well as withstand pounding waves and storm surges of a not-so-pacific ocean.

Bob's legacy is defined by his charisma and his brilliant mentoring of generations of ecologists, as much as by his research. He kindled curiosity, independent thinking and a willingness to observe closely and then manipulate nature to discern her secrets. Even after retiring, Bob actively supported his ever-expanding family of academic (as well as biological) children, grandchildren and great-grandchildren.

Now recognized as one of the greatest ecologists in history, Bob was not afraid to be provocative, but understood that what mattered were results — especially experimental ones. His towering stature easily intimidated students until they spent time with him and discovered an encouraging and inspiring mentor and often a friend.

Even early on, another giant in ecology, Robert MacArthur, who in the 1960s had championed the importance of competition in structuring ecological communities, understood how profound Bob's keystone-species findings were. Writing to him three months after the initial starfish results were published, MacArthur stated simply: "This changes everything." And so it did. ■

Jane Lubchenco *is distinguished professor of integrative biology at Oregon State University, Corvallis, Oregon, USA, and the first US Science Envoy for the Ocean. She switched fields in graduate school to work with an ecologist who opened her eyes and expanded her world: Bob Paine.*
e-mail: lubchenco@oregonstate.edu

For News & Views online, go to nature.com/newsandviews

CLIMATE SCIENCE

Cooling in the Antarctic

The Antarctic Peninsula has been warming for many decades, but an analysis now reveals that it has cooled since the late 1990s. Inspection of the factors involved suggests that this is consistent with natural variability. SEE LETTER P.411

ERIC J. STEIG

The Antarctic Peninsula is a triangular, mountainous land with a coastline of dramatic, calving glaciers and rich wildlife, and it exemplifies the popular image of Antarctica (Fig. 1). Over the past half century, it has been one of the most rapidly warming places on Earth. This warming is associated with major physical and biological changes, including a decline in the Adélie penguin population[1] and the disintegration in 2002 of a large portion of the Larsen B ice shelf, a major geographical feature that had existed for millennia[2]. It is natural to view the changes at this northernmost point in Antarctica as part of the inexorable southward march of anthropogenic climate change. It may thus seem remarkable that Turner and colleagues[3] now report (page 411) that the Antarctic Peninsula has actually cooled in the past two decades.

Turner *et al.* show that the average temperature on the peninsula has decreased by about 0.5 °C per decade since the late 1990s, about the same rate at which it warmed in the preceding five decades. To understand this apparent reversal, one has to recognize that the average warming trend observed since the middle of the twentieth century reflects several aspects of Antarctic Peninsula climate. Which aspect dominates varies by both location and season. For example, the oft-heard claim that the peninsula is the fastest-warming place on Earth is accurate only during the winter, as recorded at the Faraday/Vernadsky station on the west coast. Winter warming at this station — more than 6 °C since records began in 1947 — is unambiguously associated with a rapid decrease in sea ice[4].

By contrast, significant summer warming has been largely restricted to the peninsula's east coast and is related to poleward migration of the circumpolar westerly winds, commonly described by an increase in the Southern Annular Mode (SAM) index[5]. The SAM is a mode of natural atmospheric variability, but changes in the SAM index have been associated with increased greenhouse gases and the decline of stratospheric ozone[6]. Autumn is the only season during which both coasts of the Antarctic Peninsula have warmed together over multiple decades[7]. The autumn temperature trend has been associated with features of large-scale atmospheric circulation known as Rossby waves, which link changes in tropical convection (associated with El Niño ocean-warming events, for example) with temperatures on the Antarctic Peninsula[7].

Turner *et al.* show that most of the factors that determine the peninsula's temperatures have changed in such a way as to favour regional cooling, rather than warming, since the end of the twentieth century. They find that there has been no increase in the SAM index since the late 1990s, but that there have been stronger easterly and southeasterly near-surface flows towards the peninsula, countering the long-term trend of increasing westerlies during the summer. Because southeasterlies tend to push sea ice towards the peninsula's east coast, there has been greater sea-ice cover

TOM TOBIN

Figure 1 | Glacier ice at James Ross Island, Antarctic Peninsula. Turner *et al.*[3] report that the peninsula has cooled during the past 20 years.

there during the past two decades, reducing the flux of heat from the ocean and further amplifying the cooling effects of the changes in atmospheric circulation.

Moreover, the authors show that the average state of the tropical Pacific Ocean has changed, with the dominance of strong El Niño events during the 1990s giving way to colder, predominantly La Niña conditions during the 2000s. Although the relationship between the state of the tropics and Antarctic Peninsula temperatures is complex, the net result during autumn and winter has been increased easterlies and southeasterlies, similar to those that occur during summer. The changing state of the tropical Pacific similarly explains why temperatures over central West Antarctica — south of the peninsula — increased markedly through the 1990s, but have since remained relatively stable[8].

A crucial point made by Turner *et al.* is that both the warming since the 1950s and the cooling since the late 1990s are entirely consistent with natural climate variability. This is to be expected: none of the known drivers of Antarctic Peninsula temperature change can be clearly associated with anthropogenic effects, apart from the summertime trend in the SAM index. Although recent changes in the peninsula's climate have been large, the natural decadal-scale variability is also large, making short-term fluctuations inherently unpredictable even in the presence of strong forcing.

Even before Turner and colleagues' analysis, there was little evidence that the rapid warming in Antarctica falls outside the range of natural variability. Indeed, the palaeoclimate record from ice cores has strongly suggested that it does not[8,9] (with the possible exception of summer warming on the northernmost part of the peninsula, at James Ross Island[10]). In short, Turner and co-workers' findings should not be surprising.

A potentially controversial aspect of the new findings is the authors' conclusion that the observed peninsula cooling is independent of the recent period of relatively modest global warming, sometimes dubbed the hiatus. An objective choice for the start of the cooling period is 1998, the year commonly cited for the start of the hiatus. Although several explanations for the hiatus have been proposed, there is little doubt that exchange of heat between the atmosphere and the tropical ocean has a major role. This heat exchange is sometimes discussed in terms of a negative phase of a phenomenon called the Interdecadal Pacific Oscillation (IPO, detected as warm or cool surface waters in the Pacific)[11]. Turner *et al.* argue that negative phases of the IPO index tend to increase temperatures on the Antarctic Peninsula, which implies that the observed cooling is not connected to the hiatus. But relationships between tropical dynamics, global temperatures and Antarctic climate aren't likely to be captured by a single index.

Climate models[12] suggest that the signal of anthropogenic climate change is damped by the tendency of mean ocean transport to carry heat northward. This, combined with the large magnitude of natural variability, suggests that anthropogenic climate change may not be unambiguously detectable in Antarctica for several more decades. Many decades of data are required to meaningfully characterize decadal climate variability. Looking at surface-air temperatures[13] collected for more than 60 years, the long-term trend is one of warming. Importantly, the authors do not claim that this long-term warming has ended, and it would indeed be premature to come to such a conclusion. ■

Eric J. Steig *is in the Department of Earth and Space Sciences, University of Washington, Seattle, Washington 98195, USA.*
e-mail: steig@uw.edu

1. Lynch, H. J., Naveen, R., Trathan, P. N. & Fagan, W. F. *Ecology* **93,** 1367–1377 (2012).
2. Domack, E. *et al. Nature* **436,** 681–685 (2005).
3. Turner, J. *et al. Nature* **535,** 411–415 (2016).
4. Turner, J. *et al. Int. J. Climatol.* **25,** 279–294 (2005).
5. Marshall, G. J. *Int. J. Climatol.* **27,** 373–383 (2007).
6. Thompson, D. W. J. *et al. Nature Geosci.* **4,** 741–749 (2011).
7. Ding, Q. & Steig, E. J. *J. Clim.* **26,** 7570–7585 (2013).
8. Steig, E. J. *et al. Nature Geosci.* **6,** 372–375 (2013).
9. Mulvaney, R. *et al. Nature* **489,** 141–144 (2012).
10. Abram, N. J. *et al. Nature Geosci.* **6,** 404–411 (2013).
11. Fyfe, J. C. *et al. Nature Clim. Change* **6,** 224–228 (2016).
12. Armour, K. C., Marshall, J., Scott, J. R., Donohoe, A. & Newsom, E. R. *Nature Geosci.* **9,** 549–554 (2016).
13. Nicolas, J. P. & Bromwich, D. H. *J. Clim.* **27,** 8070–8093 (2014).

MOLECULAR BIOLOGY

A surprise beginning for RNA

Organic molecules called coenzymes are central to metabolism, but have also been found to act as components of RNA in bacteria. A study reveals how coenzymes are incorporated into RNA. **SEE LETTER P.444**

KATHARINA HÖFER & ANDRES JÄSCHKE

The absence of a molecular cap structure at the start of messenger RNA molecules has long been considered to be a hallmark of bacteria[1]. However, in the past decade[2,3], chemical modifications have been discovered in bacterial RNA that structurally resemble the caps found in mRNA from eukaryotes (organisms whose cells contain a nucleus). These modified building blocks are coenzymes, which are well known to biochemists for their role as helpers in enzyme-catalysed metabolic reactions. On page 444, Bird *et al.*[4] report that the bacterial capping mechanism is fundamentally different from that of eukaryotes. The authors then extend their study to unravel why some RNA sequences carry this cap, whereas others do not.

> ***"The study provides a first explanation for how coenzyme-modified RNA is synthesized in bacteria."***

RNA is generally composed of only four building blocks — the nucleoside molecules adenosine, cytidine, guanosine and uridine — linked by phosphate groups. However, many site-specific chemical modifications decorate RNA molecules, supporting diverse coding, structural and catalytic functions[5]. The cap at the 5′ end of mRNA is one of the most prominent eukaryotic modifications, influencing processes as diverse as RNA splicing, intracellular transport and protein biosynthesis[1]. The attachment of this cap occurs in parallel with RNA transcription, thanks to the combined efforts of different enzymes[6] (Fig. 1a).

First, the enzyme RNA polymerase (RNAP) binds to a specific sequence called the promoter in DNA, and initiates RNA synthesis immediately downstream of this, at the transcription start site (denoted as the +1 position). RNAP assembles the RNA chain complementary to the DNA template strand by linking nucleosides that have three phosphate groups attached (nucleoside triphosphates; NTPs), each linkage causing the concurrent release of two phosphate groups. The RNA carries a triphosphate group at its leading 5′ end, stemming from the NTP incorporated at the +1 position. Once the growing RNA chain reaches a certain length, a cap structure is added to this end: enzymes first clip off a monophosphate group, then add a guanosine monophosphate molecule, and finally add a methyl group to the guanosine, thereby producing a mature cap structure.

Bacteria do not possess this capping machinery, so textbooks say that their transcripts carry a 5′ triphosphate. But mass

spectrometry indicates[3,7] that this is not wholly accurate. Analysis of chopped-down bacterial RNA revealed unexpected constituents that, owing to their structure, could reside only at the 5′ end of RNA. These constituents were two old acquaintances, nicotinamide adenine dinucleotide (NAD^+) and 3′-dephospho-coenzyme A (dpCoA), central coenzymes in bacterial physiology.

In 2015, the combination of a NAD^+-specific enrichment protocol and high-throughput sequence analysis revealed[2] a set of bacterial regulatory small RNAs to have cap-like NAD^+ attachments that protect them from degradation and modification. An enzyme called NudC can remove the cap[2,8], but it was not clear how NAD^+ got into these RNA strands in the first place.

The sequence of all reported NAD^+–RNA molecules starts with adenosine[2], and NAD^+ and dpCoA contain an adenosine substructure. As a result, Bird *et al.* hypothesized that the coenzymes compete with the regular NTP, adenosine triphosphate, in the initiation step of transcription, therefore becoming incorporated into the RNA chain at the +1 position[4] (Fig. 1b). The authors' cell-free transcription assays confirmed that bacterial RNAP can efficiently incorporate NAD^+, its reduced form NADH, and dpCoA into full-length RNA transcripts. However, incorporation is efficient only if the promoter sequence of the corresponding DNA is the same as those in the bacterium *Escherichia coli* that are transcribed to highly NAD^+-capped RNAs[2].

Systematic investigation revealed that the promoter nucleoside immediately upstream of +1 (the nucleoside in the −1 position) is a key determinant of coenzyme incorporation, with the presence of adenosine at −1 conferring much higher levels of incorporation than cytidine. In a crucial experiment, the authors analysed the ability of various *E. coli* promoters to initiate transcription of NAD^+-modified RNAs *in vivo*, and so demonstrated that these *in vitro* findings also apply in living cells. Furthermore, they showed that coenzyme capping results in a large increase in RNA stability *in vivo*.

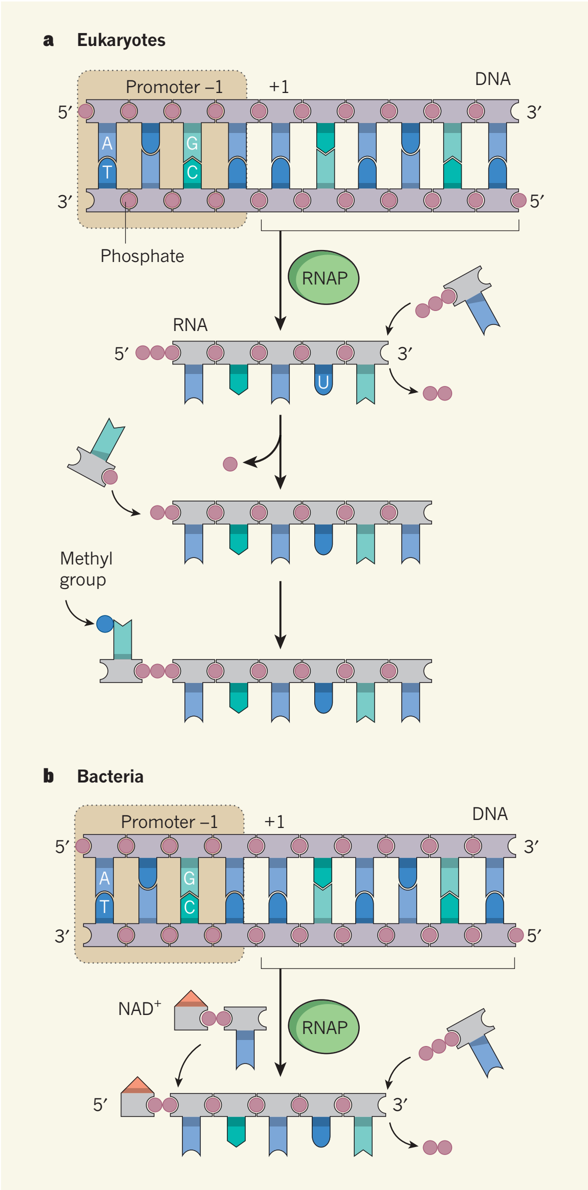

Figure 1 | Capping mechanisms. a, During eukaryotic transcription, the RNA polymerase (RNAP) enzyme begins synthesizing RNA from DNA immediately downstream of the DNA promoter sequence, at position +1. RNAP links nucleosides — adenosine (A), cytidine (C), guanosine (G) and uridine (U), with U being incorporated in place of the DNA nucleoside thymidine (T) — that harbour three phosphate groups. The enzyme removes two phosphates as each molecule is added to the chain. After RNA reaches a certain length, other enzymes (not shown) cap the 5′ end: a phosphate group is removed, a guanosine monophosphate added and a methyl group added to that. **b**, By contrast, Bird *et al.*[4] report that bacterial RNA is capped during the initiation of transcription. A coenzyme molecule (here, NAD^+) that contains an adenosine substructure competes with adenosine triphosphate for position +1 and is therefore directly incorporated at the 5′ end of RNA by RNAP. The nucleoside present at DNA position −1 determines the efficiency of coenzyme incorporation.

Finally, Bird *et al.* used X-ray crystallography to analyse the structural basis for coenzyme incorporation. They soaked crystals of an RNAP–promoter complex in a solution containing the coenzymes and NTPs, and observed that coenzyme capping could initiate RNA formation in the crystal.

The current study provides a first explanation for how coenzyme-modified RNA is synthesized in bacteria and demonstrates the fundamental differences between this process and typical eukaryotic capping. Furthermore, the work establishes the functional relevance of NAD^+ capping *in vivo* — increasing RNA stability. The existence[2] of the decapping enzyme NudC indicates that the stabilized transcripts can be destabilized and targeted for degradation if the metabolic need arises.

It remains to be seen whether selective stabilization and degradation are the only functions of these unconventional RNA ends. We recently proposed[8] that coenzymes and metabolites attached to RNA provide a layer of 'epitranscriptomic' information that modifies the activity of RNA without altering its sequence. Such information could endow RNAs with additional functions and facilitate their interaction with other biomolecules. If this is the case, there must be a high level of specificity in the linking of a particular coenzyme to an RNA. Bird and colleagues' study does not reveal whether RNAP can distinguish between different adenosine-containing coenzymes *in vivo*. An interesting question is therefore whether there are other structural determinants of coenzyme incorporation besides the −1 nucleoside. It will also be interesting to see whether RNAP can incorporate, through similar mechanisms, uridine-, cytidine- and guanosine-containing biomolecules.

Finally, Bird *et al.* demonstrated *in vitro* that eukaryotic RNAP can also incorporate coenzymes into RNA. Thus, this atypical capping might not be limited to bacteria. The diversity of cap structures and capping mechanisms in eukaryotes may well be greater than currently anticipated. ■

Katharina Höfer *and* **Andres Jäschke** *are at the Institute of Pharmacy and Molecular Biotechnology, Heidelberg University, 69120 Heidelberg, Germany.*
e-mail: jaeschke@uni-hd.de

1. Topisirovic, I., Svitkin, Y. V., Sonenberg, N. & Shatkin, A. J. *Wiley Interdisciplin. Rev. RNA* **2,** 277–298 (2011).
2. Cahová, H., Winz, M.-L., Höfer, K., Nübel, G. & Jäschke, A. *Nature* **519,** 374–377 (2015).
3. Kowtoniuk, W. E., Shen, Y., Heemstra, J. M., Agarwal, I. & Liu, D. R. *Proc. Natl Acad. Sci. USA* **106,** 7768–7773 (2009).
4. Bird, J. G. *et al. Nature* **535,** 444–447 (2016).
5. Machnicka, M. A. *et al. Nucleic Acids Res.* **41,** D262–D267 (2013).
6. Martinez-Rucobo, F. W. *et al. Mol. Cell* **58,** 1079–1089 (2015).
7. Chen, Y. G., Kowtoniuk, W. E., Agarwal, I., Shen, Y. & Liu, D. R. *Nature Chem. Biol.* **5,** 879–881 (2009).
8. Jäschke, A., Höfer, K., Nübel, G. & Frindert, J. *Curr. Opin. Microbiol.* **30,** 44–49 (2016).

This article was published online on 6 July 2016.

CONSERVATION

Fishing for lessons on coral reefs

A global study has identified coral reefs with greater fish biomass than would be predicted given human and environmental pressures. These outliers might teach us something about sustainable coral-reef management. SEE LETTER P.416

KRISTY J. KROEKER

The human population is expected to reach 9.7 billion by mid-century[1], with many of us concentrated in the narrow, coastal zones of the world. The inevitable growing demand for food is of great concern to conservationists. Seafood is a key source of nutrition for people worldwide, yet unsustainable fishing practices have already led to the degradation of many coastal ecosystems[2], and these degraded ecosystems have a reduced capacity to support stable fisheries[3]. Strong fishing restrictions are in place for only 2% of the world's oceans[4], leaving the vast majority of marine ecosystems at risk from overfishing and continued degradation. On page 416, Cinner *et al.*[5] provide key insights into the social and economic conditions linked to declines in the biomass of coral-reef fish.

Although there is a well-established link between overfishing and coral-reef health, we know less about the social, cultural and economic conditions that cause some communities to overfish while others fish more sustainably. Understanding the root causes of overfishing may allow individuals and organizations to address, and potentially alleviate, the conditions that contribute to overfishing, and to promote the socio-economic conditions associated with sustainable fisheries.

Cinner *et al.* compiled ecological and environmental data for some 2,500 coral reefs worldwide, as well as the socio-economic data for the use of these reefs. The authors then compared how the biomass of fish on coral reefs varied with numerous social and economic factors, such as human population growth and levels of tourism, on both local and national scales, while also accounting for some environmental conditions (largely beyond human control) that influence reef fish populations.

The authors find that conventional conservation approaches such as well-enforced reserves (areas that are not fished) generally increase fish biomass, but they also describe other socio-economic factors that lead to reef-fish declines. In particular, there are fewer fish in locations with shorter travel times to large markets where people can sell fish.

The effect of increasing market-based forces on decreasing fish biomass was stronger than the effects of many of the other factors that influence reef-fish biomass, including human population pressures, environmental conditions or local management actions. This result is crucial for coral-reef conservation because it suggests that market forces contribute to overfishing and that market-based interventions — such as eco-labelling or creating markets for sustainably harvested fish — may be necessary to support sustainable fisheries on coral reefs.

The authors also report a second compelling result. They identify 15 reefs that have much greater fish biomass than would be expected given the human and environmental pressures. These reefs constitute what are called 'bright spots' (Fig. 1), and can now be analysed to learn lessons that may point conservationists in new directions.

Identifying and scaling up the lessons learned from individuals or populations that are outperforming those around them has been done successfully in the fields of human health, development (such as agricultural practices or resource use) and business management, but this strategy is not a standard approach in marine-conservation studies. The benefits of understanding the factors that underlie outperformers — whether in coral-reef conservation or human health — are manifold and include the potential to generate local community involvement by identifying proven and practical solutions that can be


REINHARD DIRSCHERL/ULLSTEIN BILD/GETTY

Figure 1 | Bright spots. Cinner *et al.*[5] carried out a global analysis of fish biomass on coral reefs and identified locations (such as Raja Ampat, Indonesia, shown here) known as bright spots, where fish stocks were higher than expected given local human and environmental pressures.

scaled up in other locations.

Five of the fifteen bright spots identified by Cinner and colleagues are in unpopulated areas. This leaves only ten other sites with which to explore how different socio-economic conditions might affect decisions to fish sustainably when access to markets is not limiting. The authors' preliminary analyses suggest that bright spots tend to be associated with communities that are actively engaged in reef-management decisions, and which are highly dependent on the resources, or in communities that have customs in place to control usage. On the basis of these results, strategies that promote community engagement and local enforcement may be crucial for sustainable management.

The new results are compelling, but 10 sites out of 2,500 reefs is an extremely limited number for a robust, quantitative analysis of bright spots (although the low number is interesting in its own right, suggesting that there are very few outliers among the world's reefs). More in-depth socio-economic studies are needed to fully understand why these conditions support high reef-fish biomass in some locations but not in others.

One limitation of this study is the tight focus on the market-based causes of coral-reef degradation at a time when coral reefs are increasingly threatened by accelerating environmental changes[6]. The precarious health of coral reefs was heart-breakingly illustrated in early 2016, when warm ocean temperatures caused severe bleaching (the expulsion of photosynthetic algae from corals, which can result in the death of the coral) of reefs globally[7], including at the iconic Great Barrier Reef[8]. In their study, Cinner *et al.* also find that coral reefs that have experienced recent environmental shocks, such as bleaching or cyclones, have lower fish biomass than would be expected on the basis of pressures such as market influences. In addition, the coral reefs located near cooler, deeper waters where animals can hide during unfavourable conditions had higher fish biomass.

"Preliminary analyses suggest that bright spots tend to be associated with communities that are actively engaged in reef-management decisions."

Lessons can also be learned from the 'dark spots' (reefs that support fewer fish than would be predicted on the basis of human and environmental pressures) that were identified by Cinner and colleagues. Not surprisingly, several of these reefs were recently exposed to environmental disturbances, such as cyclones, highlighting the importance of considering how climate change will continue to affect reefs in the future.

Although analysis of bright spots may help to identify market-based management approaches for sustaining coral-reef fishes, a portfolio of conservation approaches is probably still needed to address the numerous threats to coral-reef ecosystems, including climate change. Without sustainable fisheries, we will not be able to maintain healthy coral reefs. And without healthy coral reefs, we will not be able to sustain the fisheries needed to feed the world's growing population. ■

Kristy J. Kroeker *is in the Department of Ecology and Evolutionary Biology, University of California, Santa Cruz, Santa Cruz, California 95060, USA.*
e-mail: kkroeker@ucsc.edu

1. United Nations Department of Economic and Social Affairs. *World Population Prospects: The 2015 Revision, Key Findings and Advance Tables* (2015).
2. Jackson, J. B. C. *et al. Science* **293,** 629–637 (2001).
3. Wilson, S. K. *et al. Ecol. Appl.* **20,** 442–451 (2010).
4. Lubchenco, J. & Grorud-Colvert, K. *Science* **350,** 382–383 (2015).
5. Cinner, J. E. *et al. Nature* **535,** 416–419 (2016).
6. Pandolfi, J. M., Connolly, S. R., Marshall, D. J. & Cohen, A. L. *Science* **333,** 418–422 (2011).
7. Normile, D. *Science* http://dx.doi.org/10.1126/science.aaf9845 (2016).
8. Normile, D. *Science* http://dx.doi.org/10.1126/science.aaf9933 (2016).

CONDENSED-MATTER PHYSICS

Attractive electrons from nanoengineering

Electrons repel each other because they are negatively charged. An experiment now confirms a fifty-year-old theory that electrons can also attract one another as a result of repulsion from other electrons. SEE LETTER P.395

TAKIS KONTOS

Coulomb's law describes the force that exists between two charged particles, such as the mutual repulsion of negatively charged electrons, and has been confirmed by a multitude of experiments. However, electrons in matter can also attract each other. On page 395, Hamo *et al.*[1] demonstrate an attraction mechanism that is purely electronic. They prove that the repulsion of electrons in solids can be turned into an attraction with the help of other electrons, validating a long-standing theory proposed by the physicist William Little[2].

The idea that electrons can attract each other is central to the theory of how conventional superconductors such as aluminium work. In the Bardeen–Cooper–Schrieffer (BCS) theory of superconductivity[3], electrons attract one another through lattice vibrations called phonons. This mechanism imposes constraints — for example, the characteristic energy of phonons, the Debye frequency, governs the temperature below which a material can superconduct (the critical temperature).

Soon after the advent of the BCS theory, Little proposed a different 'excitonic' attraction scheme, whereby electrons attract each other because of repulsion from other electrons, in close analogy with the attraction through phonons[2] (Fig. 1a). To illustrate the excitonic mechanism, he considered two electrons (the system) interacting with a polarizable molecule (the polarizer; let's consider a diatomic molecule for simplicity). The polarizer has one electron that is free to move between the molecule's two atoms. An electron in the system can repel the polarizer electron, leaving behind a positively charged region. The other electron in the system is then attracted to this region and, consequently, the two system electrons are attracted to one another.

The characteristic energy of the excitonic mechanism is simply the energy difference between two electronic states of the polarizer (the bonding and anti-bonding states)[4], which can, in principle, be much larger than the Debye frequency of most metals. The excitonic mechanism was therefore expected to provide a higher critical temperature than the few kelvin that was, at the time, thought to be required by its phononic counterpart. Such high-temperature superconductivity is desirable for practical applications, and the possibility of achieving it triggered intense theoretical and experimental activity. It was thought that the excitonic mechanism could be responsible for the superconductivity of organic superconductors; however, after years of intense debate, it is now generally accepted that it is not[5].

Efforts to find a superconductor whose activity is based on the excitonic mechanism face two key problems: a material must be discovered in which Little's proposal can be applied, and the excitonic mechanism in that material must lead to superconductivity[4]. Hamo *et al.* decided to separate the two problems. They aimed to demonstrate the basic attractive mechanism in a material without

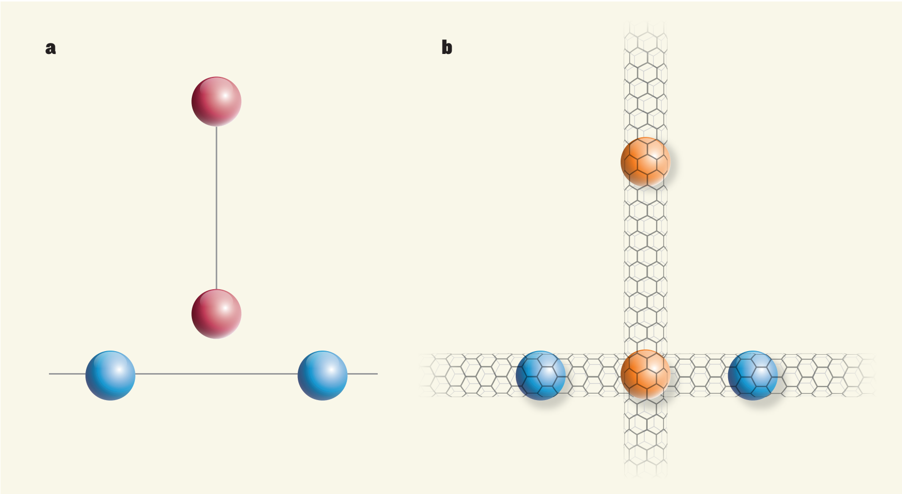

Figure 1 | The excitonic mechanism for attractive electrons. **a**, In 1964, the physicist William Little proposed a set-up to demonstrate his theory that electrons can attract one another because of repulsion from other electrons[2]. There are two key components to his proposal: a pair of electrons (blue) within an electron chain (the 'system'), and a polarizable molecule (the 'polarizer'), composed here of two atoms (red). **b**, Hamo *et al.*[1] use nanoengineering to realize Little's set-up. In their experiment, the system consists of two electrons within a carbon nanotube and the polarizer is a pair of potential-energy wells (orange) within a separate carbon nanotube. The two nanotubes are placed perpendicularly to each other such that one of the polarizer's potential wells is directly above the system. As the separation between the two nanotubes is reduced, the presence of the polarizer causes the system electrons to attract each other.

requiring superconductivity. Furthermore, instead of trying to find the desired material in nature, the authors fabricated it using nanometre-scale engineering techniques.

Unlike Little's original proposal, the authors' polarizer is an artificial molecule: a pair of potential-energy wells within a carbon nanotube, which is placed on a microchip. The electron system is constructed inside a separate carbon nanotube, on its own microchip. The two nanotubes are then placed perpendicularly to each other (Fig. 1b), one above the other, inside a scanning probe microscope. After the apparatus is cooled to a low temperature (about 10 millikelvin), the nanotubes are moved closer together until they are about 100 nanometres apart. The authors can then observe the effect of the polarizer on the behaviour of the system electrons and, in particular, confirm whether or not the electrons attract one another.

Hamo and collaborators' experiment has several key assets. Their nanotube material is almost entirely free from impurities, which allows the electrical force acting on the electrons inside each nanotube to be carefully controlled. The particular set-up used by the authors also allows them to accurately assemble or disassemble the basic elements of Little's proposal — the system and the polarizer — and study their formation and interactions.

In contrast to work with real molecules, the researchers' electrical-current measurements and charge-sensing of artificial molecules allow direct characterization of all of the relevant energy scales in the experiment. For example, the interaction between the system electrons can be determined by measuring the signal from electrometers built inside the carbon nanotubes, or simply from the current flowing through the devices as a function of the applied voltages. Using these techniques, the authors concluded that the electrons were attractive, confirming Little's excitonic mechanism.

In light of Hamo and colleagues' findings, one may now dream of engineering new types of superconductor. However, making a whole crystal — or even a short chain — of the authors' material would be a formidable task. Furthermore, because the excitonic mechanism seems to be optimal in fewer than three spatial dimensions, superconductivity will inevitably compete with other phenomena that affect electrical behaviour (such as insulating charge-density waves)[4]. In addition, the bonding–antibonding splitting produced in the authors' set-up requires low temperatures (in the sub-kelvin range).

Nevertheless, the purely electronic attraction demonstrated is so generic that it could be transposed to any type of material in which some, or possibly all, of these constraints could be lifted. Although Hamo and collaborators' set-up will not form the basis of a practical excitonic superconductor, it will be useful as a 'quantum simulator' of such superconductors for basic research. It is therefore likely to become a key feature of the quantum toolbox of nanoscience. ■

Takis Kontos *is at the Laboratoire Pierre Aigrain, Ecole Normale Supérieure, 75231 Paris, France.*
e-mail: kontos@lpa.ens.fr

1. Hamo, A. *et al. Nature* **535,** 395–400 (2016).
2. Little, W. A. *Phys. Rev.* **134,** A1416–A1424 (1964).
3. Bardeen, J., Cooper, L. N. & Schrieffer, J. R. *Phys. Rev.* **106,** 162–164 (1957).
4. Hirsch, J. E. & Scalapino, D. J. *Phys. Rev. B* **32,** 117–134 (1985).
5. Jérome, D. in *The Physics of Organic Superconductors and Conductors* (ed. Lebed, A) 3–16 (Springer, 2008).

BIOGEOCHEMISTRY

Nocturnal escape route for marsh gas

A field study of methane emissions from wetlands reveals that more of the gas escapes through diffusive processes than was thought, mostly at night. Because methane is a greenhouse gas, the findings have implications for global warming.

KATEY WALTER ANTHONY & SALLY MACINTYRE

Global wetlands are the largest natural source of atmospheric methane, a potent greenhouse gas. Methane is produced by microbes decomposing organic matter in oxygen-free sediment, and escapes from wetlands by three main pathways: through plants; by bubbling out of water (ebullition); and by diffusion of methane molecules across the microscopically thin air–water interface (Fig. 1). Most of the methane emissions from lakes and wetlands have been credited to the first two pathways. But writing in *Geophysical Research Letters*, Poindexter *et al.*[1] report evidence indicating that diffusive emissions are larger than previously thought, and occur mostly at night.

Diffusive emission of sparingly soluble gases such as methane from wetlands is controlled by passage across the air–water interface. Field data show that the emission can be quantified using a model in which the near-surface water is renewed by upwelling motions, for instance, those caused by

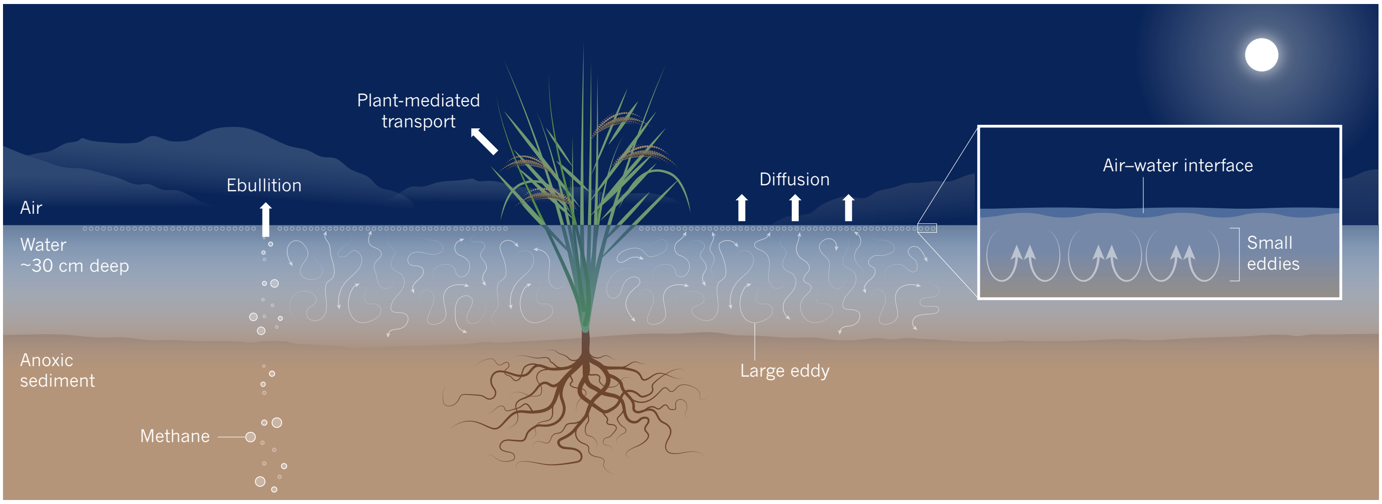

Figure 1 | Methane-transport pathways from wetland soils. Methane is generated in oxygen-free sediments in wetlands, and can escape to the atmosphere by bubbling to the surface (ebullition), by transport through plants (which is highest during the day), or by diffusion of molecules across the air–water interface. Heat loss from wetlands at night can cause convection that generates turbulent eddies, which renew dissolved methane just below the air–water interface, accelerating diffusive emissions. The larger eddies transport methane throughout the water column, whereas the smaller ones thin the diffusive layer immediately below the air–water interface. The size of the smaller eddies (500 micrometres to 1 centimetre across) and the rate of methane renewal varies with the intensity of turbulence. Poindexter *et al.*[1] find that diffusive methane emissions from wetlands are much greater than was previously thought. Figure adapted from ref. 13.

turbulent eddies, associated with wind or cooling[2,3]. Methane transport across the air–water interface accelerates as turbulence intensifies, for example as the wind increases. Poindexter *et al.* are the first to quantify how heat loss from wetland surfaces accelerates diffusive emissions over seasonal and annual cycles, using a heat-flux-based equation that is similar to the surface-renewal model[2–4].

On clear, still nights, heat is emitted from the water surface by radiation; additional cooling from evaporation and conduction may occur even with light winds. Cooling surface water sinks, displacing the underlying water and forming eddies. Large eddies circulate dissolved methane throughout the water column, whereas smaller, near-surface eddies renew the methane at the air–water interface, increasing methane flux to the atmosphere. Poindexter *et al.* use the term 'hydrodynamic transport' to describe this convective mixing driven by cooling; however, hydrodynamic transport is an umbrella term that usually pertains to multiple processes that transport dissolved gases through water, including convection, internal waves (which occur within the body of the water), and the breaking of surface waves.

Past field measurements (see refs 5 and 6, for example) of wetland methane emissions led scientists to conclude that diffusive transport was the least important of the processes that release methane to the atmosphere, but most of those measurements were made during daylight hours, when sunlight warms wetland surface water and creates stable density gradients that retard convective mixing. Using sensors mounted several metres high on a tower, Poindexter *et al.* took continuous, year-round measurements of wind speed, energy inputs and outputs to and from the water (including heat flux), total methane flux and temperature from a shallow wetland dominated by tall emergent plants in the Sacramento–San Joaquin Delta, a temperate region in California. Day- and night-time measurements of the concentration of methane dissolved in surface water were also made on 24 days distributed throughout the year.

The authors calculated that convection-enhanced diffusion caused 18% of total daytime emissions on average. But when they incorporated the effect of nocturnal cooling, they found that convection-enhanced diffusion was the dominant transport pathway at night, contributing 54% of total night-time fluxes. Moreover, because the authors make several assumptions about the nature of flow near the air–water interface, their estimates are conservative. This discrepancy points to the need for more effort to quantify the effect of surfactants and near-surface turbulence on parameters used in the authors' calculations[4].

Poindexter and colleagues' results do not imply that total wetland emissions are higher than previously thought. Rather, they require a reassessment of how emissions are partitioned among the three methane-escape pathways in large-scale regional and global models of wetland emissions[7–9]. A larger convection-enhanced diffusive flux implies lower emissions by plants and/or ebullition. The partitioning will be system specific, because several factors — including plant type and coverage, water depth and landscape geomorphology — work together to control the relative contribution from each pathway.

The demonstration that convection-enhanced diffusion is a larger source of atmospheric methane from wetlands than was previously thought is valuable for several reasons. First, it suggests that nocturnal cooling — which is not well accounted for in commonly used wind-based formulations of diffusive emissions — is probably a significant factor in other sheltered systems such as thermokarst (thaw) ponds and flooded forests. Second, it has implications for tropical wetlands, which are particularly poised for strong convection-enhanced diffusive emissions because heat losses associated with evaporation and with radiation emitted from the water surface are enhanced when surface waters are warm. Methane concentrations in tropical wetlands are high and do not exhibit a strong winter decline as in temperate wetlands, which means that the fraction of convection-enhanced emissions from tropical ecosystems could be higher than those reported in the current study from a temperate wetland.

A third implication of the work stems from the lack of day-to-night differences in surface-water methane concentrations in the shallow California wetland, which implies that there was no strong vertical gradient in methane concentration. Pronounced concentration gradients occur beneath the surface layer in many other water bodies, such that the lower part of the water column is methane-rich. Mixing from convection will entrain methane from the lower water column in those bodies, bringing it to the surface where it can escape to the atmosphere[10]. In addition, convection reduces the time that dissolved methane spends in water and thus reduces its consumption by microbes; this shorter residence time has the potential to further increase methane fluxes.

Convection-enhanced methane emissions are probably largest in warm climatic regions, but most small, methane-rich water bodies are located in cooler locations at high northern latitudes[11]. However, these cooler areas are projected to undergo temperature increases of up to 7.5 °C by the end of this century[12]. This warming

will lead to higher methane production and to convection-enhanced diffusion becoming an increasingly significant mechanism for releasing this methane to the atmosphere, constituting a newly recognized positive feedback to climate warming. In the meantime, Poindexter and colleagues' results underscore the need to consider wetlands and lakes as dynamic systems, even on clear, calm nights. ■

Katey Walter Anthony *is at the Water and Environmental Research Center, University of Alaska Fairbanks, Fairbanks, Alaska 9775-7340, USA.* **Sally MacIntyre** *is at the Marine Science Institute, University of California Santa Barbara, Santa Barbara, California 93106-6150, USA.*
e-mails: kmwalteranthony@alaska.edu; sally.macintyre@ucsb.edu

1. Poindexter, C. M., Baldocchi, D. D., Matthes, J. H., Knox, S. H. & Variano, E. A. *Geophys. Res. Lett.* http://dx.doi.org/10.1002/2016GL068782 (2016).
2. Zappa, C. J. *et al. Geophys. Res. Lett.* **34,** L10601 (2007).
3. MacIntyre, S. A. *et al. Geophys. Res. Lett.* **37,** L24604 (2010).
4. Wang, B., Liao, Q., Fillingham, J. H. & Bootsma, H. A. *J. Geophys. Res. Oceans* **120,** 2129–2146 (2015).
5. Morrissey, L. A. & Livingston, G. P. *J. Geophys. Res. Atmos.* **97,** 16661–16670 (1992).
6. Whiting, G. J., Chanton, J. P., Bartlett, D. S. & Happell, J. D. *J. Geophys. Res. Atmos.* **96,** 13067–13071 (1991).
7. Bohn, T. J. & Lettenmaier, D. P. *Geophys. Res. Lett.* **37,** L22401 (2010).
8. Riley, W. J. *et al. Biogeosciences* **8,** 1925–1953 (2011).
9. Walter, B. P. & Heimann, M. *Global Biogeochem. Cycles* **14,** 745–765 (2000).
10. Crill, P. M. *et al. J. Geophys. Res. Atmos.* **93,** 1564–1570 (1988).
11. Bastviken, D., Tranvik, L. J., Downing, J. A., Crill, P. M. & Enrich-Prast, A. *Science* **331,** 50–50 (2011).
12. IPCC. *Climate Change 2013: The Physical Science Basis. Contribution of Working Group I to the Fifth Assessment Report of the Intergovernmental Panel on Climate Change* (eds Stocker, T. F. *et al.*) 1535 (Cambridge Univ. Press, 2013).
13. MacIntyre, S., Wanninkhof, R. & Chanton, J. P. In *Methods in Ecology, Biogenic Trace Gases: Measuring Emissions from Soil and Water* (eds Matson, P. A. & Harriss, R. C.) 52–97 (Blackwell Science, 1995).

PHYSIOLOGY

Pancreatic β-cell heterogeneity revisited

Two analyses of insulin-producing β-cells reveal differences in what has long been considered a homogeneous population. These differences might reflect changes during maturation or ageing, or distinct cell lineages. SEE LETTER P.430

SUSAN BONNER-WEIR & CRISTINA AGUAYO-MAZZUCATO

Diabetes is associated with an inadequate supply of functional pancreatic β-cells, which normally maintain healthy blood-glucose levels by secreting insulin in response to raised levels and shutting off secretion when glucose is scarce. These cells have been regarded as a single, homogeneous population, even though studies have shown that β-cells are functionally immature in the neonatal period immediately after birth[1,2], and that adult β-cells are not all identical[3,4]. Now, two papers (Bader *et al.*[5] on page 430 and Dorrell *et al.*[6] in *Nature Communications*), identify genetic markers that allow subpopulations of β-cells to be isolated and studied. These studies are bound to revive interest in β-cell heterogeneity and highlight the relevance of this research area for understanding and enhancing cell-replacement therapies for diabetes.

Although all adult β-cells may seem the same when analysed using stains for insulin, subpopulations can differ in terms of insulin secretion[3,4] and insulin-expression levels[7], length of chromosome end structures called telomeres[8] (which correlates with the number of times the cell has divided) and expression of the gene *p16Ink4a*, a marker and effector of β-cell growth arrest (senescence)[9]. Bolstering the idea that this heterogeneity is functional are differences in β-cell sensitivity to glucose[10] and the fact that the cells can be recruited by increased glucose levels to adopt biosynthetic[11,12] or active secretory states[12–15], adapting to the demand for more insulin secretion.

Pancreatic islets are micro-organs composed of several hormone-secreting cell types, including β-cells. During the development of islets, cells are organized into a 3D architecture through a mechanism called planar polarity. Bader *et al.* investigated β-cell expression of a planar-polarity protein called Flattop (Fltp) in mice.

The authors replaced the gene encoding Fltp with a gene that encodes a fluorescent reporter protein dubbed FVR, so that cells that normally express Fltp fluoresced. In this way, they defined two β-cell subpopulations — proliferative immature cells that did not express Fltp or fluoresce (FVR$^-$), and

50 Years Ago

It is not surprising that the Prime Ministers of France and Britain should have been grateful for a few crumbs of agreement to fill out the communique after a recent meeting in London. By all accounts, British membership of the European Economic Community was not a fruitful topic of conversation. It is therefore paradoxical that the two Prime Ministers should have considered this a suitable time for a decision in principle that the tunnel beneath the English Channel should in due course be built … The case for a tunnel is wearing thin. Alternative ways of crossing what is, after all, a narrow strip of water have become more attractive … It looks very much as if the two governments may be making the right decision at the wrong time ... it is to be hoped that the two governments will have another close look at the wisdom of the course to which they have committed themselves before the digging of a tunnel actually begins.
From *Nature* 23 July 1966

100 Years Ago

Like ourselves, the industrial cities of the United States are beginning to realise the serious economic and hygienic effects caused by the unscientific combustion of coal … Dr W. F. M. Goss has contributed to a paper on "Smoke as a Source of Atmospheric Pollution" … The author is not very optimistic in his outlook, for he considers that a revolution in practice which will result in the elimination of existing sources of atmospheric pollution is not to be expected "because present-day knowledge is insufficient to supply necessary means" … We are throwing away … a valuable inheritance which should belong to coming generations, and which they will never be able to recover.
From *Nature* 20 July 1916

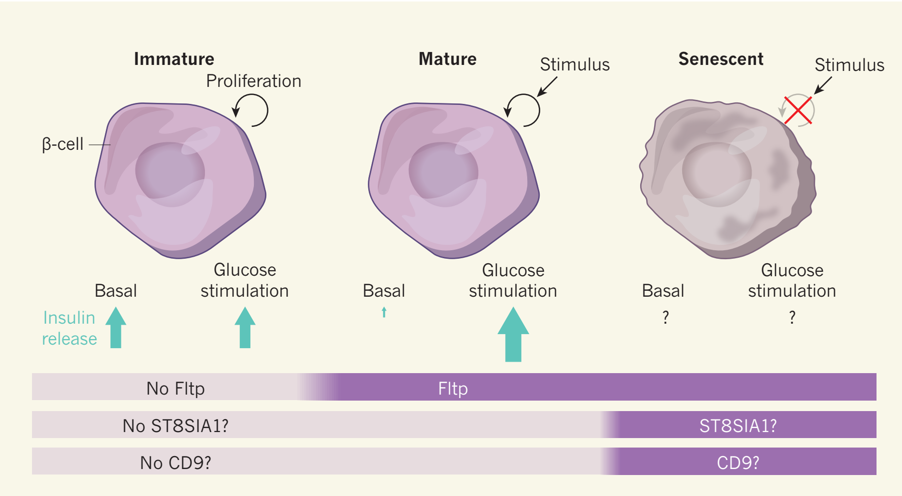

Figure 1 | Separating β-cell subtypes. The insulin-secreting β-cells of the pancreas are thought to renew slowly, so, at any one time, cells of different ages will be present in the tissue. Immature cells are highly proliferative and do not respond robustly to glucose stimulation, but secrete some insulin even at basal (low) blood-glucose levels. Mature cells proliferate in response to external stimuli and release insulin robustly, secreting little or no insulin under basal conditions. Old cells cease to proliferate (they become senescent) and may be dysfunctional. Bader *et al.*[5] show that immature cells do not express the protein Flattop (Fltp), but mature cells do. Dorrell *et al.*[6] find that subsets of β-cells express the proteins ST8SIA1 and/or CD9. Although it was not tested, it could be hypothesized that these cells might be senescent, because they show impaired glucose-stimulated insulin secretion compared with the β-cells from the same samples that lack these markers.

mature, quiescent fluorescing cells (FVR$^+$). Eighty per cent of β-cells were FVR$^+$ in adult mice, as were about 50% of other islet cells. It is of considerable interest that 20% of adult cells are FVR$^-$, because it has been reported[3,10] that 20% of β-cells in adult rodents are unresponsive to glucose.

The authors next separated and further analysed each subpopulation for gene expression, ultrastructure and insulin secretion. These experiments supported the idea that Fltp is a marker of mature β-cells. Furthermore, an *in vitro* tracing analysis confirmed that β-cells progress from FVR$^-$ to FVR$^+$ over time. FVR$^-$ cells proliferated more than FVR$^+$ cells during the normal β-cell population expansion seen during the neonatal period and pregnancy. By contrast, when mice were fed a high-fat diet, which increases the demand on β-cells, cells in the FVR$^+$ subpopulation increased in size, thus presumably increasing their insulin-secreting capacity.

Fltp seems to be a marker, rather than an effector, of the β-cell transition from immature and proliferative to mature and quiescent — deletion of Fltp in mice did not impair β-cell development, proliferation or maturation. Adult mice that lacked the protein had normal glucose tolerance, insulin sensitivity and levels of pancreatic insulin and glucagon, a hormone that raises blood glucose. However, Bader *et al.* found that activation of a signalling cascade called the Wnt/planar cell-polarity pathway, of which Fltp is a downstream effector, enhanced human and mouse β-cell maturation *in vitro*. Moreover, manipulating cells into 3D aggregates had the same effect, indicating that planar polarity is important for β-cell maturation. In the future, the development of specific antibodies that bind Fltp will facilitate a range of experiments to study its role in the human pancreas.

In the second study, Dorrell *et al.* provide further evidence for the existence of β-cell heterogeneity, this time in humans. Previously[16], the same group used antibodies that bind cell-surface proteins to identify hormone-secreting cell types in partially purified isolated human islets. In the current paper, they report the development of two more antibodies that allowed them to distinguish four subtypes of β-cell in the adult human pancreas. The antibodies bind molecules whose role in β-cells is unknown — CD9, a cell-surface glycoprotein that in other systems suppresses cell proliferation, and ST8SIA1, a membrane-bound glycosphingolipid involved in cell adhesion and cell growth.

The authors found consistent proportions of the four β-cell subtypes in healthy adults. Expression of genes crucial for β-cell identity was similar in each subgroup, but expression of around 100 other genes of mostly unknown function in β-cells differed. Cells that expressed both CD9 and ST8SIA1 released more insulin in basal conditions and were less responsive to glucose stimulation than those negative for both markers. This impaired responsiveness may be relevant for disease, because β-cell function is impaired in type 2 diabetes, and Dorrell and colleagues showed that the two ST8SIA1-expressing subtypes accounted for 45% of β-cells in people with this disease, compared with 18% in healthy adults.

What is the biological reason for β-cell heterogeneity? We have hypothesized[17] that young β-cells differ from those in the early stages of maturation or in midlife, those that are mature and have stopped dividing, and those that are old or dying. If this is true, the observed subtypes might reflect different stages of the β-cell life cycle (Fig. 1).

Although Bader *et al.* showed that mouse cells transition from the Fltp-lacking to the Fltp-expressing subgroup over time, it is unclear whether the four human β-cell subtypes observed by Dorrell and colleagues have a temporal relationship or are independent lineages. It also remains unclear whether the increased proportion of ST8SIA1-expressing subtypes in people with type 2 diabetes is the result of selective loss of functionally active β-cells that lack ST8SIA1, or arises because of progressive dysfunction of β-cells owing to the cellular stress of diabetes. Regardless of whether the four human subtypes are separate lineages or sequential stages, their heterogeneity should be considered in research that aims to generate optimal cells for β-cell replacement therapy, because these subgroups may differ in their proliferative capacity or vulnerability to cellular stress.

Together, these papers revisit and underscore the need to consider β-cells as a heterogeneous population comprising cells at different stages of development with different functional and proliferative characteristics. Thanks to the current studies, the tools to explore these differences further are now available. ■

Susan Bonner-Weir *and* **Cristina Aguayo-Mazzucato** *are in the Joslin Diabetes Center, Harvard Medical School, Boston, Massachusetts 02215, USA.*
e-mail: susan.bonner-weir@joslin.harvard.edu

1. Jermendy, A. *et al. Diabetologia* **54,** 594–604 (2011).
2. Blum, B. *et al. Nature Biotechnol.* **30,** 261–264 (2012).
3. Salomon, D. & Meda, P. *Exp. Cell Res.* **162,** 507–520 (1986).
4. Pipeleers, D. G. *Diabetes* **41,** 777–781 (1992).
5. Bader, E. M. A. *et al. Nature* **535,** 430–434 (2016).
6. Dorrell, C. S. J. *et al. Nature Commun.* http://dx.doi.org/10.1038/ncomms11756 (2016).
7. Katsuta, H. *et al. Endocrinology* **153,** 5180–5187 (2012).
8. Peng, S. W. *et al. Endocrinology* **150,** 3058–3066 (2009).
9. Tschen, S. I., Dhawan, S., Gurlo, T. & Bhushan, A. *Diabetes* **58,** 1312–1320 (2009).
10. Van Schravendijk, C. F., Kiekens, R. & Pipeleers, D. G. *J. Biol. Chem.* **267,** 21344–21348 (1992).
11. Schuit, F. C., In't Veld, P. A. & Pipeleers, D. G. *Proc. Natl Acad. Sci. USA* **85,** 3865–3869 (1988).
12. Bosco, D. & Meda, P. *Endocrinology* **129,** 3157–3166 (1991).
13. Hiriart, M. & Ramirez-Medeles, M. C. *Endocrinology* **128,** 3193–3198 (1991).
14. Ling, Z., Wang, Q., Stangé, G., In't Veld, P. & Pipeleers, D. *Diabetes* **55,** 78–85 (2006).
15. Karaca, M. *et al. PLoS ONE* **4,** e5555 (2009).
16. Dorrell, C. *et al. Diabetologia* **54,** 2832–2844 (2011).
17. Weir, G. C. & Bonner-Weir, S. *Ann. NY Acad. Sci.* **1281,** 92–105 (2013).

This article was published online on 11 July 2016.

ARTICLE

doi:10.1038/nature18637

A comprehensive transcriptional map of primate brain development

Trygve E. Bakken[1*], Jeremy A. Miller[1*], Song-Lin Ding[1*], Susan M. Sunkin[1], Kimberly A. Smith[1], Lydia Ng[1], Aaron Szafer[1], Rachel A. Dalley[1], Joshua J. Royall[1], Tracy Lemon[1], Sheila Shapouri[1], Kaylynn Aiona[1], James Arnold[1], Jeffrey L. Bennett[2], Darren Bertagnolli[1], Kristopher Bickley[1], Andrew Boe[1], Krissy Brouner[1], Stephanie Butler[1], Emi Byrnes[1], Shiella Caldejon[1], Anita Carey[1], Shelby Cate[1], Mike Chapin[1], Jefferey Chen[1], Nick Dee[1], Tsega Desta[1], Tim A. Dolbeare[1], Nadia Dotson[1], Amanda Ebbert[1], Erich Fulfs[1], Garrett Gee[1], Terri L. Gilbert[1], Jeff Goldy[1], Lindsey Gourley[1], Ben Gregor[1], Guangyu Gu[1], Jon Hall[1], Zeb Haradon[1], David R. Haynor[3], Nika Hejazinia[1], Anna Hoerder-Suabedissen[4], Robert Howard[1], Jay Jochim[1], Marty Kinnunen[1], Ali Kriedberg[1], Chihchau L. Kuan[1], Christopher Lau[1], Chang-Kyu Lee[1], Felix Lee[1], Lon Luong[1], Naveed Mastan[1], Ryan May[1], Jose Melchor[1], Nerick Mosqueda[1], Erika Mott[1], Kiet Ngo[1], Julie Nyhus[1], Aaron Oldre[1], Eric Olson[1], Jody Parente[1], Patrick D. Parker[1], Sheana Parry[1], Julie Pendergraft[1], Lydia Potekhina[1], Melissa Reding[1], Zackery L. Riley[1], Tyson Roberts[1], Brandon Rogers[1], Kate Roll[1], David Rosen[1], David Sandman[1], Melaine Sarreal[1], Nadiya Shapovalova[1], Shu Shi[1], Nathan Sjoquist[1], Andy J. Sodt[1], Robbie Townsend[1], Lissette Velasquez[1], Udi Wagley[1], Wayne B. Wakeman[1], Cassandra White[1], Crissa Bennett[1], Jennifer Wu[1], Rob Young[1], Brian L. Youngstrom[1], Paul Wohnoutka[1], Richard A. Gibbs[5], Jeffrey Rogers[5], John G. Hohmann[1], Michael J. Hawrylycz[1], Robert F. Hevner[6], Zoltán Molnár[4], John W. Phillips[1], Chinh Dang[1], Allan R. Jones[1], David G. Amaral[2], Amy Bernard[1] & Ed S. Lein[1]

The transcriptional underpinnings of brain development remain poorly understood, particularly in humans and closely related non-human primates. We describe a high-resolution transcriptional atlas of rhesus monkey (*Macaca mulatta*) brain development that combines dense temporal sampling of prenatal and postnatal periods with fine anatomical division of cortical and subcortical regions associated with human neuropsychiatric disease. Gene expression changes more rapidly before birth, both in progenitor cells and maturing neurons. Cortical layers and areas acquire adult-like molecular profiles surprisingly late in postnatal development. Disparate cell populations exhibit distinct developmental timing of gene expression, but also unexpected synchrony of processes underlying neural circuit construction including cell projection and adhesion. Candidate risk genes for neurodevelopmental disorders including primary microcephaly, autism spectrum disorder, intellectual disability, and schizophrenia show disease-specific spatiotemporal enrichment within developing neocortex. Human developmental expression trajectories are more similar to monkey than rodent, although approximately 9% of genes show human-specific regulation with evidence for prolonged maturation or neoteny compared to monkey.

The primate brain develops through a series of stereotyped processes that are conserved across mammals[1], including the specification, migration, and maturation of diverse cell types and the formation and refinement of functional neuronal circuits. There are also primate-specific features of brain development that increase anatomical[2], cognitive[3], and behavioural complexity[4], and may explain why many human neurological and neuropsychiatric diseases are inadequately modelled in rodents[5]. These features include a larger cortical progenitor pool in the outer subventricular zone not present in rodents[2] and protracted myelination[6], synapse production[7], and pruning[8]. Rhesus monkeys and humans share a greatly expanded neocortex and specialization of areas (most notably primary visual cortex[2]), compared to mouse brains, reflecting the more recent common ancestor of humans and rhesus monkeys (25 million years ago) than humans and mice (70 million years ago)[9]. Likewise, the rhesus monkey and human brain[10] share more similar patterns of gene expression than do mouse and human brains[11]. The rhesus monkey thus provides a valuable proxy for human brain development, particularly during prenatal and early postnatal development stages that are difficult to sample in humans, and also provides a comparator to study human-specific features such as prolonged maturation or neoteny[6,12,13].

Molecular programs responsible for brain development remain incompletely understood in any species, due to the spatiotemporal complexity of these processes and the resource intensity of methods needed to probe them. Transcriptome-based approaches have accelerated understanding of variation in gene expression programs related to brain structure and function in adult and developing humans[14–17] and rhesus monkeys[10,18], albeit with limited anatomical resolution and developmental coverage. Recent studies in adult mice[19,20] and humans[21] have profiled individual cortical cells and demonstrated robust transcriptional differences between neuronal and non-neuronal cell types and large-scale changes over the course of development. Although these approaches offer cellular resolution in targeted domains, a global picture of gene expression changes over development across the complete cellular milieu has been lacking.

This project had the aim of creating a transcriptional atlas of non-human primate brain, combining fine anatomical precision with dense temporal coverage across prenatal and postnatal development

[1]Allen Institute for Brain Science, Seattle, Washington 98109, USA. [2]Department of Psychiatry and Behavioral Science, California National Primate Research Center, The M.I.N.D. Institute, University of California, Davis, Sacramento, California 95817, USA. [3]Department of Radiology, University of Washington, Seattle, Washington 98195, USA. [4]Department of Physiology, Anatomy and Genetics, University of Oxford, South Parks Road, Oxford OX1 3QX, UK. [5]Human Genome Sequencing Center and Department of Molecular and Human Genetics, Baylor College of Medicine, Houston, Texas 77030, USA. [6]Center for Integrative Brain Research, Seattle Children's Research Institute, Seattle, Washington 98101, USA.
*These authors contributed equally to this work.

in regions associated with neuropsychiatric disease. These transcriptional data are complemented by imaging and histology-based anatomical reference and cellular-resolution *in situ* hybridization (ISH) data sets, all publicly accessible through the NIH Blueprint Non-Human Primate (NHP) Atlas (http://www.blueprintnhpatlas.org and http://www.brain-map.org).

Spatiotemporal transcriptome analysis

This resource characterizes rhesus monkey forebrain development with three modalities: (1) anatomical reference data sets consisting of magnetic resonance imaging (MRI) and corresponding densely sampled Nissl stains; (2) cellular-resolution gene expression data generated with a high throughput ISH platform; and (3) fine anatomical resolution transcriptome time series data generated with a combination of laser microdissection (LMD) and DNA microarrays (Fig. 1a). Molecular analyses focused on discrete progenitor and postmitotic cell populations in neocortex (medial prefrontal and visual cortical areas), hippocampus, striatum, and amygdala (Fig. 1b and Supplementary Tables 1 and 2). Ten developmental time points (the ten 'ages' referred to hereafter) were chosen to correspond to peak periods of neurogenesis for neurons destined for different layers and glial cell types of V1 (prenatal)[22] and major developmental epochs: neonate, infant, juvenile, and young adult (Fig. 1c, postnatal). Anatomical parcellation at each time point was based on prior work in monkey and human brain development[2,17] (Extended Data Fig. 1). Canonical genes marking different neural cell types showed expected spatiotemporal patterning across development, shown as heat maps (Fig. 1d and Extended Data Fig. 2) laid out following the anatomical organization in Fig. 1c.

To gain a high-level understanding of transcriptional dynamics during cortical development, we represented the similarity between cortical samples using multidimensional scaling (MDS) based on correlated expression (Fig. 1e–g). Layer and age explained almost 90% of the variation across all samples ($n = 922$; Fig. 1e) and prenatal samples ($n = 542$; Fig. 1f). To examine smaller differences between neuronal populations (grey circles in Fig. 1f), we repeated the MDS analysis only on V1 cortical layers (containing different types of excitatory neurons; $n = 175$; Fig. 1g). Transcriptional similarity of layers reflects spatial proximity and birth date, as described in adult rhesus monkey[10]. Moreover, continuous variation across prenatal development suggests gradual changes in gene expression.

There were few sex-related differences in expression, although the study was not powered to detect subtle differences restricted to specific brain regions or developmental stages. Only one autosomal gene (*LOC693361*, NADH-ubiquinone oxidoreductase chain 1-like) showed robust increased expression in males across brain regions during prenatal development (Extended Data Fig. 3 and Supplementary Table 3). However, the microarray probe for *LOC693361* also targets an unannotated region of rhesus monkey Y chromosome[23], so there are probably no autosomal genes with persistent male- or female-specific expression differences across development.

Developmental transcriptional dynamics

Previous work has demonstrated that different cortical layers have distinct transcriptomic profiles both in adult and developing cortex, where the largest differences are seen between germinal and postmitotic cell populations[17]. In grossly dissected developing human prefrontal cortex, gene expression changes fastest prenatally and slows sharply just after birth[14]. If dividing cells drive most expression change, then depletion of the progenitor pool would explain decreased rates. In contrast, we find that all layers of V1 and prefrontal cortex (anterior cingulate gyrus; ACG) have similar rates of expression change across development (Fig. 2a). Thus transcriptional programs change dramatically both in progenitor cell populations as they give rise to different neuronal and non-neuronal cell types, as well as in postmitotic neuronal cell types as they differentiate and mature into adulthood.

Similar developmental trajectories were seen in hippocampus, basal ganglia and amygdala (Extended Data Fig. 4a). However, the genes changing dynamically could differ by region or age. We identified the top 1,000 genes with the largest increase and decrease in relative expression between all pairs of ages for each structure and visualized the overlap of these gene lists as a heat map (Fig. 2b). This threshold was selected because at least 1,000 genes significantly changed expression (ANOVA false discovery rate (FDR) <0.05, fold change >1.25) between all adjacent ages in the majority of regions (Extended Data Fig. 4b). Genes changing over time were remarkably synchronized across different cell populations. At every age, approximately half of the top increasing and decreasing genes were shared by most brain regions, and unsupervised clustering grouped samples almost perfectly by age (age index bar in Fig. 2b). Genes increasing with age showed substantial overlap across ages within, but much less between, prenatal and postnatal ages. This suggests that distinct transcriptional programs are active in prenatal and postnatal development, and that many of these programs progress gradually. At early stages, samples grouped by proliferative state independently of brain region (mitotic index bar in Fig. 2b) reflecting a common set of cell division genes. Postnatally, samples grouped more by anatomical structure, reflecting increased regional identity during brain maturation (structure index bar in Fig. 2b).

To interpret these dynamic gene expression patterns, we searched for enrichment of Gene Ontology (GO) terms at each region and age (Supplementary Tables 4 and 5) and represented significant enrichments as heat maps ordered as above (Fig. 2c). For example, genes related to onset (positive regulation) of axonal projection were enriched during prenatal periods as expected. Surprisingly, this process appears to be actively repressed during late postnatal development, as genes associated with offset (negative regulation) of axonal projection showed increased expression from juvenile (12 months) to young adult (48 month) stages. Processes associated with synapse development are temporally enriched in late prenatal and early postnatal periods, and also synchronized between presynaptic (synaptic vesicle localization) and postsynaptic (dendrite development) neurons. Interestingly, the region-specific blocks of coordinated expression in postnatal visual cortex (V1 and V2) and hippocampus (Fig. 2b, arrows) were enriched for autophagy genes (Extended Data Fig. 4c), which may reflect early dendritic spine pruning[24] and grey matter volume reduction[25] in visual cortex.

Regional timing of biological processes

Some biological processes, such as synaptogenesis and myelination, are protracted over development[6,24], and we find that process activation, inferred from increased expression of process-related genes at each age ('increasing'), is longer than inactivation ('decreasing'; Fig. 3a). Biological processes persist longer in all regions pooled together (black lines) than in any individual region (coloured lines), so developmental timing must vary between regions. We quantified synchrony between pairs of regions as the proportion of ages during which a process is active in both versus either region, for processes active in all regions at some age (for example, Extended Data Fig. 5a). Remarkably, despite major differences in cellular and functional makeup of brain regions sampled, all pairs of regions showed similar degrees of synchrony across all GO terms. This synchrony was centred on overlap of approximately half of all ages (Extended Data Fig. 5b), far greater than expected by chance. Few processes—cell proliferation, projection, and adhesion—were synchronized across all regions and ages (Supplementary Table 5).

Processes usually started before birth in all regions, but sometimes at strikingly different times in different regions (Fig. 3b). Consistent with known early maturation of subcortical circuits[1], rank ordering age of onset for each process across regions showed earlier subcortical onset, particularly in the amygdala, and similar timing for neocortex and hippocampus (Extended Data Fig. 5c). For example, subcortical globus pallidus is myelinated before cortical white matter[26] and shows early increased expression of genes specific to myelinating oligodendrocytes

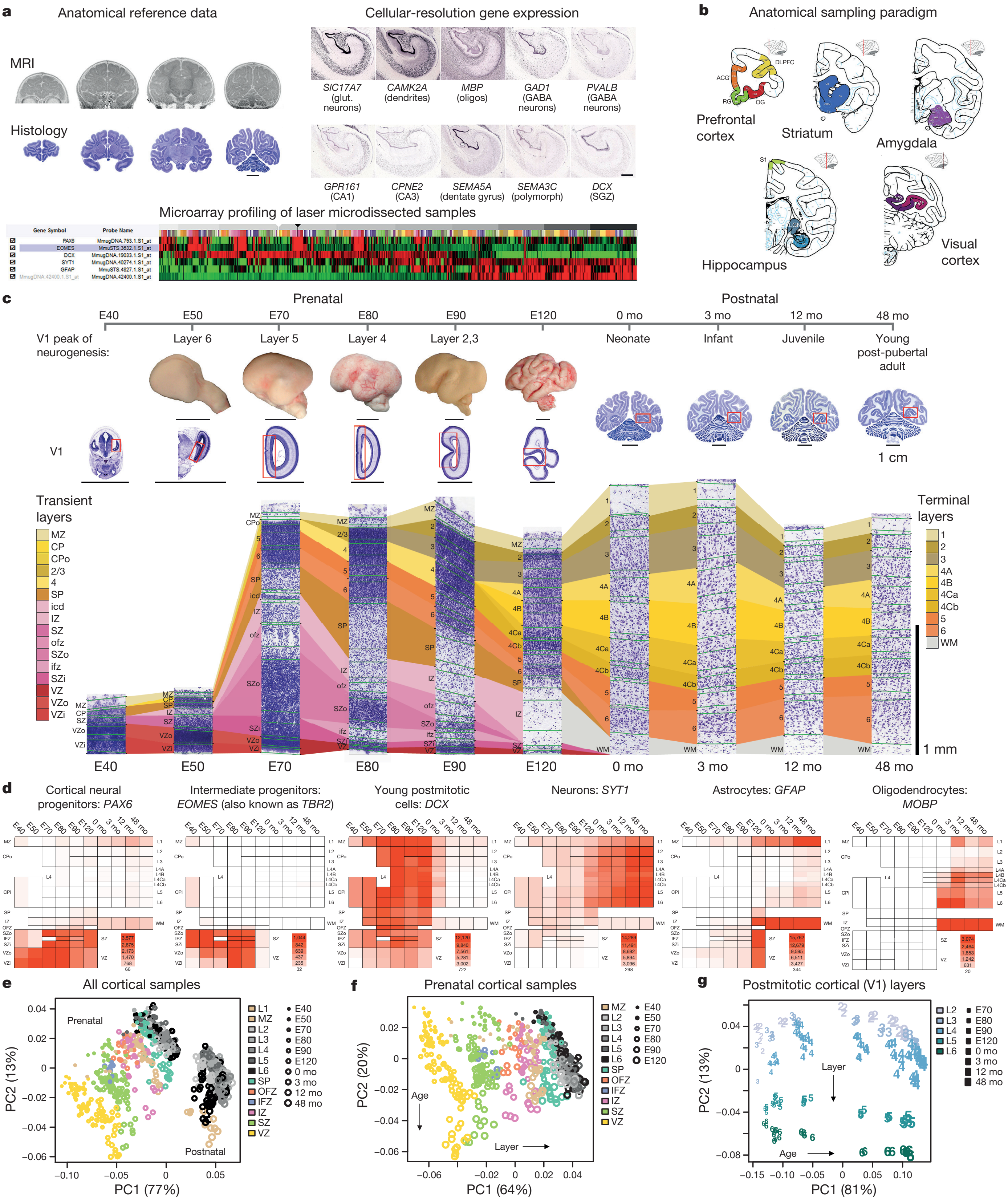

Figure 1 | High-resolution transcriptional profiling of rhesus monkey brain development. a, Neuroimaging, histological and transcriptome data components. **b**, Brain regions analysed. **c**, Primary visual cortex (V1) sampling paradigm for transcriptome analysis spanning ages from 40 embryonic days (E40) to 48 months (mo) after birth, with salient developmental events or stages noted (top row). Whole brain or hemisphere sections are shown for each age (V1, red box outline), as well as a high magnification Nissl image detailing laminar microdissections. Cortical layers profiled at each stage are colour-coded by predominant mitotic (red, pink) or postmitotic (orange, yellow, tan) cell makeup. **d**, Heat maps of canonical cell type marker gene expression organized anatomically as in **c**. **e**–**g**, Multi-dimensional scaling (MDS) plots showing the first two principal axes of variation for all cortical samples ($n = 922$) (**e**), prenatal samples ($n = 542$) (**f**) and postmitotic layers in V1 ($n = 175$) (**g**). Scale bars in **c**: 1 cm (top and middle rows) or 1 mm (bottom row). Structure abbreviations are given in Supplementary Table 1.

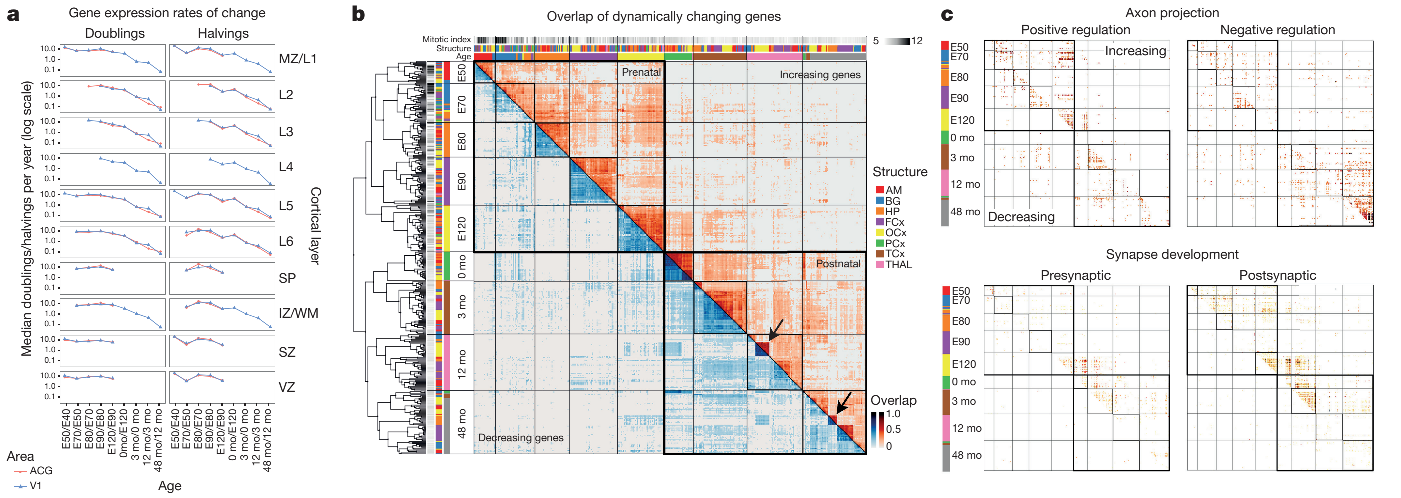

Figure 2 | Transcriptional dynamics across brain regions and ages. **a**, Similar decreasing rates of gene expression change across cortical layers (rows, ordered from basal to apical) and areas (anterior cingulate gyrus, ACG, red; primary visual cortex, V1, blue). **b**, Overlap of temporally dynamic genes across brain regions and ages. Proportion of the top 1,000 genes with increasing (red, upper triangle) or decreasing (blue, lower triangle) expression for each region between pairs of adjacent ages (for example, E50 compared to E40) that are shared with other ages and regions. Note large overlap between all regions at each age and within prenatal and postnatal periods. Arrows highlight region-specific blocks of coordinated expression. AM, amygdala; BG, basal ganglia; HP, hippocampus; FCx, frontal; OCx, occipital; PCx, parietal cortex; TCx, temporal cortex; THAL, thalamus. **c**, Timing of neuronal connectivity-related events revealed by enrichment of GO terms in overlapping gene lists from **b**.

(*MOG*, *MOBP*, and *ERMN*) (Fig. 3c and Extended Data Fig. 5d). Interestingly, three other oligodendrocyte markers (*MAL*, *ASPA*, and *OPALIN*) turned on synchronously in all regions, suggesting a temporal and regional dissociation of different stages of myelination.

Late emergence of mature cortical identity

The neocortex is composed of diverse neuronal subtypes organized into layers that have distinct connectivity and transcriptional signatures in the adult[10,20,27] with graded and discrete variation between cortical areas[15,16,28]. A neuron develops its mature molecular identity through cell-autonomous processes and environmental interactions during migration, process extension, and synapse formation. If early generated neurons closely resemble their mature states, then environmental interactions must have small effects on their terminal molecular identities. As we found extensive expression changes within postmitotic cortical layers (see Fig. 2a), there is a role for either or both of these mechanisms.

To examine the emergence of mature laminar signatures, we compared layer-enriched expression patterns across development from the earliest stage at which all postmitotic layers are present (embryonic day 80 (E80)) to adulthood. We calculated the average expression correlation, across layers and between all pairs of ages, of the top 2.5% of genes most specific for each layer in V1 at each age (see Methods and Supplementary Table 6). Adult identity emerged gradually (Fig. 4a), as evidenced by decreased expression similarity with increased age separation. In fact, laminar expression patterns in young adulthood barely resembled mid-fetal cortex ($R < 0.1$).

These correlation trends result from nearly complete shifts in genes showing robust layer-specific expression (fold change >1.5; Fig. 4b). Most genes were enriched only for a subset of contiguous ages at early, middle, and late stages, while few genes showed persistent laminar enrichment (Fig. 4b, c and Supplementary Table 7). Sets of laminar genes tile smoothly across development, suggesting a graded emergence of functional characteristics of neuronal subtypes, as well as shifting proportions of subtypes within layers. Genes with early laminar expression are enriched for GO terms related to early developmental events such as neuron differentiation ($P = 1.6 \times 10^{-7}$) and axon generation ($P = 6.7 \times 10^{-6}$), whereas later laminar genes are enriched for axon guidance ($P = 6.5 \times 10^{-5}$) and innervation ($P = 9.8 \times 10^{-6}$).

Different anatomical and functional neocortical areas have distinct gene expression patterns in the adult, most prominently in V1 (refs 15, 16, 28). During development, intrinsic (protomap)[29] and extrinsic (protocortex)[30] factors shape cortical area identity. To ask whether the temporal dynamics of areal expression support intrinsic versus extrinsic areal specification, we first identified genes differentially expressed between caudal (V1, blue) and rostral (ACG, red) cortex in different layers at each developmental stage (Fig. 4d and Supplementary Table 8). More genes were differentially expressed between cortical areas in postmitotic layers during late postnatal than during prenatal development. These genes were enriched for cell adhesion ($P = 3.9 \times 10^{-6}$) and synaptic transmission ($P = 7.3 \times 10^{-4}$) GO terms, suggesting a role for extrinsic factors related to the functional maturation of cortical circuitry. Developmental process timing varies across primate cortex, with neurogenesis occurring earlier in frontal than caudal cortex, but circuit maturation persisting later in frontal cortex[6,8], and this was recapitulated by an even more protracted emergence of enriched genes in ACG (12 to 48 months) compared to V1 (3 to 12 months).

To test for genes that may contribute to intrinsic specification, we searched for genes with persistent areal enrichment beginning before the arrival of thalamic[31] or other extrinsic inputs. Although 38% of genes showed regional differences, only 1% were persistent over development (Supplementary Table 8). These genes were primarily expressed in postmitotic cortical layers, for example *CBLN2* (ref. 17), and only 20 genes (0.2%) were expressed in germinal zones, including the well-known caudal-to-rostral gradient genes *FGFR3* (ref. 17, 29) and *NR2F1* (also known as *COUP-TFI*)[29]. Thus, although there is evidence for a small number of genes clearly reflecting early intrinsic areal specification, there are many more adult differences that could be due to extrinsic interactions and activity-dependent mechanisms[32].

Some areal differences are probably due to differences in the proportion and maturation state of specific cell types, such as dividing neural progenitors and postmitotic neurons and glia. We identified spatiotemporal locations with significant enrichment in V1 or ACG for markers of cell cycle (that is, actively dividing progenitor cells), GABAergic and glutamatergic neurons in adult mouse V1, and astrocytes (Fig. 4e–h). Cell cycle markers were enriched in V1 subventricular zone from E80 to E90 (Fig. 4e), reflecting extended generation of superficial excitatory neurons in V1 relative to ACG. Likewise, markers for excitatory neurons (Fig. 4g) were enriched in ACG prenatally, corresponding to earlier generation and maturation of these cells. Postnatal enrichment in V1 is probably secondary to using markers derived

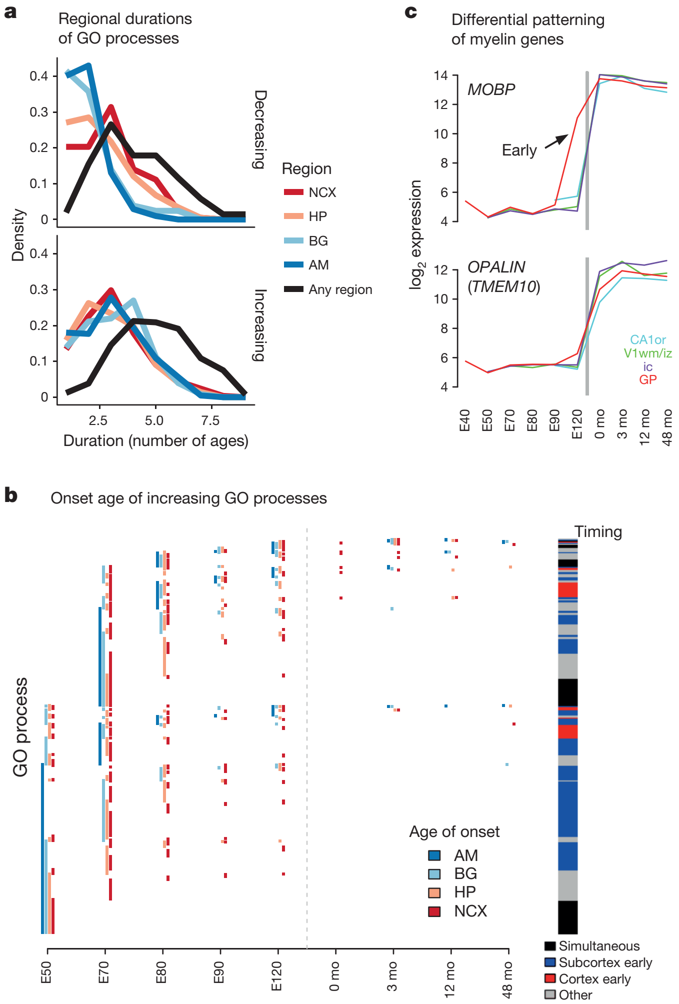

Figure 3 | Variable onset of biological processes between brain regions. **a**, Prolonged duration of biological GO processes. Number of ages at which increasing and decreasing GO processes are active in each region (colours) or in any region (black). **b**, Synchronous and asynchronous onset of GO processes between regions, mainly beginning in prenatal development. Left: age of onset for all increasing GO processes ordered by onset in subcortical and then cortical regions (AM, BG, HP, then neocortex (NCX)). Right: GO processes predominantly begin earlier in subcortical than cortical regions. **c**, Early onset (arrow) of mature oligodendrocyte marker *MOBP* in subcortical globus pallidus (arrow) compared to cortical myelin-enriched regions. Other myelin genes such as *OPALIN* show synchronous developmental timing. CA1or, hippocampal CA1 stratum oriens; V1 iz/wm, intermediate zone/white matter; ic, internal capsule.

from adult mouse V1. Astrocyte marker enrichment in prenatal ACG progressed from proliferative to postmitotic layers (Fig. 4h), tracking astrocyte generation and migration in these layers. Finally, markers of inhibitory GABAergic interneurons showed early enrichment in V1 subventricular zone (SZ), followed by ACG enrichment in several layers (Fig. 4f), a potential signature of early interneuron migration from medial ganglionic eminence to caudal cortex.

The majority of areal genes showed intermediate expression in primary somatosensory cortex (S1), located approximately midway between rostral ACG and caudal V1 (Extended Data Fig. 6). Therefore, rostro-caudal expression gradients, rather than specific features of ACG and V1, probably drive many of these areal expression differences.

Mapping disease genes to development

Highly heritable but genetically complex neurodevelopmental disorders will be more tractable if we can identify common pathways linking many candidate risk genes. For example, recent work on autism spectrum disorder (ASD) demonstrated that candidate genes are co-expressed in mid-fetal human cortical neurons[17,33,34] and converge on synaptic development pathways. Large-scale genetic association studies have identified high-confidence risk genes associated with primary autosomal recessive microcephaly (MCPH), ASD, intellectual disability, and schizophrenia. We localized these disease genes in developing cortex using this new high-resolution map.

We used weighted gene co-expression network analysis (WGCNA) to identify sets of genes with correlated patterning (modules) in cortical samples at each age, linked modules with overlapping genes between adjacent ages, and annotated modules for enrichment in different cortical layers and cell types (Fig. 5a and Supplementary Table 9). Next, we tested disease gene sets for significant enrichment (hypergeometric test, empirically corrected $P < 0.1$). As expected, MCPH genes showed early- to mid-fetal enrichment in neuronal progenitor-enriched modules (Fig. 5b), where they are positioned to alter cell cycle kinetics to reduce neuron numbers and brain size. Many ASD genes showed coordinated expression in postmitotic neurons prenatally (Fig. 5c), as previously reported[17,33,34], but also postnatally. In contrast, schizophrenia genes were selectively enriched only in postmitotic neuronal modules from infancy through adulthood (Fig. 5d).

Intellectual-disability-associated genes were not enriched in any gene modules, consistent with the view that disruption of many biological pathways can undermine cognitive development[34]. To investigate whether these diverse molecular pathways converge on intermediate phenotypes within intellectual disability such as structural brain malformations, we looked for correlated expression among the 71 intellectual disability genes across prenatal and postnatal cortex. We identified four major expression patterns: (1) postnatal cortical plate, (2) prenatal germinal layers, (3) prenatal subventricular zone and cortical plate, and (4) more complex patterns spanning development (Fig. 5e). Consistent with the module analysis above, MCPH-associated genes had significantly similar expression profiles (multivariate distance matrix regression, $P < 0.001$) and were enriched in prenatal germinal zones in clusters 2 and 3 in either the ventricular zone or subventricular zone. In contrast, other phenotypes did not share expression patterns, including cortical atrophy, seizures and even microcephaly with other brain malformations. Furthermore, genes with similar patterns can give rise to different phenotypes. *ASXL3* and *GRIP1* are co-expressed ($R = 0.80$) in cluster 3, but are associated with MCPH and corpus callosum agenesis, respectively.

Human-specific developmental trajectories

Humans exhibit unique cortical and cognitive developmental trajectories compared to other mammals[5] that are probably correlated with differences in gene expression. To identify conserved and divergent genes, we compared gene expression trajectories across prenatal and postnatal development in frontal cortex between rat, rhesus monkey, and two independent human data sets, normalizing timescales by developmental event scores[1]. Expression conservation varied across species (Kruskal–Wallis rank sum test, $P < 10^{-21}$), with greater similarity within humans than within primates (Wilcoxon signed rank test, $P < 10^{-6}$), as expected based on evolutionary distance (Fig. 6a). Surprisingly, there was no significant difference in conservation of rat trajectories with either human or rhesus monkey, indicating transcriptional patterning has evolved at the same average rate in human and rhesus monkey since our last common ancestor. On average, 69% of genes had conserved expression trajectories ($R > 0.5$) across all three species, and genes with the most dynamic expression change over development were even more highly conserved (Extended Data Fig. 7a, b). For example, *EMX2*, a transcription factor critical to cortical arealization[35], and *CNTN1*, a cell adhesion gene that guides neuronal migration and connectivity (Fig. 6b), are highly conserved.

A minority (13%) of genes differed between primates and rat (validated for a subset of genes in developing mouse; Supplementary Table 10) and approximately 9% had human-specific expression trajectories.

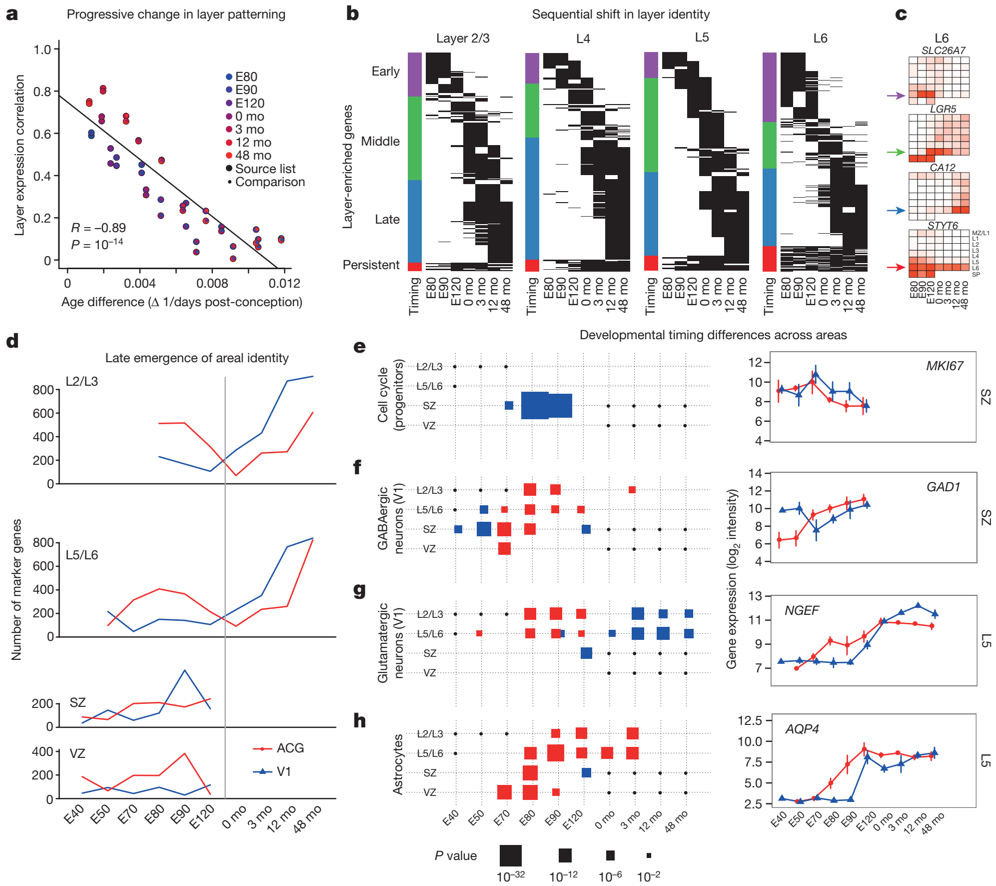

Figure 4 | Protracted maturation of neocortex through young adulthood. a, Expression patterns of genes best marking each cortical layer progressively change with time. Each dot represents the average across-layer expression correlation of the 10% of genes best distinguishing layers at one age (source list) with their expression levels in another age (comparison). Values are plotted against a scaled difference in age. **b**, Layer-enriched gene expression shows progressive and extensive change with age. Binary heat map showing expression of layer-enriched genes (rows) across ages (columns). Genes are ordered and divided based on the median age of laminar expression into four chronological groups: early (median age < E120), middle (E120–3 months), late (>3 months) and persistent. **c**, Developmental expression of representative genes from each chronological group in layer 6. **d**, Number of genes differentially expressed between rostral (ACG) and caudal (V1) cortex in superficial (L2/3), deep (L5/6) and proliferative (SZ, VZ) layers across development. Most differences are found in postmitotic layers during early prenatal and late postnatal development. **e**–**h**, Genes marking specific cell classes show regional enrichment consistent with earlier neurogenesis and gliogenesis in ACG compared to V1. Left column: enrichment of regional genes (**d**) with markers for cell cycle (progenitors) (**e**); GABAergic (**f**) and glutamatergic (**g**) neurons in V1; and astrocytes (**h**). Size of box indicates significance of cell type enrichment in a given layer, region, and age. Right column: expression levels (mean ± s.e.) of canonical marker genes for each cell type in V1 (blue) and ACG (red).

The proportion of genes showing different conservation patterns was robust to gene selection and correlation threshold (Extended Data Fig. 7b). Some of these differences were dramatic; for example, *BMP3* decreases over primate development but increases in rodents (Fig. 6b). *BMP3* is a *WNT* signalling growth factor that has been linked to craniofacial variation in dogs[36]. *CNTN2*, a close family member of the conserved adhesion gene *CNTN1*, likewise shows opposite developmental trajectories in primates and rodents. In both human data sets, *LGALS1* and *LIN7A* increase or decrease expression, respectively, in opposite directions to other species. *LGALS1* has a different adult laminar pattern of cortical expression in humans compared to mice[11], whereas deletion of *LIN7A* is associated with human intellectual disability and disrupted neuronal migration and axonal pathfinding in mouse[37].

Some aspects of cortical development, such as myelination[6] and synaptic pruning[8], are protracted or neotenous between cortical areas or between species. Reasoning that abrupt changes in expression may represent important developmental milestones, we compared developmental timing by identifying distinct changes in expression trajectories, or breakpoints. A total of 179 increasing and 179 decreasing genes met these criteria in all three species, being well fit by segmented linear regression (Supplementary Table 11). Consistent with different developmental rates of these species, breakpoints for genes with increasing (Fig. 6c) and decreasing (Extended Data Fig. 7c) expression often occurred earliest in rat, at intermediate times for rhesus monkey, and latest in human. Almost half (81) of genes with increasing expression were synapse related (dashed lines, Fig. 6c), and breakpoints coincided with ages of peak synaptic density estimated in these species (shaded rectangles, Fig. 6c and Extended Data Fig. 7d). There was no significant difference in the breakpoints for synapse-related genes in human V1 versus prefrontal cortex, and only a short delay in rhesus monkey V1 (42 days, $P = 9.6 \times 10^{-9}$, Extended Data Fig. 7e), consistent with synchronous synaptogenesis reported in primates[7,38–40]. A later study reported protracted synaptogenesis in human[41], but this study suffered from sparse sampling and no statistical analysis and does not appear consistent with the bulk of evidence.

Although the timing of gene expression breakpoints (a change in the slope of a developmental trajectory) was largely conserved between species, particularly between rhesus monkey and rat (Extended Data Fig. 7f), human breakpoints were clearly bimodally distributed (Fig. 6c), suggesting that some genes had different developmental timing. For example, *OLIG1* is expressed in maturing oligodendrocytes and had a late breakpoint relative to rhesus monkey (Fig. 6d), consistent with prolonged myelination in several human cortical areas compared to rhesus monkey and chimpanzee[6]. Surprisingly, many more genes

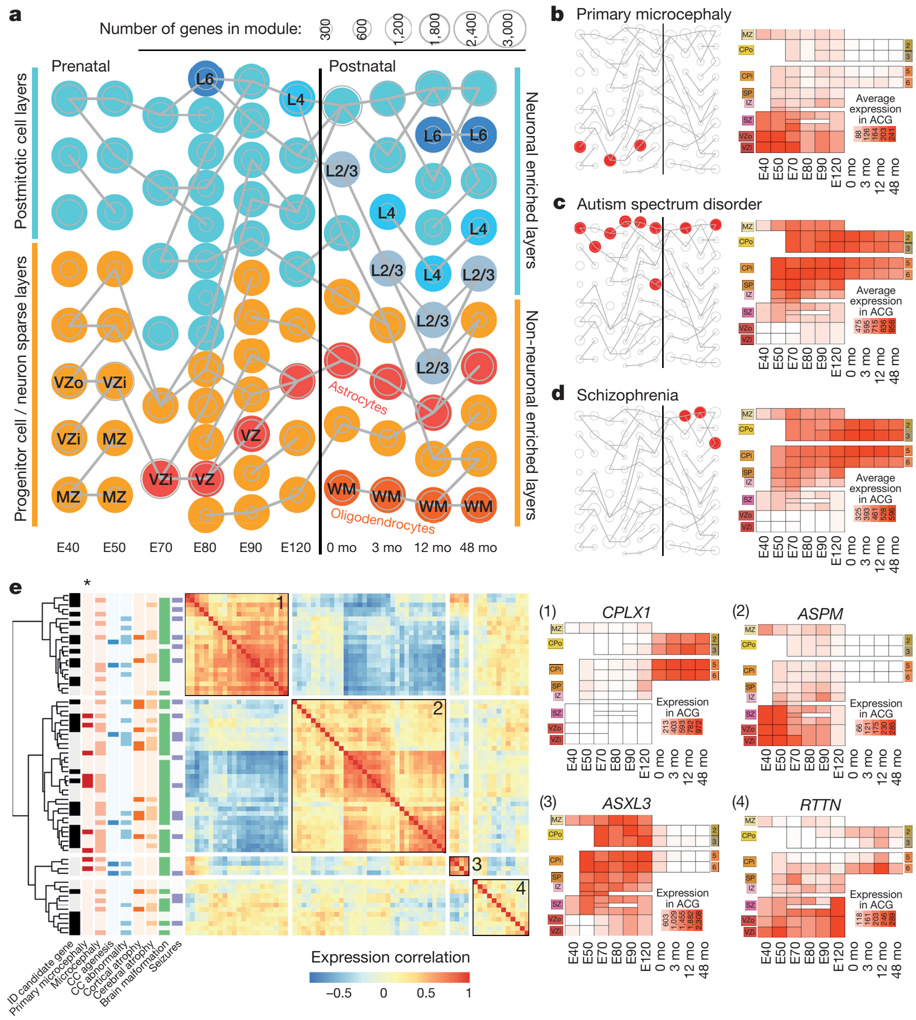

Figure 5 | Spatiotemporal localization of disease-specific associations in developing cortex. a, WGCNA gene co-expression networks (modules; Supplementary Table 9) based on pooled V1 and ACG samples ($n = 603$) analysed independently at each age (columns). Modules were tested for significant gene set enrichment and overlap with hypergeometric tests. Modules significantly enriched for markers of glial cell classes ($P < 10^{-15}$) or cortical layers ($P < 10^{-30}$) are colour-coded and annotated. Remaining modules are coloured or labelled based on maximal expression in postmitotic (neuron-enriched; cyan) layers or progenitor or largely non-neuronal (WM, layer 1; orange) layers. Modules from adjacent ages with the most highly significant gene overlap ($P < 10^{-50}$) are connected by grey lines. **b–d**, Left: modules significantly enriched for risk genes associated with neurodevelopmental disorders (empirically corrected $P < 0.1$; red discs). Right: average expression pattern of genes found in at least two enriched modules. **b**, Genes related to primary autosomal recessive microcephaly are enriched in early non-neuronal modules, and show maximal expression in prenatal ventricular zone. **c**, Genes related to autism spectrum disorder are enriched in modules associated with cortical neurons, and show highest expression in cortical plate across development. **d**, Genes related to schizophrenia show similar neuronal layer enrichment to autism genes, but restricted to postnatal ages. **e**, Left: genes related to intellectual disability (ID) are associated with different brain malformations and/or seizures and show four major expression patterns over cortical development. Right: expression heat maps of known and candidate disease genes representing developmental profiles of each cluster. Intellectual disability genes also associated with primary microcephaly are significantly enriched in cortical progenitor-enriched pattern 2 (*$P < 0.001$; multivariate distance matrix regression permutation test). CC, corpus callosum.

had an early rather than late breakpoint in human prefrontal cortex (Fig. 6e), in contrast to previous work[12,13] showing human-specific delayed peak expression in this brain region. However, we found that many early genes continued to increase expression through adulthood (Fig. 6e), such as *SYT7* (Fig. 6d), a presynaptic calcium-binding protein important for modifying neurotransmitter release[42]. In rhesus monkey, gene expression often did not change significantly after breakpoints. Genes with an early breakpoint and late maximal expression may mark developmental processes that are protracted in human relative to non-human primates and that underlie our extended cognitive development. Interestingly, we found this transcriptional signature of neoteny between species in both prefrontal cortex and V1, but much less so in evolutionarily older structures including hippocampus, amygdala and striatum (Fig. 6e and Extended Data Fig. 7g).

Discussion

The current project transcriptionally profiled primate brain development with fine anatomical detail from early gestation to young adulthood. Although expression rates of change decreased more than 100-fold over development, we observed small but coherent changes from juvenile to adult, a period of enormous cognitive change and susceptibility to neuropsychiatric disease. These changes related to the late emergence of mature laminar and areal signatures, biological pathways such as negative regulation of axonal pathfinding, and the appearance of gene modules significantly associated with ASD and schizophrenia.

Two unexpected characteristics of expression trajectories support extrinsic influences on developmental transcriptional regulation. First, there was a striking synchrony among genes changing in disparate brain regions and cell populations, suggesting a mechanism for global

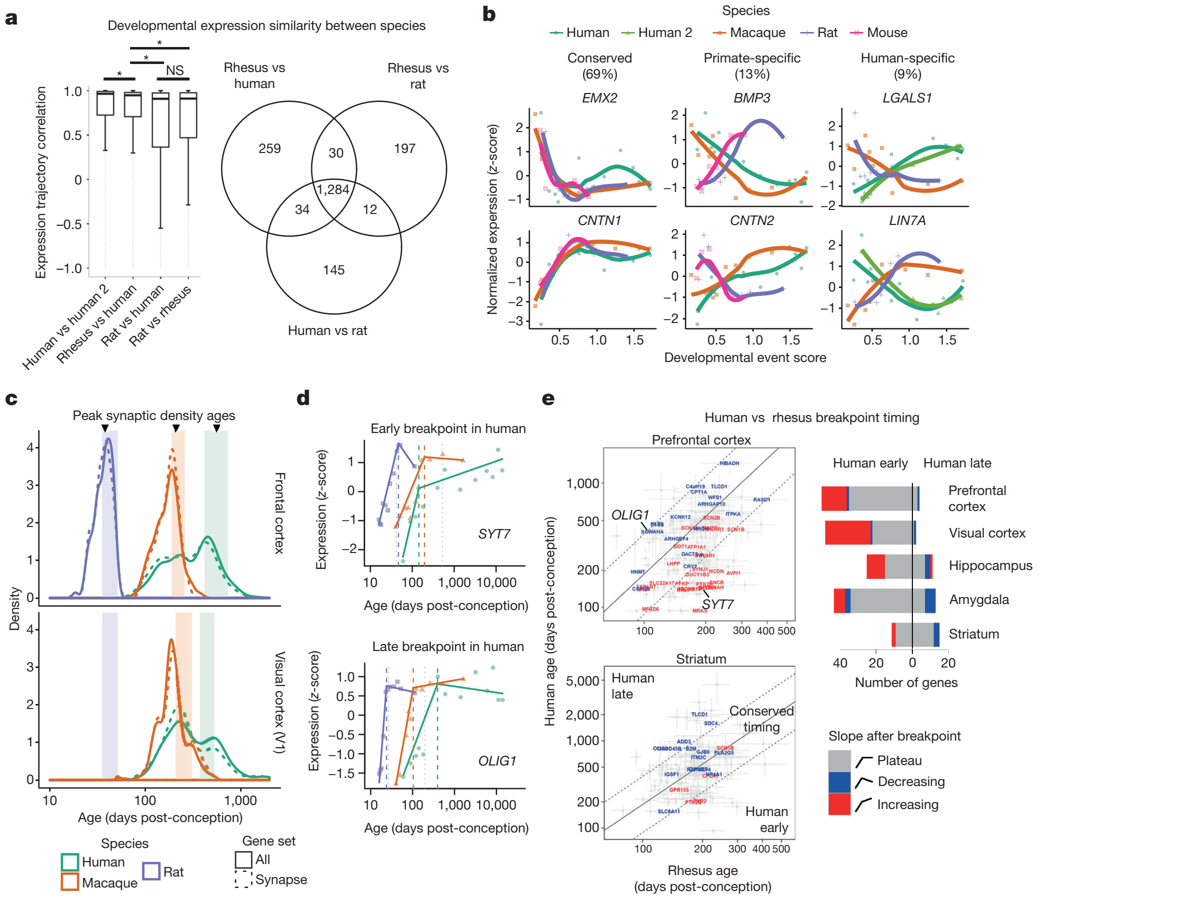

Figure 6 | Conserved and human-specific gene expression trajectories in frontal cortex. a, Left: box plots of pairwise correlations between developmental expression trajectories (median ± 25th and 75th percentiles, whiskers at 1.5 times the interquartile range) of orthologous genes profiled in rhesus monkey, rat and two human data sets. Kruskal–Wallis rank sum test, post hoc Wilcoxon signed rank paired tests: *$P < 0.001$ (Bonferroni-corrected), NS, not significant. Right: Venn diagram showing the number of conserved ($R > 0.5$) genes between each pair of species. **b**, Examples of conserved and species-specific gene trajectories. Colours and symbols are consistent in **b**–**d**. **c**, Distribution of breakpoint ages for 179 orthologues (solid lines) of which 81 were synapse related (dashed lines) in frontal cortex and V1. Shaded bars indicate periods of peak synaptic density (95% confidence intervals) in each species (Extended Data Fig. 7b). **d**, Genes with unexpectedly early (*SYT7*) and late (*OLIG1*) breakpoints in expression trajectories in human. Observed breakpoints (dashed lines) compared to expected breakpoints (dotted lines) based on timing in rhesus monkey. **e**, Many genes in human cortex have early breakpoints followed by prolonged increase in expression. Left: comparison of breakpoint timing (points with 95% confidence intervals) between human and rhesus shows a biased population of early breakpoint genes in human cortex but not striatum. Many of these early breakpoint genes continue to increase expression through young adulthood (red) in contrast to genes with relatively conserved timing that tend to plateau (grey) or decrease (blue). Ages corresponding to equivalent (solid lines) or nearby (dashed lines) developmental stages (event scores within ± 0.2; see Methods) in human and rhesus monkey are shown. Right: bar plot summarizing the number of genes that have an early or late breakpoint in human in different brain regions.

regulation such as circulating hormones. Second, the surprisingly late acquisition of adult-like cortical areal and laminar molecular phenotypes points to an important role for contextual and activity-dependent mechanisms in sculpting mature cellular phenotypes[43,44].

We show that 22% of genes have different developmental trajectories in rat and human, comparable to 25% of genes that have different laminar patterns in adult mouse and human cortex[11]. In contrast, approximately 9% of genes have different trajectories in rhesus monkey and human, including genes with delayed peak expression solely in human cortex. Therefore, rhesus monkey is an important comparator for understanding human-specific features of brain development, but cannot fully model protracted circuit formation and associated diseases that are seen only in humans.

A recently expanded set of ASD candidate genes[45] were significantly enriched in newborn neurons during prenatal development, as previously reported[17,33,34], but also enriched throughout postnatal development. Schizophrenia risk genes were also enriched in neurons but not until infancy, suggesting a larger role for dysfunction in circuit refinement than prenatal processes such as neurogenesis. Schizophrenia and ASD were enriched in the same neuron-enriched module in infancy despite only 5% overlap in candidate genes, pointing to a shared aetiology that is being increasingly appreciated[46].

This data resource (http://www.blueprintnhpatlas.org and http://www.brain-map.org) has many potential applications. For example, it could be used to establish an *in vivo* baseline against which to compare the identity and maturity of *in vitro* stem-cell-derived neurons[47]. Recent technical advances enable profiling the full transcriptome[19–21], epigenome[48], and ultimately proteome of single cells. These techniques promise to refine this broad survey to a causal understanding of molecular programs driving the complete lineage of primate brain cells and the maturation of specific neuron types in functional circuits.

Online Content Methods, along with any additional Extended Data display items and Source Data, are available in the online version of the paper; references unique to these sections appear only in the online paper.

Received 6 August 2015; accepted 10 June 2016.
Published online 13 July; corrected online 20 July 2016
(see full-text HTML version for details).

1. Workman, A. D., Charvet, C. J., Clancy, B., Darlington, R. B. & Finlay, B. L. Modeling transformations of neurodevelopmental sequences across mammalian species. *J. Neurosci.* **33,** 7368–7383 (2013).

2. Smart, I. H. M., Dehay, C., Giroud, P., Berland, M. & Kennedy, H. Unique morphological features of the proliferative zones and postmitotic compartments of the neural epithelium giving rise to striate and extrastriate cortex in the monkey. *Cereb. Cortex* **12,** 37–53 (2002).
3. MacLean, E. L. *et al.* The evolution of self-control. *Proc. Natl Acad. Sci. USA* **111,** E2140–E2148 (2014).
4. Caldwell, C. A. & Whiten, A. in *Primates in Perspective* 652–662 (Oxford Univ. Press, 2011).
5. Izpisua Belmonte, J. C. *et al.* Brains, genes, and primates. *Neuron* **86,** 617–631 (2015).
6. Miller, D. J. *et al.* Prolonged myelination in human neocortical evolution. *Proc. Natl Acad. Sci. USA* **109,** 16480–16485 (2012).
7. Rakic, P., Bourgeois, J. P., Eckenhoff, M. F., Zecevic, N. & Goldman-Rakic, P. S. Concurrent overproduction of synapses in diverse regions of the primate cerebral cortex. *Science* **232,** 232–235 (1986).
8. Petanjek, Z. *et al.* Extraordinary neoteny of synaptic spines in the human prefrontal cortex. *Proc. Natl Acad. Sci. USA* **108,** 13281–13286 (2011).
9. Gibbs, R. A. *et al.* Evolutionary and biomedical insights from the rhesus macaque genome. *Science* **316,** 222–234 (2007).
10. Bernard, A. *et al.* Transcriptional architecture of the primate neocortex. *Neuron* **73,** 1083–1099 (2012).
11. Zeng, H. *et al.* Large-scale cellular-resolution gene profiling in human neocortex reveals species-specific molecular signatures. *Cell* **149,** 483–496 (2012).
12. Somel, M. *et al.* Transcriptional neoteny in the human brain. *Proc. Natl Acad. Sci. USA* **106,** 5743–5748 (2009).
13. Liu, X. *et al.* Extension of cortical synaptic development distinguishes humans from chimpanzees and macaques. *Genome Res.* **22,** 611–622 (2012).
14. Colantuoni, C. *et al.* Temporal dynamics and genetic control of transcription in the human prefrontal cortex. *Nature* **478,** 519–523 (2011).
15. Hawrylycz, M. J. *et al.* An anatomically comprehensive atlas of the adult human brain transcriptome. *Nature* **489,** 391–399 (2012).
16. Kang, H. J. *et al.* Spatio-temporal transcriptome of the human brain. *Nature* **478,** 483–489 (2011).
17. Miller, J. A. *et al.* Transcriptional landscape of the prenatal human brain. *Nature* **508,** 199–206 (2014).
18. Bakken, T. E. *et al.* Spatiotemporal dynamics of the postnatal developing primate brain transcriptome. *Hum. Mol. Genet.* **24,** 4327–4339 (2015).
19. Molyneaux, B. J. *et al.* DeCoN: genome-wide analysis of *in vivo* transcriptional dynamics during pyramidal neuron fate selection in neocortex. *Neuron* **85,** 275–288 (2015).
20. Zeisel, A. *et al.* Cell types in the mouse cortex and hippocampus revealed by single-cell RNA-seq. *Science* **347,** 1138–1142 (2015).
21. Darmanis, S. *et al.* A survey of human brain transcriptome diversity at the single cell level. *Proc. Natl Acad. Sci. USA* **112,** 7285–7290 (2015).
22. Rakic, P. Neurons in rhesus monkey visual cortex: systematic relation between time of origin and eventual disposition. *Science* **183,** 425–427 (1974).
23. Hughes, J. F. *et al.* Strict evolutionary conservation followed rapid gene loss on human and rhesus Y chromosomes. *Nature* **483,** 82–86 (2012).
24. Elston, G. N., Oga, T. & Fujita, I. Spinogenesis and pruning scales across functional hierarchies. *J. Neurosci.* **29,** 3271–3275 (2009).
25. Scott, J. *et al.* Longitudinal analysis of the developing rhesus monkey brain using magnetic resonance imaging: birth to adulthood. *Brain Struct. Funct.* **221,** 2847–2871 (2016).
26. Hasegawa, M. *et al.* Development of myelination in the human fetal and infant cerebrum: a myelin basic protein immunohistochemical study. *Brain Dev.* **14,** 1–6 (1992).
27. Sorensen, S. A. *et al.* Correlated gene expression and target specificity demonstrate excitatory projection neuron diversity. *Cereb. Cortex* **25,** 433–449 (2015).
28. Pletikos, M. *et al.* Temporal specification and bilaterality of human neocortical topographic gene expression. *Neuron* **81,** 321–332 (2014).
29. O'Leary, D. D. M. & Chou, S.-J. J. & Sahara, S. Area patterning of the mammalian cortex. *Neuron* **56,** 252–269 (2007).
30. De la Rossa, A. *et al. In vivo* reprogramming of circuit connectivity in postmitotic neocortical neurons. *Nat. Neurosci.* **16,** 193–200 (2013).
31. Rakic, P. Prenatal development of the visual system in rhesus monkey. *Phil. Trans. R. Soc. Lond. B* **278,** 245–260 (1977).
32. Tropea, D. *et al.* Gene expression changes and molecular pathways mediating activity-dependent plasticity in visual cortex. *Nature Neurosci.* **9,** 660–668 (2006).
33. Willsey, A. J. *et al.* Coexpression networks implicate human midfetal deep cortical projection neurons in the pathogenesis of autism. *Cell* **155,** 997–1007 (2013).
34. Parikshak, N. N. *et al.* Integrative functional genomic analyses implicate specific molecular pathways and circuits in autism. *Cell* **155,** 1008–1021 (2013).
35. Bishop, K. M., Goudreau, G. & O'Leary, D. D. Regulation of area identity in the mammalian neocortex by Emx2 and Pax6. *Science* **288,** 344–349 (2000).
36. Schoenebeck, J. J. *et al.* Variation of *BMP3* contributes to dog breed skull diversity. *PLoS Genet.* **8,** e1002849 (2012).
37. Matsumoto, A. *et al.* LIN7A depletion disrupts cerebral cortex development, contributing to intellectual disability in 12q21-deletion syndrome. *PLoS One* **9,** e92695 (2014).
38. Bianchi, S. *et al.* Synaptogenesis and development of pyramidal neuron dendritic morphology in the chimpanzee neocortex resembles humans. *Proc. Natl Acad. Sci. USA* **110** (Suppl 2), 10395–10401 (2013).
39. Huttenlocher, P. R. Synaptic density in human frontal cortex — developmental changes and effects of aging. *Brain Res.* **163,** 195–205 (1979).
40. Rakic, P., Bourgeois, J. P. & Goldman-Rakic, P. S. Synaptic development of the cerebral cortex: implications for learning, memory, and mental illness. *Prog. Brain Res.* **102,** 227–243 (1994).
41. Huttenlocher, P. R. & Dabholkar, A. S. Regional differences in synaptogenesis in human cerebral cortex. *J. Comp. Neurol.* **387,** 167–178 (1997).
42. Jackman, S. L., Turecek, J., Belinsky, J. E. & Regehr, W. G. The calcium sensor synaptotagmin 7 is required for synaptic facilitation. *Nature* **529,** 88–91 (2016).
43. Pouchelon, G. *et al.* Modality-specific thalamocortical inputs instruct the identity of postsynaptic L4 neurons. *Nature* **511,** 471–474 (2014).
44. De Marco García, N. V., Karayannis, T. & Fishell, G. Neuronal activity is required for the development of specific cortical interneuron subtypes. *Nature* **472,** 351–355 (2011).
45. Iossifov, I. *et al.* Low load for disruptive mutations in autism genes and their biased transmission. *Proc. Natl Acad. Sci. USA* **112,** E5600–E5607 (2015).
46. de Lacy, N. & King, B. H. Revisiting the relationship between autism and schizophrenia: toward an integrated neurobiology. *Annu. Rev. Clin. Psychol.* **9,** 555–587 (2013).
47. Stein, J. L. *et al.* A quantitative framework to evaluate modeling of cortical development by neural stem cells. *Neuron* **83,** 69–86 (2014).
48. Cusanovich, D. A. *et al.* Multiplex single cell profiling of chromatin accessibility by combinatorial cellular indexing. *Science* **348,** 910–914 (2015).

Supplementary Information is available in the online version of the paper.

Acknowledgements The authors thank the Allen Institute for Brain Science founders, P. G. Allen and J. Allen, for their vision, encouragement, and support. The authors also thank J. Montiel and W. Zhi Wang for their advice on developmental neuroanatomy and experimental design. We also wish to acknowledge the California National Primate Research Center (NIH Award Number RR00169) for providing tissues and Covance Genomics Laboratory (Seattle, Washington) for microarray probe generation, hybridization and scanning. The project was supported by NIH Blueprint for Neuroscience Research contract HHSN-271-2008-0047 (PI: E. Lein, Allen Institute for Brain Science) from the National Institute of Mental Health. Its contents are solely the responsibility of the authors and do not necessarily represent the official views of the National Institutes of Health or the National Institute of Mental Health.

Author Contributions T.E.B., J.A.M., S.-L.D., L.N., A.S., R.A.D., J.J.R., S.Sha., M.J.H., D.G.A., A.Be. and E.S.L. contributed significantly to the analysis. K.A.S., L.N., A.S., R.A.D., J.G.H., R.F.H., Z.M., C.D., D.G.A., A.Be. and E.S.L. contributed significantly to the experimental and technical design. T.E.B., J.A.M., T.L., S.Sha., and A.Be. contributed significantly to generation of the data. S.M.S., K.A.S., L.N., T.L., P.W., J.G.H., M.J.H., J.W.P., C.D., A.R.J., D.G.A., A.Be. and E.S.L. contributed significantly to supervision and management of the project. K.A., N.De., T.D., J.G., G.Gu., C.L.K., C.L., C.-K.L., P.D.P., T.R., K.R. and D.S. contributed to the analysis. N.De, T.A.D., A.E., J.G., R.A.G., G.Gu., D.R.H., A.H.-S., J.J., C.L.K., C.L., C.-K.L., F.L., J.N., J.R., Z.L.R. and W.B.W. contributed to the experimental and technical design. K.A., J.A., C.B., J.L.B., D.B., K.Bi., A.Bo., K.Br., S.B., E.B., S.Cal., A.C., S.Cat., M.C., J.C., N.De., T.A.D., N.Do., G.Ge., T.L.G., J.G., L.G., B.G., G.Gu., J.H., Z.H., N.H., R.H., M.K., A.K., C.L.K., C.L., C.-K.L., F.L., N.Ma., R.M., J.M., N.Mo., E.M., K.N., J.N., A.O., E.O., J.Pa., S.P., J.Pe., L.P., M.R., Z.L.R., T.R., B.R., K.R., D.R., M.S., N.Sh., S.Shi., N.Sj., A.J.S., R.T., L.V., U.W., W.B.W., C.Wh., J.W., R.Y. and B.L.Y. contributed to generation of the data. A.Bo., E.B., M.C., T.D., T.A.D., A.E., E.F., B.G., M.K., C.L., L.L., N.Ma., S.P., M.R. and A.J.S. contributed to supervision and management of the project. T.E.B., J.A.M. and E.S.L. wrote the manuscript.

Author Information Detailed technical protocol documents describing tissue processing and microarray profiling are available at the Allen Brain Atlas portal (http://www.brain-map.org) through the non-human primate link, or directly from the NIH Blueprint NHP Atlas website (http://www.blueprintnhpatlas.org), under the documentation tab. Microarray data can be viewed online by selecting microdissection under the microarray tab and can be downloaded under the download tab. Reprints and permissions information is available at www.nature.com/reprints. The authors declare no competing financial interests. Readers are welcome to comment on the online version of the paper. Correspondence and requests for materials should be addressed to E.S.L. (EdL@alleninstitute.org).

Reviewer Information *Nature* thanks P. Carninci and C. Sherwood and the other anonymous reviewer(s) for their contribution to the peer review of this work.

METHODS

No statistical methods were used to predetermine sample size, and the experiments were not randomized or blinded. More complete descriptions of the experimental and data processing methods are available in protocol documents at the NIH Blueprint NHP Atlas website (http://www.blueprintnhpatlas.org; documentation tab).

Animals. Frozen post-mortem tissue samples from prenatal rhesus macaque (*Macaca mulatta*) of predominantly Indian origin (Extended Data Table 1) were provided by the Time-Mated Breeding Program at the California National Research Primate Center (CNPRC; http://www.cnprc.ucdavis.edu). Prenatal brain material was acquired following fetectomy using standard operating procedures (SOPs) at the CNPRC. Timed pregnancy derived biological replicate specimens (2 males, 2 females) at each of six prenatal developmental stages (E40, E50, E70, E80, E90, and E120) were profiled. These time points were selected to coincide with peak periods of neurogenesis for the different layers of primary visual cortex based on birthdating experiments[22]. Frozen postmortem tissue samples from postnatal rhesus macaque were also provided by CNPRC. Brain regions were systematically collected from well-characterized rhesus monkeys born and raised at the CNPRC in outdoor, half-acre enclosures that provide a naturalistic setting and normal social environment. For transcriptome analysis, three male specimens at each of four postnatal developmental stages representing the neonate (0 months), infant (3 months), juvenile (12 months) and post-pubertal adult (48 months) were profiled. Extensive health, family lineage and dominance information were maintained on all animals. All procedures were approved by the Institutional Animal Care and Use Committee (IACUC) at UC Davis.

Postnatal MRI and histological reference series. An interleaved anatomical atlas of magnetic resonance imaging (MRI), histology, and block face photographs was created from four male rhesus macaques at 2 weeks, 3, 12 and 48 months after birth as described in the 'reference series' protocol document available at (http://www.blueprintnhpatlas.org). In addition, ISH data were generated serially across complete hemispheres of three post-pubertal adult (48 months) male specimens. Genes were selected to mark specific cell populations and cortical areas and to represent gene families important to neural function and associated with neuropsychiatric disease and brain evolution. Several histological stains (Nissl, acetylcholinesterase and SMI-32) of complete hemispheres were combined with ISH data to provide an unprecedented cellular-resolution view of gene expression in the whole post-pubertal adult brain. High-throughput colorimetric ISH methods are described in detail elsewhere[49] and in the '*in situ* hybridization' protocol document available at (http://www.blueprintnhpatlas.org).

Tissue processing. Following collection, brain tissues were partitioned in a manner dependent on specimen stage, gradually frozen, and then stored at −80°C until processing. For a subset of E40 specimens, following specimen collection, the calvarium was frozen intact in an isopentane/dry ice slurry maintained at −40 °C to −45 °C, gradual freezing at a steady rate. For the majority of E40 specimens, the specimens were embedded in OCT (optimal cutting temperature compound) during the freezing process. In brief, chilled OCT was placed around the calvarium. A disposable embedding chamber was filled with approximately 5 mm^3 chilled OCT. The specimen was carefully oriented and centred in the OCT, posterior surface down in the OCT. Then, the specimen was aligned along the medial/lateral axis using the bilateral ocular fiduciaries as a frame of reference. Next, the specimen was aligned in the coronal plane. After alignment along all axes, OCT was added to encase the specimen in its entirety. The top of the specimen was covered with approximately 3 mm of OCT. The chamber containing the specimen was directly placed onto a level bed of dry ice. The specimen and OCT were allowed to freeze completely. After demarcation of the orientation of the brain in the OCT block, the frozen tissue block was stored at −80 °C.

For the E50 specimens, following removal of the brain from the skull, the whole brain was frozen intact in an isopentane/dry ice slurry maintained at −40 °C to −45 °C, gradual freezing at a steady rate. For a subset of E50 specimens, the specimens were embedded in OCT during the freezing process. In brief, chilled OCT was placed around the intact brain. Freestanding aluminium bars were assembled onto a Teflon coated plate and sized to the appropriate specifications for the E50 brain. The internal chamber was filled with approximately 5 mm^3 chilled OCT. The specimen was carefully oriented and centred in the OCT dorsal surface down in the OCT. Then, the specimen was aligned along the medial/lateral axis using the longitudinal fissure as the frame of reference. Next, the specimen was aligned in the coronal plane. After alignment along all axes, OCT was added to encase the specimen in its entirety. The top of the specimen was covered with approximately 3 mm of OCT. The Teflon plate containing the specimen was directly placed onto the level bed of dry ice. The specimen and OCT were allowed to freeze completely. After demarcation of the orientation of the brain in the OCT block, the aluminium bars were removed and the frozen tissue block was stored at −80 °C.

For the E70, E80, E90, and E120 specimens, the hemispheres were bisected along the midline and individually frozen by placing the medial aspect of each hemisphere down onto an aluminium-Teflon coated plate that was slowly lowered into an isopentane/dry ice slurry maintained at −40 °C to −45 °C. Only approximately a third of the tissue was submerged in the slurry to allow the tissue to gradually freeze and to keep freezing artefacts to a minimum. Frozen hemispheres were stored at −80 °C.

Depending on the prenatal time point, different approaches were taken for generating coronal slabs. When possible, the number of slabs per specimen was kept to a minimum. The E40, E50, and E70 specimens were not slabbed. For E80, the first slab contained up through the temporal pole and the second slab contained the occipital pole. For E90, the first slab contained the frontal lobe anterior of the temporal pole and the second slab contained temporal pole posterior through the occipital lobe. For E120, three coronal slabs were made. The first slab consisted of the frontal lobe anterior of the temporal pole. The second slab consisted of the temporal pole posterior to the cerebellum including all of the mid-brain. The third slab included primarily the occipital lobe.

For postnatal brains, after dissection brains were sectioned into coronal slabs approximately 1 to 1.5 cm in thickness and the left hemisphere was prepared for sectioning onto microscope slides for ISH. Structures for microarray analysis were isolated from the right hemisphere slabs, and these samples were then frozen at −80 °C until processed further.

Laser microdissection and RNA isolation. Tissue spanning five anatomically distinct brain regions—frontal cortex, visual cortex, hippocampus, striatum, and amygdala (Fig. 1 and Supplementary Table 1)—was selected from each specimen and processed for further thin sectioning and LMD using a standard protocol. Specifically, frozen tissue was cryosectioned at 14 μm onto polyethylene naphthalate (PEN) slides (Leica Microsystems, Bannockburn, IL) and a 1:10 Nissl series was generated for neuroanatomical reference for all prenatal time points. In addition, for the E40, E50, E70, E80, and E90 time points, a 1:10 *GAP43* and 1:10 *ENC1 in situ* hybridization (ISH) series was generated for neuroanatomical reference, as they often clearly delineate nuclei and layers at early developmental stages. For E120, a 1:10 acetylcholinesterase series was generated for neuroanatomical reference. In total, 127 transient and terminal anatomical structures were isolated using this strategy[50–53]. After drying for 30 min at room temperature, PEN slides were frozen at −80 °C. Slides were lightly Nissl stained with cresyl violet to allow cytoarchitectural visualization. Slides were fixed in ice-cold 70% ethanol for 30 s, washed for 15 s in nuclease-free water, stained in 0.7% cresyl violet in 0.05% NaOAc, pH 3.4 for 2 min, nuclease-free water for 15 s, followed by 15 s each in 50%, 75%, and 95% ethanol, followed by 20 s in 100% ethanol, and then a final 100% ethanol wash for 25 s. Slides were air-dried for 2 min, and desiccated in a vacuum for 1 h, then frozen at −80 °C until microdissection. Laser microdissection was performed on a Leica LMD6000 (Leica Microsystems, Bannockburn, IL), using the Nissl stain and GAP43 and ENC1 ISH or acetylcholinesterase histological staining as a guide to identify target brain regions in prenatal samples. Microdissected tissue was collected directly into RLT buffer from the RNeasy Micro kit (Qiagen, Valencia, CA) with β-mercaptoethanol. Samples were volume-adjusted with water to 75 μl, vortexed, centrifuged, and frozen at −80 °C. RNA was isolated for each structure following the manufacturer's directions for the RNeasy Micro kit. RNA samples were eluted in 14 μl and 1 μl was run on the Agilent 2100 Bioanalyzer (Agilent Technologies, Santa Clara, CA) using the Pico assay. Due to low sample volume and incompatibility of the eluant with the Nanodrop spectrophotometer (Thermo Scientific, Wilmington, DE), samples were quantitated using the Bioanalyzer concentration output. This was done by running a 1 $ng\,\mu l^{-1}$ RNA standard on the same Pico chip and then dividing the sample concentration output by the output of the standard concentration. For prenatal samples, 2 ng of total RNA was almost always used as the input amount for the labelling reaction, and the average RNA integrity number (RIN) of passed samples was 7.5, with RINs typically lower than 4.5 failing. For postnatal samples, 5 ng of total RNA was almost always used as the input, and the average RIN of passed samples was 7.5, with RINs typically lower than 5 failing.

Histological stains. *Nissl.* For the Nissl neuroanatomical reference slides, slides were stored at 37 °C for 1–5 days before staining. Sections were defatted with xylene or the xylene substitute Formula 83, and hydrated through a graded series containing 100%, 95%, 70%, and 50% ethanol. After incubation in water, the sections were stained with 0.213% thionin, then differentiated and dehydrated in water and a graded series containing 50%, 70%, 95% and 100% ethanol. Finally, slides were incubated in xylene or Formula 83, and coverslipped with the mounting agent DPX. After drying, slides were cleaned before digital imaging.

Acetylcholinesterase. A modified acetylcholinesterase protocol was used to assist in neuroanatomical delineations in E120. Unlike acetylcholinesterase staining in fixed tissue, staining in fresh frozen tissue does not elucidate cholinergic fibres commonly seen in the cortex, but instead provides demarcation of various subcortical nuclei. Acetylcholinesterase staining was performed using a direct colouring

thiocholine method combined with a methyl green nuclear counterstain to improve tissue visibility[54]. Glass slides with fresh frozen tissue sections were removed from 4 °C, allowed to equilibrate to room temperature, fixed in 10% neutral buffered formalin (NBF) and washed briefly in ultra-pure water. Sections were then incubated for 25 min in a solution of acetylthiocholine iodide, sodium citrate, cupric sulphate, and potassium ferricyanide in a 0.1 M sodium acetate buffer (pH 6.0), washed in 0.1 M Tris-HCl buffer (pH 7.2), and incubated with 0.5% diaminobenzidine (DAB) in 0.1 M Tris-HCl with 0. 03% hydrogen peroxide for 8 min. Slides were incubated in 0.2% methyl green, briefly dipped in 100% ethanol, cleared with Formula 83 and coverslipped with DPX. After drying, slides were cleaned before digital imaging.

***In situ* hybridization (ISH).** High-throughput colorimetric ISH methods are described in detail elsewhere (see ref. 49) and in the *in situ* hybridization protocol document located under the documentation tab at (http://www.blueprintnhpatlas.org). In brief, fresh frozen tissue sections (from either E40, E50, E70, E80, or E90) on slides were fixed in 4% PFA in PBS, acetylated, and dehydrated through graded alcohols. Endogenous peroxidase activity was blocked with 3% hydrogen peroxide in methanol. Proteinase K digestion at 0.0135 U ml^{-1} was carried out. Digoxigenin (DIG)-labelled riboprobes (either *GAP43* or *ENC1*) were hybridized at 63.5 °C for 5.5 h, followed by stringency washes and a series of enzymatic reaction steps for detection and amplification of DIG signal. Sections were washed with EDTA, fixed in 4% PFA, and washed with acid alcohol (70% ethanol, adjusted to pH = 2.1 with 12 N HCl) to reduce background signal. Slides were coverslipped with Hydromatrix, subjected to quality control analysis and cleaned before digital imaging. The complete list of 46 ISH gene targets for ISH in postnatal rhesus monkey is also available in the documentation tab at (http://www.blueprintnhpatlas.org).

Digital imaging and processing of histologically stained sections. Digital imaging was done using the ScanScope XT (Aperio Technologies, Vista, CA). The final resolution of images was 1 μm per pixel. All images were databased and preprocessed, then subjected to quality control analysis to ensure optimal focus and that no process artefacts were present in the images. Images that passed this initial quality control were further assessed to ensure that the staining data were as expected. Once all quality control criteria were met, images became available for annotation of anatomic structures.

mRNA profiling. Prenatal samples passing RNA quality control were amplified and profiled. Briefly, samples were amplified and labelled using a custom 2 cycle Ultra Low Input procedure, using components of MessageAmp II aRNA Amplification kit (AM1751) for the first amplification cycle (using oligodT), and components of MessageAmp II Biotin Enhanced Single Round aRNA Amplification kit (AM1791) for the second amplification cycle (using both random hexamers and oligodT). For prenatal samples, 2 ng of total RNA was added to the initial reaction mix together with 250 ng of pBR322 (Invitrogen). Following the first cycle of IVT, the plasmid carrier was removed with a DNaseI (Qiagen) treatment. The first cycle IVT products were purified using the QiagenMinElute Kit (Qiagen). Input into the second cycle was normalized to 400 ng. Hybridization was to catalogue GeneChip Rhesus Macaque Genome Arrays from Affymetrix containing 52,803 probe sets/sequences. For detailed information about this macaque microarray, see the Affymetrix website (http://www.affymetrix.com/browse/products.jsp?productId=131496&navMode=34000&navAction=jump&aId=productsNav#1_3). Labelling and scanning were completed following the manufacturer's recommendations. Quality control assessment failed a small number of microarray samples. Sample amplification, labelling, and microarray processing were performed by Covance in Seattle, WA.

Postnatal samples passing RNA quality control were amplified and profiled as described in Winrow *et al.*[55] with a few modifications. Briefly, samples were amplified and labelled using a custom 2 cycle version, using 2 kits of the GeneChip HT One-Cycle cDNA Synthesis Kit from Affymetrix. For postnatal samples, 5 ng of total RNA was added to the initial reaction mix together with 250 ng of pBR322 (Invitrogen). *In vitro* transcription (IVT) for the first cycle was performed using a 5X MEGAscript T7 Kit (Ambion). Following the first round of IVT, the plasmid carrier was removed with a DNaseI (Qiagen) treatment. The first round IVT products were purified using the QiagenMinElute Kit (Qiagen). Input into the second round was normalized to 150 ng for postnatal samples. Hybridization was to catalogue GeneChip Rhesus Macaque Genome Arrays. Labelling and scanning were completed following the manufacturer's, recommendations and profiles were normalized using robust multi-array (RMA). Sample amplification, labelling, and microarray processing were performed by Covance in Seattle, WA.

Microarray processing and normalization. To account for differences in mRNA processing, prenatal and postnatal samples were first normalized separately using a standard procedure, and then scaled together to minimize the effects of technical biases (for example, due to differences in mRNA processing of prenatal and postnatal samples) while preserving biological variance. For prenatal samples, the BioConductor "affy" package was used to read in the Affymetrix microarray data and RMA method[56], consisting of background normalization, $\log_2$ transformation, and quantile normalization, was applied to summarize the probe level data into gene expression measurements for each batch. Control samples from macrodissected adult cortex were included in each batch to normalize the data across batches by aligning their mean gene expression values. Postnatal samples from each batch were preprocessed using the same RMA method as for prenatal samples. ComBat (http://www.bu.edu/jlab/wp-assets/ComBat/)[57] was then applied to reduce more severe non-biological batch-to-batch bias. The postnatal microarray data are unchanged since the original public release. Finally, the normalized prenatal data was scaled to postnatal data by sorting probes by average expression across developed regions in E80 and older animals, finding the difference in average expression levels (postnatal – prenatal) of each group of 100 probes, and then scaling each probe by the corresponding value.

The purpose of normalization was to minimize the effects of these non-biological biases while keeping biological variance intact so that within and across brain comparisons primarily reveal differences and similarities that are biologically relevant. As a data-driven quality control process, for each batch, we applied clustering/MDS to detect any outlier in the batch by checking whether samples from the same structure/age were grouped together. IAC (inter-array connectivity) was also calculated to numerically measure how one microarray was similar to the other microarrays in the batch. The same quality control process was applied over multiple batches to identify outliers. After normalization and outlier removal, a total of 1,212 prenatal and 724 postnatal samples remained.

Probe set filtering and gene symbol assignments. From the 52,865 probe sets included on the microarray, we identified 12,441 high-confidence probe sets mapping to unique genes (Supplementary Table 2). First, to assess the targeting specificity of each probe set, we pooled mRNA from 20 prenatal and 20 postnatal discrete anatomical and temporal populations and ran these mRNA pools both on Affymetrix microarrays and using RNA-seq as previously described[58]. Since a high quality transcriptome was not available for rhesus macaque, we used GSNAP to map RNA-seq reads to the rheMac2 (January 2006) genome and identified expression values for 50,648 putative transcripts. We used Galaxy (http://usegalaxy.org)[59–61] to intersect rheMac2 genomic coordinates of probes (Affymetrix annotation version 34; 30 January 2014), GSNAP transcripts and NCBI rhesus gene information (downloaded 6 February 2014). 34,646 probe sets mapped unambiguously to 15,577 genes (rhesus Entrez IDs) and were further considered. For each probe set, we calculated the correlation between probe set intensity and FPKM values for all RNA-seq transcripts corresponding to the same gene and retained the most highly correlated probe set for each gene. We omitted 3,136 genes that did not have any probe sets significantly correlated (FDR <0.1) between methods. We annotated the final set of 12,441 genes with 10,715 human and 10,403 mouse orthologues using NCBI Homologene (downloaded 7 January 2014).

Comparing gene expression across neocortex. Heat maps were independently generated for each gene by mapping expression levels in neocortex to a colour vector of white (low expression) to red (high expression). Samples were organized in a grid corresponding to layer (vertical axis, from ventricular to pial surface), age (horizontal axis, from young to old), and cortical region (ordered rostral to caudal within each age). Each sample is labelled on the axes as well as within the corresponding boxes, with missing data points (either due to incomplete sampling or if a structure does not exist) left blank. The size of each box is chosen for clarity and is unrelated to gene expression.

We calculated the correlation between all neocortical samples based on the expression correlation of 12,441 genes. We converted correlations into distances with the transformation $1 - (0.5 \times 1 + \text{correlation})$, applied metric multi-dimensional scaling using the *cmdscale* R function to represent these distances in two dimensions, and estimated per cent variance explained for the first two principal coordinates. We plotted samples with point colour representing cortical layer and point size representing age. For clarity, samples that were annotated as cortical plate were assigned to postmitotic layers (L2–L6) that were most transcriptionally similar. We repeated this analysis for two subsets of samples: prenatal cortical layers and V1 postmitotic layers (layers 2–6).

Sex differential expression. Brain samples with data from both male and female donors included all prenatal ages and were included in a linear mixed model with sex as a fixed effect and brain region, age and donor as random effects. One model was fit for each gene individually using the "nlme" R package and *P* values were estimated using Satterthwaite's approximation to degrees of freedom as implemented in the "lmerTest" R package (see Supplementary Table 3). A permutation based correction for multiple comparisons was then performed. For each of 6 prenatal ages, donor sex labels (2 males, 2 females) were shuffled to generate 64 permuted data sets. For each of these permutations, an identical linear mixed model was fit to all genes, and genes were ordered by the magnitude of the fixed effect of sex. Median and 95% confidence interval (2.5% and 97.5% quantiles) were calculated for each rank ordered fixed effect. Finally, a quantile–quantile plot (Extended Data Fig. 3) was created to compare observed fixed effects to median

expected (permuted) effects. 11 genes had sex effects lying outside of the 95% confidence interval (greater expression in males), and 7 of these genes were nominally significant (mixed model P value <0.05).

For probes that showed differential sex expression greater than expected by chance or for Y chromosome probes, target sequences were downloaded from Affymetrix (https://www.affymetrix.com/analysis/index.affx). These sequences were compared to a primate nucleotide database using NCBI Blastn[62], and the best match (query coverage >80%, sequence identity >90%) was reported in Supplementary Table 3. Note that 5 of 6 Y chromosome probes probably measured expression of highly similar paralogues on the X chromosome or autosomes, a consequence of the Affymetrix rhesus macaque microarray having been developed several years before the rhesus monkey Y chromosome was sequenced[23].

Analysis of dynamic genes using GO. We first calculated average gene expression in all brain regions ($n = 3$–4 monkeys) at 10 ages, and then calculated rates of expression change as the difference in $\log_2$-transformed expression between adjacent ages in each region and expressed as doublings or halvings per year. Note that rates of expression change could not be calculated for the earliest time point (E40) or for regions without sampling at adjacent ages. For each of 419 distinct brain regions, we rank ordered genes by rates of expression change, and selected the top 1,000 increasing and decreasing genes. We compared all of these genes lists ($419 \times 418 = 175{,}142$ comparisons). For each gene list comparison, we found the number of overlapping genes and calculated an overlap similarity score based on the weighted rank order of the lists ('OrderedList' package in R). We then generated a null distribution of similarity scores by shuffling gene lists 10 million times and calculated P values for observed similarity scores. We found that 56,540 gene lists were significantly (Bonferroni corrected $P < 0.05$) overlapping.

We visualized the number of overlapping genes as a heat map and reordered rows and columns based on the correlated patterns of overlapping increasing genes. Specifically, we calculated the distance between 419 brain samples as (1 – correlation) / 2 and used unsupervised hierarchical clustering with complete linkage to order samples. The dendrogram was reordered (while preserving the tree structure) by weighting branches by median ages of samples and rotating branches to group similar ages. Samples from the same age were highlighted with grid lines aligned to this dendrogram (Fig. 2b). The heat map was also annotated with brain structure and a mitotic index approximated by mean expression of *MKI67* (Ki-67 protein).

We performed GO enrichment with the Bioconductor 'GOstats' package in R with a background set of 10,715 human orthologues included in this study. We repeated GO enrichment analysis on each of 56,540 gene lists (32,053 increasing and 24,487 decreasing), and found 11,899 biological process terms were nominally significant ($P < 0.05$) for at least one list. To reduce false positive associations, we calculated the level of statistical support for each GO term as the proportion of children of that term (based on the GO hierarchy) that were nominally enriched. For example, if a GO term had 10 associated children and four were enriched, then the term had a support of 0.4. For each term, we plotted a heat map of statistical support for all 56,540 gene lists (on a scale of 0 to 1), and many of these heat maps showed distinct patterns of enrichment (for example, Fig. 2c and Extended Data Fig. 4). We summarized GO enrichment as a table by calculating the average support for all 419 regions and considered a GO term active if mean support was greater than 0.01. We transformed this table into a binary matrix showing when and where GO terms were active. We removed terms associated with fewer than 10 of 419 regions, as these terms probably represented noise, and this resulted in 3,704 processes increasing and/or decreasing over development (Supplementary Table 4).

We repeated the previous gene overlap and GO enrichment analyses with a set of five major brain regions including neocortex, hippocampus, basal ganglia and amygdala at nine ages and thalamus at four ages (40 total brain regions). We found that 556 of 1,600 gene list comparisons were significantly overlapping and 1,012 biological processes were active in these regions (Supplementary Table 5). For each GO term, we calculated commonality as the number of ages (maximum nine) that term was active in each brain region and in any region. We plotted the distribution of commonalities across all terms in different regions as density line plots separately for increasing and decreasing processes (Fig. 2d).

Relative timing of developmental processes. We calculated the relative timing of GO term activity using the binary matrix representing when and where terms were active in the four brain regions (neocortex, hippocampus, basal ganglia and amygdala) for which we had information across development. For each of six possible region comparisons, we divided the number of ages a GO term was active in both regions by the number of ages it was active in either region (for example, Extended Data Fig. 5a). For each term, we averaged the six age overlap calculations to summarize overall timing differences. We repeated these calculations for all 1,012 GO terms and plotted the distribution of age overlaps for increasing and decreasing processes (Extended Data Fig. 5b).

For 837 increasing processes, we plotted the earliest age of activity in four brain regions and ordered terms by age of onset in amygdala, basal ganglia, hippocampus and neocortex (Fig. 3c). We characterized timing as either simultaneous (equal age of onset in all regions), subcortex early (either amygdala or hippocampus onset earlier than both hippocampus and neocortex), or cortex early (either hippocampus or neocortex onset earlier than both amygdala and hippocampus). Next, for each term, we rank ordered the four brain regions based on age of onset. Ties were broken by assigning the average rank to all tied regions. For example, if a process was first active at E50 in amygdala and at E70 in the other three regions, then amygdala was assigned a rank of 1 while the other regions were assigned a rank of 3 (average of ranks 2, 3 and 4). This tie-breaking method highlighted terms that were earlier and later than all other regions. We calculated region ranks for 837 terms and plotted a heat map of the proportion of terms with each rank for each region (columns sum to one in Extended Data Fig. 5c) and used these proportions to calculate the weighted mean rank of each region.

We selected the top 40 genes enriched in myelinating oligodendrocytes in adult mouse[63] and identified 23 orthologues with expression data in rhesus. Six genes (*MOG*, *MOBP*, *ERMN*, *MAL*, *ASPA* and *OPALIN*) were highly correlated ($R > 0.9$) with each other across all brain regions over development (Extended Data Fig. 5d). We calculated average expression of these genes ($n = 3$–4 subjects) in the highly myelinated regions that were sampled in this study.

Transcriptional signatures of V1 layers. We compared gene expression across postmitotic layers in V1 for each age starting from E80, the earliest age at which all layers were sampled. Samples from L2 and L3 were considered together as L2/3, and samples from sub-layers of L4 were considered together as L4. For each subject and age, we calculated the average $\log_2$ scaled gene expression of layers 2/3, 4, 5 and 6, as well as adjacent layers marginal zone/L1 and intermediate zone/white matter for comparison. For each age, we fit a linear model to the expression data with a dummy variable coding for layer. The proportion of variance explained by each layer was estimated using the CAR metric[64] in the 'relaimpo' R package. For each layer and age, we rank ordered genes based on the proportion of variance explained (Supplementary Table 6).

Layer signatures between ages were compared by identifying the top 10% most laminar genes evenly allocated between layers (top 2.5% each in L2/3, L4, L5, and L6), and then calculating their average across-layer correlation between ages. Specifically, for each 'source' list of marker genes, we found the average expression by layer of these genes at the 'source' age and at every other 'target' age, resulting in two expression tables of 1,224 genes by 4 layers. Gene by gene, expression across layers was compared using Pearson correlation and the average correlation across all 1,224 genes was determined.

Differential expression between the layer and all other layers was calculated using the 'limma' R package. Genes were considered layer-enriched if they explained at least 25% of the expression variance in all layers (see description of analysis above) and had expression >1.5-fold higher than other layers combined. Genes marking the same layer in at least two ages were further defined as persistent if they were laminar during at least 5 out of 7 ages, or early, middle, or late if their median age of laminar enrichment was <E120, between E120 and 3 months, or >3 months, respectively (Supplementary Table 7). Selected marker genes were visualized using heat maps as described above, but only showing the subset of data considered in this analysis (L1-WM in V1 from E80 to 48 months). To characterize the function of genes from each laminar timing group, we grouped genes from all layers with the same timing and performed gene ontology (GO) enrichment using all "Biological Process" terms with fewer than 500 associated genes. We identified significantly associated terms (nominal $P < 10^{-4}$ and five or more genes enriched for at least one timing group) and visualized $-\log_{10} P$ values using a heat map.

Differential expression between neocortical regions. We compared gene expression in V1 and ACG independently for each age in the outer (L2/L3) and inner (L5/L6) cortical layers, in the subventricular zone (SZ), and in the ventricular zone (VZ). First, we averaged gene expression (logarithmically scaled) within specimen across all relevant samples for each layer in V1 and ACG independently (that is, L2 and L3 in V1 were averaged in each brain). For each age and layer, nominal P values for differential regional expression were calculated using a paired test ($n = 3$–4 monkeys), and genes with $P < 0.05$ and average fold change >2 were considered significantly enriched in ACG or V1 (Supplementary Table 8). We then defined persistent regional markers as genes significantly enriched in either ACG or V1 in at least two-thirds of the ages in which a layer was present ($n \geq 5$ in L2/L3; $n \geq 6$ in L5/L6; $n \geq 4$ in SZ and VZ). We visualized the expression patterns of select regional markers using line plots, where each point shows the average (± standard deviation) $\log_2$-scaled gene expression levels of that gene in ACG (red) or V1 (blue) for a particular layer (specified to the right of the plot).

We quantified regional enrichment of several cell types in each layer and at each age using a hypergeometric test. Specifically, we compared 242 lists of marker genes derived from the literature against each set of V1 and ACG enriched genes

described above, calculated a P value based on the significance of overlap using the *phyper* function in R. P values were Bonferroni corrected for multiple comparisons and visualized as boxes in a grid of layers (vertical axis) and ages (horizontal axis). Cell type lists were derived as follows: dividing cell markers were defined as any marker of any phase of cell cycle as presented in supplementary fig. 3 of Bar-Joseph *et al.*[65]. Markers for excitatory neurons in adult mouse V1 were derived from Tasic *et al.*[66] by identifying all genes expressed in at least 2.2× as many excitatory as inhibitory cells (based on proportion) and that have expression in the 80th percentile excitatory cell that is both 2.2× higher than the 80th percentile inhibitory cell and also higher than RPKM = 2.5. Inhibitory neuron markers were defined the same way, but swapping excitatory and inhibitory above. Finally, astrocyte marker genes were defined as genes which showed at least tenfold enrichment in sorted astrocytes compared with both neurons and oligodendrocytes in Cahoy *et al.*[67]

To address the issue of timing of gene expression in prenatal cortical development, we extended these analyses to S1 by considering the set of genes showing rostral enrichment during the phase in which V1 corticogenesis lags ACG (E70–E90), and asked to what extent these genes also show higher expression in S1 vs V1. We do this in two ways. First, we re-plot genes presented in Fig. 4 with S1 also shown for direct comparison. Second, we calculate the average enrichment of these genes in S1 relative to V1 (using $\log_2$ fold change across all samples from the relevant layers between E70–E90), and compare it directly to the average enrichment in ACG relative to V1 (Extended Data Fig. 6).

Network profiling of disease genes. We used weighted gene co-expression network analysis (WGCNA)[68,69] to generate 10 unbiased gene co-expression networks (one at each age) using cortical structures (ACG and V1) with the goal of quantifying the distribution of disease-related genes throughout these networks. Initial networks were generated using an automated strategy with the following function call in R:

blockRun = blockwiseModules(datExprRun, checkMissingData = TRUE, maxBlockSize = 17500,power = 14, networkType = "signed", deepSplit = 1, minModuleSize = 50, minCoreKMESize = 17, minKMEtoStay = 0.4, mergeCutHeight = 0.1, numericLabels = TRUE, verbose = 1)

where *datExprRun* is the $\log_2$ normalized microarray data from the top 9,331 (75%) most variable genes (at each time point). For postnatal time points these values in V1 and ACG were scaled to the mean interquartile expression of samples from layers 2, 3, 5, and 6. The goal of this scaling was to de-emphasize regional patterning differences or batch effects and maximize laminar and cell type patterning. After running the network (and after performing the merging steps described below) module eigengenes (ME; the first principal component of genes in the module) were calculated for each module, and all genes were reassigned to the module to which it is most highly correlated to the ME (referred to as the gene's module membership, or kME). Genes with kME <0.4 for all modules in a given age are left unassigned (defined as module 0). While there is no agreed upon value for a kME cut-off in the literature, we have successfully used a cut-off of kME <0.4 in the past as the cut-off for assigned versus unassigned genes (for example, Hawrylycz *et al.* (ref. 70)).

If the resulting network at any time point contained more than 15 modules, the module pair with the most highly correlated ME were iteratively merged until 15 modules remained. Since networks are unaffected by changes in labelling, modules were then re-ordered manually such that modules with strong enrichment for cortical plate neurons had low numbers, modules with strong enrichment for progenitor or glial cells had higher numbers, and modules between ages with a highly significant number of overlapping genes were ordered similarly across development. To do this third step, every pair of modules in networks from adjacent ages were compared using a hypergeometric test, and pairs with overlap significance of $P < 10^{-50}$ were linked (using grey lines in Fig. 5). We note that several additional pairs of modules show significant overlap (but with $P \geq 10^{-50}$)—these modules pairs are not shown in the plot for readability and because we are interesting in finding only the most significant overlaps. Finally, modules which were split into two modules at a single age but not at both adjacent ages were merged. At each age, modules are numbered by row number in Fig. 5a with the top row being Module 01 at each age. Module assignments for each gene at each age are provided in Supplementary Table 9.

We have broadly annotated many of these modules based on cortical layer, cell type, and disease enrichments, and provide the annotated network as a resource to the community. Module assignments of postmitotic vs progenitor cell layer in prenatal neocortex was done by comparing mean expression in cortical plate (CP) and subplate (SP) vs all other layers, and noting which mean value is highest. Similarly, assignments of cortical vs glial cell layers in postnatal neocortex was done by comparing mean expression in postmitotic layers 2–6 vs white matter and layer 1. Module assignments based on cortical layer were performed by finding the average expression of all module genes in all layers included in them and finding the layer in which expression is highest (select layer enrichments are labelled in Fig. 5a). Additional assignments for primarily postmitotic cortical layers (from E80 to 48 months) were found by performing a hypergeometric test on every module against layer markers identified in the analysis in Fig. 4b for each age. Significant enrichments ($P < 10^{-30}$) are colour-coded in Fig. 5a. This P value cut-off ensured that modules selected were only enriched with markers for a single layer, whereas with lower cut-offs, some modules had markers for multiple layers. Module enrichments for astrocytes and oligodendrocytes were calculated by performing hypergeometric test comparisons, and plotting these P values as coloured discs in Fig. 5a for modules that are highly significant ($P < 10^{-15}$). Astrocyte marker genes were defined as genes which showed at least tenfold enrichment in sorted astrocytes compared with both neurons and oligodendrocytes in Cahoy *et al.*[67] (likewise for the oligodendrocyte markers).

We used empirical rather than Bonferroni correction of the significance of disease gene enrichments because the tests were correlated due to high module gene overlap. Hypergeometric P values were calculated by comparing each module against genomics-based disease genes for autosomal recessive primary microcephaly (13 genes)[71], autism spectrum disorder (*a posteriori* probability >0.8; 171 genes)[45] and schizophrenia (206 genes)[72] with homologues in this data set. Module assignments were then permuted 999 times per disease, and the minimum P value across all modules for each of the permuted comparisons was recorded. Nominal P values were corrected with this empirical null distribution of minimum P values. For example, a nominal P value less than the minimum P value in 90% of the permutations had an empirically corrected P value equal to 0.1 that controlled the family-wise error rate at 10%. This is a much more stringent criterion than FDR <0.1 because it means that there is a less than 10% chance that any of the enriched modules is a false positive enrichment. Modules that were significantly enriched for disease-associated genes were plotted as red discs in Fig. 5b–d. For each disease, expression heatmaps for genes present in at least two enriched modules were plotted to show different developmental profiles.

A recent study of intellectual disability with and without brain malformations in consanguineous families identified 89 known and candidate disease related genes[73]. For each pair of 71 genes profiled in this data set, we calculated the Pearson correlation of expression in all ACG and V1 cortical samples across development. We used hierarchical clustering of the Euclidean distance of correlations to group genes with similar spatiotemporal expression profiles into 4 major clusters and visualized correlations as a heat map with the "pheatmap" R package. Genes were annotated with colour bar tracks indicating phenotypes present in one or more individuals with likely pathological mutations in these genes. Primary microcephaly was defined as microcephaly without other brain malformations and corpus callosum abnormalities included agenesis and various hypogenesis and dysgenesis phenotypes. Multivariate distance matrix regression (MDMR) was used to test whether each phenotype explained a significant proportion of variation in the expression based distance matrix, and P values were calculated based on a permutation test as previously described[74]. Expression heat maps for a representative gene from each cluster were plotted to show different developmental profiles.

Conservation of developmental expression trajectories. Developmental expression data were downloaded for rat frontal cortex[75] and five human brain regions (medial frontal cortex, MFC; primary visual cortex, V1; hippocampus; amygdala; and striatum)[16] homologous to regions profiled in this study. To compare rhesus monkey to gross cortical samples in rat and human, we calculated average expression across all sub-regions of anterior cingulate gyrus (ACG, partially overlapping with MFC in human), V1, hippocampus, amygdala and striatum at each age. We aligned ages across species by estimating event scores based on the conserved timing of developmental events[1] and found that prenatal and postnatal development were well sampled in all species.

For frontal cortical samples, 4,125 orthologous genes were identified using NCBI Homologene, and we selected 2,062 genes that were among the top 50% most variable genes over development in rhesus. This filter removed genes that had relatively constant expression and therefore would be difficult to compare trajectories between species. Independently for each gene and species, we estimated the shape of expression trajectories by smoothed local linear regression ("loess" R function) with degree zero to allow for complex dynamics while reducing overfitting. With these smoothed fits, we estimated expression at 8 approximately evenly spaced event scores (ranging from 0.27 to 1.32) for each species. We correlated expression trajectories between each pair of species and plotted a Venn diagram showing the number of conserved (Pearson correlation $R > 0.5$) genes between each pair of species. Genes were assigned to one of five sets based on the pattern of species conservation. 'Conserved' genes were conserved between at least two species pairs and 'not conserved' were not conserved between any species pair and may represent noise. 'Primate-specific' genes were conserved between human and rhesus but not between rat and either primate. 'Human-specific' genes were conserved between rhesus and rat but not between human and either other species.

'Rhesus-specific' genes were conserved between human and rat but not between rhesus and either other species.

Next, we downloaded developmental expression profiles from an independent human data set (dorsolateral prefrontal cortex, dlPFC, GEO accession code GSE30272)[14]. For 1,848 of 2,062 variable genes with dlPFC data, we calculated Pearson correlations of expression trajectories between human MFC and dlPFC as described above. Expression correlations between all pairs of species were compared with box plots (median $\pm$ 25th and 75th percentiles, whiskers at 1.5 times the interquartile range, and outliers plotted as points). Correlation distributions deviated significantly from normality based on a Shapiro–Wilk test ("shapiro.test" function in R), and so differences were tested with a Kruskal–Wallis rank sum test ("kruskal.test") followed by paired Wilcoxon signed rank tests ("wilcox.test") to test for significant differences in conservation between species. Finally, we repeated the analysis described above for a larger set of 8,683 orthologous genes in human and rhesus macaque. First, we rank ordered genes based on the standard deviation of expression across rhesus monkey development. For the top 100 most variable genes, we calculated expression correlations between human data sets and between human and rhesus. We repeated this analysis 86 times, each time including the next set of 100 most variable genes. Finally, we plotted the median correlation within and between species as a function of developmental expression variability.

We downloaded expression data (average ISH density) for 2,024 genes in the dorsal pallium (which includes frontal cortex) of developing mouse[76] (http://developingmouse.brain-map.org/) using the Allen Brain Atlas Application Programming Interface (API) and calculated Spearman correlations between 305 mouse and rat orthologous genes. All pair-wise species correlations are included in Supplementary Table 10.

We used DAVID[77,78] v6.7 (https://david.ncifcrf.gov/home.jsp) to test different sets of conserved genes for significant enrichment in gene ontology categories, tissue specificity and disease association relative to a background set of all 1,848 variable genes. Gene paralogues were downloaded from Ensembl with BioMart[79]. We checked genes for evidence of positive selection on different evolutionary branches using Selectome[80,81] (http://selectome.unil.ch/).

Developmental breakpoint analysis. For 4,125 orthologous genes in homologous brain regions of human, rhesus monkey and rat, we fit expression trends (log-transformed intensity versus age in embryonic days) using segmented linear regression ("segmented" R package) with a single breakpoint and two slopes. Breakpoints were initialized at the mid-point of development, and standard errors for breakpoint and slope estimates were calculated using 20 bootstrap iterations (Supplementary Table 11). 95% confidence intervals (CI) were calculated for slopes based on bootstrapped standard errors ($\pm 1.96 \times$ s.e.). Genes with a good model fit ($R^2 > 0.8$) and significantly increasing (95% CI did not include zero) or decreasing initial slopes in all three species were included for further analysis. Breakpoint densities of $\log_{10}$(age) in frontal and primary visual cortical areas were plotted for different species for all genes and for synapse related genes downloaded from SynaptomeDB[82] (http://metamoodics.org/SynaptomeDB). For each brain region, species pairwise comparisons of breakpoints and standard errors were plotted and genes with significantly increasing or decreasing second slopes (95% CI did not include zero) were highlighted (Fig. 6e and Extended Data Fig. 7d, e). For each pair of species, ages corresponding to equivalent (that is, equal event scores) or nearby developmental stages (event scores within ± 0.2) were plotted. Genes with significantly different breakpoints between species (95% CI of breakpoints did not overlap) were counted and summarized for each brain region as a stacked bar plot indicating the expression slope after human breakpoints. Breakpoint timing was also compared between frontal and primary visual areas in rhesus and human with a paired Wilcoxon signed rank test and plotted (Extended Data Fig. 7c). In total, expression breakpoints were identified for 179 significantly increasing and 179 decreasing genes in human and rhesus monkey V1 and ACG.

Synaptic density measurements were obtained from previously published studies for V1 in rat[83], and V1 and prefrontal cortex in human[41] and rhesus[40]. Segmented linear regression was fit to synaptic density trends (percentage maximum synaptic density versus age in embryonic days), and breakpoints corresponded to ages of peak density (Extended Data Fig. 7b). Breakpoint 95% CIs were calculated and plotted as shaded bands in density plots.

Code availability. All results and figures from this study can be reproduced using R code and data files available from GitHub (https://github.com/AllenBrainAtlas/DevRhesusLMD). The software is free and can be modified and redistributed under the terms of the GNU General Public License, version 3 (GPLv3).

49. Lein, E. S. *et al.* Genome-wide atlas of gene expression in the adult mouse brain. *Nature* **445,** 168–176 (2007).
50. Bystron, I., Blakemore, C. & Rakic, P. Development of the human cerebral cortex: Boulder Committee revisited. *Nature Rev. Neurosci.* **9,** 110–122 (2008).
51. Price, J., Russchen, F. & Amaral, D. in *Handbook of Chemical Neuroanatomy* (eds Hokfelt, B. & Swanson, L.) 279–381 (Elsevier, 1987).
52. Berger, B. & Alvarez, C. Neurochemical development of the hippocampal region in the fetal rhesus monkey, III: calbindin-D28K, calretinin and parvalbumin with special mention of cajal-retzius cells and the retrosplenial cortex. *J. Comp. Neurol.* **366,** 674–699 (1996).
53. Paxinos, G. *The Rhesus Monkey Brain in Stereotaxic Coordinates* (Academic Press, 2009).
54. Karnovsky, M. J. & Roots, L. A 'direct-coloring' thiocholine method for cholinesterases. *J. Histochem. Cytochem.* **12,** 219–221 (1964).
55. Winrow, C. J. *et al.* Refined anatomical isolation of functional sleep circuits exhibits distinctive regional and circadian gene transcriptional profiles. *Brain Res.* **1271,** 1–17 (2009).
56. Bolstad, B. M., Irizarry, R. A., Astrand, M. & Speed, T. P. A comparison of normalization methods for high density oligonucleotide array data based on variance and bias. *Bioinformatics* **19,** 185–193 (2003).
57. Johnson, W. E., Li, C. & Rabinovic, A. Adjusting batch effects in microarray expression data using empirical Bayes methods. *Biostatistics* **8,** 118–127 (2007).
58. Miller, J. A. *et al.* Improving reliability and absolute quantification of human brain microarray data by filtering and scaling probes using RNA-seq. *BMC Genomics* **15,** 154 (2014).
59. Goecks, J., Nekrutenko, A. & Taylor, J. Galaxy: a comprehensive approach for supporting accessible, reproducible, and transparent computational research in the life sciences. *Genome Biol.* **11,** R86 (2010).
60. Blankenberg, D. *et al.* Galaxy: a web-based genome analysis tool for experimentalists. *Curr. Protoc. Mol. Biol.* **Chapter 19,** Unit 19.10.1–21 (2010).
61. Giardine, B. *et al.* Galaxy: a platform for interactive large-scale genome analysis. *Genome Res.* **15,** 1451–1455 (2005).
62. Altschul, S. F., Gish, W., Miller, W., Myers, E. W. & Lipman, D. J. Basic local alignment search tool. *J. Mol. Biol.* **215,** 403–410 (1990).
63. Zhang, Y. *et al.* An RNA-sequencing transcriptome and splicing database of glia, neurons, and vascular cells of the cerebral cortex. *J. Neurosci.* **34,** 11929–11947 (2014).
64. Zuber, V. & Strimmer, K. High-dimensional regression and variable selection using CAR scores. *Stat. Appl. Genet. Mol. Biol.* **10,** 1–22 (2011).
65. Bar-Joseph, Z. *et al.* Genome-wide transcriptional analysis of the human cell cycle identifies genes differentially regulated in normal and cancer cells. *Proc. Natl Acad. Sci. USA* **105,** 955–960 (2008).
66. Tasic, B. *et al.* Adult mouse cortical cell taxonomy revealed by single cell transcriptomics. *Nature Neurosci.* **19,** 335–346 (2016).
67. Cahoy, J. D. *et al.* A transcriptome database for astrocytes, neurons, and oligodendrocytes: a new resource for understanding brain development and function. *J. Neurosci.* **28,** 264–278 (2008).
68. Langfelder, P. & Horvath, S. WGCNA: an R package for weighted correlation network analysis. *BMC Bioinformatics* **9,** 559 (2008).
69. Langfelder, P. & Horvath, S. Fast R functions for robust correlations and hierarchical clustering. *J. Stat. Softw.* **46,** http://dx.doi.org/10.18637/jss.v046.i11 (2012).
70. Hawrylycz, M. *et al.* Canonical genetic signatures of the adult human brain. *Nat. Neurosci.* **18,** 1832–1844 (2015).
71. Verloes, A., Drunat, S., Gressens, P. & Passemard, S. in *GeneReviews* (eds Pagon, R. A. *et al.*) (Univ. Washington, 2013).
72. Schizophrenia Working Group of the Psychiatric Genomics Consortium. Biological insights from 108 schizophrenia-associated genetic loci. *Nature* **511,** 421–427 (2014).
73. Karaca, E. *et al.* Genes that affect brain structure and function identified by rare variant analyses of Mendelian neurologic disease. *Neuron* **88,** 499–513 (2015).
74. Zapala, M. A. & Schork, N. J. Multivariate regression analysis of distance matrices for testing associations between gene expression patterns and related variables. *Proc. Natl Acad. Sci. USA* **103,** 19430–19435 (2006).
75. Stead, J. D. H. *et al.* Transcriptional profiling of the developing rat brain reveals that the most dramatic regional differentiation in gene expression occurs postpartum. *J. Neurosci.* **26,** 345–353 (2006).
76. Thompson, C. L. *et al.* A high-resolution spatiotemporal atlas of gene expression of the developing mouse brain. *Neuron* **83,** 309–323 (2014).
77. Huang, W., Sherman, B. T. & Lempicki, R. A. Systematic and integrative analysis of large gene lists using DAVID bioinformatics resources. *Nature Protocols* **4,** 44–57 (2009).
78. Huang, W., Sherman, B. T. & Lempicki, R. A. Bioinformatics enrichment tools: paths toward the comprehensive functional analysis of large gene lists. *Nucleic Acids Res.* **37,** 1–13 (2009).
79. Smedley, D. *et al.* The BioMart community portal: an innovative alternative to large, centralized data repositories. *Nucleic Acids Res.* **43,** W589–W598 (2015).
80. Proux, E., Studer, R. A., Moretti, S. & Robinson-Rechavi, M. Selectome: a database of positive selection. *Nucleic Acids Res.* **37,** D404–D407 (2009).
81. Moretti, S. *et al.* Selectome update: quality control and computational improvements to a database of positive selection. *Nucleic Acids Res.* **42,** D917–D921 (2014).
82. Pirooznia, M. *et al.* SynaptomeDB: an ontology-based knowledgebase for synaptic genes. *Bioinformatics* **28,** 897–899 (2012).
83. Blue, M. E. & Parnavelas, J. G. The formation and maturation of synapses in the visual cortex of the rat. II. Quantitative analysis. *J. Neurocytol.* **12,** 697–712 (1983).

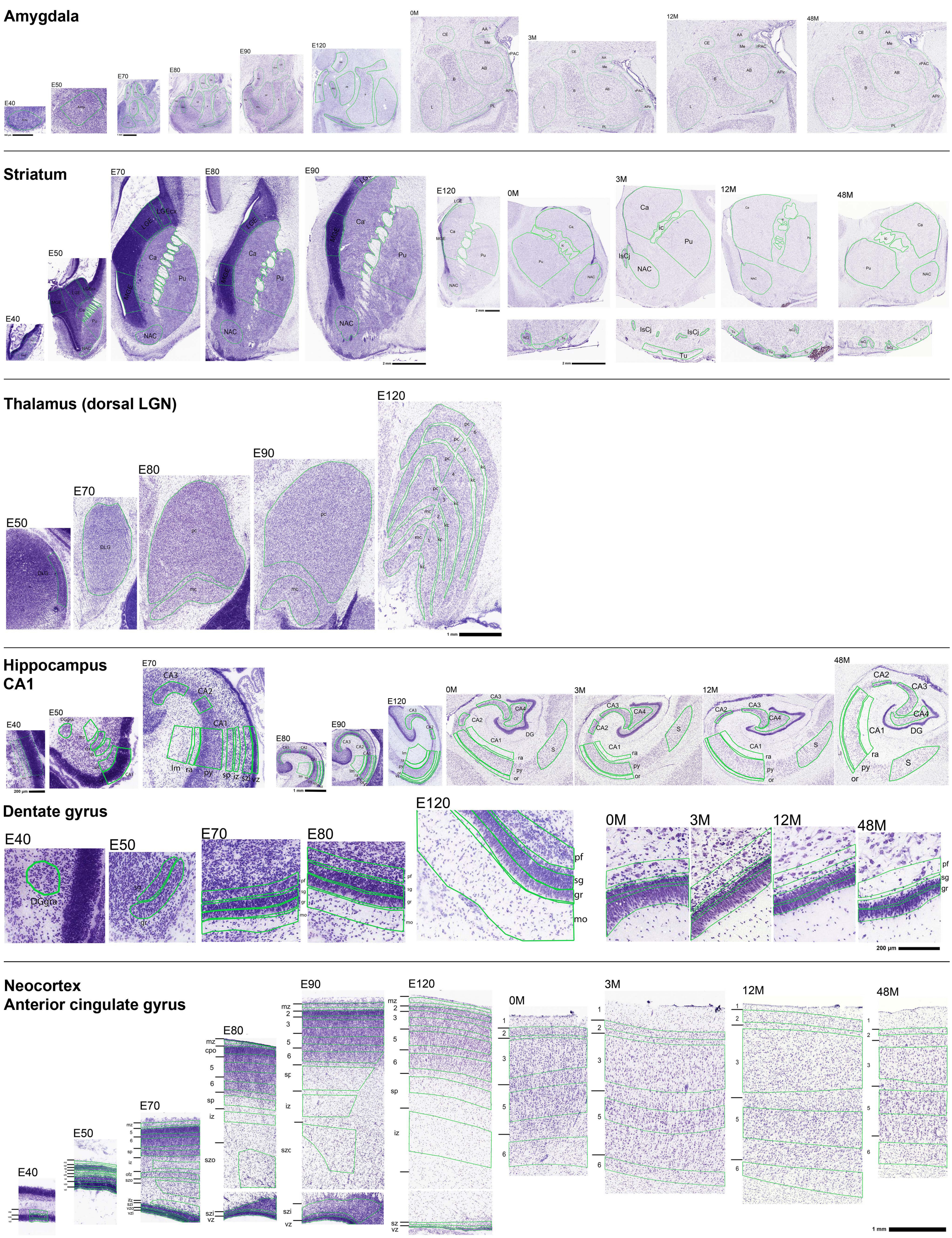

Extended Data Figure 1 | Anatomical parcellations of developing cortical and subcortical regions. Nissl stained sections of major brain regions sampled in this resource. Green lines demarcate subregions that were isolated by laser capture microdissection and transcriptionally profiled.

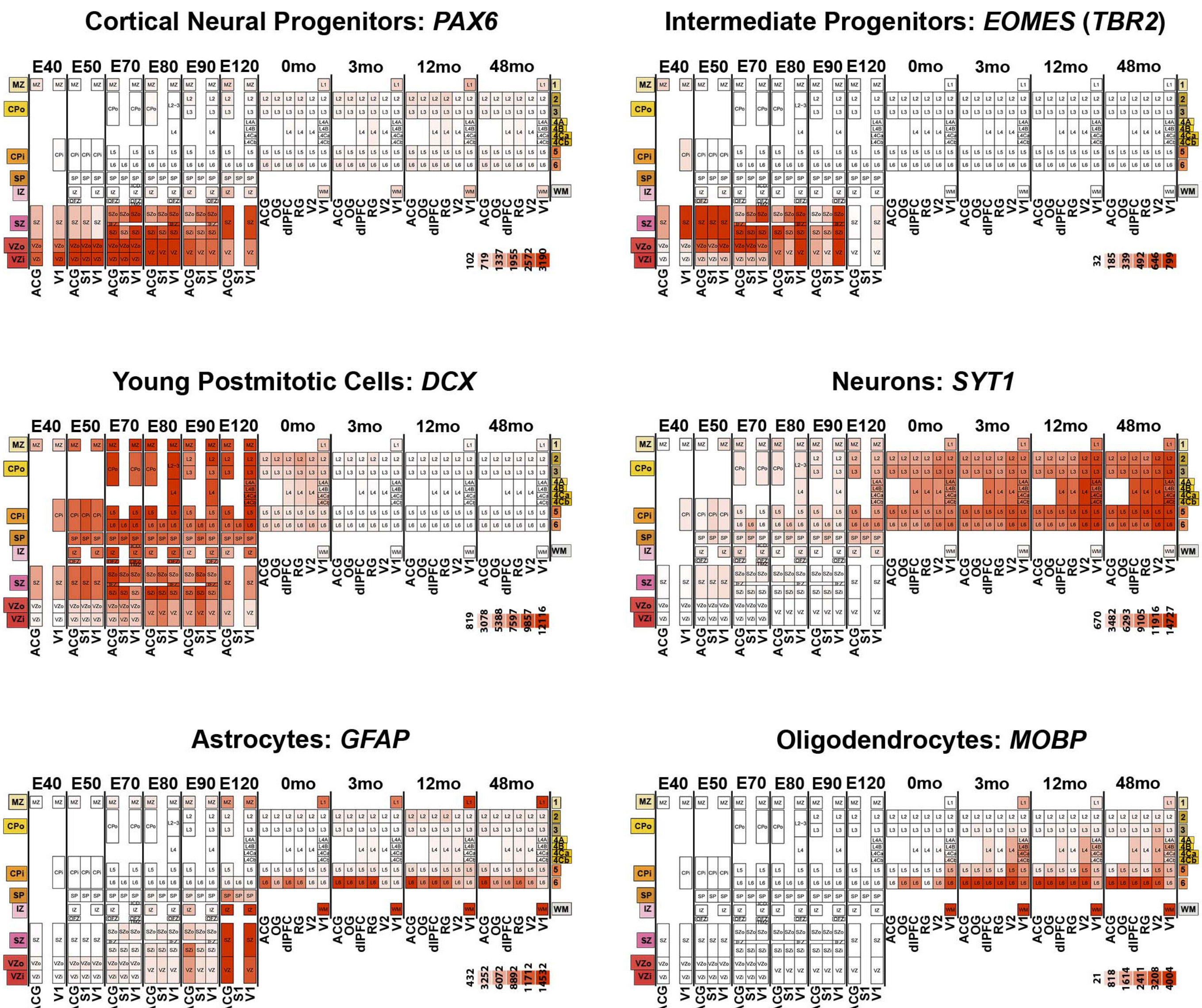

Extended Data Figure 2 | Canonical cell type marker gene expression across cortical development. Heat maps of average gene expression in cortical layers at different prenatal (E40–E120) and postnatal ages (0–48 months). Anterior cingulate gyrus (ACG) and primary visual cortex (V1) were sampled at all ages, while primary somatosensory cortex (S1) was sampled in a limited set of layers prenatally. Several additional prefrontal and visual areas were sampled postnatally: orbital gyrus (OG), dorsolateral prefrontal cortex (dlPFC), rectal gyrus (RG) and secondary visual cortex (V2).

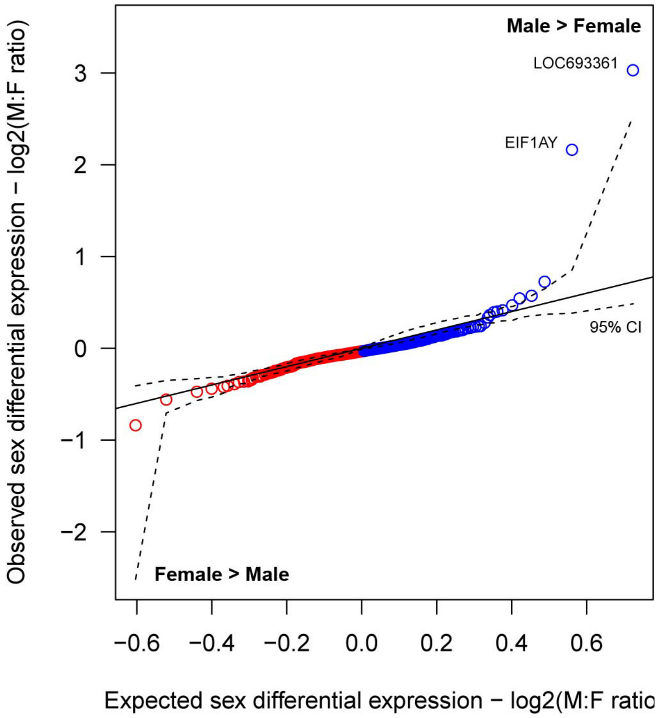

Extended Data Figure 3 | Sex differential expression is limited to two Y chromosome genes. a, Quantile–quantile plot of observed versus expected sex differential expression for all 12,441 genes across brain regions during prenatal development. A linear mixed model was fit to all prenatal brain samples with a fixed effect for sex and random effects for brain region, age and donor (see Supplementary Table 11). Genes were ordered by the observed sex effect and plotted versus the expected sex effect based on permutation testing. A 95% confidence interval was calculated (dashed line) based on permutations, and 11 genes in males and no genes in females were more highly expressed than expected by chance. Seven of these 11 genes were nominally significant and included at least two Y chromosome genes (*EIF1AY*, *LOC720563*) and potentially a third gene (*LOC693361*) whose microarray probe maps to an unannotated region of the Y chromosome.

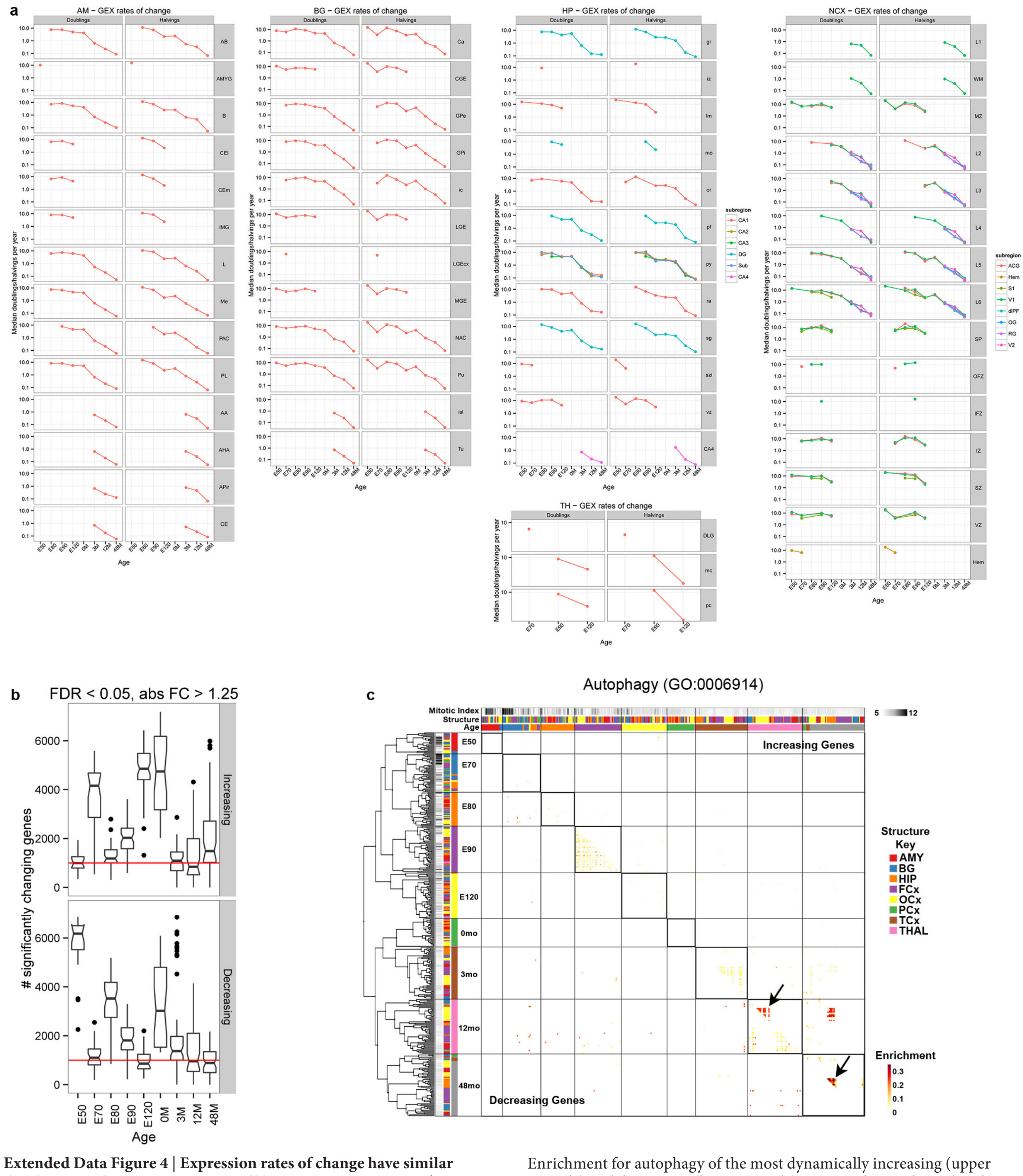

Extended Data Figure 4 | Expression rates of change have similar developmental trajectories across all brain regions. a, Rates of expression change in all available brain subregions and ages. **b**, Box plots summarizing the number of significantly increasing or decreasing genes between adjacent time points in all subregions. At all ages, the majority of subregions had at least 1,000 genes (red line) that were significantly changing (ANOVA FDR < 0.05, fold change > 1.25). **c**, Regional specificity of increased autophagy may reflect differential timing of synaptic pruning. Enrichment for autophagy of the most dynamically increasing (upper triangle) and decreasing (lower triangle) genes with samples ordered and labelled as in Fig. 3b. For each gene list, the colour corresponds to the proportion of GO terms that are more specific (that is, 'child') terms subsumed under autophagy (GO:0006914) based on the GO hierarchy and that are significantly enriched (nominal $P < 0.05$). Note that autophagy was selectively turned on in occipital cortex after infancy and in hippocampus after juvenility (arrows).

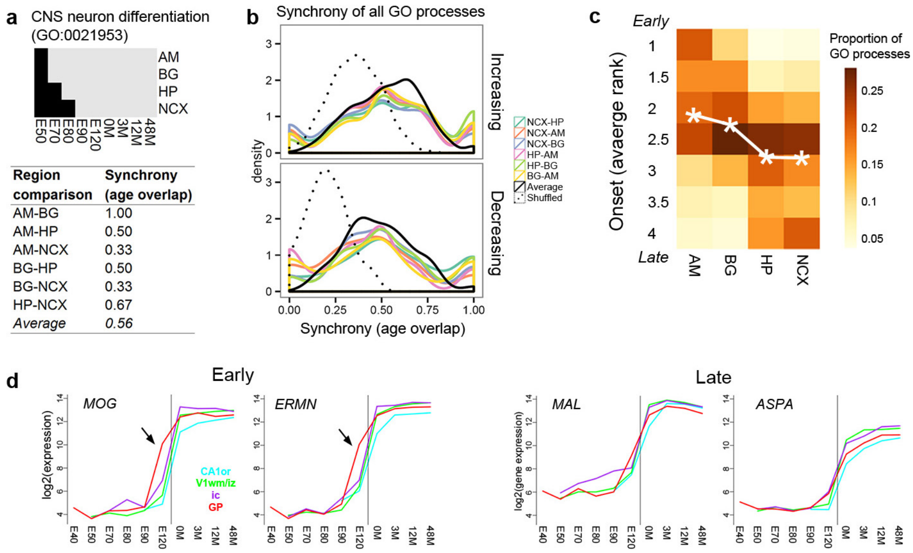

Extended Data Figure 5 | Variable synchrony of biological processes between brain regions. a, Example of variable timing of GO process activity (black boxes) between regions, resulting in different age overlaps (mini-table below). Note that E50 was the earliest age for which we could calculate expression change. AM, amygdala; BG, basal ganglia; HP, hippocampus; NCX, neocortex. **b**, Average pairwise age overlaps (black, solid line) for all increasing (top) and decreasing (bottom) GO processes were greater than expected by chance (black, dotted line). **c**, Rank ordered timing of GO processes in Fig. 4c with weighted average rank for each region (asterisks). **d**, Developmental expression of mature oligodendrocyte markers in four myelin-enriched brain subregions with early increased expression in globus pallidus (arrows) for *MOG* and *ERMN*, but not *MAL* and *ASPA*.

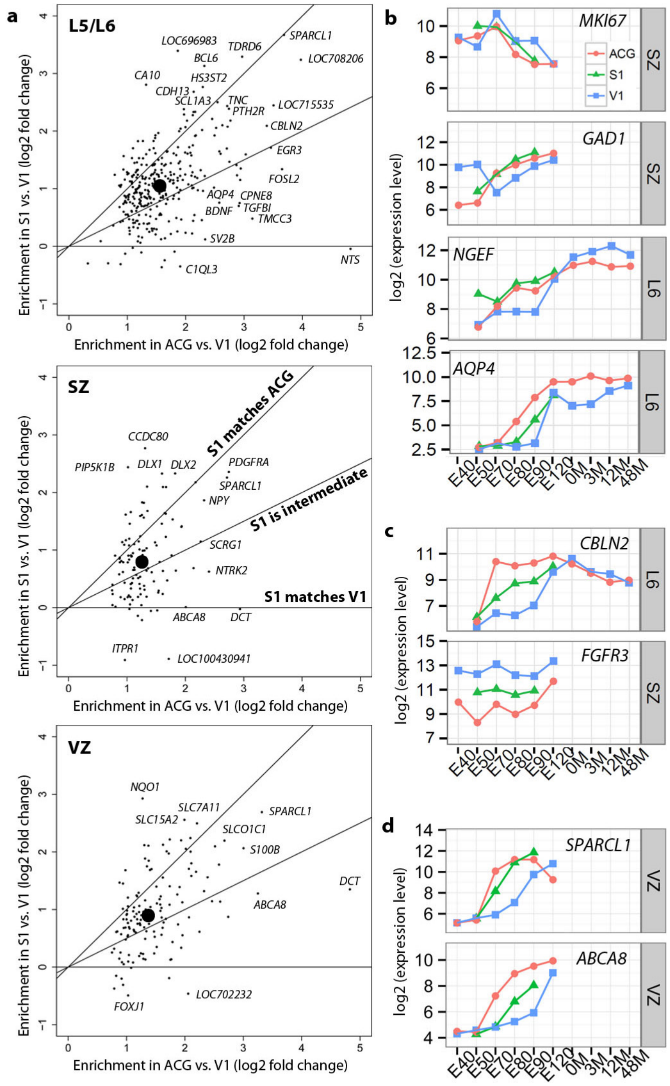

Extended Data Figure 6 | Neurogenesis and gliogenesis in S1 occur at a time course intermediate between V1 and ACG. a, Genes with enriched expression in ACG relative to V1 between E70–E90 also show enriched expression in S1 relative to V1, suggesting that the timing of primary sensory regions is non-uniform in L5/L6 (top), subventricular zone (SZ) (middle), and ventricular zone (VZ) (bottom). Each plot shows the average enrichment ($\log_2$ fold change) in S1 vs V1 (*y* axis) compared with the average enrichment in ACG vs V1 (*x* axis) between E70–E90 for all genes significantly enriched in ACG in at least two of the three ages between E70–E90 (Fig. 5a). **b**, Marker genes for cell types (compare with Fig. 5e–h) show expression patterns in S1 which are either consistent with ACG (that is, *GAD1*) or intermediate between V1 and ACG (that is, *AQP4*). **c**, Genes with enriched expression for V1 (*FGFR3*) or ACG (*CBLN2*) across development show intermediate expression in S1, suggesting that these genes may show cortical gradients rather than specific expression in V1 or ACG. **d**, Genes with common expression patterning in V1 and ACG can show different patterns in S1, suggesting that rate of neuron and glia development is not the whole story. For example, *SPARCL1* and *ABCA8* both show increased expression with time in VZ with V1 showing a delay relative to ACG; however, these two genes show different temporal delays in S1.

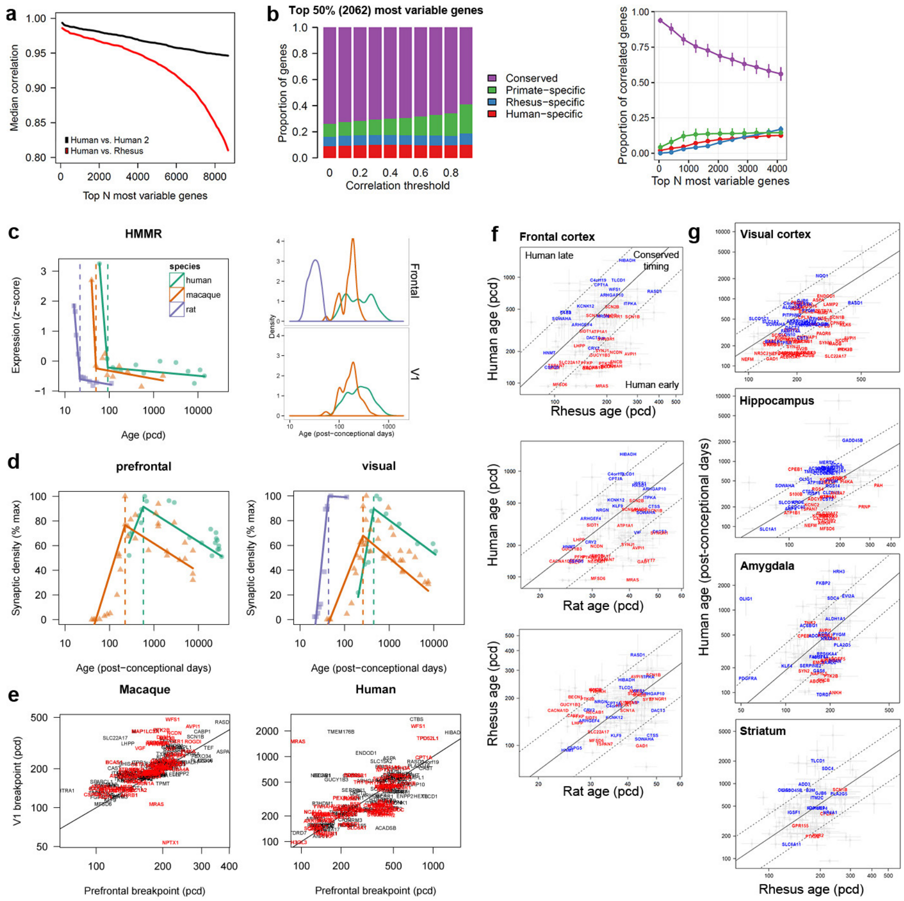

Extended Data Figure 7 | Evolutionary conservation of developmental expression. **a**, Median pairwise correlations of expression trajectories in prefrontal cortex within human (black) and between human and rhesus monkey (red) decrease for less variable genes in rhesus monkey (genes ordered by standard deviation of expression across ages). **b**, Left: proportion of genes assigned to different conservation categories is robust to correlation threshold. Right: developmentally dynamic genes are more highly conserved (genes ordered by same method as in **a**). For each set of genes, the average ± standard deviation of the proportion of genes in each conservation category was estimated using correlation thresholds ranging from 0 to 0.9. **c**, Left: segmented linear fits of expression for example gene with estimated breakpoints in each species (dashed lines). Right: distribution of breakpoint ages for 179 decreasing genes with good fits to the model in frontal and primary visual cortex. Colours and symbols are consistent in **c** and **d**. **d**, Segmented linear fits with breakpoint estimation of synaptic density for prefrontal and primary visual cortex based on previously published studies (see Methods). **e**, Breakpoint comparison of 179 increasing genes including 81 synapse related genes (red) between cortical areas within species. Genes that fall on the lines peak at the same age in primary visual and prefrontal cortex. **f**, **g**, Comparison of breakpoint timing between human, rhesus monkey and rat in prefrontal cortex (**f**) and additional brain regions (**g**). Genes that plateau in expression after their breakpoint in human (grey points), and genes that significantly decrease (blue symbols) or increase (red symbols) expression with 95% confidence intervals (grey lines) of breakpoints. Black lines correspond to equal (solid) ± a window (dashed) of developmental ages between species. pcd, post-conceptional days.

Extended Data Table 1 | Rhesus monkey donor information

Animal ID	Age	SX date	Sex	Indian origin (proportion)	Chinese origin (proportion)
MMU37857	E40	2/9/2012	Female	15/16	1/16
MMU38481	E40	5/2/2012	Male	1	0
MMU31370	E40	3/26/2013	Male	1	0
MMU36477	E40	4/16/2012	Female	1	0
DAM37624	E50	1/13/2012	Male	5/8	3/8
MMU36725	E50	4/23/2012	Male	1	0
MMU30213	E50	3/6/2012	Male	1	0
MMU38099	E50	2/23/2012	Female	15/16	1/16
DAM35650	E70	1/23/2012	Female	1	0
MMU32143	E70	3/9/2012	Female	1	0
MMU33757	E70	3/5/2012	Male	15/16	1/16
MMU35475	E70	3/5/2012	Male	7/8	1/8
MMU35058	E80	2/2/2012	Female	15/16	1/16
MMU37852	E80	3/29/2012	Female	1	0
MMU34624	E80	4/19/2012	Male	3/4	1/4
MMU36435	E80	4/30/2012	Male	15/16	1/16
MMU34326	E90	4/16/2012	Male	1	0
MMU35674	E90	4/13/2012	Female	1	0
MMU38285	E90	4/13/2012	Female	13/16	3/16
MMU38521	E90	4/27/2012	Male	1	0
MMU27052	E120	3/23/2012	Male	1	0
MMU30021	E120	3/7/2012	Female	1	0
MMU34501	E120	7/30/2012	Male	3/4	1/4
MMU29380	E120	3/12/2012	Female	1	0
MMU39867	0M	NA	Male	NA	NA
MMU39893	0M	4/12/2013	Male	3/4	1/4
MMU40864	0M	4/21/2014	Male	1	0
MMU40944	0M	4/29/2014	Male	1	0
MMU39465	3M	11/13/2008	Male	1	0
MMU39538	3M	5/10/2013	Male	1	0
MMU39766	3M	7/15/2013	Male	7/8	1/8
MMU40525	3M	6/9/2014	Male	1	0
MMU39420	12M	6/26/2013	Male	1	0
MMU39620	12M	3/9/2014	Male	7/8	1/8
MMU39645	12M	3/9/2014	Male	7/8	1/8
MMU36322	48M	7/11/2013	Male	1	0
MMU36358	48M	7/14/2013	Male	5/8	3/8
MMU36468	48M	6/26/2013	Male	5/8	3/8

Subject information for 38 rhesus macaque monkeys included in study. Surgery (SX) date, age, sex, and ancestry based on origin of parents and grandparents.

ARTICLE

doi:10.1038/nature18646

Human gut microbes impact host serum metabolome and insulin sensitivity

Helle Krogh Pedersen[1*], Valborg Gudmundsdottir[1*], Henrik Bjørn Nielsen[1*], Tuulia Hyotylainen[2,3,4*], Trine Nielsen[5*], Benjamin A. H. Jensen[6], Kristoffer Forslund[7], Falk Hildebrand[7,8,9], Edi Prifti[10,11], Gwen Falony[9,12], Emmanuelle Le Chatelier[10], Florence Levenez[10], Joel Doré[10,13], Ismo Mattila[4,14], Damian R. Plichta[1], Päivi Pöhö[4,15], Lars I. Hellgren[1], Manimozhiyan Arumugam[5], Shinichi Sunagawa[7,16], Sara Vieira-Silva[9,12], Torben Jørgensen[17,18], Jacob Bak Holm[6], Kajetan Trošt[14], MetaHIT Consortium†, Karsten Kristiansen[6,19], Susanne Brix[1], Jeroen Raes[8,9,12], Jun Wang[6,19,20,21,22], Torben Hansen[5,23], Peer Bork[7,24,25,26], Søren Brunak[1,27], Matej Oresic[3,4,14], S. Dusko Ehrlich[10,28] & Oluf Pedersen[5,17]

Insulin resistance is a forerunner state of ischaemic cardiovascular disease and type 2 diabetes. Here we show how the human gut microbiome impacts the serum metabolome and associates with insulin resistance in 277 non-diabetic Danish individuals. The serum metabolome of insulin-resistant individuals is characterized by increased levels of branched-chain amino acids (BCAAs), which correlate with a gut microbiome that has an enriched biosynthetic potential for BCAAs and is deprived of genes encoding bacterial inward transporters for these amino acids. *Prevotella copri* and *Bacteroides vulgatus* are identified as the main species driving the association between biosynthesis of BCAAs and insulin resistance, and in mice we demonstrate that *P. copri* can induce insulin resistance, aggravate glucose intolerance and augment circulating levels of BCAAs. Our findings suggest that microbial targets may have the potential to diminish insulin resistance and reduce the incidence of common metabolic and cardiovascular disorders.

Insulin resistance (IR) and metabolic syndrome are risk factors for both type 2 diabetes and ischaemic cardiovascular diseases, pathologies that are in epidemic growth worldwide. Mounting evidence suggests a link between the gut microbiome and human metabolic health[1–4], with transferability of insulin resistance phenotypes through faecal microbiome transplants[5,6]. These effects may partly be mediated through the metabolome[7]. Serum levels of amino acids, most consistently the BCAAs[8,9], triacylglycerols with low carbon number and double bonds[10,11], as well as specific membrane phospholipids[12], have previously been associated with IR and future risk of metabolic and cardiovascular morbidities. However, the origin of the abnormal IR-associated serum metabolome is largely unknown[13].

To explore the relationships between the fasting serum metabolome and the gut microbiome in the states of IR and metabolic syndrome, we examined 291 non-diabetic Danish adults, of whom 277 had available gut microbial data from the MetaHIT[1] study population. IR was estimated by homeostatic model assessment (HOMA-IR), which in epidemiological studies is a widely applied measure of IR, primarily as an estimate of hepatic IR[14]. Since IR is largely influenced by body mass index (BMI), we also estimated the IR index adjusted for BMI (HOMA-IR_{BMIadj}). Metabolic syndrome was defined according to recommendations by the International Diabetes Federation[15] (see Methods). For comparative analyses we further included 75 Danish type 2 diabetes patients[4] with quantitative gut metagenomics data generated by the same experimental protocol. Characteristics of the study samples are given in Supplementary Table 1 and Extended Data Fig. 1.

Results

In the present study, we assessed the role of the gut microbiome as a source for key features of the serum metabolome profile, predicting metabolic and cardiovascular disorders in non-diabetic lean and obese people. Untargeted metabolome profiles were generated on fasting serum samples, applying two mass spectrometry-based analytical platforms and providing information about 325 polar metabolites (94 known, 231 unknown) and 876 molecular lipids (289 known, 587 unknown), respectively (here collectively termed serum metabolites). These were binned into 74 co-abundance clusters across all individuals (Fig. 1a, Supplementary Tables 2 and 3). We found 19 of the 74 metabolite clusters (26%), comprising 26 polar metabolites and 367 lipids, to be significantly associated with both IR and metabolic syndrome, with consistent directionality across the 291 non-diabetic

[1]Center for Biological Sequence Analysis, Dept. of Systems Biology, Technical University of Denmark, DK-2800 Kongens Lyngby, Denmark. [2]University of Örebro, SE-702 81 Örebro, Sweden. [3]Turku Centre for Biotechnology, University of Turku and Åbo Akademi University, FI-20520 Turku, Finland. [4]VTT Technical Research Centre of Finland, FI-02044 Espoo, Finland. [5]The Novo Nordisk Foundation Center for Basic Metabolic Research, Faculty of Health and Medical Sciences, University of Copenhagen, DK-2200 Copenhagen, Denmark. [6]Laboratory of Genomics and Molecular Biomedicine, Department of Biology, University of Copenhagen, DK-2100 Copenhagen, Denmark. [7]European Molecular Biology Laboratory, 69117 Heidelberg, Germany. [8]Department of Bioscience Engineering, Vrije Universiteit Brussel, 1050 Brussels, Belgium. [9]Center for the Biology of Disease, VIB, 3000 Leuven, Belgium. [10]MGP MetaGénoPolis, INRA, Université Paris-Saclay, 78350 Jouy en Josas, France. [11]Institute of Cardiometabolism and Nutrition (ICAN), 75013 Paris, France. [12]Department of Microbiology and Immunology, Rega Institute, KU Leuven, 3000 Leuven, Belgium. [13]Micalis Institute, INRA, AgroParisTech, Université Paris-Saclay, 78350 Jouy-en-Josas, France. [14]Steno Diabetes Center, DK-2820 Gentofte, Denmark. [15]Faculty of Pharmacy, University of Helsinki, FI-00014 Helsinki, Finland. [16]Institute of Microbiology, ETH Zurich, CH-8092 Zurich, Switzerland. [17]Faculty of Health and Medical Sciences, University of Copenhagen, DK-2200 Copenhagen, Denmark. [18]Research Centre for Prevention and Health, Centre for Health, Capital region, Glostrup Hospital, DK-2600 Glostrup, Denmark. [19]BGI-Shenzhen, 518083 Shenzhen, China. [20]Princess Al Jawhara Albrahim Center of Excellence in the Research of Hereditary Disorders, King Abdulaziz University, Jeddah, Saudi Arabia. [21]Macau University of Science and Technology, Avenida Wai long, Taipa, Macau. [22]Department of Medicine and State Key Laboratory of Pharmaceutical Biotechnology, University of Hong Kong, Hong Kong. [23]Faculty of Health Sciences, University of Southern Denmark, DK-5000 Odense, Denmark. [24]Molecular Medicine Partnership Unit, University of Heidelberg and European Molecular Biology Laboratory, 69120 Heidelberg, Germany. [25]Max Delbrück Centre for Molecular Medicine, D-13125 Berlin, Germany. [26]Department of Bioinformatics, University of Wuerzburg, D-97074 Würzburg, Germany. [27]Novo Nordisk Foundation Center for Protein Research, Disease Systems Biology, Faculty of Health and Medical Sciences, University of Copenhagen, DK-2200 Copenhagen, Denmark. [28]King's College London, Centre for Host–Microbiome Interactions, Dental Institute Central Office, Guy's Hospital, SE1 9RT London, UK.
*These authors contributed equally to this work.
†Lists of participants and their affiliations appear in the Supplementary Information.

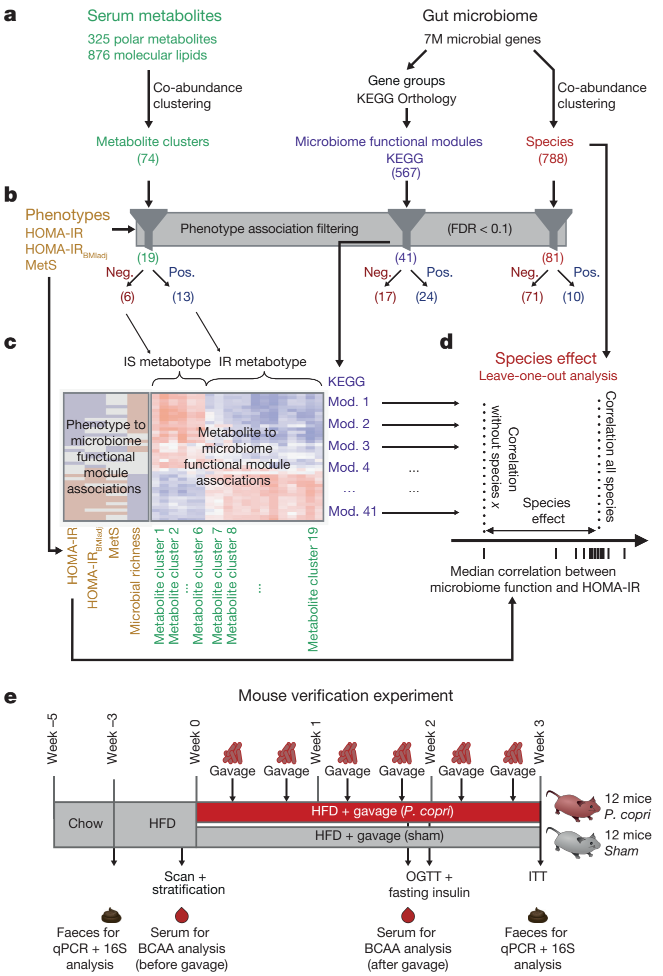

Figure 1 | Overview of the workflow integrating human phenotypes, fasting serum metabolome, gut microbiome data and mouse feeding experiments. a, Metabolites were summarized as co-abundance clusters, and functional module and species abundance profiles extracted from gut microbiome data. **b**, Features were filtered for significant positive or negative associations with HOMA-IR, HOMA-IR_{BMIadj} or metabolic syndrome. **c**, Metabolite clusters were divided into IR- and IS-metabotypes and associated with microbiome functional modules. **d**, Microbial driver species for the functional module associations with HOMA-IR were identified using a leave-one-out analysis. **e**, Experimental design for *P. copri* feeding mouse experiment. HFD, high-fat diet; OGTT, oral glucose tolerance test; ITT, insulin tolerance test; MetS, metabolic syndrome.

individuals (Spearman rank correlation test, false discovery rate (FDR) < 0.1, Extended Data Fig. 2 and Supplementary Tables 4 and 5). These 19 metabolite clusters separated into two groups that were either positively or negatively correlated with both IR and metabolic syndrome, referred hereafter to as the IR-metabotype and insulin sensitivity (IS)-metabotype, respectively (Fig. 1b, Supplementary Table 6, Supplementary Results and Extended Data Fig. 3). Most of these associations were confirmed in type 2 diabetes patients (see Supplementary Results for details).

In accordance with previous reports, the identifiable serum metabolites constituting the IR-metabotype mainly comprised amino acids (including BCAAs; see Supplementary Discussion), tricarboxylic acid cycle metabolites, and a large number of triacylglycerols (Supplementary Table 6, previous findings referenced therein). Interestingly, we found that serum BCAAs clustered with hydrocinnamic and indole-3-lactic acids (metabolite cluster M10, Supplementary Table 2), both of which belong to a class of phenolic compounds that are associated with gut microbial metabolism[16]. Serum levels of hydrocinnamic acid are affected by gut microbiota in mice[17] and hydrocinnamic acid is a known inhibitor of branched-chain α-keto acid dehydrogenase kinase, which regulates the breakdown of BCAAs[18]. By contrast, the IS-metabotype consisted solely of serum lipids, primarily phospholipids and triacylglycerols with odd carbon number and high double bond content (Supplementary Table 6). Hence, our results confirm previous reports of odd-chain fatty acids and polyunsaturated fatty acids as associated with reduced risk of type 2 diabetes[10,19]. Plasma odd-chain fatty acids are often considered to be a product of microbial metabolism or a marker of dietary intake, especially of dairy products, although recent findings show that C15:0 and C17:0 are also endogenously produced in adipocytes through α-oxidation of palmitic and stearic acid[20,21]. Based on our data, however, it is not possible to distinguish if these odd-chain fatty acids originate from dietary intake or bacterial metabolism. Surprisingly, the IS-metabotype also included C16:0-ceramide and sphingomyelin. Elevated circulating concentrations of ceramides[22], including the C16:0 ceramide[23,24], are generally implicated in the pathogenesis of IR. However, our data suggest that C16:0-ceramide may play a more complex role in the regulation of host insulin sensitivity than recognized until now.

Some of the IR- and metabolic-syndrome-associated fasting serum metabolites, such as the essential BCAAs, cannot be synthesized by humans and must therefore originate from ingested food or gut microbial synthesis. Therefore, we investigated the metabolic potential of the gut microbiome in relation to these metabolites using KEGG functional modules (Fig. 1a), that is, a set of manually curated functional and pathway units from the KEGG database, each consisting of a number of KEGG orthologous gene groups[25].

Forty-one of the 567 microbiome functional modules (7%) were significantly associated (Mann–Whitney *U*-test, FDR < 0.1) with one or more of the IR and metabolic syndrome phenotypes (Extended Data Fig. 2, Supplementary Table 7). All 41 functional modules were furthermore associated with the IR- and IS-metabotypes (Figs 1c and 2), with a majority also differing in abundance in the expected direction in type 2 diabetes patients (Supplementary Results). A majority (23/33) of the HOMA-IR associated modules remained significant after adjusting for BMI, while six additional modules were identified upon the BMI adjustment (Extended Data Fig. 2, Supplementary Table 7). The results suggest that, in this sample of lean and obese individuals, the functional microbial shift in IR is largely independent of BMI, which should be further validated in population-based cohorts. Furthermore, we found this functional shift to also partly overlap with functional characteristics of a low richness gut microbiome, as the IR associations of many functional modules (24/33) were attenuated after adjusting for microbial gene richness (Supplementary Results). We observed only a minor separation in the microbiome or metabolomic data corresponding to patient subgroups based on the five clinical components of the metabolic syndrome (Supplementary Results).

The cross-domain associations between the IR and metabolic syndrome phenotypes, the serum metabolome and the gut microbiome described above may suggest functional relationships. Notably, the functional modules of the microbiome that were positively associated with both HOMA-IR and the IR-metabotype contained enzymes for biosynthesis of BCAAs, cofactors, vitamins, lipopolysaccharides and various transport systems, some of which have elevated expression in gut microbiomes transplanted into mice from obese donors[6]. In contrast, the microbiome negatively associated with HOMA-IR and the IR-metabotype contained functional modules important for methanogenesis, pyruvate oxidation and transport systems, including inward transport of BCAAs. Noticeably, the microbiome functional modules that were associated with the two metabotypes showed a large overlap with the metabolic pathways essential for microbiome–host interactions mediated through metabolites, including the BCAAs, as highlighted in a recent *Caenorhabditis elegans* study[26].

Coherently, the majority (60/81) of the microbial species associated with IR or metabolic syndrome (Supplementary Table 8) correlated significantly with the IR- and IS-metabotypes (Supplementary Results,

Extended Data Figs 4 and 5). To identify the species that contributed the most to the associations between the microbiome functional modules and HOMA-IR, we iterated the correlation analysis, leaving out genes from a single species in each iteration (see Fig. 1d and Methods for details). For several functional modules, the correlations with HOMA-IR were driven by only a few species (Supplementary Table 9). Notably, the positive associations between HOMA-IR and the biosynthesis modules of BCAA, tryptophan and lipopolysaccharides were largely driven by *P. copri* followed by *B. vulgatus*, as they were almost abolished when genes from these species were omitted. Although these two species were the main drivers for many of the same functional modules, they were at the same time significantly anti-correlated (Spearman correlation coefficient $= -0.38$, $P = 9.0 \times 10^{-11}$, Extended Data Fig. 6), consistent with the previously reported trade-off between these genera[27]. Still, the abundance of each of these species (when present) correlated positively with HOMA-IR (Extended Data Fig. 7, Supplementary Table 10), as did their combined abundance across all individuals (Spearman correlation coefficient $= 0.20$, $P = 0.001$, Extended Data Fig. 6). The possible importance of *P. copri* is further highlighted by its positive correlation with the BCAA-containing metabolite cluster M10 in the 94 individuals with detectable levels of the species (Spearman correlation coefficient $= 0.22$, $P = 0.034$, Extended Data Fig. 7, Supplementary Table 10). However, the correlations of *P. copri* to the BCAA-containing metabolite cluster M10 and HOMA-IR were abolished in the full cohort of 277 non-diabetic individuals ($P = 0.44$ and $P = 0.67$, respectively), suggesting that in the absence of *P. copri* other species may influence the levels of the M10 metabolite cluster and HOMA-IR. *P. copri*, a hallmark species of the *Prevotella* enterotype[28] (see Supplementary Results for further discussion), has been associated with rheumatoid arthritis[29] but not with IR in humans. *B. vulgatus* is reported to correlate positively with fat mass and other markers of IR in humans[30], whereas a mouse study suggested protection against the development of metabolic disorders, although only in the context of a low-fat diet[6]. Thus, the role of *B. vulgatus* in IR and metabolic disorders seems complex and is probably context-specific. Among other driver species for the microbial functional modules positively correlated with HOMA-IR were *Escherichia coli*, *Sutterella wadsworthensis* and unclassified *Sutterella* and *Prevotella* species (Extended Data Fig. 8, Supplementary Table 9).

In contrast to the functional modules enriched in the gut microbiome of insulin-resistant individuals, which were driven by relatively few microbial species each with high impact, all microbial functional modules associated with increased insulin sensitivity were driven by multiple species, all with minor effect (Supplementary Results).

The microbial functional module analysis presented in Fig. 2 highlighted an increased BCAA biosynthesis potential, but depletion for genes encoding the transport system for bacterial BCAA uptake (referred to as inward BCAA transport) in the gut microbiome of insulin-resistant individuals (Fig. 3a). These findings synergistically contribute to an increased BCAA pool and are of considerable interest

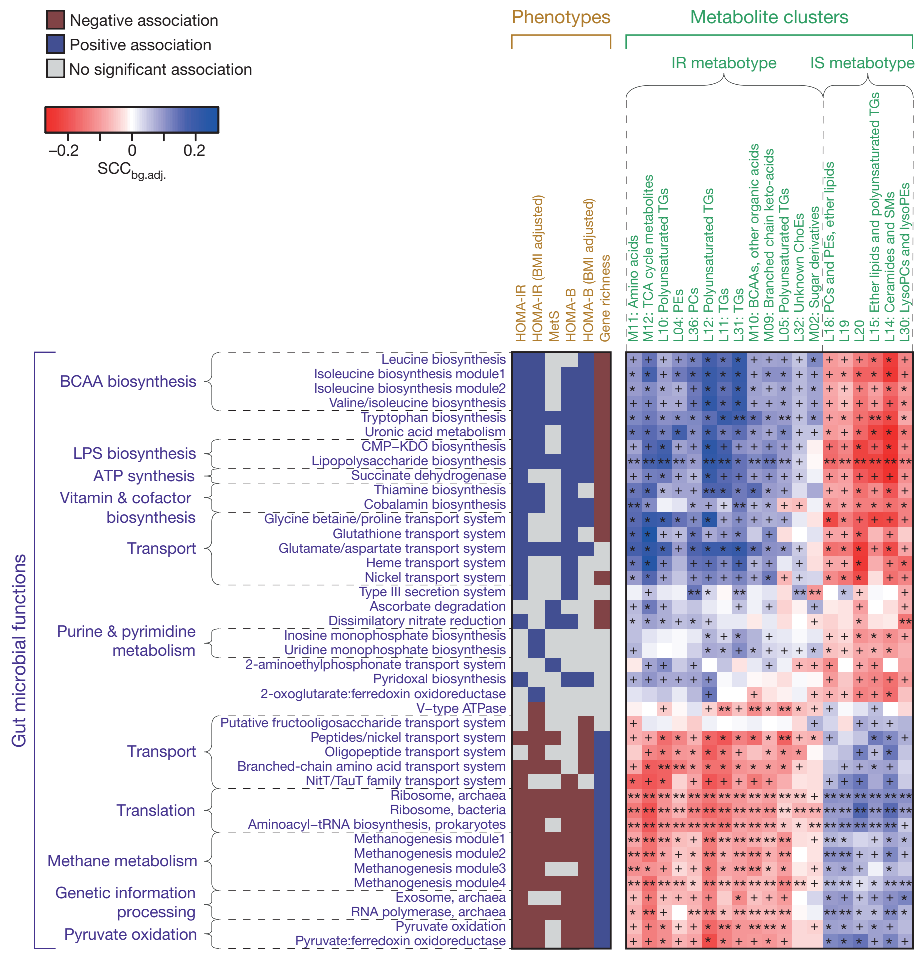

Figure 2 | Association map of the three-tiered analyses integrating the phenome, the gut microbiome and the fasting serum metabolome in 277 non-diabetic individuals with available metagenomic data. The left panel shows significant associations (Mann–Whitney *U*-test FDR < 0.1) between microbial functional modules and the indicated phenotypes; colouring indicates direction of association. The right panel shows associations between the same modules and serum metabolite clusters. Colouring represents the median Spearman correlation coefficient between metabolite clusters and the indicated functional modules, corrected for background distribution ($SCC_{bg.adj.}$, see Methods), where MWU FDRs are denoted: +, FDR < 0.1; *, FDR < 0.01; **, FDR < 0.001.

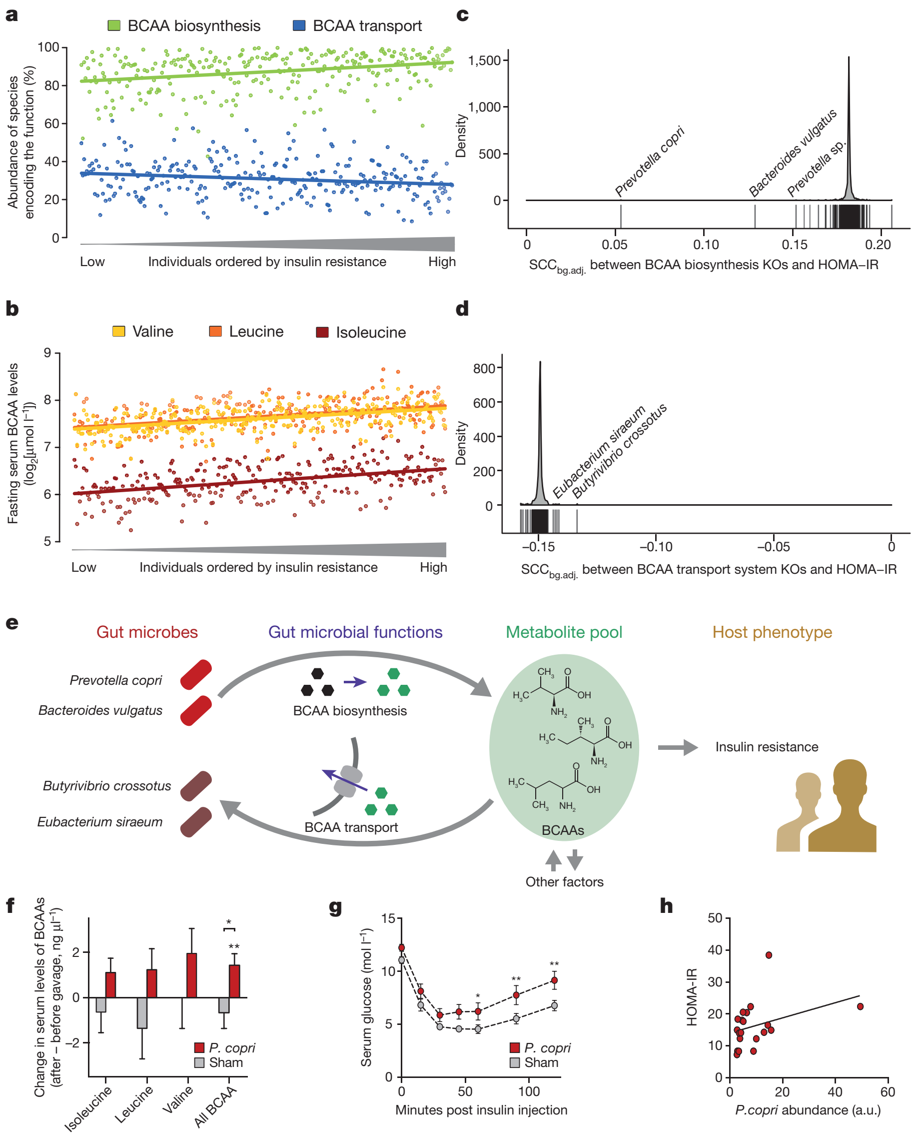

Figure 3 | The ratio between the gut microbiome potential for BCAA biosynthesis and inward transport is linked to fasting serum BCAA levels and IR in humans and can be attributed to a few driver species, including *P. copri* that induces an aggravation of glucose intolerance in mice concomitantly with elevated serum BCAA levels. a, The total abundance of all microbial species containing genes coding for BCAA biosynthesis (Spearman correlation coefficient (SCC) = 0.30, $P = 5.3 \times 10^{-7}$) and inward transport (SCC = −0.17, $P = 4.5 \times 10^{-3}$) potential is shown in green and blue, respectively, for 277 non-diabetic individuals ordered by their HOMA-IR levels. The slopes are significantly different ($P = 4.0 \times 10^{-8}$, see Methods). **b**, Fasting serum BCAA levels in 291 non-diabetic individuals ordered by HOMA-IR levels (SCC: leucine = 0.40, isoleucine = 0.44, valine = 0.49, $P < 4 \times 10^{-12}$). **c**, **d**, The effect of specific microbial species on associations between BCAA biosynthesis and transport, respectively, and HOMA-IR in 277 non-diabetic individuals; illustrated by the change in background-adjusted median SCC ($SCC_{bg.adj}$) between HOMA-IR and the BCAA biosynthesis/transport functional modules when a given species has been excluded from the analysis (see Methods). **e**, Suggested model of the microbiome contribution to serum BCAA levels and IR. Fasting serum BCAA levels are influenced by microbial BCAA biosynthesis and uptake; these levels in turn may influence host insulin sensitivity. **f**, Changes in mouse serum BCAA levels (mean ± s.e.m.) after *P. copri* or sham gavaging for two weeks before challenge. Asterisks indicate significance between *P. copri*-gavaged ($n = 12$) and sham-gavaged control mice ($n = 12$) and significance relative to before challenge (likelihood ratio test, $*P < 0.05$; $**P < 0.01$). **g**, Insulin tolerance test. The *P. copri*-gavaged mice ($n = 12$) had significantly higher serum glucose levels compared to sham-gavaged controls ($n = 12$, $P = 0.032$, repeated measures two-way ANOVA) after three weeks challenge. Mean ± s.e.m. is depicted. Asterisks indicate significant differences at individual time points (repeated measures two-way ANOVA): $*P < 0.05$; $**P < 0.01$. **h**, Faecal *P. copri* abundance (arbitrary units, quantitative PCR normalized 16S rDNA) as a function of HOMA-IR two weeks post bacterial challenge (SCC = 0.46, $P = 0.040$).

in the light of the report demonstrating that serum BCAA levels are increased in mice following transplantation of stools from insulin-resistant individuals[6]. The described gut microbiome features are consistent with the elevated serum levels of BCAAs in insulin-resistant individuals (Fig. 3b), suggesting that an increased ratio between gut microbial biosynthesis and uptake of BCAAs contributes to elevated serum BCAA concentrations, which are known to associate with IR[31]. Moreover, the difference between the potential for BCAA biosynthesis and inward BCAA transport of the gut microbiome was even more significantly associated with the serum BCAA concentrations than either of the two functional modules alone (Supplementary Table 11). Importantly, while the IR-associated increase in the microbial potential for BCAA biosynthesis was largely driven by *P. copri* or *B. vulgatus* (see above), the reduced capacity for bacterial BCAA uptake was driven by reduced abundance of multiple species, including *B. crossotus* and *E. siraeum* (Fig. 3c, d).

Consistent correlations with HOMA-IR were observed for almost all of the enzymes and transport system subunits within the BCAA

biosynthesis and transport modules respectively, lending further credence to the importance of these modules (Extended Data Fig. 9, Supplementary Table 12). Notably, of the BCAA biosynthesis enzymes, D-citramalate synthase showed the strongest individual positive correlation with HOMA-IR (Spearman correlation coefficient = 0.24, $P = 4.89 \times 10^{-5}$). D-citramalate synthase constitutes the first step in a less common threonine-independent isoleucine biosynthesis pathway[32]. While most microorganisms synthesize isoleucine from threonine[33], 87 gut microbial species identified in our cohort (including both *P. copri* and *B. vulgatus*, Supplementary Table 13), contained the D-citramalate synthase gene, highlighting the importance of this less common pathway in the human gut microbiome.

Our findings are summarized in the model shown in Fig. 3e, which offers a mechanistic explanation for the increased circulating BCAA concentrations that are known to correlate positively with IR[31] and type 2 diabetes[8]. The difference in functional potential between microbial BCAA biosynthesis and BCAA uptake explained 2.4–3.1% of the variance in serum BCAA levels (Supplementary Table 11). In comparison, less than 1% of variance is explained by currently identified variants in the human genome, although the heritability of fasting serum BCAA levels[34] is estimated to be 0.41–0.49.

P. copri was the strongest driver species for the positive association between microbial BCAA biosynthesis in the gut and IR, suggesting a possible causal relation. This assumption is further supported by several reports associating Prevotellaceae[35–37], and more specifically *P. copri*[29,38], with intestinal inflammation, an important contributor to host IR. To experimentally address the relation between *P. copri* and abnormal glucose metabolism, we compared *P. copri* ($n = 12$) and sham-gavaged ($n = 12$) C57BL/6J male mice on a high-fat diet (Fig. 1e). Notably, two weeks of *P. copri* challenge aggravated glucose intolerance (Extended Data Fig. 10a) and increased serum total BCAA levels (compared with baseline: likelihood ratio test, $P = 0.004$, Fig. 3f). Insulin sensitivity was reduced after three weeks of *P. copri* challenge (Fig. 3g, $P = 0.032$), suggesting a potentially causal role of *P. copri* in mediating the increase in serum BCAA and IR. The relatively modest effect of the *P. copri* inoculation on serum BCAA levels may reflect that *P. copri* correlated more strongly to HOMA-IR than to BCAAs in the human cohort (Supplementary Table 10). Importantly, upon glucose challenge, the plasma insulin excursion rates were indistinguishable between groups (Extended Data Fig. 10b; $P = 0.80$), hence negating beta cell malfunction as a confounding variable. It should be noted that Prevotellaceae (and thus *P. copri*) were a minor component of the mouse microbiome in both groups upon feeding with a high-fat diet, as evidenced by faecal 16S rDNA amplicon analysis (Extended Data Fig. 10c). Despite minor compositional changes in the gut microbiota (adonis, $P = 0.04$), we found no alterations of the relative abundances of any single family component thereof to be significant upon gavage (Extended Data Fig. 10c, FDR > 0.05). In contrast, *P. copri* was significantly increased (Extended Data Fig. 10d, $P = 0.0058$), suggesting that it contributed to the observed pathophysiological changes. This conclusion is further supported by the direct correlation between *P. copri* abundances and HOMA-IR (Fig. 3h, Spearman correlation coefficient = 0.46, $P = 0.040$). Interestingly, an inverse relationship between glucose intolerance and *P. copri* challenge was recently reported[39]. However, in the latter study a completely different dietary regimen, high in fibre and low in fat, was used, suggesting that the effect of *P. copri* is diet-dependent. Furthermore, it should be noted that the feed used in the present study contained soy protein, which is low in BCAAs, as the protein source, contrasting the use of casein, high in BCAAs, in the study by Kovatcheva-Datchary *et al.*[39].

Discussion

By integrating data on host insulin sensitivity and metabolic syndrome, gut microbiome, and fasting serum metabolome, we were able to demonstrate clear metabolome signatures of IR phenotypes among non-diabetic individuals and validate them in patients with type 2 diabetes. The IR-associated metabolome associates with functional components of the IR-linked gut microbiome: notably the increased potential for lipopolysaccharide and BCAA biosynthesis, and reduced potential for BCAA transport into bacterial cells, methanogenesis and pyruvate oxidation.

Studies demonstrating the association of fasting serum BCAA levels with incident type 2 diabetes[8], the normalization of BCAA levels in obese individuals after bariatric surgery[40] and the development of IR in rats after BCAA diet supplementation[31] suggest a potentially causative role of the BCAAs, or their breakdown products[41,42], in metabolic disorders, although the reason as to why they are elevated in the first place is not well established. Potential explanations include reduced BCAA breakdown in adipose tissue[43,44] and liver[45]. Consistent relationships in our data between serum concentrations of BCAAs, bacterial BCAA biosynthesis and inward transport potentials, and the severity of IR phenotypes are reinforced by the intriguing findings that BCAAs co-vary tightly with fasting serum metabolites known to be of microbial origin. This suggests that the gut microbiota is another independent contributing source of elevated serum BCAA levels in common human states of IR. Furthermore, positive correlations between microbial functions—including BCAA biosynthesis—and IR are largely driven by a few species only, notably *P. copri* and *B. vulgatus*, suggesting that they may directly impact host metabolism. We tested this hypothesis in mice fed a high-fat diet, and found that a challenge with *P. copri* led to increased circulating serum levels of BCAAs, insulin resistance and an aggravation of glucose intolerance. We conclude that dysbiosis of the human gut microbiota impacts the serum metabolome and contributes to insulin resistance.

Importantly, while our findings relate to non-diabetic individuals and type 2 diabetes patients with preserved insulin secretion, they cannot yet be generalized to patients with impaired insulin secretion (Supplementary Discussion). Future physiological studies are needed to elucidate how the intestinal BCAAs and other amino acids enter the bloodstream and from which intestinal location they are absorbed. Furthermore, investigations of how dietary changes alone or in combination with microbial or pharmacological interventions may impact the microbiome and, in particular, influence *P. copri* modulation of serum BCAA levels will open novel avenues to counter the pathogenesis of IR and its linked epidemics of common metabolic and cardiovascular disorders.

Online Content Methods, along with any additional Extended Data display items and Source Data, are available in the online version of the paper; references unique to these sections appear only in the online paper.

Received 18 January; accepted 14 June 2016.
Published online 13 July 2016.

1. Le Chatelier, E. *et al.* Richness of human gut microbiome correlates with metabolic markers. *Nature* **500,** 541–546 (2013).
2. Qin, J. *et al.* A metagenome-wide association study of gut microbiota in type 2 diabetes. *Nature* **490,** 55–60 (2012).
3. Karlsson, F. H. *et al.* Gut metagenome in European women with normal, impaired and diabetic glucose control. *Nature* **498,** 99–103 (2013).
4. Forslund, K. *et al.* Disentangling type 2 diabetes and metformin treatment signatures in the human gut microbiota. *Nature* **528,** 262–266 (2015).
5. Vrieze, A. *et al.* Transfer of intestinal microbiota from lean donors increases insulin sensitivity in individuals with metabolic syndrome. *Gastroenterology* **143,** 913–916 (2012).
6. Ridaura, V. K. *et al.* Gut microbiota from twins discordant for obesity modulate metabolism in mice. *Science* **341,** 1241214 (2013).
7. Holmes, E., Li, J. V., Marchesi, J. R. & Nicholson, J. K. Gut microbiota composition and activity in relation to host metabolic phenotype and disease risk. *Cell Metab.* **16,** 559–564 (2012).
8. Wang, T. J. *et al.* Metabolite profiles and the risk of developing diabetes. *Nat. Med.* **17,** 448–453 (2011).
9. Lee, C. C. *et al.* Branched-chain amino acids and insulin metabolism: The Insulin Resistance Atherosclerosis Study (IRAS). *Diabetes Care* **39,** 582–588 (2016).
10. Rhee, E. P. *et al.* Lipid profiling identifies a triacylglycerol signature of insulin resistance and improves diabetes prediction in humans. *J. Clin. Invest.* **121,** 1402–1411 (2011).

11. Kotronen, A. *et al.* Serum saturated fatty acids containing triacylglycerols are better markers of insulin resistance than total serum triacylglycerol concentrations. *Diabetologia* **52,** 684–690 (2009).
12. Floegel, A. *et al.* Identification of serum metabolites associated with risk of type 2 diabetes using a targeted metabolomic approach. *Diabetes* **62,** 639–648 (2013).
13. Roberts, L. D., Koulman, A. & Griffin, J. L. Towards metabolic biomarkers of insulin resistance and type 2 diabetes: progress from the metabolome. *Lancet Diabetes Endocrinol*. **2,** 65–75 (2014).
14. Matthews, D. R. *et al.* Homeostasis model assessment: insulin resistance and beta-cell function from fasting plasma glucose and insulin concentrations in man. *Diabetologia* **28,** 412–419 (1985).
15. Alberti, K. G. M. M., Zimmet, P. & Shaw, J. Metabolic syndrome – a new world-wide definition. A consensus statement from the International Diabetes Federation. *Diabet. Med.* **23,** 469–480 (2006).
16. Aura, A. M. Microbial metabolism of dietary phenolic compounds in the colon. *Phytochem. Rev.* **7,** 407–429 (2008).
17. Velagapudi, V. R. *et al.* The gut microbiota modulates host energy and lipid metabolism in mice. *J. Lipid Res.* **51,** 1101–1112 (2010).
18. Tso, S. C. *et al.* Structure-based design and mechanisms of allosteric inhibitors for mitochondrial branched-chain α-ketoacid dehydrogenase kinase. *Proc. Natl Acad. Sci. USA* **110,** 9728–9733 (2013).
19. Forouhi, N. G. *et al.* Differences in the prospective association between individual plasma phospholipid saturated fatty acids and incident type 2 diabetes: the EPIC-InterAct case-cohort study. *Lancet Diabetes Endocrinol*. **2,** 810–818 (2014).
20. Roberts, L. D., Virtue, S., Vidal-Puig, A., Nicholls, A. W. & Griffin, J. L. Metabolic phenotyping of a model of adipocyte differentiation. *Physiol. Genomics* **39,** 109–119 (2009).
21. Collins, J. M. *et al.* De novo lipogenesis in the differentiating human adipocyte can provide all fatty acids necessary for maturation. *J. Lipid Res.* **52,** 1683–1692 (2011).
22. Summers, S. A. Ceramides in insulin resistance and lipotoxicity. *Prog. Lipid Res.* **45,** 42–72 (2006).
23. Raichur, S. *et al.* CerS2 haploinsufficiency inhibits β-oxidation and confers susceptibility to diet-induced steatohepatitis and insulin resistance. *Cell Metab.* **20,** 687–695 (2014).
24. Turpin, S. M. *et al.* Obesity-induced CerS6-dependent C16:0 ceramide production promotes weight gain and glucose intolerance. *Cell Metab.* **20,** 678–686 (2014).
25. Kanehisa, M. *et al.* KEGG for linking genomes to life and the environment. *Nucleic Acids Res.* **36,** D480–D484 (2008).
26. Watson, E. *et al.* Interspecies systems biology uncovers metabolites affecting *C. elegans* gene expression and life history traits. *Cell* **156,** 759–770 (2014).
27. Yatsunenko, T. *et al.* Human gut microbiome viewed across age and geography. *Nature* **486,** 222–227 (2012).
28. Arumugam, M. *et al.* Enterotypes of the human gut microbiome. *Nature* **473,** 174–180 (2011).
29. Scher, J. U. *et al.* Expansion of intestinal *Prevotella copri* correlates with enhanced susceptibility to arthritis. *eLife* **2,** e01202 (2013).
30. Dewulf, E. M. *et al.* Insight into the prebiotic concept: lessons from an exploratory, double blind intervention study with inulin-type fructans in obese women. *Gut* **62,** 1112–1121 (2013).
31. Newgard, C. B. *et al.* A branched-chain amino acid-related metabolic signature that differentiates obese and lean humans and contributes to insulin resistance. *Cell Metab.* **9,** 311–326 (2009).
32. Charon, N. W., Johnson, R. C. & Peterson, D. Amino acid biosynthesis in the spirochete Leptospira: evidence for a novel pathway of isoleucine biosynthesis. *J. Bacteriol.* **117,** 203–211 (1974).
33. Umbarger, H. E. Amino acid biosynthesis and its regulation. *Annu. Rev. Biochem.* **47,** 532–606 (1978).
34. Shin, S.-Y. *et al.* An atlas of genetic influences on human blood metabolites. *Nat. Genet.* **46,** 543–550 (2014).
35. Elinav, E. *et al.* NLRP6 inflammasome regulates colonic microbial ecology and risk for colitis. *Cell* **145,** 745–757 (2011).
36. Henao-Mejia, J. *et al.* Inflammasome-mediated dysbiosis regulates progression of NAFLD and obesity. *Nature* **482,** 179–185 (2012).
37. Heimesaat, M. M. *et al.* Gram-negative bacteria aggravate murine small intestinal Th1-type immunopathology following oral infection with Toxoplasma gondii. *J. Immunol.* **177,** 8785–8795 (2006).
38. Dillon, S. M. *et al.* Gut dendritic cell activation links an altered colonic microbiome to mucosal and systemic T-cell activation in untreated HIV-1 infection. *Mucosal Immunol.* **9,** 24–37 (2016).
39. Kovatcheva-Datchary, P. *et al.* Dietary fiber-induced improvement in glucose metabolism is associated with increased abundance of *Prevotella*. *Cell Metab.* **22,** 971–982 (2015).
40. Laferrère, B. *et al.* Differential metabolic impact of gastric bypass surgery versus dietary intervention in obese diabetic subjects despite identical weight loss. *Sci. Transl. Med.* **3,** 80re2 (2011).
41. Lynch, C. J. & Adams, S. H. Branched-chain amino acids in metabolic signalling and insulin resistance. *Nat. Rev. Endocrinol.* **10,** 723–736 (2014).
42. Jang, C. *et al.* A branched-chain amino acid metabolite drives vascular fatty acid transport and causes insulin resistance. *Nat. Med.* **22,** 421–426 (2016).
43. Herman, M. A., She, P., Peroni, O. D., Lynch, C. J. & Kahn, B. B. Adipose tissue branched chain amino acid (BCAA) metabolism modulates circulating BCAA levels. *J. Biol. Chem.* **285,** 11348–11356 (2010).
44. Pietiläinen, K. H. *et al.* Global transcript profiles of fat in monozygotic twins discordant for BMI: pathways behind acquired obesity. *PLoS Med.* **5,** e51 (2008).
45. Shin, A. C. *et al.* Brain insulin lowers circulating BCAA levels by inducing hepatic BCAA catabolism. *Cell Metab.* **20,** 898–909 (2014).

Supplementary Information is available in the online version of the paper.

Acknowledgements The authors wish to thank S. Castillo, M. Sysi-Aho, A. Ruskeepää, U. Lahtinen, A. Forman, T. Lorentzen, B. Andreasen, G. J. Klavsen, M. J. Nielsen, B. Pedersen, M. T. F. Damgaard and L. B. Rosholm for technical assistance, D. R. Mende and J. R. Kultima for their help in data processing and tool provision, C. Ekstøm and S. Ditlevsen for statistical and mathematical assistance, respectively, and T. F. Toldsted and G. Lademann for management assistance. C. B. Newgard and A. Vaag are thanked for critical comments on our manuscript. The present study is initiated and funded by the European Community's Seventh Framework Program (FP7/2007-2013): MetaHIT, grant agreement HEALTH-F4-2007-201052. Additional funding came from The Lundbeck Foundation Centre for Applied Medical Genomics in Personalized Disease Prediction, Prevention and Care (LuCamp, http://www.lucamp.org), Metagenopolis grant ANR-11-DPBS-0001 and FP7 METACARDIS HEALTH-F4-2012-305312. J.R., S.V.-S. and G.F. are funded by the Rega institute for Medical Research, KU Leuven, the Agency for Innovation by Science and Technology (IWT), Marie Curie Actions FP7 People COFUND - Proposal 267139 and the Fund for Scientific Research Flanders (FWO). M.O. is also supported by Academy of Finland (Centre of Excellence in Molecular Systems Immunology and Physiology Research, Decision No. 250114) and EU FP7 Project TORNADO (project 222720). F.H. has received funding from the European Union's Horizon 2020 research and innovation programme under the Marie Skłodowska-Curie grant agreement No. 600375. The Center for Biological Sequence Analysis and the Novo Nordisk Foundation Center for Basic Metabolic Research have in addition received support from the Innovative Medicines Initiative Joint Undertaking under grant agreement no. 115317 (DIRECT), resources of which are composed of financial contribution from the European Union's Seventh Framework Programme (FP7/2007-2013) and EFPIA companies' in kind contribution. The Novo Nordisk Foundation Center for Protein Research received funding from the Novo Nordisk Foundation (grant agreement NNF14CC0001). The Novo Nordisk Foundation Center for Basic Metabolic Research is an independent Research Center at the University of Copenhagen partially funded by an unrestricted donation from the Novo Nordisk Foundation (http://www.metabol.ku.dk).

Author Contributions O.P., S.D.E. and P.B. devised the study. O.P., S.D.E., S.Bru. and H.B.N. designed the study protocol and supervised all parts of the project. H.B.N. and S.Bru. led the data integration, the bioinformatics analyses and did the primary interpretation of analytical outcomes in close collaboration with H.K.P. and V.G. H.K.P., V.G., B.A.H.J., T.Hy., E.P., D.P., S.S., F.H., K.F., J.B.H. and S.V.-S. performed data analyses. T.N., T.Ha. and O.P. composed the clinical protocol, carried out phenotyping of study participants including collection of biological samples and physiological data generation and interpretation. F.L. performed DNA extraction and J.D. supervised DNA extraction. J.W. supervised DNA sequencing and gene profiling. M.O., T.Hy., I.M., K.T. and P.P. performed profiling of serum metabolomics and serum lipidomics. B.A.H.J., K.K., J.B.H. and S.Bri. performed mouse experiments. H.B.N., H.K.P. and V.G. drafted the first versions of the paper with critical and substantial contributions from O.P., S.Bru., T.N., J.R., K.F., F.H., M.O., L.I.H., D.P., G.F., P.B. and S.D.E. All authors approved the final version. MetaHIT consortium members provided support and constructive criticism throughout MetaHIT research operations.

Author Information Raw nucleotide data can be found for all samples used in the study in the European Nucelotide Archive (accession numbers: ERP003612, ERP004605, MetaHIT samples; ERP014713, 16S rDNA from mouse experiment). The metabolomics data has been deposited in the MetaboLights database (http://www.ebi.ac.uk/metabolights/) under accession number: MTBLS351. Reprints and permissions information is available at www.nature.com/reprints. The authors declare no competing financial interests. Readers are welcome to comment on the online version of the paper. Correspondence and requests for materials should be addressed to S.Bru. (soren.brunak@cpr.ku.dk), M.O. (matej.oresic@gmail.com), S.D.E. (dusko.ehrlich@jouy.inra.fr) or O.P. (oluf@sund.ku.dk).

Reviewer Information *Nature* thanks J. Garrett, L. Groop, C. Lozupone, G. Siuzdak and the other anonymous reviewer(s) for their contribution to the peer review of this work.

METHODS

Human study population. The study population comprised 291 normoglycaemic and middle-aged Danish MetaHIT individuals as previously reported[1], as well as 75 Danish type 2 diabetes patients[4]. All analyses involving gut microbiome data were restricted to 75 type 2 diabetes patients and 277 out of the 291 of the non-diabetic individuals whose data passed all quality control criteria (see details below), whereas all non-microbiome analyses involved the full set of 291 non-diabetic individuals. No statistical methods were used to predetermine sample size.

Of the 75 type 2 diabetes patients, ten patients (13%) received no hyperglycaemic medications, 58 patients (77%) received the biguanide compound, metformin; of these 28 patients (37%) received metformin as the only anti-hyperglycaemic medication, 10 patients (13%) received sulfonylurea alone or in combination with metformin, 14 patients (19%) received a combination of oral anti-diabetic drugs and insulin treatment and 4 patients (5%) were on insulin treatment only. Eleven patients (15%) were treated with dipeptidyl peptidase-4 (DPP4) inhibitors or glucagon-like peptide-1 (GLP-1), all of them in combination with metformin. Patients were reported as receiving anti-hypertensive treatment if at least one of the following drugs were reported: spironolactone, thiazides, loop diuretics, beta-blockers, calcium channel blockers, moxonidin or drugs affecting the renin-angiotensin system (in total $n=55$; 73%). Patients receiving statins were reported as receiving lipid-lowering medication (in total $n=56$; 75%). We have previously shown that metformin has impact on the configuration and functional potential of human gut microbiota whereas no significant differences were observed for other anti-diabetic medications, diuretics, or lipid lowering- and blood pressure lowering drugs[4].

In short, all study participants (Caucasian Danes) were recruited from the population-based Inter99 study[46] or from the outpatient clinic at Steno Diabetes Center. Study volunteers were invited for two visits with approximately 14 days apart. At the first visit the participants were examined in the morning after an overnight fast of at least 10 h and without prior morning physical activity. At the second visit a DEXA scan was performed to evaluate body fat percentage. All samples (from both non-diabetic and diabetic individuals) were generated within the Danish part of the MetaHIT consortium (http://www.metahit.eu), and the infrastructure of this project was constructed specifically to make all samples comparable by ensuring similar handling and by minimizing the risk of batch effects. All of these samples were collected individually as participant recruitment proceeded, by the same staff and using the same protocol for both stool and blood samples. Serum for metabolomics and stool for metagenomics were stored at −80 °C until the planned analyses took place.

The study was approved by the Ethical Committees of the Capital Region of Denmark (HC-2008-017 and H-15000306) and was in accordance with the principles of the Declaration of Helsinki. All individuals gave written informed consent before participating in the study.

Phenotyping. Clinical phenotyping and fasting biochemistry were performed and analysed as reported[1]. HOMA-IR was calculated as: (fasting plasma glucose (mmol/l) × fasting serum insulin (mU/l))/22.5[14] and HOMA-B (a measure of pancreatic beta-cell function) calculated as (20 × fasting plasma insulin)/(fasting plasma glucose − 3.5)[14]. Due to the confounding effects of anti-diabetic treatment, HOMA-IR and HOMA-B were only assessed in non-diabetic individuals. BMI was calculated as weight (kg) divided by height (m^2) and obesity defined as BMI >30 kg/m^2. Metabolic syndrome was defined according to the International Diabetes Federation[15]. Non-diabetic individuals classified as having the metabolic syndrome in accordance with the IDF ($n=163$) were characterized by central obesity defined by gender-specific increased waist circumference as well of two of four additional risk factors for cardiovascular disease: raised levels of fasting plasma glucose or triglycerides, or reduced fasting plasma level of HDL-cholesterol, or raised blood pressure. In order to account for differences in age, sex and BMI, we matched the 75 Danish type 2 diabetes patients with 75 age-, sex- and BMI-matched individuals chosen from the non-diabetic study samples of 277 Danish individuals (Supplementary Table 1).

Generation of serum metabolome data set. The metabolomics analyses were performed on all human samples together, in randomized order, both related to the sample preparation and instrumental analysis. Similarly, all 48 mouse samples were analysed for BCAAs together in randomized order. Control serum samples consisting of pooled human serum were included in equal intervals as part of the sample run for both human and mouse samples ($n=30$ for humans and $n=4$ for mice), as well as a set of pure standard samples (pure standards in a solvent for evaluation of instrument performance and robustness), extracted standard samples (standards going through the same sample preparation to monitor the performance on the whole analytical procedure), blank samples (only solvent to observe possible background peaks) and calibration samples.

Metabolomics analyses were also conducted on previously reported Danish type 1 diabetes patients[4] ($n=30$ for polar metabolites, $n=31$ for molecular lipids). These data were only used for the co-abundance clustering of metabolites (see below) to increase sample size for finding inter-variable conditions. Type 1 diabetes patients are distinctive from type 2 diabetes patients as they represent both a very different pathology and lifelong medical/lifestyle treatment and were consequently not used for any other analyses.

Human and mouse samples were analysed at VTT Technical Research Centre of Finland (Espoo, Finland) and Steno Diabetes Center (Gentofte, Denmark), respectively, using the same type of instrument with identical analytical conditions.

Analysis of fasting serum polar metabolites by GC × GC-TOFMS. Serum polar metabolites were analysed in 396 human and 48 mouse serum samples (24 pre- and 24 post-gavage samples) using comprehensive two-dimensional gas chromatography combined with time-of-flight mass spectrometry (GC × GC-TOFMS, a LECO Pegasus 4D equipped with a cryogenic modulator from LECO Corp.) with a method described previously[47]. Specifically, 400 μl methanol and 10 μl internal standard mixture (C17:0 (186.5 mg/l), deuterated valine (37 mg/l) and succinic acid-d_4 (63 mg/l)) were added to 30 μl of serum samples. The samples were vortex mixed and centrifuged for 5 min at 10,000 r.p.m. and half of the supernatant was evaporated to dryness. This was followed by two-step derivatization using methoximation and silylation by first adding 25 μl methoxamine (45 °C, 60 min) and then 25 μl *N*-trimethylsilyl-*N*-methyl trifluoroacetamide (45 °C, 60 min). Finally, a retention index standard mixture (*n*-alkanes, 25 μl, concentration = 8 mg/l) and an injection standard (4,4′-dibromooctafluorobiphenyl, 50 μl, concentration = 10 mg/l), both in hexane, were added to the mixture. The calibration consisted of six points for each quantified metabolite.

The columns were as follows: a methyl-deactivated retention gap (1.5 m × 0.53 mm i.d.) was connected to 10 m × 0.18 mm Rxi-5MS (phase thickness 0.18 μm) and to 1.5 m × 0.1 mm BPX-50 (phase thickness 0.1 μm). Helium was used as the carrier gas at a constant pressure mode (40 psig). A 4-s separation time was used in the second dimension. The temperature program was as follows for the first-dimension column: 50 °C (2 min), at 7 °C/min to 240 °C and at 25 °C/min to 300 °C (3 min). The second-dimension column temperature was 20 °C higher than the corresponding first-dimension column throughout the program.

The analytical method used allows for combined targeted and untargeted analysis, where a selected subset of metabolites can be quantified[47]. In the present study, quantitation of 27 target metabolites (stearic acid, oleic acid, linoleic acid, palmitic acid, citric acid, glutamic acid, 3,4-dihydroxybutanoic acid, 3-hydroxybutyric acid, threonine, 2,4-dihydroxybutanoic acid, phenylalanine, tyrosine, 2-hydroxybutyric acid, serine, glyceric acid, methionine, glycine, leucine, isoleucine, valine, ornithine, proline, cholesterol, arachidonic acid, alanine and aspartic acid) was done by external calibration curves for each individual metabolite.

ChromaTOF vendor software (LECO) was used for within-sample data processing, and the Guineu software[47] was used for alignment, normalization and peak matching across samples. The normalization was performed by correction for internal standards and specific target metabolites were additionally quantified using external calibration curves. Other mass spectra from the GC × GC-TOFMS analysis were searched against the NIST Mass Spectral Library and Golm Metabolome Database[48], also using retention index data in the identification. Artefact peaks due to chemical background and compounds outside the linear range of the method were removed from the data set. Control serum samples ($n=30$ for human, $n=4$ for mouse analyses) were analysed together with the samples. The relative standard deviation (RSD) for internal standards, spiked into the samples, was on average of 12.8% for the human serum sample analyses. The RSD% of the quantified metabolites in the control serum samples ($n=30$) was on average 18.5% for the analysis of human serum samples. For quantitative analysis of BCAAs in mice serum samples, the RSD% was 13.3% for isoleucine, 11.2% for leucine and 24.2% for valine in control serum samples ($n=4$), and for internal standards in mice serum the RSD was on average 16.6%. Neither sample preparation nor analysis order showed any significant effect on the results.

All serum metabolite peaks that were present (non-zero value) in more than 50% of samples were included in the data analyses, including the unidentified ones. We reasoned that inclusion of complete data as obtained from the platform best represent the global metabolome as covered by the platform. The unidentified peaks were annotated with their structural class from the Golm Metabolome Database[48] using functional group prediction based on the fragmentation patterns[47]. In total 325 (94 known and 231 unknown) serum polar metabolites were measured in the human study.

Analysis of serum molecular lipids using UHPLC-QTOFMS. Serum molecular lipids were analysed in 397 human serum samples using ultra-high-performance liquid chromatography coupled with time-of-flight mass spectrometry (UHPLC-QTOFMS Q-Tof Premier mass spectrometer, Waters, Inc.) using electrospray ionization in positive ionization mode with a methodology described earlier[49]. Specifically, a standard mixture 1 (20 μl) containing LPC(17:0), PC(17:0/17:0), PE(17:0/17:0) and Cer(d18:1/17:0) (Avanti Polar Lipids, Inc.)

and TG(17:0/17:0/17:0) (Larodan Fine Chemicals AB), all at concentration of 10 mg/l, was added to 10 μl of serum samples and the samples were extracted with chloroform and methanol (2:1; 100 μl). The lower phase (60 μl) was collected after centrifugation and 20 μl of internal standard mixture 2 (LPC(16:1D$_3$), concentration: 10 mg/l, PC(16:1/16:1-D$_6$), concentration: 15 mg/l, and TG(16:0/16:0/16:0-^{13}C3), concentration: 15 mg/l, was added. The extracts were analysed on an Acquity UPLCTM BEH C18 2.1 × 100 mm column packed with 1.7 μm particles. The solvent system included 1% 1 M NH_4Ac, 0.1% HCOOH and acetonitrile/isopropanol (1:1, 1% 1M NH_4Ac, 0.1% HCOOH) in gradient elution mode with a flow rate of 0.4 ml/min. The serum lipid profiling was carried out at a mass range of m/z 300–1,200 with scan duration of 0.2 s.

The data processing using MZmine 2 (ref. 50) included alignment of peaks, peak integration, isotopic grouping, normalization, and peak identification. Serum lipids were identified using an internal spectral library or with tandem MS and data were normalized using the internal standards representatives of each class of serum lipid present in the samples as previously described[49]. Sphingomyelins were normalized with the PC standard. All lipid peaks were included in the data analyses, including the unidentified ones. Control serum samples ($n = 30$), extracted standard samples ($n = 22$) as well as blanks and pure standard samples were analysed together with the study samples. The standard deviation (RSD) for internal standards, spiked into the samples, was 8–13% in serum samples ($n = 397$) and 9.1% in the extracted standards ($n = 22$). The RSD% of the identified lipids in the control serum samples was on average 12.8%. In total 876 molecular serum lipids, 289 known and 587 unknown, were measured. Neither sample preparation nor analysis order showed any significant effect on the results.

Clustering of co-abundant serum metabolites. Clusters of co-abundant serum metabolites were identified using the R package WGCNA[51] (Fig. 1a). Serum polar metabolites and serum molecular lipids (see above) were analysed separately but are collectively referred to as serum metabolites. Signed, weighted metabolite co-abundance correlation (biweight midcorrelations (a median-based correlation measure that is more robust to outliers than Pearson correlation[52,53]) after $\log_2$ transformation) networks were calculated across all examined individuals. A scale-free topology criterion was used to choose the soft threshold $\beta = 13$ for the polar metabolites and $\beta = 14$ for molecular lipid correlations. Clusters were identified with the dynamic hybrid tree-cutting algorithm[54], using deepSplit of 4 and a minimum cluster size of 3 and 5 for polar metabolite and molecular lipid clusters, respectively. Serum metabolites that did not fit the clustering criteria were combined in a group named 'remaining'. The profile of each serum metabolite cluster was summarized by the cluster eigenvector (that is, the first principal component of the metabolite abundances across individuals). Similar clusters were subsequently merged if the biweight mid-correlation between the cluster's eigenvectors exceeded 0.8 and 0.75 for serum polar metabolite and serum molecular lipid clusters, respectively. The serum polar metabolite and serum molecular lipid clusters (labelled M00–M35 and L00–L39, respectively) are collectively termed metabolite clusters.

Construction of a non-redundant metagenomics reference gene catalogue. The reference gene catalogue used in the present study was constructed from Illumina shotgun sequencing data from 620 publically available faecal samples[4,55]. The data was processed using the MOCAT software package (version 1.1)[56]. Reads were trimmed (option read_trim_filter) using a quality and length cut-off of 20 and 30 bp, respectively. Trimmed reads were subsequently screened against a custom database of Illumina adapters (option screen_fastafile) and the human genome version 19 using a 90% identity cut-off (option screen). The resulting high-quality reads were assembled (option assembly) and assemblies revised (option assembly_revision). Genes were predicted on scaftigs with a minimum length of 500 bp (option gene_prediction).

Predicted protein-coding genes with a minimum length of 100 bp were clustered at 95% sequence identity using CD-HIT (version 4.6.1)[57] with parameters set to: -c 0.95, -G 0 -aS 0.9, -g 1, -r 1). The representative genes of the resulting clusters were 'padded' (that is, extended up to 100 bp at each end of the sequence using the sequence information available from the assembled scaftigs), resulting in the final reference gene catalogue used in this study. The reference gene catalogue was functionally annotated using SmashCommunity (version 1.6)[58] after aligning the amino acid sequence of each gene to the KEGG database (version 62)[25].

Profiling of metagenomics samples. We obtained metagenomics data for the 291 non-diabetic individuals and 75 type 2 diabetes patients as previously described[1,4]. The DNA extraction protocol was standardized for all samples and all sequencing was done using Illumina platforms, using paired-end reads (Supplementary Table 14). Of the 291 non-diabetic samples, 14 that were sequenced with the Illumina Solexa technology had average read length below 42 nt (leading to less certain mappings) and were thus excluded from further analyses to avoid unnecessary biases, resulting in a final set of 277 non-diabetic individuals with gut microbiome data. All 75 type 2 diabetes samples passed all quality control criteria. Sequencing statistics for each sample have previously been described[4] and are repeated in Supplementary Table 14. Raw insert (sequenced fragments of DNA represented by single or paired-end reads) count profiles were generated using MOCAT[56] by mapping high-quality reads from each metagenome to the reference gene catalogue (option screen) using an alignment length and identity cut-off of 45% and 95%, respectively. The abundance profile for each catalogue gene was calculated as the sum of uniquely mapped sequence reads (97% identity) using 7M sequence reads per sample (downsized). KEGG Orthology (KO) gene group abundance profiles were calculated by summing the abundance of genes annotated to the respective KO gene group. KOs were mapped to microbiome functional KEGG modules based on annotations downloaded on 14 January 2014 from the KEGG BRITE database. Gene richness was calculated as the number of genes with abundance higher than zero in the given sample (downsized). For negative binominal statistics all uniquely mapped sequence reads were used to estimate abundances.

Metagenomics species construction. The gene catalogue was clustered by co-abundance as described by Nielsen *et al.*[59], which defined 10,754 co-abundance gene groups (CAGs) with high correlations (Pearson correlation coefficient >0.9). The 925 largest of these, with more than 700 genes, were considered as metagenomics species (MGS) and referred to as species throughout the article. The abundance profiles of the CAGs and MGS were determined as the medium gene abundance (7M reads per sample) throughout the samples. Furthermore, the CAGs and MGSs were taxonomically annotated, by summing up the taxonomical annotation of their genes as described by Nielsen *et al.*[59]. Each gene was annotated by sequence similarity to known reference genomes (blastN, E-value < 0.001 against imomi4 genome databank, August 2012 release).

Mouse intervention study with *Prevotella copri*. *P. copri* (CB7, DSMZ) was cultivated under anaerobic conditions in PYG medium (SSI Diagnostica), harvested in log phase, aliquoted and stored in 10% glycerol at −80 °C until use. Mice (24 male WT C57BL/6J, Taconic, 10 weeks of age) were housed in cages of four and kept at 22 °C in a specific-pathogen-free facility under a 12 h light-dark cycle, fed *ad libitum* and had free access to water. Number of mice (sample size) was selected based on previous experience in measurement of dysglycaemic phenotype in a mouse model, but was not arrived at through formal analysis. After 2 weeks of acclimatization on a standard chow diet (Altromin 1310, Altromin), mice were transferred to a soy protein-based 60% high-fat diet low in BCAAs (12492D, Ssniff) in order to prime for later development of glucose intolerance and insulin resistance and sham-gavaged (1% glycerol in PBS) twice a week. After three weeks on high-fat diet, mice were divided into two equal groups of 12 mice each (three cages per group, minimizing the influence of potential cage effects). The groups were not randomized but stratified by magnetic resonance (MR)-based fat mass and weight. For the following three weeks, mice were gavaged twice weekly with 100 μl of either *P. copri* (5×10^8 CFU/mouse, 1% glycerol in PBS) or sham while remaining on the high-fat diet. Blood for BCAA measurements was drawn 3 days before diet change and 11 days post diet change in EDTA-coated tubes kept on ice and centrifuged at 4 °C for 10 min at 1,000*g* before storage at −80 °C until metabolomics analysis.

An oral glucose tolerance test (OGTT) was performed after two weeks of *P. copri* challenge. The mice were fasted for 5 h with free access to water and gavaged with 3 g glucose/kg lean mass. Blood glucose was measured in tail vein blood before and 15, 30, 45, 60, 90, and 120 min post the glucose bolus, using standard Contour Next Test Strips that met 2013 accuracy criteria requirements from International Organization for standardization of diagnostic tests (Bayer Contour).

Insulin secretion capacity was evaluated by measuring plasma insulin before (T0) and 15 min post glucose bolus (T15) using an electrochemiluminescence assay (Meso Scale Diagnostics) following the manufacturer's instructions.

An insulin tolerance test was performed after 3 weeks of bacterial challenge. The mice were acclimatized in clean cages without bedding for 2 h and injected intra peritoneally with 0.75 U insulin/kg lean mass in alternating order. Insulin was diluted in succinulated gelatin (Gelofusine B. Braun Melsungen AG), allowing increased efficacy of insulin administration, thus minimizing intra experimental standard variations. Blood glucose was measured immediately before and 15, 30, 45, 60, 90 and 120 min post insulin bolus, using standard Contour Next Test Strips that met accuracy criteria requirements from International Organization for standardization of diagnostic tests (Bayer Contour).

In all mouse experiments performed, mice were handled in alternating order. During ITT and OGTT the operator was semi-blinded as each mouse was assigned a random number corresponding to the time (minute) for insulin/glucose bolus administration.

For quantitative PCR and 16 rDNA amplicon sequencing, bacterial DNA from faecal samples were extracted using a NucleoSpin soil kit (Macherey-Nagel) according to manufacturer's instructions. DNA yield and integrity

were assessed using a Nanodrop and agarose gel electrophoresis, respectively. Quantitative PCR analyses were performed using the SYBR Green qPCR Master mix (Thermo Scientific) and the Stratagene Mx3000P qPCR System. The relative abundance of *P. copri* was determined by normalization to the reference 16S rDNA gene using the comparative C_T method[75] for relative gene expression. Primer sequences were previously published[29] and are as follows: Universal 16S forward: 5′-ACTCCTACGGGAGGCAGCAGT-3′, Universal 16S reverse: 5′-ATTACCGCGGCTGCTGGC-3′, *P. copri* forward: 5′-CCGGACTCCTGCCCCTGCAA-3′, *P. copri* reverse: 5′-GTTGCGCCA GGCACTGCGAT-3′.

The PCR-based library formation for the 16S rDNA amplicon sequencing was performed using 10 ng DNA, 0.2 μM of each barcoded forward and reverse primer, 0.2 mM dNTPs and 0.5 units Phusion high fidelity DNA polymerase (Thermo Scientific) in a total volume of 25 μl. To target the 16S rRNA gene's variable region 4 (V4) a forward primer 515F (5′-AATGATACGGCGACCACCGAGATCTACAC NNNNNNNN TATGGTAATTGTGTGCCAGCMGCCGCGGTAA-3′; 'N' indicates the nucleotides of the barcode sequence) and a reverse primer 806R (5′-CAAGCAGAAGACGGCATACGAGAT NNNNNNNNNNNNAGTCAGT CAG CC GGACTACHVGGGTWTCTAAT-3′) were used, both with Illumina adaptor sequences in the 5′ end[60,61]. Cycling condition was as follows: 98 °C for 30 s followed by 35 cycles of 98 °C for 5 s, 56 °C for 20 s and 70 °C for 20 s. PCR products were purified using Agencourt AMPure XP (Beckman Coulter) beads. Subsequently, samples were pooled in equal concentrations and sequenced using an Illumina MiSeq with V2 PE500 cartridge (500 cycles).

For 16S rDNA data analysis, generated sequences were analysed using QIIME v.1.9.1 with default settings. Chimaera checking was performed using UCHIME[62] and *de novo* OTU-picking was performed using UCLUST[63] with 97% sequence similarity. Representative sequences were assigned taxonomy against the Greengenes database v.13_8[64] using the RDP-classifier[65]. Subsequent analyses were performed in R v.3.2.3 using the metagenomeSeq[66], PhyloSeq[67], vegan[68] and ggplot2[69] packages. Data was filtered for low-abundance OTUs by removal of OTUs present in fewer than 3 of the 48 samples and with a relative abundance across all samples 0.005%. Analyses in R were performed with an average of $51{,}912 \pm 15{,}173$ (s.d.) sequences per sample after filtering. For bacteria, differential abundance analysis we normalized read counts with metagenomeSeq[66] using cumulative-sum scaling. Statistical analysis was performed on data filtered based on effective sample sizes where taxa were not included if they had fewer than X effective number of positive samples, where X is the median of estimated effective samples per feature calculated using metagenomeSeq.

All animal experiments were conducted in accordance with national Danish guidelines (Amendment #1306 of 23 November 2007) as approved by the Danish Animal Inspectorate, Ministry of Justice, permission #2014-15-2934-01027. Mice were kept under specific-pathogen-free conditions and experimental protocols were validated by in-house standard operation procedures.

Statistical analysis. Apart from the mouse experiment, in which Graphpad Prism version 6, Treestar, was used, all statistical analyses were performed in the statistical computing language R[70]. As the non-diabetic study sample comprised both non-obese and obese individuals, a number of the physiological variables were not normally distributed (Extended Data Fig. 1). Consequently, non-parametric tests were applied in the statistical analysis. For all analyses involving microbiome data, we only included microbial species and KOs present in at least three non-diabetic individuals to avoid artefactual results. All comparisons with a Benjamini–Hochberg false discovery rate (FDR) <0.1 were considered significantly different throughout the analysis. To focus the analysis on phenotype-relevant variables, we employed an initial filtering of significant phenotype association of the serum metabolite clusters, microbial species and microbiome-derived KEGG modules (Fig. 1b). Serum metabolite clusters and species associations with HOMA-IR were conducted with a Spearman rank correlation test. Partial Spearman rank correlation tests[71] were used to adjust the correlations for BMI (HOMA-$\mathrm{IR_{BMIadj}}$), or gene richness (HOMA-$\mathrm{IR_{GeneRichness.adj}}$) where applicable, using the ppcor R package[72]. Serum metabolite clusters and species abundance differences between individuals with and without metabolic syndrome were tested with a Mann–Whitney U-test. We focused the downstream analysis on the serum metabolite clusters associated with all three phenotypes (HOMA-IR, HOMA-$\mathrm{IR_{BMIadj}}$ and metabolic syndrome), but other metabolite clusters were significantly associated with one or more of the three phenotypes that were not retained for further study. Owing to the low number of microbiome functional modules and species associated with all three phenotypes, we included all functional modules and species associated with HOMA-IR, HOMA-$\mathrm{IR_{BMIadj}}$ or metabolic syndrome in further analysis.

All associations for microbial functional modules were identified using a Mann–Whitney U-test, where the ranks of KOs within a given KEGG functional module were compared with the ranks of all other KOs. For associations of microbial functional modules with HOMA-IR, gene richness and serum metabolite clusters the ranks were based on Spearman correlation coefficients, whereas partial Spearman correlation coefficients were used to rank KOs for association with HOMA-$\mathrm{IR_{BMIadj}}$, and HOMA-$\mathrm{IR_{GeneRichness.adj}}$, as it allows adjusting for BMI and gene richness, respectively. To quantify the shift in (partial) Spearman correlation for a given KEGG module compared to the background distribution, we calculated the background adjusted median Spearman correlation ($\mathrm{SCC_{bg.adj}}$) for a given KEGG module m as:

$$\mathrm{SCC_{bg.adj}} = \mathrm{median}(\mathrm{SCC}_{\mathrm{KOs} \in \mathrm{KEGG\ module}\ m}) - \mathrm{median}(\mathrm{SCC}_{\mathrm{KOs} \notin \mathrm{KEGG\ module}\ m})$$

where $\mathrm{SCC_{KO}}$ is the (partial) Spearman correlation coefficient between the KO and HOMA-IR, HOMA-$\mathrm{IR_{BMIadj}}$, HOMA-$\mathrm{IR_{GeneRichness.adj}}$, gene richness or serum metabolite clusters. For associations of microbial functional modules with metabolic syndrome and type 2 diabetes, the ranks were based on Wald statistics for testing differentially abundant KOs with a negative binomial test, using the DESeq2 R package[73]. In contrast to all other tests, analyses using the negative binomial test were based on the non-rarefied gene counts.

To identify the main microbial species driving the association between functional KEGG modules and HOMA-IR described above, the calculation of the KO gene group abundance profiles was iterated excluding the genes from a different species, in each iteration (leave-one-out analysis). The effect of a given species on a specified association was defined as the change in median Spearman correlation coefficient between KOs and HOMA-IR when genes from the respective species were left out (DeltaSCC), that is, for species s and KEGG module m:

$$\mathrm{DeltaSCC}_m^s = \mathrm{median}\left(\mathrm{SCC}^{\mathrm{all\ species}}_{\mathrm{KOs} \in \mathrm{KEGG\ module}\ m}\right) - \mathrm{median}\left(\mathrm{SCC}^{\mathrm{excluding\ species}\ s}_{\mathrm{KOs} \in \mathrm{KEGG\ module}\ m}\right)$$

For visualizing the species' effect on the association between HOMA-IR and a given KEGG module m, $\mathrm{SCC}_{\mathrm{bg.adj},m}$ (the background-adjusted median SCC between HOMA-IR and KOs in module m when including all species) was used as reference, that is:

$$\begin{aligned}\mathrm{Plottedvalue}_m^s &= \mathrm{SCC}_{\mathrm{bg.adj},m} - \mathrm{DeltaSCC}_m^s \\ &= \mathrm{median}\left(\mathrm{SCC}^{\mathrm{excluding\ species}\ s}_{\mathrm{KOs} \in \mathrm{KEGG\ module}\ m}\right) - \mathrm{median}\left(\mathrm{SCC}^{\mathrm{all\ species}}_{\mathrm{KOs} \notin \mathrm{KEGG\ module}\ m}\right)\end{aligned}$$

In addition, the magnitude of each species' relative contribution to the correlation was summarized as the percentage change compared to the original median Spearman correlation coefficient (% SCC), that is:

$$\%\mathrm{SCC}_m^s = \frac{\mathrm{DeltaSCC}_m^s}{\mathrm{SCC}_{\mathrm{bg.adj},m}} \times 100$$

When testing whether regression slopes were significantly different we used the z score as suggested by Paternoster *et al.*[74] and converted it to a P value using a 2-sided t distribution.

For analysis of the data from the mouse intervention, the repeated blood glucose measurements from the OGTT were compared between the two groups of mice using repeated measurements two-way ANOVA, Tukey's post hoc test (Sigmaplot). The area under the curve (AUC) (GraphPad) was compared using a Mann–Whitney U-test (GraphPad). The effect of the *P. copri* gavage challenge on the combined BCAA measures (leucine, isoleucine and valine) was tested on log-transformed metabolite values using a likelihood ratio test (linear model using generalized least squares), which does not assume independence between the amino acid measurements from the same mouse. For this, the variances of the three amino acids were modelled independently. To test for differences in the gut microbiota composition between sham and *P. copri*-gavaged mice we performed adonis test on the 16S data using weighted UniFrac distance. To test for bacteria families differentially abundant between sham and *P. copri*-gavaged mice we used the fitZig function in the metagenomeSeq R package[66].

46. Jørgensen, T. *et al.* A randomized non-pharmacological intervention study for prevention of ischaemic heart disease: baseline results Inter99. *Eur. J. Cardiovasc. Prev. Rehabil.* **10,** 377–386 (2003).
47. Castillo, S., Mattila, I., Miettinen, J., Orešič, M. & Hyötyläinen, T. Data analysis tool for comprehensive two-dimensional gas chromatography/time-of-flight mass spectrometry. *Anal. Chem.* **83,** 3058–3067 (2011).
48. Kopka, J. *et al.* GMD@CSB.DB: the Golm Metabolome Database. *Bioinformatics* **21,** 1635–1638 (2005).
49. Nygren, H., Seppänen-Laakso, T., Castillo, S., Hyötyläinen, T. & Orešič, M. Liquid chromatography-mass spectrometry (LC-MS)-based lipidomics for studies of body fluids and tissues. *Methods Mol. Biol.* **708,** 247–257 (2011).
50. Pluskal, T., Castillo, S., Villar-Briones, A. & Oresic, M. MZmine 2: modular framework for processing, visualizing, and analyzing mass spectrometry-based molecular profile data. *BMC Bioinformatics* **11,** 395 (2010).
51. Langfelder, P. & Horvath, S. WGCNA: an R package for weighted correlation network analysis. *BMC Bioinformatics* **9,** 559 (2008).

52. Langfelder, P. & Horvath, S. Fast R functions for robust correlations and hierarchical clustering. *J. Stat. Softw.* **46,** i11 (2012).
53. Mosteller, F. & Tukey, J. W. *Data Analysis and Regression. A Second Course in Statistics*, 203–209 (Addison–Wesley, 1977).
54. Langfelder, P., Zhang, B. & Horvath, S. Defining clusters from a hierarchical cluster tree: the Dynamic Tree Cut package for R. *Bioinformatics* **24,** 719–720 (2008).
55. Li, J. *et al.* An integrated catalog of reference genes in the human gut microbiome. *Nat. Biotechnol.* **32,** 834–841 (2014).
56. Kultima, J. R. *et al.* MOCAT: a metagenomics assembly and gene prediction toolkit. *PLoS One* **7,** e47656 (2012).
57. Li, W. & Godzik, A. Cd-hit: a fast program for clustering and comparing large sets of protein or nucleotide sequences. *Bioinformatics* **22,** 1658–1659 (2006).
58. Arumugam, M., Harrington, E. D., Foerstner, K. U., Raes, J. & Bork, P. SmashCommunity: a metagenomic annotation and analysis tool. *Bioinformatics* **26,** 2977–2978 (2010).
59. Nielsen, H. B. *et al.* Identification and assembly of genomes and genetic elements in complex metagenomic samples without using reference genomes. *Nat. Biotechnol.* **32,** 822–828 (2014).
60. Caporaso, J. G. *et al.* QIIME allows analysis of high-throughput community sequencing data. *Nat. Methods* **7,** 335–336 (2010).
61. Kozich, J. J., Westcott, S. L., Baxter, N. T., Highlander, S. K. & Schloss, P. D. Development of a dual-index sequencing strategy and curation pipeline for analyzing amplicon sequence data on the MiSeq Illumina sequencing platform. *Appl. Environ. Microbiol.* **79,** 5112–5120 (2013).
62. Edgar, R. C., Haas, B. J., Clemente, J. C., Quince, C. & Knight, R. UCHIME improves sensitivity and speed of chimera detection. *Bioinformatics* **27,** 2194–2200 (2011).
63. Edgar, R. C. Search and clustering orders of magnitude faster than BLAST. *Bioinformatics* **26,** 2460–2461 (2010).
64. DeSantis, T. Z. *et al.* Greengenes, a chimera-checked 16S rRNA gene database and workbench compatible with ARB. *Appl. Environ. Microbiol.* **72,** 5069–5072 (2006).
65. Wang, Q., Garrity, G. M., Tiedje, J. M. & Cole, J. R. Naive Bayesian classifier for rapid assignment of rRNA sequences into the new bacterial taxonomy. *Appl. Environ. Microbiol.* **73,** 5261–5267 (2007).
66. Paulson, J. N., Stine, O. C., Bravo, H. C. & Pop, M. Differential abundance analysis for microbial marker-gene surveys. *Nat. Methods* **10,** 1200–1202 (2013).
67. McMurdie, P. J. & Holmes, S. phyloseq: an R package for reproducible interactive analysis and graphics of microbiome census data. *PLoS One* **8,** e61217 (2013).
68. Oksanen, J. *et al.* vegan: Community Ecology Package. R package version 2.3-3. https://cran.r-project.org/web/packages/vegan/index.html (2016).
69. Wickham, H. *ggplot2: Elegant Graphics for Data Analysis*. (Springer, 2009).
70. R Development Core Team. R: A language and environment for statistical computing. R Foundation for Statistical Computing, Vienna, Austria. (2012).
71. Whittaker, J. *Graphical models in applied multivariate statistics.* (John Wiley & Sons, 1990).
72. Seongho, K. ppcor: Partial and semipartial (Part) correlation. R package version 1.0. https://cran.r-project.org/web/packages/ppcor/index.html (2012).
73. Love, M. I., Huber, W. & Anders, S. Moderated estimation of fold change and dispersion for RNA-seq data with DESeq2. *Genome Biol.* **15,** 550 (2014).
74. Paternoster, R., Brame, R., Mazerolle, P. & Piquero, A. Using the correct statistical test for the equality of regression coefficients. *Criminology* **36,** 859–866 (1998).
75. Lee, S., Chang, J. & Blackstone, C. FAM21 directs SNX27–retromer cargoes to the plasma membrane by preventing transport to the Golgi apparatus. *Nat. Commun.* **7,** http://dx.doi.org/10.1038/ncomms10939 (2016).

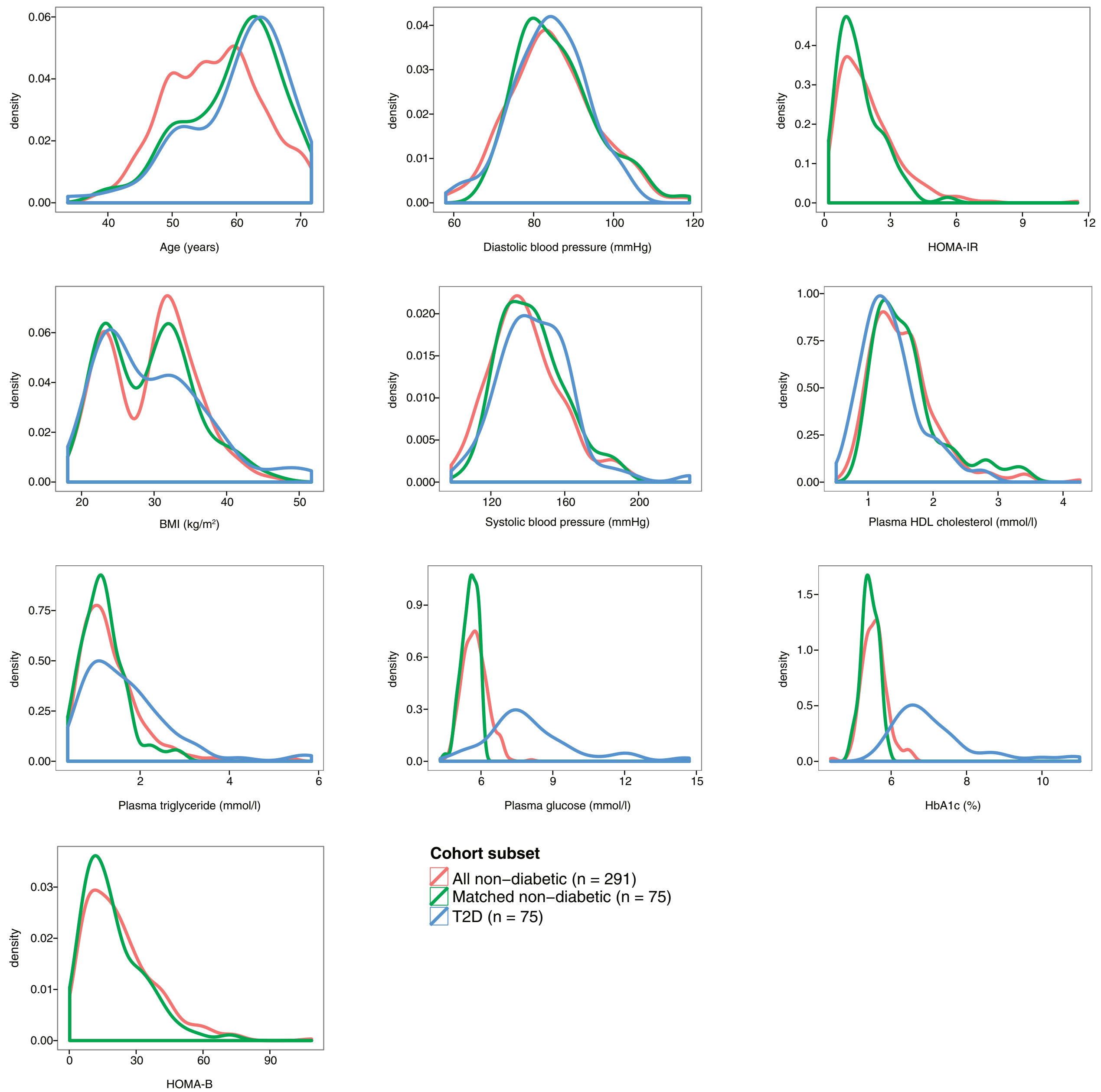

Extended Data Figure 1 | Distributions of continuous physiological traits for the 291 non-diabetic individuals, 75 type 2 diabetes patients and 75 matched non-diabetic controls. An overview of the same traits is shown in Supplementary Table 1. The 75 non-diabetic controls are a subset of the 291 non-diabetic individuals matched to the type 2 diabetes patients by age, sex and BMI and used for comparative analyses.

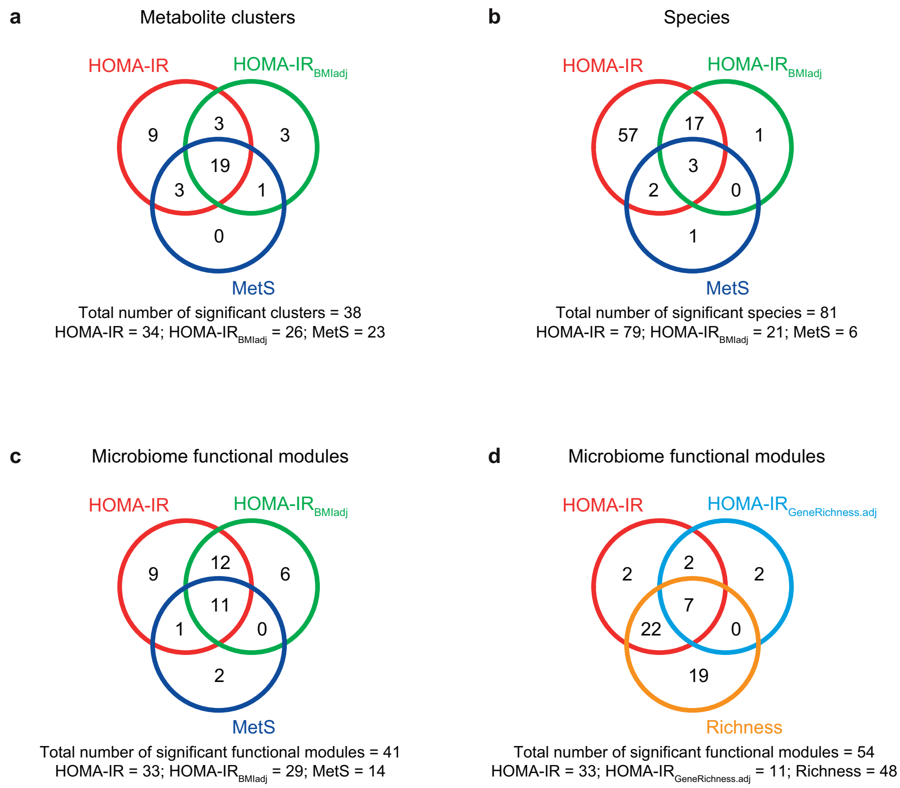

Extended Data Figure 2 | The number of metabolite clusters, species and microbiome functional modules significantly associated with HOMA-IR, HOMA-IR$_{BMIadj}$, and metabolic syndrome. a–c, Venn diagrams resuming the number of serum metabolite clusters (**a**), species (**b**) and microbiome functional modules (**c**) that are associated with the three HOMA-IR, HOMA-IR$_{BMIadj}$ and metabolic syndrome phenotypes at FDR < 0.1. **d**, The number of microbiome functional modules associated with HOMA-IR, gene richness and HOMA-IR$_{GeneRichness.adj}$. The metabolite cluster associations are based on all 291 non-diabetic individuals whereas the species and KEGG module associations were estimated on the 277 non-diabetic individuals with microbiome data. MetS, metabolic syndrome.

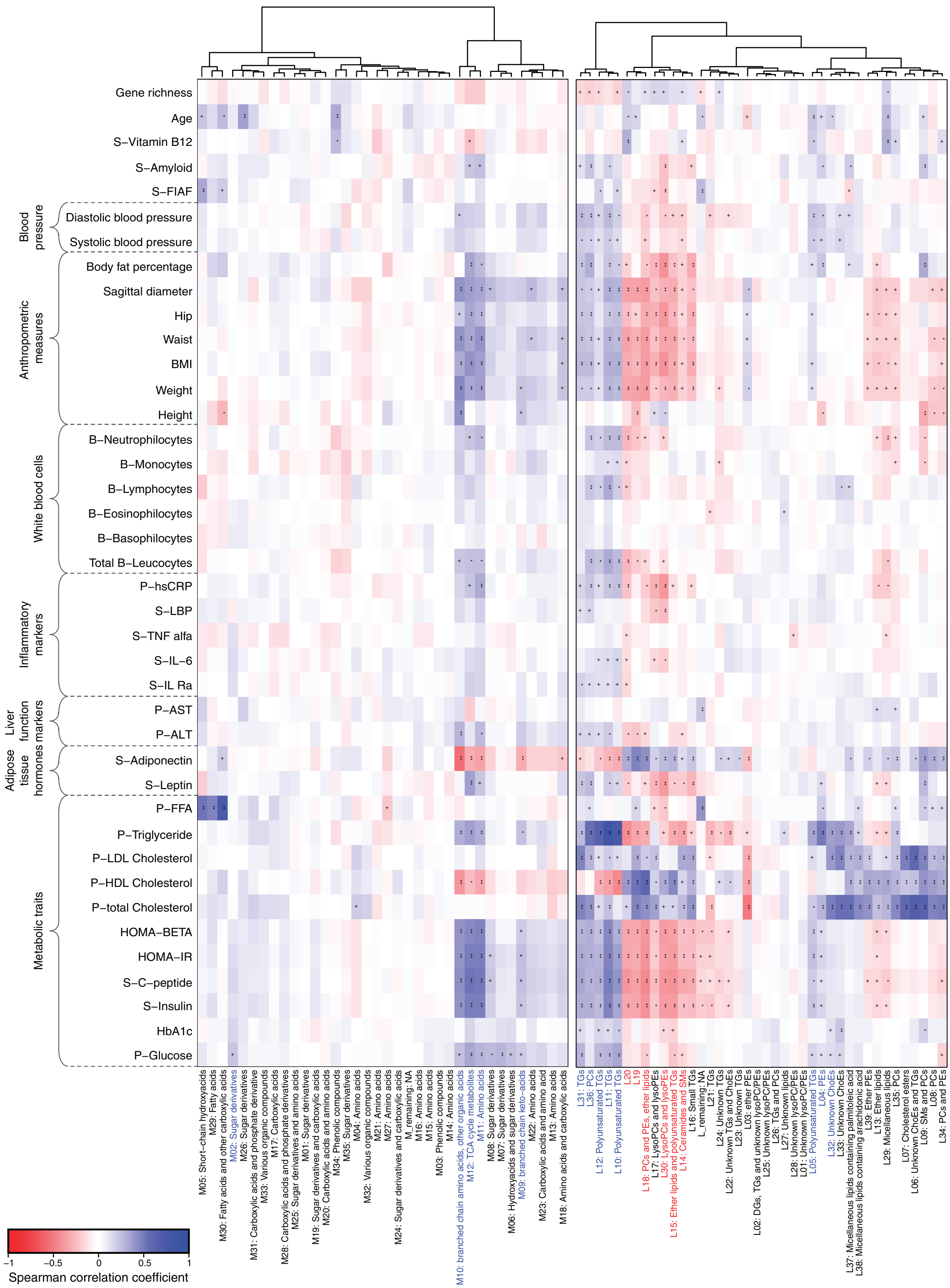

Extended Data Figure 3 | Fine-grained correlation profile of fasting serum metabolite clusters and physiological traits in 291 non-diabetic individuals. Spearman correlations between all fasting serum metabolite clusters (top panel, molecular lipids; bottom panel, polar metabolites) and clinical phenotypes. The metabolites in each panel are clustered by their correlation profile (see dendrogram). The colour represents positive (blue) or negative (red) correlations and FDRs are denoted: +, FDR < 0.1; *, FDR < 0.01; **, FDR < 0.001. The names of the 19 metabolite clusters making up the IR- and IS-metabotypes are highlighted with blue (IR-metabotype) and red (IS-metabotype), respectively.

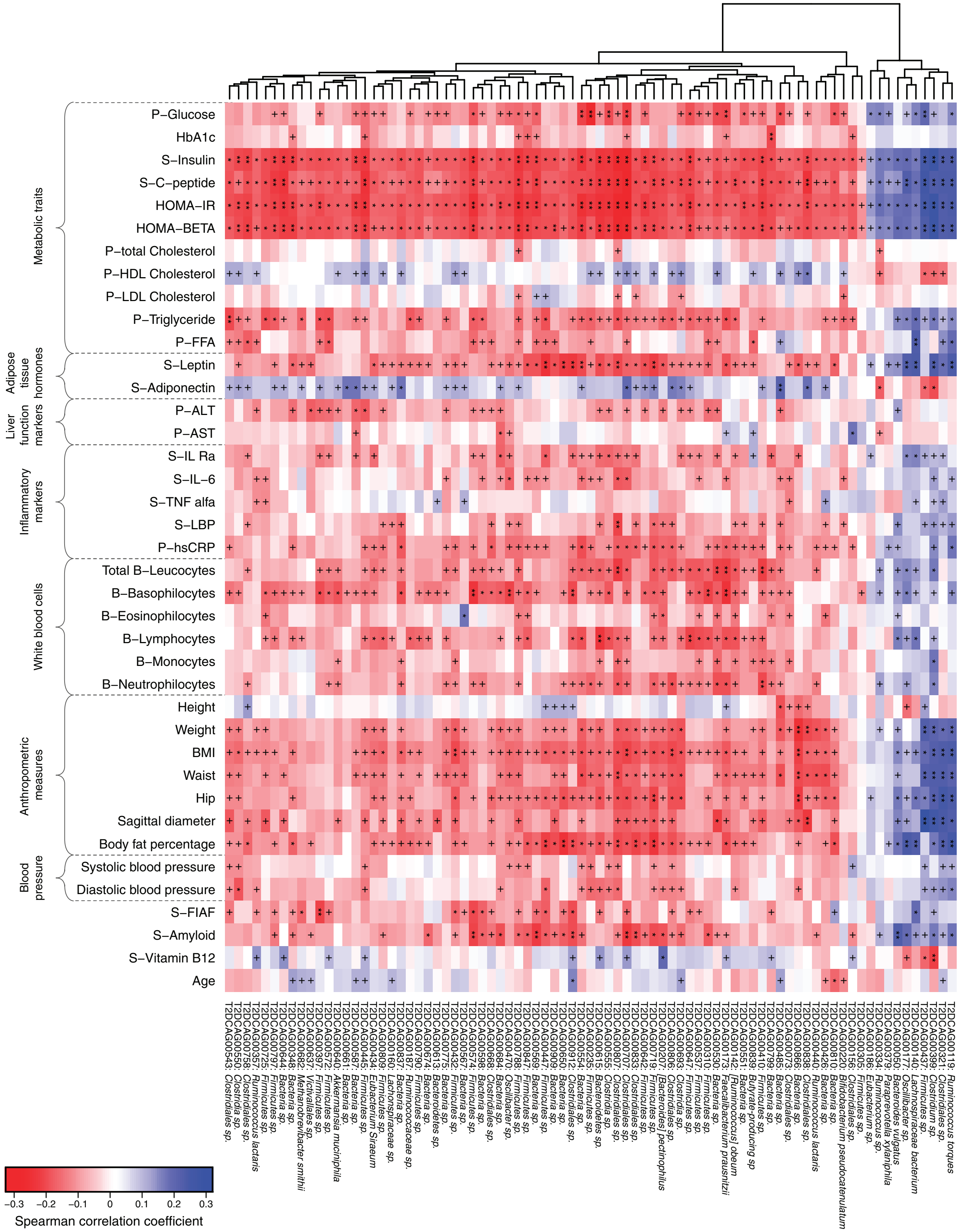

Extended Data Figure 4 | Fine-grained correlation profile of IR- and metabolic-syndrome-associated microbial species and physiological traits in 277 non-diabetic individuals. Spearman correlations between continuous physiological traits and the 81 species significantly associated (FDR < 0.1) with HOMA-IR, HOMA-IR$_{BMIadj}$ or metabolic syndrome phenotypes (Extended Data Fig. 1). The species are clustered by their correlation profile. The colour represents positive (blue) or negative (red) correlations and FDRs are denoted: +, FDR < 0.1; *, FDR < 0.01; **, FDR < 0.001.

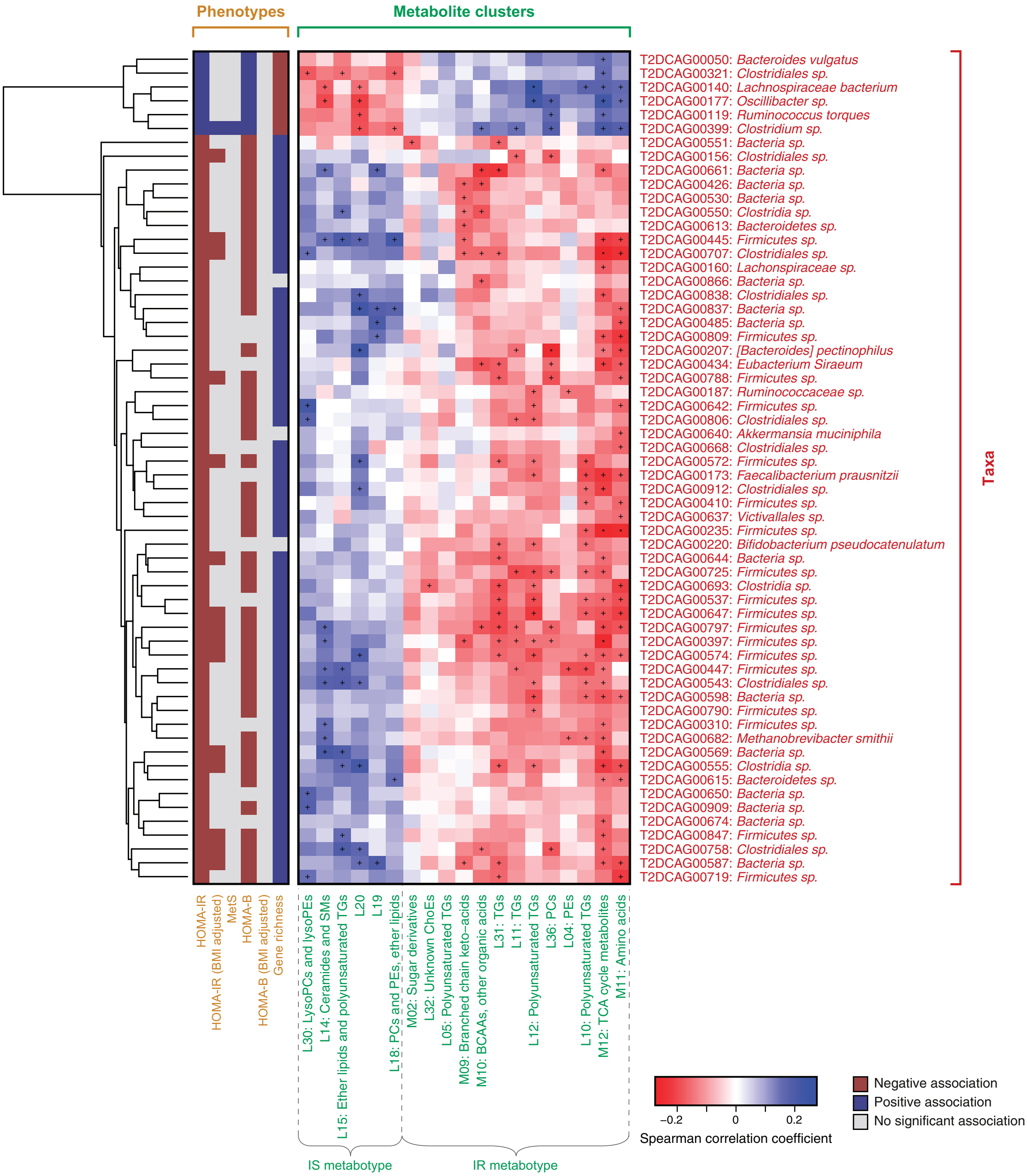

Extended Data Figure 5 | Correlations between IR- and metabolic syndrome-associated microbial species and fasting serum metabolite clusters in 277 non-diabetic individuals. Spearman correlations between species that were significantly associated (FDR < 0.1) with HOMA-IR, HOMA-IR$_{BMIadj}$ or metabolic syndrome phenotypes and the 19 metabolite clusters making up the IR- and IS-metabotypes. The colour represents positive (blue) or negative (red) correlations and FDRs are denoted: +, FDR < 0.1; *, FDR < 0.01; **, FDR < 0.001. The left sidebar represents positive (blue) or negative (red) correlations between the species and the indicated phenotypes (FDR < 0.1). MetS, metabolic syndrome.

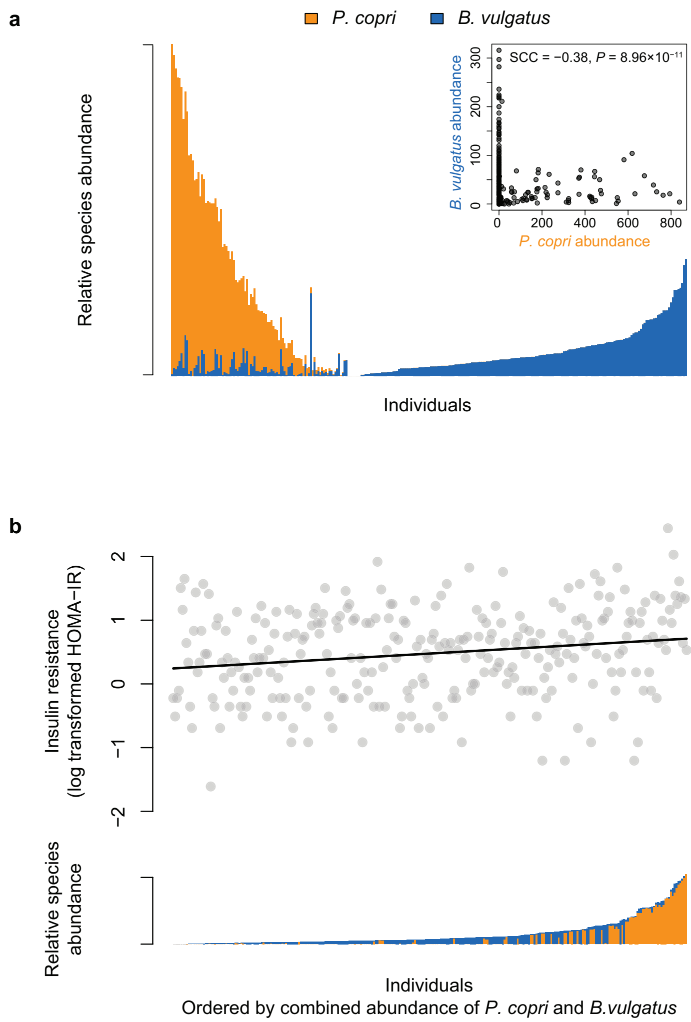

Extended Data Figure 6 | Abundances of *P. copri* and *B. vulgatus* anti-correlate and their combined abundance correlates with HOMA-IR in 277 non-diabetic individuals. a, **b**, The abundances of T2DCAG00385: *P. copri* (orange) and T2DCAG00050: *B. vulgatus* (blue), shown for all non-diabetic individuals arranged by decreasing *P. copri* abundance and increasing *B. vulgatus* abundance (**a**), and arranged by total abundance of both species with HOMA-IR levels shown above (**b**).

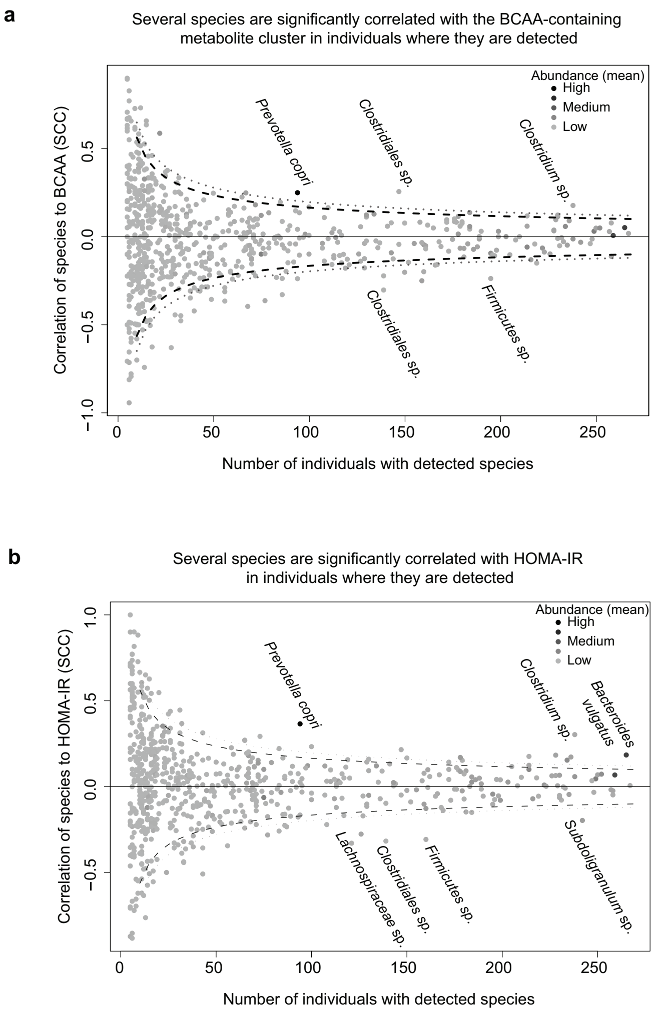

Extended Data Figure 7 | Correlations between microbial species and both HOMA-IR and the BCAA-containing metabolite cluster (M10) in 277 non-diabetic individuals. a, **b**, Spearman correlations between species and both the BCAA-containing metabolite cluster (**a**, M10) and insulin resistance (**b**, HOMA-IR) in individuals with detectable abundances of the respective species. FDRs of 0.1 and 0.05 are denoted with dotted and dashed lines, respectively. Colour intensity represents mean species abundance in individuals where the species was observed.

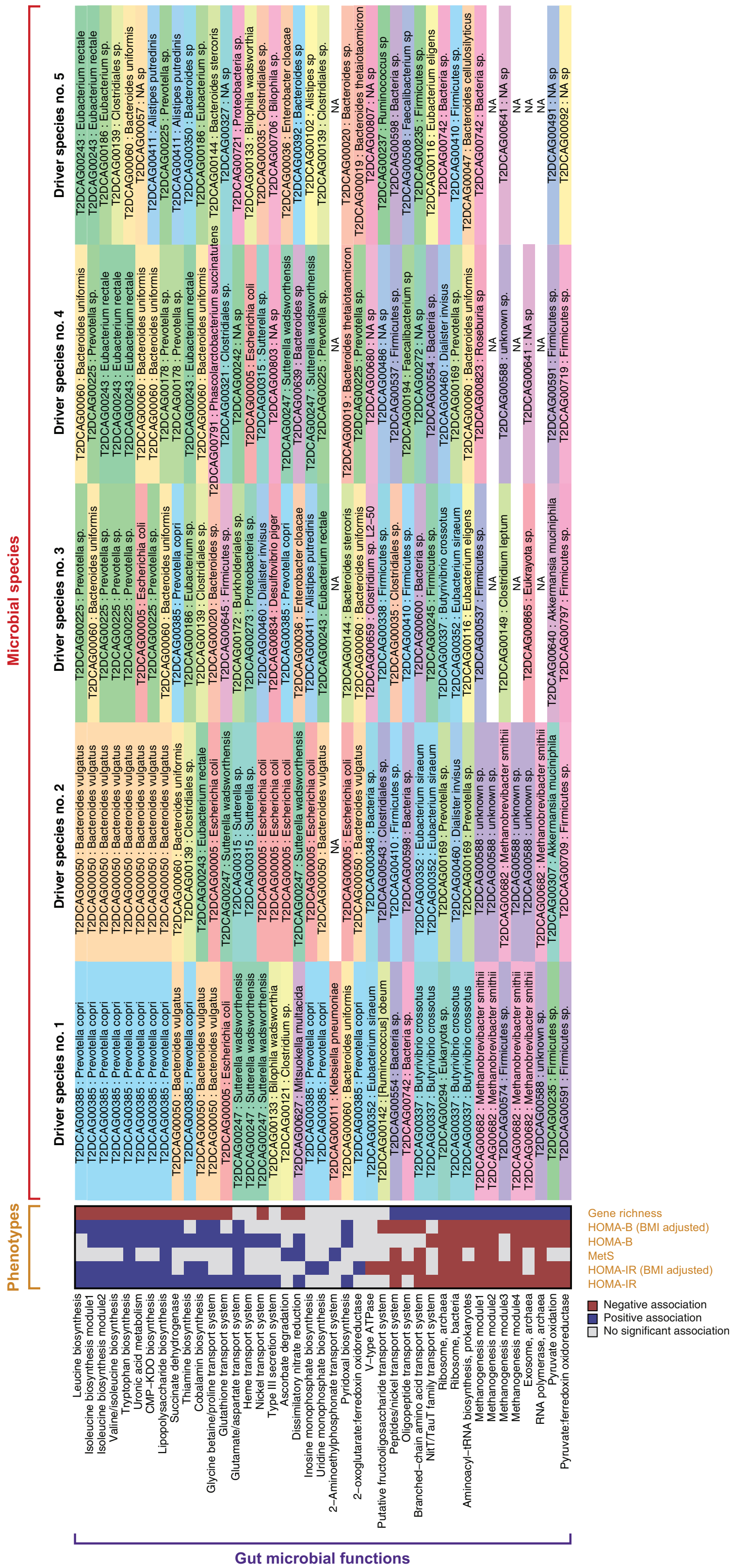

Extended Data Figure 8 | Microbial driver species for associations between microbiome functional modules and insulin resistance in 277 non-diabetic individuals. The five most important microbial species driving the association between the indicated microbiome functional modules and insulin resistance (HOMA-IR) are shown (see Supplementary Table 9 for effect sizes). Each species is highlighted with a different colour. The left sidebar represents positive (blue) or negative (red) associations between the functional modules and the indicated phenotypes (FDR <0.1). MetS, metabolic syndrome.

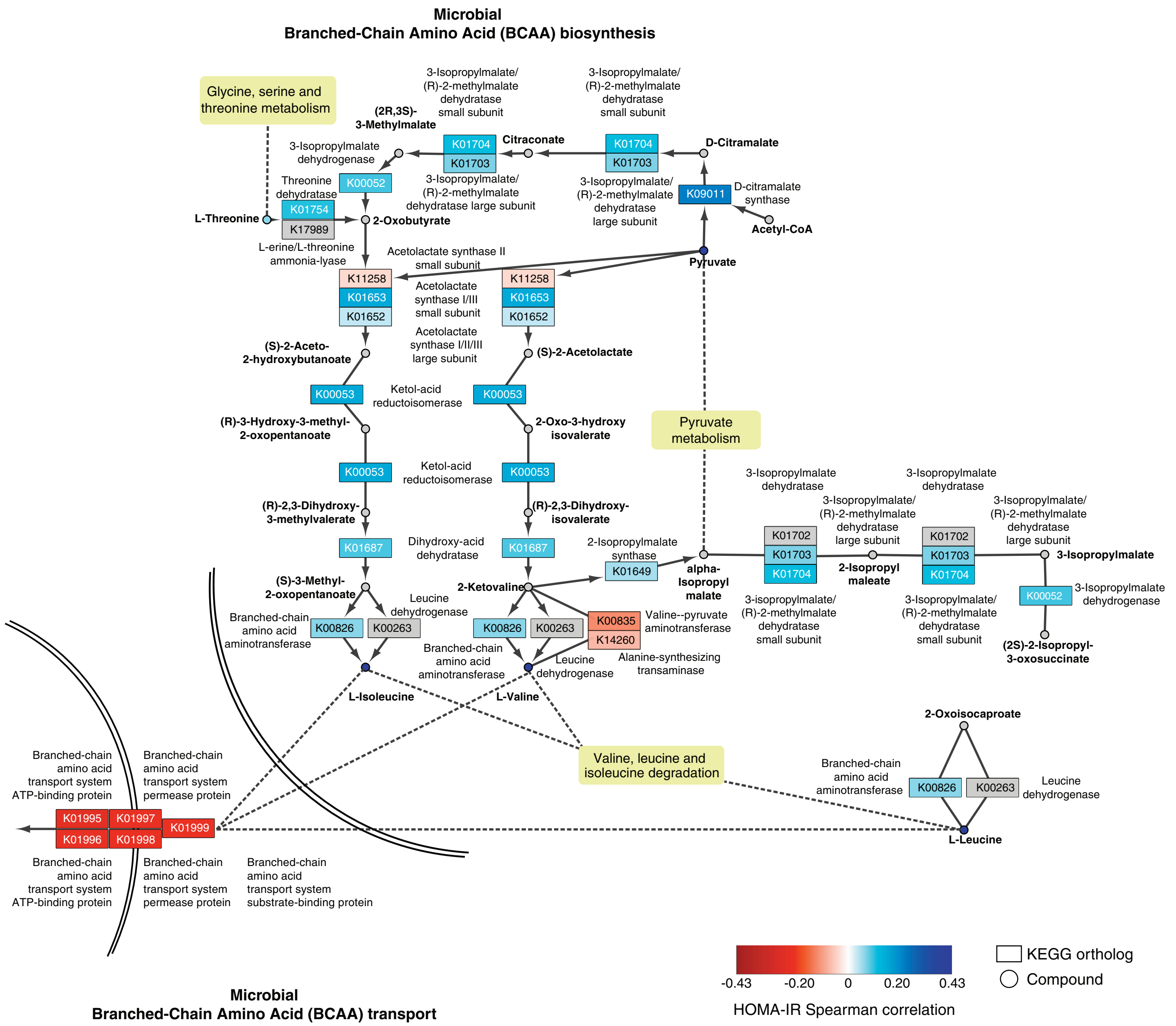

Extended Data Figure 9 | An in-depth view of the microbial BCAA biosynthesis pathway and BCAA inward transport system, illustrating the correlations between microbial KEGG orthologous gene groups and serum metabolites with human insulin resistance. KEGG orthologous gene groups (squares) and metabolites (circles) are coloured by their Spearman correlation with HOMA-IR in the non-diabetic individuals ($n = 277$ for KEGG orthologous gene groups, $n = 291$ for metabolites), or coloured grey if no information was available. The network is adapted from KEGG pathway maps (pathways hsa00290 and hsa02010).

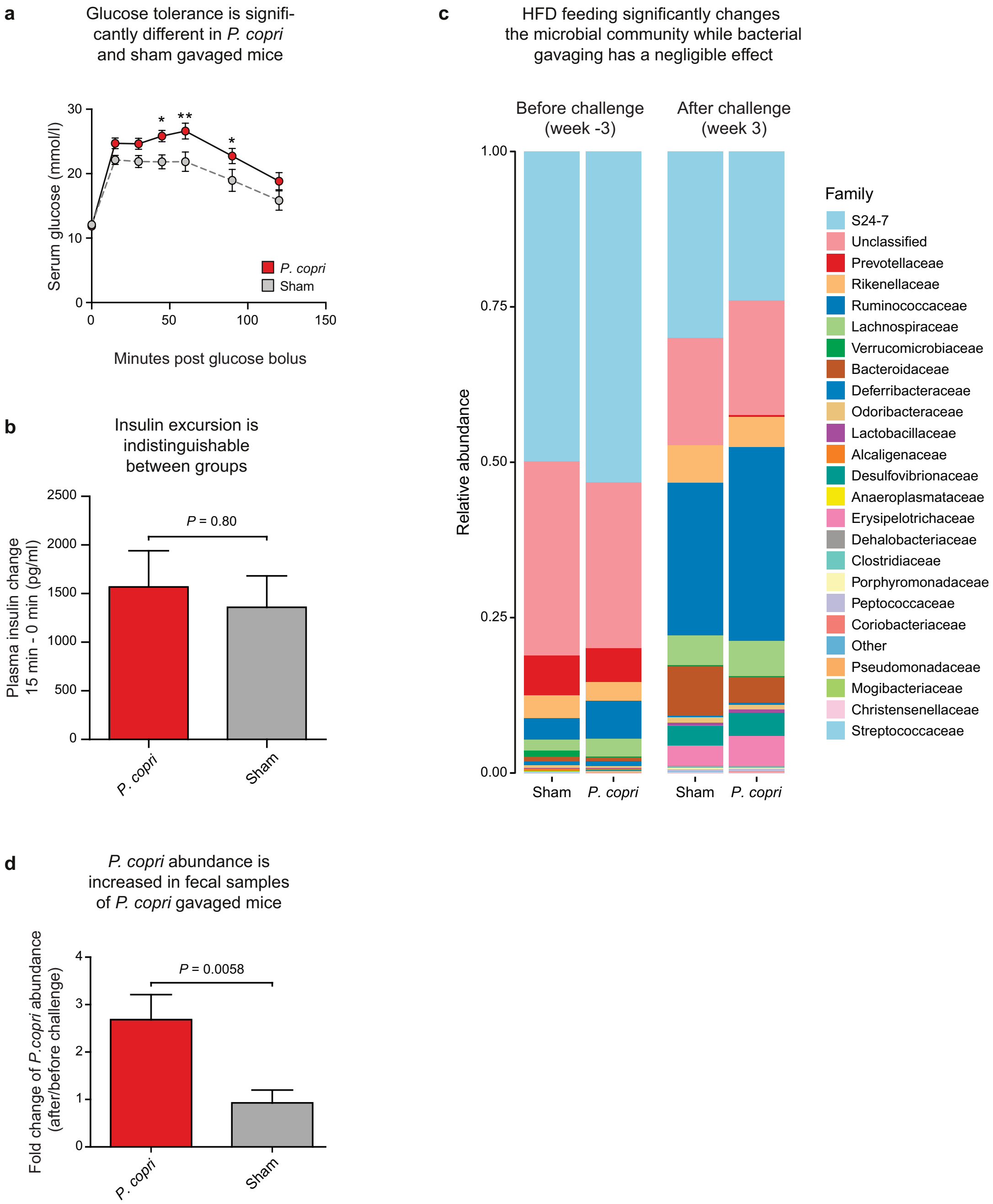

Extended Data Figure 10 | Oral glucose tolerance test after two weeks of *P. copri* or sham gavaging and 16S rDNA amplicon sequencing of faecal samples from mice after three weeks of treatment with *P.copri* or *sham*. a, Oral glucose tolerance test. The *P. copri*-gavaged mice ($n = 12$) had significantly higher serum glucose levels compared to sham-gavaged controls ($n = 12$, $P = 0.02$, Mann–Whitney *U*-test for AUC) after two weeks of the gavage challenge. Mean ± s.e.m. is depicted. Stars indicate significant differences at individual time points (repeated measurements two-way ANOVA): $*P < 0.05$; $**P < 0.01$. **b**, Plasma insulin was measured before and 15 min post glucose bolus, $P = 0.80$, Mann–Whitney *U*-test, bars represents mean ± s.e.m., $n = 12$. **c**, Microbiota taxa summary plots on family level after the two given time points, that is, pre high-fat diet (HFD) and post HFD plus gavage. HFD feeding significantly changed the microbial community (adonis $P = 0.001$) while bacterial gavaging had negligible effect. Data represent mean values. $n = 12$ per group (one sample from the sham group at time point −3 weeks did not go successfully through the 16S rDNA amplicon sequencing and is therefore represented by 11 samples). 'Unclassified' refers to reads that could not be classified to any taxonomy. 'Other' refers to reads that could not be classified at family level. **d**, *P. copri* changes in mouse faecal samples after *P. copri* gavaging as determined by quantitative PCR. Bars show the change in *P. copri* levels relative to before *P. copri* or sham challenge (bars represents mean ± s.e.m., $n = 12$, $P = 0.0058$, Mann–Whitney *U*-test).

doi:10.1038/nature18325

Replication fork stability confers chemoresistance in BRCA-deficient cells

Arnab Ray Chaudhuri[1]*, Elsa Callen[1]*, Xia Ding[2], Ewa Gogola[3], Alexandra A. Duarte[3], Ji-Eun Lee[4], Nancy Wong[1], Vanessa Lafarga[5], Jennifer A. Calvo[6], Nicholas J. Panzarino[6], Sam John[1], Amanda Day[1], Anna Vidal Crespo[1], Binghui Shen[7], Linda M. Starnes[8], Julian R. de Ruiter[3], Jeremy A. Daniel[8], Panagiotis A. Konstantinopoulos[9], David Cortez[10], Sharon B. Cantor[6], Oscar Fernandez-Capetillo[5], Kai Ge[4], Jos Jonkers[3], Sven Rottenberg[3,11], Shyam K. Sharan[2] & André Nussenzweig[1]

Cells deficient in the *Brca1* and *Brca2* genes have reduced capacity to repair DNA double-strand breaks by homologous recombination and consequently are hypersensitive to DNA-damaging agents, including cisplatin and poly(ADP-ribose) polymerase (PARP) inhibitors. Here we show that loss of the MLL3/4 complex protein, PTIP, protects *Brca1/2*-deficient cells from DNA damage and rescues the lethality of *Brca2*-deficient embryonic stem cells. However, PTIP deficiency does not restore homologous recombination activity at double-strand breaks. Instead, its absence inhibits the recruitment of the MRE11 nuclease to stalled replication forks, which in turn protects nascent DNA strands from extensive degradation. More generally, acquisition of PARP inhibitors and cisplatin resistance is associated with replication fork protection in *Brca2*-deficient tumour cells that do not develop *Brca2* reversion mutations. Disruption of multiple proteins, including PARP1 and CHD4, leads to the same end point of replication fork protection, highlighting the complexities by which tumour cells evade chemotherapeutic interventions and acquire drug resistance.

The role of BRCA1 and BRCA2 in the repair of double-strand breaks (DSBs) is thought to be central to their tumour-suppressor activities, and underlies the hypersensitivity of *Brca*-deficient cells to DNA-damaging agents. While cisplatin and PARP inhibitors (PARPi) have been shown to be effective chemotherapeutic agents, most *Brca*-mutant carcinomas acquire resistance[1]. Besides reduced uptake and increased efflux of drugs, the most well-described mechanism that drives chemotherapeutic resistance in *Brca1/2*-deficient tumours is through the restoration of homologous recombination (HR)[1]. Identification of additional mechanisms underlying resistance to DNA damage is crucial for improving therapies and predicting tumour responses in *Brca*-deficient cancers.

PTIP loss protects RFs in *Brca*-deficient cells

In addition to their roles in HR, recent studies have uncovered DSB-independent functions for BRCA1 and BRCA2 during replication stress[2–6]. Since MRE11 has been implicated in mediating replication fork (RF) degradation in cell lines[2–4], we tested whether primary cells deficient in BRCA1 or BRCA2 also showed degradation of nascent replication tracts. We therefore conditionally inactivated BRCA1 and BRCA2 in B lymphocytes (*Brca1*$^{f/f}$CD19Cre; *Brca2*$^{f/f}$*Cd19Cre*). B cells were sequentially labelled with CldU-(red) followed by IdU-(green), after which the active RFs were stalled with hydroxyurea (HU) (Fig. 1a). The relative shortening of the IdU tract after HU treatment serves as a measure of RF degradation (Fig. 1a). Upon HU treatment, wild-type (WT) cells showed a mean IdU/CldU tract ratio close to 1 (Fig. 1b). However, *Brca1*- and *Brca2*-deficient B cells exhibited a 30–45% reduction in the IdU tract length (Fig. 1b–e and Extended Data Fig. 1a–c).

Consistent with previous data[2,3], RF degradation in B lymphocytes was dependent on MRE11 exonuclease activity (Extended Data Fig. 1a–c). We also tested the role of DNA2 and the Werner syndrome helicase/nuclease (WRN) in degradation of forks in *Brca2*-deficient B cells. Treatment of *Brca2*-deficient cells with WRN inhibitor did not result in fork protection, whereas MRE11 and DNA2 were epistatic (Extended Data Fig. 1c).

Since 53BP1, RIF1, and PTIP counteract BRCA1-dependent HR by inhibiting MRE11-dependent DSB resection[7–15], we examined whether these factors might also function in RF stability. We thus inactivated BRCA1, BRCA2, RIF1, PTIP and 53BP1 in B lymphocytes (Extended Data Fig. 2a). Short exposure to HU did not promote significant DSB formation (Extended Data Fig. 2b), and fork progression rates were comparable across all genotypes (Extended Data Fig. 2c–f).

Absence of 53BP1 did not protect *Brca1*-deficient B cells from degradation of RFs (Fig. 1b), consistent with the finding that BRCA1 acts in RF stabilization in a manner independent of DSB repair[2,3]. Nascent strands also shortened considerably in the absence of the 53BP1 effector *Rif1* and in *Brca1/Rif1* doubly deficient cells (Fig. 1c). In striking contrast, loss of *Ptip* protected RFs from HU-induced degradation in both *Brca1*- and *Brca2*-deficient cells (Fig. 1d, e). Moreover, while *Brca1*$^{-/-}$, *Rif1*$^{-/-}$, and *Brca1*$^{-/-}$*Rif1*$^{-/-}$ B cells displayed increased genomic instability when treated with HU (Extended Data Fig. 3a), *Brca1/Ptip* doubly deficient cells exhibited 2.4-fold fewer chromosomal aberrations and increased viability compared with *Brca1*$^{-/-}$ (Fig. 1f). Similarly, loss of *Ptip* decreased the number of chromosomal aberrations in *Brca2*$^{-/-}$cells challenged with HU (Extended Data Fig. 3b), suggesting that PTIP has functions at

[1]Laboratory of Genome Integrity, National Cancer Institute, National Institutes of Health, Bethesda, Maryland 20892, USA. [2]Mouse Cancer Genetics Program, National Cancer Institute, National Institutes of Health, Frederick, Maryland 21702, USA. [3]Division of Molecular Pathology and Cancer Genomics Centre, The Netherlands Cancer Institute, Plesmanlaan 121, 1066 CX Amsterdam, The Netherlands. [4]Laboratory of Endocrinology and Receptor Biology, National Institute of Diabetes and Digestive and Kidney Diseases, National Institutes of Health, Bethesda, Maryland 20892, USA. [5]Genomic Instability Group, Spanish National Cancer Research Centre (CNIO), Madrid 28029, Spain. [6]Department of Molecular, Cell, and Cancer Biology, University of Massachusetts Medical School, UMASS Memorial Cancer Center, Worcester, Massachusetts 01605, USA. [7]Department of Radiation Biology, Beckman Research Institute of City of Hope, 1500 East Duarte Road, Duarte, California 91010, USA. [8]The Novo Nordisk Foundation Center for Protein Research, Faculty of Health and Medical Sciences, University of Copenhagen, Copenhagen 2200, Denmark. [9]Departments of Gynecologic Medical Oncology, Dana Farber Cancer Institute, Harvard Medical School, Boston, Massachusetts 02215, USA. [10]Department of Biochemistry, Vanderbilt University School of Medicine, 2215 Garland Avenue, Nashville, Tennessee 37232, USA. [11]Institute of Animal Pathology, Vetsuisse Faculty, University of Bern, Länggassstrasse 122, 3012 Bern, Switzerland.
*These authors contributed equally to this work.

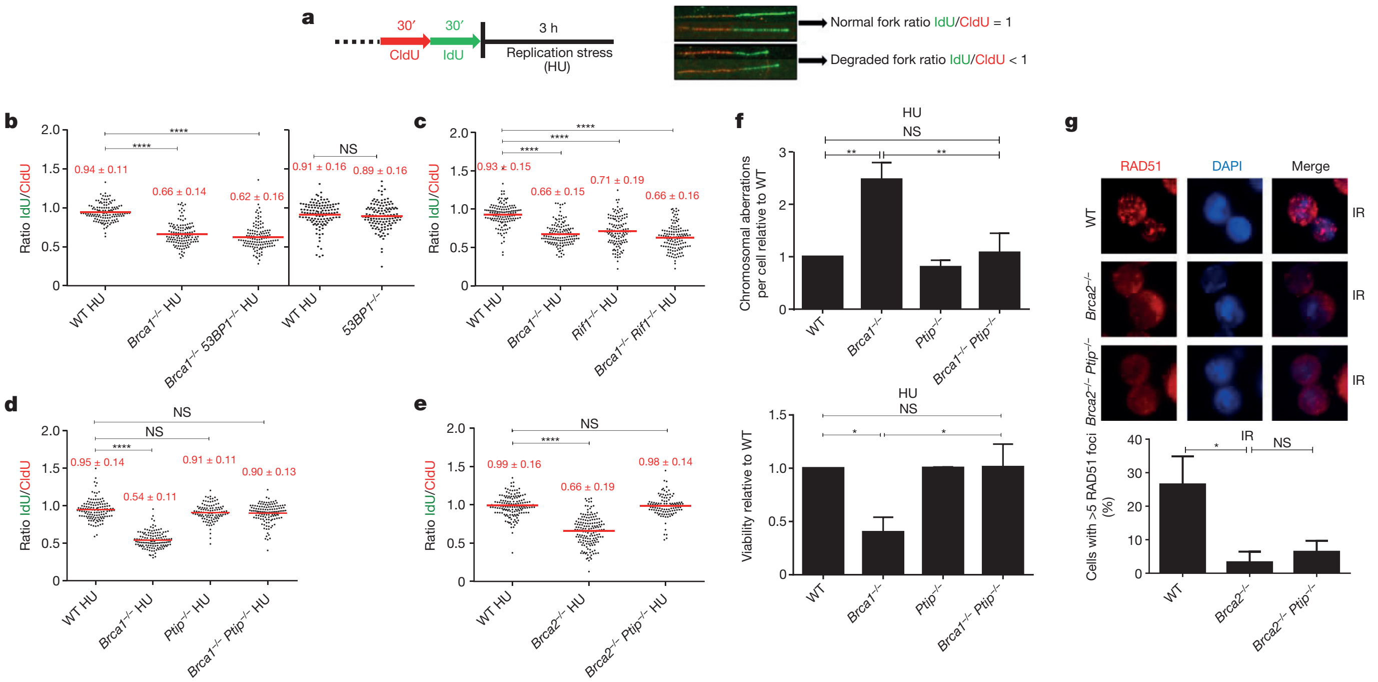

Figure 1 | Loss of *Ptip* in *Brca1/2*-deficient B cells protects nascent DNA from degradation without restoring HR. a, Schematic for labelling B cells with CldU and IdU. **b**–**e**, Ratio of IdU versus CldU upon HU treatment. Numbers in red indicate the mean ± s.d. (NS, not significant, $^{****}P \leq 0.0001$, Mann–Whitney test). One hundred and twenty-five replication forks were analysed for each genotype. **f**, Genomic instability (top) and viability upon HU treatment (bottom) relative to WT upon 6 h of 10 mM HU treatment. ($^{**}P \leq 0.001$, $^{*}P \leq 0.05$, unpaired *t*-test.) Fifty metaphases were analysed. **g**, Representative images (top) and quantification (below) of irradiation (IR)-induced RAD51 foci. $^{*}P \leq 0.05$, unpaired *t*-test ($n = 120$ cells examined). Experiments were repeated three times.

stalled RFs distinct from its DSB-dependent interactions with 53BP1 and RIF1.

We hypothesized that HU-induced degradation would impact RF progression rates. We therefore assayed the ability of WT and mutant cells to incorporate nucleotide analogues in the presence of low concentrations of HU. We observed a significant decrease in IdU tract lengths during HU exposure across all genotypes. However, *Brca2*-deficient cells had significantly decreased progression rates upon HU treatment, whereas *Ptip*$^{-/-}$ and *Brca2*$^{-/-}$*Ptip*$^{-/-}$ cells displayed significantly longer replication tracts (Extended Data Fig. 3c). We also tested the effect of *Ptip*-deficiency on recovery after replication stalling with high concentrations of HU. We found that although the percentage of restarted RFs did not change among genotypes (Extended Data Fig. 3d), loss of *Brca2* resulted in a delayed restart, whereas *Brca2/Ptip* doubly deficient cells restarted normally (Extended Data Fig. 3e). Thus, loss of PTIP promotes RF progression and timely restart in *Brca2*-deficient cells, which correlates with decreased RF degradation.

PTIP loss rescues lethality of *Brca2*-null ESCs

Since elevated levels or stabilized RAD51 filaments could protect RFs from degradation[2,3,16], we asked whether PTIP deficiency leads to overexpression of RAD51 or enhanced RAD51 activity. RAD51 levels were similar in WT, *Ptip*$^{-/-}$, *Brca2*$^{-/-}$, and *Brca2*$^{-/-}$*Ptip*$^{-/-}$ cells (Extended Data Fig. 3f), but the ability of RAD51 to relocalize to sites of DNA DSBs was severely impaired in *Brca2/Ptip*-deficient B cells (Fig. 1g and Extended Data Fig. 3g) and embryonic stem cells (ESCs) (see Fig. 2c, d). Moreover, loss of *Ptip* did not enhance the loading of RAD51 on nascent chromatin (see Fig. 3f).

Loss of *Brca2* in ESCs is incompatible with cell survival[17]. To test whether PTIP deficiency could promote ESC survival we knocked down PTIP in PL2F7 mouse ESCs, which have one null and one conditional allele of *Brca2* (*Brca2*$^{f/-}$, Fig. 2a and Extended Data Fig. 4a)[17]. After CRE transfection in *Brca2*$^{f/-}$ ESCs and selection in HAT medium, very few resistant colonies were obtained and these remained *Brca2*$^{f/-}$ rather than *Brca2*-null, reflecting the essential role of BRCA2 in ESC viability (Fig. 2b)[17]. Strikingly, 12.5% and 5% of the HAT-resistant colonies were *Brca2*-null when targeted by *Ptip* short hairpin RNAs (shRNAs) 1 and 2 respectively (Fig. 2b and Extended Data Fig. 4b). Consistent with our analysis of *Brca2*$^{-/-}$*Ptip*$^{-/-}$ B cells (Fig. 1g), irradiation-induced RAD51 foci formation was defective in *Brca2/Ptip*-deficient ESCs (Fig. 2c, d). Moreover, while efficient gene targeting to the *Pim-1* locus was observed in WT ESCs using a promoterless hygromycin cassette (100% of the hygromycin-resistant WT clones were targeted integrations), we did not observe a single targeted clone in *Brca2/Ptip*-deficient ESCs (Fig. 2e) indicative of defective HR. Similarly, the synthetic HR reporter substrate DR–GFP revealed impaired HR in *Brca2/Ptip*-deficient ESCs (Extended Data Fig. 4c). Nevertheless, stalled RFs in PTIP-deficient *Brca2*$^{-/-}$ ESCs displayed RF protection compared with *Brca2* hypomorphic mutant ESCs (Y3308X)[17] (Fig. 2f). Thus, deficiency in PTIP protects RFs from degradation and rescues the lethality of *Brca2* knockout ESCs without restoring DSB-induced HR.

BRCA2 is dispensable for HR at RFs

It has been suggested that HR at stalled forks is regulated differently from HR at DSBs[18]. As a readout for HR at RFs, we assayed for sister chromatid exchanges (SCEs) in WT and Y3308X ESCs. Although Y3308X cells show undetectable levels of irradiation-induced RAD51 formation and loss of targeted integration, indicative of a defect in DSB-induced HR[17], the basal frequency of SCE was normal in Y3308X cells (Extended Data Fig. 4d). Moreover, RAD51 was enriched on nascent DNA in Y3308X during normal replication and in presence of HU as measured by isolation of proteins on native DNA (iPOND) analysis (Extended Data Fig. 4e). We also observed similar frequencies of spontaneously generated and DNA damage-induced SCEs in WT, *Brca2-null* and *Brca2/Ptip*-deficient B cells (Extended Data Fig. 4f). Thus, in contrast to RAD51 which is required for DSB- and replication-associated HR[19], BRCA2 appears to be dispensable for HR

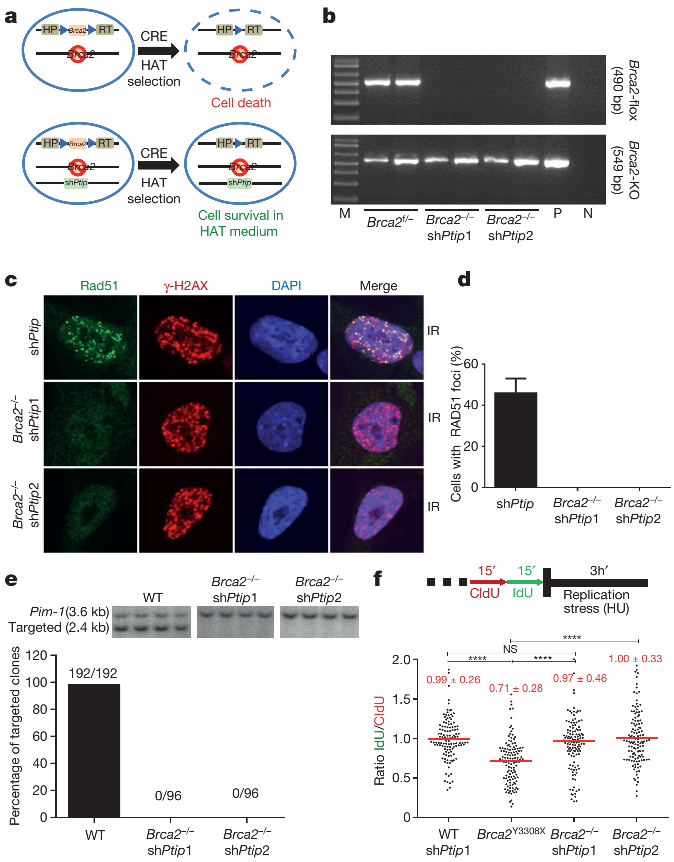

Figure 2 | PTIP deficiency rescues the lethality of *Brca2*-null mouse ESCs and confers fork protection. **a**, Schematic for deletion of *Brca2*. **b**, PCR genotyping of ESC clones (M, marker; P, positive control for *Brca2*$^{f/-}$; N, no DNA control). **c**, **d**, Representative images (**c**) and quantification (**d**) of irradiation-induced foci in *shPtip* and *Brca2*$^{-/-}$/sh*Ptip* ESCs ($n = 110$ cells examined). **e**, Representative Southern blot images (top) and quantification for targeting efficiency (bottom) for 59xDR–GFP[36] gene targeting to the *Pim-1* locus. **f**, Ratio of IdU versus CldU (****$P \leq 0.0001$, Mann–Whitney test). One hundred and twenty-five replication forks were analysed.

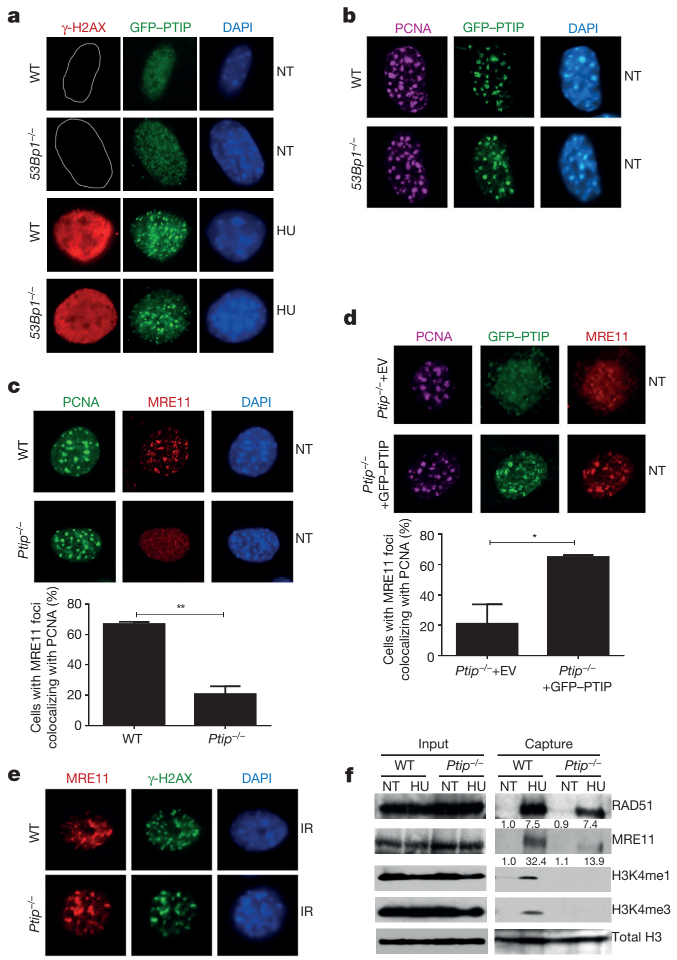

Figure 3 | PTIP localizes to sites of replication and recruits MRE11 to active and stalled replication forks. **a**, WT and *53Bp1*$^{-/-}$ MEFs expressing GFP-tagged PTIP were either treated or not (NT) with 4 mM HU and assessed for γ-H2AX (red) and PTIP (green). DAPI (4′,6-diamidino-2-phenylindole) indicated in blue. Quantification in Extended Data Fig. 5c. **b**, Co-localization of PCNA (magenta) and PTIP (green). Quantification in Extended Data Fig. 5d. **c**, Co-localization of PCNA (green) and MRE11 (red). Quantification in lower panel ($n = 150$ cells examined). **d**, *Ptip*$^{-/-}$ MEFs infected with either empty vector (EV, containing IRES–GFP) or full-length PTIP (GFP–PTIP) and probed for GFP (green), MRE11 (red) and PCNA (magenta). Quantification in lower panel ($n = 150$ cells examined). **e**, MRE11 (red) and γ-H2AX (green) irradiation-induced foci. Quantification in Extended Data Fig. 5g. **f**, iPOND analyses of proteins at replication forks (capture). Input represents 0.25% of the total cellular protein content. RAD51 and MRE11 levels (shown below) were normalized to total H3. Experiments were repeated three times.

that uses the nascent sister chromatid to repair DNA lesions during replication.

MRE11 association at RFs depends on PTIP–MLL3/4

Although the recruitment of PTIP to DSBs after irradiation is dependent on 53BP1 (Extended Data Fig. 5a, b)[10], we hypothesized that PTIP might be recruited to sites of stalled RFs independently of its interactions with 53BP1. Consistently, we observed PTIP accumulation at sites of replication stalling marked by pan-nuclear γ-H2AX staining[20]. Among cells exhibiting pan γ-H2AX signal, 71.4% of WT and 78% of *53Bp1*$^{-/-}$ mouse embryonic fibroblasts (MEFs) exhibited PTIP foci following HU treatment (Fig. 3a and Extended Data Fig. 5c). Even in the absence of HU treatment, PTIP exhibited extensive co-localization with proliferating cell nuclear antigen (PCNA) during late S phase both in WT and in *53Bp1*-deficient cells (Fig. 3b and Extended Data Fig. 5d, e). Collectively, these data suggest that PTIP might function during normal or perturbed replication in a DSB- and 53BP1-independent manner.

Like PTIP, MRE11 also associates with chromatin in a DNA damage-independent but DNA replication-dependent manner[21] (Fig. 3c). Loss of PTIP resulted in a marked decrease of MRE11 association with PCNA foci in unperturbed cycling MEFs (Fig. 3c) and defective MRE11 recruitment to ssDNA regions upon HU treatment (Extended Data Fig. 5f). Re-introduction of WT full-length PTIP into *Ptip*$^{-/-}$ MEFs restored MRE11 co-localization with PCNA in late S phase (Fig. 3d). Thus, in contrast to irradiation-induced MRE11 foci, localization of MRE11 to sites of DNA replication is PTIP-dependent (Fig. 3c–e and Extended Data Fig. 5g).

To monitor MRE11 and RAD51 association with active and stalled RFs we performed iPOND analysis in WT and *Ptip*$^{-/-}$ MEFs (Extended Data Fig. 5h)[22]. WT cells showed an increase in MRE11 and RAD51 association with stalled RFs (Fig. 3f). *Ptip*-deficient cells also showed an increase in RAD51 association at RFs, but MRE11 association with nascent DNA was reduced upon HU treatment (Fig. 3f), consistent with our immunofluorescence analysis (Fig. 3c and Extended Data Fig. 5f). Thus, MRE11 deposition on newly synthesized DNA is dependent on PTIP, which itself is recruited to stalled forks upon HU treatment (Extended Data Fig. 5i)[22].

PTIP is also known to constitutively associate with PA1 and with MLL3/MLL4 histone methyltransferases which catalyse methylation of histone H3 at lysine 4 (refs 23, 24). To identify the region of PTIP that promotes RF degradation in *Brca2*-deficient cells, we expressed EV (empty vector), FL (full-length PTIP), W165R (disrupting interactions with PA1)[25,26], W663R (disrupting interactions with 53BP1 at DSBs)[25] or Del-BRCT5-6 (disrupting interaction with MLL3/4 independently of DSBs)[23,24,26] in *Brca2/Ptip* doubly deficient cells. We observed that only reconstitution of *Brca2/Ptip*-deficient cells with PTIP-Del-BRCT5-6 maintained fork protection (Extended Data Fig. 6a).

We therefore tested whether the recruitment of MRE11 at stalled forks was dependent on MLL3/4. We observed that MRE11 association at RFs was dependent on MLL3/4 as monitored by iPOND and immunofluorescence analysis (Extended Data Fig. 6b, c). We also observed an enrichment of H3K4me1 and H3K4me3 at nascent forks upon HU treatment that was PTIP- and MLL3/4-dependent (Fig. 3f and Extended Data Fig. 6b). Thus, deposition of MRE11 on newly synthesized or stalled chromatin correlates with the establishment of H3K4me1 and H3K4me3 at RFs.

To determine whether MLL4 contributes to degradation of stalled forks in *Brca*-deficient cells, we examined RF degradation in *Brca1*$^{-/-}$*Mll4*$^{-/-}$ and *Brca2*$^{-/-}$*Mll4*$^{-/-}$ B cells. *Brca1*$^{-/-}$*Mll4*$^{-/-}$ and *Brca2*$^{-/-}$*Mll4*$^{-/-}$ cells displayed a partial rescue of fork degradation (Extended Data Fig. 6d, e). To test whether MLL4 methyltransferase activity is critical, we targeted the catalytic SET domain of MLL4 in *Brca1*-deficient B cells. We observed a significant rescue of fork degradation in *Brca1*$^{-/-}$*Mll4*-SET$^{-/-}$ cells, suggesting that the methyltransferase activity is important for promoting fork degradation (Extended Data Fig. 6f).

RF protection confers chemoresistance

RF protection contributes to genome stability in a manner independent of DSB-induced HR[2,3,5]. Consistently, we observed that *Brca2*$^{-/-}$*Mll4*$^{-/-}$ B cells showed a partial rescue of chromosomal aberrations upon PARPi and cisplatin treatment compared with *Brca2*$^{-/-}$ cells alone (Extended Data Fig. 6g). However, *Rif1*-deficient cells, characterized by extensive RF degradation (Fig. 1c) but normal irradiation-induced RAD51 foci formation (Extended Data Fig. 7a), showed increased chromosomal aberrations in response to replication poisons PARPi, HU and cisplatin (Extended Data Figs 3a and 7b, c)[27]. We therefore speculated that RF stability mediated by loss of PTIP (Fig. 1d, e) might confer genome stability to *Brca*-deficient cells exposed to chemotherapeutics that poison DNA replication. Indeed, we found that *Ptip* deficiency reduced the levels of chromosomal aberrations both in *Brca1*$^{-/-}$ and in *Brca2*$^{-/-}$ B cells (Fig. 4a, b).

To test whether differential levels of PTIP expression could be an indicator of patient responses to platinum chemotherapy, we queried clinical information from The Cancer Genome Atlas (TCGA) of patients with *Brca1/Brca2*-mutated ovarian serous adenocarcinoma treated with platinum chemotherapy (Extended Data Fig. 8a, b). Survival analysis demonstrated that platinum-treated *Brca2* mutants with high PTIP expression were correlated with a longer progression-free survival (PFS) (Extended Data Fig. 8a). Lower expression of PTIP also predicted a shorter PFS in *Brca2*-associated ovarian cancers (Extended Data Fig. 8b). Taken together, these data suggest that PTIP levels could be a biomarker for acquired resistance to platinum-based chemotherapy in *Brca1/2*-mutated ovarian cancers.

An unbiased shRNA screen recently demonstrated that reduced levels of the nucleosome remodelling factor CHD4 in *Brca2* mutant cancers correlated with poor patient response to chemotherapy, and increased tolerance to DNA-damaging agents without restoration of RAD51-dependent HR[28]. To test whether the resistance mechanism in this case occurs through RF protection, we knocked down CHD4 in the *Brca2* mutant ovarian cancer cell line PEO1 (Extended Data Fig. 8c, d). While CHD4 depletion in *Brca2* mutant cells did not restore HR[28], we observed that it largely conferred protection to nascent replication tracts from degradation upon HU treatment (Fig. 4c).

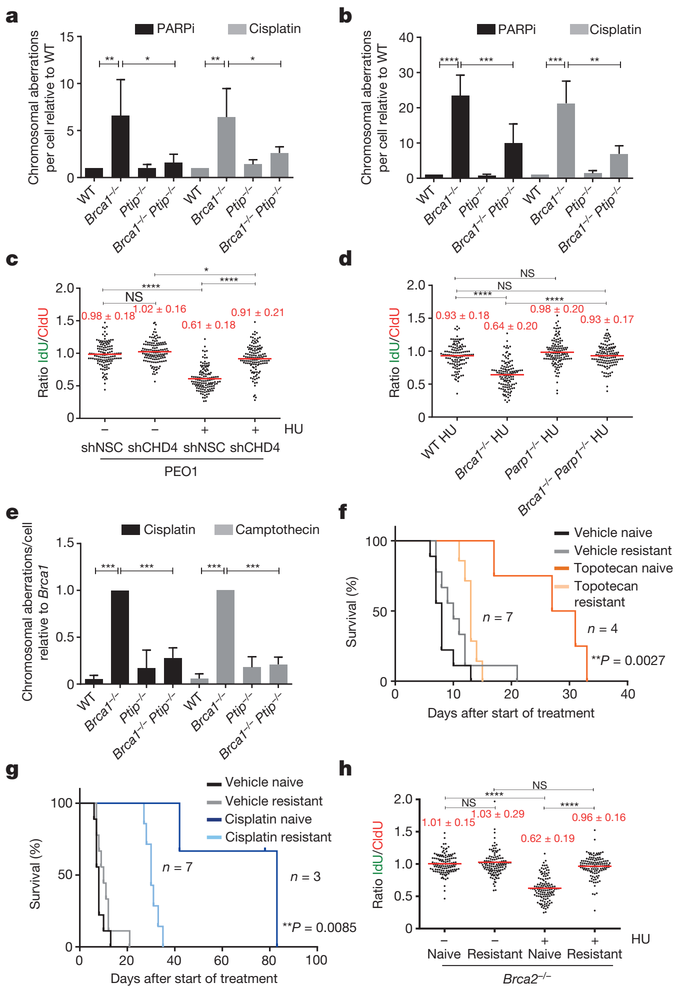

Figure 4 | Replication fork protection confers genome stability and chemotherapeutic resistance. a, b, Genomic instability measured in metaphase spreads from B cells ($n = 50$; $*P \leq 0.05$, $**P \leq 0.01$, $***P \leq 0.001$, $****P \leq 0.0001$, unpaired t-test). Experiments were repeated four times. **c**, Ratio of IdU versus CldU in *BRCA2*-mutated PEO1 cells either mock (shNSC) infected or infected with shRNA against CHD4 (shCHD4) ($*P \leq 0.05$, $****P \leq 0.0001$, Mann–Whitney test). One hundred and twenty-five replication forks were analysed. **d**, Ratio of IdU versus CldU in HU-treated B cells ($*P \leq 0.05$, $****P \leq 0.0001$, Mann–Whitney test). One hundred and twenty-five replication forks were analysed. **e**, Genomic instability in B cells ($n = 50$; $***P \leq 0.001$, unpaired t-test). Experiments repeated four times. **f**, **g**, Kaplan–Meier survival curves in mice implanted with either PARPi-naive or -resistant tumours and treated with either topotecan (**f**) or cisplatin (**g**) using log-rank (Mantel–Cox) test. **h**, Ratio of IdU versus CldU in untreated or HU-treated tumours (PARPi naive versus PARPi resistant) ($****P \leq 0.0001$, Mann–Whitney test). One hundred and twenty-five replication forks were analysed.

Moreover, depletion of CHD4 resulted in significantly decreased recruitment of MRE11 upon HU treatment in *Brca2* mutant cells (Extended Data Fig. 8e, f).

These results suggest that MRE11-mediated degradation contributes to genome instability upon treatment with replication poisons. To test this idea, we pre-incubated *Brca2*-deficient B cells with the MRE11 nuclease inhibitor mirin before treating with PARP inhibitor or cisplatin. Mirin treatment did not alter the frequency of replicating cells monitored by EdU incorporation (Extended Data Fig. 8g). However, incubation with mirin reduced the levels of PARPi-induced chromosomal aberrations approximately twofold. Similarly, *Brca2*-deficient cells were partly protected from cisplatin-induced DNA damage when MRE11 nuclease activity was inhibited (Extended Data Fig. 8h).

We conclude that MRE11 nuclease promotes genomic instability in *Brca2*-deficient cells.

Since PARP1 (ARTD1) is required for MRE11 localization to stalled replication forks[29] and its loss rescues the embryonic lethality in *Brca2*-null ESCs[30], we tested the contribution of PARP1 to RF stability and genome integrity by generating *Brca1*$^{-/-}$*Parp1*$^{-/-}$ B cells (*Brca1*$^{f/f}$; *Parp1*$^{-/-}$; *Cd19Cre*). Interestingly, loss of *Parp1* protected *Brca1*-deficient RFs from degradation and resulted in a significant reduction in chromosomal aberrations (Fig. 4d, e). Nevertheless, *Parp1* deficiency failed to rescue irradiation-induced RAD51 foci formation in *Brca1*-deficient cells (Extended Data Fig. 8i). Thus, despite the fact that treatment with PARP inhibitor increases levels of DNA damage in *Brca1*-deficient cells[31,32], loss of *Parp1* before *Brca1* loss protects against genome instability.

To determine whether *Brca2*-deficient tumour cells acquire chemotherapy resistance via RF protection, we induced PARPi-resistance using the KB2P mouse model for *Brca2*-deficient breast cancer (Extended Data Fig. 9a)[33]. A mammary tumour from KB2P mice was transplanted into syngeneic FVB mice and, when the tumour reached a size $>200\,\text{mm}^3$, mice were treated with PARPi (AZD2461) for 28 consecutive days (Extended Data Fig. 9b, c). The tumour was initially responsive to treatment but eventually grew, upon which treatment was repeated until PARPi resistance was achieved (Extended Data Fig. 9c). The stability of acquired resistance was confirmed by re-transplanting matched naive and resistant tumours and treating the animals with vehicle or AZD2461 (Extended Data Fig. 9d). PARPi-resistant tumours also showed cross-resistance to replication poisons topotecan and cisplatin (Fig. 4f, g).

Both naive and resistant *Brca2*-deficient tumours showed impaired irradiation-induced RAD51 foci formation (Extended Data Fig. 9e, f). We therefore assayed naive and resistant tumours *ex vivo* for RF stability. The mean length of the CldU and the IdU tracts were similar in all samples that were not treated with HU (Fig. 4h and Extended Data Fig. 9g). While naive tumour cells showed degradation of nascent tracts upon HU treatment, resistant tumour cells were protected (Fig. 4h). These data suggest that RF protection rather than restoration of HR may be the main mechanism for acquired resistance in this mammary tumour. However, in this case, acquired resistance was not simply due to loss of PTIP or MRE11 proteins (Extended Data Fig. 9h).

Discussion

Our study and the accompanying paper[30] provide the first examples of genetic alterations that bypass the essential requirement for DSB-induced HR, evidenced by the finding that reduction in PTIP or PARP1 (ARTD1) levels rescues the lethality of *Brca2*-null ESCs. We speculate that the reason *Brca2* nullizygosity is compatible with viability is because RAD51 is able to perform essential HR functions (such as SCE) by loading onto RFs independently of BRCA2 (Extended Data Fig. 4e), even if RAD51 loading onto processed DSBs is strictly dependent on BRCA2 (Fig. 1g and Fig. 2c, d). We also show that loss of PTIP, PARP1 and CHD4 confers resistance to a variety of DNA-damaging agents in *Brca*-deficient cells. Resistance to PARPi and cisplatin both in primary and in tumour cells grown *in vitro* or *in vivo* correlates with protection from RF degradation. While 53BP1 disruption rescues the viability of *Brca1*-deficient mice by restoration of HR[8,9], cells from these animals show residual levels of chromosomal aberration. The significant level of RF degradation observed in *Brca1*$^{-/-}$*53Bp1*$^{-/-}$ cells (Fig. 1b) may contribute to this genome instability.

Since RF degradation is mediated by MRE11, we propose that persistence of MRE11 at stalled forks is toxic and normally counteracted by BRCA1/2. One possibility is that MRE11 could initially be recruited to stalled forks to mediate RF restart[4], and that BRCA1/2 is necessary to subsequently disengage MRE11 from already-processed DNA termini. Consistently, we have found a significant increase in chromatin-bound MRE11 in *Brca2*-deficient cells treated with HU or cisplatin (Extended Data Fig. 10 a, b)[4]. In *Saccharomyces cerevisiae*, failure to remove MRE11 from single-stranded DNA can lead to hypersensitivity to a variety of clastogens[34,35]. We therefore propose that deficiencies in PTIP, CHD4 and PARP1 could confer drug resistance in *Brca*-deficient cells by limiting the access of MRE11 to single-strand DNA at stalled RFs.

In summary, we have shown that protection of nascent DNA from degradation provides a mechanism that can promote synthetic viability and drug resistance in *Brca*-deficient cells without restoring HR at DSBs.

Online Content Methods, along with any additional Extended Data display items and Source Data, are available in the online version of the paper; references unique to these sections appear only in the online paper.

Received 30 July 2015; accepted 15 April 2016.

1. Lord, C. J. & Ashworth, A. Mechanisms of resistance to therapies targeting BRCA-mutant cancers. *Nature Med.* **19,** 1381–1388 (2013).
2. Schlacher, K. *et al.* Double-strand break repair-independent role for BRCA2 in blocking stalled replication fork degradation by MRE11. *Cell* **145,** 529–542 (2011).
3. Schlacher, K., Wu, H. & Jasin, M. A distinct replication fork protection pathway connects Fanconi anemia tumor suppressors to RAD51-BRCA1/2. *Cancer Cell* **22,** 106–116 (2012).
4. Ying, S., Hamdy, F. C. & Helleday, T. Mre11-dependent degradation of stalled DNA replication forks is prevented by BRCA2 and PARP1. *Cancer Res.* **72,** 2814–2821 (2012).
5. Pathania, S. *et al.* BRCA1 haploinsufficiency for replication stress suppression in primary cells. *Nature Commun.* **5,** 5496 (2014).
6. Pathania, S. *et al.* BRCA1 is required for postreplication repair after UV-induced DNA damage. *Mol. Cell* **44,** 235–251 (2011).
7. Bunting, S. F. *et al.* BRCA1 functions independently of homologous recombination in DNA interstrand crosslink repair. *Mol. Cell* **46,** 125–135 (2012).
8. Bunting, S. F. *et al.* 53BP1 inhibits homologous recombination in Brca1-deficient cells by blocking resection of DNA breaks. *Cell* **141,** 243–254 (2010).
9. Bouwman, P. *et al.* 53BP1 loss rescues BRCA1 deficiency and is associated with triple-negative and BRCA-mutated breast cancers. *Nature Struct. Mol. Biol*. **17,** 688–695 (2010).
10. Callen, E. *et al.* 53BP1 mediates productive and mutagenic DNA repair through distinct phosphoprotein interactions. *Cell* **153,** 1266–1280 (2013).
11. Chapman, J. R. *et al.* RIF1 is essential for 53BP1-dependent nonhomologous end joining and suppression of DNA double-strand break resection. *Mol. Cell* **49,** 858–871 (2013).
12. Escribano-Díaz, C. *et al.* A cell cycle-dependent regulatory circuit composed of 53BP1-RIF1 and BRCA1-CtIP controls DNA repair pathway choice. *Mol. Cell* **49,** 872–883 (2013).
13. Feng, L., Fong, K. W., Wang, J., Wang, W. & Chen, J. RIF1 counteracts BRCA1-mediated end resection during DNA repair. *J. Biol. Chem.* **288,** 11135–11143 (2013).
14. Di Virgilio, M. *et al.* Rif1 prevents resection of DNA breaks and promotes immunoglobulin class switching. *Science* **339,** 711–715 (2013).
15. Zimmermann, M., Lottersberger, F., Buonomo, S. B., Sfeir, A. & de Lange, T. 53BP1 regulates DSB repair using Rif1 to control 5′ end resection. *Science* **339,** 700–704 (2013).
16. Hashimoto, Y., Ray Chaudhuri, A., Lopes, M. & Costanzo, V. Rad51 protects nascent DNA from Mre11-dependent degradation and promotes continuous DNA synthesis. *Nature Struct. Mol. Biol*. **17,** 1305–1311 (2010).
17. Kuznetsov, S. G., Liu, P. & Sharan, S. K. Mouse embryonic stem cell-based functional assay to evaluate mutations in BRCA2. *Nature Med.* **14,** 875–881 (2008).
18. Willis, N. A. *et al.* BRCA1 controls homologous recombination at Tus/Ter-stalled mammalian replication forks. *Nature* **510,** 556–559 (2014).
19. Sonoda, E. *et al.* Sister chromatid exchanges are mediated by homologous recombination in vertebrate cells. *Mol. Cell. Biol.* **19,** 5166–5169 (1999).
20. Toledo, L. I. *et al.* A cell-based screen identifies ATR inhibitors with synthetic lethal properties for cancer-associated mutations. *Nature Struct. Mol. Biol*. **18,** 721–727 (2011).
21. Mirzoeva, O. K. & Petrini, J. H. DNA replication-dependent nuclear dynamics of the Mre11 complex. *Mol. Cancer Res.* **1,** 207–218 (2003).
22. Dungrawala, H. *et al.* The replication checkpoint prevents two types of fork collapse without regulating replisome stability. *Mol. Cell* **59,** 998–1010 (2015).
23. Cho, Y. W. *et al.* PTIP associates with MLL3- and MLL4-containing histone H3 lysine 4 methyltransferase complex. *J. Biol. Chem.* **282,** 20395–20406 (2007).
24. Patel, S. R., Kim, D., Levitan, I. & Dressler, G. R. The BRCT-domain containing protein PTIP links PAX2 to a histone H3, lysine 4 methyltransferase complex. *Dev. Cell* **13,** 580–592 (2007).
25. Gong, Z., Cho, Y. W., Kim, J. E., Ge, K. & Chen, J. Accumulation of Pax2 transactivation domain interaction protein (PTIP) at sites of DNA breaks via RNF8-dependent pathway is required for cell survival after DNA damage. *J. Biol. Chem.* **284,** 7284–7293 (2009).

26. Starnes, L. M. *et al.* A PTIP-PA1 subcomplex promotes transcription for IgH class-switching independently from the associated MLL3/MLL4 methyltransferase complex. *Genes Dev* **30,** 149–163 (2016).
27. Buonomo, S. B., Wu, Y., Ferguson, D. & de Lange, T. Mammalian Rif1 contributes to replication stress survival and homology-directed repair. *J. Cell Biol.* **187,** 385–398 (2009).
28. Guillemette, S. *et al.* Resistance to therapy in BRCA2 mutant cells due to loss of the nucleosome remodeling factor CHD4. *Genes Dev.* **29,** 489–494 (2015).
29. Bryant, H. E. *et al.* PARP is activated at stalled forks to mediate Mre11-dependent replication restart and recombination. *EMBO J.* **28,** 2601–2615 (2009).
30. Ding, X. *et al.* Synthetic viability by BRCA2 and PARP1/ARTD1 deficiencies. *Nature Commun*. http://dx.doi.org/10.1038/ncomms12425 (2016).
31. Bryant, H. E. *et al.* Specific killing of BRCA2-deficient tumours with inhibitors of poly(ADP-ribose) polymerase. *Nature* **434,** 913–917 (2005).
32. Farmer, H. *et al.* Targeting the DNA repair defect in BRCA mutant cells as a therapeutic strategy. *Nature* **434,** 917–921 (2005).
33. Jonkers, J. *et al.* Synergistic tumor suppressor activity of BRCA2 and p53 in a conditional mouse model for breast cancer. *Nature Genet.* **29,** 418–425 (2001).
34. Chen, H. *et al.* Sae2 promotes DNA damage resistance by removing the Mre11-Rad50-Xrs2 complex from DNA and attenuating Rad53 signaling. *Proc. Natl Acad. Sci. USA* **112,** E1880–E1887 (2015).
35. Puddu, F. *et al.* Synthetic viability genomic screening defines Sae2 function in DNA repair. *EMBO J.* **34,** 1509–1522 (2015).
36. Moynahan, M. E., Pierce, A. J. & Jasin, M. BRCA2 is required for homology-directed repair of chromosomal breaks. *Mol. Cell* **7,** 263–272 (2001).

Supplementary Information is available in the online version of the paper.

Acknowledgements We thank A. Bhandoola for discussions; K. Wolcott for flow cytometry; R. Faryabi for help with statistical analysis; T. de Lange for *Rif1*$^{f/f}$ mice, J. Tainer for PFM39, R. Brosh for WRNi and J. Petrini for Mre11 antibodies. This work was supported by the Intramural Research Program of the National Institutes of Health (NIH), the National Cancer Institute and the Center for Cancer Research, and by a Department of Defense grant to A.N. (BCRP DOD Idea Expansion Award, grant 11557134), and the Netherlands Organization for Scientific Research, the Dutch Cancer Society and the Swiss National Science Foundation to S.V. A.R.C. was supported by a Prospective Researcher Award from Swiss National Science Foundation (PBZHP3_147302) and Human Frontier Science Program Long-Term Fellowship (LT000393/2013). S.C. was supported by NIH grant R01 CA176166-01A1; B.S. was supported by NIH grant R01CA085344; and J.A.D. was supported by a grant to the Center for Protein Research from the Novo Nordisk Foundation (NNF14CC0001).

Author Contributions A.R.C., E.C., S.S. and A.N. conceived and planned the study. A.R.C., E.C. and X.D. designed, performed experiments and analysed data on B cells, MEFS and ESCs. E.G. and A.A.D. generated and performed experiments on PARPi-resistant tumours. J.J. and S.R. supervised the studies on PARPi-resistant tumours. N.W., A.D. and S.J. helped with experimentation. J.E.L. and K.G. generated *Mll4*- and *Mll4*-SET-deficient mice. L.S. and J.D. generated PTIP deletion constructs. B.S. provided reagents for experiments. D.C. provided advice on performing iPOND experiments and supervised iPOND mass spectrometry. J.C., N.P. and S.C. provided shCHD4 PEO1 cells and performed immunofluorescence experiments. P.K. analysed TCGA databases. V.F. and O.F.C. performed high-throughput image analysis of MRE11. S.S. supervised the ESC studies. A.R.C., E.C. and A.N. wrote the manuscript and all authors reviewed it.

Author Information Source tumour measurement data are provided in Supplementary Information. Reprints and permissions information is available at www.nature.com/reprints. The authors declare no competing financial interests. Readers are welcome to comment on the online version of the paper. Correspondence and requests for materials should be addressed to A.N. (andre_nussenzweig@nih.gov).

METHODS

Mice, MEFs, and B cell cultures. The *53Bp1*$^{-/-}$ (ref. 37), *Brca1*$^{f(\Delta 11)/f(\Delta 11)}$ (NCI mouse repository), *Brca2*$^{f/f}$ (NCI mouse repository), *Rif1*$^{f/f}$ (ref. 27), *Ptip*$^{f/f}$ (ref. 24) and *Mll4*$^{f/f}$ (ref. 38) mice have been described. To generate *Mll4*-SET-flox/flox mice, exons 50–51 of the *Mll4*/*Kmt2d* gene were flanked by *loxP* sites. Cre-mediated deletion of the floxed exons 50–51 causes frame shift and generates a stop codon in exon 52. The resulting protein lacks the carboxy (C)-terminal 276 amino acids including the entire enzymatic SET domain. Resting splenic B cells were isolated from 8- to 12-week-old WT or mutant spleen with anti-CD43 microbeads (anti-Ly48; Miltenyi Biotech) and were cultured with LPS (25 μg/ml; Sigma), IL-4 (5 ng/ml; Sigma) and RP105 (0.5 μg/ml; BD) as described[10]. Stimulated B cells were additionally infected with CRE to ensure a high level of gene deletion in these cells. All mice were randomly distributed in experimental groups after genotyping. WT MEFs were immortalized by SV40 retroviral infection, and SV40 immortalized *Ptip*$^{f/f}$ (ref. 39) and *Mll3*$^{-/-}$*Mll4*$^{f/f}$ MEFs[38] were infected with a CRE retrovirus to delete *Ptip* and *Mll4* respectively. Coding sequences for mouse Ptip–GFP were cloned into the MIGR1 retroviral vector as previously described[10]. All cell lines used were tested for mycoplasma using a Mycoplasma Detection Kit (Invitrogen) and relevant cell lines were authenticated either by genotyping or western blot analysis. PARP inhibitor (KU58948) was obtained from AstraZeneca. Mirin was obtained from Sigma, PFM39 and WRN inhibitors were gifts from J. Tainer and R. Brosh respectively. DNA2 inhibitor has been described[40]. Cisplatin and HU were obtained from Sigma. For FISH analysis, metaphases were prepared and imaged as described[10]. Animal experiments were approved by the Animal Care and Use Committee of NCI-Bethesda and the Animal Ethical Committee of The Netherlands Cancer Institute.

Generation of CHD4-deficient PEO1 lines using RNAi. *BRCA2*-mutated ovarian cancer cell lines PEO1 were grown in DMEM with 10% FBS and 1% Glutmax. RNAi for CHD4 was performed as previously described[28].

ESC lines, shRNA knockdowns and rescue of BRCA2 viability. PL2F2 mouse ESCs were maintained in M15 media (Knockout DMEM with 15% fetal bovine serum, 0.00072% β-mercaptoethanol, 100 U/ml penicillin, 100 μg/ml streptomycin and 0.292 mg/ml L-glutamine) at 37 °C, 5% CO_2. ESCs were plated on a monolayer of mitotically inactive feeder cells as described previously[17]. BRCA2 conditional knockout ESCs were generated as previously described[17]. Two different shRNAs against *Ptip* mRNA were cloned into pSuperior vector (Oligoengine). shRNA sequences are listed below with the targeted sequences underlined: *mPtip shRNA-1* sense, 5′GATCCCC <u>GTGGCGCTCTCCTGCCAGT</u> TTCAAGAGA <u>ACTGGCAGGAGAGCGCCAC</u> TTTTTA 3′; *mPtip shRNA-1* antisense, 5′ AGCTTAAAAA <u>GTGGCGCTCTCCTGCCAGT</u> TCTCTTGAA <u>ACTGGCAGGAGAGCGCCAC</u> GGG 3′; *mPtip shRNA-2* sense, 5′GATCCCC <u>CCGTAGCAACACAGTCCTC</u> TTCAAGAGA <u>GAGGACTGTGTTGCTACGG</u> TTTTTA 3′; *mPtip shRNA-2* antisense, 5′ AGCTTAAAAA <u>CCGTAGCAACACAGTCCTC</u> TCTCTTGAA <u>GAGGACTGTGTTGCTACGG</u> GGG 3′.

shRNA vectors were linearized by ScaI and electroporated into ESCs using a Bio-Rad gene pulser. Cells were selected in G418 (0.18 mg/ml) 24 h after electroporation for 5 days. Individual colonies were picked and PTIP levels were determined by western blotting. The PGK-Cre plasmid was electroporated into *Ptip* shRNA knockdown cells (20 μg DNA for 1×10^7 cells). Thirty-six hours after electroporation, HAT (hypoxanthine–aminopterin–thymidine) selection was performed for 5 days, after which cells were switched to HT (hypoxanthine–thymidine) media for 2 days and then transferred to normal media. Colonies were picked when visible, genomic DNA was extracted and Southern blotting was performed as described previously[17]. For PCR genotyping, the following primers were used to amplify the *Brca2* cko allele and *Brca2*-KO allele: *Brca2*-KO forward, 5′ GCCACCTCTGCCTGATTCTA; *Brca2*-KO reverse, 5′ AAAGAACCAGCTGGGGCTCGAG; *Brca2*-flox forward, 5′ TGAAGTGGACCCTGTAACCC; *Brca2*-flox reverse, 5′ AGTTCTCTCCTTTCAGCCTTCT.

Gene targeting and the gene conversion HR assay. For gene targeting, ESCs were electroporated with 75 μg of linear targeting fragment from p59xDR–GFP, followed by selection for 5 days in 110 μg/ml hygromycin; then they were allowed to grow in normal ESC media[36]. Colonies were picked, and targeted clones were identified by Southern hybridization as described[36]. For the DSB-induced HR assay, ESCs were transiently electroporated with 20 μg of either pDR–GFP only or pDR–GFP plus I-SceI expressing vectors for 48 h. Gene conversion was read-out as the percentage of GFP-positive cells by flow cytometry analysis[41].

DNA fibre analysis. Asynchronous B cells, *BRCA2*-mutated PEO1 cells and *Brca2*-deficient K2BP tumours were labelled with 30 μM CldU, washed with PBS and exposed to 250 μM IdU. After exposure to IdU, the cells were washed again in warm PBS and treated or not with HU before collection. Cells were then lysed and DNA fibres stretched onto glass slides, as described[42]. The fibres were denatured with 2.5 M HCl for 1 h, washed with PBS and blocked with 2% BSA in phosphate buffered saline Tween-20 for 30 min. The newly replicated CldU and IdU tracts were revealed with anti-BrdU antibodies recognizing CldU and IdU respectively. Images were taken at 60 × magnification (Zeiss Axio Observer.Z1), and statistical analysis was performed using GraphPad Prism.

DSB detection by PFGE. DSB detection by PFGE was done as described[42]. Ethidium-bromide-stained gels were analysed using an UVP EC3 imaging system. Quantification was performed using ImageJ normalizing DSB signals to unsaturated DNA signals in the well. Relative DSB levels were obtained by comparing treatment results to the background DSB signals observed for untreated conditions.

Western blotting and immunofluorescence. Primary antibodies were used at the following dilutions: anti-tubulin (1:15,000, Sigma), anti-H3K4me3 (1:5,000, Millipore), anti-H3K4me1 (1:5,000, Millipore), anti-RAD51 (1:50, Santa Cruz), anti-PCNA (1:2,000, Santa Cruz), anti-total H3 (1:1,000 Millipore) and anti-Mre11 (1:10,000, gift from J. Petrini, MSKCC). MEFs were prepared for immunofluorescence by growth on 18 mm × 18 mm glass cover slips. Lymphocytes were dropped onto slides coated with CellTak (BD Biosciences). Cells were fixed with methanol and incubated with primary antibody as indicated.

iPOND and flow cytometry. iPOND was performed essentially as described[22]. One hundred and fifty million WT, *Ptip*$^{-/-}$ and *Mll3*$^{-/-}$*Mll4*$^{-/-}$ MEFs were labelled with 10 μM EdU (Life Technologies) and treated with HU as indicated. Two hundred million cells were use for iPOND experiments with ESCs. Cells were cross-linked with 1% formaldehyde for 10 min at room temperature, quenched with 0.125 M glycine and washed with PBS. For the conjugation of EdU with biotin azide, cells were permeabilized with 0.25% Triton X-100/ PBS, and incubated in click reaction buffer (10 mM sodium-L-ascorbate, 20 μM biotin azide (Life Technologies), and 2 mM CuSO4) for 2 h at room temperature. Cells were resuspended in lysis buffer (50 mM Tris-HCl, pH 8.0, and 1% SDS) supplemented with protease inhibitors (Roche), and chromatin was solubilized by sonication in a Bioruptor (Diagenode-Pico) at 4 °C for 24 min. After centrifugation, clarified supernatants were incubated for 1 h with streptavidin-MyOne C1 beads (Life Technologies). Beads were washed and captured proteins were eluted by boiling beads in 2 × NuPAGE LDS Sample Buffer (Life Technologies) containing 200 mM DTT for 40 min at 95 °C. Proteins were resolved by electrophoresis using NuPAGE Novex 4–12% Bis-Tris gels and detected by western blotting with the indicated antibodies. For flow cytometric analysis, asynchronous B cells were pulsed with 10 mM EdU for 20 min at 37 °C and stained using the Click-IT EdU Alexa Fluor 488 Flow Cytometry Assay Kit according to the manufacturer's specifications (ThermoFisher C-10425).

Generation of AZD2461-resistant KB2P tumours and *in situ* RAD51 assay. *Brca2*$^{-/-}$*;p53*$^{-/-}$ mammary tumours were generated in *K14-cre;Brca2*$^{f/f}$*; p53*$^{f/f}$ (KB2P) female mice and genotyped as described previously[33]. Orthotopic transplantations into WT FVB/N/OLA (F1) mice, tumour monitoring, and sampling were conducted as described[43]. Starting from 2 weeks after transplantation, tumour size was monitored at least three times a week. All treatments were started when tumours reached a size of approximately 200 mm^3. AZD2461 (100 mg/kg) was given orally for 28 consecutive days. If tumours did not shrink below 100% of the initial volume, treatment was continued for another 28 days. AZD2461 was diluted in 0.5% w/v hydroxypropyl methylcellulose in deionized water to a concentration of 10 mg/ml. For testing cross-resistance, mice were given a single treatment regimen of topotecan (2 mg/kg intraperitoneally, days 0–4 and 14–18) or cisplatin (Mayne Pharma, 6 mg/kg intravenously, day 0). Statistical analysis was performed using GraphPad Prism (log-rank Mantel–Cox test). The *in situ* RAD51 irradiation induced formation assay has been described[44].

Statistics. Statistics was performed by two-tailed *t*-test, Mann–Whitney test or by log-rank Mantel–Cox test unless otherwise specified. Statistical tests were justified appropriate for every figure. The data were normally distributed and the variance between groups being statistically compared was similar. No statistical methods or criteria were used to estimate sample size or to include/exclude samples. The investigators were not blinded to the group allocation during the experiments; however, the samples were coded before analysis unless otherwise specified.

37. Ward, I. M. *et al.* 53BP1 is required for class switch recombination. *J. Cell Biol.* **165,** 459–464 (2004).
38. Lee, J. E. *et al.* H3K4 mono- and di-methyltransferase MLL4 is required for enhancer activation during cell differentiation. *eLife* **2,** e01503 (2013).
39. Cho, Y. W. *et al.* Histone methylation regulator PTIP is required for PPARγ and C/EBPα expression and adipogenesis. *Cell Metab.* **10,** 27–39 (2009).
40. Liu, W. *et al.* A selective small molecule DNA2 inhibitor for sensitization of human cancer cells to chemotherapy. *EBioMedicine* **6,** 73–86 (2016).
41. Pierce, A. J., Johnson, R. D., Thompson, L. H. & Jasin, M. XRCC3 promotes homology-directed repair of DNA damage in mammalian cells. *Genes Dev.* **13,** 2633–2638 (1999).
42. Ray Chaudhuri, A. *et al.* Topoisomerase I poisoning results in PARP-mediated replication fork reversal. *Nature Struct. Mol. Biol*. **19,** 417–423 (2012).
43. Rottenberg, S. *et al.* Selective induction of chemotherapy resistance of mammary tumors in a conditional mouse model for hereditary breast cancer. *Proc. Natl Acad. Sci. USA* **104,** 12117–12122 (2007).
44. Xu, G. *et al.* REV7 counteracts DNA double-strand break resection and affects PARP inhibition. *Nature* **521,** 541–544 (2015).

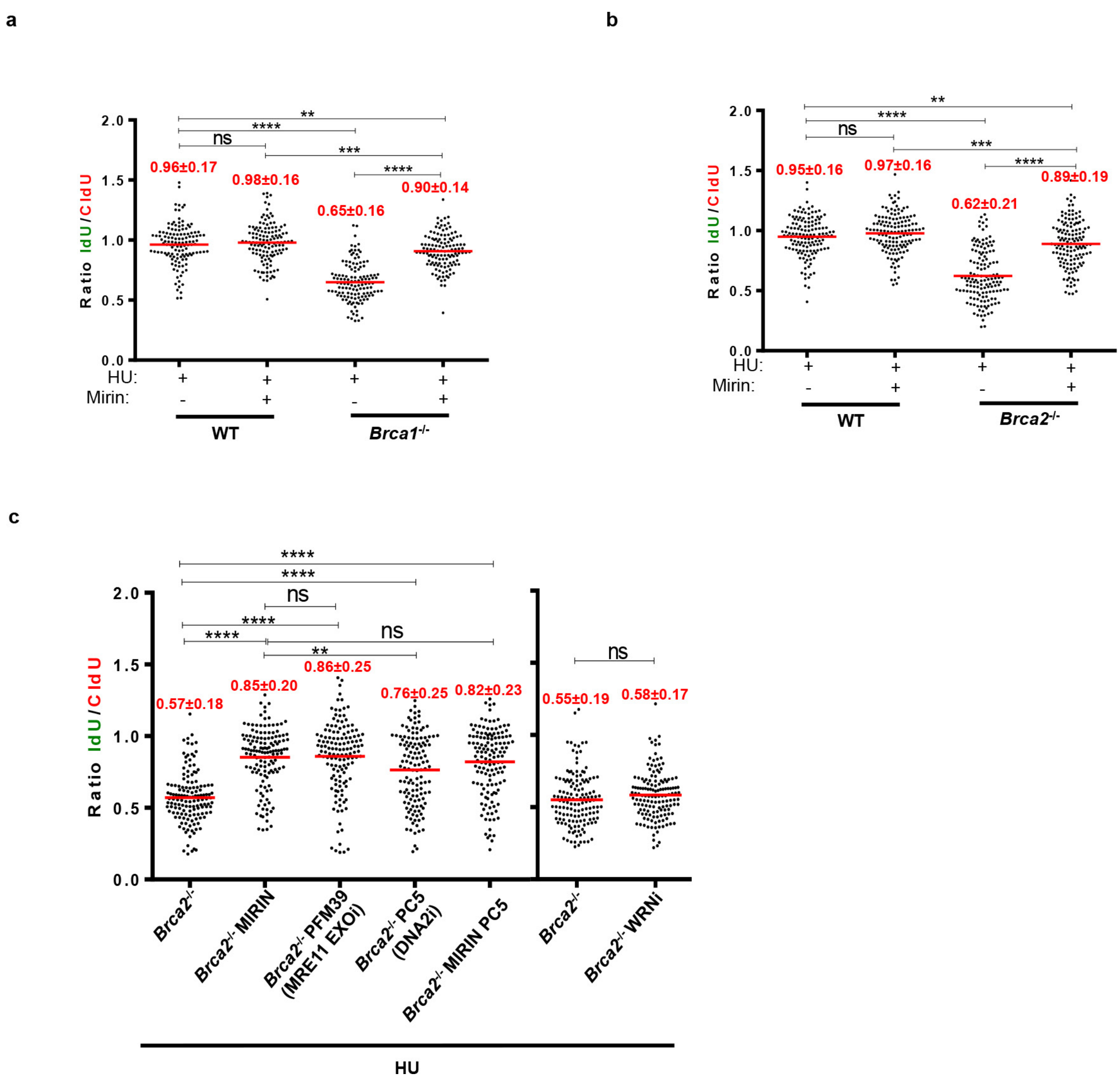

Extended Data Figure 1 | Fork degradation in *Brca*-deficient B lymphocytes is mediated by MRE11 exonuclease activity. a, b, Ratio of IdU versus CldU upon HU treatment in WT, *Brca1*$^{-/-}$ (**a**) and WT, *Brca2*$^{-/-}$ (**b**) B lymphocytes with or without mirin pre-treatment. Numbers in red indicate the mean ± s.d. for each sample (**$P \leq 0.05$, ***$P \leq 0.001$, ****$P \leq 0.0001$, Mann–Whitney test). One hundred and twenty-five replication forks were analysed for each genotype. **c**, Ratio of IdU versus CldU upon HU treatment in *Brca2*$^{-/-}$ B lymphocytes with or without mirin, PFM39 (MRE11 exonuclease inhibitor), PC5 (DNA2 inhibitor) or WRNi pre-treatment. Numbers in red indicate the mean ± s.d. for each sample (**$P \leq 0.05$, ****$P \leq 0.0001$, Mann–Whitney test). One hundred and twenty-five replication forks were analysed for each genotype.

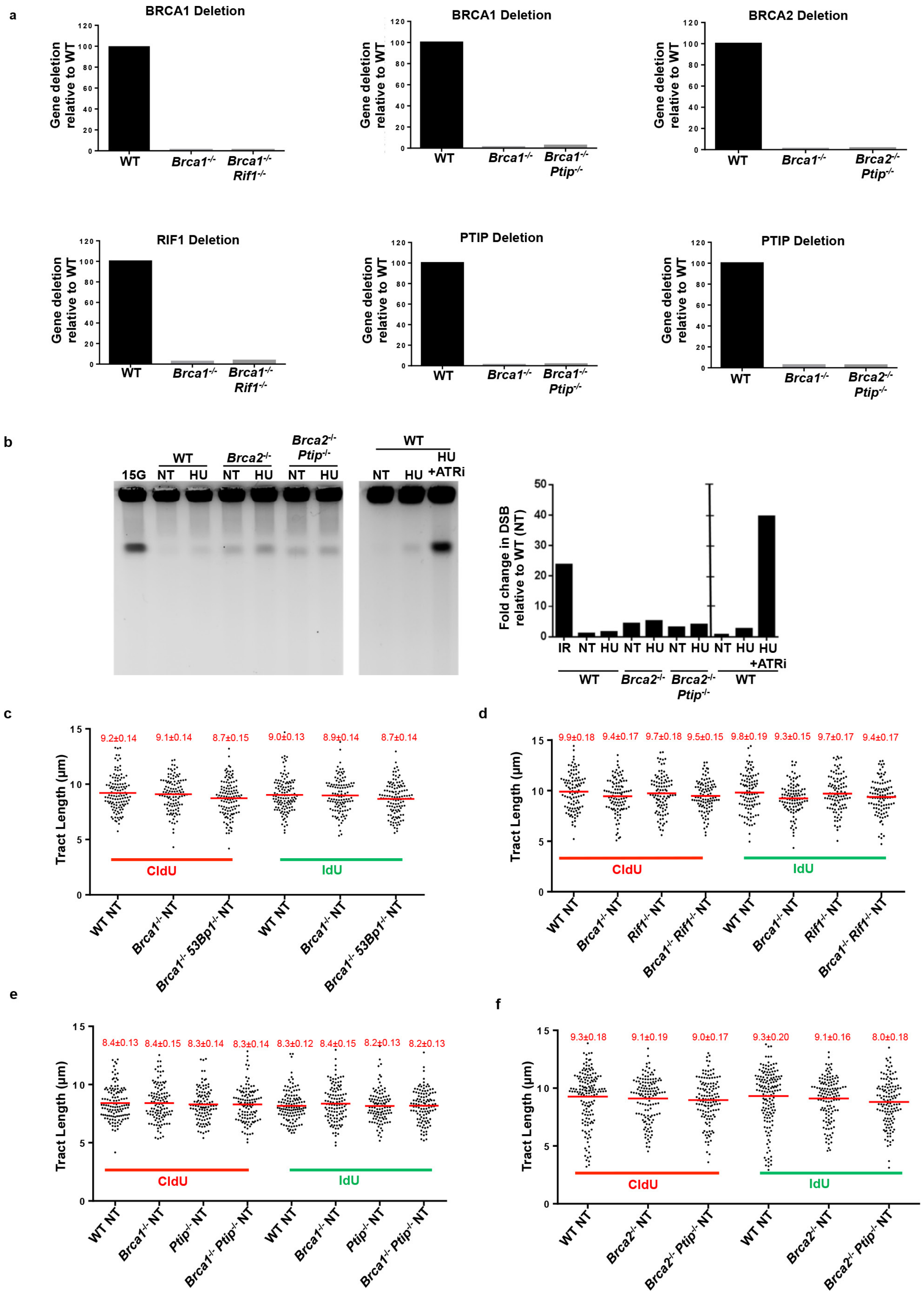

Extended Data Figure 2 | Replication fork progression rates and DSBs in B lymphocytes. **a**, Quantificative PCR analysis for *Brca1*, *Brca2*, *Ptip* and *Rif1* gene deletions in WT, $Brca1^{-/-}$, $Brca1^{-/-}$ $Rif1^{-/-}$, $Brca1^{-/-}Ptip^{-/-}$, $Brca2^{-/-}$ and $Brca2^{-/-}$ $Ptip^{-/-}$ primary B lymphocytes after infection with CRE. **b**, PFGE analysis for detection of DSBs in WT, $Brca2^{-/-}$ and $Brca2^{-/-}$ $Ptip^{-/-}$ B lymphocytes treated with or without 4 mM HU for 3 h. Positive control for DSBs includes treatment of 15 Gy irradiation and HU +ATRi treatment for 3 h. Quantification of fold change in DSBs across genotypes relative to non-treated WT is plotted on the right. **c–f**, Replication fork progression rates, measured by tract lengths in micrometres, of CldU (red) and IdU (green) in WT, $Brca1^{-/-}$, $Brca1^{-/-}$ $53Bp1^{-/-}$, $Rif1^{-/-}$, $Brca1^{-/-}$ $Rif1^{-/-}$, $Ptip^{-/-}$, $Brca1^{-/-}$ $Ptip^{-/-}$, $Brca2^{-/-}$ and $Brca2^{-/-}$ $Ptip^{-/-}$ primary B lymphocytes. Samples were not treated with HU. Numbers in red indicate the mean ± s.d. for each sample. One hundred and twenty-five replication forks were analysed for each genotype.

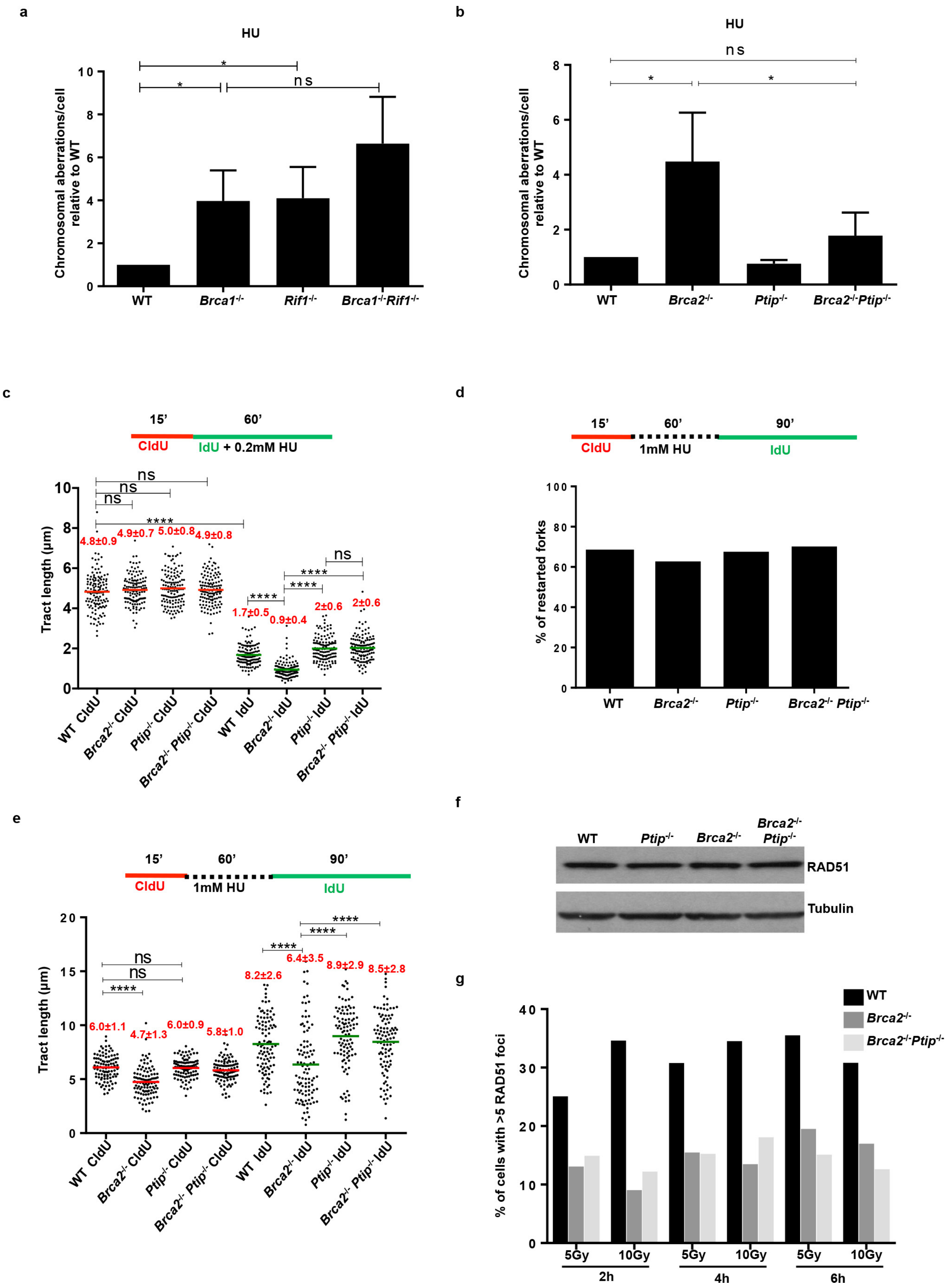

Extended Data Figure 3 | See next page for caption.

Extended Data Figure 3 | Loss of PTIP rescues fork progression and restart defects in *Brca2*-deficient B lymphocytes but does not affect RAD51 IRIF. a, Genomic instability measured in metaphase spreads from B lymphocytes derived from WT, *Brca1*$^{-/-}$, *Rif1*$^{-/-}$, *Brca1*$^{-/-}$*Rif1*$^{-/-}$ mice treated for 6 h with 10 mM HU (*$P \leq 0.05$, unpaired *t*-test). Fifty metaphases were analysed per condition. Experiments were repeated three times. **b**, Genomic instability measured in metaphase spreads from B lymphocytes derived from WT, *Brca2*$^{-/-}$, *Ptip*$^{-/-}$, *Brca2*$^{-/-}$*Ptip*$^{-/-}$ mice treated for 6 h with 10 mM HU (*$P \leq 0.05$, unpaired *t*-test). Fifty metaphases were analysed per condition. Experiments were repeated three times. **c**, Fork progression in B lymphocytes derived from WT, *Brca2*$^{-/-}$, *Ptip*$^{-/-}$, *Brca2*$^{-/-}$*Ptip*$^{-/-}$ mice treated for 1 h with 0.2 mM HU. The *y* axis represents the tract lengths in micrometres. Numbers in red indicate the mean ± s.d. for each sample (****$P \leq 0.0001$, Mann–Whitney test). One hundred and fifty replication forks were analysed for each genotype. **d**, Percentage of restarted replication forks in WT, *Brca2*$^{-/-}$, *Ptip*$^{-/-}$, *Brca2*$^{-/-}$*Ptip*$^{-/-}$ B cells treated for 1 h with 1 mM HU followed by 90 min recovery. Two hundred replication forks were analysed for each genotype. **e**, Tract lengths of restarted replication forks in WT, *Brca2*$^{-/-}$, *Ptip*$^{-/-}$, *Brca2*$^{-/-}$*Ptip*$^{-/-}$ B cells treated for 1 h with 1 mM HU followed by 90 min recovery. The *y* axis represents the tract lengths in micrometres. Numbers in red indicate the mean ± s.d. for each sample (NS, not significant, ****$P \leq 0.0001$, Mann–Whitney test). One hundred and fifty replication forks were analysed for each genotype. **f**, Western blot analysis for RAD51 levels in WT, *Ptip*$^{-/-}$, *Brca2*$^{-/-}$ and *Brca2*$^{-/-}$*Ptip*$^{-/-}$ B cell extracts. Tubulin was used as loading control. **g**, Quantification of RAD51 foci formation in WT, *Brca2*$^{-/-}$ and *Brca2*$^{-/-}$*Ptip*$^{-/-}$ B cells upon treatment with 5 and 10 Gy irradiation and recovery for 2, 4 and 6 h ($n = 150$ cells analysed).

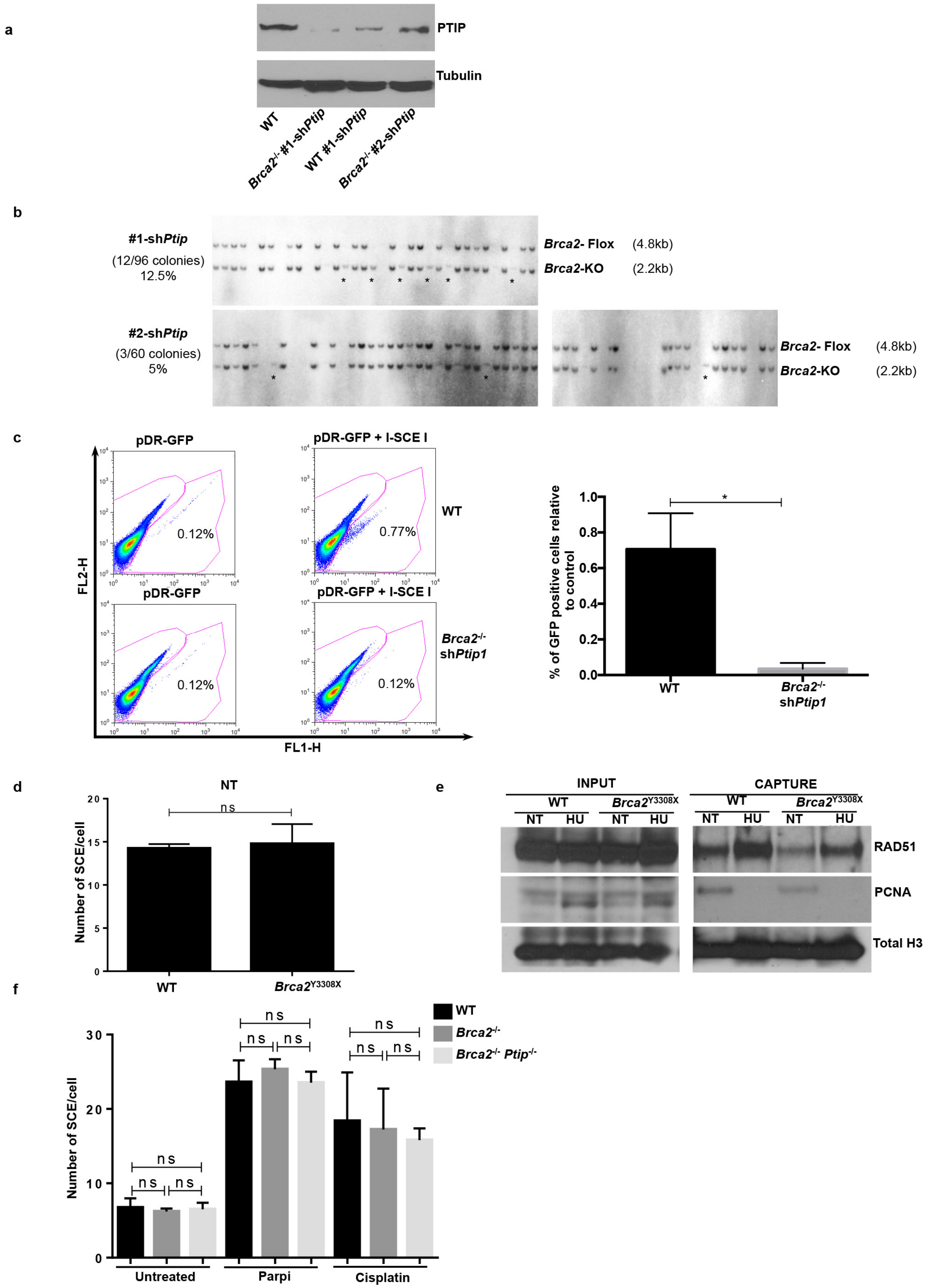

Extended Data Figure 4 | See next page for caption.

Extended Data Figure 4 | Depletion of PTIP rescues the lethality of *Brca2*-deficient ESCs. a, Western blot analysis for PTIP levels in WT and two different clones of *Brca2*$^{-/-}$ ESCs electroporated with sh*Ptip*. **b**, Southern blot analysis for determination of *Brca2* deletion in surviving clones electroporated with sh*Ptip*. Probes distinguishing the *Brca2*-flox allele (4.8 kb) (upper band) and *Brca2* KO allele (2.2 kb) (lower band) were used. *Surviving ESC clones with *Brca2* deletion and simultaneous downregulation of PTIP (12/96 *Brca2*-deleted colonies were found with sh*Ptip*1 and 3/60 colonies were found with sh*Ptip*2). Genotyping was confirmed by PCR (Fig. 2b). **c**, Top, representative FACS profiles of WT and *Brca2*$^{-/-}$/sh*Ptip* ESCs electroporated with either pDR–GFP plasmid only (control) or pDRGFP and I-SceI expressing vector for 48 h. Gene conversion of the pDR–GFP construct by HR is determined by the percentage of GFP-positive cells (FL1, green-detection filter; FL2, red-detection filter). Bottom, quantification of the percentage of GFP-positive cells in WT and *Brca2*$^{-/-}$/sh*Ptip* ESCs across three independent experiments. NS, not significant, *$P \leq 0.05$, unpaired *t*-test. **d**, Sister chromatid exchange (SCE) analysis in WT and *Brca2*^{Y3308X} hypomorphic ESCs. Twenty metaphases were analysed per condition; experiments were repeated three times. **e**, WT and *Brca2*^{Y3308X} hypomorphic ESCs were preincubated with mirin, EdU-labelled for 15 min and treated with 4 mM HU for 2 h. Proteins associated with replication forks were isolated by iPOND and detected by western blotting with the indicated antibodies. **f**, SCEs in WT, *Brca2*$^{-/-}$ and *Brca2*$^{-/-}$ *Ptip*$^{-/-}$ B cells either untreated or treated overnight with 1 μM PARPi or with 0.5 μM cisplatin (NS, not significant, *$P \leq 0.05$, **$P \leq 0.001$, unpaired *t*-test). Twenty metaphases were analysed per condition; experiments were repeated three times.

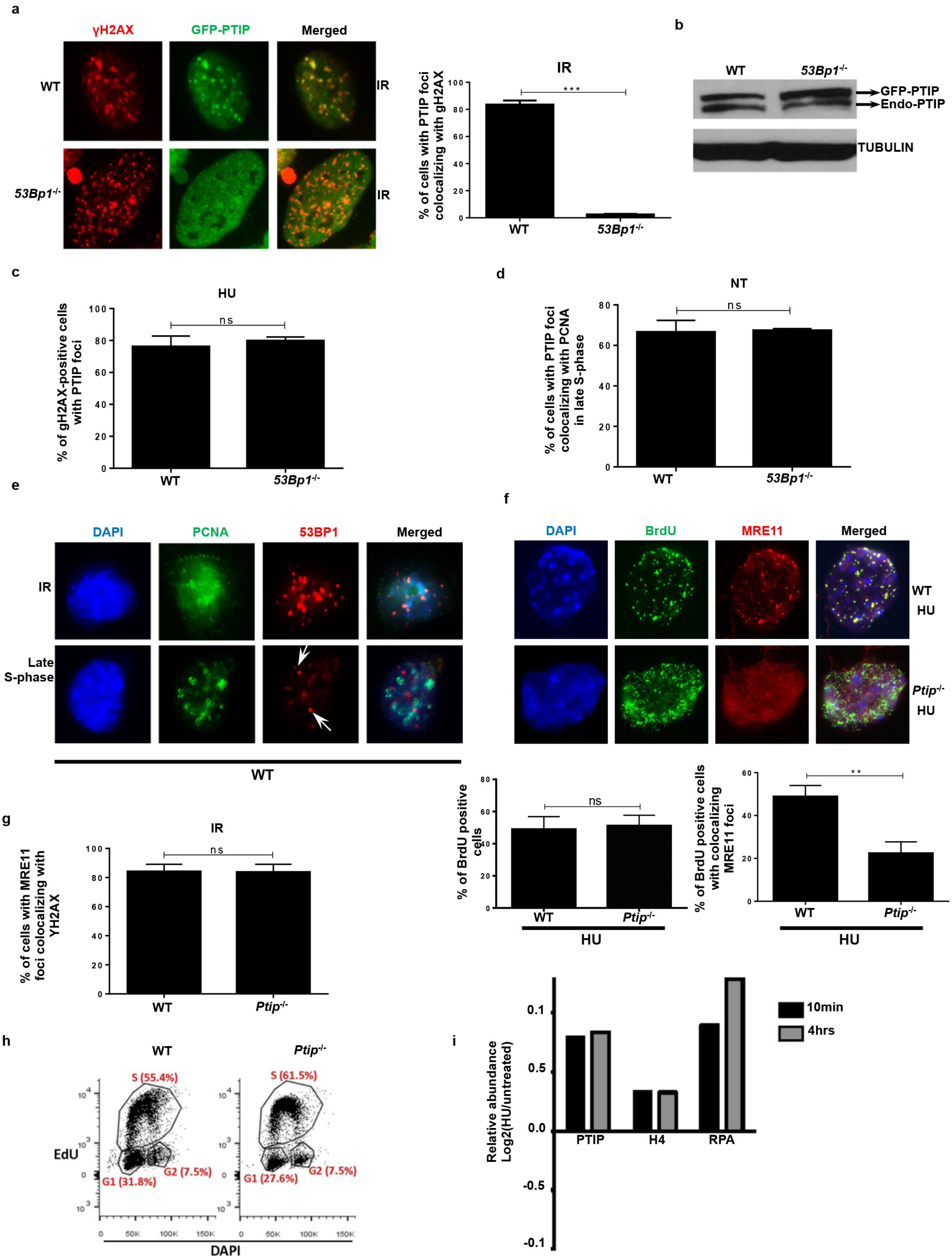

Extended Data Figure 5 | See next page for caption.

Extended Data Figure 5 | PTIP localizes to sites to DNA replication independently of DSBs. **a**, WT and *53Bp1*$^{-/-}$ MEFs were retrovirally infected with a GFP-tagged PTIP construct. Cells were then irradiated with 10 Gy and allowed to recover. Co-localization of γ-H2AX (red) and PTIP (green) was assessed. Adjoining graph quantifies the percentage of cells with γ-H2AX foci co-localizing with PTIP upon irradiation ($n = 150$ cells analysed). Experiments were repeated three times. **b**, Western Blot analysis for endogenous and overexpressed PTIP levels in WT and *53Bp1*$^{-/-}$ MEFs retrovirally infected with a GFP-tagged PTIP construct (GFP–PTIP). **c**, Quantification of the percentage of pan-nuclear γ-H2AX-positive cells with PTIP foci in WT and *53Bp1*$^{-/-}$ MEFs upon treatment with HU (related to Fig. 3a) ($n = 150$ cells analysed). Experiments were repeated three times. **d**, Quantification of the percentage of cells with PTIP foci co-localizing with PCNA in WT and *53Bp1*$^{-/-}$ MEFs in late S phase (related to Fig. 3b) ($n = 150$ cells analysed). Experiments were repeated three times. **e**, Representative immunofluorescence images of PCNA and 53BP1 co-staining in irradiated WT cells (10 Gy) or in late S-phase sites. White arrows indicate that the few 53BP1 foci observed in late S-phase cells do not co-localize with PCNA. ($n = 50$ cells analysed). Experiments were repeated three times. **f**, Representative immunofluorescence images of WT and *Ptip*$^{-/-}$ MEFs treated with 4 mM HU for 2 h and analysed for ssDNA (BrdU) and MRE11 co-localization. Bottom panels shows the quantification of BrdU-positive cells (left) and the percentage of MRE11 co-localization in BrdU-positive cells (right) upon HU treatment in WT and *Ptip*$^{-/-}$ MEFs. ($n = 150$ cells analysed). Experiments were repeated three times. **g**, Quantification of the percentage of cells with MRE11 foci co-localizing with γ-H2AX upon irradiation treatment (10 Gy) in WT and *Ptip*$^{-/-}$ MEFs (related to Fig. 3e) ($n = 150$ cells analysed). Experiments were repeated three times. **h**, Cell cycle profiles in WT and *Ptip*$^{-/-}$ MEFs as measured by the incorporation of EdU (*y* axis) vs. DAPI (*x* axis). **i**, iPOND coupled to SILAC Mass-Spectrometry analysis for PTIP, H4 and RPA enrichment at stalled forks in 293T cells upon 3 mM HU treatment for 10 min and 4 h (ref. 22). The *y* axes represent the relative abundance of the indicated proteins on a $\log_2$ scale.

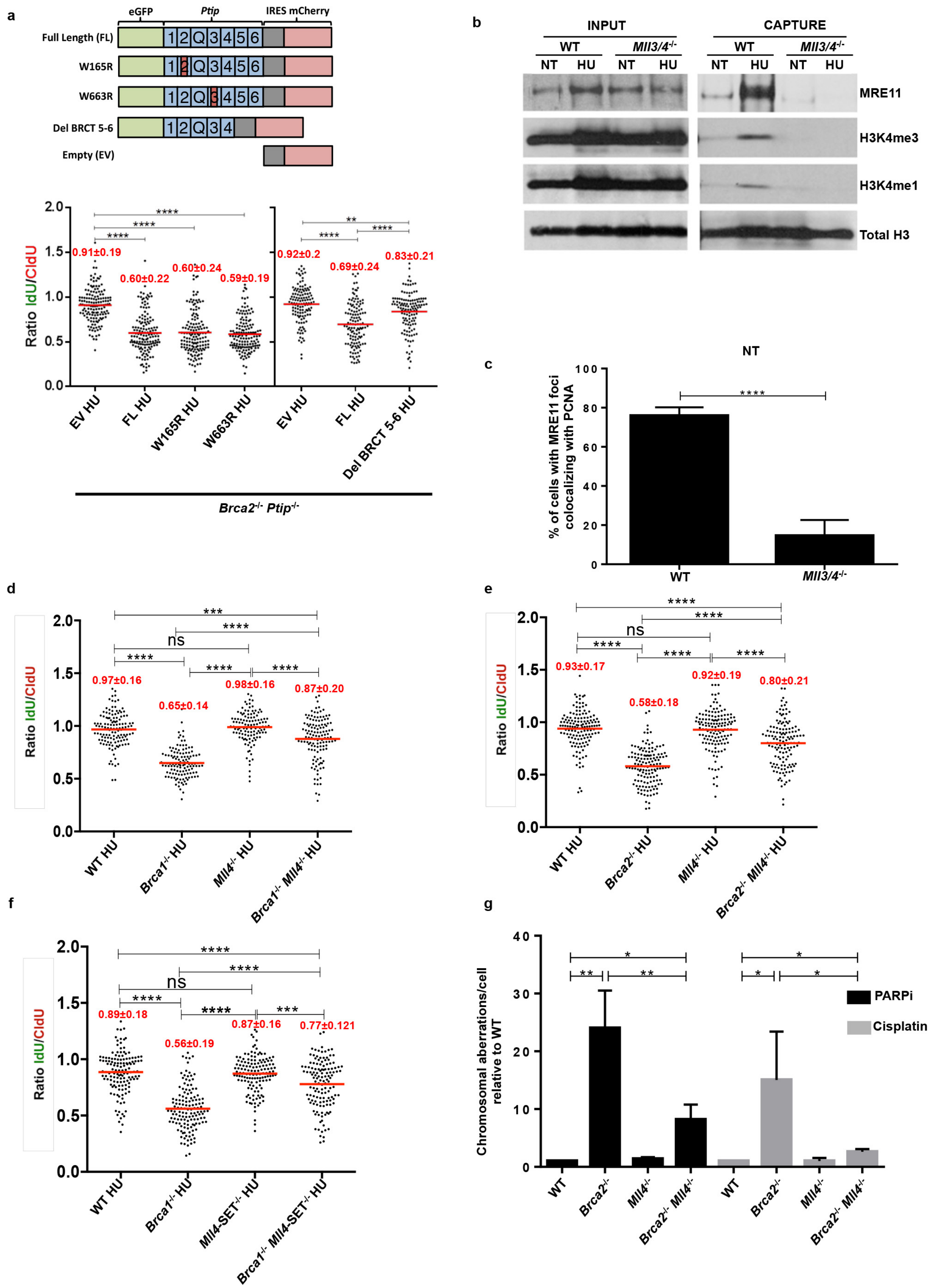

Extended Data Figure 6 | See next page for caption.

Extended Data Figure 6 | MLL3/4 promotes replication fork degradation in *Brca2*–deficient cells. a, Top, schematic of the retroviral PTIP mutant constructs used to identify the domain of PTIP involved in driving replication fork degradation. Different BRCT domains in PTIP are numbered and Q represents the glutamine rich region between the second and the third BRCT domains. Bottom, ratio of IdU versus CldU upon HU treatment of *Brca2*$^{-/-}$ *Ptip*$^{-/-}$ B lymphocytes retrovirally infected with either EV, FL, W165R, W663R and Del BRCT 5-6 PTIP-mutant constructs and sorted for GFP or mCherry expression. Numbers in red indicate the mean ± s.d. for each sample (**$P \leq 0.01$, ****$P \leq 0.0001$, Mann–Whitney test). One hundred and twenty-five replication forks were analysed for each condition. **b**, WT and *Mll3/4*$^{-/-}$ MEFs were EdU-labelled for 15 min and treated with 4 mM HU for 4 h. Proteins associated with replication forks were isolated by iPOND and detected by western blotting with the indicated antibodies. **c**, Quantification of the percentage of cells with MRE11 foci co-localizing with PCNA in late S phase in WT and *MLL3/4*$^{-/-}$ MEFs ($n = 150$ cells analysed). Experiments were repeated three times. **d–f**, Ratio of IdU versus CldU upon HU treatment in WT, *Brca1*$^{-/-}$, *Brca2*$^{-/-}$ *Mll4*$^{-/-}$, *Mll4*-SET$^{-/-}$, *Brca1*$^{-/-}$*Mll4*$^{-/-}$, *Brca2*$^{-/-}$*Mll4*$^{-/-}$ and *Brca1*$^{-/-}$*Mll4*-SET$^{-/-}$ B cells. Numbers in red indicate the mean ± s.d. for each sample (NS, not significant, ****$P \leq 0.0001$, Mann–Whitney test). At least 125 replication forks were analysed for each genotype. **g**, Genomic instability measured in metaphase spreads from splenic B cells derived from WT, *Brca2*$^{-/-}$, *Mll4*$^{-/-}$, *Brca2*$^{-/-}$*Mll4*$^{-/-}$ B cells treated overnight with 1 μM PARPi or with 0.5 μM cisplatin (**$P \leq 0.01$, ***$P \leq 0.001$, unpaired *t*-test). Fifty metaphases were analysed per condition. Experiments were repeated three times.

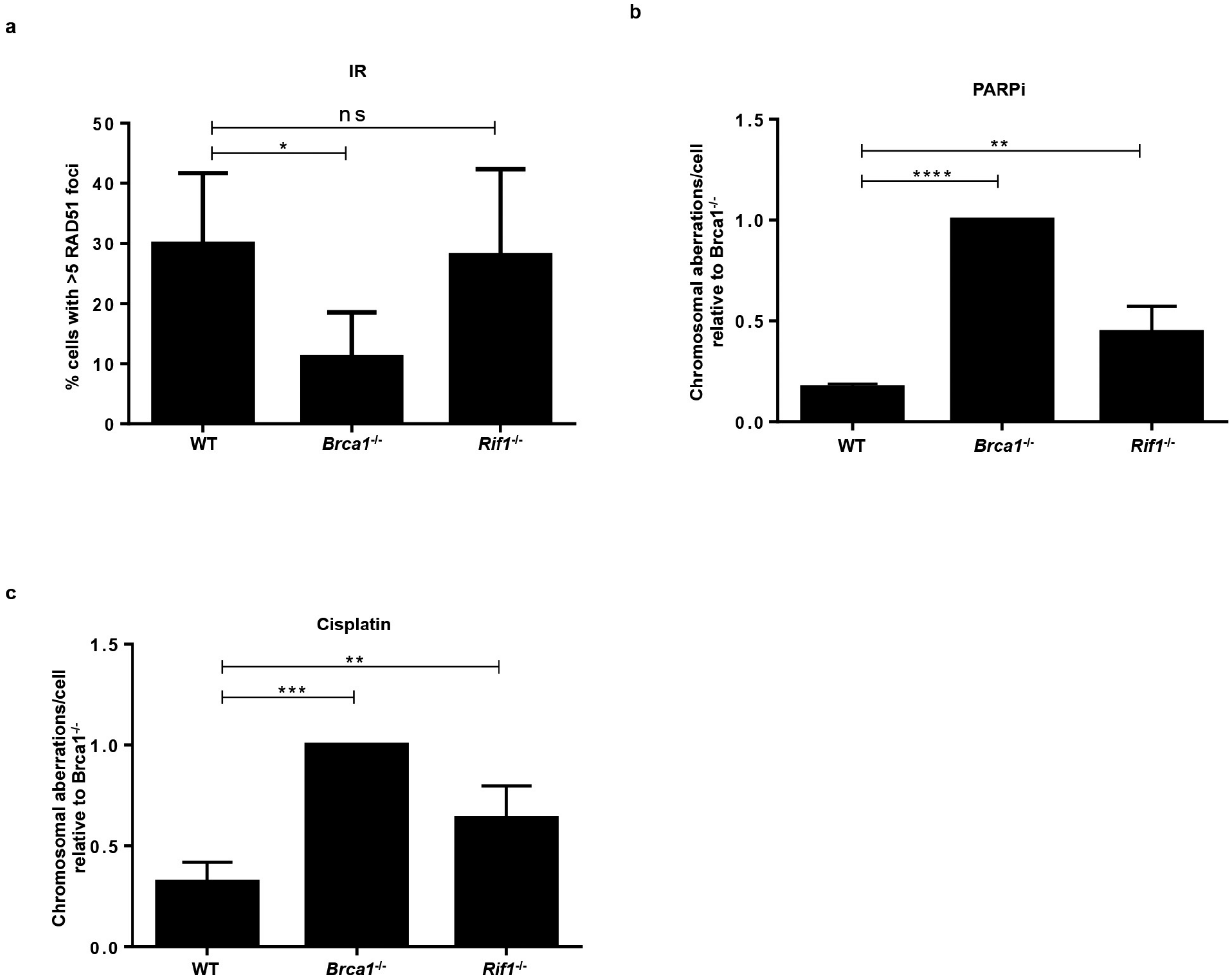

Extended Data Figure 7 | Loss of RIF1 results in chromosomal instability. a, Quantification of RAD51 foci formation in WT, *Brca1*$^{-/-}$ and *Rif1*$^{-/-}$ B cells. Cells were treated with 10 Gy and harvested 4 h after irradiation (NS, not significant, *$P \leq 0.05$). At least 100 cells were analysed per condition; experiments were repeated three times. **b**, **c**, Genomic instability measured in metaphase spreads from splenic B cells derived from WT, *Brca1*$^{-/-}$ and *Rif1*$^{-/-}$ mice treated overnight with 1 μM PARPi (**b**) or with 0.5 μM cisplatin (**c**) (NS, not significant, **$P \leq 0.01$, ***$P \leq 0.001$, ****$P \leq 0.0001$, unpaired *t*-test). Fifty metaphases were analysed per condition; experiments were repeated three times.

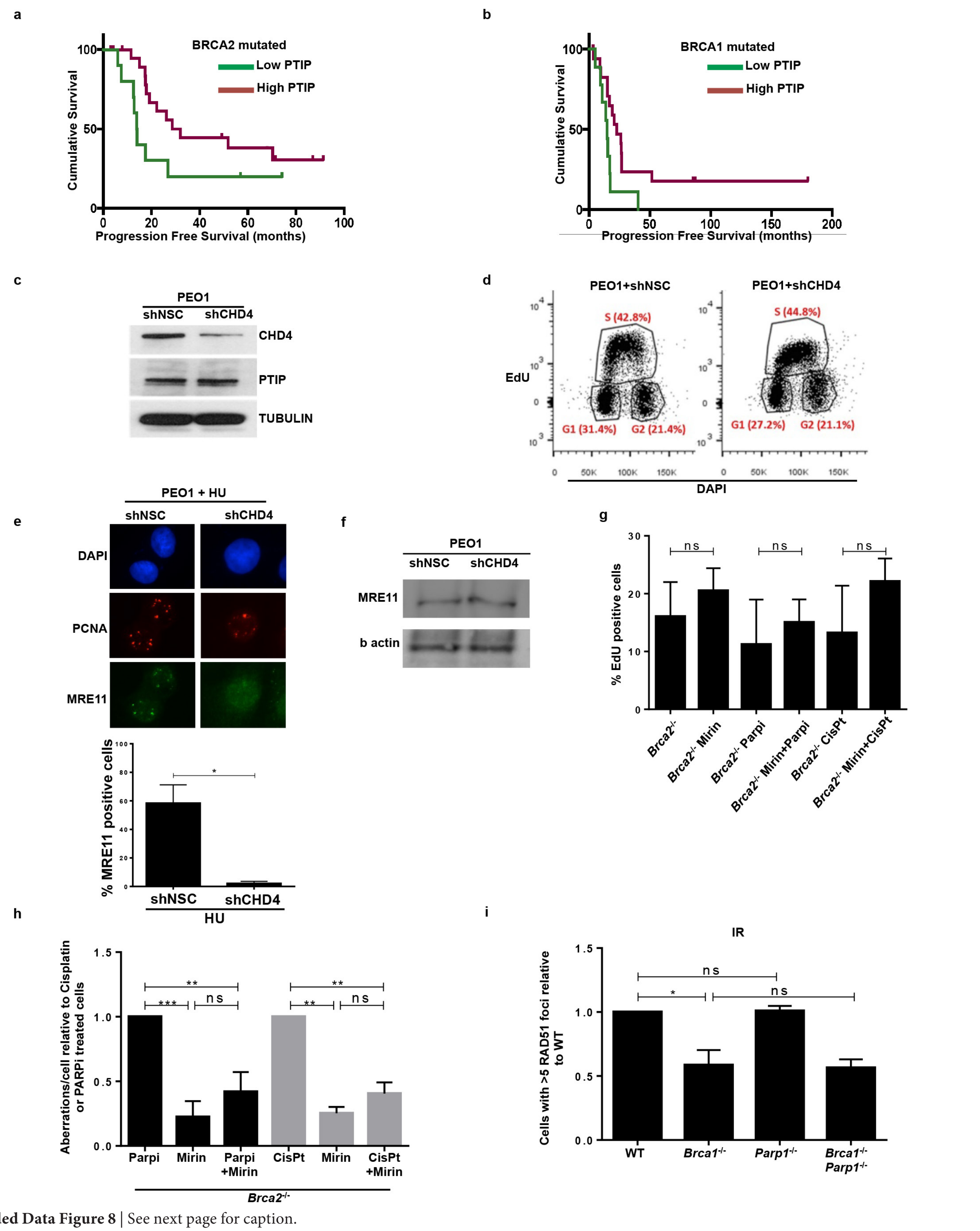

Extended Data Figure 8 | See next page for caption.

Extended Data Figure 8 | Multiple mutations can cause resistance to DNA-damaging agents in *Brca*-deficient cells. a, **b**, Difference in progression-free survival (PFS) of *BRCA2*- and *BRCA1*-mutated ovarian serous adenocarcinoma patients with standard platinum-based regimens. Data were obtained from the TCGA project. Patients were separated into PTIP low- or high-expression on the basis of the 33rd percentile of PTIP expression *z*-scores. The difference between the PFS of PTIP-low versus PTIP-high was assessed by univariate log-rank P value ($P < 0.072$ and $P < 0.032$ in **a** and **b**, respectively). Analysis included 38 tumours with *BRCA1* mutations and 34 tumours with *BRCA2* mutations out of 316 high-grade serous ovarian cancers that underwent whole-exome sequencing. PFS curves for PTIP-low and PTIP-high expressing tumours were generated by the Kaplan–Meier method. All reported P values are two-sided. **c**, Western blot analysis for CHD4 and PTIP levels in PEO1 cells infected with shNSC and shCHD4. Tubulin was used as loading control. **d**, Cell cycle profiles in PEO1 cells infected with shNSC and shCHD4 as measured by the incorporation of EdU (*y* axis) versus DAPI (*x* axis). **e**, Immunostaining for MRE11 and PCNA in PEO1 cells infected with shNSC and shCHD4 upon treatment with 4 mM HU. Bottom, quantification for MRE11 recruitment upon HU treatment. At least 100 cells were analysed per condition; experiments were repeated three times. **f**, Western blot analysis for CHD4 and MRE11 levels in PEO1 cells infected with shNSC and shCHD4. Actin was used as loading control. **g**, Percentage of EdU-positive cells was analysed 20 h after *Brca2*$^{-/-}$ B cells were treated with mirin alone, mirin+PARPi or mirin+cisplatin (NS, not significant). EdU was pulsed for 20 min before FACS analysis. Experiments were repeated three times. **h**, Genomic instability measured in metaphase spreads from B cells derived from *Brca2*$^{-/-}$ mice pretreated with 25 μM mirin for 2 h followed by overnight treatment with 1 μM PARPi or 0.5 μM cisplatin (NS, not significant, *$P \leq 0.05$, **$P \leq 0.001$, unpaired *t*-test). Fifty metaphases were analysed per condition. Experiments were repeated three times. **i**, Quantification of RAD51 foci formation in WT, *Brca1*$^{-/-}$, *Parp1*$^{-/-}$ and *Brca1*$^{-/-}$*Parp1*$^{-/-}$ B cells treated with 10 Gy irradiation and harvested 4 h after treatment. At least 100 cells were analysed per condition; experiments were repeated three times.

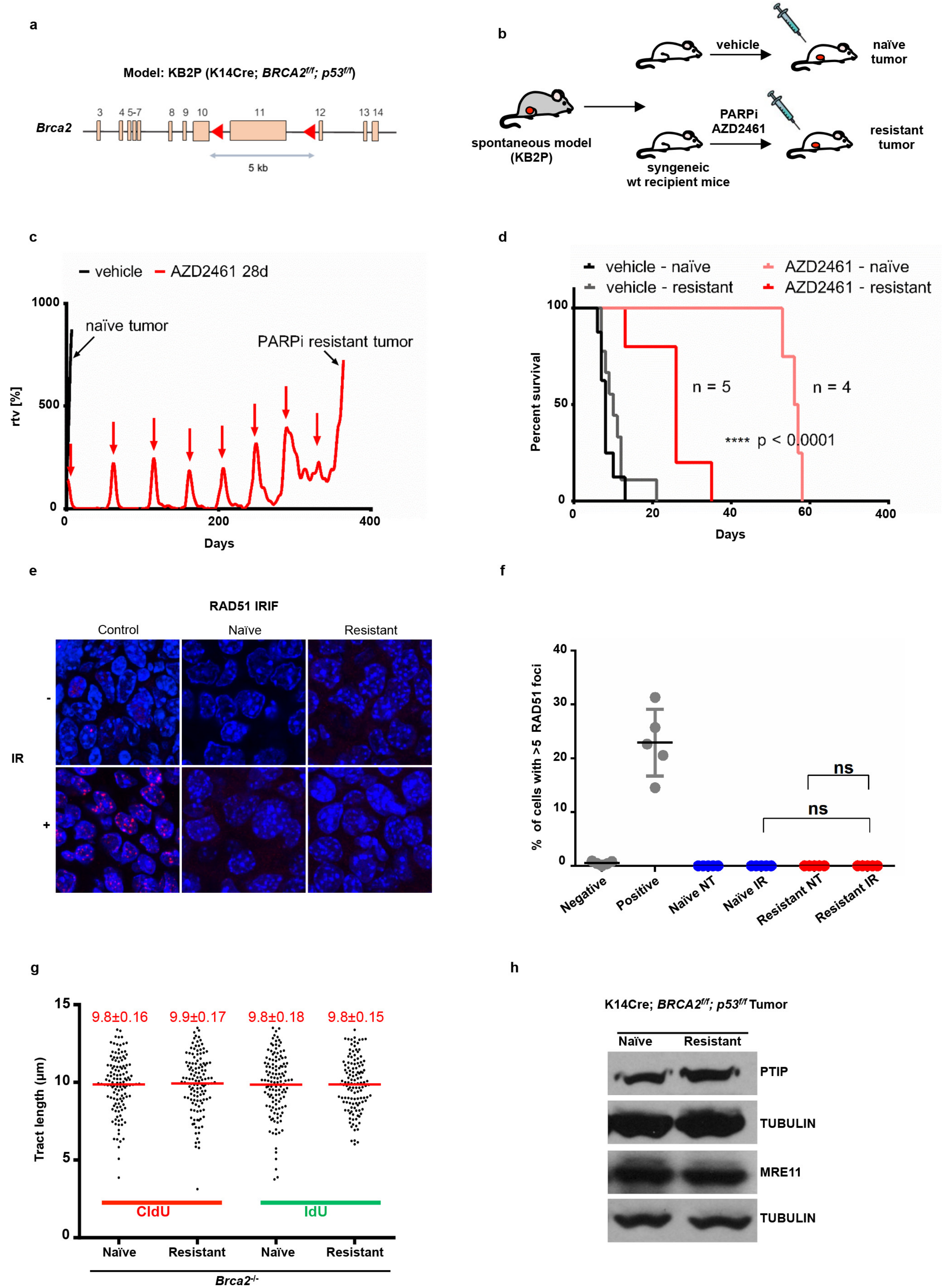

Extended Data Figure 9 | See next page for caption.

Extended Data Figure 9 | *Brca2*-deficient tumours acquire PARPi resistance without restoration of RAD51 foci formation. a, Schematic depicting the conditional *BRCA2* allele of the KB2P (*K14CRE*;*Brca2*$^{f/f}$;*p53*$^{f/f}$) spontaneous tumour model. **b**, Outline of the PARPi intervention study. A spontaneous BRCA2-/p53-deficient tumour was generated and re-transplated into syngeneic WT mice. When the tumours reached 200 mm^3, they were treated either with vehicle or PARPi AZD2461. **c**, PARPi response curve of the KB2P tumour (relative tumour volume (rtv) versus days). The treatment for 28 consecutive days was started when the tumour reached 200 mm^3 (rtv = 100%). In response to the treatment, the tumour shrank but eventually grew back. When it reached 100% relative tumour volume, the treatment was repeated (as indicated with red arrows) for another 28 days. This regime was continued until the tumour became resistant to PARPi (black arrow). **d**, The stability of acquired resistance of the KB2P tumour was confirmed by re-transplanting matched naive and resistant tumours and treating animals either with vehicle or AZD2461 (only one 28-day cycle). Kaplan–Meier survival curve indicates that resistant tumours did not respond to the AZD2461 treatment, while naive tumours exhibited high sensitivity, indicative of a stable genetic mechanism of resistance. **e**, **f**, Irradiation-induced RAD51 foci were detected by immunofluorescence in the KB2P donor: RAD51 foci formation was undetectable in naive and resistant tumours, suggesting that HR restoration is not an underlying mechanism of PARPi resistance. Spontaneous tumours from *K14 Cre; p53*$^{f/f}$ mice treated with irradiation were used as positive control for RAD51 foci. Unirradiated *K14 Cre; p53*$^{f/f}$ cells were used as a negative control. **g**, Replication fork progression rates measured by tract lengths in micrometres of CldU (red) and IdU (green) in PARPi-naive or PARPi-resistant tumours. Numbers in red indicate the mean ± s.d. for each sample. One hundred and twenty-five replication forks were analysed for each condition. **h**, Western blot analysis for PTIP and MRE11 levels in PARPi-naive or PARPi-resistant tumours. Tubulin was used as loading control.

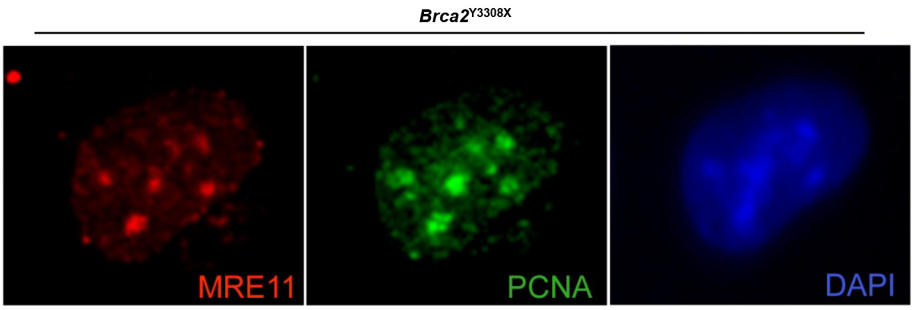

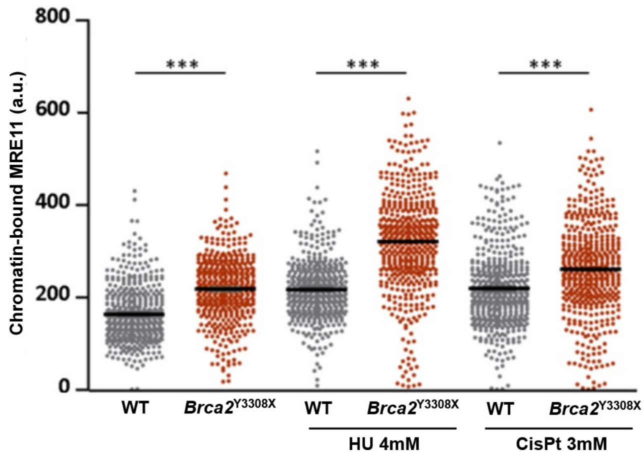

Extended Data Figure 10 | *Brca2*-deficient ESCs have higher levels of chromatin-bound MRE11. a, Representative image of a *Brca2* hypomorph mouse ESC (denoted *Brca2*^{Y3308X}) showing MRE11 foci (red) in S phase (identified by PCNA foci (green)). DNA was stained with DAPI (blue). **b**, High-throughput microscopy analysis quantifying the overall levels of chromatin-bound MRE11 per individual nucleus in WT and *Brca2*^{Y3308X} cells treated as indicated (a.u., arbitrary units).

LETTER

doi:10.1038/nature18007

Relativistic reverberation in the accretion flow of a tidal disruption event

Erin Kara[1,2,3], Jon M. Miller[4], Chris Reynolds[1,3] & Lixin Dai[3,5]

Our current understanding of the curved space-time around supermassive black holes is based on actively accreting black holes, which make up only ten per cent or less of the overall population. X-ray observations of that small fraction reveal strong gravitational redshifts that indicate that many of these black holes are rapidly rotating[1]; however, selection biases suggest that these results are not necessarily reflective of the majority of black holes in the Universe[2]. Tidal disruption events, where a star orbiting an otherwise dormant black hole gets tidally shredded and accreted onto the black hole[3], can provide a short, unbiased glimpse at the space-time around the other ninety per cent of black holes. Observations of tidal disruptions have hitherto revealed the formation of an accretion disk and the onset of an accretion-powered jet[4–8], but have failed to reveal emission from the inner accretion flow, which enables the measurement of black hole spin. Here we report observations of reverberation[9–12] arising from gravitationally redshifted iron Kα photons reflected off the inner accretion flow in the tidal disruption event Swift J1644+57. From the reverberation timescale, we estimate the mass of the black hole to be a few million solar masses, suggesting an accretion rate of 100 times the Eddington limit or more[13]. The detection of reverberation from the relativistic depths of this rare super-Eddington event demonstrates that the X-rays do not arise from the relativistically moving regions of a jet, as previously thought[5,14].

Swift J1644+57 was detected by the Swift Burst Alert Telescope on 28 March 2011 as it reached an isotropic X-ray luminosity greater than 10^{48} erg s^{-1}. Follow-up radio, optical and infrared observations located the position of the source at the centre of a compact, non-interacting, star-forming galaxy (redshift $z = 0.3534$). The spatial coincidence with a normal galaxy and the decay in luminosity over time t as $L \propto t^{-5/3}$ led to the conclusion that this transient was a tidal disruption event (TDE)[4,6,15]. The peak luminosity exceeds the Eddington limit by four orders of magnitude (for a 10^6-solar-mass black hole), which suggests that the X-ray emission is highly anisotropic, possibly originating from a relativistic jet pointed in our line of sight[4]. These energetics arguments suggesting a relativistic jet were bolstered by the detection of a strong radio afterglow at the nucleus of this previously inactive galaxy[5]. Although the broadband observations all suggest that this TDE resulted in super-Eddington accretion and the launching of jets, the powering of the jets (whether magnetically driven or radiation-pressure-driven) and the role of geometric beaming remains unknown[14,16].

Follow-up X-ray observations of Swift J1644+57 were taken soon after the initial discovery, and found the source to be highly variable, further suggesting accretion onto a compact object. A 200 s quasi-periodic signal was reported in the 2–10 keV light curve of the brightest two observations at >99.99% and >99.73% confidence[17]. Although the exact nature of the quasiperiodic oscillation is unknown, it does confirm the formation of an accretion disk just 10 days after the initial TDE. It was suggested[17] that this quasiperiodicity could originate from orbits at the inner edge of the accretion disk, resonances in the relativistic jet or variability in a turbulent accretion flow. Here, we reanalyse the early XMM-Newton and Suzaku observations to look at properties of the variability at all other timescales (Extended Data Table 1). We use a new technique, X-ray reverberation mapping, which combines spectral and timing techniques to understand the physical nature of the rapid X-ray variability.

We proceed by extracting XMM-Newton light curves in narrow energy bands from 0.3 keV to 10 keV (observed frame) and then use Fourier techniques to extract the relative time delays between these bands as a function of the temporal frequency (see Methods). We find a coherent soft excess lag in the frequency range 0.0002–0.001 Hz (Extended Data Fig. 1), and by averaging the interband time delays over these frequencies produce the lag–energy spectrum shown in Fig. 1. We find that the 5.5–8 keV rest-frame emission is delayed by ~100 s relative to the 4–5 keV and 8–13 keV emission (the same time delay can be seen directly between the rest-frame 5.5–8 keV and 8–13 keV light curves in Extended Data Fig. 2). The iron K lag is found with >99.9% confidence (see Methods for details). We also find the same iron K lag in the Suzaku observation taken 10 days earlier at >99.8% confidence (Extended Data Figs 3 and 4). The asymmetry of the line is confirmed at >98% confidence (Extended Data Fig. 5, Extended Data Table 2). The iron K lag is characteristic of emission that reverberates

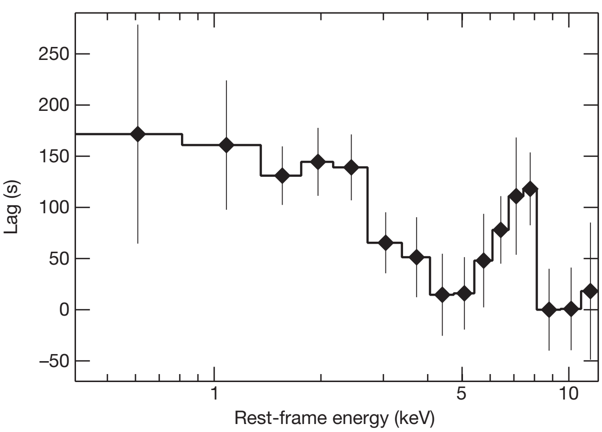

Figure 1 | Lag–energy spectrum of Swift J1644+57. The lag–energy spectrum with 1σ error bars in the frequency range $(2–10) \times 10^{-4}$ Hz. The zero point lag has been shifted so that zero lag corresponds to the emission that varies first and larger lags correspond to the correlated emission that varies later. This lag–energy spectrum shows that the emission from ~4–5 keV and 8–13 keV (primary continuum-dominated bands) vary first, and the iron line from ~7–8 keV responds ~100 s later, consistent with short-timescale reverberation off an ionized accretion disk. The asymmetric profile of the iron K lag shows that the emission is gravitationally redshifted and therefore much of the emission originates close to the central massive black hole.

[1]Department of Astronomy, University of Maryland, College Park, Maryland 20742, USA. [2]X-ray Astrophysics Laboratory, NASA/Goddard Space Flight Center, Greenbelt, Maryland 20771, USA. [3]Joint Space Science Institute, University of Maryland, College Park, Maryland 20742, USA. [4]Department of Astronomy, University of Michigan, Ann Arbor, Michigan 48103, USA. [5]Department of Physics, University of Maryland, College Park, Maryland 20742, USA.

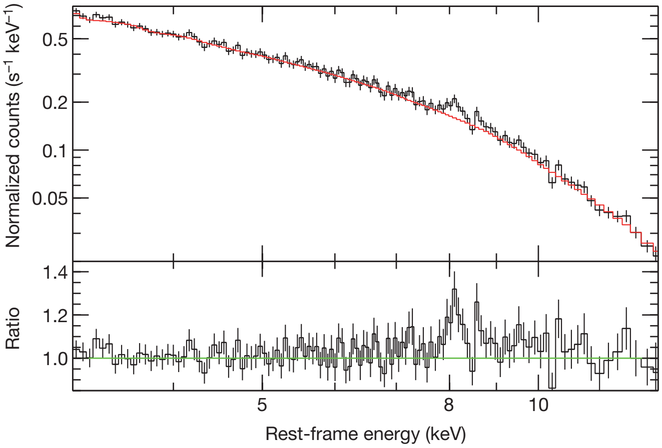

Figure 2 | The energy spectrum of Swift J1644+57. The time-integrated energy spectrum in normalized counts units of the observation shown in Fig. 1. The top panel shows the data in black and the best-fit power-law model for 2–10 keV (observer's frame) in red. Errors are at the 1σ level. The fit includes intrinsic absorption of $\sim 10^{22}$ cm^{-2}, similar to previous analyses[17]. The bottom panel shows the ratio of the data to that of the absorbed power-law model. The green line indicates a ratio of one, corresponding to agreement between the model and the data. The residuals show a clear excess at 8 keV, the same energy as the peak of the lag–energy spectrum in Fig. 1.

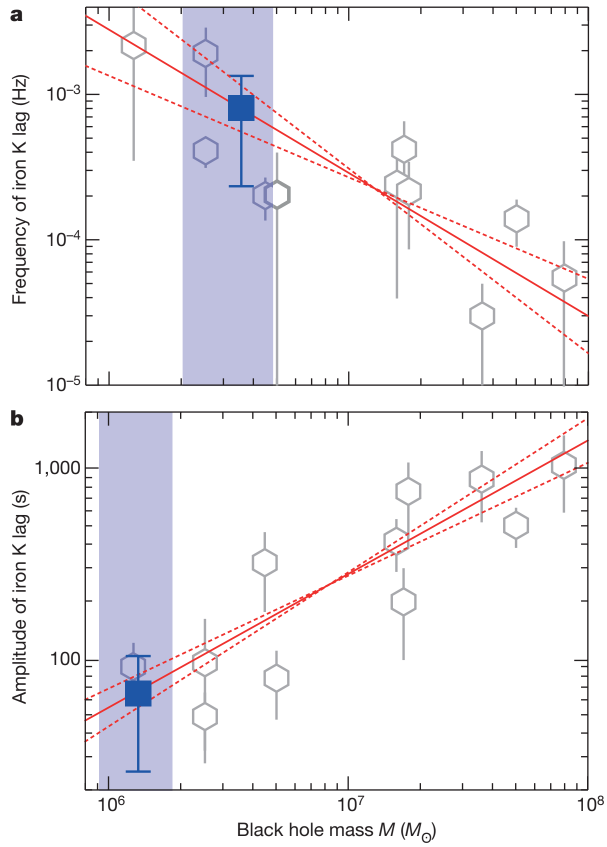

Figure 3 | Comparison of lags in Swift J1644+57 with other Seyfert galaxies. a, The rest-frame frequency range of the iron K lag versus black hole mass (in units of solar masses, $M_\odot$) for several Seyfert galaxies (grey hexagons; error bars indicate the frequency range). The solid red line indicates the best-fit linear model (in log–log space) with 1σ errors (red dashed lines). The blue square and error bars indicate the rest-frame frequency range of the iron K lag in Swift J1644+57, and the blue shaded region shows the 1σ range in mass suggested by this correlation. **b**, As in **a** except the correlation is with the amplitude of the lag (with 1σ error bars) versus black hole mass. The amplitude of the lag in Swift J1644+57 is calculated between 4–5.5 keV and the peak of the line at 6.5–8 keV. Both correlations suggest a black hole mass of a few million solar masses.

off the inner accretion flow and is re-emitted as a relativistically broadened iron Kα line. Such short-timescale lags between the direct emission and the reprocessed emission indicate that the emitting region is very small, within tens of gravitational radii of the central black hole. The asymmetric profile of the iron K lag indicates that the iron Kα emission line is gravitationally redshifted from within 10 gravitational radii. Relativistic reverberation lags associated with the broad iron Kα line are commonly found in rapidly varying local Seyfert galaxies[18–20] (see Extended Data Fig. 6 for examples).

Time lag analysis is a powerful technique because it disentangles the variable and correlated emissions from other emissions in the time-integrated energy spectrum. We examined the time-integrated energy spectrum in detail to search for further evidence of the iron K emission line. The resulting spectrum is shown in Fig. 2 compared with the best-fit absorbed power law for 2–10 keV. There is an excess in the energy spectrum at rest-frame 8 keV, the same energy as the peak in the lag–energy spectrum. To estimate the strength of the spectral feature, we fit it with a simple Gaussian function and find the equivalent width (that is, the area of the Gaussian above the continuum) to be 60 ± 10 eV. If this line corresponds to highly ionized iron Kα emission at 6.97 keV, then the emission is blueshifted by a line-of-sight velocity of $\sim 0.15c$.

With our new timing results, we estimate the mass of the central black hole by comparing the lag amplitude and lag frequency of Swift J1644+57 to Seyfert galaxies with known reverberating broad iron lines. The time lag of the broad iron line is determined by the light travel time between the continuum-emitting region and the X-ray photosphere. The temporal frequency at which the iron K reverberation lag is found is determined by how fast the continuum is varying. Both the light travel time and the variability timeframe are expected to scale with the mass of the central black hole. These two correlations have been seen in Seyfert galaxies for which X-ray reverberation is detected[19,21]. In Fig. 3, we plot (as grey hexagons) the known correlations of the rest-frame temporal frequency of the iron K lag versus the black hole mass (Fig. 3a) and the rest-frame amplitude of the iron K lag versus black hole mass (Fig. 3b) for several Seyfert galaxies. The red solid lines in both panels show the best-fit line to these correlations using an orthogonal-distance regression fitting procedure to account for the error in both the x and y variables. For clarity, we do not plot the error bars on the mass in the figure, but they were included in the model fitting (see Extended Data Table 3 for the names and references of individual sources). The blue squares indicate the redshift-corrected temporal frequency (Fig. 3a) and lag amplitude (Fig. 3a) for our TDE source placed at the black hole mass suggested by the best-fit line. Both the lag amplitude and frequency correlations suggest a mass of a few million solar masses (as shown by the blue shaded region), confirming that this source achieves isotropic luminosities exceeding the Eddington limit by a factor of >10. The TDE fall-back rate for such a black hole mass is sufficient to produce a luminosity of $\sim 10^{46}$ erg s^{-1} assuming a radiative efficiency of $\sim$10%. See Methods for a discussion on the spread in this correlation, and the possible biases in mass that such a spread may imply.

The detection of iron K reverberation in this super-Eddington accretion event puts strong constraints on the geometry of the flow and the launching mechanism of the jet. It definitively shows that the optically thick accretion flow is being irradiated by a variable X-ray source. Although blazars sometimes show soft lags[22], there is no evidence of iron K reflection in either their lags or their time-integrated energy spectra. Therefore, the detection of iron K reverberation in Swift J1644+57 strongly disfavours a model in which the X-ray emission is produced by a highly relativistic (Lorentz factor >10), magnetically powered, blazar-like jet, as previously discussed[3]. Following recent theoretical developments in our understanding of super-Eddington accretion flows[23–26], we believe that we are looking down

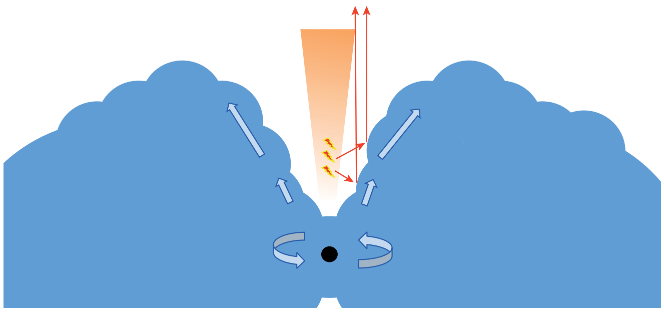

Figure 4 | Schematic of reverberation off a super-Eddington accretion flow. Swift J1644+57 is thought to be a super-Eddington accreting source, with a very thick, face-on accretion disk (blue) and a relativistic radio jet (orange). We suggest that the iron K lag originates from the light travel time between a flaring X-ray source and an irradiated outflowing funnel wall. In this schematic of the cross-section of the thick disk, the observer is looking down the funnel into the relativistic depths close to the central black hole. Variable X-ray continuum emission (lightning bolts) follows several light paths (two of which are shown as red arrows). The continuum emission reflects off the walls of the funnel and into the observer's line of sight. The strong blueshift of the iron lag is due to special relativistic Doppler shifts, and the asymmetric red wing is due to gravitational redshift from the strong gravity of the black hole. The blue arrows represent the dynamics in the disk: the accretion flow rotates around the central black hole and the walls of the funnel are outflowing at $\sim$0.1c–0.5c.

the polar funnel of a geometrically thick, radiation-supported flow (see Fig. 4 for a schematic). Therefore, the blueshift of the peak in the iron line is probably not due to disk rotation (requiring an edge-on disk), but rather due to the Doppler shift from outflowing material on the funnel wall that has been radiatively accelerated to 0.1c–0.5c. In such a flow, a substantial part of the beaming is geometric (radiation preferentially escapes down the funnel) and the slow jet is probably launched by radiation pressure (see Methods and Extended Data Fig. 7 for an application of this simple model).

Relativistic reverberation off an optically thick super-Eddington accretion flow tells us that much of the X-ray emission originates close to the event horizon. In principle, therefore, the X-ray emission can be used to measure the spin of the central black hole. However, our current models for measuring black hole spin from the broadening of the iron K emission assume a geometrically thin disk extending to the innermost stable circular orbit (ISCO), an assumption that is not likely to be relevant for this super-Eddington source, which has a very thick accretion disk that possibly extends beyond the ISCO to the marginally bound orbit[27,28]. Therefore, at this time we cannot claim an estimate of the black hole spin; but, with future developments in modelling such flows, relativistic reverberation from TDEs offers a potentially powerful technique for measuring spin—not only in the 10% of black holes that are persistently accreting, but also in the 90% of dormant black holes in the Universe.

Online Content Methods, along with any additional Extended Data display items and Source Data, are available in the online version of the paper; references unique to these sections appear only in the online paper.

Received 16 December 2015; accepted 4 April 2016.
Published online 22 June 2016.

1. Reynolds, C. S. The spin of supermassive black holes. *Class. Quant. Grav*. **30,** 244004 (2013).
2. Vasudevan, R. V., Fabian, A. C., Reynolds, C. S., Dauser, T. & Gallo, L. C. A selection effect boosting the contribution from rapidly spinning black holes to the cosmic X-ray background. *Mon. Not. R. Astron. Soc.* **458,** 2012–2023 (2016).
3. Rees, M. J. Tidal disruption of stars by black holes of 10^6–10^8 solar masses in nearby galaxies. *Nature* **333,** 523–528 (1988).
4. Burrows, D. N. *et al.* Relativistic jet activity from the tidal disruption of a star by a massive black hole. *Nature* **476,** 421–424 (2011).
5. Zauderer, B. A. *et al.* Birth of a relativistic outflow in the unusual gamma-ray transient Swift J164449.3+573451. *Nature* **476,** 425–428 (2011).
6. Bloom, J. S. *et al.* A possible relativistic jetted outburst from a massive black hole fed by a tidally disrupted star. *Science* **333,** 203–206 (2011).
7. Miller, J. M. *et al.* Flows of X-ray gas reveal the disruption of a star by a massive black hole. *Nature* **526,** 542–545 (2015).
8. Komossa, S. Tidal disruption of stars by supermassive black holes: status of observations. *J. High Energy Astrophys*. **7,** 148–157 (2015).
9. Fabian, A. C. *et al.* Broad line emission from iron K- and L-shell transitions in the active galaxy 1H 0707-495. *Nature* **459,** 540–542 (2009).
10. Zoghbi, A., Fabian, A. C., Reynolds, C. S. & Cackett, E. M. Relativistic iron K X-ray reverberation in NGC 4151. *Mon. Not. R. Astron. Soc.* **422,** 129–134 (2012).
11. Cackett, E. M. *et al.* Modelling the broad Fe Kα reverberation in the AGN NGC 4151. *Mon. Not. R. Astron. Soc.* **438,** 2980–2994 (2014).
12. Uttley, P., Cackett, E. M., Fabian, A. C., Kara, E. & Wilkins, D. R. X-ray reverberation around accreting black holes. *Astron. Astrophys. Rev.* **22,** 72 (2014).
13. Evans, C. R. & Kochanek, C. S. The tidal disruption of a star by a massive black hole. *Astrophys. J.* **346,** L13–L16 (1989).
14. Tchekhovskoy, A., Metzger, B. D., Giannios, D. & Kelley, L. Z. Swift J1644+57 gone MAD: the case for dynamically important magnetic flux threading the black hole in a jetted tidal disruption event. *Mon. Not. R. Astron. Soc.* **437,** 2744–2760 (2014).
15. Levan, A. J. *et al.* An extremely luminous panchromatic outburst from the nucleus of a distant galaxy. *Science* **333,** 199–202 (2011).
16. Coughlin, E. R. & Begelman, M. C. Hyperaccretion during tidal disruption events: weakly bound debris envelopes and jets. *Astrophys. J.* **781,** 82 (2014).
17. Reis, R. C. *et al.* A 200-second quasi-periodicity after the tidal disruption of a star by a dormant black hole. *Science* **337,** 949–951 (2012).
18. Zoghbi, A. *et al.* Discovery of Fe Kα X-ray reverberation around the black holes in MCG-5-23-16 and NGC 7314. *Astrophys. J.* **767,** 121 (2013).
19. Kara, E. *et al.* Discovery of high-frequency iron K lags in Ark 564 and Mrk 335. *Mon. Not. R. Astron. Soc.* **434,** 1129–1137 (2013).
20. Alston, W. N. *et al.* Discovery of a $\sim$2-h high-frequency X-ray QPO and iron Kα reverberation in the active galaxy MS 2254.9−3712. *Mon. Not. R. Astron. Soc.* **449,** 467–476 (2015).
21. De Marco, B. *et al.* Discovery of a relation between black hole mass and soft X-ray time lags in active galactic nuclei. *Mon. Not. R. Astron. Soc.* **431,** 2441–2452 (2013).
22. Ravasio, M. *et al.* Observing Mkn 421 with XMM-Newton: the EPIC-PN point of view. *Astron. Astrophys.* **424,** 841–855 (2004).
23. Sądowski, A. & Narayan, R. Powerful radiative jets in supercritical accretion discs around non-spinning black holes. *Mon. Not. R. Astron. Soc.* **453,** 3213–3221 (2015).
24. Jiang, Y.-F., Stone, J. M. & Davis, S. W. A global three-dimensional radiation magneto-hydrodynamic simulation of super-Eddington accretion disks. *Astrophys. J.* **796,** 106 (2014).
25. McKinney, J. C., Dai, L. & Avara, M. J. Efficiency of super-Eddington magnetically-arrested accretion. *Mon. Not. R. Astron. Soc.* **454,** L6–L10 (2015).
26. Abramowicz, M. A., Czerny, B., Lasota, J. P. & Szuszkiewicz, E. Slim accretion disks. *Astrophys. J.* **332,** 646–658 (1988).
27. Abramowicz, M. A. *et al.* Leaving the innermost stable circular orbit: the inner edge of a black-hole accretion disk at various luminosities. *Astron. Astrophys.* **521,** A15 (2010).
28. Krolik, J. H. & Hawley, J. F. Where is the inner edge of an accretion disk around a black hole? *Astrophys. J.* **573,** 754–763 (2002).

Acknowledgements E.K. thanks A. Zoghbi, M. C. Miller, F. Tombesi, E. Miller and L. Denby for discussions. E.K. also thanks the Hubble Fellowship Program for support under grant number HST-HF2-51360.001-A from the Space Telescope Science Institute, which is operated by the Association of Universities for Research in Astronomy, Incorporated, under NASA contract NAS5-26555. J.M.M. acknowledges N. Schartel and XMM-Newton for executing target-of-opportunity observations of Swift J1644+57. C.R. acknowledges support from NASA under grant number NNX14AF86G. L.D. thanks J. McKinney for discussions. L.D. acknowledges support from NASA/NSF/TCAN (NNX14AB46G), NSF/XSEDE/TACC (TG- PHY120005) and NASA/Pleiades (SMD-14-5451). This work is based on observations made with XMM-Newton, a European Space Agency (ESA) science mission with instruments and contributions directly funded by ESA member states and the US (NASA) and the Suzaku satellite, a collaborative mission between the space agencies of Japan (JAXA) and the US (NASA).

Author Contributions E.K. led the XMM-Newton and Suzaku time lag analysis, simulations, interpretation of the results and manuscript preparation. J.M.M. performed the XMM-Newton spectral analysis and contributed to the interpretation of the results. C.R. developed the analytical toy model for reverberation in a super-Eddington flow and contributed to the interpretation of the results. L.D. had the idea of examining X-ray time lags in a TDE and contributed to the interpretation of the results.

Author Information Reprints and permissions information is available at www.nature.com/reprints. The authors declare no competing financial interests. Readers are welcome to comment on the online version of the paper. Correspondence and requests for materials should be addressed to E.K. (ekara@astro.umd.edu).

METHODS

XMM-Newton data reduction. XMM-Newton[29] observed Swift J1644+57 with the EPIC-pn camera[30] for 25 ks in large-window imaging mode with a medium optical block filer. We reduced the data using the XMM-Newton Science Analysis System (SAS version 14.0.0) and the newest calibration files. The events were filtered with conditions PATTERN ≤ 4 and FLAG $= 0$. See Extended Data Table 1 for a summary of the observations used in this analysis.

For the spectral analysis we used an annulus source region, excising the central pixels as the spectrum is clearly affected by pile-up. We excised the central 12 arcsec of the circular source region of 60 arcsec. We could not use the same source region for the detailed timing analysis because this source region spanned two chips that have slightly different readout times that affect the timing analysis. We therefore used a smaller circular source region of 35 arcsec contained on a single chip. For the timing analysis we did not need to excise the central pixels because pile-up does not affect the measurement of the lag. Pile-up is a random process and therefore does not contribute to the correlated variability between energy bands from which the lags are determined[31].

For both the spectral and timing analyses we used a circular background region with a radius of 70 arcsec. There were no strong background flares during the observation and the 0.3–10 keV background count rate (corrected for region size) never exceeded 0.4 counts per second, $\sim$4% of the source count rate. The response matrices were produced using the rmfgen and arfgen tools in SAS.

We used the epiclccorr tool to produced background subtracted light curves with 10 s bins in several small energy bands in the range 0.3–10 keV. The 0.3–10 keV background-subtracted light curve is shown in Extended Data Fig. 2. The inset of Extended Data Fig. 2 shows a zoom-in of the light curves during the brightest, most variable part of the observation. We specifically examine the 4–6 keV light curve (red) and the 6–10 keV light curve (blue). By examining closely the light curves, one can see that on average the 4–6 keV band lags with respect to the 6–10 keV band (as shown in the lag–energy spectrum of Fig. 1). Although a lag is evident even in the time domain, the Fourier domain offers a clearer look at the lags on particular timescales.

We attempted to extract lags and spectra from an XMM-Newton observation taken shortly after the original one. Unfortunately, this observation was heavily affected by background flares, as noted previously[17]. Only 4 ks of the entire 21 ks exposure had a background level lower than the suggested maximum rate of 0.4 counts per second in the 10–12 keV background light curve. No iron K line or lag was detected, but given the poor quality of the data we cannot say whether this non-detection is intrinsic to the source.

Fourier time lag analysis of the XMM-Newton data. The Fourier time lag analysis follows the standard procedure[12,32]. In short, for every energy bin shown in the lag–energy spectrum (Fig. 1), the time lag is computed between the light curve in that particular bin of interest and the large reference-band light curve from 0.3–10 keV. We remove the bin of interest from the reference band so we do not have correlated errors. As the lag is measured in each bin of interest relative to essentially the same reference band, the lag–energy spectrum displays the relative lag between different energy bins.

To compute the lag we take the Fourier transform of the light curve and the reference-band light curve and compute the cross spectrum by multiplying one band and the complex conjugate of the other band. The argument of the cross spectrum is the phase difference between the two bands. For the lag–energy spectrum, we focus on the average phase lag over a particular frequency range. We convert the phase lag into a time lag by dividing by the midpoint frequency. In practice, the lag–energy spectrum is read from bottom to top—the bins with the smallest lag respond first, whereas the bins with larger lags are delayed with respect to the other bins.

We choose the frequency range in the usual way, on the basis of the lag–frequency spectrum between rest-frame 0.3–1 keV and 1–4 keV (Extended Data Fig. 1). These bands are chosen because the 0.3–1 keV band is typically the band dominated by the soft excess and the 1–4 keV band is typically the band most dominated by the continuum[9,19]. We find a negative lag (that is, the soft band lagging the hard band) from $(2–10) \times 10^{-4}$ Hz and therefore our lag–energy analysis is focused on this particular frequency range.

The power of the cross-spectral Fourier technique is that we pick out variability features that are correlated between energy bands. This, in principle, allows us to pick out components that may be lost in the time-averaged spectrum.

Suzaku data reduction. We process the unfiltered event files for each of the XIS CCDs. The source and background regions were $\sim$3.5 arcmin in radius. XSELECT was used to extract the spectral products, and medium-resolution responses were generated using XISRESP. The front- and back-illuminated light curves were combined for the time lag analysis. We extracted light curves between 1–8 keV in 1 keV energy bins and 128 s time bins. We include the 1.8–2.2 keV band where there are known calibration uncertainties because they do not affect the time lag analysis. The signal was too low in the 8–10 keV bins, and the maximum-likelihood analysis could not converge. We therefore exclude these highest-energy bins from the analysis. The total Suzaku exposure is 52 ks.

The Suzaku spectrum does not show a clear iron K emission line. We find an upper limit of 7 eV on an iron line of equivalent width at the same energy as the XMM-Newton spectrum. We closely examined the spectrum above 3 keV, ignoring the Au edge at $\sim$2.3 keV, which resulted in additional residuals to the fit. We find that the 3–10 keV spectrum shows slight hardening above $\sim$6 keV. This hardening is not likely to be due to pile-up because the observation was taken in the one-quarter window mode and the observed count rate is well below the nominal pile-up limit of 100 incident counts per second for the one-quarter window mode. Furthermore, excising the central 20 arcsec of the source region does not remove the hardening. We checked the Suzaku Hard X-ray Detector (HXD) spectrum and found that the excess hardening was also present above 20 keV. Extended Data Fig. 3 shows the ratio of the Suzaku X-ray Imaging Spectrometer (XIS) and HXD data to an absorbed power-law fit to the 3–6 keV range (this includes a normalization cross-calibration constant of 1.16 between front-illuminated XIS and HXD, as suggested in the Suzaku ABC guide). This ratio plot displays the hard tail above $\sim$6 keV and the excess above 20 keV. The excess hardening and curvature above 20 keV are reminiscent of the Compton hump. The presence of a Compton hump without the accompanying detection of an iron line is puzzling, but could suggest the presence of an iron line that is so severely broadened that it is rendered undetectable. This in turn would suggest that the reflection features were produced much closer to the black hole (and that our line of sight extended down to this region) during the Suzaku observation compared with the later XMM-Newton observation.

Maximum likelihood analysis of Suzaku data. As Suzaku is in a low-Earth orbit there are gaps in the observations approximately every 3,000 s. The timescales relevant to this system are longer than 3,000 s and therefore we cannot rely on the Fourier method. Instead we chose the maximum-likelihood method[33], which is used to analyse the lags in NuSTAR observations[34,35]; for further details of the method and Monte Carlo simulations that compare it with the Fourier method see the indicated references.

The Suzaku lag–energy spectrum is shown in Extended Data Fig. 4. The lag increases up to the same at the same energy as in the XMM-Newton observation (8 keV rest frame) and then drops again at higher energies. We note that the iron K lag amplitude that we measure is roughly the same size as the time bin of the light curve. The lag amplitude that we measure is an average time lag, and therefore the observed lag amplitude is not directly set by the bin size. The only clear difference between the Suzaku lags and those found in XMM-Newton are from 1–2 keV. The 1–2 keV bin in the Suzaku data are 110 ± 50 s less than the XMM-Newton lags. We hesitate to over-interpret one bin, but note that differences in the soft excess are also seen between Seyfert galaxies that show similar iron K lag features[19].

This analysis shows that we detect iron K reverberation in a TDE in two observations taken at different times, made with different observatories and analysed using different techniques.

Significance of the lag. In this section we present several statistical tests to confirm the detection. We start by testing whether the observed lags are due to random fluctuations in the data. Next we test whether the observed lags are consistent with the behaviour of the iron K lags seen in other Seyfert galaxies. Once we determine the significance of the detection of the iron K lag, we test whether this line profile is broad and asymmetric, as these features have important implications for the interpretation of the iron K emission originating from close to the central black hole.

We start by testing the detection of the lags using Monte Carlo simulations. We simulate light curves using the method described in ref. 36. We obtain our underlying power spectral density model (PSD) by fitting the 0.3–10 keV observed PSD with a broken power law (plus a constant for the white noise). With this relatively short observation, we do not observe a break in the PSD and so we assume a break frequency of 10^{-4} Hz to a low-frequency power law with index 1 (consistent with previous results[37] on the low-frequency variability of Swift J1644+57). Above 10^{-4} Hz we find a high-frequency power-law index of 2.1.

We simulate 10,000 light curves in each energy bin, scaled to the observed variance, count rate and exposure for that bin. We compute the time lag between each bin and the large reference band and assume zero intrinsic lag. Extended Data Fig. 5 shows the 1σ distribution of the lags in each energy bin overlaid with the observed XMM-Newton lag–energy spectrum to check the probability that the observed 0.3–10 keV lag–energy spectrum could be due to random fluctuations. Summing $\chi^2 = (x - \mu)2/\sigma^2$ for each independent energy bin (where x is the observed lag, μ is the mean of our zero-lag null hypothesis and σ is the standard deviation based on the Monte Carlo simulations), we obtain χ^2/d.o.f. = 33/17.

Our simulations therefore rule out a zero-lag null hypothesis with >99% confidence. This statistical test does not, however, account for the fact that the lags are coherently distributed above and below the zero-lag null hypothesis and not simply randomly distributed. The distribution of lags is Gaussian for all energy bins.

Next we test whether the 3–10 keV lags that we observe are associated with iron K emission lagging behind the continuum. Most sources with iron K lags show the smallest lag at the red wing of the iron line, a gradual increase in the lags up to the line centroid and a sharp drop above the line centroid back to small lags[12]. Phenomenologically, this behaviour is well described by a power-law continuum plus an asymmetric and broad emission line peaking at the line centroid. We use the diskline model as a phenomenological model to test for the presence of an iron K lag similar to those seen in Seyfert galaxies, however, we emphasize that the diskline (which describes the line broadening from a rotating, inclined, thin accretion disk) is formally not an appropriate model to describe emission from a face-on thick accretion flow. For the purposes of this simple statistical test for the presence of an iron K line in the lag–energy spectrum, the diskline model is simply employed in its role as a 'generic' skewed line profile and is sufficient.

To test for the presence of the iron K lag in Swift J1644+57, we compare two nested models in the 3–10 keV band: one of only a constant fitted to the 3–10 keV lag–energy spectrum and other containing an additional diskline model. For the diskline model we leave the line energy and inclination free (to allow some freedom in the width of the line profile) and freeze the inner and outer radii to $6r_g$ and $200r_g$, respectively (where $r_g = GM/c^2$ is the gravitational radius), with a power-law disk emissivity. We use an F-test to compare two nested models. Because the normalization of the lag can be negative, we avoid the problem of fitting too close to the parameter space boundary[38]. The resulting F-statistic value is $\Delta\chi^2/\chi^2 = 23.8$ and therefore the constant plus diskline model is preferred with >99.9% confidence. If we assume that the iron K lag found in Suzaku data has the same diskline energy and inclination as the XMM-Newton lag, then the F test indicates that the constant plus diskline model is preferred to >99.8% confidence. The same test with a Gaussian rather than a diskline model results in the Gaussian being preferred at >99.2% confidence for the XMM-Newton data and 98.8% confidence for the Suzaku data. This suggests that an asymmetric diskline model is preferred over the Gaussian, though this needs to be tested rigorously (see below).

Now that we have tested for the presence of an iron K lag, similar to those seen in Seyfert galaxies, we test whether the iron line is broad and whether the iron line is asymmetric. For the first test, we simply use the function steppar in XSPEC, which steps through the parameter space to calculate $\Delta\chi^2$ at each step. We find that the Gaussian is inconsistent with a narrow line at >99% confidence. Next we compare the best-fit broad Gaussian model with the asymmetrically broadened diskline model. Although the diskline model provides a lower χ^2 value for the same number of degrees of freedom, both models result in formally acceptable fits (that is, result in a reduced χ^2 less than 1). See a comparison of the Gaussian and diskline models in the right panels in Extended Data Fig. 5. We follow a Bayesian formalism[43] to quantify the improvement of the asymmetric diskline. To compare the broad Gaussian fit with the asymmetric diskline model, we compute the ratio of the evidences—the so-called Bayes' factor[38]. The Bayes' factor is the ratio of the posterior probabilities of our two models given the observed data, which we determine by stepping through the free parameters of each model and computing χ^2 at each point. We convert χ^2 into a probability for each step and sum the probabilities over the domain (in effect, integrating the probability over our defined parameter space). The free parameters and their domains for each model are shown in Extended Data Table 2. For simplicity, we freeze the normalization of the power law for both models to be the average lag from 3–4 keV and 6–10 keV. We find the Bayes' factor (the ratio of the diskline-integrated probability to the Gaussian probability) to be 55. This corresponds to the asymmetric diskline being favoured over the Gaussian at >98% confidence.

Comments on the reverberation lag–mass relation. In Fig. 3, we compared the frequency and amplitude of the iron K lag with the black hole mass for several Seyfert galaxies with known reverberation lags. Those sources are shown in Extended Data Table 3. We use all published iron K lag results, excluding the iron K lag in MS 22549−3712, which is associated with a quasiperiodic oscillation and may not have the same variability mechanism as the other sources[20].

Where possible, we use optical reverberation mass estimates with scale factor $\langle f \rangle = 4.3$ (ref. 39). These were obtained from the AGN (active galactic nuclei) Black Hole Mass Database (http://astro.gsu.edu/AGNmass). Most masses were calculated using the relation between the broad line region (BLR) radius and the luminosity, $R_{\rm BLR} \propto L^{\alpha}$ (refs 40–42), with $\alpha = 0.5$. For sources that do not have an optical reverberation mass estimate, we assumed an error of 0.5 dex.

Some of the spread in the correlation between the lag amplitude and black hole mass in Seyfert galaxies is probably due to differences in the accretion flow geometry and orientation. To this effect, if the geometry of the tidal disruption is very different to that of Seyfert galaxies (as we expect), then Swift J1644+57 may not lie on this correlation. Therefore, some caution should be exercised in using the lag amplitude as a definitive indicator of the mass. We do note however, that although the amplitude of the lag is dependent on the geometry of the flow (that is, dilution effects, different light travel times, the effect of inclination), the frequency at which the lag is found is less dependent on geometry and is therefore likely to be a more trustworthy indicator.

In Extended Data Fig. 6 we compare the reverberation lags of three rapidly variable Seyfert galaxies and the TDE Swift J1644+57. The sources are 1H 0707−405, IRAS 13224−3809 and Swift J2127.4+5654. To compare the shapes of the lag–energy spectra of different mass objects, we have scaled the lags so that they have the same iron K lag amplitude. There are clearly similarities in the overall spectra (for example, the lag of the soft excess, broad iron K line and Compton hump with respect to the continuum), although there are differences in the shapes of the line profiles. Swift J644+57 has a slightly narrower iron K line profile than 1H 0707−495 and IRAS 13224−3809. The energy of the line centroid in Swift J1644+57 is also slightly higher than the line centroid in Swift J2127.4+5654. We discuss possible physical reasons for this in the next sections.

Theoretical framework of super-Eddington accretion in TDEs. During a TDE the black hole goes from being dormant to radiating at or above the Eddington luminosity within around one month, and then decays in around a year to sub-Eddington levels[13]. The dynamical mass fallback rate of the debris is super-Eddington when the black hole mass is less than 50 million solar masses[13]. If the circularization of the debris is efficient enough[44–46], then the accretion on the black hole is also super-Eddington.

The small super-Eddington accretion disk in a TDE has not been well studied, but very recently numerical simulations have been employed to understand super-Eddington disks in persistent sources such as AGN or X-ray binaries[23–25]. Although the overall radiative efficiency and luminosity are still debated, in all simulations the disk structure is geometrically thick and optically thick, deviating from the standard thin disk picture[47]. A strong optically thick outflow is also generated and radiation can only leak through a narrow funnel along the polar direction. Close to the black hole, simulations show that a jet can help to carve out the inner accretion flow, thus exposing the X-ray emitting region of the disk[25]. In the final section, we present a toy model of the X-ray emission based on the geometry suggested by these numerical simulations.

Iron line reverberation from the outflowing eye-wall of a super-Eddington accretion flow. XMM-Newton shows that the iron line peaks at 7.5–8 keV in both the direct energy spectrum and in the lag–energy spectrum. Even in the case of hydrogen-like iron (with an iron-Kα line energy of 6.97 keV) the observed energies necessitate a significant blueshift. In the case of sub-Eddington AGN that possess geometrically thin accretion disks such blueshifts would suggest a high-inclination accretion disk. In the case of Swift J1644+57, however, multiple lines of evidence[4,5] point to a low-inclination (pole-on) geometry. Given the robust theoretical expectation (discussed in the previous section) that the accretion disk of such a super-Eddington source should be very geometrically thick, we suggest that the blueshifts seen in the iron line correspond to (radiation-driven) outflows in the funnel, or 'eye wall', of a geometrically thick accretion flow. In addition to the blue wing, the strong red wing of the iron line necessitates gravitational redshift (neglecting the small effect of multiple scattering events that can Compton downscatter some iron K photons to lower energies). This therefore suggests that the base of the geometrically thick funnel reaches deep into the potential well of the black hole, within 10 gravitational radii.

As proof of principle we construct a simple toy model of iron line reverberation in a funnel geometry (see Fig. 4). The funnel is assumed to be conical with a half-opening angle of θ, and we consider X-ray line reverberation driven by some variable X-ray source on-axis in the funnel at distance $R_{\rm X}$ from the black hole. We suppose that line emission can be excited along the walls of the funnel from radii $R_{\rm min}$ (within which we assume the accretion flow to be completely optically thick) to $R_{\rm max}$ (beyond which the disk starts to flatten off and cannot see the X-ray source). In this toy model, we neglect the rotation of the flow and simply prescribe a radial outflow velocity profile for the wall material:

$$v(R) = v_0 + (v_{\rm t} - v_0)\frac{R - R_{\rm min}}{R + R_{\rm acc}}$$

where v_0 is an initial velocity, $v_{\rm t}$ is a terminal velocity, and $R_{\rm acc}$ is the characteristic radius over which the acceleration proceeds. We then calculate the line profile in both the flux–energy and lag–energy spectra, assuming that we are viewing the funnel exactly pole-on. We include the effects of the relativistic Doppler shifts, relativistic beaming and gravitational redshift on both the excitation of the line

emission by the source and the observed energy/lags. We do not, however, account for general relativistic light bending.

Example results for a range of terminal velocities are shown in Extended Data Fig. 7 for the following illustrative parameters: $\theta = \pi/4$, $R_{\min} = 6r_g$, $R_{\max} = 200r_g$, $R_X = 30r_g$, $v_0 = 0$. To calculate time-lags in physical units, we also need to assume a black hole mass: we take $M = 2 \times 10^6 M_{\odot}$. Strongly blueshifted line peaks can readily be obtained—with this parameter set, we find that a terminal velocity of $v_t \approx 0.5c$ is required to have the line peak at 7.8 keV. We also obtain lag–energy spectra comparable to those seen in the data, peaking at 7.8 keV with a tail to lower energies. We obtain qualitatively similar results if we have a narrower opening angle (that is, $\theta = \pi/6$) and slower terminal velocity ($v_t \approx 0.3c$). Because of this degeneracy, we do not make a strong claim of the funnel opening angle.

An important technical point to note is that the time-lags derived in a reverberation analysis are smaller than the actual time-lags (that is, the light travel time of the extra path-length traversed by the reflected emission) due to dilution of the line-band by the coherent component of the direct continuum emission. In the toy model results shown here, we derive the observed (diluted) lags by multiplying the actual lags by the fraction that the line emission contributes at each energy, normalizing so that the peak of the line is 30% of its local continuum (motivated by the observed total energy spectrum, Fig. 2). It remains a distinct possibility that some fraction of the observed X-ray continuum is incoherent, meaning that we have overcorrected for dilution and hence underpredicted the dilution-corrected lags. A full treatment of dilution in any theoretical model requires a consideration of the full reflection spectrum and a Fourier-domain treatment that parallels that applied to the real data.

Code availability. The model fitting of spectra and lag–energy spectra was completed with XSPEC, which is available at the HEASARC website (http://heasarc.gsfc.nasa.gov). The code used for the time lag analysis and Monte Carlo simulations is not currently available. All figures were made in Veusz (http://home.gna.org/veusz).

29. Jansen, F. *et al.* XMM-Newton observatory. I: the spacecraft and operations. *Astron. Astrophys.* **365,** L1–L6 (2001).
30. Strüder, L. *et al.* The European Photon Imaging Camera on XMM-Newton: the pn-CCD camera. *Astron. Astrophys.* **365,** L18–L26 (2001).
31. Zoghbi, A. & Fabian, A. C. X-ray reverberation close to the black hole in RE J1034+396. *Mon. Not. R. Astron. Soc.* **418,** 2642–2647 (2011).
32. Nowak, M. A., Vaughan, B. A., Wilms, J., Dove, J. B. & Begelman, M. C. Rossi x-ray timing explorer observation of Cygnus X-1. II. Timing analysis. *Astrophys. J.* **510,** 874–891 (1999).
33. Zoghbi, A., Reynolds, C. & Cackett, E. M. Calculating time lags from unevenly sampled light curves. *Astrophys. J.* **777,** 24 (2013).
34. Zoghbi, A. *et al.* Observations of MCG-5-23-16 with Suzaku, XMM-Newton and NuSTAR: disk tomography and Compton hump reverberation. *Astrophys. J.* **789,** 56 (2014).
35. Kara, E. *et al.* Iron K and Compton hump reverberation in SWIFT J2127.4+5654 and NGC 1365 revealed by NuSTAR and XMM-Newton. *Mon. Not. R. Astron. Soc.* **446,** 737–749 (2015).
36. Timmer, J. & König, M. On generating power law noise. *Astron. Astrophys.* **300,** 707–710 (1995).
37. Saxton, C. J., Soria, R., Wu, K. & Kuin, N. P. M. Long-term X-ray variability of Swift J1644+57. *Mon. Not. R. Astron. Soc.* **422,** 1625–1639 (2012).
38. Kass, R. & Raftery, A. Bayes factors. *J. Am. Stat. Assoc.* **90,** 773–795 (1995).
39. Grier, C. J. *et al.* Stellar velocity dispersion measurements in high-luminosity quasar hosts and implications for the AGN black hole mass scale. *Astrophys. J.* **773,** 90 (2013).
40. Kaspi, S. Reverberation measurements for 17 quasars and the size-mass-luminosity relations in active galactic nuclei. *Astrophys. J.* **533,** 631–649 (2000).
41. Bentz, M. C. *et al.* The radius-luminosity relationship for active galactic nuclei: the effect of host-galaxy starlight on luminosity measurements. II. The full sample of reverberation-mapped AGNs. *Astrophys. J.* **697,** 160–181 (2009).
42. Bentz, M. C. *et al.* The low-luminosity end of the radius-luminosity relationship for active galactic nuclei. *Astrophys. J.* **767,** 149 (2013).
43. Protassov, R., van Dyk, D. A., Connors, A., Kashyap, V. L. & Siemiginowska, A. Statistics, handle with care: detecting multiple model components with the likelihood ratio test. *Astrophys. J.* **571,** 545–559 (2002).
44. Guillochon, J., McCourt, M., Chen, X., Johnson, M. D. & Berger, E. Unbound debris streams and remnants resulting from the tidal disruptions of stars by supermassive black holes. Preprint at http://arxiv.org/abs/1509.08916 (2015).
45. Shiokawa, H., Krolik, J. H., Cheng, R. M., Piran, T. & Noble, S. C. General relativistic hydrodynamic simulation of accretion flow from a stellar tidal disruption. *Astrophys. J.* **804,** 85 (2015).
46. Dai, L., McKinney, J. C. & Miller, M. C. Soft X-ray temperature tidal disruption events from stars on deep plunging orbits. *Astrophys. J.* **812,** L39 (2015).
47. Shakura, N. I. & Sunyaev, R. A. Black holes in binary systems: observational appearance. *Astron. Astrophys.* **24,** 337–355 (1973).
48. Bentz, M. C. *et al.* A reverberation-based mass for the central black hole in NGC 4151. *Astrophys. J.* **651,** 775–781 (2006).
49. Kara, E., Fabian, A. C., Cackett, E. M., Miniutti, G. & Uttley, P. Revealing the X-ray source in IRAS 13224-3809 through flux-dependent reverberation lags. *Mon. Not. R. Astron. Soc.* **430,** 1408–1413 (2013).
50. Bian, W. & Zhao, Y. On X-ray variability in narrow-line and broad-line active galactic nuclei. *Mon. Not. R. Astron. Soc.* **343,** 164–168 (2003).
51. Kara, E. *et al.* The closest look at 1H0707-495: X-ray reverberation lags with 1.3 Ms of data. *Mon. Not. R. Astron. Soc.* **428,** 2795–2804 (2013).
52. Zhou, X.-L. & Wang, J.-M. Narrow iron K lines in active galactic nuclei: evolving populations? *Astrophys. J.* **618,** L83–L86 (2005).
53. Zhang, E.-P. & Wang, J.-M. The unified model of active galactic nuclei. I: non-hidden broad-line region Seyfert 2 and narrow-line Seyfert 1 galaxies. *Astrophys. J.* **653,** 137–151 (2006).
54. Grier, C. J. *et al.* A reverberation lag for the high-ionization component of the broad-line region in the narrow-line Seyfert 1 Mrk 335. *Astrophys. J.* **744,** L4 (2012).
55. Kara, E., Cackett, E. M., Fabian, A. C., Reynolds, C. & Uttley, P. The curious time lags of PG 1244+026: discovery of the iron K reverberation lag. *Mon. Not. R. Astron. Soc.* **439,** L26–L30 (2014).
56. Jin, C., Done, C., Middleton, M. & Ward, M. A long XMM-Newton observation of an extreme narrow-line Seyfert 1: PG 1244+026. *Mon. Not. R. Astron. Soc.* **436,** 3173–3185 (2013).
57. Marinucci, A. *et al.* Simultaneous NuSTAR and XMM-Newton 0.5–80 keV spectroscopy of the narrow-line Seyfert 1 galaxy SWIFT J2127.4+5654. *Mon. Not. R. Astron. Soc.* **440,** 2347–2356 (2014).
58. Malizia, A. *et al.* First high-energy observations of narrow-line Seyfert 1s with INTEGRAL/IBIS. *Mon. Not. R. Astron. Soc.* **389,** 1360–1366 (2008).
59. Simien, F. & Prugniel, P. Kinematical data on early-type galaxies. VI. *Astron. Astrophys.* **384,** 371–382 (2002).
60. Alston, W. N., Vaughan, S. & Uttley, P. The flux-dependent X-ray time lags in NGC 4051. *Mon. Not. R. Astron. Soc.* **435,** 1511–1519 (2013).
61. Denney, K. D. *et al.* A revised broad-line region radius and black hole mass for the narrow-line Seyfert 1 NGC 4051. *Astrophys. J.* **702,** 1353–1366 (2009).

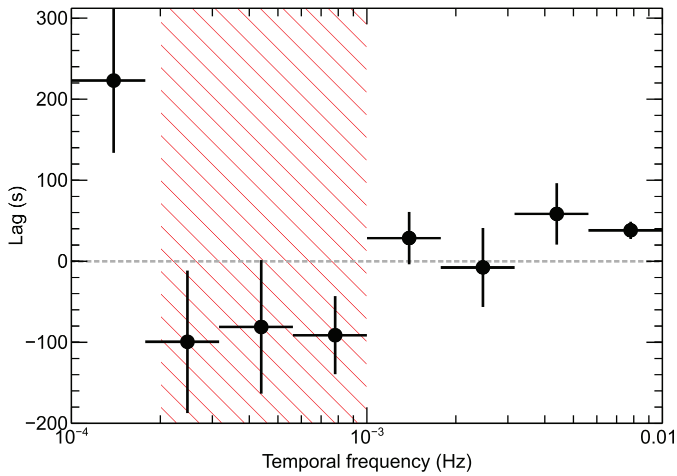

Extended Data Figure 1 | XMM-Newton lag–frequency spectrum. The lag–frequency spectrum between rest frame 0.3–1 keV and 1–4 keV (the usual soft and hard bands chosen for reverberation studies[9,21]). The lag–frequency spectrum shows a negative lag (that is, the soft band lagging behind the hard band) from $(2–10) \times 10^{-4}$ Hz (highlighted by the red hashed region). Because the lag–frequency spectrum shows a soft lag at these frequencies, we examined further the lag–energy spectrum at this particular frequency range (see Fig. 1). Error bars are at the 1σ level.

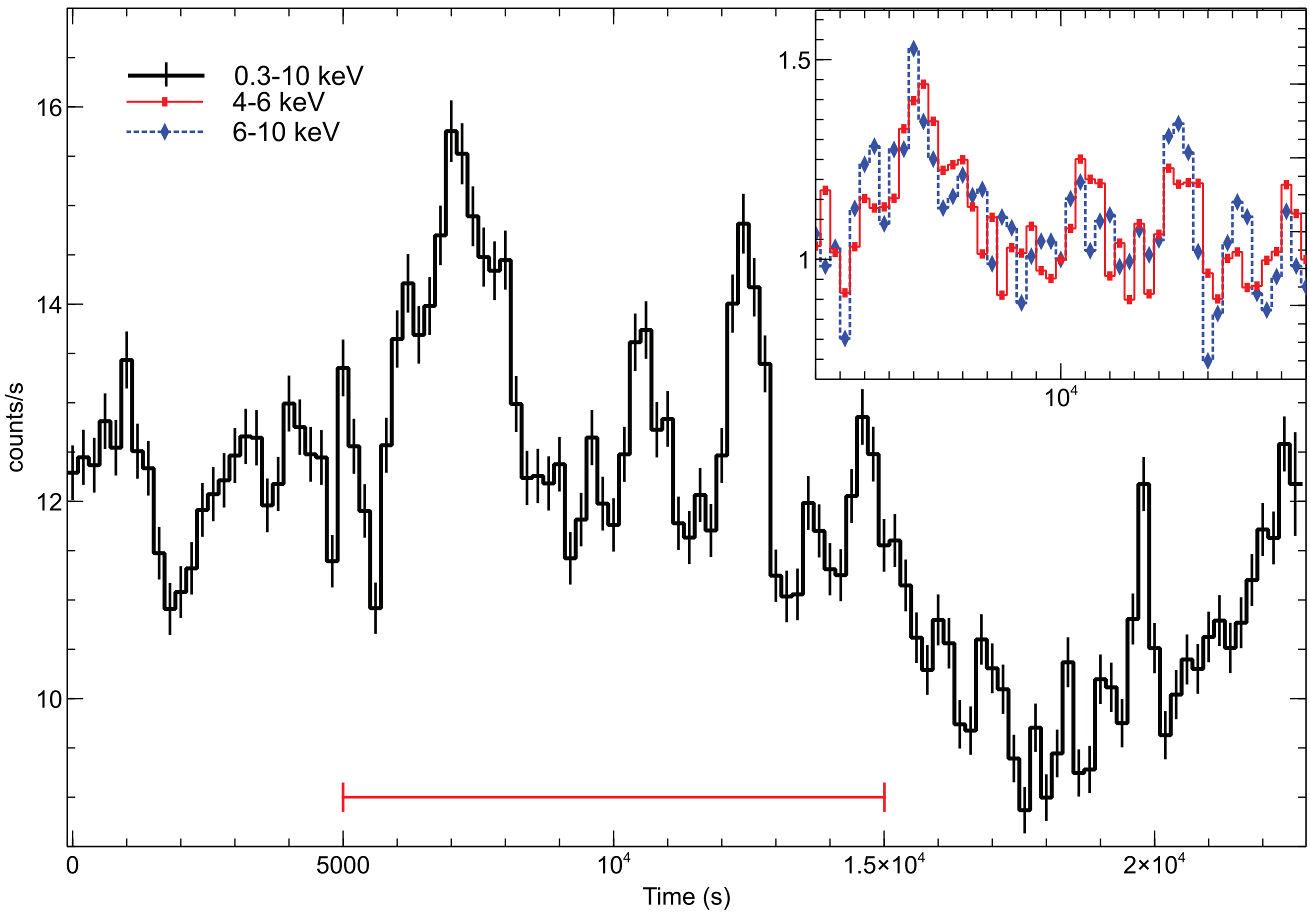

Extended Data Figure 2 | XMM-Newton light curve of Swift J1644+57. The observed 0.3–10 keV light curve in 200 s bins showing the rapid variability in this 25 ks observation. Note that the *y* axis does not extend to zero count rate. Error bars are at the 1σ level. Inset, the 4–6 keV (~5.5–8 keV rest frame) light curve (red) and the 6–10 keV (~8–13 keV rest frame) light curve (blue) zoomed in on the most variable part of the light curve from 5,000 s to 15,000 s (indicated by the red line in the main figure). The *y* axis is in units of count rate divided by the mean of the entire light curve. This illustrates (in the time domain) that on average the 6–10 keV variability leads the 4–6 keV variability. We emphasize that the time delay seen in these coarsely binned light curves places an upper limit on the actual amplitude of the lag. The detailed Fourier analysis (Fig. 1) allows us to obtain a better estimate of the average time lag.

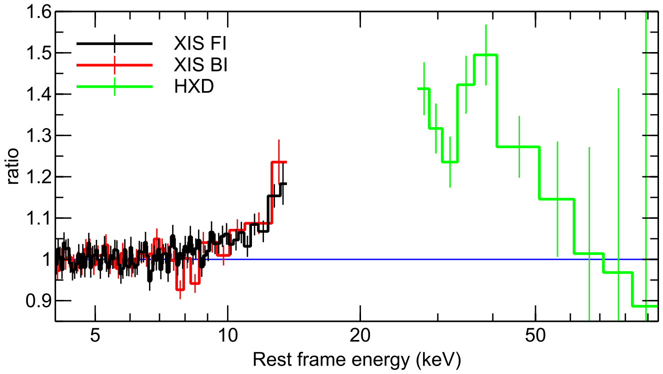

Extended Data Figure 3 | Suzaku XIS and HXD spectra. A ratio plot of the time-integrated energy spectra of the front-illuminated (black) and back-illuminated (red) XIS detectors and the HXD (green) to an absorbed power-law fit from 3–6 keV. The blue line at a ratio of one indicates where the data would be fully described by the absorbed power-law model. Error bars are at the 1σ level. This fit exhibits the potential hardening in the spectrum above $\sim$6 keV that appears to continue up to $\sim$30 keV, beyond which the spectrum turns over. There is no obvious iron line in the XIS spectra.

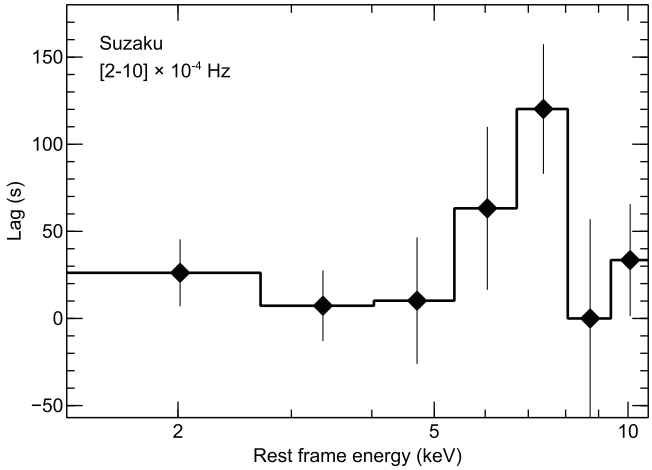

Extended Data Figure 4 | Suzaku lag–energy spectrum. The lag–energy spectrum of the Suzaku observation taken 10 days before the XMM-Newton observation. An iron K lag at the same frequency and same energy as the XMM-Newton iron K lag is detected in the data. This confirms the presence of an iron K lag with an amplitude of $\sim$120 s in two separate observations, taken with different instruments and analysed using different techniques. Error bars are at the 1σ level.

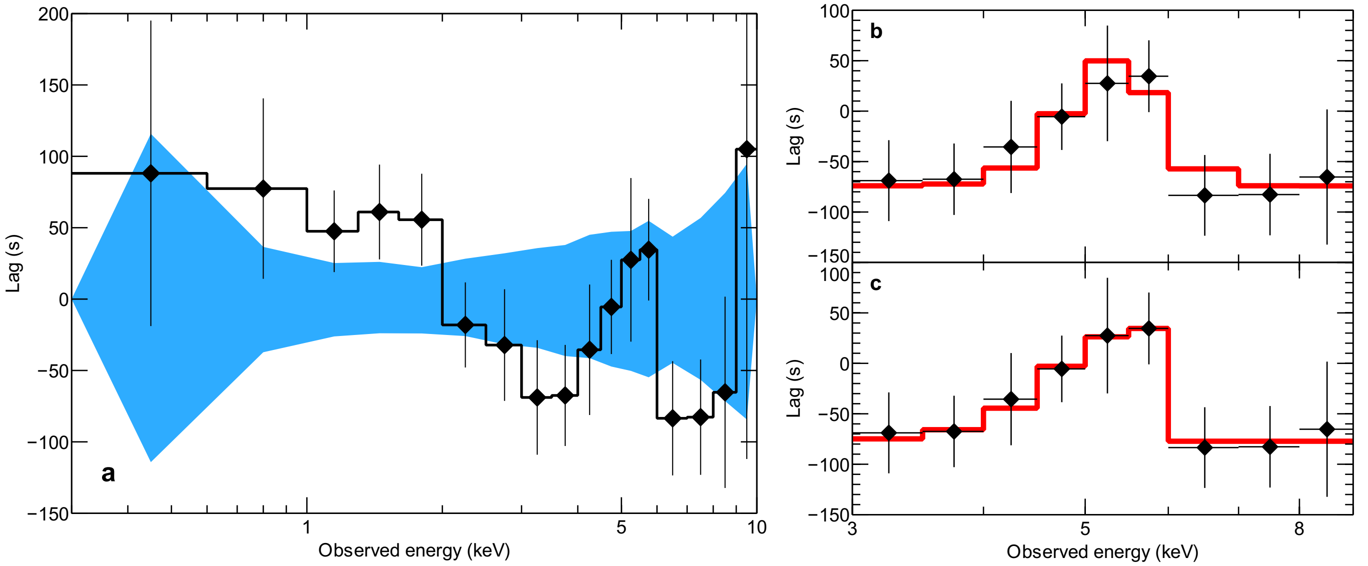

Extended Data Figure 5 | Statistical significance of the XMM-Newton lag–energy spectrum. a, The observed lag–energy spectrum (black points; same as Fig. 1 except the zero-point lag has not been shifted) compared with the 1σ distribution of 10,000 simulated Monte Carlo light curve pairs in each energy bin with zero lag (blue shaded region). This plot shows that the observed 0.3–10 keV lag energy is inconsistent with zero lag at >99% confidence. See Methods for details of the simulations. **b**, **c**, The best Gaussian (**b**) and asymmetric diskline (**c**) model fits (red lines) to the 3–10 keV lag–energy spectrum. We compute the Bayes' factor between the models and find that the diskline is preferred at >98% confidence.

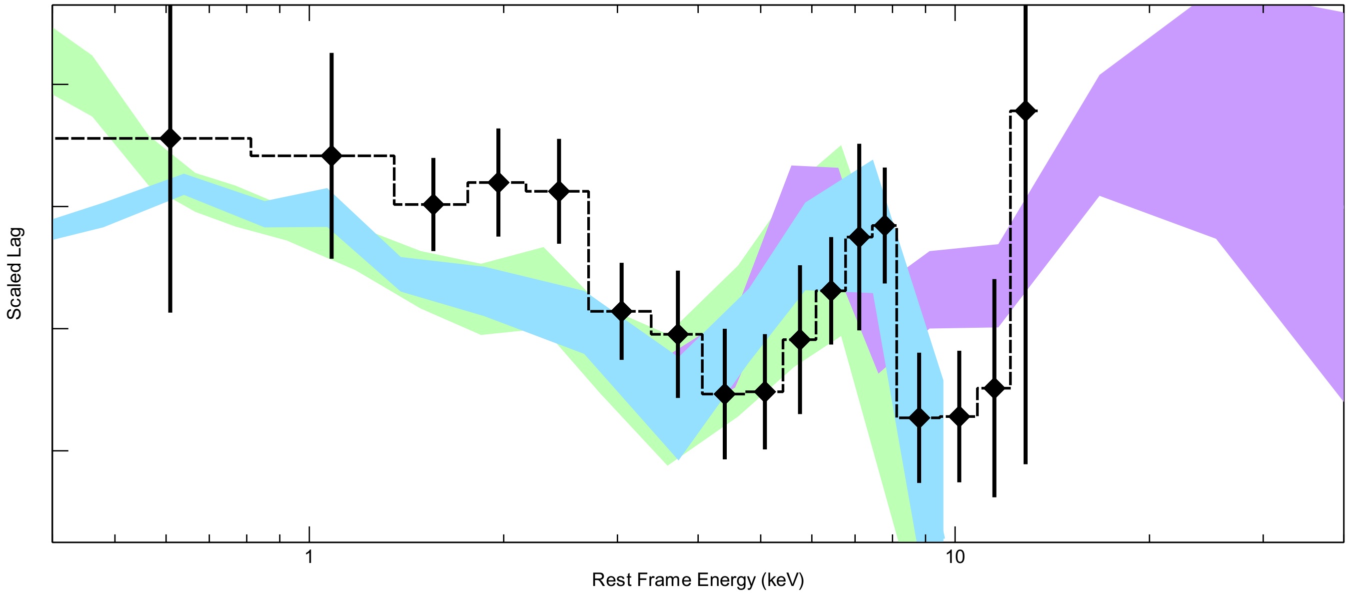

Extended Data Figure 6 | Swift J1644+57 lag–energy spectrum compared with Seyfert galaxies. Overlay of the reverberation signatures in nearby variable Seyfert galaxies compared with Swift J1644+57 (black diamonds). We show IRAS 13224−3809 in green, 1H 0707−495 in blue and Swift J2127.4+5654 in purple. The *y* axis shows arbitrary time lag units that have been scaled so that all of the sources have the same iron K lag amplitude. We show the scaled lag because all of the sources have different black hole masses (see Fig. 3). There is similarity in the broadband shape, although the iron K line profile of Swift J1644+57 appears to be slightly narrower and peaks at higher energies.

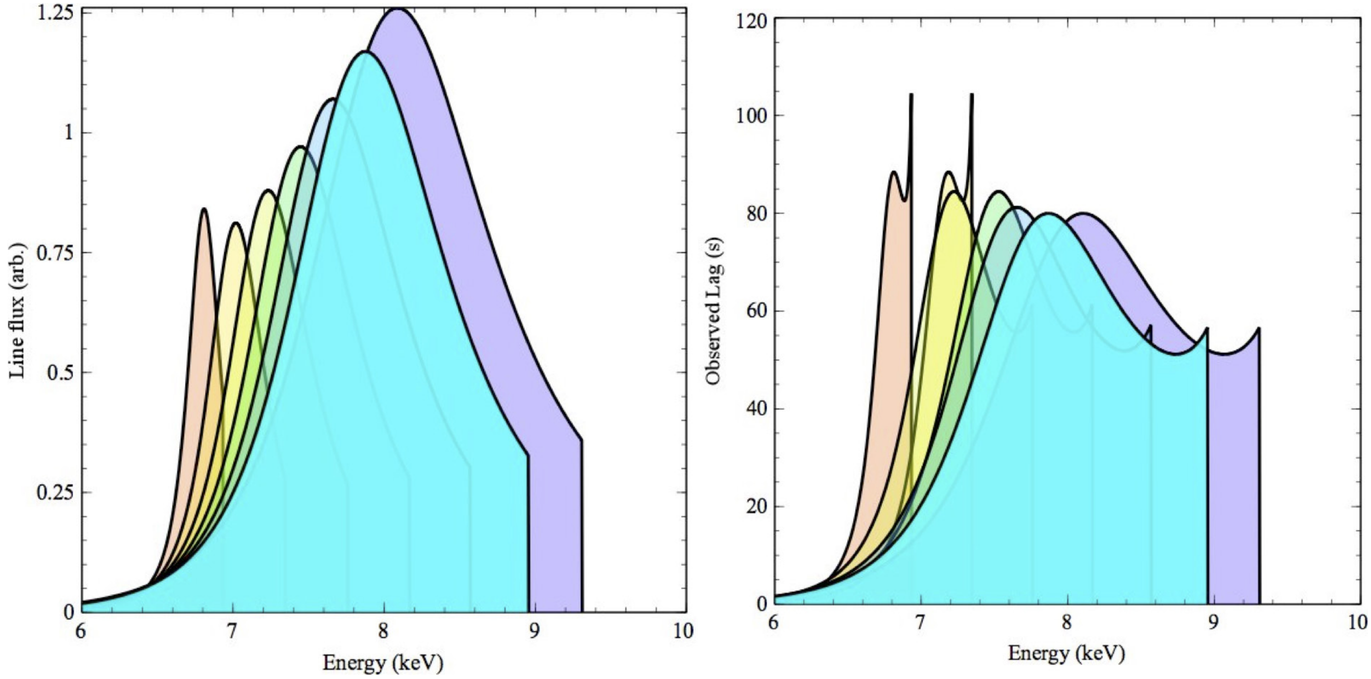

Extended Data Figure 7 | Flux–energy and lag–energy spectra of reflection in super-Eddington flow. Flux–energy (left) and lag–energy (right) spectra derived from our toy model for iron XXVI (rest-frame 6.97 keV) Kα line reverberation from an outflowing funnel wall. The results for terminal velocities of 0, 0.1*c*, 0.2*c*, 0.3*c*, 0.4*c*, 0.5*c* and 0.6*c* are shown (from left to right in peak energies).

Extended Data Table 1 | Observations used in this analysis

Instument	Date (YYYY-MM-DD)	OBSID	Exposure (s)
XMM-Newton	2011-04-16	0678380101	25000
Suzaku	2011-04-06	906001010	52000

A summary of the data used in this work, including the name of the telescope, the date of the observation, the OBSID unique identifier and the observation exposure length.

Extended Data Table 2 | Results of the fits to the lag–energy spectrum

Gaussian Model			Diskline Model		
Parameter	**Best-fit**	**Domain**	**Parameter**	**Best-fit**	**Domain**
Line energy (keV)	5.3	[3, 10]	Line energy (keV)	5.3	[3, 10]
Width (keV)	0.67	[0, 3]	Inclination (deg)	42	[0, 90]
Normalization (s)	188	[0, 500]	Normalization (s)	167	[0, 500]
Bayes' Factor ($P_{\text{diskline}}/P_{\text{Gaussian}}$): 55					
Probability: $> 98\%$					

The free parameters in the Gaussian and diskline models. We show the best-fit parameters, the domain over which we step through the parameters, the corresponding Bayes' factor and the probability. Note that for fitting in XSPEC we have shifted the lag amplitudes up by a constant value of 1,000 s so that none of the normalizations would be negative.

Extended Data Table 3 | Lags and masses of Seyfert galaxies with reverberation detections

Name	Lag Amplitude (s)	Lag Frequency (10^{-4} Hz)	Mass ($\log(M/M_{\odot})$)
NGC 4151 [10,48]	880±360	0.1–0.5	7.55±0.05
1H 0707-495 [49,50]	47±16	10–30	6.4±0.5
IRAS 13224-3809 [51,52]	299±135	1.4–2.8	6.6±0.5
MCG-5-23-16 [18,52]	1037±455	0.1–10	7.9±0.5
NGC 7314 [18,52]	77±30	0.1–4	6.9±0.5
Ark 564 [19,53]	92±65	3.2–5.2	6.4±0.5
Mrk 335 [19,54]	193±98	1.9–6.7	7.23±0.04
PG 1244+026 [55,56]	762±306	0.9–3.6	7.3±0.5
Swift J2127.4+5654 [57,58]	407±127	0.4–4.5	7.2±0.5
NGC 1365 [35,59]	500±120	0.9–1.9	7.7±0.5
NGC 4051 [60,61]	90±30	3.5–40	6.1±0.1

The observed iron K lag amplitude (measured between 3–4 keV and 5–7 keV) with 1σ errors, observed iron K lag frequency range and black hole mass with 1σ errors are shown for all Seyfert galaxies with known iron K reverberation detections. The two references listed in brackets after each object correspond to the reference[10,18,19,35,49,51,55,57,60] for the iron K lag amplitude and frequency, and the reference[48,50,52–54,56,58,59,61] for the black hole mass. These data correspond to the plot shown in Fig. 3 (although the error on the mass has not been plotted, for clarity).

LETTER

doi:10.1038/nature18278

Origin and implications of non-radial Imbrium Sculpture on the Moon

Peter H. Schultz[1] & David A. Crawford[2]

Rimmed grooves, lineations and elongate craters around Mare Imbrium shape much of the nearside Moon. This pattern was coined the Imbrium Sculpture[1], and it was originally argued that it must have been formed by a giant oblique (∼30°) impact, a conclusion echoed by later studies[2]. Some investigators, however, noticed that many elements of the Imbrium Sculpture are not radial to Imbrium, thereby implicating an endogenic or structural origin[3,4]. Here we use these non-radial trends to conclude that the Imbrium impactor was a proto-planet (half the diameter of Vesta), once part of a population of large proto-planets in the asteroid belt. Such independent constraints on the sizes of the Imbrium and other basin-forming impactors markedly increase estimates for the mass in the asteroid belt before depletion caused by the orbital migration of Jupiter and Saturn[5]. Moreover, laboratory impact experiments, shock physics codes and the groove widths indicate that multiple fragments (up to 2% of the initial diameter) from each oblique basin-forming impactor, such as the one that formed Imbrium, should have survived planetary collisions and contributed to the heavy impact bombardment between 4.3 and 3.8 billion years ago.

Previous interpretations for the Imbrium Sculpture included expressions of both structural features and secondary ejecta[6,7]. Horsts and graben crossing the Imbrium basin rim (the Apennine Mountains)[6] and subsurface radial dikes detected from Gravity Recovery and Interior Laboratory (GRAIL) data[8] support this interpretation in certain locations. Most of the features comprising the facies surrounding Imbrium, however, relate to ballistic emplacement[9,10]. Grooves and secondary craters with breached down-range rims record the momentum of ballistic debris but many do not radiate from the centre of the basin. Moreover, grooves that radiate from near the basin centre superpose those non-radial grooves and lineations originating well up range (Fig. 1a), in contrast to the traditional single-stage sequence of ejecta emplacement where the ejecta curtain advances outward systematically[10]. Rimmed grooves (sculptured terrains) characterize first-arriving debris, whereas lower-relief radial lineations (mobilized ejecta deposits) and elongated secondaries generally characterize late-arriving ejecta. Previous studies combined both facies into the single term Imbrium Sculpture, but differences in expression, direction and scale suggest that part of the sculpturing component (as originally described in Earth-based telescopic observations) may have a different cause.

The distribution of basin and ejecta asymmetries (see Extended Data Figs 1–4) indicates a northwest–southeast Imbrium-impactor trajectory[1,2]. Mapped endpoints of each groove/secondary (lineation) defined great circles that were traced back until they intersected the great circle delineating the impactor trajectory. The selected northwest–southeast trajectory was then readjusted until all great circles from Imbrium-related ejecta converged within the basin. Sets of these great circles were then subdivided according to where they crossed the readjusted trajectory line: up range from the basin centre, down range from the centre, and within a radius of 300 km around the centre. Laboratory and hydrocode impact experiments previously documented evolving source regions where the ejecta launch positions migrated within the growing excavation crater (see Extended Data Fig. 5)[11–13]. The pattern becomes most evident when the impactor-diameter to crater-diameter ratio becomes large, for example, very large scales, oblique trajectories, strength-controlled targets or low-speed impacts. The pattern far to the east resembles one side of a butterfly pattern (the western counterpart masked by Oceanus Procellarum and Orientale ejecta) that reaches the lunar far side, about 2,700 km (90°) east of Mare Marginis. One set of lineations, however, never converges within the basin rim and parallels the optimized trajectory (Fig. 1b). We propose that this set is an expression of the failed impactor. Maps of the different sets of groove and lineation trends are included in Extended Data Figs 2–4.

Hypervelocity impact experiments[11,12] and numerical models[13] reveal sets of ejecta trajectories converging well up range of the final crater centre, just as is observed for Imbrium. In impact experiments (∼5 km s^{-1} at 15°) with solid targets, rays and surface scouring down range subtend an angle to either side of the trajectory comparable to the impact angle (Fig. 2b). The outermost set converges up range of the final crater rim and relates to the sheared-off portions of the impactor[13,14]. Nearly parallel scours, however, originate from either side of the projectile (Extended Data Fig. 6). For large-body impacts, surface curvature becomes important, and portions of the projectile escape re-impacting the surface entirely (Fig. 2b). Captured fragments, crater sizes in down-range witness plates, and in-flight imaging in laboratory experiments (see also Extended Data Fig. 7) reveal that 5–8 large, intact and unmelted fragments survive, which is indicative of a non-catastrophic failure process[15]. Collectively, the larger fragments comprise about half the initial mass, each of which represents 40–46% of the original impactor diameter.

This observed physical process in the laboratory should apply at much larger scales. A numerical simulation used the CTH shock-physics analysis package for a 100 km monolithic dunite asteroid hitting the Moon at an impact velocity of 10 km s^{-1} at 30° from horizontal and incorporating a localized shear-failure material model (see Methods). Just as in experiments, projectile components scour the surface down range well before crater excavation and ejecta emplacement; moreover, their trajectories can be traced back to the projectile at the region of first contact, with some sets that extend back to the sides of the original impactor (Fig. 3a). This simulation closely matches the orientation of mapped grooves around the Moscoviense basin on the Moon (Fig. 3b and Extended Data Fig. 8b).

Consequently, grooves and lineations comprising the Imbrium Sculpture reveal several important clues about the excavation process. First, the initial stage of excavation originated well up range of the basin centre, consistent with experiments and numerical models. Debris ejected at this stage has very high speeds and low angles directed generally down range[11,12]. Second, sheared-off (decapitated) portions of the original asteroid retain speeds close to its original impact speed and extend far down range due to surface curvature[15–18]. Proposed remnants include heavily degraded elongate craters and grooves

[1]Brown University, Department of Earth, Environmental, and Planetary Sciences, 324 Brook Street, Providence, Rhode Island 02912, USA. [2]Sandia National Laboratories, P. O. Box 5800, MS 0840, Sandia National Laboratories, Albuquerque, New Mexico 87185, USA.

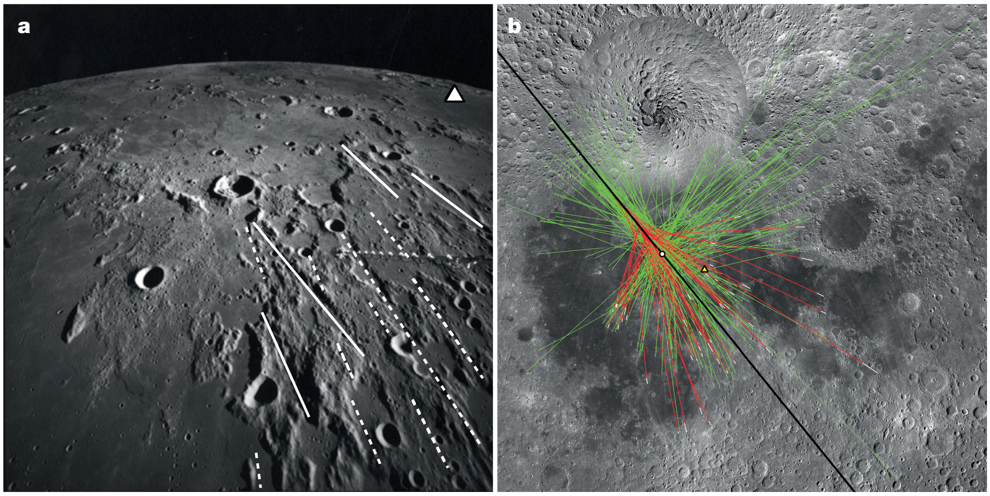

Figure 1 | Views and trends of Imbrium Sculpture. a, Imbrium Sculpture from south of the 24-km-diameter crater Lalande in the centre of view (looking to the northwest) with the crater Mösting at the top right. Dashed white lines trace secondaries originating from near the basin centre cross or truncate grooves originating well up range from the centre of Imbrium (solid lines). Triangle identifies the Surveyor 6 landing site in Sinus Medii (top right). Apollo 16 metric frame (A16-M-1413). **b**, Convergence of all grooves and highly elongated secondary craters on an Imbrium-centred map in a Lambert-stereographic conformal projection centred on Imbrium (offset from centre here). Yellow triangle locates the Apollo 15 landing site just inside the southeast Imbrium rim (white dot). Green lines correspond to subsets that converge along a great circle northwest of the basin centre. Red lines correspond to elongate secondaries converging up range of the basin centre, but a notable set of near-parallel trends up range (green) never converges within the basin. Black line indicates the proposed trajectory of the Imbrium impact (from the northwest); white dot indicates the basin centre. Image is a re-projected composite from the wide-angle Lunar Reconnaissance Orbiter Camera (LROC; circular region at top is an artefact around the North Pole). Sample size was determined by the ability to discern a clear orientation (based on length and expression) of each groove or elongated secondary crater, yielding over 230 mapped orientations (total set shown in Extended Fig. 3a).

beyond the southern rim of Imbrium (for example, Boscovich). Last, ejecta during later crater excavation stage (created by shock rarefactions off the free surface) become more radial to the centre of the final basin and superpose scouring from the earliest stages. Whether caused by ballistic ejecta from low-speed impacts or grazing impactor fragments, the width of each groove or crater should be

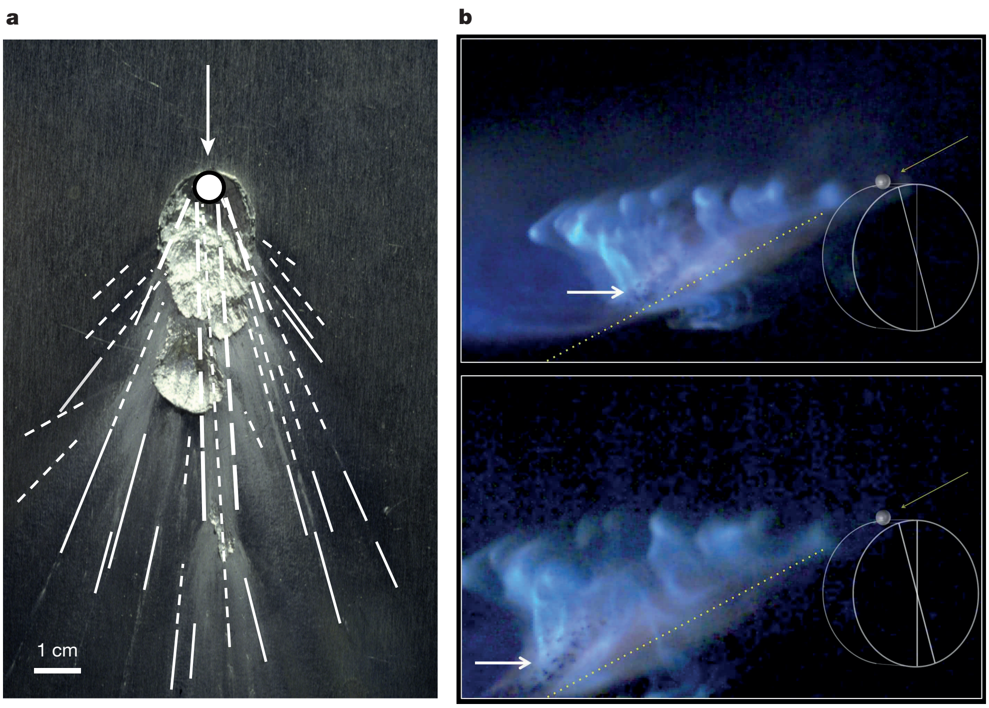

Figure 2 | An oblique impact experiment into a planar aluminium and cylindrical target by aluminium projectile impacting at 5.2 km s^{-1}. a, Scours originating from the point of first contact converge up range and result from projectile fragments re-impacting the surface downrange (impact angle was at 15° from the horizontal). **b**, An oblique impact into a curved surface prevents fragments from re-impacting the surface, as in planar targets. Fragments (arrows) surviving a 5 km s^{-1} impact into a 6.7-cm aluminium disk (faintly outlined) by a 0.635-cm aluminium sphere (represented graphically). About 40 μs after impact (top), downrange fragmental debris (just above the yellow dotted line) separates from the vapour plume (blue) along the initial trajectory. The bottom image shows the evolution 15 μs later with 8–10 large fragments (1–3 mm across) travelling close to the same speed as the initial impactor. Additional images can be found in Extended Data Fig. 7. The experiments shown here have been replicated numerous (more than 30) times for both similar and different conditions of impactor speed and angle.

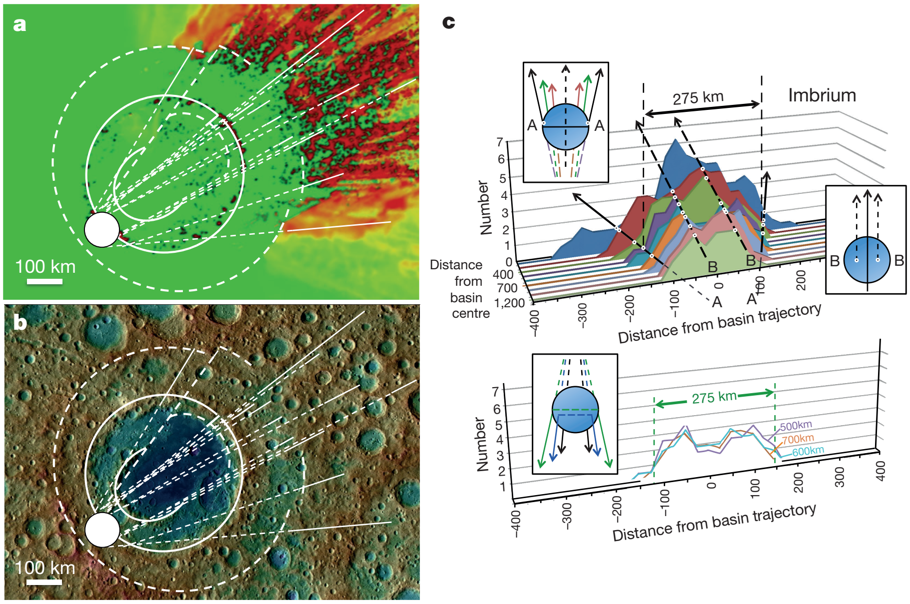

Figure 3 | Hydrocode simulation tracing impactor fragments from a basin-forming impact compared with scours from the Moscoviense basin. a, Hydrocode simulation of a 100 km asteroid impacting the Moon at 30° (dunite at 10 km s^{-1}) resulting in the same non-radial pattern observed in hypervelocity impact experiments. Red coloration is the pattern of asteroid relics interacting with the target surface. **b**, Mapped scours (degraded) on the Moscoviense basin for comparison with the hydrocode model. Images without overlays are included in the Extended Data Fig. 8. **c**, Histograms generated from intersections between great circles extending a subset of grooves (not converging within Imbrium) and great circles orthogonal to the Imbrium trajectory at different distances from the basin centre (out to 1,200 km). Top view shows all sets between 400 km and 1,200 km from the basin centre, with down range to the top. The limits of intersections correspond to the sides of the projectile (A–A and B–B in the insets). Bottom view selects just those intersections between 500 km and 700 km from the basin centre where the impact point occurred. The diameter of the Imbrium impactor is estimated to have been between 220 km and 275 km in diameter. See also Extended Data Fig. 2d. Intersection points composing the histograms have observational errors that depend on the length and distance of the measured grooves and scours. Repeat measurements indicate errors no more than 30 km.

controlled by the target strength and only a few times the size of the impacting debris (see Methods).

Such observations indicate that debris scoured the surface down range before reaching the final transient cavity dimension, well before the arrival of ejecta from the excavation stage. Expressions of pre-ejecta scouring include breaches in the southeast Imbrium rim within the Apennines and the arcuate region southeast of Imbrium (extending from craters Julius Caesar to near Flamarian). Similarly, the extension of the inner ring and degraded scour zones crossing the outer ring in Moscoviense illustrate this process (Fig. 3b), in contrast with the up-range rim[17].

The evolving flow field from an oblique impact accounts for the different groove orientations and enigmatic sequence of the Imbrium Sculpture. On the basis of experiments and models, certain sets of Sculpture probably originated from surviving impactor fragments and can be used to constrain the size of the Imbrium projectile, provided the Imbrium impact point can be determined. The farthest up-range location of the impact point must be well within the outermost Imbrium ring to the north (outer edge of Mare Frigoris). Groove trends up range intersecting the Imbrium trajectory line, however, constrain the farthest down-range location for the impact point, close to Montes Jura (Fig. 1b).

To provide a quantitative estimate for the Imbrium impactor size, great circle segments were placed orthogonal to the trajectory at incremental distances up range from the basin centre, as illustrated in laboratory experiments (Extended Data Figs 2–4). Intercepts between the extended great circles and this series of orthogonal lines generate a histogram as a function of distance from the basin centre (Fig. 3c). Those trends never crossing the original Imbrium trajectory originated from the sides of the impactor that detached soon after the moment of impact. On the basis of this strategy, the diameter of the Imbrium asteroid is estimated to have been 275 km, with statistical (and measurement) uncertainty constraining the outermost limit. If the shoulder of the distribution is used, then the derived diameter reduces to 220 km. The best determination between these two values becomes ~250 km ± 25 km. With the same approach, preliminary data indicate that the impactor diameters for the Schrödinger, Moscoviense and Orientale basins were ~45 km, ~100 km and ~110 km, respectively[17].

The derived impactor diameters can be used to calculate the diameter of the apparent transient crater (see Methods). The apparent transient diameter here refers to the diameter measured at the pre-impact surface before collapse. For a non-porous, gravity-controlled scaling[19], the Imbrium body (250 km in diameter) impacting at 30° (25 km s^{-1}) would result in a pre-collapse apparent transient diameter of ~850 km (compared to the observed diameter of ~1,250 km) and closely corresponds to the next most inner ring, from Montes Alpes to inside the Archimedes plateau. Decreasing the impact speed to 15 km s^{-1} decreases the transient crater sizes to ~700 km.

This reinterpretation of some components of the Imbrium Sculpture leads to other insights including impact speed, impactor signatures and sizes of proto-planets in the early Solar System. First, the derived sizes for the Orientale and Moscoviense impactors are nearly the same size, yet their basin diameters are very different (930 km and 445 km). Since both were formed by oblique impacts, this difference in crater size now requires a low impact speed for Moscoviense, consistent with the hydrocode model (Fig. 3b).

Second, impactor components surviving impact provide an explanation for meteoritic signatures within certain basins and highland lunar samples (see Methods). A previous study suggested that portions of the impactor could survive low-speed vertical impacts (based on a two-dimensional model)[20]. Here we find that the three-dimensional hydrocode model indicates that impactor components should line the basin interior but were buried by late-arriving ejecta beyond the rim. Down-range dispersal of the Imbrium impactor also could account for similar meteoritic compositions in Apollo 16 regolith breccias[21].

Last, Imbrium is among the largest among all lunar basins created during the Late Heavy Bombardment (LHB) between 4.1 and 3.7 billion years ago. On the basis of our independent estimate for its diameter, the Imbrium impactor would have been $\sim 2.5 \times 10^{22}$ g (for an asteroid with a bulk density of $2.5\,\mathrm{g\,cc^{-1}}$). Consequently, the total mass intersecting just the Moon during the LHB significantly exceeded the 10^{21} g previously proposed[5]. But the Imbrium impactor was only one of many proto-planets in the proposed E-belt, which was destabilized by late giant planet migration[22]. Large-body oblique impacts on both the terrestrial planets and asteroids should have generated large debris injected into planet-crossing orbits due to surface curvature, for example, Rheasilvia on Vesta, Hellas on Mars, Crisium, and even the earlier South Pole–Aitken basin[18] on the Moon. Fragments as large as 2% of the original diameter survived these collisions (see Methods) and generated numerous multi-kilometre-size objects in planet-crossing orbits that would have led to numerous craters 20–50 km in diameter.

Online Content Methods, along with any additional Extended Data display items and Source Data, are available in the online version of the paper; references unique to these sections appear only in the online paper.

Received 28 August 2015; accepted 18 April 2016.

1. Gilbert, G. K. The Moon's face: a study of the origin of its features. *Science* **21,** 305–307 (1893).
2. Baldwin, R. B. *The Measure of the Moon* (Univ. of Chicago Press, 1963).
3. Hartmann, W. K. Radial structures surrounding lunar basins, I: the Imbrium System. *Commun. Lunar Planet. Lab.* **2,** 1–16 (1964).
4. Strom, R. G. Analysis of lunar lineaments, I: tectonic maps of the Moon. *Commun. Lunar Planet. Lab.* **2,** 205–216 (1964).
5. Gomes, R., Levison, H. F., Tsiganis, K. & Morbidelli, A. Origin of the cataclysmic Late Heavy Bombardment period of the terrestrial planets. *Nature* **435,** 466–469 (2005).
6. Spudis, P. D. *The Geology of Multi-Ring Impact Basins* (Cambridge Univ. Press, 1993).
7. Wilhelms, D. E. Secondary impact craters of lunar basins. *Proc. Lunar Planet. Sci. Conf.* **7,** 2883–2901 (1976).
8. Andrews-Hannah, J. C. *et al.* The structure and evolution of the lunar Procellarum region as revealed by GRAIL. *Nature* **514,** 68–71 (2014).
9. Wilhelms, D. E. *The Geologic History of the Moon* Professional Paper 1348 (US Geological Survey, 1987).
10. Oberbeck, V. R. The role of ballistic erosion and sedimentation. *Rev. Geophys. Space Phys.* **13,** 337–362 (1975).
11. Anderson, J. L. B., Schultz, P. H. & Heineck, J. T. Asymmetry of ejecta flow during oblique impacts using three-dimensional particle image velocimetry. *J. Geophys. Res.* **108,** 5094 (2003).
12. Hermalyn, B., Schultz, P. H. & Heineck, J. T., Early-stage coupling for oblique impacts into granular material. *41st Lunar Planet. Science Conf.* Abstract no. 2565 (2010).
13. Schultz, P. H. & Wrobel, K. Downrange impact melt and related effects from Hale Crater on Mars. *J. Geophys. Res.* **117,** E04001 (2012).
14. Schultz, P. H. & Gault, D. E. Prolonged global catastrophes from oblique impacts. *Spec. Pap. Geol. Soc. Am.* **247,** 239–261 (1992).
15. Crawford, D. A. & Schultz, P. H. A model of localized shear heating with implications for the morphology and paleomagnetism of complex craters. *Large Meteorite Impacts Planet. Evol. V* 047 (2013).
16. Schultz, P. H., Stickle, A. M. & Crawford, D. A. Effect of asteroid decapitation on craters and basins. *43rd Lunar Planet. Science Conf.* Abstract no. 2428 (2012).
17. Schultz, P. H. & Crawford, D. A. Lunar basin-forming projectiles. *45th Lunar Planet. Science Conf.* Abstract no. 1961 (2014).
18. Schultz, P. H. & Crawford, D. A. Origin of the nearside structural and geochemical anomalies on the Moon. *Spec. Pap. Geol. Soc. Am.* **477,** 141–159 (2011).
19. Schmidt, R. M. & Housen, K. R. Some recent advances in scaling of impact and explosion cratering. *Int. J. Impact Eng.* **5,** 543–560 (1987).
20. Yue, Z. *et al.* Projectile remnants in central peaks of lunar impact craters. *Nature Geosci*. **6,** 435–437 (2013).
21. Joy, K. H. *et al.* Direct detection of projectile relics from the end of the lunar basin-forming epoch. *Science* **336,** 1426–1429 (2012).
22. Bottke, W. F. *et al.* An Archeaean heavy bombardment from a destabilized extension of the asteroid belt. *Nature* **485,** 78–81 (2012).

Acknowledgements NASA Grant NNX13AB75G provided support for the study. We acknowledge the technical support of the NASA Ames Vertical Gun Range at NASA Ames Research Center for the hypervelocity impact experiments and the image resources of the Northeast Planetary Data Center. Sandia is a multi-program laboratory operated by Sandia Corporation, a Lockheed Martin Company, for the United States Department of Energy under Contract DE-AC04-94AL85000.

Author Contributions P.H.S. conceived the idea and collected data for the Moon as well as the experiments; D.A.C. performed the shock physics model; P.H.S. and D.A.C. co-wrote the paper.

Author Information Reprints and permissions information is available at www.nature.com/reprints. The authors declare no competing financial interests. Readers are welcome to comment on the online version of the paper. Correspondence and requests for materials should be addressed to P.H.S. (peter_schultz@brown.edu).

METHODS

Imbrium grooves and elongated secondary craters. The Imbrium Sculpture reflects a sequence of arrival and source regions from Imbrium, even in the same region of the Moon, as illustrated by several examples. For reference, Extended Data Fig. 1 identifies the concentric rings of Imbrium defined by relic mountains and wrinkle ridges. The northern part of the outer ring (corresponding to Mare Frigoris) is poorly expressed due to collapse of the up-range rim. Extended Data Figure 2a includes a region southeast of Imbrium, close to the proposed trajectory. Farther west in this region, trends of some grooves diverge, trending more to the northwest. Extensions of these trends converge (and indicate a source) up range of the basin centre, characteristic of oblique impacts. This contrast in source regions becomes more apparent farther southwest (Extended Data Fig. 2b) and southeast of Imbrium (Extended Data Fig. 2c). Flow lines directed more radial to the basin centre overlap those secondaries and grooves originating up range. Up range from Imbrium (Extended Data Fig. 2d), grooves are narrower and closer to the basin than in other directions and also exhibit different source regions within the basin.

Expression of the initial trajectory for each set varies with impact angle. At higher impact angles (>45°), returning ejecta create slightly elongate craters. At lower angles (<30°), they produce elongate secondary craters with breached down-range rims, as down-range-directed debris interferes with excavation. At very low impact angles (10°), however, speeds need to increase in order to achieve a given ballistic range, thereby scouring the surface and producing rimmed grooves and scours that retain signatures of their initial momentum. The long grooves and elongated secondaries comprising the Imbrium Sculpture indicate that the impact angles must have been at very low angles (<10°).

Complete distribution of grooves and elongated secondary craters. The entire set of mapped grooves and elongated secondary craters with extensions along great circles towards Imbrium (Extended Data Fig. 3a). Some secondaries northeast of Mare Marginis (lateral) originate from a region up range of the basin centre. No statistical methods were used to predetermine the sample size. Many trends that converge up range from the basin centre are shown in Extended Data Fig. 3b. Source regions for a subset of grooves and elongate secondaries found up range of Imbrium cross the trajectory line well up range of the basin centre (illustrated in Fig. 1b and Extended Data Fig. 3c) and constrain the region of first contact by the Imbrium impactor to a region northwest of Sinus Iridum in what is now Mare Frigoris. Most trends, however, converge within 300 km of the centre of Imbrium (Extended Data Fig. 3d). The extended ballistic ranges to the east–northeast give the impression of a butterfly pattern, characteristic of an oblique impact, whereas the paucity of examples west and southwest reflect burial by later volcanic units of Oceanus Procellarum.

Some mapped sets indicate a source region down range of the basin centre as the result of a migrating ejecta flow centre. Such flow migration characterizes the early stages of oblique impacts and becomes more evident at very large scales as cratering efficiency reduces due to the role of gravity limiting crater growth. A subset of trends, however, never crosses the trajectory line or converges beyond the up-range rim of Imbrium (Extended Data Fig. 4). These sets are interpreted as grooves and secondary craters created by decapitated fragments from the Imbrium impactor and are used to constrain estimates for its size. Those great circles delineating the lateral limit represent fragments from the sides of the impactor, whereas those close to the trajectory are from the top. We suggest that a portion of Rheita Vallis is actually associated with Imbrium, rather than Nectaris. A fraction of the initial kinetic energy is lost during large-body oblique impacts. In laboratory experiments[14] (at 5 km s^{-1} to 6 km s^{-1}), as much as 22% at 15° and 10% at 30° of the initial kinetic energy decouples from crater formation in planar impacts. Curved surfaces allow impactor debris to extend farther beyond the rim (or lost to space, if not re-accreted) before impacting the surface (shown in Fig. 2b). Such decoupling results in dramatic reductions in crater depth, in evidence from both laboratory experiments and numerical codes[18].

Late-stage ejecta typically bury or mask earlier stages originating up range. Ejecta from Imbrium, however, are not simply deposited but are mobilized after striking the surface due to their initial momentum, thereby resulting in extensive mixing[10]. Hence, deposit thicknesses are difficult to measure, if not predict. Mapping of the different sets directly down range (near Julius Caesar; Extended Data Fig. 2c) illustrates such burial or extensive modification. In other directions (Extended Data Fig. 2a), ejecta deposits may stagnate in lows, which exposes crossing patterns at higher elevations (for example, Sinus Aestuum, near the horizon in Fig. 1a). At greater distances from Imbrium, thinning of the ejecta deposits allows recognition of the different orientations more clearly (Extended Data Fig. 2b).

Strategy for determining impact first contact and impactor size. Laboratory impact experiments capture ejecta in ballistic flight through a pulsed laser sheet[11]. Extended Data Figure 5 illustrates the evolution of ejecta trajectories as they evolve during crater growth and clearly reveals that the source region for ejecta evolves from a position near the impact point (Extended Data Fig. 5a, red dot) to a position close to the centre of the final crater (Extended Data Fig. 5b). In laboratory-scale experiments using loose particulates, the size of the region of coupling between the projectile and target is small relative to the final crater, best expressed at early stages of formation[11,12]. Specifically, the ratio between crater diameter and projectile diameter ranges from 20:1 to 50:1, depending on impact angle and impact speed. For strength-controlled targets (Fig. 2a), however, this ratio ranges from 4 to 8, also depending on angle and speed. This ratio reduces as a function of increasing size for gravity-controlled growth[19] and approaches that for a strength-controlled crater at basin scales. Hence, the evolving source region establishes a strategy not only for determining the point of impact but also constrains the size of the projectile, provided that the crater-to-projectile diameter ratio is small as illustrated in Fig. 2.

The point of first contact is constrained by the convergence of up-range ejecta, whereas the size of the projectile can be determined from the convergence of the down-range ejecta (Extended Data Fig. 6a). Such pronounced asymmetries disappear through time in laboratory experiments using gravity-controlled particulate targets (Extended Data Fig. 5b). Trends established by scouring extend up range, where they cross two orthogonal lines placed at different distances from the up-range rim for both a 15° and 30° impact (Extended Data Fig. 6b). Crossing the orthogonal line at the up-range crater rim provides a reasonable prediction for the projectile diameter. In these images, the slight offset from the trajectory line is the result of the spin of the projectile due to rifling in the launch tube. This spin imparts a centrifugal force to sheared and spalled fragments as demonstrated by reversed offsets between left- and right-hand twist tubes.

A subset of trends of impacting ejecta (grooves and elongate craters) northwest of Imbrium (up range) converges within the Atlas Mountains, but none originates northward of Mare Frigoris (Extended Data Fig. 3c). Consequently, the region of first contact must be confined to this region (Extended Data Fig. 3a). Those great-circle trends determined from inferred down-range ejecta trajectories, extending back to the region of first contact, then can be used to constrain an estimate for the lateral dimension of the object that formed this basin, independent of any a priori information about the impact angle or speed (only the trajectory needs to be assumed or determined). Results of the CTH moel of the Moscoviense impact further justify this strategy (Fig. 2b).

CTH model. The average impact speed by asteroids at the Moon is ~23 km s^{-1}, but for this numerical simulation (Fig. 3a) we assumed a relatively low-speed impact to demonstrate that the process does occur at much larger scales (and at only slightly higher speeds than in the experiments). The CTH model[23] will be described more fully in a separate contribution but is summarized eleswhere[15]. This new modification includes a damage model[24] incorporating the pressure-dependent melt curve[25]. Specifically, the yield strength of fully damaged material follows a Coulomb friction law. As conditions approach the melting point, thermal softening of the bulk material occurs. The model also included a method to estimate strain-dependent statistical crack spacing, shear heating within cracks, and heat loss via conduction away from cracks. As the temperature within a crack approaches the melting temperature, these additions now incorporate thermal softening. The combination of these modifications to the code results in a Brittle Damage with Localized Thermal Softening (BDL) model. This model depends on crack spacing (L), which is assumed to follow a power law in strain rate ($\dot{\varepsilon}$), that is, $L = L_0\dot{\varepsilon}^{-n}$.

Here we chose L_0 and n to produce crack spacing of 2–7 m for strain rates encountered during formation of terrestrial craters with diameters of 1–280 km. The BDL model predicts thermal crack widths of 0.3–3 cm and characteristic cooling times of 10–1,000 s for the equation of state (EOS), strength and conductivity properties appropriate for silicates. Frictional heating within each crack is proportional to $\mu L\dot{\varepsilon}P$, where μ is the friction coefficient (which decreases with temperature) and P is pressure. With the crack spacing and widths used here, 0.1–1% of rock volume is affected by this process. Surface curvature is an important factor for tracking the fate of decapitated projectile fragments from the formation of a basin the size of Imbrium, but such a model would be computationally expensive. Instead, we modelled the Moscoviense impact to demonstrate the basic processes, sequence of arrival, and migrating source regions for impactor debris.

Basin scaling. With the determined impactor size and reasonably constrained impact angle (20° to 30°), well-established crater scaling relations[19] can be used to estimate the size of the transient (pre-collapse) cavity for Imbrium, both for consistency and comparison with observable surface features.

$$D_g/2r = (\rho/\delta)^{1/3} k[(v\sin\theta)^2/gr)]^{\alpha/3} \quad (1)$$

Variables are defined as the following: D_g, transient crater diameter limited by gravity; r, impactor radius; ρ, projectile density; δ, lunar density; v, impact speed; θ, impact angle from the horizontal; k, an empirically derived material-dependent constant; α, an exponent dependent on the relative role of momentum and gravity controlling excavation; and g, gravitational acceleration of the Moon. The chosen

exponents and constants are based on experimental values for near-gravity scaling for loose particulates[26] with the following: $\alpha = 0.51$; and $k = 1.07$, a constant (including a shape factor for the diameter). The basis for this approach is that the initial collision generates a strong shock that converts the target into loose material under extension during the excavation stage. Wet sand scaling also has been used to represent gravity-controlled growth of non-porous materials[19] with the same dimensionless scaling equation but different values for the exponent ($\alpha = 0.65$) and constant ($k = 0.8$). These two approaches bracket the extrapolations. The average speed impact speed for the Moon today is around 23 km s^{-1} but uncertainties require consideration of a range of possibilities. Comparison between these two scaling relations and the range of impact speeds is summarized in Extended Data Table 1.

The two scaling approaches yield similar values of ~830–860 km (25 km s^{-1}) and ~700 km (15 km s^{-1}) for the Imbrium transient apparent diameter (different from the final diameter found today). Prior estimates based on the ejected volumes of material[6] yielded a slightly smaller transient diameter of 685 ± 88 km, which could indicate a lower speed impact. More recent estimates[27] based on the annular crustal bulge and numerical models also indicate a range of transient diameters (~500 km to 740 km) that depends on the thermal profile of the crust at the time. In this case, the numerical model assumed both a vertical impact at 15 km s^{-1} and a much smaller impactor diameter (80 km). Transient diameters estimated by other studies can be found in that study. The much larger diameter derived from the observations here suggests that three-dimensional models with a curved surface are needed to estimate the Imbrium transient crater diameter.

The derived transient rim diameters from the analytical scaling relations are also larger than recent estimates based on the positive gravity anomalies from the GRAIL mission and other gravity data[8]. This contradiction, however, can be reconciled if the interior gravity anomalies of Imbrium and other basins correspond to the shape and diameter of the deformed and displaced lower crust at depth[28,29], rather than a transient diameter referenced to the surface. Such an interpretation also would account for the offset of the gravity anomalies up range of the basin centre relative to the final basin rim, for example, Moscoviense, Orientale, Imbrium and Crisium[16].

Estimates for the transient crater diameters for other basins can be made based on other observed impactor diameters using the same approach described here[17]. For the peak-ring basin Schrödinger, the predicted transient apparent diameter is ~200 km ($v = 25$ km s^{-1}, $\theta = 30°$) based on extrapolation from sand experiments[26] or 280 km for wet soil[19]. The observed (post-collapse) rim–rim diameter is 290 km; consequently, the latter calculation must represent an overestimate. Decreasing the speed to 15 km s^{-1} only partly corrects this discrepancy. For Moscoviense (445 km in diameter), an assumed impact speed of 25 km s^{-1} and a derived impactor diameter of 100 km in diameter yield nearly the same apparent transient crater diameters of 390 km (sand) and 380 km (wet soil). Both estimates, however, are unreasonable because rim collapse (25%) would increase the diameter beyond the observed diameter. Reducing the impact speed to 10 km s^{-1} (matching the hydrocode model) results in a rim–rim transient diameter of 350 km and collapsed rim of 440 km, which is close to the result from the CTH hydrocode model (485 km) for same inputs for projectile size, speed and angle.

The final diameter of Imbrium depends on the selected physical expression. For example, the outer diameter (1,250 km) is delineated from the northern shores of Mare Frigoris to the Apennines. It should be pointed out, however, that the transient crater diameter here (~830–860 km) is only about 3.5 times the impactor diameter. Such a small ratio reflects the role of gravity preventing ejecta from escaping the transient cavity. Nevertheless, high shock pressures extended well outside this limit and material still remained in motion, even though the crater would later collapse. Increasing the apparent transient diameter by 25% (for the transient rim–rim diameter) results in the calculated transient rim-to-rim basin diameter ranging from 1,040 km to 1,080 km, which would extend from the northwest rim of Sinus Iridum (region of first contact) to just inside the Apennines. The final crater, however, undergoes collapse. Up range (to the northwest), the transient crater profile would have been unstable due to over-steepening of the up-range wall and result in greater rim/wall collapse (for example, extending to Mare Frigoris). Shallower excavation down range[16], however, would have preserved the uplifted rim, now represented by the Apennines.

Surviving impactor fragments and the Late Heavy Bombardment. Laboratory impact experiments can be used to assess the size and state of fragments surviving oblique impacts. Oblique impacts into planar targets generate considerable down-range debris, largely derived from the impactor as recorded in witness plates placed down range[14]. Estimates for the size of the fragments can be derived from a combination of the size of the craters in a vertical witness plate (facing the debris down range) and the observed speed (from high-speed imaging) or the momentum generated by the collision. These experiments revealed two different processes: catastrophic disruption resulting in a strain-dependent power-law fragment size distribution; and non-catastrophic disruption following a very different distribution revealed only at low impact angles (<15°). The strain dependence on the largest fragment size resembled the consequences for impact disruption of asteroids, the reverse of the case considered here. The non-catastrophic distribution, however, resulted in 5–8 similar size fragments travelling very close to the initial impactor speed. The sizes of these largest isolated fragments do not depend strongly on strain rate, consistent with these fragments formed by a different process (for example, shear)[14].

The derived sizes, however, do not represent the initial fragment dimensions following the first contact because they impacted the surface down range and fragmented still further, before impacting the witness plate. Hence, this approach underestimates the true projectile-fragment size distribution, except at the lowest impact angles (<10°). Impacting a sphere or cylinder, however, prevents some fragments impacting the surface down range[18]. Such experimental designs reveal that (1) some large fragments avoid re-impact with trajectories only slightly deflected from the initial trajectory, and (2) impacts into surfaces with sufficient curvature expose their true physical state and size following first contact (planar targets designed to avoid down-range impacts near the primary crater also preserve the original fragment sizes).

We further illustrate these results in a sequence of images that capture the size, trajectory and physical state of projectile fragments revealed in the high-speed image sequence shown in Fig. 2b and more completely in Extended Data Fig. 7. The 0.635-cm-diameter aluminium sphere impacted a 6.7-cm-diameter disk. Although the launch angle was actually 30° (from the horizontal), the impact point is slightly down range from the top, thereby resulting in an effective impact angle of 20° from the surface tangent on top of the disk. The collision resulted in about ten large fragments following close to the original trajectory, behind the vapour plume and jetting plasma. The largest fragment is about 0.2 cm in diameter, among other fragments 0.1–0.2 cm, consistent with measurements from impacted witness plates[14]. Smaller fragments leading this debris are cold (in silhouette) and near the initial trajectory, while others trail at slightly higher angles. In addition, a reddish glow surrounds this debris to either side of the trajectory and corresponds to a cloud of melt droplets. This distribution of debris is reflected in the arrival sequence observed on the witness plates with high-speed imaging.

The physical state of the Imbrium impactor after the collision depends on the impact angle and whether or not it fully decouples before hitting down range. In general, the peak pressure should reduce as $(\sin\theta)^2$ of the level for a vertical impact. For a 30° impact from the horizontal, this angle dependence means that the peak pressure would be reduced by a factor of 4. Two additional processes reduce the pressure even further. First, the density of the upper crust of the mega-regolith of the Moon reduces the impedance, thereby further reducing the peak pressure in the impactor. Second, the response in the impactor is more complicated than in the target because of the large amount of free surface, which reduces the expected peak pressures even further, along with the role of shear failure[18]. A prior modelling study[30] for a 5 km diameter at impact speeds comparable to this study for Imbrium (20 km s^{-1}) calculated peak pressures in the projectile during impacts into planar targets and found that a 30° impact allows 16% of the projectile to remain as a solid, whereas a 15° impact allows 100% to survive, generally consistent with laboratory experiments[14].

At the scale of the Imbrium basin, the widths of the parallel grooves down range provide a measure of the debris diameters based on crater scaling. At very low angle impacts (<5°) with speeds slightly less than the initial impactor speed, gravity-scaling relations for 10 km s^{-1} debris reveal that a 20-km-wide groove would have been produced by debris 4.5 km in diameter (equation (1)). At such low impact angles, however, groove widths should be controlled by strength scaling relations, which would predict even greater sizes for the debris. Grooves extending from near the region of first contact range from 10 km to 20 km across. Consequently, a conservative estimate predicts that some of the larger down-range fragments from the Imbrium impactor were conservatively 2 km to 4.5 km across, that is, less than 1–2% of the original diameter. Because a longer groove was probably not the result of a single impactor, grooves could represent more than one fragment while others could have escaped the Moon entirely.

If the impacting bodies were differentiated, the core would have a different distribution relative to the crust. For example, if the Moscoviense impactor was differentiated into a core and mantle, three-dimensional models reveal that projectile remnants line the interior ring while the crustal component is generally distributed beyond the rim[17]. This contrasts with prior results for the South Pole–Aitken basin, where the core is distributed beyond the rim[31]. The difference in distribution reflects the size of the impactor relative to the radius of the Moon.

More generally, recent studies indicate that ancient regolith breccias sampled at the Apollo 16 landing site have similar compositions (highly magnesian) poorly represented in current meteorite collections[21]. After the LHB, meteoritic contamination in the Apollo regolith shifted to a greater range of compositions. The

results of the study presented here suggest that the Imbrium impactor would have dispersed its signature across the Southern Highlands and account for the observed unique meteoritic contamination of Apollo 16 regolith preserved in regolith breccias, reflecting post-Imbrium reworking[32].

Consequently, large basin-forming collisions at angles less than 35° on the Moon (or any planet) should have generated considerable amounts of debris just from the surviving impactor mass that escaped the gravity field. The experiments, models and observations of groove width all show that this component should be composed of large masses (or weakly held masses) departing at speeds nearly the same as the original impact speed and along the original trajectory. This contrasts with excavated debris from the parent body that would have been heavily shocked to achieve comparable speeds and ejected over broad angles. Our observations indicate that the basin-forming impactors are much larger than those previously assumed to accommodate the surviving asteroids in the Hungaria region[21]. One important implication, then, is that this picture may be incomplete. For example, the E-belt dynamical model assumed an arbitrary number of test particles and then compared the fit of those dynamically surviving particles constrained by assumptions about crater and basin scaling. If our assessment is correct, then asteroids in the Hungaria region may be only a small fraction of the original total mass (and sizes), but not necessarily the number of bodies. Either the basin-forming bodies during the LHB did not all come from the proposed E-belt[33], or the E-belt was originally composed of larger bodies that underwent collisional fragmentation and dispersal during planet migration, a process that was acknowledged to be missing in that study.

23. McGlaun, J. M., Thompson, S. L. & Elrick, M. G. A three-dimensional shock wave physics code. *Int. J. Impact Eng.* **10,** 351–360 (1990).
24. Collins, G. S., Melosh, H. J. & Ivanov, B. A. Modeling damage and deformation in impact simulations. *Meteorit. Planet. Sci.* **39,** 217–231 (2004).
25. Senft, L. E. & Stewart, S. T. Dynamic fault weakening and the formation of large impact craters. *Earth Planet. Sci. Lett.* **287,** 471–482 (2009).
26. Schultz, P. H., Ernst, C. E. & Anderson, J. L. B. Expectations for crater size and photometric evolution from the Deep Impact Collision. *Space Sci. Rev.* **117,** 207–239 (2005).
27. Potter, R. W. K., Kring, D. A., Collins, G. S., Kiefer, W. S. & McGovern, P. J. Estimating transient crater size using the crustal annular bulge: insights from numerical modeling of lunar basin-scale impacts. *Geophys. Res. Lett.* **39,** L18203 (2012).
28. Schultz, P. H., Orphal, D. L., Miller, B., Borden, W. F. & Larson, S. A. in *Multi-Ring Basins* (eds Schultz, P. H. & Merrill, R. B.) Vol. 12A, 181–195 (1981).
29. Schultz, P. H. Atmospheric effects on ejecta emplacement and crater formation on Venus from Magellan. *J. Geophys. Res.* **97,** 16183–16248 (1992).
30. Pierazzo, E. & Melosh, H. J. Hydrocode modeling of oblique impacts: the fate of the projectile. *Meteorit. Planet. Sci.* **35,** 117–130 (2000).
31. Wieczorek, M. A., Weiss, B. P. & Stewart, S. T. An impactor origin for lunar magnetic anomalies. *Science* **335,** 1212–1215 (2012).
32. Korotev, R. L. Some things we can infer about the Moon from the composition of the Apollo 16 regolith. *Meteorit. Planet. Sci.* **32,** 447–478 (1997).
33. Minton, D. A., Richardson, J. E. & Fassett, C. I. Reexamining the main asteroid belt as the primary source of ancient lunar craters. *Icarus* **247,** 172–190 (2015).

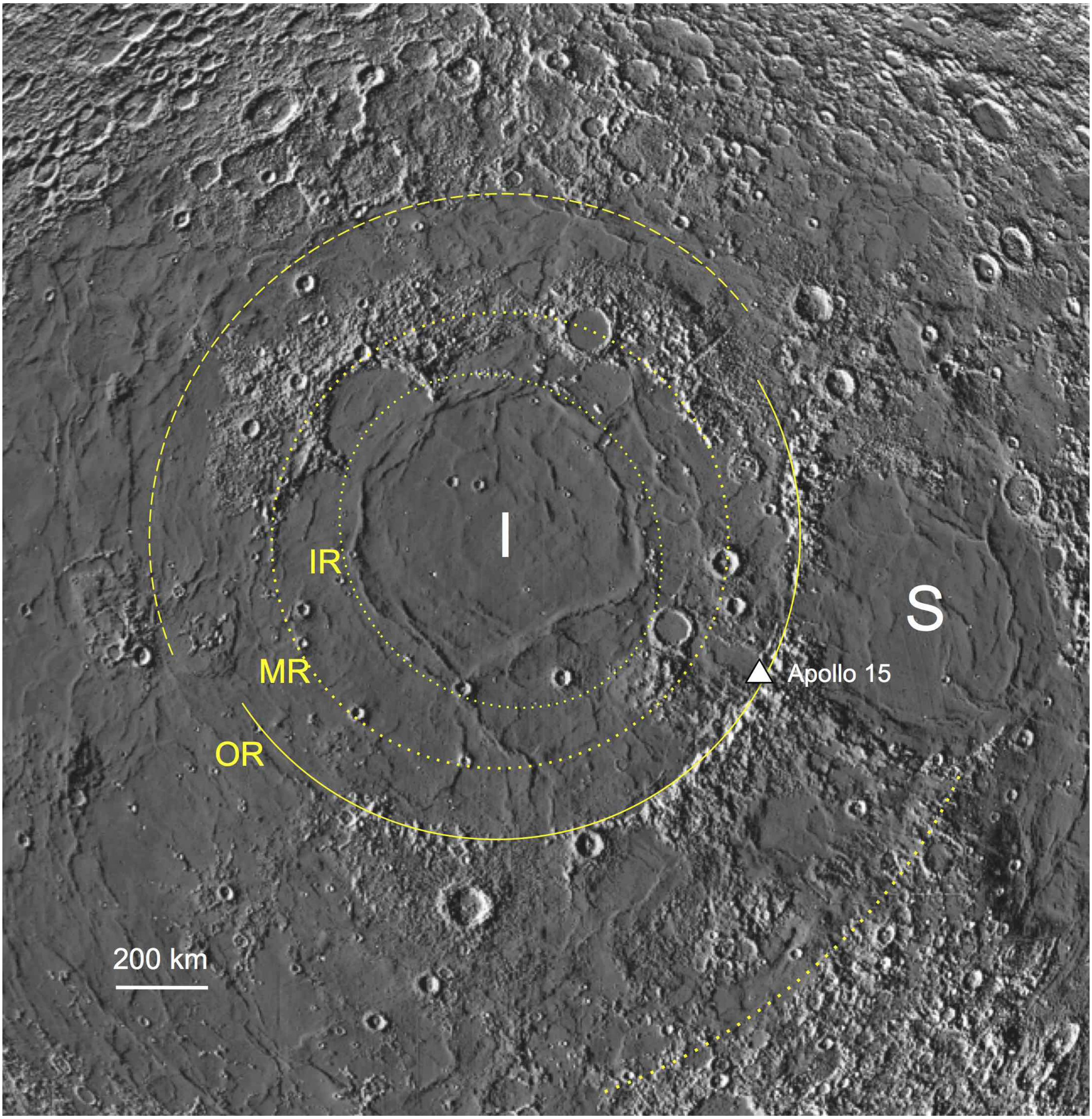

Extended Data Figure 1 | Mapped rings and features of the Imbrium basin that reveal asymmetries due to the impact trajectory and identify features for reference in the discussion. The rings comprising the Imbrium basin (I), including an outer ring, corresponding to the Apennines (OR), a middle ring extending to the Alpes Mountains (MR), and an oblong interior ring (IR) delineated by isolated massifs (mountains) and wrinkle ridges. An additional scarp-ring extends farther to the southeast (dotted line). The poorly expressed outer ring to the northwest is detached from the boundary to the southeast due to enhanced rim collapse in the up-range direction. The middle ring is incomplete but is recognized by isolated massifs and re-direction of tectonic features (wrinkle ridges). The inner ring is oblong (northwest–southeast) but truncated to the southeast. Nevertheless, wrinkle ridges do extend along the proposed trajectory. Such a pattern is consistent with portions of the impactor being decapitated after first contact but continuing to interact with the near surface down range. The Apollo 15 landing site at the base of the OR is also shown. 'S' indicates the Serenitatis basin. (Base map is an orthographic projection of Lunar Orbiter Laser Altimeter (LOLA) reproduced with permission from M. Collins.)

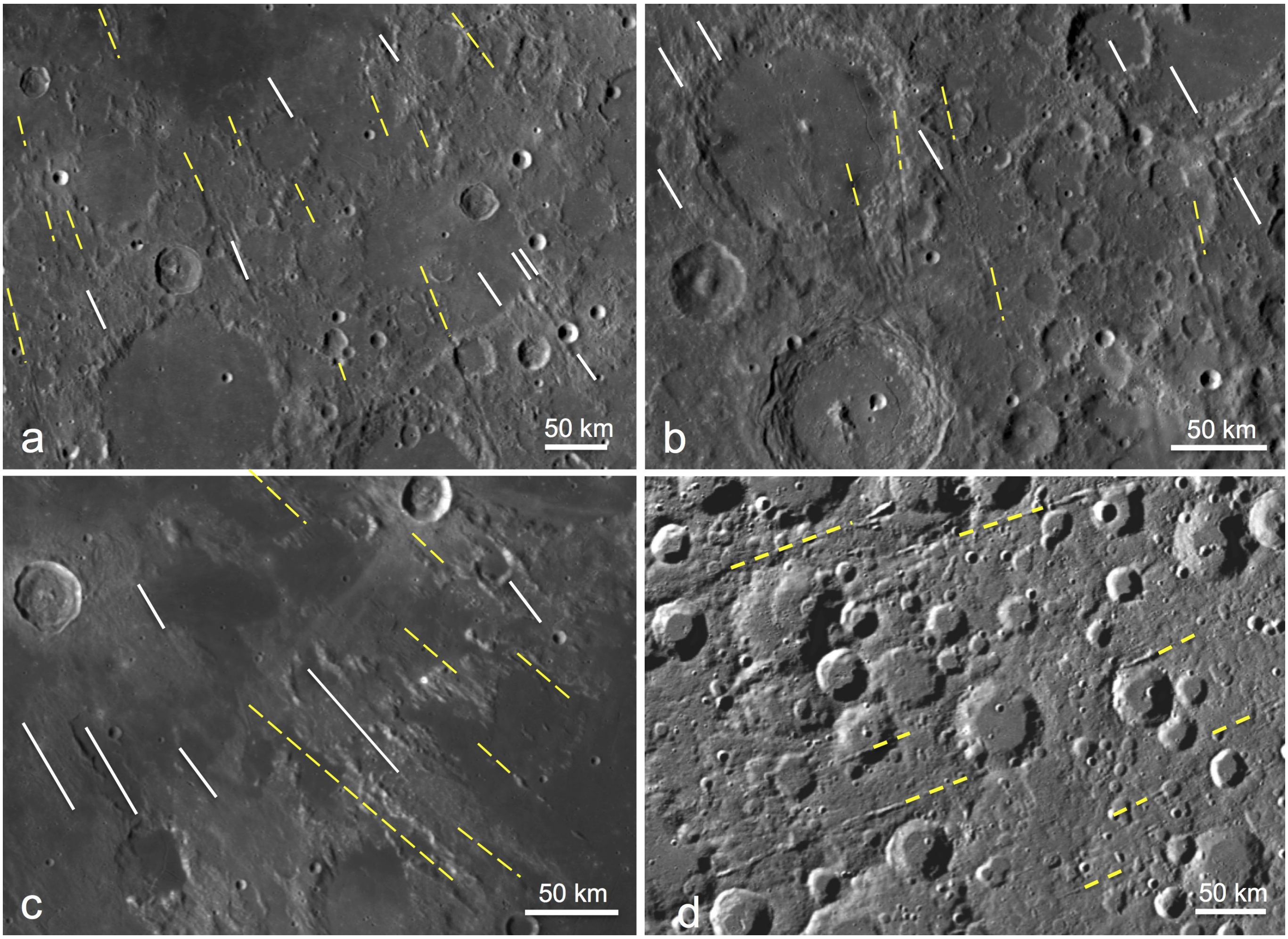

Extended Data Figure 2 | Mapped trends corresponding to grooves, scours and lineations in different directions around the Imbrium impact basin on the Moon. a, Region south–southeast of the Imbrium basin centred (latitude −6.693, longitude 6.491) near the trajectory line with the degraded crater Hipparchus in the right centre. White solid lines illustrate trends that converge up range of the basin centre (close to the point of first contact), whereas yellow dashed line trends converge closer to the centre of Imbrium (crater excavation). **b**, Region farther west from the trajectory line for Imbrium and south of Fig. 1a (centred at latitude −14.823, longitude −0.798). Certain grooves (white) have trends directed northwest (source up range of basin centre), and indicate first-arriving debris, in contrast to other sets (yellow), which are radial from the basin centre and correspond to later-arriving material. The crater Alphonsus is in the top left. **c**, Grooves and elongate secondaries near the Julius Caesar crater (bottom centre) and Boscovich craters (bottom left) southeast of Imbrium (latitude 12.496, longitude 15.681). Grooves/secondaries trending more northwest (solid white lines radial to the Imbrium) superpose those trending more westerly (dashed yellow lines converging on the proposed point of first contact). **d**, Region northwest (up range) of Imbrium (latitude, 68.304, longitude −114.03). The crater at the very top (only partial) is named Niepce. Most sets here indicate a source region towards the basin centre.

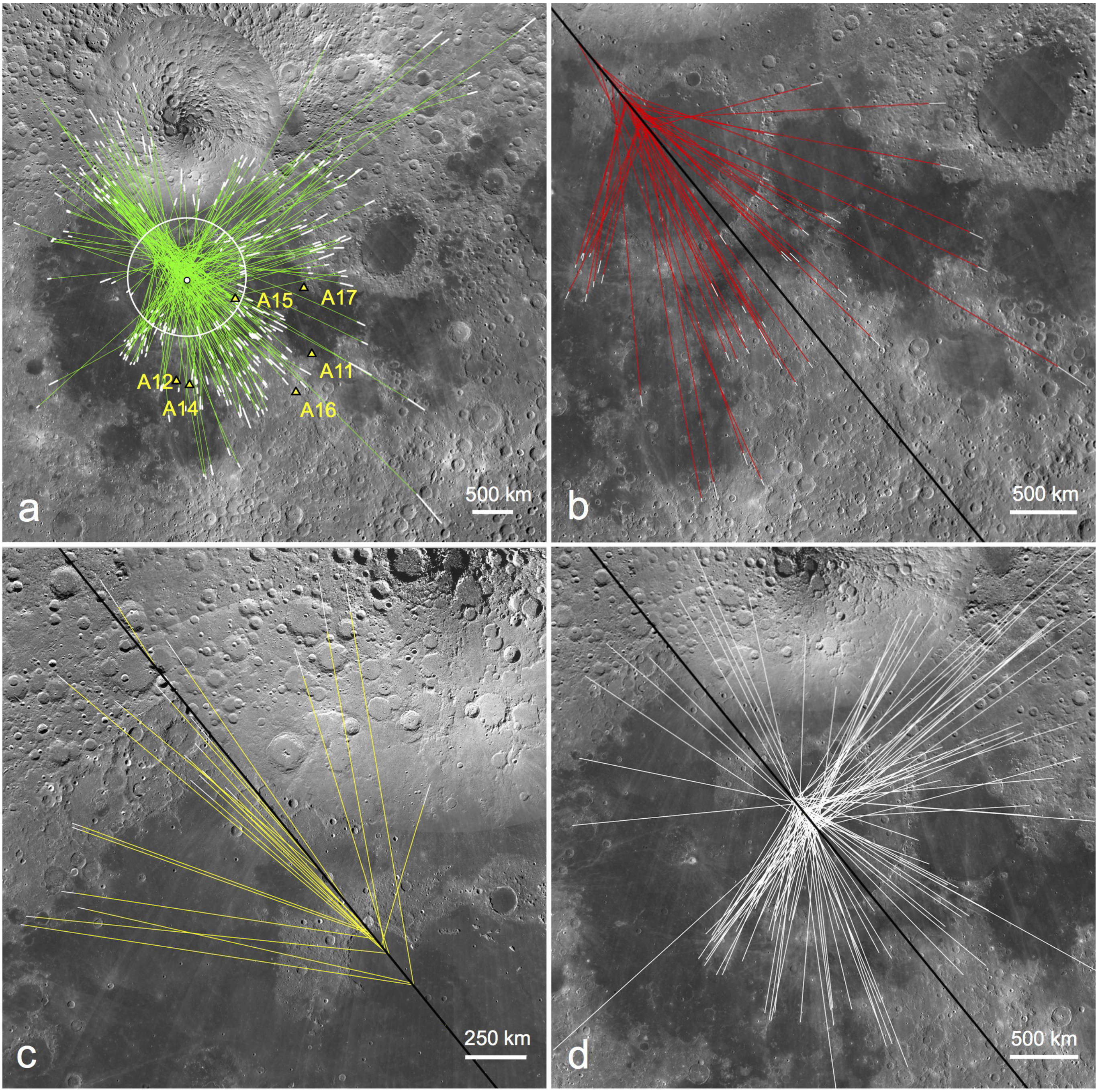

Extended Data Figure 3 | Mapped lineations extended as great circles into the Imbrium basin to assess sources during formation. a, Great circles extended from trends established by over 230 mapped grooves and elongate secondary craters related to the Imbrium basin (white circle). Locations of different Apollo landing sites are also identified. Lambert-conformal stereographic projection centred on Imbrium. **b**, Subset of trends from down-range secondaries that cross the trajectory more than 300 km northwest of the Imbrium centre. **c**, Subset of trends north of Imbrium intersecting the trajectory line well up range from the basin centre. **d**, Subset of great circles that cross the inferred Imbrium trajectory within a 300 km radius of its centre. The most distant secondaries have trends that converge slightly up range.

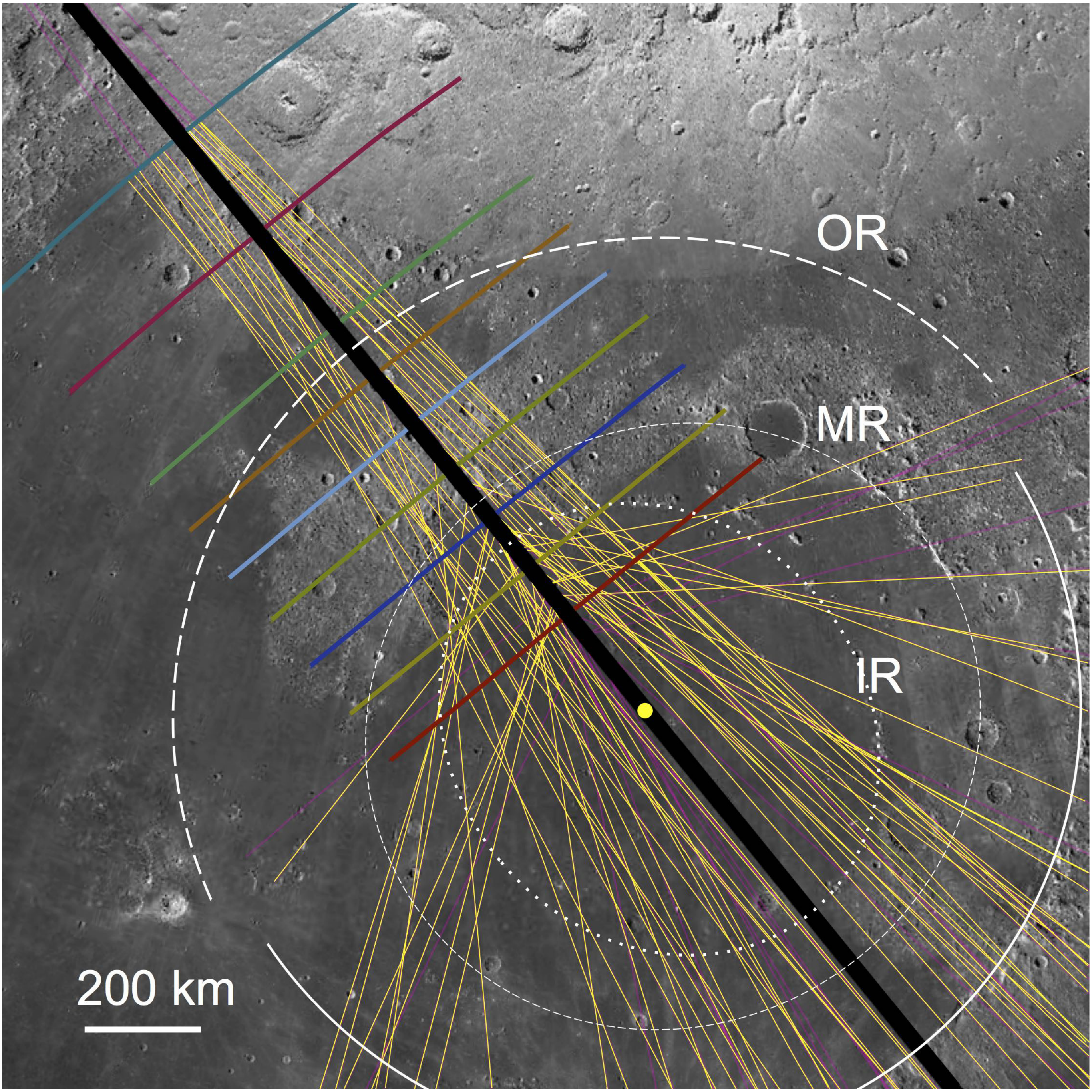

Extended Data Figure 4 | Subset of great circles of trends associated with down-range secondaries and grooves that cross the trajectory 300 km up range of its centre. One subset forms trends nearly paralleling the trajectory, consistent with sheared impactor fragments. Coloured lines orthogonal to the trajectory (black) are used to constrain the size of the impactor (Fig. 3c). Circles correspond to basin rings defined by relict massifs and wrinkle ridges. IR, inner oblong ring; MR, middle ring; OR, outer ring, which is delineated by two different arcs resulting from the up-range rim collapse.

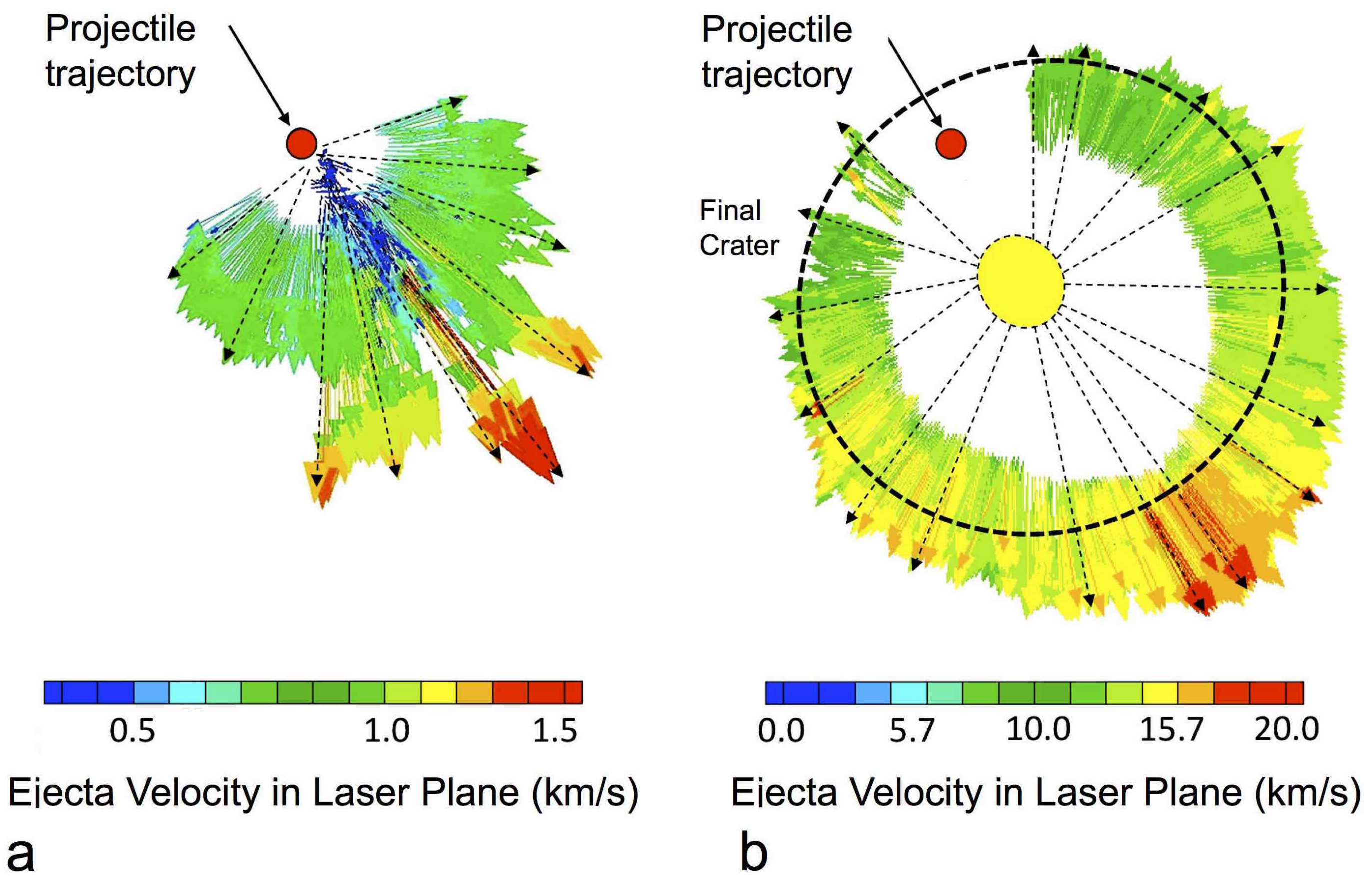

Extended Data Figure 5 | Evolution of trajectories from hypervelocity oblique impact experiments, illustrating the evolving source region during excavation. **a**, Early trajectory. **b**, Late trajectory. Packets of ejecta passing through a horizontal laser beam (using three-dimensional particle velocimetry) were captured in multiple cameras to establish in-flight trajectories at different times of crater growth. Modified from ref. 13 (**a**) and ref. 11 (**b**).

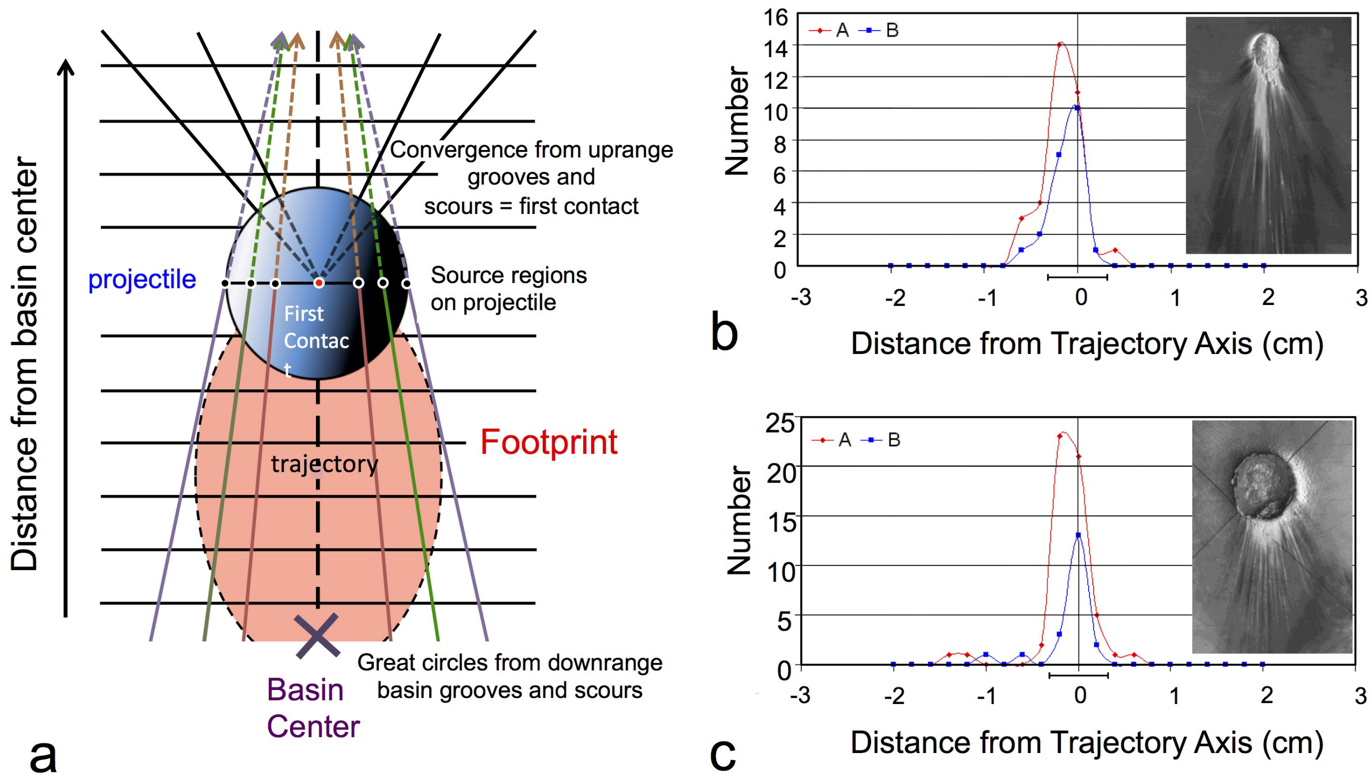

Extended Data Figure 6 | Strategies for determining the position of the impact point from mapped patterns on a target surface. **a**, Mapped trends of grooves and elongated trajectories down range that do not converge near the crater centre allow estimation of the size of the projectile. Convergence of trends from the up-range direction constrains the region of first contact. Convergence of trends intercepting a line orthogonal to the trajectory at the location set by the region of first contact constrains the diameter of the projectile. **b**, **c**, Convergence diagrams for 15° (**b**) and 30° (**c**) hypervelocity impacts into aluminium by 0.635 cm aluminium spheres onto planar targets. Grooves created by hypervelocity projectile debris converge and cross a reference line perpendicular to the trajectory at the up-range rim of the crater (line A) and 1.5 projectile diameters up range (line B). Well beyond the up-range rim (line B), the spray originates from spalls and shears from either side of the projectile and travels down range with little relative velocities directed away from the initial trajectory. Therefore, these components can be used to estimate the impactor diameter, consistent with 0.635 cm (indicated by the scale bar below).

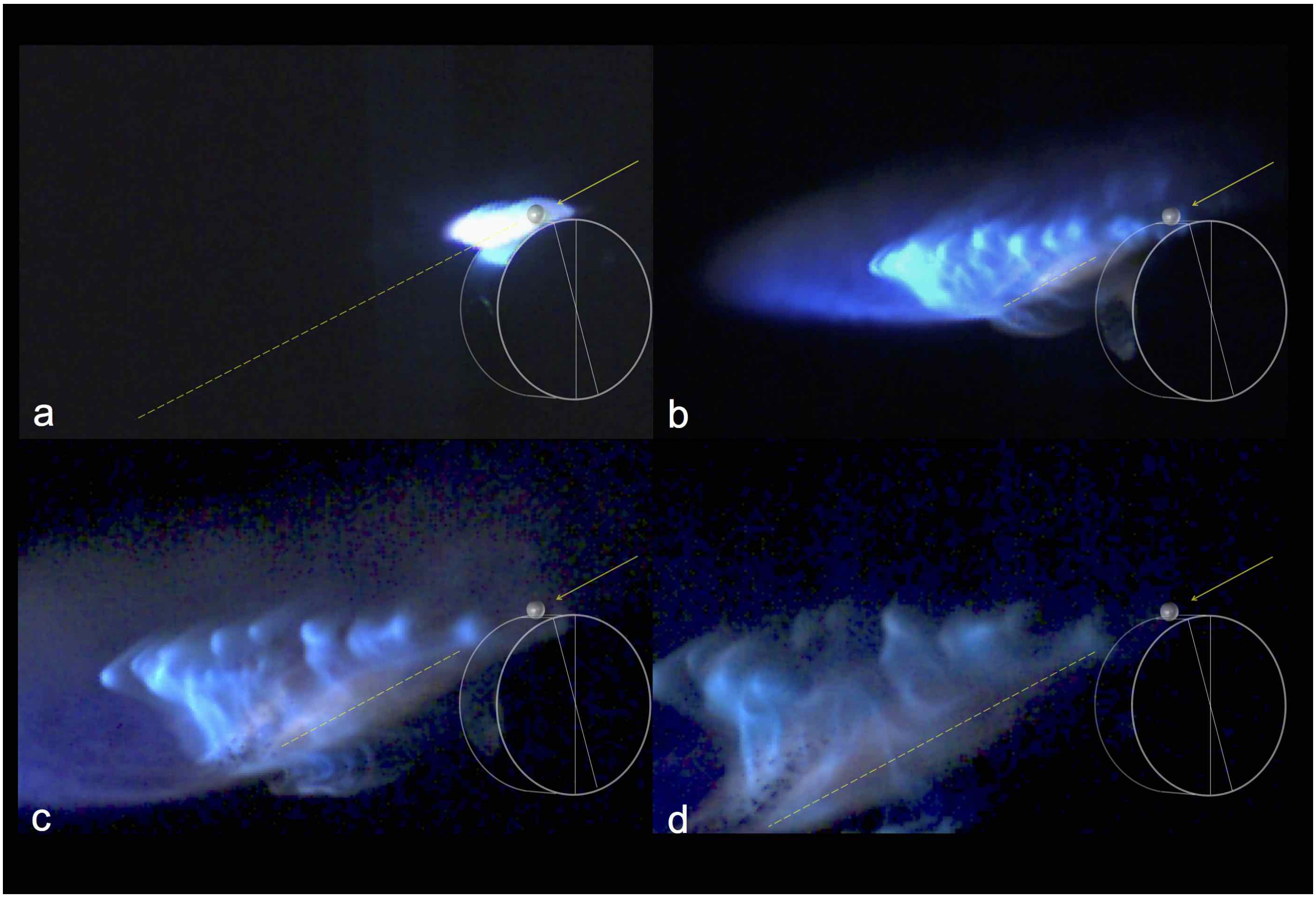

Extended Data Figure 7 | Fragmental debris resulting from a 0.635 cm aluminium sphere impacting a 6.7 cm aluminium disk at ~5 km s^{-1}. **a**–**d**, The launch angle was 30°, but because the impact point was not at the top of the disk, the actual impact angle was 20°. **a**, The top left frame shows the jetting phase (blue–white tongue-like extension). **b**, The jetting phase (15 μs later) shows the jetting phase, now a faint blue haze, and vapour (turbulent blue gas) with fragments emerging near and above the yellow dashed line (the crater seen below the impact on the disk was from a prior experiment). **c**, Still later, leading fragmental debris down range (near the yellow dotted line immersed in plasma) separate from the vapour phase along the initial trajectory. **d**, The fourth frame shows 8–10 large fragments (1–3 mm across) travelling close to the same speed as the initial impactor. Experiments were performed without artificial illumination and shows that the fragments are not notably heated. The aluminium sphere is represented graphically, and the aluminium disk is faintly outlined.

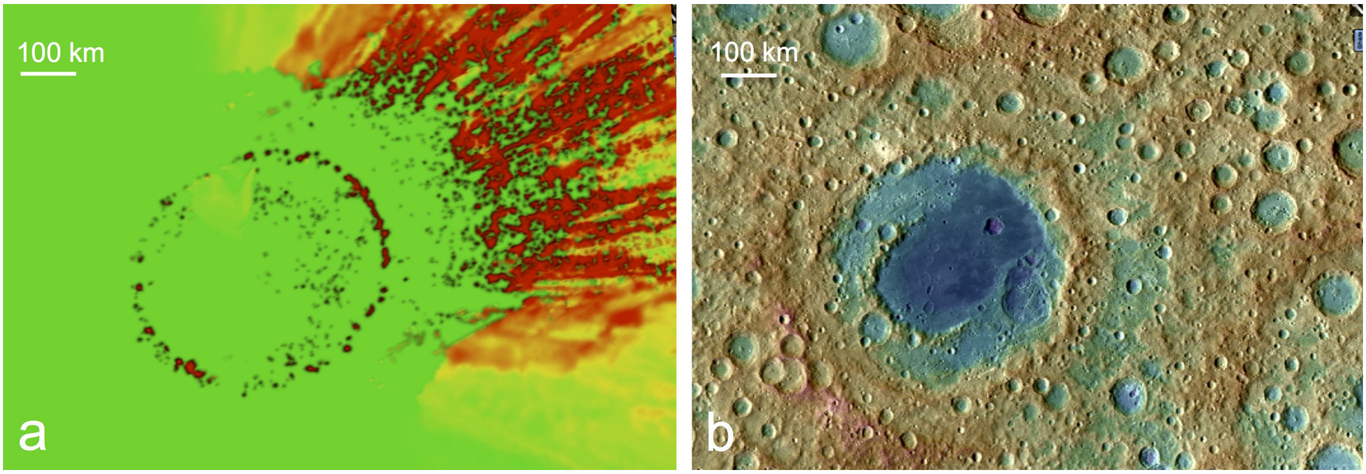

Extended Data Figure 8 | Comparing results of the CTH numerical model and the Moscoviense basin on the Moon from corresponding LOLA-DEM data without mapped lineations. a, The CTH model tracked where impactor fragments intersected the surface (in red). Beyond the rim, the linear red areas point towards the region of first contact, rather than the centre of the basin. See Fig. 3a for mapped lineations. Later ejecta (not shown) cover this evidence as identifiable units but their effects (grooves) remain preserved. **b**, The shaded relief map from the Lunar Laser Altimeter is shown here without the mapped lineations shown in Fig. 3b. Mapped lineations in Fig. 3b were based not only on topographic data but available images from Lunar Orbiter, Apollo and LROC wide-angle cameras.

Extended Data Table 1 | Comparison of selected transient basin diameters calculated from two scaling equations

Basin	Assumed impact speed	Actual rim-rim diameter (km)	Impactor diameter* (km)	Sand†		Wet Sand‡	
				D_{tA} (km)	D_{tR} (km)	D_{tA} (km)	D_{tR} (km)
Schrödinger		290	45				
	25 km/s			200	(250)	(280)	(440)
	15 km/s			170	210	230	350
Moscoviense		445	100				
	25 km/s			(390)	(480)	(380)	(480)
	15 km/s			320	(400)	(340)	(420)
	10 km/s			280	350	280	350
Orientale		930	110				
	25 km/s			420	520	460	570
	15 km/s			350	440	360	460
Imbrium		1250	250				
	25 km/s			830	1040	860	1080
	15 km/s			700	880	690	860

D_{tA} is the apparent transient crater diameter (referenced to the pre-impact surface). D_{tR} approximates the rim–rim transient crater (pre-collapse); rim collapse increases the diameter by another 25%. Parentheses indicate unreasonable values. Impact angles are assumed to be at 30° (except where noted). Values are rounded to two figures.

*Estimates for impactor diameter for Schrödinger and Orientale are from ref. 17.

†Constants and exponents from ref. 27.

‡Constants and exponents from ref. 19.

doi:10.1038/nature18639

Electron attraction mediated by Coulomb repulsion

A. Hamo[1]*, A. Benyamini[1]*, I. Shapir[1]*, I. Khivrich[1], J. Waissman[1]†, K. Kaasbjerg[1]†, Y. Oreg[1], F. von Oppen[2] & S. Ilani[1]

One of the defining properties of electrons is their mutual Coulomb repulsion. However, in solids this basic property may change; for example, in superconductors, the coupling of electrons to lattice vibrations makes the electrons attract one another, leading to the formation of bound pairs. Fifty years ago it was proposed[1] that electrons can be made attractive even when all of the degrees of freedom in the solid are electronic, by exploiting their repulsion from other electrons. This attraction mechanism, termed 'excitonic', promised to achieve stronger and more exotic superconductivity[2–6]. Yet, despite an extensive search[7], experimental evidence for excitonic attraction has yet to be found. Here we demonstrate this attraction by constructing, from the bottom up, the fundamental building block[8] of the excitonic mechanism. Our experiments are based on quantum devices made from pristine carbon nanotubes, combined with cryogenic precision manipulation. Using this platform, we demonstrate that two electrons can be made to attract each other using an independent electronic system as the 'glue' that mediates attraction. Owing to its tunability, our system offers insights into the underlying physics, such as the dependence of the emergent attraction on the underlying repulsion, and the origin of the pairing energy. We also demonstrate transport signatures of excitonic pairing. This experimental demonstration of excitonic pairing paves the way for the design of exotic states of matter.

Following the development of the Bardeen–Cooper–Schrieffer (BCS) theory of superconductivity[9], W. A. Little[1] proposed the idea that two electrons can attract each other not via phononic-based attraction, but via their repulsion from other electrons. He predicted that if electrons, which are much lighter than ions, mediate the attraction, then the electron pairing would be much stronger than in conventional superconductors. To test this new form of attraction, Little proposed a one-dimensional conducting organic chain (Fig. 1a, green) that has an array of polarizable sidechains ('polarizers', purple). Each polarizer has a single electron that can hop between two sites—one closer to and one further away from the main chain. Owing to Coulomb repulsion, an electron travelling down the main chain polarizes the side chains, which in turn attracts another electron in the main chain. This mechanism rapidly became popular in attempts to engineer unconventional superconductivity; it was extended to two dimensions[2,3], generalized to attraction at localized sites[10–14] and used in early attempts to explain high-T_c superconductivity[15]. It is considered a candidate for the unusual superconductivity[16,17] and pairing[18] observed in $SrTiO_3$ interfaces, and it has analogues in optical systems[19]. Numerous attempts have been made to directly synthesize organic materials that have the essential microscopic components[7]; however, so far there has not been any experimental evidence for an excitonic attraction between electrons.

At the core of Little's proposal is the idea that electrons separate into two groups: some form the 'system' (Fig. 1a, green), where their mutual interaction is to become attractive, while others make up the surrounding 'medium' (purple) that produces the 'glue' for the attraction. To make electrons attractive, this medium should perform the unusual feat of flipping the sign of the potential generated by the system electrons, making them look like holes to other system electrons (Fig. 1b). This suggests that the medium should effectively have a negative dielectric constant. Little suggested that this property can be achieved in the dynamic (retarded) limit, in which the system electrons respond faster than the medium, thus leaving a positive polarization cloud in their wake that creates an exponentially weak BCS-like pairing. However, Hirsch and Scalapino showed[5] that the interesting regime of Little's model is instead the static (instantaneous) limit. Only in that limit does superconductivity dominate over competing orders (such as charge and spin density waves) and the superconducting phase exhibit strong Bose–Einstein-condensation-like pairing.

Here we demonstrate that excitonic pairing is indeed possible and that the key ingredient is the discreteness of the electrons in the medium. We take a bottom-up approach and construct the minimal building block of Little's model that features excitonic attraction[8]—a two-site system and a single polarizer (Fig. 1a, dashed circle)—and show that when the polarizer interacts strongly with the system, it can render its electrons attractive.

The system and polarizer are created within two separate carbon nanotubes, each on its own microchip. We use our recently developed nano-assembly technique[20] to suspend each nanotube between two metallic contacts and above an array of gates (Supplementary Information section S1). In both devices we bias the gates to produce a double-well electrostatic potential along the nanotube length (Fig. 1c). In the polarizer device, the energy levels in the two wells are placed far from the chemical potential in the leads, but close to each other, such that a single electron can hop between the wells, but cannot escape to the leads. The polarizer thus operates as an isolated dipole whose sole degree of freedom is the polarization of its electron (Supplementary Information section S2). Conversely, in the system device, a large central barrier inhibits tunnelling between the two wells, but small side barriers allow electrons to enter from their corresponding leads. On a separately contacted side segment of the system nanotube, we create an independent quantum dot that serves as a charge detector, detecting the population of individual system electrons via weak electrostatic coupling. We then mount the two chips, oppositely facing and perpendicular to each other, in a custom-built scanning probe microscope inside a dilution refrigerator (Fig. 1d). The microscope allows us to control the distance and the coupling between the polarizer nanotube and the system nanotube (Fig. 1d inset) and, hence, to test whether the polarizer alters the behaviour of the system electrons in a fundamental way.

We first measure the charge stability diagram of the bare system, without the polarizer. Using the left and right gates of the system, we scan the potential detuning between the two wells, $\delta V = (V_L - V_R)/2$, and their mean potential, $V = (V_L + V_R)/2$. Changes in the electronic occupation of the system appear as steps in the charge-detector current, I_{CD} (Supplementary Information section S2). This measurement (Fig. 2a) yields the well-known charge stability diagram of a double

[1]Department of Condensed Matter Physics, Weizmann Institute of Science, Rehovot 76100, Israel. [2]Dahlem Center for Complex Quantum Systems and Fachbereich Physik, Freie Universität Berlin, 14195 Berlin, Germany. †Present addresses: Department of Physics, Harvard University, Cambridge, Massachusetts 02138, USA (J.W.); Department of Micro- and Nanotechnology, Technical University of Denmark, DK-2800 Kongens Lyngby, Denmark (K.K.).
*These authors contributed equally to this work.

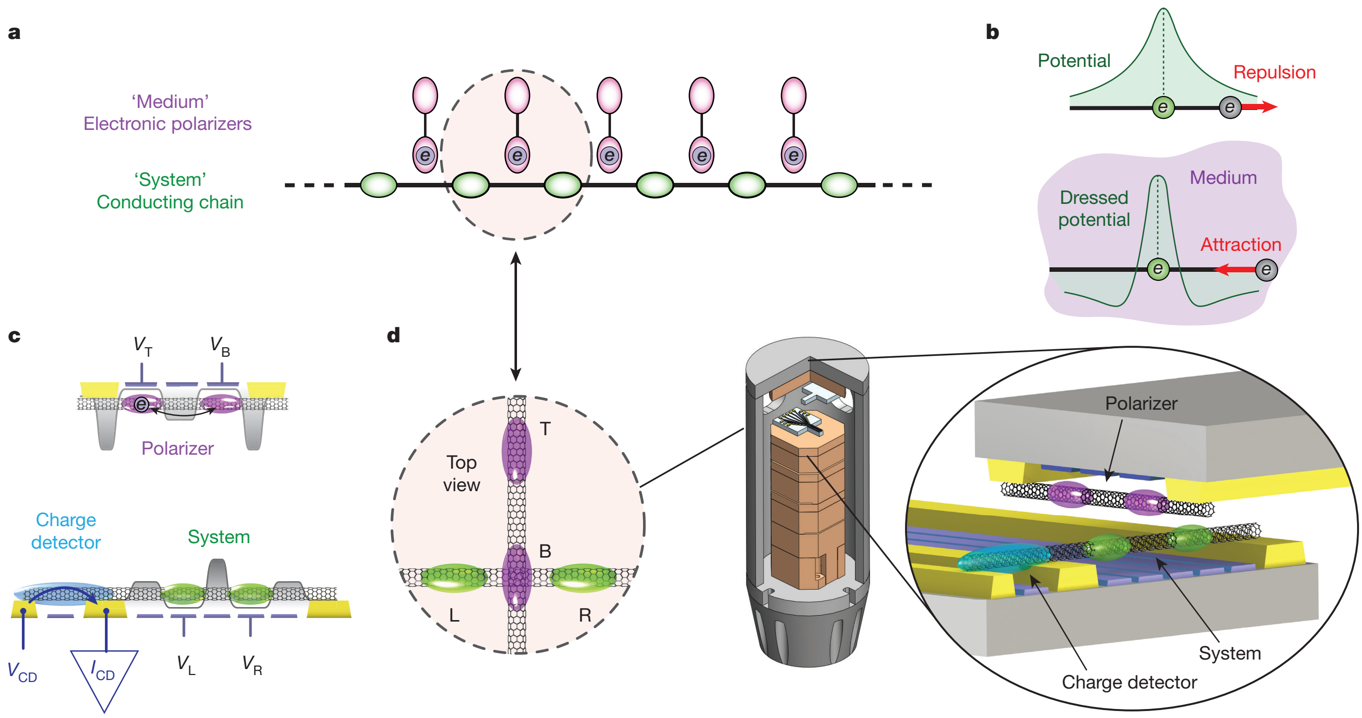

Figure 1 | Model system and experimental realization of its fundamental building block. a, The organic-molecule model system proposed by Little[1], consisting of two parts: the 'system', a one-dimensional conducting chain (individual lattice sites marked in green), and the 'medium', an array of side-chain 'polarizers' (purple) each having a single electron that can hop between a site close to, and a site further away from, the chain. The fundamental unit block that manifests attraction is a two-site system with one polarizer (dashed circle). **b**, In a bare electronic system (top) an electron creates a repulsive Coulomb potential (green). Embedding it in a medium that flips the sign of its potential (bottom) will make this electron attractive to other electrons. **c**, Implementation of the two components ('polarizer' and 'system') that make up the fundamental building block. These are fabricated as two separate devices, each having a pristine nanotube assembled on contacts (yellow) and suspended above an array of gates (blue), which set the potential landscape for the electrons (grey) (see Supplementary Information section S1 for dimensions). The polarizer device (top) has two gate voltages, V_B and V_T, that control the potentials of the bottom and top dots (purple), and is operated as an isolated dipole, whose sole degree of freedom is that of a single electron hopping between the sites. The system device (bottom) has two gate voltages, V_L and V_R, that control the potentials of the right and left dots (green). Here the central barrier is opaque and the side barriers are relatively transparent such that electrons enter the two dots from their corresponding leads. An additional dot on a side segment of the same nanotube (blue) serves as a single electron transistor charge detector: a voltage bias across it, V_{CD}, leads to current, I_{CD}, that is sensitive to the population of the system dots through weak electrostatic coupling. **d**, A custom-built scanning probe microscope (centre), operating inside a dilution refrigerator, brings the two oppositely facing devices into proximity (about 100–150 nm apart) such that the polarizer nanotube is perpendicular to the system nanotube (right) and such that one of its dots is directly above the system while the other is further away (left), creating a structure that is analogous to that of Little's molecule.

quantum dot with repulsive electrons (explained in Supplementary Information section S3). Tilted charging lines reflect the addition of a single electron to the right or left dot. Near their crossing, the charging lines exhibit a vertical shift (Fig. 2a, dashed black line), reflecting the fact that if one dot is occupied the energy to populate the other dot is increased by the Coulomb repulsion between the neighbouring electrons. This vertical shift is thus a direct fingerprint of the nearest-neighbour electron repulsion, and its magnitude normalized to energy units yields the strength of this repulsion, $W = 830\,\mu\text{eV}$.

Fundamentally different behaviour is observed when the polarizer is brought into close proximity to the system. In this case, we measure a charge stability diagram with an interaction line that is rotated from vertical to horizontal (Fig. 2b). This rotation implies that the polarizer inverts the interaction between the system electrons from repulsive to attractive. The inversion is best understood by realizing that the ground states at the centre of the two charge stability diagrams are fundamentally different: in the bare system it is a degenerate state between having a single electron on the left or the right dot (labelled (1, 0) and (0, 1)); with the polarizer nearby it becomes a paired ground state having a degeneracy between the two states with an even electron number (labelled (0, 0) and (1, 1)). The odd states, (1, 0) and (0, 1), become excited states, separated from the ground state by a pairing gap Δ. This gap is maximal at the centre of the horizontal vertex, where its magnitude is given by the length of this vertex (2Δ after normalization; see Supplementary Information section S4), reaching $\Delta = 790\,\mu\text{eV} \approx 8\,\text{K}$.

A medium can transform repulsive system electrons to attractive electrons only if it can flip the sign of the electrostatic potential produced by these electrons. The Coulomb potential of a bare electron is positive in its local and neighbouring sites, implying on-site and nearest-neighbour repulsion (Fig. 2c). If the on-site repulsion is retained while flipping the potential sign at the nearest-neighbour site, then the system remains stable, but acquires nearest-neighbour attraction. However, any medium based on continuum classical electrostatics can at best screen a potential to zero, but cannot flip its sign (Fig. 2d). We therefore seek to understand what the special feature of our polarizer medium is that enables such sign inversion.

The key element for a sign-inverting medium is charge discreteness[21] and, more fundamentally, the fact that a single electron does not repel itself. To understand this, compare the screening by a single-electron dipole to that of a metallic object of similar geometry (Fig. 2e). In a small external field, the charge in the metal will polarize slightly to exactly null the internal field. Conversely, in a dipole with small inter-site tunnelling, an entire electron will polarize between the two sites, creating an internal field that is much larger than, and of opposite sign to, the external field. This behaviour is the basis for our basic 'sign-inverter'. Unlike continuous charge in a metal that experiences its own field and thus minimizes the electrostatic energy by nulling the internal

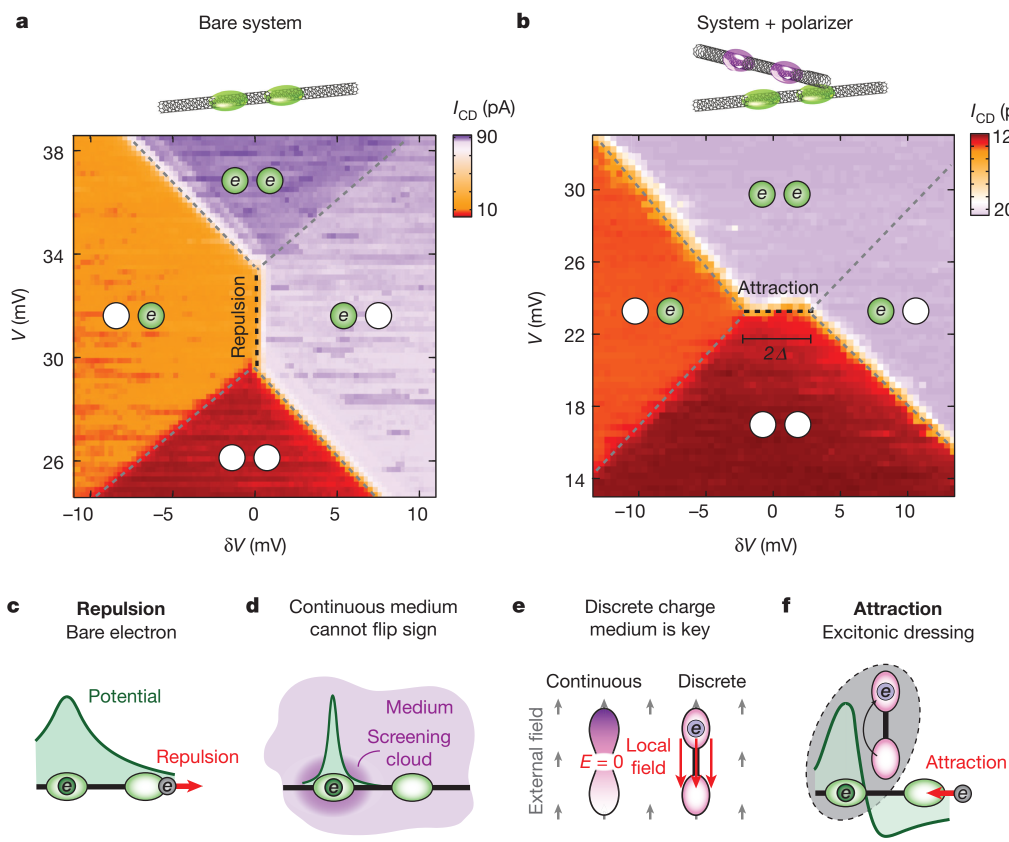

Figure 2 | From repulsive to attractive electrons. **a**, Measured charge stability diagram of the bare system: charge detector current (I_{CD}, colour scale) plotted as a function of the voltage detuning between its right (R) and left (L) sites, $\delta V = (V_{\mathrm{L}} - V_{\mathrm{R}})/2$, and the mean gate voltage, $V = (V_{\mathrm{L}} + V_{\mathrm{R}})/2$. Steps in I_{CD} (dashed grey lines) correspond to single electrons populating the L/R sites (green/white circles label an electron presence/absence). The middle vertical shift (black dashed line) is a direct measure of the Coulomb repulsion between the neighbouring electrons (see text). **b**, Similar charge stability diagram to **a**, but with the polarizer nanotube positioned nearby (approximately 125-nm separation between the nanotubes). The interaction vertex is now horizontal, reflecting an attraction between the electrons. Along this line (dashed black) the ground state is degenerate between the two even states (0, 0) and (1, 1) ((n_{L}, n_{R}) represents the number of electrons in the L and R dots), whereas the odd states (1, 0) and (0, 1) are the excited states, separated by a pairing gap Δ from the ground state. This gap is maximal at the centre of the horizontal line, and its magnitude there is equal to the length of this line (2Δ when normalized to energy units; see Supplementary Information section S4). Note that the charge detector is far away from the right dot and that when the polarizer is close their mutual capacitance is strongly screened and so the charging lines of this dot are harder to observe. **c**, In the bare system, an electron populating the L site generates a Coulomb potential (green) that is positive (repulsive) in both the L and R sites. **d**, Embedding the system in a medium based on continuum electrostatics (purple) can at best screen the potential to zero far away from the electron, but cannot flip its sign. **e**, The key element for sign inversion is charge discreteness: a single-electron dipole (right) and a similarly shaped metal (left) will screen an external field differently (grey arrows). In the latter the internal field is nulled, whereas in the former it is larger and of opposite sign to the external field (red arrows; over-screening). This behaviour is rooted in the fact that an electron does not repel itself (see text). **f**, With a nearby polarizer, an electron charging the system gets dressed by the polarization (grey ellipse). The electrostatic potential (green) of the dressed particle will be substantially different to that of the bare electron (calculated in Supplementary Information section S4). Note that all the measurements presented here were done with single holes instead of single electrons, but to avoid unnecessary confusion we presented the physics in the language of electrons.

field, a single electron does not feel its own field and so can generate a large over-screening internal field, as long as this minimizes its single-particle energy.

To analyse the sign inversion microscopically, for the geometry of our system, we describe the polarizer by the Hamiltonian

$$H_{\mathrm{pol}} = \frac{1}{2}\delta\hat{\sigma}_Z + t\hat{\sigma}_X \qquad (1)$$

in which $\hat{\sigma}_Z = \psi_{\mathrm{T}}^{\dagger}\psi_{\mathrm{T}} - \psi_{\mathrm{B}}^{\dagger}\psi_{\mathrm{B}}$, $\hat{\sigma}_X = \psi_{\mathrm{T}}^{\dagger}\psi_{\mathrm{B}} + \psi_{\mathrm{B}}^{\dagger}\psi_{\mathrm{T}}$, $\psi_{\mathrm{T}}^{\dagger}$ (ψ_{T}) and $\psi_{\mathrm{B}}^{\dagger}$ (ψ_{B}) are creation (annihilation) operators of electrons in the two polarizer sites ('T', top; 'B', bottom), $\delta = \epsilon_{\mathrm{T}} - \epsilon_{\mathrm{B}}$ is the energy detuning between these sites, t is the tunnelling amplitude, and we ignored a constant energy offset. The repulsion between system and polarizer electrons leads to a charge–dipole coupling

$$H_{\mathrm{coup}} = \frac{1}{2}U(n_{\mathrm{L}} + n_{\mathrm{R}})(\hat{I} - \hat{\sigma}_Z) \qquad (2)$$

in which n_{L} and n_{R} are the populations of the left and right system sites, U is the repulsion between an electron in one of these sites and an electron in the bottom site of the polarizer (assuming negligible interaction with the top site), and $\hat{I} = \psi_T^{\dagger}\psi_T + \psi_B^{\dagger}\psi_B$. This coupling dresses an electron entering the system with a dipolar excitation of the polarizer (Fig. 2f). In the strong coupling limit[5] ($U > t$, applicable to the measurements in Fig. 2b), the electron is dressed by a fully polarized dipole, and the effective potential of the dressed particle is considerably different from that of the bare electron (Supplementary Information section S4). If the charge–dipole coupling exceeds the charge–charge repulsion within the system

$$H_{\mathrm{repulsion}} = W n_{\mathrm{L}} n_{\mathrm{R}} \qquad (3)$$

that is, $U > W$, then the dressed potential at the neighbouring site has a flipped sign, implying that another electron is attracted to the dressed particle. This attraction reflects the fact that the neighbouring electron is more strongly attracted to the vacancy formed in the bottom site of

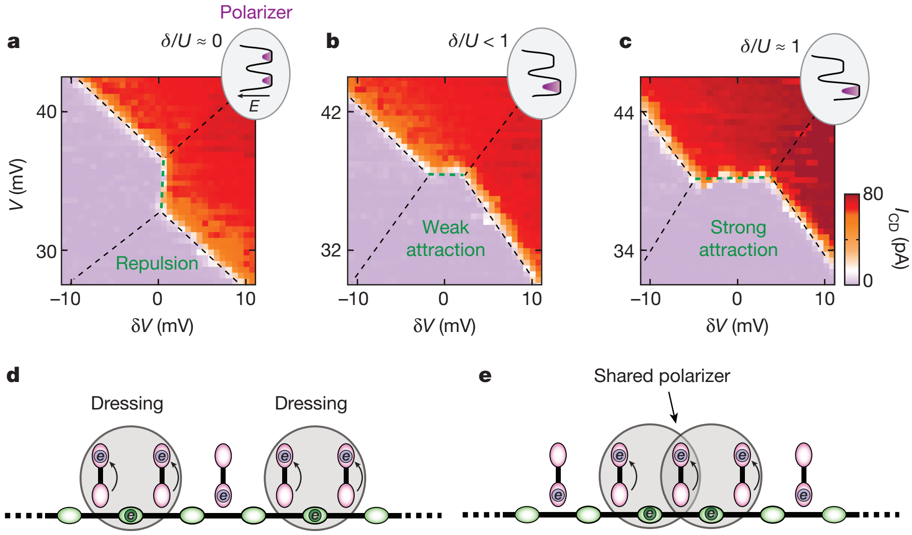

Figure 3 | Dependence of pairing energy on the polarizer detuning and the origin of the pair binding energy. **a**–**c**, Charge stability diagrams similar to those in Fig. 2b, measured for different energy detunings of the polarizer: $\delta = 0.39$ meV (**a**), 1.01 meV (**b**) and 2.57 meV (**c**). The observed attraction increases linearly with δ (more data in Supplementary Information section S6). The insets show the polarizer potential wells for the different detuning values. **d**, **e**, Rationalizing this observation using a toy model of the chain: two spatially separated electrons in the chain are each dressed by the polarization of their two adjacent polarizers (**d**); when the electrons are nearest neighbours, they share the centre polarizer and thus need to polarize one fewer polarizer (**e**). The energy gain, which gives the pairing energy, is consequently equal to δ, as we observe in the experiments in **a**–**c**. A similar polarizer-sharing argument holds for the two-site case, as is explained in Supplementary Information section S6.

the polarizer than it is repelled by the original electron that triggered the polarization.

A central prediction of the above model is a direct relationship between the emergent attraction and the underlying repulsion. We test this prediction by changing the separation between the nanotubes, which modifies the repulsion between system and polarizer electrons (U) while keeping the repulsion between the system electrons (W) fixed. The measured dependence of 2Δ on U (Supplementary Fig. 6) shows a linear dependence with unit slope. This result follows from equations (1)–(3) in the strong coupling limit (Supplementary Information section S4) and is a demonstration that the observed attraction is driven by repulsion.

Because the ability of the polarizer to dress an electron depends on its polarizability, one might expect that the optimal polarizer detuning for creating the strongest pairing would be at zero detuning ($\delta = 0$). At this detuning, the electronic wavefunction of the polarizer is symmetrically split between its top and bottom sites and its polarizability is maximal. However, the measured charge stability diagrams at different detunings (Fig. 3a–c) show that the attractive correction to the bare repulsion is not maximal at $\delta = 0$, but rather increases linearly with δ. This observation captures an important point about the origin of the pair binding energy, which is most easily rationalized by considering a toy model of a multisite chain (Fig. 3d, e): two far-apart electrons on the chain would each be dressed by two adjacent polarizers (Fig. 3d). In contrast, nearest-neighbour electrons share one polarizer and thus gain the polarization energy of one polarizer (Fig. 3e). This energy gain constitutes the pair binding energy, which is exactly equal to δ, the stored energy in a polarizer. This is indeed what we observe experimentally. The same mechanism of sharing the dressing costs, leading to a pairing energy of magnitude δ, also holds in our two-site case, as we explain in Supplementary Information section S6.

Beyond the ground-state stability diagram, we also examine whether pairing is reflected in transport, that is, whether electrons enter the system in pairs. In our set-up, we can measure the current through the polarizer and deduce the behaviour of the system via its strong correlations with the polarizer. To simplify the measurement, we open the barrier to one of the polarizer dots to strongly couple it to the lead, making the polarizer effectively a single quantum dot coupled to two leads (Fig. 4a). Now, the polarization is between dot and lead rather than between two dots. Although these two cases are electrostatically quite similar, they are fundamentally very different: whereas the excitonic polarization of an isolated double dot preserves the overall fermion parity of the combined system and polarizer, tunnelling of an electron to a lead in the polarizer does not. Yet, establishing pairing also in the latter configuration opens possibilities to create quantum systems with engineered dissipation, which may help to stabilize one-dimensional superconductivity[22].

Figure 4b shows the measured polarizer current, I_{pol}, with source–drain bias $V_{SD} = -1.3$ mV as a function of its local gate voltage, V_B, exhibiting a standard Coulomb blockade peak when the occupation of the polarizer dot is free to fluctuate. Owing to the strong coupling to the system, the peak position depends strongly on the electronic occupation of the system (Fig. 4b). If we fix V_B at 241.5 mV (dashed line in Fig. 4b), then the polarizer conducts for the odd system occupations (1, 0) and (0, 1), but is blocked for the even states. The Coulomb peak is pushed well below the Fermi energy for the (0, 0) state and well above it for the (1, 1) state. This behaviour persists throughout the charge stability diagram of the system (Fig. 4c, $V_{SD} = 100\,\mu$V), showing finite current (red) for odd states and negligible current (blue) for even states. Notably, the attraction survives even in the dynamic regime with tunnelling rates being a substantial fraction of the repulsion ($\Gamma_{pol}/U \approx 0.2$, $\Gamma_R/U \approx 0.45$ and $\Gamma_L/U \approx 0.23$, where $\Gamma_{L,R,pol}$ are the tunnelling rates to the left and right contacts of the system and to the polarizer contacts, respectively). Although neither the (0, 0) nor the (1, 1) states support single-particle current, we observe a finite current peak along their degeneracy line[23,24] (indicated by the arrow in Fig. 4c). Theoretical calculations (Fig. 4d) reproduce this peak only when including correlated many-body events in which an electron hopping in and out of the polarizer is accompanied by a pair of electrons simultaneously co-tunnelling out of and into the system (Supplementary Information section S7).

To better understand the processes underlying the observed current peak, we measure the current along a cut perpendicular to the degeneracy line, as a function of αV (where α, the independently measured lever-arm, normalizes V to energy units) and for varying V_{SD} (Fig. 4e). In different bias ranges we observe conductance regimes that differ in their turn-on slope, $s = dV_{SD}/d(\alpha V)$, which reflects the number of system electrons participating coherently in the dominant conductance

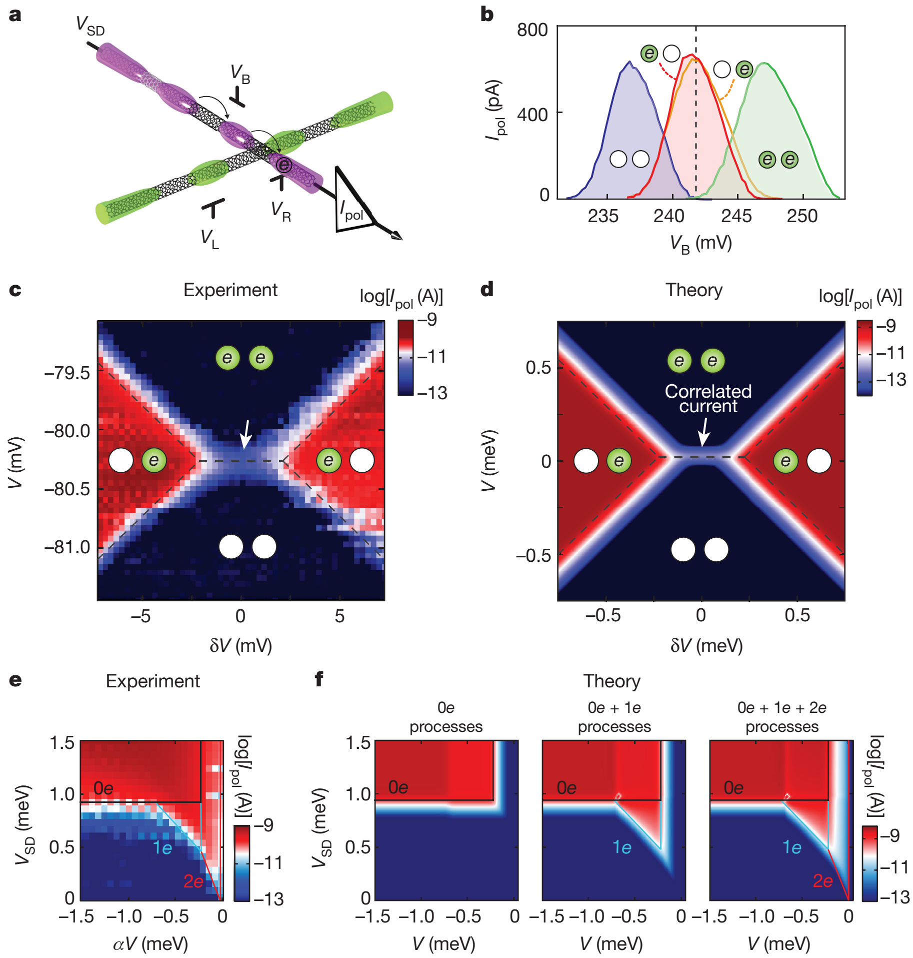

Figure 4 | Transport measurements. a, Experimental configuration. The polarizer current, I_{pol}, is measured with a finite bias on one lead, V_{SD}. The barrier between this lead and its nearby dot is reduced such that the dot becomes strongly connected to the lead, effectively making the polarizer nanotube a single quantum dot device with two leads. Compared to the experiments presented in Figs 2 and 3, in which the polarization occurred internally between two dots, here the polarization is between the dot and its lead. **b**, I_{pol} measured as a function of the local gate voltage, V_B, for four different population states of the system: blue, (0, 0); red, (1, 0); orange, (0, 1); green, (1, 1). In these measurements, the system charge remained fixed by staying far away from the charging lines of the system. This measurement was performed at a high bias, $V_{SD} = -1.3$ mV, which widens the observed charging lines. The vertical dashed line indicates the gate voltage V_B used in **c**. **c**, I_{pol} (colour scale) measured at $V_{SD} = 100\,\mu$V as a function of the voltage detuning between the L and R system sites, $\delta V = (V_L - V_R)/2$, and the mean voltage, $V = (V_L + V_R)/2$. Finite current (red) is observed for the odd system states, (1, 0) and (1, 0), and negligible current (blue) is measured for the even states, (0, 0) and (1, 1), except for a special peak of finite current (indicated by the white arrow) appearing along their degeneracy line. **d**, A theoretical master-equation calculation of I_{pol} for the parameters of the experiment (Supplementary Information section S7). The theoretical result features a finite current peak on the degeneracy line between the (0, 0) and (1, 1) states only when considering correlated processes that involve co-tunnelling of a pair of electrons into the system in concert with an electron tunnelling out of the polarizer. **e**, I_{pol} (colour scale) measured along a line cutting through the centre of the degeneracy line as a function αV and V_{SD} (the independently measured lever-arm, $\alpha = 0.61$, normalizes V to energy units). Three regimes appear at different bias ranges, differing in their turn-on slope, $s = dV_{SD}/(\alpha V)$, the value of which ($s \approx 0$, black line; $s \approx 1$, blue line; $s \approx 2$, red line) reflects the number of system electrons participating in the dominant transport process (0e, 1e or 2e, respectively) (see Supplementary Information section S7). **f**, Theoretical master-equation calculation of I_{pol} versus αV and V_{SD} with only a 0e system process considered (left), with 0e + 1e processes (middle) and with 0e + 1e + 2e processes (left). The 2e processes, which involve a pair tunnelling in the system, are the dominant processes at low bias, as is observed experimentally, although their calculated amplitude is lower than in the experiment, probably because the theory considers them to only the lowest order in tunnelling (Supplementary Information section S7).

process ($s = 0$, 1 and 2 corresponds to processes with zero, one and two system electrons, respectively). At high bias, $V_{SD} > 925\,\mu\text{eV} \approx U$, we observe $s \approx 0$ (Fig. 4e, black line), showing that a polarizer electron with enough energy to overcome its interaction with the system electrons (U) can flow without their cooperation. At intermediate bias, $V_{SD} > 490\,\mu$eV, the observed slope is $s \approx 1$ (Fig. 4e, blue line), reflecting simultaneous co-tunnelling of one system electron. Below this, and down to zero bias, the slope is $s \approx 2$ (Fig. 4e, red line), indicating that at low energies a pair of electrons co-tunnels into the system in concert with an electron tunnelling out of the polarizer. Theoretical calculations (Fig. 4f and Supplementary Information section S7) reproduce the main features, although they give a smaller two-electron current than is observed experimentally, probably because they consider these processes to only the lowest order in tunnelling.

Our work experimentally establishes the fundamental concept of excitonic pairing of electrons that was theorized half a century ago. The ability to construct the basic building block of electronic attraction raises many questions regarding the possibility of engineering exotic states of matter by generalizing this concept to larger systems, for example, whether it would be possible to create an artificial superconductor, what kind of pairing such a superconductor would have, and whether it would be stable against competing ground states (see Supplementary Information section S8 for further discussion). The benefit of repulsion-driven attraction is that the pairing energy of the

attraction increases linearly with decreasing device dimensions. Our experiments achieved pairing energies of about 8 K with rather large quantum dots (approximately 400 nm). By extrapolating this value to the nanometre scale, we postulate that it should be possible to reach energies well in excess of room temperature. Given the tremendous progress in engineering quantum dots in two-dimensional semiconductors[25–28], down to almost single-atom scale[29], the possibilities to engineer interesting states of matter based on electronic attraction now seem very promising.

Received 17 January; accepted 26 May 2016.

1. Little, W. A. Possibility of synthesizing an organic superconductor. *Phys. Rev.* **134,** A1416–A1424 (1964).
2. Ginzburg, V. L. Concerning surface superconductivity. *Sov. Phys. JETP* **20,** 1549–1550 (1964).
3. Allender, D. & Bardeen, J. Model for an exciton mechanism of superconductivity. *Phys. Rev. B* **7,** 1020–1029 (1973).
4. Ginzburg, V. L. High-temperature superconductivity—dream or reality? *Sov. Phys. Usp*. **19,** 174–179 (1976).
5. Hirsch, J. E. & Scalapino, D. J. Excitonic mechanism for superconductivity in a quasi-one-dimensional system. *Phys. Rev. B* **32,** 117–134 (1985).
6. Micnas, R., Ranninger, J. & Robaszkiewicz, S. Superconductivity in narrow-band systems with local nonretarded attractive interactions. *Rev. Mod. Phys.* **62,** 113–171 (1990).
7. Jérome, D. in *The Physics of Organic Superconductors and Conductors* (ed. Lebed, A.) 3–16 (Springer, 2008).
8. Raikh, M. E., Glazman, L. I. & Zhukov, L. E. Two-electron state in a disordered 2D island: pairing caused by the coulomb repulsion. *Phys. Rev. Lett.* **77,** 1354–1357 (1996).
9. Bardeen, J., Cooper, L. & Schrieffer, J. Microscopic theory of superconductivity. *Phys. Rev.* **106,** 162–164 (1957).
10. Hirsch, J. E. & Scalapino, D. J. Double-valence-fluctuating molecules and superconductivity. *Phys. Rev. B* **32,** 5639–5643 (1985).
11. Varma, C. Missing valence states, diamagnetic insulators, and superconductors. *Phys. Rev. Lett.* **61,** 2713–2716 (1988).
12. Matsushita, Y., Bluhm, H., Geballe, T. H. & Fisher, I. R. Evidence for charge Kondo effect in superconducting Tl-doped PbTe. *Phys. Rev. Lett.* **94,** 157002 (2005).
13. Butler, M. R., Movaghar, B., Marks, T. J. & Ratner, M. A. Electron pairing in designer materials: a novel strategy for a negative effective Hubbard U. *Nano Lett.* **15,** 1597–1602 (2015).
14. Oganesyan, V., Kivelson, S., Geballe, T. & Moyzhes, B. Josephson tunneling spectroscopy of negative-U centers. *Phys. Rev. B* **65,** 172504 (2002).
15. Hirsch, J. E., Tang, S., Loh, E. Jr & Scalapino, D. J. Pairing interaction in two-dimensional CuO_2. *Phys. Rev. Lett.* **60,** 1668–1671 (1988).
16. Ge, J. *et al.* Superconductivity above 100 K in single-layer FeSe films on doped $SrTiO_3$. *Nat. Mater.* **14,** 285–289 (2015).
17. Richter, C. *et al.* Interface superconductor with gap behaviour like a high-temperature superconductor. *Nature* **502,** 528–531 (2013).
18. Cheng, G. *et al.* Electron pairing without superconductivity. *Nature* **521,** 196–199 (2015).
19. Firstenberg, O. *et al.* Attractive photons in a quantum nonlinear medium. *Nature* **502,** 71–75 (2013).
20. Waissman, J. *et al.* Realization of pristine and locally tunable one-dimensional electron systems in carbon nanotubes. *Nat. Nanotechnol.* **8,** 569–574 (2013).
21. Averin, D. V. & Bruder, C. Variable electrostatic transformer: controllable coupling of two charge qubits. *Phys. Rev. Lett.* **91,** 057003 (2003).
22. Lobos, A. M., Iucci, A., Müller, M. & Giamarchi, T. Dissipation-driven phase transitions in superconducting wires. *Phys. Rev. B* **80,** 214515 (2009).
23. Goldstein, M., Berkovits, R. & Gefen, Y. Population switching and charge sensing in quantum dots: a case for a quantum phase transition. *Phys. Rev. Lett.* **104,** 226805 (2010).
24. Yoo, G., Park, J., Lee, S.-S. B. & Sim, H.-S. Anisotropic charge Kondo effect in a triple quantum dot. *Phys. Rev. Lett.* **113,** 236601 (2014).
25. Medford, J. *et al.* Quantum-dot-based resonant exchange qubit. *Phys. Rev. Lett.* **111,** 050501 (2013).
26. Braakman, F., Barthelemy, P., Reichl, C., Wegscheider, W. & Vandersypen, L. M. K. Long-distance coherent coupling in a quantum dot array. *Nat. Nanotechnol.* **8,** 432–437 (2013).
27. Seo, M. *et al.* Charge frustration in a triangular triple quantum dot. *Phys. Rev. Lett.* **110,** 046803 (2013).
28. Delbecq, M. R. *et al.* Full control of quadruple quantum dot circuit charge states in the single electron regime. *Appl. Phys. Lett.* **104,** 183111 (2014).
29. Fölsch, S., Martínez-Blanco, J., Yang, J., Kanisawa, K. & Erwin, S. C. Quantum dots with single-atom precision. *Nat. Nanotechnol.* **9,** 505–508 (2014).

Supplementary Information is available in the online version of the paper.

Acknowledgements We thank E. Altman, E. Berg, Y. Gefen, M. Goldstein, U. Leonhardt, G. Refael and A. Yacoby for discussions and D. Mahalu for the e-beam writing. K.K. acknowledges support from the Carlsberg Foundation. Y.O. acknowledges support by Minerva, BSF and ERC Adg grant (FP7/2007-2013 340210). F.v.O. acknowledges support through SPP 1459 and SFB 658. S.I. acknowledges financial support by the ERC Cog grant (See-1D-Qmatter, No. 647413).

Author Contributions A.H., A.B., I.S. and S.I. performed the experiments, analysed the data, contributed to its theoretical interpretation and wrote the paper. I.S. built the scanning probe microscope. I.K. built the custom measurement instrumentation for the experiment. J.W. designed and fabricated the devices. K.K., Y.O. and F.v.O. developed the theoretical model. K.K. performed the theoretical simulations.

Author Information Reprints and permissions information is available at www.nature.com/reprints. The authors declare no competing financial interests. Readers are welcome to comment on the online version of the paper. Correspondence and requests for materials should be addressed to S.I. (shahal.ilani@weizmann.ac.il).

Reviewer Information *Nature* thanks R. Egger, T. Kontos and E. Scheer for their contribution to the peer review of this work.

doi:10.1038/nature18287

Engineering and mapping nanocavity emission via precision placement of DNA origami

Ashwin Gopinath[1], Evan Miyazono[2], Andrei Faraon[2] & Paul W. K. Rothemund[1,3,4]

Many hybrid devices integrate functional molecular or nanoparticle components with microstructures, as exemplified by the nanophotonic devices that couple emitters to optical resonators[1] for potential use in single-molecule detection[2,3], precision magnetometry[4], low threshold lasing[5,6] and quantum information processing[7–12]. These systems also illustrate a common difficulty for hybrid devices: although many proof-of-principle devices exist, practical applications face the challenge of how to incorporate large numbers of chemically diverse functional components into microfabricated resonators at precise locations. Here we show that the directed self-assembly[13,14] of DNA origami[15] onto lithographically patterned binding sites allows reliable and controllable coupling of molecular emitters to photonic crystal cavities (PCCs). The precision of this method is sufficient to enable us to visualize the local density of states within PCCs by simple wide-field microscopy and to resolve the antinodes of the cavity mode at a resolution of about one-tenth of a wavelength. By simply changing the number of binding sites, we program the delivery of up to seven DNA origami onto distinct antinodes within a single cavity and thereby digitally vary the intensity of the cavity emission. To demonstrate the scalability of our technique, we fabricate 65,536 independently programmed PCCs on a single chip. These features, in combination with the widely used modularity of DNA origami[16–20], suggest that our method is well suited for the rapid prototyping of a broad array of hybrid nanophotonic devices.

Solution-synthesized molecules and colloidal nanoparticles offer unique optical properties, such as tunable photoluminescence (PL) spectra, which are difficult to achieve in the materials we can most easily craft into microfabricated optical cavities. Thus hybrid nanophotonic systems, in which the strongly localized optical fields within microfabricated cavities further enhance the optical properties of molecules and nanoparticles[1] or create new properties such as lasing[5,6] or nonlinear phenomena[8], are of interest.

To reliably build such systems, it is necessary to have a fabrication method which can both introduce well defined numbers (often exactly one) of optically active components into a single cavity, and position those components relative to the antinodes of the cavity mode with a precision that is well below the wavelength of light (tens of nanometres). Further, advanced hybrid devices would organize two or more kinds of chemically diverse subcomponents—organic molecules, nitrogen–vacancy centres, quantum dots, ions, or metallic nanoparticles—in intimate contact at the length scale of the subcomponents (0.1–10 nm). Finally, whether the hybrid device is imagined to be part of a hand-held biomedical diagnostic machine, or part of a quantum circuit embedded within a classical computer which controls it, large numbers of devices must be scalably integrated on chips, using CMOS-compatible techniques.

A complete solution for hybrid device fabrication would address all of the above challenges, achieving control of component number within a cavity, precise positioning in a cavity mode, modular incorporation of diverse materials, finer subcomponent-scale arrangement, and large-scale integration. No current technique suffices. Three approaches are used to integrate heterogeneous components into microstructures: (1) fully stochastic assembly, (2) fully deterministic scanning-probe assembly, and (3) directed self-assembly. In (1), fully stochastic assembly[6–9], molecules or nanoparticles are either deposited or grown at random locations on a substrate. When resonator locations are predefined[8], the yield of functional devices in which a single component has landed within a resonator is limited by Poisson statistics to 37%, but yields can be lower since positioning within the cavity is uncontrolled. Alternatively, via 'select and post-process'[1], randomly arranged components can be mapped using atomic force microscopy (AFM), scanning electron microscopy (SEM), or super-resolution fluorescence microscopy and a resonator can be built around the component[7,9]. Scanning probe assembly (2) involves pushing components into a resonator using the scanning probe tip, one at a time[10,11]. Neither fully stochastic nor scanning-probe approaches can be scaled up. In contrast, directed self-assembly (3) uses lithographically defined growth sites or binding sites to localize components to microstructures with high probability, and is thus inherently scalable. But while previous directed self-assembly techniques control emitter number and position[12], they do not generalize to other component types, or address subcomponent organization.

Structural DNA nanotechnology[21] can create organic/inorganic hybrid components at a resolution unachievable by top-down fabrication. Particularly versatile in this regard is DNA origami[15,22], in which a long single strand of DNA is folded by the concerted action of hundreds of much shorter DNA 'staple strands': coupling diverse subcomponents to the staple strands yields modular DNA 'breadboards' that carry up to 200 different elements (these can range from organic dyes[16,17], metal nanoparticles[16,17], nitrogen–vacancy centres[23] and quantum dots[17–19] to carbon nanotubes[20] and proteins), simultaneously juxtaposed[16–19] with 3–5 nm resolution. Large-scale integration of the functionalized DNA shapes can then be achieved through electrostatic immobilization onto ~100-nm binding sites that have been lithographically defined on desired substrates. When optimized, this 'placement' technique[13,14] successfully positions single origami at 94% of binding sites with ~20-nm precision. Together, origami and placement thus meet all five of the above challenges in the context of a general hybrid nanophotonics platform: the former provides modularity and fine subcomponent-scale organization, the latter control over component number, positioning and scalability. Below we give examples in which origami and placement work together to control the emission of thousands of silicon nitride (SiN) PCCs.

Solution-synthesized DNA origami triangles (Fig. 1a and Extended Data Fig. 1) serve both as components and adaptors, carrying either 3 or 15 cyanine dye subcomponents (Cy5, Fig. 1b) to triangular binding sites within PCCs. To form the origami, a long circular scaffold strand

[1]Department of Bioengineering, California Institute of Technology, Pasadena, California 91125, USA. [2]Department of Applied Physics and Materials Science, California Institute of Technology, Pasadena, California 91125, USA. [3]Computing and Mathematical Sciences, California Institute of Technology, Pasadena, California 91125, USA. [4]Computation and Neural Systems, California Institute of Technology, Pasadena, California 91125, USA.

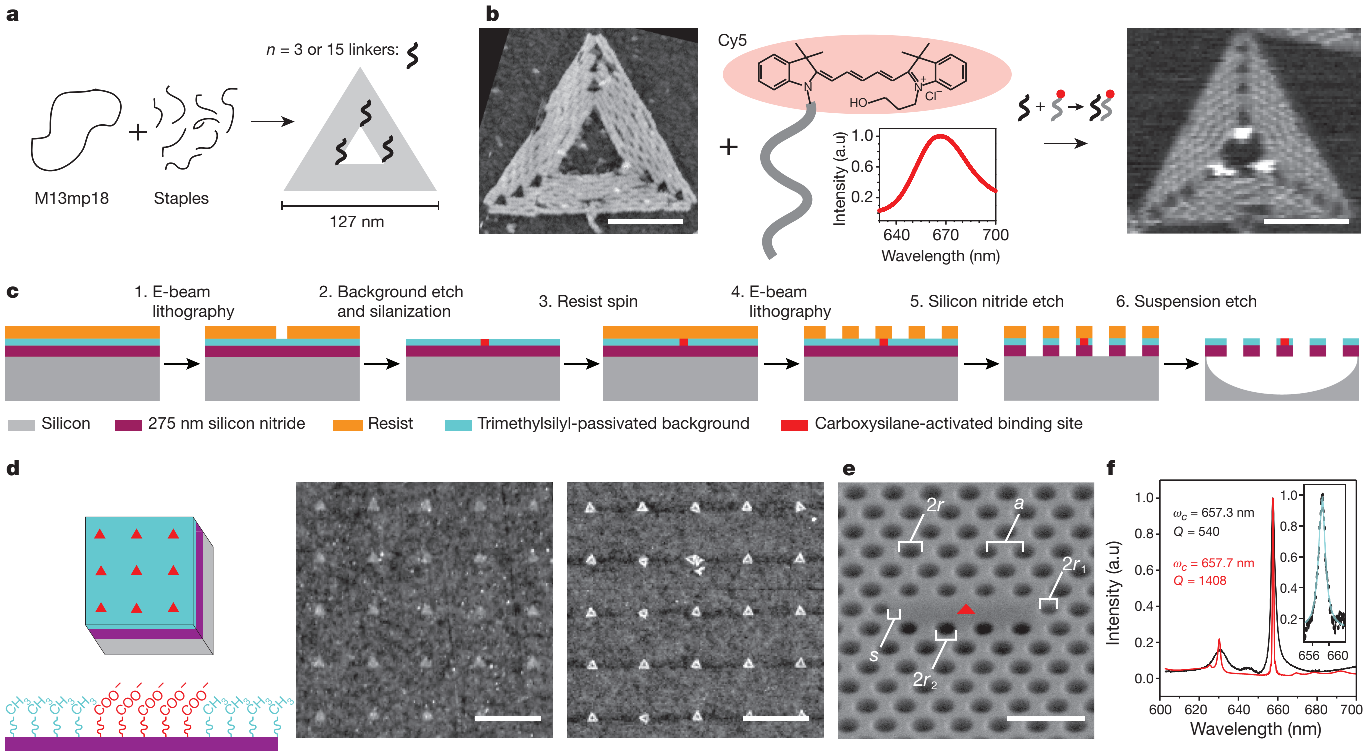

Figure 1 | DNA origami, binding sites for placement, and photonic crystal cavities. **a**, A single-stranded M13mp18 scaffold is annealed with staples to form origami triangles with single-stranded linkers (black squiggles) for the attachment of subcomponents. **b**, Fluid AFM of origami without (leftmost image) and with (rightmost image) subcomponent strands (middle, grey squiggles) labelled with Cy5 (red oval or red dots) bound to linkers (black squiggles). The inset spectrum shows Cy5's broad emission, centred at 670 nm). **c**, Fabrication of a single binding site (red), within a passivation layer (blue), followed by construction of a photonic crystal cavity (PCC) around it (details in Extended Data Fig. 2). **d**, Diagram shows test substrate for placement fidelity (without PCCs), and the groups which mediate binding (carboxylate), and non-binding (methyl). AFM images show binding sites before (left) and after (right) placement; 24 of 25 sites have a single origami (full test substrate: 600 sites, 98% single origami). **e**, SEM of a PCC; $a = 256$ nm, $r/a = 0.3$, $r_1/a = 0.2$, $r_2/a = 0.25$, $s = 0.22a$. **f**, Low resolution PCC reflectance spectra (black) is compared to FDTD prediction (red); fundamental mode ω_c agrees within 1 nm, lower Q is attributed to fabrication defects[24]. Inset, high resolution fit to ω_c (blue). Scale bars: **b**, 50 nm; **d**, 400 nm; **e**, 500 nm.

(the genome of bacteriophage M13mp18) is annealed (90–20 °C, 6 h) with ~200 short computer-designed staple strands, and a Cy5-labelled subcomponent strand (grey strands with a red dot) which binds to linkers (black) projecting from a subset of the staple strands. Figure 1c outlines the fabrication steps (details in Extended Data Fig. 2) used to create both binding sites and PCCs from a 275-nm-thick SiN layer (purple) on a Si wafer (grey). Binding sites are created (steps 1 and 2) via electron beam (e-beam) patterning of negatively charged carboxylate groups (red, which bind negatively charged origami strongly via positively charged Mg^{2+} ions from solution) within a background of hydrophobic methyl groups (blue, which bind origami poorly). Directed self-assembly proceeds by incubating a solution of purified DNA origami over the patterned substrate which results in a high yield of single origami binding events. Figure 1d depicts placement reoptimized for SiN, which achieves 98% single-origami occupancy. PCCs based on previous designs[24] are fabricated after the binding sites via additional e-beam and etching (steps 3–6). Each cavity (Fig. 1e) is simply a row of three missing holes within a two-dimensional (2D) triangular lattice of air holes. In 2D, light is confined to the cavity because the spacing of the air holes creates an optical bandgap. Vertical confinement is achieved by total internal reflection at the interface of the SiN membrane and the air above and below. Cavity geometry was optimized using finite-difference time domain (FDTD) simulations to set up a high-quality mode (Fig. 1f) between 655 nm and 660 nm, near the emission peak of Cy5.

A large variation in cavity emission, as a function of Cy5-origami position, highlights the importance of emitter placement in both theory and experiment (Fig. 2, Extended Data Fig. 4). Because emitters are located on the 2D cavity surface, total spontaneous emission S_T from a Cy5 at location $\mathbf{r} = (x, y)$ for wavelength ω has three components[11]: direct emission into free space, indirect emission into the cavity (eventually scattered into free space by imperfect confinement), and interference between the two. The measurement set-up (Extended Data Fig. 5) sets coefficients C_{dir}, C_{cav} and C_{int}, which govern the relative contribution of each component to the total spontaneous emission:

$$S_T(\mathbf{r}, \omega) = C_{\mathrm{dir}} + C_{\mathrm{cav}} P(\mathbf{r}, \omega) + C_{\mathrm{int}} I(\mathbf{r}, \omega)$$

where the enhancement of emission into the cavity mode, $P(\mathbf{r}, \omega)$, has a Lorentzian line shape centred about the cavity resonance ω_c, and an interference factor $I(\mathbf{r}, \omega)$ accounts for the interference between direct and indirect emission at the collection point. Because photons are coupled multimodally through free space into the monochromator, and because Cy5-origami carry multiple emitters, we neglect C_{int} and assume that any observed dependence on emitter position is due to $P(\mathbf{r}, \omega)$. In particular, $P(\mathbf{r}, \omega_c)$, the Purcell factor, is proportional to the local density of states (LDOS) at $\mathbf{r}$, which exhibits strong periodic features with a spacing below the diffraction limit (116 nm from central maxima to adjacent minima; see simulations in Figs 2c and 3b). To measure these features experimentally, PL spectra (Fig. 2b) were recorded for a series of isolated cavities each with a Cy5-origami positioned at one of 21 different x-offsets along their horizontal midlines (Extended Data Fig. 4a). Oscillations were less sharp than expected, but predicted antinodes were still prominent and emission from single Cy5-origami varied up to fourfold (Fig. 2c, data are Lorentzian fits to spectra). For comparison, we modelled random placement by creating PCCs filled with tightly packed origami (Extended Data Fig. 4b). Reference patches with the same average

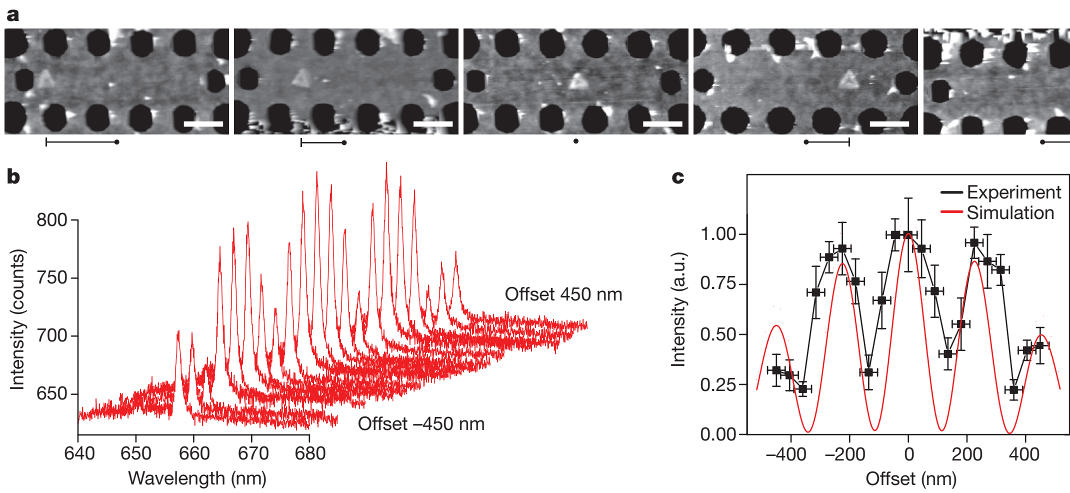

Figure 2 | PL spectra as a function of emitter position. a, Dry AFM of PCCs with a single origami ($n = 15$ Cy5/origami) at different x-offsets; dots marks cavity centres. Scale bars, 250 nm. **b**, PL spectra from PCCs with x-offsets from -450 nm to $+450$ nm, with Δx of 45 nm. **c**, Comparison of background-subtracted and normalized PL peak emission from spectra in **b** with the normalized LDOS calculated via FDTD. Intensity error bars are ± 1 standard deviation for 6–8 measurements; x-offset error bars are ± 1 standard deviation for 2–3 post-fabrication AFM measurements, averaging ± 28 nm.

number (26) of Cy5-origami were constructed on open SiN. After measuring spectra (Extended Data Fig. 4c) for five copies of each, we computed the ratio of enhanced to unenhanced emission; randomly placed emitters experience only a 1.5 enhancement, on average. Thus, placement of emitters is important to realize both maximal and reproducible emitter–cavity coupling.

The ability to spectrally characterize single cavities (Fig. 2b) is important, but for mode mapping (Fig. 2c) this approach is tedious and sensitive to alignment errors. A variety of scanning probe[10,11,25–27] and cathodoluminescence techniques[28] have been used to map microcavity modes in 1D[10,11] and 2D[25,26,28], but they require complex instrumentation. By fabricating a 2D array of PCCs whose microscale X–Y coordinates reflect the nanoscale x–y coordinates of a Cy5-origami within each cavity (Fig. 3a), wide-field epifluorescence microscopy (Fig. 3c) affords direct super-resolution visualization of the 2D LDOS (Fig. 3b). Although the predicted subdiffraction mode pattern is clearly visible in an image of a single array (Extended Data Fig. 6a), Fig. 3c shows an average of five arrays with better signal-to-noise. A 1D slice through the map (Fig. 3d) matches the simulated LDOS better than data in Fig. 2c (perhaps due to better e-beam alignment for close-packed PCC arrays), and emission varies by >5-fold. Resolution is limited by the spatial arrangement of emitters on the origami, the precision of placement, and the resolution with which e-beam lithography can maintain registration between the micrometre-scale PCCs.

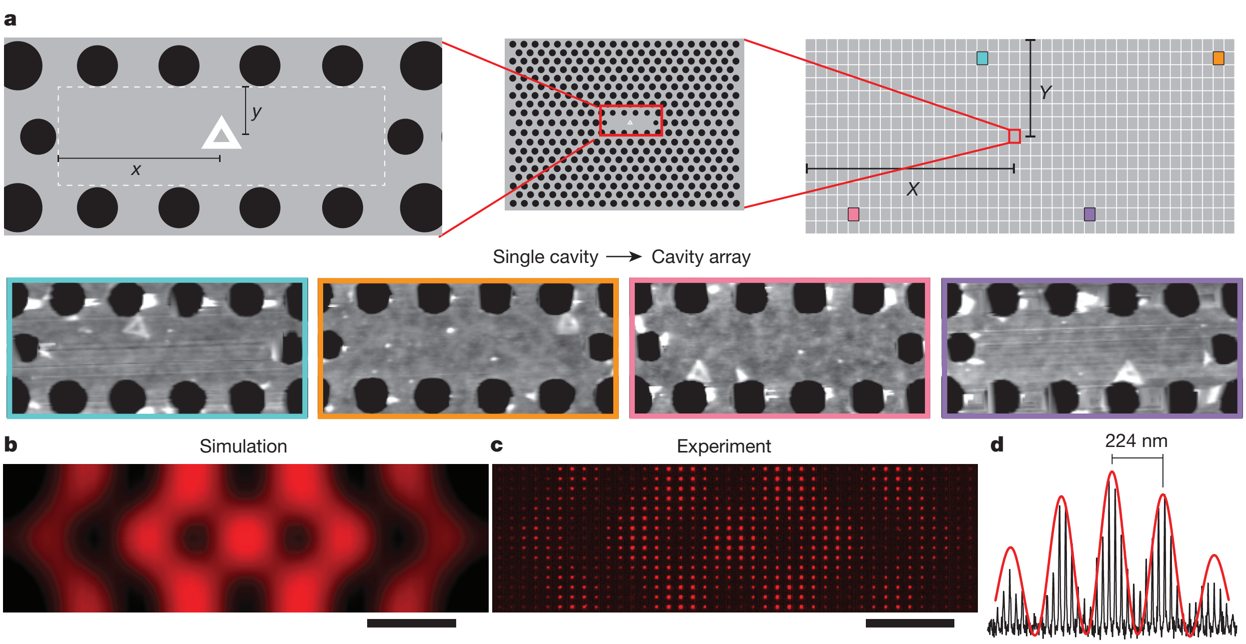

Figure 3 | Visualization of the LDOS via wide-field microscopy. a, Top, the x–y location of a Cy5-origami (left) within a single PCC (centre) translates to that PCC's X–Y location within a 40×15 PCC array (right; 176 μm × 77 μm). Dashed rectangle in left image shows the area over which origami position was varied, in increments of $\Delta x = 26.5$ nm and $\Delta y = 22.5$ nm. Bottom, AFM of four cavities; outline colours indicate positions in array shown at top right. **b**, Simulated LDOS for a single PCC. **c**, Wide-field epifluorescence microscopy average of five copies of the PCC array. **d**, Comparison of **b** to **c** along their horizontal midlines; data (black) normalized to simulated LDOS (red) at central antinode. Scale bars: **b**, 200 nm; **c**, 32 μm.

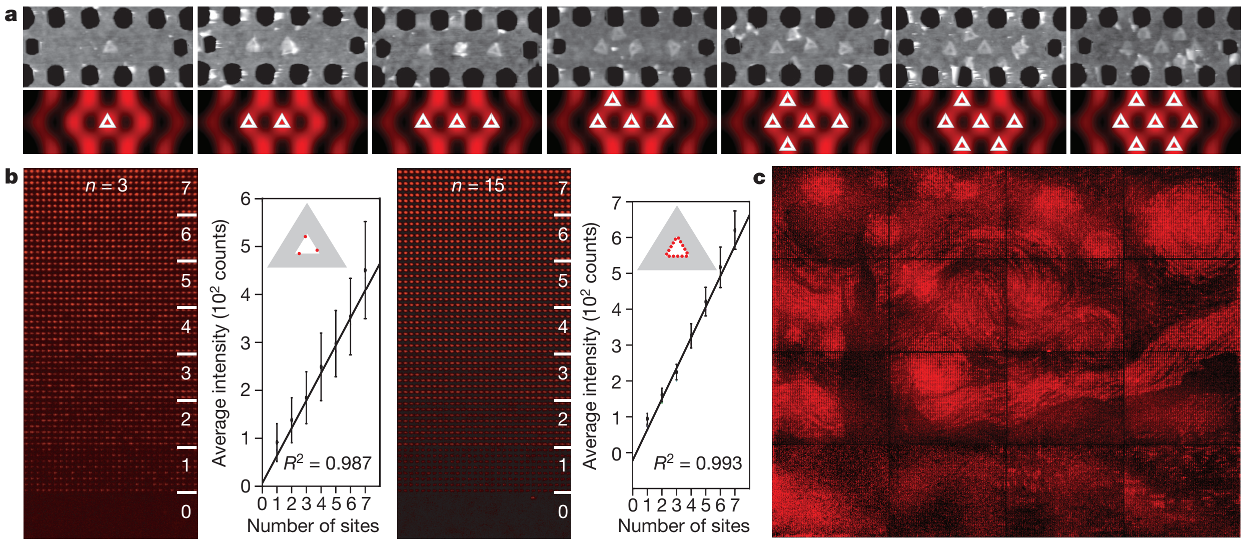

Figure 4 | Digital control of cavity emission. a, AFM and schematics show that up to seven origami can be placed in distinct antinodes of a single PCC. **b**, Epifluorescence images show test patterns of each of the seven configurations from **a** plus an array of zero-site controls for $n=3$ and $n=15$ Cy5/origami. 240 copies of each configuration are shown, see Extended Data Fig. 7 for all 512 copies studied. Plots show means from Gaussian fits to intensity histograms (Extended Data Fig. 8); error bars are ± 1 standard deviation. **c**, Van Gogh's *The Starry Night* approximated with 65,536 cavities each having from zero to seven binding sites. See Extended Data Fig. 9 for details.

Here emitters lie equally spaced along the ~50 nm ($<\lambda/10$) inner edge of origami triangles and so emitter arrangement dominates other factors, but designs with more densely arranged emitters should allow the method to be tested down to 10-nm resolution.

We have shown that origami placement in PCCs enables super-resolution mapping of cavity modes, but the method's implications are much broader. Our expanded-scale mode map (Fig. 3c) relies on the reproducible fabrication of 3,000 devices with precise emitter–cavity coupling, and its success implies the ability to create devices with arbitrary coupling, up to the maximum available within a single antinode. To show that we could further engineer emission through coupling to multiple antinodes, we created cavities for which a variable number of origami components, from one to seven, were positioned within the seven strongest antinodes of the cavity (Fig. 4a). Device reproducibility was assessed by creating 64×64 arrays of cavities, each with eight 512-cavity sub-arrays having the same number (from 0 to 7) of origami positioned within them. To demonstrate subcomponent-scale organization, we repeated the experiment for two different numbers and sublithographic arrangements of dyes (Fig. 4b, $n=3$ Cy5 and $n=15$ Cy5). Predicted antinode variability was small (~15% peak intensity difference between the central and six surrounding antinodes) and so a roughly linear relationship between emission and origami number was expected and observed. This allowed us to use sixteen 64×64 PCC arrays on the same chip to recognizably approximate a 65,536-pixel grayscale image (Extended Data Fig. 9) with eight intensity levels (Fig. 4c).

More quantitatively, single-origami devices in Fig. 4b had emission variabilities of $\pm 22.6\%$ (that is, ± 1 coefficient of variation, which is the standard deviation divided by the mean) for 3 Cy5 and $\pm 10.9\%$ for 15 Cy5. We modelled device emission as having a binomially distributed component, governed by the number n of Cy5 and the fraction p of functional Cy5 (simultaneously capturing the purity of Cy5-labelled strands, coupling efficiency of these strands to origami, and fraction of unbleached Cy5) multiplied by a Gaussian component, simultaneously capturing both placement and fabrication errors, which should be independent of n. Minimizing squared error between modelled and observed device variability for $n=3$ and $n=15$ simultaneously suggests that $p=87.2\%$ of emitters were coupled and intact, and Gaussian noise was 4.5% (± 1 standard deviation). However, the effect of Gaussian noise on total variability was small ($<10\%$): assuming a placement and fabrication error of 0%, and solving for p in $\sigma = \sqrt{np(1-p)}/np$, where $np(1-p)$ is the variance and np the mean of the binomial distribution, gives similar values for both 3 emitters (86.7%) and 15 emitters (85%). We did not explore $n=1$ because of bleaching and instrument sensitivity, but this analysis suggests that with longer-lived emitters, 85% yield for single-photon light sources could be easily achieved.

Here we have used DNA origami as modular adaptors to quickly switch between two different tightly distributed numbers of emitting subcomponents (achieving 2.6 ± 0.6 for $n=3$ and 13 ± 1.4 for $n=15$; ± 1 standard deviation) simply by changing a few DNA strands. Because any material that can be attached to DNA can now be coupled to resonators, diverse applications can be explored. For label-free (emitter-less) single-molecule detection[2,3], origami modularity will allow specificity to be switched quickly between small molecules, proteins and nucleic acids. For applications in quantum information or magnetometry which require emitters with better photophysics, recent advances in nanodiamond nitrogen[29] and silicon[30] vacancy centres may provide suitable emitters. Even without emitter improvements, hybrid nanophotonics based on origami placement will enable the cavity amplification of many phenomena, ranging from plasmonic enhancement[16] and lifetime engineering[19] (where origami provide metal nanoparticle and emitter integration) to superradiance and low-threshold lasing[5,6] (where origami can tightly control emitter number and density). Beyond hybrid nanophotonics, our work may apply to hybrid nanoelectronics[20], and to any heterogeneous fabrication wherein molecular or nanoparticulate components are integrated with microstructures—the end of low-yield methods such as 'select and post-process' is in sight.

Online Content Methods, along with any additional Extended Data display items and Source Data, are available in the online version of the paper; references unique to these sections appear only in the online paper.

Received 27 October 2015; accepted 19 April 2016.
Published online 11 July 2016.

1. Benson, O. Assembly of hybrid photonic architectures from nanophotonic constituents. *Nature* **480,** 193–199 (2011).
2. Armani, A. M. *et al.* Label-free, single-molecule detection with optical microcavities. *Science* **317,** 783–787 (2007).
3. Yang, D. *et al.* High sensitivity and high Q-factor nanoslotted parallel quadrabeam photonic crystal cavity for real-time and label-free sensing. *Appl. Phys. Lett.* **105,** 063118 (2014).

4. Jensen, K. *et al.* Cavity-enhanced room-temperature magnetometry using absorption by nitrogen-vacancy centers in diamond. *Phys. Rev. Lett.* **112,** 160802 (2014).
5. Yakunin, S. *et al.* Low-threshold amplified spontaneous emission and lasing from colloidal nanocrystals of caesium lead halide perovskites. *Nat. Commun.* **6,** 8056 (2015).
6. Strauf, S. *et al.* Self-tuned quantum dot gain in photonic crystal lasers. *Phys. Rev. Lett.* **96,** 127404 (2006).
7. Hennessy, K. *et al.* Quantum nature of a strongly coupled single quantum dot–cavity system. *Nature* **445,** 896–899 (2007).
8. Englund, D. *et al.* Controlling cavity reflectivity with a single quantum dot. *Nature* **450,** 857–861 (2007).
9. Sapienza, L., Davanço, M., Badolato, A. & Srinivasan, K. Nanoscale optical positioning of single quantum dots for bright and pure single-photon emission. *Nat. Commun.* **6,** 7833 (2015).
10. Barth, M., Nüsse, N., Löchel, B. & Benson, O. Controlled coupling of a single-diamond nanocrystal to a photonic crystal cavity. *Opt. Lett.* **34,** 1108–1110 (2009).
11. Englund, D. *et al.* Deterministic coupling of a single nitrogen vacancy center to a photonic crystal cavity. *Nano Lett.* **10,** 3922–3926 (2010).
12. Lyasota, A. *et al.* Integration of multiple site-controlled pyramidal quantum dot systems with photonic-crystal membrane cavities. *J. Cryst. Growth* **414,** 192–195 (2015).
13. Kershner, R. J. *et al.* Placement and orientation of individual DNA shapes on lithographically patterned surfaces. *Nat. Nanotechnol.* **4,** 557–561 (2009).
14. Gopinath, A. & Rothemund, P. W. K. Optimized assembly and covalent coupling of single-molecule DNA origami nanoarrays. *ACS Nano* **8,** 12030–12040 (2014).
15. Rothemund, P. W. K. Folding DNA to create nanoscale shapes and patterns. *Nature* **440,** 297–302 (2006).
16. Acuna, G. P. *et al.* Fluorescence enhancement at docking sites of DNA-directed self-assembled nanoantennas. *Science* **338,** 506–510 (2012).
17. Schreiber, R. *et al.* Hierarchical assembly of metal nanoparticles, quantum dots and organic dyes using DNA origami scaffolds. *Nat. Nanotechnol.* **9,** 74–78 (2014).
18. Bui, H. *et al.* Programmable periodicity of quantum dot arrays with DNA origami nanotubes. *Nano Lett.* **10,** 3367–3372 (2010).
19. Ko, S. H., Du, K. & Liddle, J. A. Quantum-dot fluorescence lifetime engineering with DNA origami constructs. *Angew. Chem. Int. Ed.* **52,** 1193–1197 (2013).
20. Maune, H. T. *et al.* Self-assembly of carbon nanotubes into two-dimensional geometries using DNA origami templates. *Nat. Nanotechnol.* **5,** 61–66 (2010).
21. Seeman, N. C. DNA in a material world. *Nature* **421,** 427–431 (2003).
22. Douglas, S. M. *et al.* Self-assembly of DNA into nanoscale three-dimensional shapes. *Nature* **459,** 414–418 (2009).
23. Zhang, T. *et al.* DNA-based self-assembly of fluorescent nanodiamonds. *J. Am. Chem. Soc.* **137,** 9776–9779 (2015).
24. Barth, M. *et al.* Modification of visible spontaneous emission with silicon nitride photonic crystal nanocavities. *Opt. Express* **15,** 17231–17240 (2007).
25. Louvion, N. *et al.* Local observation and spectroscopy of optical modes in an active photonic-crystal microcavity. *Phys. Rev. Lett.* **94,** 113907 (2005).
26. Mivelle, M. *et al.* Light funneling from a photonic crystal laser cavity to a nano-antenna: overcoming the diffraction limit in optical energy transfer down to the nanoscale. *Opt. Express* **22,** 15075–15087 (2014).
27. Rotenberg, N. & Kuipers, L. Mapping nanoscale light fields. *Nat. Photon.* **8,** 919–926 (2014).
28. Sapienza, R. *et al.* Deep-subwavelength imaging of the modal dispersion of light. *Nat. Mater.* **11,** 781–787 (2012).
29. Knowles, H. S., Kara, D. M. & Atatüre, M. Observing bulk diamond spin coherence in high-purity nanodiamonds. *Nat. Mater.* **13,** 21–25 (2014).
30. Neu, E. *et al.* Low-temperature investigations of single silicon vacancy colour centres in diamond. *New J. Phys.* **15,** 043005 (2013).

Supplementary Information is available in the online version of the paper.

Acknowledgements We acknowledge funding from the Army Research Office (award W911NF-11-1-0117), the Office of Naval Research (award N000141410702), the Air Force Office of Scientific Research (Young Investigator award FA9550-15-1-0252), and the US National Science Foundation (Expeditions in Computing numbers 0832824 and 1317694, Molecular Programming Project; http://molecular-programming.org). We thank J. Fakonas for discussions and B. Fultz for use of his spectrometer. Device fabrication was done at Caltech's Kavli Nanoscience Institute.

Author Contributions A.G. and P.W.K.R. conceived the project. A.G. performed origami synthesis, nanofabrication, AFM, SEM and fluorescence microscopy. A.G. and E.M. built the set-up for microphotoluminescence spectroscopy. All authors contributed to data interpretation and manuscript preparation.

Author Information Reprints and permissions information is available at www.nature.com/reprints. The authors declare no competing financial interests. Readers are welcome to comment on the online version of the paper. Correspondence and requests for materials should be addressed to A.G. (ashwing@caltech.edu) or P.W.K.R. (pwkr@dna.caltech.edu).

METHODS

DNA origami

Design. A variation of the 'sharp triangle' design described previously[15] was chosen because the sharp triangle is rigid and it has a low tendency to aggregate. The 'sameside sharp triangle' used here (details of design in Extended Data Fig. 1) has the same scaffold path as the original sharp triangle, and the scaffold strand shares the same alignment as in the original structure. (For sequences and the caDNAno design, unzip Supplementary Data: specifically, files 'ETSamSide_15Cy5_StapleList.xls' and 'Sameside-sharp-triangle-bridged.json' which unzip into the directory 'OrigamiDesignFiles'.) The difference between the original sharp triangle and the sameside sharp triangle lies in the pattern of nicks along the phosphate backbone of the staple strands: in the original sharp triangle, nick positions alternate between the two faces of the triangle, whereas the new sameside sharp triangle has all nick positions on the same face of the triangle. Additionally, 15 staples on the inner edge of the triangle occur in two versions. The first version is an unmodified staple. The second version has an 18-nucleotide poly-T extension, which serves as a linker that binds to a 21-nucleotide poly-A 'subcomponent' strand bearing a single Cy5 on its 5′ end. Using this basic design we prepared two version of the origami: one had $n=15$ Cy5 molecules along its inner edge and the second had only $n=3$ Cy5 in along its inner edge.

Synthesis. Staple strands (Integrated DNA Technologies, 100 μM each in water) and the scaffold strand (single-stranded M13mp18, Bayou Biolabs, P-107) were mixed together to target concentrations of 100 nM (each staple) and 40 nM, respectively (a 2.5:1 staple:scaffold ratio) in 10 mM Tris Base, 1 mM EDTA buffer (adjusted to pH 8.35 with HCl) with 12.5 mM magnesium chloride. (We refer to the buffer used for origami synthesis, with the above combination of Tris Base, EDTA, and Mg^{2+}, as 'TE/Mg^{2+}'.) Staples with the poly-T linker and the Cy5 label were added at 5× and 150× excess respectively. 50 μl volumes of staple/scaffold mixture were heated to 90 °C for 5 min and annealed from 90 °C to 20 °C at −0.2 °C min^{-1} in a PCR machine. We used 0.5 ml DNA LoBind tubes (Eppendorf) to minimize loss of origami to the sides of the tubes.

Purification. Since a high concentration of excess staples interferes with origami placement, the synthesized origami were purified away from excess staples using 100 kD molecular weight cut-off spin filters ('Amicon Ultra-0.5 Centrifugal Filter Units with Ultracel-100 membranes'). By the following protocol, recovery is generally 40%–50% and staples are not visible by agarose gel. Wet the filter by adding 500 μl TE/Mg^{2+}. Spin filter at 2,000 r.c.f. (relative centrifugal force) for 6 min at 4 °C, until the volume in the filter is 50 μl. Discard the filtrate. Add 50 μl of unpurified origami and 400 μl TE/Mg^{2+}. Spin at 2,000 r.c.f. for 6 min at 4 °C. Wash the origami three more times by discarding the filtrate, adding 450 μl TE/Mg^{2+} and spinning at 2,000 r.c.f. for 6 min at 4 °C. Invert the filter onto a clean tube and spin at 2,000 r.c.f. for 6 min at 4 °C to collect purified origami (~50 μl). Total time for this purification is roughly 40 min.

All of the work reported in this Letter was performed with spin-column purified origami. Other protocols, which may give higher yield via PEG precipitation or magnetic bead separation, are available[31,32] although we have not verified that these methods would give quantitatively similar results for placement.

Quantification. Post-purification, origami were quantified using a NanoDrop spectrophotometer (Thermo Scientific). We estimated the molar extinction coefficient of the origami triangles as that of a fully double-stranded M13mp18 molecule ($\varepsilon = 123{,}735{,}380\,M^{-1}\,cm^{-1}$; we did not correct for a small single-stranded loop present on one edge of the origami). The typical working concentration for origami during placement was 100 pM, which is too small to be measured with the NanoDrop, so serial dilutions were performed. For all of the experiments performed reported here, we used a single 300 μl stock of 20 nM origami solution that was diluted to 100 pM immediately before each use.

Handling origami. After purification and quantification, it is especially important to use DNA LoBind tubes (Eppendorf) for storage and dilution of low concentration DNA origami solutions. Low dilutions, for example, 100 pM, must be made fresh from more concentrated solutions and used immediately—even overnight storage can result in total loss of origami to the sides of the tube. Addition of large amounts of carrier DNA to prevent origami loss may prevent origami placement, just as excess staples do. We have not yet determined whether other blocking agents such as BSA might both prevent origami loss and preserve placement.

Photonic crystal cavity nanofabrication. We fabricated PCCs similar to previous designs[24] using two slightly different approaches. For isolated PCCs occurring in widely spaced arrays, like those which appear in Fig. 2, we suspended the PCC membranes using a front etch. For large, close-packed arrays of PCCs like those which appear in Figs 3 and 4, we suspended the PCC membranes using a back etch. Schematics for both fabrication processes are given in Extended Data Fig. 2. All fabrication was carried out in Caltech's Kavli Nanoscience Institute.

Widely spaced PCC arrays. A schematic of the fabrication process is shown in Extended Data Fig. 2a; SEM images of these arrays are given in Extended Data Fig. 3. Fabrication began with 275 nm LPCVD (low-pressure chemical vapour deposition) growth of SiN on a 100 mm single-side polished (SSP, 525 ± 25 μm thick) ⟨100⟩ silicon wafer as the base substrate (Rogue Valley Microdevices). The wafer was cleaned and alignment markers were defined in the SiN layer by e-beam lithography and modified Bosch ICP (inductively coupled plasma) etching. The substrate was cleaned again and silanized with a trimethylsilyl passivation layer by vapour deposition of HMDS (hexamethyldisilazane). Next, binding sites in the shape of a DNA origami were defined at specific locations using the alignment markers (defined *a priori*) by e-beam lithography. Binding sites were then activated with a short O_2 plasma etch and the resist was stripped. Surface silanols on binding sites were converted to carboxylate groups via a second silanization. Lastly, a PCC was defined around the carboxylated binding site by e-beam lithography and modified Bosch ICP etching of the SiN layer. Finally, PCCs were suspended using a XeF_2 isotropic etch of the underlying Si layer.

Here we note that all modified Bosch ICP etching of SiN, whether for definition of PCCs or alignment marks, was performed in an ICP-RIE (inductively coupled plasma-reactive ion etcher, Oxford Instruments System 100 ICP 380) at a pressure of 4 mtorr, with a flow rate of 25 sccm for SF_6 and 35 sccm for C_4F_8, an RF generator power of 25 W, an ICP power of 1,000 W, at 4 °C. Further, we note that this modified Bosch process does not involve alternating applications of SF_6 and C_4F_8, but rather introduces them as a mixed gas.

Definition of alignment markers. Substrates were sonicated with isopropanol (IPA) and dried in a stream of N_2 to remove any particulate contaminants. Substrates were spin coated with 600 nm of ZEP 520A (10 s, 500 rpm; 10 s, 1,500 rpm; 120 s, 3,000 rpm; ZEP 520A is a high-resolution positive electron beam resist from Zeon Chemicals). Alignment marker patterns were defined by e-beam. Patterns were developed in ZED N50 (Zeon Chemicals electron beam resist developer) for 1 min. Patterns were transferred into the substrate using the modified Bosch process for about 30 min. Remaining resist was stripped with hot (50 °C) n-methyl pyrrolidone (NMP).

Surface passivation with trimethylsilyl groups. Substrates were sonicated with IPA and dried in a stream of N_2, to remove any particulate contaminants. Substrates were cleaned with O_2 plasma in a Plasmatherm Dual-chamber SLR-720 RIE (reactive ion etcher), with a flow rate of 50 sccm, a pressure of 50 mtorr and a power setting of 80 W (110 W cm^{-2}), for 5 min to create surface silanols. Substrates were dehydrated on a hot plate at 150 °C for 5 min. Substrates were incubated in a 4 l chamber saturated with HMDS vapour (a 20 cm × 20 cm × 10 cm Tupperware with a 90 mm Petri dish in the corner holding 10 ml HMDS) for 20 min. This step resulted in the formation of a monolayer of trimethylsilyl groups on the surface. Substrates were heated on a hot plate at 150 °C for 30 min, to stabilize the silanized surface. It is important to bake the substrate both before and after HMDS vapour-priming to ensure high quality surface silanization and increase the robustness of the monolayer to hydrolysis. Failure to perform either of these steps leads to increased background binding of origami.

Definition of carboxylated binding sites. Binding sites were defined by e-beam lithography on a freshly prepared and silanized substrates as follows. Substrates were spin-coated with a 170–180 nm resist layer of poly(methyl methacrylate) (MicroChem Corp., 950 PMMA, A3) at 2,500 rpm for 90 s. The resist was baked at 180 °C for 30 s. Binding sites were defined in the resist using e-beam lithography with a 100 keV beam at 500 pA current. The dosage ranged from 600 to 850 μC cm^{-2} and patterns were proximity corrected. The resist was developed for 70 s in a 1:3 solution of methyl isobutyl ketone (MIBK) and isopropanol (IPA). Surface silanols were created in the lithographically defined regions by an O_2 plasma etch (Plasmatherm Dual chamber SLR-720 RIE, a flow rate of 20 sccm, a pressure of 20 mtorr and a power setting of 50 W (92 W cm^{-2}), for 18 s). The resist was stripped by sonicating the wafer in bath of NMP at 50 °C for 10 min. The surface silanols that were created by O_2 plasma was converted to carboxylate groups by incubating the substrate in a disodium carboxyethylsilanetriol (CTES from Gelest, 25% w/v in water Catalog #SIC2263.0) silanization buffer (0.01% CTES, 10 mM Tris, pH 8.3 for 10 min) followed by sonication in milliQ water. During the last step, ensure that the silanization buffer is at pH 8.3. Higher pH leads to the trimethylsilyl background being hydrolysed and inadvertently carboxylated.

Definition of isolated PCCs. After binding site definition, the substrate was cleaned with IPA. A 600 nm thick layer of ZEP 520A was spin-coated on the substrate and baked at 180 °C for 1 min. PCCs were defined using e-beam lithography with a 100 keV beam at a current of 500 pA. The dosage ranged from 200 to 300 μC cm^{-2} and patterns were proximity corrected. The exposed resist was developed in ZED N50 for 1 min. PCC structures were created via modified Bosch etch for 9–12 min, depending on the etch rate observed that day. The Si under the PCC was isotropically etched with a custom-built pulsed XeF_2 etcher (5 cycles of 20 s each, 500 mtorr XeF_2). The resist was stripped by overnight soaking of the chip in a bath of NMP at 50 °C. It is important not to sonicate the substrate after the PCC has been suspended as it leads to the collapse of the PCC membrane.

Close-packed PCC arrays. A schematic of the fabrication process is given in Extended Data Fig. 2b. The process is a modification of procedures in ref. 33 in which extremely large SiN membranes were created (up to 2.4 mm × 2.4 mm). The fabrication process is similar to that described for isolated cavities above, with the exception that PCC arrays were created on a SiN window supported by a thin Si layer (which is removed at the very last step with an XeF_2 etch). Fabrication began with double-side polished silicon wafers (DSP, ⟨100⟩, 380 ± 10 nm thick, University Wafers, Rogue Valley Microdevices) with 275 nm layers of LPCVD-grown SiN on both sides of each wafer.

Etching of large SiN windows. Wafers were cleaned and alignment marker were defined by e-beam lithography and ICP/modified Bosch etch (30 min) in the SiN layers on both sides, using the wafer flat for alignment. Substrates were spin-coated with a 600 nm layer of ZEP 520A on the back side of the wafer. Substrates were spin-coated with ProTEK PSB (Brewer Science) on the top side of the wafer to protect it from contamination and physical scratches. A 650 μm × 650 μm window was defined via e-beam using back-side alignment markers. The resist was developed in ZED N50 for 1 min. The SiN layer (on the back side) was etched for 1 h by the modified Bosch process, to punch through to the Si layer. Si exposed in the previous step was etched for 12 h in 50% KOH solution to a depth of approximately 300–350 μm. This created an SiN window of approximately 400 μm × 400 μm supported by an Si layer less than 80 μm thick. The ProTEK PSB was stripped using hot (50 °C) NMP.

Notes on fabrication. After Si-supported SiN windows were etched, origami binding sites and PCC arrays were defined on the top surfaces using earlier-defined top-side alignment. We note that the alignment error between patterns on the top and bottom of the wafers sometimes reached a few tens of micrometres. However the most crucial alignment errors, between the origami binding site and the PCC array, were limited to tens of nanometres, because both binding sites and PCCs were created using the same set of alignment markers on the top of the wafer. Finally, the thin Si support remaining underneath the PCC array was removed using XeF_2 pulsed etching. The suspended membranes are extremely delicate so it is crucial that substrate is handled with care. It is important not to sonicate suspended photonic crystal membranes as this will break them.

Origami placement on PCCs. Here the placement DNA origami on binding sites is mediated by Mg^{2+} binding to surface carboxylate groups, rather than surface silanols, as in our previous work[14]. We have observed that the use of carboxylated binding sites allows high-quality origami placement and orientation on SiN at a much lower Mg^{2+} concentration (15 mM) than that required (35 mM) for binding sites activated only by an O_2 plasma (and which we presume are covered with silanols). We have not measured the density of carboxylate groups or silanols in either case, but we suggest that the effect is due to the difference in pK_as between these two functional groups: similar surface carboxylate groups[34] have a pK_a of ~6, while silanol groups have a pK_a of 8.3. Thus binding sites with carboxylate groups should carry a higher negative charge at our working pH of 8.3, they should bind more Mg^{2+}, and they should enable the observed binding of origami at lower Mg^{2+} concentration.

In addition to decreasing the potential for Mg^{2+} salt artefacts during drying, the use of carboxylate groups has a further important added benefit. Over the course of the extensive PCC fabrication process, different areas experience many different specific series of treatments, which results in many different surface types. Some of these, for example the inside of the PCC holes or the back side of the PCC membranes, are not passivated with trimethylsilyl groups, and appear to bind some DNA origami at higher Mg^{2+} concentration. Thus the use of carboxylated binding sites (and hence a lower Mg^{2+} concentration for placement) decreases nonspecific DNA origami binding and ensures that under our buffer conditions the only locations at which origami can stably bind are the intended binding sites.

Below, we describe the placement protocol in five steps, which apart from the use of a lower Mg^{2+} concentration and carboxylated binding sites, is similar to that in our previous work[14]. Photographs in supplementary figure 3 of ref. 14 show how substrates should look at different steps of the placement process. (Note that our previous work uses carboxylation of binding sites at a different step, after origami placement, as part of a method to achieve covalent coupling of origami to substrates.)

Binding. A 50 mm Petri dish was prepared with a moistened piece of laboratory tissue paper to limit evaporation. Solution with 100 pM origami was prepared in 'placement buffer' (10 mM Tris, 15 mM Mg^{2+}, pH 8.3) and a 20 μl drop was deposited in the middle of the chip, on top of the PCCs. The chip was placed in the closed, humid Petri dish and the origami solution was allowed to incubate on the chip for 1 h.

Initial wash. After the 1 h incubation, excess origami (in solution) were washed away with at least 8 buffer washes by pipetting 60 μl of fresh placement buffer onto the chip, and pipetting 60 μl off the chip. Each of the 8 washes consisted of pipetting the 60 μl volume up and down 2–3 times to mix the fresh buffer with existing buffer on the chip. This initial wash took about 2 min.

Tween wash. Next, in order to remove origami that were non-specifically bound to the passivated background, the chip was buffer-washed 5 times using a 'Tween washing buffer' with 0.1% Tween 20 (v/v in placement buffer). This took about 1 min. Because of the low surface tension of the Tween washing buffer, these washes were difficult to perform: they involve adding 20–40 μl of wash buffer, just enough to cover most of the chip, but not enough to spill over the chip and wet the back side of the chip (this may introduce dust contamination from the Petri dish). After the fifth wash, the chip was left to incubate for 30 min. (It is important to use Tween 20, rather than other surfactants. Tween 80 and SDS, which are two other common surfactants, lead to markedly different results—Tween 80 leads to the total removal of placed origami from the substrate, and SDS does not remove excess origami from the trimethylsilyl background. It is important that chips are not exposed to Tween 20 until after the origami have been deposited. Tween 20 applied before binding completely inactivates the binding sites.)

Final stabilizing wash. Last, the chip was buffer-washed 8 times back into a higher pH 'stabilizing buffer' (10 mM Tris, 15 mM Mg^{2+}, pH 8.9) so that origami bound strongly and artefacts were minimized during subsequent drying. This took about 2 min. These washes were relatively high volume (60 μl) and were intended to completely remove the Tween 20. The amount of Tween 20 left was monitored qualitatively by the surface tension of the drop (roughly, by eye). When a 20 μl drop covered roughly the same area as the initially deposited drop, it was assumed that the Tween 20 had been sufficiently removed. In the last wash the chip was left with roughly 20 μl of stabilizing buffer, and was ready for drying.

Drying. Chips were dried by serial dilution into ethanol. The chips were dipped in 50% ethanol in water (v/v%) for 10 s, 75% ethanol in water (v/v%) for 10 s and then 120 s in 90% ethanol in water. Then the chips were air-dried. (If nanoarrays are subjected to ethanol solutions with less than 80% ethanol for more than 60–90 s, origami begin to detach from the surface. After the 90% ethanol immersion, it is necessary to let the samples air-dry rather than using N_2 or compressed air, since streaking or other drying artefacts are observed in instances of forced air drying.)

Troubleshooting origami placement. If low binding, high multiple binding, or high background binding artefacts are observed, see the troubleshooting guide in Extended Data Table 1. Below we provide notes emphasizing some of the more important aspects of the placement protocol, which may be helpful in troubleshooting. Do not allow the patterned region with binding sites to dry at any point during the binding step or subsequent buffer washes. Inadvertent dewetting of the binding sites leads to distortion of the origami (causing them to ball up) as well as the formation of salt crystals on top of them. Do not use EDTA in placement, Tween washing, or imaging buffers. It is unnecessary in this context and will change the effective Mg^{2+} concentration for placement slightly. Make fresh buffer solutions every week. Here and elsewhere in this work, we use buffers at low strength (typically 10 mM) to minimize background binding and to make complete washing into different buffers easier. This means the buffers have low buffering capacity and the pH will decrease (and placement may cease to work, depending on conditions). For example, weak buffers made to read pH 8.35 can lose 0.05 pH units and read pH 8.3 after one week.

AFM characterization. After the cavities were fabricated and the origami were placed within the cavities, we quantified the quality of placement using dry AFM. While the presence of origami (and the fluorophores they carry) can be inferred from the optical experiments, we have used AFM because it provides the ability to unambiguously verify the presence of single origami, as well as measure the precise location of the origami (and hence fluorophores) with respect to the cavity. Unless otherwise specified (images in Fig. 1b were taken under aqueous buffer with a Bruker Fastscan AFM), all AFM images were taken in air in tapping mode with a Dimension Icon AFM/Nanoscope V Scanner (Bruker) using the short, fat cantilever from an SNL probe B ("sharp nitride lever", 2 nm tip radius, Bruker) resonating at approximately 60 kHz. Imaging origami on suspended resonators was challenging. All images had to be acquired at the lowest possible force in order to reduce tip–sample interaction. We optimized imaging conditions on an unsuspended region near the alignment markers and then moved onto the cavity with precise stage movements. Minimization of imaging force was important: if imaging force was increased, imaging became unstable. We noticed that imaging near the edge of suspended regions was easier than at the middle; we suggest that the suspended SiN membrane is interfering with AFM measurement by acting as a mechanical resonator itself.

Each AFM image was processed using Gwyddion (http://gwyddion.net/). In assessing the quality of placement, we measured both the binding site occupancy (the percentage of sites with one or more origami), and the number of origami at a given site (0, 1, 2, or >3). In previous work[14], we measured the quality of placement over dozens of repetitions of placement, where each repetition had more than 500 binding sites. Here, because of the difficulty of AFM measurements on

PCC resonators, we performed a test for the quality of placement by analysing a single array of 600 binding sites on SiN (Fig. 1d), without any PCCs. Carboxylate-mediated placement on SiN resulted in no empty binding sites, and few sites with multiple bindings (∼2% of sites). Thus, we measured a single origami occupancy of 98%, consistent with that previously achieved.

For experiments in which single origami binding sites were written inside PCCs (Figs 2 and 3), AFM imaging of selected cavities showed that the fabrication steps added to create the PCCs did not degrade the quality of placement: all PCCs inspected (Fig. 2a, Fig. 3a, and Extended Data Fig. 4) had binding sites occupied by single origami, within ∼10 nm of the desired location. We attribute the low rate of multiple bindings to the low Mg^{2+} concentration (enabled by carboxylated binding sites), the Tween 20 washes, and the proximity correction (which enables accurate patterning of the binding sites) that we used. We attribute the low positional error to our use of multiple alignment markers within the single e-beam field, and the use of the same markers for the patterning of both the PCCs and the binding sites. As far as we can tell, the quality of the binding sites is not affected by their proximity to etched features, such as the holes in the PCCs.

For experiments in which multiple origami binding sites were written inside resonators (Fig. 4, Extended Data Figs 7 and 9), we observed that resonators with larger numbers of binding sites (that is, 5, 6 or 7) had a greater number of multiple bindings (which increase the number of origami in the resonator above that desired). We did not quantify this effect, because linear fits of emission as a function of the number of binding sites suggest that it is not a large effect (Fig. 4b). In our previous work[14], we observed that crowding of binding sites over large arrays decreased site occupancy, because sites filled mostly via 2D diffusion of weakly surface-bound origami from the edges of the array. Here, crowding of binding sites within PCCs seems to have an opposite effect. The context is quite different, however. The PCC structure blocks 2D diffusion of origami to binding sites from the background, and sites are positioned closely in a different configuration which may allow extra origami to bind partially to two adjacent binding sites. The effect of the spacing between origami binding sites in different contexts thus deserves more study.

Spectroscopy. For all cross-polarization reflectance and microphotoluminescence (fluorescence) spectroscopy we used the set-up illustrated in Extended Data Fig. 5. For cross-polarization reflectance measurements, we used a Fianium supercontinuum laser as an excitation source. Broad-spectrum excitation light was polarized used a linear polarizer (polarizer 1) and focused onto the PCC sample through a 50× (0.8 NA) infinity-corrected objective. The sample was oriented at 45° to the incident polarization, and reflected signal collected by the objective passed through another polarizer (polarizer 2, orthogonal to polarizer 1) before being coupled into a monochromator (a SpectraPro-2500i with a grating of 1,800 grooves per millimetre from Princeton Instruments).

For fluorescence spectroscopy we use the same basic set-up but replaced the supercontinuum laser with a 15 mW, 638 nm laser, bandpass filtered at 635 ± 5 nm (635 BP). After being expanded to ∼500 μm in size, the laser beam was focused onto the sample through the same 50× (0.8 NA) objective. On the sample surface, the laser spot was approximately 5 μm in size, as measured by a CCD camera. Fluorescence emission was filtered through a 650-nm longpass filter (650 LP) to remove excitation light, before being coupled into the monochromator. A marked reduction in fluorescence signal was observed after illumination times of 30–45 s. Thus the potential effects of bleaching were minimized by limiting total illumination time to 10 s: final spectra were produced by averaging 10 spectral scans, each taken with an integration time of 1 s.

Wide-field epifluorescence microscopy. All fluorescence imaging was performed with an Olympus BX-61 microscope with a xenon excitation source. Excitation light was filtered with a 640-nm shortpass filter, and passed through a 645-nm dichroic to the sample. After returning through the dichroic, emission light was bandpass filtered at 655 ± 5 nm. The narrow bandpass filter was important for emission; longpass filtering of the emission light admitted too much direct Cy5 emission, rather than indirect emission through the cavity, and this made it impossible to image the 2D mode map. Fluorescence emission was imaged using a 50× (0.8 NA) objective onto a Hamamatsu EMCCD cooled to −80 °C. Complete bleaching of samples was observed at illumination times of approximately 2 min. For a particular PCC array, each final image was created by averaging 10 image acquisitions. For $n = 3$ Cy5, integration time for each of these acquisitions was 1 s; for $n = 15$ Cy5, integration time for each acquisition was 200 ms. In the case of 2D modemaps, a single final image of a particular PCC array (Extended Data Fig. 6a) was somewhat noisy, and five final images of different PCC arrays were averaged to yield the final data (Fig. 3c and Extended Data Fig. 6b). Features of the experimental images and 2D LDOS are qualitatively similar, but we did not attempt to fit experimental images to simulation, and instead matched their features by eye.

FDTD simulations for PCC design and analysis. Three dimensional (3D) finite-difference time domain (FDTD) simulation was used both for PCC design and to generate simulated LDOS for comparison with experimental maps of the resonant cavity modes. All simulations were performed using FDTD Solutions from Lumerical Solutions, Inc (https://www.lumerical.com/). Lumerical simulation files can be found by unzipping the Supplementary Data, in the directory 'LumericalScripts'. Matlab files for creating Autocad versions of optimized resonators can also be found by unzipping the Supplementary Data, in the directory 'AutocadScriptGenerator'.

Cavity geometry (Fig. 1e) was based on previous designs[24] featuring soft confinement[35]. To design the photonic crystal we fixed the refractive index of SiN at 2.05, the thickness of the SiN membrane at 275 nm, and adjusted r, r/a, r_1, r_2 and s to maximize quality factor within the wavelength range 655–660 nm. Photonic crystal size was set to $20a$ in the x-direction and $34.64a$ in the y-direction. Boundary conditions were implemented by introducing a perfect matching layer around the structure. The simulation discretization was set to a/R in the x-direction, $0.866a/R$ in the y-direction, and a/R in the z-direction, where the variable R was set to 10 for PCC design (so that PCC parameters could be quickly optimized), and set to 20 to generated simulated LDOS of higher resolution for comparison with experimental mode maps. The simulation modelled emission from a single dipole with polarization $P(x, y, z) = (1, 1, 0)$, located at a weak symmetry point close the cavity surface.

Code availability. The code used to design and simulate the PCCs as well as code to generate Autocad files for electron beam lithography defining PCCs and binding sites is available as the zip-encoded Supplementary Data file.

31. Stahl, E., Martin, T. G., Praetorius, F. & Dietz, H. Facile and scalable preparation of pure and dense DNA origami solutions. *Angew. Chem. Int. Ed.* **53,** 12735–12740 (2014).
32. Shaw, A., Benson, E. & Högberg, B. Purification of functionalized DNA origami nanostructures. *ACS Nano* **9,** 4968–4975 (2015).
33. Klein, M. J. K. *Wafer-Scale Fabrication of Thin SiN Membranes and Au Films and Membranes with Arrays of Sub-micron Holes Using Nanosphere Lithography*. PhD thesis, École Polytechnique Fédérale de Lausanne (2010).
34. Noy, A. *Handbook of Molecular Force Spectroscopy* (Springer, 2007).
35. Akahane, Y., Asano, T., Song, B.-S. & Noda, S. High-Q photonic nanocavity in a two-dimensional photonic crystal. *Nature* **425,** 944–947 (2003).

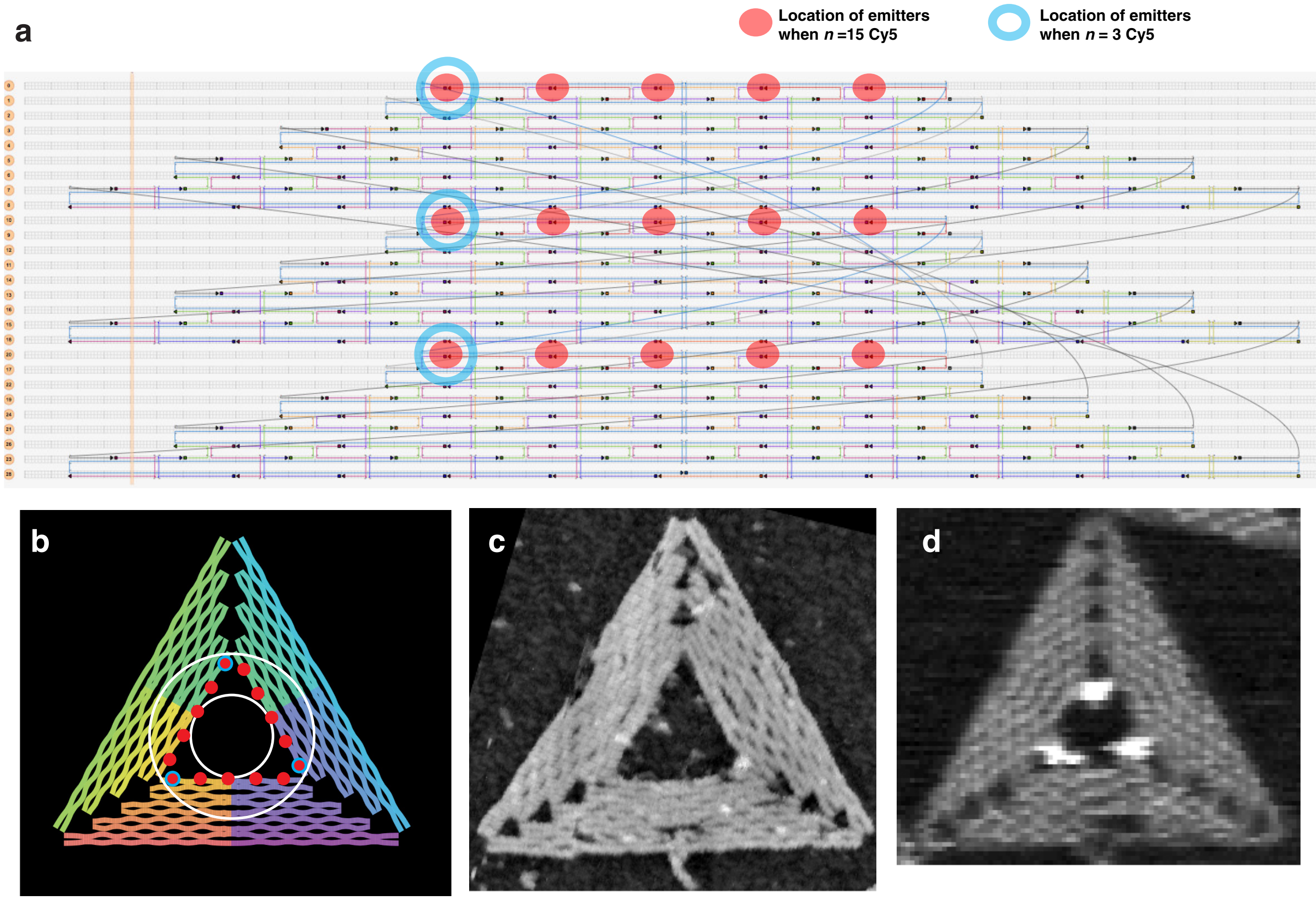

Extended Data Figure 1 | DNA origami design showing position of Cy5 fluorophores. a, We used a triangular DNA origami shape, ~130 nm on each edge, as an adaptor to position fluorophores within a photonic crystal cavity (PCC). The origami is composed of a 7,249-nucleotide (nt) single-stranded scaffold (the commercially available single-stranded genome of the M13mp18 bacteriophage) and approximately 200 commercially synthesized 'staple strands' which are typically 32 nucleotides in length. Mixed together and annealed from 90 to 20 °C over the course of about 6 h, the strands self-assemble to form equilateral triangles in high yield. Three trapezoidal domains make up this 'sameside sharp triangle' design. Red filled circles indicate 15 positions at which staples were extended on their 5′ end with 18-nt poly-T linkers for the synthesis of origami bearing $n = 15$ Cy5. Blue rings indicate the subset of positions used for origami bearing $n = 3$ Cy5. To these linkers, 21-nt poly-A 'subcomponent' strands modified with a 5′ Cy5 were hybridized. Because the Cy5 modification is on their 5′ ends, subcomponent strands put Cy5 within a few nucleotides of the origami surface, less than 1 nm from where linkers extend from the origami surface (rather than at the 6-nm-away distal end of the linker/Cy5 strand hybrid). **b**, Schema showing both components of the fine structure of a DNA origami (gaps between helices, and crossover positions, where helices are tangent) with linker/Cy5-label positions noted as in **a**. The white outer ring has a 62.4-nm diameter and the white inner ring has a 31.2-nm diameter. As in **a**, red dots indicate the subset of positions used for origami bearing $n = 15$ Cy5 and blue rings around red dots indicate positions used for origami bearing $n = 3$ Cy5. Rainbow colours on the origami trace the path of the scaffold as it progresses through the origami structure, from red to purple. **c**, Buffer AFM image showing fine structure of origami without linkers/Cy5 strands for comparison with **b**. **d**, Buffer AFM image showing origami with $n = 3$ linkers and Cy5 strands. In this AFM image the Cy5-labelled duplexes appear to fall on the inside of the inner triangular hole, perhaps due to adhesion to the mica substrate used in these high-resolution experiments. High-resolution imaging of origami dried onto SiN is difficult, and so the exact conformation of Cy5-labelled duplexes on resonators was not determined. However, because the carboxylated sites bind DNA strongly, it seems likely that Cy5-labelled duplexes would behave similarly and fall within the 54-nm triangular hole of the origami, between 30 and 60 nm from the centre of the origami.

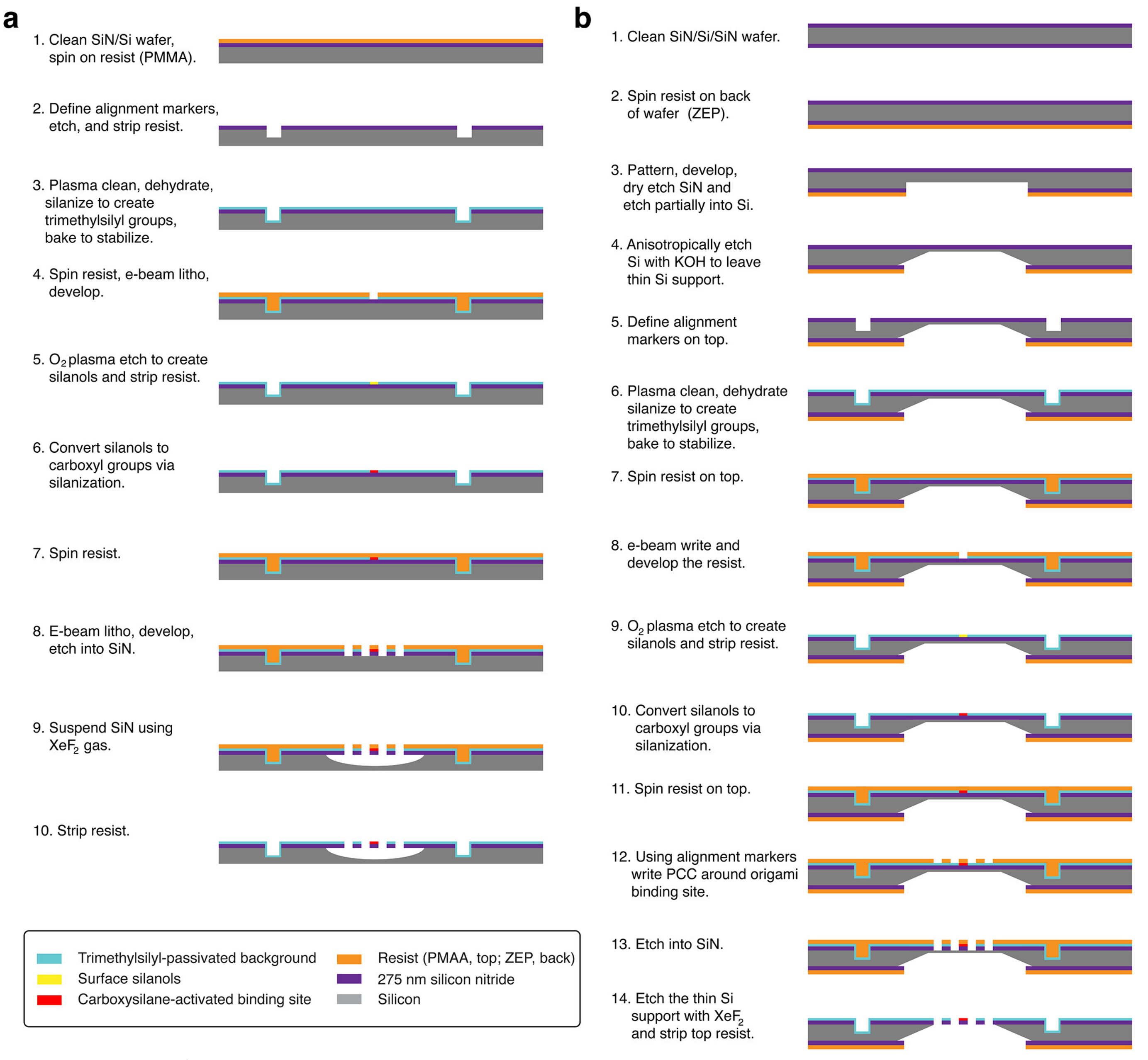

Extended Data Figure 2 | Process flow for fabricating PCCs. a, Fabrication of isolated PCCs for widely spaced arrays (Fig. 2). **b**, Fabrication of PCCs in close-packed arrays (Figs 3, 4). Note that back-side alignment markers are omitted from **b** for clarity. After either fabrication process substrates are incubated in origami solution, rinsed of excess origami, subjected to an ethanol dilution series, and air-dried.

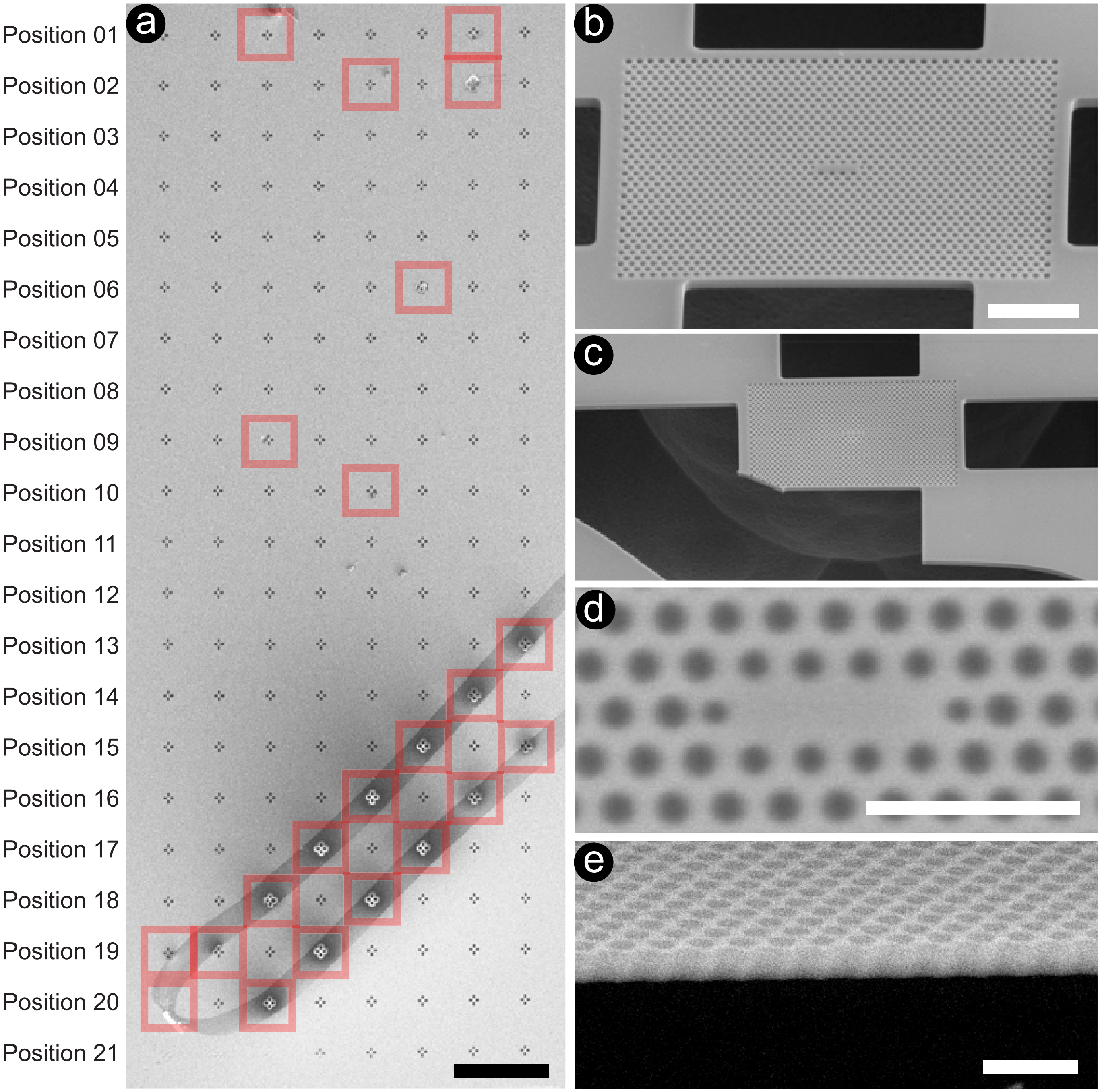

Extended Data Figure 3 | SEM imaging of isolated PCCs used for taking fluorescence spectra as a function of *x*-position. An 8 × 21 array was used. **a**, Positions 01 to 21 each indicate a row of eight copies of isolated PCCs having origami positioned at the same *x*-offset, as exemplified in Extended Data Fig. 4. Red squares indicate broken PCC membranes which were not used. **b**, Intact membrane. **c**, Typical broken membrane. **d**, Zoom-in of PCC. **e**, Cross-section of PCC membrane. Scale bars: **a**, 300 µm; **b**, 2 µm; **d**, 1 µm; **e**, 500 nm.

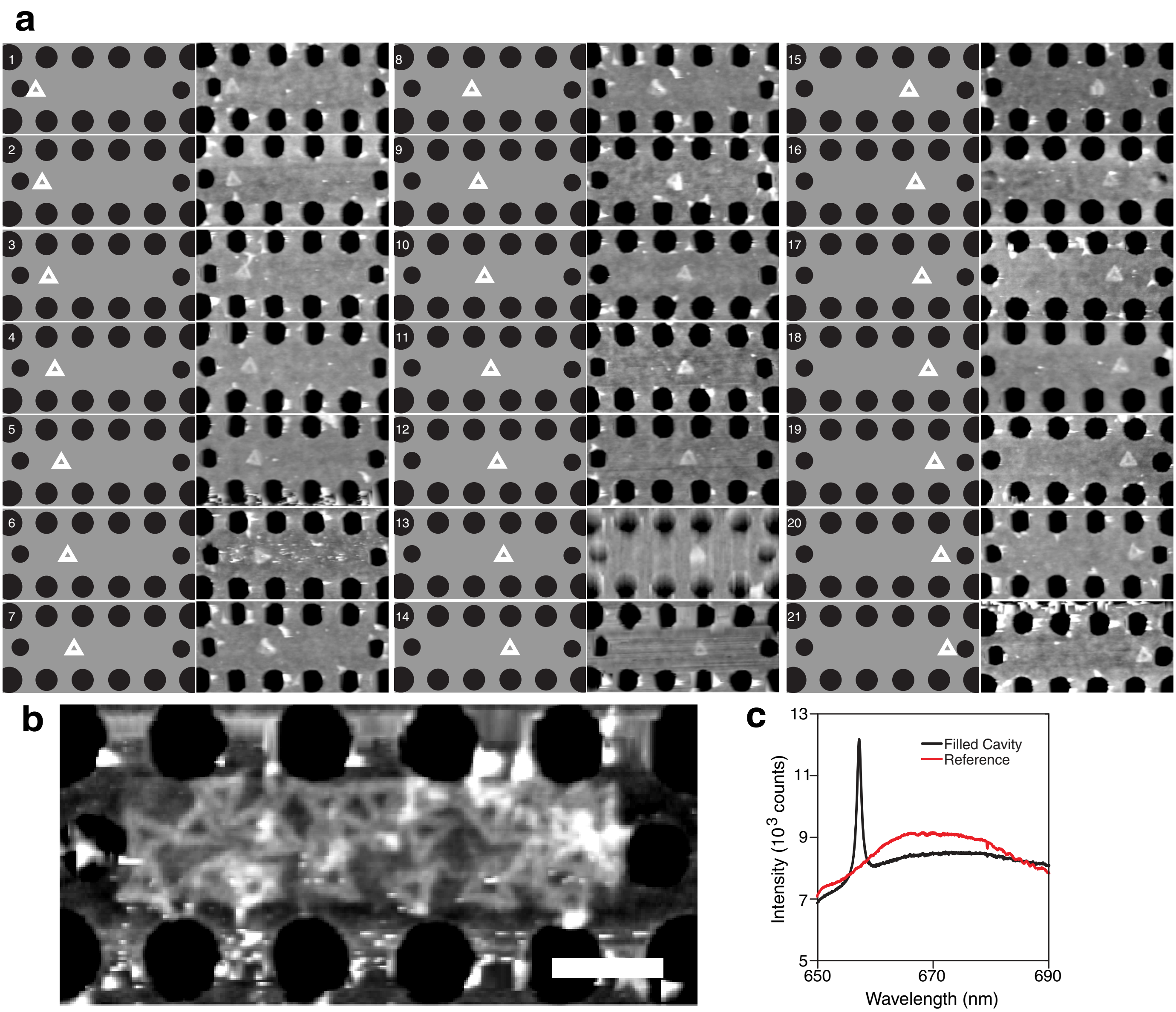

Extended Data Figure 4 | AFM of isolated PCCs and control cavity. a, Schema and representative AFM for each of 21 offsets at which spectra (Fig. 2b) were measured. **b**, Dry AFM of a control PCC filled with origami ($n = 15$ Cy5/origami). Scale bar, 250 nm. **c**, PL reference spectra (red) for Cy5-origami on open SiN, and for Cy5-origami filling a cavity, as in **b**.

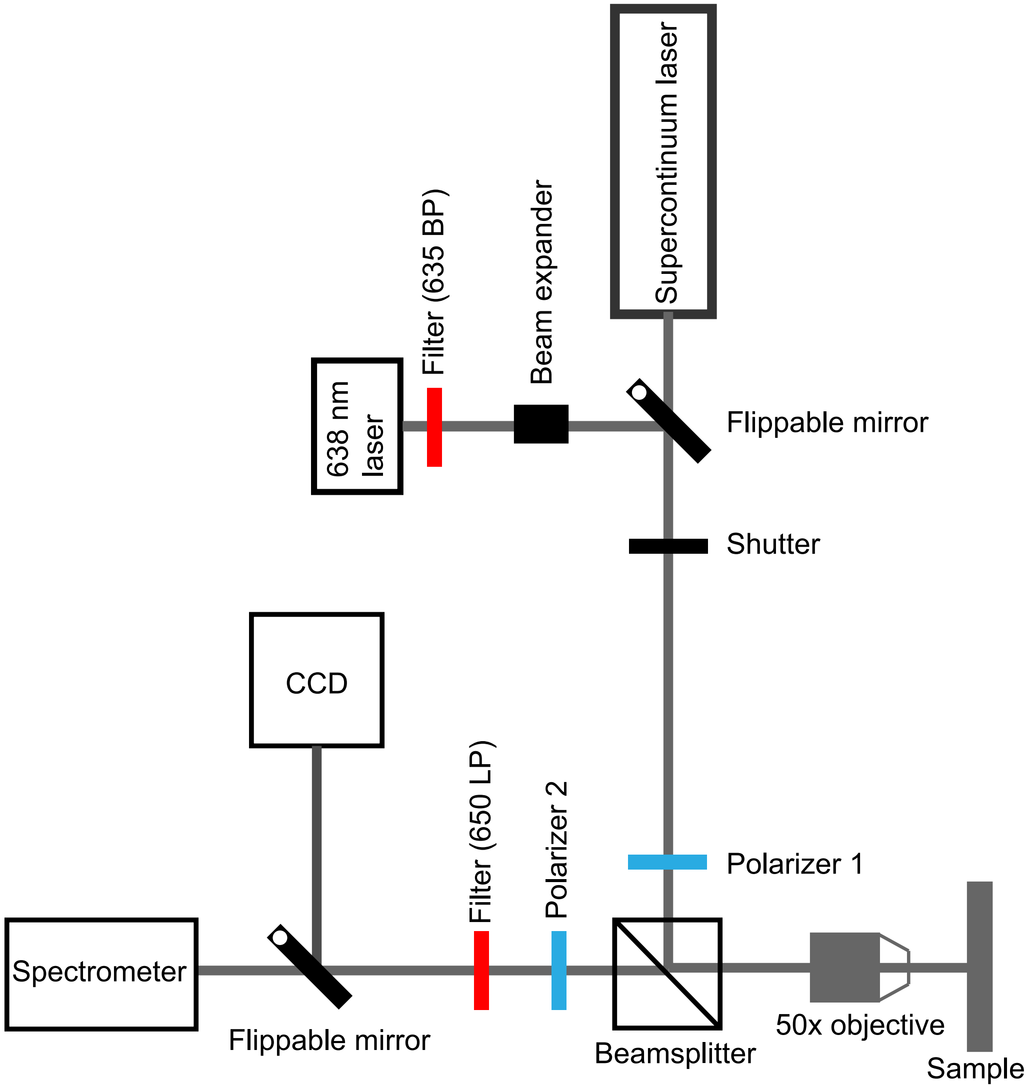

Extended Data Figure 5 | Optical set-up for reflectance and fluorescence spectroscopy. The 650-nm long-pass filter (650 LP) was used only for fluorescence spectroscopy. Details in Methods.

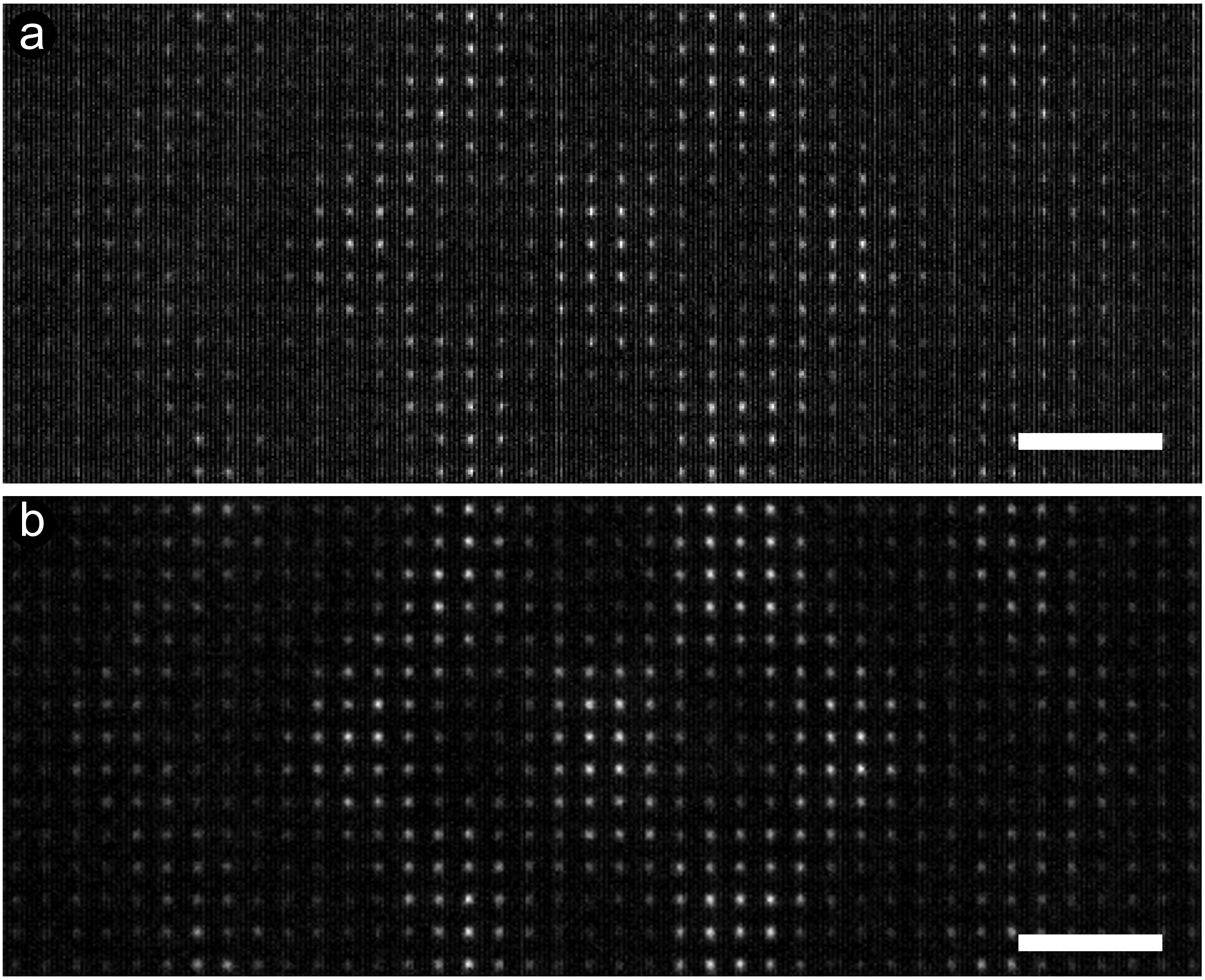

Extended Data Figure 6 | Comparison of unaveraged and averaged epifluorescence images of PCC array used for 2D mode map. a, A single epifluorescence image of a single array. **b**, An average of five images taken of five different PCC arrays, as in Fig. 3c. Scale bars, 23 μm.

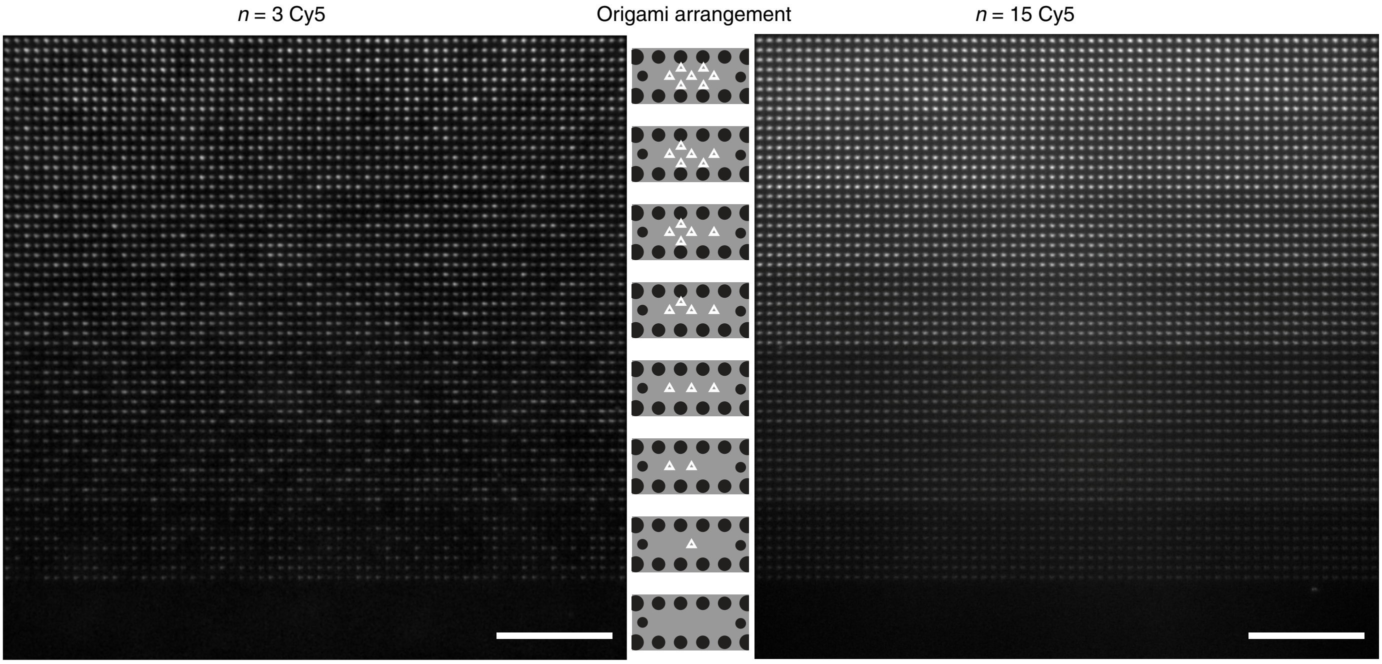

Extended Data Figure 7 | Raw fluorescence data demonstrating digital control of cavity emission. The central panel diagrams eight different arrangements of origami (white triangles) within PCCs, with the number of origami ranging from zero to seven. The left panel shows an epifluorescence image of eight PCC arrays, each containing 512 copies of a PCC with the origami arrangement diagrammed in the adjacent row of the central panel; each origami has $n = 3$ Cy5. The right panel shows an analogous epifluorescence image of eight PCC arrays for which each origami has $n = 15$ Cy5. Histograms summarizing these epifluorescence data are given in Extended Data Fig. 8. See Fig. 4b for plots showing the linearity of intensity as the number of origami are increased. Scale bars, 50 μm.

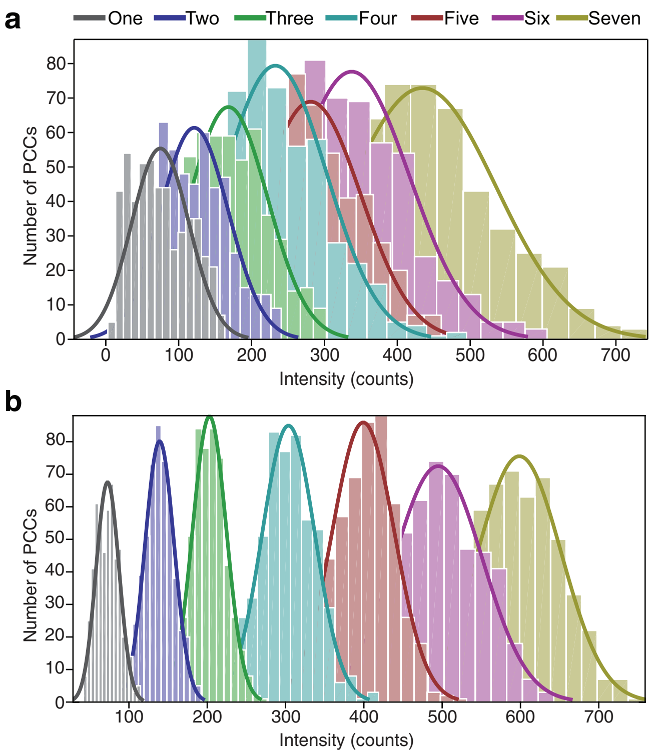

c

Binding Sites	3-Cy5-Origami	15-Cy5-Origami
1	111.53 ± 25.2	83.75 ± 9.1
2	171.24 ± 29.9	150.17 ± 11.5
3	231.36 ± 34.6	213.55 ± 13.4
4	313.92 ± 45.1	314.68 ± 21.1
5	375.95 ± 44.2	409.78 ± 24.9
6	448.11 ± 51.1	507.87 ± 35.2
7	572.45 ± 64.8	609.03 ± 33.4

Extended Data Figure 8 | Histograms of numerical data demonstrating digital control of cavity emission. Eight different arrangements of origami were loaded into PCCs, with the number of origami ranging from zero to seven (see centre panel, Extended Fig. 7). 512 identical PCCs of each of the nonzero arrangements were imaged by epifluorescence microscopy (Extended Data Fig. 7, left and right panels) and their intensity was quantified. These data, for $n = 3$ Cy5 origami (**a**) and $n = 15$ Cy5 origami (**b**) are represented by coloured histograms labelled 'one' through 'seven'. The number of PCCs with a given fluorescence intensity is plotted on the y-axis. **c**, Summary of means and standard deviations (for intensity measured as counts) from Gaussian fits in **a**, **b**. The peaks of these histograms are plotted in Fig. 4b.

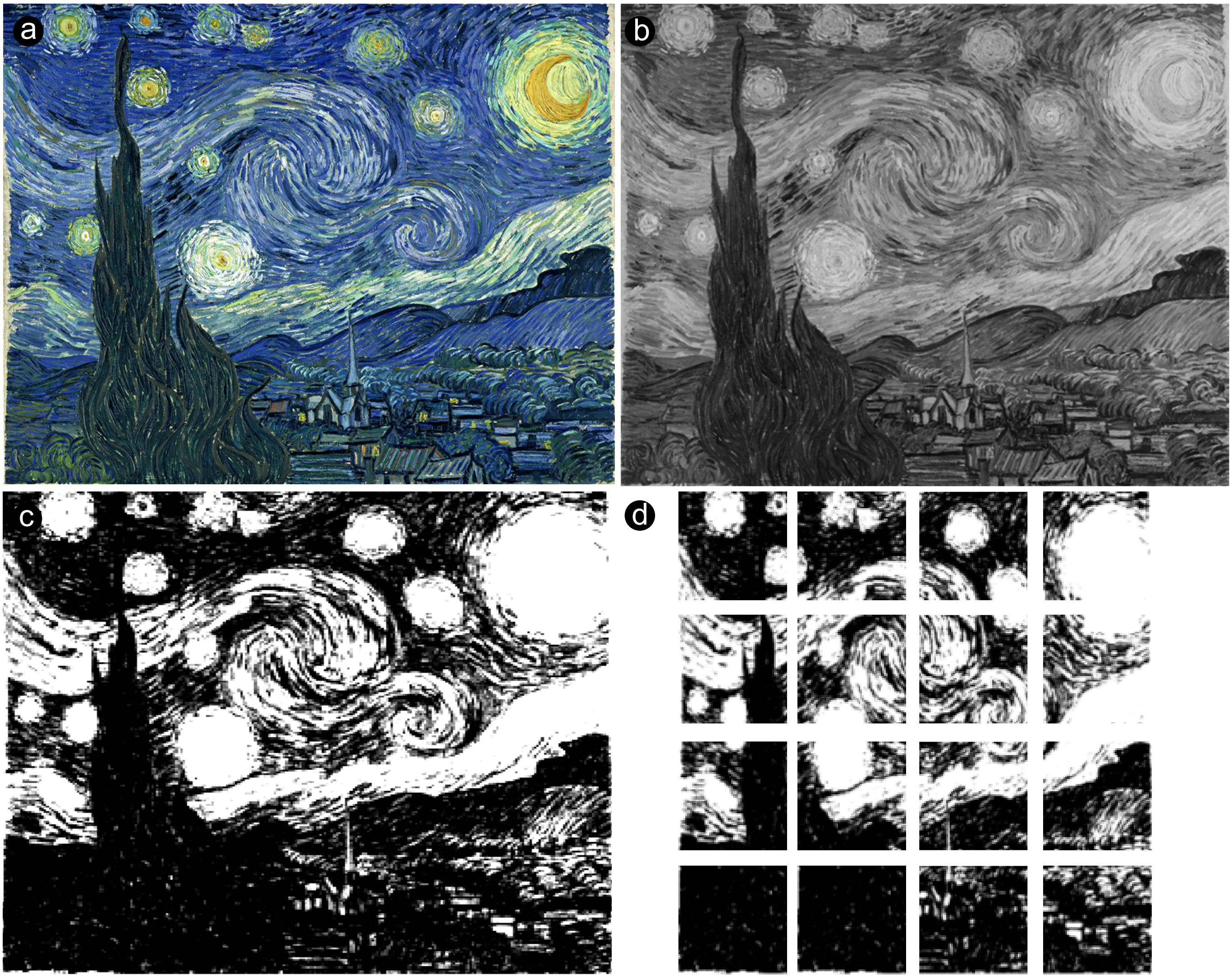

Extended Data Figure 9 | Schema for recreation of Vincent van Gogh's painting *The Starry Night* (1889). See Fig. 4c for recreation. **a**, Original image from Wikimedia Commons (https://commons.wikimedia.org/wiki/File:VanGogh-starry_night_ballance1.jpg). Because our current emitters and cavities provide only one color, with only eight levels of intensity, the original image was converted to greyscale (**b**) and then further converted to have three-bit colour depth (**c**). Because of the difficulty of handling extremely large suspended SiN membranes (which easily break) we limited our recreation to a low-resolution $256 \times 256 = 65{,}536$ pixel version, which was then further broken down into sixteen 64×64 pixel arrays (**d**). With one PCC per pixel, these arrays were small enough that we could fabricate and handle the resulting SiN membranes without too much breakage, image them separately, and then reassemble the sixteen images into a 4×4 array for the final recreation (Fig. 4c).

Extended Data Table 1 | Troubleshooting guide for origami placement

Problem	Likely cause	Solution
Site occupancy below 90%.	• Old chip with inactive sites. • Low origami concentration. • Short incubation time. • Low Mg^{2+} or pH, esp. if site occupancy $< 30\%$.	• Chips work best ≤ 24 hours after activation. • Use ~100 pM origami. Prepare dilution fresh. Use Lo-Bind tubes. • Incubate origami for an hour. • Use 15 mM Mg^{2+}. • Use pH 8.3–8.5.
High multiple binding.	Primarily: • High origami concentration. • Long incubation time. • Oversized features. Secondarily: • High pH. • High Mg^{2+}.	First try: • Use ~100 pM origami. • Keep incubation between 30 and 90 min. • Look at features in resist by SEM and adjust e-beam write (feature size, dose) and/or minimize O_2 activation time. Second try: • Keep pH in the range 8.3–8.5. • Use 15 mM Mg^{2+}.
Poor alignment of origami with few multiple bindings.	• High pH. • High Mg^{2+}.	• Keep pH in the range 8.3–8.5. • Use 15 mM Mg^{2+}.
High background binding. • Whole or partial origami on background in AFM. • Unstable AFM, e.g. whole scanlines of identical value (“scars”). • For fluorescent origami, high background under optical imaging.	Problem with trimethylsilyl (TMS) background passivation. • Poor initial TMS quality. • TMS hydrolyzed by high pH. • TMS hydrolyzed by long incubation. • Failure to wash weakly bound origami from TMS.	• Dehydrate the wafer by baking before and after TMS formation. • Keep pH< 9 preferably in the range 8.3–8.5. • Keep incubation between 30 and 90 minutes. • Remove weakly bound origami with 8× Tween 20 washes.
Large particulates on sites but few or no origami.	• Sample dewetted or dried. Salts and origami aggregates occupy the site.	• Do not let chip dewet during origami deposition or subsequent buffer washes.
Small particles on background.	• Overbaked PMMA. • Acetate causes fine precipitate.	• Bake PMMA for 30 s at 180 °C . • Use non-acetate salts/acids when preparing buffers, e.g. use $MgCl_2$, and HCl to adjust.
Origami fall off during ethanol drying.	• Too much time spent in dilute ethanol $< 80\%$.	• Move quickly from low to high % ethanol.
Origami ball up into site during ethanol drying and corners are double height.	• Origami project onto non-sticky TMS surface.	• Hydrolyze TMS surface before drying by incubating in pH 8.9 stabilization buffer.
CTES-mediated placement yields binding of origami everywhere.	• High pH of CTES solution has hydrolyzed TMS (before placement).	• Use 0.01% CTES in a buffer adjusted to a pH of ≤ 8.3 for carboxylation step.

Origami placement[13,14] is a robust technique for the delivery of components into microfabricated structures, but the quality of the results is nonlinear in a number of variables, including pH, origami concentration, Mg^{2+} ion concentration, and incubation time. To aid reproduction of the technique, we give a guide to the effects that occur, and the remedies to apply, when experimental variables are outside the optimal range.

doi:10.1038/nature18008

Cooperative electrocatalytic alcohol oxidation with electron–proton–transfer mediators

Artavazd Badalyan[1] & Shannon S. Stahl[1]

The electrochemical oxidation of alcohols is a major focus of energy and chemical conversion efforts, with potential applications ranging from fuel cells to biomass utilization and fine-chemical synthesis[1–7]. Small-molecule electrocatalysts for processes of this type are promising targets for further development[8], as demonstrated by recent advances in nickel catalysts for electrochemical production and oxidation of hydrogen[9–11]. Complexes with tethered amines that resemble the active site of hydrogenases[12] have been shown both to catalyse hydrogen production (from protons and electrons) with rates far exceeding those of such enzymes[11,13] and to mediate reversible electrocatalytic hydrogen production and oxidation with enzyme-like performance[14]. Progress in electrocatalytic alcohol oxidation has been more modest. Nickel complexes similar to those used for hydrogen oxidation have been shown to mediate efficient electrochemical oxidation of benzyl alcohol, with a turnover frequency of 2.1 per second. These compounds exhibit poor reactivity with ethanol and methanol, however[15]. Organic nitroxyls, such as TEMPO (2,2,6,6-tetramethyl-1-piperidine *N*-oxyl), are the most widely studied electrocatalysts for alcohol oxidation[5–7,16–19]. These catalysts exhibit good activity (1–2 turnovers per second) with a wide range of alcohols[18] and have great promise for electro-organic synthesis[7]. Their use in energy-conversion applications, however, is limited by the high electrode potentials required to generate the reactive oxoammonium species. Here we report (2,2′-bipyridine)Cu/nitroxyl co-catalyst systems for electrochemical alcohol oxidation that proceed with much faster rates, while operating at an electrode potential a half-volt lower than that used for the TEMPO-only process. The (2,2′-bipyridine)Cu(II) and TEMPO redox partners exhibit cooperative reactivity and exploit the low-potential, proton-coupled TEMPO/TEMPOH redox process rather than the high-potential TEMPO/TEMPO$^+$ process. The results show how electron-proton-transfer mediators, such as TEMPO, may be used in combination with first-row transition metals, such as copper, to achieve efficient two-electron electrochemical processes, thereby introducing a new concept for the development of non-precious-metal electrocatalysts.

Cu/TEMPO and related catalyst systems have been studied extensively for aerobic alcohol oxidation[20]. An early report suggested that the Cu component of this co-catalyst system mediates aerobic oxidation of the hydroxylamine to the oxoammonium form of the nitroxyl co-catalyst (see Fig. 1c)[21]. Later studies[22–24], however, highlighted the mechanistic relationship between these catalysts and galactose oxidase (Fig. 1d and e), an enzyme that features a tyrosine-derived phenoxyl radical coordinated to a Cu(II) centre in the active site[25,26]. Both the chemical (Cu/TEMPO) and enzyme-based reactions mediate alcohol oxidation via the cooperative reactivity of Cu(II) and an oxyl radical as oxidants. This joint participation of two one-electron oxidants contrasts the many alcohol oxidation methods in organic chemistry that use a two-electron oxidant, such as TEMPO$^+$ (see Fig. 1c), Cr(VI) or I(III) reagents, or noble-metal catalysts (such as Pd(II) and Ir(III)) that undergo facile two-electron redox steps.

The unique Cu/TEMPO mechanism has important implications for electrocatalytic alcohol oxidation because, under appropriate conditions, it should be possible to generate TEMPO$^•$ at much lower electrode potentials than needed for TEMPO$^+$. To test this hypothesis, preliminary studies probed the electrochemical behaviour of (bpy)Cu/TEMPO (where bpy is 2,2′-bipyridine) solutions under anaerobic conditions. A cyclic voltammogram, recorded with a solution of Cu(I)OTf (where OTf is trifluoromethanesulfonate), bpy and TEMPO (1 mM each) in acetonitrile, revealed (quasi)reversible features associated with the (bpy)Cu(II)/(bpy)Cu(I) and TEMPO$^{+/•}$ redox processes at −0.18 V and +0.24 V, respectively, versus ferrocenium/ferrocene ($Cp_2Fe^{+/0}$) (Fig. 2a). No TEMPO/TEMPOH redox feature was observed in the cyclic voltammogram, reflecting the lack of a proton source in solution. Electrochemical oxidation of TEMPOH often requires a large overpotential[17], which could reduce the efficiency of TEMPO regeneration during catalytic turnover. Independent experiments, however, highlighted an alternative pathway for TEMPOH reoxidation: (bpy)Cu(II)$(OTf)_2$ was found to mediate efficient oxidation of TEMPOH to TEMPO under anaerobic conditions in the presence of 2,6-lutidine as a Brønsted base (that is, as a proton acceptor). The relevance of this process to alcohol oxidation was demonstrated via spectrophotometric study of the anaerobic oxidation of benzyl alcohol by (bpy)Cu(II)$(OTf)_2$ in the presence of 2,6-lutidine and catalytic TEMPO (0.1 equivalents). This mixture led to rapid reduction of Cu(II), affording a solution that was spectroscopically identical to an independently prepared solution of Cu(I)OTf/bpy (1:1) (Fig. 2b). The reaction did not stop or slow after 10% conversion (that is, after complete consumption of TEMPO), and no benzyl alcohol oxidation or (bpy)Cu(II) reduction was observed in the absence of TEMPO. These observations indicated that (bpy)Cu(II) promoted the oxidation of both benzyl alcohol and TEMPOH, as shown in the reaction cycle in Fig. 2b, and suggested that electrochemical regeneration of (bpy)Cu(II) could provide the basis for electrocatalytic alcohol oxidation.

Cyclic voltammetry studies in the absence of a Brønsted base showed that the electrochemical behaviour of (bpy)Cu(II)$(OTf)_2$ was not affected by the presence of TEMPO and/or benzyl alcohol. A slight increase in the anodic peak current was observed for the (bpy)Cu(II)/(bpy)Cu(I) wave at −0.14 V upon addition of 2,6-lutidine, presumably reflecting catalytic turnover of the Cu(II) (and TEMPO) species on the timescale of the cyclic voltammogram scan (see Supplementary Fig. 1). This result prompted us to evaluate other Brønsted bases, including *N*-methylimidazole (NMI), 4-(dimethylamino)pyridine, 2-(dimethylamino)pyridine, 1,4-diazabicyclo[2.2.2]octane, triethylamine, diisopropylamine, isopropylamine, tributylamine, dibutylamine, *n*-butylamine and aqueous NaOH (see Supplementary Figs 2 and 3). Significant catalytic features were evident in the cyclic voltammograms with several of these bases, and triethylamine (Et_3N) was particularly effective (Fig. 3a).

The reaction conditions were optimized to permit assessment of the catalytic performance of the (bpy)Cu/TEMPO/Et_3N catalyst system, and the analysis was performed at a scan rate at which the catalytic

[1]Department of Chemistry, University of Wisconsin-Madison, 1101 University Avenue, Madison, Wisconsin 53706, USA.

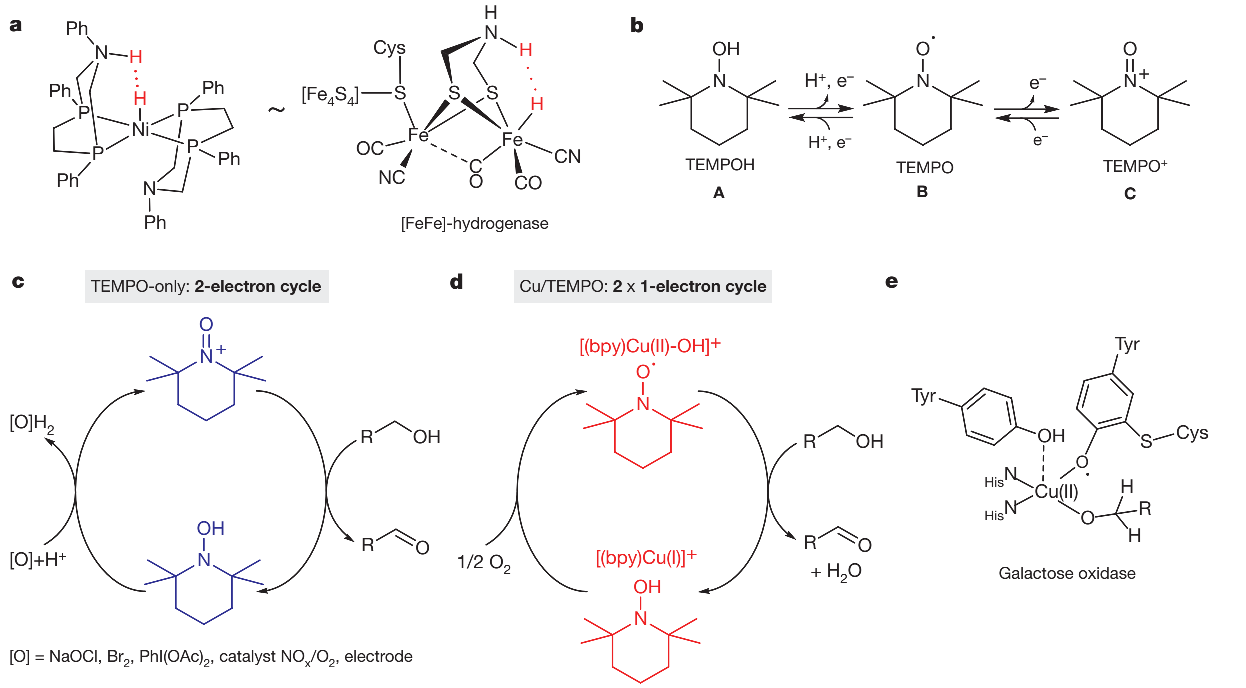

Figure 1 | Molecular electrocatalysts and related homogeneous and enzymatic catalysts. a, Synthetic Ni complex that catalyses H_2 formation, with pendant amines that function as proton relays, and the analogous structure of the [FeFe] hydrogenase active site. **b**, The redox reactions of TEMPO. **c**, **d**, Simplified catalytic cycles for oxoammonium- and (bpy)Cu/TEMPO-based alcohol oxidation pathways. **e**, The oxidized active site of galactose oxidase.

current (which is proportional to the reaction rate) does not exhibit a scan-rate dependence (150 mV s^{-1}, Supplementary Fig. 4). The catalytic current exhibited a saturation dependence on both [Et_3N] and [TEMPO], and the concentrations of these components were chosen within the concentration-independent-rate regimes (50 mM and 5 mM, respectively; see Supplementary Figs 5 and 6). Under these conditions, the catalytic current exhibited a linear, first-order dependence on [(bpy)Cu] and a half-order dependence on [$PhCH_2OH$] (see Fig. 3b and c; the intercept in Fig. 3c corresponds to the anodic current of the (bpy)Cu(II)/(bpy)Cu(I) redox couple in the absence of alcohol).

These results may be analysed within the kinetic framework formulated by ref. 27 (see Supplementary Information for more details). The S-shaped voltammograms indicate that the electrocatalysis is not affected by the diffusion of base, substrate or TEMPO to the electrode and corresponds to the 'kinetic regime' in which the

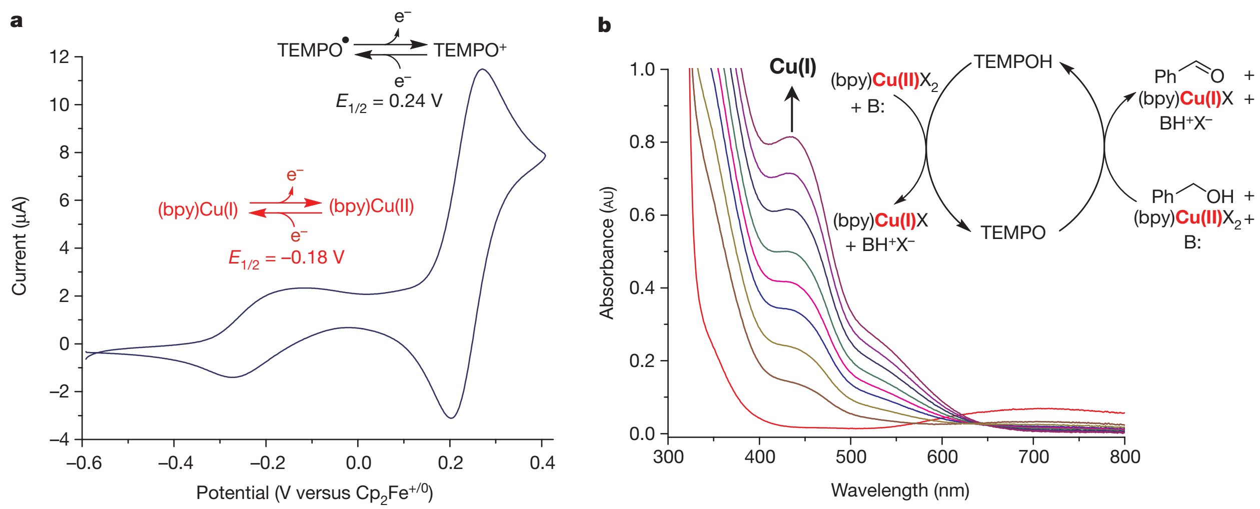

Figure 2 | Cyclic voltammogram of a solution of (bpy)Cu(OTf) and TEMPO and spectrophotometric evidence for (bpy)Cu(II)-mediated oxidation of TEMPOH (and benzyl alcohol) under anaerobic conditions. a, Conditions: 1 mM (bpy)Cu(OTf), 1 mM TEMPO, 10 mV s^{-1}, glassy carbon working electrode, 0.1 M Bu_4NClO_4/CH_3CN. **b**, Conditions: 1 mM $Cu(II)(OTf)_2$, 1 mM bpy, 0.1 mM TEMPO, 50 mM 2,6-lutidine, 100 mM $PhCH_2OH$, 2 ml, 25 °C, 0.1 M Bu_4NClO_4/CH_3CN. 20 min reaction time. The final spectrum corresponds to an independently prepared solution of 1 mM (bpy)Cu(I)OTf. The lack of isosbestic behaviour at early time points reflects changes in the Cu(II)/Cu(I)/bpy speciation under the reaction conditions. We note that the difference in peak currents for (bpy)Cu and TEMPO species in **a** reflects differences in the diffusion properties of these species. See Supplementary Information section 2 for further discussion. B: is the Brønsted base 2,6-lutidine. AU, absorbance units; $E_{1/2}$, half-wave potential.

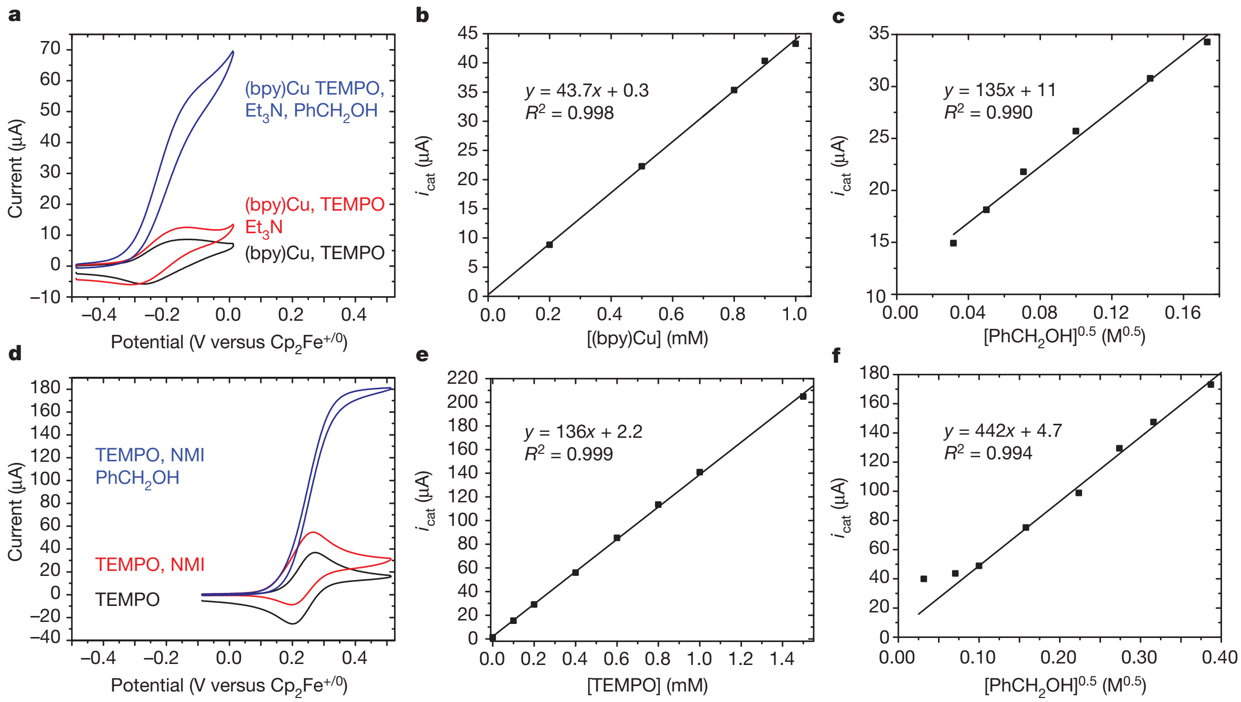

g

Catalyst system	(bpy)Cu/TEMPO	TEMPO
Kinetic order in catalyst	1st	1st
Kinetic order in benzyl alcohol	1st*	1st*
Potential of current plateau (versus $Cp_2Fe^{+/0}$)	–0.14 V	0.36 V
k_{obs} (20 mM $PhCH_2OH$)	11.6 s^{-1}	2.3 s^{-1}

*The kinetic order here reflects the first order $C^0_{substrate}$ dependence in the k_{obs} expression in equation (1).

Figure 3 | Electrochemical oxidation of benzyl alcohol with (bpy)Cu/TEMPO and TEMPO catalysts. Cyclic voltammograms, kinetic data and performance comparison. **a**, Cyclic voltammograms recorded with solutions of (bpy)Cu/TEMPO, corresponding to 1 mM Cu(I)OTf, 1 mM bpy, 5 mM TEMPO (black), upon addition of 50 mM Et_3N (red), and then addition of 100 mM $PhCH_2OH$ (blue). **b**, Plot of i_{cat} versus [(bpy)Cu(I)OTf]. Conditions: 5 mM TEMPO, 50 mM Et_3N, 100 mM $PhCH_2OH$. **c**, Plot of i_{cat} versus $[PhCH_2OH]^{0.5}$. Conditions: 1 mM (bpy)Cu(I), 5 mM TEMPO, 50 mM Et_3N. **d**, Cyclic voltammograms recorded with solutions of TEMPO, corresponding to 1 mM TEMPO (black), upon addition of 450 mM NMI (red), and then addition of 100 mM $PhCH_2OH$ (blue). **e**, Plot of i_{cat} versus [TEMPO]. Conditions: 450 mM NMI, 100 mM $PhCH_2OH$. **f**, Plot of i_{cat} versus $[PhCH_2OH]^{0.5}$. Conditions: 1 mM TEMPO, 450 mM NMI. **g**, Performance comparison between (bpy)Cu/TEMPO- and TEMPO-based electrocatalytic oxidation of benzyl alcohol. All experiments in 0.1 M Bu_4NClO_4/CH_3CN, at 150 mV s^{-1} for (bpy)Cu/TEMPO and at 100 mV s^{-1} for TEMPO-only reaction.

catalytic current is limited only by chemical steps involving the catalyst. The current measured for the catalytic reaction, i_{cat}, is described by

$$i_{cat} = nFAC^0_{cat}\sqrt{D_{cat}2k_{obs}} \qquad (1)$$

where $k_{obs} = kC^0_{substrate}$ and

$$\frac{i_{cat}}{i_p} = \frac{1}{0.4463}\sqrt{\frac{RT2k_{obs}}{Fnv}} \qquad (2)$$

Equation (1) is derived for two-electron oxidation of a substrate, where n is the number of electrons for the (bpy)Cu redox couple ($n = 1$), F is Faraday's constant, A is the surface area of the electrode, C^0_{cat} is the electrocatalyst concentration, D_{cat} is the diffusion constant of the catalyst, 2 is the stoichiometric factor and k_{obs} is the observed rate constant. This expression accounts for the first-order dependence of the catalytic current on the (bpy)Cu concentration (C^0_{cat}) and the half-order dependence on substrate concentration ($C^0_{substrate}$) (compare Fig. 3b and c; the half-order dependence of the catalytic current on $C^0_{substrate}$ corresponds to a first-order dependence of the chemical reaction rate (k_{obs}) on $C^0_{substrate}$; see Fig. 3g). The ratio i_{cat}/i_p in equation (2), where i_p is the peak current of the electrocatalyst in the absence of substrate, provides a convenient means to determine k_{obs} (where R is the ideal gas constant, T is the reaction temperature, and v is the scan rate). The catalytic wave for (bpy)Cu/TEMPO-mediated oxidation of benzyl alcohol does not exhibit a clearly defined plateau, so the catalytic current was recorded at the peak potential of the (bpy)Cu complex. This approach will underestimate k_{obs}, but it avoids the uncertainties of identifying a plateau. A k_{obs} value of 11.6 s^{-1} at an applied potential of −0.14 V was determined for the Cu/TEMPO/Et_3N catalyst system using this method (Fig. 3g).

Similar studies of electrocatalytic benzyl alcohol oxidation with a TEMPO-only catalyst were performed to provide a benchmark for comparison. The cyclic voltammogram of TEMPO shows a reversible one-electron redox feature corresponding to the TEMPO/$TEMPO^+$ couple at $E_{1/2} = 0.24$ V (versus $Cp_2Fe^{+/0}$) (Fig. 3d). Et_3N cannot be used as a base with TEMPO because Et_3N undergoes oxidation at the electrode surface in this potential range, and it also undergoes a background reaction with $TEMPO^+$. NMI has a basicity similar to Et_3N (pK_a values for NMI-H^+ and Et_3N-H^+ are 17.1 and 18.8, respectively, in CH_3CN), and it was identified as an effective Brønsted base. TEMPO exhibited an S-shape catalytic wave at the TEMPO/$TEMPO^+$ couple in the presence of NMI and benzyl alcohol (Fig. 3d). The catalytic current exhibited a saturation dependence on the NMI

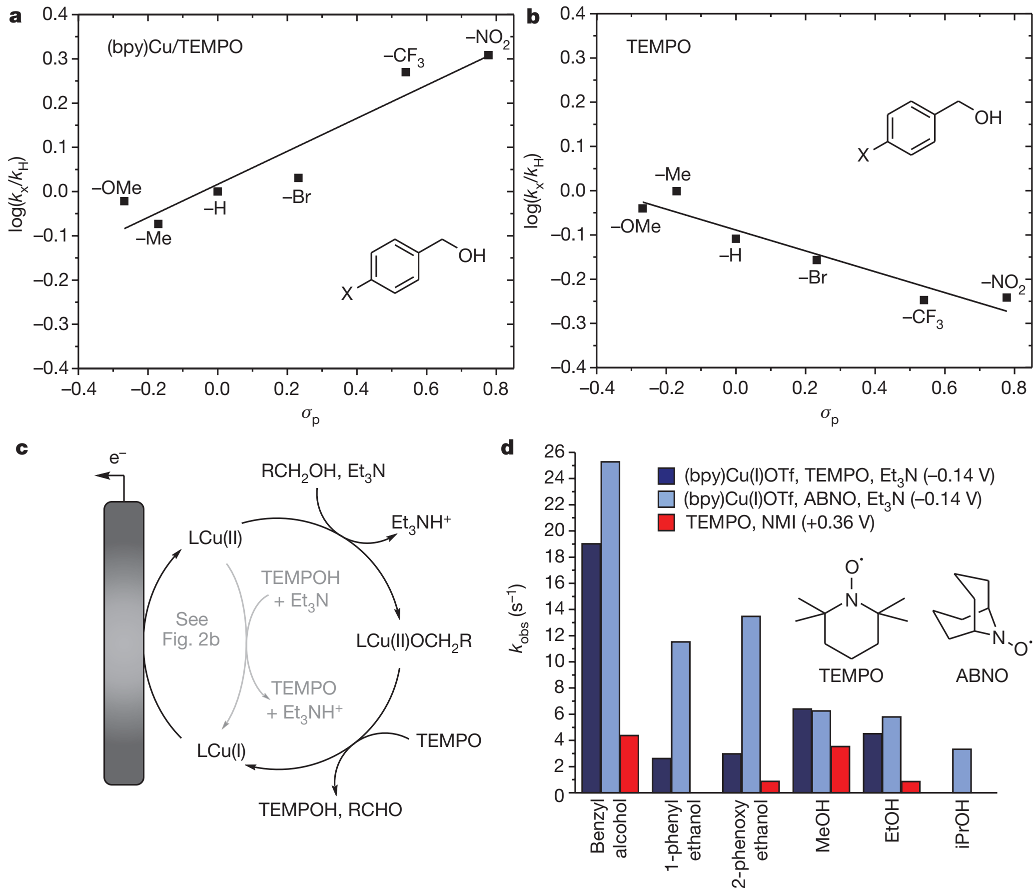

Figure 4 | Electronic effects and comparative reactivity of different catalyst systems with different alcohols. a, **b**, Hammett plots of independent rate measurements of *para*-substituted benzyl alcohols with (bpy)Cu/TEMPO (**a**) and TEMPO (**b**) electrocatalysts. See Fig. 3 for conditions. **c**, The proposed mechanism of (bpy)Cu/TEMPO-mediated alcohol oxidation. **d**, Relative catalytic activity of three different catalyst systems [Cu/TEMPO, Cu/ABNO, and TEMPO-only] with six different benzylic, aliphatic, primary and secondary alcohols. Conditions: 100 mM alcohol concentration and 0.1 M Bu_4NClO_4 in CH_3CN, in all cases. Cu/TEMPO: 1 mM (bpy)Cu(I)(OTf), 5 mM TEMPO, 50 mM Et_3N; Cu/ABNO: 1 mM (bpy)Cu(I)(OTf), 1 mM ABNO, 50 mM Et_3N. TEMPO: 1 mM TEMPO, 450 mM NMI. Rate constants were calculated according to equations (1) and (2) (see Supplementary Information for details).

concentration, and the NMI concentration was chosen to be within the concentration-independent-rate regime (450 mM; see Supplementary Fig. 9). Under these conditions, the catalytic current exhibited a linear, first-order dependence on [TEMPO] and a half-order dependence on benzyl alcohol concentration (Fig. 3e and f; see equation (2)). The kinetic constants calculated according to equation (2) revealed a k_{obs} value of 2.3 s^{-1} at an applied potential of 0.36 V for the TEMPO/NMI catalyst system (Fig. 3g).

Additional insights into the (bpy)Cu/TEMPO and TEMPO-only catalyst systems were obtained from kinetic isotope effects and Hammett studies. Independent rate measurements for the oxidation of $PhCH_2OH$ and $PhCD_2OH$ revealed a kinetic isotope effect of 1.0 for (bpy)Cu/TEMPO, while a kinetic isotope effect of 3.2 was observed for the TEMPO-only catalyst system. The oxidation rates of six *para*-substituted benzyl alcohols were then measured with both catalyst systems. Hammett plots of the data (Fig. 4a and b) reveal relatively weak, but opposite, electronic trends: electron-deficient alcohols are oxidized more readily with the (bpy)Cu/TEMPO catalyst system, with a slope (ρ) of +0.37, while electron-rich alcohols react more rapidly with the TEMPO-only catalyst ($\rho = -0.24$). Previous studies of these catalyst systems with chemical oxidants supported the formation of (bpy) Cu(II)/alkoxide[23,24] and $TEMPO^+$/alkoxide[16,28] adducts, respectively, which afford the aldehyde or ketone product via intramolecular hydrogen transfer to the TEMPO fragment. With the Cu/TEMPO catalyst, the kinetic studies, isotope effects, and Hammett data in Figs 3 and 4a may be rationalized by rate-limiting formation of a Cu(II)–alkoxide, which will proceed more rapidly with electron-deficient (that is, more acidic) alcohols (Fig. 4c). With the TEMPO-only catalyst, the data in Figs 3 and 4b are consistent with rate-limiting hydrogen transfer from the alcohol to $TEMPO^+$ within the $TEMPO^+$/alkoxide adduct, wherein the hydrogen has a slightly hydridic character.

The modular composition of the (bpy)Cu/TEMPO electrocatalyst makes it well suited for further optimization and development. In a preliminary assessment of this opportunity, TEMPO was replaced with the sterically less-hindered bicyclic nitroxyl, ABNO (9-azabicyclo [3.3.1]nonane *N*-oxyl)[20]. Six sterically and electronically different alcohols were tested with the three catalyst systems, (bpy)Cu/TEMPO, (bpy)Cu/ABNO and TEMPO-only (Fig. 4d). The (bpy)Cu/nitroxyl catalysts exhibited substantially higher rates than the TEMPO-only catalyst for all substrates tested, including excellent reactivity with methanol and ethanol. The high activity of both (bpy)Cu/nitroxyl catalysts was especially notable because it occurred at an applied potential 0.5 V lower than for the TEMPO-only catalyst (−0.14 V versus +0.36 V, respectively). The (bpy)Cu/ABNO catalyst exhibited higher activity than (bpy)Cu/TEMPO for nearly all alcohols, presumably reflecting the role of steric effects on the reaction[20]. Methanol, the smallest available alcohol, was an exception and exhibited nearly identical rates with the two catalysts.

The results presented above show that electrochemical alcohol oxidation with (bpy)Cu/nitroxyl catalysts occurs at the (bpy)Cu(II)/(bpy) Cu(I) redox potential. The nitroxyl is also required for catalytic activity, however, and the data are consistent with cooperative reactivity

involving the (bpy)Cu(II) and nitroxyl species in a concerted one-proton/two-electron oxidation of the Cu(II)-coordinated alkoxide ligand. This step affords the aldehyde or ketone product and is reminiscent of 'β-hydride elimination' steps commonly observed with noble metals[24]. However, rather than direct hydride transfer to a single metal centre, the proton and two electron equivalents associated with the hydride are partitioned between Cu and nitroxyl co-catalysts, affording (bpy) Cu(I) and hydroxylamine (for example, TEMPOH) (compare Fig. 1b and d). Thus, Cu(II) serves as a one-electron oxidant, while the nitroxyl serves as an electron-proton acceptor.

These observations have important implications for the development of electrocatalysts composed of non-precious metals, with applications extending beyond alcohol oxidation. The role of the nitroxyl as an electron-proton-transfer mediator (in which both an electron and a proton are transferred) in the (bpy)Cu/nitroxyl-catalysed reactions may be compared to the role of Brønsted bases in many other electrocatalytic reactions, including the tethered amines of the hydrogenase mimics in Fig. 1a. Brønsted bases play a crucial role in promoting proton-coupled electron transfer steps, in which deprotonation of a catalytic intermediate is coupled to one-electron transfer to the catalytic metal centre or to the electrode. Such concerted steps can greatly enhance catalytic rates by avoiding energetically unfavourable intermediates that would arise from independent proton- and electron-transfer steps[29,30]. Electron-proton-transfer mediators, such as nitroxyls, expand upon this concept in an important way because such entities are equipped to accept both a proton and an electron. By working in cooperation with a first-row transition metal, electron-proton-transfer mediators provide the basis for efficient proton-coupled two-electron reactivity. The present study illustrates this concept, and shows how it can lead to much faster electrocatalytic rates and lower overpotentials, both of which are crucial in energy-conversion applications. Two-electron redox steps are intrinsic to electrochemical reactions involving H_2, O_2, N_2, CO_2 and numerous other molecules, and the development of new cooperative electrocatalysts composed of non-precious metals and electron-proton-transfer mediators could lead to important breakthroughs in these applications.

Online Content Methods, along with any additional Extended Data display items and Source Data, are available in the online version of the paper; references unique to these sections appear only in the online paper.

Received 23 December 2015; accepted 13 April 2016.
Published online 27 June 2016.

1. Kakati, N. *et al.* Anode catalysts for direct methanol fuel cells in acidic media: do we have any alternative for Pt or Pt−Ru? *Chem. Rev.* **114,** 12397–12429 (2014).
2. Bianchini, C. & Shen, P. K. Palladium-based electrocatalysts for alcohol oxidation in half cells and in direct alcohol fuel cells. *Chem. Rev.* **109,** 4183–4206 (2009).
3. Cheung, K.-C., Wong, W.-L., Ma, D.-L., Lai, T.-S. & Wong, K.-Y. Transition metal complexes as electrocatalysts—development and applications in electro-oxidation reactions. *Coord. Chem. Rev.* **251,** 2367–2385 (2007).
4. Trincado, M., Banerjee, D. & Grützmacher, H. Molecular catalysts for hydrogen production from alcohols. *Energy Environ. Sci.* **7,** 2464–2503 (2014).
5. Hickey, D. P., McCammant, M. S., Giroud, F., Sigman, M. S. & Minteer, S. D. Hybrid enzymatic and organic electrocatalytic cascade for the complete oxidation of glycerol. *J. Am. Chem. Soc.* **136,** 15917–15920 (2014).
6. Cha, H. G. & Choi, K.-S. Combined biomass valorization and hydrogen production in a photoelectrochemical cell. *Nat. Chem.* **7,** 328–333 (2015).
7. Ciriminna, R., Palmisano, G. & Pagliaro, M. Electrodes functionalized with the 2,2,6,6-tetramethylpiperidinyloxy radical for the waste-free oxidation of alcohols. *ChemCatChem* **7,** 552–558 (2015).
8. Francke, R. & Little, R. D. Redox catalysis in organic electrosynthesis: basic principles and recent developments. *Chem. Soc. Rev.* **43,** 2492–2521 (2014).
9. Rakowski Dubois, M. & Dubois, D. L. Development of molecular electrocatalysts for CO_2 reduction and H_2 production/oxidation. *Acc. Chem. Res.* **42,** 1974–1982 (2009).
10. Le Goff, A. *et al.* From hydrogenases to noble metal-free catalytic nanomaterials for H_2 production and uptake. *Science* **326,** 1384–1387 (2009).
11. Raugei, S. *et al.* Experimental and computational mechanistic studies guiding the rational design of molecular electrocatalysts for production and oxidation of hydrogen. *Inorg. Chem.* **55,** 445–460 (2016).
12. Rauchfuss, T. B. Diiron azadithiolates as models for the [FeFe]-hydrogenase active site and paradigm for the role of the second coordination sphere. *Acc. Chem. Res.* **48,** 2107–2116 (2015).
13. Helm, M. L., Stewart, M. P., Bullock, R. M., Rakowski DuBois, M. & DuBois, D. L. A synthetic nickel electrocatalyst with a turnover frequency above 100,000 s^{-1} for H_2 production. *Science* **333,** 863–866 (2011).
14. Rodriguez-Maciá, P., Dutta, A., Lubitz, W., Shaw, W. J. & Rüdiger, O. Direct comparison of the performance of a bio-inspired synthetic nickel catalyst and a [NiFe]-hydrogenase, both covalently attached to electrodes. *Angew. Chem. Int. Ed.* **54,** 12303–12307 (2015).
15. Weiss, C. J., Wiedner, E. S., Roberts, J. A. S. & Appel, A. M. Nickel phosphine catalysts with pendant amines for electrocatalytic oxidation of alcohols. *Chem. Commun.* **51,** 6172–6174 (2015).
16. Bobbitt, J. M., Brückner, C. & Merbouh, N. Oxoammonium- and nitroxide-catalyzed oxidations of alcohols. *Org. React.* **74,** 103–424 (2009).
17. Semmelhack, M. F., Chou, C. S. & Cortes, D. A. Nitroxyl-mediated electrooxidation of alcohols to aldehydes and ketones. *J. Am. Chem. Soc.* **105,** 4492–4494 (1983).
18. Rafiee, M., Miles, K. C. & Stahl, S. S. Electrocatalytic alcohol oxidation with TEMPO and bicyclic nitroxyl derivatives: driving force trumps steric effects. *J. Am. Chem. Soc.* **137,** 14751–14757 (2015).
19. Hickey, D. P. *et al.* Predicting electrocatalytic properties: modeling structure-activity relationships of nitroxyl radicals. *J. Am. Chem. Soc.* **137,** 16179–16186 (2015).
20. Ryland, B. L. & Stahl, S. S. Practical aerobic oxidations of alcohols and amines with homogeneous copper/TEMPO and related catalyst systems. *Angew. Chem. Int. Ed.* **53,** 8824–8838 (2014).
21. Semmelhack, M. F., Schmid, C. R., Cortes, D. A. & Chou, C. S. Oxidation of alcohols to aldehydes with oxygen and cupric ion, mediated by nitrosonium ion. *J. Am. Chem. Soc.* **106,** 3374–3376 (1984).
22. Dijksman, A., Arends, I. W. C. E. & Sheldon, R. A. Cu(II)-nitroxyl radicals as catalytic galactose oxidase mimics. *Org. Biomol. Chem.* **1,** 3232–3237 (2003).
23. Hoover, J. M., Ryland, B. L. & Stahl, S. S. Mechanism of copper(I)/TEMPO-catalyzed aerobic alcohol oxidation. *J. Am. Chem. Soc.* **135,** 2357–2367 (2013).
24. Ryland, B. L., McCann, S. D., Brunold, T. C. & Stahl, S. S. Mechanism of alcohol oxidation mediated by copper(II) and nitroxyl radicals. *J. Am. Chem. Soc.* **136,** 12166–12173 (2014).
25. Whittaker, J. W. Free radical catalysis by galactose oxidase. *Chem. Rev.* **103,** 2347–2364 (2003).
26. Chirik, P. J. & Wieghardt, K. Radical ligands confer nobility on base-metal catalysts. *Science* **327,** 794–795 (2010).
27. Costentin, C. & Savéant, J.-M. Multielectron, multistep molecular catalysis of electrochemical reactions: benchmarking of homogeneous catalysts. *ChemElectroChem* **1,** 1226–1236 (2014).
28. Semmelhack, M. F., Schmid, C. R. & Cortes, D. A. Mechanism of the oxidation of alcohols by 2,2,6,6-tetramethylpiperidine nitrosonium cation. *Tetrahedr. Lett.* **27,** 1119–1122 (1986).
29. Huynh, M. H. V. & Meyer, T. J. Proton-coupled electron transfer. *Chem. Rev.* **107,** 5004–5064 (2007).
30. Warren, J. J., Tronic, T. A. & Mayer, J. M. Thermochemistry of proton-coupled electron transfer reagents and its implications. *Chem. Rev.* **110,** 6961–7001 (2010).

Supplementary Information is available in the online version of the paper.

Acknowledgements Financial support for this project was provided by the Great Lakes Bioenergy Research Center (Department of Energy Biological and Environmental Research Office of Science DE-FC02-07ER64494).

Author Contributions S.S.S. conceived the idea for the Cu/nitroxyl electrocatalytic alcohol oxidation, and A.B. and S.S.S. collaborated to design the project. A.B. performed all experimental work and led the data interpretation and analysis, in consultation with S.S.S. A.B. and S.S.S. wrote the manuscript.

Author Information Reprints and permissions information is available at www.nature.com/reprints. The authors declare no competing financial interests. Readers are welcome to comment on the online version of the paper. Correspondence and requests for materials should be addressed to S.S.S. (stahl@chem.wisc.edu).

LETTER

doi:10.1038/nature18645

Absence of 21st century warming on Antarctic Peninsula consistent with natural variability

John Turner[1], Hua Lu[1], Ian White[1], John C. King[1], Tony Phillips[1], J. Scott Hosking[1], Thomas J. Bracegirdle[1], Gareth J. Marshall[1], Robert Mulvaney[1] & Pranab Deb[1]

Since the 1950s, research stations on the Antarctic Peninsula have recorded some of the largest increases in near-surface air temperature in the Southern Hemisphere[1]. This warming has contributed to the regional retreat of glaciers[2], disintegration of floating ice shelves[3] and a 'greening' through the expansion in range of various flora[4]. Several interlinked processes have been suggested as contributing to the warming, including stratospheric ozone depletion[5], local sea-ice loss[6], an increase in westerly winds[5,7], and changes in the strength and location of low–high-latitude atmospheric teleconnections[8,9]. Here we use a stacked temperature record to show an absence of regional warming since the late 1990s. The annual mean temperature has decreased at a statistically significant rate, with the most rapid cooling during the Austral summer. Temperatures have decreased as a consequence of a greater frequency of cold, east-to-southeasterly winds, resulting from more cyclonic conditions in the northern Weddell Sea associated with a strengthening mid-latitude jet. These circulation changes have also increased the advection of sea ice towards the east coast of the peninsula, amplifying their effects. Our findings cover only 1% of the Antarctic continent and emphasize that decadal temperature changes in this region are not primarily associated with the drivers of global temperature change but, rather, reflect the extreme natural internal variability of the regional atmospheric circulation.

While global mean surface air temperature (SAT) has increased over recent decades, the rate of regional warming has varied markedly[10], with some of the most rapid SAT increases recorded in the polar regions[11–13]. In Antarctica, the largest SAT increases have been observed in the Antarctic Peninsula (AP) and especially on its west coast[1]: in particular, Vernadsky (formerly Faraday) station (Fig. 1) experienced an increase in annual mean SAT of 2.8 °C between 1951 and 2000.

The AP is a challenging area for the attribution of the causes of climate change because of the shortness of the *in situ* records, the large inter-annual circulation variability[14] and the sensitivity to local interactions between the atmosphere, ocean and ice. In addition, the atmospheric circulation of the AP and South Pacific are quite different between summer (December–February) and the remainder of the year.

Since the late 1970s, the springtime loss of stratospheric ozone has contributed to the warming of the AP, particularly during summer[7]. However, during the extended winter period of March–September, when teleconnections between the tropics and high southern latitudes are strongest[15], tropical sea surface temperature (SST) anomalies in the Pacific and Atlantic Oceans[16] can strongly modulate the climate of the AP. The teleconnections are further affected by the mid-latitude jet, which influences regional cyclonic activity and AP SATs. While the jet is strong for most of the year, during the summer it is weaker, there are fewer cyclones, and tropical forcing plays little part in AP climate variability.

The annual mean SAT records from six coastal stations located in the northern AP (Fig. 1) show a warming through the second half of the twentieth century, followed by little change or a decrease during the first part of the twenty-first century[17]. We investigate the differences in high and low latitude forcing on the climate of the AP during what we henceforth term the 'warming' and 'cooling' periods, focusing particularly on the period since 1979, since this marks the start of the availability of reliable, gridded atmospheric analyses and fields of sea-ice concentration (SIC). We use a stacked and normalized SAT anomaly record (Fig. 2a) based on the six station SAT time series (see Methods) to investigate the broad-scale changes that have affected the northern AP since 1979. To provide an objective measure of the timing of the change in trend we used the sequential Mann–Kendall test (see Methods). This identified the middle of 1998 to early 1999 as the most likely turning point between the warming and cooling periods (indicated by shading on Fig. 2). The trends in the stacked SAT during the warming (0.32 ± 0.20 per decade (dec^{-1}), 1979–1997) and cooling (-0.47 ± 0.25 dec^{-1}, 1999–2014) periods are both statistically significant at $P < 0.05$ (Extended Data Table 1). To confirm that the change in trend is not simply an artefact of the extreme El Niño conditions during 1997–1998, we repeated the analysis for 1979–1996 and 2000–2014. The trends were still significant at $P < 0.05$, although magnitudes were slightly smaller.

While the stacked SAT increased in all seasons during the warming period of 1979–1997 (Extended Data Table 1), the warming was largest during the summer, although the significance of the trend is lower ($P < 0.10$). During this period there was a positive trend in the Southern Annular Mode (SAM)[5], primarily during summer (Extended Data Fig. 1) in response to stratospheric ozone depletion and increasing greenhouse gas concentrations[5,18]. The trend in the SAM led to a greater flow of mild, northwesterly air onto the AP (Extended Data Fig. 2a), with SAT on the northeastern side increasing most because of amplification through the foehn effect[7]. This atmospheric circulation trend contributed to the large decrease in SIC in summer (Extended Data Fig. 3a) and for the year as a whole (Fig. 3a). However, there was no significant trend in annual mean sea-level pressure (SLP) across the AP during the warming period (Fig. 3b). During the summer, tropical climate variability had little influence on the AP SATs[15] and the trend in the SAM had the greatest impact.

Over the cooling period of 1999–2014 there was a significant increase in annual mean SIC around the northern AP and across the northern part of the Weddell Sea (Fig. 3c). This occurred as a result of increasingly cyclonic conditions in the Drake Passage and northwestern Weddell Sea (Fig. 3d), associated with a strengthening mid-latitude jet, which advected cold air towards the AP.

The stacked SAT decreased in all seasons over 1999–2014, but with the greatest cooling during summer, when the trend was moderately significant ($P < 0.10$) (Extended Data Table 1). In this season the trends during the warming and cooling periods are different at a 90% confidence level (see Methods).

During the summer the SAM index remained predominantly positive (Extended Data Fig. 1), and SLP was on average lower over the

[1]British Antarctic Survey, Natural Environment Research Council, High Cross, Madingley Road, Cambridge CB3 0ET, UK.

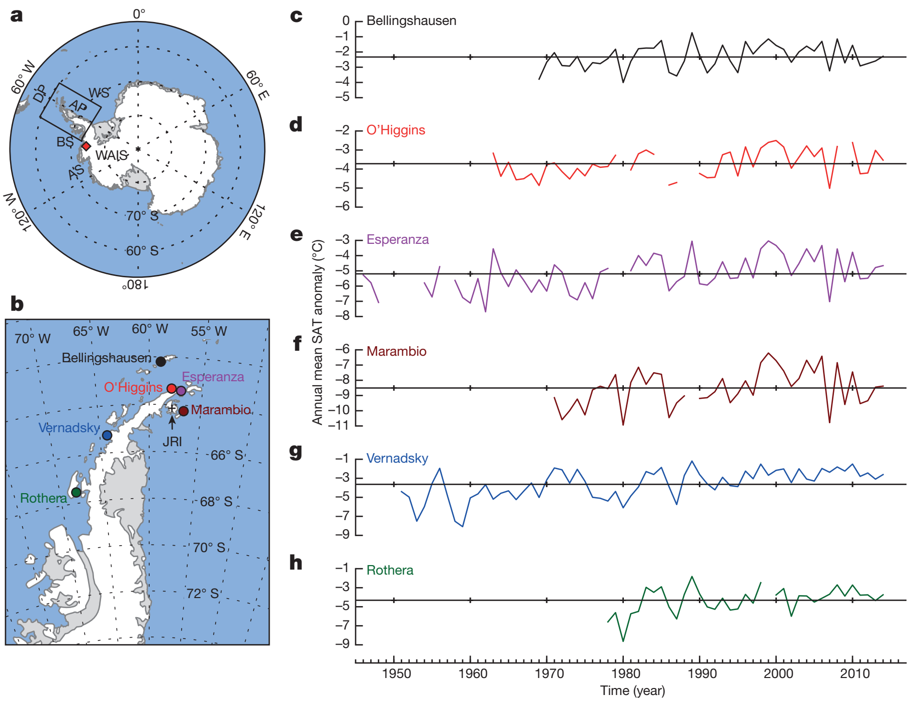

Figure 1 | SAT changes at the six AP stations. **a**, **b**, Map of the Antarctic (**a**) with a blow up of the AP showing the locations of stations referred to in the text (**b**). The locations of the drilling sites for the Ferrigno and James Ross Island ice cores are indicated by a red diamond and an arrowed cross, respectively. **c**–**h**, The time series of annual mean SAT anomalies are shown for Bellingshausen (**c**), O'Higgins (**d**), Esperanza (**e**), Marambio (**f**), Vernadsky (**g**) and Rothera (**h**), with each horizontal line indicating the mean for the whole time series. AS, Amundsen Sea; BS, Bellingshausen Sea; DP, Drake Passage; WAIS, West Antarctic Ice Sheet; WS, Weddell Sea.

Antarctic than during the warming period (Fig. 4a). However, there was no significant trend in the SAM, probably owing to there being little change in the depth of the ozone hole.

The summer cooling resulted from strong east-to-southeasterly near-surface flow towards the AP as SLP decreased (increased) over the South Atlantic (Bellingshausen Sea) (Extended Data Fig. 4a). The greater cyclonic conditions over the South Atlantic occurred in association with a mid-latitude jet that was significantly ($P < 0.05$) stronger than during the warming period (Fig. 4b), and which was located at the northern limit of a cold trough extending from Antarctica. The stronger east-to-southeasterly flow advected sea ice towards the east coast of the AP, giving a positive SIC trend that extended across the whole of the northern Weddell Sea (Extended Data Fig. 5a). This greater ice extent limited the flux of heat from the ocean and amplified the effects of the circulation changes.

During the extended winter, the circulation over the South Pacific is marked by a clearly defined climatological split jet structure, with the subtropical jet (STJ) near 30° S and the polar front jet (PFJ) close to 60° S (ref. 19). The PFJ is sensitive to both zonally symmetric forcing, such as SAM variability, and regional factors, such as the stationary Rossby waves propagating from the tropical Pacific Ocean[15], and the meridional gradient of extratropical SSTs. In general, the STJ (PFJ) is

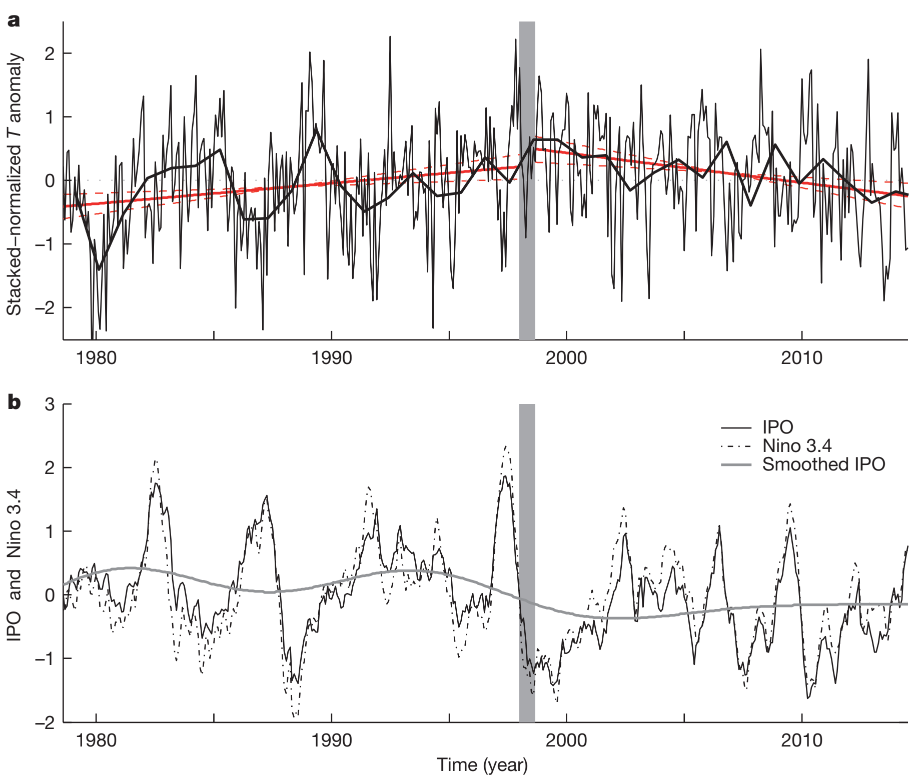

Figure 2 | AP temperature and measures of tropical climate variability since 1979. a, The stacked–normalized SAT anomalies for 1979–2014 (thin black line), with the thick black line showing the annual mean values. The solid red lines show the linear trends for the warming and cooling periods, with the 95% confidence limits for the trends indicated by the broken lines. **b**, The monthly mean IPO index (continuous black line) and Niño 3.4 temperature anomaly (broken line), with the grey line showing the IPO index with decadal smoothing. The vertical grey-shaded area on both figures indicates the period of transition from warming to cooling identified by the Mann–Kendall test.

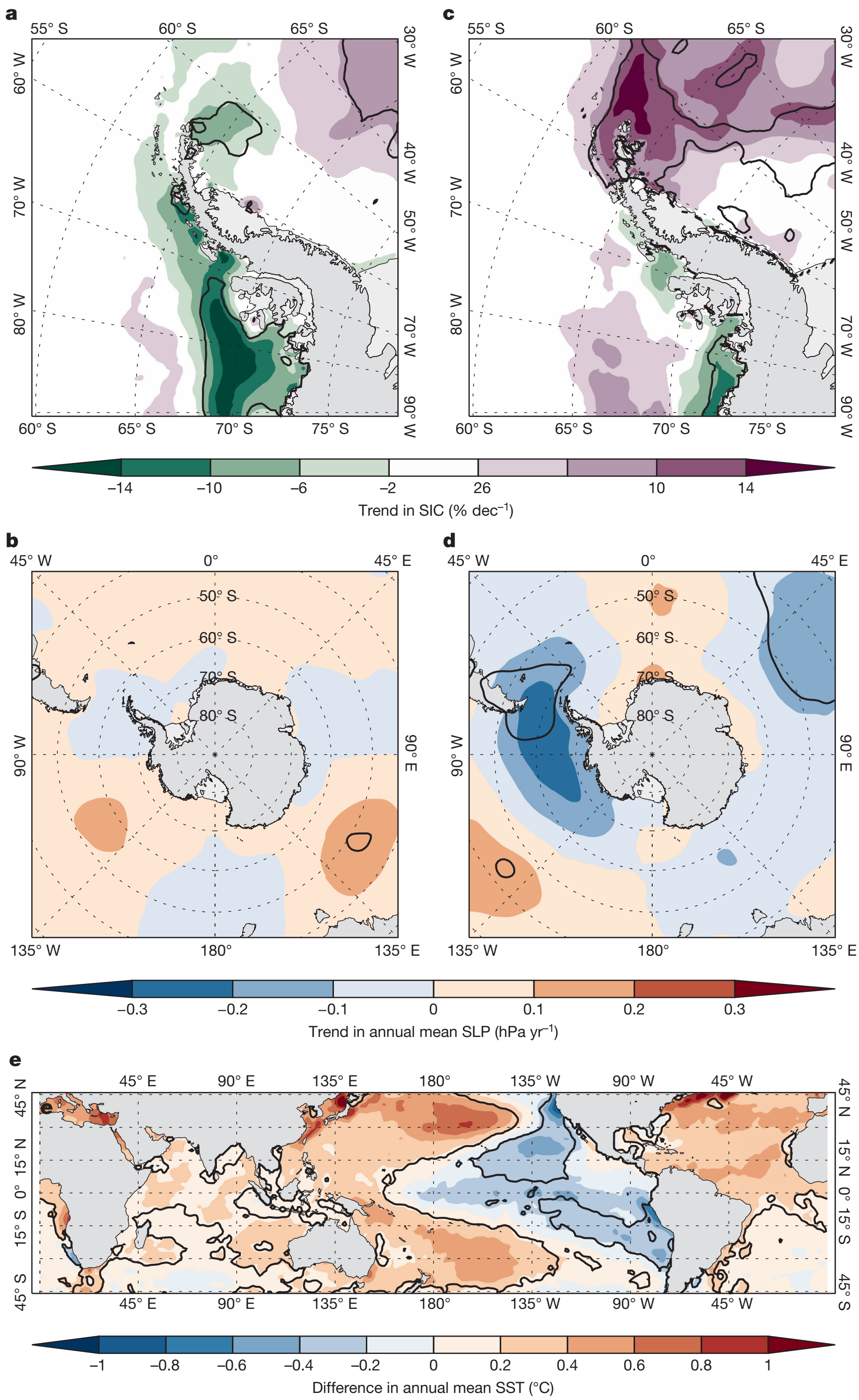

Figure 3 | Trends and differences in atmospheric and oceanic conditions. **a**, The trend in annual mean SIC for 1979–1997. **b**, The trend in annual mean SLP for 1979–1997. **c**, The trend in annual mean SIC for 1999–2014. **d**, The trend in annual mean SLP for 1999–2014. **e**, The difference in annual mean SSTs between 1999–2014 and 1979–1997. Areas where the difference or trend is significant at $P < 0.05$ are indicated by a bold line.

stronger during El Niño/positive Interdecadal Pacific Oscillation (IPO) (La Niña/negative IPO)[20,21]. Nevertheless, their combined effect on the AP regional circulation is complex and may involve nonlinear wave–mean flow feedbacks[22].

The tropical–high-latitude linkages during the extended winter were examined through an analysis of large-scale Rossby wave propagation via the horizontal stationary Eliassen–Palm fluxes[23] at 300 hPa (see Methods). During the 1979–1997 warming period, tropical SSTs were characterized by relatively high SSTs across the eastern tropical Pacific Ocean with relatively more frequent El Niño conditions and a more positive IPO (Fig. 2b), and thus a relatively weak (strong) PFJ (STJ). The generation of quasi-stationary Rossby waves occurred primarily close to 180° E, consistent with higher SSTs in this area, and the wave propagation from the tropics to the South Pacific was limited by a strengthened STJ.

During the 1999–2014 cooling period, a major change in tropical Pacific SSTs occurred with SSTs higher over the Maritime Continent and lower over the eastern Pacific Ocean (Fig. 3e). There was also enhanced transmission of quasi-stationary Rossby waves from the tropics towards the Antarctic, which can be seen in the differences in 300 hPa stream function (Fig. 4f). However, at higher latitudes wave propagation was reduced or prohibited because of enhanced

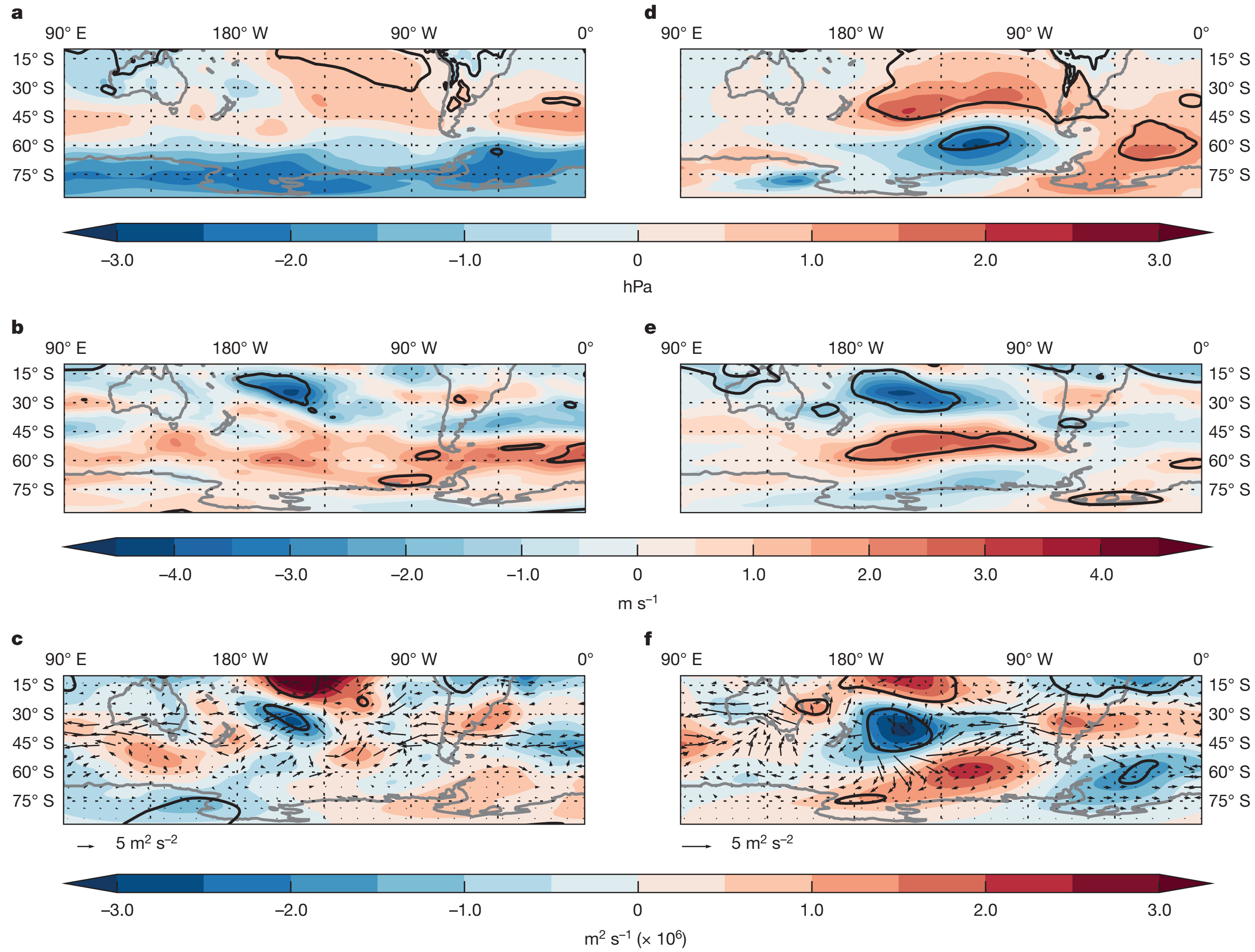

Figure 4 | Differences in atmospheric conditions between the cooling and warming periods (1999–2014 minus 1979–1997). a–f, SLP December–February (DJF) (**a**), 300 hPa zonal wind component DJF (**b**), stream function (colours) and wave propagation (arrows) DJF (**c**), SLP March–September (**d**), 300 hPa zonal wind component March–September (**e**), stream function (colours) and wave propagation (arrows) March–September (**f**). Areas where the differences are significant at $P < 0.05$ are indicated by a bold line.

equatorward wave refraction or reflection from the PFJ region (Fig. 4f). The PFJ was significantly stronger across the South Pacific during the cooling period (Fig. 4e), which is consistent with the higher frequency of La Niña-like conditions and an enhanced meridional temperature gradient between mid- and high latitudes, corresponding to a negative IPO (Fig. 2b). The stronger PFJ resulted in greater surface cyclonic activity to the west of the AP during the cooling period (Fig. 4d), which typically gives higher SATs across the AP[20]. However, critically over 1999–2014 there was a climatological trough in the Drake Passage, giving enhanced easterly flow across the northern Weddell Sea towards the AP. The progressively stronger easterly flow is shown by a decrease of SLP (significant at $P < 0.05$ in March–May (MAM) and June–August (JJA)) in the Drake Passage (Extended Data Fig. 4b–d) and a positive trend in SIC around the northern AP (Extended Data Fig. 5b–d). The cold, east-to-southeasterly circulation negated the warming effect from the tropics usually found in association with La Niña-like conditions, resulting in a cooling trend in SAT during the extended winter period over 1999–2014.

The start of the AP cooling in 1998 coincided with the so-called 'global warming hiatus'. There has been extensive discussion over the factors responsible for this reduction in the rate of increase in mean global SAT[24,25], with the negative phase of the IPO, volcanic and solar activity, and aerosol forcing being cited as possible causes. As discussed earlier, the phase of the IPO can affect the climate of the AP, but the negative phase is usually associated with higher SATs during the extended winter. Since the late 1990s, AP SATs have decreased throughout the year, with local factors playing a greater part than tropical variability, indicating that the absence of AP SAT warming is independent of the global warming hiatus.

The recent change in SAT trend can be set in a longer-term perspective through examination of regional ice core records. An ice core from James Ross Island[26] (Fig. 1), which is close to Marambio station, showed that the region experienced several periods of rapid warming and cooling in the last 1,000 years, and that the warming trend over the last 100 years was 'highly unusual', although not unprecedented. However, the period since the late 1970s includes the ozone hole, which is unique in the record. The Ferrigno ice core from the coast of West Antarctica (Fig. 1) shows a warming from the 1950s to the early twenty-first century that agrees well with the warming observed at Vernadsky[27]. In the longer term, this record revealed marked decadal variability and, importantly, resolved a 50-year period in the eighteenth century when SATs increased at a faster rate than observed at Vernadsky over the second half of the twentieth century. Such long-term variability is also expected from analysis of station SAT records, which exhibit statistical long-term persistence[28]. Therefore all these studies suggest that the rapid warming on the AP since the 1950s and subsequent cooling since the late-1990s are both within the bounds of the large natural decadal-scale climate variability of the region. This result is also consistent with

the very high level of decadal-scale natural internal variability of the regional atmospheric circulation seen in long control runs of climate models[29]. Climate model projections forced with medium emission scenarios indicate the emergence of a large anthropogenic regional warming signal, comparable in magnitude to the late twentieth century Peninsula warming, during the latter part of the current century[30].

Online Content Methods, along with any additional Extended Data display items and Source Data, are available in the online version of the paper; references unique to these sections appear only in the online paper.

Received 5 February; accepted 6 June 2016.

1. Turner, J. *et al.* Antarctic climate change during the last 50 years. *Int. J. Climatol.* **25,** 279–294 (2005).
2. Cook, A. J., Fox, A. J., Vaughan, D. G. & Ferrigno, J. G. Retreating glacier fronts on the Antarctic Peninsula over the past half-century. *Science* **308,** 541–544 (2005).
3. Vaughan, D. G. Implications of the break-up of Wordie Ice Shelf, Antarctica for sea level. *Antarct. Sci.* **5,** 403–408 (1993).
4. Convey, P. in *Antarctic Peninsula Climate Variability: Historical and Palaeoenvironmental Perspectives* (eds Domack, E. *et al.)* 145–158 (American Geophysical Union, 2003).
5. Thompson, D. W. J. & Solomon, S. Interpretation of recent Southern Hemisphere climate change. *Science* **296,** 895–899 (2002).
6. Turner, J., Maksym, T., Phillips, T., Marshall, G. J. & Meredith, M. P. Impact of changes in sea ice advance on the large winter warming on the western Antarctic Peninsula. *Int. J. Climatol.* **33,** 852–861 (2013).
7. Marshall, G. J., Orr, A., van Lipzig, N. P. M. & King, J. C. The impact of a changing Southern Hemisphere Annular Mode on Antarctic Peninsula summer temperatures. *J. Clim.* **19,** 5388–5404 (2006).
8. Ding, Q., Steig, E. J., Battisti, D. S. & Kuttel, M. Winter warming in West Antarctica caused by central tropical Pacific warming. *Nature Geosci*. **4,** 398–403 (2011).
9. Clem, K. R. & Fogt, R. L. Varying roles of ENSO and SAM on the Antarctic Peninsula climate in austral spring. *J. Geophys. Res. Atmos.* **118,** 11481–11492 (2013).
10. Brohan, P., Kennedy, J. J., Harris, I., Tett, S. F. B. & Jones, P. D. Uncertainty estimates in regional and global observed temperature changes: a new data set from 1850. *J. Geophys. Res. Atmos.* **111,** D12106 (2006).
11. Screen, J. A. & Simmonds, I. The central role of diminishing sea ice in recent Arctic temperature amplification. *Nature* **464,** 1334–1337 (2010).
12. Vaughan, D. G. *et al.* Recent rapid regional climate warming on the Antarctic Peninsula. *Clim. Change* **60,** 243–274 (2003).
13. Bromwich, D. H. *et al.* Central West Antarctica among the most rapidly warming regions on Earth. *Nature Geosci*. **6,** 139–145 (2013).
14. Connolley, W. M. Variability in annual mean circulation in southern high latitudes. *Clim. Dyn.* **13,** 745–756 (1997).
15. Trenberth, K. E., Fasullo, J. T., Branstator, G. & Phillips, A. S. Seasonal aspects of the recent pause in surface warming. *Nature Clim. Chang*. **4,** 911–916 (2014).
16. Li, X. C., Holland, D. M., Gerber, E. P. & Yoo, C. Impacts of the north and tropical Atlantic Ocean on the Antarctic Peninsula and sea ice. *Nature* **505,** 538–542 (2014).
17. Carrasco, J. F. Decadal changes in the near-surface air temperature in the western side of the Antarctic Peninsula. *Atmos. Clim. Sci* **3,** 275–281 (2013).
18. Gillett, N. P. *et al.* Attribution of polar warming to human influence. *Nature Geosci*. **1,** 750–754 (2009).
19. Bals-Elsholz, T. M. *et al.* The wintertime Southern Hemisphere split jet: structure, variability, and evolution. *J. Clim.* **14,** 4191–4215 (2001).
20. Turner, J. The El Niño-Southern Oscillation and Antarctica. *Int. J. Climatol.* **24,** 1–31 (2004).
21. Chen, B., Smith, S. R. & Bromwich, D. H. Evolution of the tropospheric split jet over the South Pacific Ocean during the 1986–89 ENSO cycle. *Mon. Weath. Rev*. **124,** 1711–1731 (1996).
22. Lorenz, D. J. & Hartmann, D. L. Eddy-zonal flow feedback in the Northern Hemisphere winter. *J. Clim.* **16,** 1212–1227 (2003).
23. Plumb, R. A. On the 3-dimensional propagation of stationary waves. *J. Atmos. Sci.* **42,** 217–229 (1985).
24. Fyfe, J. C. *et al.* Making sense of the early-2000s warming slowdown. *Nature Clim. Chang*. **6,** 224–228 (2016).
25. Trenberth, K. E. Has there been a hiatus ? *Science* **349,** 691–692 (2015).
26. Mulvaney, R. *et al.* Recent Antarctic Peninsula warming relative to Holocene climate and ice-shelf history. *Nature* **489,** 141–144 (2012).
27. Thomas, E. R., Bracegirdle, T. J., Turner, J. & Wolff, E. W. A 308 year record of climate variability in West Antarctica. *Geophys. Res. Lett.* **40,** 5492–5496 (2013).
28. Ludescher, J., Bunde, A., Franzke, C. L. E. & Schellnhuber, H. J. Long-term persistence enhances uncertainty about anthropogenic warming of Antarctica. *Clim. Dyn.* **46,** 263–271 (2016).
29. Turner, J., Hosking, J. S., Marshall, G. J., Phillips, T. & Bracegirdle, T. J. Antarctic sea ice increase consistent with intrinsic variability of the Amundsen Sea Low. *Clim. Dyn.* **46,** 2391–2402 (2016).
30. Bracegirdle, T. J., Connolley, W. M. & Turner, J. Antarctic climate change over the Twenty First Century. *J. Geophys. Res.* **113,** D03103 (2008).

Supplementary Information is available in the online version of the paper.

Acknowledgements This work was financially supported by the UK Natural Environment Research Council under grant NE/K00445X/1. It forms part of the Polar Science for Planet Earth programme of the British Antarctic Survey. We are grateful to D. G. Vaughan for valuable discussions during this study. We are grateful to ECMWF for the provision of reanalysis fields and to the US National Snow and Ice Data Center for the sea-ice data. The data used in this study are available from the authors upon request.

Author Contributions J.T. conceived the study and led the writing of the manuscript. J.T., H.L., T.P., J.S.H., G.J.M., T.J.B. and J.C.K. analysed the results. P.D. investigated the role of tropical forcing. T.P. managed the data and prepared some of the figures. H.L. carried out the statistical analysis. R.M. compared the recent trends with palaeoclimate data. I.W. computed the stationary eddy fluxes.

Author Information Reprints and permissions information is available at www.nature.com/reprints. The authors declare no competing financial interests. Readers are welcome to comment on the online version of the paper. Correspondence and requests for materials should be addressed to J.T. (jtu@bas.ac.uk).

Reviewer Information *Nature* thanks W. Hobbs and E. Steig for their contribution to the peer review of this work.

METHODS

Data. The monthly mean SAT data for the stations were obtained primarily from the Scientific Committee on Antarctic Research (SCAR) Reference Antarctic Data for Environmental Research (READER) data base[31]. These values are derived as the mean of the synoptic (6-hourly) observations. A monthly value was produced only if 90% of the 6-hourly data were available. To maximize the number of these data, if a value was missing, but adjacent 3-hourly values were available, then an estimate of the 6-hourly value was made by linearly interpolating between these two adjacent values; for example, if a value at 06Z was missing but values existed at 03Z and 09Z then the mean of those values would be used to estimate a value for 06Z. Any resultant bias will be random and should have a negligible effect on the monthly mean. Similar to READER, if there were insufficient synoptic observations to derive a monthly mean, a value was taken from the monthly CLIMAT message if available.

To account for differences in temperature variability between the six stations, we have generated a monthly mean stacked SAT anomaly record. These values are the mean of the available normalized temperature anomalies, of which at least five are available from 1979 onwards. Anomalies are calculated relative to the 1981–2010 period. Our use of the stacked temperature anomalies is justified by the fact that SATs at all six stations have a similar relationship to mean SLP (Extended Data Fig. 6) and therefore the broad-scale atmospheric circulation, despite there being differences in local effects. Indeed, Ding and Steig[32] also demonstrated that trends computed from a stacked AP SAT record showed good, broad-scale agreement with trends determined from satellite and reanalysis data.

To investigate atmospheric circulation variability for 1979–2014, we use the fields from the European Centre for Medium-range Weather Forecasting (ECMWF) Interim reanalysis (ERA-Interim), which have a grid spacing of $0.7° \times 0.7°$ and are considered to be the best reanalysis for depicting recent Antarctic climate[33]. Fields of mean SIC, computed using the Bootstrap version 2 algorithm[34] were obtained on a 25-km-resolution grid from the US National Snow and Ice Data Center (http://www.nsidc.org).

Statistical methods. A non-parametric statistical technique called the sequential Mann–Kendall test[35–37] was employed to detect the period when a significant change of trend occurred in the monthly mean stacked temperature anomalies. Note that the sequential Mann–Kendall test has been widely used to detect approximate potential trend turning points in time series[36–38].

The null hypothesis we tested was that there is no turning point in the trend of the monthly temperature anomaly time series under investigation. To prove or to disprove the null hypothesis, our calculation follows the procedure given by Gerstengarbe and Werner[36]. Let a temperature time series $X = \{X_1,\ldots, X_n\}$ be separated into $n-1$ subseries (that is, the first subseries includes the sample values $X_1, X_2,\ldots$, the second include the values $X_2, X_3,\ldots$, and so on). The $n-1$ Mann–Kendall test statistic variables[35] determined by these subseries are given as:

$$W_t = \sum_{i=1}^{t} R_i$$

where R_i is the rank of the t-th sub-series $\{X_1, X_2,\ldots, X_{t+1}\}$, that is, the number of the elements $X_i\{i > j\}$ such that $X_i > X_j$ with $i = 2,\ldots, t$ and $j = 1,\ldots, i-1$. Consequently, for each of the $n-1$ subseries, the corresponding progressive row $U(t)$ is defined as

$$U(t) = \frac{W_t - E(W_t)}{\sqrt{\mathrm{Var}(W_t)}}$$

where $E(W_t)$ is the expected value of the respective subseries with

$$E(W_t) = \frac{l_t(l_t - 1)}{4}$$

and $\mathrm{Var}(W_t)$ is the respective variance given by

$$\mathrm{Var}(W_t) = \frac{l_t(l_t - 1)(2l_t - 5)}{72}$$

which assumes that, for $l_t \to \infty$ (l_t = the length of the subseries), W_t is approximately Gaussian and the normalized $U(t)$ is assumed to be a standard Gaussian distribution. Similarly, for a given t, the corresponding rank series $V(t)$, the so-called retrograde row can be calculated using the reversed time series $\{X_{t+1}, X_{t-2},\ldots,X_1\}$.

Once the progressive and retrograde rank series $U(t)$ and $V(t)$ are calculated for all $t = 1,\ldots, n-1$, the temporal locations where $U(t)$ and $V(t)$ cross each other are determined and considered as potential trend turning points. When either the progressive $U(t)$ or retrograde $V(t)$ row exceeds certain confidence limits (for example, the absolute values of $U(t)$ and $V(t)$ become greater than 2 in our case) before and after the crossing point, the null hypothesis that the sampled time series has no change points is rejected.

The statistical significance of the linear trends during the warming and cooling periods is estimated using the non-parametric Mann–Kendall Tau and Sens slope test[36,38], where the P values are calculated as two-sided. To test the significance of the trend differences between two periods, we compute the confidence intervals at 90% and 95% levels for individual trends and examine whether or not they overlap[39].

As the sequential Mann–Kendall test can only detect the approximate time when a change of the trend may occur, we find that it is often the case that multiple changes can be detected over a couple of years. Namely, the trend change may actually take a couple of years to occur in the real world.

Correlations, linear trends and composite differences from gridded data sets were computed using monthly anomalies based on a standard least-squares method, with the methodology used to calculate the significance levels based upon Santer *et al.*[39]. An effective sample size was calculated based on the lag 1 autocorrelation coefficient of the regression residuals. This effective sample size was used for the computation of the standard error and in indexing the critical values of Student's t distribution. On figures showing the differences of means between the warming and cooling periods, significance levels were calculated using t-tests performed without the assumption of equal variances between the periods being compared. For the computation of the correlations, the time series of SST and atmospheric fields were all detrended.

Determination of the stationary wave fluxes. The formulation of Plumb[23] was used to estimate the difference in stationary wave activity between the warming and cooling periods in the upper troposphere (for example, 300 hPa). The fluxes give an indication of the direction of wave propagation and take the form:

$$\mathbf{F} = \frac{p\cos\varphi}{2}\left(v'^2 - \frac{\Phi'}{af\cos\varphi}\frac{\partial v'}{\partial\lambda},\ \ -v'u' + \frac{\Phi'}{af\cos\varphi}\frac{\partial u'}{\partial\lambda}\right)$$

where λ, φ are the zonal and meridional coordinates, u, v are the zonal and meridional velocity components, p represents normalized pressure, which is pressure divided by a standard reference pressure p_s, here p_s is taken as 1,000 hPa, a is the Earth's radius, $f = 2\Omega\sin\varphi$ is the Coriolis parameter with Ω the Earth's rotation rate and Φ the geopotential. Primes represent deviations from the zonal-mean. Note that $\mathbf{F}$ has been written in terms of the geopotential Φ by using the geostrophic wind relations $u = -\frac{\psi_\varphi}{a}$, $v = \frac{\psi_\lambda}{a\cos\varphi}$, where ψ is the geostrophic stream function. This is to reduce the possible amplification of noise due to successive derivatives and to facilitate the physical understanding of each components. All differentiation is performed using centred differences. Also, $\mathbf{F}$ is calculated on a monthly basis to isolate the stationary perturbations and then a time-average is taken over the selected period for each year.

31. Turner, J. *et al.* The SCAR READER project: towards a high-quality database of mean Antarctic meteorological observations. *J. Clim.* **17,** 2890–2898 (2004).
32. Ding, Q. H. & Steig, E. J. Temperature change on the Antarctic Peninsula linked to the tropical Pacific. *J. Clim.* **26,** 7570–7585 (2013).
33. Bracegirdle, T. J. & Marshall, G. J. The reliability of Antarctic tropospheric pressure and temperature in the latest global reanalyses. *J. Clim.* **25,** 7138–7146 (2012).
34. Comiso, J. C. Variability and trends in Antarctic surface temperatures from *in situ* and satellite infrared measurements. *J. Clim.* **13,** 1674–1696 (2000).
35. Mann, H. B. Non parametric test against trend. *Econometric* **13,** 245–259 (1945).
36. Gerstengarbe, F. W. & Werner, P. C. Estimation of the beginning and end of recurrent events within a climate regime. *Clim. Res.* **11,** 97–107 (1999).
37. Li, Y., Lu, H., Jarvis, M. J., Clilverd, M. A. & Bates, B. Nonlinear and nonstationary influences of geomagnetic activity on the winter North Atlantic Oscillation. *J. Geophys. Res. Atmos.* **116,** D16109 (2011).
38. Burkey, J. A non-parametric monotonic trend test computing Mann-Kendall Tau, Tau-b, and Sens Slope written in MathWorks MATLAB (King County, Department of Natural Resources and Parks, Science and Technical Services section, 2006).
39. Santer, B. D. *et al.* Statistical significance of trends and trend differences in layer-average atmospheric temperature time series. *J. Geophys. Res.* **105,** 7337–7356 (2000).
40. Marshall, G. J. Trends in the Southern Annular Mode from observations and reanalyses. *J. Clim.* **16,** 4134–4143 (2003).

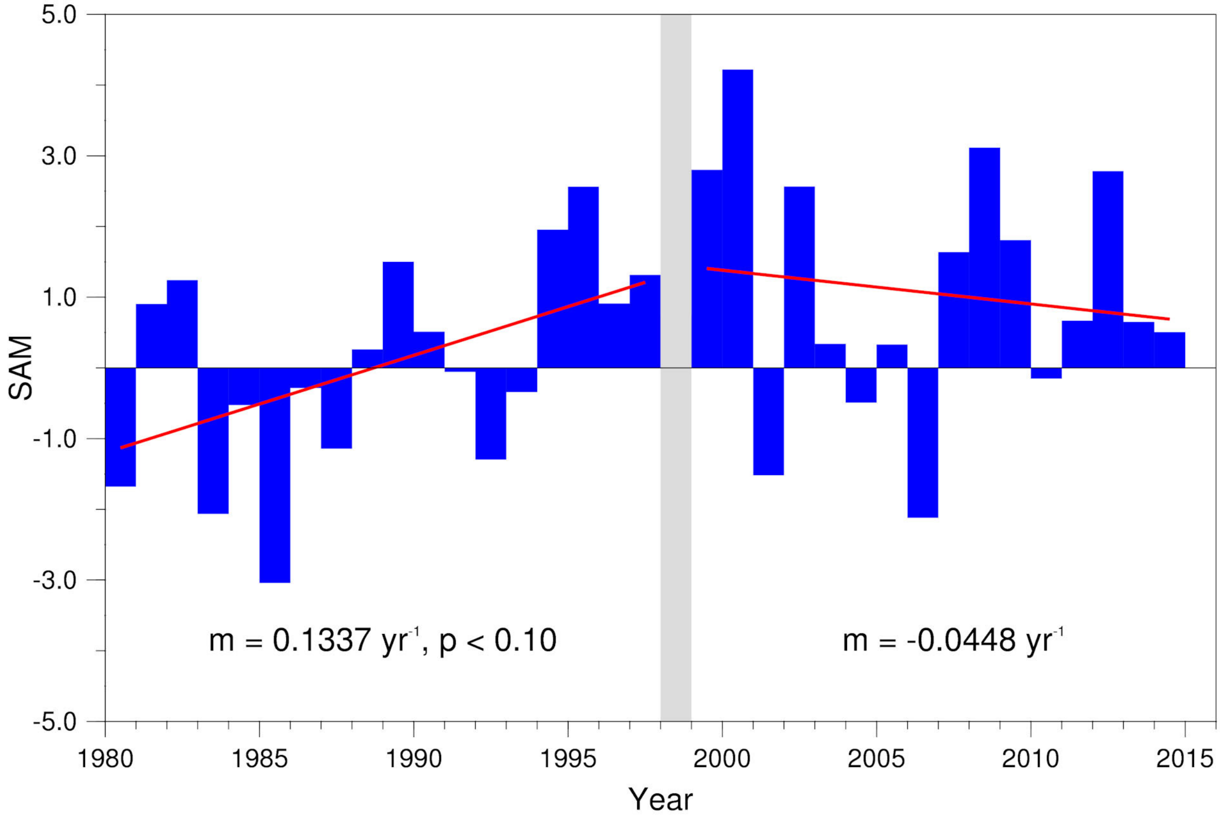

Extended Data Figure 1 | The Southern Annular Mode. The austral summer (December–February) SAM index[40] for December 1979–February 2014. The linear trends for 1980–1997 and 1999–2014 are shown in red. The data were obtained from https://legacy.bas.ac.uk/met/gjma/sam.html.

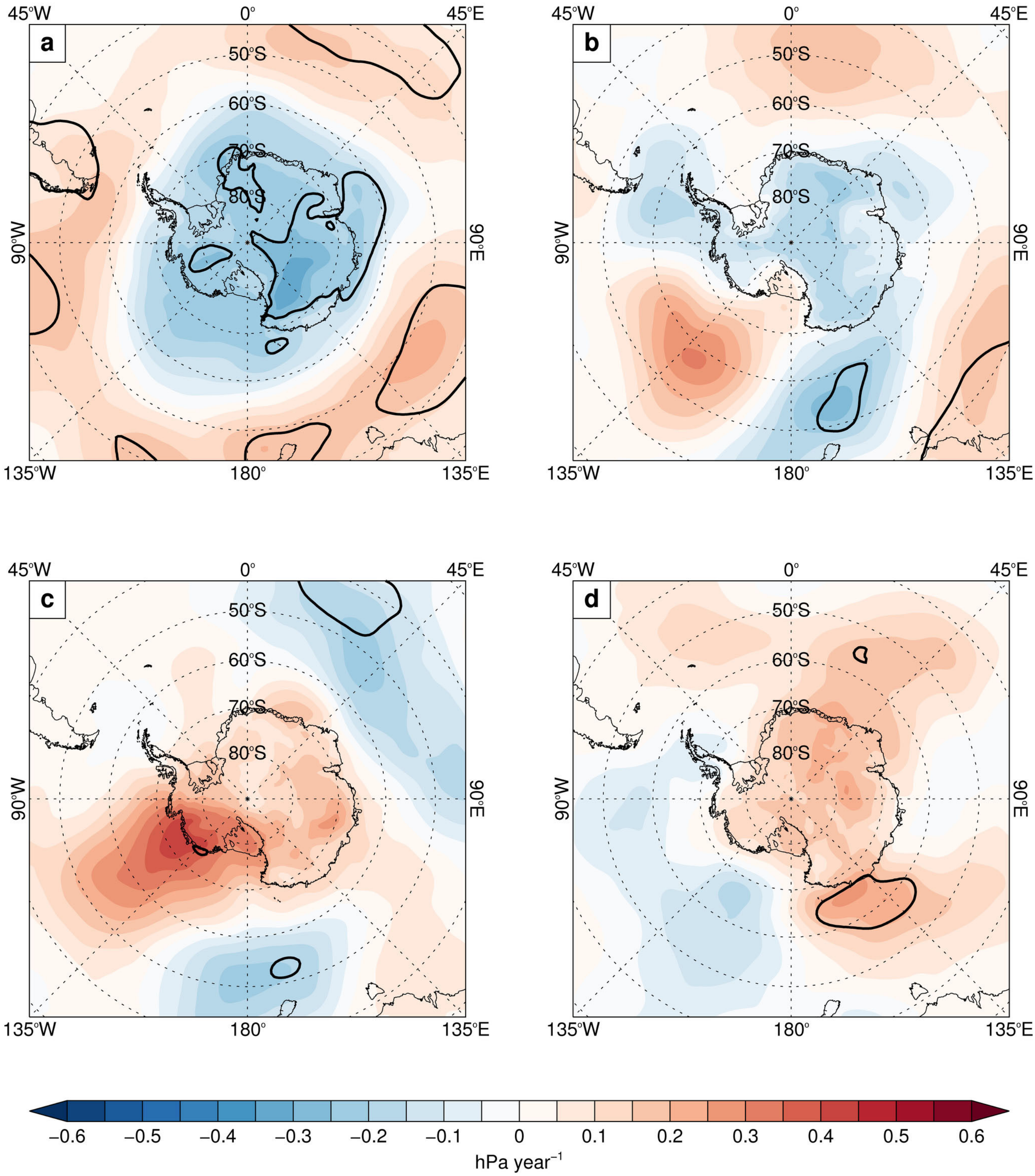

Extended Data Figure 2 | Seasonal SLP trends during the warming period. a–d, DJF December 1979–February 1998 (**a**), MAM 1979–1997 (**b**), JJA 1979–1997 (**c**) and September–November (SON) 1979–1997 (**d**). Areas where the trends are significant at $P < 0.05$ are indicated by a bold line.

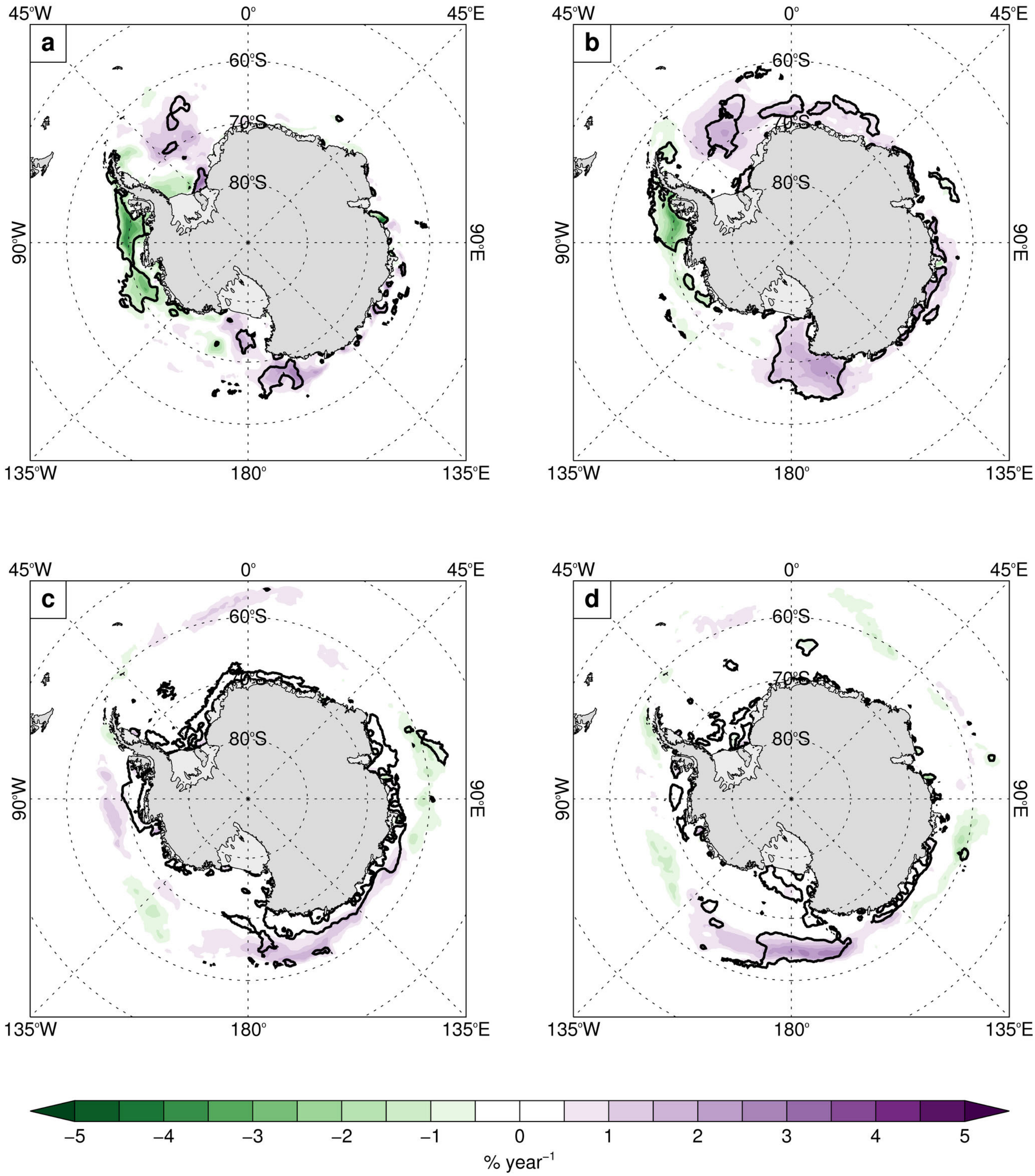

Extended Data Figure 3 | Seasonal trends in sea-ice concentration during the warming period. a–d, DJF December 1979–February 1998 (**a**), MAM 1979–1997 (**b**), JJA 1979– 1997 (**c**) and SON 1979–1997 (**d**). Areas where the trends are significant at $P < 0.05$ are indicated by a bold line.

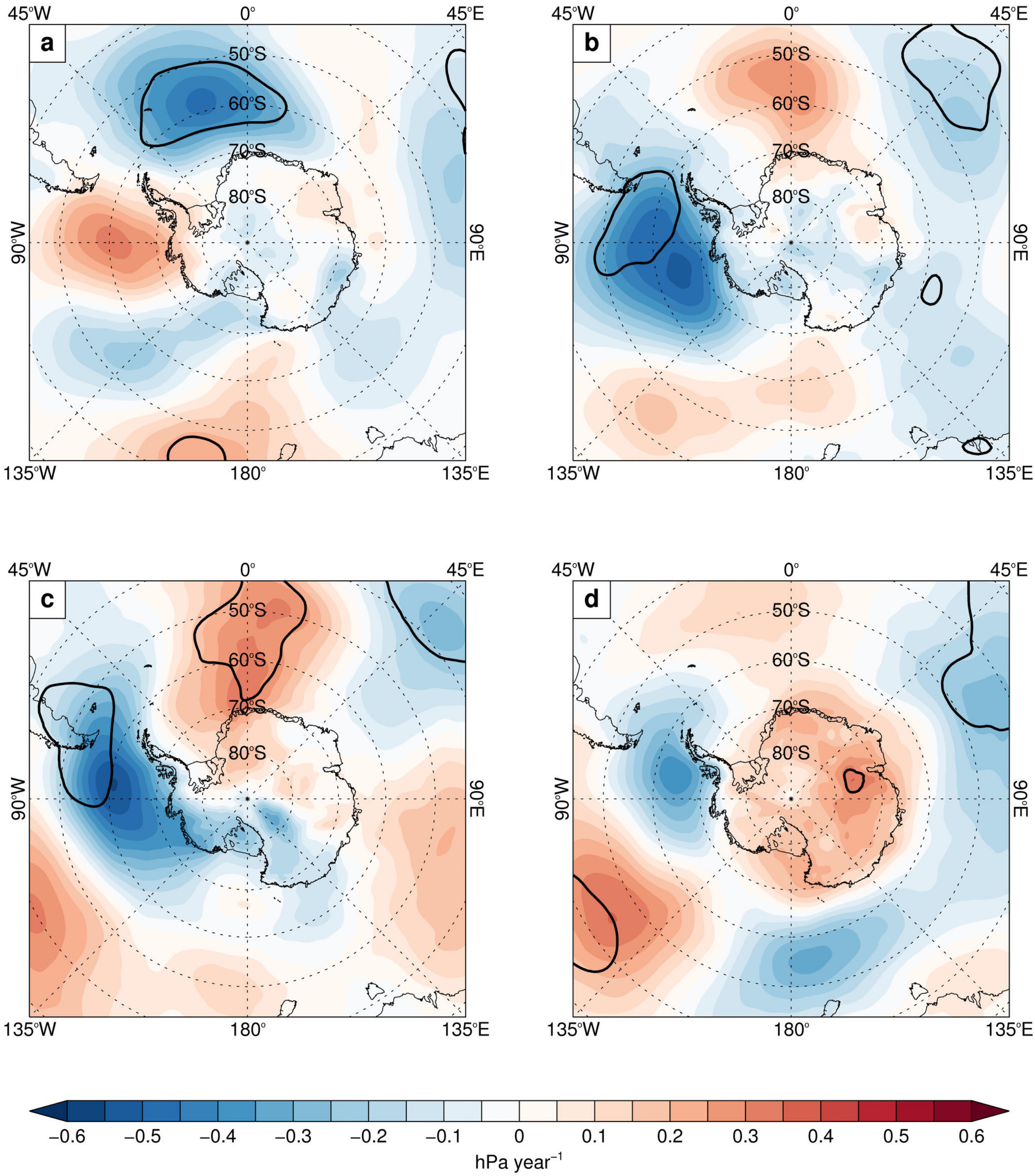

Extended Data Figure 4 | Seasonal SLP trends during the cooling period. a–d, DJF December 1999–February 2014 (**a**), MAM 1999–2014 (**b**), JJA 1999–2014 (**c**) and SON 1999–2014 (**d**). Areas where the trends are significant at $P < 0.05$ are indicated by a bold line.

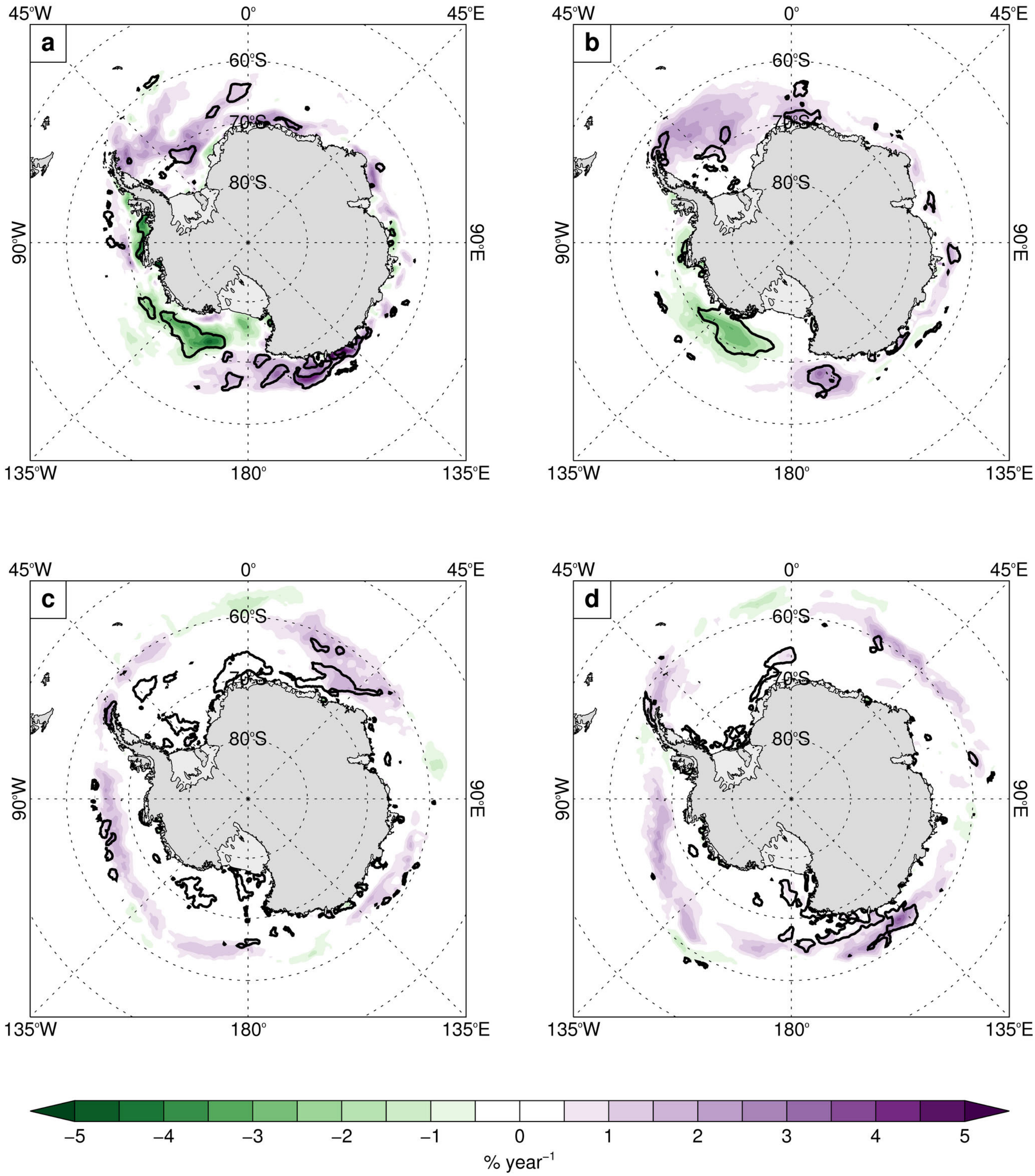

Extended Data Figure 5 | Seasonal trends in sea-ice concentration during the cooling period. a–d, DJF December 1999–February 2014 (**a**), MAM 1999–2014 (**b**), JJA 1999–2014 (**c**) and SON 1999–2014 (**d**). Areas where the trends are significant at $P < 0.05$ are indicated by a bold line.

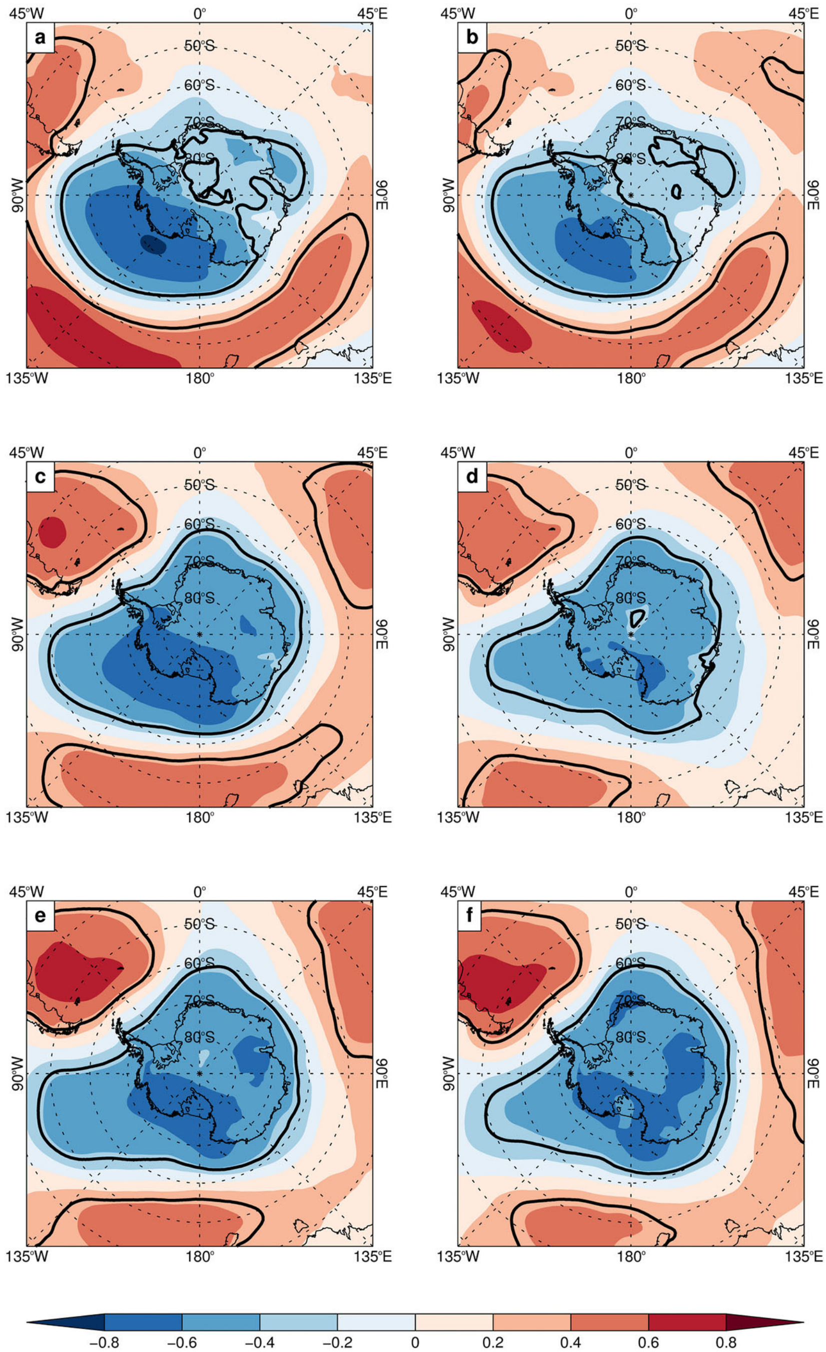

Extended Data Figure 6 | The correlation of annual mean SAT from the stations with annual mean SLP for 1979–2014. a–f, Areas where the correlation is significant at $P < 0.05$ are indicated by a bold line. Rothera (**a**), Vernadsky (**b**), Bellingshausen (**c**), O'Higgins (**d**), Esperanza (**e**) and Marambio (**f**).

Extended Data Table 1 | Annual and seasonal trends of the stacked, normalized temperature record

	Annual	DJF	MAM	JJA	SON
1979 – 1997	0.32**	0.51*	0.18	0.04	0.33
1999 - 2014	-0.47**	-0.72*	-0.39	-0.09	-0.36

Trends are given for the warming (1979–1997) and cooling (1999–2014) periods and are per decade. Significance of the trends is indicated as $^{**}P < 0.05$ and $^{*}P < 0.10$. Note, the DJF trends are for the summer seasons over December 1979–February 1998 and December 1999–February 2014.

LETTER

doi:10.1038/nature18607

Bright spots among the world's coral reefs

Joshua E. Cinner[1], Cindy Huchery[1], M. Aaron MacNeil[1,2,3], Nicholas A.J. Graham[1,4], Tim R. McClanahan[5], Joseph Maina[5,6,7], Eva Maire[1,8], John N. Kittinger[9,10], Christina C. Hicks[1,4,9], Camilo Mora[11], Edward H. Allison[12], Stephanie D'Agata[5,7,13], Andrew Hoey[1], David A. Feary[14], Larry Crowder[9], Ivor D. Williams[15], Michel Kulbicki[16], Laurent Vigliola[13], Laurent Wantiez[17], Graham Edgar[18], Rick D. Stuart-Smith[18], Stuart A. Sandin[19], Alison L. Green[20], Marah J. Hardt[21], Maria Beger[6], Alan Friedlander[22,23], Stuart J. Campbell[5], Katherine E. Holmes[5], Shaun K. Wilson[24,25], Eran Brokovich[26], Andrew J. Brooks[27], Juan J. Cruz-Motta[28], David J. Booth[29], Pascale Chabanet[30], Charlie Gough[31], Mark Tupper[32], Sebastian C. A. Ferse[33], U. Rashid Sumaila[34] & David Mouillot[1,8]

Ongoing declines in the structure and function of the world's coral reefs[1,2] require novel approaches to sustain these ecosystems and the millions of people who depend on them[3]. A presently unexplored approach that draws on theory and practice in human health and rural development[4,5] is to systematically identify and learn from the 'outliers'—places where ecosystems are substantially better ('bright spots') or worse ('dark spots') than expected, given the environmental conditions and socioeconomic drivers they are exposed to. Here we compile data from more than 2,500 reefs worldwide and develop a Bayesian hierarchical model to generate expectations of how standing stocks of reef fish biomass are related to 18 socioeconomic drivers and environmental conditions. We identify 15 bright spots and 35 dark spots among our global survey of coral reefs, defined as sites that have biomass levels more than two standard deviations from expectations. Importantly, bright spots are not simply comprised of remote areas with low fishing pressure; they include localities where human populations and use of ecosystem resources is high, potentially providing insights into how communities have successfully confronted strong drivers of change. Conversely, dark spots are not necessarily the sites with the lowest absolute biomass and even include some remote, uninhabited locations often considered near pristine[6]. We surveyed local experts about social, institutional, and environmental conditions at these sites to reveal that bright spots are characterized by strong sociocultural institutions such as customary taboos and marine tenure, high levels of local engagement in management, high dependence on marine resources, and beneficial environmental conditions such as deep-water refuges. Alternatively, dark spots are characterized by intensive capture and storage technology and a recent history of environmental shocks. Our results suggest that investments in strengthening fisheries governance, particularly aspects such as participation and property rights, could facilitate innovative conservation actions that help communities defy expectations of global reef degradation.

Despite substantial international conservation efforts, diversity and abundance continue to decline within many of the world's ecosystems[1,7]. Most conservation approaches aim to identify and protect places of high ecological integrity under minimal threat[8]. Yet, with escalating social and environmental drivers of change, conservation actions are also needed where people and nature coexist, especially where human effects are already severe[9]. Here, we highlight an approach for implementing conservation in coupled human–natural systems focused on identifying and learning from outliers—places that are performing substantially better than expected, given the socioeconomic and environmental conditions they are exposed to. By their very nature, outliers deviate from expectations, and consequently can provide novel insights into confronting complex problems where conventional solutions have failed. This type of positive deviance, or bright spot analysis has been used in fields such as business, health, and human development to uncover local actions and governance systems that work in the context of widespread failure[10,11], and holds much promise in informing conservation.

To demonstrate this approach, we compiled data from 2,514 coral reefs in 46 countries, states, and territories (hereafter 'nations/states') and developed a Bayesian hierarchical model to generate expected conditions of how standing reef fish biomass (a key indicator of resource availability and ecosystem functions[12]) was related to 18 key environmental variables and socioeconomic drivers (Fig. 1; Extended Data Tables 1–4; Extended Data Figs 1–3; Methods). Drawing on a broad body of theoretical and empirical research in the social sciences[13–15] and ecology[2,6,16] on coupled human–natural systems, we quantified how reef fish biomass (Fig. 1a) was related to distal social drivers such as markets, affluence, governance, and population (Fig. 1b, c), while controlling for well-known environmental conditions such as depth,

[1]Australian Research Council Centre of Excellence for Coral Reef Studies, James Cook University, Townsville, Queensland 4811, Australia. [2]Australian Institute of Marine Science, PMB 3 Townsville MC, Townsville, Queensland 4810, Australia. [3]Department of Mathematics and Statistics, Dalhousie University, Halifax, Nova Scotia B3H 3J5 Canada. [4]Lancaster Environment Centre, Lancaster University, Lancaster LA1 4YQ, UK. [5]Wildlife Conservation Society, Global Marine Program, Bronx, New York 10460, USA. [6]Australian Research Council Centre of Excellence for Environmental Decisions, Centre for Biodiversity and Conservation Science, University of Queensland, Brisbane St Lucia, Queensland 4074, Australia. [7]Department of Environmental Sciences, Macquarie University, North Ryde, New South Wales 2109, Australia. [8]MARBEC, UMR 9190, IRD-CNRS-UM-IFREMER, Université Montpellier, 34095 Montpellier Cedex, France. [9]Center for Ocean Solutions, Stanford University, California 94305, USA. [10]Conservation International Hawaii, Betty and Gordon Moore Center for Science and Oceans, 7192 Kalaniana'ole Hwy, Suite G230, Honolulu, Hawaii 96825, USA. [11]Department of Geography, University of Hawaii at Manoa, Honolulu, Hawaii 96822, USA. [12]School of Marine and Environmental Affairs, University of Washington, Seattle, Washington 98102 USA. [13]Institut de Recherche pour le Développement, UMR IRD-UR-CNRS ENTROPIE, Laboratoire d'Excellence LABEX CORAIL, BP A5, 98848 Nouméa Cedex, New Caledonia. [14]Ecology & Evolution Group, School of Life Sciences, University Park, University of Nottingham, Nottingham NG7 2RD, UK. [15]Coral Reef Ecosystems Division, NOAA Pacific Islands Fisheries Science Center, Honolulu, Hawaii 96818, USA. [16]UMR Entropie, Labex Corail, –IRD, Université de Perpignan, 66000 Perpignan, France. [17]EA4243 LIVE, University of New Caledonia, BPR4 98851 Nouméa Cedex, New Caledonia. [18]Institute for Marine and Antarctic Studies, University of Tasmania, Hobart, Tasmania 7001, Australia. [19]Scripps Institution of Oceanography, University of California, San Diego, La Jolla, California 92093, USA. [20]The Nature Conservancy, Brisbane, Queensland 4101, Australia. [21]Future of Fish, 7315 Wisconsin Ave, Suite 1000W, Bethesda, Maryland 20814, USA. [22]Fisheries Ecology Research Lab, Department of Biology, University of Hawaii, Honolulu, Hawaii 96822, USA. [23]National Geographic Society, Pristine Seas Program, 1145 17th Street NW, Washington DC 20036-4688, USA. [24]Department of Parks and Wildlife, Kensington, Perth, Western Australia 6151, Australia. [25]Oceans Institute, University of Western Australia, Crawley, Western Australia 6009, Australia. [26]The Israeli Society of Ecology and Environmental Sciences, Kehilat New York 19 Tel Aviv, Israel. [27]Marine Science Institute, University of California, Santa Barbara, California 93106-6150, USA. [28]Departamento de Ciencias Marinas., Recinto Universitario de Mayaguez, Universidad de Puerto Rico, San Juan 00680, Puerto Rico. [29]School of Life Sciences, University of Technology, Sydney, New South Wales 2007, Australia. [30]UMR ENTROPIE, Laboratoire d'Excellence LABEX CORAIL, Institut de Recherche pour le Développement, CS 41095, 97495 Sainte Clotilde, La Réunion. [31]Blue Ventures Conservation, 39-41 North Road, London N7 9DP, UK. [32]Coastal Resources Association, St. Joseph St., Brgy. Nonoc, Surigao City, Surigao del Norte 8400, Philippines. [33]Leibniz Centre for Tropical Marine Ecology (ZMT), Fahrenheitstrasse 6, D-28359 Bremen, Germany. [34]Fisheries Economics Research Unit, University of British Columbia, 2202 Main Mall, Vancouver, British Columbia V6T 1Z4, Canada.

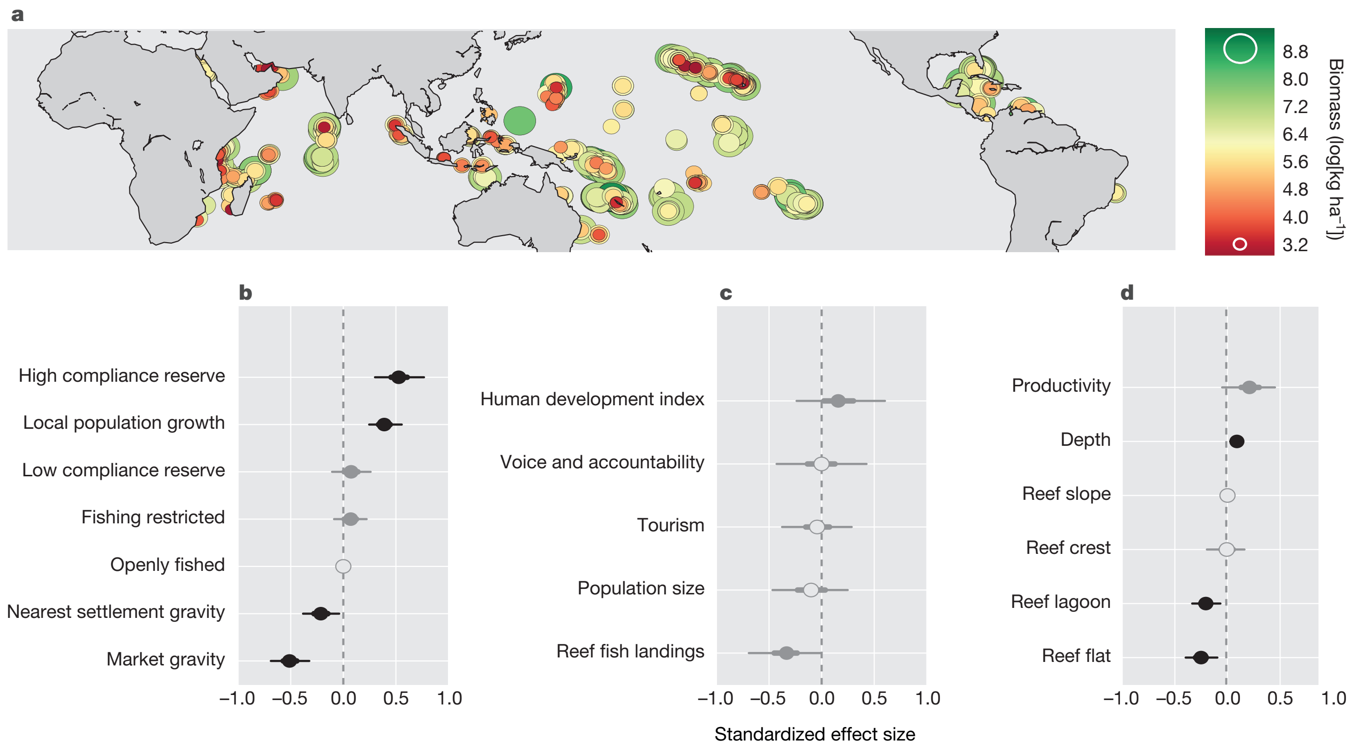

Figure 1 | Global patterns and drivers of reef fish biomass. a, Reef fish biomass among 918 study sites. Points vary in size and colour proportional to the amount of fish biomass. **b**–**d**, Standardized effect size of local-scale social drivers, nation/state-scale social drivers, and environmental covariates, respectively. Parameter estimates are Bayesian posterior median values, 95% uncertainty intervals (UI; thin lines), and 50% UI (thick lines). Black dots indicate that the 95% UI does not overlap 0; grey closed circles indicates that 75% of the posterior distribution lies to one side of 0; and grey open circles indicate that the 50% UI overlaps 0.

habitat, and productivity (Fig. 1d) (Extended Data Table 1; Methods). In contrast to many global studies of reef systems that are focused on demonstrating the severity of human effects[6], our examination seeks to uncover potential policy levers by highlighting the relative role of specific social drivers. A key finding from our global analysis is that our metric of potential interactions with urban centres, called market

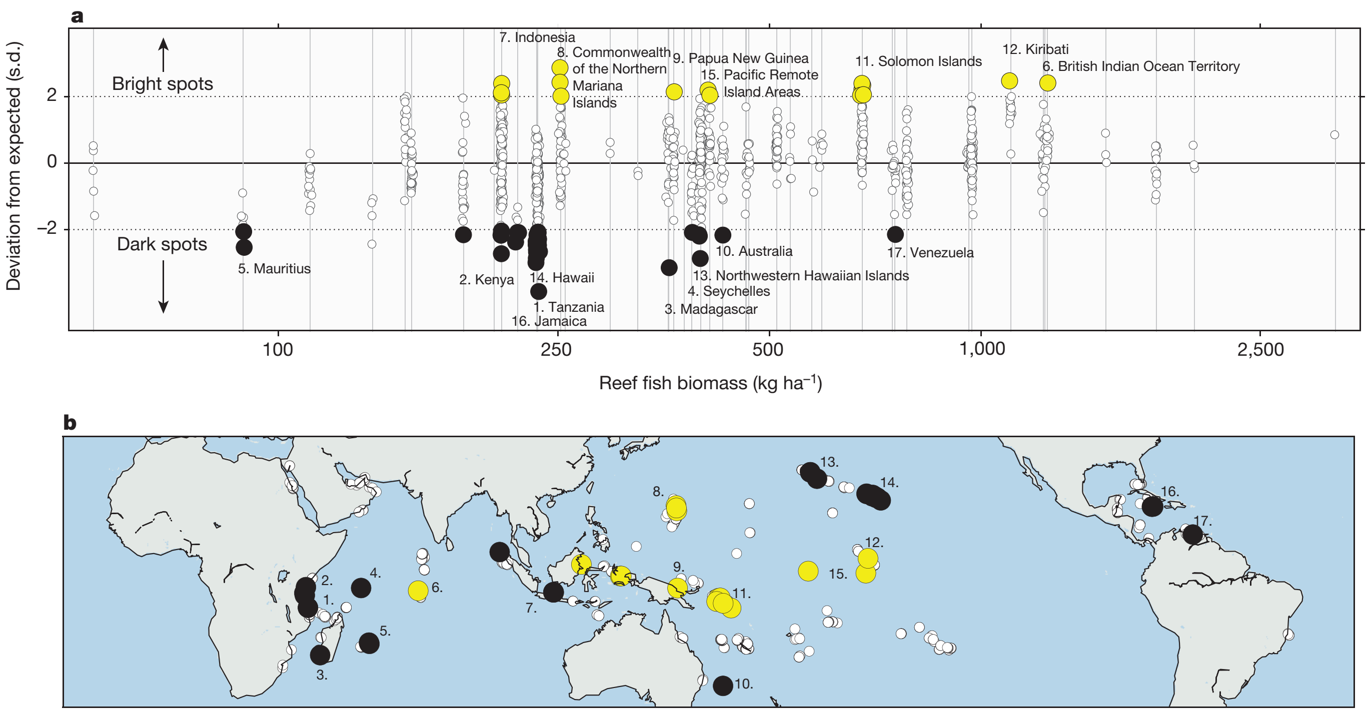

Figure 2 | Bright and dark spots among the world's coral reefs. a, Each site's deviation from expected biomass (y axis) along a gradient of nation/state mean biomass (x axis). The 50 sites with biomass values >2 standard deviations above or below expected values were considered bright (yellow) and dark (black) spots, respectively. Each grey vertical line represents a nation/state; those with bright or dark spots are labelled and numbered. There can be multiple bright or dark spots in each nation/state. **b**, Map highlighting bright and dark spots with large circles, and other sites in small circles. Numbers correspond to panel **a**.

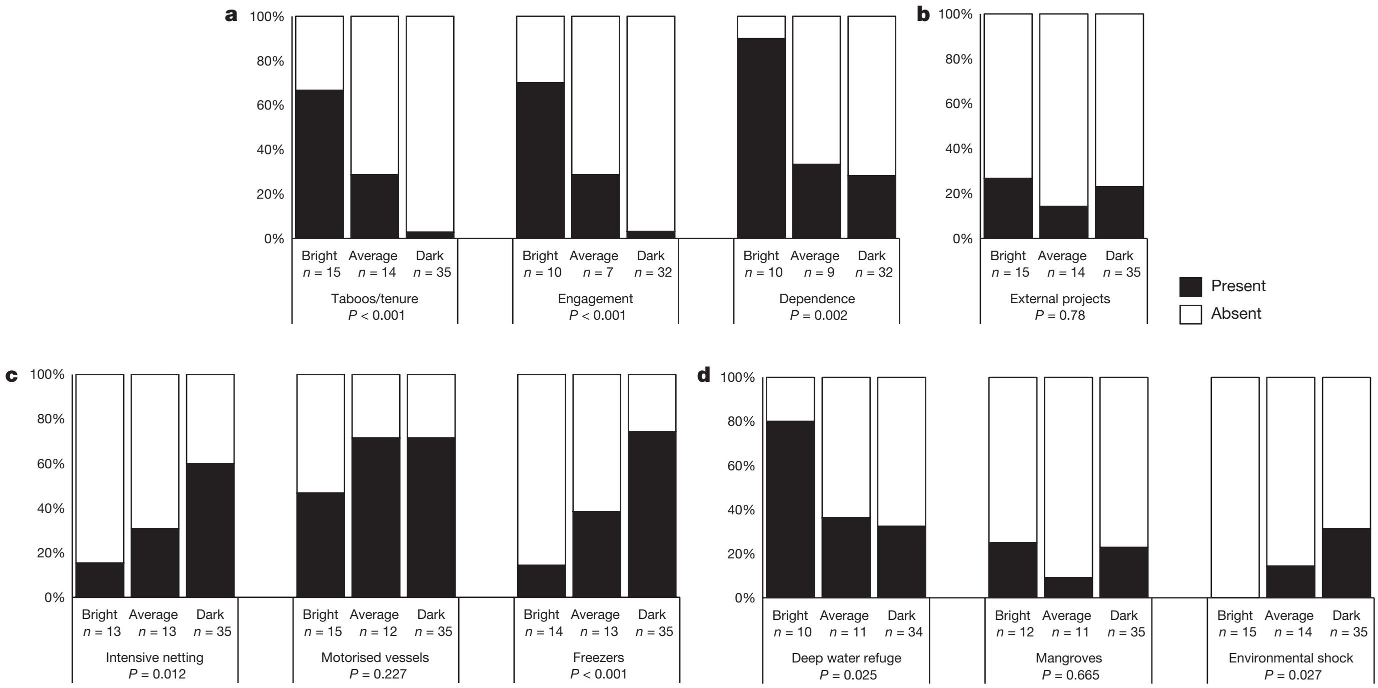

Figure 3 | Differences in key social and environmental conditions between bright spots, dark spots, and 'average' sites. a, Social and institutional conditions; **b**, external- or donor-driven projects; **c**, technologies; **d**, environmental conditions. *P* values are determined using Fisher's exact test. Intensive netting includes beach seine nets, surround gill nets, and muro-ami.

gravity[17] (Methods), more so than local or national population pressure, management, environmental conditions, or national socioeconomic context, had the strongest relationship with reef fish biomass (Fig. 1). Specifically, we found that reef fish biomass decreased as the size and accessibility of markets increased (Extended Data Fig. 1b). Somewhat counter-intuitively, fish biomass was higher in places with high local human population growth rates, probably reflecting human migration to areas of better environmental quality[18]—a phenomenon that could result in increased degradation at these sites over time. We found a strong positive, but less certain relationship (that is, a high standardized effect size, but only >75% of the posterior distribution above zero) with the Human Development Index, meaning that reefs tended to be in better condition in wealthier nations/states (Fig. 1c). Our analysis also confirmed the role that marine reserves can play in sustaining biomass on coral reefs, but only when compliance is high (Fig. 1b), reinforcing the importance of fostering compliance for reserves to be successful.

Next, we identified 15 bright spots and 35 dark spots among the world's coral reefs, defined as sites with biomass levels more than two standard deviations higher or lower than expectations from our global model, respectively (Fig. 2; Methods; Extended Data Table 5). Rather than simply identifying places in the best or worst condition, our bright spots approach reveals the places that most strongly defy expectations. Using them to inform the conservation discourse will certainly challenge established ideas of where and how conservation efforts should be focused. For example, remote places far from human impacts are conventionally considered near-pristine areas of high conservation value[6], yet most of the bright spots we identified occur in fished, populated areas (Extended Data Table 5), some with biomass values below the global average. Alternatively, some remote places such as parts of the northwest Hawaiian Islands underperform (that is, were identified as dark spots).

Detailed analysis of why bright spots can evade the fate of similar areas facing equivalent stresses will require a new research agenda gathering detailed site-level information on social and institutional conditions, technological innovations, external influences, and ecological processes[19] that are simply not available in a global-scale analysis. As a hypothesis-generating exploration to begin uncovering why bright and dark spots may diverge from expectations, we surveyed data providers who sampled the sites and other experts with first-hand knowledge about the presence or absence of ten key social and environmental conditions at the 15 bright spots, 35 dark spots, and 14 average sites with biomass values closest to model expectations (see Methods and Supplementary Information for details). Our initial exploration revealed that bright spots were more likely to have high levels of local engagement in the management process, high dependence on coastal resources, and the presence of sociocultural governance institutions such as customary tenure or taboos (Fig. 3; Methods). For example, in one bright spot, Karkar Island, Papua New Guinea, resource use is restricted through an adaptive rotational harvest system based on ecological feedbacks, marine tenure that allows for the exclusion of fishers from outside the local village, and initiation rights that limit individuals' entry into certain fisheries[20]. Bright spots were also generally proximate to deep water, which may help provide a refuge from disturbance for corals and fish[21] (Fig. 3; Extended Data Fig. 4). Conversely, dark spots were distinguished by having fishing technologies allowing for more intensive exploitation, such as fish freezers and potentially destructive netting, as well as a recent history of environmental shocks (for example, coral bleaching or cyclone; Fig. 3). The latter is particularly worrisome in the context of climate change, which is likely to lead to increased coral bleaching and more intense cyclones[22].

Our global analyses highlight two novel opportunities to inform coral reef governance. The first is to use bright spots as agents of change to expand the conservation discourse from the current focus on protecting places under minimal threat[8], towards harnessing lessons from places that have successfully confronted numerous or severe stressors. Our bright spots approach can be used to inform the types of investments and governance structures that may help to create more sustainable pathways for impacted coral reefs. Specifically, our initial investigation highlights how investments that strengthen fisheries governance, particularly issues such as participation and property rights, could help communities to innovate in ways that allow them to defy expectations. Conversely, the more typical efforts to provide capture and storage infrastructure, particularly where there are environmental shocks and local-scale governance is weak, may lead to

social–ecological traps[23] that reinforce resource degradation beyond expectations. Effectively harnessing the potential to learn from both bright and dark spots will require scientists to increase research efforts in these places, NGOs to catalyse lessons from other areas, donors to start investing in novel solutions, and policy makers to ensure that governance structures foster flexible learning and experimentation. Indeed, bright spots may have much to offer in terms of how to creatively confront drivers of change and prioritize conservation actions. Likewise, dark spots can help identify development strategies to avoid. Critically, the bright spots we identified span the development spectrum from low to high income (for example, Solomon Islands and territories of the USA, respectively; Fig. 2), showing that lessons about effective reef management can emerge from diverse places.

A second opportunity stems from a renewed focus on managing the socioeconomic drivers that shape reef conditions. Many social drivers are amenable to governance interventions, and our comprehensive analysis (Fig. 1) suggests that an increased policy focus on social drivers such as markets and development could result in improvements to reef fish biomass. For example, given the important influence of markets in our analysis, reef managers, donor organizations, conservation groups, and coastal communities could improve sustainability by developing interventions that dampen the negative influence of markets on reef systems. A portfolio of market interventions, including eco-labelling and sustainable harvesting certifications, fisheries improvement projects, and value chain interventions have been developed within large-scale industrial fisheries to condition access to markets based on sustainable harvesting[24,25]. Although there is considerable scope for adapting these interventions to artisanal coral reef fisheries in both local and regional markets, effectively dampening the negative influence of markets may also require developing novel interventions that address the range of ways in which markets can lead to overexploitation. Existing research suggests that markets create incentives for overexploitation not only by affecting price and price variability for reef products[26], but also by influencing people's behaviour[27,28], including their willingness to cooperate in the collective management of natural resources[29].

The long-term viability of coral reefs will ultimately depend on international action to reduce carbon emissions[22]. However, fisheries remain a pervasive source of reef degradation, and effective local-level fisheries governance is crucial to sustaining ecological processes that give reefs the best chance of coping with global environmental change[30]. Seeking out and learning from bright spots is a novel approach to conservation that may offer insights into confronting the complex governance problems facing coupled human–natural systems such as coral reefs.

Online Content Methods, along with any additional Extended Data display items and Source Data, are available in the online version of the paper; references unique to these sections appear only in the online paper.

Received 5 January; accepted 27 May 2016.
Published online 15 June 2016.

1. Pandolfi, J. M. *et al.* Global trajectories of the long-term decline of coral reef ecosystems. *Science* **301,** 955–958 (2003).
2. Bellwood, D. R., Hughes, T. P., Folke, C. & Nyström, M. Confronting the coral reef crisis. *Nature* **429,** 827–833 (2004).
3. Hughes, T. P., Bellwood, D. R., Folke, C., Steneck, R. S. & Wilson, J. New paradigms for supporting the resilience of marine ecosystems. *Trends Ecol. Evol.* **20,** 380–386 (2005).
4. Sternin, M. *et al.* in *The Hearth Nutrition Model: Applications in Haiti, Vietnam, and Bangladesh.* (eds O Wollinka, E Keeley, B Burkhalter, & N Bashir) 49–61 (VA: BASICS, 1997).
5. Pretty, J. N. *et al.* Resource-conserving agriculture increases yields in developing countries. *Environ. Sci. Technol.* **40,** 1114–1119 (2006).
6. Knowlton, N. & Jackson, J. B. C. Shifting baselines, local impacts, and global change on coral reefs. *PLoS Biol.* **6,** e54 (2008).
7. Naeem, S., Duffy, J. E. & Zavaleta, E. The functions of biological diversity in an age of extinction. *Science* **336,** 1401–1406 (2012).
8. Devillers, R. *et al.* Reinventing residual reserves in the sea: are we favouring ease of establishment over need for protection? *Aquat. Conserv.* **25,** 480–504 (2014).
9. Pressey, R. L., Visconti, P. & Ferraro, P. J. Making parks make a difference: poor alignment of policy, planning and management with protected-area impact, and ways forward. *Philos. Trans. R. Soc. B* **370,** 20140280 (2015).
10. Pascale, R. T. & Sternin, J. Your company's secret change agents. *Harv. Bus. Rev.* **83,** 72–81, 153 (2005).
11. Levinson, F. J., Barney, J., Bassett, L. & Schultink, W. Utilization of positive deviance analysis in evaluating community-based nutrition programs: an application to the Dular program in Bihar, India. *Food Nutr. Bull.* **28,** 259–265 (2007).
12. McClanahan, T. R. *et al.* Critical thresholds and tangible targets for ecosystem-based management of coral reef fisheries. *Proc. Natl Acad. Sci. USA* **108,** 17230–17233 (2011).
13. York, R. *et al.* Footprints on the earth: The environmental consequences of modernity. *Am. Sociol. Rev.* **68,** 279–300 (2003).
14. Lambin, E. F. *et al.* The causes of land-use and land-cover change: moving beyond the myths. *Glob. Environ. Change* **11,** 261–269 (2001).
15. Cinner, J. E. *et al.* Comanagement of coral reef social-ecological systems. *Proc. Natl Acad. Sci. USA* **109,** 5219–5222 (2012).
16. Hughes, T. P., Huang, H. & Young, M. A. The wicked problem of China's disappearing coral reefs. *Conserv. Biol.* **27,** 261–269 (2013).
17. Dodd, S. C. The interactance hypothesis: a gravity model fitting physical masses and human groups. *Am. Sociol. Rev.* **15,** 245–256 (1950).
18. Wittemyer, G., Elsen, P., Bean, W. T., Burton, A. C. & Brashares, J. S. Accelerated human population growth at protected area edges. *Science* **321,** 123–126 (2008).
19. Noble, A. *et al.* in *Bright spots demonstrate community successes in African agriculture* (ed. F. W. T. Penning de Vries) 7 (International Water Management Institute, 2005).
20. Cinner, J. *et al.* Periodic closures as adaptive coral reef management in the Indo-Pacific. *Ecol. Soc.* **11,** 31 (2006).
21. Lindfield, S. J. *et al.* Mesophotic depths as refuge areas for fishery-targeted species on coral reefs. *Coral Reefs* **35,** 125–137 (2016).
22. Cinner, J. E. *et al.* A framework for understanding climate change impacts on coral reef social–ecological systems. *Reg. Environ. Change* **16,** 1133–1146 (2016).
23. Cinner, J. E. Social-ecological traps in reef fisheries. *Glob. Environ. Change* **21,** 835–839 (2011).
24. O'Rourke, D. The science of sustainable supply chains. *Science* **344,** 1124–1127 (2014).
25. Sampson, G. S. *et al.* Sustainability. Secure sustainable seafood from developing countries. *Science* **348,** 504–506 (2015).
26. Schmitt, K. M. & Kramer, D. B. Road development and market access on Nicaragua's Atlantic coast: implications for household fishing and farming practices. *Environ. Conserv.* **36,** 289–300 (2009).
27. Falk, A. & Szech, N. Morals and markets. *Science* **340,** 707–711 (2013).
28. Sandel, M. J. *What Money Can't Buy: The Moral Limits Of Markets.* (Macmillan, 2012).
29. Ostrom, E. *Governing the Commons: The Evolution of Institutions for Collective Action.* (Cambridge University Press, 1990).
30. Graham, N. A., Jennings, S., MacNeil, M. A., Mouillot, D. & Wilson, S. K. Predicting climate-driven regime shifts versus rebound potential in coral reefs. *Nature* **518,** 94–97 (2015).

Supplementary Information is available in the online version of the paper.

Acknowledgements The ARC Centre of Excellence for Coral Reef Studies, Stanford University, and University of Montpellier funded working group meetings. This work was supported by J.E.C.'s Pew Fellowship in Marine Conservation and ARC Australian Research Fellowship. Thanks to M. Barnes for constructive comments.

Author Contributions J.E.C. conceived of the study with support from M.A.M., N.A.J.G., T.R.M., J.K., C.Hu., D.M., C.M., E.H.A., and C.C.Hi.; C.Hu. managed the database; M.A.M., J.E.C., and D.M. developed and implemented the analyses; J.E.C. led the manuscript with M.A.M. and N.A.J.G. All other authors contributed data and made substantive contributions to the text.

Author Information This is the Social-Ecological Research Frontiers (SERF) working group contribution no. 11. Reprints and permissions information is available at www.nature.com/reprints. The authors declare no competing financial interests. Readers are welcome to comment on the online version of the paper. Correspondence and requests for materials should be addressed to J.E.C. (Joshua.cinner@jcu.edu.au).

Reviewer Information *Nature* thanks S. Qian, B. Walker and the other anonymous reviewer(s) for their contribution to the peer review of this work.

METHODS

No statistical methods were used to predetermine sample size.

Scales of data. Our data were organized at three spatial scales:

(i) Reef ($n = 2,514$). The smallest scale, which had an average of 2.4 surveys/transects.

(ii) Site (a cluster of reefs; $n = 918$). We clustered reefs together that were within 4 km of each other, and used the centroid of these clusters to estimate site-level social and site-level environmental covariates (Extended Data Table 1). To make these clusters, we first estimated the linear distance between all reefs, then used a hierarchical analysis with the complete-linkage clustering technique based on the maximum distance between reefs. We set the cut-off at 4 km to select mutually exclusive sites where reefs cannot be more distant than 4 km. The choice of 4 km was informed by a 3-year study of the spatial movement patterns of artisanal coral reef fishers, corresponding to the highest density of fishing activities on reefs based on GPS-derived effort density maps of artisanal coral reef fishing activities[31]. This clustering analysis was carried out using the R functions hclust and cutree, resulting in an average of 2.7 reefs per site.

(iii) Nation/state (nation, state, or territory; $n = 46$). A larger scale in our analysis was nation/state, which are jurisdictions that generally correspond to individual nations (but could also include states, territories, overseas regions, or extremely remote areas within a state such as the northwest Hawaiian Islands; Extended Data Table 2), within which sites and reefs were nested for analysis.

Estimating biomass. Reef fish biomass can reflect a broad selection of reef fish functioning and benthic conditions[12,32–34], and is a key metric of resource availability for reef fisheries. Reef fish biomass estimates were based on instantaneous visual counts from 6,088 surveys collected from 2,514 reefs. All surveys used standard belt-transects, distance sampling, or point-counts, and were conducted between 2004 and 2013. Where data from multiple years were available from a single reef, we included only data from the year closest to 2010. Within each survey area, reef associated fishes were identified to species level, abundance counted, and total length (TL) estimated, with the exception of one data provider who measured biomass at the family level. To make estimates of biomass from these transect-level data comparable among studies, we:

(iv) Retained families that were consistently studied and were above a minimum size cut-off. Thus, we retained counts of >10-cm diurnally active, non-cryptic reef fish that are resident on the reef (20 families, 774 species), excluding sharks and semi-pelagic species. We also excluded three groups of fishes that are strongly associated with coral habitat conditions and are rarely targets for fisheries (Anthiinae, Chaetodontidae, and Cirrhitidae). Families included are: Acanthuridae, Balistidae, Diodontidae, Ephippidae, Haemulidae, Kyphosidae, Labridae, Lethrinidae, Lutjanidae, Monacanthidae, Mullidae, Nemipteridae, Pinguipedidae, Pomacanthidae, Serranidae, Siganidae, Sparidae, Synodontidae, Tetraodontidae and Zanclidae. We calculated the total biomass of fish on each reef using standard published species-level length–weight relationship parameters or those available on FishBase[35]. When length–weight relationship parameters were not available for a species, we used the parameters for a closely related species or genus.

(v) Directly accounted for depth and habitat as covariates in the model (see Environmental conditions section below).

(vi) Accounted for any potential bias among data providers (capturing information on both inter-observer differences, and census methods) by including each data provider as a random effect in our model.

Biomass means, medians, and standard deviations were calculated at the reef-scale. All reported log values are the natural log.

Social drivers

Local population growth. We created a 100 km buffer around each site and used this to calculate human population within the buffer in 2000 and 2010 based on the Socioeconomic Data and Application Centre (SEDAC) gridded population of the world database[36]. Population growth was the proportional difference between the population in 2000 and 2010. We chose a 100 km buffer as a reasonable range at which many key human impacts from population (for example, land-use and nutrients) might affect reefs[37].

Management. For each site, we determined if it was unfished, that is, whether it fell within the borders of a no-take marine reserve (we asked data providers to further classify whether the reserve had high or low levels of compliance); restricted—whether there were active restrictions on gears (for example, bans on the use of nets, spear guns, or traps) or fishing effort (which could have included areas inside marine parks that were not necessarily no take); or fished, that is, regularly fished without effective restrictions. To determine these classifications, we used the expert opinion of the data providers, and triangulated this with a global database of marine reserve boundaries[38].

Gravity. We adapted the economic geography concept of 'gravity'[17,39–41], also called interactance[42], to examine potential interactions between reefs and: (i) major urban centres/markets (defined as provincial capital cities, major population centres, landmark cities, national capitals, and ports); and (ii) the nearest human settlements. This application of the gravity concept infers that potential interactions increase with population size, but decay exponentially with the effective distance between two points. Thus, we gathered data on both population estimates and a surrogate for distance: travel time.

Population estimations. We gathered population estimates for: (i) the nearest major markets (which includes national capitals, provincial capitals, major population centres, ports, and landmark cities) using the World Cities base map from ESRI; and (ii) the nearest human settlement within a 500 km radius using LandScan 2011 database. The different data sets were required because the latter is available in raster format while the former is available as point data. We chose a 500 km radius from the nearest settlement as the maximum distance any non-market fishing activities for fresh reef fish are likely to occur.

Travel time calculation. Travel time was computed using a cost–distance algorithm that computes the least 'cost' (in minutes) of travelling between two locations on a regular raster grid. In our case, the two locations were either the centroid of the site (that is, reef cluster) and the nearest settlement, or the centroid of the site and the major market. The cost (that is, time) of travelling between the two locations was determined by using a raster grid of land cover and road networks with the cells containing values that represent the time required to travel across them[43]:

- Tree cover, broadleaved, deciduous and evergreen, closed; regularly flooded tree cover, shrub, or herbaceous cover (fresh, saline, & brackish water) = speed of 1 km h^{-1}
- Tree cover, broadleaved, deciduous, open (open = 15–40% tree cover) = speed of 1.25 km h^{-1}
- Tree cover, needle-leaved, deciduous and evergreen, mixed leaf type; shrub cover, closed-open, deciduous and evergreen; herbaceous cover, closed-open; cultivated and managed areas; mosaic: cropland/tree cover/other natural vegetation, cropland/shrub or grass cover = speed of 1.5 km h^{-1}
- Mosaic: tree cover/other natural vegetation; tree cover, burnt = speed of 1.25 km h^{-1}
- Sparse herbaceous or sparse shrub cover = speed of 2.5 km h^{-1}
- Water = speed of 20 km h^{-1}
- Roads = speed of 60 km h^{-1}
- Track = speed of 30 km h^{-1}
- Artificial surfaces and associated areas = speed of 30 km h^{-1}
- Missing values = speed of 1.4 km h^{-1}

We termed this raster grid a friction-surface (with the time required to travel across different types of surfaces analogous to different levels of friction). To develop the friction-surface, we used global data sets of road networks, land cover, and shorelines:

- Road network data was extracted from the Vector Map Level 0 (VMap0) from the National Imagery and Mapping Agency's (NIMA) Digital Chart of the World (DCW). We converted vector data from VMap0 to 1 km resolution raster.
- Land cover data were extracted from the Global Land Cover 2000 (ref. 44).
- To define the shorelines, we used the GSHHS (Global Self-consistent, Hierarchical, High-resolution Shoreline) database version 2.2.2.

These three friction components (road networks, land cover, and water bodies) were combined into a single friction surface with a Behrmann map projection. We calculated our cost-distance models in R[45] using the accCost function of the gdistance package. The function uses Dijkstra's algorithm to calculate least-cost distance between two cells on the grid and the associated distance taking into account obstacles and the local friction of the landscape[46]. Travel time estimates over a particular surface could be affected by the infrastructure (for example, road quality) and types of technology used (for example, types of boats). These types of data were not available at a global scale but could be important modifications in more localized studies.

Gravity computation. To compute the gravity to the nearest market, we calculated the population of the nearest major market and divided that by the squared travel time between the market and the site. Although other exponents can be used[47], we used the squared distance (or in our case, travel time), which is relatively common in geography and economics. This decay function could be influenced by local considerations, such as infrastructure quality (for example, roads), the types of transport technology (that is, vessels being used), and fuel prices, which were not

available in a comparable format for this global analysis, but could be important considerations in more localized adaptations of this study.

To determine the gravity of the nearest settlement, we located the nearest populated pixel within 500 km, determined the population of that pixel, and divided that by the squared travel time between that cell and the reef site.

As is standard practice in many agricultural economics studies[48], an assumption in our study is that the nearest major capital or landmark city represents a market. Ideally we would have used a global database of all local and regional markets for coral reef fish, but this type of database is not available at a global scale. As a sensitivity analysis to help justify our assumption that capital and landmark cities were a reasonable proxy for reef fish markets, we tested a series of candidate models that predicted biomass based on: (1) cumulative gravity of all cities within 500 km; (2) gravity of the nearest city; (3) travel time to the nearest city; (4) population of the nearest city; (5) gravity to the nearest human population above 40 people km^{-2} (assumed to be a small peri-urban area and potential local market); (6) the travel time between the reef and a small peri-urban area; (7) the population size of the small peri-urban population; (8) gravity to the nearest human population above 75 people km^{-2} (assumed to be a large peri-urban area and potential market); (9) the travel time between the reef and this large peri-urban population; (10) the population size of this large peri-urban population; and (11) the total population size within a 500 km radius. Model selection revealed that the best two models were gravity of the nearest city and gravity of all cities within 500 km (with a 3 AIC value difference between them; Extended Data Table 3). Importantly, when looking at the individual components of gravity models, the travel time components all had a much lower AIC value than the population components, which is broadly consistent with previous systematic review studies[49]. Similarly, travel time to the nearest city had a lower AIC score than any aspect of either the peri-urban or urban measures. This suggests our use of capital and landmark cities is likely to better capture exploitation drivers from markets rather than simple population pressures. This may be because market dynamics are difficult to capture by population threshold estimates; for example some small provincial capitals where fish markets are located have very low population densities, while some larger population centres may not have a market. Downscaled regional or local analyses could attempt to use more detailed knowledge about fish markets, but we used the best proxy available at a global scale.

Human Development Index (HDI). HDI is a summary measure of human development encompassing: a long and healthy life, being knowledgeable, and having a decent standard of living. In cases where HDI values were not available specific to the State (for example, Florida and Hawaii), we used the national (for example, USA) HDI value.

Population size. For each nation/state, we determined the size of the human population. Data were derived mainly from census reports, the CIA fact book, and Wikipedia.

Tourism. We examined tourist arrivals relative to the nation/state population size (above). Tourism arrivals were gathered primarily from the World Tourism Organization's Compendium of Tourism Statistics.

National reef fish landings. Catch data were obtained from the Sea Around Us Project (SAUP) catch database (http://www.seaaroundus.org), except for Florida, which was not reported separately in the database. We identified 200 reef fish species and taxon groups in the SAUP catch database[50]. Note that reef-associated pelagics such as scombrids and carangids normally form part of reef fish catches. However, we chose not to include these species because they are also targeted and caught in large amounts by large-scale, non-reef operations.

Voice and accountability. This metric, from the World Bank survey on governance, reflects the perceptions of the extent to which a country's citizens are able to participate in selecting their government, as well as freedom of expression, freedom of association, and a free media. In cases where governance values were not available specific to the nation/state (for example, Florida and Hawaii), we used national (for example, USA) values.

Environmental drivers

Depth. The depth of reef surveys were grouped into the following categories: <4 m, 4–10 m, >10 m to account for broad differences in reef fish community structure attributable to a number of inter-linked depth-related factors. Categories were necessary to standardise methods used by data providers and were determined by pre-existing categories used by several data providers.

Habitat. We included the following habitat categories:

(i) Slope. The reef slope habitat is typically on the ocean side of a reef, where the reef slopes down into deeper water.
(ii) Crest. The reef crest habitat is the section that joins a reef slope to the reef flat. The zone is typified by high wave energy (that is, where the waves break). It is also typified by a change in the angle of the reef from an inclined slope to a horizontal reef flat.
(iii) Flat. The reef flat habitat is typically horizontal and extends back from the reef crest for 10's to 100's of metres;
(iv) Lagoon/back reef. Lagoon reef habitats are where the continuous reef flat breaks up into more patchy reef environments sheltered from wave energy. These habitats can be behind barrier/fringing reefs or within atolls. Back reef habitats are similar broken habitats where the wave energy does not typically reach the reefs and thus forms a less continuous 'lagoon style' reef habitat. Due to minimal representation among our sample, we excluded other less prevalent habitat types, such as channels and banks. To verify the sites' habitat information, we used the Millennium Coral Reef Mapping Project (MCRMP) hierarchical data[51], Google Earth, and site depth information.

Productivity. We examined ocean productivity for each of our sites in mg of C per m^2 per day (http://www.science.oregonstate.edu/ocean.productivity/). Using the monthly data for years 2005 to 2010 (in hdf format), we imported and converted those data into ArcGIS. We then calculated yearly average and finally an average for all these years. We used a 100 km buffer around each of our sites and examined the average productivity within that radius. Note that ocean productivity estimates are less accurate for near-shore environments, but we used the best available data.

Analyses. We first looked for collinearity among our covariates using bivariate correlations and variance inflation factor estimates (Extended Data Fig. 2 and Extended Data Table 4). This led to the exclusion of several covariates (not described above): (i) geographic basin (tropical Atlantic, western Indo-Pacific, central Indo-Pacific, or eastern Indo-Pacific); (ii) gross domestic product (purchasing power parity); (iii) rule of law (World Bank governance index); (iv) control of corruption (World Bank governance index); and (v) sedimentation. Additionally, we removed an index of climate stress, developed by Maina *et al.*[52], which incorporated 11 different environmental conditions, such as the mean and variability of sea surface temperature due to repeated lack of convergence for this parameter in the model, likely indicative of unidentified multicollinearity. All other covariates had correlation coefficients 0.7 or less and variance inflation factor scores less than 5 (indicating multicollinearity was not a serious concern). Care must be taken in causal attribution of covariates that were significant in our model, but demonstrated collinearity with candidate covariates that were removed during the aforementioned process. Importantly, the covariate that exhibited the largest effect size in our model, market gravity, was not strongly collinear with other candidate covariates.

To quantify the multi-scale social, environmental, and economic factors affecting reef fish biomass we adopted a Bayesian hierarchical modelling approach that explicitly recognized the three scales of spatial organization: reef (j), site (k), and nation/state (s).

In adopting the Bayesian approach we developed two models for inference: a null model, consisting only of the hierarchical units of observation (that is, intercepts-only) and a full model that included all of our covariates (drivers) of interest. Covariates were entered into the model at the relevant scale, leading to a hierarchical model whereby lower-level intercepts (averages) were placed in the context of higher-level covariates in which they were nested. We used the null model as a baseline against which we could ensure that our full model performed better than a model with no covariate information. We did not remove 'non-significant' covariates from the model because each covariate was carefully considered for inclusion and could therefore reasonably be considered as having an effect, even if small or uncertain; removing factors from the model is equivalent to fixing parameter estimates at exactly zero—a highly-subjective modelling decision after covariates have already been selected as potentially important[53].

The full model assumed the observed, reef-scale observations of fish biomass (y_{ijks}) were modelled using a non-central t distribution, allowing for fatter tails than typical log-normal models of reef fish biomass[32]. We chose the non-central t after having initially used a log-normal model because our model diagnostics suggested that several model parameters had not converged. We ran a supplementary analysis to support our use of the non-central t distribution with 3.5 degrees of freedom (see Supplementary Information). Therefore our model was:

$$\log[y_{ijks}] \sim \text{non-central } t(\mu_{ijks}, \tau_{\text{reef}}, 3.5)$$

$$\mu_{ijks} = \beta_{0jks} + \beta_{\text{reef}} \boldsymbol{X}_{\text{reef}}$$

$$\tau_{\text{reef}} \sim \text{U}(0,100)^{-2}$$

with $\boldsymbol{X}_{\text{reef}}$ representing the matrix of observed reef-scale covariates and β_{reef} array of estimated reef-scale parameters. The τ_{reef} (and all subsequent τ values) were assumed common across observations in the final model and were minimally

informative[53]. Using a similar structure, the reef-scale intercepts (β_{0jks}) were structured as a function of site-scale covariates ($\boldsymbol{X}_{\mathrm{sit}}$):

$$\beta_{0jks} \sim \mathrm{N}(\mu_{jks}, \tau_{\mathrm{sit}})$$

$$\mu_{jks} = \gamma_{0ks} + \gamma_{\mathrm{sit}}\boldsymbol{X}_{\mathrm{sit}}$$

$$\tau_{\mathrm{sit}} \sim \mathrm{U}(0,100)^{-2}$$

with γ_{sit} representing an array of site-scale parameters. Building upon the hierarchy, the site-scale intercepts (γ_{0ks}) were structured as a function of state-scale covariates ($\boldsymbol{X}_{\mathrm{sta}}$):

$$\gamma_{0ks} \sim \mathrm{N}(\mu_{ks}, \tau_{\mathrm{sta}})$$

$$\mu_{ks} = \gamma_0 + \gamma_{\mathrm{sta}}\boldsymbol{X}_{\mathrm{sta}}$$

$$\tau_{\mathrm{sta}} \sim \mathrm{U}(0,100)^{-2}$$

Finally, at the top scale of the analysis we allowed for a global (overall) estimate of average log-biomass (γ_0):

$$\gamma_0 \sim \mathrm{N}(0.0,1000)$$

The relationships between fish biomass and reef, site, and state-scale drivers was carried out using the PyMC package[54] for the Python programming language, using a Metropolis-Hastings (MH) sampler run for 10^6 iterations, with a 900,000 iteration burn-in thinned by 10, leaving 10,000 samples in the posterior distribution of each parameter; these long burn-in times are often required with a complex model using the MH algorithm. Convergence was monitored by examining posterior chains and distributions for stability and by running multiple chains from different starting points and checking for convergence using Gelman–Rubin statistics[55] for parameters across multiple chains; all were at or close to 1, indicating good convergence of parameters across multiple chains.

Overall model fit. We conducted posterior predictive checks for goodness of fit (GoF) using Bayesian *P* values[43] (BpV), whereby fit was assessed by the discrepancy between observed or simulated data and their expected values. To do this we simulated new data (y_i^{new}) by sampling from the joint posterior of our model (θ) and calculated the Freeman–Tukey measure of discrepancy for the observed (y_i^{obs}) or simulated data, given their expected values (μ_i):

$$D(y|\theta) = \sum_i (\sqrt{y_i} - \sqrt{y_i})^2$$

yielding two arrays of median discrepancies $D(y^{\mathrm{obs}}/\theta)$ and $D(y^{\mathrm{new}}/\theta)$ that were then used to calculate a BpV for our model by recording the proportion of times $D(y^{\mathrm{obs}}/\theta)$ was greater than $D(y^{\mathrm{new}}/\theta)$ (Extended Data Fig. 3a). A BpV above 0.975 or under 0.025 provides substantial evidence for lack of model fit. Evaluated by the deviance information criterion (DIC), the full model greatly outperformed a null model that included no covariates ($\Delta\mathrm{DIC} = 472$).

To examine homoscedasticity, we checked residuals against fitted values. We also checked the residuals against all covariates included in the model, and several covariates that were not included in the model (primarily due to collinearity), including: (i) Atoll, a binary metric of whether the reef was on an atoll or not; (ii) control of corruption, perceptions of the extent to which public power is exercised for private gain, including both petty and grand forms of corruption, as well as 'capture' of the state by elites and private interests, derived from the World Bank survey on governance; (iii) geographic basin, whether the site was in the tropical Atlantic, western Indo-Pacific, central Indo-Pacific, or eastern Indo-Pacific; (iv) connectivity, we examined three measures based on the area of coral reef within a 30 km, 100 km, and 600 km radius of the site; (v) sedimentation; (vi) coral cover (which was only available for a subset of the sites); (vii) climate stress[52]; and (viii) census method. The model residuals showed no patterns with these eight additional covariates, suggesting they would not explain additional information in our model.

Bright and dark spot estimates. Because the performance of site scale locations are of substantial interest in uncovering novel solutions for reef conservation, we defined bright and dark spots at the site scale. To this end, we defined bright (or dark) spots as locations where expected site-scale intercepts (γ_{0ks}) differed by more than two standard deviations from their nation/state-scale expected value (μ_{ks}), given all the covariates present in the full hierarchical model:

$$\mathrm{SS}_{\mathrm{spot}} = |(\mu_{ks} - \gamma_{0ks})| > 2[\mathrm{s.d.}(\mu_{ks} - \gamma_{0ks})]$$

This, in effect, probabilistically identified the most deviant sites, given the model, while shrinking sites towards their group-level means, thereby allowing us to overcome potential bias due to low and varying sample sizes that can lead to extreme values from chance alone. After an initial log-normal model formulation, where we were not confident in model convergence, we employed a non-central *t* distribution at the observation scale, which facilitated model convergence and dampened any effects of potentially extreme reef-scale observations on the bright and dark spot estimates. Further, we did not consider a site a bright or dark spot if the group-level (that is, nation/state) mean included fewer than five sites.

Analysing conditions at bright spots. For our preliminary exploration into why bright and dark spots may diverge from expectations, we surveyed data providers and other experts about key social, institutional, and environmental conditions at the 15 bright spots, 35 dark spots, and 14 sites that performed most closely to model specifications. Specifically, we developed an online survey (SI) using Survey Monkey (http://www.surveymonkey.com) software, which we asked data providers who sampled those sites to complete with input from local experts, where necessary. Data providers generally filled in the survey in consultation with nationally based field team members who had detailed local knowledge of the socioeconomic and environmental conditions at each of the sites. Research on bright spots in agricultural development[19] highlights several types of social and environmental conditions that may lead to bright spots, which we adapted and developed proxies for as the basis of our survey into why our bright and dark spots may diverge from expectations. These include:

(i) Social and institutional conditions. We examined the presence of customary management institutions such as taboos and marine tenure institutions, whether there was substantial engagement by local people in management (specifically defined as there being active engagement by local people in reef management decisions; token involvement and consultation were not considered substantial engagement), and whether there were high levels of dependence on marine resources (specifically, whether a majority of local residents depend on reef fish as a primary source of food or income). All social and institutional conditions were converted to presence/absence data. Dependence on resources and engagement were limited to sites that had adjacent human populations. All other conditions were recorded regardless of whether there is an adjacent community.

(ii) Technological use/innovation. We examined the presence of motorized vessels, intensive capture equipment (such as beach seine nets, surround gill nets, and muro-ami nets), and storage capacity (that is, freezers).

(iii) External influences (such as donor-driven projects). We examined the presence of NGOs, fishery development projects, development initiatives (such as alternative livelihoods), and fisheries improvement projects. All external influences were recorded as present/absent then summarized into a single index of whether external projects were occurring at the site.

(iv) Environmental/ecological processes (for example, recruitment and connectivity). We examined whether sites were within 5 km of mangroves and deep-water refuges, and whether there had been any major environmental disturbances such as coral bleaching, tsunami, and cyclones within the past 5 years. All environmental conditions were recorded as present/absent.

As an exploratory analysis of associations between these conditions and whether sites diverged more or less from expectations, we used two complementary approaches. The link between the presence/absence of the aforementioned conditions and whether a site was bright, average, or dark was assessed using a Fisher's exact test. Then we tested whether the mean deviation in fish biomass from expected was similar between sites with presence or absence of the mechanisms in question (that is, the presence or absence of marine tenure/taboos) using an ANOVA assuming unequal variance. The two tests yielded similar results, but provide slightly different ways to conceptualize the issue, the former is correlative while the latter explains deviation from expectations based on conditions, so we provide both (Fig. 3 and Extended Data Fig. 4). It is important to note that some of these social and environmental conditions were significantly associated (that is, Fisher's exact probabilities <0.05), and further research is required to uncover how these and other conditions may make sites bright or dark.

31. Daw, T. *et al. The Spatial Behaviour of Artisanal Fishers: Implications for Fisheries Management and Development (Fishers in Space).* (WIOMSA, 2011).
32. MacNeil, M. A. *et al.* Recovery potential of the world's coral reef fishes. *Nature* **520,** 341–344 (2015).
33. Mora, C. *et al.* Global human footprint on the linkage between biodiversity and ecosystem functioning in reef fishes. *PLoS Biol.* **9,** e1000606 (2011).
34. Edwards, C. B. *et al.* Global assessment of the status of coral reef herbivorous fishes: evidence for fishing effects. *Proc. Biol. Sci.* **281,** 20131835 (2014).
35. Froese, R. & Pauly, D. *FishBase*. http://www.fishbase.org (2014).
36. Center for International Earth Science Information Network (CIESIN). *Gridded population of the world. Version 3 (GPWv3)* http://sedac.ciesin.columbia.edu/gpw (2005).

37. MacNeil, M. A. & Connolly, S. R. in *Ecology of Fishes on Coral Reefs* (ed C. Mora) Ch. 12, 116–126 (2015).
38. Mora, C. *et al.* Ecology. Coral reefs and the global network of Marine Protected Areas. *Science* **312,** 1750–1751 (2006).
39. Ravenstein, E. G. The laws of migration. *J. R. Stat. Soc.* **48,** 167–235 (1885).
40. Anderson, J. E. A theoretical foundation for the gravity equation. *Am. Econ. Rev.* **69,** 106–116 (1979).
41. Anderson, J. E. *The Gravity Model.* (National Bureau of Economic Research, 2010).
42. Lukermann, F. & Porter, P. W. Gravity and potential models in economic geography. *Ann. Assoc. Am. Geogr.* **50,** 493–504 (1960).
43. Nelson, A. *Travel Time to Major Cities: A Global Map of Accessibility.* (Ispra, Italy, 2008).
44. Bartholomé, E. *et al. GLC 2000: Global Land Cover Mapping for the Year 2000: Project Status November 2002.* (Institute for Environment and Sustainability, 2002).
45. R Core Team. *R: A language and environment for statistical computing*. https://www.R-project.org (2016).
46. Dijkstra, E. W. A note on two problems in connexion with graphs. *Numer. Math.* **1,** 269–271 (1959).
47. Black, W. R. An analysis of gravity model distance exponents. *Transportation* **2,** 299–312 (1973).
48. Emran, M. S. & Shilpi, F. *The Extent of the Market and Stages of Agricultural Specialization.* Vol. 4534 (World Bank Publications, 2008).
49. Cinner, J. E., Graham, N. A., Huchery, C. & Macneil, M. A. Global effects of local human population density and distance to markets on the condition of coral reef fisheries. *Conserv. Biol.* **27,** 453–458 (2013).
50. Teh, L. S. L., Teh, L. C. & Sumaila, U. R. A Global Estimate of the Number of Coral Reef Fishers. *PLoS One* **8,** e65397 (2013).
51. Andréfouët, S. *et al.* in *10th International Coral Reef Symposium* (eds Y. Suzuki *et al.*) 1732–1745 (Japanese Coral Reef Society, 2006).
52. Maina, J., McClanahan, T. R., Venus, V., Ateweberhan, M. & Madin, J. Global gradients of coral exposure to environmental stresses and implications for local management. *PLoS One* **6,** e23064 (2011).
53. Gelman, A. *et al. Bayesian Data Analysis.* Vol. 2 (Taylor & Francis, 2014).
54. Patil, A., Huard, D. & Fonnesbeck, C. J. PyMC: Bayesian stochastic modelling in Python. *J. Stat. Softw.* **35,** 1–81 (2010).
55. Gelman, A. & Rubin, D. B. Inference from iterative simulation using multiple sequences. *Stat. Sci.* **7,** 457–472 (1992).

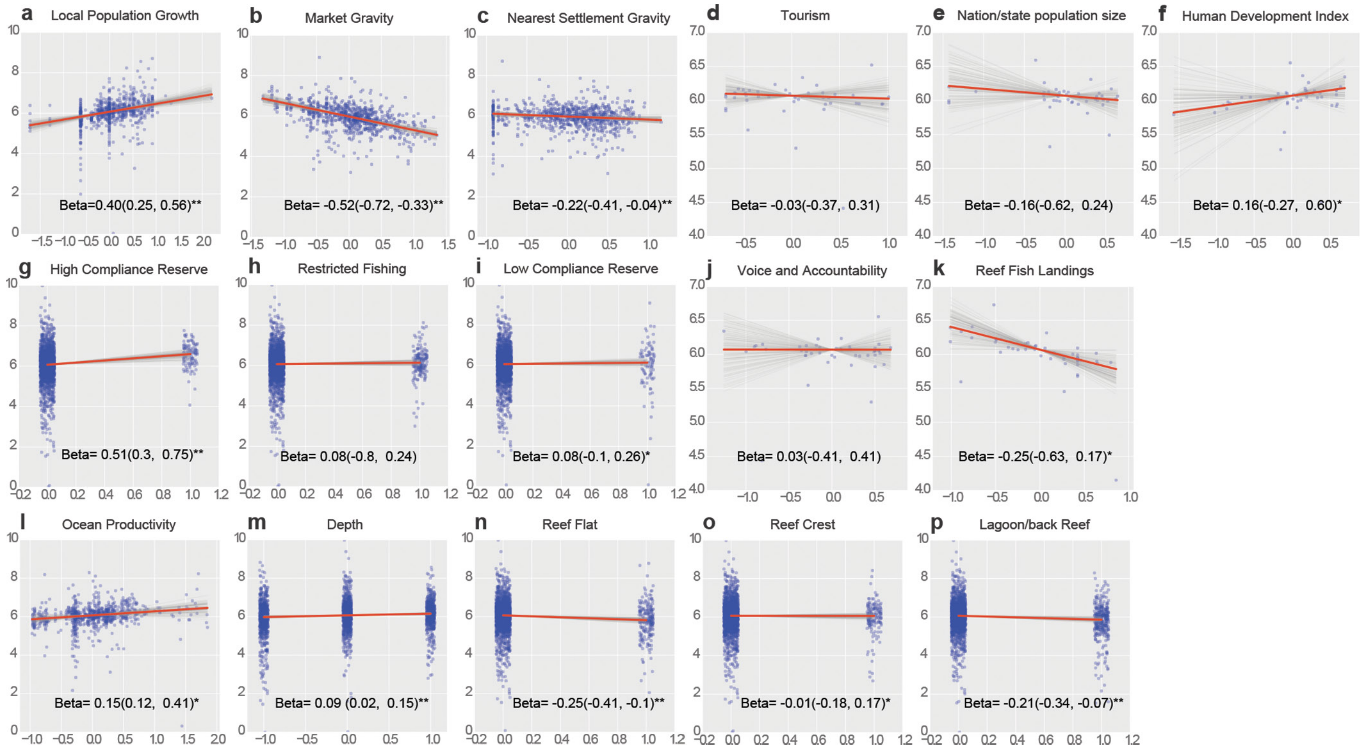

Extended Data Figure 1 | Marginal relationships between reef fish biomass and social drivers. **a**, Local population growth; **b**, market gravity; **c**, nearest settlement gravity; **d**, tourism; **e**, nation/state population size; **f**, Human Development Index; **g**, high compliance marine reserve (0 is fished baseline); **h**, restricted fishing (0 is fished baseline); **i**, low-compliance marine reserve (0 is fished baseline); **j**, voice and accountability; **k**, reef fish landings; **l**, ocean productivity; **m**, depth ($-1 = 0$–4 m, $0 = 4$–10 m, $1 = >10$ m); **n**, reef flat (0 is reef slope baseline); **o**, reef crest flat (0 is reef slope baseline); **p**, lagoon/back reef flat (0 is reef slope baseline). All variables displayed on the *x* axis are standardized. Red lines are the marginal trend line for each parameter as estimated by the full model. Grey lines are 100 simulations of the marginal trend line sampled from the posterior distributions of the intercept and parameter slope, analogous to conventional confidence intervals. Two asterisks indicate that 95% of the posterior density is in either a positive or negative direction (Fig. 1b–d); a single asterisk indicates that 75% of the posterior density is in either a positive or negative direction.

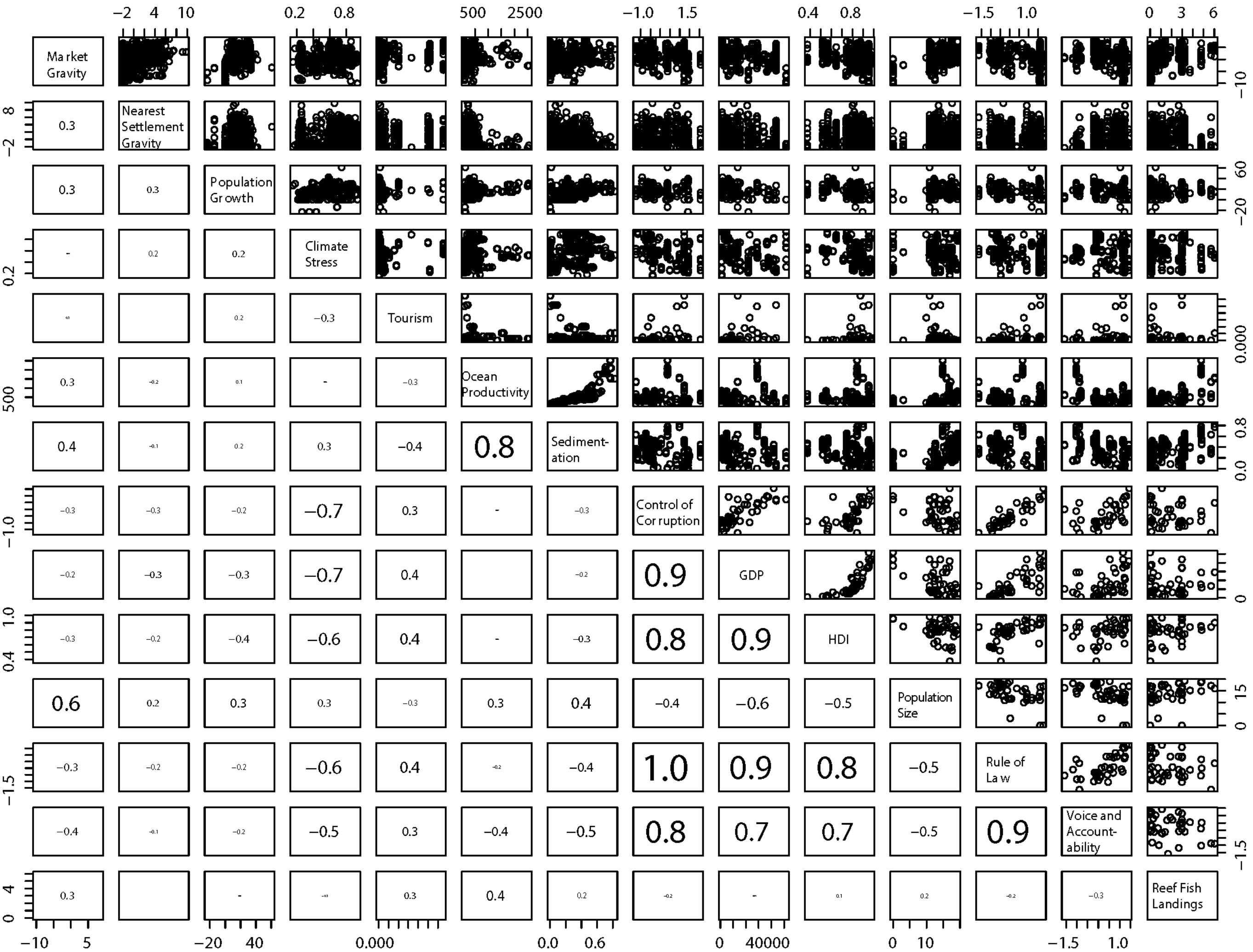

Extended Data Figure 2 | Correlation plot of candidate continuous covariates before accounting for collinearity (Extended Data Table 4). Collinearity between continuous and categorical covariates (including biogeographic region, habitat, protection status, and depth) were analysed using box plots.

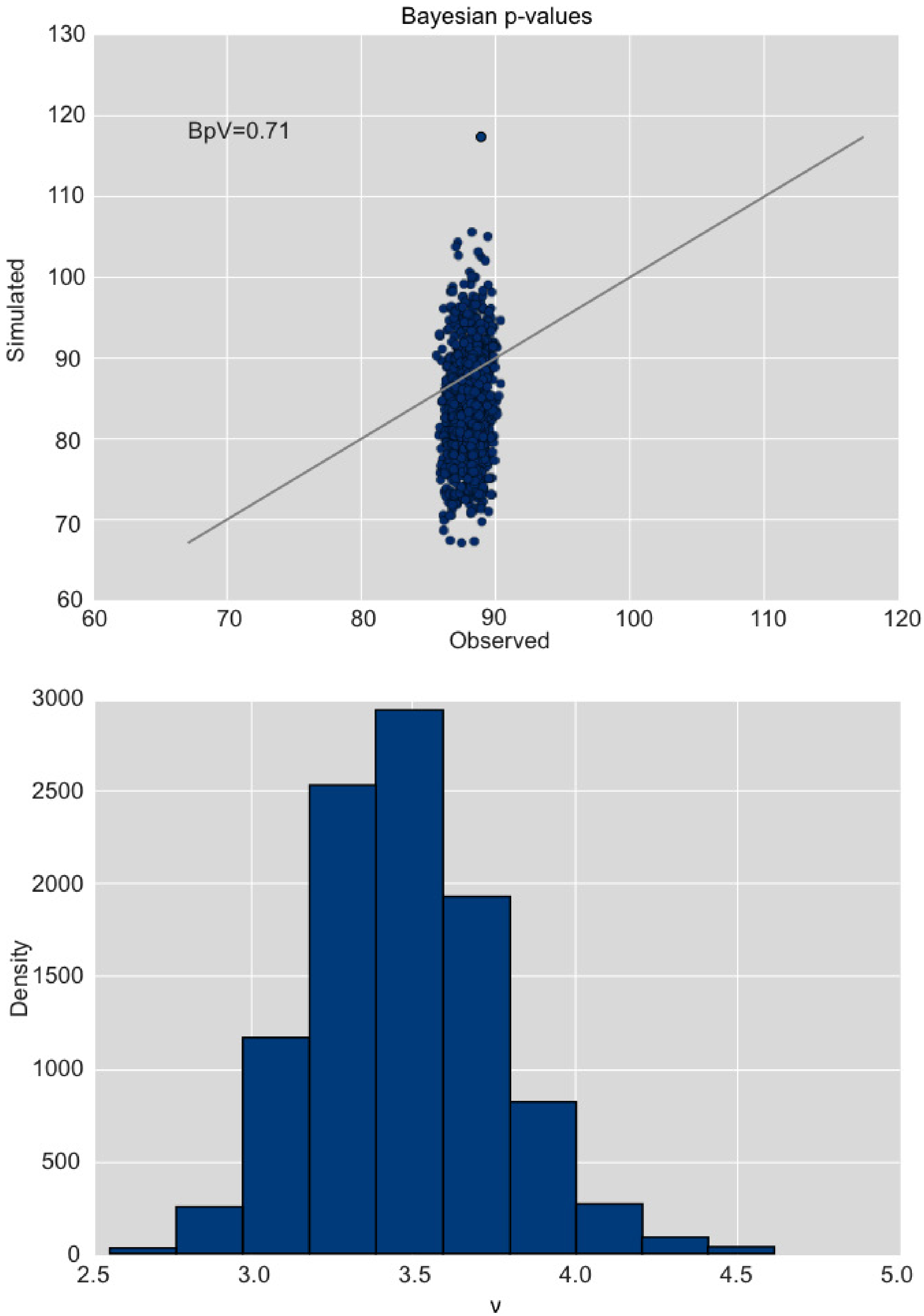

Extended Data Figure 3 | Model fit statistics. Top, Bayesian *P* values (BpV) for the full model indicating goodness of fit, based on posterior discrepancy. Points are Freeman–Tukey differences between observed and expected values, and simulated and expected values within the MCMC scheme ($n = 10{,}000$). Plot shows no evidence for lack of fit between the model and the data. Bottom, Posterior distribution for the degrees of freedom parameter (ν) in our supplementary analysis of candidate distributions. The highest posterior density of 3.46, with 97.5% of the total posterior density below 4 provides strong evidence in favour of a non-central *t* distribution relative to a normal distribution and supports the use of 3.5 for ν.

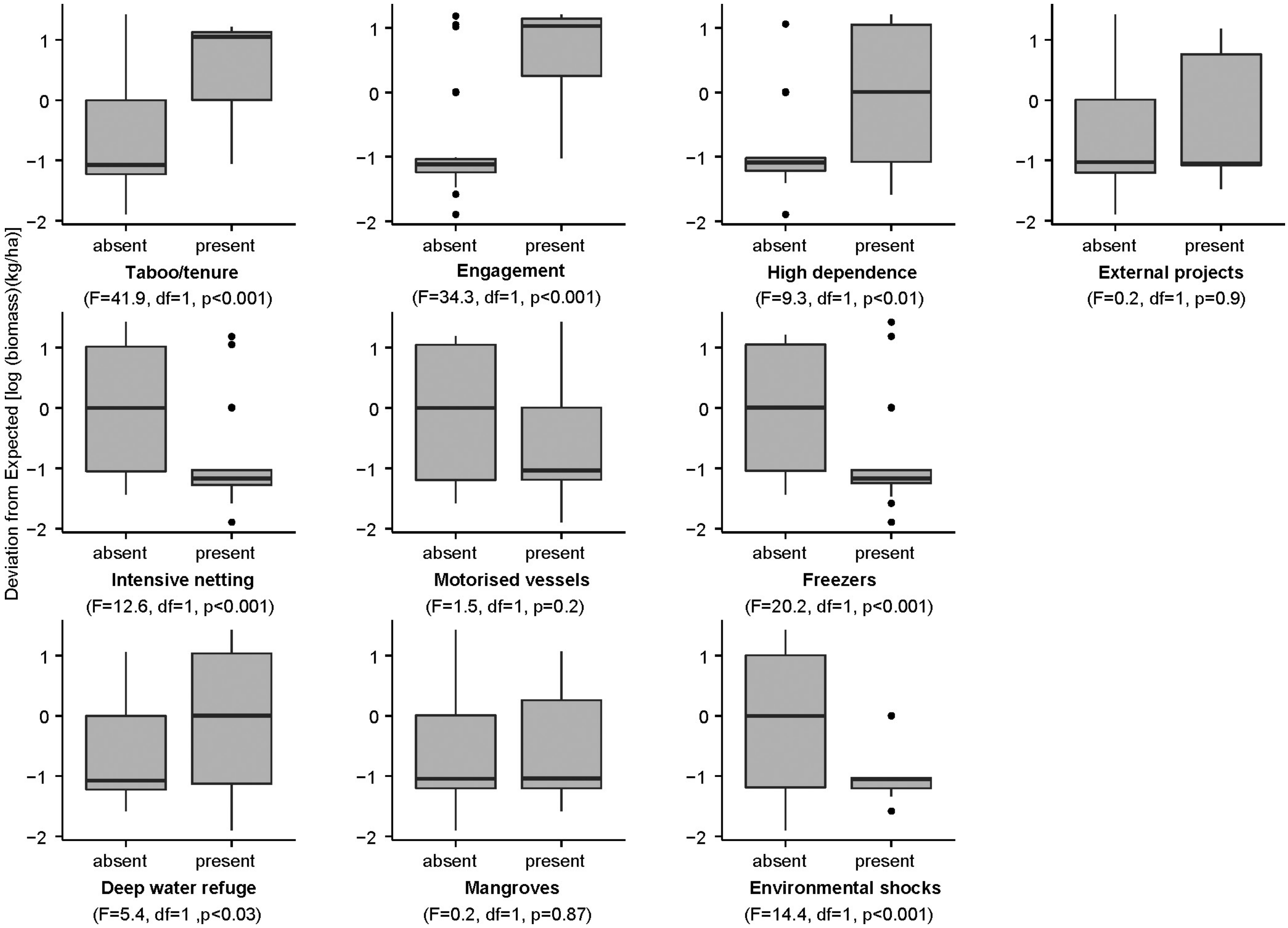

Extended Data Figure 4 | Box plot of deviation from expected as a function of the presence or absence of key social and environmental conditions expected to produce bright spots. Boxes range from the first to third quartile and whiskers extend to the highest value that is within 1.5× the inter-quartile range (that is, distance between the first and third quartiles). Data beyond the end of the whiskers are outliers, which are plotted as points.

Extended Data Table 1 | Summary of social and environmental covariates

Covariate	Description	Scale	Key data sources
Local population growth	Difference in local human population (i.e. 100km buffer around our sites) between 2000-2010	Site	Socioeconomic Data and Application Centre (SEDAC) gridded population of the work database[36]
'Gravity' of major markets within 500km	The population of the major market divided by the squared travel time between the reef sites and the market. This value was summed for all major markets within 500km of the site.	Site	Human population size, land cover, road networks, coastlines
'Gravity' of the closest human settlement	The population of the nearest human settlement divided by the squared travel time between the reef site and the settlement.	Site	Human population size, land cover, road networks, coastlines
Protection status	Whether the reef is openly fished, restricted (e.g. effective gear bans or effort restrictions), or unfished	Reef	Expert opinion, global map of marine protected areas.
Human Development index	A summary measure of human development encompassing: a long and healthy life, being knowledgeable and have a decent standard of living. We used linear and quadratic functions for HDI.	Nation/state	United Nations Development Programme
Population Size	Total population size of the jurisdiction	Nation/ state	World Bank, census estimates, Wikipedia
Tourism	Proportion of tourist visitors to residents	Nation/ state	World Tourism Organization's Compendium of Tourism Statistics, census estimates
Voice and accountability	Perceptions of the extent to which a country's citizens are able to participate in selecting their government.	Nation/ state	World Bank
Fish landings	Landings of reef fish (tons) per Km^2 of reef	Nation/ state	Teh et al.[50]
Productivity	The average (2005-2010) ocean productivity in mg C / m2 / day	Site	http://www.science.oregonstate.edu/ocean.productivity/
Habitat	Whether the reef is a slop, crest, flat, or back reef/lagoon	Reef	Primary data
Depth	Depth of the ecological survey (<4m, 4.1-10m, >10m)	Reef	Primary data

Further details can be found in the Methods. The smallest scale is the individual reef. Sites consist of clusters of reefs within 4 km of each other. Nations/states generally correspond to countries, but can also include or territories or states, particularly when geographically isolated (for example, Hawaii). Refs 36 and 50 are cited in this table.

Extended Data Table 2 | List of nations/states covered in study and their respective average biomass (kg ha^{-1} ± standard error)

Nation/states	Average biomass	(± SE)
American Samoa	235.93	(± 17.75)
Australia	735.01	(± 136.85)
Belize	981.16	(± 65.32)
Brazil	663.35	(± 115.17)
British Indian Ocean Territory (Chagos)	2975.58	(± 603.99)
Cayman Islands	464.09	(± 25.41)
Colombia	846.07	(± 162.49)
Commonwealth of the Northern Mariana Islands	505.54	(± 99.3)
Comoros Islands	305.62	(± 38.73)
Cuba	2107.37	(± 466.34)
Egypt	552.73	(± 70.18)
Farquhar	2665.48	(± 492.62)
Federated States of Micronesia	377.90	NA (n=1)
Fiji	1464.54	(± 144.39)
Florida	1661.35	(± 198.42)
French Polynesia	1077.20	(± 101.4)
Guam	118.98	(± 16.81)
Hawaii	380.45	(± 25.11)
Indonesia	275.76	(± 19.89)
Israel	445.16	(± 105.13)
Jamaica	275.77	(± 50.75)
Kenya	335.25	(± 65.81)
Kiribati	1219.93	(± 93.2)
Madagascar	409.48	(± 46.1)
Maldives	688.64	(± 97.07)
Marshall Islands	707.72	(± 174.38)
Mauritius	166.93	(± 73.7)
Mayotte	631.43	(± 68.25)
Mexico	1930.81	(± 737.09)
Mozambique	461.01	(± 60.14)
Netherlands Antilles	428.01	(± 53.99)
New Caledonia	1460.27	(± 143.18)
NW Hawaiian Islands	729.71	(± 46.33)
Oman	282.79	(± 70.22)
Palau	3212.26	(± 332.02)
Panama	373.78	(± 85.41)
Papua New Guinea	566.70	(± 31.76)
Philippines	202.62	NA (n=1)
Pacific Remote Island Areas (PRIA), USA	641.47	(± 79.25)
Reunion	172.32	(± 30.67)
Seychelles	446.99	(± 46.6)
Solomon Islands	1280.30	(± 216.74)
Tanzania	346.29	(± 41.51)
Tonga	1149.97	(± 151.27)
United Arab Emirates	81.35	(± 28.66)
Venezuela	1472.39	(± 496.95)

In most cases, nation/state refers to an individual country, but can also include states (for example, Hawaii or Florida), territories (for example, British Indian Ocean Territory), or other jurisdictions. We treated the northwestern Hawaiian islands and Farquhar as separate 'nation/states' from Hawaii and the Seychelles, respectively, because they are extremely isolated and have little or no human population. In practical terms, this meant different values for a few nation/state scale indicators that ended up having relatively small effect sizes (Fig. 1b): population, tourism visitations, and in the case of the northwestern Hawaiian islands, fish landings.

Extended Data Table 3 | Model selection of potential gravity indicators and components

Model	Covariates	AIC	Delta AIC
M2	Gravity of nearest city	2666.4	0
M1	Gravity of all cities in 500km	2669.5	3.1
M3	Travel time to nearest city	2700.0	33.6
M5	Gravity of nearest small peri-urban area (40 people/km2)	2703.9	37.5
M11	Total Population in 500km radius	2712.0	45.6
M9	Travel time to the nearest large peri-urban area (75 people/km2)	2712.1	45.7
M6	Travel time to nearest small peri-urban area (40 people/km2)	2713.8	47.4
M8	Gravity to the nearest large peri-urban area (75 people/km2)	2722.9	56.5
M7	Population of nearest small peri-urban area (40 people/km2)	2792.7	126.3
M4	Population of the nearest city	2812.8	146.5
M10	Population of the nearest large peri-urban area (75 people/km2)	2822.2	155.8
M0	Intercept only	2827.7	161.27

Extended Data Table 4 | Variance inflation factor (VIF) scores for continuous data before and after removing variables due to collinearity

Covariate	starting VIF	ending VIF
Market gravity (log)	1.9	1.5
Nearest settlement gravity	1.4	1.3
Population growth	1.4	1.3
Climate stress	2.7	X
Ocean productivity	6.5	2.2
Sedimentation	6.0	X
Tourism	2.5	2.0
Control Corruption	10.5	X
GDP	8.2	X
HDI	5.5	3.3
Population size	1.9	1.8
Reef fish landings	3.1	2.2
Rule of Law	33.8	x
Voice and Accountability	3.2	3.2

X = covariate removed.

Extended Data Table 5 | List of bright and dark spot locations, population status, and protection status

Bright or Dark	Nation/State	Location	Populated	Protection
Bright	British Indian Ocean Territory	Chagos	Unpopulated	Unfished (high compliance)
	Commonwealth of the Northern Mariana Islands	Agrihan	Unpopulated	Fished
		Guguan	Unpopulated	Fished
	Indonesia	Raja Ampat 1	Populated	Restricted
		Raja Ampat 2	Populated	Restricted
		Kalimantan	Populated	Restricted
	Kiribati	Tabueran 1	Populated	Fished
		Tabueran 2	Populated	Fished
	Papua New Guinea	Karkar	Populated	Restricted
	PRIA	Baker	Unpopulated	Restricted
		Jarvis Island	Unpopulated	Restricted
	Solomon Islands	Choiseul	Populated	Fished
		Isabel	Populated	Fished
		Makira	Populated	Fished
		New Georgia	Populated	Fished
Dark	Australia	Lord Howe	Populated	Unfished (high compliance)
	Hawaii	Hawaii	Populated	Fished
		Kauai 1	Populated	Fished
		Kauai 2	Populated	Fished
		Lanai	Populated	Fished
		Maui 1	Populated	Fished
		Maui 2	Populated	Fished
		Molokai	Populated	Fished
		Oahu 1	Populated	Fished
		Oahu 2	Populated	Fished
		Oahu 3	Populated	Fished
		Oahu 4	Populated	Fished
		Oahu 5	Populated	Fished
		Oahu 6	Populated	Fished
	Indonesia	Karimunjawa 1	Populated	Fished
		Karimunjawa 2	Populated	Unfished (low compliance)
		Karimunjawa 3	Populated	Unfished (low compliance)
		Pulau Aceh	Populated	Fished
	Jamaica	Montego Bay 1	Populated	Unfished (low compliance)
		Montego Bay 2	Populated	Fished
		Rio Bueno	Populated	Fished
	Kenya	Diani	Populated	Fished
	Madagascar	Toliara	Populated	Fished
	Mauritius	Anse Raie	Populated	Fished
		Grand Sable	Populated	Fished
	NW Hawaii	Lisianski	Unpopulated	Unfished (high compliance)
		Pearl & Hermes 1	Unpopulated	Unfished (high compliance)
		Pearl & Hermes 2	Unpopulated	Unfished (high compliance)
	Reunion	Reunion	Populated	Fished
	Seychelles	Bel Ombre	Populated	Restricted
	Tanzania	Bongoyo	Populated	Unfished (high compliance)
		Chapwani	Populated	Fished
		Mtwara	Populated	Fished
		Stone Town, Zanzibar	Populated	Fished
	Venezuela	Chuspa	Populated	Fished

doi:10.1038/nature18630

Prefrontal neuronal assemblies temporally control fear behaviour

Cyril Dejean[1,2]*, Julien Courtin[1,2,3]*, Nikolaos Karalis[1,2,4]*, Fabrice Chaudun[1,2], Hélène Wurtz[1,2], Thomas C. M. Bienvenu[1,2] & Cyril Herry[1,2]

Precise spike timing through the coordination and synchronization of neuronal assemblies is an efficient and flexible coding mechanism for sensory and cognitive processing[1–6]. In cortical and subcortical areas, the formation of cell assemblies critically depends on neuronal oscillations, which can precisely control the timing of spiking activity[7,8]. Whereas this form of coding has been described for sensory processing and spatial learning[9–12], its role in encoding emotional behaviour remains unknown. Fear behaviour relies on the activation of distributed structures, among which the dorsal medial prefrontal cortex (dmPFC) is known to be critical for fear memory expression[13–16]. In the dmPFC, the phasic activation of neurons to threat-predicting cues, a spike-rate coding mechanism, correlates with conditioned fear responses and supports the discrimination between aversive and neutral stimuli[14,17–19]. However, this mechanism does not account for freezing observed outside stimuli presentations, and the contribution of a general spike-time coding mechanism for freezing in the dmPFC remains to be established. Here we use a combination of single-unit and local field potential recordings along with optogenetic manipulations to show that, in the dmPFC, expression of conditioned fear is causally related to the organization of neurons into functional assemblies. During fear behaviour, the development of 4 Hz oscillations coincides with the activation of assemblies nested in the ascending phase of the oscillation. The selective optogenetic inhibition of dmPFC neurons during the ascending or descending phases of this oscillation blocks and promotes conditioned fear responses, respectively. These results identify a novel phase-specific coding mechanism, which dynamically regulates the development of dmPFC assemblies to control the precise timing of fear responses.

To evaluate the contribution of prefrontal spike-time coding mechanisms to fear behaviour, mice were implanted with recording electrodes targeting the dmPFC and submitted to discriminative fear conditioning (Fig. 1a). In this behavioural model, mice learned to discriminate between two auditory stimuli of different frequency. The conditioned stimulus termed CS^+ is associated with the delivery of a mild foot-shock (the unconditioned stimulus, US) whereas a control stimulus, termed CS^-, is not. Twenty-four hours after conditioning, when re-exposed to the CS^+ but not the CS^-, mice displayed a selective increase in conditioned freezing, a characteristic fear immobilization reaction (Fig. 1a). Freezing was not only driven by CS sensory stimulations but was also observed between CS presentations, suggesting the involvement of internally generated mechanisms triggering/maintaining freezing responses (Extended Data Fig. 1). Interestingly, during freezing, a subset of putative principal neurons (PNs) synchronized briefly and repeatedly, which represents a main characteristic of neuronal assemblies. To identify whether the formation of dmPFC assemblies may encode freezing, we investigated the presence of freezing-specific coactivation patterns in simultaneously recorded dmPFC PNs (Extended Data Fig. 2). We calculated correlation matrices between spike trains of dmPFC PNs within a sliding window of 150 ms and performed principal component analyses on these correlation matrices (see Methods and Extended Data Fig. 3). In each animal, these analyses identified a discrete pattern of correlation that was freezing specific. This pattern corresponded to a subpopulation of PNs repeatedly recruited during freezing (Fig. 1b–d and Extended Data Fig. 3g). These dmPFC PNs displayed enhanced firing and coactivation each time the correlation pattern occurred, hence forming assemblies of PNs. These assembly neurons (ANs) were functionally segregated from ONs as coactivation between those two populations was not different from chance (Fig. 1d–f and Extended Data Fig. 3). Importantly, AN firing rate was stable during freezing, indicating that assembly detection was not due to tonic increase in firing (Fig. 1c and Extended Data Fig. 4a). During CS^+ presentations, the firing profile of dmPFC neurons was highly heterogeneous, with AN and ON exhibiting undifferentiated CS-evoked excitation, inhibition or no responses, as recently observed[14,17] (Extended Data Fig. 4c–f). In addition, the probability of observing assembly activation during freezing was similar inside or outside CS^+ presentations and did not vary around CS^+ presentations (Extended Data Fig. 4b, g). Together, these data indicate that a specific subpopulation of dmPFC PNs participates in functional assemblies during fear expression.

After conditioning, analyses of dmPFC local field potentials (LFPs) revealed a prominent oscillation in the 3–6 Hz range, with a peak around 4 Hz, which develops during freezing and temporally matched the recruitment of dmPFC assemblies (Fig. 2a–b). Consistent with our previous observations[20], power spectral and spectrogram analyses indicated that dmPFC 4 Hz oscillation power was significantly higher during freezing compared with mobility periods, and that freezing onset and offset coincided with an increase and decrease of 4 Hz power, respectively (Fig. 2c–d). Strikingly, frequency-specific correlational analyses revealed a significant and maximum correlation between dmPFC LFP 4 Hz power and assembly probability within epochs surrounding freezing onset and offset (Fig. 2e). To evaluate whether the development of 4 Hz oscillations and the formation of dmPFC assemblies was predictive of freezing, we computed the first time point around freezing onset and offset for which 4 Hz oscillations and assembly probability significantly changed. These analyses indicated that both 4 Hz power and assembly activation significantly increased and decreased before freezing onset and offset, respectively (Fig. 2f). Importantly, the increase in 4 Hz power preceded the changes in assembly activation, which indicates that 4 Hz oscillations are a prerequisite process for dmPFC assembly activation and freezing onset. These data indicate that freezing dynamics are precisely controlled by a 4 Hz-mediated recruitment of dmPFC assemblies.

To understand how 4 Hz oscillations dynamically shape dmPFC assemblies during freezing, we evaluated the phase locking of

[1]INSERM, Neurocentre Magendie, U862, 146 Rue Léo-Saignat, 33077 Bordeaux, France. [2]Université de Bordeaux, Neurocentre Magendie, U862, 146 Rue Léo-Saignat, 33077 Bordeaux, France. [3]Friedrich Miescher Institute for Biomedical Research, Maulbeerstrasse 66, CH-4058 Basel, Switzerland. [4]Faculty of Medicine, Ludwig-Maximilians Universität München, 82152 Planegg-Martinsried, Germany.
*These authors contributed equally to this work.

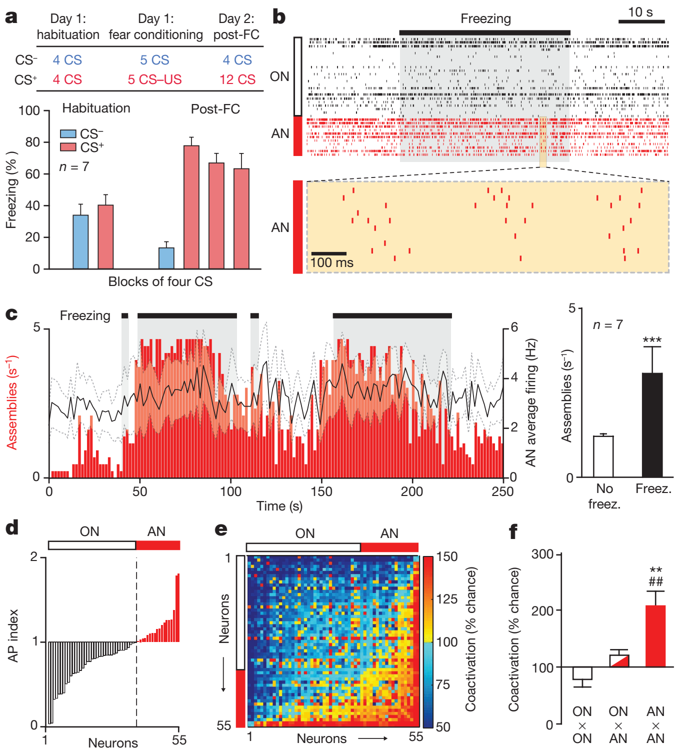

Figure 1 | dmPFC PNs participate in neuronal assemblies during freezing. a, Protocol and behavioural results. During habituation, mice ($n = 7$) exhibited low freezing during CS$^-$ and CS$^+$. After conditioning (post-FC), CS$^+$ induced high freezing compared with CS$^-$ (Friedman repeated-measures one-way analysis of variance (ANOVA) on ranks test, $P < 0.01$; Student–Newman–Keuls post-hoc test, CS$^-$ versus each CS$^+$ block, all $P < 0.05$). **b**, Example of dmPFC ANs exhibiting temporal organization during freezing compared with no freezing and to ON. **c**, Left: representative example of assembly activation during freezing versus no freezing and averaged firing for AN ($n = 16$, black line; white shaded area, s.e.m.). Grey shaded area represents freezing periods. Right: average numbers of assemblies activated during no freezing (No freez.) and freezing (Freez.) ($n = 7$ mice, Wilcoxon signed-rank test, no-freezing versus freezing, $***P < 0.001$). **d**, Distribution of the assembly participation index (AP index) for 55 dmPFC PNs recorded in a mouse. The individual neuron AP index shows which PNs are significantly active (AN), or inhibited/unchanged (ON) within freezing patterns detected by principal component analysis (1, chance level). **e**, Coactivation matrix averaged over freezing epochs from the same 55 dmPFC PNs. The strength of the coactivation between neuron pairs is expressed as the percentage of coactivation compared with chance. **f**, Averaged coactivation for AN and/or ON pairs (one sample t-test, coactivation versus 100% hypothetical mean, $P < 0.01$; one-way ANOVA, $P < 0.001$; Bonferroni post-hoc test, AN × AN versus any other group, $**P < 0.01$). Shaded areas and error bars, mean ± s.e.m.

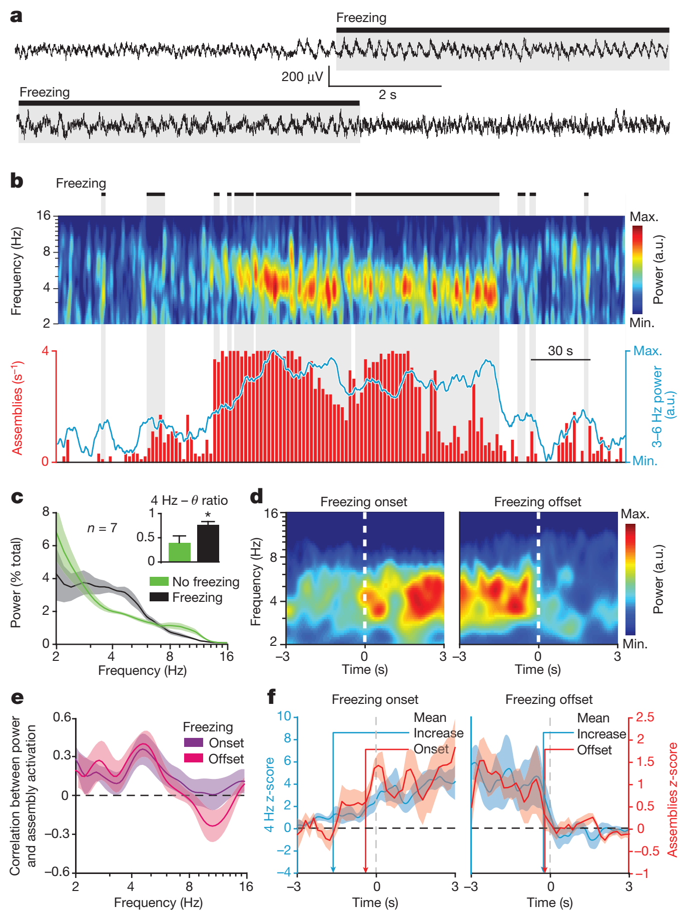

Figure 2 | Temporal matching of 4 Hz oscillations and dmPFC assemblies during freezing. a, Examples of raw dmPFC LFP traces at the onset (top) and offset (bottom) of a freezing episode. **b**, Freezing episodes (top, black lines and grey boxes), LFP spectrogram in the 2–16 Hz frequency band (middle, $\log_2$ scale), assembly activation and LFP power averaged in the 3–6 Hz band (bottom). **c**, Normalized LFP power spectra for freezing and no freezing in the 2–16 Hz band ($n = 7$ mice; $\log_2$ scale). Inset: 4 Hz to θ ratio for freezing and no freezing ($n = 7$ mice, Wilcoxon signed-rank test, non-freezing versus freezing, $*P < 0.05$). **d**, Averaged peri-event spectrogram in the 2–16 Hz frequency band ($\log_2$ scale) centred on freezing onset (left, $n = 7$ mice) and offset (right, $n = 7$ mice). **e**, Correlation between power and assembly activation as a function of LFP frequency ($\log_2$ scale) during epochs surrounding freezing onset (−3 s to +3 s, purple line, $n = 7$ mice) and offset (−3 s to +3 s, pink line, $n = 7$ mice). The y axis represents the Spearman correlation coefficient. **f**, Normalized 3–6 Hz power and assembly activation z-score centred on freezing onset (left, $n = 7$ mice) and offset (right, $n = 7$ mice). Arrows indicate the first time point with a significant increase around freezing onset or decrease around freezing offset. Shaded areas and error bars, mean ± s.e.m.; a.u., arbitrary units.

individual AN and ON to 4 Hz oscillations (Fig. 3a, b). The fraction of dmPFC neurons significantly phase-locked to 4 Hz oscillations was larger for ANs than ONs (Fig. 3c). Remarkably, phase-locked ANs were highly selectivity of 4 Hz ascending phase, while the preferred phase distribution of ONs was homogenous (Fig. 3d, e). To control if ANs might only synchronize because of their 4 Hz phase locking or to 4 Hz power increase, we first evaluated the averaged pairwise co-firing activity between pairs of ANs or ONs as a function of 4 Hz phase. This co-firing activity was corrected for the temporal and phase relation between pairs of neurons using a shuffling and shift predictor approach (see Methods and Fig. 3f). The corrected co-firing activity of AN was significantly stronger in the ascending compared with the descending phase of 4 Hz oscillation, which rules out the possibility that AN synchronization is solely due to AN phase locking (Fig. 3f). Next, we computed the corrected co-firing of AN pairs as a function of 4 Hz power levels and phases (Fig. 3g). We observed that, for different power levels, synchronization among AN, but not ON, was restricted to the ascending phase of the oscillations and larger than ON synchronization (Fig. 3g). These data indicate that the coordination of dmPFC PNs into cell assemblies during freezing is orchestrated by 4 Hz oscillations.

To evaluate whether the formation of dmPFC assemblies was causally related to freezing expression, we used an optogenetic strategy based on the selective activation of dmPFC parvalbumin-expressing interneurons (PV$^+$) in the ascending or descending phase of 4 Hz oscillations (see Methods, Fig. 4 and Extended Data Fig. 5a, b). Conditional adeno-associated virus (AAV) encoding for channelrhodopsin (ChR2) was injected in the dmPFC of mice expressing the Cre recombinase under the control of a PV promoter to specifically infect PV$^+$ interneurons (Fig. 4 and Extended Data Fig. 5a, b). Because

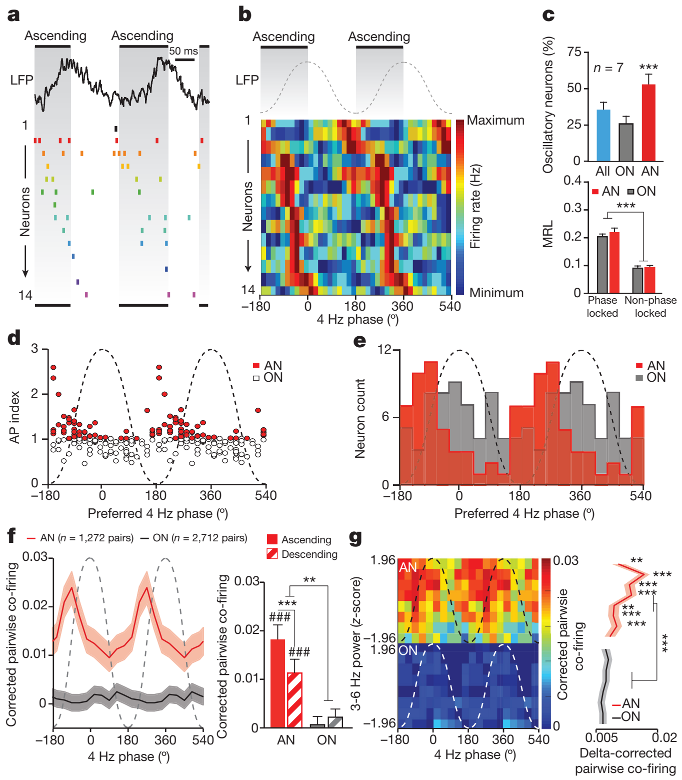

Figure 3 | Four-hertz oscillations organize dmPFC PNs into assemblies during freezing. **a**, Representative example of an LFP recorded in the dmPFC showing prominent 4 Hz oscillations and simultaneous sequential activation of 14 AN recorded in the same animal during freezing. **b**, Averaged firing of individual AN displayed in **a** as a function of 4 Hz LFP oscillation phase. Each AN was significantly modulated by 4 Hz phase (Rayleigh test, all $P < 0.05$). **c**, Top: average percentage of neurons significantly phase-locked to 4 Hz oscillations among all neurons (blue), AN (red) and ON (white) ($n = 7$ mice, one way repeated-measures ANOVA, $P < 0.001$; Bonferroni post-hoc test, $^{***}P < 0.001$). Bottom: averaged mean resultant length vector (MRL) for phase-locked and non-phase-locked AN and ON neurons ($n = 7$ mice, AN: $n = 50/90$ phase-locked neurons; ON: $n = 61/200$ phase-locked neurons; two-way ANOVA, F_1: AN versus ON, $P = 0.206$; F_2: phase-locking, $P < 0.001$; $F_1 \times F_2$: $P = 0.324$; Bonferroni post-hoc test, $^{***}P < 0.001$). **d**, Distribution of all phase-locked dmPFC PNs assembly participation indices (AP index) as a function of preferred phase (left axis, red dots: AN, AP index > 1, $n = 50$ neurons; white dots: ON, AP index < 1, $n = 61$ neurons; bin: 18°, $n = 7$ mice). **e**, Distribution of phase-locked AN and ON preferred phases (AN: $n = 50$ neurons; ON: $n = 61$ neurons; bin: 18°, $n = 7$ mice). **f**, Left: corrected pairwise co-firing activity of pairs of AN and ON as a function of 4 Hz phase (AN = 1,272 pairs; ON = 2,712 pairs recorded in 7 mice). Right: averaged corrected pairwise co-firing for AN and ON neurons during the ascending or descending phase of 4 Hz oscillations ($n = 7$ mice, AN: $n = 1{,}272$ pairs, ON: n 2,712 pairs, two-way ANOVA, F_1: AN versus ON, $P = 0.003$; F_2: ascending versus descending, $P < 0.001$; $F_1 \times F_2$: $P < 0.001$; Bonferroni post-hoc test, $^{**}P < 0.01$, $^{***}P < 0.001$; one sample t-test against hypothetical mean $= 0$, $P < 0.001$). **h**, Left: corrected pairwise co-firing activity as a function of the phase and power (z-score) of 4 Hz oscillations. Right: delta-corrected pairwise co-firing activity (maximum ascending minus minimum descending phase) of pairs of AN and ON (AN = 1,272 pairs; ON = 2,712 pairs recorded in 7 mice; two-way ANOVA, F_1: AN versus ON, $P < 0.001$; F_2: power, $P < 0.001$; $F_1 \times F_2$: $P < 0.001$; Bonferroni post-hoc AN versus ON, $^{**}P < 0.01$, $^{***}P < 0.001$; one sample t-test against hypothetical mean $= 0$, $P < 0.001$). Error bars, mean ± s.e.m.

dmPFC assemblies are both phase- and freezing-specific, we recorded and performed online detection of freezing, high instantaneous power and ascending phase of 4 Hz oscillations in the period after a train of CS$^+$ presentations (See methods, Extended Data Fig. 6). Each time these conditions were fulfilled, we optogenetically activated dmPFC PV$^+$ interneurons to inhibit PN firing at the ascending or descending phase of 4 Hz oscillations (Fig. 4a, d and Extended Data Figs 5–7). During post-CS$^+$ presentations, green fluorescent protein (GFP) controls exhibited high fear levels on day 2 and low fear levels on days 3 and 4, which represent a natural timing effect, not a bias of our experimental conditions (Extended Data Fig. 6c). Importantly, activating or inhibiting PV$^+$ interneurons in the ascending or descending phase of 4 Hz oscillations did not modify 4 Hz power compared with periods without stimulation or GFP controls (Extended Data Fig. 5d–i). In contrast, the activation or inhibition of PV$^+$ interneurons in the ascending or descending phase of 4 Hz oscillations respectively reduced and increased the co-firing activity of dmPFC PNs in the phase targeted (Extended Data Fig. 8c, d). Optogenetic-mediated inhibition of dmPFC PNs in the ascending phase of the oscillation significantly reduced freezing compared with control conditions (Fig. 4b, c, g, h and Extended Data Fig. 6). To evaluate the temporal specificity of our manipulation, we inhibited the firing of dmPFC PNs in the descending phase of the oscillation during freezing, when dmPFC ANs are less likely to be coactive (Fig. 3d–f). This manipulation significantly increased freezing compared with control conditions (Fig. 4e–h and Extended Data Fig. 6). Importantly, because we performed these optogenetic manipulations over 2 days (Extended Data Fig. 6d), we ensured that the stimulation in the ascending phase of 4 Hz oscillations on the first day had no influence on CS$^+$-evoked freezing the next day (Extended Data Fig. 6g). Finally, we repeated our stimulation experiment in mice in which PV$^+$ interneurons expressed archeorhodopsin (ArchT) to inhibit dmPFC PV$^+$ interneurons and thereby disinhibit dmPFC PNs (Extended Data Fig. 9). When applied in the descending phase of the oscillation, stimulation had no effect on freezing (Extended Data Fig. 9b, c). However, in the ascending phase of the oscillation, PN disinhibition produced a significant increase in freezing (Extended Data Fig. 9d, e). Together, these results demonstrate that the formation of dmPFC assemblies at the ascending phase of 4 Hz oscillations and their suppression in the descending phase are necessary for the precise temporal coding of fear behaviour.

Using single-unit and LFP recordings and optogenetic manipulations, we demonstrated that a subset of dmPFC PNs participate in the formation of functional assemblies, dynamically coordinated by 4 Hz oscillations during freezing. Our results indicate that the formation of dmPFC assemblies at specific phases of 4 Hz oscillations is causally related to freezing expression. Importantly, although the strength of phase locking or the increase in 4 Hz power might impact neuronal synchronization among ANs, our analyses indicate that they cannot explain alone the specific and stronger synchronization we observed between AN (Fig. 3f, g). Therefore the temporal organization of ANs in the ascending phase of 4 Hz oscillations appears as a specific encoding mechanism for freezing. Modification of dmPFC spiking activity after presentations of threat-predicting cues, a form of rate coding mechanism that correlates with fear responses, has been described in the past[14,17,18,21] and could be related to plasticity mechanisms or attentional processes. Our data indicate that, in addition to this mechanism, the expression of conditioned freezing is also encoded in the dynamic organization of internally generated dmPFC assemblies. To our knowledge, these data represent the first causal demonstration of a phase-specific coding mechanism during conditioned fear behaviour. In a recent study, we imposed a 4 Hz analogue stimulation to the dmPFC through PV$^+$ interneurons and showed that this artificial rhythm was sufficient to elicit freezing and fear memory[20]. The concept in the present model is radically different in that we did not impose the rhythm but intended to interfere with dmPFC assemblies nested in the ascending phase of 4 Hz oscillations, which were specifically activated during fear expression (see Supplementary Information for further discussion). Whereas 4 Hz oscillations have already been described in different structures during various behavioural tasks[20,22–25], the origin of this slow oscillation is still unknown. It was suggested that this oscillation originates from the ventral tegmental area[24], or

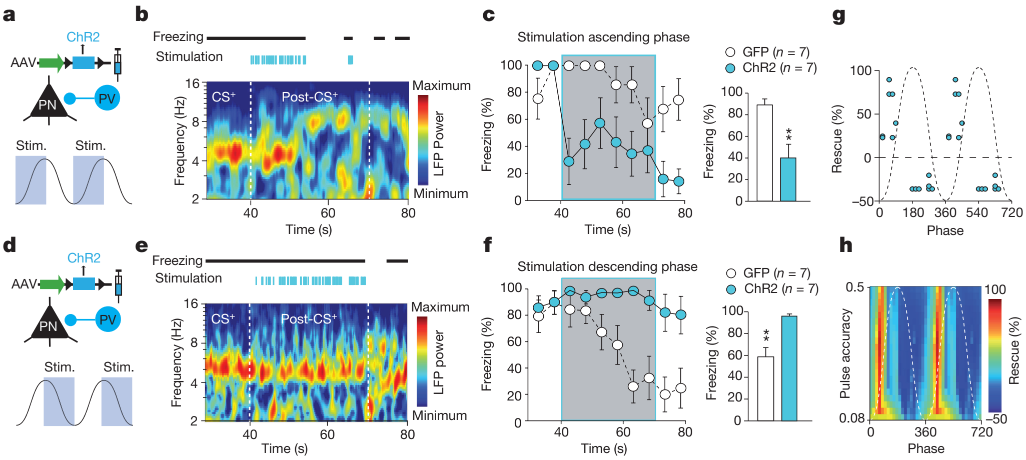

Figure 4 | Phase-specific optogenetic inhibition of dmPFC PNs controls freezing. **a**, **d**, Schematic of the strategy used to inhibit dmPFC PNs during the ascending or descending phase of 4 Hz oscillation. Stim., stimulation. **b**, **e**, Top: representative example of freezing (black line) and kinetics of light pulse stimulations (blue ticks) during and after CS$^+$ presentations 24 h (**b**) and 48 h (**e**) after conditioning. Bottom: corresponding LFP spectrogram in the 2–16 Hz band (binary logarithmic scale) during light-mediated inhibition of dmPFC assemblies in the ascending (**b**) or descending (**e**) phase of the oscillation. **c**, **f**, Left: time-resolved changes in freezing during light-mediated inhibition of dmPFC assemblies in the ascending (**c**) or descending (**f**) phase of the 4 Hz oscillation in PV-IRES-Cre mice infected within the dmPFC with ChR2 (ascending phase: first CS$^+$, $n=7$; descending phase: first CS$^+$, $n=7$) or GFP (ascending phase: first CS$^+$, $n=7$; descending phase: first CS$^+$, $n=7$; ascending phase: two-way ANOVA, factor 1: ChR2 versus GFP, $P<0.001$; factor 2: time, $P<0.001$; $F_1 \times F_2$, $P<0.05$; descending phase: two-way ANOVA, factor 1: ChR2 versus GFP, $P<0.001$; factor 2: time, $P<0.001$; $F_1 \times F_2$, $P<0.05$). Shaded area represents light stimulation period. Right: averaged freezing from PV-IRES-Cre mice infected in dmPFC with ChR2 ($n=7$) or GFP ($n=7$) during the stimulation (Mann–Whitney test, ChR2 versus GFP, $^{**}P<0.01$). **g**, **h**, Percentage of freezing rescue (freezing for ChR2 minus average freezing for GFP) as a function of the phase of the stimulation (**g**), or as a function of both the phase and pulse stimulation accuracy (**h**) for mice stimulated in the ascending or descending phase of the 4 Hz oscillation ($n=25$ sessions in 16 animals). Pulse stimulation accuracy to the phase of 4 Hz oscillations was quantified using MRL of pulse locking on 4 Hz phase. Error bars, mean ± s.e.m.

the whisker barrel cortex[26]. Our data demonstrate that the encoding of distinct behavioural states occurs through the dynamic organization of dmPFC assemblies by 4 Hz oscillations. However, it is still not clear how this phase-specific code is relayed to downstream structures to actively drive or suppress freezing. Recent data demonstrated that the synchronization of slow oscillations between dmPFC and amygdala circuits correlates with freezing[19,27,28]. This could represent an effective mechanism for the coincident activation of neurons within distributed brain regions. To model the relationship between dmPFC phase-coding and freezing expression, we propose a functional scheme where dmPFC assembly activation is at the core of an emitter–receiver system for fear expression (Extended Data Fig. 10a). In this system, dmPFC assembly activity emerges from background activity because of its phase specificity. This temporal constraint provides a clear signal-to-noise ratio within an entire 4 Hz cycle (SNR) for a receiver, which could be the amygdala as recently suggested[19,20,27,28]. In this model, the effects of the optogenetic manipulations on freezing can be explained by alterations of the transmission of this dmPFC-to-receiver fear signal. On the one hand, upregulation of SNR through dmPFC PN inhibition during the descending phase (Extended Data Fig. 10b) or disinhibition during the ascending phase (Extended Data Fig. 10c) enhanced fear expression. On the other hand, downregulation of SNR through dmPFC PN ascending phase inhibition (Extended Data Fig. 10b) reduced freezing. Beyond the field of emotions, this mechanism is likely to apply to other brain functions that depend on the activation of assemblies through oscillatory processes[1–6]. Finally, as previously hypothesized[29], our data confirm that the persistence of fear, which is a core symptom of anxiety disorders, could be precisely controlled by the modulation of activity in relation to specific slow oscillations.

Online Content Methods, along with any additional Extended Data display items and Source Data, are available in the online version of the paper; references unique to these sections appear only in the online paper.

Received 11 November 2015; accepted 8 June 2016.
Published online 13 July 2016.

1. Gire, D. H. *et al.* Temporal processing in the olfactory system: can we see a smell? *Neuron* **78,** 416–432 (2013).
2. Friedrich, R. W., Habermann, C. J. & Laurent, G. Multiplexing using synchrony in the zebrafish olfactory bulb. *Nature Neurosci.* **7,** 862–871 (2004).
3. Igarashi, K. M., Lu, L., Colgin, L. L., Moser, M. B. & Moser, E. I. Coordination of entorhinal-hippocampal ensemble activity during associative learning. *Nature* **510,** 143–147 (2014).
4. Pastalkova, E., Itskov, V., Amarasingham, A. & Buzsáki, G. Internally generated cell assembly sequences in the rat hippocampus. *Science* **321,** 1322–1327 (2008).
5. Huxter, J., Burgess, N. & O'Keefe, J. Independent rate and temporal coding in hippocampal pyramidal cells. *Nature* **425,** 828–832 (2003).
6. O'Neill, J., Senior, T. J., Allen, K., Huxter, J. R. & Csicsvari, J. Reactivation of experience-dependent cell assembly patterns in the hippocampus. *Nature Neurosci.* **11,** 209–215 (2008).
7. Harris, K. D., Csicsvari, J., Hirase, H., Dragoi, G. & Buzsáki, G. Organization of cell assemblies in the hippocampus. *Nature* **424,** 552–556 (2003).
8. Buzsáki, G. Neural syntax: cell assemblies, synapsembles, and readers. *Neuron* **68,** 362–385 (2010).
9. Dupret, D., O'Neill, J., Pleydell-Bouverie, B. & Csicsvari, J. The reorganization and reactivation of hippocampal maps predict spatial memory performance. *Nature Neurosci.* **13,** 995–1002 (2010).
10. Huxter, J. R., Senior, T. J., Allen, K. & Csicsvari, J. Theta phase-specific codes for two-dimensional position, trajectory and heading in the hippocampus. *Nature Neurosci.* **11,** 587–594 (2008).
11. Richmond, B. J., Optican, L. M., Podell, M. & Spitzer, H. Temporal encoding of two-dimensional patterns by single units in primate inferior temporal cortex. I. Response characteristics. *J. Neurophysiol.* **57,** 132–146 (1987).
12. Laurent, G., Wehr, M. & Davidowitz, H. Temporal representations of odors in an olfactory network. *J. Neurosci.* **16,** 3837–3847 (1996).
13. Corcoran, K. A. & Quirk, G. J. Activity in prelimbic cortex is necessary for the expression of learned, but not innate, fears. *J. Neurosci.* **27,** 840–844 (2007).
14. Courtin, J. *et al.* Prefrontal parvalbumin interneurons shape neuronal activity to drive fear expression. *Nature* **505,** 92–96 (2014).
15. Vidal-Gonzalez, I., Vidal-Gonzalez, B., Rauch, S. L. & Quirk, G. J. Microstimulation reveals opposing influences of prelimbic and infralimbic cortex on the expression of conditioned fear. *Learn. Mem.* **13,** 728–733 (2006).
16. Do-Monte, F. H., Quiñones-Laracuente, K. & Quirk, G. J. A temporal shift in the circuits mediating retrieval of fear memory. *Nature* **519,** 460–463 (2015).
17. Burgos-Robles, A., Vidal-Gonzalez, I. & Quirk, G. J. Sustained conditioned responses in prelimbic prefrontal neurons are correlated with fear expression and extinction failure. *J. Neurosci.* **29,** 8474–8482 (2009).
18. Chang, C. H., Berke, J. D. & Maren, S. Single-unit activity in the medial prefrontal cortex during immediate and delayed extinction of fear in rats. *PLoS ONE* **5,** e11971 (2010).

19. Likhtik, E., Stujenske, J. M., Topiwala, M. A., Harris, A. Z. & Gordon, J. A. Prefrontal entrainment of amygdala activity signals safety in learned fear and innate anxiety. *Nature Neurosci.* **17,** 106–113 (2014).
20. Karalis, N. *et al.* 4-Hz oscillations synchronize prefrontal–amygdala circuits during fear behavior. *Nature Neurosci.* **19,** 605–612 (2016).
21. Livneh, U. & Paz, R. Amygdala-prefrontal synchronization underlies resistance to extinction of aversive memories. *Neuron* **75,** 133–142 (2012).
22. Dzirasa, K. *et al.* Lithium ameliorates nucleus accumbens phase-signaling dysfunction in a genetic mouse model of mania. *J. Neurosci.* **30,** 16314–16323 (2010).
23. Dzirasa, K., Fuentes, R., Kumar, S., Potes, J. M. & Nicolelis, M. A. Chronic *in vivo* multi-circuit neurophysiological recordings in mice. *J. Neurosci. Methods* **195,** 36–46 (2011).
24. Fujisawa, S. & Buzsáki, G. A 4 Hz oscillation adaptively synchronizes prefrontal, VTA, and hippocampal activities. *Neuron* **72,** 153–165 (2011).
25. Tort, A. B. *et al.* Dynamic cross-frequency couplings of local field potential oscillations in rat striatum and hippocampus during performance of a T-maze task. *Proc. Natl Acad. Sci. USA* **105,** 20517–20522 (2008).
26. Ito, J. *et al.* Whisker barrel cortex delta oscillations and gamma power in the awake mouse are linked to respiration. *Nature Commun.* **5,** 3572 (2014).
27. Lesting, J. *et al.* Patterns of coupled theta activity in amygdala-hippocampal-prefrontal cortical circuits during fear extinction. *PLoS ONE* **6,** e21714 (2011).
28. Stujenske, J. M., Likhtik, E., Topiwala, M. A. & Gordon, J. A. Fear and safety engage competing patterns of theta-gamma coupling in the basolateral amygdala. *Neuron* **83,** 919–933 (2014).
29. Dejean, C. *et al.* Neuronal circuits for fear expression and recovery: recent advances and potential therapeutic strategies. *Biol. Psychiatry* **78,** 298–306 (2015).

Supplementary Information is available in the online version of the paper.

Acknowledgements We thank the members of the Herry laboratory for comments on the manuscript, and K. Deisseroth and E. Boyden for sharing material. Microscopy was done in the Bordeaux Imaging Center of the CNRS-INSERM and Bordeaux University, a member of France BioImaging. This work was supported by grants from the French National Research Agency (ANR-10-EQPX-08 OPTOPATH; LABEX BRAIN ANR 10-LABX-43, LABEX TRAIL ANR 10-LABX-57), the European Research Council (ERC) under the European Union's Seventh Framework Program (FP7/2007-2013)/ERC grant agreement number 281168, and the Conseil Regional d'Aquitaine.

Author Contributions F.C., J.C., C.D., N.K., T.C.M.B. and H.W. performed the experiments and analysed the data. J.C., C.D. and C.H. designed the experiments and wrote the paper.

Author Information Reprints and permissions information is available at www.nature.com/reprints. The authors declare no competing financial interests. Readers are welcome to comment on the online version of the paper. Correspondence and requests for materials should be addressed to C.D. (cyril.dejean@scilight.eu) or C.H. (cyril.herry@inserm.fr).

Reviewer Information *Nature* thanks A. Holmes, P. O'Donnell and the other anonymous reviewer(s) for their contribution to the peer review of this work.

METHODS

Animals. Male C57BL6/J mice (3 months old, Janvier), PV-IRES-Cre mice (3 months old, Jackson Laboratory, B6;129P2-Pvalb$^{tm1(cre)Arbr}$/J) and CamKIIalpha-Cre mice (3 months old, Jackson Laboratory, B6.Cg-Tg(Camk2A-cre)T29-1Stl/J) were individually housed for at least 7 days before all experiments, under a 12-h light–dark cycle, and provided with food and water *ad libitum*. All procedures were performed in accordance with standard ethical guidelines (European Communities Directive 86/60-EEC) and were approved by the committee on Animal Health and Care of Institut National de la Santé et de la Recherche Médicale and French Ministry of Agriculture and Forestry (agreement A3312001). Representative examples and traces displayed in the main figures were observed for the seven animals used in these experiments.

Behaviour. Fear conditioning and testing took place in two different contexts (contexts A and B). The conditioning and testing boxes were cleaned with 70% ethanol and 1% acetic acid before and after each session, respectively. To score freezing behaviour, an automated infrared beam detection system located on the bottom of the experimental chambers was used (Coulbourn Instruments). Because the detection of our dependent variable (freezing) was independent of the experimenter, we did not use a blinding process for group allocation or behaviour scoring. The animals were considered to be freezing if no movement was detected for 2 s. On day 1, C57BL6/J mice were submitted to a habituation session in context A, in which they received four presentations of the CS$^+$ and the CS$^-$ (total CS duration 30 s, consisting of 50-ms pips at 0.9 Hz repeated 27 times, 2 ms rise and fall; pip frequency 7.5 kHz or white-noise, 80 dB sound pressure level). Discriminative fear conditioning was performed on the same day by pairing the CS$^+$ with a US (1-s foot-shock, 0.6 mA, 5 CS$^+$–US pairings; inter-trial intervals, 20–180 s). The onset of the US coincided with the offset of the CS$^+$. The CS$^-$ was presented after each CS$^+$–US association but was never reinforced (five CS$^-$ presentations; inter-trial intervals, 20–180 s). The frequencies used for CS$^+$ and CS$^-$ were counterbalanced across animals and randomization of CS$^-$ and CS$^+$ allocation was performed using an online randomization algorithm (http://www.randomization.com/). On day 2, conditioned mice were submitted to a post-fear-conditioning session in context B during which they received 4 and 12 presentations of the CS$^-$ and CS$^+$, respectively. Seven naive C57BL6/J mice were included in this experiment and the data were collected in two distinct replicates. For optogenetic experiments using channelrhodopsin (ChR2), archeorhodopsin (ArchT) or GFP controls, PV-IRES-Cre mice were submitted to the same conditioning protocol described above except that on days 2, 3 and 4, conditioned mice were submitted to post-fear-conditioning sessions in context B during which they received four presentations of the CS$^-$ followed by four presentations of the CS$^+$. The number of CS$^+$ was limited to four to prevent fear memory extinction from day 2 to days 3 and 4. Blue (ChR2) or Yellow (ArchT) light stimulation was applied during 30 s after the last pip of the four CS$^+$. The rationale behind this stems from our previous study[12] showing that manipulation of CS$^+$-evoked dmPFC activity impacted fear expression. To avoid interference with this activity period, the present manipulations were restricted to those 30 s immediately after sound presentation. Importantly, freezing levels on day 1 were of similar magnitude in GFP control and wild-type animals used in the first part of this study (Extended Data Fig. 6a, b). Typically, freezing levels in GFP controls during CS$^+$ were not different from day 2 to days 3 and 4 (Extended Data Fig. 6c). However, freezing level observed in the 30 s time windows after CS$^+$ went from high on day 2 to moderate on days 3 and 4 (Extended Data Fig. 6c). Our hypothesis predicts that 4 Hz ascending phase inhibition of PNs will decrease freezing and conversely for a stimulation in the descending phase. To evaluate the changes in freezing levels upon optogenetic stimulation, this behavioural pattern brought us to test ascending phase stimulation on day 2 and descending phase on day 3 to avoid floor and ceiling effect respectively (Extended Data Fig. 6d). For the same reasons, 4 Hz descending and ascending phase disinhibition of PNs were performed on days 3 and 4, respectively (Extended Data Fig. 9a). We also noticed a tendency for optogenetic stimulation to decrease freezing level around subsequent CS$^+$ on the same day in the ChR2 group (Extended Data Fig. 6e, f). To rule out the possibility that changes in freezing behaviour upon optogenetic stimulation were not solely due to the direct action of the stimulation but also to a cumulative effect of past manipulations, our analyses were restricted to the 30 s epoch after the first CS$^+$ on days 2, 3 and 4. Although this decrease was not observed with ArchT animals (Extended Data Fig. 9b, d) we used the same restriction with this group for the sake of consistency with ChR2 group. Note that within these 30 s, light application was conditioned to the behaviour and the brain state of the animal (see section on 'Closed-loop stimulation'). To score freezing behaviour, the aforementioned automated infrared beam detection was used in addition to a Cineplex video tracking system (Plexon) that was used for online detection of freezing and subsequent conditional optogenetic stimulation. For optogenetic experiments, four distinct behavioural experiments were performed to collect the entire data set. The impact of stimulation pulse phase specificity on freezing behaviour was assessed by calculating freezing rescue as a function of pulses preferred 4 Hz phase as well as phase locking strength. Freezing rescue was calculated as the difference between the average freezing levels of GFP control and that of ChR2 animal during optical stimulation epochs. Stimulation pulses preferred phase was retrieved through the pulse phase histogram and tested for significance (Rayleigh's test *P*). Pulse accuracy was quantified by phase locking strength using the mean resultant length (MRL): that is, the length of the mean vector. Low or high MRL values are respectively indicative of a spread or a concentrated circular distribution of pulses around the preferred phase. In a first set of analyses we considered only those experiments with canonic features (Fig. 4a–g): that is, where pulse phase distribution was significant ($P < 0.05$), preferred phase was in the intended range (ascending phase, −180 to 0°; descending phase, 0–180°) and MRL was above 0.2. For ArchT experiments, five animals fulfilled the criteria on days 3 and 4. For ChR2 experiments, on day 2 (ascending phase) seven animals fulfilled the criteria; on day 3 (descending phase) seven animals fulfilled the criteria. In a second set of experiment (Fig. 4h) we addressed the joint impact of phase and pulse accuracy on freezing level. For that purpose, we added sessions with weak MRL values to the previous set of analysed data. On day 2 (ascending phase) 14 sessions fulfilled the criteria; on day 3 (descending phase) 11 sessions fulfilled the criteria. That is a total of 25 sessions that were acquired in 16 animals as follows: 9 animals on both days 2 and 3; 5 animals only on day 2; and 2 animals only on day 3. The distributions of pulse accuracy (MRL) and preferred phase were then two-dimensionally interpolated to create a linearly spaced grid of freezing rescue value (bin MRL 0.02; bin phase 36°).

Surgery and recordings. Mice were anaesthetized with isoflurane (induction 3%, maintenance 1.5%) in oxygen. Body temperature was maintained at 37 °C with a temperature controller system (FHC). Mice were secured in a stereotaxic frame and unilaterally implanted in the left dorsomedial prefrontal cortex (dmPFC) with a multi-wire electrode array aimed at the following coordinates: 2 mm anterior to bregma; 0.3 mm lateral to the midline; and 0.8–1.4 mm ventral to the cortical surface. The electrodes consisted of 16 or 32 individually insulated nichrome wires (13 μm diameter, impedance 30–100 kΩ; Kanthal) contained in a 26-gauge stainless-steel guide cannula. The wires were attached to an 18-pin connector (Omnetics) or 2 connectors in the case of a 32-wire assembly. All implants were secured using Super-Bond cement (Sun Medical). After surgery mice were allowed to recover for 7 days and were habituated to handling. Analgesia was applied before, and 1 day after surgery (Metacam, Boehringer). Electrodes were connected to one or two headstages (Plexon) containing 16 unity-gain operational amplifiers. Each headstage was connected to a 16-channel preamplifier (gain 100 × bandpass filter from 150 Hz to 9 kHz for unit activity and from 0.7 Hz to 170 Hz for field potentials, Plexon). Spiking activity was digitized at 40 kHz and bandpass filtered from 250 Hz to 8 kHz, and isolated by time-amplitude window discrimination and template matching using a Multichannel Acquisition Processor system (Plexon). At the conclusion of the experiment, recording sites were marked with electrolytic lesions before perfusion, and electrode tips locations were reconstructed with standard histological techniques.

Virus injections and optogenetics. For optical control of PV interneurons, conditional AAV encoding ChR2 (AAV-EF1a-DIO-hChR2(H134R)-EYFP, serotype 5, Vector Core, University of North Carolina) or ArchT (AAV-FLEX-ArchT-GFP, serotype 9, Vector Core, University of North Carolina) were bilaterally injected into the dmPFC of PV-IRES-Cre mice from glass pipettes (tip diameter 10–20 μm) connected to a picospritzer (Parker Hannifin Corporation; approximately 0.4 μL per hemisphere) at the following coordinates: 2 mm anterior to bregma; 0.4 mm lateral to midline and 0.9 to 1.2 mm ventral to the cortical surface. One to two weeks after the injection mice were implanted bilaterally with optic fibres (diameter: 200 μm; numerical aperture: 0.37; flat tip; Doric Lenses) at the same coordinates. Control experiments were performed using an AAV containing the DNA construct for only GFP (AAV-FLEX-GFP, Vector Core, University of North Carolina). All implants were secured using Super-Bond cement (Sun Medical). For experiments using optogenetic stimulation coupled to single-unit recordings, one of the two optic fibres was combined to the array of 16 or 32 individually insulated nichrome wires. Single-unit recordings during the manipulation of PV interneurons were performed as described in the 'Surgery and recordings' section. Behavioural and recording experiments were performed 3–5 weeks after injection. The light (approximately 14 mW per implanted fibre) was bilaterally conducted from the laser (OptoDuet 473/593 nm, Ikecool) to the mice via two fibre-optic patch cords (diameter 200 μm, Doric Lenses), connected to a rotary joint (1 × 2 fibre-optic rotary joint, Doric Lenses) that allowed mice to freely move in the behavioural apparatus. Instead of directly manipulating dmPFC PNs, we capitalized on the properties of cortical PV$^+$ interneurons, which are a particular class of GABAergic interneurons regulating efficiently the output activity of cortical principal excitatory neurons[30,31]. Because a single PV$^+$ interneuron can contact more than 1,500 PNs[32], the optogenetic activation or inhibition of

population of PV$^+$ represents an efficient tool for controlling PN activity[14,33–35]. This strategy was motivated by the fact that optogenetic manipulation of PNs was associated with large artefacts, which prevented the simultaneous recording of LFPs (Extended Data Fig. 5c). For optogenetic manipulation of PV$^+$ interneurons during behaviour, we used 30 ms light pulses delivered under specific behavioural and neurophysiological conditions (see section on 'Closed-loop stimulation'). After behavioural and recording experiments, mice were perfused and histological analysis was performed.

Anatomical and histological analysis. Mice were euthanized with isoflurane and perfused through the left ventricle with 4% w/v paraformaldehyde in 0.1 M PBS. Brains were dissected out and postfixed for 4 h at 4 °C in the same solution. Sections (60 μm thick) were cut, mounted on gelatin-coated microscope slides and dried. Sections were stained with toluidine blue, dehydrated and mounted. Electrolytic lesions were identified with conventional transmission light microscopy. Only recordings with confirmed lesions in cingulate and prelimbic areas of dmPFC were included in our analyses. It is important to note that because the electrode bundles are manually fabricated in the laboratory and individual wires can be slightly displaced during insertion in the brain, the distance between each electrode cannot be measured precisely. It is therefore technically impossible to determine from which layer the single unit and LFP recorded from the same electrode were performed. For verification of viral injections in dmPFC (which include the cingulate cortex ACC and the prelimbic area), serial 80-μm-thick slices containing the dmPFC were imaged using an epifluorescence system (Leica DM 5000) fitted with a 10× dry objective. The location and the extent of the injections/infections were visually controlled. Only infections accurately targeted to dmPFC were considered for behavioural and electrophysiological analyses.

Single-unit analyses. Single-unit spike sorting was performed using Off-Line Sorter software (Plexon) for all behavioural sessions. Principal component scores were calculated for unsorted waveforms and plotted in a three-dimensional space defined by principal components and/or timing and voltage features of the waveforms; clusters containing similar valid waveforms were manually defined. A group of waveforms were considered to be generated from a single neuron if the waveforms formed a discrete, isolated, cluster in the three-dimensional space and did not contain a refractory period less than 1 ms, as assessed using inter-spike interval analysis. To avoid analysis of the same neuron recorded on different channels, we computed cross-correlation histograms. If a target neuron presented a peak of activity at a time that the reference neuron fired, only one of the two neurons was considered for further analysis. To separate putative inhibitory interneurons from putative excitatory PNs we used an unsupervised cluster algorithm based on Ward's method. In brief, the Euclidian distance was calculated between all neuron pairs on the basis of the three-dimensional space defined by each neuron's average half-spike width (measured from trough to peak), the firing rate and the area under the late positive deflection phase of the spike. An iterative agglomerative procedure was then used to combine neurons into groups based on the matrix of distances such that the total number of groups was reduced to return the smallest possible increase in within-group sum of square deviation. Cross-correlation analysis was then performed to evaluate the excitatory or inhibitory nature of each neuron on other simultaneously recorder units. To assess the significance of cross-correlogram analyses performed between pairs of recorded neurons, a mean firing rate with 95% confidence limits of the target neuron firing rate was calculated. Significant short-latency inhibitory or excitatory interactions were retained if the number of action potentials of the target neuron was inferior or superior to these 95% confidence limits, respectively. Note that among the clusters of PNs and interneurons, no PNs were found to inhibit another cell and no interneurons were found to excite another cell. To identify the main firing patterns among PNs, we used an unbiased principal component analysis based on the neuronal activity evoked by CS$^+$ presentations (z-score 500 ms before and after CS$^+$ presentations, CS$^+$ presentations one to four in the post-fear-conditioning sessions, each CS$^+$ consisting of 27 individual sound pips; bin size of 10 ms). Only the first principal component was considered (PC1) because it explained most of the variance of our data set. One neuron was excluded from analysis on the motive of an absence of spiking activity around the time of CS$^+$ presentation. Neurons ($n = 289$) were classified as correlated, indifferent of inversely correlated with PC1 at the $P < 0.05$ significance level.

Neuronal assembly isolation. We hypothesized that single neurons of the dmPFC functionally aggregate into discrete assemblies to code for fear expression. We used a previously published method[36] to evaluate the possibility that a subset of PNs is coactivated during discrete time windows inside freezing epochs. We calculated single-unit rate histograms with a sliding window of 150 ms and 100 ms overlap, to minimize potential slicing of assembly realizations. In this study we were interested in identifying which neurons were coactivated rather than how much they were coactivated. We therefore focused on the sole presence or absence of activity for a neuron inside each time bin independently of its actual firing rate. To this end, the rate histograms were binarized in such a way that any bin value strictly above zero was given a value of 1 (otherwise 0, Extended Data Fig. 3a, top). Binarized histograms for n simultaneously recorded PNs were then concatenated and we calculated the $n \times n$ coactivation matrix of the PN population for each time bin (Extended Data Fig. 3a, bottom). To investigate the emergence of specific coactivation pattern during the recording session, principal component analysis was performed on the coactivation matrix. We considered only the score on the first principal component (PC1) that explains the greatest part of the coactivation matrix variance. To extract putative coactivation matrix pattern related to fear expression, we then analysed the distribution of PC1 scores as a function of animal freezing behaviour. Note that we also investigated the impact of sliding window length on PC1 score distributions inside and outside freezing epochs to define the optimal window length to isolate freezing-related neuronal assemblies. The optimal window length was found to be 150 ms, as shorter windows were not as efficient in discriminating freezing versus no-freezing epochs and larger windows were not further ameliorating that discrimination (Extended Data Fig. 3c). The probability of a certain PC1 score predicting freezing was analysed using a bootstrap method as follows. PC1 score was binned (0.1 units) and we calculated the freezing probability associated with each score bin. The same procedure was applied to a set of surrogate data for which freezing intervals were shuffled 50 times. Actual and surrogate freezing probabilities as a function of PC1 score were then compared to retrieve the threshold above which PC1 score predicted freezing behaviour above chance level (red dotted line in Extended Data Fig. 3b, d–e, h–m). This threshold was then used to isolate coactivation matrix patterns predicting freezing behaviour (hereafter named coactivation matrix freezing patterns). Finally, we identified and analysed which single neurons were coactive inside coactivation matrix freezing patterns associated with freezing behaviour (Extended Data Fig. 3f, top). Note that the weight of a neuron within the coactivation matrix freezing pattern can be solely due to its random probability of spiking (for example, neurons that increase firing during freezing would be more likely to co-fire). To correct for this potential bias, we tested the significance of each single neuron contribution to the coactivation matrix freezing pattern against that of a surrogate data set (50 time shuffling of the spike train inter-spike intervals, Extended Data Fig. 3f, bottom). The average coactivation matrix was normalized by dividing it by the average surrogate coactivation matrix (Fig. 1e, all other examples see Extended Data Fig. 3h–m). Each neuron was then given an assembly participation index (AP index) defined as the ratio between its average and surrogate firing rates for coactivation matrix freezing patterns (Fig. 1d, e). Each neuron displaying an AP index significantly above the chance level (chance: AP index = 1) defined by the confidence interval of surrogate data was considered as an AN (AP index > 1). Units with an AP index inferior or equal to chance level were classified as ONs (ON, AP index < 1).

LFP analyses. LFPs were analysed using custom scripts from Matlab, as well as an open source Matlab toolbox for the analysis of circular statistics[37]. LFP signals were filtered in the 4 Hz range (3–6 Hz) using a second-order Butterworth filter. To evaluate 4 Hz phase locking of individual neurons, we calculated the instantaneous phase of the 3–6 Hz filtered LFPs using the Hilbert transform. For a given neuron, each spike was assigned its corresponding LFP 4 Hz phase value from the LFP signal recorded on the same wire. Phase locking was calculated using Rayleigh's test for circular uniformity and statistical significance was assessed using Rayleigh's test P and z values. For significantly phased-locked PNs, we quantified the preferred phase as well as phase locking strength using the MRL. Importantly, MRL estimate is highly dependent on the sample size. To account for this bias, we computed MRL only for significantly phase-locked neurons displaying at least 50 spikes. Therefore, at least the relative comparisons of 4 Hz modulation strength between conditions should not be affected by sample sizes (number of spikes). For time–frequency analysis, we used wavelet decomposition of LFP signals. LFPs were convolved by a family of Morlet's wavelets, one for each frequency between 2 and 16 Hz (with a $\log_2$ scale) as a function of time. Power spectral density for freezing and non-freezing epochs was retrieved by averaging the results of the time-resolved wavelet analysis across those specific time intervals. To average LFP power across animals, we first normalized the power spectral density histogram as the percentage of total power between 2 and 16 Hz. To compare θ (8–12 Hz) and 4 Hz frequencies in freezing and non-freezing epochs we calculated the 4 Hz to θ ratio:

$$\frac{\sum \mathrm{PSD}_{4\mathrm{Hz}} - \sum \mathrm{PSD}_{\theta}}{\sum \mathrm{PSD}_{4\mathrm{Hz}} + \sum \mathrm{PSD}_{\theta}}$$

We addressed the correlation in time between freezing episode onset and offset and LFP oscillations in the 2–16 Hz frequency range by calculating the average peri-event time spectrograms of dmPFC LFP around the onset or offset of freezing epochs. We then addressed the putative relationship between neuronal assembly occurrence and the modulation of certain frequency components in the LFP at the time of freezing onset and offset. For this we computed a linear correlation between

assembly rate (occurrence per second) and LFP power at each frequency between 2 and 16 Hz. To assess 4 Hz and assembly dynamics inside freezing and no freezing episodes, we normalized the length of freezing and no-freezing intervals to express time as the percentage of time elapsed inside each interval.

To evaluate the average pairwise co-firing between pairs of PN as a function of 4 Hz phase, spike trains were binned according to LFP 4-Hz phase (36° bin size), and for each bin class the pairwise co-firing index was calculated as the ratio of co-occurring (common) spikes to the total number of spikes in the bin class for the two units. This provides a simple yet direct measure of the co-occurrence of unit spikes as a function of phase. To ensure the pairwise co-firing of AN neurons was not artificially enhanced by (1) the temporal relation between pairs of AN neurons or (2) the cycle-to-cycle relation between AN neurons (phase relation), we computed a shuffled co-firing (1) and phase-shift predictor (2) as follows. For the shuffled co-firing analysis, for each pair of PNs, one spike train inter-spike intervals were time-shuffled 50 times and the mean surrogate co-firing for each phase bin value recalculated. We then averaged over all AN or ON neuron pairs. This analysis conserves the overall firing rate of the shuffled spike train but destroys the temporal relationship between the two spike trains. Since ANs and ONs present different firing rates and different modulations of firing rates in relation to freezing (Extended Data Fig. 4a), this correction allows the comparison of co-firing between both populations. For the shift predictor analysis, for each 36° phase bin and each pair of AN neurons, 4 Hz cycles were given an index from 1 to n, n corresponding to the total number of 4 Hz cycles in the recording. Indices were then shuffled 50 times for the reference neuron and the mean surrogate co-firing was calculated. This analysis destroys the cycle-to-cycle relation between the two spike trains while preserving the firing modulation by behaviour. We then calculated the corrected pairwise co-firing by subtracting both the shuffled co-firing and the shift predictor to the actual co-firing and subsequently evaluated the sole contribution of freezing or phase to the co-firing of PN. In addition we assessed the impact of the instantaneous power of 4 Hz oscillations on PN co-firing. To this end we calculated pairwise co-firing as a function of phase for different classes of 4 Hz power. Power during freezing was z-scored and binned (0.49 s.d.) and pairwise co-firing was calculated as a function of phase and power. The analysis was restricted to the -1.96 s.d. to $+1.96$ s.d. power range (eight bins) encompassing 95% of power values to exclude extreme values with low occurrence. To compare ANs and ONs on the way their phase-specific pairwise co-firing is impacted by 4 Hz power change, we calculated the difference in corrected co-firing between ascending and descending phases as follows: $\Delta CF = \max(CF_{ascending})/\min(CF_{descending})$.

Closed-loop stimulation. Neurons forming a functional assembly cannot be specifically manipulated using a standard optogenetic approach. Although such cellular specificity is unattainable to this day, a certain temporal specificity exists as the activation of fear coding neuronal assemblies is specific of 4 Hz ascending phase. To apply our stimulation in a functionally specific manner, we performed optogenetic inhibition of PNs as a function of the phase (ascending or descending) of the ongoing 4 Hz oscillation in dmPFC LFP. To that end we designed a closed-loop stimulation protocol where animal behaviour (freezing) and dmPFC LFP (4 Hz power and phase) were monitored online and simultaneously analysed to drive a laser beam. Animal position was sampled at 80 Hz and LFP at 1 KHz, then uploaded every 10 ms in Matlab for online analysis. The former served, on the one hand, to quantify animal speed in the last 1,000 ms of uploaded signal and on the other hand to bandpass filter the LFP signal (3–6 Hz range) and retrieve both 4 Hz power in the last 500 ms and 4 Hz phase for the last recorded data point. Animal speed was calculated as the average distance travelled over the last 1,000 ms time window and compared with the freezing threshold. Bandpass filtering was applied using a second-order Butterworth filter and Hilbert transform was used to estimate both 4 Hz power in the last 500 ms and LFP instantaneous phase for the last data point. Three conditions were defined for the stimulation. For the most recent 10 ms upload if (1) animal speed was below freezing threshold, (2) 4 Hz power was above that of baseline level and (3) 4 Hz phase was encompassed within the range of choice (ascending, 0–180°; or descending, 180–360°), then stimulation was triggered. The stimulation consisted of a 1 ms pulse sent from Matlab to a pulse generator (Master 9, AMPI) that in turn sent a 30 ms pulse to a blue/yellow laser generator to deliver optical stimulation to the dmPFC. The whole computation from neuronal data read to laser onset was achieved in 30 ms maximum (data retrieval 10 ms; computation 5–20 ms). Hence, at the end of the 30 ms light pulse, a new analysis loop was completed and if the three conditions were again fulfilled in the most recent 10 ms upload then a new stimulation pulse was triggered.

Statistical analyses. For each statistical analysis provided in the manuscript, the Kolmogorov–Smirnov normality test was first performed on the data to determine whether parametric or non-parametric tests were required. Two different approaches were used to calculate the sample size. For studies in which we had sufficient information on response variables, power analyses were performed to determine the number of mice needed. For studies in which the behavioural effect of the manipulation could not be pre-specified, such as optogenetic experiments, we used a sequential stopping rule. In essence this method enables null-hypothesis tests to be used in sequential stages, by analysing the data at several experimental points using t-tests. Usually the experiment started by testing only a few animals and if the P value was below 0.05, the investigator declared the effect significant and stopped testing. If the P value was greater than 0.36, the investigator stopped the experiment and retained the null hypothesis. For sample size estimation using power analyses, we used an online power analysis calculator (G*power 3). For each analysis, sample size was determined using a power > 0.9 and alpha error $= 0.05$. All tests were two sided. Sample size determination using sequential stopping rule analyses were used for optogenetic experiments in which it was not possible to determine a priori the effect of the optical manipulation. We used P values of 0.05 and 0.36 for lower and upper criteria. Using this strategy, we ended up with a value of n comprising between five and seven animals per group. No randomization or investigator blinding was done.

30. Markram, H. *et al.* Interneurons of the neocortical inhibitory system. *Nature Rev. Neurosci.* **5,** 793–807 (2004).
31. Somogyi, P., Freund, T. F. & Cowey, A. The axo-axonic interneuron in the cerebral cortex of the rat, cat and monkey. *Neuroscience* **7,** 2577–2607 (1982).
32. Sik, A., Penttonen, M., Ylinen, A. & Buzsáki, G. Hippocampal CA1 interneurons: an *in vivo* intracellular labeling study. *J. Neurosci.* **15,** 6651–6665 (1995).
33. Kvitsiani, D. *et al.* Distinct behavioural and network correlates of two interneuron types in prefrontal cortex. *Nature* **498,** 363–366 (2013).
34. Wolff, S. B. *et al.* Amygdala interneuron subtypes control fear learning through disinhibition. *Nature* **509,** 453–458 (2014).
35. Stark, E. *et al.* Inhibition-induced theta resonance in cortical circuits. *Neuron* **80,** 1263–1276 (2013).
36. Peyrache, A., Benchenane, K., Khamassi, M., Wiener, S. I. & Battaglia, F. P. Principal component analysis of ensemble recordings reveals cell assemblies at high temporal resolution. *J. Comput. Neurosci.* **29,** 309–325 (2010).
37. Berens, P. CircStat: a MATLAB toolbox for circular statistics. *J. Stat. Softw.* **31,** 1–21 (2009).

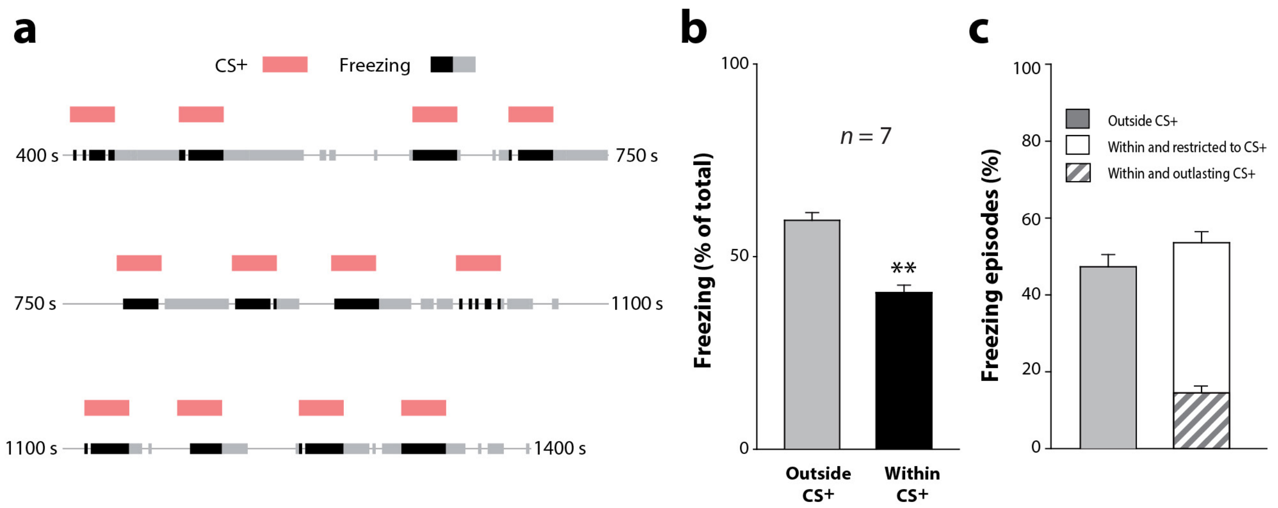

Extended Data Figure 1 | CS$^+$-triggered and spontaneous occurrence of conditioned freezing responses. **a**, Representative examples of conditioned freezing behaviour periods recorded 24 h after auditory fear conditioning (post-FC session). Freezing epochs occurred either independently of any sensory stimulation (thick grey lines) or were induced by CS$^+$ presentations (thick black lines). **b**, Averaged percentage of freezing behaviour recorded 24 h after auditory fear conditioning (post-FC session) within or outside CS$^+$ presentations ($n = 7$ mice, paired t-test, within versus outside CS$^+$, $^{**}P < 0.01$). **c**, Averaged percentage of freezing episodes initiated outside or within CS$^+$ presentations and restricted or outlasting CS$^+$ presentations ($n = 7$ mice). Error bars, mean ± s.e.m.

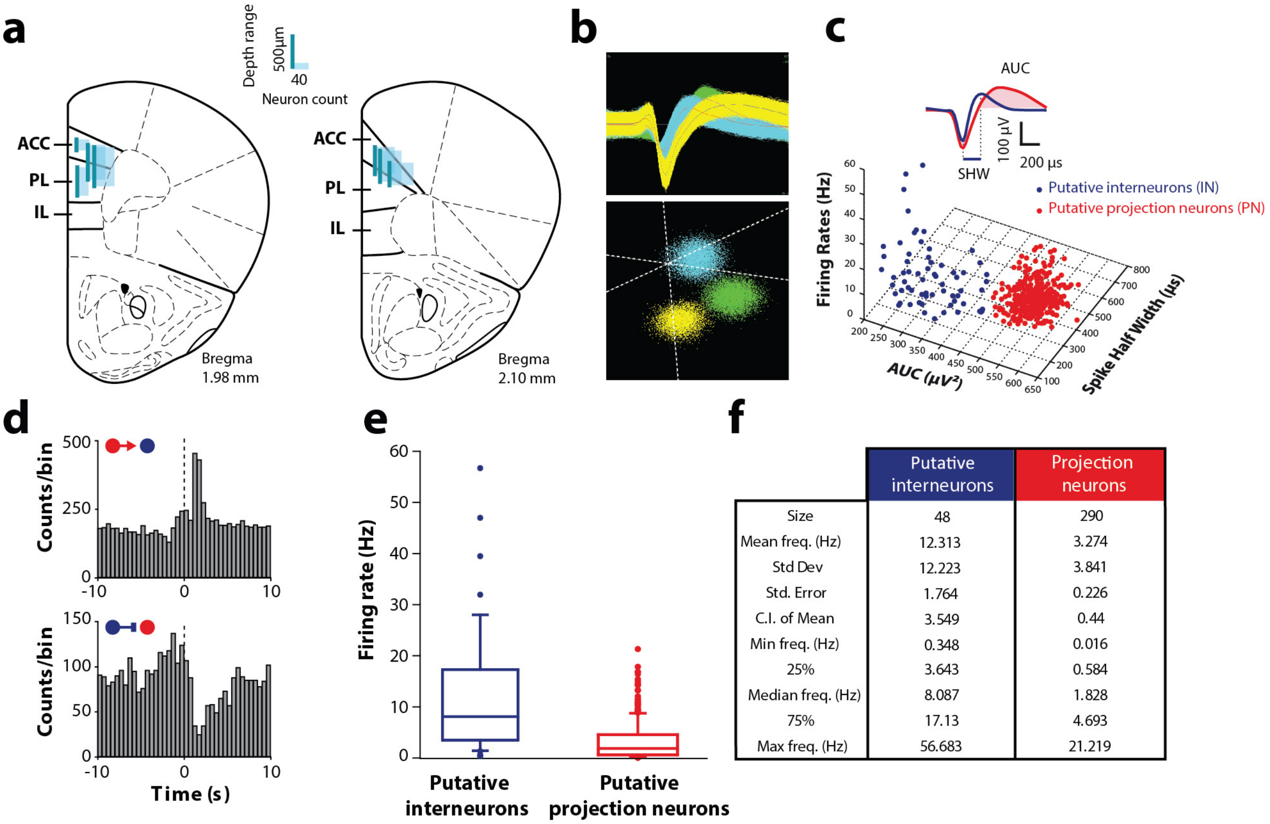

	Putative interneurons	Projection neurons
Size	48	290
Mean freq. (Hz)	12.313	3.274
Std Dev	12.223	3.841
Std. Error	1.764	0.226
C.I. of Mean	3.549	0.44
Min freq. (Hz)	0.348	0.016
25%	3.643	0.584
Median freq. (Hz)	8.087	1.828
75%	17.13	4.693
Max freq. (Hz)	56.683	21.219

Extended Data Figure 2 | Separation of putative PNs and putative interneurons. a, Location and depth of recording sites in the dmPFC and number of neurons recorded ($n = 7$ mice). **b**, Top: superimposed waveforms recorded from three different units. Bottom: spikes originating from individual units were sorted using three-dimensional principal component analysis. **c**, Among the population of neurons recorded, 86% were classified as putative projection neurons (PN, red circles, $n = 290$) and 14% as putative interneurons (IN, blue circles, $n = 48$) using an unbiased unsupervised cluster separation algorithm based on three electrophysiological properties: firing frequency, spike half width (SHW) and spike area under waveform peak. Inset, average waveform of a representative PN and interneuron illustrating the methodology used to quantify SHW and the spike segment used to calculate the spike area under waveform. **d**, Top: representative cross-correlogram performed between a PN and interneuron showing a short-latency, presumably monosynaptic, excitatory interaction (no inhibitory interaction identified among all significant cross-correlograms identified). Bottom: representative cross-correlogram between an interneuron and a PN showing a short-latency, possibly monosynaptic, inhibitory interaction (no excitatory interaction identified among all significant cross-correlograms identified). Reference events correspond to the spikes of the presynaptic neuron (dashed line at time 0, bins of 0.5 ms). Red and blue circles represent PNs and interneurons, respectively. **e**, Box plot of the firing rate of PNs ($n = 290$ in 7 mice) and interneurons ($n = 48$ in 7 mice). For each box plot, the middle, bottom and top lines correspond to the median, lower quartile and upper quartile firing rates. Blue and red dots below and above the boxes correspond to outlier data points.
f, Corresponding firing frequency statistics for PNs and interneurons.

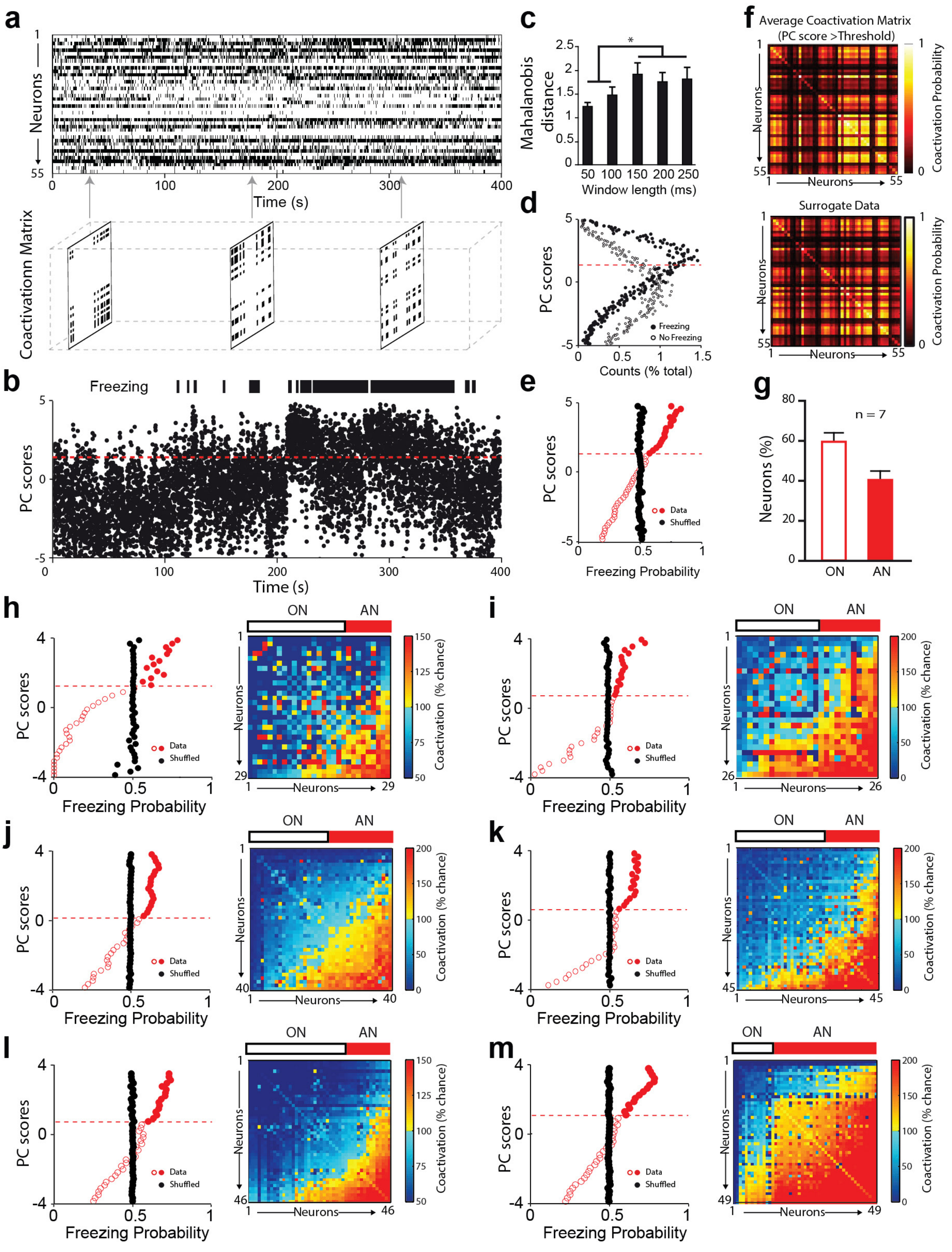

Extended Data Figure 3 | See next page for caption.

Extended Data Figure 3 | Isolation of dmPFC neuronal assemblies. **a**, Top: example of a binarized rate histogram matrix computed from 55 PNs recorded in a single animal. Bottom: examples of correlation matrices computed for particular time bins from the same 55 PNs (bin size: 150 ms). **b**, Corresponding example of principal component scores for the same population of 55 PNs and freezing behaviour as a function of time. For the displayed component (first principal component), the distribution of scores is different for freezing and no freezing periods. This shows that freezing episodes are associated with a specific profile of activity for the simultaneously recorded neurons taken as a population. **c**, Averaged Mahalanobis distance between neuronal population profiles correlated with freezing and no freezing epochs as a function of the length of the sliding window used to produce the binarized rate histograms (see Methods). The optimal separation for neuronal population profiles correlated with freezing and no freezing epochs was obtained with sliding window lengths between 150 and 250 ms ($n = 7$ mice, Friedman repeated-measures one-way ANOVA on ranks test, $*P < 0.05$). Error bars, mean $\pm$ s.e.m. **d**, Corresponding example distribution of principal component scores for neuronal population profiles correlated with freezing (black dots) and no freezing (white dots) epochs (Wilcoxon signed rank test, $P < 0.05$). **e**, Corresponding example of freezing probability as a function of neuronal population principal component score. Freezing probability associated with each score is compared with surrogate data (black dots) for which freezing intervals have been shuffled. Plain and open red dots represent neuronal population profiles that are significantly over-represented compared with chance during freezing and no freezing periods, respectively (one sample t-test, surrogate data versus actual freezing probability for each score, for scores equal to or above 1.15, freezing probability superior to chance level and $P < 0.05$). The red dotted line represents the boundary between neuronal population profiles correlated with freezing and no freezing epochs. **f**, Top: coactivation matrix averaged over freezing epochs from the same 55 dmPFC PNs recorded in a single animal. The strength of the coactivation between pairs of neurons is expressed as the percentage of coactivation compared with chance. Bottom: surrogate data. Coactivation matrix averaged over freezing epochs from the same 55 dmPFC PNs recorded in a single animal for which spike trains have been shuffled 50 times. **g**, Average percentage of ANs (AP index > 1) and ONs (AP index < 1) to freezing-activated neuronal assemblies ($n = 7$ mice, ON: 59.6 $\pm$ 4.5%; AN: 40.4 $\pm$ 4.5%). **h**–**m**, Left: example of freezing probability as a function of neuronal population principal component score for individual mice as in **e**. Right: normalized coactivation matrix averaged over freezing predicting epochs from dmPFC PNs recorded in individual animals ($n = 29$, 40, 46, 26, 45 and 49 neurons). The strength of the coactivation between pairs of neuron is expressed as the percentage of coactivation compared with chance. Error bars, mean $\pm$ s.e.m.

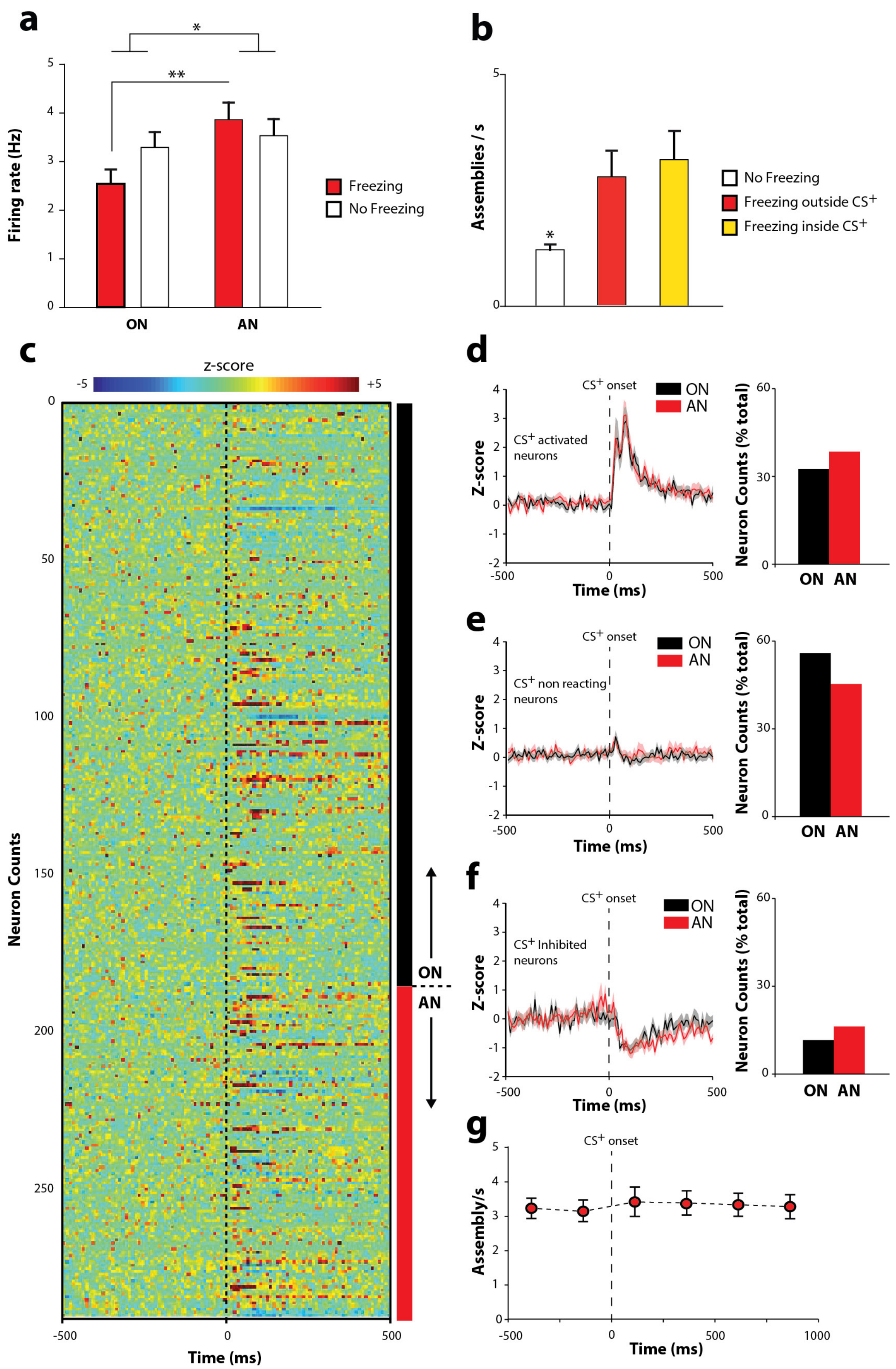

Extended Data Figure 4 | CS$^+$-evoked firing activity of dmPFC PNs. **a**, Averaged firing rate during freezing and no freezing periods for ANs and ONs ($n = 7$ mice, two-way ANOVA, factor 1: AN versus ON, $P < 0.05$; factor 2: freezing versus no freezing, $P > 0.05$; $F_1 \times F_2$: $P > 0.05$; Student–Newman–Keuls post-hoc test within freezing, $^{**}P < 0.01$, $^{*}P < 0.05$). **b**, Average neuronal assembly rate during no freezing periods and during freezing episodes within or outside CS$^+$ presentations ($n = 7$ mice, Friedman repeated-measures one-way ANOVA on ranks test, no freezing versus freezing (inside or outside CS$^+$), $P < 0.05$; Student–Newman–Keuls post-hoc test, $^{*}P < 0.05$). **c**, *Z*-score-normalized peri-stimulus time histograms of individual dmPFC ANs ($n = 117$) and ONs ($n = 172$) during freezing episodes. **d–f**, Left: mean *z*-score of CS$^+$-evoked significant excitatory (**d**), unchanged (**e**) or significant inhibited (**f**) neuronal responses for dmPFC AN and ON. Grey and pink shaded areas correspond to mean ± s.e.m. Right: corresponding percentage of AN and ON ($n = 7$ mice, χ^2 test, $P > 0.05$ in all cases; CS$^+$-evoked excitation: AN: 38.5%, ON: 32.6%; CS$^+$-evoked no changes: AN: 45.3%, ON: 55.8%; CS$^+$-evoked inhibition: AN: 16.2%, ON: 11.6%). **g**, The probability of observing assembly activation is not affected by CS$^+$ (repeated-measures one-way ANOVA on ranks, $P > 0.05$). Error bars, mean ± s.e.m.

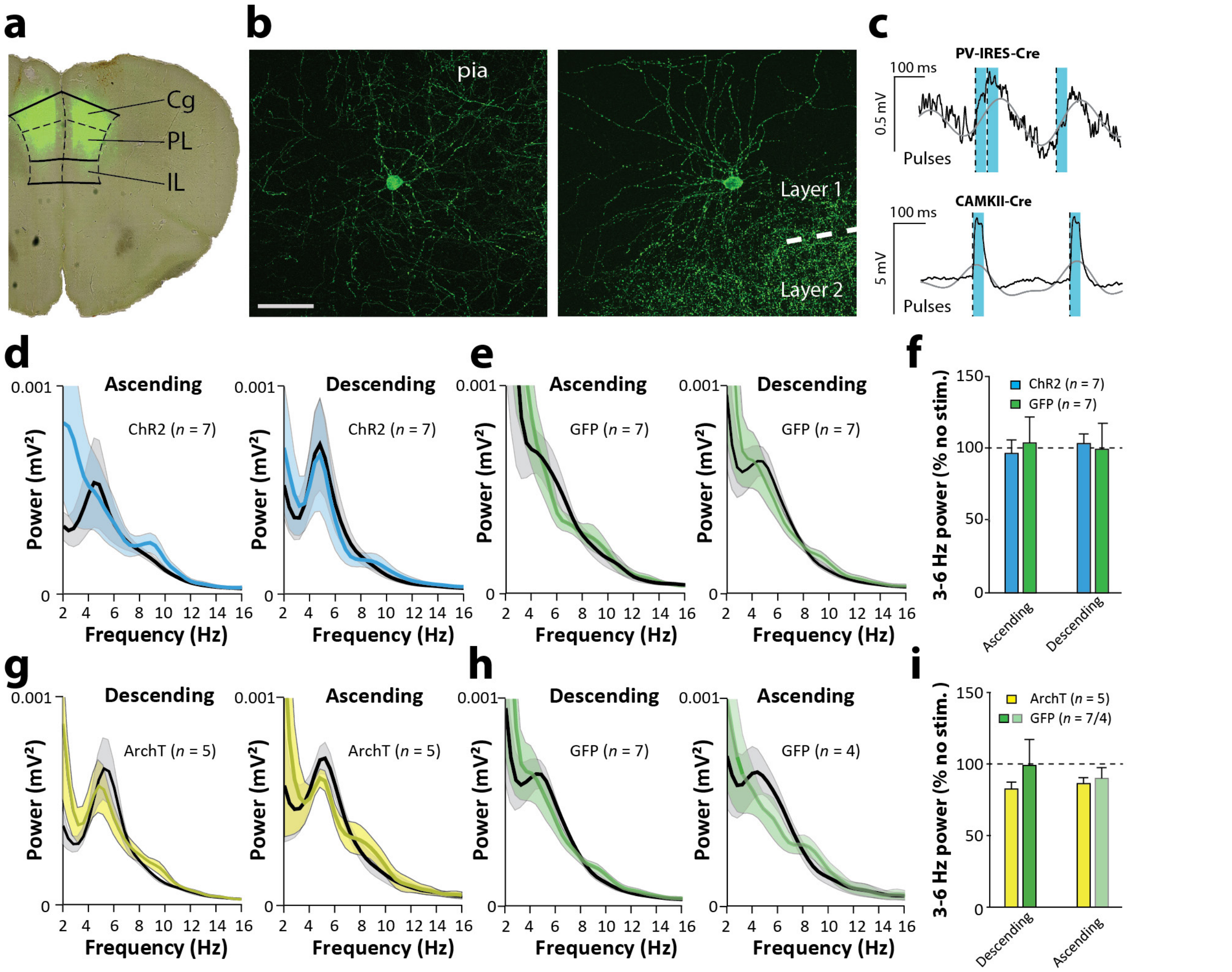

Extended Data Figure 5 | Histological controls and closed-loop stimulation technique. a, Representative micrograph used for dmPFC GFP expression assessment. **b**, Representative dmPFC PV interneurons with distinct dendritic arborizations were infected. Left: multipolar neuron with a round soma, corresponding to a putative basket cell. Right: interneuron with an ovoid soma at the layer 1–2 border, displaying asymmetric and tufted dendrites. Some branches extend towards the pia, bend and follow the pial surface. This neuron corresponds to the typical description of axo-axonic (chandelier) cells in mPFC. **c**, Top: representative raw (black trace) and filtered (grey trace, 3–6 Hz) dmPFC LFP recorded in PV-IRES-Cre mice during 4 Hz oscillations (top) or in CAMKII-Cre mice outside 4 Hz oscillations infected with ChR2 (bottom) upon light activation (30 ms square pulses; black line, pulse start; red bar, pulse length). **d**, **e**, Averaged LFP power spectra obtained in ChR2-infected mice and GFP controls during stimulated (coloured traces) and non-stimulated (grey traces) periods when the stimulation was applied in the ascending (ChR2, $n = 7$ mice; GFP, $n = 7$ mice) or descending (ChR2, $n = 7$ mice; GFP, $n = 7$ mice) phase. **f**, Averaged 3–6 Hz LFP power for ChR2 and GFP mice during stimulation in the ascending or descending phase of 4 Hz oscillations expressed as a percentage of no stimulation periods (ChR2, $n = 7$ mice; GFP, $n = 7$ mice; two-way ANOVA, factor 1: GFP versus ChR2, $P = 0.848$; factor 2: descending versus ascending, $P = 0.879$; $F_1 \times F_2$, $P = 0.618$). **g**, **h**, Averaged LFP power spectra obtained in ArchT infected mice and GFP controls during stimulated (coloured traces) and non-stimulated (grey traces) periods when the stimulation was applied in the descending (ArchT, $n = 5$ mice; GFP, $n = 7$ mice) or ascending phase (ChR2, $n = 5$ mice; GFP, $n = 4$ mice). **i**, Averaged 3–6 Hz LFP power for ArchT and GFP mice during stimulation in the descending or ascending phase of 4 Hz oscillations expressed as a percentage of no stimulation periods (ArchT, $n = 5$ mice; GFP, $n = 7/4$ mice; two-way ANOVA, factor 1: GFP versus ChR2, $P = 0.872$; factor 2: descending versus ascending, $P = 0.183$; $F_1 \times F_2$, $P = 0.5$). Error bars, mean ± s.e.m.

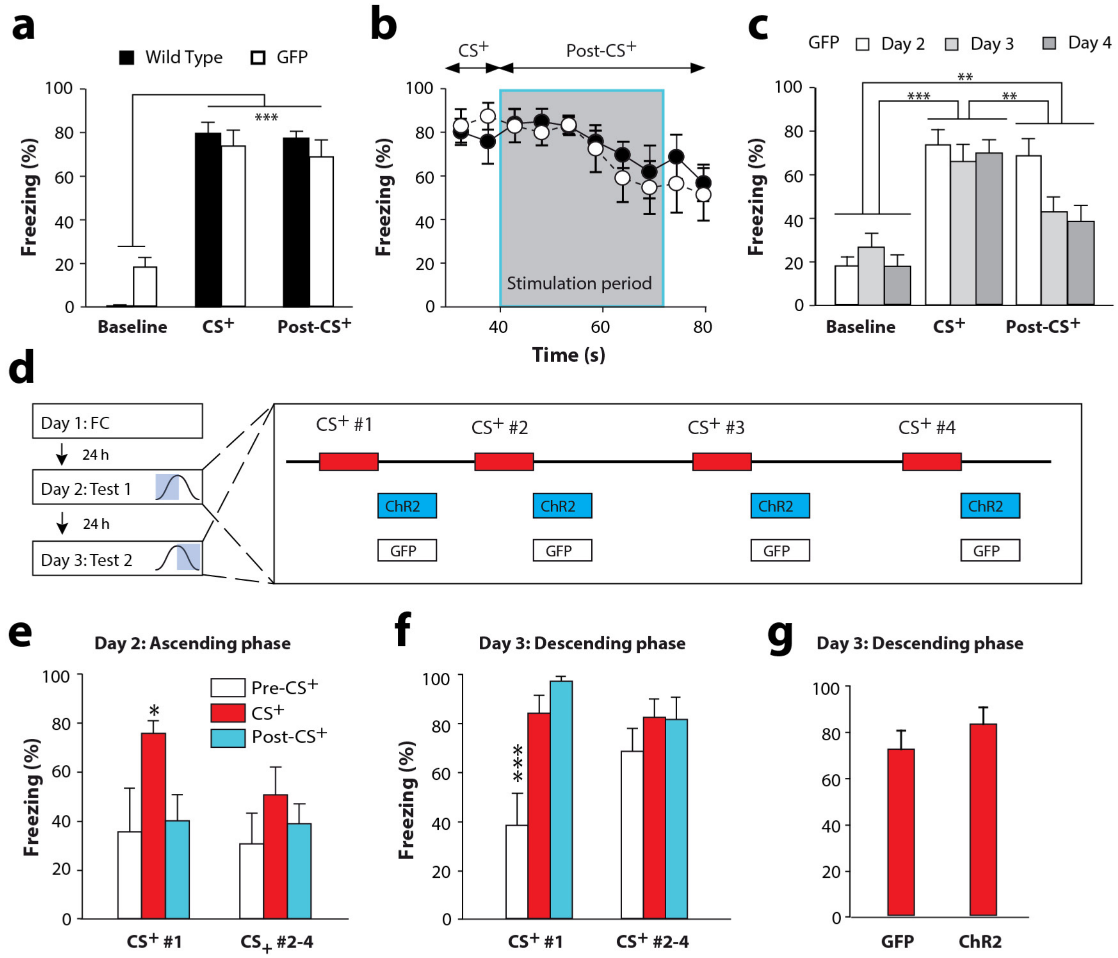

Extended Data Figure 6 | Phase-specific optogenetic inhibition of dmPFC PNs. a, Twenty-four hours after conditioning, levels of freezing in wild type ($n = 7$) and GFP ($n = 7$) control animals where similar (2 min baseline, four CS$^+$ and four post-CS$^+$ periods of 30 s averaged, two-way ANOVA, factor 1: wild type versus GFP, $P > 0.05$; factor 2: time, $P < 0.001$; $F_1 \times F_2$, $P < 0.01$, Student–Newman–Keuls post-hoc test within wild type and GFP, ***$P < 0.001$). **b**, Corresponding time-resolved changes in freezing behaviour around CS$^+$ offset for wild type and GFP control animals (two-way ANOVA, factor 1: wild type versus GFP, $P > 0.05$; factor 2: time, $P > 0.05$; $F_1 \times F_2$, $P > 0.05$). **c**, Comparison of GFP control levels of freezing during (CS$^+$) and 30 s after CS$^+$ (post-CS$^+$) on days 2 ($n = 7$), 3 ($n = 7$) and 4 ($n = 4$) (2 min baseline, four CS$^+$ and four post-CS$^+$ periods of 30 s averaged; two-way ANOVA, factor 1: day, $P > 0.05$; factor 2: time, $P < 0.001$; $F_1 \times F_2$, $P > 0.05$; Bonferroni post-hoc test between epochs, **$P < 0.01$, ***$P < 0.001$). **d**, Timeline scheme for the optogenetic stimulation protocol on day 2 with stimulation targeting the ascending phase of 4 Hz oscillation cycle (top) and day 3 with stimulation targeting the descending phase of 4 Hz oscillation cycle (bottom). **e**, **f**, Comparison of freezing levels between CS$^+$ 1 and CS$^+$ 2–4 for epochs 10 s preceding, during and 30 s after CS$^+$ during optogenetic stimulation (pre-CS$^+$, CS$^+$ and post-CS$^+$ respectively) on day 2 (**e**) and day 3 (**f**). On day 2, ascending phase stimulation after CS$^+$ 1 induced a decrease of freezing levels during subsequent CS$^+$ epochs as no more difference was observed between pre CS$^+$, CS$^+$ and post CS$^+$ for CS$^+$ 2–4 compared with CS$^+$ 1 ($n = 7$ mice, repeated-measures two-way ANOVA, factor 1: CS$^+$ 1 versus CS$^+$ 2–4, $P > 0.05$; factor 2: epoch, $P < 0.05$; $F_1 \times F_2$, $P > 0.05$; Student–Newman–Keuls post-hoc test within factor 1, *$P < 0.05$ compared with both pre- and post-CS$^+$ epochs). On day 3, descending phase stimulation after CS$^+$ 1 induced an increase in freezing levels during pre-CS$^+$ epochs as no more difference was observed between pre-CS$^+$, CS$^+$ and post-CS$^+$ for CS$^+$ 2–4 compared with CS$^+$ 1 ($n = 7$ mice, repeated-measures two-way ANOVA, factor 1: CS$^+$ 1 versus CS$^+$ 2–4, $P > 0.05$; factor 2: epoch, $P < 0.05$; $F_1 \times F_2$, $P < 0.05$; Student–Newman–Keuls post-hoc test within factor 1, *$P < 0.001$ compared with both CS$^+$ and post-CS$^+$ epochs). **g**, Averaged freezing behaviour evoked by CS$^+$ 1 presentation on day 3 if day 2 stimulation was in the ascending phase (GFP $n = 7$, ChR2 with day 2 ascending $n = 7$, Mann–Whitney rank sum test, $P = 0.259$).

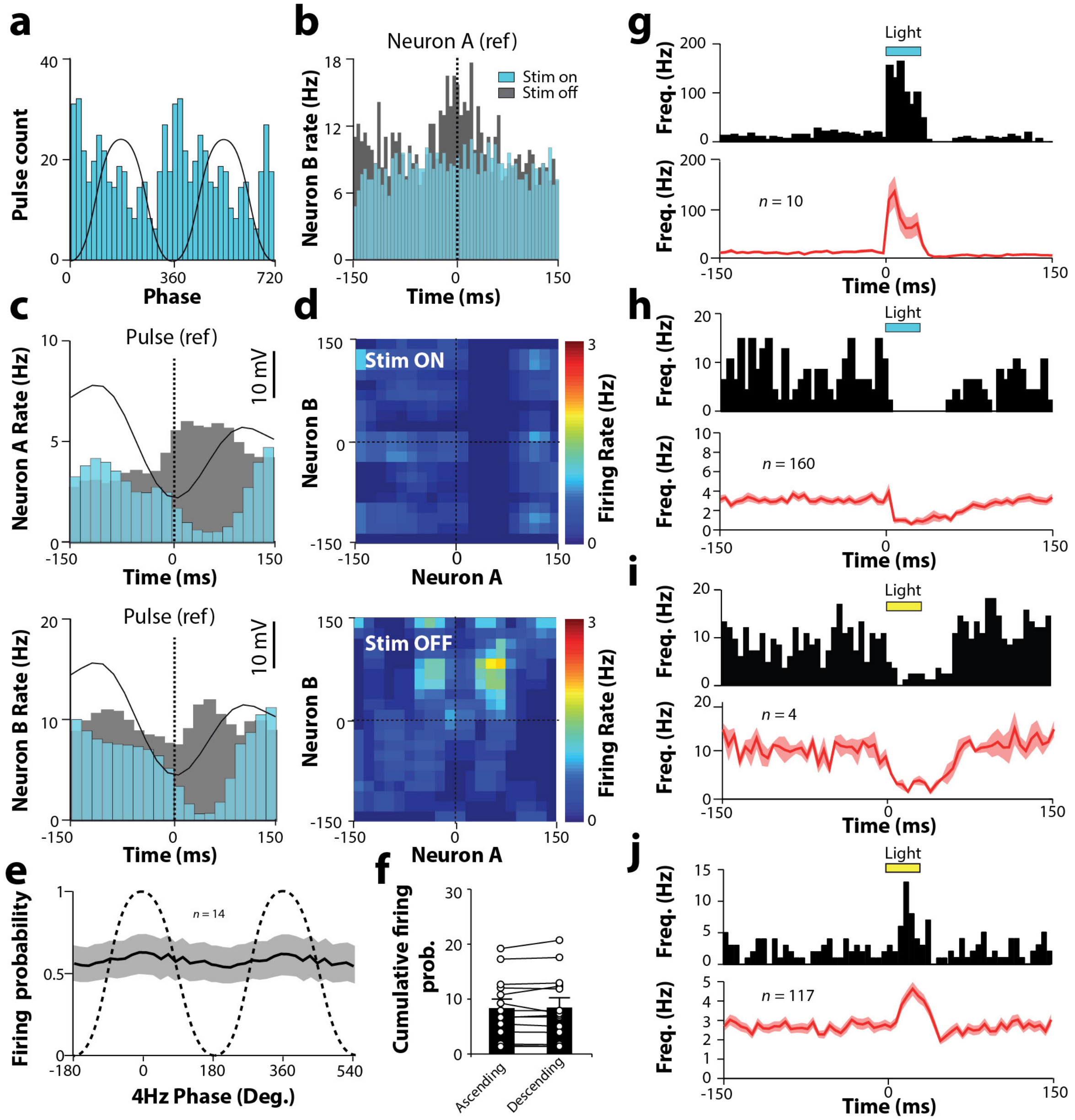

Extended Data Figure 7 | Phase specificity of the close loop stimulation technique. a, Representative distribution of stimulation pulses in relation to the phase of the 4 Hz oscillation (black line, filtered LFP 3–6 Hz) when the stimulation was applied in the ascending phase of the oscillation (bins of 18°). **b**, Representative cross-correlogram between two dmPFC PNs (neurons A and B) participating to neuronal assemblies during (blue bars), or outside (grey bars) optogenetic inhibition of PV interneurons. Note the reduction in joint firing activity when the stimulation was on. Reference events correspond to the spikes of the neuron A (dashed line at time 0, bins of 5 ms). **c**, Firing frequency of dmPFC neurons A (top) and B (bottom) without optogenetic stimulation (grey bars, bins of 15 ms) or when the pulse was applied in the ascending phase of the 4 Hz oscillation (blue bars, bins of 15 ms) (black line, filtered LFP 3–6 Hz). **d**, Corresponding joint peri-stimulus time histograms performed between the same dmPFC neurons A and B when the pulse was applied in the ascending phase of the 4 Hz oscillation (top) or without stimulation (bottom). Note the inhibition of the co-firing activity when the stimulation was on. **e**, Firing probability per degree of identified PV$^+$ interneurons as a function of 4 Hz oscillations phase ($n = 14$ PV$^+$ interneurons). **f**, Cumulative firing probability per degree for individual PV$^+$ interneurons (open circles) during the ascending or descending phase of 4 Hz oscillations and corresponding averaged cumulative firing probability (black bars, $n = 14$ PV$^+$ interneurons, Wilcoxon signed rank test, $P = 0.733$). **g**, **i**, Top: firing of a PV$^+$ interneuron in a mouse expressing ChR2 or ArchT in PV$^+$ interneurons in the dmPFC in response to blue or yellow light (light-pulse duration 30 ms; 150 trials). Bottom: mean peri-stimulus time histograms of all PV$^+$ interneurons displaying significant light-evoked excitation or inhibition ($n = 10$ PV$^+$ from five mice infected with ChR2; $n = 4$ PV$^+$ from two mice infected with ArchT, light-pulse duration, 30 ms). Bins of 5 ms. **h**, **j**, Top: firing of a PN in a mouse expressing ChR2 or ArchT in PV$^+$ interneurons in the dmPFC in response to blue or yellow light activation of PV$^+$ interneurons (light-pulse duration, 30 ms; 150 trials). Bottom: mean peri-stimulus time histograms of all PNs displaying significant light-evoked inhibition or excitation ($n = 160$ PNs from seven mice infected with ChR2; $n = 117$ PNs from five mice infected with ArchT; light-pulse duration, 30 ms). Bins of 5 ms. Error bars, mean ± s.e.m.

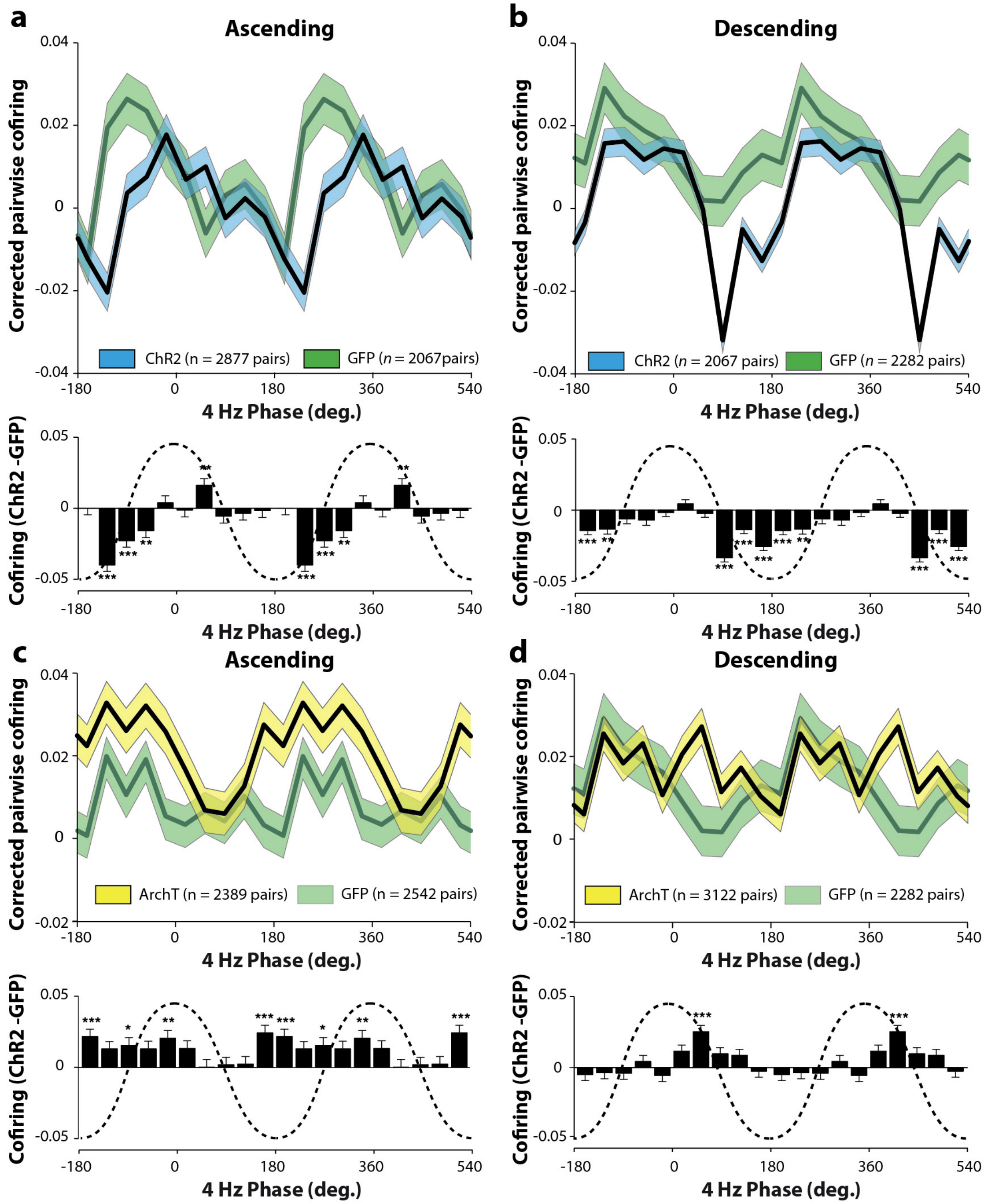

Extended Data Figure 8 | Effect of phase-specific PV manipulation on dmPFC co-firing activity. a, **b**, Top: corrected pairwise co-firing for pairs of dmPFC neurons recorded in mice infected with ChR2 or GFP during stimulation in the ascending (**a**, ChR2, $n = 2{,}877$ pairs; GFP, $n = 2{,}067$ pairs) or descending (**b**, ChR2, $n = 2{,}067$ pairs; GFP, $n = 2{,}282$ pairs) phase of 4 Hz oscillations. Bottom: averaged delta-corrected pairwise co-firing activity (delta = ChR2 minus GFP) as a function of 4 Hz phase (one sample *t*-test with Bonferroni correction, hypothetical mean = 0, $^{**}P < 0.01$, $^{***}P < 0.001$). **c**, **d**, Top: corrected pairwise co-firing for pairs of dmPFC neurons recorded in mice infected with ArchT or GFP during stimulation in the ascending (**a**, ArchT, $n = 2{,}389$ pairs; GFP, $n = 2{,}542$ pairs) or descending (**b**, ArchT, $n = 3{,}122$ pairs; GFP, $n = 2{,}282$ pairs) phase of 4 Hz oscillations. Bottom: averaged delta-corrected pairwise co-firing activity (delta = ArchT minus GFP) as a function of 4 Hz phase (one-sample *t*-test with Bonferroni correction, hypothetical mean = 0, $^{*}P < 0.05$, $^{**}P < 0.01$, $^{***}P < 0.001$). Error bars, mean ± s.e.m.

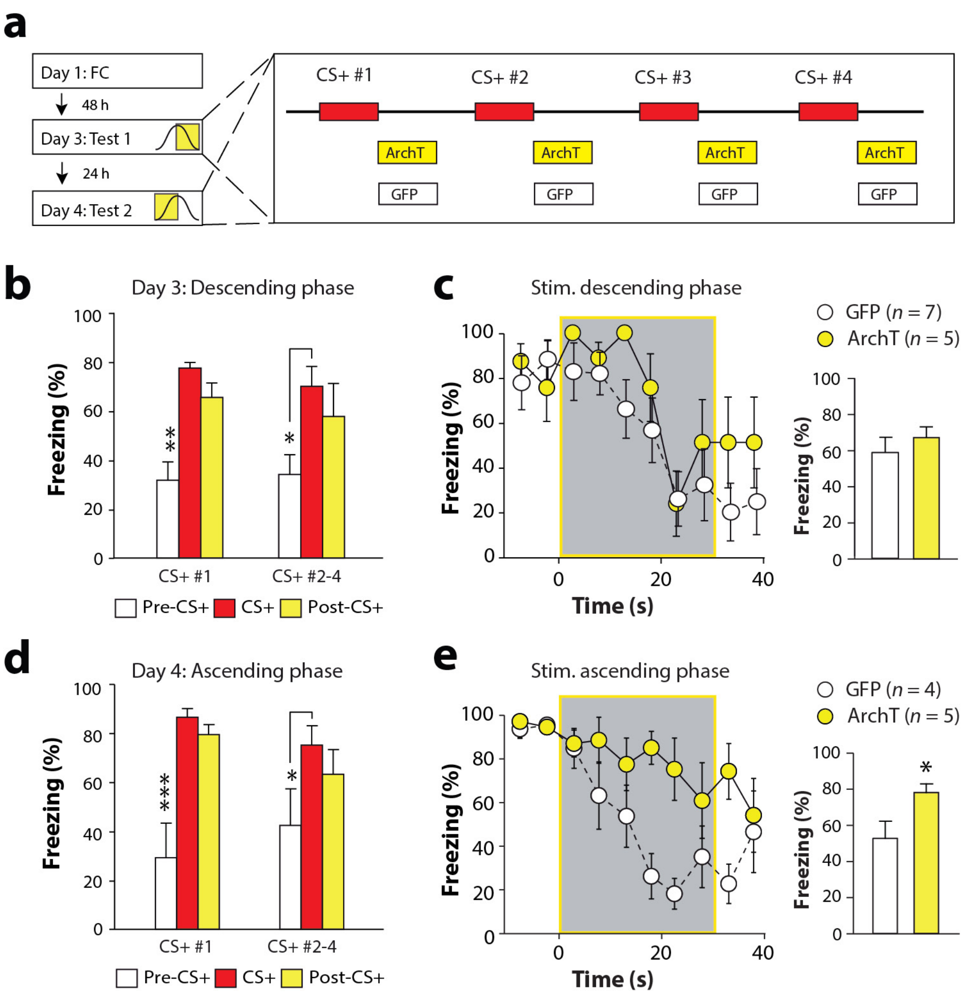

Extended Data Figure 9 | Phase-specific optogenetic disinhibition of dmPFC PNs enhanced fear behaviour. **a**, Timeline scheme for the optogenetic stimulation protocol on day 3 with stimulation targeting the descending phase of 4 Hz oscillation cycle (top) and day 4 with stimulation targeting the ascending phase of 4 Hz oscillation cycle (bottom). **b**, **d**, Comparison of freezing levels between CS$^+$ 1 and CS$^+$ 2–4 for epochs 10 s preceding, during and 30 s after CS$^+$ during optogenetic stimulation of PV-IRES-Cre mice infected within the dmPFC with ArchT (pre-CS$^+$, CS$^+$ and post-CS$^+$ respectively) on day 3 (**b**) and day 4 (**d**). On day 3, descending phase stimulation after CS$^+$ 1 had no effect on freezing levels during subsequent CS$^+$ epochs before, during or after CS$^+$ ($n = 5$ ArchT mice, repeated-measures two-way ANOVA, factor 1: CS$^+$ 1 versus CS$^+$ 2–4, $P > 0.05$; factor 2: epoch, $P < 0.05$; $F_1 \times F_2$, $P > 0.05$; Student–Newman–Keuls post-hoc test within factor 1, $^{**}P < 0.01$ compared with both pre- and post-CS$^+$ epochs, $^{*}P < 0.05$ comparing pre-CS$^+$ with CS$^+$ epochs). On day 4, ascending phase stimulation after CS$^+$ 1 had no effect on freezing levels during subsequent CS$^+$ epochs before, during or after CS$^+$ ($n = 5$ ArchT mice, repeated-measures two-way ANOVA, factor 1: CS$^+$ 1 versus CS$^+$ 2–4, $P > 0.05$; factor 2: epoch, $P < 0.05$; $F_1 \times F_2$, $P < 0.05$; Student–Newman–Keuls post-hoc test within factor 1, $^{***}P < 0.001$ compared with both CS$^+$ and post-CS$^+$ epochs, $^{*}P < 0.05$ comparing pre-CS$^+$ with CS$^+$ epochs). **c**, **e**, Left: time-resolved changes in freezing behaviour during light-mediated inhibition of dmPFC neuronal assemblies in the descending (**c**) or ascending (**e**) phase of the 4 Hz oscillation in PV-IRES-Cre mice infected within the dmPFC with ArchT (descending phase: first CS$^+$, $n = 5$; ascending phase: first CS$^+$, $n = 5$) or GFP (descending phase: first CS$^+$, $n = 7$; ascending phase: first CS$^+$, $n = 4$; descending phase: two-way ANOVA, factor 1: ArchT versus GFP, $P > 0.05$; factor 2: time, $P > 0.05$; $F_1 \times F_2$, $P > 0.05$; ascending phase: two-way ANOVA, factor 1: ArchT versus GFP, $P < 0.01$; factor 2: time, $P < 0.01$; $F_1 \times F_2$, $P < 0.01$). Shaded area represents the period during which the light stimulation was applied. Right: averaged freezing behaviour during the stimulation in the descending (**c**) (ArchT $n = 5$; GFP $n = 7$, Mann–Whitney test, ArchT versus GFP, $P > 0.05$) or ascending phase (**e**) (ArchT $n = 5$; GFP $n = 4$, Mann–Whitney test, ArchT versus GFP, $^{*}P < 0.05$). Error bars, mean ± s.e.m.

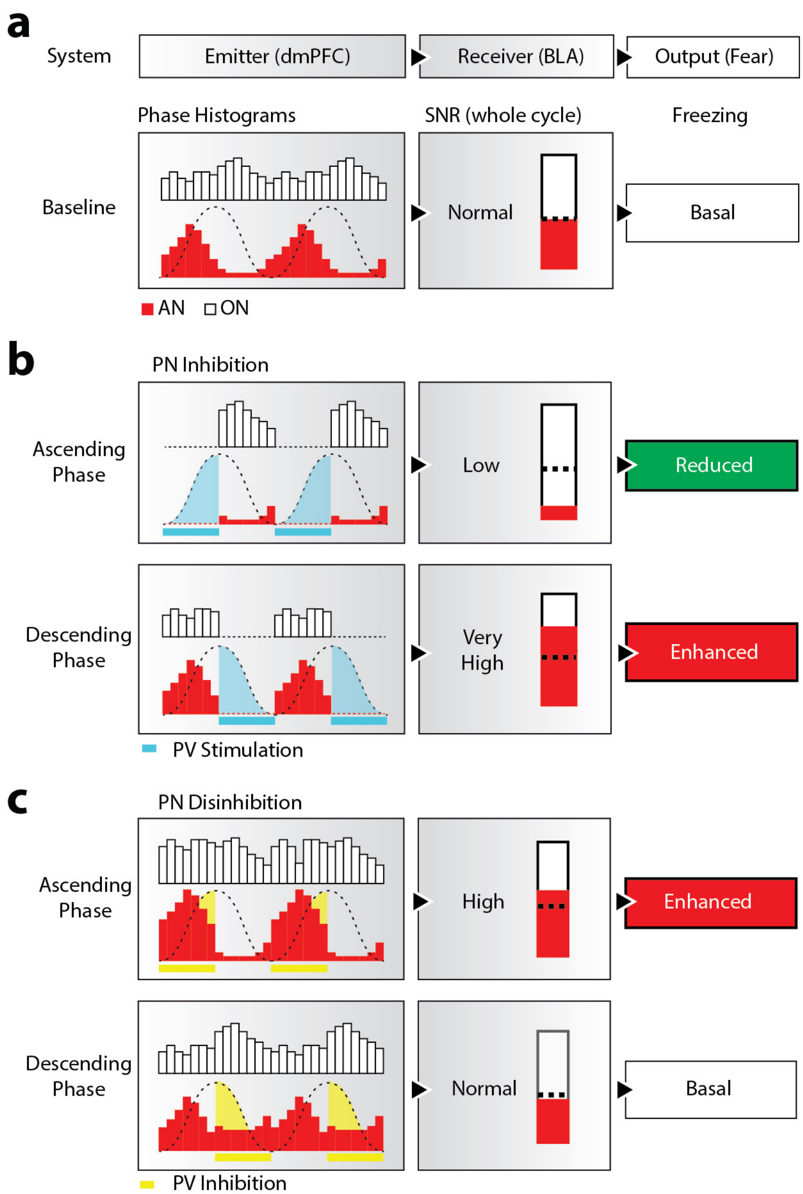

Extended Data Figure 10 | Functional model of phase-specific coding for freezing behaviour. This schematic illustrates how, within a 4 Hz cycle, the phase specificity and relative influence of dmPFC assembly and non-assembly neurons (AN, ON, respectively) could represent a functional signal for downstream structures implicated in the expression of freezing behaviour. **a**, In normal freezing conditions, the prevalence and restriction of AN activation in the ascending phase combined with the monotonic phase distribution of ONs provides downstream structures with a signal-to-noise ratio (SNR) over an entire 4 Hz cycle that allows freezing expression. **b**, During optogenetic PN inhibition this SNR is altered. Top: when stimulating in the ascending phase, the bulk of AN activity over a cycle is shut down. This dramatically reduces SNR and prevents freezing expression. Bottom: when stimulating in the descending phase, AN activity is largely preserved over a cycle while that of ONs is diminished to a large extent. This strongly increases SNR and exacerbates freezing expression. **c**, During optogenetic PN disinhibition the SNR is also altered. Top: when stimulating in the ascending phase, the AN activity over a cycle is promoted compared with non-ensemble activity. This increases SNR and enhances freezing expression. Bottom: when stimulating in the descending phase, both assembly and non-assembly neuron activities over a cycle are increased. This does not affect SNR and freezing remains similar to normal conditions. In this model the dmPFC can be seen as an emitter whose signal transmission conditions the SNR for the receiver and the further expression of fear behaviour. Our optogenetic dissection of phase specificity for dmPFC neuronal assemblies shows that SNR can be manipulated to either.

LETTER

doi:10.1038/nature18626

Unexpected role of interferon-γ in regulating neuronal connectivity and social behaviour

Anthony J. Filiano[1,2], Yang Xu[3], Nicholas J. Tustison[4], Rachel L. Marsh[1,2], Wendy Baker[1,2], Igor Smirnov[1,2], Christopher C. Overall[1,2], Sachin P. Gadani[1,2,5,6], Stephen D. Turner[7], Zhiping Weng[8], Sayeda Najamussahar Peerzade[3], Hao Chen[8], Kevin S. Lee[1,2,5,9], Michael M. Scott[5,10], Mark P. Beenhakker[5,10], Vladimir Litvak[3]* & Jonathan Kipnis[1,2,5,6]*

Immune dysfunction is commonly associated with several neurological and mental disorders. Although the mechanisms by which peripheral immunity may influence neuronal function are largely unknown, recent findings implicate meningeal immunity influencing behaviour, such as spatial learning and memory[1]. Here we show that meningeal immunity is also critical for social behaviour; mice deficient in adaptive immunity exhibit social deficits and hyper-connectivity of fronto-cortical brain regions. Associations between rodent transcriptomes from brain and cellular transcriptomes in response to T-cell-derived cytokines suggest a strong interaction between social behaviour and interferon-γ (IFN-γ)-driven responses. Concordantly, we demonstrate that inhibitory neurons respond to IFN-γ and increase GABAergic (γ-aminobutyric-acid) currents in projection neurons, suggesting that IFN-γ is a molecular link between meningeal immunity and neural circuits recruited for social behaviour. Meta-analysis of the transcriptomes of a range of organisms reveals that rodents, fish, and flies elevate IFN-γ/JAK-STAT-dependent gene signatures in a social context, suggesting that the IFN-γ signalling pathway could mediate a co-evolutionary link between social/aggregation behaviour and an efficient anti-pathogen response. This study implicates adaptive immune dysfunction, in particular IFN-γ, in disorders characterized by social dysfunction and suggests a co-evolutionary link between social behaviour and an anti-pathogen immune response driven by IFN-γ signalling.

Social behaviour is beneficial for many processes critical to the survival of an organism, including foraging, protection, breeding, and, for higher-order species, mental health[2,3]. Social dysfunction manifests in several neurological and mental disorders such as autism spectrum disorder, frontotemporal dementia, and schizophrenia, among others[4]. Likewise, imbalance of cytokines, a disparity of T-cell subsets, and overall immune dysfunction is often associated with the above-mentioned disorders[5–7]. However, the fundamental mechanism(s) by which dysfunctional immunity may interfere with neural circuits and contribute to behavioural deficits remain unclear.

To test whether adaptive immunity is necessary for normal social behaviour, we tested SCID mice (deficient in adaptive immunity) using the three-chamber sociability assay[8] (Extended Data Fig. 1a). This assay quantifies the preference of a mouse for investigating a novel mouse versus an object, and has been used to identify deficits in multiple mouse models of disorders that present with social dysfunction[9]. Unlike wild-type mice, SCID mice lacked social preference for a mouse over an object (Fig. 1a). Importantly, SCID mice did not show anxiety, motor, or olfactory deficits (Extended Data Fig. 1b–j). We confirmed that SCID mice have social deficits by analysing social interactions in a home cage (Extended Data Fig. 1k). To test whether social deficits were reversible, we repopulated 4-week-old SCID mice with wild-type lymphocytes (Extended Data Fig. 1l–n) and measured social behaviour 4 weeks after transfer. SCID mice repopulated with lymphocytes, unlike those injected with the vehicle, showed social preference indistinguishable from wild-type mice (Fig. 1b).

Recent clinical findings indicate that disturbed circuit homeostasis, resulting in hyper-connectivity, is a feature of children with autism spectrum disorder[10]. Imaging studies using task-free resting-state fMRI (rsfMRI), revealed hyper-connectivity among frontal cortical nodes in patients with autism spectrum disorder[11]. Disturbances in resting state connectivity are also observed in mice with social deficits[12]. rsfMRI is an unbiased technique used to assess synchrony between brain regions over time by comparing spontaneous fluctuations in blood oxygenation level-dependent (BOLD) signals[13]. To assess the influence of adaptive immunity on functional connectivity, we analysed resting-state BOLD signals from wild-type and SCID mice (Extended Data Fig. 2a). SCID mice exhibited hyper-connectivity between multiple frontal and insular regions (Fig. 1c, d, Extended Data Fig. 2b and Supplementary Table 1) implicated in social behaviour and autism spectrum disorder. Notably, repopulating SCID mice with lymphocytes rescued aberrant hyper-connectivity observed in vehicle-treated SCID controls (Fig. 1c, d and Extended Data Fig. 2b). Interestingly, other functionally connected regions, not directly implicated in social function, such as interhemispheric connectivity between motor and somatosensory cortex, were not affected by a deficiency in adaptive immunity (Supplementary Table 1). Using another approach to analyse neuronal activation in a task-based system, we demonstrated that SCID mice exposed to a social stimulus exhibited hyper-responsiveness in the prefrontal cortex (PFC; increased number of c-fos$^+$ cells in PFC; Fig. 1e, f) but not the hippocampus (Extended Data Fig. 2c).

We previously demonstrated that T cells influence learning behaviour and exert their beneficial effects presumably from the meninges[1,14]. To address the role of meningeal T cells in social behaviour, we decreased the extravasation of T cells into the meninges of wild-type mice using antibodies against VLA4 (ref. 15), an integrin expressed on T cells (among other immune cells) required for CNS homing. Partial elimination of T cells from meninges (Extended Data Fig. 3) was sufficient to cause a loss in social preference (Fig. 1g). Despite their proximity to the brain, meningeal T cells do not enter the brain parenchyma, suggesting their effect is mediated by soluble factors. To

[1]Center for Brain Immunology and Glia, School of Medicine, University of Virginia, Charlottesville, Virginia 22908, USA. [2]Department of Neuroscience, School of Medicine, University of Virginia, Charlottesville, Virginia 22908, USA. [3]Department of Microbiology and Physiological Systems, University of Massachusetts Medical School, Worcester, Massachusetts 01655, USA. [4]Department of Radiology and Medical Imaging, School of Medicine, University of Virginia, Charlottesville, Virginia 22908, USA. [5]Neuroscience Graduate Program, School of Medicine, University of Virginia, Charlottesville, Virginia 22908, USA. [6]Medical Scientist Training Program, School of Medicine, University of Virginia, Charlottesville, Virginia 22908, USA. [7]Department of Public Health Sciences, School of Medicine University of Virginia, Charlottesville, Virginia 22908, USA. [8]Department of Biochemistry and Molecular Pharmacology, University of Massachusetts Medical School, Worcester, Massachusetts 01655, USA. [9]Department of Neurosurgery, School of Medicine, University of Virginia, Charlottesville, Virginia 22908, USA. [10]Department of Pharmacology, School of Medicine, University of Virginia, Charlottesville, Virginia 22908, USA.
*These authors jointly supervised this work.

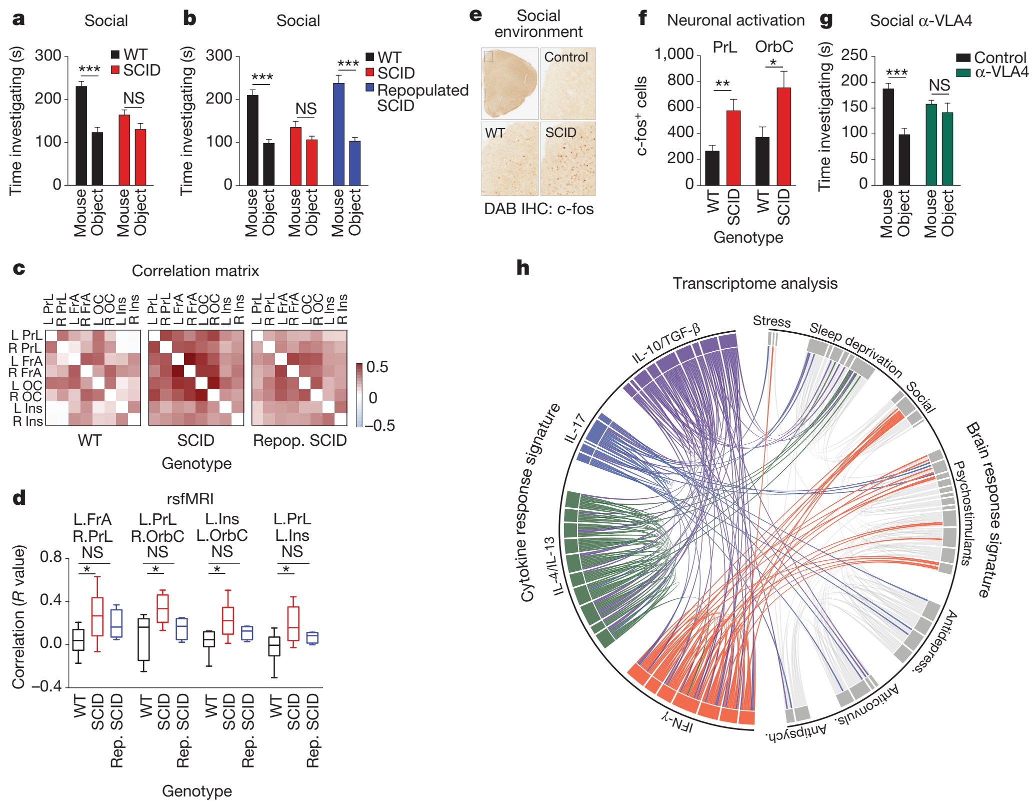

Figure 1 | Meningeal T-cell compartment is necessary for supporting neuronal connectivity and social behaviour. a, Wild-type mice exhibit social preference absent in SCID mice (ANOVA for genotype ($F_{1,26}$) = 6.370, P = 0.0181; n = 14 mice per group; $^{**}P < 0.01$, Sidak's post hoc test; pooled two independent experiments). **b**, Repopulating the adaptive immune system in SCID mice restored normal social behaviour (n = 17, 16, 15 mice per group; ANOVA for genotype ($F_{2,45}$) = 8.282, P = 0.0009 and interaction ($F_{2,45}$) = 9.146, P = 0.0005; $^{***}P < 0.001$; $^{**}P < 0.01$, Sidak's post hoc test; pooled three independent experiments). **c**, Correlation matrices from wild-type, SCID, and repopulated (Repop.) SCID mice were generated by rsfMRI. L, left; R, right; FrA, frontal association area; PrL, prelimbic cortex; Ins, insula; OrbC, orbital cortex. **d**, Correlation values from rsfMRI. Box and whisker plots extend to the 25th and 75th percentiles with the centre-line showing the mean. Whiskers represent the minimum and maximum data points (n = 8, 9, 4 mice per group; ANOVA < 0.05; $^{*}P < 0.05$, Sidak's post hoc test; pooled two independent experiments). **e**, Immunohistochemistry of c-fos in the PFC. **f**, Elevated numbers of c-fos^{+} cells in the prefrontal and orbital cortices of SCID compared with wild-type mice (n = 9;10 mice per group; $^{**}P < 0.01$; $^{*}P < 0.05$, t-test; single experiment). **g**, Acute partial depletion of meningeal T cells caused social deficits (n = 12, 13 mice per group; ANOVA for interaction ($F_{1,23}$) = 7.900, $P < 0.01$; $^{***}P < 0.001$, Sidak's post hoc test; pooled two independent experiments). **h**, Circos plot showing the connectivity map derived from the pairwise comparison of transcriptome data sets. The representations of IFN-γ, IL-4/IL-13, IL-17, and IL-10/TGF-β data set connectivity are shown in orange, green, blue, and purple, respectively. Each line represents a pairwise data set overlap, which was determined using GSEA analysis and filtered by $P < 0.05$ and normalized enrichment score (NES) > 1.5. See Extended Data Fig. 5 for labels. Data from the three-chamber test (**a**, **b**, **g**) were analysed by applying a two-way ANOVA for social behaviour and genotype/treatment, followed by Sidak's post hoc test. Bars, mean times investigating ± s.e.m. Antidepress., antidepressants; anticonvuls., anticonvulsants; antipsych., antipsychotics.

identify which T-cell-mediated pathways are involved in regulating social behaviour, we used gene set enrichment analysis (GSEA) to search for T-cell-mediated response signatures (IFN-γ, IL-4/IL-13, IL-17, Il-10, TGF-β) in 41 transcriptomes from mouse and rat brain cortices. GSEA assesses whether the expression of a previously defined group of related genes is enriched in one biological state. In this case, we used GSEA to identify which cytokine-induced response signatures were enriched in the transcriptomes of mice and rats exposed to different stimuli. The stimuli included social aggregation, sleep deprivation, stress, psychostimulants, antidepressants, anticonvulsants, and antipsychotics. Transcriptomes from cortices of animals exposed to social aggregation and psychostimulants were enriched for IFN-γ regulated genes (Fig. 1h, Extended Data Fig. 4 and Supplementary Tables 2 and 3).

A substantial number of meningeal T cells are capable of expressing IFN-γ (41.95% ± 6.34 of TCR^{+} cells; Extended Data Fig. 5a) and recent work has proposed a role for IFN-γ in T-cell trafficking into meningeal spaces[16]. To assess the potential role of IFN-γ in mediating the influence of T cells on social behaviour, we first examined the social behaviour of IFN-γ-deficient mice and determined that they had social deficits (Fig. 2a). Importantly, IFN-γ-deficient mice did not show anxiety or motor deficits (Extended Data Fig. 5b–g). Similar to SCID mice, IFN-γ-deficient mice also exhibited aberrant hyper-connectivity in fronto-cortical/insular regions (Fig. 2b, c and Supplementary Table 1). Although repopulating SCID mice with lymphocytes from wild-type mice restored a social preference, repopulating SCID mice with lymphocytes from *Ifng*$^{-/-}$ mice did not have such an effect (Extended Data Fig. 6a). Remarkably, a single injection of recombinant IFN-γ into the cerebrospinal fluid (CSF) of *Ifng*$^{-/-}$ mice was sufficient to restore their social preference when tested 24 h after injection (Fig. 2d) and reduce overall hyper-connectivity in the PFC (Extended Data Fig. 6b). To further validate a role for IFN-γ signalling in social behaviour, we tested mice deficient for the IFN-γ receptor (*Ifngr1*$^{-/-}$ mice) and found that they had a similar social deficit as observed in *Ifng*$^{-/-}$ mice (Extended Data Fig. 6c), which, as expected, was not rescued by injecting recombinant IFN-γ into the CSF (Extended Data Fig. 6d). On the basis of our previous demonstration of a role for IL-4 produced by meningeal T cells in spatial learning behaviour[1], we assessed whether deficiency in IL-4 would also result in social deficits. IL-4-deficient mice did not demonstrate social deficits; in fact, they spent more time investigating a novel mouse than a novel object compared with wild-type mice (Extended Data Fig. 6e).

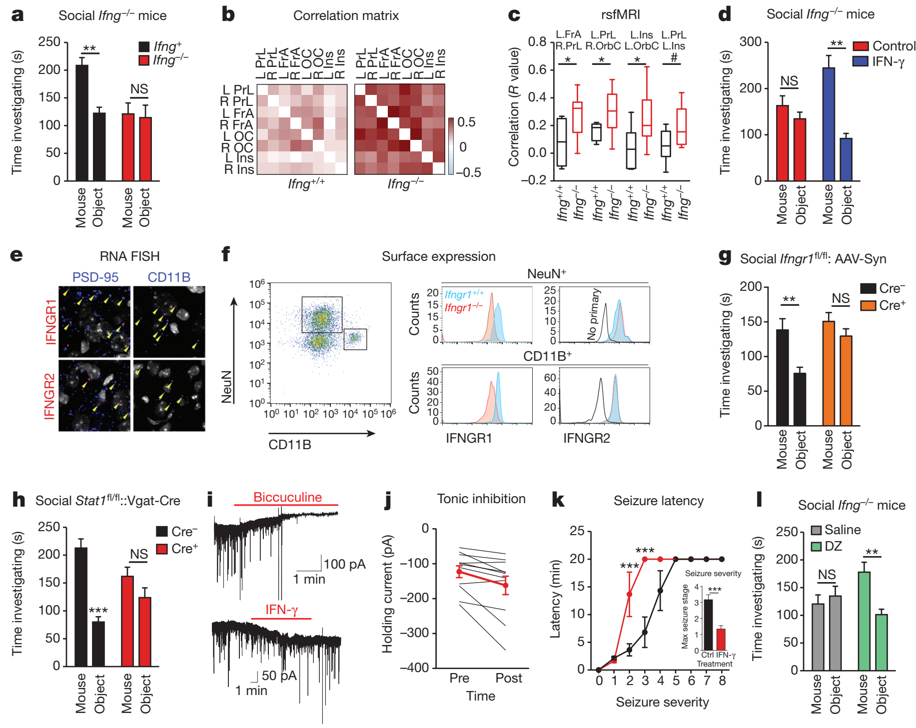

Figure 2 | IFN-γ supports proper neural connectivity and social behaviour. a, *Ifng*$^{-/-}$ mice exhibit social deficits ($n = 16$, 12 mice per group; ANOVA for genotype ($F_{1,52}) = 8.327$, $P < 0.01$; $**P < 0.01$, Sidak's post hoc test; pooled two independent experiments). **b**, Correlation matrix from *Ifng*$^{+/+}$ and *Ifng*$^{-/-}$ mice. **c**, Box and whisker plots of correlation values ($n = 8$ mice per group; $*P < 0.05$; # $P = 0.06$, *t*-test; repeated twice. **d**, A single CSF injection of IFN-γ (20 ng) was sufficient to rescue social deficits in *Ifng*$^{-/-}$ mice 24 h after injection ($n = 14$, 11 mice per group; ANOVA for interaction ($F_{1,46}) = 10.22$ $P < 0.01$; $***P < 0.001$, Sidak's post hoc test; pooled two independent experiments). **e**, Expression of IFN-γ receptor subunit mRNA by fluorescent *in situ* hybridization in slices from mouse PFC. RNA probes and corresponding colours: left, psd95-blue (neurons); right, CD11B-blue (microglia); top, IFNGR1-red; bottom, IFGR2-red. Yellow arrowheads denote co-localization. **f**, Expression of IFN-γ receptor subunit protein by flow cytometry. Cells were gated on Hoechst+/live/single then neurons and microglia were gated on NeuN and CD11B, respectively. *Ifngr1*$^{-/-}$ mice and no primary antibody for IFNGR2 were included as negative controls. **g**, Deleting *Ifngr1* from neurons in the PFC caused social deficits. *Ifngr1*$^{fl/fl}$ mice were injected with AAV-Syn-CRE–GFP into the PFC and tested for social behaviour 3 weeks after injection ($n = 11$, 12 mice per group; ANOVA for genotype ($F_{1,21}) = 10.62$, $P < 0.01$; $*P < 0.05$, Sidak's post hoc test; pooled three independent experiments). **h**, *Vgat*^{Cre}::*Stat1*$^{fl/fl}$ mice exhibit social deficits ($n = 10$, 11 mice per group; ANOVA for interaction ($F_{1,19}) = 10.30$, $P < 0.01$; $***P < 0.001$, Sidak's post hoc test; pooled three independent experiments). **i**, Layer II/III neurons in slices from wild-type mice are held under tonic GABAergic inhibition (top), which is blocked by the GABA-A receptor antagonist bicuculline. IFN-γ increases tonic GABAergic inhibitory current ($n = 11$ cells from four mice; bottom). **j**, Holding current before and during IFN-γ ($P = 0.01$ *t*-test). **k**, IFN-γ increased latency to reach each seizure stage ($n = 6$ mice per group; ANOVA with repeated measures <0.001; $***P < 0.001$, Sidak's post hoc test) and (inset) reduced the maximum severity of seizures ($***P < 0.001$, *t*-test; repeated twice). **l**, Diazepam rescued social deficits in *Ifng*$^{-/-}$ mice ($n = 12$ mice per group; ANOVA for interaction ($F_{1,22}) = 9.204 < 0.01$; $**P < 0.01$, Sidak's post hoc test; repeated twice). Data from the three-chamber test (**a**, **d**, **g**, **h**, **i**) were analysed by applying a two-way ANOVA for social behaviour and genotype/treatment, followed by a Sidak's post hoc test. Bars represent average mean times investigating ± s.e.m. All experiments were repeated at least once.

To determine which cell types in the brain respond to IFN-γ, we analysed mouse PFC for the expression of IFN-γ receptor subunits 1 and 2 and found that both neurons and microglia express mRNA and protein for R1 and R2 subunits of the IFN-γ receptor (Fig. 2e, f and Extended Data Fig. 7). Microglia are CNS-resident macrophages and are known to express the IFN-γ receptor[17]. However, genetically deleting STAT1, the signalling molecule downstream of the IFN-γ receptor, from microglia (and other cells of myeloid origin), did not disturb normal social preference (Extended Data Fig. 8). These results led us to focus on neuronal responses to IFN-γ as they relate to social behaviour.

To assess a role for IFN-γ in neuronal signalling, we deleted *Ifngr1* in PFC neurons via adeno-associated virus (AAV) delivery of Cre recombinase under the Synapsin I promoter (Extended Data Fig. 9). Attenuating IFN-γ signalling in PFC neurons was sufficient to alter mouse behaviour in a three-chamber social task and result in a lack of social preference (Fig. 2g), reinforcing the importance of IFN-γ signalling on neurons for social behaviour. Injecting recombinant IFN-γ into the CSF activated layer I neocortical neurons as assessed by c-fos immunoreactivity (Extended Data Fig. 10a, b). These neurons are almost entirely inhibitory[18], suggesting that IFN-γ may drive regional inhibition of circuits by directly activating layer I inhibitory neurons located in close proximity to the brain surface and CSF. To investigate mechanisms downstream of the IFN-γ receptor, we used *Vgat*^{cre}::*Stat1*$^{fl/fl}$ mice. Deletion of STAT1 from GABAergic inhibitory neurons was sufficient to induce deficits in social behaviour (Fig. 2h), suggesting that the IFN-γ may be signalling through inhibitory neurons.

To directly assess if IFN-γ can drive inhibitory tone in the PFC, we measured inhibitory currents in layer II/III pyramidal cells from acutely prepared brain slices from wild-type mice. In addition to receiving phasic inhibitory synaptic input, these cells are also held under a tonic GABAergic current that serves to hyperpolarize their resting membrane potential (Fig. 2i). Tonic GABAergic currents are extrasynaptic and can yield long-lasting network inhibition[19]. We observed that IFN-γ augmented tonic current (Fig. 2i, j and Extended Data Fig. 10c, d), suggestive of elevated levels of ambient GABA during application of IFN-γ. Deleting the IFN-γ receptor from inhibitory neurons (*Vgat*^{cre}::*Ifngr1*$^{fl/fl}$ mice) prevented IFN-γ from augmenting tonic inhibitory current (Extended Data Fig. 10c). Given that IFN-γ promotes inhibitory tone, we tested whether IFN-γ could prevent aberrant neural discharges by injecting IFN-γ into the CSF and then chemically inducing seizures with the GABA type A receptor antagonist pentylenetetrazole (PTZ). Mice injected with IFN-γ were less

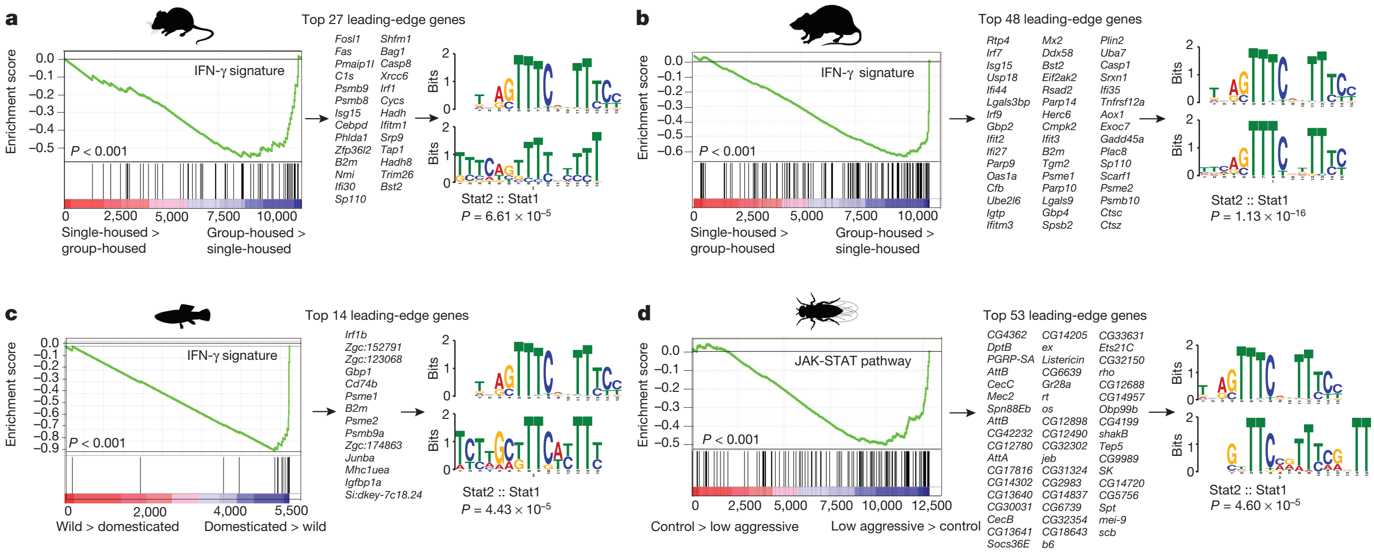

Figure 3 | Over-representation of IFN-γ transcriptional signature genes in social behaviour-associated brain transcriptomes of rat, mouse, zebrafish, and *Drosophila*. **a**–**c**, GSEA plots demonstrate the over-representation of IFN-γ transcriptional signatures (derived from Molecular Signature Database C2, GSE33057, or from ref. 30) in brain transcriptomes of (**a**) mice and (**b**) rats subjected to social or isolated housing and in brain transcriptomes of (**c**) domesticated zebrafish compared with a wild zebrafish strain. **d**, Over-representation of JAK/STAT pathway transcriptional signature genes (derived from GSE2828) in head transcriptomes of flies selected for low aggressive behaviour (behavioural readout for social behaviour in flies (see Methods section 'Meta-data analysis' for more details)). Genes are ranked into an ordered list according to their differential expression. The middle part of the plot is a bar code demonstrating the distribution of genes in the IFN-γ transcriptional signature gene set against the ranked list of genes. The list on the right shows the top genes in the leading-edge subset. Promoter regions of these genes were scanned for transcription factor binding sites using MEME suite. MEME output demonstrates significant STAT transcription factor binding site enrichment *in cis*-regulatory regions of leading-edge genes upregulated in a social context.

susceptible to PTZ-induced seizures: IFN-γ delayed seizure onset and lowered seizure severity (Fig. 2k). Further, to test whether over-excitation causes social deficits in IFN-γ-deficient mice, we treated $Ifng^{-/-}$ mice with diazepam to augment GABAergic transmission[20]. Diazepam successfully rescued social behaviour of $Ifng^{-/-}$ mice, similar to the effect observed with recombinant IFN-γ treatment (Fig. 2l), suggesting that social deficits, caused by a deficiency in IFN-γ, may arise from inadequate control of GABAergic inhibition by IFN-γ.

It is intriguing that IFN-γ, predominately thought of as an anti-pathogen cytokine, can play such a profound role in maintaining proper social function. Since social behaviour is crucial for the survival of a species and aggregation increases the likeliness of spreading pathogens, we hypothesized that there was co-evolutionary pressure to increase an anti-pathogen response as sociability increased, and that the IFN-γ pathway may have influenced this co-evolution. To test this hypothesis, we analysed metadata of publically available transcriptomes from multiple organisms including the rat, mouse, zebrafish, and fruit fly. Using GSEA, we determined that transcripts from social rodents (acutely group-housed) are enriched for an IFN-γ responsive gene signature (Fig. 3a, b and Supplementary Tables 3–7). Conversely, rodents that experienced social isolation demonstrated a dramatic loss of the IFN-γ responsive gene signature (Supplementary Tables 3–7). Zebrafish and flies showed a similar association between anti-pathogen and social responses (Fig. 3c, d). We observed that immune response programs were highly enriched in the brain transcriptomes of flies selected for low aggressiveness traits (a physiological correlate for socially experienced flies[21]; Fig. 3d and Supplementary Tables 3–7). We next analysed the promoters of these highly upregulated social genes and found them to be enriched for STAT1 transcription factor binding motifs (Fig. 3a–d). These data suggest that, even in the absence of infection, an IFN-γ gene signature is upregulated in aggregated organisms. This is consistent with an interaction between social behaviour and the anti-pathogen response, a dynamic that could be mediated by the IFN-γ pathway. Since low-aggressive flies upregulate genes in the JAK/STAT pathway (canonically downstream of IFN-γ receptors in higher species), yet lack IFN-γ or T cells, it is intriguing to speculate that T-cell-derived IFN-γ may have evolved in higher species to more efficiently regulate an anti-pathogen response during increased aggregation of individuals.

Our results reveal a novel role for meningeal immunity in regulating neural activity and social behaviour through IFN-γ. The role of immune molecules has been previously shown to control brain development and function[22–26], and a role for cytokines in influencing behaviour has been proposed, primarily in the context of sickness behaviour and pain[27,28]. These examples, however, have predominately focused on peripheral nerves and non-neuronal targets. Here we show that CNS neurons directly respond to IFN-γ derived from meningeal T cells to elevate tonic GABAergic inhibition and prevent aberrant hyper-excitability in the PFC. These data suggest that social deficits in numerous neurological and psychiatric disorders may result from impaired circuitry homeostasis derived from dysfunctional immunity. On the basis of our findings, it is also plausible that subtle homeostatic changes in meningeal immunity may also contribute to modulating neuronal circuits that are responsible for our everyday behaviours and personality. Given this communication between immunity and neuronal circuits[29], it is intriguing to hypothesize that these pathways might be vulnerable to manipulation by fast-evolving pathogens. Improved comprehension of these pathways could improve our understanding of the aetiology of neurodevelopmental and neuropsychiatric disorders associated with maternal infections and/or aberrant inflammation and may result in the development of new therapeutic targets.

Online Content Methods, along with any additional Extended Data display items and Source Data, are available in the online version of the paper; references unique to these sections appear only in the online paper.

Received 30 December 2015; accepted 3 June 2016.
Published online 13 July 2016.

1. Derecki, N. C. *et al.* Regulation of learning and memory by meningeal immunity: a key role for IL-4. *J. Exp. Med.* **207,** 1067–1080 (2010).
2. Bourke, A. F. Hamilton's rule and the causes of social evolution. *Phil. Trans. R. Soc. B* **369,** 20130362 (2014).
3. Cacioppo, S., Capitanio, J. P. & Cacioppo, J. T. Toward a neurology of loneliness. *Psychol. Bull.* **140,** 1464–1504 (2014).

4. Kennedy, D. P. & Adolphs, R. The social brain in psychiatric and neurological disorders. *Trends Cogn. Sci.* **16,** 559–572 (2012).
5. Ashwood, P. *et al.* Altered T cell responses in children with autism. *Brain Behav. Immun.* **25,** 840–849 (2011).
6. Gupta, S., Aggarwal, S., Rashanravan, B. & Lee, T. Th1- and Th2-like cytokines in $CD4^+$ and $CD8^+$ T cells in autism. *J. Neuroimmunol.* **85,** 106–109 (1998).
7. Waisman, A., Liblau, R. S. & Becher, B. Innate and adaptive immune responses in the CNS. *Lancet Neurol.* **14,** 945–955 (2015).
8. Moy, S. S. *et al.* Sociability and preference for social novelty in five inbred strains: an approach to assess autistic-like behavior in mice. *Genes Brain Behav.* **3,** 287–302 (2004).
9. Silverman, J. L., Yang, M., Lord, C. & Crawley, J. N. Behavioural phenotyping assays for mouse models of autism. *Nature Rev. Neurosci.* **11,** 490–502 (2010).
10. Nelson, S. B. & Valakh, V. Excitatory/inhibitory balance and circuit homeostasis in autism spectrum disorders. *Neuron* **87,** 684–698 (2015).
11. Supekar, K. *et al.* Brain hyperconnectivity in children with autism and its links to social deficits. *Cell Reports* **5,** 738–747 (2013).
12. Zhan, Y. *et al.* Deficient neuron-microglia signaling results in impaired functional brain connectivity and social behavior. *Nature Neurosci.* **17,** 400–406 (2014).
13. Shen, H. H. Core concept: resting-state connectivity. *Proc. Natl Acad. Sci. USA* **112,** 14115–14116 (2015).
14. Brynskikh, A., Warren, T., Zhu, J. & Kipnis, J. Adaptive immunity affects learning behavior in mice. *Brain Behav. Immun.* **22,** 861–869 (2008).
15. Yednock, T. A. *et al.* Prevention of experimental autoimmune encephalomyelitis by antibodies against $\alpha4\beta1$ integrin. *Nature* **356,** 63–66 (1992).
16. Kunis, G. *et al.* IFN-γ-dependent activation of the brain's choroid plexus for CNS immune surveillance and repair. *Brain* **136,** 3427–3440 (2013).
17. Tsuda, M. *et al.* IFN-γ receptor signaling mediates spinal microglia activation driving neuropathic pain. *Proc. Natl Acad. Sci. USA* **106,** 8032–8037 (2009).
18. Prieto, J. J., Peterson, B. A. & Winer, J. A. Morphology and spatial distribution of GABAergic neurons in cat primary auditory cortex (AI). *J. Comp. Neurol.* **344,** 349–382 (1994).
19. Oláh, S. *et al.* Regulation of cortical microcircuits by unitary GABA-mediated volume transmission. *Nature* **461,** 1278–1281 (2009).
20. Han, S., Tai, C., Jones, C. J., Scheuer, T. & Catterall, W. A. Enhancement of inhibitory neurotransmission by GABAA receptors having α2,3-subunits ameliorates behavioral deficits in a mouse model of autism. *Neuron* **81,** 1282–1289 (2014).
21. Wang, L., Dankert, H., Perona, P. & Anderson, D. J. A common genetic target for environmental and heritable influences on aggressiveness in *Drosophila*. *Proc. Natl Acad. Sci. USA* **105,** 5657–5663 (2008).
22. Datwani, A. *et al.* Classical MHCI molecules regulate retinogeniculate refinement and limit ocular dominance plasticity. *Neuron* **64,** 463–470 (2009).
23. Djurisic, M. *et al.* PirB regulates a structural substrate for cortical plasticity. *Proc. Natl Acad. Sci. USA* **110,** 20771–20776 (2013).
24. Steinman, L. Inflammatory cytokines at the summits of pathological signal cascades in brain diseases. *Sci. Signal.* **6,** pe3 (2013).
25. Smith, L. K. *et al.* β2-microglobulin is a systemic pro-aging factor that impairs cognitive function and neurogenesis. *Nature Med.* **21,** 932–937 (2015).
26. Baruch, K. *et al.* Aging-induced type I interferon response at the choroid plexus negatively affects brain function. *Science* **346,** 89–93 (2014).
27. McCusker, R. H. & Kelley, K. W. Immune-neural connections: how the immune system's response to infectious agents influences behavior. *J. Exp. Biol.* **216,** 84–98 (2013).
28. Scholz, J. & Woolf, C. J. The neuropathic pain triad: neurons, immune cells and glia. *Nature Neurosci.* **10,** 1361–1368 (2007).
29. Bhat, R. *et al.* Inhibitory role for GABA in autoimmune inflammation. *Proc. Natl Acad. Sci. USA* **107,** 2580–2585 (2010).
30. López-Muñoz, A. *et al.* Evolutionary conserved pro-inflammatory and antigen presentation functions of zebrafish IFNγ revealed by transcriptomic and functional analysis. *Mol. Immunol.* **48,** 1073–1083 (2011).

Supplementary Information is available in the online version of the paper.

Acknowledgements This work was supported by grants from the National Institutes of Health (AG034113 and NS081026 to J.K.), (T32-AI007496 to A.J.F.), and the Hartwell Foundation (to A.J.F.). We thank all the members of the Center for Brain Immunology and Glia (BIG) for their comments during numerous discussions of this manuscript. We also thank J. Roy for his expertise in MRI, B. Tomlin and N. Al Hamadani for animal care, as well as S. Rich, S. Onengut-Gumuscu, and E. Farber for sequencing the cDNA library.

Author Contributions A.J.F. and J.K. designed and performed experiments and wrote the manuscript. Y.X. and V.L. provided intellectual contributions and analysed all transcriptome data. S.D.T., Z.W., S.N.P., and H.C. analysed transcriptome data. N.T. and C.C.O. analysed BOLD data. R.L.M., W.B., I.S., S.P.G., M.M.S. and M.P.B. provided intellectual contributions and assisted with experimental procedures. M.P.B. performed all electrophysiological experiments. K.S.L. critically reviewed the manuscript.

Author Information RNA-seq data have been deposited in the Gene Expression Omnibus under accession number GSE81783. Reprints and permissions information is available at www.nature.com/reprints. The authors declare no competing financial interests. Readers are welcome to comment on the online version of the paper. Correspondence and requests for materials should be addressed to A.J.F. (afiliano@virginia.edu), V.L. (Vladimir.Litvak@umassmed.edu) or J.K. (kipnis@virginia.edu).

Reviewer Information *Nature* thanks M. Kano, L. Steinman and the other anonymous reviewer(s) for their contribution to the peer review of this work.

METHODS

Mice. All mice (C57BL/6) were either bred in-house or purchased from the Jackson Laboratory. For each individual experiment, the control mice were obtained from the same institution as test mice. In the case that mice were purchased, they were maintained for at least 1 week to habituate before manipulation/experimentation. When possible, mice used for experiments were littermates. These include all electrophysiology experiments, all cohorts using *Stat1*$^{fl/fl}$ mice, experiments analysing induced seizures, experiments counting c-fos^{+} neurons, and experiments using *Il4*$^{-/-}$ mice. Experiments assessing the social behaviour of SCID mice using the three-chamber assay included mice bred in-house and mice purchased from the Jackson Laboratory. All other experiments used mice purchased from the Jackson Laboratory. Experimental groups were blinded and randomly assigned before the start of experimentation and remained blinded until all data were collected. Mice were housed under standard 12 h light/dark cycle conditions in rooms equipped with control for temperature and humidity. Unless stated otherwise, male mice were tested at 8–10 weeks of age. Sample sizes were chosen on the basis of a power analysis using estimates from previously published experiments. All experiments were approved by the Institutional Animal Care and Use Committee of the University of Virginia.

Behaviour. For cohorts tested with multiple behavioural assays, the elevated plus-maze was performed first and then followed by the open field before any other assay. Before all experiments, mice were transported to the behaviour room and given 1 h to habituate. All behavioural testing was conducted during daylight hours.

Elevated plus-maze. Mice were placed into the centre hub and allowed to explore the plus-maze for 10 min. Video tracking software (CleverSys) was used to quantify time spent in the open arms.

Open field. Mice were placed into the open field (35 cm × 35 cm) and allowed to explore for 15 min. Total distance and time spent in the centre (23 cm × 23 cm) were quantified using video tracking software (CleverSys).

Rotarod. Mice were placed on an accelerating rotarod (MedAssociates) that accelerated from 4.0 to 40 rpm over 5 min. Infrared beams were used to quantify the latency of a mouse to fall of the rod. Mice were given six trials with a 4-h break between trials 3 and 4.

Three-chamber sociability assay. The three-chamber sociability test was conducted as previously described[31]. Briefly, mice were transported to the testing room and habituated for at least 1 h. The room was maintained in dim light and a white noise generator used to mitigate any unforeseen noises. Test boxes were fabricated, in-house, by a machine shop. Test mice were placed in the centre chamber with the two outer chambers containing empty wire cages (Spectrum Diversified Designs) and allowed to explore for 10 min (habituation phase). After the habituation phase, mice were returned to the centre chamber. A novel mouse (an 8- to 10-week-old male C57BL/6J, ∼18–22g) was placed under one cup and an object placed under the other. Before testing, the novel mouse was habituated to the cup by being placed under the cup for 10 min, three times a day for 5 days. Mice were allowed to explore for an additional 10 min (social phase). A video tracking system (CleverSys) was used to quantify the time spent around each target. For three-chamber experiments comparing social behaviour between wild-type and SCID mice, data collected using males and females were combined because no significant effects were found between genders. When females were tested, juvenile C57BL/6J male (approximately 4 weeks old) mice were used as novel demonstrators.

Novel/social environment. Mice were single housed and maintained unmanipulated for 5 days, then placed in a novel/social environment with a mouse (opposite sex and identical *scid* genotype) under video surveillance as previously described[31]. After 2 h, mice were euthanized and prepared for immunohistochemistry as described below. The time spent interacting was measured by a blinded observer for 5 min at the 30, 60, and 90 min post-introduction time points.

Resting-state fMRI. The protocol for rsfMRI was adapted from Zhan *et al.*[12]. Mice were maintained under light anaesthesia with (1–1.25%) isoflurane and images were acquired on a 7.0 T MRI Clinscan system (Bruker, Etlingen, Germany) using a 30-mm inner-diameter mouse whole-body radiofrequency coil. High-resolution structural images were acquired by collecting 16 0.7-mm-thick coronal slices using TR/TE 5,500/65 ms and an 180° flip angle. A BOLD rsfMRI time series of 16 0.7-mm-thick coronal slices was collected using TR/TE 4,000/17 ms and a 60° flip angle. For analysis, a structural template[32] was custom labelled using *The Mouse Brain* by Paxinos and Franklin as reference (Extended Data Fig. 3). The non-rigid transformation between the template and each individual mouse was estimated using the open source Advanced Normalization Tools (ANTs) package[33] that was then used to propagate the regional labels to each subject. Cleaning of the bold fMRI data was performed using tools available in ANTsR[34]—a statistical and visualization interface between ANTs and the R statistical project. fMRI preprocessing consisted of motion correction[35], bandpass filtering (frequency = 0.002–0.1), and CompCor estimation[36]. The correlation matrix was determined from the clean fMRI data using the regions labels. To determine whether the functional connectivity between sample groups was significantly different, we tested for the equality of their corresponding correlation matrices. First, an aggregate correlation matrix was constructed for each group by calculating the median value for each connection, and then the aggregate matrices were compared using the Jennrich test[37], as implemented in the cortest.jennrich function in the R psych package. To create a functional connectivity network for a sample group, a correlation threshold was applied to the connections between regions of interest. If a connection strength was above the threshold, it was kept as an edge in the network, otherwise it was discarded. When comparing networks from multiple sample groups, the threshold was determined by calculating the maximum threshold that left one of the networks connected (that is, it was possible to reach any node in the network from any other node).

Immunohistochemistry. Mice were killed under Euthasol then transcardially perfused with PBS with heparin. Brains were removed and drop fixed in 4% PFA for 48 h. After fixation, brains were washed with PBS, cryoprotected with 30% sucrose, then frozen in O.C.T. compound (Sakura Finetek) and sliced (40 μM) with a cryostat (Leica). Free-floating sections were maintained in PBS + Azide (0.02%) until further processing. Immunohistochemistry for c-fos (1:1,000 dilution; Millipore) on free-floating sections was performed as previously described[38].

Depletion of meningeal T cells. A rat monoclonal antibody to murine VLA4 (clone PS/2) was affinity purified from hybridoma supernatants and was used with the permission of K. Ley (La Jolla Institute of Allergy and Immunology, San Diego, CA). Mice were given two separate injections (intraperitoneal; 0.2 mg in saline per mouse), 4 days apart, of either anti-VLA4 or rat anti-HRP for control (clone HRPN; BioXcell), then tested 24 h after final injection.

Dissection of meninges and flow cytometry. Meninges were dissected as previously described[1]. Briefly, after killing and perfusing, skulls caps were removed by making an incision along the parietal and squamosal bones. The meninges were removed from the internal side of the skull cap and gently pressed through a 70 μm nylon mesh cell strainer with sterile plastic plunger (BD Biosciences) to isolate a single cell suspension. Cells were then centrifuged at 300*g* at 4 °C for 10 min, resuspended in cold FACS buffer (pH 7.4; 0.1 M PBS; 1 mM EDTA; 1% BSA), and stained for extracellular markers using the following antibodies at a 1:200 dilution: CD45 PerCP-Cyanine5.5 (eBioscience), TCR BV510 (BD Bioscience), CD4 FITC (eBioscience), L/D Zombie NIR (BioLegend). To measure intracellular IFN-γ, single-cell isolates from meninges were maintained in T-cell isolation buffer (RPMI + 2% FBS, 2 mM L-glutamine, 1 mM sodium pyruvate, 10 mM HEPES, 1× non-essential amino acids, and 1× Antibiotic-Antimycotic (Thermo Fisher) and stimulated with PMA/ionomycin (Cell Stimulation Cocktail – eBioscience) + 10 μg/ml brefeldin A at 37 °C before extracellular staining as stated above. Cells were then permeabilized with Cytofix/Cytoperm (BD Biosciences) and stained with IFN-γ APC (eBioscience; clone XMG1.2).

To measure expression of IFN-γ receptors, brains were removed and placed in Neurobasal media containing 10% fetal bovine serum. The meninges were removed from the brain and the frontal cortex was micro-dissected under a dissection microscope. Using a 2 ml dounce homogenizer, brains were homogenized in Neurobasal media with 50 U/ml Dnase I. The homogenate was passed through a 70 μm nylon filter and washed with cold FACS buffer. IFNGR were labelled with anti-IFNGR1 Biotin (BD Pharmingen; GR20) or rabbit anti-IFNGR2 (Santa Cruz; M-20). Cells were washed with FACS buffer and incubated with FITC conjugated streptavidin or 488 conjugated chicken anti-rabbit. Next, cells were washed again then incubated with CD11B PE-Cyanine7 (eBioscience), L/D Zombie NIR (BioLegend), and Hoechst for 45 min. Cells were washed, then permeabilized and fixed with Cytofix/Cytoperm (BD Biosciences). After another wash with permeabilization wash buffer (PBS with 10% fetal bovine serum, 1% sodium azide, and 1% saponin; pH 7.4), cells were incubated overnight with NeuN PE (Millipore). Cells underwent a final wash and again passed through a 70 μm nylon filter. Samples were run on a flow cytometer Gallios (Beckman Coulter) then analysed using FlowJo software (Treestar).

SCID repopulation. SCID mice were repopulated with cells from spleen and lymph nodes (axillary, brachial, cervical, inguinal, and lumbar). Spleen and lymph nodes were collected from a 3- to 4-week-old donor and passed through a 70 μm nylon mesh cell strainer with a sterile plastic plunger. ACK buffer was used to lyse red blood cells before washing with saline. Cells were counted on an automated cell counter (Nexcelom) and injected (intravenously) at 5×10^6 cells in 250 μl of saline (control mice were injected with 250 μl of saline only). For injections, the animal technician was blinded to the genotype of the mice and the content of the injection. Thus, all groups were handled identically. Mice aged 3–4 weeks were carefully placed into a tail vein injection platform. Their tails were briefly warmed using a heating pad and saline with cells or saline alone was slowly injected into the tail vein using a 28-gauge needle. After the injection, mice were returned to their home cage.

IFN-γ injections. Mice were anaesthetized with a ketamine/xylazine (ketamine (100 mg/kg) and xylazine (10 mg/kg)) injection (intraperitoneal) or isoflurane (2%), then placed into a stereotaxic frame with the head at an approximately 45° angle. The skin above the cisterna magna was cleaned and sanitized before a 1 cm incision was made. The underlying muscles were separated with forceps, retracted, and a small Hamilton syringe (33-gauge) was used to slowly inject 1 μl of saline or IFN-γ (20 ng; eBioscience) into the cisterna magna. After injection the syringe was held in place for 5 min to avoid back-flow of CSF. After the syringe was removed, muscles were put back in place and skin was sutured. Mice were placed on a heating pad and given ketoprofen and baytril for recovery.

Induced seizures. IFN-γ was injected into the CSF through the cisterna magna as described above, 24 h before inducing seizures. Control mice were injected with the same volume of saline. To induce seizures, mice were injected with PTZ (40 mg/kg; intraperitoneally). After injection, mice were placed into an empty housing cage and recorded for video analysis. Seizures were analysed by a blinded observer using a behaviour scoring system previously published[39].

Diazepam treatment. Diazepam (1.25 mg/kg) was delivered intraperitoneally for 30 min before testing for social behaviour.

Fluorescence *in situ* hybridization. Mice were euthanized then transcardially perused with PBS with heparin followed by 4% PFA. Brains were then removed and drop fixed in 4% PFA for 24 h, frozen in OCT, and 12 μM sections were cut on a cryostat. Fluorescence *in situ* hybridization was performed using RNA ISH tissue assay kits (Affymetrix) following the manufacturer's protocol. Tissues were treated with protease for 20 min at 40 °C. Images at 63× magnification were acquired on a Leica TCS SP8 confocal system (Leica Microsystems) using LAS AF Software.

AAV delivery. AAV1.hSyn.HI.eGFP–Cre.WPRE.SV40 and AAV1.hSyn.eGFP.WPRE.bGH were purchased from Penn Vector Core. *Ifngr1*$^{fl/fl}$ mice were purchased from the Jackson Laboratory. After 1 week of habituation, mice were anaesthetized with 2% isoflurane and injected bilaterally with 2×10^{10} genome copies of AAV virus in 1 μl at stereotaxic coordinates +2.5 μm bregma A/P, 0.25 μm lateral, 1.25 μm deep.

Measuring inhibitory currents. Visualized whole-cell patch-clamp recordings were performed on layer II/III prefrontal cortical neurons prepared from acute brain slices (adult) using the protective recovery method[40]. Recordings were performed in 34 °C artificial cerebrospinal fluid (ACSF) containing (in mM) 131.5 NaCl, 25 $NaHCO_3$, 12 D-glucose, 2.5 KCl, 1.25 NaH_2PO_4, 2 $CaCl_2$, and 1 $MgCl_2$. ACSF also contained 3 mM kynurenic acid to block synaptic excitation and 2.5 mM NO-711 to enhance tonic inhibition[41]. Slices were incubated in this ACSF for 5–10 min before placement in the recording chamber. The patch pipette solution with elevated chloride contained (in mM) 140 CsCl, 4 NaCl, 1 $MgCl_2$, 10 HEPES, 0.05 EGTA, 2 Mg-ATP, and 0.4 Mg-GTP[41]. Once recordings equilibrated, baseline holding current in ACSF was measured for 3.5 min, after which ACSF containing IFN-γ (20 pg/ml) was applied for 8.5 min and then washed. Data presented show the mean holding current during the last minute of control (ACSF) and drug (ACSF + IFN-γ) conditions.

RNA isolation and sequencing. Eight-week-old male mice were purchased from the Jackson Laboratory and housed in standard housing boxes with either four mice per cage or isolated for 6 days. Mice were euthanized as described above and the PFC was microdissected under a dissection microscope. RNA was isolated using an RNAeasy mini kit (Qiagen) and a cDNA library was generated with a TruSeq Stranded mRNA Library Prep Kit (Illumina) with Agencourt AMPure XP beads for PCR cleanup. Samples were loaded onto a NextSeq 500 High-output 75 cycle cartridge and sequenced on a NextSeq 500 (Illumina).

Transcriptome analysis. Raw FASTQ sequencing reads were chastity filtered to remove clusters having outlying intensity corresponding to bases other than the called base. Filtered reads were assessed for quality using FastQC[42]. Reads were splice-aware aligned to the UCSC mm9 genome using STAR[43], and reads overlapping UCSC mm9 gene regions were counted using featureCounts[44]. The DESeq2 Bioconductor package[45] in the R statistical computing environment[46] was used for normalizing count data, performing exploratory data analysis, estimating dispersion, and fitting a negative binomial model for each gene comparing the expression from the PFC of mice in a social environment versus isolation. After obtaining a list of differentially expressed genes, log(fold changes), and *P* values, Benjamini–Hochberg false discovery rate procedure was used to correct *P* values for multiple testing. A gene set enrichment analysis (GSEA) algorithm[47] was applied to identify the enrichment of transcriptional signatures and molecular pathways in PFC transcriptomes of mice exposed to group and isolation housing conditions. Four thousand seven hundred and twenty-six publicly available transcriptional signatures were obtained from the molecular Signature Database C2 version 4.0, and GSEA was used to examine the distribution of these curated gene sets in lists of genes ordered according to differential expression between group and isolation housing conditions. We analysed statistics by evaluating nominal *P* value and normalized enrichment score (NES) on the basis of 1,000 random sample permutations.

Meta-data analysis. The custom-made IFN-γ and pathogen-induced transcriptional signatures (Supplementary Table 2) were generated by retrieving genes upregulated at least twofold following IFN-γ stimulation or pathogen infection. All custom signatures were derived from publicly available transcriptomes downloaded from Gene Expression Omnibus (GEO). Specifically, mammalian IFN-γ transcriptional signatures were derived from transcriptomes GSE33057, GSE19182, GSE36287, GSE9659, GSE1432, and GSE6353. Zebrafish IFN-γ transcriptional signature was used as described[48]. *Drosophila* pathogen-induced JAK/STAT-dependent transcriptional signatures were derived from transcriptomes GSE54833 and GSE2828.

A GSEA algorithm was applied to identify the enrichment of custom-made mammalian IFN-γ transcriptional signatures in the publicly available brain cortex transcriptomes of mice and rats exposed to social aggregation, sleep deprivation, stress, psychostimulants (DOI, cocaine, amphetamine, methamphetamine, methylphenidate, caffeine, nicotine, and modafinil), antipsychotics (olanzapine, haloperidol, and risperidone), anticonvulsants (levetiracetam, phenytoin, ethosuximide, and oxcarbazepine), and antidepressants (iproniazid, moclobemide, paroxetine, and phenelzine). In total, 41 transcriptomes were analysed as indicated in Supplementary Table 2. We analysed statistics by evaluating nominal *P* value and NES on the basis of 1,000 random sample permutations.

Zebrafish are social fish that aggregate into shoals[49–52]. Various zebrafish strains differ in their preference for social interaction and novelty, resembling the phenotypic variation of inbred mouse strains[8,53]. Notably, domesticated zebrafish strains demonstrate higher social interaction and social novelty preference[54–56] compared with wild zebrafish strains. Therefore, a GSEA algorithm was used to identify the enrichment of zebrafish IFN-γ transcriptional signature in the publicly available whole-brain transcriptomic profiles of behaviourally distinct strains of domesticated and wild zebrafish (Supplementary Table 7). The brain transcriptomic profiles of domesticated (Scientific Hatcheries (SH) and Transgenic Mosaic 1 (TM1)) and wild (Nadia, Gaighata) zebrafish strains were derived from publicly available transcriptome data set GSE38729. We analysed statistics by evaluating nominal *P* value and NES on the basis of 1,000 random gene set permutations.

Social interactions in *Drosophila melanogaster* flies play an important role in courtship, mating, egg-laying, circadian timing, food search, and even lifespan determination[57–62]. Notably, a number of studies have demonstrated that social isolation leads to an aggressive behaviour in *Drosophila* flies, whereas group housing suppresses the aggressiveness[21,63,64]. Therefore, we employed a GSEA algorithm to identify the enrichment of JAK/STAT-dependent transcriptional signatures in the publicly available brain transcriptomes of *Drosophila* populations that were socially-induced or genetically-selected for low-aggressive (that is, social) behaviour (Supplementary Table 7). The transcriptomic profiles were derived from publicly available transcriptome data sets GSE5404 and GSE6994. We analysed statistics by evaluating nominal *P* value and NES on the basis of 1,000 random gene set permutations.

Promoter motif analysis. A GSEA algorithm was used to identify genes that are differentially expressed in brain transcriptomes of mice and rats exposed to social aggregation, domesticated zebrafish strains, and low-aggressive *Drosophila melanogaster* populations, compared with their control counterparts. High-scoring differentially expressed 'leading-edge' social genes were selected on the basis of their presence in the IFN-γ and pathogen-induced transcriptional signatures. Specifically, as shown in Fig. 3, we have identified 31, 48, 14, and 53 leading-edge genes in brain transcriptomes of mice and rats exposed to social aggregation, domesticated Zebrafish strain, and low-aggressive *Drosophila melanogaster* population, respectively. We next extracted promoter sequences of 200 bp upstream of transcription start sites of these 'leading-edge' genes using UCSC Genome Browser (https://genome.ucsc.edu/). The MEME suite was then used to discover overrepresented transcription factor binding motifs, as described[65]. MEME parameters used were any number of motif repetitions per sequence, with a minimum motif width of 5 bases and maximum motif width of 15 bases. The discovered MEME motifs were compared using Tomtom analysis. In this case, the Tomtom motif similarity analysis ranks the MEME motif most similar to the vertebrates *in vivo* and *in silico*. The statistics were determined using Euclidean distance.

Circos plot. A GSEA algorithm was applied to identify the enrichment of IFN-γ, IL-4/IL-13, IL-17, and IL-10/TGF-β signalling pathways in the brain transcriptomes of rodent animals exposed to social aggregation, stress, psychostimulants, antipsychotics, and antidepressants. All custom signatures were derived from publicly available rodent transcriptomes downloaded from Gene Expression Omnibus. Statistical significance of GSEA results was assessed using 1,000 sample permutations. A NES greater than 1.5 and a nominal *P* value less than 0.05 was used to determined pairwise transcriptome connectivity. A Circos graph was generated using Circos package 0.68.12 (ref. 66).

Statistics. Data were analysed using the statistical methods stated in each figure legend. For the three-chamber assay, a two-way ANOVA was performed using genotype/treatment and sociability as main effects, followed by applying a Sidak's post hoc comparison to assess if the group had a significant social preference. Before running an ANOVA, an equality of variance was determined by using a Brown–Forsythe test. Bars display the means, and error bars represent ranges of the standard error of the mean. For rsfMRI, data were analysed using a one-way ANOVA followed by a post hoc Tukey's test. The box and whisker plots extend to the 25th and 75th percentiles and the centre line indicates the mean. The whiskers represent the min and max data points. Data for seizure latency were analysed using a two-way ANOVA with repeated measures followed by Sidak's post hoc test. Additional details of statistical analysis are supplied in Supplementary Table 8.

31. Filiano, A. J. *et al.* Dissociation of frontotemporal dementia-related deficits and neuroinflammation in progranulin haploinsufficient mice. *J. Neurosci.* **33,** 5352–5361 (2013).
32. Johnson, G. A. *et al.* Waxholm space: an image-based reference for coordinating mouse brain research. *Neuroimage* **53,** 365–372 (2010).
33. Avants, B. B. *et al.* A reproducible evaluation of ANTs similarity metric performance in brain image registration. *Neuroimage* **54,** 2033–2044 (2011).
34. Avants, B. B. *et al.* The pediatric template of brain perfusion. *Sci. Data* **2,** 150003 (2015).
35. Power, J. D., Barnes, K. A., Snyder, A. Z., Schlaggar, B. L. & Petersen, S. E. Spurious but systematic correlations in functional connectivity MRI networks arise from subject motion. *Neuroimage* **59,** 2142–2154 (2012).
36. Behzadi, Y., Restom, K., Liau, J. & Liu, T. T. A component based noise correction method (CompCor) for BOLD and perfusion based fMRI. *Neuroimage* **37,** 90–101 (2007).
37. Jennrich, R. I. An asymptotic χ^2 test for the equality of two correlation matrices. *J. Am. Stat. Assoc.* **65,** 904–912 (1970).
38. Palop, J. J., Mucke, L. & Roberson, E. D. Quantifying biomarkers of cognitive dysfunction and neuronal network hyperexcitability in mouse models of Alzheimer's disease: depletion of calcium-dependent proteins and inhibitory hippocampal remodeling. *Methods Mol. Biol.* **670,** 245–262 (2011).
39. Li, Z., Hall, A. M., Kelinske, M. & Roberson, E. D. Seizure resistance without parkinsonism in aged mice after tau reduction. *Neurobiol. Aging* **35,** 2617–2624 (2014).
40. Ting, J. T., Daigle, T. L., Chen, Q. & Feng, G. Acute brain slice methods for adult and aging animals: application of targeted patch clamp analysis and optogenetics. *Methods Mol. Biol.* **1183,** 221–242 (2014).
41. Nusser, Z. & Mody, I. Selective modulation of tonic and phasic inhibitions in dentate gyrus granule cells. *J. Neurophysiol.* **87,** 2624–2628 (2002).
42. Andrews, S. FastQC: a quality control tool for high throughput sequence data (2010).
43. Dobin, A. *et al.* STAR: ultrafast universal RNA-seq aligner. *Bioinformatics* **29,** 15–21 (2013).
44. Liao, Y., Smyth, G. K. & Shi, W. featureCounts: an efficient general purpose program for assigning sequence reads to genomic features. *Bioinformatics* **30,** 923–930 (2014).
45. Love, M. I., Huber, W. & Anders, S. Moderated estimation of fold change and dispersion for RNA-seq data with DESeq2. *Genome Biol.* **15,** 550 (2014).
46. R Core Team. R: a language and environment for statistical computing (R Foundation for Statistical Computing, 2010).
47. Subramanian, A. *et al.* Gene set enrichment analysis: a knowledge-based approach for interpreting genome-wide expression profiles. *Proc. Natl Acad. Sci. USA* **102,** 15545–15550 (2005).
48. López-Muñoz, A., Roca, F. J., Meseguer, J. & Mulero, V. New insights into the evolution of IFNs: zebrafish group II IFNs induce a rapid and transient expression of IFN-dependent genes and display powerful antiviral activities. *J. Immunol.* **182,** 3440–3449 (2009).
49. Engeszer, R. E., Patterson, L. B., Rao, A. A. & Parichy, D. M. Zebrafish in the wild: a review of natural history and new notes from the field. *Zebrafish* **4,** 21–40 (2007).
50. Krause, J., Butlin, R. K., Peuhkuri, N. & Pritchard, V. L. The social organization of fish shoals: a test of the predictive power of laboratory experiments for the field. *Biol. Rev. Camb. Phil. Soc.* **75,** 477–501 (2000).
51. Miller, N. & Gerlai, R. Quantification of shoaling behaviour in zebrafish (*Danio rerio*). *Behav. Brain Res.* **184,** 157–166 (2007).
52. Saverino, C. & Gerlai, R. The social zebrafish: behavioral responses to conspecific, heterospecific, and computer animated fish. *Behav. Brain Res.* **191,** 77–87 (2008).
53. Barba-Escobedo, P. A. & Gould, G. G. Visual social preferences of lone zebrafish in a novel environment: strain and anxiolytic effects. *Genes Brain Behav.* **11,** 366–373 (2012).
54. Moretz, J. A., Martins, E. P. & Robison, B. D. Behavioral syndromes and the evolution of correlated behavior in zebrafish. *Behav. Ecol.* **18,** 556–562 (2007).
55. Wright, D., Butlin, R. K. & Carlborg, O. Epistatic regulation of behavioural and morphological traits in the zebrafish (*Danio rerio*). *Behav. Genet.* **36,** 914–922 (2006).
56. Zala, S. M., Määttänen, I. & Penn, D. J. Different social-learning strategies in wild and domesticated zebrafish, *Danio rerio*. *Anim. Behav.* **83,** 1519–1525 (2012).
57. Levine, J. D., Funes, P., Dowse, H. B. & Hall, J. C. Resetting the circadian clock by social experience in *Drosophila melanogaster*. *Science* **298,** 2010–2012 (2002).
58. Mery, F. *et al.* Public versus personal information for mate copying in an invertebrate. *Curr. Biol.* **19,** 730–734 (2009).
59. Ruan, H. & Wu, C. F. Social interaction-mediated lifespan extension of *Drosophila* Cu/Zn superoxide dismutase mutants. *Proc. Natl Acad. Sci. USA* **105,** 7506–7510 (2008).
60. Sarin, S. & Dukas, R. Social learning about egg-laying substrates in fruitflies. *Proc. R. Soc. B* **276,** 4323–4328 (2009).
61. Sokolowski, M. B. Social interactions in "simple" model systems. *Neuron* **65,** 780–794 (2010).
62. Wertheim, B., van Baalen, E. J., Dicke, M. & Vet, L. E. Pheromone-mediated aggregation in nonsocial arthropods: an evolutionary ecological perspective. *Annu. Rev. Entomol.* **50,** 321–346 (2005).
63. Hoffmann, A. A. A laboratory study of male territoriality in the sibling species *Drosophila melanogaster* and *D. simulans*. *Anim. Behav.* **35,** 807–818 (1987).
64. Kamyshev, N. G. *et al.* Plasticity of social behavior in *Drosophila*. *Neurosci. Behav. Physiol.* **32,** 401–408 (2002).
65. Bailey, T. L. *et al.* MEME SUITE: tools for motif discovery and searching. *Nucleic Acids Res.* **37,** W202–W208 (2009).
66. Krzywinski, M. *et al.* Circos: an information aesthetic for comparative genomics. *Genome Res.* **19,** 1639–1645 (2009).

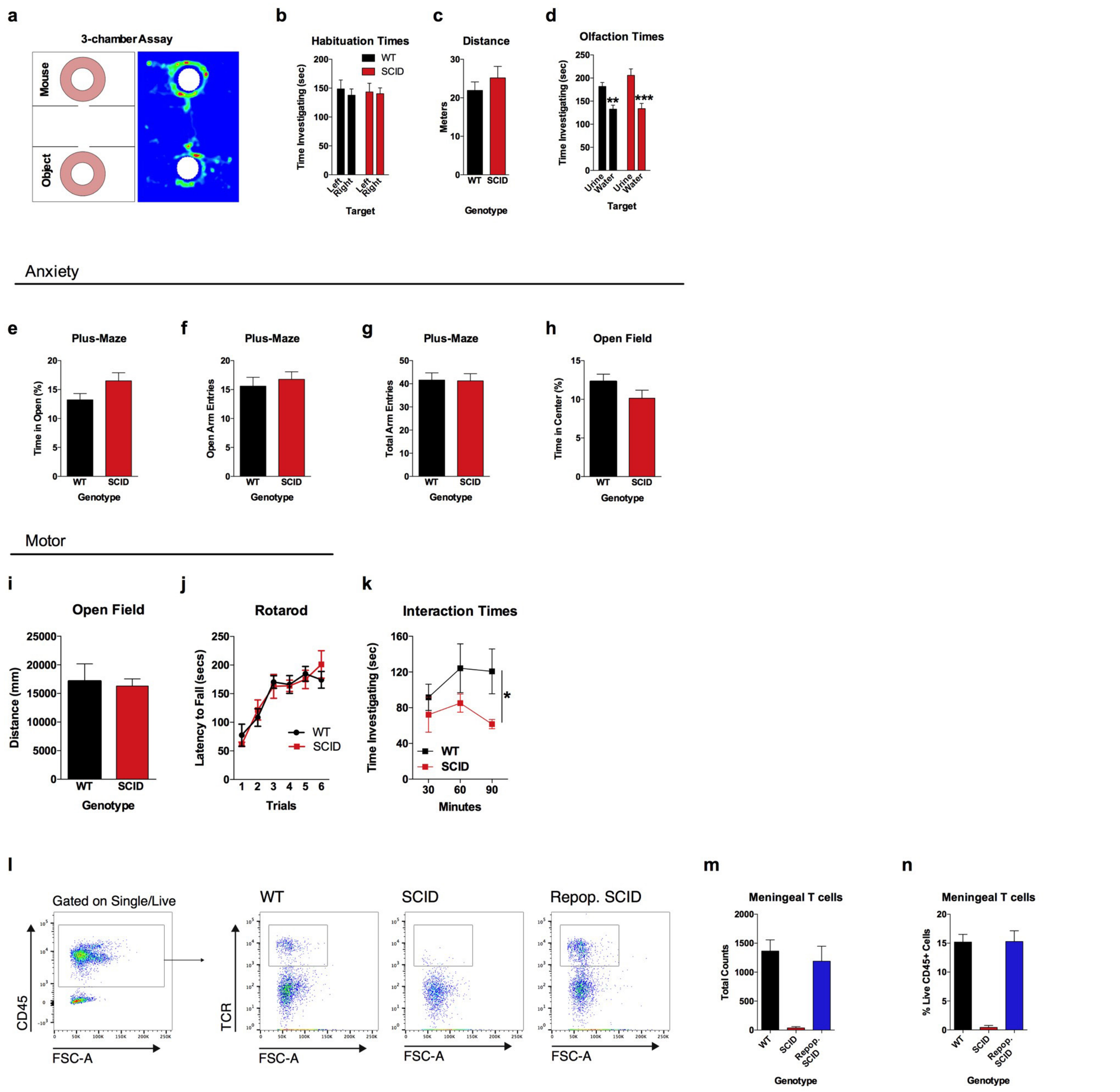

Extended Data Figure 1 | SCID mice have no observable anxiety, motor, or olfactory deficits. a, The three-chamber sociability assay was used to test social behaviour. **b**, Neither wild-type nor SCID mice had a side bias in the habituation phase (empty cups) of the three-chamber assay ($n=6$; repeated at least three times). **c**, There was no effect of genotype on distance travelled in the three-chamber assay during the habituation phase ($n=6$; repeated at least three times). **d**, Both wild-type and SCID mice had an olfactory preference to urine, suggesting normal olfactory behaviour ($n=8$ mice per group; ANOVA for urine preference $F_{1,28}=31.01$; $P<0.0001$; $***P<0.001$, $**P<0.01$, Sidak's post hoc test; single experiment). **e**, Percentage time spent in the open arms of plus-maze ($n=22$ mice per group; pooled two independent experiments). **f**, Number of entries into the open arms of the plus-maze ($n=22$ mice per group; pooled two independent experiments). **g**, Total arm entries of plus-maze ($n=22$ mice per group; pooled two independent experiments). **h**, Percentage time spent in the centre of the open field ($n=22$ mice per group; pooled two independent experiments). **i**, Total ambulatory distance in the open field ($n=22$ mice per group; pooled two independent experiments). **j**, Latency to fall off the accelerating rotarod ($n=8$ mice per group; single experiment). **k**, SCID mice spent less time investigating each other than wild-type mice spent investigating each other when placed into a novel social environment ($n=5$ mice per group; repeated-measures ANOVA for genotype $F_{1,21}=5.708$ $*P<0.05$; single experiment). **l**, Repopulated SCID mice have similar numbers (**m**) and percentages (**n**) of meningeal T cells as wild-type mice ($n=4$–5 mice per group; repeated at least three times). Cells were gated on singlets, live, $CD45^+$, and TCR.

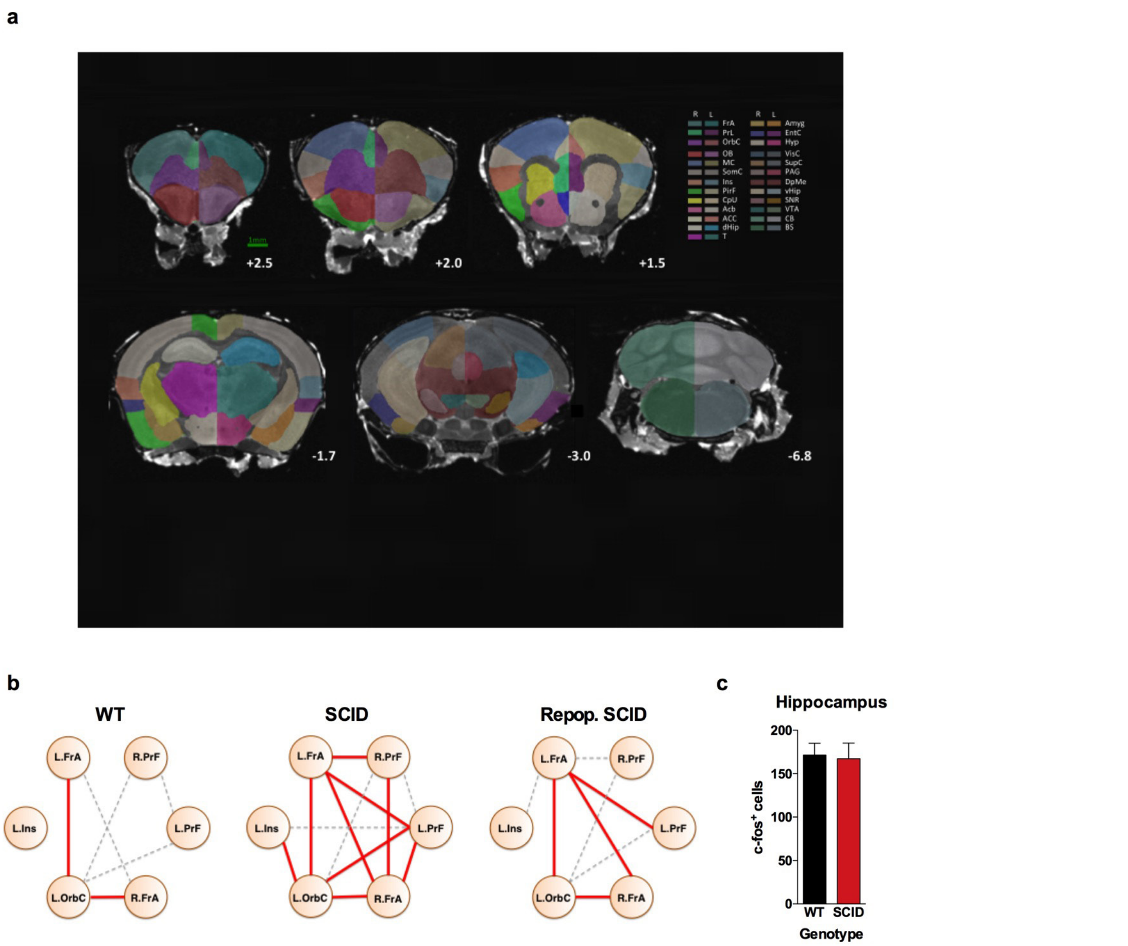

Extended Data Figure 2 | Neuroanatomical structures analysed by rsfMRI. a, Regions of interests (ROIs) were generated using *The Mouse Brain* by Paxinos and Franklin as a reference. Representative slices were extracted from ref. 32. Abbreviations are as follows: FrA, frontal association cortex; PrL, prelimbic cortex; OrbC, orbital cortex; OB, olfactory bulb; MC, motor cortex; SocC, somatosensory cortex; Ins, insula; PirF, piriform cortex; CpU, caudate putamen; Acb, accumbens; ACC, anterior cingulate cortex; dHip, dorsal hippocampus; *T*, thalamus; Amyg, amygdala; EntC, entorhinal cortex; Hyp, hypothalamus; VisC, visual cortex; SupC, superior colliculus; PAG, periductal grey; DpMe, deep mesencephalic nucleus; vHip, ventral hippocampus; SNR, substantia nigra; VTA, ventral tegmental area; CB, cerebellum; BS, brain stem. **b**, Connectivity of local PFC/insular nodes. Correlation thresholds were applied to visualize the strength of the connection. Connections that pass a high threshold are shown in red; connections that pass a lower threshold are shown in dashed grey. SCID mice have aberrant hyper-connectivity in the PFC ($n = 8$–9 mice per group; $P < 0.05$, Jennrich test; two pooled independent experiments). **c**, c-fos^{+} cells in the hippocampus ($n = 9$–10 mice per group; single experiment).

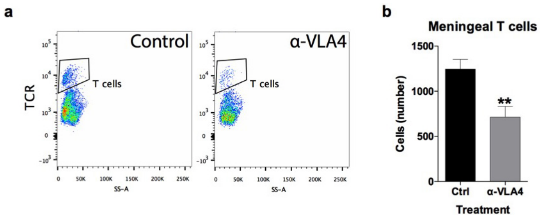

Extended Data Figure 3 | Acute reduction of meningeal T cells with anti-VLA4. a, Anti-VLA4 depletes meningeal T cells. Meninges were dissected and single-cell suspensions were immunostained. T cells were gated on live, single, $CD45^+$, TCR^+ events and counted by flow cytometry. **b**, Acute injection of anti-VLA4 reduced the amount of TCR^+ T cells in the meninges ($n = 4$ mice per group; $*P < 0.01$; repeated at least twice).

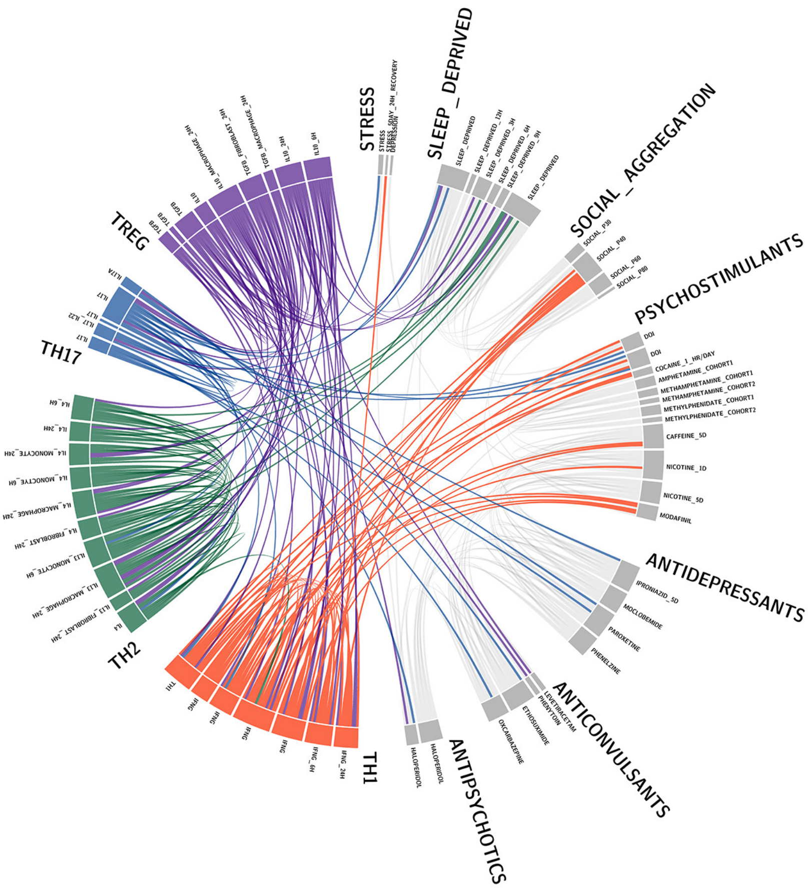

Extended Data Figure 4 | Circos plot showing the connectivity of Th1 response and social aggregation. Labels are shown for the data sets analysed and presented in Fig. 1h.

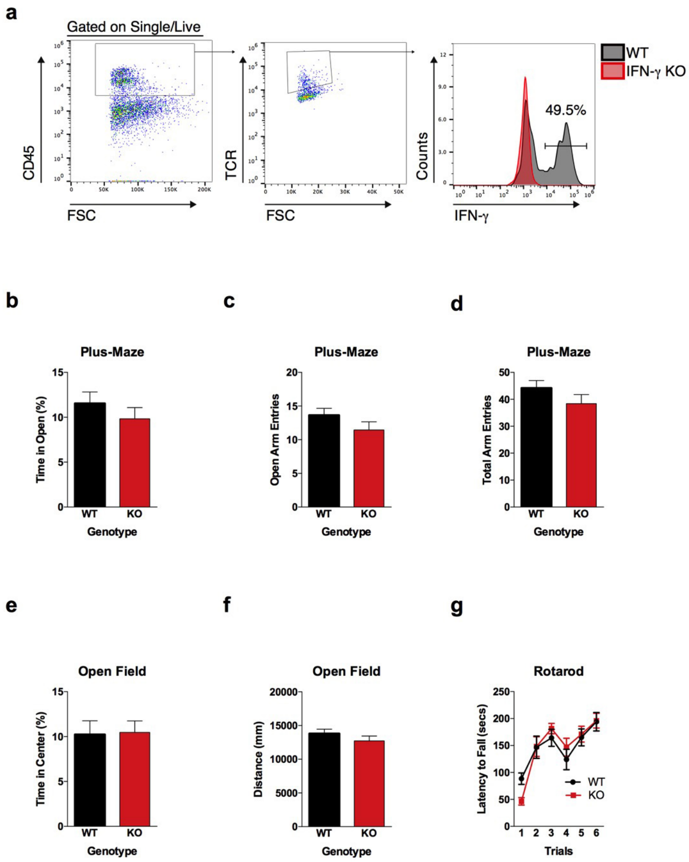

Extended Data Figure 5 | T cells in the meninges produce IFN-γ and IFN-γ-deficient mice have normal levels of anxiety and motor behaviour. a, A substantial percentage of meningeal T cells produce IFN-γ. Cells were gated for live, singlets, CD45$^+$, and TCR$^+$. *Ifng*$^{-/-}$ mice were used to gate for IFN-γ staining. **b**, Percentage time spent in open arms of the plus-maze ($n = 20$ mice per group; pooled two independent experiments). **c**, Entries into the open arms of plus-maze ($n = 20$ mice per group; pooled two independent experiments). **d**, Total entries into all arms of the plus-maze ($n = 20$ mice per group; pooled two independent experiments). **e**, Percentage time spent in the centre of the open field ($n = 20$ mice per group; pooled two independent experiments). **f**, Total ambulatory distance in the open field ($n = 20$ mice per group; pooled two independent experiments). **g**, Latency to fall off the accelerating rotarod ($n = 8$ mice per group; single experiment).

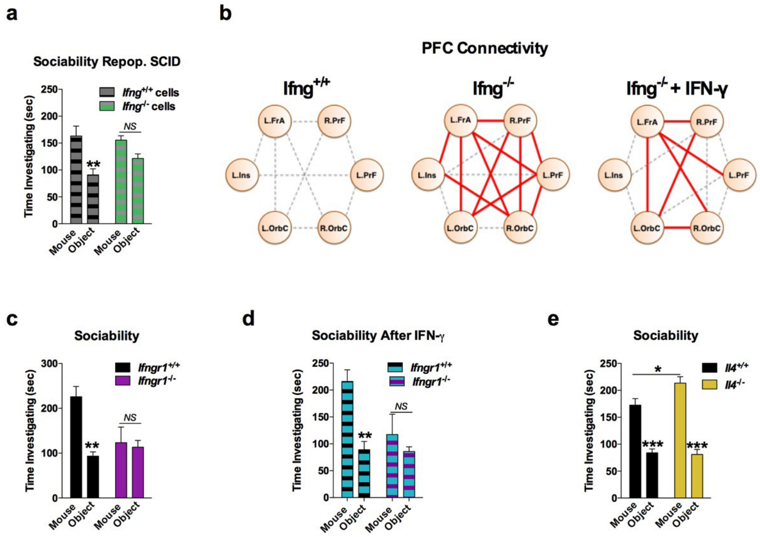

Extended Data Figure 6 | IFN-γ signalling is necessary for normal social behaviour. a, Repopulating SCID mice with wild-type lymphocytes rescued a social preference; repopulating with *Ifng*$^{-/-}$ lymphocytes did not rescue a social preference; ANOVA for social behaviour $F_{1,14} = 11.99$; $P = 0.0038$ ($^{**}P < 0.01$; $n = 8$ mice per group; single experiment). **b**, Connectivity of local PFC/insular nodes. Correlation thresholds were applied to visualize the strength of the connection. Connections that pass a high threshold are shown in red; connections that pass a lower threshold are shown in dashed grey. *Ifng*$^{-/-}$ mice have more connections than wild-type mice (Jennerich test; $P = 0.0006$). These connections were reduced by IFN-γ (Jennerich test; $P = 0.02$; pooled two independent experiments). **c**, *Ifngr1*$^{-/-}$ mice have social deficits ($n = 6$ mice per group; ANOVA for interaction $P = 0.01$; $^{**}P < 0.01$ Sidak's post hoc test) that were not rescued by injecting IFN-γ into the CSF (**d**; $n = 5$–6 mice per group; ANOVA for interaction $P = 0.01$; $^{**}P < 0.01$ Sidak's post hoc test; single experiment). **e**, *Il4*$^{-/-}$ mice spend more time than wild-type mice investigating a novel mouse; ANOVA for genotype $F_{1,32} = 5.397$; $P = 0.0267$ ($^{*}P < 0.05$ Sidak's post hoc test; $n = 16$–18 mice per group; pooled three independent experiments).

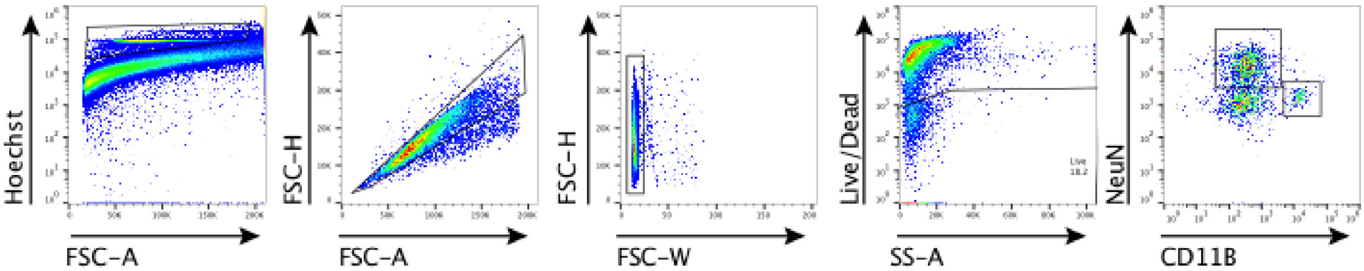

Extended Data Figure 7 | Gating strategy for neurons and microglia. Brain homogenates were stained and analysed by flow cytometry. Cells were gated on nucleated, singlets, and live. Neurons were then gated on NeuN-positive and microglia on CD11B-positive cells.

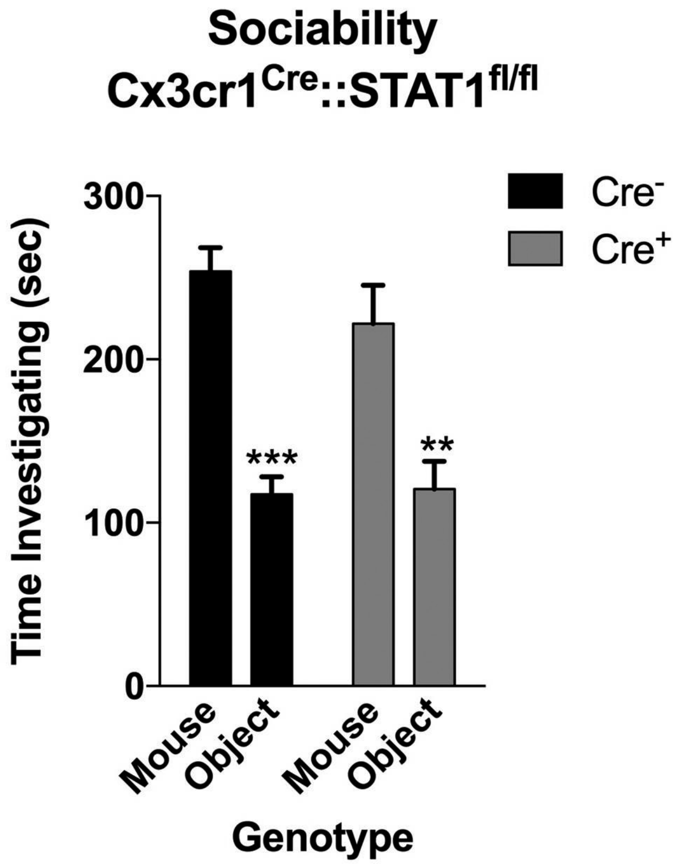

Extended Data Figure 8 | IFN-γ signalling in microglia is not necessary for normal social function. Mice deficient for STAT1 in microglia have normal social preference ($n = 9$ mice per group; ANOVA for Cre $F_{1,16} = 1.809$ and sociability $F_{1,16} = 30.10$; $P < 0.0001$; $^{**}P < 0.01$; $^{***}P < 0.001$ Sidak's post hoc test; pooled two independent experiments).

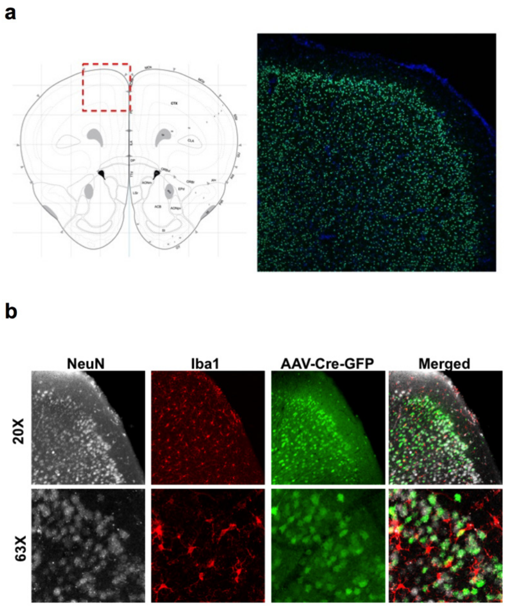

Extended Data Figure 9 | Deleting IFNGR1 by AAV transduction. Mice were injected with AVVs expressing Cre and GFP under a synapsin promoter. **a**, GFP fluorescence in the PFC. Atlas image adapted from 2015 Allen Institute for Brain Science, Allen Brain Atlas. Available from: http://www.brain-map.org. **b**, GFP fluorescence is only observed in NeuN^{+} neurons, not Iba^{+} microglia (top, 20×; bottom 63× objective).

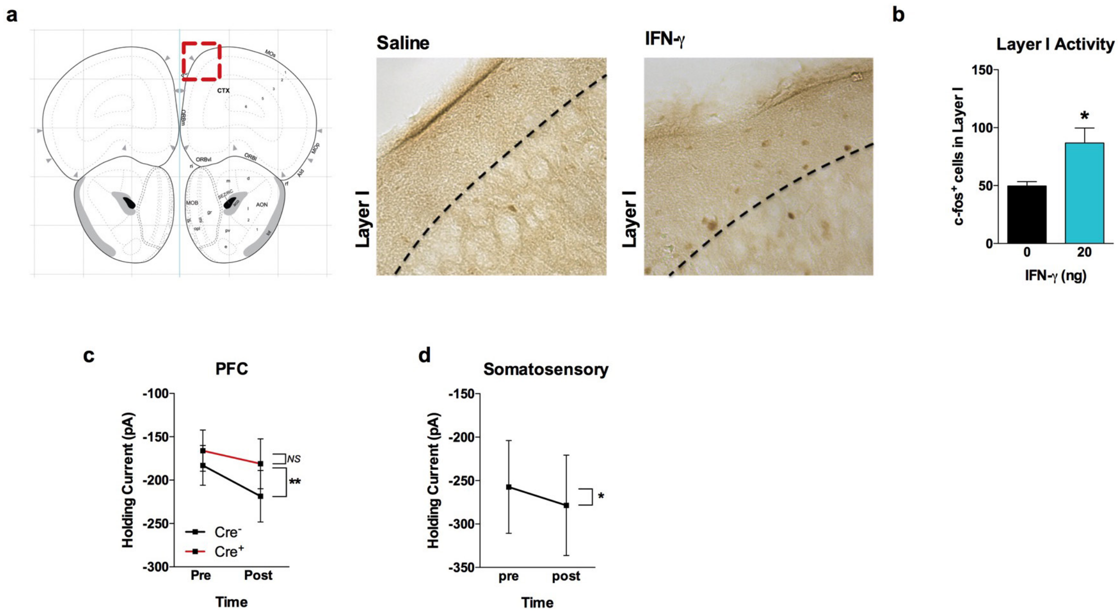

Extended Data Figure 10 | IFN-γ increased the number of c-fos$^+$ cells in layer I of the PFC. **a**, IFN-γ was injected into the CSF (into the cisterna magna) 2 h before killing and processing brains for immunohistochemistry. Slices were stained for c-fos. Atlas image adapted from 2015 Allen Institute for Brain Science, Allen Brain Atlas. Available from: http://www.brain-map.org. **b**, Total c-fos$^+$ cells in layer I of the PFC ($n = 3$ mice per group; $*P < 0.05$; single experiment). Holding current pre and post IFN-γ application on acute slices from the PFC (**c**) and somatosensory cortex (**d**; $n = 6$ neurons from three mice). **c**, *Vgat*^{cre}::*Ifngr1*$^{fl/fl}$ mice. IFN-γ increased tonic inhibition in Cre$^-$ mice ($n = 6$–7 cells from four mice per group; $**P < 0.01$ Sidak's post hoc test).

doi:10.1038/nature18624

Identification of proliferative and mature β-cells in the islets of Langerhans

Erik Bader[1,2,3]*, Adriana Migliorini[1,2]*, Moritz Gegg[1,2], Noah Moruzzi[1,4], Jantje Gerdes[1], Sara S. Roscioni[1], Mostafa Bakhti[1], Elisabeth Brandl[1], Martin Irmler[5,6], Johannes Beckers[5,6,7], Michaela Aichler[8], Annette Feuchtinger[8], Christin Leitzinger[9], Hans Zischka[9], Rui Wang-Sattler[3], Martin Jastroch[5,10], Matthias Tschöp[5,10], Fausto Machicao[5,11], Harald Staiger[5,11,12], Hans-Ulrich Häring[5,11,12], Helena Chmelova[5,13,14], Julie A. Chouinard[5,13,14], Nikolay Oskolkov[15], Olle Korsgren[16], Stephan Speier[5,13,14] & Heiko Lickert[1,2,5,7]

Insulin-dependent diabetes is a complex multifactorial disorder characterized by loss or dysfunction of β-cells. Pancreatic β-cells differ in size, glucose responsiveness, insulin secretion and precursor cell potential[1–5]; understanding the mechanisms that underlie this functional heterogeneity might make it possible to develop new regenerative approaches. Here we show that *Fltp* (also known as *Flattop* and *Cfap126*), a Wnt/planar cell polarity (PCP) effector and reporter gene[6], acts as a marker gene that subdivides endocrine cells into two subpopulations and distinguishes proliferation-competent from mature β-cells with distinct molecular, physiological and ultrastructural features. Genetic lineage tracing revealed that endocrine subpopulations from Fltp-negative and -positive lineages react differently to physiological and pathological changes. The expression of Fltp increases when endocrine cells cluster together to form polarized and mature 3D islet mini-organs[7–9]. We show that 3D architecture and Wnt/PCP ligands are sufficient to trigger β-cell maturation. By contrast, the Wnt/PCP effector Fltp is not necessary for β-cell development, proliferation or maturation. We conclude that 3D architecture and Wnt/PCP signalling underlie functional β-cell heterogeneity and induce β-cell maturation. The identification of Fltp as a marker for endocrine subpopulations sheds light on the molecular underpinnings of islet cell heterogeneity and plasticity and might enable targeting of endocrine subpopulations for the regeneration of functional β-cell mass in diabetic patients.

The islet of Langerhans is a complex mini-organ that regulates energy metabolism[10]. Pancreatic β-cells are organized in polarized rosette-like structures around blood vessels[7] and are coupled by gap junctions to allow them to sense glucose and secrete appropriate amounts of insulin into the blood stream[11]. The conserved Wnt/planar cell polarity (PCP) pathway regulates the orientation of cells and organelles within the plane of a tissue and thus determines the function of cells in an organ[12,13]. As self-organized 3D tissue architecture is required for organ formation and terminal differentiation[14,15], we tested whether acquisition of tissue polarity and architecture could influence β-cell heterogeneity and maturation.

To analyse the establishment of tissue polarity at the molecular level, we used the $Fltp^{ZV}$ knock-in/knockout mouse, in which the entire open-reading frame of *Fltp* is replaced by a multicistronic lacZ–Venus reporter cassette[6]. In this model, Fltp promoter-driven histone 2B (H2B)–Venus reporter (FVR) activity is confined to terminally differentiated cells with established PCP[6]. We first analysed reporter activity in the pancreas of $Fltp^{ZV/+}$ heterozygous embryos at embryonic day (E)18.5, when endocrine cells are still organized in cord-like structures outside the ductal tubules and start to aggregate and form 3D mini-organs (Extended Data Fig. 1). Notably, we detected heterogeneous reporter activity in β-cells that expressed high levels of Nkx6.1 in compacted islet structures, but not in scattered pre-β-cells in cord-like structures that expressed low levels of Nkx6.1. This finding suggests that FVR is activated in endocrine cells during islet compaction and establishment of polarization. Because β-cell maturation occurs in the first two weeks after birth[9], we analysed reporter activity in postnatal and adult islets from heterozygous $Fltp^{ZV/+}$ mice. At postnatal day (P)1, reporter activity was detectable in less than 50% of $Nkx6.1^{+}$ β-cells; activity was significantly increased at P11 and reached a maximum of 80% in adult islets (Fig. 1a, b). In adult islets, FVR was expressed in ~50% of glucagon-secreting α-cells, ~80% of insulin-secreting $Nkx6.1^{+}$ β-cells, ~50% of somatostatin-secreting δ-cells and ~50% of pancreatic polypeptide-secreting PP-cells (Fig. 1c, d). Together, these observations suggest that islet cell heterogeneity develops during islet neogenesis and is likely to be determined by the terminal differentiation and planar polarization status of endocrine cells.

To understand the biological relevance of islet cell heterogeneity in more detail, we specifically focused on β-cells in heterozygous $Fltp^{ZV/+}$ mice. We first compared the proliferation rate of FVR^{-} and FVR^{+} β-cells during homeostasis, postnatal β-cell expansion and physiological insulin resistance. FVR^{-} $Nkx6.1^{+}$ β-cells showed a significantly increased replication rate during the postnatal expansion phase at P1, at P11 and upon metabolic demand during pregnancy at gestational day (G)15.5, as measured by Ki-67 immunoreactivity (Fig. 1e, f) and EdU incorporation (Extended Data Fig. 2a, b), when compared to FVR^{+} $Nkx6.1^{+}$ β-cells; by contrast, FVR^{+} $Nkx6.1^{+}$ β-cells showed increased levels of the cell-cycle inhibitor p27 (Extended Data Fig. 2h–j). When we compared the head and tail regions and different-sized islets, we noticed remarkable intra-islet and inter-islet heterogeneity in terms of FVR marker expression and proliferation rate (Extended Data Fig. 2c–g), probably due to different cell-type compositions in the islet niches[16]. Collectively, our data show that β-cell subpopulations, depending on their niche and environmental conditions, show

[1]Institute of Diabetes and Regeneration Research, Helmholtz Zentrum München, 85764 Neuherberg, Germany. [2]Institute of Stem Cell Research, Helmholtz Zentrum München, 85764 Neuherberg, Germany. [3]Institute of Epidemiology II, Helmholtz Zentrum München, 85764 Neuherberg, Germany. [4]Department of Molecular Medicine and Surgery, Karolinska University Hospital, SE-17176 Stockholm, Sweden. [5]German Center for Diabetes Research (DZD), 85764 Neuherberg, Germany. [6]Institute of Experimental Genetics, Helmholtz Zentrum München, 85764 Neuherberg, Germany. [7]Technische Universität München, Ismaninger Straße 22, 81675 München, Germany. [8]Research Unit Analytical Pathology, Helmholtz Zentrum München, 85764 Neuherberg, Germany. [9]Institute of Molecular Toxicology and Pharmacology, Helmholtz Zentrum München, 85764 Neuherberg, Germany. [10]Institute of Diabetes and Obesity, Helmholtz Zentrum München, 85764 Neuherberg, Germany. [11]Institute for Diabetes Research and Metabolic Diseases, Helmholtz Zentrum München, University of Tübingen, 72076 Tübingen, Germany. [12]Department of Internal Medicine, Division of Endocrinology, Diabetology, Vascular Disease, Nephrology and Clinical Chemistry, University of Tübingen, 72076 Tübingen, Germany. [13]Paul Langerhans Institute Dresden (PLID), Helmholtz Zentrum München, University Clinic Carl Gustav Carus, Technische Universität Dresden, 01307 Dresden, Germany. [14]DFG-Center for Regenerative Therapies Dresden (CRTD), Faculty of Medicine, Technische Universität Dresden, 01307 Dresden, Germany. [15]Diabetes and Endocrinology, Lund University Diabetes Centre, 205 02 Malmö, Sweden. [16]Department of Immunology, Genetics and Pathology, Uppsala University, 751 05 Uppsala, Sweden.
*These authors contributed equally to this work.

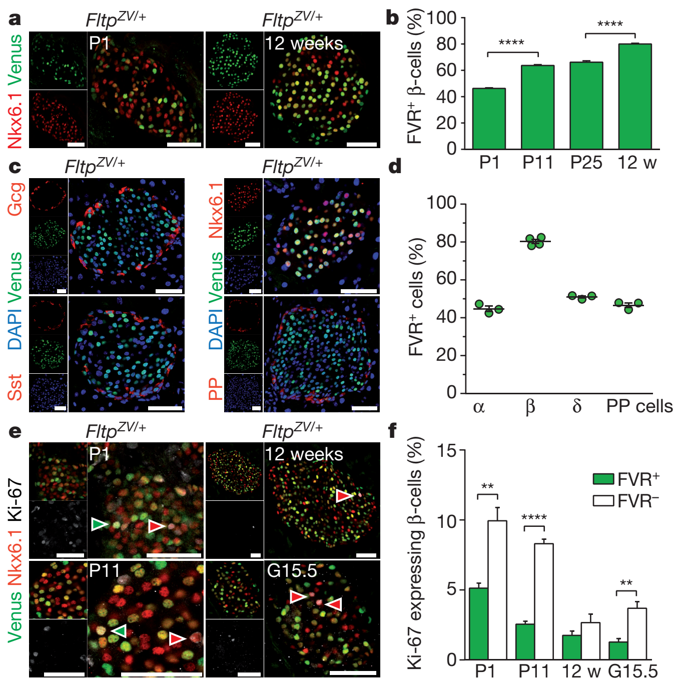

Figure 1 | FVR expression increases during postnatal β-cell maturation, is heterogeneous in endocrine cell lineages and is absent in β-cells with high proliferative capacity. a, b, Laser scanning confocal microscopy (LSM) images (**a**) and quantification (**b**) of FVR$^+$ β-cell distribution during postnatal β-cell maturation (P1, P11, P25) and in adulthood (12 weeks (w)) (P1: *n* (mice) = 5 (14,766 Nkx6.1$^+$ cells), P11: *n* (mice) = 6 (13,789 Nkx6.1$^+$ cells), P25: *n* (mice) = 5 (8,733 Nkx6.1$^+$ cells), 12 weeks: *n* (mice) = 9 (17,369 Nkx6.1$^+$ cells); ****$P < 0.0001$). **c, d**, LSM images (**c**) and quantification (**d**) of FVR expression in endocrine cell lineages in adulthood (*n* (mice) = 3, 1,676 PP$^+$ cells, 1,656 Sst$^+$ (δ-)cells and 1,975 Gcg$^+$ (α-)cells); *n* (mice for β-cells) = 5, β-cells (7,327 Nkx6.1$^+$ cells)). **e, f**, LSM images (**e**) and quantification (**f**) of Ki-67-expressing cells among FVR$^-$ and FVR$^+$ β-cell subpopulations at P1, P11, 12 weeks and in pregnant mice (G15.5; arrowheads indicate proliferating cells; red arrowheads, Nkx6.1; green arrowheads, Venus and Nkx6.1; P1: *n* (mice) = 5 (14,766 Nkx6.1$^+$ cells), P11: *n* (mice) = 6 (13,789 Nkx6.1$^+$ cells), 12 weeks: *n* (mice) = 5 (10,042 Nkx6.1$^+$ cells) and pregnant G15.5: *n* (mice) = 5 (12,691 Nkx6.1$^+$ cells); (P1) **$P = 0.0048$, (P11) ****$P < 0.0001$, (G15.5) **$P = 0.0039$). Scale bars, 50 μm (**a**, **c**, **e**). Two-sided unpaired *t*-test was performed (**b**, **e**). Data represent mean ± s.e.m. Source data for all graphs and quantifications are provided online.

markedly different FVR expression levels correlating with their proliferative capacity.

The data presented so far suggest that the expression of FVR probably subdivides β-cells into proliferative and more mature β-cells. To test this idea directly, we isolated adult islets from *Fltp*$^{ZV/+}$ mice and purified the FVR endocrine subpopulations for genome-wide mRNA expression profiling (Fig. 2a, b). We found 997 genes that showed more than 1.5-fold differences in expression between FVR$^-$ and FVR$^+$ endocrine cells (Fig. 2c and Supplementary Table 1). Strikingly, unbiased gene ontology term (Fig. 2g and Supplementary Table 2) and ingenuity analysis (Fig. 2h and Supplementary Table 3) revealed that the FVR$^-$ subpopulation showed significant enrichment of genes associated with G-protein coupled receptor (GPCR), Wnt and MAPK signalling transduction, whereas the FVR$^+$ subpopulation showed significant enrichment of genes that are important for mature β-cell function. This difference is reflected by differential mRNA expression of hormones, β-cell maturation markers, mitochondrial and metabolic genes, receptors and signalling components, as revealed by microarray analysis (Fig. 2d–f) and confirmed by qPCR analysis on highly enriched β-cell subpopulations (Extended Data Fig. 3a–h). Mitochondrial gene expression (Fig. 2e, g, h), ultrastructural (Extended Data Fig. 4) and biochemical analysis (Fig. 2k, l), and mitochondrial network architecture (Extended Data Fig. 5e–k) collectively suggest that the two isolated β-cell subpopulations have similar numbers of mitochondria (Extended Data Fig. 3i) but that the mitochondria differ in architecture and physiology. Measuring the oxygen consumption rate of sorted FVR$^-$ and FVR$^+$ β-cells from *Fltp*$^{ZV/+}$ islets using an XF96 extracellular flux analyser revealed that glucose-induced ATP synthesis and glucose responsiveness were not significantly different between the two subpopulations (Extended Data Fig. 5a–d), whereas static glucose-stimulated and arginine-stimulated insulin secretion were significantly enhanced in the sorted and reaggregated FVR$^+$ β-cell enriched subpopulation (Extended Data Fig. 5l). These results are consistent with the differences in the expression of genes involved in glucose sensing and insulin secretion (Fig. 2 and Extended Data Fig. 3g). Finally, the high expression of the proprotein convertase subtilisin/kexin type-1 gene (*Pcsk1*) in the FVR$^+$ cells (Extended Data Fig. 3g) and the higher number of mature secretory granules in Fltp-lineage$^+$ cells (Fig. 2i, j and see below) further support the idea that FVR$^+$ and Fltp-lineage$^+$ cells are mature β-cells.

The differential expression of signalling components and the distinct physiologies of the two β-cell subpopulations suggested that they might react differently to environmental changes. To test this hypothesis, we used a Cre recombinase/*loxP*-mediated genetic lineage tracing approach, which allowed us to follow the cell populations over time (Fig. 3a). We isolated *Fltp*$^{T2AiCre/+}$;*Gt(ROSA)26*^{mTmG} islets (refs 17, 18) and performed *in vitro* single cell-tracking experiments. This showed that Fltp-lineage$^-$ endocrine cells turned into Fltp-lineage$^+$ cells (Fig. 3b). As FVR$^-$ and FVR$^+$ β-cells are molecularly and biologically distinct, these results suggest that FVR$^-$ precursor β-cells differentiate into FVR$^+$ mature β-cells. Notably, the FVR$^-$ β-cell enriched subpopulation expressed low levels of *Slc2a2* (Extended Data Fig. 3g), which has been recently shown to be expressed in insulin-positive pancreatic multipotent precursor cells in mouse and human islets[3,4].

To analyse the *in vivo* β-cell subpopulation dynamics at the time when compensatory β-cell proliferation reaches peak levels[19], we isolated adult islets from non-pregnant female mice and from pregnant female mice at G15.5 (Fig. 3c, d). Quantitative analysis showed that the Fltp-lineage$^-$ β-cell subpopulation compensates for the increased metabolic demand in pregnant mice by proliferating. The higher number of mTmG double-positive cells in pregnant mice further suggested that Fltp-lineage$^-$ cells differentiate into mature β-cells *in vivo*. Next, we transplanted *Fltp*$^{T2AiCre/+}$;*Gt(ROSA)26*^{mTmG} islets into the anterior chamber of the eye in mice for noninvasive longitudinal *in vivo* imaging[20]. After donor islet isolation and transplantation onto the iris, islets first shrank in volume during engraftment, owing to the lack of nutritional supply, before revascularization counteracted islet degeneration (Extended Data Fig. 6d). Concomitant with the revascularization and decrease in islet size we observed a relative increase in the Fltp-lineage$^-$ and decrease in the Fltp-lineage$^+$ subpopulation volume (Fig. 3f, g) and number (Extended Data Fig. 6e) 13 days after transplantation, suggesting that the more mature and metabolic active endocrine subpopulation undergoes apoptosis, probably due to hypoxia, until revascularization. Four weeks after transplantation the Fltp-lineage$^+$ subpopulation had recovered, probably owing to the maturation of Fltp-lineage$^-$ cells into mature Fltp-lineage$^+$ cells (Fig. 3e). Finally, we investigated the endocrine subpopulation dynamics in a high-fat diet (HFD) mouse model. HFD causes insulin resistance and compensatory β-cell hyperplasia followed by hypertrophy, but the exact pathomechanism of β-cell failure remains unclear[21]. Over an eight-week period, we observed increased glucose intolerance (Extended Data Fig. 6c) and a steady increase in islet volume accompanied by a significant increase in the cross-sectional area of the Fltp-lineage$^+$ endocrine cell population, indicating that mature endocrine cells are more metabolically active and prone to hypertrophy commonly associated with cytotoxic stress (Fig. 3h–k and Extended Data Fig. 6a, b). This observation might explain why the Fltp-lineage$^+$ subpopulation predominantly decreased

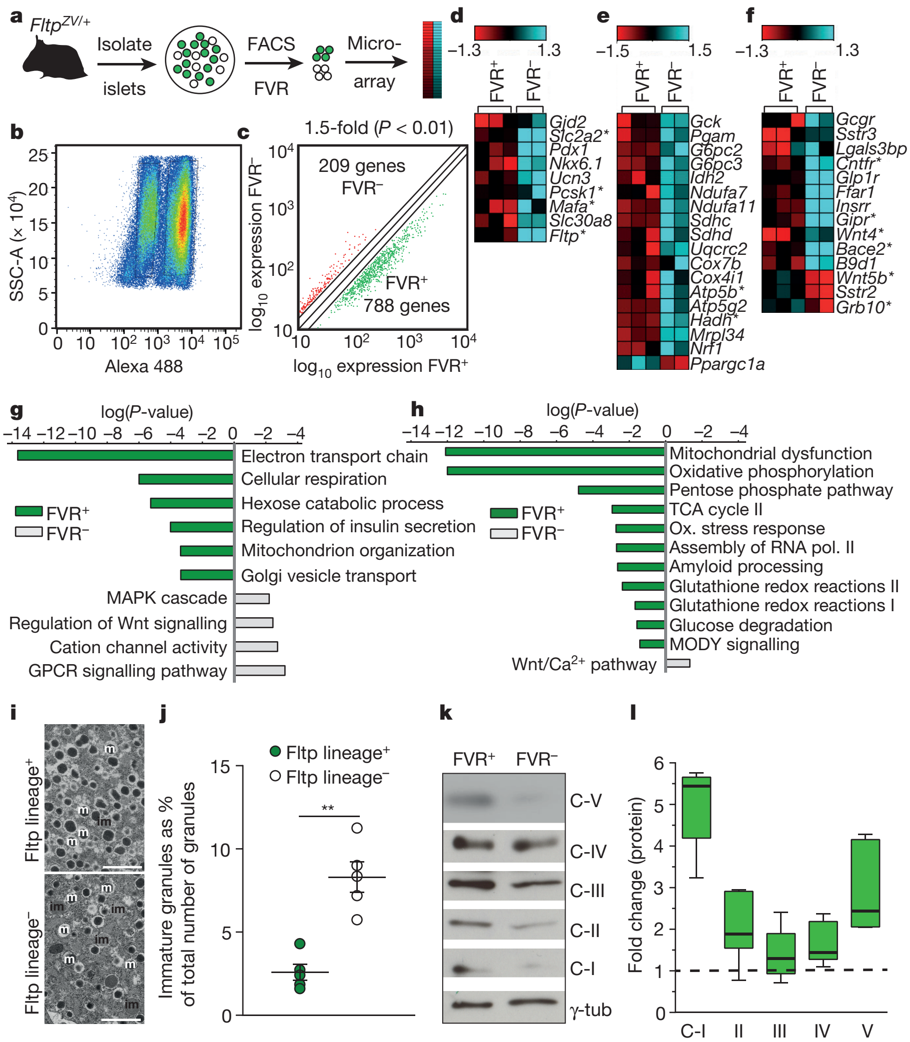

Figure 2 | FVR distinguishes between two endocrine subpopulations with distinct molecular, physiological and ultrastructural features. **a**, Experimental design for microarray analysis of endocrine subpopulations from isolated *Fltp*$^{ZV/+}$ islets. **b**, Fluorescent activated cell sorting (FACS) separation of FVR$^+$ and FVR$^-$ endocrine subpopulations. **c**, Scatter plot of the 997 genes that were differentially regulated in FVR$^+$ and FVR$^-$ endocrine cells (1.5-fold regulated, $P < 0.01$, limma t-test). **d–f**, Heatmaps depicting regulated genes among FVR subpopulations involved in β-cell function (**d**), mitochondrial function (**e**) and receptors and signalling (**f**) (*validated by qPCR, median centre was applied to each gene of the heatmaps across different samples). **g**, **h**, Bar graph of selected, significantly enriched gene ontology terms (**g**) and ingenuity pathways (**h**) of regulated genes among FVR subpopulations shown in **c**. **i**, **j**, Transmission electron microscopy images (**i**; scale bars, 1 nm) and quantification (**j**) of insulin granules in immunogold-labelled β-cells from *Fltp*$^{T2AiCre/+}$;*Gt(ROSA)26*$^{mTmG/+}$ mice (m, mature; im, immature) (n (independent experiments) = 5, n (β-cells) = 50, n (granules) = 12,254; $^{**}P = 0.0015$, two sided unpaired t-test). **k**, **l**, Western blot (**k**) and quantification (**l**) of mitochondria complexes I–V from FACS-sorted FVR$^+$ and FVR$^-$ subpopulations (protein expression normalized to γ-tubulin and to the FVR$^-$ population (dotted line), n (independent experiments) = 5, whiskers represent minimum and maximum values). Data in **j** represent mean ± s.e.m. See Supplementary Fig. 1 for gel source data.

after transplantation (Fig. 3g). Together, our results suggest that, in pregnant mice, Fltp$^-$ endocrine cells undergo compensatory proliferation, whereas more mature Fltp-lineage$^+$ endocrine cells probably account for islet cell hypertrophy and seem more sensitive to cytotoxic stress.

In our molecular analysis we noticed that apical–basal polarity and expression of Wnt/PCP genes were increased in FVR$^+$ β-cells (Fig. 2 and Extended Data Fig. 3g, j). Notably, cellular polarization and compaction in 3D pseudo-islet cultures[22,23] strongly induced protein expression of a variety of β-cell maturation markers, including Nkx6.1, MafA and Ucn3, as revealed by quantitative PCR (qPCR) and immunocytochemistry in time-course experiments in Min6 insulinoma cells (Extended Data Fig. 7a–j). Consistent with the induction of the Wnt/PCP effector Fltp and Nkx6.1 during islet neogenesis (Extended Data Fig. 1), we observed that treatment of dispersed and reaggregated P5 islet cells (Fig. 4a–c) and pseudo-islets of Min6 insulinoma cells (Extended Data Fig. 7k–n) with the Wnt/PCP ligand Wnt5a significantly upregulated β-cell maturation makers. Human microislets and human islets show heterogenous expression of WNT4 in endocrine and β-cells, consistent with the differential expression of *Wnt4* and *Wnt5b* in the FVR$^-$ and FVR$^+$ subpopulations (Fig. 4d–g and Extended Data Fig. 3g). Treatment of human EndoC-β H1 β-cells with the canonical Wnt ligand WNT3A increased proliferation, whereas treatment with WNT4 or WNT5A did not (Extended Data Fig. 8a–e). Notably, WNT4 induced JNK activation (Extended Data Fig. 8f, g) and increased levels of NKX6.1 and PDX1 protein in human EndoC-β H1 β-cells (Fig. 4h, i) and human islets (Fig. 4j, k), suggesting that WNT4 triggers the non-canonical Wnt/PCP pathway. Finally, WNT5A increased glucose-stimulated insulin secretion (GSIS) in human microislets (Extended Data Fig. 8h). Together, these results suggest that 3D architecture and Wnt/PCP pathway activation induce β-cell maturation and increase GSIS.

Finally, we investigated whether the Wnt/PCP effector Fltp is required for β-cell function beyond its role as a maturation marker.

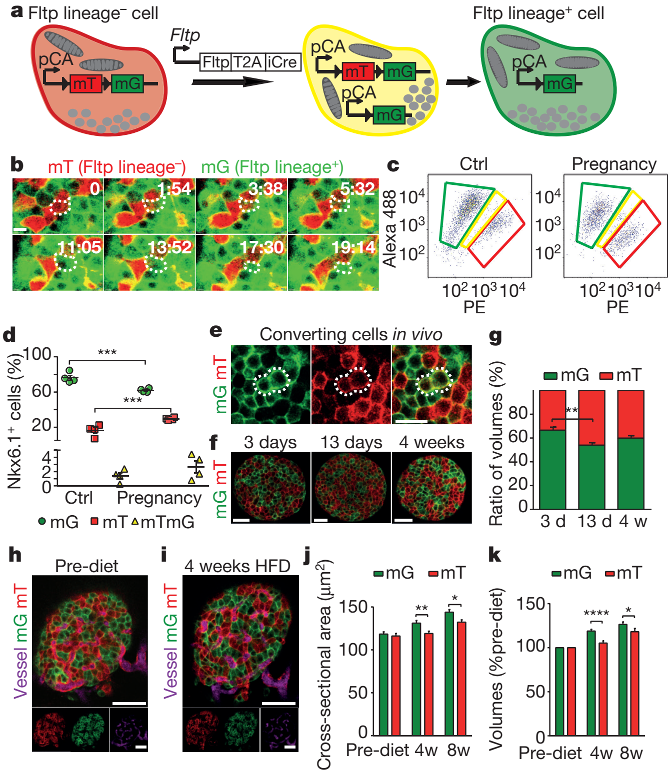

Figure 3 | *Fltp* genetic lineage tracing reveals differential responses of endocrine and β-cell subpopulations upon physiological and pathological insulin resistance. a, $Fltp^{T2AiCre/+}$;$Gt(ROSA)26^{mTmG/+}$ lineage-tracing model. Fltp lineage⁻ cells (mT, red) convert into Fltp lineage⁺ cells (mG, green) upon Fltp-promoter driven Cre expression via an intermediate (mTmG, yellow) cell state. **b**, **e**, Time-lapse imaging of *in vitro* cultured $Fltp^{T2AiCre/+}$;$Gt(ROSA)26^{mTmG/+}$ islets (**b**; *n* (cells) = 7) and *in vivo* islets transplanted into the anterior chamber of the eye (AC) using laser scanning confocal microscopy (LSM) (**e**) shows conversion of endocrine Fltp lineage⁻ cells (mT) into Fltp lineage⁺ cells (mG) (white dotted line shows converting cells). **c**, **d**, FACS analysis (**c**) and quantification (**d**) of mT, mTmG and mG Nkx6.1⁺ β-cells from control (Ctrl) and pregnant mice (G15.5) (*n* (mice per group) = 4, $***P = 0.0001$, $***P = 0.0003$, Bonferroni's multiple comparison test). **f**, **g**, LSM images (**f**) and quantification (**g**) of a $Fltp^{T2AiCre/+}$;$Gt(ROSA)26^{mTmG/+}$ islet transplanted into the AC over engraftment time (*n* (islets) = 15 islets from 4 mice; $**P = 0.0086$, two sided unpaired *t*-test). **h**, **i**, LSM images of a $Fltp^{T2AiCre/+}$;$Gt(ROSA)26^{mTmG/+}$ islet in the AC before (Pre-diet; **h**) and after 4 weeks on a high-fat diet (HFD; **i**). **j**, **k**, Quantification of mT and mG cell cross-sectional areas (**j**) and compartment volume change among mT and mG endocrine cells (**k**) of intraocular $Fltp^{T2AiCre/+}$;$Gt(ROSA)26^{mTmG/+}$ islets before and during HFD (4 w, 8 w) (**j**, *n* (islets) = 34, $*P = 0.0112$, $**P = 0.00732$; **k**, *n* (islets) = 34, $*P = 0.026$, $****P < 0.0001$, Sidak's multiple comparison test). Scale bars, 10 µm (**b**); 20 µm (**e**, **f**); 50 µm (**h**, **i**). Data shown as mean ± s.e.m.

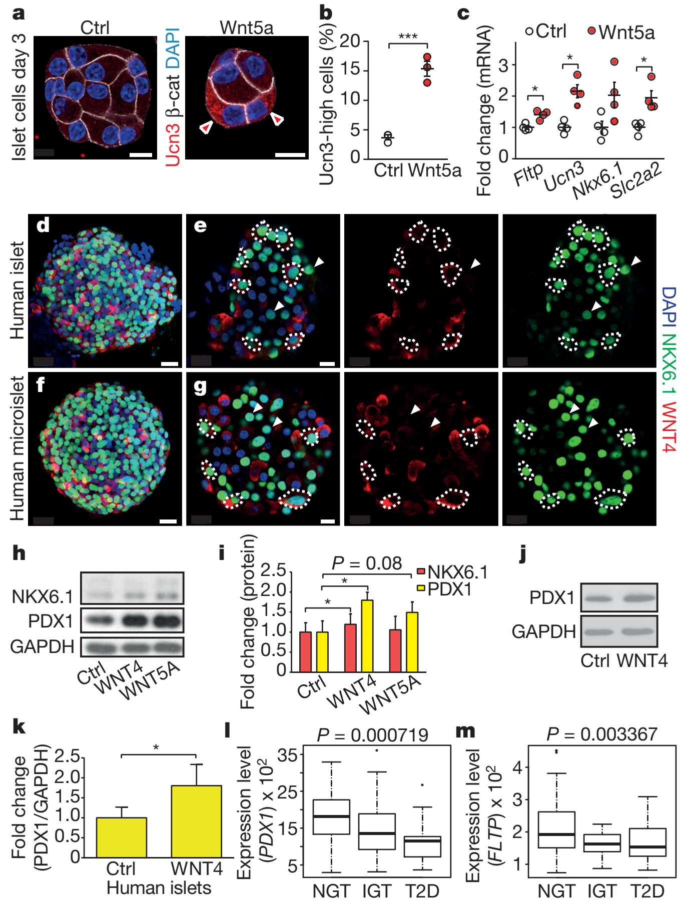

Figure 4 | The Wnt/PCP pathway triggers β-cell maturation. a, **b**, LSM images (**a**) and quantification (**b**) of Ucn3 protein in reaggregated islet cells from P5 wild-type mice treated with or without Wnt5a (*n* (independent experiments) = 3 (DAPI⁺ cells control = 680, DAPI⁺ cells Wnt5a = 877), $***P = 0.001$, two sided unpaired *t*-test). **c**, Wnt5a stimulation of mRNA expression of β-cell maturation markers in P5 reaggregated islet cells (*n* (independent experiments) = 4, $*P < 0.05$, two sided unpaired *t*-test). **d**–**g**, LSM images of a human islet (**d**, **e**) and a human microislet (**f**, **g**) showing heterogeneity of WNT4-expressing NKX6.1⁺ β-cells (white dotted lines and arrowheads). **h**, **i**, Western blot (**h**) and quantification (**i**) of NKX6.1 and PDX1 in EndoC-β H1 β-cells after 4 days of treatment with WNT4 and WNT5A (*n* (independent experiments) = 5; $*P = 0.030$ for PDX1, $*P = 0.0349$ for NKX6.1, two-sided paired *t*-test). **j**, **k**, Western blot (**j**) and quantification (**k**) of PDX1 expression in human islet after 4 days of treatment with WNT4 (*n* (independent experiments) = 9, 4 human donors, two-sided paired *t*-test). **l**, **m**, RNA sequencing expression data of *FLTP* and *PDX1* in human pancreatic islets from healthy donors (normal glucose tolerance (NGT), *n* = 66), pre-diabetic donors (impaired glucose tolerance (IGT), *n* = 21) and type 2 diabetic donors (T2D, *n* = 19; one-way ANOVA). Scale bars, 10 µm (**a**, **d**–**g**). Data represent mean ± s.e.m. See Supplementary Fig. 1 for gel source data.

Terminally differentiated cell types in the inner ear and lung depend on Fltp function as a modulator of the actin and microtubule cytoskeleton[6] and mature β-cells require cell polarity[24] and the cytoskeleton[25] for proper insulin secretion. *Fltp* knockout ($Fltp^{ZV/ZV}$) β-cells do not show impaired development, proliferation or maturation (Extended Data Figs 9, 10a, c, d) or altered glucose tolerance or insulin sensitivity (Extended Data Fig. 10b, e). However, when we analysed basal glucose and insulin levels in adult mice we found small but significantly reduced levels in starved $Fltp^{ZV/ZV}$ mice, suggesting that *Fltp* knockout causes a minor defect in insulin secretion (Extended Data Fig. 10b, f). To rule out systemic effects on basal insulin levels in $Fltp^{ZV/ZV}$ animals, we isolated islets from adult mice and performed GSIS. Consistent with the finding that insulin secretion depends on cell polarity and the cytoskeleton[24,25] we found reduced GSIS in $Fltp^{ZV/ZV}$ islets (Extended Data Fig. 10g). To investigate whether the human *FLTP* orthologue (*CFAP126*, also known as *C1orf192*) is associated with metabolic traits, we genotyped seven single nucleotide polymorphisms (SNPs) tagging all the common variation in this gene (minor allele frequency ≥ 0.01) and analysed their associations with insulin secretion, insulin sensitivity and body fat content and distribution in a cohort of 2,228 human prediabetic subjects[26]. The results showed that the intronic SNP *rs75715534* (minor allele frequency 0.037) was significantly associated with increased insulin secretion in lean subjects (body mass index (BMI) < 25), whereas the same SNP was associated with decreased insulin secretion in obese people (BMI ≥ 35) (Extended Data Fig. 8j, k and Supplementary Table 4). *CFAP126, SLC2A2* and *PDX1* were significantly downregulated in isolated human islets from

pre-diabetic (IGT) when compared to non-diabetic (NGT) subjects and further downregulated in islets from type 2 diabetic (T2D) individuals (Fig. 4l, m and Extended Data Fig. 8i), suggesting that Wnt/PCP signalling and β-cell maturation or function are impaired by glucolipotoxicity.

We have demonstrated that proliferative and mature β-cells can be distinguished by expression of the Wnt/PCP effector and reporter gene *Fltp*. Several studies have indicated that loss of β-cell identity and maturation underlies the pathogenesis of type 2 diabetes[27–30]. The availability of a unique marker for mature β-cells opens new ways to explore pathways regulating islet heterogeneity and might allow researchers to target β-cell maturation for cell-replacement and regenerative therapy.

Online Content Methods, along with any additional Extended Data display items and Source Data, are available in the online version of the paper; references unique to these sections appear only in the online paper.

Received 5 May 2015; accepted 1 June 2016.
Published online 11 July 2016.

1. Salomon, D. & Meda, P. Heterogeneity and contact-dependent regulation of hormone secretion by individual B cells. *Exp. Cell Res.* **162,** 507–520 (1986).
2. Heimberg, H. *et al.* Heterogeneity in glucose sensitivity among pancreatic β-cells is correlated to differences in glucose phosphorylation rather than glucose transport. *EMBO J.* **12,** 2873–2879 (1993).
3. Smukler, S. R. *et al.* The adult mouse and human pancreas contain rare multipotent stem cells that express insulin. *Cell Stem Cell* **8,** 281–293 (2011).
4. Razavi, R. *et al.* Diabetes enhances the proliferation of adult pancreatic multipotent progenitor cells and biases their differentiation to more β-cell production. *Diabetes* **64,** 1311–1323 (2015).
5. Katsuta, H. *et al.* Single pancreatic β cells co-express multiple islet hormone genes in mice. *Diabetologia* **53,** 128–138 (2010).
6. Gegg, M. *et al.* Flattop regulates basal body docking and positioning in mono- and multiciliated cells. *eLife* **3,** e03842 (2014).
7. Bonner-Weir, S. Morphological evidence for pancreatic polarity of β-cells within islets of Langerhans. *Diabetes* **37,** 616–621 (1988).
8. Gu, C. *et al.* Pancreatic beta cells require NeuroD to achieve and maintain functional maturity. *Cell Metab.* **11,** 298–310 (2010).
9. Blum, B. *et al.* Functional β-cell maturation is marked by an increased glucose threshold and by expression of urocortin 3. *Nat. Biotechnol.* **30,** 261–264 (2012).
10. In't Veld, P. & Marichal, M. Microscopic anatomy of the human islet of Langerhans. *Adv. Exp. Med. Biol.* **654,** 1–19 (2010).
11. Meda, P., Perrelet, A. & Orci, L. Increase of gap junctions between pancreatic B-cells during stimulation of insulin secretion. *J. Cell Biol.* **82,** 441–448 (1979).
12. Wang, Y. & Nathans, J. Tissue/planar cell polarity in vertebrates: new insights and new questions. *Development* **134,** 647–658 (2007).
13. Wallingford, J. B. Planar cell polarity and the developmental control of cell behavior in vertebrate embryos. *Annu. Rev. Cell Dev. Biol.* **28,** 627–653 (2012).
14. Eiraku, M. *et al.* Self-organizing optic-cup morphogenesis in three-dimensional culture. *Nature* **472,** 51–56 (2011).
15. McCracken, K. W. *et al.* Modelling human development and disease in pluripotent stem-cell-derived gastric organoids. *Nature* **516,** 400–404 (2014).
16. Orci, L. *et al.* A morphological basis for intercellular communication between α- and β-cells in the endocrine pancreas. *J. Clin. Invest.* **56,** 1066–1070 (1975).
17. Lange, A. *et al.* Fltp(T2AiCre): a new knock-in mouse line for conditional gene targeting in distinct mono- and multiciliated tissues. *Differentiation* **83,** S105–S113 (2012).
18. Muzumdar, M. D., Tasic, B., Miyamichi, K., Li, L. & Luo, L. A global double-fluorescent Cre reporter mouse. *Genesis* **45,** 593–605 (2007).
19. Rieck, S. & Kaestner, K. H. Expansion of β-cell mass in response to pregnancy. *Trends Endocrinol. Metab.* **21,** 151–158 (2010).
20. Speier, S. *et al.* Noninvasive *in vivo* imaging of pancreatic islet cell biology. *Nat. Med.* **14,** 574–578 (2008).
21. Golson, M. L., Misfeldt, A. A., Kopsombut, U. G., Petersen, C. P. & Gannon, M. High fat diet regulation of β-cell proliferation and β-cell mass. *Open Endocrinol. J.* **4,** (2010). 10.2174/1874216501004010066
22. Kitsou-Mylona, I., Burns, C. J., Squires, P. E., Persaud, S. J. & Jones, P. M. A role for the extracellular calcium-sensing receptor in cell-cell communication in pancreatic islets of Langerhans. *Cell. Physiol. Biochem.* **22,** 557–566 (2008).
23. Schulze, T., Morsi, M., Bruning, D., Schumacher, K. & Rustenbeck, I. Different responses of mouse islets and MIN6 pseudo-islets to metabolic stimulation: a note of caution. *Endocrine* **51,** 440–447 (2016).
24. Granot, Z. *et al.* LKB1 regulates pancreatic β cell size, polarity, and function. *Cell Metab.* **10,** 296–308 (2009).
25. Kalwat, M. A. & Thurmond, D. C. Signaling mechanisms of glucose-induced F-actin remodeling in pancreatic islet β cells. *Exp. Mol. Med.* **45,** e37 (2013).
26. Staiger, H. *et al.* Common genetic variation in the human FNDC5 locus, encoding the novel muscle-derived 'browning' factor irisin, determines insulin sensitivity. *PLoS One* **8,** e61903 (2013).
27. Gao, T. *et al.* Pdx1 maintains β cell identity and function by repressing an α cell program. *Cell Metab.* **19,** 259–271 (2014).
28. Wang, Z., York, N. W., Nichols, C. G. & Remedi, M. S. Pancreatic β cell dedifferentiation in diabetes and redifferentiation following insulin therapy. *Cell Metab.* **19,** 872–882 (2014).
29. Talchai, C., Xuan, S., Lin, H. V., Sussel, L. & Accili, D. Pancreatic β cell dedifferentiation as a mechanism of diabetic β cell failure. *Cell* **150,** 1223–1234 (2012).
30. Jonas, J. C. *et al.* Chronic hyperglycemia triggers loss of pancreatic β cell differentiation in an animal model of diabetes. *J. Biol. Chem.* **274,** 14112–14121 (1999).

Supplementary Information is available in the online version of the paper.

Acknowledgements We thank A. Raducanu, A. Böttcher and E. Schlüssel for comments and discussions; A. Theis, B. Vogel and K. Diemer for technical support; the Human Tissue Laboratory (HTL) of Lund University Diabetes Centre (LUDC) for high-quality RNA sequencing expression data from human pancreatic islets donors; to InSphero for human microislets; the European Consortium for Islet Transplantation (ECIT) for human islets; and R. Scharfmann for the EndoC-β H1 cell line. The human islet research was supported by a Strategic Research Grant from the Swedish Research Council (2009-1039). A.M. was funded by the Helmholtz post-doctoral fellowship program. This work was supported by an Emmy-Noether Fellowship, the European Union (ERC starting grant Ciliary Disease) and the HumEn project from the European Union's Seventh Framework Programme for Research, Technological Development and Demonstration under grant agreement No. 602587 (http://www.hum-en.eu/). This work was funded (in part) for H.L. and J.B. by the Helmholtz Alliance ICEMED – Imaging and Curing Environmental Metabolic Diseases, through the Initiative and Networking Fund of the Helmholtz Association. We thank the Helmholtz Society, Helmholtz Portfolio Theme 'Metabolic Dysfunction and Common Disease, German Research Foundation and German Center for Diabetes Research (DZD e.V.) for financial support. This work was supported with funds for S.S. from the Emmy-Noether Program, the Center for Regenerative Therapies Dresden-DFG Research Center for Regenerative Therapies Dresden, Cluster of Excellence (CRTD), the DFG-Collaborative Research Center/Transregio 127 and the German Ministry for Education and Research to the German Centre for Diabetes Research and to the Network of Competence for Diabetes.

Author Contributions E.B., A.M. and M.G. conceived and performed the experiments and wrote the manuscript. M.B. established the 3D *in vitro* cultures. S.S.R. and E.B. helped to perform human islet experiments. N.M., C.L., H.Z., M.J., M.T. and J.G. conceived and performed mitochondria analysis. M.I. and J.B. performed the microarray analysis. M.A. and A.F. analysed mitochondria by TEM. F.M., H.S. and H-U.H. performed the SNP analysis of *FLTP* in humans. O.K. provided human islets and N.O. provided RNA sequencing data. R.W-S. supervised and trained E.B. in human epidemiology and genetics. H.C., J.A.C. and S.S. performed the islet transplantation and analyzed the data set. H.L. conceived the study and wrote the manuscript.

Author Information Microarray data have been submitted to GEO with accession number GSE68853. Reprints and permissions information is available at www.nature.com/reprints. The authors declare competing financial interests: details are available in the online version of the paper. Readers are welcome to comment on the online version of the paper. Correspondence and requests for materials should be addressed to H.L. (heiko.lickert@helmholtz-muenchen.de).

Reviewer Information *Nature* thanks C. Wollheim and the other anonymous reviewer(s) for their contribution to the peer review of this work.

METHODS

Animal studies. Animal experiments were carried out in compliance with the German Animal Protection Act and with the approved guidelines of the Society of Laboratory Animals (GV-SOLAS) and of the Federation of Laboratory Animal Science Associations (FELASA). Mouse lines used: $Fltp^{ZV}$ (C57BL/6J; ref. 6) and $Fltp^{T2AiCre/+}$ (mixed C57BL/6J, CD1 background; ref. 17) crossed with $Gt(ROSA)26^{mTmG}$ (129/SvJ, C57BL/6J mixed background; ref. 18) ($Fltp^{T2AiCre/+}$;$Gt(ROSA)26^{mTmG}$). Albino B6 mice (B6N-Tyrc/BrdCrCrl; Charles River) crossed with B6 $Rag1^{-/-}$ mice (B6.129S7-Rag1tm1Mom/J; Jackson Laboratories) were used as recipients for $Fltp^{T2AiCre/+}$;$Gt(ROSA)26^{mTmG}$ islet transplants. All experiments were performed using 3–6-month-old mice, unless indicated otherwise. Islet isolation was carried out by collagenase P (Roche) digestion and centrifugation using Optiprep density gradient (Sigma) as described[31]. Isolated islets were handpicked twice under a microscope. For analysis of islet β-cell proliferation during pregnancy, mice were euthanized at G15.5 and for histological analysis EdU was administrated 24 h before sacrifice. For HFD analysis, fourteen weeks after islet transplantation, mice were divided into two groups and either continued on a normal diet (Ssniff GmbH) or switched to HFD (60 kcal % fat; Research Diets, Inc.) with *ad libitum* access to water and chow.

For intraperitoneal glucose tolerance tests (IPGTTs) and insulin tolerance test (ITT) mice were fasted for 6 h and injected intraperitoneally with 2 g glucose per kg (BW) or 0.75 U insulin per kg (BW), respectively. Blood glucose was measured at indicated time points after glucose injection using Accu-Chek Aviva glucometer (Roche).

Cell culture and human islets. Min6 (clone 9) murine β-cell line and EndoC-β H1 were cultured in adherence (2D culture) as described previously[32,33]. For floating 3D (3D) culture Min6 were plated on uncoated ibidi chambers (ibidi) for 3, 6 or 7 days. For 3D matrigel based cultures, Min6 and EndoC-β H1 were cultured in Growth-Factor-Reduced Matrigel Matrix (BD Bioscience, Germany) diluted 1:1 in their respective medium. All the cell lines used were tested for mycoplasma and were negative. Isolated islet cells from P5 pancreata were cultured overnight in RPMI 1640 containing P/S and 5% FCS. For analysis of Wnt5a induced β-cell maturation, samples were stimulated with 400 ng/ml of Wnt5a (R&D systems, Germany) for 12 h, 3 or 6 days in RPMI1640 supplemented with P/S and 3% FCS. Human islets isolated from cadaver and pancreatic microislets were obtained from the JDRF award 31-2008-416 (ECIT Islet for Basic Research program) and from InSphero (Switzerland), respectively. All experiments with human islets were approved by the Ethical commission of the Technical University of Munich (Germany). Human islet donor data: 6 donors, 3 males and 3 females; age mean 53.6 yrs (range: 41–65); BMI, mean 24.25 (range: 20.8–30.1); purity mean 78 (range 89–45%). Human microislet donor data: 3 donors, 2 female and 1 male; age mean 40.10 yrs (range: 37–56); BMI mean 23.19 (range: 22.7–23.56).

Upon arrival, human islets were collected by centrifugation, selected by hand picking and cultured in CMRL1066 (Gibco, Thermo Fisher Scientific) supplemented with 10% human serum (Sigma), 1% P/S and 2 mM L-glutamine. Pancreatic microislets were cultured according to the manufacturer's instruction. Human islets were treated with 100 ng/ml WNT4 (R&D systems) or 400 ng/ml WNT5A in CMRL 1066 supplemented with 2% human serum albumin (Sigma), 1% P/S, 2 mM L-glutamine, 5.5 mM glucose, 100 ng/ml mouse Noggin (Peprotech) and 10 μM Y-27632 (Santa Cruz) for 4 days (medium was changed every 2 days).

Microislets were treated with 100 ng/ml WNT4 (R&D Systems) or 400 ng/ml WNT5A in CMRL 1066 supplemented with 2% human serum albumin, 1% P/S, 2 mM L-glutamine, 5.5 mM glucose and 100 ng/ml mouse Noggin (Peprotech) for 4 days (medium was changed every 2 days).

EndoC-β H1 cells were treated with 100 ng/ml WNT4 (R&D systems) or 400 ng/ml WNT5A or 200 ng/ml WNT3A (Peprotech) in their culture medium[5] supplemented with 100 ng/ml mouse Noggin (Peprotech) and 10 μM Y-27632 (Santa Cruz) for 4 h or 4 days (medium was changed every 2 days).

Islet transplantation and *in vivo* imaging of islets engrafted in the anterior chamber of the eye. For islet transplantation into the anterior chamber of the mouse eye, mice were anaesthetized by inhalation of 2% isoflurane in 100% oxygen via a face mask. The mouse head was fixed in a head holder and a 25-gauge needle used to make a small incision into the cornea, close to the corneal limbus. Next, 30–40 islets in PBS were slowly injected into the anterior chamber of the eye using a custom made beveled glass cannula (outer diameter 0.4 mm, inner diameter 0.32 mm; Hilgenberg GmbH). For *in vivo* imaging mice were intubated (BioLite, Braintree Scientific, Inc.) and anaesthetized by 2% isoflurane in 100% oxygen with 270 μl stroke volume at 250 strokes per min for ≤90 min. *In vivo* imaging was performed as previously described[34]. For confocal and two-photon imaging, an upright laser-scanning microscope (LSM780 NLO; Zeiss) with a two-photon laser (Chameleon Vision II; Coherent, Inc.) and W Plan-Apochromat 20×/1.0 DIC M27 75 mm objective (Zeiss) was used. Imaging of intraocular islets was performed during islet engraftment (days 3, 13 and 4 weeks post-transplantation) and repeated four and eight weeks after diet switch. Backscattered laser light was detected at 633 nm. Total islet volume was calculated using surface rendering (Imaris 7.4, Bitplane AG). GFP (mG) and Tomato (mT) were excited by two-photon laser at 930 nm and detected at 500–550 nm and at 575–610 nm, respectively. mG and mT islet fractions were assessed from Gaussian filtered *z*-stacks (step size of 1.5 μm) of the whole islet for the revascularization or within the top 80 μm of the islet for the HFD time points using surface rendering (Imaris 7.4). Compartment volumes were calculated in relation to total islet volume obtained from backscatter imaging. Vessels were visualized by injecting 0.8 μM Qtracker 705 (Life Technologies) in 100 μl PBS into the tail vein and detected at 690–730 nm. mG and mT cell cross-sectional areas were assessed manually in individual optical planes of the islet *z*-stacks (Fiji software)[35].

Transmission electron microscopy. Immunogold staining was performed on isolated islets from $Fltp^{T2AiCre/+}$;$Gt(ROSA)26^{mTmG/+}$ mice as follows. After islet isolation the islets were cultured overnight in RPMI1640 supplemented with 10% FCS and P/S, then fixed in 2.5% electron microscopy grade glutaraldehyde in 0.1 M sodium cacodylate buffer pH 7.4 (Science Services), stained with rabbit anti-GFP (Invitrogen, A11122, 1:500) and a gold-conjugated goat anti-rabbit antibody (Aurion, 806.011, 1:40). Isolated FACS-sorted FVR islet cells or immunogold-stained islets were fixed in 2.5% electron microscopy grade glutaraldehyde in 0.1 M sodium cacodylate buffer pH 7.4 (Science Services) as pellets, post-fixed in 2% aqueous osmium tetraoxide[36], dehydrated in gradual ethanol (30–100%) and propylene oxide, embedded in Epon (Merck) and cured for 48 h at 60 °C. Semi-thin sections were cut and stained with toluidine blue. Ultrathin sections of 50 nm were collected onto 200 mesh copper grids, stained with uranyl acetate and lead citrate before examination by transmission electron microscopy (Zeiss Libra 120 Plus, Carl Zeiss NTS GmbH). Pictures were acquired using a Slow Scan CCD-camera and iTEM software (Olympus Soft Imaging Solutions). Serial pictures for image analyses were acquired by transmission electron microscopy (Zeiss EM10CR, Carl Zeiss NTS GmbH) with a MegaView III camera system (Olympus Deutschland GmbH). Images were quantified using image analysis software Definiens Developer XD2 (Definiens AG) according to a previously published procedure[37]. Initially mitochondria were annotated manually. A rule set was developed in order to detect and quantify the length of the inner mitochondrial membrane within these marked mitochondria, based on intensity, morphology and neighbourhood. Additionally the area for each mitochondrion and the number of mitochondria per cell area were calculated. The β-cells were identified as Fltp lineage^{+} or Fltp lineage^{-} according to their immuno-gold labelling. Insulin granules were counted after their classification as immature or mature granules according to their morphology.

Immunofluorescence staining and western blot. For immunohistochemistry, pancreas samples were fixed in 4% formalin, cryoprotected by incubation in a progressive sucrose gradient and embedded in Optimum Cutting Temperature (OCT). Sorted cells, Min6 and EndoC-β H1 were fixed in 4% formalin before staining. For whole-mount staining, embryos were cleared using BABB solution and stained using a modified previously described protocol[6].

Primary antibodies used for immunostaining: goat anti-Nkx6.1 (R&D system, AF5857, 1:400), rabbit anti-Nkx6.1 (Acris/Novus, NBP1-82553, 1:100), rat anti-RFP (Chromotek, ORD003515, 1:1000), chicken anti-GFP (Aves Labs, GFP-1020, 1:800), guinea pig anti-glucagon (Millipore, 4031-01F, 1:500), goat anti-somatostatin (Santa Cruz, sc-7819, 1:300), rabbit anti-insulin (Thermo Scientific, PA-18001, 1:200), guinea pig anti-insulin (Thermo Scientific, PA-26938, 1:300), goat anti-pancreatic polypeptide (PP) (Abcam, ab77192, 1:300), rabbit anti-Ki-67 (Abcam, ab15580, 1:200), rabbit anti-MafA (Bethyl, IHC-00352-1, 1:100), mouse anti-β-catenin (BD, 610154, 1:2000), rabbit anti-Urocortin 3 (Phoenix Pharmaceuticals, H-019-29, 1:300), rabbit anti-p27 (Santa Cruz, sc-528, 1:100), goat anti-Wnt4 (R&D Systems, AF475, 1:100), Alexa Fluor 546 phalloidin (Invitrogen, A22283, 1:200), rat anti-E-cadherin (raised by E. Kremmer (Helmholtz Zentrum München), 1:200), MitoTracker Deep Red FM (Life Technologies, M22426, final concentration in the medium: 200 nM). Secondary antibodies used for indirect fluorescence staining (dilution always 1:800): goat anti-chicken Alexa Fluor 488 (Dianova, 103-545-155), donkey anti-goat Alexa Fluor 488 (Invitrogen, A11055), donkey anti-mouse Alexa Fluor 555 (Invitrogen, A31570), donkey anti-goat Alexa Fluor 555 (Invitrogen, A21432), donkey anti-rabbit Alexa Fluor 555 (Invitrogen, A31572), donkey anti-goat Alexa Fluor 594 (Invitrogen, A11058), donkey anti-mouse Alexa Fluor 594 (Invitrogen, A21203), donkey anti-guinea-pig Alexa Fluor 649 (Dianova, 706-495-148). Nuclear staining was performed with DAPI (Life Technology, 1:800). EdU staining was performed using the Click-iT Staining Kit (Life Technology) according to the manufacturer's instructions. For analysis of proliferation of EndoC-β H1, cells were pulsed with 10 μM EdU for 2 days. Cryosection imaging was performed using a Leica SP5 confocal microscope.

Analysis was performed either manually or by using IMARIS software (Bitplane) or the Leica LAS-AF (Version 2.7.3.9723) software. For western blot analysis of mitochondrial complexes, islet cells were isolated and FACS sorted in RIPA buffer. Cell lysates were resolved by SDS–PAGE, transferred to PVDF membrane (Biorad) and incubated with the following primary antibodies: anti-Rt/Ms Total OxPhos Complex Kit (Life technologies, 458099, 1:250) and γ-tubulin (Abcam, ab11316, 1:10.000). For western blot analysis of Fltp and Nkx6.1 expression, tissues and Min6 were dissociated in RIPA buffer. Cell lysates were resolved by SDS–PAGE, transferred to PVDF membrane (Biorad) and incubated with the following antibodies: rabbit anti-Fltp[38] (1:500), goat anti-Nkx6.1 (R&D system, AF5857, 1:2.000) and mouse anti-γ-tubulin (Abcam, ab11316, 1:10.000). For western blot analysis of pJNK, NKX6.1 and PDX1 expression, human islet and EndoC-β H1 were dissociated in RIPA buffer. Cell lysates were resolved by SDS–PAGE, transferred to PVDF membrane (Biorad) and incubated with the following primary antibodies: Rabbit SAPK/JNK (56G8) (New England Biolabs, 9258, 1:1.000), rabbit SAPK/JNK-Phospho (New England Biolabs, 4668, 1:1.000), goat anti-NKX6.1 (R&D Systems, AF5857, 1:2.000), rabbit anti-PDX1 (New England Biolabs, 5679, 1:500) and mouse anti GAPDH (Merck Bioscience, CB 1001, 1:5.000-10.000). Protein bands were visualized using the following horseradish peroxidase (HRP)-conjugated antibody: Goat anti-mouse HRP (Dianova, 115-036-062, 1:10.000), rabbit anti goat HRP (Dianova, 305-035-045, 1:5.000), goat anti rabbit HRP (Dianova, 111-036-045, 1:5.000) and chemiluminescence reagent (Millipore). The bands were quantified using ImageJ.

Fluorescent intensity analysis. Nkx6.1 and MafA fluorescent intensity analysis of Min6 was performed with Imaris software, using the spot function. Spots of the same size were chosen and the mean fluorescence within these spots was calculated. The median fluorescent intensity was used as a threshold to distinguish between Nkx6.1-high and -low cells.

To show the fluorescent intensity profiles a line was drawn and the fluorescence intensity over this line calculated and plotted against the length of the line.

To calculate the Fltp reporter fluorescent intensity of the BABB cleared pancreata Imaris software was used. A surface on the Nkx6.1 positive cells was calculated and the mean Fltp reporter fluorescent intensity was calculated within the described surfaces.

Nkx6.1, Venus, EdU and p27 fluorescent intensity analysis of pancreatic islet sections were performed with Imaris software, by using the surface function. Surfaces using the same threshold were rendered for the Nkx6.1 positive cells and the mean fluorescence intensity within these surfaces was calculated for Venus, EdU and p27. To discriminate between p27-high and -low cells, the total mean fluorescent intensity of all islets of one mouse was used as a threshold. The threshold for EdU was set by eye.

Mitochondria network analysis and oxygen consumption rate. The mitochondria network was analysed using Imaris. The mitochondrial surface was rendered by thresholding the Mitotracker Deep Red FM (Thermo Fisher Scientific) intensity. The analysis was performed on nine Nkx6.1–Venus double-positive cells and on four Nkx6.1 single-positive cells from two islets cultured in culture medium and on nine Nkx6.1–Venus double-positive cells and on six Nkx6.1 single-positive cells from three islets exposed to 2 mM glucose for 2 h. For the flux analysis experiment, FVR^+ and FVR^- β-cells were sorted and recovered. Around 30,000 single cells were plated in a 96-well plate for flux analysis using 2 μl Growth-Factor-Reduced Matrigel Matrix (BD Bioscience) diluted 1:2 in medium per well and rested overnight. The cells were starved for 2 h in Hank's Salt (HBSS) supplemented with 2 mM glucose and 2 mM glutamax (Thermo Fisher Scientific). Oxygen consumption was measured using an XF96 extracellular flux analyser (Seahorse Bioscience) with sequential injections of 13 mM glucose, 4 μM oligomycin (Sigma) and 10 μM antimycin + 4 μM rotenone (Sigma).

FACS analysis, gene profiling and endocrine cell reaggregation. For gene profiling, qPCR, transmission electron microscopy and western blotting, cells from isolated islets were sorted and analysed using FACS-Aria III (BD Bioscience). The percentage and purity of both endocrine populations were controlled by cytospins and quantitative PCR (qPCR) and 90% purity of Nkx6.1$^+$ β-cell subpopulations was achieved using an optimized FACS sorting scheme. For FACS analysis, cells were fixed in 4% PFA and intracellular staining for Nkx6.1 was performed by using goat anti-Nkx6.1 (R&D Systems, AF5857, 1:100) and donkey anti-goat APC (Dianova, 705-136147, 1:1.000). The ratio of Fltp lineage$^+$ and Fltp lineage$^-$ populations during pregnancy was calculated over the Nkx6.1$^+$ cells. The results were analysed using FlowJo software. For qPCR on sorted populations, total RNA was extracted from FACS-sorted endocrine cells, using a miRNeasy micro kit (Qiagen) and amplified with the Ovation PicoSL WTA System. For gene profiling, total RNA was extracted from FACS-sorted FVR endocrine cells, using a miRNeasy micro kit (Qiagen) and amplified with the Ovation PicoSL WTA System V2 in combination with the Encore Biotin Module (Nugen). Amplified cDNA was hybridized on Affymetrix Mouse Gene 1.0 ST arrays. Staining and scanning were performed according to the Affymetrix expression protocol including minor modifications as suggested in the Encore Biotion protocol. Expression console (v.1.3.0.187, Affymetrix) was used for quality control and to obtain annotated normalized RMA (robust microarray analysis) gene-level data (standard settings including median polish and sketch-quantile normalization). TaqMan qPCR was assessed using the probe list provided in Supplementary Table 5, according to the manufacturer's instructions. For quantification of mitochondrial DNA copy number, DNA from sorted cells was extracted using QIamp DNA Blood Mini kit (QiAgen) according to the manufacturer's instructions. The ratio of mtDNA to nDNA was determined by Syber green qPCR (Dynamo Flash Syber green, Byozym) using the primers listed in Supplementary Table 5. For endocrine cell re-aggregation, FVR^+ and FVR^--enriched β-cells were FACS sorted and cultured by shaking in DMEM (containing 4.5 g/l glucose, 5% FCS and 1% v/v penicillin/streptomycin) diluted 1:1 in conditioned medium (DMEM containing 4.5 g/l glucose, 5% FCS and 1% v/v penicillin/streptomycin) from MS1 cells (pancreatic islets endothelial cell line, ATCC CRL-2279, LGC Standards GmbH). Cells were aggregated for 6 days; 10 μM Y-27632 (Santa Cruz) was added on day 1 and left for the first 3 days, at which point the medium was changed. One day before the GSIS assay, the cells were cultured in DMEM (containing 11 mM glucose, 5% FCS and 1% v/v penicillin/streptomycin).

GSIS assays and pancreatic insulin and glucagon concentration. Isolated murine islets were allowed to recover overnight in islet medium (DMEM containing 11 mM glucose, 10% v/v FBS, 1% v/v penicillin/streptomycin). For the static GSIS assay, islets of the same size were handpicked and assayed with different glucose concentrations as previously described[39]. For static GSIS assays on endocrine aggregates, modified Krebs Ringer phosphate Hepes (KRPH) buffer supplemented with 0.1% BSA was used. The aggregates were incubated for 30 min in KRPH with 2.8 mM glucose and sequentially incubated with different glucose concentrations as indicated. For static GSIS assays on human microislets, sequential incubation with 2.8 mM glucose and 16.8 mM glucose in KRPH buffer was assessed for 2 h each. Assessment of pancreatic insulin and glucagon concentration was performed by acid ethanol extraction. Murine insulin and glucagon concentrations were determined using Ultrasensitive Insulin ELISA kit (Cristal Chem) and Mouse Glucagon ELISA Kit (Cristal Chem), respectively, and normalized over protein content. Human insulin concentrations were determined using an Ultrasensitive Insulin ELISA kit (Mercodia).

Association analysis. The study population consisted of 2,228 white individuals at risk for type 2 diabetes (family history of type 2 diabetes, body mass index (BMI) $\geq 27\,\mathrm{kg/m^2}$, impaired fasting glycaemia and/or previous gestational diabetes) recruited from the ongoing Tübingen Family study for type 2 diabetes. All participants underwent assessment of medical history, smoking status and alcohol consumption habits; the subjects furthermore agreed to undergo physical examination, routine blood tests and oral glucose tolerance tests (OGTTs). Only individuals with complete phenotypic and genotypic data sets and documented absence of medication known to influence glucose tolerance, insulin sensitivity or insulin secretion were included. All study participants gave informed written consent to the study and protocols adhered to the Declaration of Helsinki.

The study protocol was approved by the Ethics Committee of the Eberhard Karls University, Tübingen.

OGTT and laboratory measurements. A standardized 75 g OGTT was performed following a 10 h overnight fast. For the determination of plasma glucose, insulin and C-peptide levels, venous blood samples were drawn at baseline and at timepoints 30, 60, 90 and 120 min of the OGTT[40]. Plasma glucose levels (in mmol/l) were measured with a bedside glucose analyser (glucose oxidase method, Yellow Springs Instruments). Plasma insulin and C-peptide levels (in pmol/l) were determined by commercial chemiluminescence assays for ADVIA Centaur (Siemens Medical Solutions). BMI was calculated as weight divided by squared height (in $\mathrm{kg/m^2}$). OGTT-derived insulin sensitivity was estimated as proposed earlier[41]: $10{,}000/[c(\mathrm{Glc}_0)*c(\mathrm{Ins}_0)*c(\mathrm{Glc}_{\mathrm{mean}})*c(\mathrm{Ins}_{\mathrm{mean}})]^{½}$ (with c = concentration, Glc = glucose and Ins = insulin). OGTT-derived insulin secretion was estimated as area under the curve (AUC) $\mathrm{Cpep}_{0-30}/\mathrm{AUC}\ \mathrm{Glc}_{0-30}$ according to the formula: $[c(\mathrm{Cpep}_0)+c(\mathrm{Cpep}_{30})]/[c(\mathrm{Glc}_0)+c(\mathrm{Glc}_{30})]$ (Cpep = C-peptide).

Selection of tagging SNPs and genotyping. Based on publicly available data from the 1000 Genomes Project (http://browser.1000genomes.org/index.html), we analysed *in silico* a genomic area on human chromosome 1q23.3 spanning the *CFAP126* gene (3.143 kb, five exons, four introns, located on the reverse strand) and 2 kb of the gene's 5′-flanking region. Within the analysed *CFAP126* locus, 36 SNPs were found. Using the tagger analysis tool of Haploview (see http://www.broadinstitute.org/scientific-community/science/programs/medical-and-population-genetics/haploview/%20haploview), seven tagging SNPs were identified that cover all the other common SNPs (minor allele frequency ≥ 0.01) with an $r^2 \geq 0.8$. These SNPs were rs17399583 (C/T), rs11584714 (C/G) and

rs57835711 (C/G) in the 5′-flanking region, rs114482063 (A/T) and rs182840301 (C/A) in intron 1 and rs16832872 (G/A) and rs75715534 (C/G) in intron 3. For genotyping, DNA was isolated from whole blood using a commercial kit (NucleoSpin, Macherey & Nagel). The tagging SNPs were genotyped using the mass spectrometry system massARRAY from Sequenom and the manufacturer's iPLEX software (Sequenom). The call rates were $\geq$96.1%. The mass spectrometric results were validated in 50 randomly selected subjects by bidirectional sequencing and both methods gave 100% identical results.

RNA sequencing expression data analysis of human pancreatic islets. RNA sequencing expression data on human pancreatic islets from $n=119$ donors including $n=14$ diagnosed type 2 diabetes (T2D) donors were obtained from the Human Tissue Laboratory (HTL) of Lund University Diabetes Centre (LUDC)[42]. Gencode v14 RefSeq was used for gene annotation. Across-samples normalization was performed using the TMM normalization method[43]. HbA1c information available for 106 human pancreatic islets donors was used for classification into a) healthy/non-diabetic donors (normal glucose tolerance, NGT, $n=66$, HbA1c <6), b) pre-diabetic donors (impaired glucose tolerance, IGT, $n=21$, $6<$ HbA1c <6.5) and c) diabetic donors (T2D, $n=19$, diagnosed + HbA1c ≥ 6.5). Associations of gene expression in human pancreatic islets with blood glucose level (NGT+IGT+T2D status) was performed with ANOVA for linear testing and using the Kruskal–Wallis method for nonlinear and non-parametric testing. Correcting for multiple testing was performed with FDR procedure and 5% significance threshold was selected for the analysis. All calculations were done using R language for statistical computations[44]. The upper whisker of the boxplots represents min (max (x), Q_3 + 1.5 * IQR) and the lower whisker max (min(x), Q_1 − 1.5 * IQR). IQR represents the box length Q_3 − Q_1.

Statistical analysis. No statistical methods were used to predetermine sample size. The experiments were not randomized and the investigators were not blinded to allocation during experiments and outcome assessment. Statistical analysis was performed using GraphPad Prism 6 Software (GraphPad Software, USA). Values were compared using unpaired or paired t-tests or ANOVA as indicated for each experiment. P values of <0.05 were considered statistically significant. Data are expressed as means $\pm$ s.e.m. unless otherwise specified. Statistical analysis of microarray profile was performed using the statistical programming environment R (R Development Core Team) implemented in CARMAweb. The P value of the limma t-test was used as a criterion for significance ($P<0.01$) and in addition filtered for fold-changes >1.5 to potentially increase biological relevance. Multiple testing corrections were not applied, because with only two replicates this approach would be too stringent (the most significant gene after Benjamini-Hochberg correction had a false discovery rate $<22\%$). Heatmaps were generated with CARMAweb[45] and cluster dendrograms with the R script hclust. GO term enrichments were performed for 1.5-fold regulated genes with a P-value <0.005 using the GePS module in the Genomatix Software Suite v3.1 (Genomatix). The pathway analyses ($P<0.05$) were generated through the use of QIAGEN's Ingenuity Pathway Analysis (IPA, QIAGEN Redwood City, http://www.qiagen.com/ingenuity). For association analysis, continuous variables with non-normal distribution were $\log_e$-transformed before statistical analysis. Multiple linear regression analysis was performed using the least-squares method. In the regression models, insulin secretion was chosen as an outcome variable, the SNP genotype (in the dominant inheritance model) as an independent variable and gender, age, BMI and insulin sensitivity as confounding variables. SNP–BMI interaction effects on insulin secretion were tested by ANCOVA with gender, age and insulin sensitivity as confounding variables. When testing all seven tagging SNPs in parallel, a Bonferroni-corrected P-value <0.0073 was considered statistically significant. For all analyses, the statistical software JMP 8.0 (SAS Institute) was used.

31. Szot, G. L., Koudria, P. & Bluestone, J. A. Murine pancreatic islet isolation. *J. Vis. Exp.* **2007,** 255 (2007).
32. Ravassard, P. *et al.* A genetically engineered human pancreatic β cell line exhibiting glucose-inducible insulin secretion. *J. Clin. Invest.* **121,** 3589–3597 (2011).
33. Miyazaki, J. *et al.* Establishment of a pancreatic β cell line that retains glucose-inducible insulin secretion: special reference to expression of glucose transporter isoforms. *Endocrinology* **127,** 126–132 (1990).
34. Chmelova, H. *et al.* Distinct roles of β-cell mass and function during type 1 diabetes onset and remission. *Diabetes* **64,** 2148–2160 (2015).
35. Schindelin, J. *et al.* Fiji: an open-source platform for biological-image analysis. *Nat. Methods* **9,** 676–682 (2012).
36. Dalton, A. J. A chrome-osmium fixative for electron microscopy. *Anat. Rec.* **121,** 281 (1955).
37. Feuchtinger, A. *et al.* Image analysis of immunohistochemistry is superior to visual scoring as shown for patient outcome of esophageal adenocarcinoma. *Histochem. Cell Biol.* **143,** 1–9 (2015).
38. Gegg, M. *et al.* Flattop regulates basal body docking and positioning in mono- and multiciliated cells. *Elife* **3,** e03842 (2014).
39. Wu, Y. *et al.* Growth hormone receptor regulates β cell hyperplasia and glucose-stimulated insulin secretion in obese mice. *J. Clin. Invest.* **121,** 2422–2426 (2011).
40. Stefan, N. *et al.* Polymorphisms in the gene encoding adiponectin receptor 1 are associated with insulin resistance and high liver fat. *Diabetologia* **48,** 2282–2291 (2005).
41. Matsuda, M. & DeFronzo, R. A. Insulin sensitivity indices obtained from oral glucose tolerance testing: comparison with the euglycemic insulin clamp. *Diabetes Care* **22,** 1462–1470 (1999).
42. Fadista, J. *et al.* Global genomic and transcriptomic analysis of human pancreatic islets reveals novel genes influencing glucose metabolism. *Proc. Natl Acad. Sci. USA* **111,** 13924–13929 (2014).
43. Robinson, M. D. & Oshlack, A. A scaling normalization method for differential expression analysis of RNA-seq data. *Genome Biol.* **11,** R25 (2010).
44. R Computing Team. *R: A Language and Environment for Statistical Computing.* (R Foundation for Statistical Computing, Vienna, Austria, 2014).
45. Rainer, J., Sanchez-Cabo, F., Stocker, G., Sturn, A. & Trajanoski, Z. CARMAweb: comprehensive R- and bioconductor-based web service for microarray data analysis. *Nucleic Acids Res.* **34,** W498–W503 (2006).

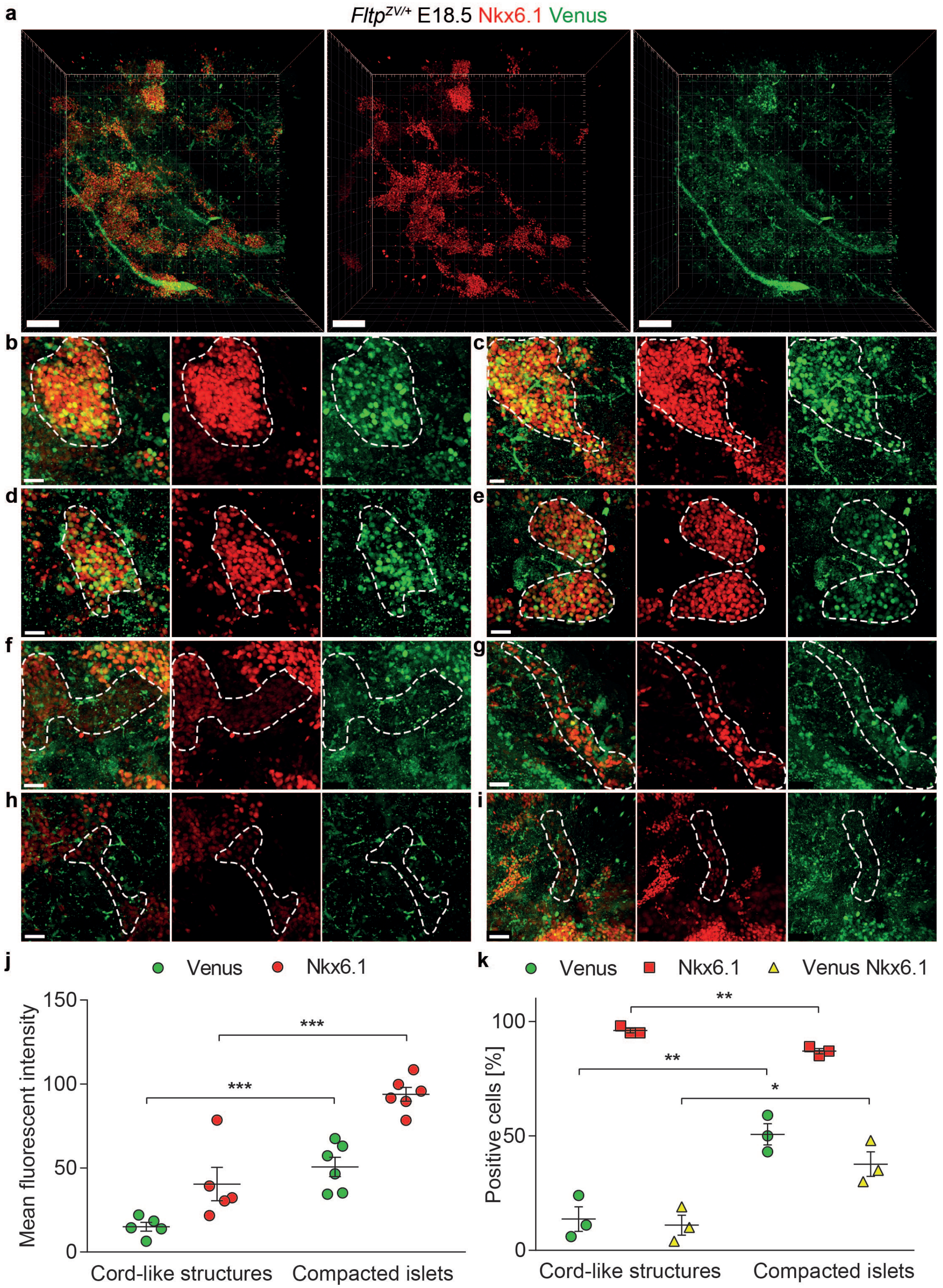

Extended Data Figure 1 | FVR expression is induced in compacted islet structures and correlates with high Nkx6.1 expression. a, Overview of a cleared whole-mount pancreas from an *Fltp*$^{ZV/+}$ mouse at E18.5, stained with anti-Nkx6.1 and anti-GFP antibodies and scanned with a laser confocal microscope. **b**–**e**, In compacted islets (dotted line), high FVR expression correlates with high Nkx6.1 expression. **f**–**i**, In cord-like structures of endocrine cells that left the ductal epithelium (dotted line), low Nkx6.1 expression correlates with low FVR expression. **j**, Quantification of the mean fluorescent intensity of Venus (FVR)$^+$ and Nkx6.1$^+$ cells in compacted and cord-like structures (n (mice) = 3, 5 cord-like structures, 6 compacted islets; $^{***}P = 0.0005$, two sided unpaired t-test). **k**, Quantification of Nkx6.1 (red) and Venus (green) single-positive cells as well as all Nkx6.1–Venus double-positive cells (yellow) in compacted and cord-like structures (n (mice) = 3, cord-like structures 570 cells, compacted islets 1,827 cells; $^{**}P = 0.0064$ for Venus, $^{**}P = 0.0041$ for Nkx6.1, $^{*}P = 0.0182$ for Venus–Nkx6.1, two-sided unpaired t-test). Scale bars, 100 μm (**a**), 20 μm (**b**–**i**). Data represent mean ± s.e.m.

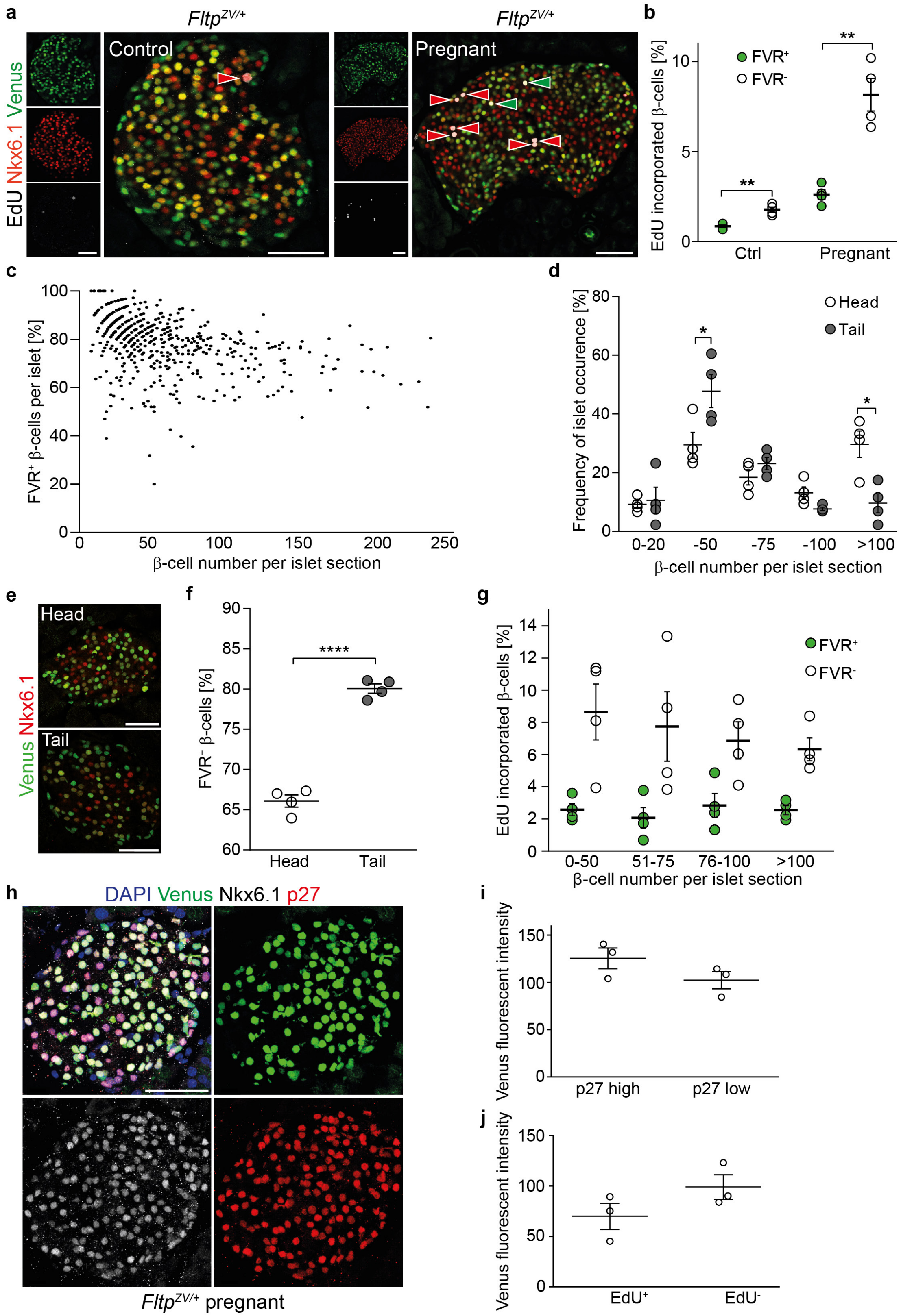

Extended Data Figure 2 | See next page for caption.

Extended Data Figure 2 | FVR$^-$ and FVR$^+$ β-cell subpopulations exhibit differential proliferative capacity and inter-islet heterogeneity in the head and tail of the pancreas. **a**, **b**, LSM images showing FVR, Nkx6.1 and EdU (**a**) and quantification (**b**) of EdU$^+$ in FVR$^-$ and FVR$^+$ β-cell subpopulations in control and pregnant (G15.5) mice (green/red arrow heads indicate proliferating FVR$^+$/FVR$^-$ β-cells. *n* (control) = 4 (8,500 Nkx6.1$^+$ cells), *n* (pregnant) = 4 (10,938 Nkx6.1$^+$ cells); $^{**}P$ (Ctrl) = 0.0049, $^{**}P$ (pregnant) = 0.0059, two-sided unpaired *t*-test). **c**, Scatter plot of FVR$^+$ β-cell distribution relative to number of β-cells per islet in *Fltp*$^{ZV/+}$ mice (*n* (mice) = 10, *n* (islets) = 512). **d**, Quantification of islet size distribution in head and tail of *Fltp*$^{ZV/+}$ pancreas sections (*n* (mice) = 4, *n* (islets) = 299; $^*P$ (20–50) = 0.0419, $^*P$ (>100) = 0.0238, two-sided unpaired *t*-test). **e**, **f**, LSM images (**e**) and quantification (**f**) of FVR$^+$ β-cell distribution in the pancreas head and tail (*n* (mice) = 4, *n* (islets) = 299, *n* (Nkx6.1$^+$ cells) = 19,054; $^{****}P < 0.0001$, two-sided unpaired *t*-test). **g**, Quantification of EdU incorporation among FVR$^-$ and FVR$^+$ β-cell subpopulations relative to number of β-cells per islet in pregnant (G15.5) *Fltp*$^{ZV/+}$ mice (*n* (mice) = 4, *n* (islets) = 196, *n* (Nkx6.1$^+$ cells) = 10,938). **h**, LSM images showing Nkx6.1-, p27- and FVR-expressing cells in islets of *Fltp*$^{ZV/+}$ pregnant (G15.5) mice. **i**, Quantification of p27 and Venus fluorescent intensity shows that p27-high cells have a higher Venus fluorescent intensity than p27-low cells in pregnant (G15.5) mice (*n* (mice) = 3, *n* (p27 and Venus positive cells) = 4,204). **j**, Quantification of Venus and EdU fluorescent intensity shows that EdU-positive cells have lower Venus fluorescent intensity than EdU-negative cells in pregnant (G15.5) mice (*n* (mice) = 3, *n* (p27$^+$, EdU$^+$ and Nkx6.1$^+$ cells) = 75, *n* (p27$^+$ EdU$^-$ Nkx6.1$^+$ cells) = 4,845). Scale bars, 50 μm (**a**, **e**, **h**). Data represent mean ± s.e.m.

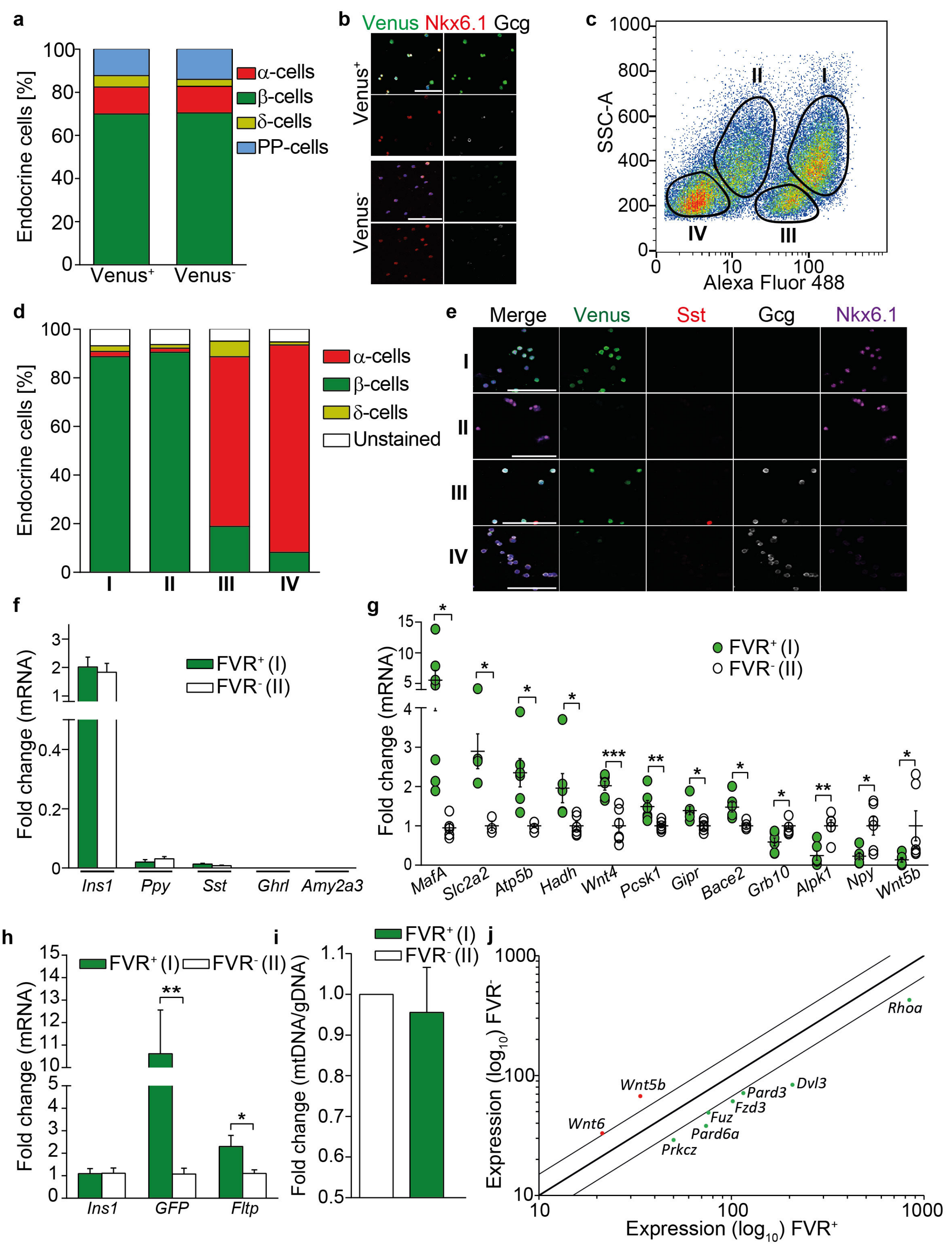

Extended Data Figure 3 | See next page for caption.

Extended Data Figure 3 | Validation of the sorting scheme and molecular and cellular analysis of FVR$^-$ and FVR$^+$ endocrine subpopulations. a, **b**, Quantification (**a**) and LSM images (**b**) of FACS-sorted FVR populations for the microarray analysis show equal numbers of endocrine cell lineages among the subpopulations (*n* (DAPI$^+$ cells) = 789). **c**, Detection and purification of four distinct endocrine subpopulations (I–IV) on the basis of granularity and Venus expression. **d**, **e**, Quantification (**d**) and LSM images (**e**) of sorted FVR subpopulations I and II confirms high enrichment of Nkx6.1$^+$ β-cells whereas III and IV exhibit high enrichment of glucagon$^+$ α-cells (*n* (DAPI$^+$ cells) = 3,275). **f**, Expression analysis of endocrine hormones and the exocrine marker *Amy2a3* reveals minimal contamination with other endocrine cell types (*n* (independent experiments) = 6 (FVR$^+$) and 5 (FVR$^-$)). **g**, **h**, Validation of the microarray analysis by real-time qPCR of β-cell-enriched subpopulations (I, II) for β-cell maturation, mitochondria and metabolic signalling pathway genes (*Atp5b*, *Hadh*, *Wnt4*, *Grb10*, *Wnt5b*, *Ins1*, *GFP*, *Fltp*, *Pcsk1*, *Gipr*, *Mafa*: *n* (independent experiments) = 6; *Bace2*, *Alpk1*, *Npy*: *n* (independent experiments) = 5, *Slc2a2*: *n* (independent experiments) = 3; *$P < 0.05$, **$P < 0.01$, ***$P < 0.001$, two-sided unpaired *t*-test). **i**, Real-time qPCR of mtDNA (S12) versus nDNA (HBB) from β-cell enriched populations (I, II) (*n* (independent experiments) = 5, expression in the FVR$^+$ subpopulation normalized on each FVR$^-$ subpopulation, error bars represent c.i.). **j**, Scatter plot of regulated polarity genes among FVR endocrine cells in microarray analysis (thin lines mark 1.5-fold difference in expression, $P < 0.05$, limma *t*-test). Scale bars, 100 μm (**b**, **e**). Data represent mean ± s.e.m. except where stated.

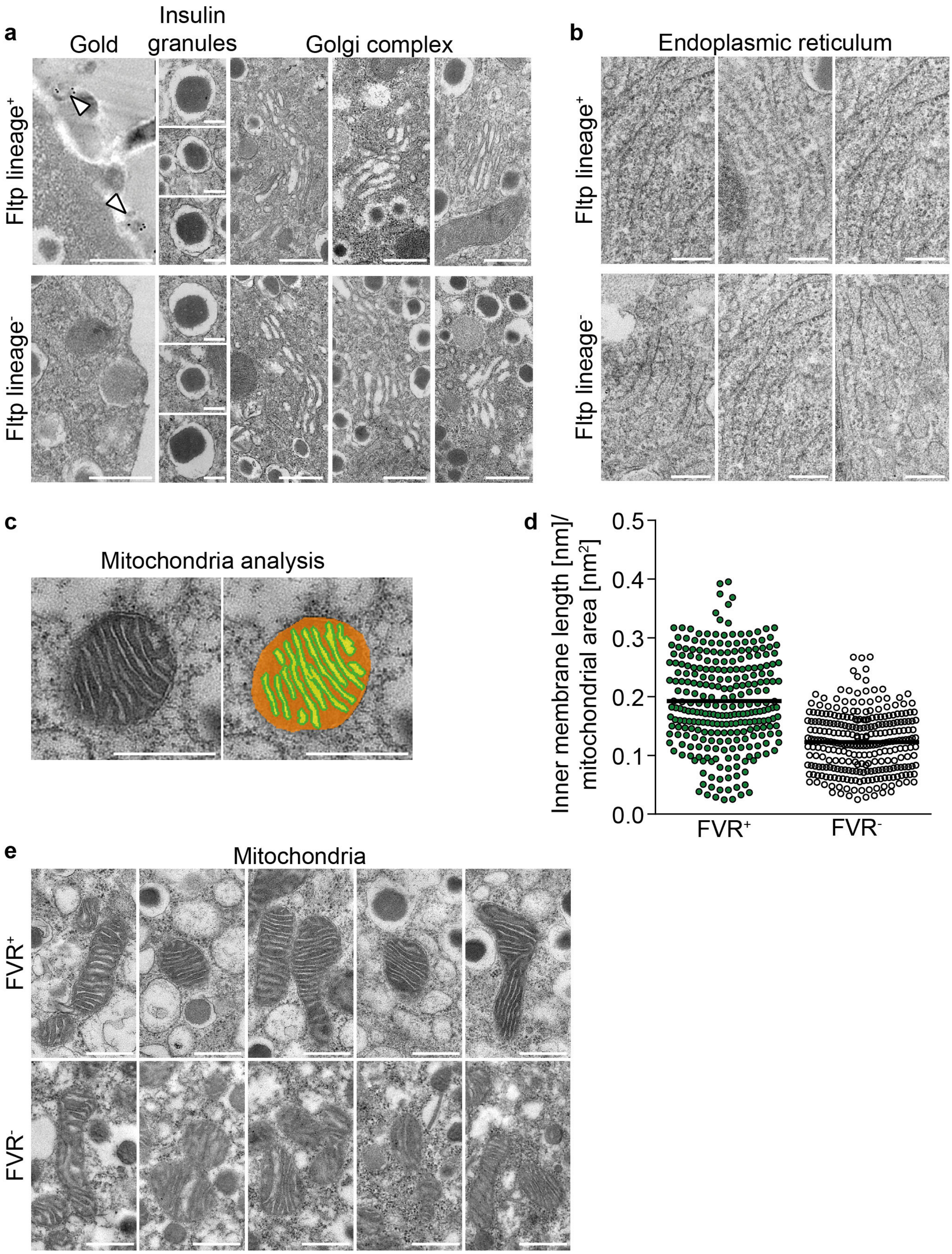

Extended Data Figure 4 | Transmission electron microscopy (TEM) analysis of Fltp$^-$ and Fltp$^+$ β-cell subpopulations and quantification of mitochondria membrane length. a, **b**, TEM images of immunogold-labelled β-cells of *Fltp*$^{T2AiCre/+}$;*Gt(ROSA)26*$^{mTmG/+}$ mice reveal no structural differences in Golgi complex (**a**) or endoplasmic reticulum (**b**). **c**, **d**, TEM images and detected areas of the algorithm used for mitochondria analysis (**c**) and analysis of inner mitochondria membrane length normalized on the mitochondria area in FVR$^+$ and FVR$^-$ β-cells (**d**) (*n* (independent experiments) = 2, *n* (FVR$^+$ cells) = 14, *n* (FVR$^-$ cells) = 16, *n* (mitochondria) = 544). **e**, TEM images of mitochondria in FVR$^+$ compared to mitochondria in FVR$^-$ β-cells. Scale bars, 500 nm (**a** (Golgi complex and gold staining), **c**, **e**), 200 nm (**a** (insulin granules), **b**). Data represent mean.

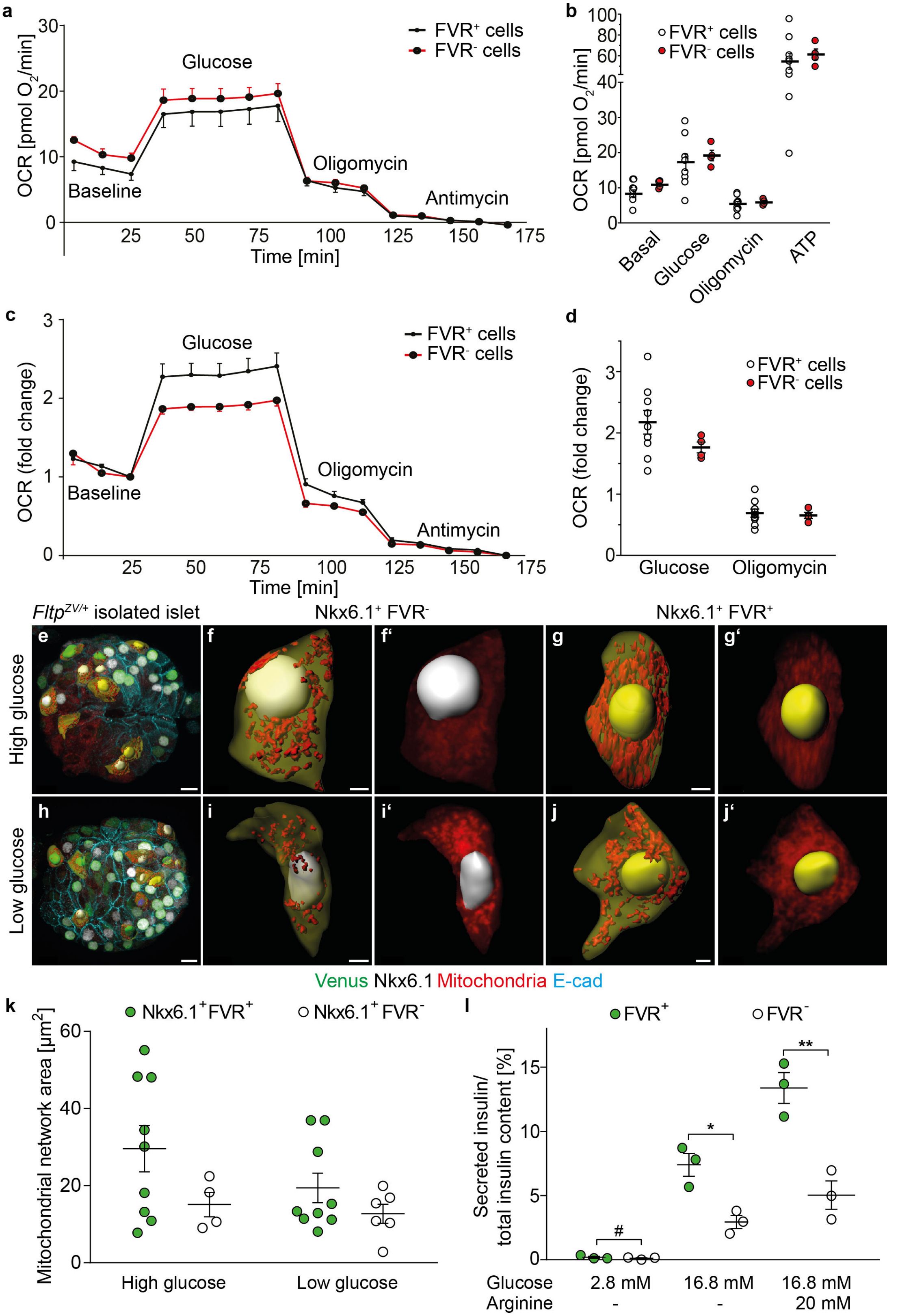

Extended Data Figure 5 | See next page for caption.

Extended Data Figure 5 | Analysis of oxygen consumption rate (OCR), mitochondria network and GSIS in FVR$^+$ and FVR$^-$ β-cells. a, OCR of FACS-sorted β-cell-enriched FVR$^+$ and FVR$^-$ subpopulations after Antimycin A subtraction. **b**, Quantification of absolute OCR rates of FACS-sorted β-cell-enriched FVR$^+$ and FVR$^-$ subpopulations after Antimycin A subtraction. FVR$^+$ n (technical replicates) = 9, FVR$^-$ n (technical replicates) = 4, for each technical replicate 3×10^4 cells were plated; endocrine cells were isolated from 9 mice; two-sided unpaired t-test. **c**, OCR of FACS-sorted β-cell-enriched FVR$^+$ and FVR$^-$ subpopulations after Antimycin A subtraction and baseline normalization. **d**, Quantification of relative OCR of FACS-sorted β-cell-enriched FVR$^+$ and FVR$^-$ subpopulations after Antimycin A subtraction and baseline normalization. FVR$^+$ n (technical replicates) = 9, FVR$^-$ n (technical replicates) = 4, two-sided unpaired t-test. **e**, **h**, LSM pictures of immunohistochemistry of isolated *Fltp*$^{ZV/+}$ mouse islets cultured under high (16.5 mM) and low (2 mM) glucose concentrations with single-cell reconstructions (Imaris) showing the reconstructed membrane (light brown), the nuclei (white, green and blue) and the mitochondria (red). **f**, **g**, **i**, **j**, Enlargement of a single Nkx6.1$^+$ cell under high (**f**) and low glucose (**i**) and an Nkx6.1$^+$ FVR$^+$ cell under high (**g**) and low glucose (**j**) with reconstruction of the nucleus, the membrane and the mitochondria. **k**, Quantification of the mitochondrial morphology of Nkx6.1–FVR double-positive cells (yellow) and Nkx6.1 single-positive cells (white) under high and low glucose stimulation (n (Nkx6.1$^+$ FVR$^+$) = 9, n (Nkx6.1$^+$ FVR$^-$ in high glucose) = 4, n (Nkx6.1$^+$ FVR$^-$ in low glucose) = 6, from three islets for low glucose and two islets for high glucose). **l**, FACS-sorted and re-aggregated β-cell-enriched subpopulations reveal differences in GSIS and arginine depolarization (n (independent experiments) = 3, n (aggregates FVR$^+$) = 16, n (aggregates FVR$^-$) = 12; *$P = 0.0206$, **$P = 0.007$, two-sided unpaired t-test). Scale bars, 10 μm (**e**, **h**), 2 μm (**f**, **j**), 3 μm (**g**, **i**). Data represent mean ± s.e.m.

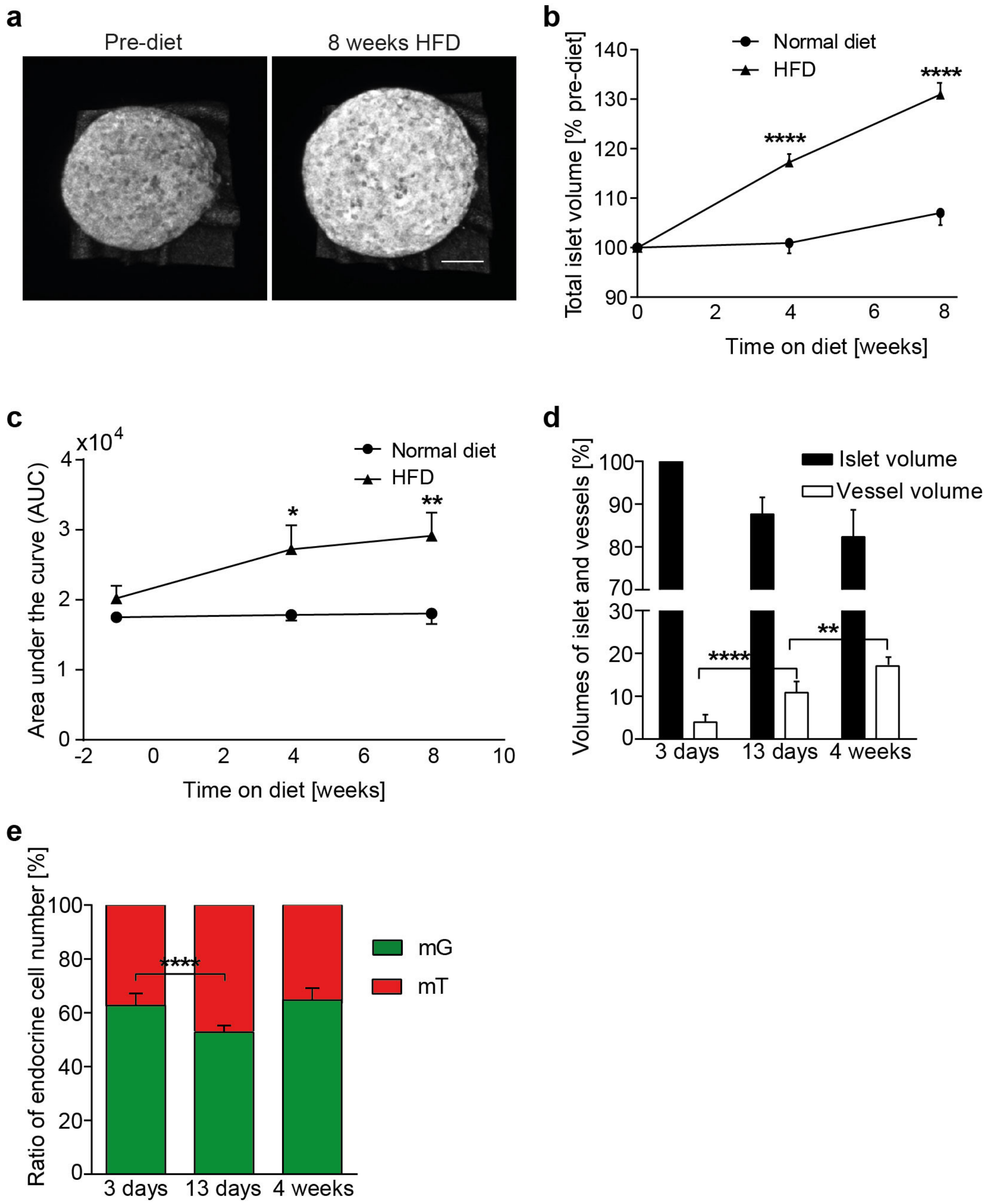

Extended Data Figure 6 | *Fltp* genetic lineage tracing of endocrine subpopulation dynamics upon islet transplantation and HFD. **a**, Maximum intensity projection of laser backscatter to determine the volume of the same transplanted *Fltp*$^{T2AiCre/+}$;*Gt(ROSA)26*$^{mTmG/+}$ islet before (Pre-diet) and after 8 weeks of HFD. **b**, Quantification of the total islet volume (transplanted *Fltp*$^{T2AiCre/+}$;*Gt(ROSA)26*$^{mTmG/+}$) in mice on normal diet and HFD (n (islets) = 25 (from 4 mice on normal diet), n (islets) = 34 (from 5 mice on HFD); ****$P < 0.0001$, Sidak's multiple comparison test). **c**, Quantification of glucose levels during intraperitoneal GTT by AUC quantification (n (mice on normal diet) = 4, n (mice on HFD) = 5; *$P = 0.0223$, **$P = 0.0064$, Sidak's multiple comparison test). **d**, Longitudinal quantification of the relative volumes of islet size and vessel volume during engraftment time (n (islets) = 15 (from 4 mice); ****$P < 0.0001$, ***$P = 0.0027$, two-sided unpaired t-test). **e**, Quantification of mG and mT endocrine cell numbers every 10 µm in a confocal z-stack during engraftment (n (islets) = 15 (from 4 mice); ****$P < 0.0001$, two-sided unpaired t-test). Scale bars, 50 µm (**a**). Data represent mean ± s.e.m.

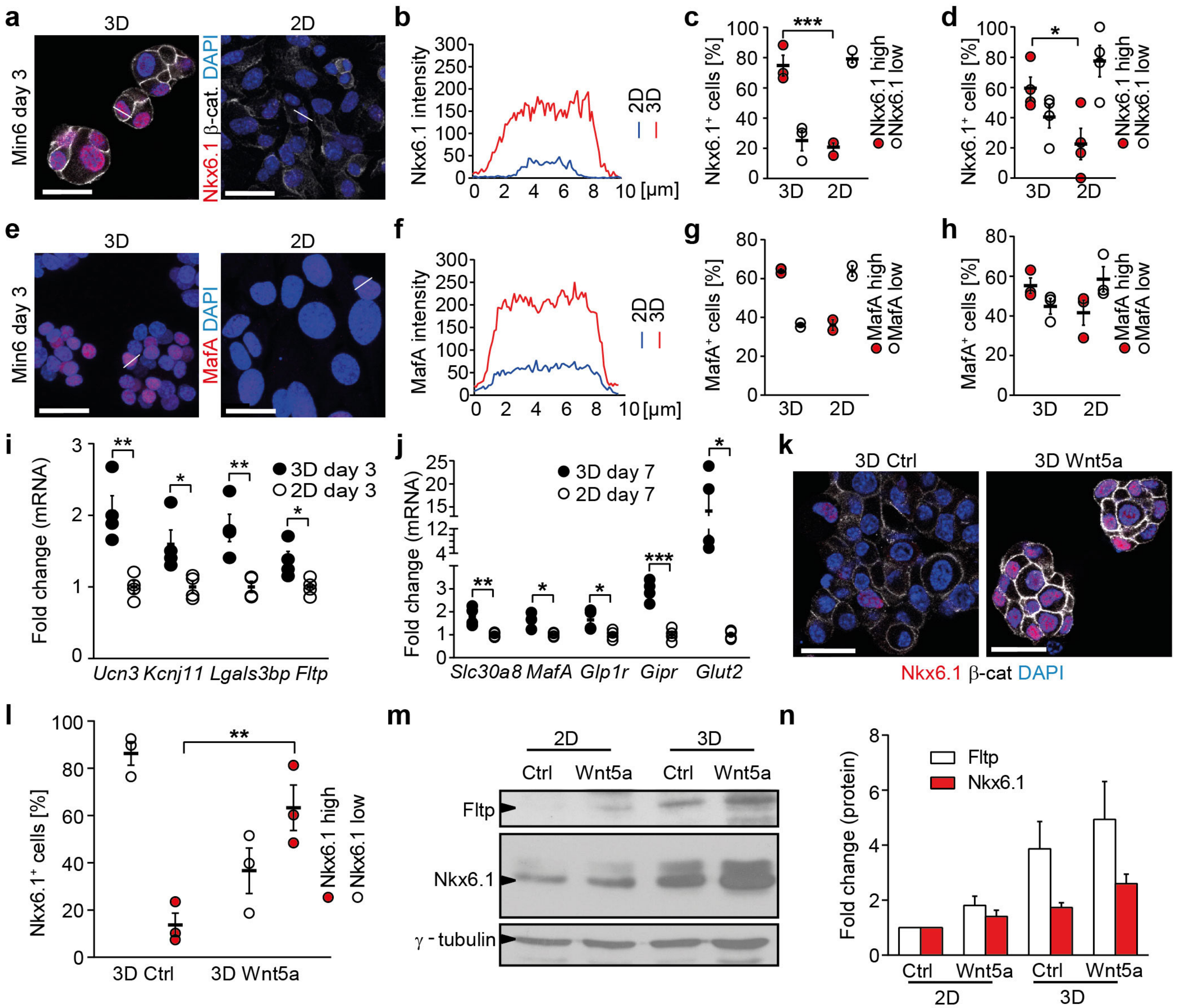

Extended Data Figure 7 | 3D architecture and Wnt/PCP induce β-cell maturation in Min6 cells. a, **c**–**e**, **g**, **h**, LSM images (**a**, **e**) and quantification (**c**, **g** (3 days culture), **d**, **h**, (7 days culture)) of Nkx6.1 and MafA mean fluorescent intensity in Min6 cells in 2D and 3D culture (**c**, *n* (independent experiments) = 3, $***P = 0.0002$; **d**, *n* (independent experiments) = 4, $*P = 0.0264$; **g**, *n* (independent experiments) = 2; **h**, *n* (independent experiments) = 3; Sidak's multiple comparison test). **b**, **f**, Fluorescent intensity of Nkx6.1 (**b**) and MafA (**f**) in a single Min6 cell in 2D and 3D culture. White lines in **a** and **e** indicate measured regions. **i**, **j**, Gene expression analysis of Min6 cells cultured in 2D and 3D culture by qPCR (*n* (independent experiments) = 4; $*P < 0.05$, $**P < 0.01$, $***P < 0.001$, two-sided unpaired *t*-test). **k**, **l**, LSM images (**k**) and quantification (**l**) of Nkx6.1$^+$ Min6 cells in floating 3D culture treated with or without Wnt5a (*n* (independent experiments) = 3; *n* (cells) = 5,419 (control), 2,419 (Wnt5a); $**P = 0.0036$, Sidak's multiple comparison test). **m**, **n**, Western blot (**m**) and quantification (**n**) of Nkx6.1 and Fltp protein in Min6 after treatment for 6 days with or without Wnt5a in 2D or 3D culture (western blots were normalized on γ-tubulin expression and standardized on 2D control, *n* (independent experiments) = 5). Scale bars, 20 μm (**a**, **e**, **k**). Data represent mean ± s.e.m.

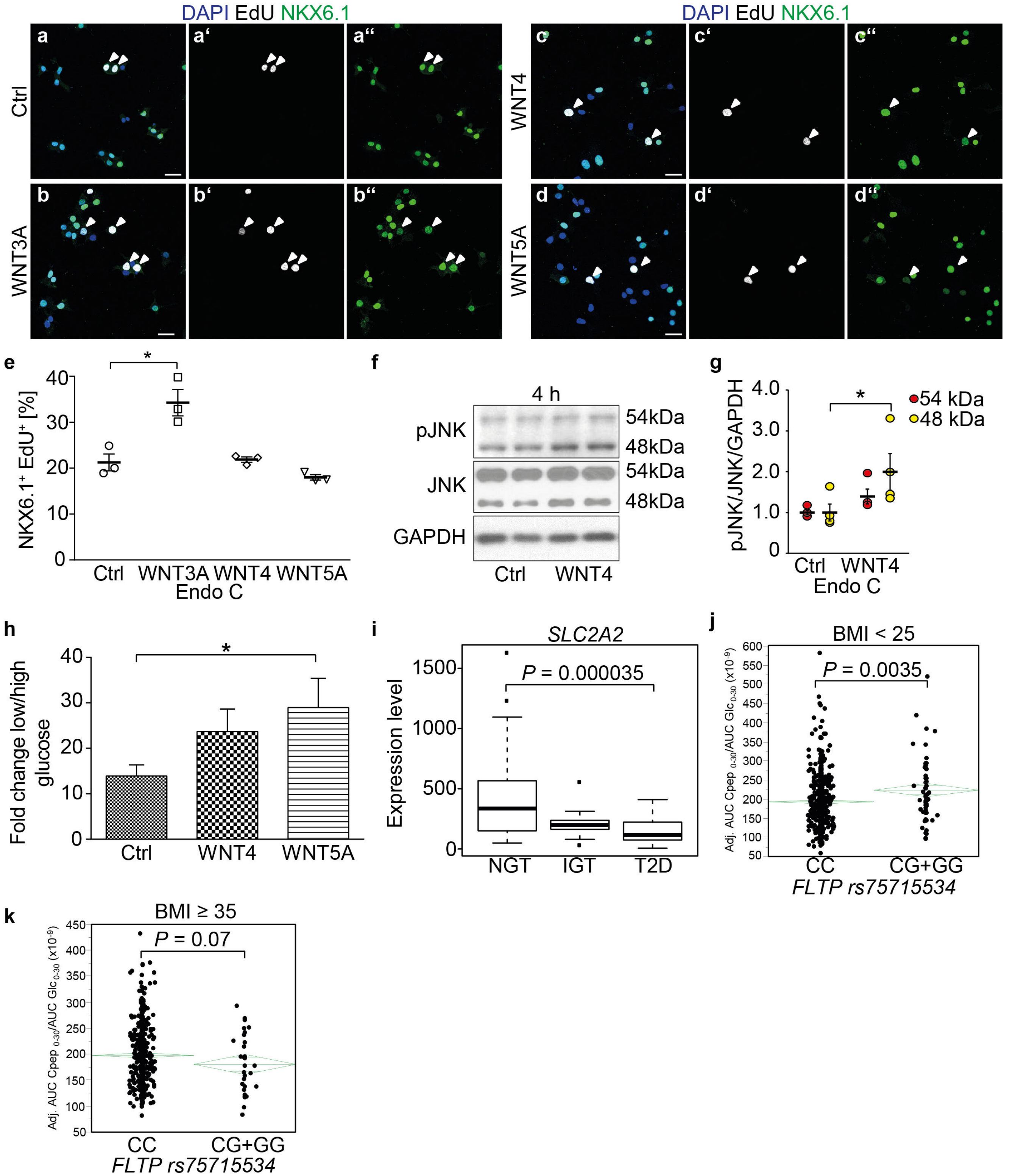

Extended Data Figure 8 | Modulation of maturation and proliferation through WNT signalling in human microislets and EndoC-β H1 human β-cell line and SNP association with insulin secretion defects in the *FLTP* gene. **a**–**e**, LSM images (**a**–**d**; proliferating cells marked by arrow heads) and quantification (**e**) of NKX6.1–EdU double-positive EndoC-β H1 cells treated with or without WNT3A, WNT4 or WNT5A (n (independent experiments) = 3, 1,617 cells counted; $^*P = 0.019$, two-sided unpaired t-test). **f**, **g**, Western blot (**f**) and quantification (**g**) of pJNK in EndoC-β H1 treated for 4 h with or without WNT4 (n (independent experiments) = 4; $^*P = 0.027$, two-sided paired t-test). **h**, Fold change in insulin secretion in response to high glucose in human microislets treated with or without WNT4 or WNT5A (3 human donors; Ctrl: n (microislets) = 23, WNT4: n (microislets) = 25, WNT5A: n (microislets) = 26; $^*P = 0.0423$, two-sided unpaired t-test). **i**, RNA sequencing expression data for *SLC2A2* in human pancreatic islets from healthy donors (NGT, $n = 66$), pre-diabetic donors (IGT, $n = 21$) and type 2 diabetic donors (T2D, $n = 19$; one-way ANOVA). **j**, **k**, The minor allele of *FLTP rs75715534* was significantly associated with increased insulin secretion in lean subjects ($P = 0.0035$), but not in obese subjects ($P = 0.07$). Adjustment of the insulin secretion index AUC $Cpep_{0-30}$/AUC Glc_{0-30} ($n = 2{,}228$) was achieved by multiple linear regression modelling with gender, age and OGTT-derived insulin sensitivity as confounding variables. Scale bars, 25 μm (**a**, **d**). Data represent mean ± s.e.m. (**e**, **g**, **h**); mean diamonds represent mean ± 95% c.i. (**j**, **k**).

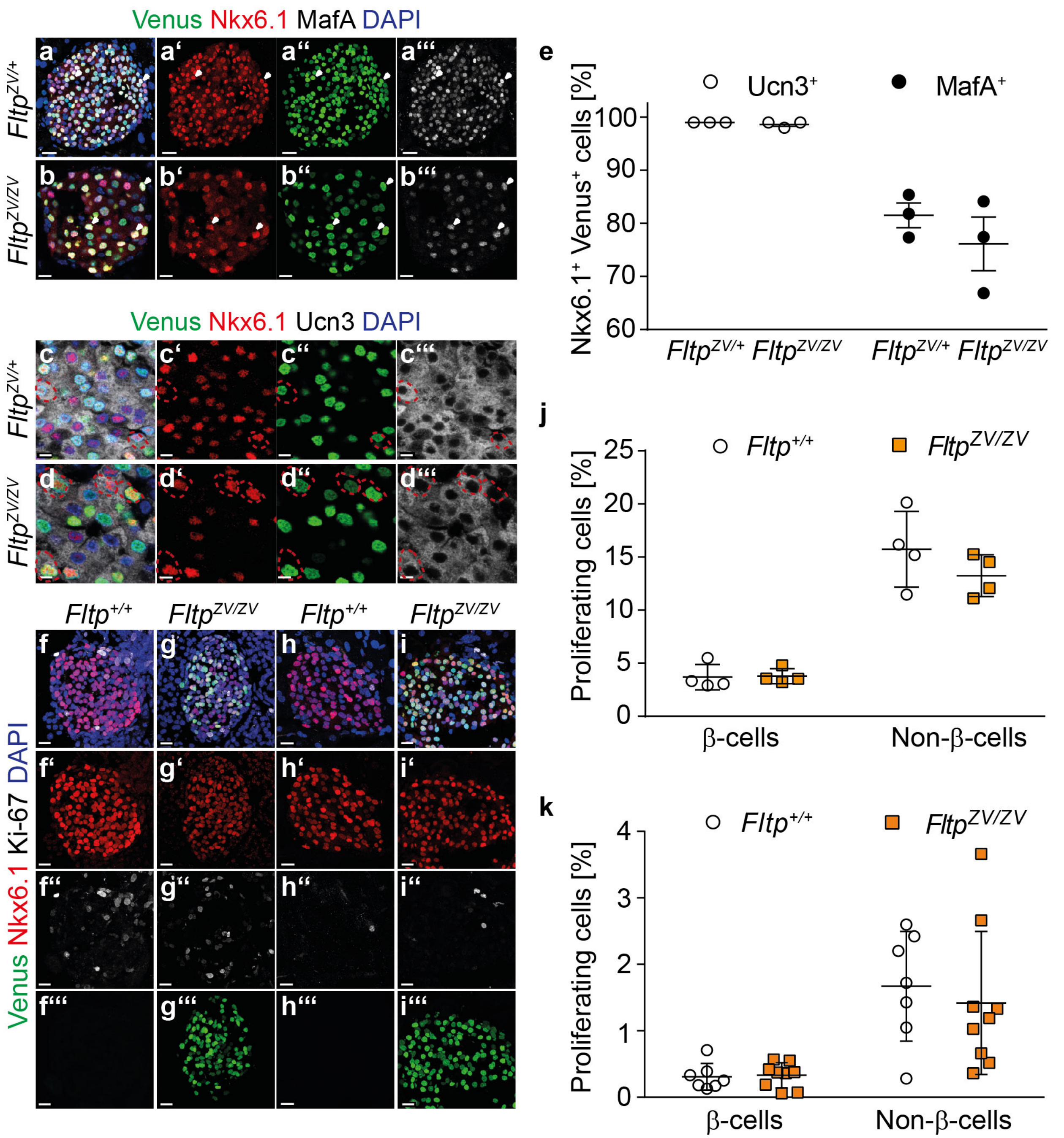

Extended Data Figure 9 | Knockout of *Fltp* has no effect on β-cell maturation or proliferation. **a**–**d**, Single plane LSM images of cryosections from adult $Fltp^{ZV/+}$ (**a**, **c**) and $Fltp^{ZV/ZV}$ (**b**, **d**) mice. Some Venus (green), Nkx6.1 (red) and MafA (white; **a**, **b**, white arrowheads) or Ucn3 (white; **c**, **d**, dashed lines) triple-positive cells are highlighted. **e**, Quantification of Venus, Nkx6.1 and Ucn3 (white) or MafA (black) triple-positive cells shows no difference in maturation status of β-cells in $Fltp^{ZV/+}$ and $Fltp^{ZV/ZV}$ mice ($Fltp^{ZV/+}$: n (mice) = 3, MafA 2,349 cells, Ucn3 1,212 cells; $Fltp^{ZV/ZV}$: n (mice) = 3, MafA 867 cells, Ucn3 1,825 cells). **f**–**i**, LSM images of immunohistochemistry on cryosections from P11 and adult $Fltp^{+/+}$ (**f**, P11; **h**, adult) and $Fltp^{ZV/ZV}$ (**g**, P11; **i**, adult) mice showing the proliferation of islet cells. **j**, **k**, Quantification of proliferating β- and non-β-cells in $Fltp^{ZV/ZV}$ and $Fltp^{+/+}$ mice at P11 (**j**) ($Fltp^{+/+}$: n (mice) = 4, 6,556 β-cells and 4,325 non-β-cells; $Fltp^{ZV/ZV}$: n (mice) = 4, 6,709 β-cells and 5,868 non-β-cells) and in adults (**k**) ($Fltp^{+/+}$: n (mice) = 7, 9,803 β-cells and 4,338 non-β-cells; $Fltp^{ZV/ZV}$: n (mice) = 9, 14,957 β-cells and 7,955 non-β-cells). Scale bar, 20 μm (**a**), 10 μm (**b**), 5 μm (**c**, **d**), 15 μm (**f**–**i**). Data represent mean ± s.d.

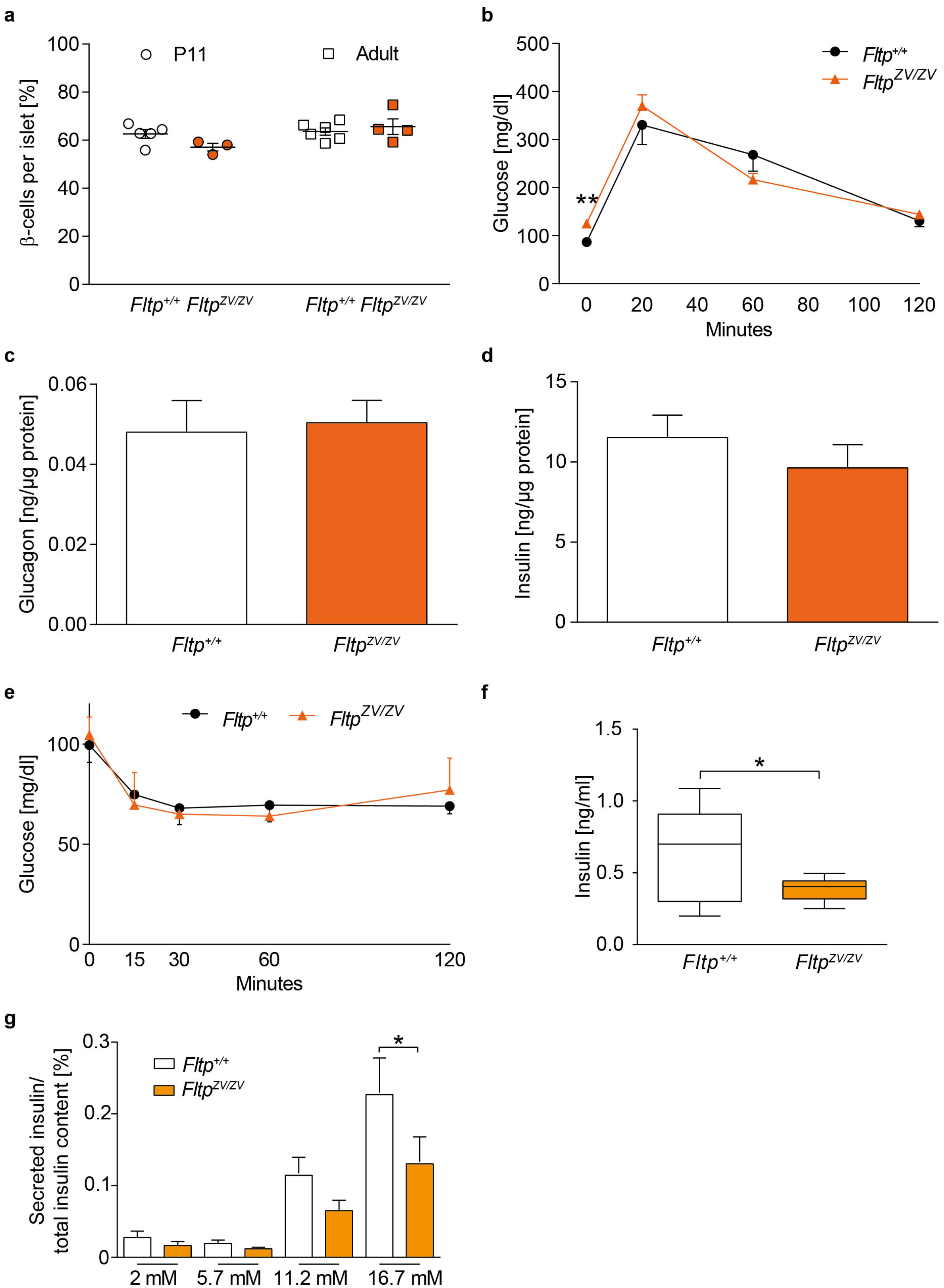

Extended Data Figure 10 | Analysis of the metabolic phenotype of *Fltp*$^{ZV/ZV}$ mice. **a**, Quantification of β-cell number in islets of Langerhans from *Fltp*$^{+/+}$ and *Fltp*$^{ZV/ZV}$ mice at P11 or adult (n (mice) = 3 (P11 *Fltp*$^{+/+}$, 6,556 Nkx6.1^{+} cells and *Fltp*$^{ZV/ZV}$, 6,791 Nkx6.1^{+} cells), n (mice) = 6 (adult *Fltp*$^{+/+}$, 3,202 Nkx6.1^{+} cells) and n (mice) = 4 (adult *Fltp*$^{ZV/ZV}$, 6,263 Nkx6.1^{+} cells)). **b**, Intraperitoneal GTT in *Fltp*$^{ZV/ZV}$ and *Fltp*$^{+/+}$ mice (*Fltp*$^{+/+}$ n (mice) = 7 and *Fltp*$^{ZV/ZV}$ n (mice) = 7; $^{**}P = 0.0022$, two-sided unpaired t-test). **c**, **d**, Concentration of glucagon (**c**) and insulin (**d**) in pancreatic tissue from *Fltp*$^{ZV/ZV}$ and *Fltp*$^{+/+}$ mice (*Fltp*$^{+/+}$ n (mice) = 5 and *Fltp*$^{ZV/ZV}$ n (mice) = 5). **e**, ITT in *Fltp*$^{ZV/ZV}$ and *Fltp*$^{+/+}$ mice (*Fltp*$^{+/+}$ n (mice) = 5 and *Fltp*$^{ZV/ZV}$ n (mice) = 3). **f**, Plasma insulin level in fasted *Fltp*$^{+/+}$ and *Fltp*$^{ZV/ZV}$ mice (*Fltp*$^{+/+}$ n (mice) = 11 and *Fltp*$^{ZV/ZV}$ n (mice) = 10; $^{*}P = 0.0405$, two-sided unpaired t-test). **g**, GSIS in isolated islets from *Fltp*$^{+/+}$ and *Fltp*$^{ZV/ZV}$ mice (*Fltp*$^{+/+}$ n (mice) = 5 and *Fltp*$^{ZV/ZV}$ n (mice) = 5; $^{*}P = 0.0263$, one-way ANOVA, Bonferroni's multiple comparison test). Data represent mean ± s.e.m.

doi:10.1038/nature18927

Mobile genes in the human microbiome are structured from global to individual scales

I. L. Brito[1,2], S. Yilmaz[3]*, K. Huang[2]*, L. Xu[2]*, S. D. Jupiter[4], A. P. Jenkins[5], W. Naisilisili[4], M. Tamminen[6,7], C. S. Smillie[1], J. R. Wortman[2], B. W. Birren[2], R. J. Xavier[2,8,9], P. C. Blainey[2], A. K. Singh[3], D. Gevers[2] & E. J. Alm[1,2,9]

Recent work has underscored the importance of the microbiome in human health, and has largely attributed differences in phenotype to differences in the species present among individuals[1–5]. However, mobile genes can confer profoundly different phenotypes on different strains of the same species. Little is known about the function and distribution of mobile genes in the human microbiome, and in particular whether the gene pool is globally homogenous or constrained by human population structure. Here, we investigate this question by comparing the mobile genes found in the microbiomes of 81 metropolitan North Americans with those of 172 agrarian Fiji islanders using a combination of single-cell genomics and metagenomics. We find large differences in mobile gene content between the Fijian and North American microbiomes, with functional variation that mirrors known dietary differences such as the excess of plant-based starch degradation genes found in Fijian individuals. Notably, we also observed differences between the mobile gene pools of neighbouring Fijian villages, even though microbiome composition across villages is similar. Finally, we observe high rates of recombination leading to individual-specific mobile elements, suggesting that the abundance of some genes may reflect environmental selection rather than dispersal limitation. Together, these data support the hypothesis that human activities and behaviours provide selective pressures that shape mobile gene pools, and that acquisition of mobile genes is important for colonizing specific human populations.

Bacteria rapidly evolve and adapt to changing environments by acquiring new genes from other bacteria in their environments. Comparison of reference genomes from the microbiomes of individuals living in different countries around the world has shown that geography does not present a substantial barrier to gene flow[6]. Moreover, there are specific examples of genes that have swept through global populations, such as the antibiotic resistance gene New Delhi metallo-beta-lactamase 1 (ref. 7). These observations raise the possibility that the mobile gene pool may be uniform across continents despite the existence of large differences in the compositions of culturally distinct microbiomes[8,9].

By contrast, there is also evidence that gene pools may be population-specific. First, horizontally transferred genes often provide a selective advantage to the host organism[6,10,11]. For example, seaweed in the traditional Japanese diet is believed to have led to selection for algal polysaccharide degradation genes that are underrepresented in North American populations[12]. Similarly, dental fillings containing mercury have led to an increase in mercury-resistance genes[13]. The use of clinical and agricultural antibiotics has resulted in the propagation of resistance genes in both pathogenic and commensal gut microbes[14,15]. Other cultural practices, including religious practices, travel, food origin and preparation, and beauty and hygiene product usage, may also shape the mobile gene pool.

Here, we combine single-cell genomics with metagenomics to survey the mobile gene pool and investigate whether mobile genes are mainly globally distributed or population-specific. We compared the mobile gene pools of 81 participants in the US-based Human Microbiome Project (HMP)[16] (Supplementary Table 1) with those of 172 Fijian islanders participating in the Fiji Community Microbiome Project (FijiCOMP) (Supplementary Table 2). FijiCOMP represents the first terabase-scale metagenomic view of the microbiome in the developing world.

Cataloguing the mobile gene pool in a large cohort using short-read metagenomic sequences is difficult, so previous analyses have been constrained to individual species[11,17] or specific mobile elements such as plasmids[18–20] and phages[21,22]. One reliable method for cataloguing mobile genes, including integrated transposons and prophages, depends on assembled genomes and is based on identifying identical or nearly identical genes present in distantly related bacterial hosts[6]. We used this method to identify 15,585 mobile genes from the 387 HMP gut microbiome reference and draft genomes[23] (Supplementary Tables 3, 5). Similar to complete genomes, even draft single-cell genomes provide enough context to link genes to hosts and to identify mobile genes. We used 180 single-cell genomes, derived from seven FijiCOMP participants, to identify an additional 22,268 mobile genes (Supplementary Tables 4, 5 and Extended Data Fig. 1). We then investigated which metagenomic libraries contained reads that mapped to this set of mobile genes to survey their abundances across individuals and populations (Extended Data Fig. 2).

Most mobile genes (62.4%) were present to some extent in both study populations, consistent with the previous finding that horizontal gene transfer (HGT) is not strongly structured by geography. Surprisingly, however, the abundance of those genes across populations was noticeably distinct (Extended Data Fig. 3a; $P < 10^{-6}$, permutational multivariate analysis of variance (PERMANOVA) based on Bray–Curtis dissimilarity,10^6 permutations), an observation that holds true even when considering a subset of the most stringently defined mobile genes (Extended Data Fig. 3b; $P < 10^{-6}$, PERMANOVA based on Bray–Curtis dissimilarity,10^6 permutations). Surveys of organisms endogenous to each population are required to fully observe both mobile gene pools (Extended Data Fig. 3c). We reasoned that diet might be a strong factor in differentiating the mobile gene pool across populations because many of the most highly consumed Fijian food items (taro, cassava breadfruit, coconut, and certain seafood) are not widely consumed in the US (see Methods).

We specifically examined genes encoding glycoside hydrolases as these include substrate-specific dietary enzymes. In the Fijian microbiomes, we found a high abundance of mobile genes from the glycoside hydrolase GH13 family (Fig. 1a, Supplementary Table 6 and Extended Data Fig. 4), which encompasses most of the dietary starch

[1]Department of Biological Engineering, Massachusetts Institute of Technology, Cambridge, Massachusetts 02139, USA. [2]Broad Institute of MIT and Harvard, Cambridge, Massachusetts 02139, USA. [3]Sandia National Laboratories, Livermore, California 94608, USA. [4]Wildlife Conservation Society, Suva, Fiji. [5]Edith Cowan University, Joondalup, Western Australia 6027, Australia. [6]Department of Aquatic Ecology, Eawag, CH-8600 Dubendorf, Switzerland. [7]Department of Environmental Systems Science, ETH Zurich, 8092 Zurich, Switzerland. [8]Massachusetts General Hospital, Boston, Massachusetts 02114, USA. [9]Center for Microbiome, Informatics and Therapeutics, Massachusetts Institute of Technology, Cambridge, Massachusetts 02139, USA.
*These authors contributed equally to this work.

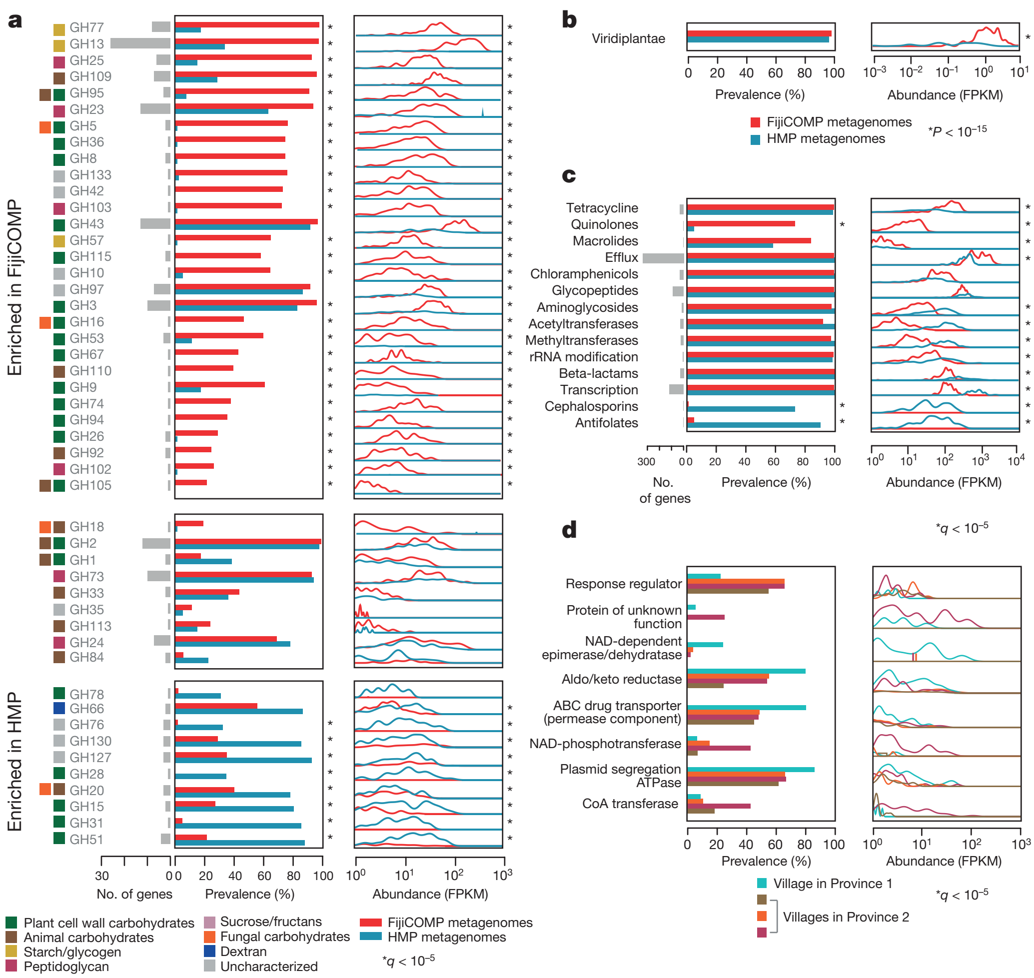

Figure 1 | Enrichment of functional mobile genes is locale-specific. **a**, Prevalence and abundance of all of the annotated mobile glycoside hydrolase families present in the FijiCOMP ($n = 172$, red) and HMP ($n = 81$, blue) metagenomic stool samples. Abundances were measured in fragments per kilobase of protein coding sequence per million mapped reads (FPKM) for each of the horizontally transferred genes, aggregated according to glycoside hydrolase family and plotted as a function of the density across samples. For each glycoside hydrolase family, the number of unique horizontally transferred genes present across the two cohorts is plotted (in grey), as are the sources of their substrates. **b**, Prevalence and abundance of plant matter (read alignments to rRNA from the kingdom Viridiplantae) in the metagenomes of stool samples from the FijiCOMP (red) and HMP (blue) populations. **c**, Prevalence and abundance of annotated mobile antibiotic resistance genes across the FijiCOMP (red) and HMP (blue) metagenomic stool samples. *P* value based on Mann–Whitney test. **d**, Prevalence and abundance of eight village-specific mobile genes (of 31 total village-specific genes) across four Fijian villages. *q* values (**a**, **b**, **d**) of prevalence comparisons based on FDR-corrected Fisher's exact tests; *q* values of abundance comparisons based on FDR-corrected Mann–Whitney tests.

degradation enzymes[24]. By contrast, glycoside hydrolases that degrade animal- and fungus-derived glycans exhibited bimodality between the American and Fijian cohorts, which may represent different dependencies on farm animals versus seafood that predominate in each of these cultures' diets. We confirmed the dietary differences between the two cohorts directly by metagenomic sequencing of stool samples, as the metagenomes of Fijians harboured significantly higher levels of plant matter ($P < 10^{-15}$, Mann–Whitney test; Fig. 1b). Thus, differences in diet-related genes in the microbiome, which have also been observed in previous cross-cultural comparisons[9,25], may be due in part to differential abundances of mobile genes, rather than to the presence of genes that can be attributed to specific taxa. There are likely to be additional non-mobile glycoside hydrolase genes that differ across populations. GH13 family genes were indeed enriched in the overall microbiomes of the FijiCOMP cohort versus the HMP cohort (see Methods), although we were unable to determine what fraction of these are mobile. The advantage of looking at mobile genes is that it narrows our focus to specific genes rather than species-level effects that might be more difficult to link directly to environmental factors such as diet.

We next hypothesized that antibiotic resistance genes might differ across populations, reflecting the high usage of beta-lactams and quinolones in Fiji (see Methods). We found that quinolone resistance was more pervasive in the Fijian cohort than the American cohort (Fig. 1c and Supplementary Table 7). Resistance to cephalosporins, which have been introduced relatively recently, was primarily an American phenomenon. Despite limited access to the full range antibiotics in Fiji, resistance genes for most classes of antibiotics were found in the Fijian population, consistent with recent findings in other developing world communities[26]. These results highlight our limited understanding of the forces that drive antibiotic resistance, and could reflect other uses of antibiotics, such as their use in agriculture, or even point to new classes of antibiotic resistance that have not yet been characterized[15].

As the distribution of mobile genes in the microbiome shows differences at a global scale, we hypothesized that gene distributions varied at even finer scales of resolution. The FijiCOMP cohort provides a unique opportunity to look at fine-scale structure because it includes individuals living in three villages in the remote Bua province and a fourth village in the agricultural Macuata province. Therefore, we checked whether any genes were specifically associated with one or more villages. Notably, we identified many village-associated mobile genes (31 genes varied significantly according to abundance, based on a Mann–Whitney test of gene abundances using FDR with $q < 0.05$,

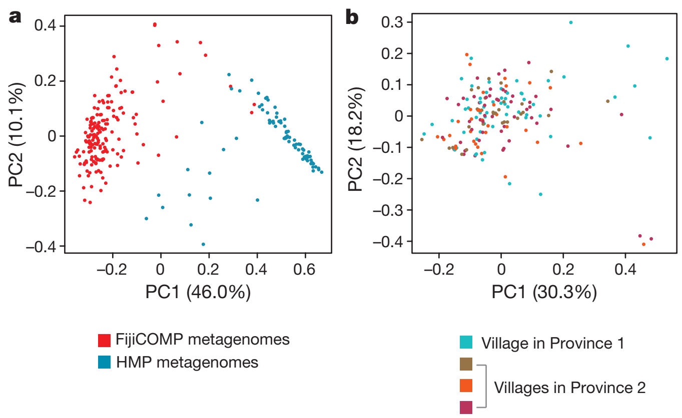

Figure 2 | Microbiome composition across global and local populations. **a**, Principal coordinates analysis of the Jenson–Shannon divergence between species compositions of the FijiCOMP ($n = 172$, red) and HMP ($n = 81$, blue) metagenomic samples. **b**, Principal coordinates analysis of the Jenson–Shannon divergence between species compositions in the FijiCOMP metagenomic samples, according to village membership.

or prevalence, based on a Fisher's exact test of village association using FDR with $q < 0.05$) (Fig. 1d and Supplementary Table 8). Village-associated mobile genes include those encoding HGT machinery, such as proteins involved in plasmid segregation, as well as proteins that may directly provide a fitness advantage to their host, such as ferredoxins.

The identification of village-associated mobile genes was unexpected because individuals' microbiomes are more similar among villages ($P > 0.05$, PERMANOVA based on Jensen-Shannon divergence, 10^5 permutations) than countries ($P < 10^{-6}$, PERMANOVA based on Jensen-Shannon divergence, 10^6 permutations) (Fig. 2, Extended Data Fig. 5 and Supplementary Table 9). Even though the mobile genes in our data set are defined by their occurrence in multiple phylogenetic backgrounds, gene exchange is known to be more frequent among closely related species[6]. We therefore investigated whether the village-associated genes were associated with species that were also partitioned unevenly across villages. For six of the 31 village-associated genes, we found a correlation with one of the ten village-associated species, although five of these six genes were also correlated with other non-village-associated species (see Methods). Overall, our findings suggest that these mobile genes are not restrained by their host genomes.

This finding prompted us to investigate the extent to which species composition determines mobile gene pool composition. First, we tested whether mobile genes originally identified in *Bacteroides* genomes or *Prevotella* genomes were more common in the metagenomes of individuals whose microbiomes were dominated by the same species. However, we did not find a significant association between the dominant taxon in an individual and their likelihood of carrying mobile genes of similar origins. Next, we investigated the taxonomy of bacteria hosting specific mobile elements by examining paired reads

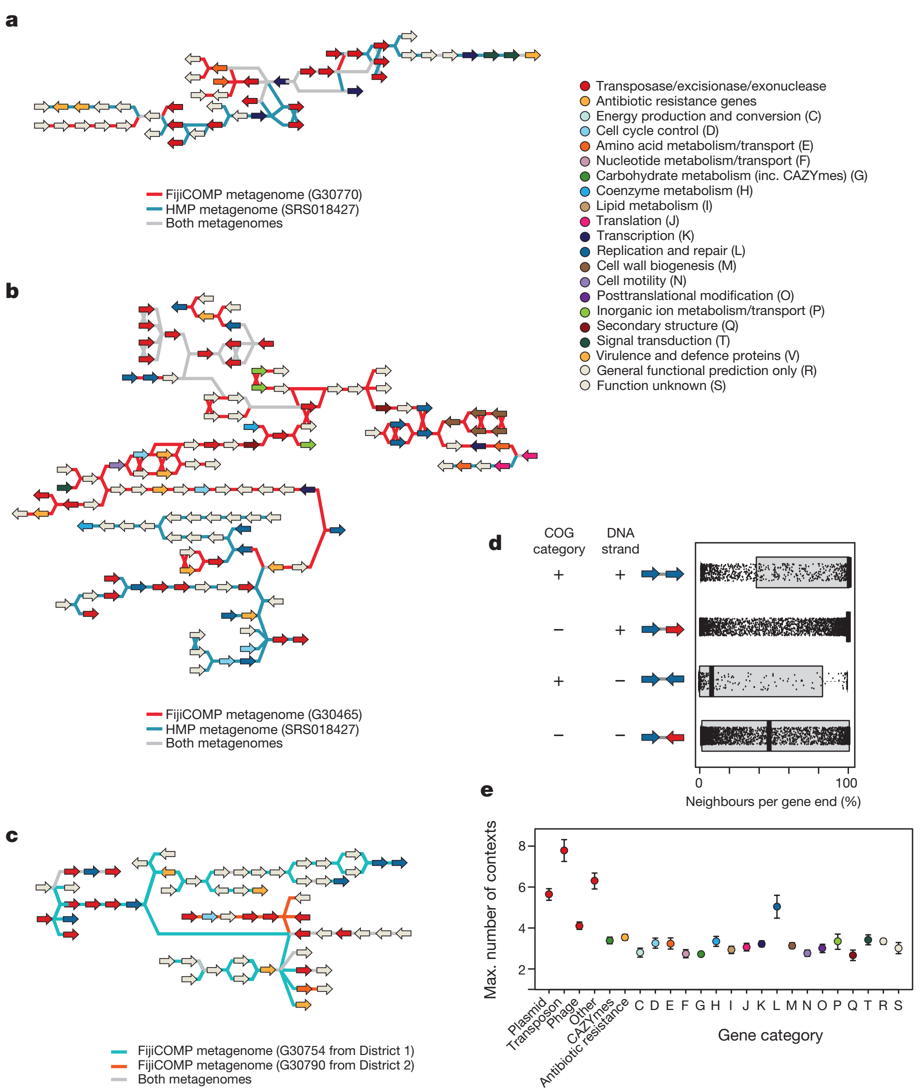

Figure 3 | Personal mobile genetic element architecture displays high variation due to recombination. **a**–**c**, Examples showing comparisons of assembled mobile genetic elements between the microbiomes of individuals from different continents (**a**, **b**) or different villages (**c**). Gene linkages between mobile genes are coloured according to the individual in whom they are present, with grey depicting linkages present in both individuals' microbiomes. Genes are coloured according to their broad COG category. **d**, For each mobile gene end, the median and quartile proportions of neighbours (as determined by the proportion of metagenomic read pairs) is plotted according to whether the adjacent gene is in broad functional concordance (determined by COG category) and whether they are situated on the same DNA strand, denoting whether they are likely to comprise the same operon. **e**, The average number of gene families connected to by mobile genes of each type of functional category, as determined by paired read linkage between mobile genes. Bars show s.e.m.

that span junctions between mobile genes integrated next to evolutionarily conserved tRNAs. Out of 838 mobile genes found adjacent to tRNAs, 65 were found near tRNAs from more than one genera, with the most promiscuous occurring next to tRNAs from 25 different genera (Supplementary Table 10; examples shown in Extended Data Fig. 6). Even within a single individual, these genes were not tied to the dominant bacteria present within that individual's microbiome, and often spanned multiple genera, including those in both Prevotellaceae and Bacteroidaceae families. Thus, horizontal gene transfer is likely to be driven by forces independent of species community composition.

The high rates of recombination observed among mobile genes support the idea that mobile genes are even less dispersal-limited than their host genomes. Following the logic of the Baas-Becking hypothesis that "everything is everywhere, but the environment selects," we might infer that environmental selection rather than dispersal drives differences in gene abundance among populations. Extending this logic from species to genes, however, is not straightforward because genes can change in abundance as a result of genetic 'hitchhiking' on mobile elements under selection at a different locus[27]. We reasoned that if recombination rates are sufficiently high, then genes should be present in many contexts. On the other hand, if gene abundances are driven by selection on larger mobile elements, then genes should appear in a limited number of contexts.

To investigate the genomic contexts of our mobile genes, we used the alignment and orientation of paired-end metagenomic reads to assemble short contigs encompassing each mobile gene (Fig. 3a–c). As expected, we found that recombination was limited, although not absent, within operons (as defined by adjacent genes in the same orientation and of the same functional category; Fig. 3d), and that horizontal transfer machinery, such as phage-, plasmid- or transposon-specific genes, had higher levels of recombination (Fig. 3e). However, despite the high prevalence of genes and broader gene functions, we found that 34.9% of the gene contexts, defined as the set of unique combinations between adjacent genes that were observed, were specific to individuals; very few of these gene contexts were conserved across populations (Fig. 4 and Extended Data Fig. 7).

Together, high recombination rates and population-specificity support the notion that environmental selection on individual genes, rather than dispersal limitation alone, plays a key role in driving gene abundances. The 'everything is everywhere' concept is reinforced for mobile genes by the observation that the majority of genes were found in both the HMP and FijiCOMP populations (Fig. 4). Even among the village-associated genes, all but five were found in all of the villages. Dispersal may play a role in shaping the distribution of a small, but abundant, subset of genes that are restricted to one population (that is, gene families (GH67, GH28 and GH110, Fig. 1a) or subsets of villages (Fig. 1e)). Nevertheless, environmental selection is underscored by the impact of diet on gene abundance. In fact, only one of the universal genes, defined as those present in more than 75% of both populations, was annotated as carbohydrate-metabolizing, despite carbohydrate-metabolizing genes being significantly enriched among population-specific genes, defined as those present in more than 50% of one population and less than 10% of the other ($P < 10^{-5}$, Pearson's χ^2 test).

How selection and dispersal affect gene exchange within physically proximal environments, that is, within a single individual's body sites, is still an open question[6]. On one hand, differences in composition and ecology may result in distinct mobile gene pools at various body sites[6,28]. On the other hand, the direct route between oral and gut communities should facilitate transmission of mobile elements, and systemic selective pressures, such as those imposed by orally administered antibiotics, may homogenize personal gene pools. Our analysis of saliva samples derived from FijiCOMP participants shows that there is little overlap between gut and oral mobile gene pools, as only 0.94% of the genes represented in the gut were detectable in any of the saliva samples. For any particular gene, there was no correlation between its presence or abundance between stool and saliva samples from the same individual. These data support the hypothesis that shared selective pressures and common ecologies structure horizontal transfer, although they do not rule out the possibility that physical proximity plays a role.

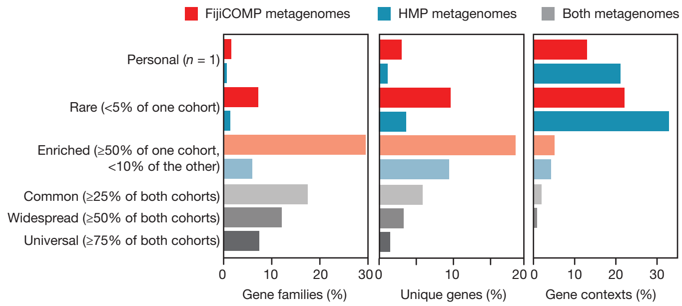

Figure 4 | Genes are widespread across global populations, but specific mobile genetic element architecture is not. The percentages of gene families (determined by functional annotations) (left), identical genes (middle), and gene contexts, defined by unique linkages between genes (right) are plotted according to their prevalence across the FijiCOMP and HMP populations. Gene families, genes and gene contexts are referred to as personal (present in a single individual), rare (in <5% of one population and absent in the other), enriched (in >50% of one population and <10% of the other), common (in ≥ 25% of both populations), widespread (in ≥ 50% of both populations) or universal (in ≥ 75% of both populations). Colour reflects association with one or both populations.

As well as presenting a data set describing the microbiome of a population in the developing world, we have also described an approach that can be used to identify environmentally relevant genes. Previous shotgun metagenome approaches have focused on the abundance of a gene as a proxy for its importance. This approach will identify important genes but also has the potential to identify many spurious genes because a single highly abundant species can carry many genes that are not specifically relevant to the environment it occupies. Instead, we look for abundant genes that are present in multiple species, using horizontal gene transfer as an additional filter for gene importance. Our approach is subject to several important caveats. First, its sensitivity for detecting mobile genes is low, and there are likely to be many more genes transferred across species than we can detect. Second, even though each of the mobile genes within our data set exists in more than one species, some of those genes may be primarily associated with a single taxon. This is especially true if a single taxon is much more abundant than the other species that carry the gene.

Despite these caveats, we found that the human-associated mobile gene pool differed between populations and carried gene functions that are likely to be associated with cultural practices; these findings provide functional insights not possible based on surveys of phylogenetic markers, such as the 16S rRNA gene, alone. These insights have the potential to improve public health at multiple levels. For example, a better understanding of the distribution of antibiotic-resistance genes among different populations' microbiomes could inform antibiotic stewardship at a regional level, by avoiding the use of specific antibiotics where resistance to them is highest. We also showed that the mobile genetic elements are highly diverse among individuals, raising the possibility that they may vary within bacterial lineages in an individual over short time spans. If this is true, then diet and drugs could modify the functions of the microbiome, even if the long-term species composition is stable[29,30]. To assess whether changes to cultural practices will influence human health via mobile genetic elements, future studies should test the speed at which selective pressures alter mobile gene frequencies within single individuals and larger populations.

Online Content Methods, along with any additional Extended Data display items and Source Data, are available in the online version of the paper; references unique to these sections appear only in the online paper.

Received 16 February 2015; accepted 15 June 2016.
Published online 13 July 2016.

1. Turnbaugh, P. J. *et al.* An obesity-associated gut microbiome with increased capacity for energy harvest. *Nature* **444,** 1027–1031 (2006).
2. Giongo, A. *et al.* Toward defining the autoimmune microbiome for type 1 diabetes. *ISME J.* **5,** 82–91 (2011).
3. Qin, J. *et al.* A metagenome-wide association study of gut microbiota in type 2 diabetes. *Nature* **490,** 55–60 (2012).
4. Scher, J. U. *et al.* Expansion of intestinal *Prevotella copri* correlates with enhanced susceptibility to arthritis. *eLife* **2,** e01202 (2013).
5. Kang, D. W. *et al.* Reduced incidence of *Prevotella* and other fermenters in intestinal microflora of autistic children. *PLoS One* **8,** e68322 (2013).
6. Parks, D. H., Imelfort, M., Skennerton, C. T., Hugenholtz, P. & Tyson, G. W. CheckM: assessing the quality of microbial genomes recovered from isolates, single cells, and metagenomes. *Genome Res.* **25,** 1043–1055 (2015).
7. Smillie, C. S. *et al.* Ecology drives a global network of gene exchange connecting the human microbiome. *Nature* **480,** 241–244 (2011).
8. Kumarasamy, K. K. *et al.* Emergence of a new antibiotic resistance mechanism in India, Pakistan, and the UK: a molecular, biological, and epidemiological study. *Lancet Infect. Dis.* **10,** 597–602 (2010).
9. De Filippo, C. *et al.* Impact of diet in shaping gut microbiota revealed by a comparative study in children from Europe and rural Africa. *Proc. Natl Acad. Sci. USA* **107,** 14691–14696 (2010).
10. Yatsunenko, T. *et al.* Human gut microbiome viewed across age and geography. *Nature* **486,** 222–227 (2012).
11. O'Donnell, M. M., O'Toole, P. W. & Ross, R. P. Catabolic flexibility of mammalian-associated lactobacilli. *Microb. Cell Fact.* **12,** 48 (2013).
12. Shapiro, B. J., David, L. A., Friedman, J. & Alm, E. J. Looking for Darwin's footprints in the microbial world. *Trends Microbiol.* **17,** 196–204 (2009).
13. Hehemann, J.-H. *et al.* Transfer of carbohydrate-active enzymes from marine bacteria to Japanese gut microbiota. *Nature* **464,** 908–912 (2010).
14. Summers, A. O. *et al.* Mercury released from dental "silver" fillings provokes an increase in mercury- and antibiotic-resistant bacteria in oral and intestinal floras of primates. *Antimicrob. Agents Chemother.* **37,** 825–834 (1993).
15. Forsberg, K. J. *et al.* The shared antibiotic resistome of soil bacteria and human pathogens. *Science* **337,** 1107–1111 (2012).
16. Forslund, K. *et al.* Country-specific antibiotic use practices impact the human gut resistome. *Genome Res.* **23,** 1163–1169 (2013).
17. Coyne, M. J., Zitomersky, N. L., McGuire, A. M., Earl, A. M. & Comstock, L. E. Evidence of extensive DNA transfer between bacteroidales species within the human gut. *MBio* **5,** e01305–e01314 (2014).
18. Human Microbiome Project Consortium. Structure, function and diversity of the healthy human microbiome. *Nature* **486,** 207–214 (2012).
19. Jones, B. V., Sun, F. & Marchesi, J. R. Comparative metagenomic analysis of plasmid encoded functions in the human gut microbiome. *BMC Genomics* **11,** 46 (2010).
20. Brown Kav, A. *et al.* Insights into the bovine rumen plasmidome. *Proc. Natl Acad. Sci. USA* **109,** 5452–5457 (2012).
21. Sentchilo, V. *et al.* Community-wide plasmid gene mobilization and selection. *ISME J.* **7,** 1173–1186 (2013).
22. Breitbart, M. *et al.* Metagenomic analyses of an uncultured viral community from human feces. *J. Bacteriol.* **185,** 6220–6223 (2003).
23. Reyes, A. *et al.* Viruses in the faecal microbiota of monozygotic twins and their mothers. *Nature* **466,** 334–338 (2010).
24. The Human Microbiome Jumpstart Reference Strains Consortium A catalog of reference genomes from the human microbiome. *Science* **328,** 994–999 (2010).
25. Cantarel, B. L., Lombard, V. & Henrissat, B. Complex carbohydrate utilization by the healthy human microbiome. *PLoS One* **7,** e28742 (2012).
26. Clemente, J. C. *et al.* The microbiome of uncontacted Amerindians. *Sci. Adv.* **1,** e1500183 (2015).
27. Shapiro, B. J. *et al.* Population genomics of early events in the ecological differentiation of bacteria. *Science* **336,** 48–51 (2012).
28. Dutilh, B. E. *et al.* A highly abundant bacteriophage discovered in the unknown sequences of human faecal metagenomes. *Nat. Commun.* **5,** 4498 (2014).
29. Faith, J. J. *et al.* The long-term stability of the human gut microbiota. *Science* **341,** 1237439 (2013).
30. David, L. A. *et al.* Host lifestyle affects human microbiota on daily timescales. *Genome Biol.* **15,** R89 (2014).

Supplementary Information is available in the online version of the paper.

Acknowledgements We thank our field collaborators in the Fiji Islands: the Wildlife Conservation Society, Fiji, Wetlands International-Oceania, K. Jenkins, S. Korovou, N. Litidamu, and K. Kishore. We thank T. Poon for sample, sequencing, and data coordination, and A. Materna (QIAGEN) for technical assistance. This work was supported by grants from the National Human Genome Research Institute (U54HG003067) to the Broad Institute, the Center for Environmental Health Sciences at MIT, the Center for Microbiome Informatics and Therapeutics at MIT, and the Fijian Ministry of Health. Additional support was provided by a Columbia University Earth Institute Fellowship (I.L.B.); a Broad Institute Lawrence Summers Fellowship (L.X.); a Burroughs Wellcome Fund Career Award at the Scientific Interface (P.C.B.); and an R01 DE020891 funded by the NIDCR and ENIGMA and a Lawrence Berkeley National Laboratory Scientific Focus Area Program supported by the US Department of Energy, Office of Science, Office of Biological and Environmental Research (S.Y. and A.K.S.). Sandia is a multi-program laboratory operated by Sandia Corp., a Lockheed Martin Co., for the United States Department of Energy under Contract DE-AC04-94AL85000.

Author Contributions I.L.B. and E.J.A. designed the study. I.L.B., S.D.J., A.P.J. and W.N. oversaw and performed the field collection of FijiCOMP data and samples. I.L.B., L.X., S.Y., and M.T. performed all experimental work. D.G., B.W.B., J.R.W., P.C.B., R.J.X. and A.K.S. oversaw the DNA sequencing production. I.L.B. and K.H. processed the shotgun data and performed alignments. I.L.B., K.H., and D.G. provided new analytical tools. I.L.B., K.H. and C.S.S. performed computational analysis. I.L.B. and E.J.A. wrote the manuscript.

Author Information Reprints and permissions information is available at www.nature.com/reprints. The authors declare no competing financial interests. Readers are welcome to comment on the online version of the paper. Correspondence and requests for materials should be addressed to E.J.A. (ejalm@mit.edu).

Reviewer Information *Nature* thanks P. Bork, K. Forslund, P. Hugenholtz and C. Rinke for their contribution to the peer review of this work.

METHODS

Overview of the Fiji Community Microbiome Project. The Fiji Community Microbiome Project was developed to characterize the role of human-associated bacteria in health and disease from a developing world population recruited in the Fiji Islands. The study sought to understand the transmission of microbiome components among individuals and their environmental surroundings. The goal was to be as comprehensive as possible in the study villages. The study included 300 individuals, regardless of health status, each of whom chose to provide any or all of stool, saliva or skin swab samples. To date, this is one of the largest cohorts on which metagenomic sequencing has been performed. Surveys were performed by visiting all households within each community. Individuals under the age of 5 years were excluded, as were individuals who were deemed mentally incapable of providing informed consent. Informed consent was received from all participants and parental consent was additionally required for all minors. IRB approval was received from Institutional Review Boards at Columbia University, the Massachusetts Institute of Technology and the Broad Institute and ethics approvals were received from the Research Ethics Review Committees at the Fiji National University and the Ministry of Health in the Fiji Islands. Whole genome metagenomic shotgun sequencing was performed on individuals' stool and saliva samples, in addition to environmental samples from individuals' proximal environments. More information and links to the data set can be found at http://www.fijicomp.org.

Samples used in this study. Saliva samples were collected in 20% glycerol and frozen within 30 min of collection. Stool samples to be used for metagenomic sequencing were collected within 30 min of voiding, stored in RNALater (QIAGEN) and frozen at 80 °C. Stool samples used for retrieval of intact cells for single-cell analysis were collected within 30 min of voiding, stored in 20% glycerol and PBS, and frozen at −80 °C. Seven individuals' samples were selected from the FijiCOMP cohort for isolation of single-cell genomes (Supplementary Table 2). Samples destined for single-cell isolation were prepared using two different single-cell amplification approaches: one based on sorting individual cells and a second based on capturing individual cells within a hydrogel.

Flow-sorted single-cell amplification. For the sorting method, thawed cells were resuspended in PBS-glycerol (20%) to a concentration of 10^6 cells per ml. Samples were serially filtered through 30-μl and 11-μl membranes then briefly sonicated (20 s) and diluted 50–100-fold. They were sorted into individual wells of a 384-well plate containing 0.5 μl PBS. Single cells then underwent alkaline lysis for 15 min at room temperature, after which the solution was neutralized. Genomes were then amplified using multiple displacement amplification[31] for 16 h at 30 °C using high-purity Φ29 polymerase expressed in *Escherichia coli* strain BL21_DE3. To initially identify amplified cells, the V68 region of the 16S rDNA locus was amplified using 1:10 dilution of the MDA product and universal 16S primers 926F and 1392R and then Sanger sequenced. Taxonomic classification was performed using the RDP naive Bayesian rRNA classifier (v. 2.6)[32]. We chose cells from this group to sequence that maximized the likelihood of observing lateral transfer between cells by accounting for the previously observed rates of HGT between organisms of a specified phylogenetic distance (the per cent identity between pairs of 16S sequences were used as a proxy)[6].

MDA reactions were sonicated to shear large fragments of DNA. Samples then underwent end-repair using the NEB Quick Blunting Kit and were purified using a QIAGEN MinElute column. Illumina adapters containing 5-bp barcodes were ligated to the genomic amplicon using the NEB Quick Ligation Kit. The double-stranded adapters were modified using 5′ and 3′-amino modified bases at one end to prevent self-ligation. Size selection was then performed using SPRI beads. Libraries then underwent nick translation using NEB Bst polymerase. Libraries were each amplified using Phusion Polymerase (New England Biolabs). The final pooled library was then gel purified to retain fragments of sizes 250–600 bp and sequenced on an Illumina HiSeq. The average size of the final library constructs was 397 bp. The total sequencing depth was 310 million reads. Single-cell libraries were barcoded and sequenced. We took several precautions to ensure the fidelity of our final single-cell libraries. Barcodes used in library preparation were designed so that each barcode would require 2 base-pair shifts to mimic any other barcode in the study; that no indel would result in a different barcode; and that barcodes contained no more than two consecutive identical basepairs. Only reads containing exact barcode matches were incorporated into libraries.

Hydrogel-based single-cell amplification. For the hydrogel method, 10 μl of thawed cells were resuspended in 500 μl PBST (0.1%). Samples were sonicated for 20 s and first filtered through a 35-μm nylon mesh, followed by a 5-μm membrane (Pall Corp.) with a 500-μl PBST wash. Samples were further diluted 500–2,000-fold in PBST to reach the final concentration of ~30 cells per μl. The diluted cell samples (2 μl) then underwent alkaline lysis for 15 min at room temperature, after which the solution was neutralized. Hydrogel monomer mix (1.3 mg 4 Arm PEG Acrylate and 0.9 mg SH-PEG-SH) and MDA master mix, including Φ29 buffer (NEB), 50 μM random hexamers with two phosphorothioate bonds at the 3′ termini, 2.5% DMSO, 0.4 mM dNTP, 0.5 mg/mL BSA, 500 nM SYTOX Orange (Invitrogen) and 1 μl REPLI-g sc Polymerase (Qiagen), were added to the side wall of the tube that contained the lysed cell sample. 25 μl of each microbial concentration was added into a frame seal chamber and the sealed chamber was incubated at 30 °C for 12 h. Fluorescent DNA clusters were imaged and selected for hydrogel cluster retrieval. Approximately 0.24 μl hydrogel and 10 pg DNA was captured in each cluster. This was dissolved and denatured in 1 μl 400 mM KOH with 0.1 mM EDTA and 0.1 M DTT at 72 °C for 10 min before neutralization. The neutralized product underwent a second MDA reaction (for 10 h) within a new hydrogel. The gel was then denatured and neutralized.

MDA products were purified and quantified using the Quant-iT HS assay (Thermo Fisher Scientific) and normalized to 5 ng/μl. Tagmentation reactions (Nextera) were carried out on 10 ng of purified DNA, and were followed by a SPRI cleanup. Unique PCR library barcoding using Index primers N7 and S5 (Illumina) was performed, followed with SPRI twice using equal volumes of beads to DNA. Libraries of were sequenced to a depth of ~1.5M 125-bp paired-end reads on Illumina's Hiseq 2500. The Broad Institute's Internal Genomics Platform's custom designed paired-end library barcodes were used. Final library size was 200–300 bp.

Assembly of single-cell genomes. Single genome amplicons were quality filtered (Phred score ≥ 3), and filtered for reads that were less than 45 bp and for those that aligned with the human genome, the *P. aeruginosa* PAO1 genome (a laboratory contaminant) and the *E. coli* BL21_DE3 genome (from which the Φ29 polymerase used in the MDA reaction was expressed and purified) using BMTagger. A small number of adaptor sequences were found in the raw data due to small inserts or primer-dimers. These adaptor sequences (30–61 bp in length) were easily identified using BLASTn and were removed before analysis. Amplicons were then assembled into genomes using either CLC Assembly Cell (v. 4.2), for the flow-sorted cells, or SPADES[33] (with the–careful flag) (v.3.6.0) for the hydrogel-captured cells. We retained assembled contigs that were at least 500 bp and resultant genomes where at least 100 kb could be assembled.

Filtering single-cell assemblies. To further vet the quality and purity of our assemblies, we used BLASTp to assign taxonomies to a set of 31 predetermined core genes that are both phylogenetically conserved and single copy in almost all genomes[34]. Although we could not identify the full set of 31 core genes in any of the assemblies, we removed several cells in which the core genes reflected mixed taxonomies. Additional validations of the single cell assemblies included quantifying the levels of contamination using CheckM[6]. We retained cells with less than 10% putative contamination. We used RNAMMER[35] to identify 16S sequences present in the assembled genome. We discarded a small number of cells that had multiple 16S sequences or those in which the RNAMMER-identified 16S rRNA sequence conflicted with the Sanger-sequenced 16S rRNA V68 region. Our final data set included 196 single cell assemblies (Supplementary Table 4).

Identification of horizontally transferred genes between divergent genomes. To identify horizontally transferred regions, we used a previously benchmarked method[6]. All assembled and reference genomes were compared in a pairwise manner using default in BLAST+ (v. 2.2.24). Recent DNA transfers are defined as the presence of near-identical DNA fragments (99% per cent identity or greater) with a length of ≥500 bp in two distantly related genomes. Note that the identification of identical DNA does not imply direct transfer between two cells. We found that approximately two-thirds of the identified transferred regions contained at least one SNP, suggesting that they could not have been the result of contamination. We restricted our analysis to comparisons between genomes whose full length 16S distance would be at least 3% dissimilar. This cut-off allowed us to distinguish between signatures of vertical inheritance and horizontal transfer, as 97% divergence at the 16S corresponds with roughly 75 million years of evolution, during which time well over 100 mutations would have accumulated per 500 bp. By conservatively defining horizontally transferred regions as those with such high nucleotide identity, we are likely to miss larger horizontally transferred regions that have undergone homologous recombination and rearrangement[16]. For the HMP reference genomes, most of which are draft status, the 16S rRNA sequences were identified using RNAMMER. We included only those HMP reference genomes that had less than 10% contamination as identified by CheckM and in which the annotated 16S region spanned a minimum of 200 bp of the V68 region (this excluded 79 genomes), resulting in a final set of 387 genomes (Supplementary Table 3). In 78 of the FijiCOMP single-cell assembles, RNAMMER identified full length 16S sequences. Multiple sequence alignments were performed using the RDP (v.11) Infernal aligner (http://rdp.cme.msu.edu/)[32,36], which accounts for secondary structure in the 16S. Per cent identity was calculated either on the full length 16S across sites that were present in 95% of cells or in a trimmed alignment of the V68 region, accounting for sites that were conserved in at least 95% of cells. By comparing per cent identity cut-offs of the hypervariable V68 region with the full-length 16S gene, we determined that a 95% identity cut-off within the V68 region was an equivalent cut-off to 97% identity between full-length 16S genes (Extended Data Fig. 8a).

Cells that have unusual or multiple divergent 16S sequences can cause highly conserved (e.g., ribosomal) genes to appear horizontally acquired. Although some ribosomal genes may be transferred, especially across related species, because they confer antibiotic resistance, to minimize the contribution of closely related strains, we excluded all HGT events inferred between a pair of cells for which any ribosomal gene was inferred to be transferred. HGT was observed to occur less frequently between cell pairs as the phylogenetic distance between them increased (Extended Data Fig. 8b), as previously reported[7].

To illustrate the diversity of genomes used in our study and their sources, a maximum likelihood-based phylogenetic tree was constructed with FastTree2 (v.2.1.3)[37] (GTR nucleotide substitution model) using a multiple sequence alignment generated by RDP of the full length 16S sequences where available and the 16S V68 region those were full length sequences could not be identified. 70 of the hydrogel-captured single-cell genomes lacked 16S rRNA sequences and were therefore not included in this tree. The tree was rooted using Archeal taxa as the outgroup, although placement of the root within Bacteria is unsupported.

Creating a non-redundant mobile gene set. In order to align reads to genes to attain relative gene abundances, we built a non-redundant gene data set (Extended Data Fig. 2). After pair-wise BLASTs between genomes (Step1), we clustered horizontally transferred regions using single-linkage clustering (Step2), identifying all with partial or full overlapping regions. Next, we identified ORFs within each contig using Prodigal (v.2.5)[38] (Step3). We included ORFs that overlapped at a minimum of 50% with a horizontally transferred region. This cut-off avoids false positive genes that overlap minimally with horizontally transferred regions, but allows for the inclusion of genes that may have been truncated due to highly fragmented draft genomes. We then clustered ORFs from each group of overlapping transferred regions into non-redundant sets using UCLUST[39] (v.1.5.579), with a 90% identity cut-off (Step4). The vast majority of genes were within 99–100% identity with the gene chosen for read alignment (that is, the centroid) (Extended Data Fig. 9). No gene with more than 10% ambiguous base pairs was chosen for read alignment. Since non-overlapping horizontally transferred regions may contain identical genes, we performed an additional final BLASTn search between genes to further reduce redundancy, although this step resulted in the removal of a relatively small number of genes (Step5).

Functional annotation of horizontally transferred genes. We relied on several methods for functional annotation. Details on the functional annotation of each gene are provided in Supplementary Table 5. We queried sequences using BLASTp against the Kyoto Encyclopedia of Genes and Genomes (KEGG)[40], using BLASTp to attain their KO classifications (e value 10^{-5}, per cent identity 30%); against the Clusters of Orthologous Groups (COG) database using rpsBLAST (e value 10^{-5}, per cent identity = 30%); and the TIGRFAM (v12.0) and PFAM (v.26) databases using HMMER (v.3.0) (e value 10^{-4}, score 22). KO numbers were mapped directly back to COG; and TIGRFAM roles that could not be assigned COGs retained the TIGRFAM designation. For each gene cluster, functional annotations were aggregated by retaining annotations to any gene within the cluster first according to COG classification, followed by KEGG, TIGRFAM and finally PFAM. We also assigned metabolic functions using the Automated Carbohydrate-Active Enzyme Annotation (http://csbl.bmb.uga.edu/dbCAN/)[41] (v.4.0), which employs an HMM-based search protocol. These were then assigned substrate categories[25]. To annotate antibiotics resistance genes, we used the ResFam[42] core genes database, which uses HMMs. Still, 32.8% of our HGT gene set could not be annotated by any of these means. To annotate the type of mobile genetic element specifically, we performed a keyword search amid the gene descriptions as follows:

Transposon: transpos*; insertion; resolv*; Tra[A-Z]; Tra[0-9]; IS[0-9]; "conjugate transposon"

Plasmid: resolv*; relax*; conjug*; trb; mob*; plasmid; "type IV"; toxin; "chromosome partitioning"; "chromosome segregation"

Phage: capsid; phage; tail; head; "tape measure"; antitermination

Other HGT machinery: integrase; excision*; exonuclease; recomb; toxin; CRISPR; restrict*; resolv*; topoisomerase; "reverse transcrip"

Carbohydrate-active enzymes and related proteins: Genes present in the CAZY database; glycosyltransferase; "glycoside hydrolase; xylan; monooxygenase; rhamnos*; cellulose; sialidase; *ose; acetylglucosaminidase; cellobiose; galact*; fructose; aldose; starch; mannose; mannan*; glucan; lyase; glycosyltransferase; glycosidase; pectin; SusD; SusC; fructokinase; galacto*; arabino*;

Proteins conferring antibiotic resistance: Genes present in the ARDB; multidrug; "azole resistance"; antibiotic resistance"; TetR; "; "tetracycline resistance"; VanZ; betalactam*; beta-lactam; antimicrob*; lantibio*

DNA extraction of FijiCOMP samples and sequencing. DNA from saliva samples was extracted using the Promega Maxwell Buccal Swab LEV DNA Purification Kit. Stool samples were collected within 24 h of saliva sample collection. DNA from stool samples was extracted using the MoBio Laboratories PowerSoil 96 Well DNA Isolation Kit with an added proteinase K step to aid in lysis (100 μg/ml final concentration at 55 °C for 20 min). Metagenomic samples were barcoded, multiplexed and sequenced across several lanes on the Illumina HiSeq 2000 platform (101 bp paired-end reads), in excess of 8 Gb of sequence per stool sample and 10 Gb per saliva sample.

Alignments of metagenomic data. The metagenomic samples analysed include 81 stool samples from the Human Microbiome Project (Supplementary Table 1) and 172 stool samples and 134 saliva samples from the FijiCOMP study (Supplementary Table 2). Raw metagenomic sequences from the FijiCOMP study were preprocessed in a manner equivalent to that for the HMP metagenomic samples[15]: they were initially filtered for quality (Phred score ≥ 3), minimum length (60 bp), and minimizing reads originating in human genomes, using BMTagger (ftp://ftp.ncbi.nlm.nih.gov/pub/agarwala/bmtagger/ NCBI/NLM/NIH; 07 March 2011, version 3.101). Sequencing depths of the final sample set were comparable between the FijiCOMP and HMP cohorts.

Reads were aligned to the non-redundant set of mobile genes (described above) using the BWA (v.0.7.12-r1039)[43] mem algorithm. A read pair is considered mapping when at least one read of the pair is mapped to the reference gene with 99% or greater sequence identity and aligned with at least half of the read length so as to avoid edge effects. In the vast majority of reads, the entirety of the read aligned with 99% or greater identity (Extended Data Fig. 10). After alignment, we considered only those genes which were had at least 80% coverage across the length of the gene, and had a median alignment depth of at least 4 reads per bp. In order to compare between samples that had varying read depth and across genes of varying length, we used a measure of fragments per kilobase of protein coding sequence per million mapped reads (FPKM), where each fragment is defined as a read pair. Alignments of the stool samples were observed for 88.3% of the 10,461 identified unique genes.

We did not consider minimum or maximum gene lengths for inclusion in our data set. The minimum gene length observed is 60 bp and the median length for all of the genes is 654 bp. Although genes of different lengths may be expected to be able to recruit metagenomic reads and meet the gene coverage criteria, gene length was not significantly correlated with prevalence, median or maximum abundance.

Some of the mobile genes are likely duplicated trans-acting core genes that confer antibiotic resistance, such tRNA synthetases[44–47]. FPKM values for these genes will be artificially inflated due to the false-positive recruitment of reads matching core genes. We presume that this component is small and given that they may be able to recruit reads from various genomes, their distribution across populations may serve to minimize differences between populations.

Assessing GH13 prevalence and abundance in entire metagenome. To determine whether any GH13-family genes, including those not identified here as mobile, were enriched in the FijiCOMP cohort, we aligned translated reads from each of the FijiCOMP and HMP metagenomic samples using PAUDA (v.1.0.1) to a database containing 16,244 GH13-family protein sequences annotated as such by the Carbohydrate-Active enZYmes Database (http://www.cazy.org) as well as 48 GH13-family protein sequences identified as mobile using the FijiCOMP single-cell and HMP assemblies. This database amounted to 11,236 unique protein-coding genes, of which 38 were identified as horizontally transferred. We then calculated coverage RPKMs (reads per kilobase of protein coding sequence per million mapped reads) for each of the genes in each of the samples and analysed 3,770 unique proteins with RPKM values greater than 100 RPKM. The distribution of GH13 genes differed between populations ($P < 10^{-5}$, PERMANOVA test of Jensen–Shannon divergences, 10^{4} permutations). 351 and 63 of the GH13 family genes were more prevalent in the FijiCOMP and HMP cohorts, respectively ($q < 0.001$ after FDR correction for Fisher's exact test). 347 genes (including 29 of the GH13 horizontally transferred genes) were enriched ($q < 0.001$ after FDR correction of Mann–Whitney tests) in the FijiCOMP data set, compared with only 118 (including 2 of the GH13 horizontally transferred genes) enriched in the HMP data set. We cannot conclusively determine whether the GH13 genes not identified in this study as horizontally transferred are part of the core or flexible genome.

Vector contamination. Cloning vectors may have been used in the sequencing of HMP reference and draft assemblies. (Cloning vectors were not used in the sequencing of the FijiCOMP single-cell genomes and adapters were removed before assembly.) As cloning vector sequence is sometimes retained in the assembly, these assemblies were screened for vector contamination against the UniVec database (http://www.ncbi.nlm.nih.gov/tools/vecscreen/univec/), using suggested parameters. Putative contamination was observed in all 387 of the HMP reference genomes, although only 102 cells had regions of putative contamination of at least 500 bp, which would have affected the method used to identify HGT events (Supplementary Table 3). The metagenomic libraries were not created using cloning vectors and therefore it may be possible to distinguish between those that are contamination (that is, those that failed to recruit reads) and those that are present. Only 102 genes linked to possible vector contamination failed to recruit reads.

tRNA analysis. Metagenomic alignments were also used to determine which mobile genes were adjacent to tRNA genes. We could then examine mobile elements that had integrated next to tRNAs to determine the taxonomy of the bacterial host. tRNAs have stable phylogenies that can be used for phylotyping[48]. Metagenomic alignments were filtered for paired reads that had only one read-pair aligning to a horizontally transferred gene. tRNA genes were identified using the program ARAGORN[49]. Taxonomies of the tRNA genes were ascertained through BLASTn searches against NT, requiring an alignment of 85 nucleotides at 85% identity. We identified 838 mobile genes adjacent to tRNA genes. Of these, 194 had multiple bacterial hosts, multiple isoacceptors, or multiple tRNA genes. 394 of the genes adjacent to tRNA genes had at least one bacterial host that could be taxonomically identified. Plots reflect the number of reads observed. 72.7% of genes adjacent to tRNAs that had annotatable functions were genes involved in the process of horizontal gene transfer (phage, transposon, plasmid, etc.).

Defining high confidence mobile genes. We also performed our analysis on the mobile gene pools in Fijian and American metagenomes on a subset of higher confidence mobile genes representing known HGT machinery genes and/or genes on scaffolds that have additional independent support for their phylogenetic placement. BLASTn searches were performed for each of the 1,662 FijiCOMP single-cell contigs containing a mobile gene against closely related organisms where available, resulting in 634 contigs that had additional phylogenetic support that could be compared. Additionally, phylogenetic placement was attained by examining tRNA genes on paired-reads aligning to the mobile gene set. This higher confidence set includes 6,187 unique genes (59.1% of the total mobile gene data set). Even with this smaller subset of high confidence genes, distinct functional gene pools can be observed between the HMP and FijiCOMP cohorts (Extended Data Figs 3, 4).

Statistical analysis of gene/function presence and abundance across samples. FPKMs associated with the same protein family were summed before analysis. To assess which genes were enriched in each population, the FPKMs of each gene were compared according to country/village using FDR-adjusted Mann–Whitney tests. Comparisons of prevalence were tested using Fisher's exact tests. All analyses were performed in R (v.3.1.0).

Identifying linkage between pairs of horizontally transferred genes. Metagenomic alignments were filtered for paired reads that matched two distinct genes in the mobile gene set. The HMP and FijiCOMP metagenomic libraries were both made with an average insert size of 180 bp. We required both genes to have 99% sequence identity or greater to their respective genes. We retained only paired reads that had information on alignment and orientation. Analysis of gene linkages was performed using the igraph package (v.0.7.1) in R. Multiple contexts, as determined by the linkage between mobile genes in the data set, were observed for 5,484 out of a total of 9,233 genes..

Microbiome composition. The bacterial composition of all samples was determined using MetaPhylerSR (v.0.115)[50]. The default database was supplemented with AMPHORA genes from the genome *Succinatimonas* sp. CAG:777 genome. The prevalence and abundance of plant matter was determined after aligning metagenomics reads to the SILVA database (v.115)[51]. We used FDR-adjusted *P* values of Pearson correlations to determine whether the abundances of any genes were significantly associated with the abundances of specific organisms in each cohort. We found that the abundances of 1,800 out of 8,322 genes (21.6%) and 1291 out of 6669 (19.4%) genes significantly correlated with the abundances of a single organism in the FijiCOMP and HMP cohorts, respectively.

Fijian Diet. The Fijian diet is rich in high-starch foods[52–54], including taro (*Colocasia esculenta*), giant swamp taro (*Cyrtosperma chamissonis*), giant taro (*Alocasia macrorhhiza*), tannia (*Xanthosoma sagittifolium*), cassava (*Manihot esculenta*), sweet potato (*Ipomoea batatas*), yams (*Dioscorea* spp.), breadfruit (*Artocarpus Altilis*) and plantains (*Musa* cultivars).

Fijians rely heavily on seafood as a main source of protein. Artisinal fishing is predominant in the study regions[55]. The species that are commonly fished locally by artisanal fishers are: eastern triangular butterflyfish (*Chaetodon baronessa*), swallowtail puller (*Chromis ternatensis*), blue-green damselfish (*Chromis viridis*), threadfin breams (*Pentapodus* sp.), imitator damselfish (*Pomacentrus imitator*), and two-lined monocle bream (*Scolopsis bilineata*). 27 species of sea cucumbers are commonly fished, though much of this catch is sold internationally, including those caught by artisanal fishers. The species that are commonly fished commercially, although consumed less often in the study region, are: blue finned rock cod (*Cephalopholis microprion*), blue-spotted grouper (*Cephalopholis rodeta*), daisy parrotfish (*Chlorurus sordidus*), orange-spotted emperorfish (*Lethrinus erythracanthus*), thumbprint emperor (*Lethrinus harak*), and snappers (*Macolor* spp.)[56].

Additional fish and shellfish consumed in Fiji, although not assessed for the study region include: albacore tuna (*Thunnus alalunga*), yellowfin tuna (*Thunnus albacares*), skipjack tuna (*Katsuwanas pelamis*), bigeye tuna (*Thunnus obesus*), Spanish mackerel (*Scomberomorus commerson*), striped marlin (*Tetrapturus audax*), blue marlin (*Makaira mazara*), barracuda (*Sphyraena* sp.), swordfish (*Xiphias gladius*), sailfish (*Istiophorus platypterus*), opah (*Lamprius regius*), sunfish (*Mola mola*), mahi mahi (*Coryphaena* sp.), black snapper (*Macolor niger*), goatfish (*Parupeneus barberinus*), parrotfish (*Scarus* sp.), rabbit fish (*Siganus puntatus*), peacock cod (*Cephalopholis argus*), unicornfish (*Naso unicornis*), cockles (*Anadara antiquata*), freshwater mussels (*Batissa violacea*) and other unspecified reef fish[57].

Antibiotic Use in Fiji. Specifically, we expected that orally administered antibiotics used to treat common ailments and dental infections would be the primary target of resistance, and these are limited to beta-lactams (amoxicillin, penicillin, fluxocillin), tetracycline, chloramphenicol, quinolones (ciprofloxacin), and metronidazole[58–60]. Thus, differences may reflect antibiotic use in other societal sectors, such as in livestock, historical uses of antibiotics, or the acquisition of multiple antibiotic resistance genes transferred within single cassettes. These findings highlight our relatively limited understanding of the forces that drive selection for antibiotic resistance within populations, and the reservoirs for resistance genes[61]. These topics are acutely important in Fiji, as *Shigella* infections are common and resistance to betalactamases, tetracyclines, chloramphenicol, cephalosporins and quinolones has already been reported[62].

Data availability. FijiCOMP metagenomic samples generated for this study are all deposited on NCBI's Short Read Archive under Project Number PRJNA217052. The specific SRS numbers corresponding to each study participant's gut and oral microbiome can be found in Supplementary Table 2. The single-cell assemblies can be found in the Data section at http://www.fijicomp.org.

31. Dean, F. B., Nelson, J. R., Giesler, T. L. & Lasken, R. S. Rapid amplification of plasmid and phage DNA using Phi 29 DNA polymerase and multiply-primed rolling circle amplification. *Genome Res.* **11,** 1095–1099 (2001).
32. Cole, J. R. *et al.* Ribosomal Database Project: data and tools for high throughput rRNA analysis. *Nucleic Acids Res.* **42,** D633–D642 (2014).
33. Bankevich, A. *et al.* SPAdes: a new genome assembly algorithm and its applications to single-cell sequencing. *J. Comput. Biol.* **19,** 455–477 (2012).
34. Wu, M. & Scott, A. J. Phylogenomic analysis of bacterial and archaeal sequences with AMPHORA2. *Bioinformatics* **28,** 1033–1034 (2012).
35. Lagesen, K. *et al.* RNAmmer: consistent and rapid annotation of ribosomal RNA genes. *Nucleic Acids Res.* **35,** 3100–3108 (2007).
36. Nawrocki, E. P. & Eddy, S. R. Infernal 1.1: 100-fold faster RNA homology searches. *Bioinformatics* **29,** 2933–2935 (2013).
37. Price, M. N., Dehal, P. S. & Arkin, A. P. FastTree 2—approximately maximum-likelihood trees for large alignments. *PLoS One* **5,** e9490 (2010).
38. Hyatt, D. *et al.* Prodigal: prokaryotic gene recognition and translation initiation site identification. *BMC Bioinformatics* **11,** 119 (2010).
39. Edgar, R. C. Search and clustering orders of magnitude faster than BLAST. *Bioinformatics* **26,** 2460–2461 (2010).
40. Kanehisa, M. *et al.* Data, information, knowledge and principle: back to metabolism in KEGG. *Nucleic Acids Res.* **42,** D199–D205 (2014).
41. Yin, Y. *et al.* dbCAN: a web resource for automated carbohydrate-active enzyme annotation. *Nucleic Acids Res.* **40,** W445–W451 (2012).
42. Gibson, M. K., Forsberg, K. J. & Dantas, G. Improved annotation of antibiotic resistance determinants reveals microbial resistomes cluster by ecology. *ISME J.* **9,** 207–216 (2015).
43. Li, H. & Durbin, R. Fast and accurate short read alignment with Burrows-Wheeler transform. *Bioinformatics* **25,** 1754–1760 (2009).
44. Wilson, D. N. Ribosome-targeting antibiotics and mechanisms of bacterial resistance. *Nat. Rev. Microbiol.* **12,** 35–48 (2014).
45. Gilbart, J., Perry, C. R. & Slocombe, B. High-level mupirocin resistance in Staphylococcus aureus: evidence for two distinct isoleucyl-tRNA synthetases. *Antimicrob. Agents Chemother.* **37,** 32–38 (1993).
46. Schimmel, P., Tao, J. & Hill, J. Aminoacyl tRNA synthetases as targets for new anti-infectives. *FASEB J.* **12,** 1599–1609 (1998).
47. Hurdle, J. G., O'Neill, A. J., Mody, L., Chopra, I. & Bradley, S. F. In vivo transfer of high-level mupirocin resistance from *Staphylococcus epidermidis* to methicillin-resistant *Staphylococcus aureus* associated with failure of mupirocin prophylaxis. *J. Antimicrob. Chemother.* **56,** 1166–1168 (2005).
48. Widmann, J., Harris, J. K., Lozupone, C., Wolfson, A. & Knight, R. Stable tRNA-based phylogenies using only 76 nucleotides. *RNA* **16,** 1469–1477 (2010).
49. Laslett, D. & Canback, B. ARAGORN, a program to detect tRNA genes and tmRNA genes in nucleotide sequences. *Nucleic Acids Res.* **32,** 11–16 (2004).
50. Liu, B., Gibbons, T., Ghodsi, M., Treangen, T. & Pop, M. Accurate and fast estimation of taxonomic profiles from metagenomic shotgun sequences. *BMC Genomics* **12** (Suppl. 2), S4 (2011).
51. Quast, C. *et al.* The SILVA ribosomal RNA gene database project: improved data processing and web-based tools. *Nucleic Acids Res.* **41,** D590–D596 (2013).

52. Robertson, A. F. S. (ed.) *Food and Nutrition in Fiji: Nutrition-Related Diseases and their Prevention* (Univ. South Pacific, 1991)
53. Rush, E., Hedges, R., Alsbersberg, B., Qionibaravi, D. & Laulu, M. Staple food intake in a rural village in Verata, *Fiji. Pac. Health Dialog* **8,** 44–46 (2001).
54. Food and Agricultural Organization. *Pacific Food Security Toolkit: Building Resilience to Climate Change, Root Crop and Fishery Production* (Food and Agricultural Organization, 2010)
55. Goetze, J. *Evidence of Artisanal Fishing Impacts and Depth Refuge in Assemblages of Reef Fish of a Fijian Island* (Thesis, Univ. Western Australia, 2009).
56. Jupiter, S., Saladrau, W. & Vave, R. *Assessment of Sea Cucumber Fisheries Through Targeted Surveys of Lau Province, Fiji* (Wildlife Conservation Society/University of the South Pacific/Fiji Department of Fisheries/Khaled bin Sultan Living Oceans Foundation, 2013).
57. Kumar M., Aalbersberg B. & Mosle L. *Mercury Levels in Fijian Seafoods and Potential Health Implications.* (World Health Organization, Western Pacific Region, 2004).
58. Murti, A. & Morse, Z. Dental antibiotic prescription in Fijian adults. *Int. Dent. J.* **57,** 65–70 (2007).
59. National Drugs and Therapeutics Subcommittee. *Antibiotic Guidelines* 3rd Edition (Ministry of Health, Government of Fiji, 2011).
60. Thompson, C. N. *et al.* Typhoid fever in Fiji: a reversible plague? *Trop. Med. Int. Health* **19,** 1284–1292 (2014).
61. Sommer, M. O. A., Dantas, G. & Church, G. M. Functional characterization of the antibiotic resistance reservoir in the human microflora. *Science* **325,** 1128–1131 (2009).
62. Watson, C. Death from multi-resistant shigelloses: a case study from Fiji. *Pac. Health Dialog* **13,** 111–114 (2006).

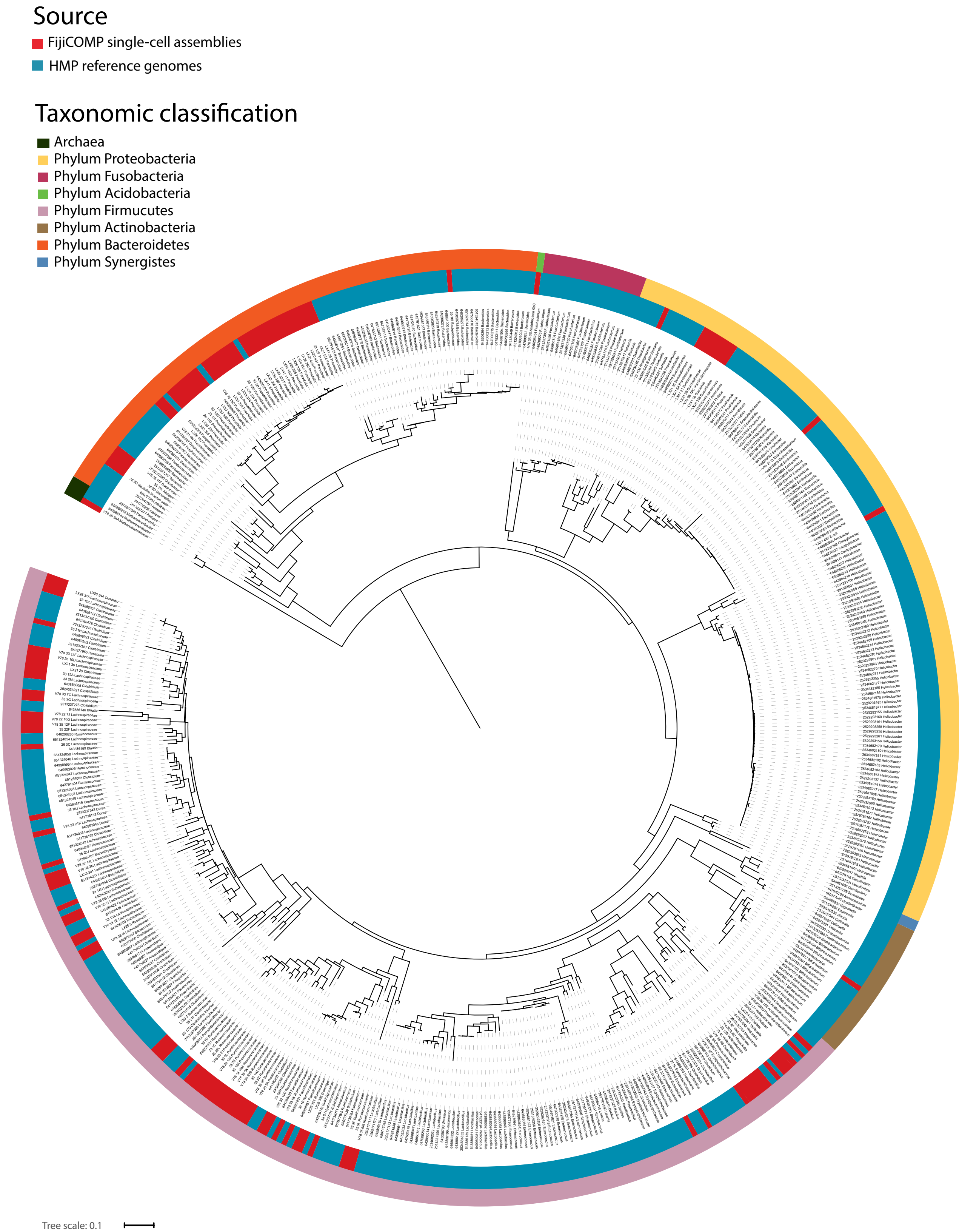

Extended Data Figure 1 | Phylogeny of assemblies used in the study span the bacterial Tree of Life. A phylogenetic tree constructed using a multiple sequence alignment of the full 16S rRNA gene or the V68 region of the 16S rRNA gene of all reference genomes and single-cell assemblies used in this analysis where available. 16S alignments were constructed using RDP. The tree was then assembled using FastTree. Support was low for all deep branches in the tree, so the archeal branch serves as the outgroup for illustrative purposes only. The outer colour bar displays taxonomic associations for archea and bacterial phyla. The inner colour bar displays the source of that operational taxonomic unit: HMP reference cells ($n = 387$ blue) and FijiCOMP single cell assemblies ($n = 110$, red). 16S rRNA gene sequences were not available for 70 FijiCOMP single-cell assembles, which are therefore not included in this tree.

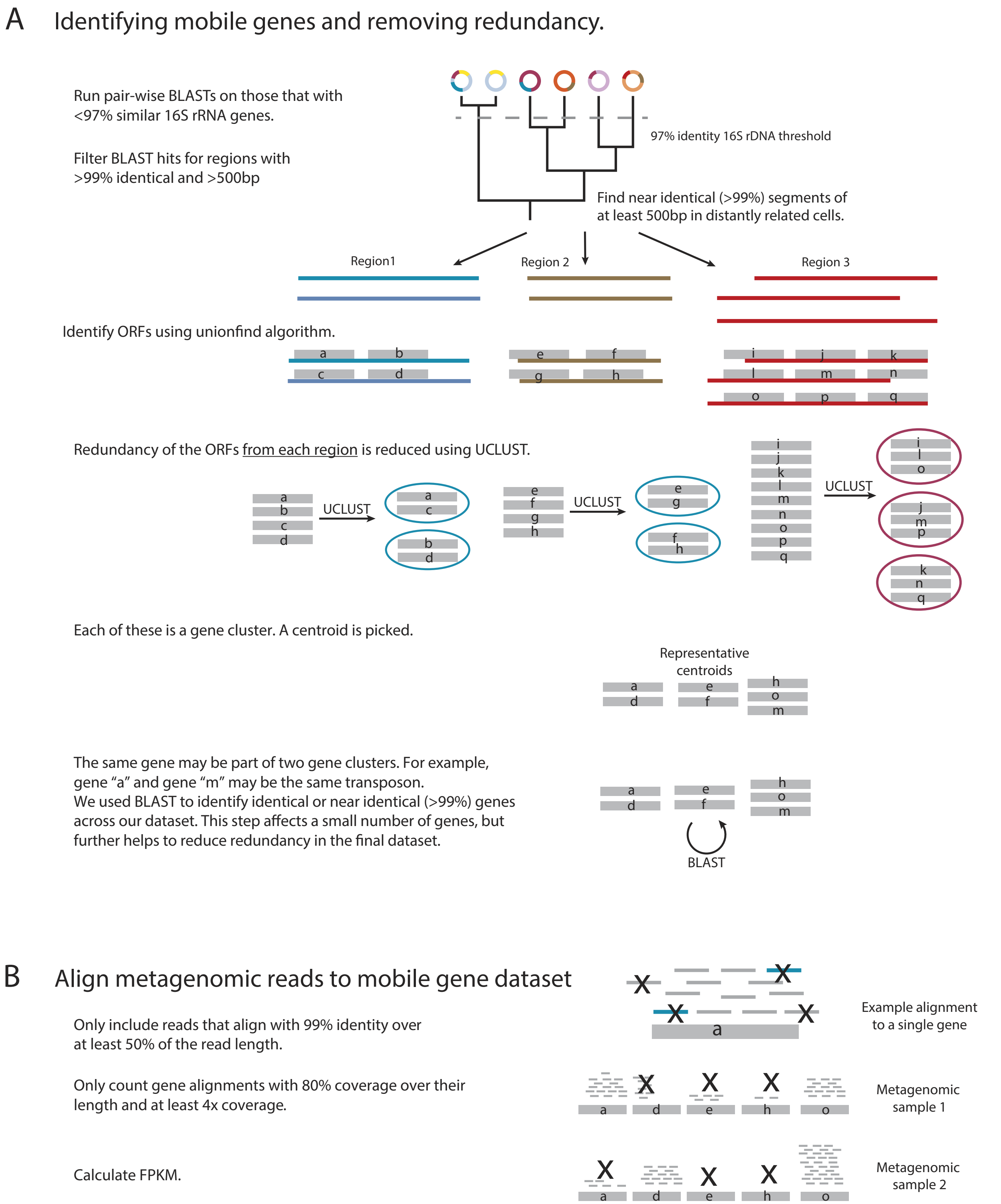

Extended Data Figure 2 | Methodology for identifying horizontally transferred genes and assessing their distribution within the metagenomic samples. Horizontally transferred regions were first identified using pair-wise BLASTs between HMP reference genomes and FijiCOMP single cell assemblies. Open reading frames were annotated within the horizontally transferred regions. Genetic redundancy was removed in the mobile gene set to ensure accurate abundance estimates using a combination of UCLUST and BLAST. Metagenomic reads were then aligned to the data set of unique mobile genes. Alignments were filtered to retain only reads that aligned with 99% identity across over 50% of their read length. Abundances of genes in the metagenomic samples were determined for genes whose alignments had a minimum of 4 × alignment depth over 80% of the gene length.

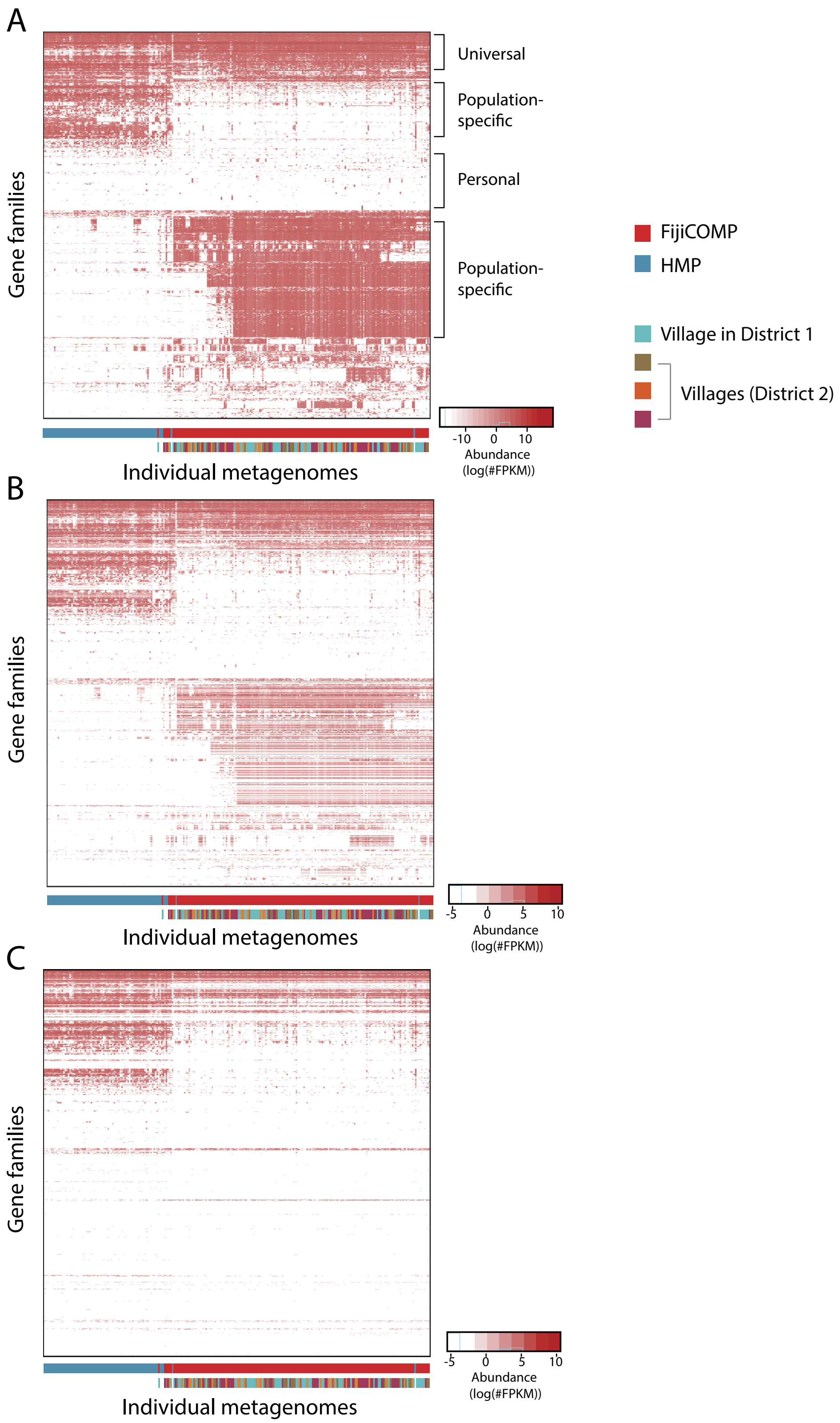

Extended Data Figure 3 | The abundance of mobile gene families is largely determine by cohort. a, A heat map is plotted showing the abundances (FPKM) of mobile genes aggregated by functional gene family (COG assignment, KEGG, TIGRFAM or PFAM family) within each of the metagenomic samples (81 HMP samples and 172 FijiCOMP samples). Hierarchical clustering using complete linkage was performed on the Euclidean distances between profiles of functional gene families across individuals and on the distances between individuals' mobile gene composition. Values are plotted on a logarithmic scale. **b**, A heat map is plotted showing the abundances (FPKM) of only those mobile gene families that were deemed of higher confidence within each of the metagenomic samples. These include mobile gene families from mobile genes that were annotated as horizontal transfer machinery or had additional support for their phylogenetic placement. The placements of gene families and individuals were maintained from **a** for comparative purposes. **c**, A heat map is plotted showing the abundances (FPKM) of only those mobile genes that were observed to be transferred between HMP reference genomes within each of the metagenomic samples. The placements of gene families and individuals were maintained from **a** for comparative purposes.

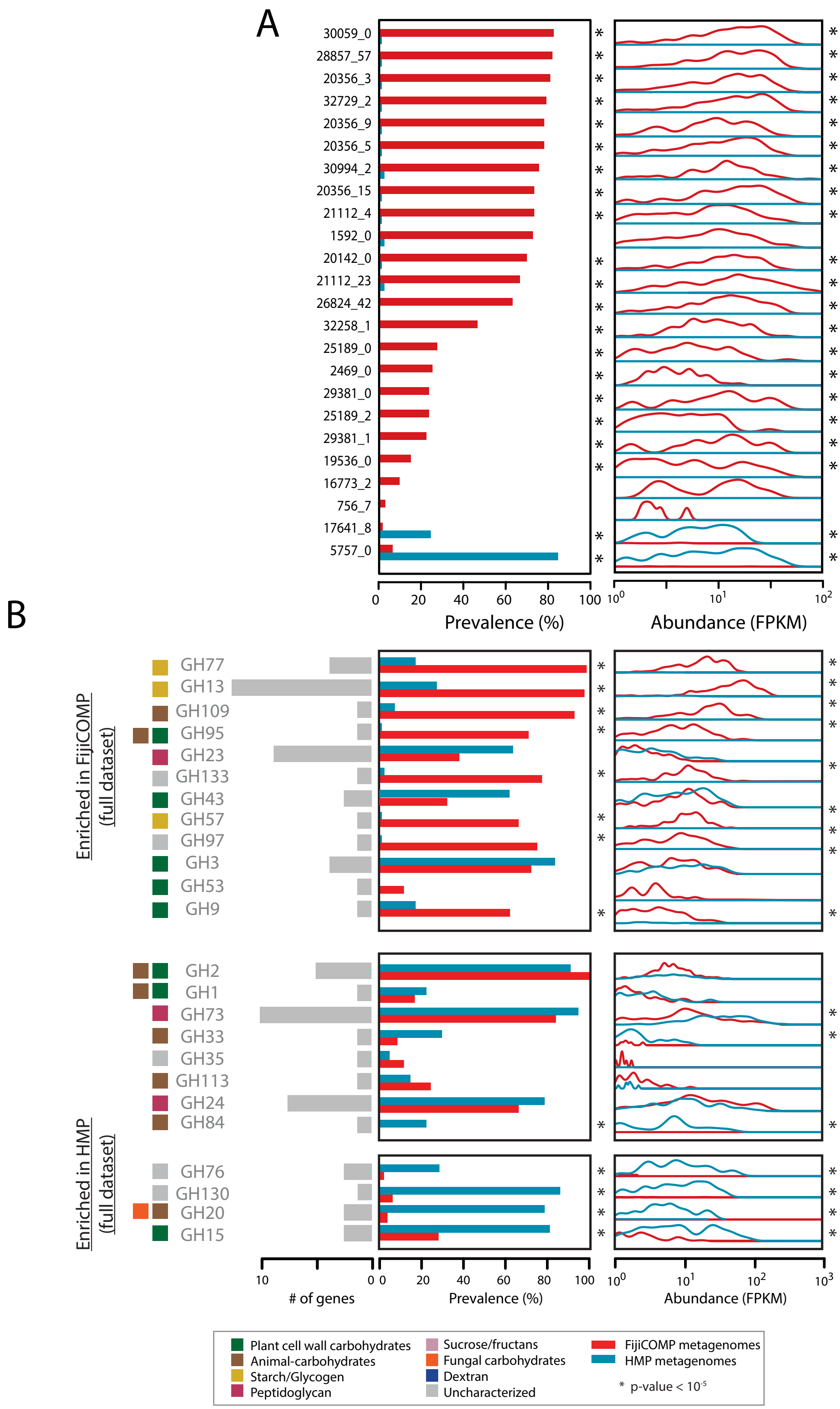

Extended Data Figure 4 | Distributions of GH13 genes and glycoside hydrolase families within mobile genes of higher confidence display population-specific enrichment. a, Prevalence and abundance (measured by FPKM) of mobile genes annotated as members of the GH13 family in the FijiCOMP ($n = 172$, red) and HMP ($n = 81$, blue) metagenomic stool samples. **b**, Prevalence and abundance of all glycoside hydrolase families within the higher confidence mobile gene subset present in the FijiCOMP (red) and HMP (blue) metagenomic stool samples. Only unique gene families from mobile genes that were annotated as horizontal transfer machinery or had additional support for their phylogenetic placement are included here. Abundances were measured by FPKM, aggregated according to glycoside hydrolase family, and plotted as a function of the density across samples. For each glycoside hydrolase family, the number of unique horizontally transferred genes observed is noted, as are the sources of their substrates.

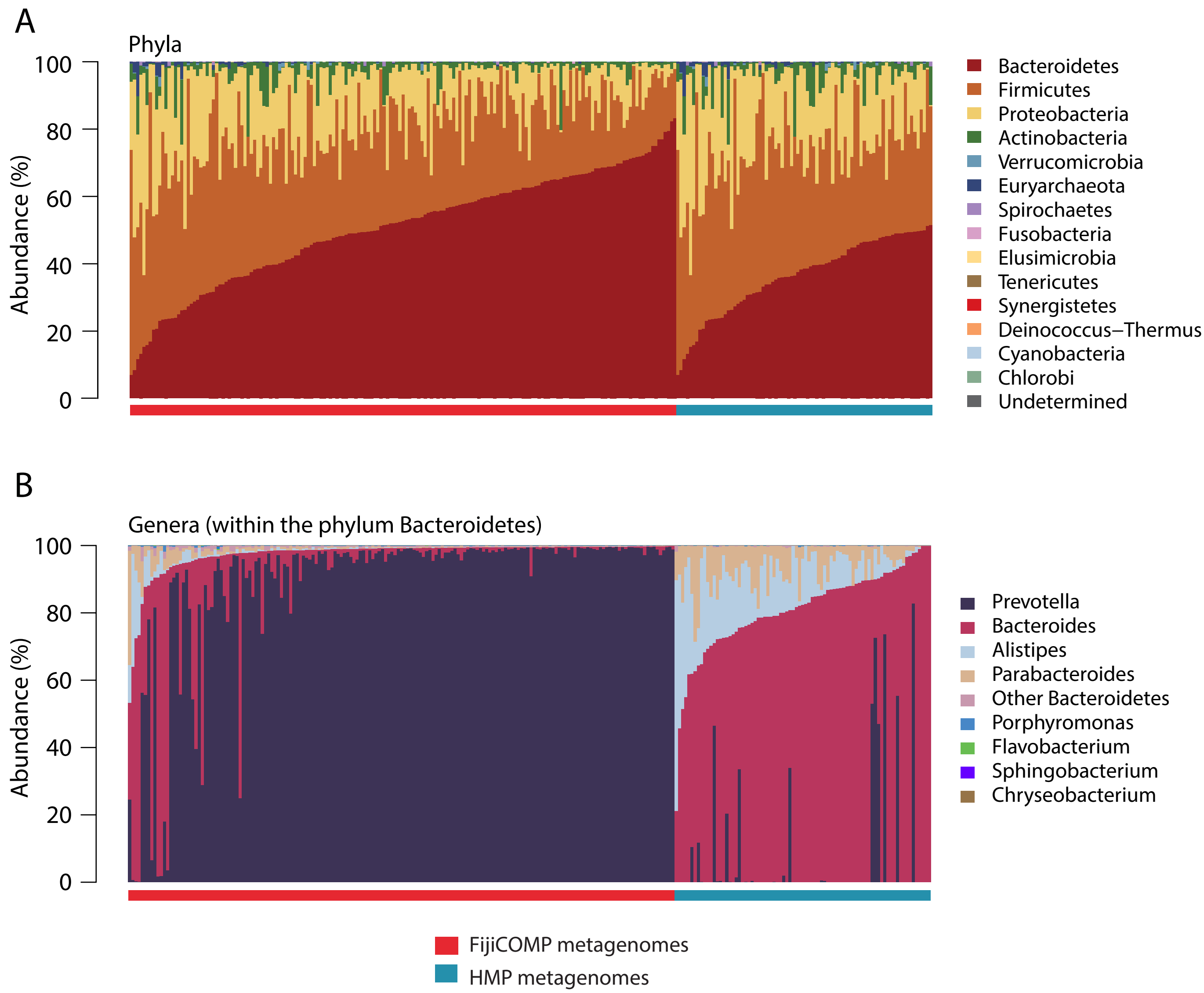

Extended Data Figure 5 | Composition of the gut microbiomes of HMP and FijiCOMP study participants. a, Relative abundances of bacteria according to phylum plotted for metagenomic samples from individuals in the HMP (n = 81, blue) and FijiCOMP (n = 172, red) cohorts. Samples are sorted according to cohort and the abundance of the dominant phyla. **b**, Relative abundances of families within the order Bacteriodales plotted for metagenomic samples from individuals in the HMP (blue) and FijiCOMP (red) cohorts. Samples are sorted according to cohort and the abundance of the top Bacteroidales member.

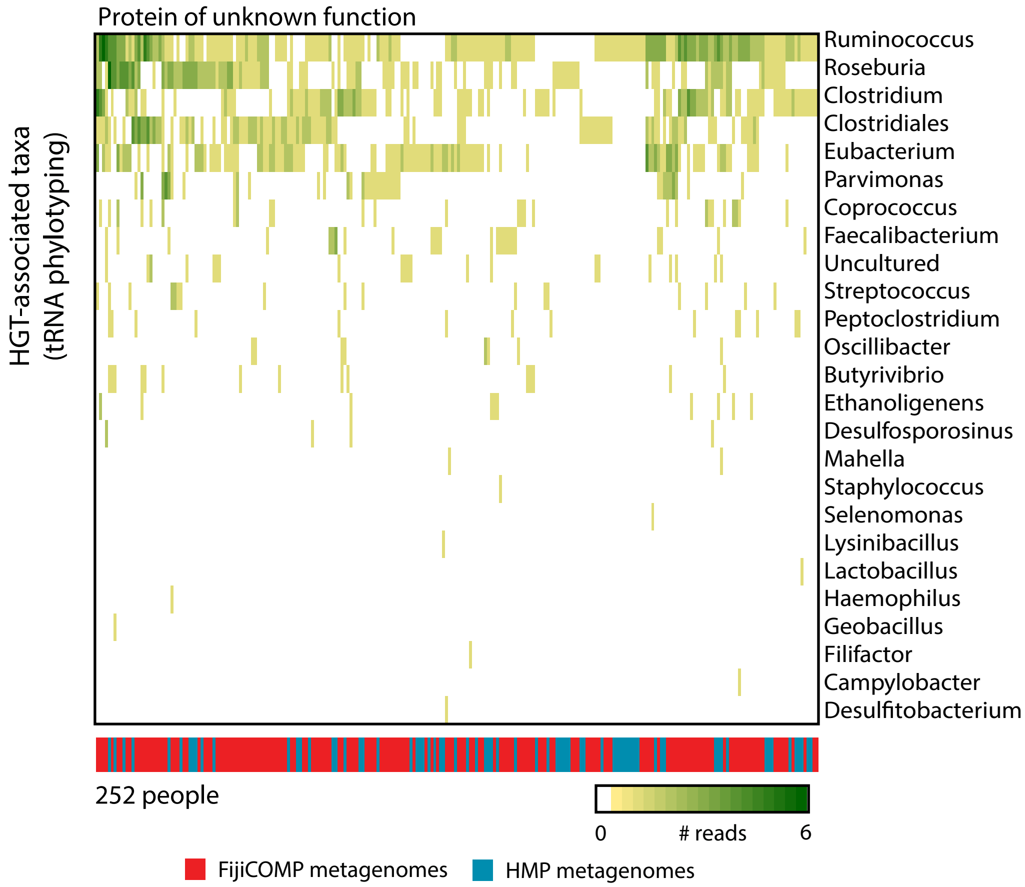

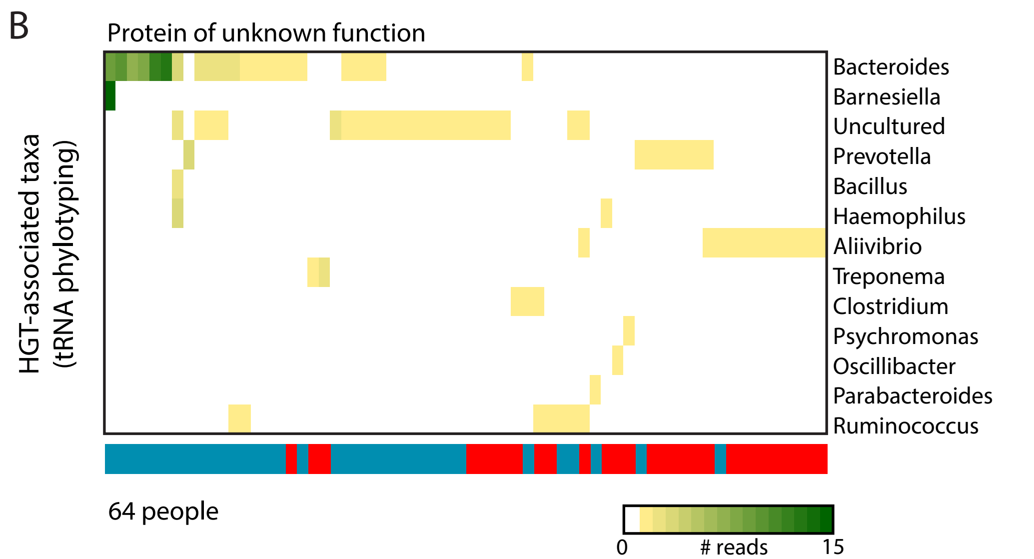

Extended Data Figure 6 | Mobile genes are observed in a wide variety of bacterial host backgrounds across the two cohorts. a, b, A heat map is plotted showing the number of read-pairs per person that aligned to both a tRNA gene and two specific horizontally transferred genes. Colours within the heat map reflect the read abundance according to the species associated with the specific tRNA gene. The colour bar shows which meteganomic cohort the reads are from: FijiCOMP (red) and HMP (blue).

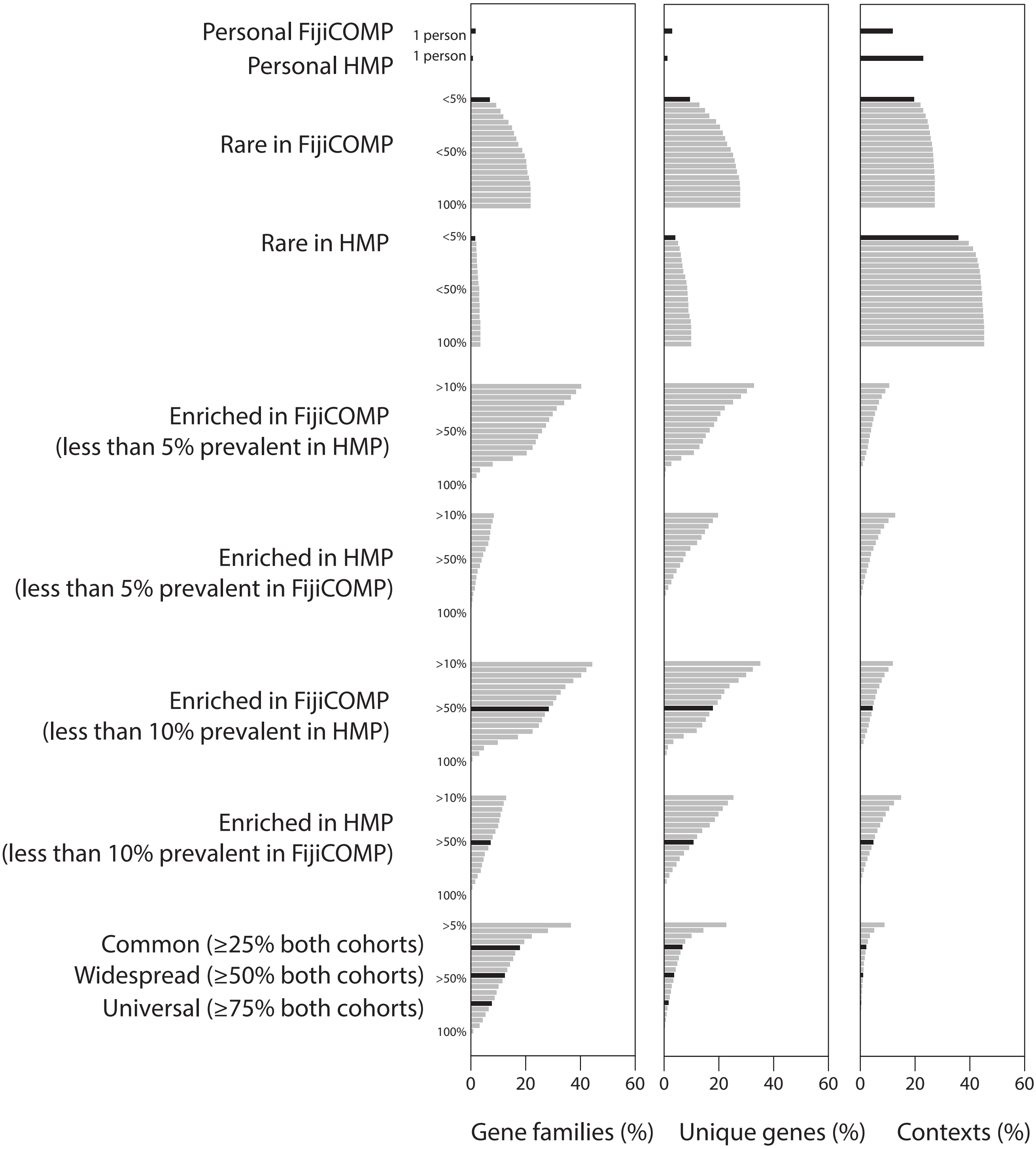

Extended Data Figure 7 | The relative abundances of genes and contexts across populations is not sensitive to precise definitions. Percentages of gene families, as determined by COG annotations (left), identical genes (middle) and gene contexts (right) between populations for a wide range of parameters. Bars are plotted in 5% increments. Bars shaded in black are the parameters that plotted in Fig. 4.

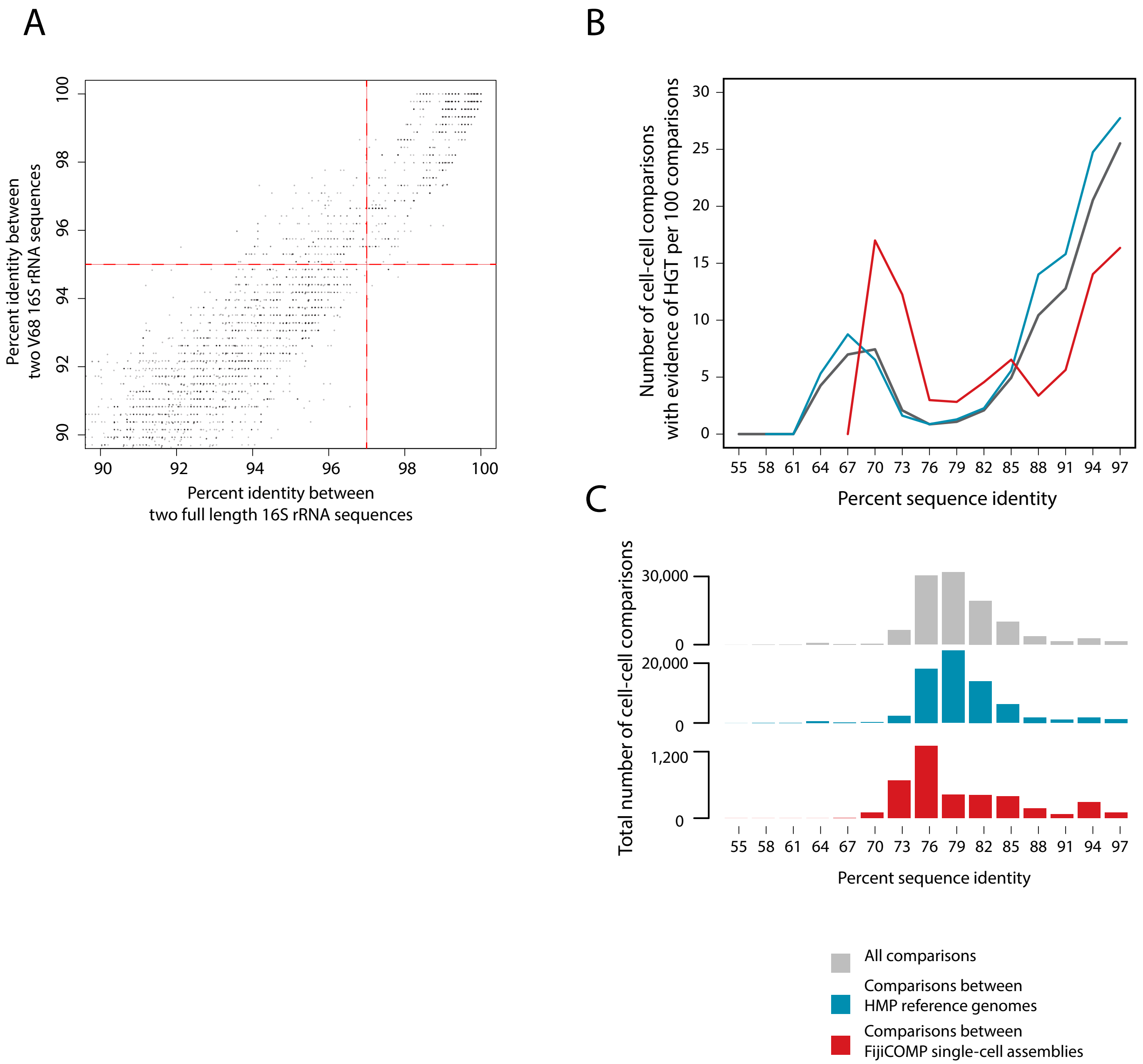

Extended Data Figure 8 | Horizontal transfer varies across cells at different phylogenetic distances. a, Nucleotide identity cut-offs for full length 16S rRNA and the V68 16S rRNA region were compared to avoid comparisons between closely related cells. For each pair of HMP reference genomes, nucleotide identity for their full-length 16S rRNA is plotted against that of their V68 regions. 97% identity of full-length 16S (corresponding to approximately 75 million years of evolution) was used as a cut-off, whereas 95% was used as a cut-off when only sequences in the V68 region were available. Only those genomes above 90% similar at both the full-length and V68 region are shown. **b**, The number of cell–cell comparisons contributing to each of the lines. **c**, HGT frequency plotted as a function of the phylogenetic divergence between species between all cell-cell comparisons (black), between HMP reference genomes only (blue) and between the FijiCOMP single cell assemblies (red). This plot includes only cells for which full-length 16S rRNA genes could be identified.

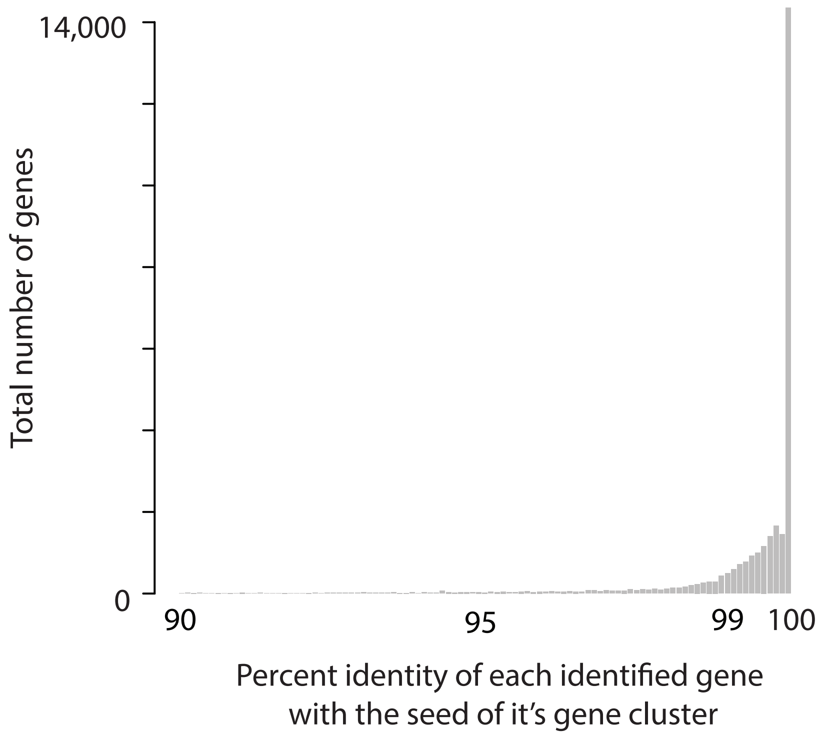

Extended Data Figure 9 | Representative genes chosen for the final mobile gene data set are highly similar to the genes that were filtered to reduce redundancy. For each overlapping horizontally transferred region observed in cell–cell BLASTn comparisons between the reference genomes and single-cell assemblies, genes were clustered to identify unique genes and reduce the redundancy of the gene set. This step is essential for accurate abundance measurements of these genes in the metagenomic data sets after read alignment. All open reading frames from each overlapping horizontally transferred region were grouped using UCLUST. The nucleotide identities of each of the filtered genes and the gene chosen for read alignment (that is, the centroid) are plotted.

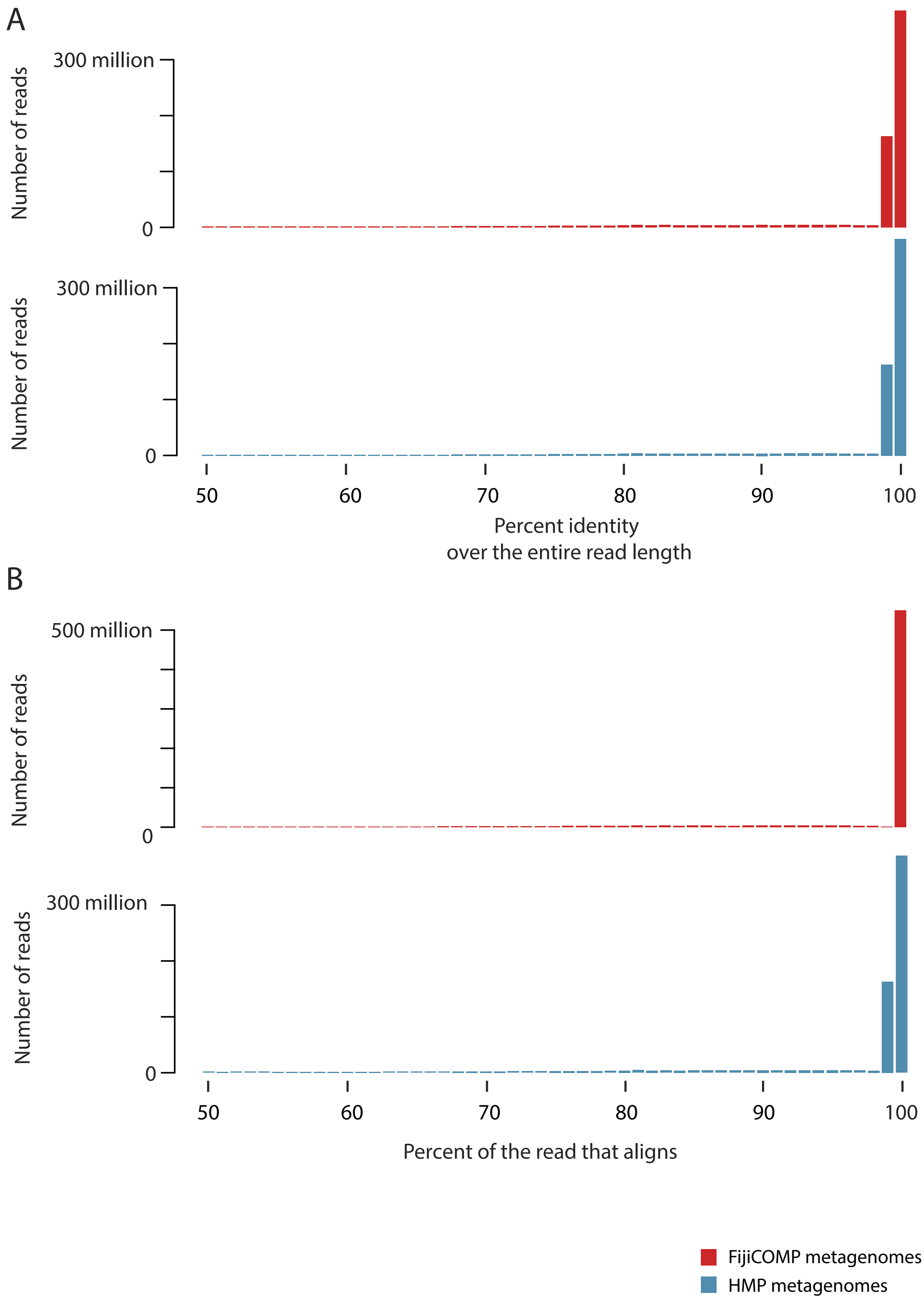

Extended Data Figure 10 | Metagenomic reads align to mobile genes with high fidelity over their entire length. Metagenomic reads were required to align with 99% identity to a mobile gene over at least 50% of the read length. Despite the seemingly low 50% cut-off, almost all reads align with near-perfect nucleotide identity over the entire length of the gene.

LETTER

doi:10.1038/nature18644

Glial-cell-derived neuroregulators control type 3 innate lymphoid cells and gut defence

Sales Ibiza[1]*, Bethania García-Cassani[1]*, Hélder Ribeiro[1], Tânia Carvalho[1], Luís Almeida[1], Rute Marques[2]†, Ana M. Misic[3]†, Casey Bartow-McKenney[3], Denise M. Larson[4], William J. Pavan[4], Gérard Eberl[2], Elizabeth A. Grice[3] & Henrique Veiga-Fernandes[1,5]

Group 3 innate lymphoid cells (ILC3) are major regulators of inflammation and infection at mucosal barriers[1]. ILC3 development is thought to be programmed[1], but how ILC3 perceive, integrate and respond to local environmental signals remains unclear. Here we show that ILC3 in mice sense their environment and control gut defence as part of a glial–ILC3–epithelial cell unit orchestrated by neurotrophic factors. We found that enteric ILC3 express the neuroregulatory receptor RET. ILC3-autonomous *Ret* ablation led to decreased innate interleukin-22 (IL-22), impaired epithelial reactivity, dysbiosis and increased susceptibility to bowel inflammation and infection. Neurotrophic factors directly controlled innate *Il22* downstream of the p38 MAPK/ERK-AKT cascade and STAT3 activation. Notably, ILC3 were adjacent to neurotrophic-factor-expressing glial cells that exhibited stellate-shaped projections into ILC3 aggregates. Glial cells sensed microenvironmental cues in a MYD88-dependent manner to control neurotrophic factors and innate IL-22. Accordingly, glial-intrinsic *Myd88* deletion led to impaired production of ILC3-derived IL-22 and a pronounced propensity towards gut inflammation and infection. Our work sheds light on a novel multi-tissue defence unit, revealing that glial cells are central hubs of neuron and innate immune regulation by neurotrophic factor signals.

ILC3 produce proinflammatory cytokines, and regulate mucosal homeostasis and anti-microbial defence[1]. In addition to their well-established developmentally regulated program, ILC3 are also controlled by microbial and dietary signals[1–6], suggesting that ILC3 possess other unexpected environment-sensing strategies. Neurotrophic factors are extracellular environmental cues to neurons and include the glial-derived neurotrophic factor (GDNF) family ligands (GFL) that activate the tyrosine kinase receptor RET in the nervous system, kidney and haematopoietic progenitors[7–11].

Analysis of gut lamina propria revealed that ILC3 express high levels of *Ret*[7,12] (Fig. 1a), a finding confirmed at the protein level and by reporter *Ret*^{GFP} knock-in mice[13] (Fig. 1b–d and Extended Data Fig. 1a–d). ILC3 subsets expressed *Ret*^{GFP} and aggregated in cryptopatches and isolated lymphoid follicles (ILF), suggesting a role of neuroregulators in ILC3 (Fig. 1b–d and Extended Data Fig. 1b–j). To explore this hypothesis, we transplanted fetal liver cells from *Ret* competent (*Ret*$^{WT/GFP}$) or deficient (*Ret*$^{GFP/GFP}$)[13] animals into alymphoid *Rag1*$^{-/-}\gamma c^{-/-}$ hosts. *Ret*-deficient chimaeras revealed unperturbed ILC3 and cryptopatch development (Fig. 1e). Notably, IL-22-expressing ILC3 were largely reduced despite normal IL-22 production by T cells (Fig. 1f, g). In contrast, innate IL-17 was unaffected by *Ret* ablation (Fig. 1f and Extended Data Fig. 2a). In agreement with this, analysis of gain-of-function *Ret*^{MEN2B} mice[14] revealed a selective

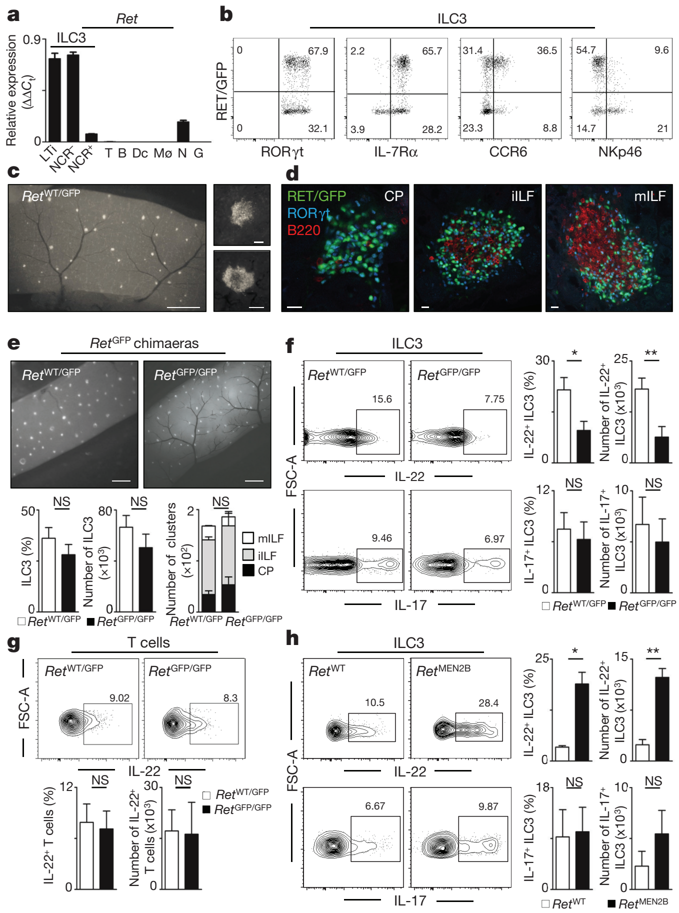

Figure 1 | The neurotrophic factor receptor RET drives enteric ILC3-derived IL-22. a, Relative expression of *Ret* in lymphoid tissue initiator cells (LTi), natural cytotoxicity receptor (NCR)$^{-}$ and NCR^{+} ILC3 subsets, T cells (T), B cells (B), dendritic cells (Dc), macrophages (Mø), enteric neurons (N) and mucosal glial cells (G). **b**, *Ret*^{GFP} ILC3 subsets in the gut. **c**, Left, *Ret*^{GFP} gut. Right, ILC3 aggregates. White, GFP. **d**, Enteric cryptopatches (CP), immature (iILF) and mature (mILF) isolated lymphoid follicles. Green, RET/GFP; blue, RORγt; red, B220. **e**, Small intestine of *Ret*^{GFP} chimaeras ($n = 15$). **f**, **g**, Enteric ILC3 and T cells from *Ret*^{GFP} chimaeras. *Ret*$^{WT/GFP}$, $n = 25$; *Ret*$^{GFP/GFP}$, $n = 22$. **h**, Enteric ILC3 from *Ret*^{MEN2B} mice ($n = 7$). Scale bars, 1 mm (**c** left, **e**); 50 μm (**c** right); 30 μm (**d**). Data are representative of 4 independent experiments. Error bars show s.e.m. $*P < 0.05$, $**P < 0.01$; NS, not significant.

[1]Instituto de Medicina Molecular, Faculdade de Medicina de Lisboa, Av. Prof. Egas Moniz, Edifício Egas Moniz, 1649-028 Lisboa, Portugal. [2]Microenvironment and Immunity Unit, Institut Pasteur, 25 Rue du Docteur Roux, 75724 Paris, France. [3]Department of Dermatology, Perelman School of Medicine, University of Pennsylvania, 421 Curie Blvd, 1007 Biomedical Research Building, Philadelphia, Pennsylvania 19104, USA. [4]Genetic Disease Research Branch, National Human Genome Research Institute, National Institutes of Health, Bethesda, Maryland 20892, USA. [5]Champalimaud Research, Champalimaud Centre for the Unknown, 1400-038 Lisboa, Portugal. †Present addresses: INSERM, U1163, Laboratory of Intestinal Immunity, and Université Paris Descartes-Sorbonne Paris Cité and Institut Imagine, Paris, France (R.M.); Center for Host-Microbial Interactions, Department of Pathobiology, School of Veterinary Medicine, University of Pennsylvania, Philadelphia, Pennsylvania 19104, USA (A.M.M).
*These authors contributed equally to this work.

increase of IL-22-producing ILC3, whereas their IL-17-producing counterparts were unaffected (Fig.1h and Extended Data Fig. 2b). To more specifically evaluate the effects of RET in ILC3, we deleted *Ret* in RORγt-expressing cells by breeding *Rorgt*-Cre with $Ret^{fl/fl}$ mice[15,16] (Extended Data Fig. 3a, b). Analysis of *Rorgt*-Cre$Ret^{fl/fl}$ (Ret^{Δ}) mice revealed selective and extensive reduction of ILC3-derived IL-22, but normal IL-22-producing T cells (Fig. 2a and Extended Data Fig. 3c, d). IL-22 acts on epithelial cells to induce reactivity and repair genes[1]. When compared to their wild-type littermate controls, the Ret^{Δ} epithelium revealed normal morphology, proliferation and paracellular permeability, but a marked reduction of epithelial reactivity and repair genes (Fig. 2b and Extended Data Fig. 3e–h). Accordingly, the Ret^{MEN2B} epithelium displayed increased levels of these molecules in an IL-22-dependent manner (Fig. 2b and Extended Data Fig. 3i). These results indicate that RET signals selectively control innate IL-22 and shape intestinal epithelial reactivity.

To determine whether neurotrophic factors regulate intestinal defence, we tested how varying degrees of RET signals control enteric aggressions. Whereas Ret^{Δ} mice treated with dextran sodium sulfate (DSS) had increased weight loss and inflammation, reduced IL-22-producing ILC3, decreased epithelial reactivity/repair genes and pronounced bacterial translocation from the gut, Ret^{MEN2B} mutants were highly protected compared to their wild-type littermate controls (Fig. 2c–j and Extended Data Fig. 4). As DSS largely causes epithelial injury, we tested whether ILC3-autonomous RET signals are required to control infection. To this end, Ret^{Δ} mice were bred with $Rag1^{-/-}$ mice to formally exclude adaptive T-cell effects. The resulting $Rag1^{-/-}Ret^{\Delta}$ mice were infected with the attaching and effacing bacteria *Citrobacter rodentium*. When compared to their littermate controls, $Rag1^{-/-}Ret^{\Delta}$ mice had marked gut inflammation, reduced IL-22-producing ILC3, increased *C. rodentium* infection and translocation, reduced epithelial reactivity genes, increased weight loss and reduced survival (Fig. 2k–n and Extended Data Fig. 5). Altogether, these data indicate that ILC3-intrinsic neurotrophic factor cues regulate gut defence and homeostasis.

We used a multi-tissue organoid system to show that IL-22 is the molecular link between RET-dependent ILC3 activation and epithelial reactivity. Addition of GFL to ILC3–epithelial organoids strongly induced epithelial reactivity genes in an IL-22- and RET-dependent manner (Fig. 3a, b and Extended Data Fig. 6a). To further examine how RET signals control innate IL-22, we investigated a gene signature

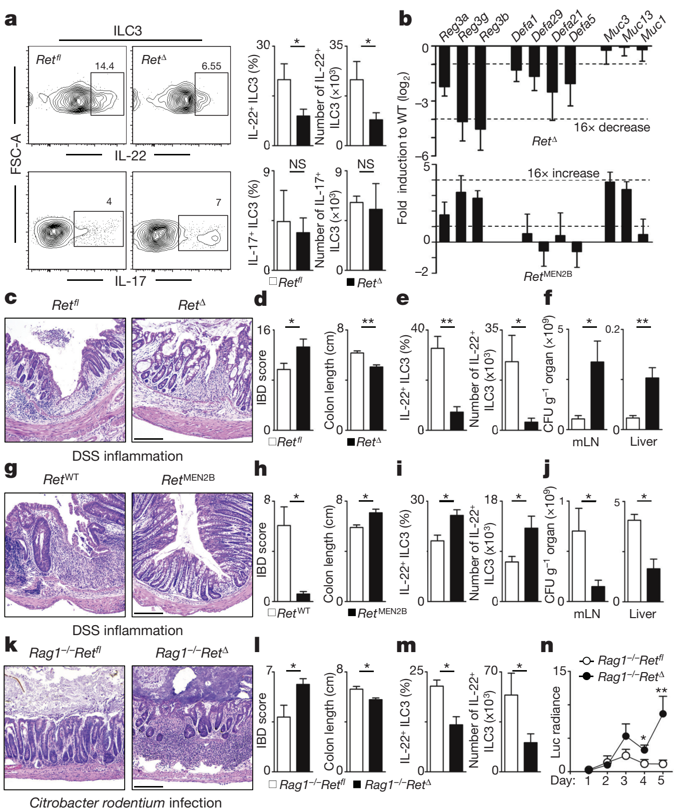

Figure 2 | ILC3-intrinsic RET signals regulate gut defence. a, ILC3-derived cytokines ($n=11$). **b**, Gene expression in the epithelium of Ret^{Δ} and Ret^{MEN2B} mice compared to their wild-type littermate controls ($n=7$). **c**–**f**, DSS treatment in Ret^{fl} and Ret^{Δ} mice ($n=8$). **c**, Histopathology. **d**, Inflammation score and colon length. **e**, Innate IL-22. **f**, Bacterial translocation. CFU, colony-forming unit. **g**–**j**, DSS treatment in Ret^{WT} and Ret^{MEN2B} mice ($n=8$). **g**, Histopathology. **h**, Inflammation score and colon length. **i**, Innate IL-22. **j**, Bacterial translocation. mLN, mesenteric lymph node. **k**–**n**, *C. rodentium* infection in $Rag1^{-/-}Ret^{fl}$ ($n=15$) and $Rag1^{-/-}Ret^{\Delta}$ ($n=17$) mice. **k**, Histopathology. **l**, Inflammation score and colon length. **m**, Innate IL-22. **n**, Infection burden. Scale bars, 200 μm. Data are representative of 4 independent experiments. Error bars show s.e.m. $*P<0.05$, $**P<0.01$.

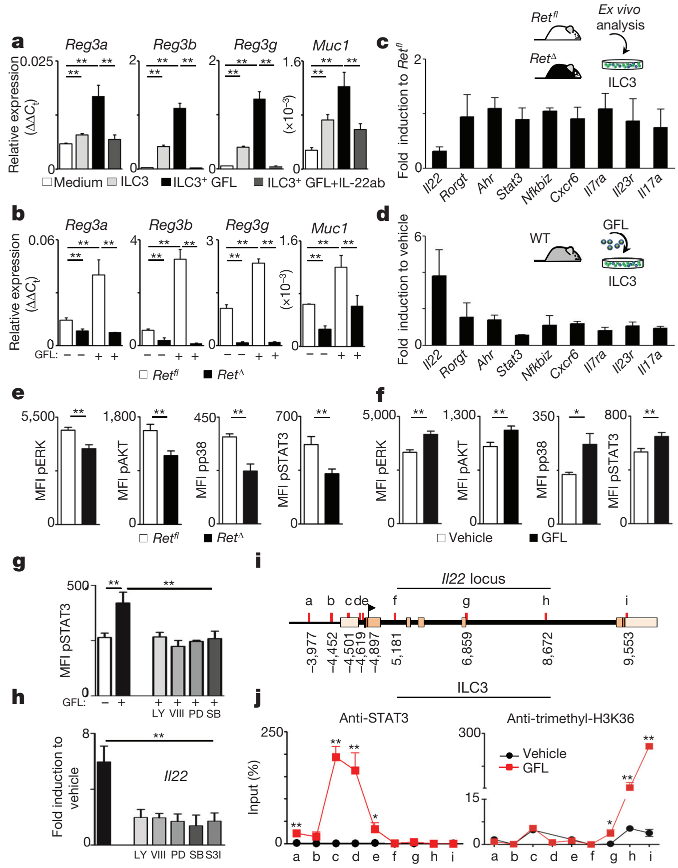

Figure 3 | ILC3-autonomous RET signals directly control *Il22* downstream of pSTAT3. a, **b**, Epithelial-ILC3 organoids ($n=9$). **c**, Gene expression in Ret^{Δ} ILC3 compared to their wild-type controls ($n=4$). **d**, Gene expression in ILC3 after activation by GFL ($n=4$). **e**, Enteric Ret^{Δ} ILC3. pERK, $n=8$; pAKT, $n=12$; phosphorylated p38/MAP kinase, $n=6$; pSTAT3, $n=14$. MFI, mean fluorescence intensity. **f**, Enteric ILC3 activation by GFL. pERK, $n=10$; pAKT, $n=16$; phosphorylated p38/MAP kinase, $n=3$; pSTAT3, $n=15$. **g**, pSTAT3 expression in enteric ILC3 cultured with medium ($n=7$), GFL ($n=11$) or GFL and inhibitors for: p38 MAPK/ERK-AKT (LY) ($n=7$); ERK (PD) ($n=7$); AKT (VIII) ($n=8$); and p38 MAPK (SB) ($n=6$). **h**, *Il22* in enteric ILC3 cultured with GFL ($n=17$) or GFL and the inhibitors LY ($n=18$); PD ($n=16$); VIII ($n=15$); SB ($n=15$); and the STAT3 inhibitor (S3I) ($n=8$). **i**, *Il22* locus. The letters a–i in this panel indicate putative STAT3 binding sites and primer location (see Methods). **j**, ChIP analysis of ILC3 stimulated with GFL ($n=10$). Data are representative of 3 independent experiments. Error bars show s.e.m. $*P<0.05$, $**P<0.01$.

associated with ILC identity[1]. Whereas the master ILC transcription factors *Runx1*, *Id2*, *Gata3*, *Rora*, *Rorgt*, *Ahr* and *Stat3* were unperturbed, *Il22* was significantly reduced in *Ret*$^{\Delta}$ ILC3 (Fig. 3c and Extended Data Fig. 6b). Accordingly, activation of ILC3 with all or distinct GFL–GFRα pairs *in trans* efficiently increased *Il22* despite normal expression of other ILC3-related genes (Fig. 3d and Extended Data Fig. 6c). Activation of RET by GFL leads to p38 MAPK/ERK-AKT cascade activation in neurons, whereas phosphorylation of STAT3 shapes *Il22* expression[7,17]. Analysis of *Ret*$^{\Delta}$ ILC3 revealed hypo-phosphorylated ERK1/2, AKT, p38/MAP kinase and STAT3 (Fig. 3e and Extended Data Fig. 6d). Accordingly, GFL-induced RET activation in ILC3 led to rapid ERK1/2, AKT, p38/MAP kinase and STAT3 phosphorylation and increased *Il22* transcription (Fig. 3d, f and Extended Data Fig. 6e, f). Accordingly, inhibition of ERK, AKT or p38/MAP kinase upon GFL activation led to impaired STAT3 activation and *Il22* expression (Fig. 3g, h). Finally, inhibition of STAT3 upon GFL-induced RET activation led to decreased *Il22* (Fig. 3h). To examine whether GFL directly regulate *Il22*, we performed chromatin immunoprecipitation (ChIP)[18] (Fig. 3i, j). Stimulation of ILC3 with GFL resulted in increased binding of pSTAT3 in the *Il22* promoter and increased trimethyl-H3K36 at the 3' end of *Il22*, indicating active *Il22*-transcribed regions[19] (Fig. 3d, j). Thus, cell-autonomous RET signals control ILC3 function and gut defence by direct regulation of *Il22* downstream of STAT3 activation.

Propensity towards inflammation and dysregulation of intestinal homeostasis have been associated with dysbiosis[20,21]. When compared to their wild-type littermates, *Ret*$^{\Delta}$ mice have altered microbial communities as evidenced by quantitative analysis, weighted UniFrac analysis and significantly altered levels of *Sutterella*, unclassified *Clostridiales* and *Bacteroides* (Fig. 4a and Extended Data Fig. 7). Discrete microbial communities may have transmissible colitogenic potential[20,21]. Nevertheless, germ-free mice colonized with the microbiota of *Ret*$^{\Delta}$ or their control littermates revealed similar susceptibility to DSS-induced colitis and identical innate IL-22 production (Fig. 4b–d). In agreement, co-housed *Ret*$^{\Delta}$ and wild-type littermates had different propensity towards intestinal inflammation (Fig. 2c, d). Together, these data indicate that dysbiosis *per se* is insufficient to cause altered innate IL-22 and susceptibility to gut inflammation as observed in *Ret*$^{\Delta}$ mice (Fig. 2c–f). Thus, we hypothesised that GFL-producing cells integrate commensal and environmental signals to control innate IL-22. Accordingly, antibiotic treatment of *Ret*$^{\Delta}$ and their wild-type littermate controls resulted in similar ILC3-derived IL-22 (ref. 22) (Fig. 4e).

Neurotrophic factors of the GDNF family were shown to be produced by enteric glial cells, which are neuron-satellites expressing the glial fibrillary acidic protein (GFAP)[7,23]. Notably, double reporter mice for ILC3 (*Ret*^{GFP}) and glial cells (*Gfap*-Cre*Rosa26*^{RFP}) revealed that stellate-shaped projections of glial cells are adjacent (4.35 ± 1.42 μm) to RORγt^{+} ILC3 within cryptopatches (Fig. 4f and Extended Data Fig. 8a). These data suggest the existence of paracrine glial–ILC3 crosstalk orchestrated by neurotrophic factors. Accordingly, lamina propria glial cells were the main producers of GFL (Extended Data Fig. 8b). Recent studies have shown that glial cells express pattern recognition receptors, notably Toll-like receptors (TLRs)[24,25]. Activation of neurosphere-derived glial cells revealed they specifically respond to TLR2, TLR4, and the alarmins IL-1β and IL-33, which efficiently controlled GFL expression and induced robust innate *Il22* in a MYD88-dependent manner (Fig. 4g–i and Extended Data Fig. 8c–g). To formally demonstrate the physiological importance of MYD88-dependent glial cell sensing on innate IL-22 production, we deleted *Myd88* in GFAP-expressing glial cells by breeding *Gfap*-Cre with *Myd88*$^{fl/fl}$ mice[26,27]. Remarkably, glial-intrinsic deletion of *Myd88* resulted in decreased intestinal GFL, increased gut inflammation, impaired ILC3-derived IL-22, and increased weight loss (Fig. 4j–m; Extended Data Fig. 9a–d). In agreement, *Gfap*-Cre*Myd88*$^{\Delta}$ mice had increased susceptible to *C. rodentium* infection (Extended Data Fig. 9e–h). Thus, mucosal glial cells orchestrate innate IL-22 via neurotrophic factors,

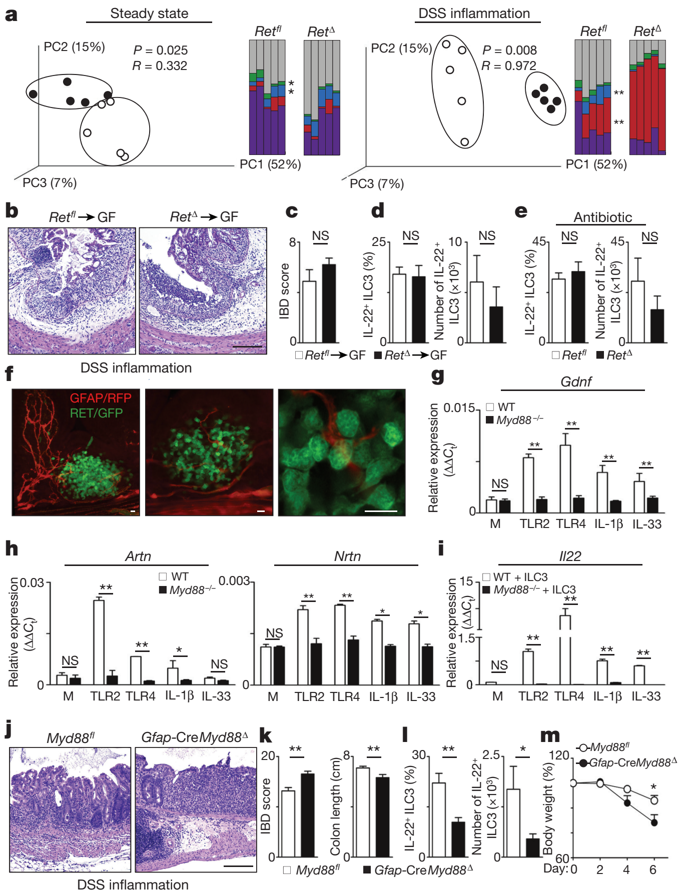

Figure 4 | Glial cells set GFL expression and innate IL-22 via MYD88-dependent sensing of the microenvironment. a, Weighted Unifrac PCoA analysis and genus-level comparisons from co-housed *Ret*^{fl} (white circles) and *Ret*$^{\Delta}$ (black circles) littermates ($n = 5$). Purple, unclassified *S24-7*; red, *Bacteroides*; green, *Sutterella*; blue, unclassified *Clostridiales*; grey, other. **b–d**, DSS treatment of germ-free (GF) mice ($n = 5$) colonized with microbiota from *Ret*^{fl} or *Ret*$^{\Delta}$ mice. **b**, Histopathology. **c**, Inflammation score. **d**, Innate IL-22. **e**, Innate IL-22 after antibiotic treatment ($n = 8$). **f**, *Ret*^{GFP}*Gfap*-Cre*Rosa26*^{RFP} mice. Green, RET/GFP; red, GFAP/RFP. **g**, **h**, Glial cell activation with TLR2, TLR4, IL-1β receptor and IL-33 receptor ligands ($n = 6$). **i**, TLR ligands, IL-1β and IL-33 activation of co-cultured ILC3 with wild-type (white bars) or *Myd88*$^{-/-}$ glial cells (black bars) ($n = 6$). **j–m**, DSS treatment of *Gfap*-Cre*Myd88*$^{\Delta}$ mice ($n = 12$). **j**, Histopathology. **k**, Inflammation score and colon length. **l**, Innate IL-22. **m**, Body weight. Scale bars, 200 μm (**b**, **j**); 10 μm (**f**). Data are representative of 3–4 independent experiments. Error bars show s.e.m. $^{*}P < 0.05$, $^{**}P < 0.01$.

downstream of MYD88-dependent sensing of commensal products and alarmins.

Defining the mechanisms by which ILC3 integrate environmental cues is critical to understanding mucosal homeostasis. Our work sheds light on the relationships between ILC3 and their microenvironment, notably through decoding a novel glial–ILC3–epithelial cell unit orchestrated by neurotrophic factors (Extended Data Fig. 10). Glial-derived neurotrophic factors operate in an ILC3-intrinsic manner by activating the tyrosine kinase RET, which directly regulates innate IL-22 downstream of p38 MAPK/ERK-AKT and STAT3 phosphorylation (Extended Data Fig. 10). Future studies will further elucidate the mechanisms inducing RET expression in ILC3.

Our data demonstrate that, in addition to their well-established capacity to integrate dendritic-cell-derived cytokines[1], ILC3 perceive distinct multi-tissue regulatory signals leading to STAT3 activity and IL-22 expression, notably by integration of glial-cell-derived neuroregulators. Thus, rather than providing hard-wired signals for

ILC3-immunity, we propose that RET signalling induces fine-tuned innate IL-22 production that leads to efficient gut homeostasis and defence.

Previous studies demonstrated that neurons may indirectly shape fetal lymphoid tissue inducer cell aggregation via regulation of mesenchymal cells and that ablation of glial cells leads to gut inflammation[28,29]; here we reveal that glial cells are central hubs of neuronal and innate immune regulation. Notably, neurotrophic factors are the molecular link between glial cell sensing, innate IL-22 and intestinal epithelial defence. Thus, it is tempting to speculate that glial–immune cell units might be also critical to the homeostasis of other barriers, notably in the skin, lung and brain[30]. From an evolutionary perspective, coordination of innate immunity and neuronal function may ensure efficient mucosal homeostasis and a co-regulated neuro-immune response to various environmental challenges, including xenobiotics, intestinal infection, dietary aggressions and cancer.

Online Content Methods, along with any additional Extended Data display items and Source Data, are available in the online version of the paper; references unique to these sections appear only in the online paper.

Received 26 November 2015; accepted 13 June 2016.
Published online 13 July 2016.

1. Artis, D. & Spits, H. The biology of innate lymphoid cells. *Nature* **517,** 293–301 (2015).
2. van de Pavert, S. A. *et al.* Maternal retinoids control type 3 innate lymphoid cells and set the offspring immunity. *Nature* **508,** 123–127 (2014).
3. Spencer, S. P. *et al.* Adaptation of innate lymphoid cells to a micronutrient deficiency promotes type 2 barrier immunity. *Science* **343,** 432–437 (2014).
4. Kiss, E. A. *et al.* Natural aryl hydrocarbon receptor ligands control organogenesis of intestinal lymphoid follicles. *Science* **334,** 1561–1565 (2011).
5. Lee, J. S. *et al.* AHR drives the development of gut ILC22 cells and postnatal lymphoid tissues via pathways dependent on and independent of Notch. *Nat. Immunol.* **13,** 144–151 (2011).
6. Qiu, J. *et al.* The aryl hydrocarbon receptor regulates gut immunity through modulation of innate lymphoid cells. *Immunity* **36,** 92–104 (2012).
7. Mulligan, L. M. RET revisited: expanding the oncogenic portfolio. *Nat. Rev. Cancer* **14,** 173–186 (2014).
8. Fonseca-Pereira, D. *et al.* The neurotrophic factor receptor RET drives haematopoietic stem cell survival and function. *Nature* **514,** 98–101 (2014).
9. Veiga-Fernandes, H. *et al.* Tyrosine kinase receptor RET is a key regulator of Peyer's patch organogenesis. *Nature* **446,** 547–551 (2007).
10. Patel, A. *et al.* Differential RET signaling pathways drive development of the enteric lymphoid and nervous systems. *Sci. Signal.* **5,** ra55 (2012).
11. Almeida, A. R. *et al.* The neurotrophic factor receptor RET regulates IL-10 production by in vitro polarised T helper 2 cells. *Eur. J. Immunol.* **44,** 3605–3613 (2014).
12. Robinette, M. L. *et al.* Transcriptional programs define molecular characteristics of innate lymphoid cell classes and subsets. *Nat. Immunol.* **16,** 306–317 (2015).
13. Hoshi, M., Batourina, E., Mendelsohn, C. & Jain, S. Novel mechanisms of early upper and lower urinary tract patterning regulated by RetY1015 docking tyrosine in mice. *Development* **139,** 2405–2415 (2012).
14. Smith-Hicks, C. L., Sizer, K. C., Powers, J. F., Tischler, A. S. & Costantini, F. C-cell hyperplasia, pheochromocytoma and sympathoadrenal malformation in a mouse model of multiple endocrine neoplasia type 2B. *EMBO J.* **19,** 612–622 (2000).
15. Sawa, S. *et al.* Lineage relationship analysis of RORγt$^+$ innate lymphoid cells. *Science* **330,** 665–669 (2010).
16. Almeida, A. R. *et al.* RET/GFRα signals are dispensable for thymic T cell development *in vivo*. *PLoS One* **7,** e52949 (2012).
17. Rutz, S., Wang, X. & Ouyang, W. The IL-20 subfamily of cytokines--from host defence to tissue homeostasis. *Nat. Rev. Immunol.* **14,** 783–795 (2014).
18. Xu, W. *et al.* NFIL3 orchestrates the emergence of common helper innate lymphoid cell precursors. *Cell Reports* **10,** 2043–2054 (2015).
19. Wen, H. *et al.* ZMYND11 links histone H3.3K36me3 to transcription elongation and tumour suppression. *Nature* **508,** 263–268 (2014).
20. Garrett, W. S. *et al.* *Enterobacteriaceae* act in concert with the gut microbiota to induce spontaneous and maternally transmitted colitis. *Cell Host Microbe* **8,** 292–300 (2010).
21. Elinav, E. *et al.* NLRP6 inflammasome regulates colonic microbial ecology and risk for colitis. *Cell* **145,** 745–757 (2011).
22. Rakoff-Nahoum, S., Paglino, J., Eslami-Varzaneh, F., Edberg, S. & Medzhitov, R. Recognition of commensal microflora by toll-like receptors is required for intestinal homeostasis. *Cell* **118,** 229–241 (2004).
23. Neunlist, M. *et al.* The digestive neuronal-glial-epithelial unit: a new actor in gut health and disease. *Nat. Rev. Gastroenterol. Hepatol.* **10,** 90–100 (2013).
24. Brun, P. *et al.* Toll-like receptor 2 regulates intestinal inflammation by controlling integrity of the enteric nervous system. *Gastroenterology* **145,** 1323–1333 (2013).
25. Kabouridis, P. S. *et al.* Microbiota controls the homeostasis of glial cells in the gut lamina propria. *Neuron* **85,** 289–295 (2015).
26. Zhuo, L. *et al.* hGFAP-cre transgenic mice for manipulation of glial and neuronal function in vivo. *Genesis* **31,** 85–94 (2001).
27. Hou, B., Reizis, B. & DeFranco, A. L. Toll-like receptors activate innate and adaptive immunity by using dendritic cell-intrinsic and -extrinsic mechanisms. *Immunity* **29,** 272–282 (2008).
28. van de Pavert, S. A. *et al.* Chemokine CXCL13 is essential for lymph node initiation and is induced by retinoic acid and neuronal stimulation. *Nat. Immunol.* **10,** 1193–1199 (2009).
29. Bush, T. G. *et al.* Fulminant jejuno-ileitis following ablation of enteric glia in adult transgenic mice. *Cell* **93,** 189–201 (1998).
30. Veiga-Fernandes, H. & Mucida, D. Neuro-Immune Interactions at Barrier Surfaces. *Cell* **165,** 801–811 (2016).

Acknowledgements We thank the Histology, Flow Cytometry, Bioimaging and Vivarium services at IMM; Sanjay Jain for providing *Ret*^{GFP} mice. Genentech for providing anti-IL-22 antibody. S.I. was supported by MEC, Spain and FCT, Portugal. B.G.-C. by FP7 (289720), EU. H.V.-F. by EMBO (1648); ERC (647274), EU; Kenneth Rainin Foundation, US; Crohn's and Colitis Foundation of America, US; and FCT, Portugal. G.E. by Institut Pasteur and ANR, France. E.A.G. by NIH NIAMS R01 AR060873. A.M.M. by NIH NIAMS T32 AR007465 and Morris Animal Foundation (D14CA-404).

Author Contributions S.I. and B.G.-C. designed, performed and analysed the experiments in Figs 1–4 and Extended Data Figs 1–9. T.C. analysed the experiments in Figs 2c, d, g, h, k, l, 4j, k, and Extended Data Figs 3e and 4e. H.R. performed and analysed the experiments in Figs 2f, j, n, 4a, m, Extended Data Figs 5a–c, e–j, 7a and 9f–h. L.A. contributed to experiments in Fig. 3a, b and Extended Data Fig. 6a. D.M.L., W.J.P., A.M.M., C.B.M. and E.A.G. performed and analysed the experiments in Fig. 4a and Extended Data Fig. 7b, c. R.M. and G.E. designed, performed and analysed the experiments in Fig. 4b–d. H.V.-F. supervised the work, planned the experiments and wrote the manuscript.

Author Information Reprints and permissions information is available at www.nature.com/reprints. The authors declare no competing financial interests. Readers are welcome to comment on the online version of the paper. Correspondence and requests for materials should be addressed to H.V.-F. (jhfernandes@medicina.ulisboa.pt or henrique.veigafernandes@research.fchampalimaud.org).

METHODS

Data reporting. The experiments were not randomized. The investigators were not blinded to allocation during experiments and outcome assessment, unless stated otherwise. Power analysis was used to estimate sample size.

Mice. C57BL/6J mice were purchased from Charles River. *Ret*^{GFP} (ref. 13), *Rag1*$^{-/-}$$\gamma c^{-/-}$ (refs 31, 32), *Ret*^{MEN2B} (ref. 14), *Rosa26*^{YFP} (ref. 33), *Rosa26*^{RFP} (ref. 34), *Ret*$^{fl/fl}$ (ref. 16), *Rorgt*-Cre[15], *Il1b*$^{-/-}$ (ref. 35) and *Myd88*$^{-/-}$ (ref. 36) were in a full C57BL/6J background. *Gfap*-Cre[26] bred to *Myd88*$^{fl/fl}$ (ref. 27) were in F8–F9 to a C57Bl/6J background. All lines were bred and maintained at IMM Lisboa animal facility. Mice were systematically compared with co-housed littermate controls. Both males and females were used in this study. Randomization and blinding were not used unless stated otherwise. All animal experiments were approved by national and institutional ethical committees, respectively, Direção Geral de Veterinária and iMM Lisboa ethical committee. Germ-free mice were housed at Instituto Gulbenkian de Ciência, Portugal, and Institut Pasteur, France, in accordance to institutional guidelines for animal care. Power analysis was performed to estimate the number of experimental mice.

Generation of fetal liver chimeras. For reconstitution experiments, 5×10^6 fetal liver cells were isolated from E14.5 *Ret*$^{WT/GFP}$ or *Ret*$^{GFP/GFP}$ mice and injected intravenously into non-lethally irradiated (200 rad) alymphoid *Rag1*$^{-/-}$$\gamma c^{-/-}$ hosts. Mice were analysed 8 weeks after transplantation.

DSS-induced colitis. Dextran sodium sulfate (DSS) (molecular mass 36,000–50,000 Da; MP Biomedicals) was added into drinking water 3% (w/v) for 5 days followed by 2 days of regular water. Mice were analysed at day 7. Body weight, presence of blood and stool consistency was assessed daily.

***Citrobacter rodentium* infection.** Infection with *Citrobacter rodentium* ICC180 (derived from DBS100 strain)[37] was performed by gavage inoculation of 10^9 colony-forming units[37,38]. Acquisition and quantification of luciferase signal was performed in an IVIS system (Caliper Life Sciences). Throughout infection, weight loss, diarrhoea and bloody stools were monitored daily.

Antibiotic treatment. Pregnant females or newborn mice were treated with streptomycin 5 g l^{-1}, ampicillin 1 g l^{-1} and colistin 1 g l^{-1} (Sigma-Aldrich) into drinking water with 3% sucrose. Control mice were given 3% sucrose in drinking water as previously described[22].

Microscopy. Intestines from *Ret*^{GFP} and *Ret*^{GFP} chimaeras were imaged in a Zeiss Lumar V12 fluorescence stereo microscope with a NeoLumar S 0.8× objective using the GFP filter. Whole-mount analysis was performed as previously described[2,9]. Briefly, adult intestines were flushed with cold PBS (Gibco) and opened longitudinally. Mucus and epithelium was removed and intestines were fixed in 4% PFA (Sigma-Aldrich) at room temperature for 10 mins and incubated in blocking/permeabilizing buffer solution (PBS containing 2% BSA, 2% goat serum, 0.6% Triton X-100). To visualise three-dimensional structures of the small intestine, samples were cleared with benzyl alcohol-benzyl benzoate (Sigma-Aldrich) before dehydration in methanol[2,9]. For analysis of thick gut sections, intestines were fixed with 4% PFA at 4 °C overnight and were then included in 4% low-melting temperature agarose (Invitrogen). Sections of 100 μm were obtained with a Leica VT1200/VT1200 S vibratome and embedded in Mowiol (Calbiochem)[2]. Slides or whole-mount samples were incubated overnight or for 1–2 days respectively at 4 °C using the following antibodies: rat monoclonal anti-B220 (RA3-6B2) (eBioscience), mouse monoclonal anti-RORγt (Q31-378) (BD Pharmigen), mouse monoclonal anti-GFAP (GA-5) (Sigma-Aldrich), mouse monoclonal anti-GFAP Cy3 (GA-5) (Abcam), anti-GDNF antibody (Abcam), DAPI (4',6-Diamidino-2-Phenylindole, Dihydrochloride) (Invitrogen). A647 goat anti-rat, A568 goat anti-rat, A647 goat anti-mouse, A488 rabbit anti-GFP, and A488 goat anti-rabbit secondary antibodies were purchased from Invitrogen. Neurospheres and cultured glial cells were fixed in PFA 4% for 10 minutes at room temperature and permeabilized in PBS-Triton 0.1% within 30 seconds. After several washing steps with PBS, cells were incubated with antibodies for 3 h at room temperature and then mounted in Mowiol[39]. Samples were acquired on a Zeiss LSM710 confocal microscope using EC Plan-Neofluar 10×/0.30 M27, Plan Apochromat 20×/0.8 M27 and EC Plan-Neofluar 40×/1.30 objectives. Three-dimensional reconstruction of images was achieved using Imaris software and snapshot pictures were obtained from the three-dimensional images. For analysis of confocal images, cells were counted using in-house software, written in MATLAB (Mathworks, Natick, MA). Briefly, single-cell ILC3 nuclei were identified by RORγt by thresholding and particle analysis. Regions of interest (ROIs) (Extended Data Fig.1i; bottom panels) were defined from each nucleus for analysis in the GFP channel, where staining was considered positive if a minimum number of pixels (usually 20) were above a given threshold. The software allows for batch processing of multiple images and generates individual report images for user verification of cell-counting results and co-expression analysis (https://imm.medicina.ulisboa.pt/en/servicos-e-recursos/technical-facilities/bioimaging).

Histopathology analysis. Colon samples were fixed in 10% neutral buffered formalin. The colon was prepared in multiple cross-sections or 'swiss roll' technique[40], routine-processed for paraffin embedding and 3–4μm sections were stained with haematoxylin and eosin. Enteric lesions were scored by a pathologist blinded to experimental groups, according to previously published criteria[41–43]. Briefly, lesions were individually scored (0–4 increasing severity) for the following criteria: 1, mucosal loss; 2, mucosal epithelial hyperplasia; 3, degree of inflammation; 4, extent of the section affected in any manner; and 5, extent of the section affected in the most severe manner as previously described[43]. Final scores were derived by summing the individual lesion and the extent scores. The internal diameter of the crypts was measured in at least five fields (10× magnification), corresponding to the hotspots in which the most severe changes in crypt architecture were seen. Measurements were performed in an average of 35 crypts per mouse, from proximal to distal colon. Intestinal villus height was measured in the jejunum. Measurements were performed in slides scanned using a Hamamatsu Nanozoomer SQ digital slide scanner running NDP Scan software.

Enteric glial cell isolation. Enteric glial cells isolation was adapted from previously described protocols[44,45]. Briefly, the muscularis layer was separated from the submucosa with surgical forceps under a dissection microscope (SteREO Lumar. V12, Zeiss). The lamina propria was scraped mechanically from the underlying submucosa using 1.5-mm cover-slips (Thermo Scientific). Isolated tissues were collected and digested with Liberase TM (7,5 μg ml^{-1}; Roche) and DNase I (0.1 mg ml^{-1}; Roche) in RPMI supplemented with 1% HEPES, sodium pyruvate, glutamine, streptomycin and penicillin and 0.1% β-mercaptoethanol (Gibco) for approximately 40 min at 37 °C. Single-cell suspensions were passed through a 100-μm cell strainer (BD Biosciences) to eliminate clumps and debris.

Flow cytometry and cell sorting. Lamina propria cells were isolated as previously described[46]. Briefly, intestines were digested with collagenase D (0.5 mg ml^{-1}; Roche) and DNase I (0.1 mg ml^{-1}; Roche) in RPMI supplemented with 10% FBS, 1% HEPES, sodium pyruvate, glutamine, streptomycin and penicillin and 0.1% β-mercaptoethanol (Gibco) for approximately 30 min at 37 °C under gentle agitation. For cytokine analysis, cell suspensions were incubated 4 h in PMA/ionomycin (Sigma-Aldrich) and brefeldin A (eBioscience) at 37 °C. Intracellular staining was performed using IC fixation/permeabilization kit (eBioscience). Cells were stained using PBS, 1% FBS, 1% HEPES and 0.6% EDTA (Gibco). Flow cytometry analysis and cell sorting was performed using FORTESSA and FACSAria flow cytometers (BD Biosciences). Data analysis was performed using FlowJo software (Tristar). Sorted populations were >95% pure. Cell suspensions were stained with anti-CD45 (30-F11), anti-TER119 (TER-119), TCRβ (H57-597), anti-CD3ε (eBio500A2), anti-CD19 (eBio1D3), anti-NK1.1 (PK136), anti-CD11c (N418), anti-Gr1 (RB6-8C5), anti-CD11b (Mi/70), anti-CCR6 (29-2L17), anti-CD127 (IL-7Rα; A7R34), anti-Thy1.2 (53-2.1), anti-CD49b (DX5), anti-TCRδ (GL3), anti-NKp46 (29A1.4), anti-IL-17 (eBio17B7), anti-IL-22 (1H8PWSR), rat IgG1 isotype control (eBRG1) antibodies, 7AAD viability dye, anti-mouse CD16/CD32 (Fc block), anti-RORγt (AFKJS-9); rat IgG2a$_\kappa$ isotype control (eBR2a) and streptavidin fluorochrome conjugates all from eBioscience; anti-CD4 (GK1.5), anti-CD31 (390), anti-CD8α (53-6.7), anti-CD24 (M1/69), anti-Epcam (G8.8) antibodies were purchased from Biolegend. Anti-RET (IC718A) antibody was purchased from R&D Systems. LIVE/DEAD Fixable Aqua Dead Cell Stain Kit was purchased from Invitrogen. Cell populations were defined as: ILC3 - CD45$^+$Lin$^-$Thy1.2^{hi}IL7Rα$^+$RORγt$^+$. For ILC3 subsets, additional markers were employed: LTi - CCR6$^+$Nkp46$^-$; ILC3 NCR$^-$ - CCR6$^-$Nkp46$^-$; ILC3 NCR$^+$ - CCR6$^-$Nkp46$^+$. Lineage was composed from CD3ε, CD8α, TCRβ, TCRγδ, CD19, Gr1, CD11c and TER119. Glial cells - CD45$^-$CD31$^-$TER119$^-$CD49b$^+$ (ref. 47); T cells - CD45$^+$CD3ε$^+$; γδ T cells - CD45$^+$CD3ε$^+$γδTCR$^+$; B cells - CD45$^+$CD19$^+$B220$^+$; macrophages - CD45$^+$CD11b$^+$F4/80$^+$; dendritic cells - CD45$^+$CD19$^-$CD3ε$^-$MHCII$^+$CD11c$^+$; enteric neurons - CD45$^-$RET/GFP$^+$ (ref. 13); epithelial cells - CD45$^-$CD24$^+$Epcam$^+$.

Quantitative RT–PCR. Total RNA was extracted using RNeasy micro kit (Qiagen) or Trizol (Invitrogen) according to the manufacturer's protocol. RNA concentration was determined using Nanodrop Spectrophotometer (Nanodrop Technologies). Quantitative real-time reverse transcription (RT)–PCR was performed as previously described[2,8,9]. *Hprt* and *Gapdh* were used as housekeeping genes. For TaqMan assays (Applied Biosystems), RNA was retro-transcribed using a High Capacity RNA-to-cDNA Kit (Applied Biosystems), followed by a pre-amplification PCR using TaqMan PreAmp Master Mix (Applied Biosystems). TaqMan Gene Expression Master Mix (Applied Biosystems) was used in real-time PCR. TaqMan Gene Expression Assays (Applied Biosystems) were the following: *Gapdh* Mm99999915_g1; *Hprt* Mm00446968_m1; *Artn* Mm00507845_m1; *Nrtn* Mm03024002_m1; *Gdnf* Mm00599849_m1; *Gfra1 Mm00439086_m1*; *Gfra2 Mm00433584_m1*; *Gfra3 Mm00494589_m1*; *Ret* Mm00436304_m1; *Il22* Mm01226722_g1; *Il17a* Mm00439618_m1; *Il23r* Mm00519943_m1; *Rorgt* Mm01261022_m1; *Il7ra* Mm00434295_m1; *Ahr* Mm00478932_m1; *Stat3* Mm01219775_m1; *Cxcr6* Mm02620517_s1; *Nfkbiz* Mm_00600522_m1; *Reg3a* Mm01181787_m1; *Reg3b* Mm00440616_g1; *Reg3g* Mm00441127_m1;

Defa1 Mm02524428_g1; *Defa29* Mm00655850_m1; *Defa5* Mm00651548_g1; *Defa21* Mm04206099_gH; *Muc1* Mm00449599_m1; *Muc3* Mm01207064_m1; *Muc13* Mm00495397_m1; *Gfap* Mm01253033_m1; *Ascl2* Mm01268891_g; *Tff3* Mm00495590_m1; *Relm-b* Mm00445845_m1; *Pla2g2a* Mm00448160_m1; *Pla2g5* Mm00448162_m1; *Wnt3* Mm00437336_m1; *Ctnnb1* Mm00483039_ m1; *Axin2* Mm00443610_m1; *Dll1b* Mm01279269_m1; *Il18* Mm00434225_m1; *Tnfa* Mm00443260_g1; *Lyz1* Mm00657323_m1; *Lrg5* Mm00438890_m1; *Tbx21* Mm00450960_m1; *Id2* Mm00711781_m1; *Runx1* Mm01213404_m1; *Notch1* Mm00435249_m1; *Notch2* Mm00803077_m1; *Gata3* Mm00484683_m1; *Bcl2* Mm00477631_m1; *Bcl2l1* Mm00437783_m1; *Arntl* Mm00500226_m1; *Glpr2* Mm01329475_m1; *Gja1* Mm01179639_s1; *Ednrb* Mm00432989; *S100b* Mm00485897_m1; *Sox10* Mm00569909_m1. Real-time PCR analysis was performed using ABI Prism 7900HT Sequence Detection System or StepOne Real-Time PCR system (Applied Biosystems).

ILC3 activation and cell signalling. Sorted intestinal ILC3 cells were starved for 3 hours in RPMI at 37 °C in order to ensure ILC3 viability. Ret^{fl} or Ret^{Δ} were analysed directly *ex vivo*. To test ERK, AKT, p38-MAPK (Cell Signaling Technology) and STAT3 (BD Pharmigen) upon GFL stimulation wild-type ILC3 were activated with 500 ng ml^{-1} (each GFL) and co-receptors (recombinant rat (rr) GFR-α1, recombinant mouse (rm) GFR-α2, rrGFR-α3 and rrGNDF from R&D Systems; recombinant human (rh) NRTN and rhARTN from PeproTech) for 10 and 30 min. When referring to the use of 'GFL', we have employed GDNF, NRTN, ARTN and their specific co-receptors in combination. For inhibition experiments cells were incubated 1 h at 37 °C before GFL stimulation, to test ERK, AKT, p38/MAPK and STAT3 phosphorylation, or during overnight stimulation with GFLs, to determine *Il22* expression levels. Inhibitors were purchased from Sigma-Aldrich; p38 MAPK/ERK-AKT, LY294002 (LY); ERK, PD98059 (PD); AKT, AKT Inhibitor VIII (VIII); p38 MAPK, SB 202190 (SB); and pSTAT3, S3I-201 (S3I).

Chromatin immunoprecipitation (ChIP) assay. Enteric ILC3 from adult C57BL/6J mice were isolated by flow cytometry. Cells were starved for 3 h with RPMI supplemented with 1% HEPES, sodium pyruvate, glutamine, streptomycin and penicillin and 0.1% β-mercaptoethanol (Gibco) at 37 °C. Cells were stimulated with GFLs (500 ng ml^{-1} each)[8], lysed, cross-linked and chromosomal DNA–protein complex sonicated to generate DNA fragments ranging from 100–300 base pairs. DNA–protein complexes were immunoprecipitated, using LowCell ChIP kit (Diagenode)[18], with 3 μg of rabbit polyclonal antibody against anti-pSTAT3 (Cell Signalling Technology), rabbit control IgG (Abcam) or H3K36me3 (07-030; Millipore). Immunoprecipitates were uncross-linked and analysed by quantitative PCR using primer pairs (5'–3') flanking putative sites on *Il22*. Vehicle (BSA)-stimulated ILC3s were used as controls. *Il22* primer sequences were previously described[48–50], briefly: (a) forward: 5′-TGCAATCAATCCCAGTATTTTG-3′ and reverse: 5′-CTTGTGCAAGCATAAGTCTCAA-3′; (b) forward: 5′-GAAGTTGGTGG GAAAATGAGTCCGTGA-3′ and reverse: 5′-GCCATGGCTTTGCCGTAG TAGATTCTG-3′; (c) forward: 5′-ACGGGAGATCAAAGGCTGCTCT-3′ and reverse: 5′-GCCAACAAGGTGCTTTTGC-3′; (d) forward: 5′-CTCACC GTGACGTTTTAGGG-3′ and reverse: 5′-GTGAATGATATGACATCAGAC-3′; (e) forward 5′-CGACGAACATGCTCCCCTGATGTTTTT-3′ and reverse: 5′-AAACTCATAGATTTCTGCAGGACAGCC-3′; (f) forward: 5′-AGCTG CATCTCTTTCTCTCCA-3′ and reverse: 5′-TATCCTGAAGGCCAA AATAGGA-3′; (g) forward: 5′-ACGACCAGAACATCCAGAAGA-3′ and reverse: 5′-GCAGAGAAAGAAATCCCCGC-3′; (h) forward: 5′-AGGGGGAC TTGCTTTGCCATTT-3′ and reverse: 5′-AACACCCCTTCTTTCC TCCTCCAT-3′; (i) forward: 5′-CTGCTCCTTCCTGCCTTCTA-3′ and reverse: 5′-CTGAGCCAGGTTTCATGTGA-3′. Primer positions are shown in Fig. 3i relative to the transcription start codon of *Il22*.

Colony-forming units and paracellular permeability. Organs were collected, weighed, and brought into suspension. Bacterial colony-forming units were determined per gram of tissue and total organ. Colony-forming units were determined by serial dilutions on Luria Broth (LB) agar and MacConkey agar (Sigma-Aldrich). Colonies were counted after 2 days of culture at 37 °C. To address intestinal paracellular permeability 16 mg per mouse of Dextran-Fitc (Sigma Aldrich) were administrated by gavage after overnight starvation. Plasma was analysed after 4 hours of Dextran-Fitc administration using a Microplate Reader TECAN Infinity F500.

BrdU administration and Ki-67 labeling. BrdU was administrated by intraperitoneal injection (1.25 mg per mouse). For flow cytometric analysis of epithelial cell proliferation anti-BrdU (Staining Kit for flow Cytometry, eBioscience) and anti-mouse Ki-67 antibody (BioLegend) were used.

Quantitative PCR analysis of bacteria in stool at the phylum level. DNA from faecal pellet samples was isolated with ZR Fecal DNA MicroPrep (Zymo Research). Quantification of bacteria was determined from standard curves established by qPCR. qPCR were performed with Power SYBR Green PCR Master Mix (Applied Biosystems) and different primer sets using a StepOne Plus (Applied Biosystems) thermocycler. Samples were normalized to 16S rDNA and reported according to the $2^{\Delta\Delta Ct}$ method. Primer sequences were: 16S rDNA, forward: 5′-ACTCCTACGGGAGGCAGCAGT-3′ and reverse: 5′-ATTACCGCGGCTGCTGGC-3′; *Firmicutes*, forward: 5′-ACTCCT ACGGGAGGCAGC-3′ and reverse: 5′-GCTTCTTAGTCAGGTACCGTCAT-3′; *Bacteroidetes*, forward: 5′-GGTTCTGAGAGGAGGTCCC-3′ and reverse: 5′-GCTGGCTCCCGTAGGAGT-3′; *Proteobacteria*, forward: 5′-GGTTC TGAGAGGAGGTCCC-3′ and reverse 5′-GCTGGCTCCCGTAGGAGT-3′.

16S rRNA quantification and gene sequencing. Faeces were isolated from co-housed Ret^{fl} or Ret^{Δ} littermates. Sequencing of the 16S *rRNA* gene was performed as previously described[51]. Briefly, barcoded primers were used to amplify the V4 region of the 16S rRNA gene, and the amplicons were sequenced on a MiSeq instrument (Illumina, San Diego, USA) using 150 bp, paired-end chemistry at the University of Pennsylvania Next Generation Sequencing Core. The paired ends were assembled and quality filtered, selecting for reads with a quality score ≥30. Reads with >10 bp homopolymers and reads shorter than 248 bp or longer than 255 bp were removed from the analysis. 16S rRNA sequence data were processed using mothur version 1.25.0 (ref. 52) and QIIME version 1.8 (ref. 53). Chimaeric sequences were removed with ChimeraSlayer[54]. Operational taxonomic units (OTUs) were defined with CD-HIT[55] using 97% sequence similarity as a cut-off. Only OTUs containing ≥2 sequences were retained; OTUs assigned to cyanobacteria or those which were not assigned to any phylum were removed from the analysis. Taxonomy was assigned using the Ribosomal Database Project (RDP) classifier v 2.2 (ref. 56), multiple sequence assignment was performed with PyNAST (v 1.2.2)[57], and FastTree[58] was used to build the phylogeny. Samples were rarified to 22,000 sequences per sample for alpha- and beta-diversity analyses. Taxonomic relative abundances are reported as the median with standard deviation. *P* values were calculated using the Wilcoxon rank-sum test. Statistical tests were conducted in R version 3.2.0. To determine which factors were associated with microbial community composition, statistical tests were performed using the non-parametric analysis of similarities (ANOSIM) with weighted UniFrac distance metrics[59].

Data accession. The sequencing data generated in this study have been submitted to the NCBI Sequence Read Archive under BioProject PRJNA314493 (SRA: http://www.ncbi.nlm.nih.gov/sra/?term=PRJNA314493).

Intestinal organoids. IntestiCult Organoid Growth Medium and Gentle Cell Dissociation Reagent were purchased from StemCell. Intestinal crypts were isolated from C57BL/6J mice according to the manufacturer's instructions and were added to previously thawed, ice-cold Matrigel at a 1:1 ratio and at a final concentration of 5,000–7,000 crypts per ml. 15 μl of this mix was plated per well of a 96-well round-bottom plate. After Matrigel solidification 100 μl of growth medium (100 U ml^{-1} penicillin/streptomycin) was added and replaced every 3 days. Organoids were grown at 37 °C with 5% CO_2 and passaged according to the manufacturer's instructions. Freshly sorted intestinal ILC3 were added to 5–8 days old epithelial organoids after plating for 24 hours with or without anti-mouse IL-22 antibody (R&D Systems).

IL-22 agonist administration *in vivo*. 150 μg of anti-IL-22 antibody (8E11; gift from Genentech) or mouse IgG1 isotype control (MOPC-21; Bio X Cell) was administered by intraperitoneal injection to Ret^{MEN2B} mice every 2 days. Animals were analysed 2 weeks after the first administration.

Neurosphere-derived glial cells. Neurosphere-derived glial cells were obtained as previously described[60]. Briefly, total intestines from E14.5 C57BL/6J and $Myd88^{-/-}$ mice were digested with collagenase D (0.5 mg ml^{-1}; Roche) and DNase I (0.1 mg ml^{-1}; Roche) in DMEM/F-12, GlutaMAX, supplemented with 1% HEPES, streptomycin/penicillin and 0.1% β-mercaptoethanol (Gibco) for approximately 30 min at 37 °C under gentle agitation. Cells were cultured for 1 week in a CO_2 incubator at 37 °C in DMEM/F-12, GlutaMAX, streptomycin and penicillin and 0.1% β-mercaptoethanol (Gibco) supplemented with B27 (Gibco), EGF (Gibco) and FGF2 (Gibco) 20 ng ml^{-1}. After 1 week of culture cells were treated with 0.05% trypsin (Gibco), transferred into PDL (Sigma-Aldrich) coated plates and culture in DMEM supplemented with 10% FBS, 1% HEPES, glutamine, streptomycin and penicillin and 0.1% β-mercaptoethanol (Gibco) until confluence. Glial cells were activated with TLR2 (5 μg ml^{-1}) (Pam3CSK4), TLR3 (100 μg ml^{-1}) (PolyI:C), TLR4 (50 μg ml^{-1}) (LPS), TLR9 (50 μg ml^{-1}) (DsDNA-EC) ligands from Invivogen and IL-1β (10 μg ml^{-1}) (401ML005), IL-18 (50 μg ml^{-1}) (B002-5), IL-33 (0.1 μg ml^{-1}) (3626ML) recombinant proteins from R&D Systems. Cells were also co-cultured with purified ILC3 from wild-type and *Il1b*-deficient mice. IL-22 expression in glial-ILC3 co-cultures upon TLR4 activation was also performed using GDNF (2 μg ml^{-1}) (AB-212–NA), NRTN (2 μg ml^{-1}) (AF-387sp) and ARTN (0.3 μg ml^{-1}) (AF-1085-sp) blocking antibodies. Cells were analysed after 24 hours of co-culture.

Statistics. Results are shown as mean ± s.e.m. Statistical analysis used Microsoft Excel. Variance was analysed using *F*-test. Student's *t*-test was performed on homoscedastic populations, and Student's *t*-test with Welch correction was applied on samples with different variances. Analysis of survival curves was performed using a MAntel–Cox test. Results were considered significant at $*P \leq 0.05$ and $**P \leq 0.01$. Statistical treatment of metagenomics analysis is described in the Methods section '16S rRNA gene sequencing and analysis'.

31. Cao, X. *et al.* Defective lymphoid development in mice lacking expression of the common cytokine receptor γ chain. *Immunity* **2,** 223–238 (1995).
32. Mombaerts, P. *et al.* RAG-1-deficient mice have no mature B and T lymphocytes. *Cell* **68,** 869–877 (1992).
33. Srinivas, S. *et al.* Cre reporter strains produced by targeted insertion of *EYFP* and *ECFP* into the *ROSA26* locus. *BMC Dev. Biol.* **1,** 4 (2001).
34. Madisen, L. *et al.* A robust and high-throughput Cre reporting and characterization system for the whole mouse brain. *Nat. Neurosci.* **13,** 133–140 (2010).
35. Horai, R. *et al.* Production of mice deficient in genes for interleukin (IL)-1α, IL-1β, IL-1α/β, and IL-1 receptor antagonist shows that IL-1β is crucial in turpentine-induced fever development and glucocorticoid secretion. *J. Exp. Med.* **187,** 1463–1475 (1998).
36. Adachi, O. *et al.* Targeted disruption of the MyD88 gene results in loss of IL-1- and IL-18-mediated function. *Immunity* **9,** 143–150 (1998).
37. Wiles, S., Pickard, K. M., Peng, K., MacDonald, T. T. & Frankel, G. In vivo bioluminescence imaging of the murine pathogen *Citrobacter rodentium*. *Infect. Immun.* **74,** 5391–5396 (2006).
38. Collins, J. W. *et al. Citrobacter rodentium*: infection, inflammation and the microbiota. *Nat. Rev. Microbiol.* **12,** 612–623 (2014).
39. Ibiza, S. *et al.* Endothelial nitric oxide synthase regulates T cell receptor signaling at the immunological synapse. *Immunity* **24,** 753–765 (2006).
40. Moolenbeek, C. & Ruitenberg, E. J. The "Swiss roll": a simple technique for histological studies of the rodent intestine. *Lab. Anim.* **15,** 57–59 (1981).
41. Burich, A. *et al.* Helicobacter-induced inflammatory bowel disease in IL-10- and T cell-deficient mice. *Am. J. Physiol. Gastrointest. Liver Physiol.* **281,** G764–G778 (2001).
42. Fort, M. M. *et al.* A synthetic TLR4 antagonist has anti-inflammatory effects in two murine models of inflammatory bowel disease. *J. Immunol.* **174,** 6416–6423 (2005).
43. Seamons, A., Treuting, P. M., Brabb, T. & Maggio-Price, L. Characterization of dextran sodium sulfate-induced inflammation and colonic tumorigenesis in *Smad3*$^{-/-}$ mice with dysregulated TGFβ. *PLoS One* **8,** e79182 (2013).
44. Bogunovic, M. *et al.* Origin of the lamina propria dendritic cell network. *Immunity* **31,** 513–525 (2009).
45. Muller, P. A. *et al.* Crosstalk between muscularis macrophages and enteric neurons regulates gastrointestinal motility. *Cell* **158,** 300–313 (2014).
46. Sanos, S. L. & Diefenbach, A. Isolation of NK cells and NK-like cells from the intestinal lamina propria. *Methods Mol. Biol.* **612,** 505–517 (2010).
47. Joseph, N. M. *et al.* Enteric glia are multipotent in culture but primarily form glia in the adult rodent gut. *J. Clin. Invest.* **121,** 3398–3411 (2011).
48. Escobar, T. M. *et al.* miR-155 activates cytokine gene expression in Th17 cells by regulating the DNA-binding protein Jarid2 to relieve polycomb-mediated repression. *Immunity* **40,** 865–879 (2014).
49. Guo, X. *et al.* Induction of innate lymphoid cell-derived interleukin-22 by the transcription factor STAT3 mediates protection against intestinal infection. *Immunity* **40,** 25–39 (2014).
50. Yeste, A. *et al.* IL-21 induces IL-22 production in CD4^{+} T cells. *Nat. Commun.* **5,** 3753 (2014).
51. Misic, A. M. *et al.* The shared microbiota of humans and companion animals as evaluated from *Staphylococcus* carriage sites. *Microbiome* **3,** 2 (2015).
52. Schloss, P. D. *et al.* Introducing mothur: open-source, platform-independent, community-supported software for describing and comparing microbial communities. *Appl. Environ. Microbiol.* **75,** 7537–7541 (2009).
53. Caporaso, J. G. *et al.* QIIME allows analysis of high-throughput community sequencing data. *Nat. Methods* **7,** 335–336 (2010).
54. Haas, B. J. *et al.* Chimeric 16S rRNA sequence formation and detection in Sanger and 454-pyrosequenced PCR amplicons. *Genome Res.* **21,** 494–504 (2011).
55. Fu, L., Niu, B., Zhu, Z., Wu, S. & Li, W. CD-HIT: accelerated for clustering the next-generation sequencing data. *Bioinformatics* **28,** 3150–3152 (2012).
56. Wang, Q., Garrity, G. M., Tiedje, J. M. & Cole, J. R. Naive Bayesian classifier for rapid assignment of rRNA sequences into the new bacterial taxonomy. *Appl. Environ. Microbiol.* **73,** 5261–5267 (2007).
57. Caporaso, J. G. *et al.* PyNAST: a flexible tool for aligning sequences to a template alignment. *Bioinformatics* **26,** 266–267 (2010).
58. Price, M. N., Dehal, P. S. & Arkin, A. P. FastTree: computing large minimum evolution trees with profiles instead of a distance matrix. *Mol. Biol. Evol.* **26,** 1641–1650 (2009).
59. Lozupone, C., Hamady, M. & Knight, R. UniFrac—an online tool for comparing microbial community diversity in a phylogenetic context. *BMC Bioinformatics* **7,** 371 (2006).
60. Mich, J. K. *et al.* Prospective identification of functionally distinct stem cells and neurosphere-initiating cells in adult mouse forebrain. *eLife* **3,** e02669 (2014).

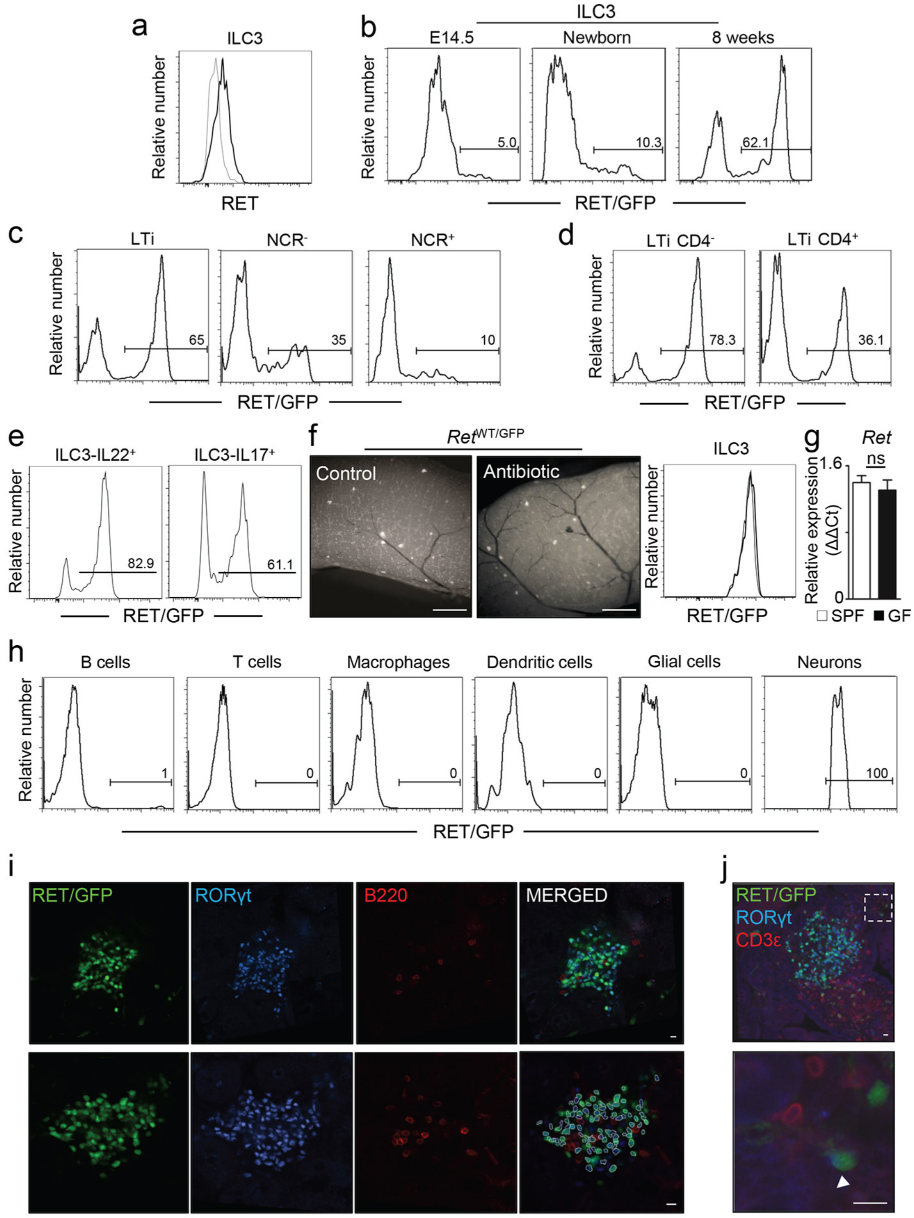

Extended Data Figure 1 | ILC3 selectively express the neurotrophic factor receptor RET. a, Expression of RET protein in gut $CD45^{+}Lin^{-}Thy1.2^{hi}IL7R\alpha^{+}ROR\gamma t^{+}$ ILC3. **b**, Analysis of gut ILC3 from Ret^{GFP} mice. Embryonic day 14.5 (E14.5). **c**, **d**, Analysis of enteric ILC3 subsets from Ret^{GFP} mice. **e**, Analysis of cytokine-producing ILC3 from Ret^{GFP} mice. **f**, Pregnant Ret^{GFP} mice were provided with antibiotic cocktails that were maintained after birth until analysis at 6 weeks of age. Left, RET/GFP (white); right, flow cytometry analysis of RET/GFP expression in ILC3. Thin line, Ab-treated; bold line, specific pathogen free (SPF). **g**, *Ret* expression in enteric ILC3 from germ-free (GF) mice and SPF controls ($n = 4$). **h**, Analysis of lamina propria populations from Ret^{GFP} mice. **i**, Enteric ILC3 clusters. Green, RET/GFP; blue, RORγt; red, B220. Bottom, quantification analysis for RET/GFP and RORγt co-expression (79.97 ± 4.72%). **j**, Rare RET-expressing ILC3 in intestinal villi. Green, RET/GFP; blue, RORγt; red, CD3ε. Scale bars, 10μm. Data are representative of 4 independent experiments. Error bars show s.e.m.

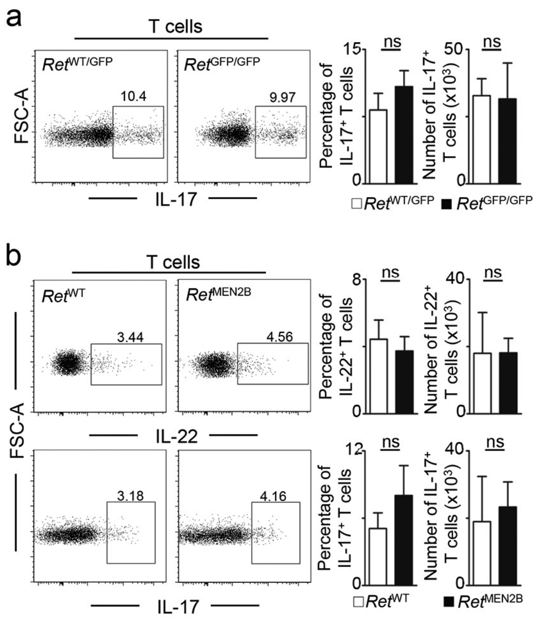

Extended Data Figure 2 | T cell-derived IL-22 and IL-17 in *Ret*^{GFP} chimaeras and *Ret*^{MEN2B} mice. **a**, T-cell-derived IL-17 in *Ret*^{GFP} chimaeras. *Ret*$^{WT/GFP}$, $n = 25$; *Ret*$^{GFP/GFP}$, $n = 22$. **b**, T-cell-derived IL-22 and IL-17 in the intestine of *Ret*^{MEN2B} mice and their wild-type littermate controls ($n = 7$). Data are representative of 4 independent experiments. Error bars show s.e.m.

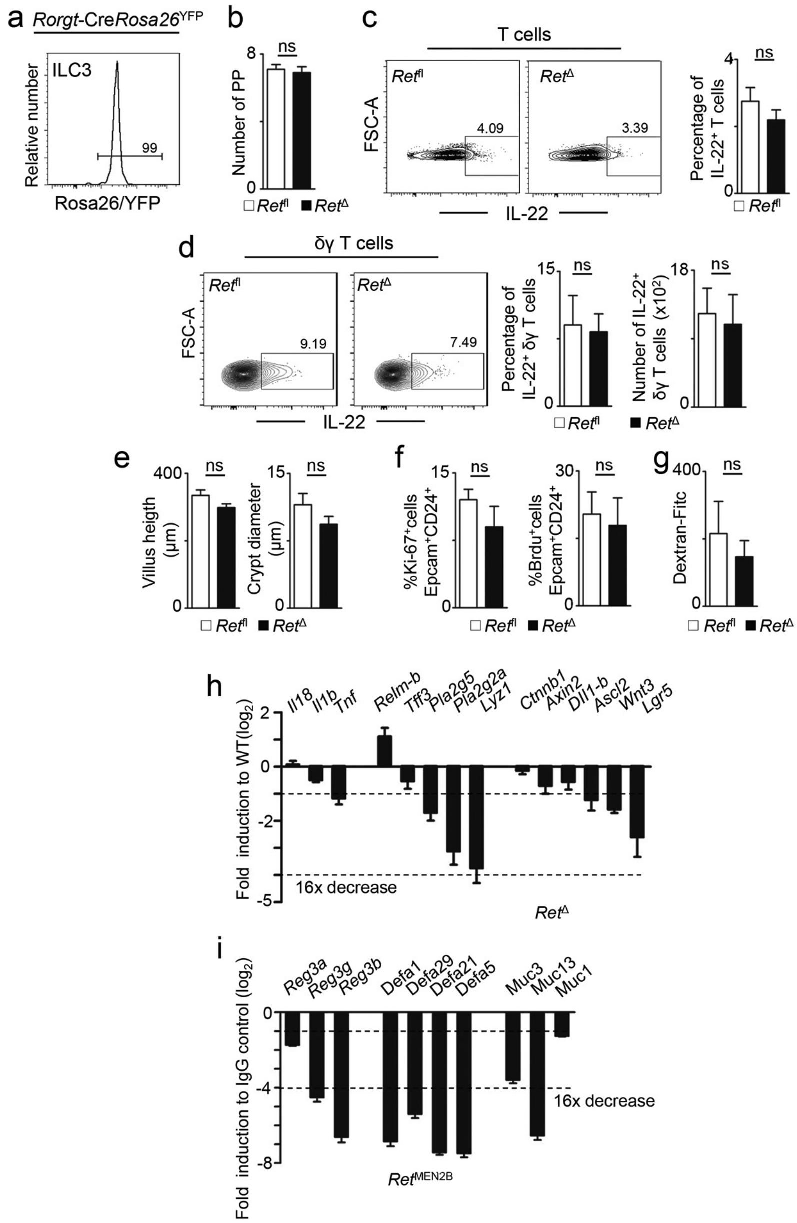

Extended Data Figure 3 | Enteric homeostasis in steady-state *Ret*$^{\Delta}$ mice. **a**, *Rorgt*-Cre mice were bread to *Rosa26*^{YFP} mice. Analysis of Rosa26/YFP expression in gut ILC3 from *Rorgt*-Cre*Rosa26*^{YFP} mice. **b**, Number of Peyer's patches (PP) ($n = 10$). **c**, T-cell-derived IL-22 in *Ret*$^{\Delta}$ mice and their wild-type littermate controls. ($n = 11$). **d**, γδ T-cell-derived IL-22 in *Ret*$^{\Delta}$ mice and their wild-type littermate controls ($n = 4$). **e**, Intestinal villus and crypt morphology ($n = 6$). **f**, Epithelial cell proliferation ($n = 5$). **g**, Intestinal paracellular permeability measured by Dextran-Fitc in the plasma ($n = 5$). **h**, Tissue repair genes in *Ret*$^{\Delta}$ intestinal epithelium in comparison to their wild-type littermate controls ($n = 8$). **i**, Reactivity genes in *Ret*^{MEN2B} mice treated with anti-IL-22 blocking antibodies compared to *Ret*^{MEN2B} intestinal epithelium. *Ret*^{MEN2B}, $n = 4$; *Ret*^{MEN2B} + anti-IL-22, $n = 4$. Data are representative of 3 independent experiments. Error bars show s.e.m.

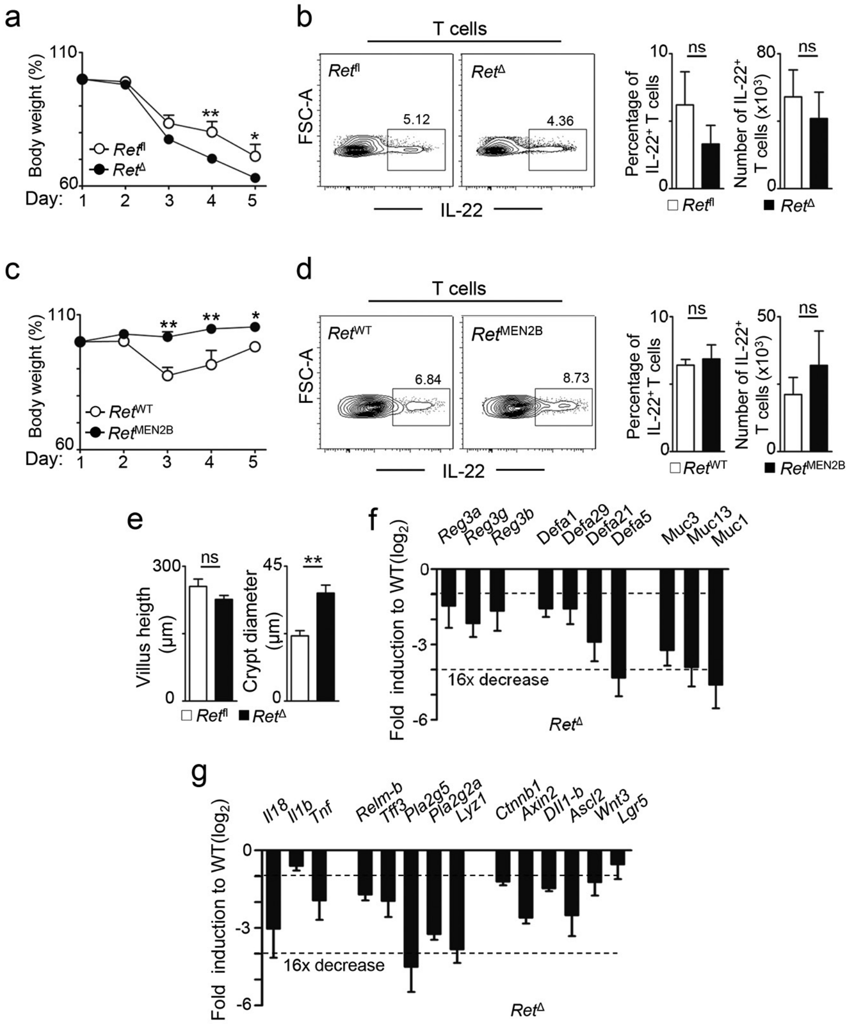

Extended Data Figure 4 | Enteric inflammation in mice with altered RET signals. Mice were treated with DSS in the drinking water. **a**, Weight loss of DSS-treated *Ret*$^{\Delta}$ mice and their littermate controls ($n = 8$). **b**, T-cell-derived IL-22 in *Ret*$^{\Delta}$ mice and their wild-type littermate controls after DSS treatment ($n = 8$). **c**, Weight loss of DSS treated *Ret*$^{\mathrm{MEN2B}}$ mice and their wild-type littermate controls ($n = 8$). **d**, T-cell-derived IL-22 in *Ret*$^{\mathrm{MEN2B}}$ mice and their wild-type littermate controls ($n = 8$). **e**, Intestinal villi and crypt morphology ($n = 6$). **f**, Epithelial reactivity gene expression in DSS treated *Ret*$^{\Delta}$ mice in comparison to their wild-type littermate controls ($n = 8$). **g**, Tissue repair gene expression in DSS treated *Ret*$^{\Delta}$ mice in comparison to their wild-type littermate controls ($n = 4$). Data are representative of 3–4 independent experiments. Error bars show s.e.m. $*P < 0.05$; $**P < 0.01$.

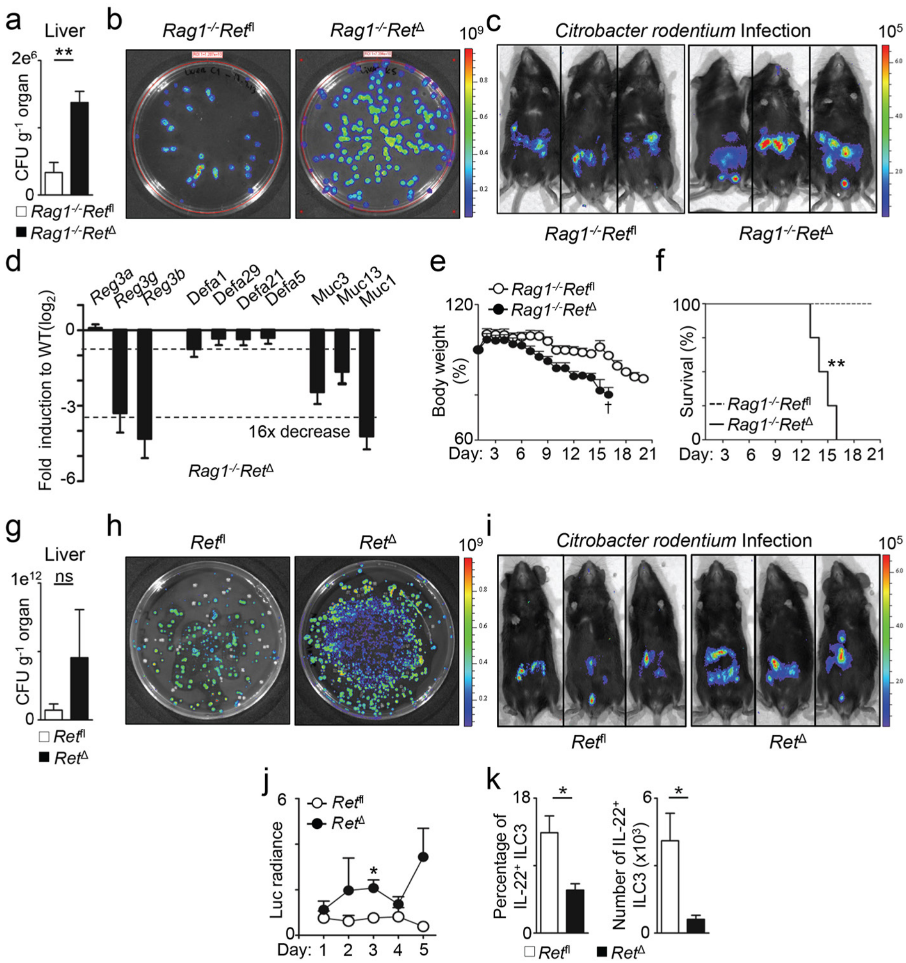

Extended Data Figure 5 | *Citrobacter rodentium* infection in *Ret*$^{\Delta}$ mice. **a**, *C. rodentium* translocation to the liver of *Rag1*$^{-/-}$*Ret*$^{\Delta}$ and their *Rag1*$^{-/-}$*Ret*^{fl} littermate controls at day 6 after infection ($n=15$). **b**, MacConkey plates of liver cell suspensions from *Rag1*$^{-/-}$*Ret*$^{\Delta}$ and their *Rag1*$^{-/-}$*Ret*^{fl} littermate controls at day 6 after *C. rodentium* infection. **c**, Whole-body imaging of *Rag1*$^{-/-}$*Ret*$^{\Delta}$ and their *Rag1*$^{-/-}$*Ret*^{fl} littermate controls at day 6 after luciferase-expressing *C. rodentium* infection. **d**, Epithelial reactivity gene expression in *C. rodentium* infected *Rag1*$^{-/-}$*Ret*$^{\Delta}$ mice (n = 17) and their *Rag1*$^{-/-}$*Ret*^{fl} littermate controls ($n=15$). **e**, Weight loss in *C. rodentium*-infected *Rag1*$^{-/-}$*Ret*$^{\Delta}$ mice and their *Rag1*$^{-/-}$*Ret*^{fl} littermate controls ($n=8$). **f**, Survival curves in *C. rodentium* infected *Rag1*$^{-/-}$*Ret*$^{\Delta}$ mice and their *Rag1*$^{-/-}$*Ret*^{fl} littermate controls ($n=8$). **g**, *C. rodentium* translocation to the liver of *Ret*$^{\Delta}$ and their *Ret*^{fl} littermate controls at day 6 after infection ($n=6$). **h**, MacConkey plates of liver cell suspensions from *Ret*$^{\Delta}$ and their *Ret*^{fl} littermate controls at day 6 after *C. rodentium* infection. **i**, Whole-body imaging of *Ret*$^{\Delta}$ and their *Ret*^{fl} littermate controls at day 6 after luciferase-expressing *C. rodentium* infection. **j**, *C. rodentium* infection burden ($n=8$). **k**, Innate IL-22 in in *C. rodentium* infected *Ret*$^{\Delta}$ mice and their *Ret*^{fl} littermate controls ($n=8$). Data are representative of 3–4 independent experiments. Error bars show s.e.m. ns, not significant. $^{*}P<0.05$; $^{**}P<0.01$.

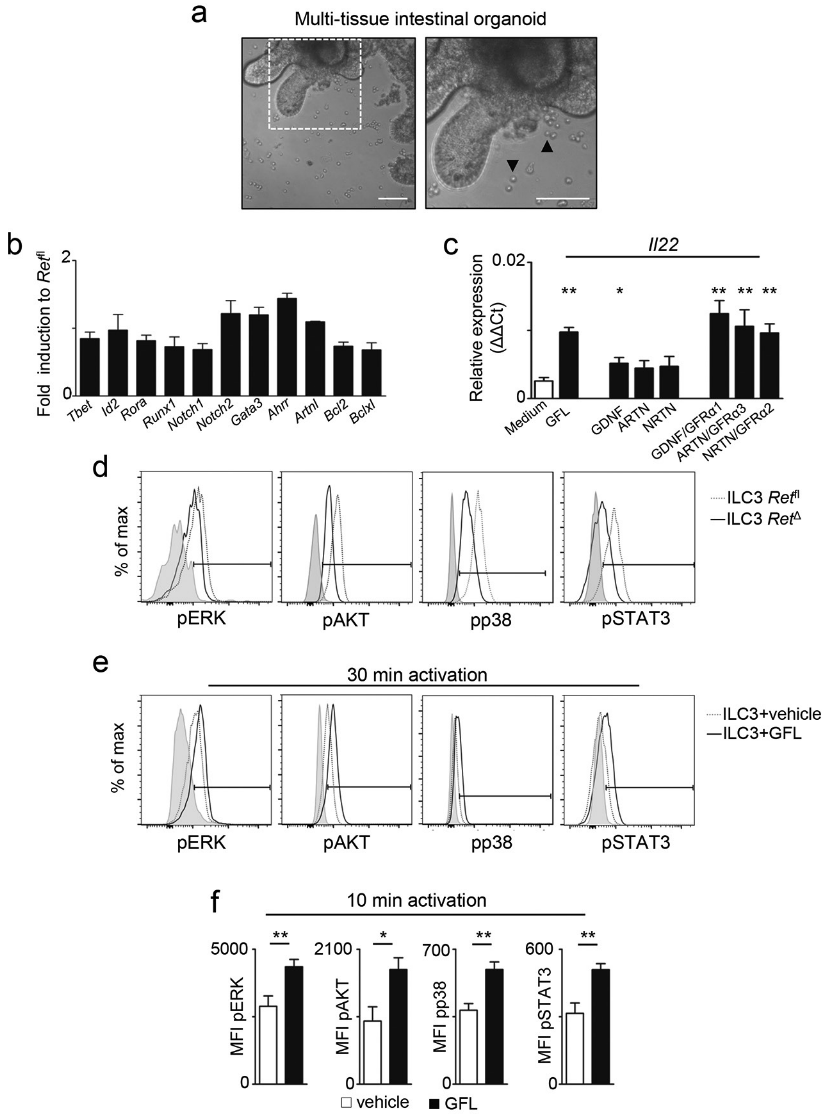

Extended Data Figure 6 | Glial-derived neurotrophic factor family ligand (GFL) signals in ILC3. a, Multi-tissue intestinal organoid system. Scale bar, 20μm. Black arrows, ILC3. **b**, Expression of ILC-related genes in ILC3 from *Ret*$^{\Delta}$ mice in comparison to their littermate controls ($n=4$). **c**, ILC3 activation with all GFL/GFRα pairs (GFL); single GDNF family ligand (GDNF, ARTN or NRTN); or single GFL/GFRα pairs (GDNF/GFRα1, ARTN/GFRα3 or NRTN/GFRα2) compared to vehicle BSA ($n=5$). **d**, ILC3 from *Ret*$^{\Delta}$ mice (open black) and their littermate controls (open dash). Isotype (closed grey). **e**, 30-min activation of ILC3 by GFL (open black) compared to vehicle BSA (open dash). Isotype (closed grey). **f**, 10-min activation of ILC3 by GFL. pERK, $n=8$; pAKT, $n=8$; phosphorylated p38/MAP kinase, $n=8$; pSTAT3, $n=8$. Similar results were obtained in at least 3–4 independent experiments. Error bars show s.e.m. *$P<0.05$; **$P<0.01$.

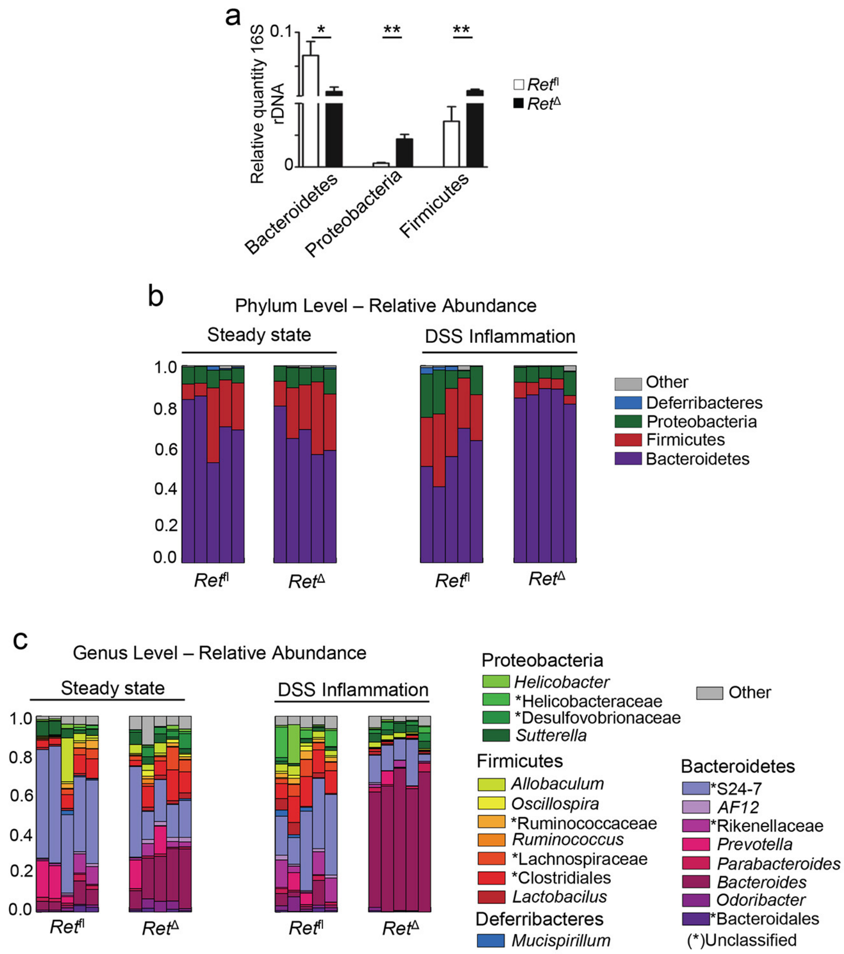

Extended Data Figure 7 | Alterations in the diversity of intestinal commensal bacteria of *Ret*$^{\Delta}$ mice. a, Quantitative PCR analysis at the phylum level in stool bacteria from co-housed *Ret*^{fl} and *Ret*$^{\Delta}$ littermates in steady state ($n = 5$). **b**, Metagenomic phylum level comparisons in stool bacterial from co-housed *Ret*^{fl} and *Ret*$^{\Delta}$ littermates in steady state (left) and after DSS treatment (right) ($n = 5$). **c**, Genus-level comparisons in stool bacteria from co-housed *Ret*^{fl} and *Ret*$^{\Delta}$ littermates in steady state (left) and after DSS treatment (right) ($n = 5$). Error bars show s.e.m. $*P < 0.05$; $**P < 0.01$.

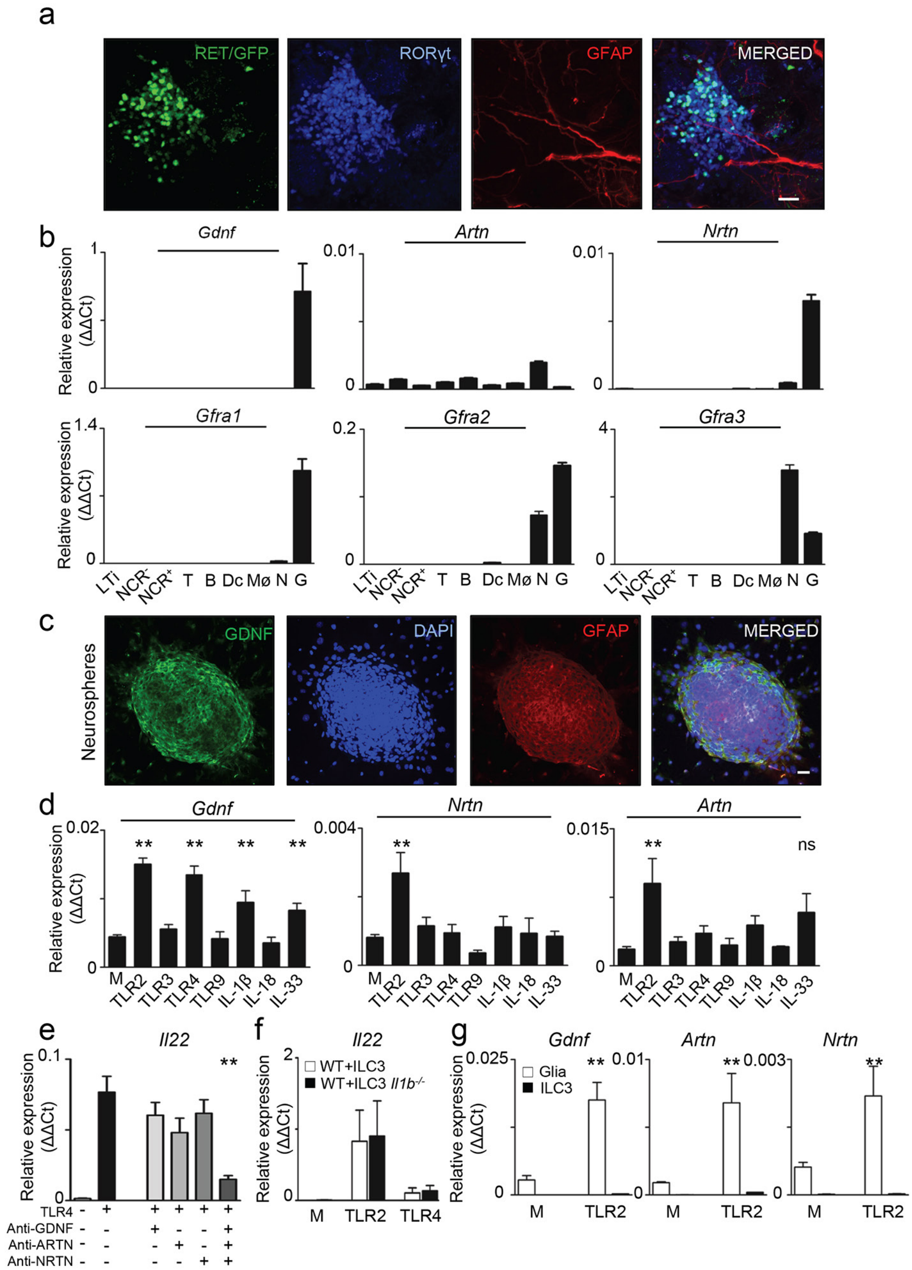

Extended Data Figure 8 | GFL-expressing glial cells anatomically co-localize with ILC3. a, Intestine of *Ret*[GFP] mice. Green, RET/GFP; red, GFAP; blue, RORγt. Similar results were obtained in 3 independent experiments. **b**, Purified lamina propria LTi, NCR$^-$ and NCR$^+$ ILC3 subsets, T cells (T), B cells (B), dendritic cells (Dc), macrophages (Mø), enteric neurons (N) and mucosal glial cells (G). **c**, Neurosphere-derived glial cells. **d**, Activation of neurosphere-derived glial cells with TLR2 (Pam3CSK4), TLR3 (Poli I:C), TLR4 (LPS) and TLR9 (DsDNA-EC) ligands, as well as IL-1β, IL-18 and IL-33 ($n=6$). M, medium. **e**, *Il22* in co-cultures of glial and ILC3 using single or combined GFL antagonists ($n=6$). **f**, *Il22* in co-cultures of ILC3 and glial cells from *Il1b*$^{-/-}$ or their wild-type controls ($n=3$). **g**, *Gdnf, Artn* and *Nrtn* expression in glial cells and ILC3 upon TLR2 stimulation ($n=3$). Scale bar, 30 μm. Similar results were obtained in at least 4 independent experiments.

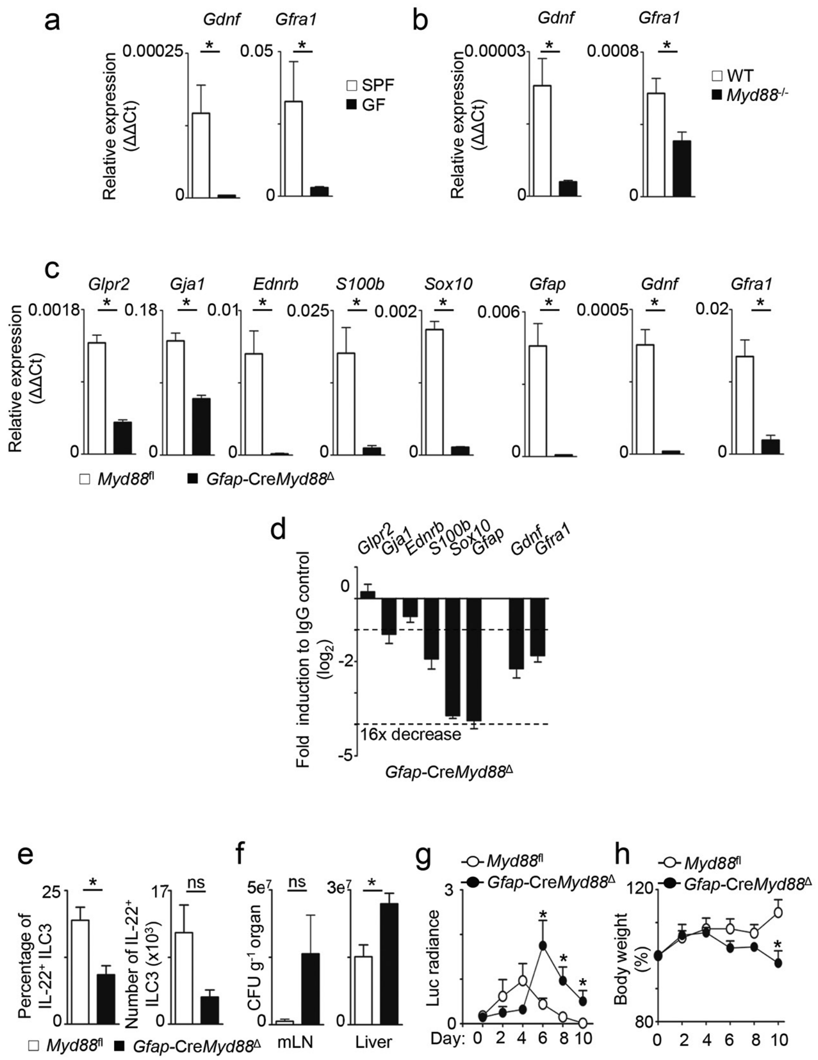

Extended Data Figure 9 | Glial cell sensing via MYD88 signals. **a**–**c**, Intestinal glial cells were purified by flow cytometry. **a**, Germ-free and their respective SPF controls ($n = 3$). **b**, Myd88$^{-/-}$ and their respective wild-type littermate controls ($n = 3$). **c**, *Gfap*-Cre*Myd88*$^{\Delta}$ and their littermate controls (*Myd88*^{fl}) ($n = 3$). **d**, Total lamina propria cells of *Gfap*-Cre*Myd88*$^{\Delta}$ and their littermate controls (*Myd88*^{fl}) ($n = 6$). **e**–**h**, *Citrobacter rodentium* infection of *Gfap*-Cre*Myd88*$^{\Delta}$ mice and their littermate controls (*Myd88*^{fl}) ($n = 6$). **e**, Innate IL-22. **f**, *Citrobacter rodentium* translocation. **g**, Infection burden. **h**, Weight loss. Data are representative of 3 independent experiments. Error bars show s.e.m. $^{*}P < 0.05$; $^{**}P < 0.01$.

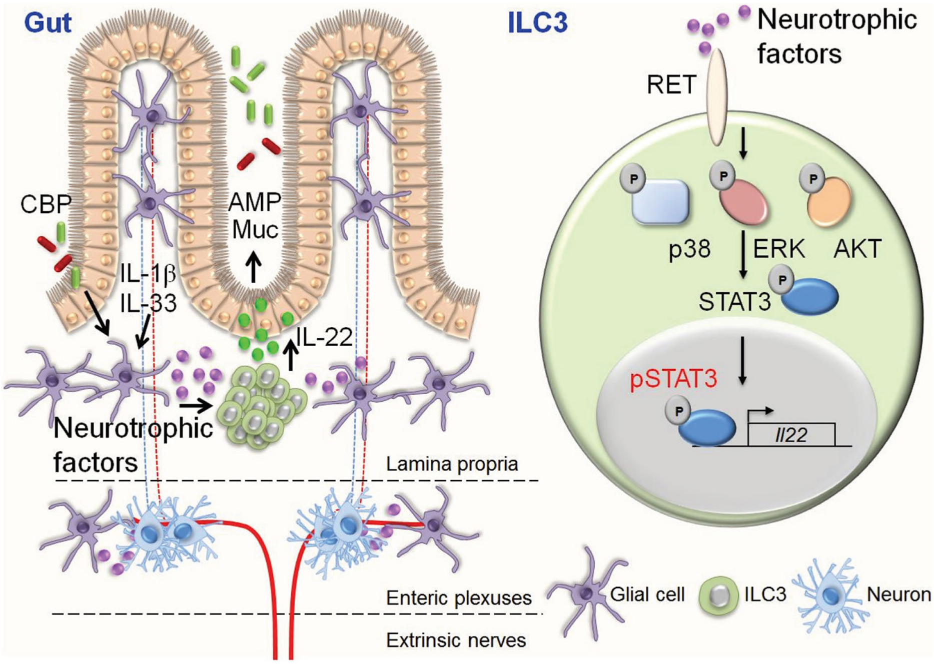

Extended Data Figure 10 | A novel glial-ILC3-epithelial cell unit orchestrated by neurotrophic factors. Lamina propria glial cells sense microenvironmental products that control neurotrophic factor expression. Glial-derived neurotrophic factors operate in an ILC3-intrinsic manner by activating the tyrosine kinase RET, which directly regulates innate IL-22 downstream of a p38 MAPK/ERK-AKT cascade and STAT3 phosphorylation. GFL induced innate IL-22 acts on epithelial cells to induce reactivity gene expression (CBP, commensal bacterial products; AMP, antimicrobial peptides; Muc, mucins). Thus, neurotrophic factors are the molecular link between glial cell sensing, innate IL-22 production and intestinal epithelial barrier defence.

doi:10.1038/nature18622

The mechanism of RNA 5′ capping with NAD$^+$, NADH and desphospho-CoA

Jeremy G. Bird[1,2*], Yu Zhang[2*], Yuan Tian[3], Natalya Panova[4], Ivan Barvík[5], Landon Greene[6], Min Liu[7], Brian Buckley[7], Libor Krásný[4], Jeehiun K. Lee[3], Craig D. Kaplan[8], Richard H. Ebright[2] & Bryce E. Nickels[1]

The chemical nature of the 5′ end of RNA is a key determinant of RNA stability, processing, localization and translation efficiency[1,2], and has been proposed to provide a layer of 'epitranscriptomic' gene regulation[3]. Recently it has been shown that some bacterial RNA species carry a 5′-end structure reminiscent of the 5′ 7-methylguanylate 'cap' in eukaryotic RNA. In particular, RNA species containing a 5′-end nicotinamide adenine dinucleotide (NAD$^+$) or 3′-desphospho-coenzyme A (dpCoA) have been identified in both Gram-negative and Gram-positive bacteria[3–6]. It has been proposed that NAD$^+$, reduced NAD$^+$ (NADH) and dpCoA caps are added to RNA after transcription initiation, in a manner analogous to the addition of 7-methylguanylate caps[6–8]. Here we show instead that NAD$^+$, NADH and dpCoA are incorporated into RNA during transcription initiation, by serving as non-canonical initiating nucleotides (NCINs) for *de novo* transcription initiation by cellular RNA polymerase (RNAP). We further show that both bacterial RNAP and eukaryotic RNAP II incorporate NCIN caps, that promoter DNA sequences at and upstream of the transcription start site determine the efficiency of NCIN capping, that NCIN capping occurs *in vivo*, and that NCIN capping has functional consequences. We report crystal structures of transcription initiation complexes containing NCIN-capped RNA products. Our results define the mechanism and structural basis of NCIN capping, and suggest that NCIN-mediated '*ab initio* capping' may occur in all organisms.

NAD$^+$, NADH, and dpCoA are nucleotides that share an adenosine-diphosphate substructure with ATP (Fig. 1a, red). Therefore, in principle, NAD$^+$, NADH, and dpCoA could serve in place of ATP as initiating nucleotides in *de novo* transcription initiation by a cellular RNAP, and thereby be incorporated *ab initio* into RNA (see Supplementary Discussion). To assess whether NAD$^+$, NADH, and dpCoA serve as initiating nucleotides for a cellular RNAP, we performed *in vitro* transcription experiments with *Escherichia coli* RNAP and DNA templates containing promoters for RNAs identified as the most-highly NAD$^+$-capped *in vivo*[6] (P_{gadY} and P_{rnaI}; Fig. 1b; Extended Data Fig. 1b). We performed reactions using ATP, NAD$^+$, NADH, or dpCoA as initiating nucleotide and [α^{32}P]-CTP as extending nucleotide. In each case, we observed efficient formation of an initial RNA product (Fig. 1b; Extended Data Fig. 1b). RppH, which processes 5′-triphosphate and 5′-diphosphate RNAs to 5′-monophosphate RNAs[9], processed the product obtained with ATP, but had no effect on products obtained with NAD$^+$, NADH, and dpCoA (Fig. 1b; Extended Data Fig. 1b). Conversely, NudC, which processes 5′-capped RNAs to 5′-monophosphate RNAs[6], had no effect on the product formed with ATP, but processed products obtained with NAD$^+$, NADH, and dpCoA (Fig. 1b; Extended Data Fig. 1b). Liquid chromatography/tandem mass spectrometry analysis confirmed the detection and structural assignment of the product of NAD$^+$-mediated transcription initiation (Extended Data Fig. 2).

To assess whether initial RNA products formed with NCINs can be extended to full-length RNA products, we performed transcription reactions with ATP, NAD$^+$, NADH, or dpCoA as initiating nucleotide and [α^{32}P]-UTP, CTP, and GTP as extending nucleotides on templates containing P_{rnaI} linked to a 100-nucleotide cassette that did not contain any adenine bases. We observed production of full-length

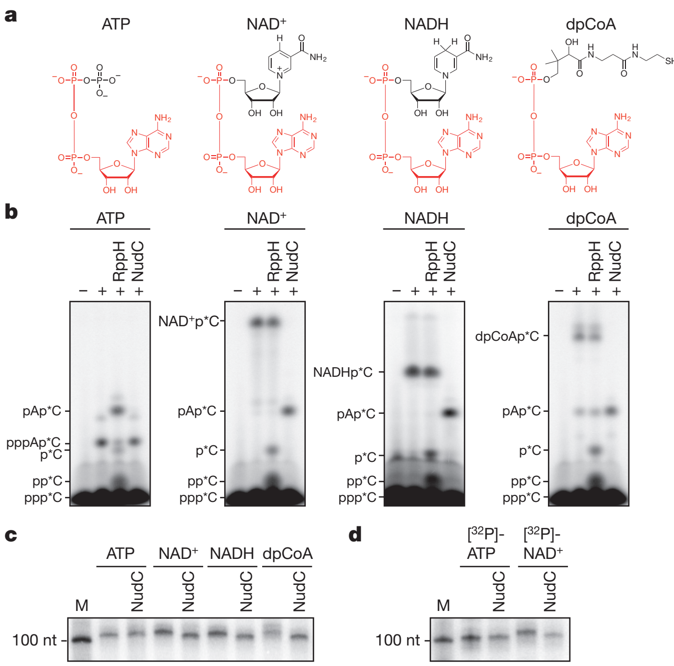

Figure 1 | *De novo* transcription initiation by ATP and NCINs. **a**, Structures of ATP, NAD$^+$, NADH, and dpCoA. Red, identical atoms. **b**, Initial RNA products of *in vitro* transcription reactions with ATP, NAD$^+$, NADH, or dpCoA as initiating nucleotide and [α^{32}P]-CTP as extending nucleotide (*E. coli* RNAP; P_{gadY}). Products were treated with RppH (processes 5′-triphosphate RNA to 5′-monophosphate RNA and 5′-NTP to 5′-NDP/5′-NMP[9,14]) or NudC (processes 5′-NAD$^+$/NADH-capped RNA to 5′-monophosphate RNA[6]) as indicated. **c**, **d**, Full-length RNA products of *in vitro* transcription reactions with ATP, NAD$^+$, NADH, or dpCoA as initiating nucleotide and [α^{32}P]-CTP, GTP, and UTP as extending nucleotides (**c**), or with [γ^{32}P]-ATP or [α^{32}P]-NAD$^+$ as initiating nucleotide and CTP, GTP, and UTP as extending nucleotides (**d**) (*E. coli* RNAP; P_{rnaI} fused to an A-less cassette). M, 100-nucleotide marker. For gel source data, see Supplementary Fig. 1.

[1]Department of Genetics and Waksman Institute, Rutgers University, Piscataway, New Jersey 08854, USA. [2]Department of Chemistry and Chemical Biology and Waksman Institute, Rutgers University, Piscataway, New Jersey 08854, USA. [3]Department of Chemistry and Chemical Biology, Rutgers University, Piscataway, New Jersey 08854, USA. [4]Institute of Microbiology, Czech Academy of Sciences, v.v.i., Vídeňská 1083, 142 20 Prague 4, Czech Republic. [5]Institute of Physics, Faculty of Mathematics and Physics, Charles University in Prague, Ke Karlovu 5, 121 16 Prague 2, Czech Republic. [6]Analytical and Bioanalytical Development, Bristol-Myers Squibb Company, One Squibb Drive, New Brunswick, New Jersey 08903, USA. [7]Environmental and Occupational Health Sciences Institute, Rutgers University, Piscataway, New Jersey 08854, USA. [8]Department of Biochemistry and Biophysics, Texas A&M University, College Station, Texas 77843, USA.
*These authors contributed equally to this work.

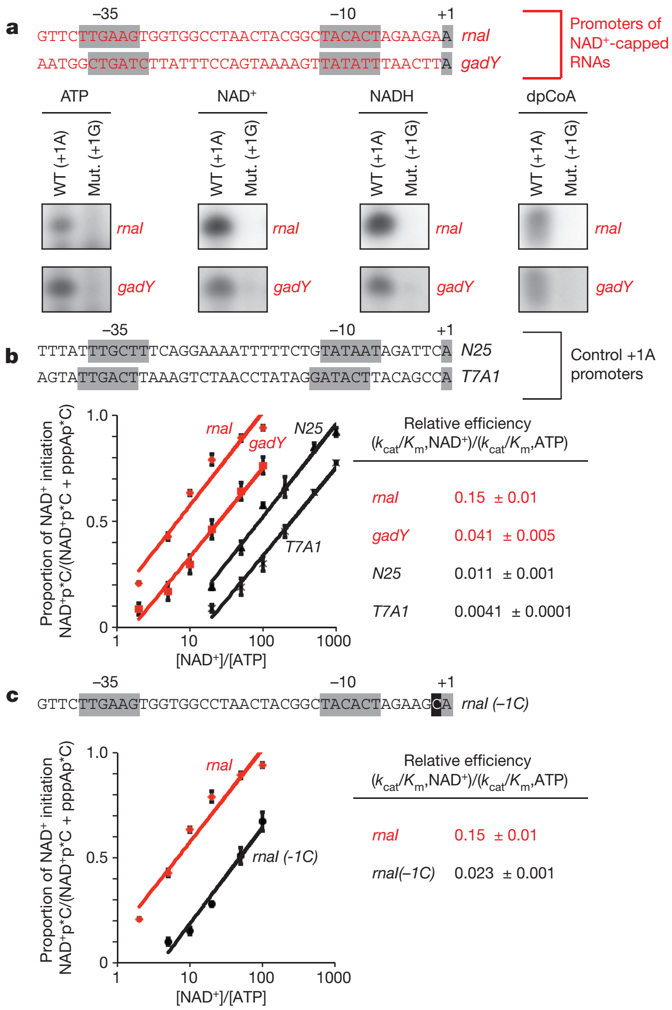

Figure 2 | Promoter-sequence effects on efficiency of NCIN-mediated transcription initiation. a, NCIN capping requires A_{+1}. Top, promoters of NAD$^+$-capped RNAs (promoter elements and start sites in grey). Bottom, initial RNA products of *in vitro* transcription reactions with ATP, NAD$^+$, NADH, or dpCoA as initiating nucleotide and [α^{32}P]-CTP as extending nucleotide (*E. coli* RNAP; WT (+1A), P_{rnaI} (upper) or P_{gadY} (lower); Mut. (+1G), +1G derivative of P_{rnaI} (upper) or P_{gadY} (lower)). **b**, Promoter sequence determinants in addition to A_{+1} affect NCIN capping. Top, control +1A promoters. Bottom left, dependence of NAD$^+$ capping on [NAD$^+$]/[ATP] ratio (mean ± s.e.m. of four determinations). Bottom right, relative efficiencies of NAD$^+$ capping. **c**, Promoter position −1 affects NCIN capping. Top, $P_{rnaI(-1C)}$ (−1 in black). Other features as in **b** (mean ± s.e.m. of three determinations). For gel source data, see Supplementary Fig. 1.

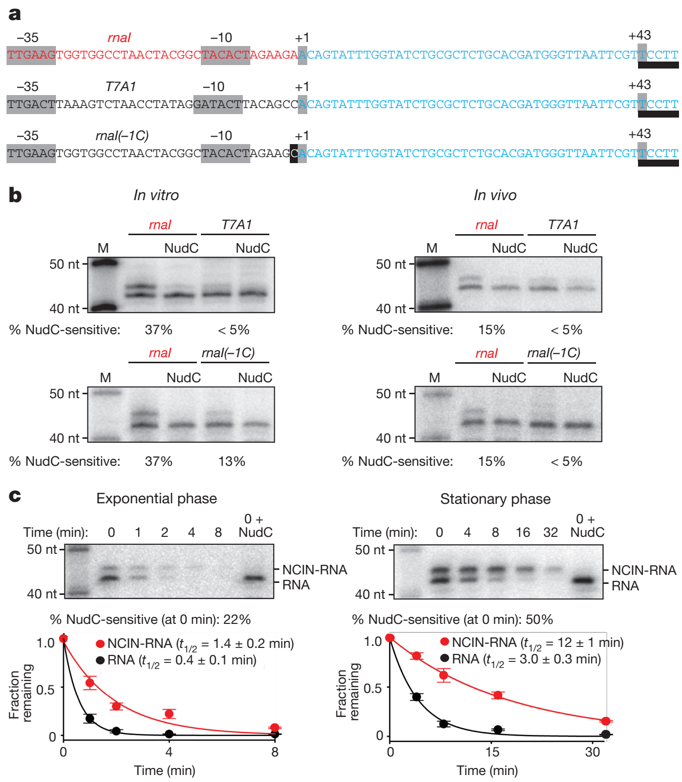

Figure 3 | NCIN-mediated transcription initiation *in vivo*. a, Templates having *rnaI*, *T7A1*, and *rnaI(−1C)* promoters fused to identical transcribed regions (promoter elements, start sites, and position of RNA 3′-end in grey; DNA that directs synthesis of reference RNA in blue; site for MazF-mt3 endoribonuclease used to generate RNA products having uniform RNA 3′-ends, underlined). **b**, NCIN capping *in vitro* (left; 1 mM NAD$^+$, 200 μM ATP, CTP, UTP, and GTP) and *in vivo* (right; RNA isolated from cells). RNA products were treated with MazF-mt3 or MazF-mt3 plus NudC, and detected by hybridization. M, 40-nucleotide and 50-nucleotide markers. **c**, Effects of NCIN capping on RNA stability *in vivo* (*rnaI* template; left, exponential-phase cells; right, stationary-phase cells; times, minutes after addition of RNA-synthesis inhibitor rifampin; half-life values are the mean ± s.e.m. of three determinations for exponential phase and five determinations for stationary phase). For gel source data, see Supplementary Fig. 1.

products in all cases, and observed that full-length products with NAD$^+$, NADH, and dpCoA contained NudC-sensitive, capped 5′-ends (Fig. 1c). Equivalent results were obtained using [^{32}P]-NAD$^+$, rather than [α^{32}P]-UTP, to detect products (Fig. 1d; Extended Data Fig. 3).

Because NAD$^+$, NADH, and dpCoA have the same Watson–Crick base pairing preferences as ATP (Fig. 1a), NCIN-mediated initiation should occur only for RNAs transcribed from promoters that contain A:T at the transcription start site +1 (+1A promoters). Consistent with this inference, we find that NCIN-mediated initiation occurs only with +1A promoters, and not with corresponding +1G promoter derivatives (Fig. 2a).

In principle, other aspects of promoter sequence, in addition to +1A at the transcription start site, could affect NCIN-mediated initiation. Consistent with this inference, we find that relative efficiencies of NAD$^+$-mediated initiation and ATP-mediated initiation, (k_{cat}/K_m,NAD$^+$)/(k_{cat}/K_m,ATP), differ over one to two orders of magnitude at different +1A promoters, with P_{rnaI} and P_{gadY} exhibiting high relative efficiencies and P_{N25} and P_{T7A1} promoters exhibiting low relative efficiencies (Figs 2a, b; Extended Data Figs 4 and 5). Substitution of the P_{rnaI} promoter position immediately upstream of the transcription start site, −1, results in an order-of-magnitude reduction in relative efficiency (Fig. 2c), indicating that position −1 is a key determinant of NAD$^+$-mediated initiation.

Having obtained results establishing that NAD$^+$, NADH, and dpCoA function as NCINs for transcription initiation *in vitro* and that promoter sequence determines the efficiency of NCIN-mediated initiation *in vitro*, we hypothesized that NCIN-mediated initiation also may occur *in vivo* and be responsible for the generation of NAD$^+$-, NADH-, and dpCoA-capped RNAs *in vivo*. Consistent with this hypothesis, the promoters for full-length RNAs identified as enriched for NAD$^+$-capping *in vivo* all are +1A promoters[6], the class of promoters competent for NAD$^+$-mediated initiation *in vitro* (Fig. 2a). Further consistent with this hypothesis, the promoters identified as most-highly enriched for NAD$^+$ capping *in vivo* are P_{rnaI} and P_{gadY}[6], the two promoters with highest efficiencies of NAD$^+$-mediated initiation *in vitro* (Fig. 2b).

To show directly that NCIN-mediated initiation occurs *in vivo*, we assessed whether the promoter sequence dependence for NCIN-mediated initiation observed *in vitro* is observed *in vivo*. We fused promoters observed *in vitro* to have high (P_{rnaI}) and low (P_{T7A1}, $P_{rnaI(-1C)}$)

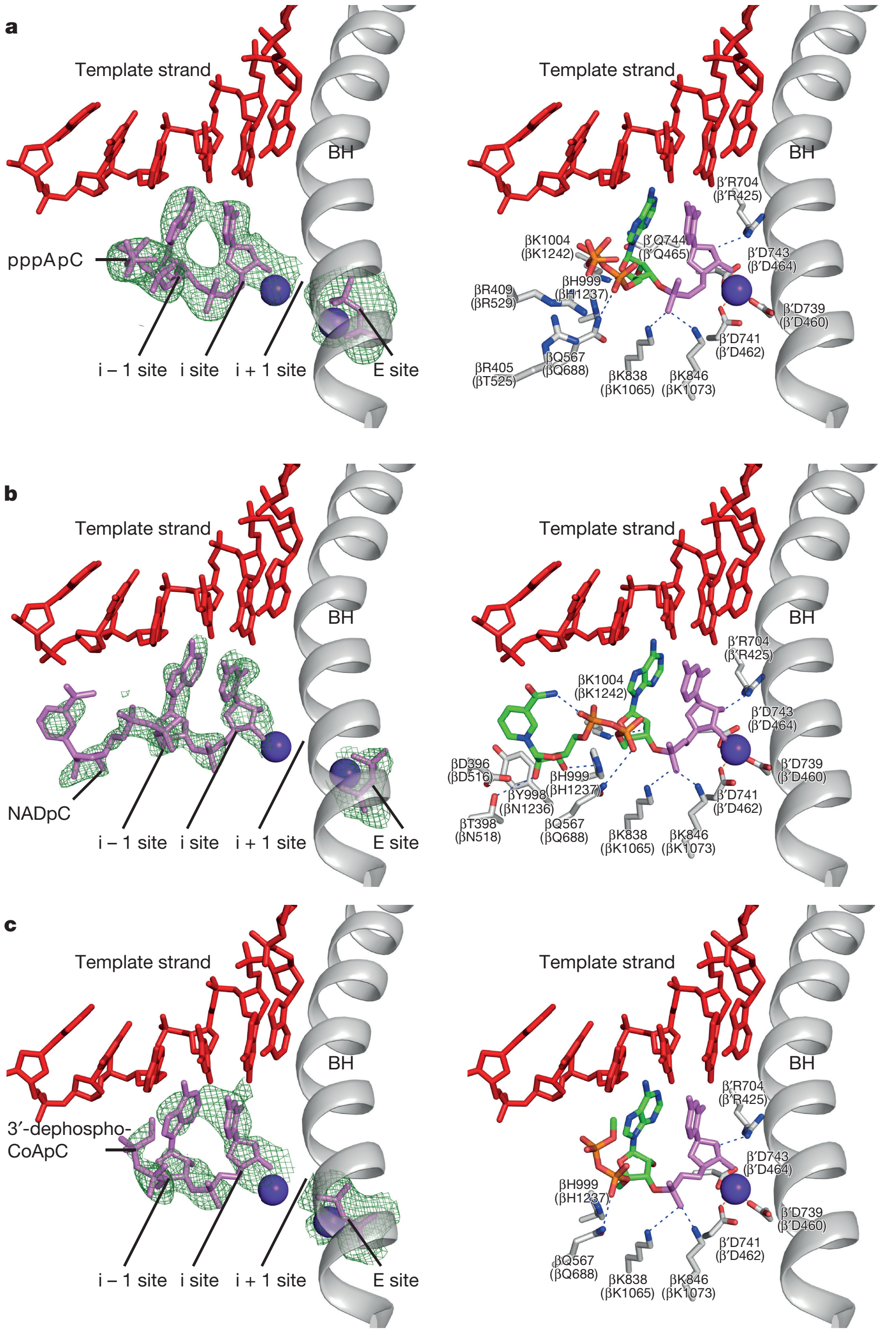

Figure 4 | Structural basis of NCIN-mediated transcription initiation. a–c, Crystal structures of RPo-pppApC, RPo-NAD$^+$pC, and RPo-dpCoApC. Left, electron density and atomic model for initial RNA product. Green mesh, $F_o - F_c$ omit map (contoured at 2.5σ in **a**, **b** and 2.2σ in **c**); red, DNA; pink, RNA product and diphosphate in 'E site' (see refs 15–17); violet spheres, Mg^{2+}(I) and Mg^{2+}(II); grey, RNAP bridge helix (BH). Right, contacts between RPo and initial RNA product. Green and orange, carbon and phosphorus atoms derived from initiating nucleotide; pink, atoms derived from extending nucleotide; red, DNA atoms and non-DNA oxygen atoms; blue, nitrogen atoms; grey sticks, RNAP carbon atoms; violet sphere, Mg^{2+}(I); grey ribbon, RNAP bridge helix.

efficiencies of NAD$^+$-mediated initiation (Figs 2b, c) to transcribed regions directing synthesis of the same RNA (reference RNA; Fig. 3a) and compared yields of NudC-sensitive, capped RNA products (Fig. 3b). We found that the promoter with high efficiency of NAD$^+$-mediated initiation *in vitro* yielded high levels of NudC-sensitive products *in vivo* (P_{rnaI}; Fig. 3b), whereas the promoters with low efficiency of NAD$^+$-mediated initiation *in vitro* yielded low, undetectable, levels of NudC-sensitive products *in vivo* (P_{T7A1}, $P_{rnaI(-1C)}$; Fig. 3b). We conclude that NCIN-mediated initiation occurs *in vivo*, and that most, or all, NCIN-capped RNA products *in vivo* arise from NCIN-mediated initiation.

To assess whether NCIN capping has functional consequences *in vivo*, we measured stabilities of NCIN capped and uncapped RNA *in vivo*, using a ΔNudC strain to eliminate NudC processing. We observe that NCIN capping results in a large, approximately three- to fourfold, increase in RNA stability (Fig. 3c), demonstrating a functional consequence of NCIN capping *in vivo*. We further observe that levels of NCIN capping are approximately twofold higher in stationary phase versus exponential phase (Fig. 3c), demonstrating a growth-phase dependence in NCIN capping.

All cellular RNAPs are members of a protein family having conserved structures and mechanisms[10–12]. To assess whether eukaryotic RNAP II, like bacterial RNAP, can use NCINs as initiating nucleotides, we performed *in vitro* transcription experiments with *Saccharomyces cerevisiae* RNAP II using ATP, NAD$^+$, or NADH as initiating nucleotide and [α-^{32}P]-UTP as extending nucleotide (Extended Data Fig. 6). The results matched those for bacterial RNAP: initiation occurred with NAD$^+$ and NADH, and products were insensitive to RppH and sensitive to NudC. We conclude that eukaryotic RNAP II can initiate transcription with NAD$^+$ and NADH, and we suggest that *ab initio* capping with NAD$^+$ and NADH also may occur in eukaryotes.

To define the structural basis of transcription initiation with ATP, NAD$^+$, and dpCoA as initiating nucleotides we determined crystal structures of product complexes obtained by soaking crystals of *Thermus thermophilus* RNAP–promoter open complex[13], RPo, with

ATP and CTP, NAD^+ and CTP, and dpCoA and CTP (Fig. 4; Extended Data Fig. 7; Extended Data Table 1). The results indicate that, in each case, the initiating entity—ATP, NAD^+, or dpCoA—and an extending nucleotide (CTP) were able to react *in crystallo* to form an initial RNA product—pppApC, NAD^+pC, or dpCoApC, respectively—and that RNAP was able to translocate *in crystallo* by one base pair relative to the nucleic-acid scaffold, yielding a complex in a post-translocated state poised for RNA extension (Fig. 4). The results for ATP provide the first structural description of an initial product complex for a cellular RNAP. The results for NAD^+ and dpCoA show graphically that NAD^+ and dpCoA serve as initiating nucleotides in transcription initiation and define the interactions that the initial RNA products make with DNA and RNAP (see Supplementary Discussion).

Our results establish that NAD^+, NADH, and dpCoA function as non-canonical initiating nucleotides (NCINs) for *de novo* transcription initiation and demonstrate the occurrence of *ab initio*, as opposed to post-transcription-initiation, capping of cellular RNAs.

Online Content Methods, along with any additional Extended Data display items and Source Data, are available in the online version of the paper; references unique to these sections appear only in the online paper.

Received 8 February; accepted 1 June 2016.
Published online 6 July 2016.

1. Topisirovic, I., Svitkin, Y. V., Sonenberg, N. & Shatkin, A. J. Cap and cap-binding proteins in the control of gene expression. *RNA* **2,** 277–298 (2011).
2. Hui, M. P., Foley, P. L. & Belasco, J. G. Messenger RNA degradation in bacterial cells. *Annu. Rev. Genet.* **48,** 537–559 (2014).
3. Jäschke, A., Höfer, K., Nübel, G. & Frindert, J. Cap-like structures in bacterial RNA and epitranscriptomic modification. *Curr. Opin. Microbiol.* **30,** 44–49 (2016).
4. Kowtoniuk, W. E., Shen, Y., Heemstra, J. M., Agarwal, I. & Liu, D. R. A chemical screen for biological small molecule-RNA conjugates reveals CoA-linked RNA. *Proc. Natl Acad. Sci. USA* **106,** 7768–7773 (2009).
5. Chen, Y. G., Kowtoniuk, W. E., Agarwal, I., Shen, Y. & Liu, D. R. LC/MS analysis of cellular RNA reveals NAD-linked RNA. *Nat. Chem. Biol.* **5,** 879–881 (2009).
6. Cahová, H., Winz, M. L., Höfer, K., Nübel, G. & Jäschke, A. NAD captureSeq indicates NAD as a bacterial cap for a subset of regulatory RNAs. *Nature* **519,** 374–377 (2015).
7. Shuman, S. RNA capping: progress and prospects. *RNA* **21,** 735–737 (2015).
8. Luciano, D. J. & Belasco, J. G. NAD in RNA: unconventional headgear. *Trends Biochem. Sci.* **40,** 245–247 (2015).
9. Deana, A., Celesnik, H. & Belasco, J. G. The bacterial enzyme RppH triggers messenger RNA degradation by 5′ pyrophosphate removal. *Nature* **451,** 355–358 (2008).
10. Ebright, R. H. RNA polymerase: structural similarities between bacterial RNA polymerase and eukaryotic RNA polymerase II. *J. Mol. Biol.* **304,** 687–698 (2000).
11. Cramer, P. & Multisubunit RNA polymerases. *Curr. Opin. Struct. Biol.* **12,** 89–97 (2002).
12. Decker, K. B. & Hinton, D. M. Transcription regulation at the core: similarities among bacterial, archaeal, and eukaryotic RNA polymerases. *Annu. Rev. Microbiol.* **67,** 113–139 (2013).
13. Zhang, Y. *et al.* Structural basis of transcription initiation. *Science* **338,** 1076–1080 (2012).
14. Xu, W., Jones, C. R., Dunn, C. A. & Bessman, M. J. Gene ytkD of *Bacillus subtilis* encodes an atypical nucleoside triphosphatase member of the Nudix hydrolase superfamily. *J. Bacteriol.* **186,** 8380–8384 (2004).
15. Westover, K. D., Bushnell, D. A. & Kornberg, R. D. Structural basis of transcription: nucleotide selection by rotation in the RNA polymerase II active center. *Cell* **119,** 481–489 (2004).
16. Zhang, Y. *et al.* GE23077 binds to the RNA polymerase ‘i’ and ‘i+1’ sites and prevents the binding of initiating nucleotides. *eLife* **3,** e02450 (2014).
17. Basu, R. S. *et al.* Structural basis of transcription initiation by bacterial RNA polymerase holoenzyme. *J. Biol. Chem.* **289,** 24549–24559 (2014).

Supplementary Information is available in the online version of the paper.

Acknowledgements We thank N. Woychik for MazF-mt3 protein. Work was supported by NSF grant CHE-1361462 (J.K.L.), Welch Foundation Grant A-1763 (C.D.K.), Czech Science Foundation 15-05228S (L.K., N.P.), and NIH grants NIEHS P30 ES005022, GM097260 (C.D.K.), GM041376 (R.H.E.), GM088343 (B.E.N.), GM096454 (B.E.N.), and GM115910 (B.E.N.).

Author Contributions L.K., J.K.L., C.D.K., R.H.E. and B.E.N. designed experiments; J.G.B., Y.Z., Y.T., N.P., I.B., L.G. and M.L. performed experiments; B.B. provided resources to perform experiments; J.G.B., Y.Z., Y.T., N.P., I.B., L.G., L.K., J.K.L., C.D.K., R.H.E. and B.E.N. performed data analysis; R.H.E. and B.E.N. wrote the paper.

Author Information The coordinates and structure factors of RPo-pppApC, RPo-NAD^+pC, and RPo-dpCoApC have been deposited in the Protein Data Bank under accession numbers 5D4C, 5D4D and 5D4E, respectively. Reprints and permissions information is available at www.nature.com/reprints. The authors declare no competing financial interests. Readers are welcome to comment on the online version of the paper. Correspondence and requests for materials should be addressed to B.E.N. (bnickels@waksman.rutgers.edu) or R.H.E. (ebright@waksman.rutgers.edu).

METHODS

No statistical methods were used to predetermine sample size. The experiments were not randomized and the investigators were not blinded to allocation during experiments and outcome assessment.

Proteins. *E. coli* RNAP core enzyme was prepared from BL21(DE3) cells transformed with plasmid pVS10 (gift from I. Artsimovitch) as described in ref. 18. σ^{70} was prepared from BL21(DE3) cells transformed with plasmid pσ^{70}-His (gift from J. Roberts) as described in refs 19,20. RppH was purchased from NEB. NudC was purified from BL21(DE3) cells from pET NudC-His, which was prepared as described previously[6]. Briefly, *nudC* was amplified by PCR from *E. coli* strain MG1655 using oligonucleotides JB221 and JB222. The PCR product was digested with XbaI and NotI and inserted into pET28c digested with XbaI and NotI. *T. thermophilus* RNAP holoenzyme was prepared as described previously[13]. *Saccharomyces cerevisiae* RNAP II was prepared as described previously[21]. MazF-mt3 protein, prepared as described previously[22], was a gift from N. Woychik.

***In vitro* transcription assays with *E. coli* RNAP: linear templates.** Linear transcription templates were synthesized by PCR using Phusion HF Polymerase master mix (Thermo) and oligonucleotides listed in Supplementary Table 1. PCR reactions contained 5 nM of the indicated template oligonucleotide, and 0.5 μM of the indicated forward and reverse primers. PCR products were purified using Qiagen PCR-clean up columns before use in transcription reactions.

Sequence of *gadY* (−65 to +35) template used in Figs 1b and 2a, b, and Extended Data Figs 4 and 5:
AGCGTATAGCTTATGTTTATAAAAAAATGG**CTGATC**TTATTTCCAGTAAAAGT**TATATT**TAACTT**A**CTGAGAGCACAAAGTTTCCCGTGCCAACAGGGAG (prepared using oligos JB224, JB230, JB231).

Sequence of *gadY* (+1G) (−65 to +35) template used in Fig. 2a:
AGCGTATAGCTTATGTTTATAAAAAAATGG**CTGATC**TTATTTCCAGTAAAAGT**TATATT**TAACTT**G**CTGAGAGCACAAAGTTTCCCGTGCCAACAGGGAG (prepared using oligos JB244, JB230, JB231).

Sequence of *rnaI* (−65 to +35) template used in Figs 2a–c and Extended Data Figs 1b, 4, and 5:
CGAGGTATGTAGGCGGTGCTACAGAGTTC**TTGAAG**TGGTGGCCTAACTACGGC**TACACT**AGAAGA**A**CTGTATTTGGTATCTGCGCTCTGCTGAAGCCAGTT (prepared using oligos JB288, JB281, JB269).

Sequence of mutant *rnaI* (+1G) (−65 to +35) template used in Fig. 2a:
CGAGGTATGTAGGCGGTGCTACAGAGTTC**TTGAAG**TGGTGGCCTAACTACGGC**TACACT**AGAAGA**G**CTGTATTTGGTATCTGCGCTCTGCTGAAGCCAGTT (prepared using oligos JB287, JB281, JB269).

Sequence of mutant *rnaI* (−1C) (−65 to +35) template used in Fig. 2c:
CGAGGTATGTAGGCGGTGCTACAGAGTTC**TTGAAG**TGGTGGCCTAACTACGGC**TACACT**AGAAGC**A**CTGTATTTGGTATCTGCGCTCTGCTGAAGCCAGTT (prepared using oligos JB367, JB281, JB269).

Sequence of *rnaI* (−65 to +112) A-less cassette template used in Figs 1c, d and Extended Data Fig. 3:
CGAGGTATGTAGGCGGTGCTACAGAGTTC**TTGAAG**TGGTGGCCTAACTACGGC**TACACT**AGAAGA**A**CTTGTTTTGGTGTCTGCGCTCCTCCTTGCCTGTTTCCTCGGTTCTTTGTGTTGGTTGCTCTGTGTTCCTTCGTTTTTCCGCCCTGCTTGGCGGTTTTTTCGTTTTCTGTGC (prepared using oligos JB288, JB281, JB251).

Sequence of *N25* (−65 to +35) template used in Fig. 2b and Extended Data Figs 4 and 5:
ATCCGTCGAGGGAAATCATAAAAAATTTAT**TTGCTT**TCAGGAAAATTTTTCTG**TATAAT**AGATTC**A**CTAATTTGAGAGAGGAGTTTAAATATGGCTGGTT (prepared using oligos JB232, JB233, JB234).

Sequence of *T7A1* (−65 to +35) template used in Fig. 2b and Extended Data Figs 4 and 5:
GATTAATTTAAAATTTATCAAAAAGAGTA**TTGACT**TAAAGTCTAACCTATAG**GATACT**TACAGCC**A**CTGAGAGGGACACGGCGAATAGCCATCCCAACGA (prepared using oligos JB235, JB228, JB229).

Promoter −35 elements, −10 elements and transcription start sites are in bold and underlined.

***In vitro* transcription assays with *E. coli* RNAP: abortive initiation assays.** 10 nM of linear template was mixed with 50 nM core RNAP and 250 nM σ^{70} in 60 μl transcription buffer (10 mM Tris-HCl pH 8.0, 40 mM KCl, 10 mM $MgCl_2$, 0.1 mM EDTA, 1 mM DTT, 0.1 mg ml^{-1} BSA, 2% glycerol) and incubated at 37 °C for 15 min to form open complexes. The indicated initiating nucleotide (0.2 mM ATP (Roche), 1 mM NAD^+ (Roche), 1 mM NADH (Roche) or 1 mM dpCoA (Sigma-Aldrich)) was added along with 6 μCi [α^{32}P]-CTP (Perkin Elmer; 3,000 Ci mmol^{-1}) and reactions were incubated at 37 °C for 10 min to allow for product formation. For the NAD^+/ATP competition assays shown in Fig. 2b, c, 1 mM NAD^+ was present in each reaction along with increasing concentrations of ATP. The data in Extended Data Fig. 4b shows initial products formed in reactions with 1 mM NAD^+ and 50 μM ATP. For the NADH/ATP competition assays shown in Extended Data Fig. 5a, 1 mM NADH was present in each reaction along with increasing concentrations of ATP. For the dpCoA/ATP competition assays shown in Extended Data Fig. 5b, 1 mM dpCoA was present in each reaction along with increasing concentrations of ATP.

For experiments shown in Fig. 2a–c and Extended Data Figs 4 and 5, reactions were stopped by addition of an equal volume of gel loading buffer (90% formamide, 100 mM Tris-HCl, pH 8.0, 18 mM EDTA, 0.025% xylene cyanol, 0.025% bromophenol blue). For the reactions shown in Fig. 1b and Extended Data Fig. 1b the samples were passed through a Nanosep Centrifugal Device (10 kDa molecular weight cut-off; Pall Corporation), the flow-through was collected, mixed with 1 U RppH (NEB), 400 nM NudC or NudC storage buffer (50 mM Tris-HCl, pH 7.9, 0.5 M NaCl, 50 mM KCl, 1 mM $MgCl_2$, 7 mM TCEP, 50% glycerol), incubated at 37 °C for 30 min, and mixed with an equal volume of gel loading buffer. Samples were run on 15% TBE-urea polyacrylamide gels (UreaGel system, National Diagnostics). Autoradiography of gels was performed using storage phosphor screens and a Typhoon 9400 variable mode imager (GE Life Science) and quantified using ImageQuant software. We note that the presence of contaminating AMP in the dpCoA stock (Extended Data Fig. 8) leads to the generation of pApC products in reactions performed with dpCoA.

For the competition assays in Fig. 2b, c and Extended Data Fig. 5, (NCIN)pC and pppApC products were quantified, the fraction of (NCIN)pC products was plotted vs. [NCIN]/[ATP], and the value of (k_{cat}/K_m,NCIN)/(k_{cat}/K_m, ATP) was calculated as the value of [NCIN]/[ATP] for which the fraction of (NCIN)pC products was 0.5. Values were obtained from averaging results of three (Fig. 2c, Extended Data Fig. 5) or four (Fig. 2b) technical replicates.

***In vitro* transcription assays with *E. coli* RNAP: run-off transcription assays.** For reactions shown in Fig. 1c, open complexes formed as described above were mixed with the indicated initiating nucleotide (0.2 mM ATP, 1 mM NAD^+, 1 mM NADH or 1 mM dpCoA) along with 6 μCi [α^{32}P]-CTP (Perkin Elmer; 3,000 Ci mmol^{-1}), 200 μM CTP, 200 μM UTP, and 200 μM GTP, and reactions were incubated at 37 °C for 10 min to allow for product formation. For the reactions shown in Fig. 1d and Extended Data Fig. 4, open complexes formed as described above were mixed with 10 μCi [γ^{32}P]-ATP (Perkin Elmer; 6,000 Ci mmol^{-1}), or 20 μCi [α^{32}P]-NAD^+ (Perkin Elmer; 800 Ci mmol^{-1}) along with 200 μM CTP, 200 μM UTP and 200 μM GTP. Reactions were incubated at 37 °C for 10 min to allow for product formation, and stopped by addition of 100 μl stop solution (0.6 M Tris-HCl, pH 8.0, 18 mM EDTA, 0.1 mg ml^{-1} glycogen). Samples were extracted with acid phenol:chloroform and RNA transcripts were recovered by ethanol precipitation, resuspended in transcription buffer and divided into 10 μl aliquots. For the experiment in Fig. 1d, 400 nM NudC was added to one aliquot while NudC storage buffer was added to the other for mock treatment. For the experiment in Extended Data Fig. 3, 0.25 U alkaline phosphatase (Thermo Fisher) was added to one aliquot, 400 nM NudC was added to one aliquot, both 0.25 U alkaline phosphatase and 400 nM NudC was added to one aliquot, and NudC storage buffer was added to another aliquot for mock treatment. Reactions were incubated at 37 °C for 30 min and stopped by addition of an equal volume of gel loading buffer and analysed by gel electrophoresis on 15% TBE-urea polyacrylamide gels as described above. Reactions were loaded alongside an Ambion Decade Marker System (Life Technologies) to enable an estimation of the approximate size of the full-length transcripts generated.

***In vitro* transcription assays with *E. coli* RNAP: transcription assays with negatively supercoiled DNA templates.** Plasmid pJB89 contains sequence for the P_{rnaI}-reference RNA fusion inserted between the XbaI and SalI sites of plasmid pSG289[23]. The sequence of the insert is:
TCTAGACGAGGTATGTAGGCGGTGCTACAGAGTTC**TTGAAG**TGGTGGCCTAACTACGGC**TACACT**AGAAGA*ACAGTATTTGGTATCTGCGCTCTGCACGATGGGTTAATTCGTTCCTTGGATCCGAATAGCCATCCCAATCGAACAGGCCTGCTGGTAATCGCAGGCCTTTTTAT*TTGGATGTCGAC.

Plasmid pJB91 contains sequence for the P_{T7A1}-reference RNA fusion inserted between the XbaI and SalI sites of plasmid pSG289[23]. The sequence of the insert is:
TCTAGAGATTAATTTAAAATTTATCAAAAAGAGTA**TTGACT**TAAAGTCTAACCTATAG**GATACT**TACAGCC*ACAGTATTTGGTATCTGCGCTCTGCACGATGGGTTAATTCGTTCCTTGGATCCGAATAGCCATCCCAATCGAACAGGCCTGCTGGTAATCGCAGGCCTTTTTAT*TTGGATGTCGAC.

Plasmid pJB95 contains sequence for the $P_{rnaI(-1C)}$-reference RNA fusion inserted between the XbaI and SalI sites of plasmid pSG289[23]. The sequence of the insert is:
TCTAGACGAGGTATGTAGGCGGTGCTACAGAGTTC**TTGAAG**TGGTGGCCTAACTACGGC**TACACT**AGAAGC*ACAGTATTTGGTATCTGCGCTCTGCACGATGGGTTAATTCGTTCCTTGGATCCGAATAGCCATCCCAATCGAACAGGCCTGCTGGTAATCGCAGGCCTTTTTAT*TTGGATGTCGAC.

Promoter −35 elements and −10 elements are in bold and underlined. DNA that directs synthesis of the reference RNA is *coloured blue*. Recognition site for MazF-mt3 (UCCUU; ref. 22) is underlined. Reference RNA includes sequence of the tR2 terminator.

For *in vitro* reactions shown in Fig. 3b, open complexes were formed using 10 nM of plasmid (pJB89, pJB91, or pJB95) and 50 nM core RNAP and 250 nM σ^{70} in 30 μl transcription buffer (see above). Transcription was carried out for 10 min at 37 °C using 1 mM NAD$^+$, 200 μM ATP, UTP, CTP and GTP. Reactions were stopped by the addition of 120 μl of stop solution and samples were extracted with acid phenol:chloroform and ethanol precipitated. The resulting RNAs were resuspended in 10 mM Tris, pH 8.0, supplemented with 2 μg of RNA isolated from wild-type MG1655 cells and treated with 2 μM MazF-mt3 for 1 h at 37 °C. Reactions were divided into two, 9 μl aliquots and 1 μl 10× transcription buffer was added to each. 1 μM NudC was added to one of these aliquots and NudC storage buffer was added to the other. Reactions were incubated at 37 °C for 90 min and stopped by addition of an equal volume of gel loading buffer.

Analysis of RNA products generated *in vivo*. For the experiments of Fig. 3b, *E. coli* MG1655 cells containing plasmids pJB89, pJB91, or pJB95 were shaken at 220 r.p.m. at 37 °C in 25 ml LB (10 g Bacto-tryptone, 5 g Bacto-yeast extract and 10 g NaCl per litre) containing 25 μg ml^{-1} chloramphenicol in 125 ml flasks (Bellco). When cell density reached an OD_{600} ~0.6, 2 ml of the cell suspension was centrifuged (30 s, 10,000*g* at room temperature) to collect cells, supernatants were removed, and cell pellets were rapidly frozen on dry ice and stored at −80 °C.

For the RNA stability experiments of Fig. 3c, strain MG1655 Δ*nudC::Kan* was constructed by P1 transduction of the Δ*nudC::Kan* cassette from JW5548[24] into MG1655. MG1655 Δ*nudC::Kan* cells containing plasmids pJB89, pJB91, or pJB95 were grown as described above to an OD_{600} ~0.6 (exponential phase) or an OD_{600} ~3.5 (stationary phase). 2 ml of the cell suspension was collected as described above (the RNA derived from these cells was used as the 0 min time point). Rifampicin was added to a final concentration of 2 mg ml^{-1} to the remainder of the culture. 2-ml aliquots were taken at the indicated times and cells were collected as described above. Frozen pellets were resuspended in 1 ml of TRI Reagent solution (Molecular Research Center). Samples were incubated at 70 °C for 10 min and then centrifuged (10 min, 21,000*g*, 4 °C) to remove insoluble material. The supernatant was transferred to a fresh tube and 200 μl of chloroform was added, samples were mixed by vortexing, and then centrifuged (10 min, 21,000*g*, 4 °C). The aqueous phase was transferred to a fresh tube, extracted with acid phenol:chloroform, and RNA transcripts were recovered by ethanol precipitation and resuspended in 10 mM Tris, pH 8.0.

5 μg of isolated RNA was treated with 2 μM MazF-mt3 in 10 mM Tris, pH 8.0 (total volume, 25 μl) and incubated for 60 min at 37 °C. Reactions were stopped by addition of an equal volume of gel loading buffer. In cases where RNA products were treated with NudC, reactions were divided into into two aliquots and 10× transcription buffer was added to each to a final concentration of 1×. 1 μM NudC was added to one of these aliquots and NudC storage buffer was added to the other. Reactions were incubated at 37 °C for 45 min and stopped by addition of an equal volume of gel loading buffer.

Detection of RNA products generated *in vitro* or *in vivo* by hybridization. In Fig. 3b, c, RNA products were detected by a procedure comprising electrophoresis on 10% 7.5 M urea slab gels (equilibrated and run in 1× TBE), transfer to and UV cross-linking to a membrane (Nytran supercharge nylon membrane, GE Healthcare Life Sciences), hybridization with a ^{32}P-labelled 'locked-nucleic-acid' probe complementary to positions +31 to +42 of the reference RNA (sequence, agCaaAttAacCc; LNA bases capitalized; purchased from Exiquon; ^{32}P-labelled using T4 polynucleotide kinase), high stringency washing (procedure as described in ref. 25), and storage-phosphor imaging. Bands were quantified using ImageQuant software. The percentage of RNA products in the upper band was determined for each sample as: $100 \times \frac{\text{upperband}}{(\text{upper band} + \text{lower band})}$. Values of the per cent of NudC-sensitive products represent the reduction in the per cent of RNA products in the upper band upon treatment with NudC. Values shown represent the average of three technical replicates (*in vitro*) or three biological replicates (*in vivo*).

For the experiments in Fig. 3c, values of half-life were determined by fitting data to a single-exponential decay function (mean ± s.e.m. of three biological replicates for exponential phase and five biological replicates for stationary phase).

***In vitro* transcription assays with *E. coli* RNAP: liquid chromatography/tandem mass spectrometry (LC/MS/MS) detection of NAD$^+$pC.** Open complexes formed as described above were mixed with 2 mM NAD$^+$ and 10 μM CTP, incubated at 37 °C for 1 h, passed through a Nanosep Centrifugal Device, and the flow-through was analysed by LC/MS/MS. (Control samples in which NAD$^+$, CTP, or RNAP were not present in the reactions were also prepared.) LC/MS/MS analyses were performed in negative ion mode with a Finnigan LTQ mass spectrometer equipped with an electrospray ionization (ESI) interface coupled with a Finnigan Surveyor HPLC system. The flow rate from the Finnigan Surveyor pump was 0.3 ml min^{-1}. The autosampler temperature was 5 °C. The liquid chromatography method used a YMC ODS-A 5 μm particle size 120 Å pore size column, 3.0 mm × 100 mm. The samples were separated using a gradient mobile phase consisting of 5 mM ammonium formate buffered to pH 7.9 in water (A) and methanol (B). The gradient condition was: 0–5 min, 100% A; 5–15 min, 100–30% A; 15–23 min, 30–0% A; 23–28 min, 0% A; 28–40 min, 100% A. Column temperature was 25 °C. The temperature of the heated capillary was 200 °C. Fragmentation was activated by collision induced dissociation (CID) with a collision energy of 20–25%. The search for NAD$^+$pC was conducted by isolating its anion ((M–2H), m/z 967) at isolation width 3 using full scan mode, and analysing its fragmentation spectrum (collision energy 20%) from $m/z = 210$ to $m/z = 1{,}000$. The characteristic fragment $m/z = 845$ (loss of nicotinamide) was used to identify NAD$^+$pC. The instrument control, data acquisition, and data analysis were performed by Xcalibur software. Ammonium formate (99%), water (HPLC grade) and methanol (HPLC grade) used in these LC/MS/MS experiments were purchased from Sigma-Aldrich.

***In vitro* transcription assays with *Saccharomyces cerevisiae* RNAP II.** Bubble templates for initiation were used following the approach in ref. 26 by mixing 2.5 nmol of oligonucleotide CKO1639 and 2.5 nmol of oligonucleotide CKO1621 (see Supplementary Table 1) in 100 μl of annealing buffer (40 mM Tris, pH 8.0, 50 mM NaCl, 1 mM EDTA), incubating at 95 °C for 3 min, and slowly cooling to 23 °C (1 °C min^{-1}) to allow annealing. The oligonucleotide mixture was run on a 2.5% agarose gel (Apex, Genesee) equilibrated and run in 1× TBE (90 mM Tris base (BioRad), 90 mM boric acid (Calbiochem), 2 mM EDTA (JT Baker)), the gel was stained with ethidium bromide and the band corresponding to the bubble template was excised from the gel, crushed, and incubated with 500 μl elution buffer (500 mM NH_4OAc, 10 mM $Mg(OAc)_2$, 1 mM EDTA, 0.1% SDS). Gel debris was removed using a Spin-X column (Costar) and nucleic acids were isolated by ethanol precipitation and re-suspended in nuclease-free water (Ambion) to a concentration of 0.5 μg μl^{-1}. 500 ng of the template was mixed with M280 magnetic streptavidin beads (Invitrogen) in 1× TE (from Ambion components) supplemented with 1 M NaCl (EMD/Calbiochem) and incubated at 25 °C for 30 min to allow binding. Templates bound to the beads were washed three times using magnetic capture to separate beads in 1× TE supplemented with 1 M NaCl, once with 1× TE, and then equilibrated into 1× transcription buffer (TB: 20 mM Tris, pH 8.0 (Ambion), 40 mM KCl (Ambion), 10 mM $MgCl_2$ (Ambion), 10% glycerol (Macron/Avantor), 0.25 mg ml^{-1} BSA (Ambion), 1 mM DTT (Gold Biotechnology)).

2.5 μg purified *Saccharomyces cerevisiae* RNAP II was added to each template in 50 μl 1× TB, and incubated with rotation at 25 °C for 20 min. Complexes were washed following magnetic capture twice with 200 μl 1× TB, and resuspended in 22 μl 2× TB containing 0.4 U μl^{-1} RNase Inhibitor (NEB). 7.5 μl of this mixture was aliquoted for reactions (four reactions per bubble template).

5 μl of 'initiator'/ [α^{32}P]-UTP mixes were added to give final concentrations of: 1 mM ATP (GE Lifesciences), 2.5 μM [α^{32}P]-UTP (from 800 Ci mmol^{-1} (12.5 μM), Perkin Elmer), 1 mM NAD$^+$, 2.5 μM [α^{32}P]-UTP (from 800 Ci mmol^{-1} (12.5 μM), Perkin Elmer); or 1 mM NADH, 2.5 μM [α^{32}P]-UTP (from 800 Ci mmol^{-1} (12.5 μM), Perkin Elmer). Reactions were incubated at 25 °C for 2 h then passed through a Nanosep Centrifugal Device (10 kDa molecular weight cut-off). The flow through was collected, mixed with 0.5 μl (2.5 U) RppH (NEB), 0.5 μl NudC (400 nM final) or 0.5 μl NudC storage buffer, incubated at 37 °C for 30 min, and mixed with an equal volume of urea gel loading buffer (10 M urea (Calbiochem), 0.5 M EDTA, pH 8.0 (JT Baker), 1 × TBE). Samples were run on 25% 19:1 acrylamide: bisacrylamide gel (from 40% 19:1 solution (BioRad), 7 M urea (Calbiochem), 1× TBE (90 mM Tris base; BioRad), 90 mM boric acid (Calbiochem), 2 mM EDTA (JT Baker)). Autoradiography of gels was performed using storage phosphor screens and a Pharos (Bio-Rad) imager. Radiolabelled products were visualized using ImageLab (Bio-Rad) software.

Structure determination: RPo-pppApC. Crystals of *T. thermophilus* RPo were prepared using a derivative of the consensus bacterial promoter nucleic acid scaffold used for analysis of RPo in ref. 13 having A in place of C at position −1 of the DNA template strand, and were grown and handled essentially as described[13]. (*T. thermophilus* RNAP is a bacterial RNAP that is homologous in structure, sequence, and mechanism to *E. coli* RNAP, but, empirically, yielding crystals of RNAP that diffract to higher resolution than *E. coli* RNAP[13,27].) Crystallization drops contained 1 μl RPo in 20 mM Tris-HCl, pH 7.7, 100 mM NaCl, and 1% glycerol, and 1 μl reservoir buffer (RB; 100 mM Tris-HCl, pH 8.4, 200 mM KCl, 50 mM $MgCl_2$, and 9.5% PEG4000), and were equilibrated against 400 μl RB in a vapour-diffusion hanging-drop tray. Rod-like crystals appeared in 1 day, and were used to micro-seed hanging drops using the same conditions. ATP and CTP (Sigma-Aldrich) were soaked into RPo crystals by addition of 0.2 μl 40 mM ATP and 40 mM CTP in 60% (v/v) RB to the crystallization drop, and incubated for 2 min at 22 °C. Crystals were transferred into reservoir solutions containing 2 mM

ATP, 2 mM CTP, and 17.5% (v/v) (2R, 3R)-(-)-2,3-butanediol (Sigma-Aldrich) and were flash-cooled with liquid nitrogen.

Diffraction data were collected at BNL beamline X29A (temperature, 100 K; wavelength, 1.08 Å), processed and scaled using HKL2000[28]. Structure factors were converted using the French-Wilson algorithm in Phenix[29] and were subjected to anisotropy correction using the UCLA MBI Diffraction Anisotropy server[30] (http://services.mbi.ucla.edu/anisoscale/). The structure was solved by molecular replacement with Molrep[31] using one RNAP molecule from the structure of *T. thermophilus* RPo (PDB 4G7H)[13] as the search model. Early-stage refinement included rigid-body refinement of each RNAP molecule, followed by rigid-body refinement of each subunit of RNAP molecules. Cycles of iterative model building with Coot[32] and refinement with Phenix[33] were performed. Atomic models of the DNA nontemplate strand, the DNA template strand, and RNA were built into $mF_o - DF_c$ omit maps, and subsequent cycles of refinement and model building were performed. The final crystallographic model of RPo-pppApC, refined to Ramachandran statistics of 97.84% favoured, 2.10% allowed, and 0.06% outliers, has been deposited in the PDB with accession code 5D4C.

Structure determination: RPo-NAD$^+$pC. NAD$^+$ (Sigma-Aldrich) and CTP were soaked into RPo crystals (prepared as described above) by addition of 0.2 μl 30 mM NAD$^+$ and 40 mM CTP in 50% (v/v) RB to the crystallization drop, and incubated for 2 h at 22 °C. Crystals were transferred into reservoir solutions containing 1.5 mM NAD$^+$, 2 mM CTP, and 17.5% (v/v) (2R, 3R)-(-)-2,3-butanediol and were flash-cooled with liquid nitrogen.

Diffraction data were collected at APS beamline 19-ID-D (temperature, 100 K; wavelength, 0.98 Å), processed and scaled using HKL2000[28], and subjected to anisotropic correction using the UCLA MBI Diffraction Anisotropy server[30] (http://services.mbi.ucla.edu/anisoscale/). The structure was solved and refined using procedures analogous to those described above for RPo-pppApC. The final crystallographic model of RPo-NAD$^+$pC, refined to Ramachandran statistics of 97.81% favoured, 2.15% allowed, and 0.04% outliers, has been deposited in the PDB with accession code 5D4D.

Structure determination: RPo-dpCoApC. dpCoA (Sigma-Aldrich) and CTP were soaked into RPo crystals (prepared as described above) by addition of 0.2 μl 60 mM 3′-desphospho-CoA and 40 mM CTP in 50% (v/v) RB to the crystallization drop, and incubated for 2 h at 22 °C. Crystals were transferred into reservoir solutions containing 3 mM 3′-desphospho-CoA, 2 mM CTP, and 17.5% (v/v) (2R, 3R)-(-)-2,3-butanediol and were flash-cooled with liquid nitrogen.

Diffraction data were collected at APS beamline 19-ID-D (temperature, 100 K; wavelength, 0.98 Å), processed and scaled using HKL2000[28], and subjected to anisotropic correction using the UCLA MBI Diffraction Anisotropy server[30] (http://services.mbi.ucla.edu/anisoscale/). The structure was solved and refined using procedures analogous to those described above for RPo-pppApC. The final crystallographic model of dpCoApC, refined to Ramachandran statistics of 97.54% favoured, 2.43% allowed, and 0.03% outliers, has been deposited in the PDB with accession code 5D4E.

Analysis of dpCoA by liquid chromatography (LC)-UV. AMP (Sigma-Aldrich) and dpCoA were diluted to 1 mM in water (HPLC grade) before injection. LC-UV analyses were performed using a Waters 2960 HPLC system coupled with a Waters 2996 photodiode array detector. The flow rate from the Finnigan Surveyor pump was 0.3 ml min^{-1}. The autosampler temperature was 5 °C. The LC method used an YMC ODS-A 5 μm particle size 120 Å pore size column, 3.0 mm × 100 mm. The samples were separated using a gradient mobile phase consisting of 25 mM triethylammonium formate buffered to pH 3.0 in water (A) and methanol (B). The gradient condition was: 0–5 min, 100% A; 5–15 min, 100–30% A; 15–23 min, 30–0% A; 23–28 min, 0% A; 28–40 min, 100% A. Column temperature was 25 °C. Detector wave length was 260 nm. The instrument control, data acquisition, and data analysis were performed by MassLynx software. Triethylammonium acetate buffer (2.0 M) and formic acid (>95%) were purchased from Sigma-Aldrich.

18. Artsimovitch, I., Svetlov, V., Murakami, K. S. & Landick, R. Co-overexpression of *Escherichia coli* RNA polymerase subunits allows isolation and analysis of mutant enzymes lacking lineage-specific sequence insertions. *J. Biol. Chem.* **278,** 12344–12355 (2003).
19. Marr, M. T. & Roberts, J. W. Promoter recognition as measured by binding of polymerase to nontemplate strand oligonucleotide. *Science* **276,** 1258–1260 (1997).
20. Perdue, S. A. & Roberts, J. W. A backtrack-inducing sequence is an essential component of *Escherichia coli* σ^{70}-dependent promoter-proximal pausing. *Mol. Microbiol.* **78,** 636–650 (2010).
21. Kaplan, C. D., Larsson, K. M. & Kornberg, R. D. The RNA polymerase II trigger loop functions in substrate selection and is directly targeted by α-amanitin. *Mol. Cell* **30,** 547–556 (2008).
22. Schifano, J. M. *et al.* An RNA-seq method for defining endoribonuclease cleavage specificity identifies dual rRNA substrates for toxin MazF-mt3. *Nat. Commun.* **5,** 3538 (2014).
23. Vvedenskaya, I. O. *et al.* Massively systematic transcript end readout, "MASTER": transcription start site selection, transcriptional slippage, and transcript yields. *Mol. Cell* **60,** 953–965 (2015).
24. Baba, T. *et al.* Construction of *Escherichia coli* K-12 in-frame, single-gene knockout mutants: the Keio collection. *Mol. Syst. Biol.* **2,** 0008 (2006).
25. Goldman, S. R., Nair, N. U., Wells, C. D., Nickels, B. E. & Hochschild, A. The primary σ factor in *Escherichia coli* can access the transcription elongation complex from solution *in vivo. eLife* **4,** 4 (2015).
26. Čabart, P., Jin, H., Li, L. & Kaplan, C. D. Activation and reactivation of the RNA polymerase II trigger loop for intrinsic RNA cleavage and catalysis. *Transcription* **5,** e28869 (2014).
27. Murakami, K. S. Structural biology of bacterial RNA polymerase. *Biomolecules* **5,** 848–864 (2015).
28. Otwinowski, Z. & Minor, W. Processing of X-ray diffraction data collected in oscillation mode. *Methods Enzymol.* **276,** 307–326 (1997).
29. French, S. & Wilson, K. On the treatment of negative intensity observations. *Acta Crystallogr. A* **34,** 517–525 (1978).
30. Strong, M. *et al.* Toward the structural genomics of complexes: crystal structure of a PE/PPE protein complex from *Mycobacterium tuberculosis*. *Proc. Natl Acad. Sci. USA* **103,** 8060–8065 (2006).
31. Vagin, A. & Teplyakov, A. MOLREP: an automated program for molecular replacement. *J. Appl. Crystallogr.* **30,** 1022–1025 (1997).
32. Emsley, P., Lohkamp, B., Scott, W. G. & Cowtan, K. Features and development of Coot. *Acta Crystallogr. D* **66,** 486–501 (2010).
33. Adams, P. D. *et al.* PHENIX: a comprehensive Python-based system for macromolecular structure solution. *Acta Crystallogr. D* **66,** 213–221 (2010).

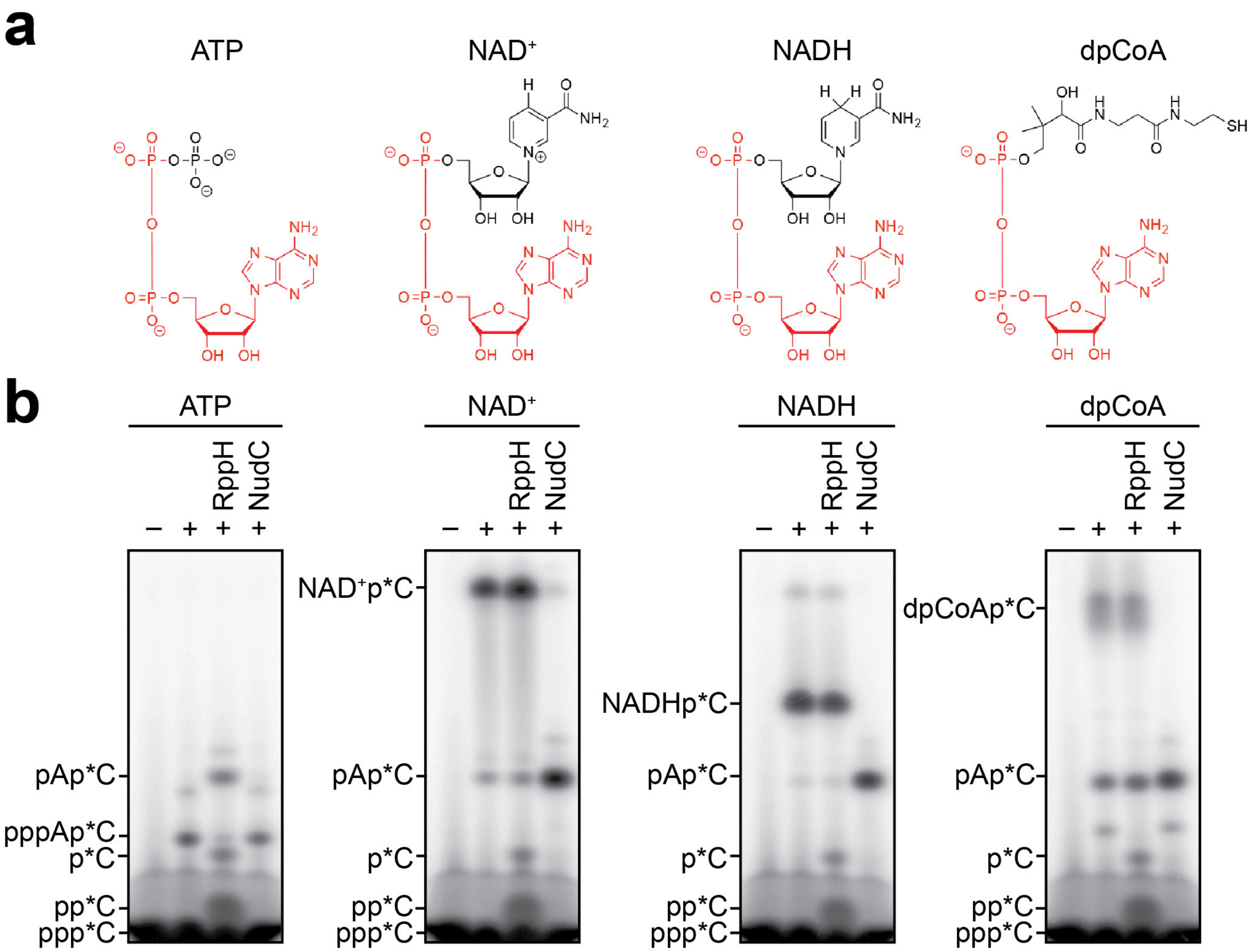

Extended Data Figure 1 | *De novo* transcription initiation by ATP and NCINs. a, Structures of ATP, NAD^+, NADH, and dpCoA. Red, identical atoms. **b**, Initial RNA products of *in vitro* transcription reactions with ATP, NAD^+, NADH, or dpCoA as initiating nucleotide and [α^{32}P]-CTP as extending nucleotide (*E. coli* RNAP; P_{rnaI}; see analogous data for P_{gadY} in Fig. 1b). Products were treated with RppH (processes 5′-triphosphate RNA to 5′-monophosphate RNA and 5′-NTP to 5′-NDP/5′-NMP[9,14]) or NudC (processes 5′-NAD^+/NADH-capped RNA to 5′-monophosphate RNA[6]) as indicated. For gel source data, see Supplementary Fig. 1.

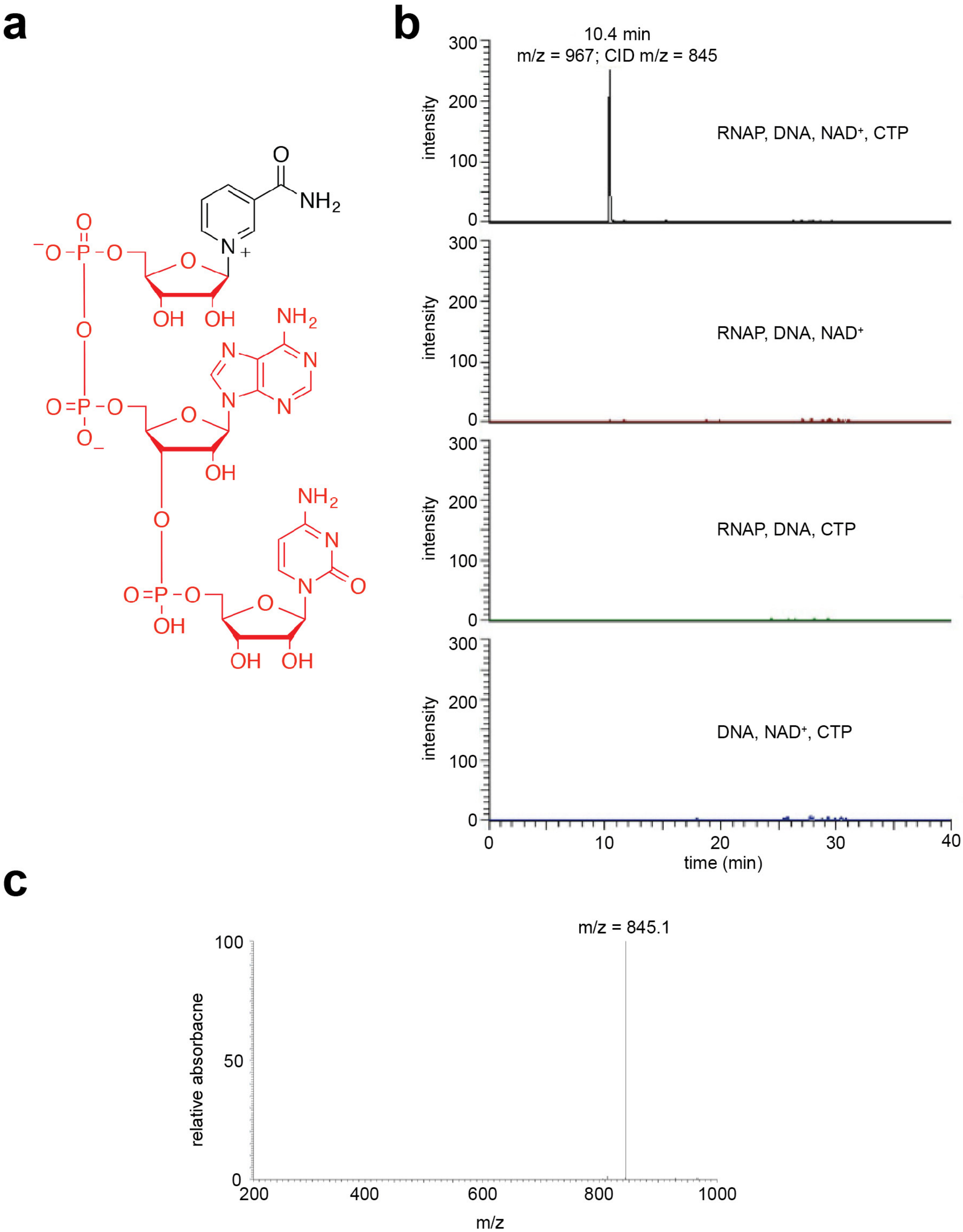

Extended Data Figure 2 | LC/MS/MS analysis of initial RNA products of *in vitro* transcription reactions with NAD$^+$ as initiating nucleotide and CTP as an extending nucleotide. a, Structure of NAD$^+$pC (red, atoms corresponding to CID-generated fragment ion). **b**, Extracted ion chromatogram (signal derived from detection of parent ion of $m/z = 967$ and CID fragment of $m/z = 845$ corresponding to NAD$^+$pC minus nicotinamide). Reactions contained the indicated components. **c**, Mass spectrum of CID fragment.

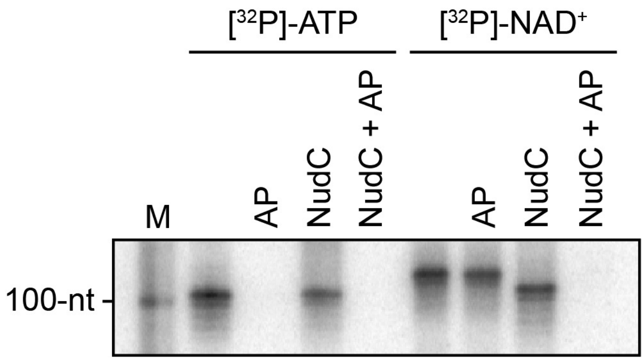

Extended Data Figure 3 | Sensitivity of full-length RNA products to alkaline phosphatase treatment. Full-length RNA products of *in vitro* transcription reactions with [γ^{32}P]-ATP or [α^{32}P]-NAD$^+$ as initiating nucleotide and CTP, GTP, and UTP as extending nucleotides (*E. coli* RNAP; P_{rnaI} fused to an A-less cassette). Products were treated with alkaline phosphatase (AP; processes 5′ phosphates) or NudC (processes 5′-NAD$^+$/NADH-capped RNA to 5′-monophosphate RNA[6]) as indicated. Results indicate that full-length RNA products generated in reactions with [α^{32}P]-NAD$^+$ as initiating nucleotides are not sensitive to AP until they are processed by NudC. M, 100-nucleotide marker. For gel source data, see Supplementary Fig. 1.

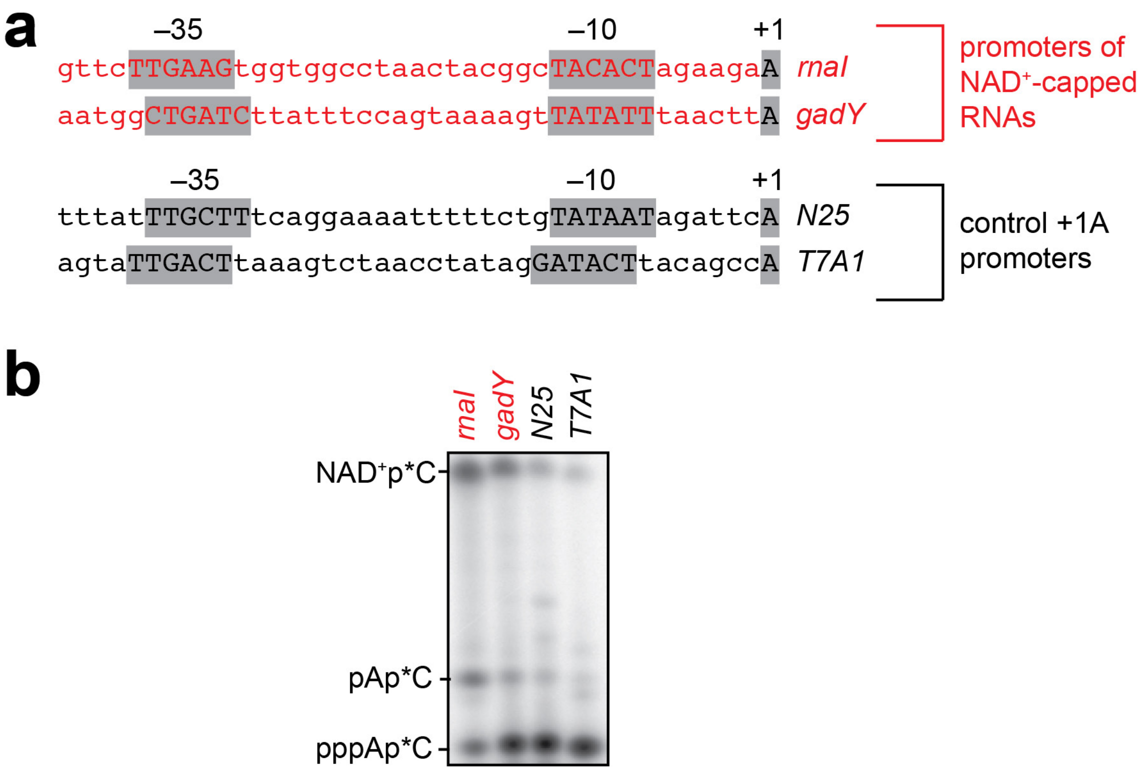

Extended Data Figure 4 | Promoter-sequence effects on efficiency of NCIN-mediated transcription initiation: NAD$^+$. a, Templates having *rnaI*, *gadY*, *N25*, and *T7A1* promoters used in the assays. **b**, Representative raw data from experiments of Fig. 2b. Initial RNA products of *in vitro* transcription reactions performed in the presence of 50 μM ATP and 1 mM NAD$^+$ as initiating nucleotides and [α^{32}P]-CTP as extending nucleotide (*E. coli* RNAP; P_{rnaI}, P_{gadY}, P_{N25}, or P_{T7A1}). (We note that contaminating AMP in the NAD$^+$ stock results in production of pAp*C.) For gel source data, see Supplementary Fig. 1.

a

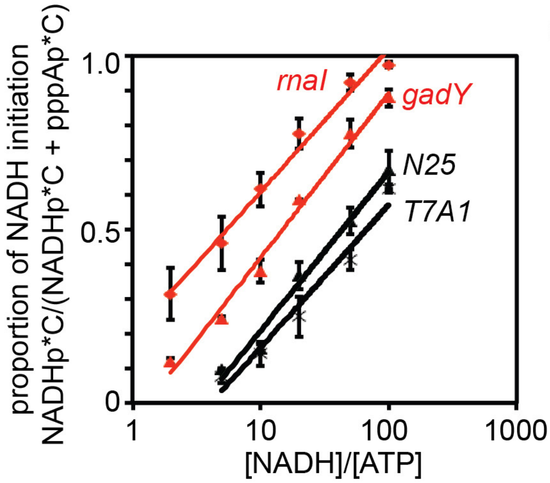

relative efficiency (kcat/Km,NADH)/(kcat/Km,ATP)	
rnaI	0.21 ± 0.05
gadY	0.067 ± 0.002
N25	0.023 ± 0.004
T7A1	0.014 ± 0.003

b

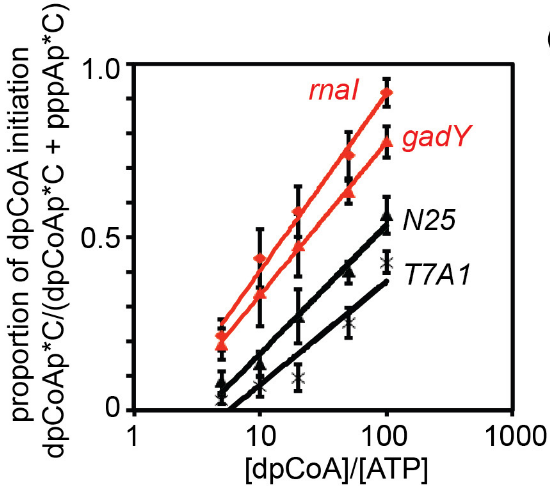

relative efficiency (kcat/Km,dpCoA)/(kcat/Km,ATP)	
rnaI	0.068 ± 0.008
gadY	0.041 ± 0.008
N25	0.018 ± 0.007
T7A1	0.0057 ± 0.002

Extended Data Figure 5 | Promoter-sequence effects on efficiency of NCIN-mediated transcription initiation: NADH and dpCoA. a, Left, dependence of NADH capping on [NADH]/[ATP] ratio (mean ± s.e.m. of three determinations). Right, relative efficiencies of NADH capping. (*E. coli* RNAP; P_{rnaI}, P_{gadY}, P_{N25}, or P_{T7A1}). **b**, Left, dependence of dpCoA-capping on [dpCoA]/[ATP] ratio (mean ± s.e.m. of three determinations). Right, relative efficiencies of dpCoA capping. (*E. coli* RNAP; P_{rnaI}, P_{gadY}, P_{N25}, or P_{T7A1}).

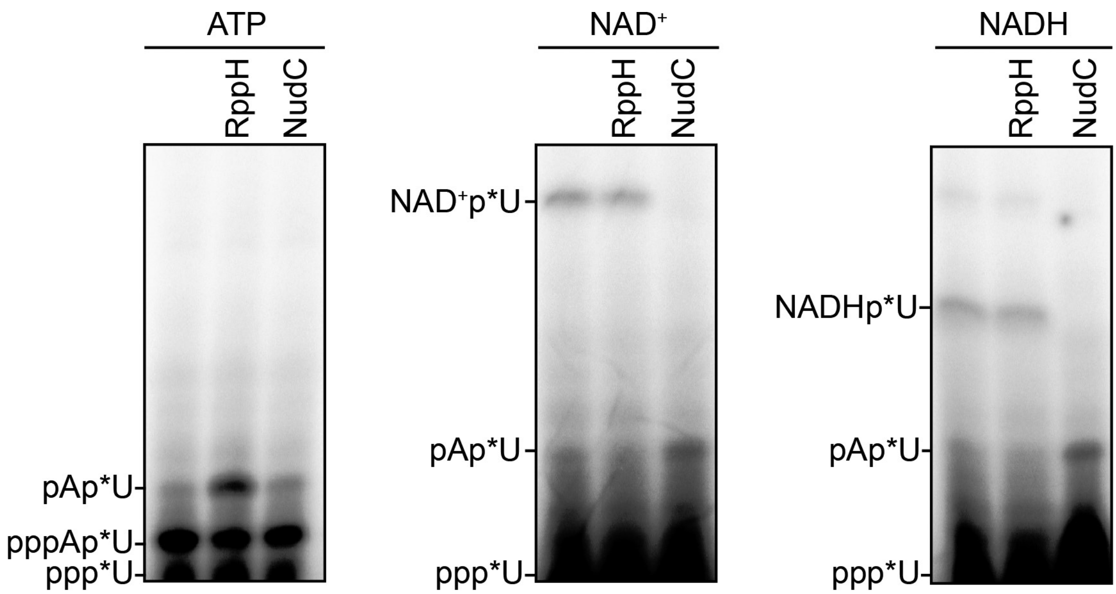

Extended Data Figure 6 | NCIN-mediated *de novo* transcription initiation by eukaryotic RNAP II. Initial RNA products of *in vitro* transcription reactions with ATP, NAD^+, or NADH as initiating nucleotide and [α^{32}P]-UTP as extending nucleotide. Reactions were performed with yeast RNAP II and an artificial bubble transcription initiation template. Products were treated with RppH or NudC as indicated. For gel source data, see Supplementary Fig. 1.

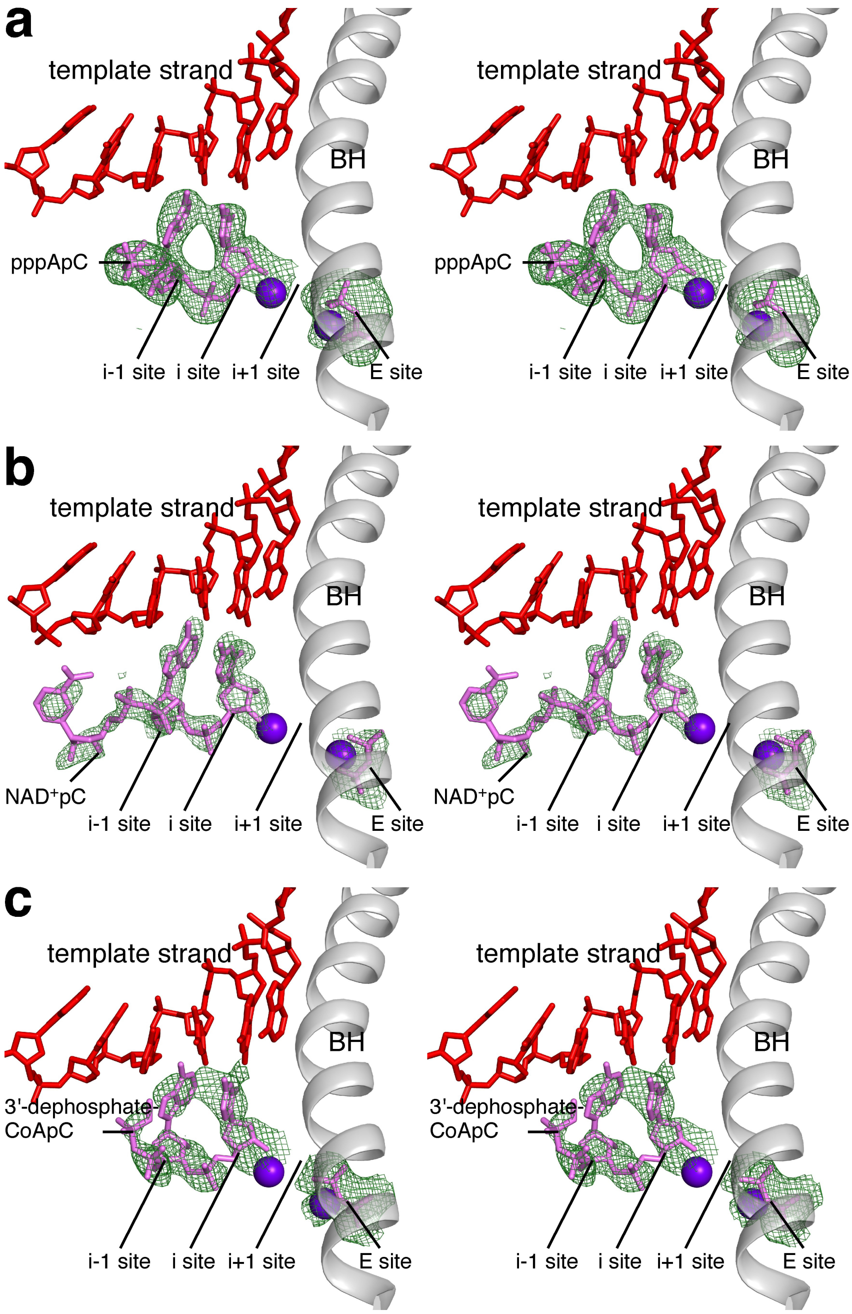

Extended Data Figure 7 | Structural basis of NCIN-mediated transcription initiation: stereoviews. a–c, Crystal structures of RPo-pppApC, RPo-NAD$^+$pC, and RPo-dpCoApC. Stereo views of density and fit for initial RNA product. Green mesh, $F_o - F_c$ omit map (contoured at 2.5σ in **a**, **b** and 2.2σ in **c**); red, DNA; pink, RNA product and diphosphate in 'E site' (see refs 15–17); violet spheres, Mg^{2+}(I) and Mg^{2+}(II); grey, RNAP bridge helix.

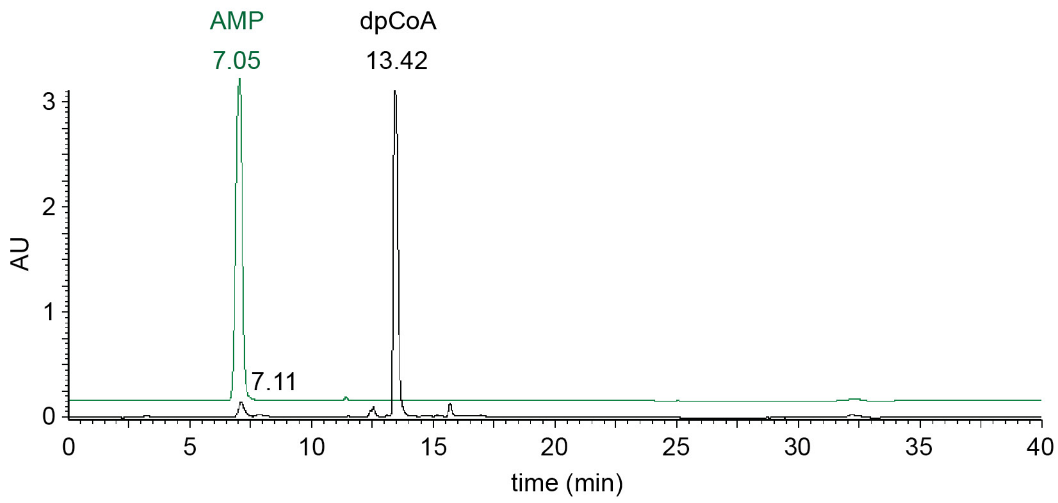

Extended Data Figure 8 | AMP content of dpCoA stock. HPLC chromatogram of dpCoA stock (Sigma-Aldrich, lot SLBJ2886V; 50 nmol). Green, HPLC chromatogram of AMP (20 nmol). Comparison of chromatograms indicates that the dpCoA stock contains ~2% AMP. The observation that the dpCoA stock contains ~2% AMP in the dpCoA stock accounts for the formation of pApC in reactions performed with dpCoA (Fig. 1b).

Extended Data Table 1 | Data collection and refinement statistics

	RPo-pppApC	RPo-NAD$^+$pC	RPo-dpCoApC
Data collection			
Space group	P2(1)	P2(1)	P2(1)
Cell dimensions			
a, *b*, *c* (Å)	186.0, 103.6, 297.4	185.0, 103.5, 296.3	185.8, 103.9, 297.1
α, β, γ (°)	90.0, 98.3, 90.0	90.0, 98.3, 90.0	90.0, 98.5, 90.0
Resolution (Å)	50.00-3.30(3.36-3.30) *	50.00-3.00(3.05-3.00) *	40.00-3.10(3.15-3.10) *
R_{sym} or R_{merge}	0.185(0.954)	0.119(0.920)	0.120(0.840)
$I/\sigma I$	8.7(1.7)	10.6(1.5)	10.4(1.4)
Completeness (%)	0.961(0.875)	0.979(0.934)	0.989(0.960)
Redundancy	5.4(5.0)	4.0(3.7)	3.8(3.5)
Refinement			
Resolution (Å)	50.00-3.30	50.00-3.00	40.00-3.10
No. reflections	154105	218773	187101
R_{work}/R_{free}	0.211/0.258	0.201/0.254	0.210/0.247
No. atoms			
Protein	55006	54790	55297
Ligand/ion	1536	1664	1651
Water	58	895	775
B-factors			
Protein	48.0	31.2	49.1
Ligand/ion	68.0	65.3	80.4
Water	12.9	11.7	27.4
R.m.s deviations			
Bond lengths (Å)	0.004	0.008	0.004
Bond angles (°)	0.79	0.95	0.69

*Highest resolution shell is shown in parentheses.

doi:10.1038/nature18636

Allosteric nanobodies reveal the dynamic range and diverse mechanisms of G-protein-coupled receptor activation

Dean P. Staus[1]*, Ryan T. Strachan[2]*, Aashish Manglik[3]*, Biswaranjan Pani[1], Alem W. Kahsai[1], Tae Hun Kim[4], Laura M. Wingler[1], Seungkirl Ahn[1], Arnab Chatterjee[1], Ali Masoudi[1], Andrew C. Kruse[5], Els Pardon[6,7], Jan Steyaert[6,7], William I. Weis[3,8], R. Scott Prosser[4], Brian K. Kobilka[3], Tommaso Costa[9] & Robert J. Lefkowitz[1,10,11]

G-protein-coupled receptors (GPCRs) modulate many physiological processes by transducing a variety of extracellular cues into intracellular responses. Ligand binding to an extracellular orthosteric pocket propagates conformational change to the receptor cytosolic region to promote binding and activation of downstream signalling effectors such as G proteins and β-arrestins. It is well known that different agonists can share the same binding pocket but evoke unique receptor conformations leading to a wide range of downstream responses ('efficacy')[1]. Furthermore, increasing biophysical evidence, primarily using the β_2-adrenergic receptor (β_2AR) as a model system, supports the existence of multiple active and inactive conformational states[2–5]. However, how agonists with varying efficacy modulate these receptor states to initiate cellular responses is not well understood. Here we report stabilization of two distinct β_2AR conformations using single domain camelid antibodies (nanobodies)—a previously described positive allosteric nanobody (Nb80)[6,7] and a newly identified negative allosteric nanobody (Nb60). We show that Nb60 stabilizes a previously unappreciated low-affinity receptor state which corresponds to one of two inactive receptor conformations as delineated by X-ray crystallography and NMR spectroscopy. We find that the agonist isoprenaline has a 15,000-fold higher affinity for β_2AR in the presence of Nb80 compared to the affinity of isoprenaline for β_2AR in the presence of Nb60, highlighting the full allosteric range of a GPCR. Assessing the binding of 17 ligands of varying efficacy to the β_2AR in the absence and presence of Nb60 or Nb80 reveals large ligand-specific effects that can only be explained using an allosteric model which assumes equilibrium amongst at least three receptor states. Agonists generally exert efficacy by stabilizing the active Nb80-stabilized receptor state (R_{80}). In contrast, for a number of partial agonists, both stabilization of R_{80} and destabilization of the inactive, Nb60-bound state (R_{60}) contribute to their ability to modulate receptor activation. These data demonstrate that ligands can initiate a wide range of cellular responses by differentially stabilizing multiple receptor states.

The allosteric behaviour of GPCRs is responsible for the complex signalling properties associated with these important regulators of human physiology. GPCR allostery, defined here as a linkage between the extracellular orthosteric ligand pocket and the intracellular G-protein-binding pocket, has long been analysed by pharmacological methods[8–10] (see Supplementary Information). Conformational changes within a GPCR induced by agonist binding can enhance the affinity and binding of intracellular signalling transducers, such as G proteins and β-arrestins. Conversely, transducer coupling further enhances agonist affinity, resulting in the formation of the ternary complex of receptor, intracellular signalling transducer, and ligand (Fig. 1a). The conceptual framework of the ternary complex model equates the magnitude of these affinity changes with the strength of transducer activation in cells[11,12], as demonstrated for several GPCR systems[13–16]. However, the structural basis underlying these allosteric relationships and how they relate to ligand efficacy is not well understood.

Ligand-dependent GPCR activation has traditionally been conceptualized as a conversion between a single inactive and a single active receptor state. However, recent studies using various spectroscopic techniques have identified multiple inactive and active receptor states, suggesting that the mechanisms underlying receptor activation may be more complex than previously thought[2–5]. To better understand how ligands with varying efficacies may differentially regulate these conformations, we sought to develop reagents to stabilize specific inactive and active conformations of the β_2AR. We and others have previously used Nb80, a Gs mimetic nanobody, to stabilize an active conformation of the β_2AR[6,7]. Indeed, competition radioligand binding assays using iodinated cyanopindolol ([^{125}I]CYP) and β_2AR reconstituted into high-density lipoprotein (HDL) particles (nanodiscs) demonstrated that Nb80 increases the affinity of the agonist isoprenaline by 75-fold (Fig. 1b), which is similar, but not identical, to the 33-fold increase seen in the presence of purified heterotrimeric Gs (Fig. 1b). To investigate the pharmacological properties of the inactive receptor, we identified a nanobody (Nb60) that preferentially bound inverse-agonist-bound β_2AR[7]. Remarkably, though the affinity of the receptor for agonist in the absence of Gs or Nb80 was presumed to reflect the pharmacological properties of the inactive state, the presence of Nb60 reduced agonist affinity by approximately 70-fold (Fig. 1b). The effects of Nb60 and Nb80 on radiotracer affinity were negligible and could not account for the large changes in affinity (Extended Data Table 1).

To further quantify the allosteric effects of Nb60, Nb80, and Gs on agonist binding, we measured isoprenaline affinity with radioligand competition binding over a range of nanobody/Gs concentrations (Extended Data Fig. 1). As the concentration of allosteric modulator increases, the effect on isoprenaline affinity becomes saturable, reaching two opposite plateau values with Nb60 and Nb80 or Gs (Fig. 1c). This is a hallmark pattern of true allosteric interactions, with

[1]Department of Medicine, Duke University Medical Center, Durham, North Carolina 27710, USA. [2]Department of Pharmacology, University of North Carolina, Chapel Hill, North Carolina 27599, USA. [3]Department of Molecular and Cellular Physiology, Stanford University School of Medicine, Stanford, California 94305, USA. [4]Department of Chemistry, University of Toronto, University of Toronto Mississauga, 3359 Mississauga Road North, Mississauga, Ontario L5L 1C6, Canada. [5]Department of Biological Chemistry and Molecular Pharmacology, Harvard Medical School, Boston, Massachusetts 02115, USA. [6]Structural Biology Brussels, Vrije Universiteit Brussel, Pleinlaan 2, 1050 Brussels, Belgium. [7]Structural Biology Research Center, VIB, Pleinlaan 2, 1050 Brussels, Belgium. [8]Department of Structural Biology, Stanford University School of Medicine, Stanford, California 94305, USA. [9]Department of Pharmacology, Istituto Superiore di Sanità, Rome 00161, Italy. [10]Department of Biochemistry, Duke University Medical Center, Durham, North Carolina 27710, USA. [11]Howard Hughes Medical Institute, Chevy Chase, Maryland 20815-6789, USA.
*These authors contributed equally to this work.

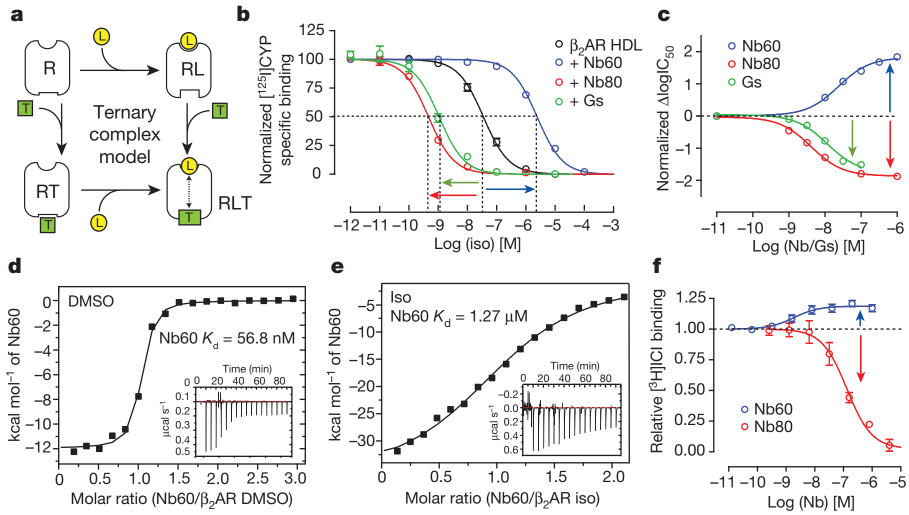

Figure 1 | Allosteric nanobodies have opposing effects on agonist affinity for the β$_2$AR. **a**, Schematic of the ternary complex model. Ligand (L) affinity to receptor (R) increases in the presence of transducer (T), this allosteric linkage is denoted by dashed line with arrows. **b**, Compared to the absence of modulator, Nb60 decreases isoprenaline affinity (negative cooperativity) and Nb80 and Gs increases affinity (positive cooperativity) as assessed by radioligand competition assays using β$_2$AR HDL particles. **c**, The effects of Nb60 and Nb80 or Gs on isoprenaline affinity are saturable functions of their concentration. **d**, **e**, The affinity of Nb60 for unliganded β$_2$AR (**d**), represented by a tight isotherm sigmoidal binding curve[23], is reduced in the presence of isoprenaline (iso) (**e**), as determined by isothermal titration calorimetry. **f**, Nb60 dose-dependently increases and Nb80 decreases the binding of the radiolabelled antagonist [^{3}H]ICI-118,551 to the β$_2$AR. All radioligand binding studies represent a minimum of three independent experiments with deviation shown as the standard error.

the net log-change in isoprenaline affinity at saturating concentration of nanobody/Gs gauging the extent of cooperativity between nanobody and agonist binding (negative for Nb60 or positive for Nb80 and Gs) (see Supplementary Information). As predicted by the ternary complex model, this coupling energy, termed α, must be constant—the effect of bound nanobody on agonist binding is reciprocal to the effect of bound agonist on nanobody binding. To verify such a prediction, we measured the affinity of Nb60 for the β$_2$AR in the absence and presence of agonist (isoprenaline) using isothermal titration calorimetry (Fig. 1d, e). As expected, the affinity of Nb60 for β$_2$AR decreased in the presence of isoprenaline. Consistent with its preference for the inactive state, Nb60 dose-dependently increased binding of the radiolabelled inverse antagonist [^{3}H]ICI-118,551 to the β$_2$AR, whereas binding was decreased in the presence of Nb80 (Fig. 1f). Together, these data show that Nb60 and Nb80 are potent allosteric modulators that can be used to stabilize inactive and active β$_2$AR states.

The decrease in isoprenaline affinity observed in the presence of Nb60 reveals a previously unappreciated 'very-low-affinity' state (K_{VL}) in competition binding experiments. The affinity of agonist for an uncoupled GPCR has traditionally been referred to as the 'low-affinity' (K_L) state; however, our results show that K_L values reflect binding of an ensemble of conformations that exchange rapidly over the course of the binding reaction. This phenomenon is probably conserved among GPCRs, as a similar K_{VL} state has been observed with the A_{2A} adenosine receptor using an antibody fragment[17]. This conformational heterogeneity is consistent with recent spectroscopic and computational studies, which have shown that the β$_2$AR exists in multiple inactive, intermediate, and active conformations that exchange within milliseconds[2–5,18]. To assess which receptor state Nb60 stabilizes, we conducted ^{19}F fluorine NMR spectroscopy of β$_2$AR labelled with a trifluoroacetanilide probe at the endogenous residue C265 located at the cytoplasmic end of transmembrane 6 (TM6). As shown previously, the unliganded β$_2$AR exists in two equally distributed inactive states (termed S1 and S2) that exchange on a fast timescale (700 ± 137 μs), and complete conversion into the active S4 state requires both agonist and transducer binding[5] (Fig. 2a, b). Using structural insights from double electron–electron resonance studies, S1 was identified as an inactive state with an interaction between TM3 residue R131$^{3.50}$ (superscripts indicate Ballesteros–Weinstein numbering for GPCRs[19]) and E268$^{6.30}$ in TM6 (ref. 5), commonly termed the ionic lock. The ionic lock has previously been shown to be important in maintaining the inactive conformation of β$_2$AR, as charge-neutralizing mutations at these positions increase receptor constitutive activity[20]. Additionally, the S2 conformation was also identified as an inactive state but with a disengaged ionic lock (Fig. 2b). The binding of G protein or other positive allosteric modulators such as Nb80 lowers the energy of the active receptor states, driving the receptor from S2 towards active conformations[5]. The ^{19}F NMR spectra showed that the addition of Nb60 to β$_2$AR bound to the inverse agonist carazolol shifted the S1–S2 equilibrium towards the inactive S2 state (Fig. 2c), providing a mechanism for its negative cooperative effects on isoprenaline affinity. Given the broad NMR line shape (Fig. 3c, red line) of the β$_2$AR when bound to carazolol and Nb60, we conducted Carr–Purcell–Meiboom–Gill (CPMG)[21] relaxation dispersion measurements to measure potential conformational heterogeneity. We found that the β$_2$AR when bound to Nb60 and carazolol interconverts (860 ± 530 s^{-1}) between S1 and S2, but is predominantly found (75–90%) in the S2 inactive state (Extended Data Fig. 1d).

To further decipher how Nb60 induces a negative cooperative effect on agonist binding, we determined a 3.2 Å X-ray crystal structure of a ternary complex comprised of β$_2$AR, Nb60, and the inverse agonist carazolol (Fig. 2d–f, Extended Data Fig. 2 and Extended Data Table 2). The complementary determining region 3 (CDR3) of Nb60 inserts into a similar β$_2$AR allosteric pocket as G protein and Nb80, located between the cytoplasmic ends of TM3, TM4, and TM6 (Fig. 2d, e). We found that T102 and Y106 in Nb60 bridge an interaction between residues R131$^{3.50}$ and E268$^{6.30}$. This interaction does not exist in the absence of Nb60 (Protein Data Bank (PDB) accession code 2RH1), indicating that Nb60 stabilizes an inactive conformation through interactions with the β$_2$AR ionic lock (Fig. 2e). However, this polar network appears 'disengaged' compared to the fully closed ionic lock in the β$_1$-adrenergic receptor (PDB accession code 2YCW)[22] (Fig. 2e), thus supporting the ^{19}F NMR data showing that Nb60 specifically stabilizes the S2 inactive state. The insertion of Nb60 F103 into a hydrophobic pocket in the β$_2$AR may also contribute to the affinity and/or negative allosteric properties of Nb60 (Extended Data Fig. 2c). Confirming the importance of T102 and F103 for the β$_2$AR–Nb60 interaction, alanine mutations at these positions inhibited Nb60 binding to the β$_2$AR and the negative cooperative effects on isoprenaline binding (Extended

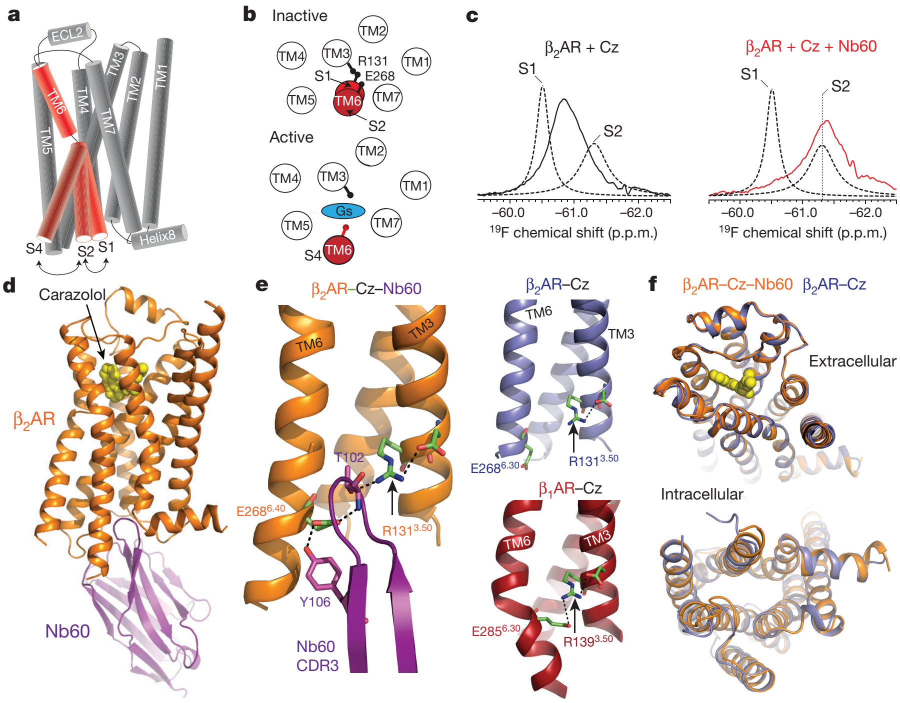

Figure 2 | Nb60 stabilizes the S2 inactive state by coordinating the β_2AR ionic lock. a, b, Cartoon depicting a side (**a**) or cytoplasmic (**b**) view of the β_2AR transmembranes (TM). Conversion from the two inactive states (S1 and S2) to the active S4 state requires both agonist and transducer (G protein) binding and is represented by a 14 Å outward movement of TM6. **c**, ^{19}F NMR spectroscopy of the β_2AR with the antagonist carazolol (Cz) ± Nb60. **d**, The 3.2 Å structure of the β_2AR bound to carazolol (Cz) and Nb60 (β_2AR–Cz–Nb60). **e**, Coordination of β_2AR ionic lock (R131 and E268) by Nb60 CDR3 residues T102 and Y106. For comparison, a disengaged and fully formed ionic lock are shown by the β_2AR–Cz (PDB accession code 2RH1) and β_1AR–Cz (PDB accession code 2YCZ), respectively. Hydrogen bonds are shown as black dotted lines. **f**, Overlay of β_2AR–Cz and β_2AR–Cz–Nb60 structures.

Data Fig. 2e, f). Other than changes within the ionic lock, the overall structure of β_2AR bound to Nb60 is highly similar to the previously determined inactive β_2AR structure bound to carazolol alone (root mean squared deviation (r.m.s.d.) of 0.3 Å for the transmembrane domains and orthosteric binding pocket, Fig. 2f). Taken together, the pharmacological, biophysical, and crystallographic studies show that Nb60 exerts its negative allosteric effect on agonist binding by stabilizing the S2 inactive β_2AR conformation.

Our observation that isoprenaline bound to the Nb80-stabilized active β_2AR with approximately 15,000-fold greater affinity than to the Nb60-stabilized inactive β_2AR (Fig. 1b, c) provides a measurement of the full allosteric power of an agonist to activate a GPCR. The large free energy difference ($-24\,\mathrm{kJ\,mol^{-1}}$) between these states is probably important for GPCR function, allowing agonist-stimulated activity to be significantly higher than that of the basal activity. As simulated for a full agonist in Fig. 3a, the overall affinity shift from inactive to active receptor (black arrow) is comprised of two components, the negative cooperative (α) effects of Nb60 (αNb60, blue) and positive effects of Nb80 (αNb80, red). Given the complexities and limitations of using NMR and crystallography to gain mechanistic insights into ligand activation of a GPCR, we used a pharmacological approach to quantify αNb60 and αNb80 for 17 β_2AR ligands of varying efficacy (Fig. 3b and Extended Data Fig. 3).

We first identified a significant positive correlation ($r = 0.8514$, $P = 0.004$) between αNb80 values (K_L/K_H ratios) and the relative intrinsic efficacies (τ values) of various ligands obtained from cellular G-protein assays (Extended Data Fig. 4a, b). This finding provides additional support for the claim that Nb80 exerts allosteric effects that mimic those of a G protein. It also confirms our previous reports that ligand efficacy is not a product of modified downstream signalling events but is rather achieved at the level of ternary complex interactions, reflecting the allosteric interactions between different ligands and transducers[12]. Interestingly, we find no significant correlation between

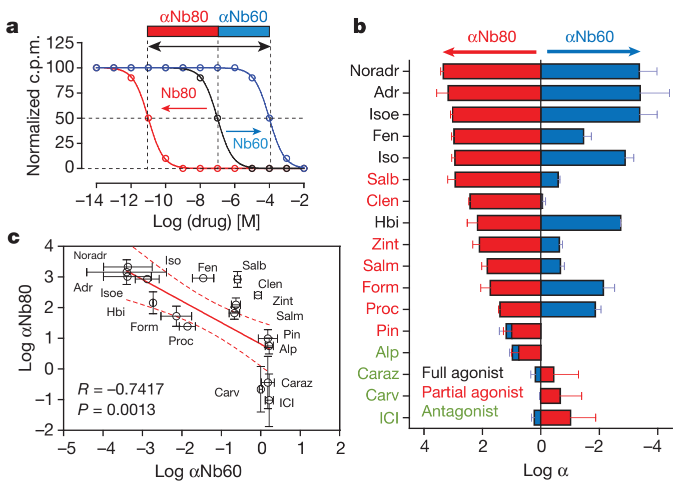

Figure 3 | Nb60 and Nb80 have varying effects on the affinity of different β_2AR ligands. a, Schematic depicting the use of equilibrium radioligand binding studies to quantify the cooperativity (α) between Nb60 or Nb80 binding and ligand affinity (see Methods and Supplementary Information). c.p.m., counts per minute. **b**, Cooperativity values for Nb60 (αNb60) and Nb80 (αNb80) for β_2AR ligands with varying efficacies. Ligands are ordered by magnitude of αNb80. **c**, Correlation plot of αNb60 and αNb80; regression shown as solid red line with 95% confidence interval (dotted red line). All α values derived from at least three independent radioligand binding experiments with the deviation depicted as standard error. Adr, adrenaline; alp, alprenolol; carv, carvedilol; caraz, carazolol; clen, clenbuterol; fen, fenoterol; form, formoterol; hbi, hydroxybenzyl isoproterenol; ICI, ICI-118,551; iso, isoprenaline; isoe, isoetharine; pin, pindolol; proc, procaterol; salb, salbutamol; salm, salmeterol; zint, zinterol.

αNb60 and ligand efficacy, providing the first evidence, to our knowledge, that ligands perceive the Nb60 and Nb80 stabilized receptor states differently (Extended Data Fig. 4c). We observed a significant negative correlation ($r = 0.7417$, $P = 0.0013$) between αNb60 and αNb80 values (Fig. 3c) across all ligands, suggesting these nanobodies stabilize functionally opposite conformations. However, the relationship between αNb60 and αNb80 was unexpectedly complex (Fig. 3b). For example, several full agonists exhibited comparable levels of positive (Nb80) and negative (Nb60) cooperativity (noradrenaline, adrenaline, and isoprenaline), whereas some partial agonists displayed patterns with surprising discrepancies (clenbuterol, salbutamol, and zinterol) (Fig. 3b). Importantly, for a subset of these ligands we confirmed that the allosteric effects of Nb80 are consistent with those elicited by the physiological transducer heterotrimeric Gs (Extended Data Fig. 5a, b), Moreover, the surprisingly divergent, ligand-specific effects of Nb60 were also observed with another inactive state-stabilizing nanobody, A11 (Extended Data Fig. 5c). Together, these data indicate that the ligand-specific effects of Nb80 and Nb60 are not nanobody-specific, but rather reflect how ligands perceive specific receptor conformations.

We next tested two different allosteric models to try to explain how the different conformations stabilized by Nb60 and Nb80 can generate the observed cooperativities. First we tested whether the dynamics of receptor states can be sufficiently modelled as a simple interconversion between two allosteric conformations, despite biophysical evidence for multiple inactive and active receptor states. Accordingly, we attempted to fit the experimentally observed αNb60 and αNb80 values for all ligands using the two-state model of receptor activation (Fig. 4a). In this simulation, the equilibrium constant J represents the distribution of inactive (R_{60}) and active (R_{80}) receptor states in the absence of ligand. The variable β describes the effect that each ligand has on the distribution of receptor states (J), with agonists displaying larger β values (that is, they stabilize more R_{80} relative to R_{60}). As shown in Fig. 4a, the theoretical curve generated by varying β in the two-state model (dotted black line) failed to accurately predict the experimentally determined αNb60 and αNb80 values for 30% of ligands tested, consisting primarily of partial agonists (dotted red oval). A different equilibrium J constant would be required to explain the cooperativity of these ligands with the same two-state model. These findings argue that ligands must modulate more than these two states to control receptor activation.

Biophysical evidence supports the existence of at least three predominant receptor states; therefore we hypothesized that a three-state model (Fig. 4b) may better explain the experimentally observed αNb60 and αNb80 values. In this model, the equilibria of R_{80} (J_1) and R_{60} (J_2) can be regulated separately by ligands, described by the allosteric factors β_1 and β_2, respectively. We found that the observed cooperativities for 12 ligands (Fig. 4b, class I, orange), which encompasses all the full agonists, can be predicted if these ligands primarily stabilize the active R_{80} state, while having negligible effects on the inactive R_{60} state. The efficacy of these ligands is thus directly proportionally related to their effect on the R_{80} equilibrium (β_1), such that highly efficacious ligands have a large β_1 (adrenaline), whereas partial agonists have a lower β_1 (clenbuterol). In contrast, the observed cooperativity of other partial agonists (classes II and III) could only be predicted by differentially modulating the R_{80} and R_{60} equilibria, suggesting these ligands regulate multiple receptor states to control receptor activation. For example, even though clenbuterol (class I), zinterol (class II), and procaterol (class III) are similar partial agonists (Extended Data Fig. 4a), the mechanism by which they promote receptor activation varies based on their ability to differentially stabilize and destabilize the active (R_{80}) and inactive (R_{60}) states, respectively (Fig. 4b). Importantly, divergences in receptor activation mechanisms can only be uncovered by studying

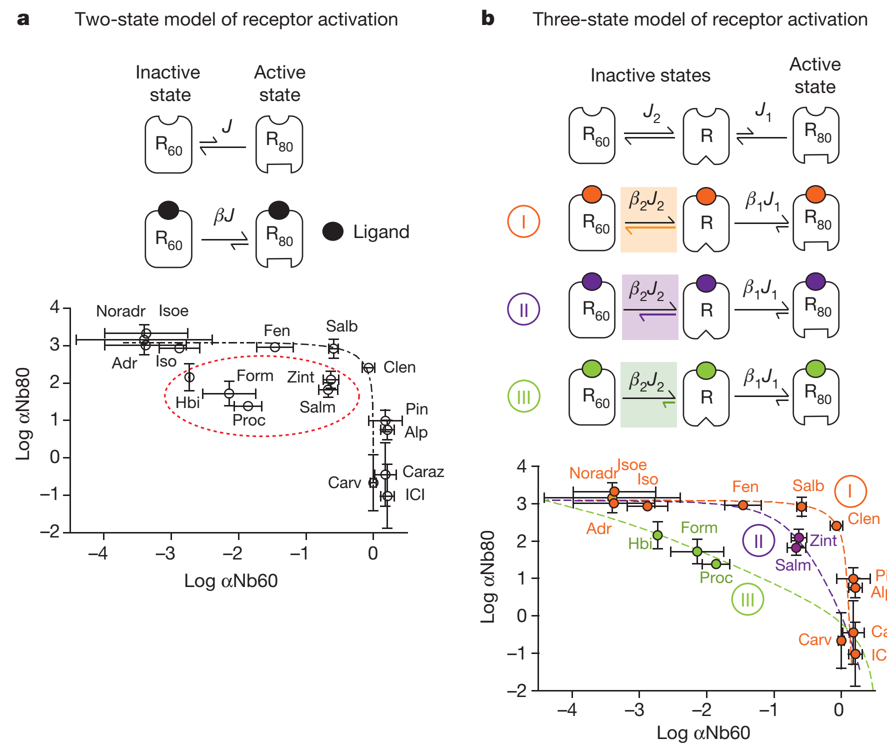

Figure 4 | β_2AR agonists differentially stabilize receptor states to regulate receptor activation. a, b, Illustration of a two-state (**a**), or three-state (**b**), model of receptor activation describing the effect of β_2AR ligands on receptor conformations stabilized by Nb60 (R_{60}) or Nb80 (R_{80}). The equilibrium (J) between receptor states can be influenced by ligand binding through the allosteric factor β. The theoretical cooperativity (α) between nanobody and ligand binding derived from the two-state model (dashed black line) fails to predict the observed α values for a subset of ligands (dashed red oval). However, the observed cooperativity values can be accurately predicted using an allosteric model in which ligands can differentially modulate three independent receptor states (three-state). Certain ligands (orange) primarily stabilize the active R_{80} state, whereas others (purple or green) can stabilize R_{80} but simultaneously destabilize the inactive R_{60} state. All α values are derived from at least three independent radioligand binding experiments with the deviation depicted as standard error.

ligand effects at both the Nb60-stabilized and Nb80-stabilized β_2AR states. The inability to accurately predict efficacy (G-protein activation) based on ligand class supports the notion that molecular efficacy is a complex process that probably involves many more unresolved receptor states.

These findings reshape our current understanding of GPCR activation. For almost 40 years, studies of these receptors have been guided by the understanding that they can exist in two forms, one of high affinity for agonists (active, coupled to the G protein) and one of low affinity (inactive, not coupled to the G protein), which are interconverted by the cooperative interaction of agonists and guanine nucleotides. We used conformationally sensitive nanobodies (Nb60 and Nb80) to reveal that Nb60-bound β_2AR has affinity ~100-fold lower than the previously described low-affinity inactive state, which is in fact an 'average' of multiple, rapidly interconverting inactive and active states. The implication is that the full allosteric potential of the β_2AR is orders of magnitude greater than formerly appreciated. Moreover, binding cooperativity between ligands of varying efficacy and Nb60 and Nb80 could only be explained by models featuring multiple (at least three) receptor states, which are differentially stabilized and/or destabilized by various agonists. Thus these data demonstrate a previously unsuspected heterogeneity in the mechanisms by which different agonists stimulate biological responses. In view of the general conservation of GPCR activation mechanisms, and a report of an A_{2A} adenosine receptor 'Nb60-like' state, these findings will probably apply to many GPCRs. Given the primacy of GPCRs as therapeutic targets, these new findings and concepts may also provide a basis for the design of drugs with potentially new therapeutic properties.

Online Content Methods, along with any additional Extended Data display items and Source Data, are available in the online version of the paper; references unique to these sections appear only in the online paper.

Received 27 November 2015; accepted 10 June 2016.
Published online 13 July 2016.

1. Kahsai, A. W. *et al.* Multiple ligand-specific conformations of the β_2-adrenergic receptor. *Nature Chem. Biol.* **7,** 692–700 (2011).
2. Liu, J. J., Horst, R., Katritch, V., Stevens, R. C. & Wüthrich, K. Biased signaling pathways in β_2-adrenergic receptor characterized by ^{19}F-NMR. *Science* **335,** 1106–1110 (2012).
3. Kofuku, Y. *et al.* Efficacy of the β_2-adrenergic receptor is determined by conformational equilibrium in the transmembrane region. *Nature Commun.* **3,** 1045 (2012).
4. Nygaard, R. *et al.* The dynamic process of β_2-adrenergic receptor activation. *Cell* **152,** 532–542 (2013).
5. Manglik, A. *et al.* Structural insights into the dynamic process of β_2-adrenergic receptor signaling. *Cell* **161,** 1101–1111 (2015).
6. Rasmussen, S. G. *et al.* Structure of a nanobody-stabilized active state of the β_2 adrenoceptor. *Nature* **469,** 175–180 (2011).
7. Staus, D. P. *et al.* Regulation of β_2-adrenergic receptor function by conformationally selective single-domain intrabodies. *Mol. Pharmacol.* **85,** 472–481 (2014).
8. Colquhoun, D. The quantitative analysis of drug-receptor interactions: a short history. *Trends Pharmacol. Sci.* **27,** 149–157 (2006).
9. Onaran, H. O. & Costa, T. Allosteric coupling and conformational fluctuations in proteins. *Curr. Protein Pept. Sci.* **10,** 110–115 (2009).
10. Colquhoun, D. Binding, gating, affinity and efficacy: the interpretation of structure–activity relationships for agonists and of the effects of mutating receptors. *Br. J. Pharmacol.* **125,** 924–947 (1998).
11. De Lean, A., Stadel, J. M. & Lefkowitz, R. J. A ternary complex model explains the agonist-specific binding properties of the adenylate cyclase-coupled β-adrenergic receptor. *J. Biol. Chem.* **255,** 7108–7117 (1980).
12. Strachan, R. T. *et al.* Divergent transducer-specific molecular efficacies generate biased agonism at a G protein-coupled receptor (GPCR). *J. Biol. Chem.* **289,** 14211–14224 (2014).
13. Wreggett, K. A. & De Léan, A. The ternary complex model. Its properties and application to ligand interactions with the D2-dopamine receptor of the anterior pituitary gland. *Mol. Pharmacol.* **26,** 214–227 (1984).
14. Ehlert, F. J. The relationship between muscarinic receptor occupancy and adenylate cyclase inhibition in the rabbit myocardium. *Mol. Pharmacol.* **28,** 410–421 (1985).
15. Samama, P., Cotecchia, S., Costa, T. & Lefkowitz, R. J. A mutation-induced activated state of the β_2-adrenergic receptor. Extending the ternary complex model. *J. Biol. Chem.* **268,** 4625–4636 (1993).
16. Onaran, H. O., Rajagopal, S. & Costa, T. What is biased efficacy? Defining the relationship between intrinsic efficacy and free energy coupling. *Trends Pharmacol. Sci.* **35,** 639–647 (2014).
17. Hino, T. *et al.* G-protein-coupled receptor inactivation by an allosteric inverse-agonist antibody. *Nature* **482,** 237–240 (2012).
18. Dror, R. O. *et al.* Identification of two distinct inactive conformations of the β_2-adrenergic receptor reconciles structural and biochemical observations. *Proc. Natl Acad. Sci. USA* **106,** 4689–4694 (2009).
19. Ballesteros, J. A. W. & Weinstein, H. Integrated methods for the construction of three-dimensional models and computational probing of structure–function relations in G protein-coupled receptors. *Methods Neurosci.* **25,** 366–428 (1995).
20. Ballesteros, J. A. *et al.* Activation of the β_2-adrenergic receptor involves disruption of an ionic lock between the cytoplasmic ends of transmembrane segments 3 and 6. *J. Biol. Chem.* **276,** 29171–29177 (2001).
21. Meiboom, S. & Gill, D. Modified spin-echo method for measuring nuclear relaxation times. *Rev. Sci. Instrum.* **29,** 688–691 (1958).
22. Moukhametzianov, R. *et al.* Two distinct conformations of helix 6 observed in antagonist-bound structures of a β_1-adrenergic receptor. *Proc. Natl Acad. Sci. USA* **108,** 8228–8232 (2011).
23. Mashalidis, E. H., Śledź, P., Lang, S. & Abell, C. A three-stage biophysical screening cascade for fragment-based drug discovery. *Nature Protocols* **8,** 2309–2324 (2013).

Supplementary Information is available in the online version of the paper.

Acknowledgements We thank D. Capel and X. Jiang for technical assistance. Administrative and secretarial support were provided by V. Ronk, K. Harley, D. Addison, and Q. Lennon. We acknowledge support from the National Institute of Health grants NS028471 (B.K.K.), T32HL007101 (D.P.S., L.M.W.), HL16037 and HL70631 (R.J.L.), from the Stanford Medical Scientist Training Program and the American Heart Association (A.M.), Italian Ministry of Health, grant RF-2011-02351158 (T.C.), and from the Mathers Foundation (B.K.K. and W.I.W.). R.J.L. is an investigator with the Howard Hughes Medical Institute.

Author Contributions D.P.S. and R.T.S. conceived the project. Pharmacological assessment of the interactions between Nb60 and Nb80 with the β_2AR were designed, performed and analysed by D.P.S., R.T.S., B.P., S.A., and A.C. Formation, purification, and crystallization of the β_2AR–Nb60–carazolol complex was conducted by D.P.S. and A. Manglik. Data collection, refinement, and structural analysis was done by A. Manglik, A.C.K., and A. Masoudi, and W.I.W. NMR spectroscopy was executed by A. Manglik, T.H.K, and supervised by R.S.P. Isothermal titration calorimetry was conducted by A.W.K. Nanobody reagents were provided by E.P. and J.S. Detailed allosteric analysis of radioligand binding data was implemented by T.C. Figures were created by D.P.S., A. Manglik, T.C., L.M.W., R.T.S., and A. Masoudi. The manuscript was written by D.P.S., T.C., R.T.S., L.M.W., A. Manglik, A.K.C., and R.J.L. Overall research was supervised by B.K.K. and R.J.L.

Author Information Coordinates and structure factors for the β_2AR–Nb60–carazolol complex are deposited in the Protein Data Bank (accession code 5JQH). Reprints and permissions information is available at www.nature.com/reprints. The authors declare no competing financial interests. Readers are welcome to comment on the online version of the paper. Correspondence and requests for materials should be addressed to R.J.L. (lefko001@receptor-biol.duke.edu), B.K.K. (kobilka@stanford.edu) or T.C. (tommaso.costa@iss.it).

Reviewer Information *Nature* thanks H. Hamm, P. Scheerer and the other anonymous reviewer(s) for their contribution to the peer review of this work.

METHODS

Data reporting. No statistical methods were used to predetermine sample size. The experiments were not randomized. The investigators were not blinded to allocation during experiments and outcome assessment.

β_2AR reconstitution in HDL particles. Human β_2AR containing an amino-terminal Flag epitope tag, carboxyl-terminal HIS-tag, and a N187E glycosylation mutation was expressed in Sf9 insect cells using the BestBac baculovirus system (Expression systems; Davis, CA). Cells were infected at a density of 3×10^6 cells per ml and harvested 66 h afterwards. Functional Flag–β_2AR was purified using Flag-M1 antibody and alprenolol affinity chromatography as previously described[24]. Flag–β_2AR was reconstituted into HDL particles (nanodiscs) according to previously published methods[25]. In brief, Flag–β_2AR was incubated with a 50-fold molar excess of membrane scaffold protein 1 (MSP1) and 8 mM POPC:POPG (3:2 molar ratio) for 1 h at 4 °C. Detergent was removed via biobeads overnight at 4 °C, and receptor-containing nanodiscs were isolated using Flag–M1 chromatography and size-exclusion chromatography.

Nanobody and Gs purification. Nanobodies were generated and purified as previously described[6]. In brief, Nb60 and Nb80 clones were originally obtained from one llama (*Lama glama*) immunized with β_2AR (truncated at residue 365) reconstituted into liposomes bound to the high affinity agonist BI-167107. Nanobody coding sequences were amplified from isolated lymphocyte RNA and cloned into phage display vector. Conformationally selective nanobodies were isolated using a series of biopanning procedures targeted against native receptor bound to agonist. Nanobodies were grown in *E. coli* WK6 cells and purified from the periplasmic extract using nickel-agarose and resource S ion exchange chromatography. Heterotrimeric Gs protein was expressed in and purified from Sf9 insect cells using nickel-agarose and ion exchange chromatography as described previously[26].

Radioligand binding assays. Competition binding assays (250 µl) contained 60 pM [^{125}I]cyanopindolol, a serial dilution of competitor, the indicated concentration of nanobody/Gs, and approximately 0.5 ng of β_2AR nanodiscs diluted in assay buffer (50 mM Tris-HCl pH 7.4, 12.5 mM $MgCl_2$, 2 mM EDTA, 0.05% BSA, 1 mM L-ascorbic acid). Total binding was determined in the absence of competitor; nonspecific binding was determined using 10 µM propranolol. Following a 90 min incubation at room temperature, binding assays were terminated by rapid filtration onto GF/B glassfibre filters treated with 0.3% PEI and washed with 8 ml of cold binding buffer using a harvester (Brandel, Gaitherburg, MD). Bound [^{125}I] was quantified using a Packard Cobra Quantum gamma counter (Packard, San Diego, CA) and expressed as specific binding. For [^{3}H]ICI-118,551 binding, 10 ng of β_2AR nanodiscs were incubated with 0.3 nM radioligand and varying concentrations of nanobody and were harvested as described above. [I^{125}] cyanopindolol affinity was determined using saturation binding (Extended Data Table 1). All binding data represent a minimum of three independent experiments with deviation represented as standard error.

Isothermal titration calorimetry (ITC). ITC experiments were carried out using the MicroCal iTC200 system. β_2AR and Nb60, purified as described above, were both dialysed against a buffer consisting of 20 mM HEPES pH 7.5, 100 mM NaCl, 0.01% lauryl maltose neopentyl glycol (MNG), and 0.001% cholesteryl hemisuccinate (CHS). Protein concentrations were determined by measurement of the absorbance at 280 nm, using molar extinction coefficient per cm parameters of each protein (ε for β_2AR: 66,350 cm^{-1} and Nb60: 21,430 cm^{-1}). Nb60 at 100 µM concentration (40 µl) was loaded into the syringe and titrated into the 200 µl sample cell containing β_2AR (10 µM) in absence or presence of 200 µM isoprenaline. Titrations were performed at 25 °C using an initial injection of 0.5 µl, followed by 2.3 µl injections (1 s duration, 300 s spacing, and 5 s filter period). Reference power was set to 10 µcal s^{-1} and stirring speed to 750 r.p.m. Reference titrations were obtained by injecting Nb60 alone or Nb60 with agonist (isoprenaline) into sample cells containing buffer alone. To obtain the stoichiometry (N) and association constant (K_A) of the interaction, the raw data were baseline corrected, peak area integrated, and fitted to a one-site nonlinear least squares fit model using the Origin7 software program. Binding experiments were performed at least twice to calculate standard deviations.

Enzyme-linked immunosorbent assay (ELISA) for determining Nb K_T. The affinity of each nanobody for the unliganded β_2AR (K_T) was required for ternary complex model data analysis. Briefly, 50 ng of carboxypeptidase-treated (to remove His$_6$ tag), biotinylated β_2AR nanodiscs were immobilized per well of a 96-well SigmaScreen Streptavidin plate in binding buffer (20 mM HEPES pH 7.4, 100 mM NaCl, 2 mM EDTA). Following a 3 h incubation at room temperature, plates were washed four times with binding buffer and incubated with serial dilutions of nanobody in binding buffer with 0.1% milk for 2 h at room temperature. Plates were quickly washed three times with binding buffer and then incubated with polyclonal anti-His HRP-conjugated antibody (1:5,000, Abcam) in binding buffer with 0.1% milk for 1 h at room temperature. Plates were quickly washed three times with binding buffer and bound nanobody was detected colorimetrically (OD_{450nm}) on a NovoStar plate reader (BMG Labtech) using TMB Ultra 1-step substrate as described by the manufacturer (Pierce).

Crystallization of β_2AR–carazolol–Nb60 complex. For crystallography trials, we used a previously described fusion protein of human β_2AR with an amino-terminal T4 lysozyme (T4L) fusion and a truncated intracellular loop three[27]. The T4L–β_2AR fusion protein was expressed and purified as described above. Purified receptor was incubated with fivefold and twofold molar excess of carazolol and Nb60, respectively. The β_2AR–carazolol–Nb60 complex was incubated overnight at 4 °C and further purified by size exclusion chromatography over a Sephadex S200 column in a buffer comprised of 20 mM HEPES pH 7.5, 100 mM NaCl, 0.01% MNG, and 0.001% CHS. The purified complex was concentrated to 37.5 mg ml^{-1} and flash frozen in liquid nitrogen for crystallization trials. We used the *in meso* crystallization method with a 10:1 (w/w) mix of 7.7 monoacylglycerol (MAG 7.7) and cholesterol as the host lipid (Avanti Polar Lipids). Samples were thawed and reconstituted with the host lipid at a 1:1 ratio with the two-syringe mixing method until a clear phase was achieved. The resulting lipidic cubic phase was dispensed in 35 nl drops onto glass sandwich plates using a GryphonLCP robot (Art Robbins Instruments). Crystals grew in a precipitant solution comprised of 100 mM HEPES pH 7.5, 20 mM EDTA, and 19–23% PEG300. Although crystals appeared in 2–3 days, the best diffraction was obtained from crystals that grew over 30 days. Crystals were harvested with mesh loops (Mitegen) and flash frozen in liquid nitrogen.

Data collection and refinement. X-ray diffraction was collected at the Advanced Photon Source GM/CA beamline 23ID-B. As with previous *in meso* crystallography of GPCRs, crystals suffered considerable radiation damage during data collection. Typically, 20–60 degree wedges of data were collected using a 20 µm beam. The resulting diffraction data from 10 crystals were processed in HKL2000 (ref. 28). The structure of the β_2AR–carazolol–Nb60 complex was solved by molecular replacement using carazolol-bound β_2AR with the T4 lysozyme removed (PDB accession code 2RH1) and a structure of Nb60 solved to 1.8 Å as search models in Phaser[29]. The model was refined iteratively in Phenix[30] with manual rebuilding in Coot[31] with and without averaging of non-crystallographic symmetry. The quality of the final model was assessed using MolProbity[32] and refinement statistics are presented in Extended Data Table 2. Figures were prepared using PyMOL (Schrödinger). The r.m.s.d. analysis for the orthosteric binding pocket was performed in PyMOL by measuring residues within 4 Å of the ligand carazolol between β_2AR–Nb60–Cz and the Protein Data Bank accession code 2RH1.

^{19}F NMR of β_2AR. ^{19}F fluorine NMR studies were conducted as previously described[5]. Briefly, full-length β_2AR with four cysteine mutations (C77V, C327S, C378A, and C406A) was expressed in Sf9 cells, extracted using dodecylmaltoside, and purified initially by M1 Flag affinity chromatography. The receptor sample was subsequently labelled with a bromotrifluoroacetanilide probe at a fivefold stoichiometric excess and purified by alprenolol–sepharose and M1 affinity chromatography. As done for previous ^{19}F NMR experiments, the detergent was gradually exchanged to 0.01% lauryl maltose neopentyl glycol (MNG, Anatrace). The final receptor sample was concentrated to 200 µM and a 2.5-fold molar excess of carazolol was added before acquisition of NMR data. After acquisition of signal for the β_2AR–carazolol complex, Nb60 was added to a 2.5-fold molar excess, and ^{19}F NMR spectra were obtained for the β_2AR–carazolol–Nb60 complex. NMR studies were performed at 25 °C on a 600 MHz Varian Innova spectrometer equipped with a cryogenic probe capable of ^{19}F NMR (600 MHz). All spectral processing was performed using Mnova 9.0.0 (Mestrelab Research). Additional information on data processing and line shape simulations are described in detail elsewhere[5]. ^{19}F CPMG relaxation data were recorded by applying CPMG frequencies ranging from 500 to 5,000 Hz at 600 MHz with a constant time of 2 ms. CPMG profiles were fitted to a two state model with Chemex as described elsewhere[33]. The ^{19}F $\pi/2$ pulse width was 19 µs.

Fitting of binding curves with the ternary complex model. The allosteric effect of nanobodies on the binding of receptor ligands is quantified by the cooperatvity factor α. Its magnitude is given by a ratio of dissociation constants (that is, K_L/K_H for Nb80 and K_L/K_{VL} for Nb60) determined from the comparison of how each ligand binds to β_2AR in the absence of versus the saturating presence of each nanobody (Extended Data Fig. 3). However, under conditions in which the nanobody concentration is sub-saturating or the radiotracer α is not exactly 1, experimental K_d ratios may underestimate the size of the cooperativity factor. To improve measurements of Nb/ligand α values, we fitted the binding curves with a mathematical function derived from TCM. This entails solving the following nonlinear system of equations that yield the concentration of free species for a binding reaction consisting of one receptor (R), one Nb (N) and n ligands (L_i) at equilibrium:

$$[R]_f = [R]_t \cdot \left\{1 + M[N]_f + \sum_{i=1}^{n} K_i[L_i]_f(1 + \alpha_i M[N]_f)\right\}^{-1}$$
$$[N]_f = [N]_t \cdot \left\{1 + M[R]_f + \left(1 + \sum_{i=1}^{n} \alpha_i K_i[L_i]_f\right)\right\}^{-1}$$
$$[L_i]_f = [L_i]_t \cdot \{1 + K_i[R]_f(1 + \alpha_i M[N]_f)\}^{-1}$$

where subscripts f and t indicate respectively free and total concentrations and the equilibrium binding constants of ligands (K) and nanobody (M) are defined as in supplementary (analysis of binding cooperativity). Exact numerical solutions were obtained using a globally convergent iterative algorithm[34], which was coded as add-in function for Excel[35]. The built-in optimizer 'solver' was used to minimize the sum of squares difference between predicted and experimental data (choosing the Newton search option and setting convergence threshold at 10^{-12}). Sets of 3 curves representing bound radiotracer as a function of increasing concentrations of unlabelled ligand, obtained in the absence and presence of Nb80 or Nb60, were fitted simultaneously. Known parameters are the M of each Nb (Extended Data Fig. 6), the K and α value of [^{125}I]cyanopindolol (Extended Data Fig. 1). Unknown fitted parameters are: non-specific tracer binding, receptor concentration and K value of the competing ligand (both shared across the 3 curves), and the individual αNb80, αNb60 values for each ligand/Nb pair. For data measured in the presence of Gs (the M value of which was not available), all ligands curves were fitted globally and constrained to share a common best-fitting M. This fitted value was close to that experimentally measured for Nb80. See supplemental information and Extended Data Figures 7 and 8 for additional information on allosteric modeling.

24. Kobilka, B. K. Amino and carboxyl terminal modifications to facilitate the production and purification of a G protein-coupled receptor. *Anal. Biochem.* **231,** 269–271 (1995).
25. Whorton, M. R. *et al.* A monomeric G protein-coupled receptor isolated in a high-density lipoprotein particle efficiently activates its G protein. *Proc. Natl Acad. Sci. USA* **104,** 7682–7687 (2007).
26. Rasmussen, S. G. *et al.* Crystal structure of the β2 adrenergic receptor–Gs protein complex. *Nature* **477,** 549–555 (2011).
27. Ring, A. M. *et al.* Adrenaline-activated structure of β_2-adrenoceptor stabilized by an engineered nanobody. *Nature* **502,** 575–579 (2013).
28. Otwinowski, Z. M. W. in *Methods in Enzymology* Vol. 276 (eds Carter, C. W. & Sweet, R. M.) 307–326 (Academic Press, 1997).
29. McCoy, A. J. *et al.* Phaser crystallographic software. *J. Appl. Crystallogr.* **40,** 658–674 (2007).
30. Adams, P. D. *et al.* PHENIX: a comprehensive Python-based system for macromolecular structure solution. *Acta Crystallogr. D* **66,** 213–221 (2010).
31. Emsley, P. & Cowtan, K. Coot: model-building tools for molecular graphics. *Acta Crystallogr. D* **60,** 2126–2132 (2004).
32. Chen, V. B. *et al.* MolProbity: all-atom structure validation for macromolecular crystallography. *Acta Crystallogr. D* **66,** 12–21 (2010).
33. Shi, L. & Kay, L. E. Tracing an allosteric pathway regulating the activity of the HslV protease. *Proc. Natl Acad. Sci. USA* **111,** 2140–2145 (2014).
34. Pradines, J. R., Hasty, J. & Pakdaman, K. Complex ligand–protein systems: a globally convergent iterative method for the n x m case. *J. Math. Biol.* **43,** 313–324 (2001).
35. Vezzi, V. *et al.* Ligands raise the constraint that limits constitutive activation in G protein-coupled opioid receptors. *J. Biol. Chem.* **288,** 23964–23978 (2013).
36. Rajagopal, S. *et al.* Quantifying ligand bias at seven-transmembrane receptors. *Mol. Pharmacol.* **80,** 367–377 (2011).

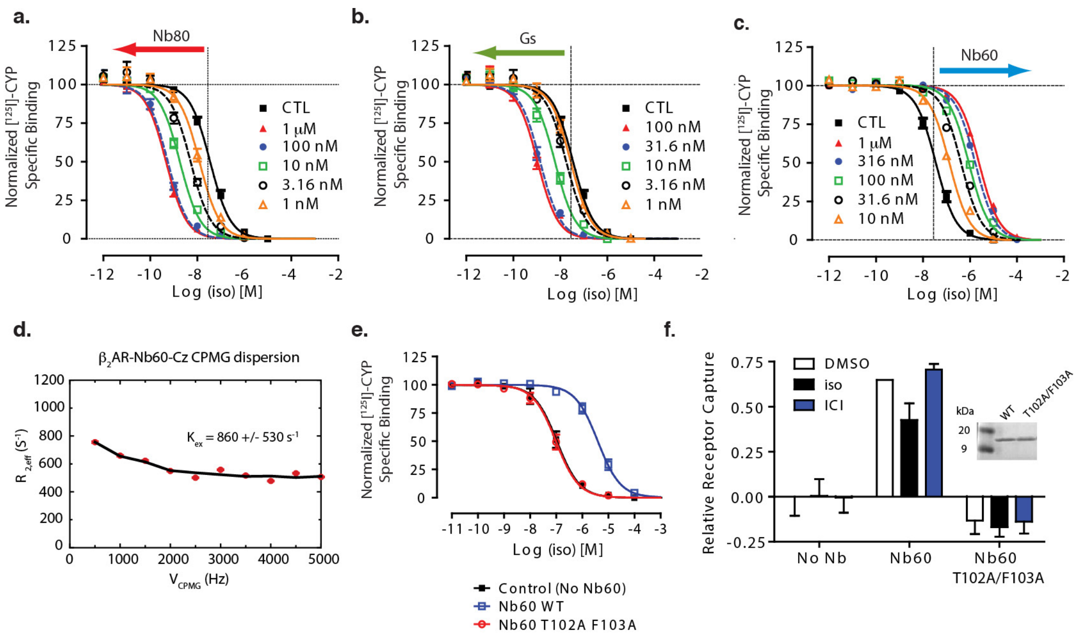

Extended Data Figure 1 | Characterization of Nb60 interaction with β$_2$AR. a–c, Competition equilibrium binding studies using [^{125}I] cyanopindolol (CYP), the cold competitor agonist isoprenaline (ISO), β$_2$AR in HDL particles, and the indicated concentration of Nb80 (**a**), Gs (**b**), or Nb60 (**c**). The dotted vertical line represents log IC$_{50}$ in absence of modulator, and the change in ligand affinity is depicted with coloured arrows. **d**, ^{19}F NMR CPMG relaxation dispersion experiment with β$_2$AR–Nb60–carazolol (Cz). K_{ex}, exchange rate. **e**, Competition equilibrium binding studies using [^{125}I]cyanopindolol, the non-labelled competitor agonist isoprenaline, β$_2$AR in HDL particles, and 1 µM wild-type Nb60 or Nb60(T102A/F103A). **f**, ELISA depicting capture of β$_2$AR by wild-type Nb60 or the T102A/F103A variant. Inset: Coomassie stain of nanobody input. Radioligand binding and ELISA experiments were performed at least three times with deviation shown as standard error.

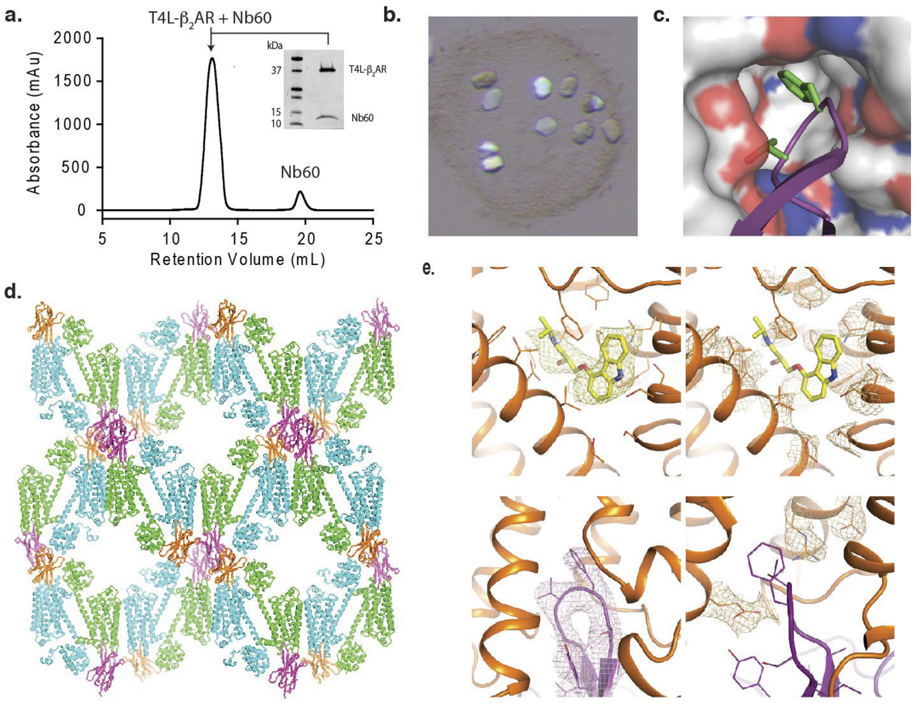

Extended Data Figure 2 | Characterization of β$_2$AR–Nb60–carazolol crystals. **a**, Monodispersity of T4L–β$_2$AR–Nb60–carazolol (β$_2$AR–Nb60–Cz) complex as assessed by size exclusion chromatography. Inset, Coomassie stain illustrating presence of β$_2$AR and Nb60 in fractions combined for crystallography. **b**, Representative picture of β$_2$AR–Nb60–Cz lipidic cubic phase (LCP) crystals. **c**, Insertion of F103 (green) from Nb60 CDR3 (purple) into hydrophobic β$_2$AR pocket, nitrogen and oxygen shown as blue and red shaded surfaces, respectively. **d**, Example of β$_2$AR–Nb60–Cz crystal lattice. **e**, Electron density 2F_o–F_c map (Sigma: 1) of carazolol binding pocket (top panels) Nb60 CDR3 binding pocket (bottom panels) within β$_2$AR.

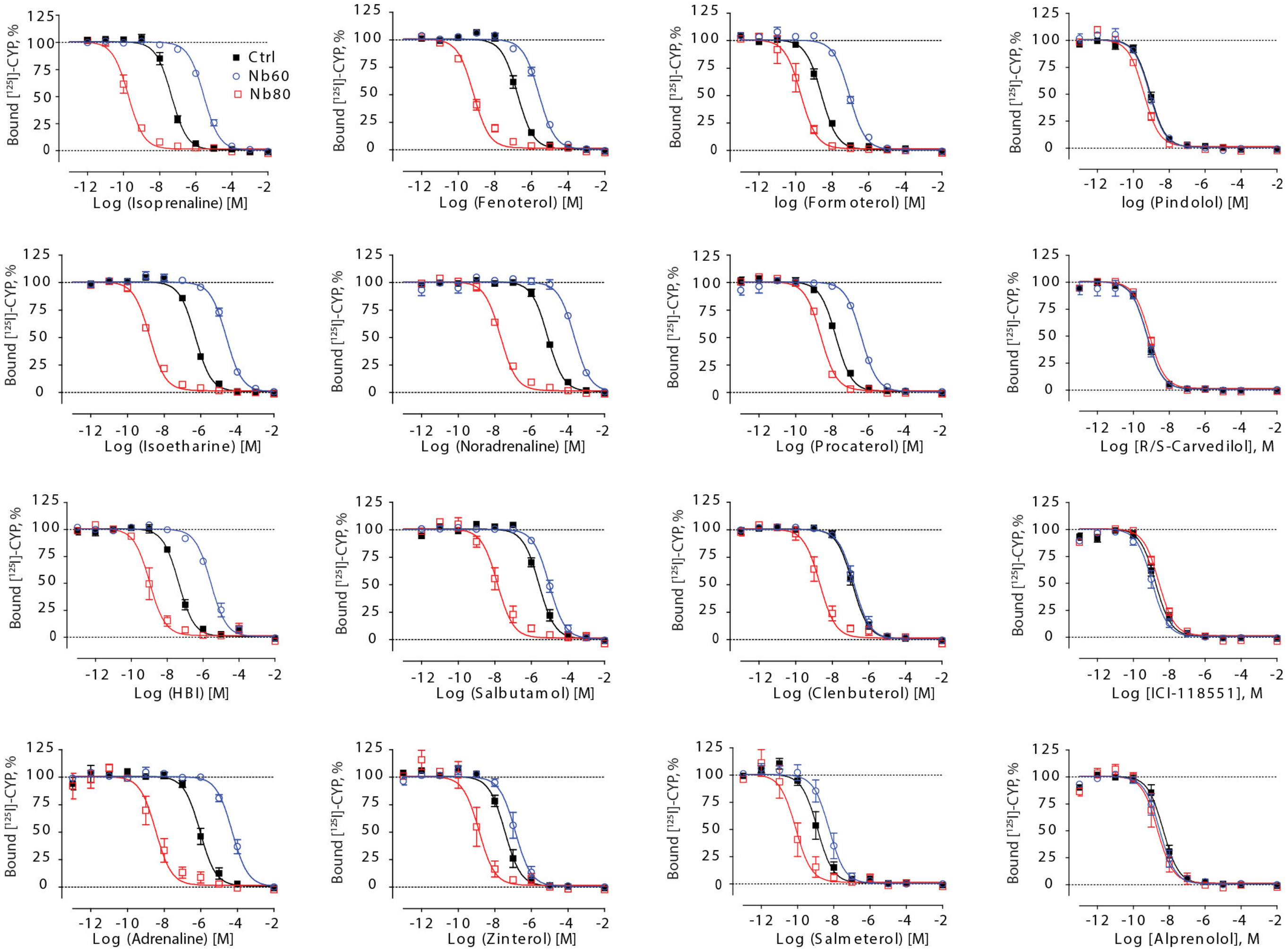

Extended Data Figure 3 | Differential effects of Nb60 and Nb80 on the affinity of 12 different β_2AR ligands. Competition equilibrium binding studies using [^{125}I]cyanopindolol, the indicated non-labelled competitor, β_2AR in HDL particles, and 1 μM of Nb60 or Nb80. Data represent at least three independent experiments with deviation depicted as standard error.

a.

	cAMP (Glosensor)		Ligand Affinity		Log Tau		Log αNb80		Log αNb60	
	LogEC50	Std. Err.	Ki	Std. Err.	Mean	Std. Err.	Mean	Std. Err.	Mean	Std. Err.
Isoprenaline	-9.622	0.046	-6.838	0.013	2.16	0.226	2.93	0.112	-2.88	0.300
Formoterol	-9.596	0.070	-8.068	0.024	1.12	0.216	1.72	0.328	-2.14	0.391
Salbutamol	-7.746	0.077	-5.868	0.023	2.23	0.186	2.92	0.257	-0.59	0.073
Salmeterol	-7.989	0.070	-8.666	0.021	0.57	0.115	1.82	0.198	-0.67	0.137
HBI	-9.579	0.097	-7.076	0.039	1.96	0.218	2.16	0.358	-2.73	0.005
Adrenaline	-8.885	0.130	-5.950	0.035	2.70	0.191	3.16	0.401	-3.40	1.010
Noradrenaline	-6.941	0.087	-4.844	0.039	1.93	0.165	3.33	0.095	-3.37	0.614
Clenbuterol	-8.499	0.075	-7.508	0.042	1.82	0.173	2.41	0.048	-0.07	0.093
Fenoterol	-9.223	0.051	-6.494	0.036	2.34	0.200	2.96	0.091	-1.46	0.270
Isoetharine	-8.646	0.070	-5.856	0.051	2.33	0.193	3.01	0.078	-3.38	0.606
Zinterol	-8.949	0.079	-7.896	0.029	1.47	0.164	2.09	0.229	-0.63	0.114
Procaterol	-9.188	0.108	-7.468	0.046	1.12	0.184	1.39	0.052	-1.86	0.204

b.

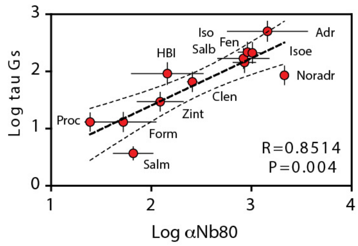

c.

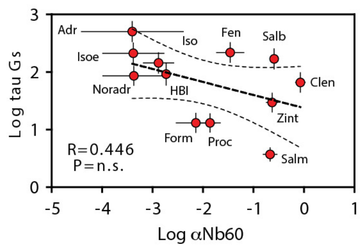

Extended Data Figure 4 | Agonist-induced G-protein activation *in cellulo* correlates with the magnitude of affinity change mediated by Nb80 *in vitro*. **a**, Table representing cell signalling and ligand affinity data. Ligand-dependent G-protein activation was quantified by measuring cAMP levels (GloSensor, Promega) from HEK293 cells overexpressing β_2AR. Ligand affinity was measured in membranes prepared from the same cells as above using competition binding assays with [^{125}I] cyanopindolol. Ligand efficacy (log τ) was calculated as previously described[36]. See methods and Supplementary Information for cooperativity (α) determination. **b**, **c**, Correlation plot of log τ and αNb80 (**b**), or αNb60 (**c**). All data represent at least three independent experiments with deviation shown as standard error.

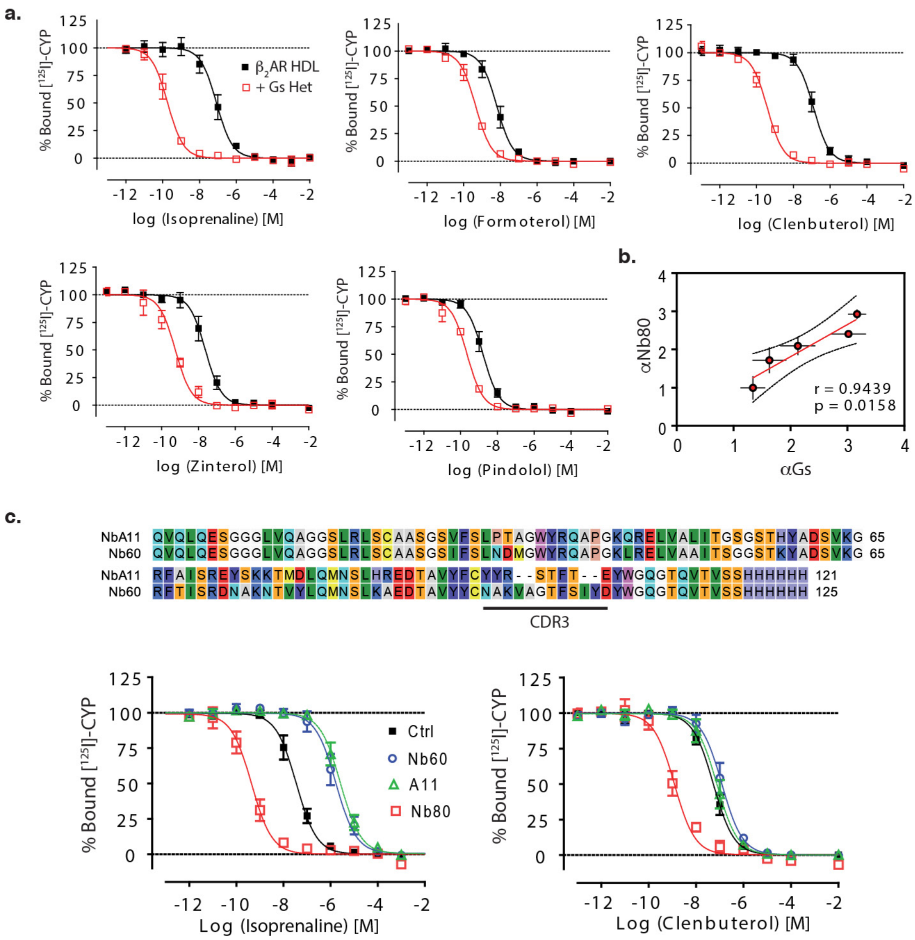

Extended Data Figure 5 | Positive correlation between allosteric properties of Nb80 and Gs. a, Equilibrium binding studies using HDL β_2AR, [^{125}I]cyanopindolol, the indicated unlabelled competitor, and 100 nM purified heterotrimeric Gs protein. **b**, Correlation plot of cooperativity values (α) for Nb80 and Gs. **c**, Sequence alignment of Nb60 and NbA11. Radioligand competition binding studies with Nb80, Nb60 or NbA11, [^{125}I]cyanopindolol, the unlabelled competitor isoprenaline or clenbuterol, and HDL β_2AR. All data represent at least three independent experiments with deviation shown as standard error.

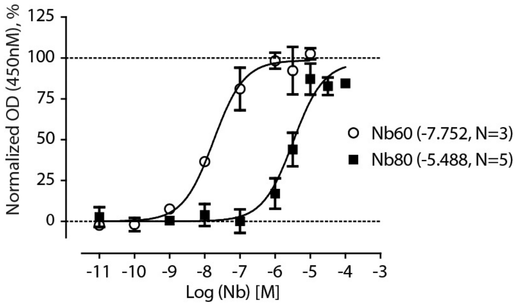

Extended Data Figure 6 | Affinity determination for Nb60 and Nb80 for unliganded β_2AR. ELISA assay detecting capture of increasing concentrations of Nb60 or Nb80 by immobilized HDL β_2AR in the absence of ligand. All data represent at least three independent experiments with deviation shown as standard error.

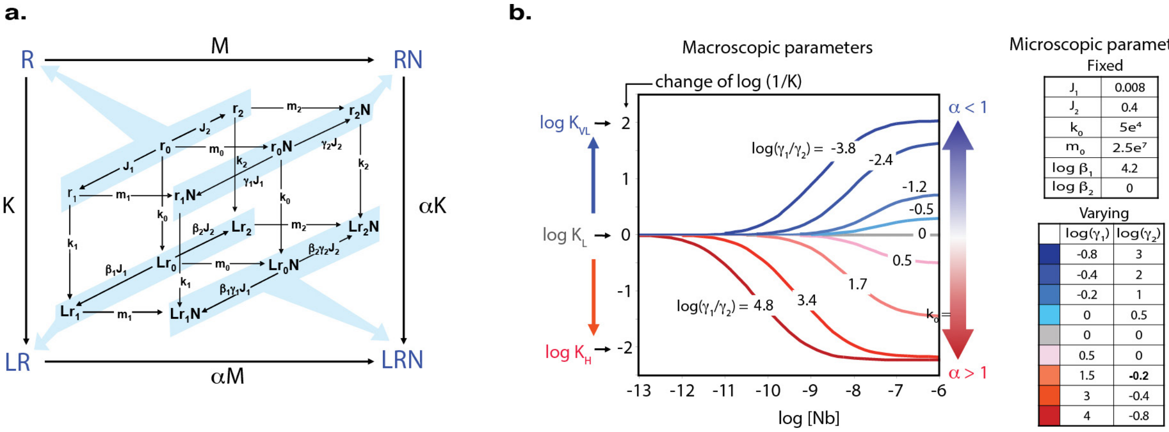

Extended Data Figure 7 | Theoretical framework illustrating the two views of allostery. a, Nested reaction schemes at equilibrium indicating the correspondence (arrowed light-blue shades) between binding site cooperativity (ternary complex model in outer box) and changes of allosteric conformations (inner cubes). Arrows stand for reversible equilibrium interactions. **b**, Change of the macroscopic dissociation constant ($1/K$) of a ligand L (shifting the equilibrium towards r_1) induced by increasing the concentrations of nine different N-ligands with diverse allosteric effects (γ_1, γ_2) on receptor states. Simulations were made using a three-state model based on the parameter values listed on the right side of the plot (curves on the left side are colour coded in red/blue tones corresponding to the boxes on the right). The change in K (that is, log difference between presence and absence of N) is calculated from equation 1 in the Supplementary Information (analysis of nanobody allostery).

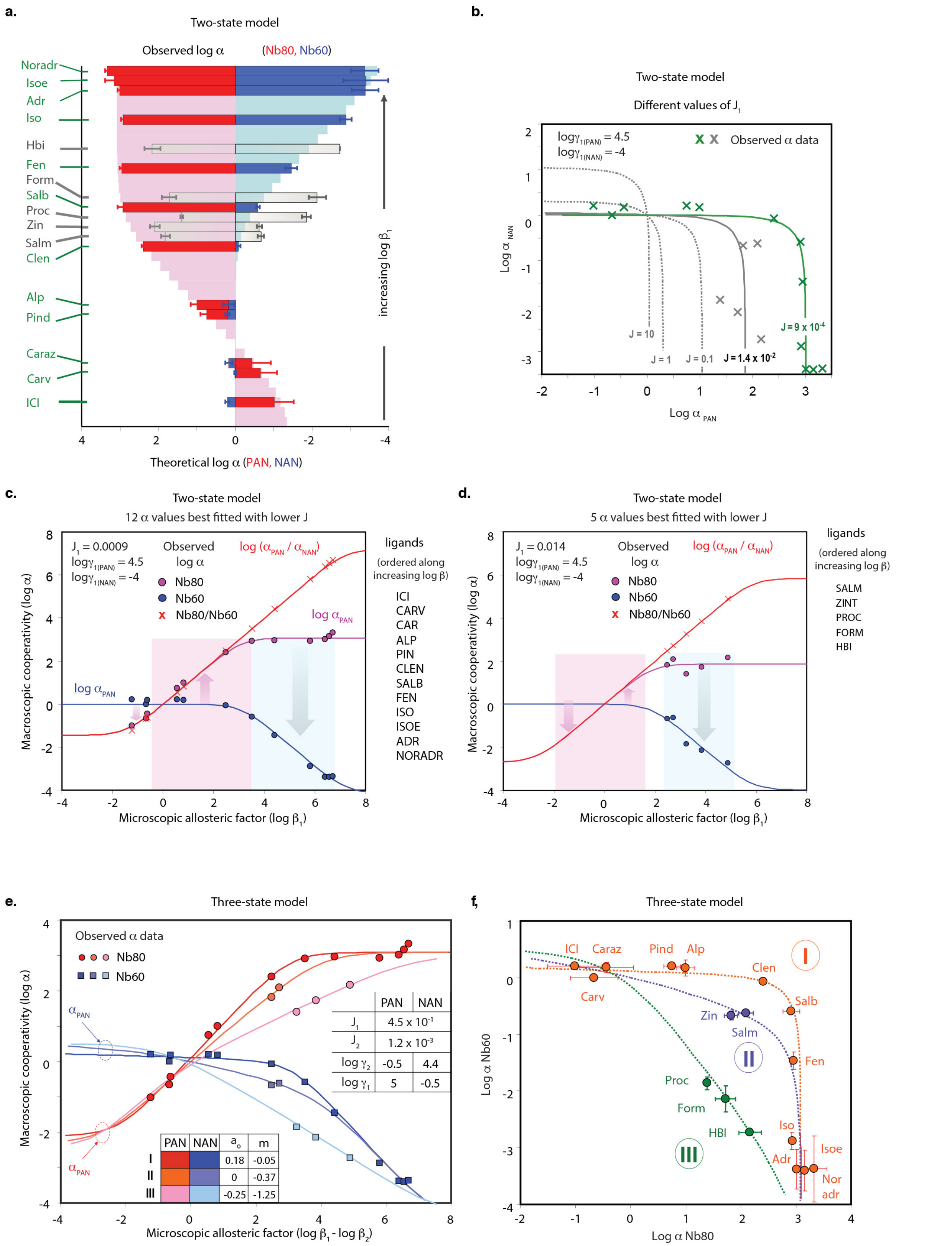

	PAN	NAN
J_1	4.5×10^{-1}	
J_2	1.2×10^{-3}	
log γ_2	-0.5	4.4
log γ_1	5	-0.5

	PAN	NAN	a_0	m
I			0.18	-0.05
II			0	-0.37
III			-0.25	-1.25

Extended Data Figure 8 | Comparison of experimental and theoretical cooperativities predicted according to a two-state or three-state allosteric model. See also the Supplementary Information section on analysis of nanobody allostery. **a**–**d**, Theoretical log α values were computed according to a two-state model for a series of hypothetical ligands (L) (log β_1 range: 4/8) and a positive (PAN, log $\gamma_1 >> 0$) or negative (NAN, log $\gamma_1 << 0$) nanobody. **a**–**d**, Observed data overlaid on values simulated at $J_1 = 8.9 \times 10^{-4}$ in histogram form (with experimental bars drawn on the closest theoretical log β_1 bin value) (**a**), or superimposed (**b**), on the log α_{NAN} versus log α_{PAN} relationships predicted for different J_1 values. The same data are replotted as separate graphs for lower J_1 (**c**) and larger J_1 (**d**) values, to show the sigmoidal relationships existing between macroscopic log αs and log β_1. **e**, **f**, Simulations made according to the three-state allosteric model. **e**, Predicted (lines) and observed (circles) log α values plotted as functions of log (β_1/β_2). Three groups of ligands (I to III, defined by the table of a0 and m parameters) produce increasingly stronger reductions of r_2 equilibrium. **f**, Same data plotted as log αNb60 versus log αNb80 relationships (see Fig. 4). All α values derived from at least three independent radioligand binding experiments with deviation depicted as standard error.

Extended Data Table 1 | Effect of Nb60 and Nb80 on [^{125}I]cyanopindolol affinity

	[^{125}I]-Cyanopindolol Affinity		Kd Ratio	
	Kd (pM)	SEM	Control / Nb	SEM
Control	737.3	92.9	----	----
Nb80	315.6	62.4	2.5	0.35
Nb60	663.0	17.7	1.1	0.12

Extended Data Table 2 | Data collection and refinement statistics (molecular replacement)

	β_2AR-Carazolol-Nb60[a]
Data collection[b]	
Space group	$P2_12_12_1$
Cell dimensions	
a, b, c (Å)	43.9, 164.5, 218.8
α, β, γ (°)	90.0, 90.0, 90.0
Resolution (Å)	32.9-3.2 (3.30-3.20)
R_{merge} (%)	17.5 (89.6)
$<I/\sigma I>$	5.3 (1.5)
$CC_{1/2}$ (%)	98.6 (82.4)
Completeness (%)	98.6 (95.5)
Redundancy	5.5 (4.6)
Refinement	
Resolution (Å)	32.9-3.2 (3.30-3.20)
Number of reflections	26,778
R_{work}/R_{free} (%)	24.7/29.0 (38.3/43.9)
Number of atoms	
Protein	7,703
Ligand (Carazolol)	44
Solvent (lipid, water, other)	56
B-factors (Å^2)	
Protein	129.81
Ligand (Carazolol)	116.36
Solvent (lipid, water, other)	157.51
R.M.S. deviation from ideality	
Bond lengths (Å)	0.003
Bond angles (°)	0.429
Ramachandran statistics[c] (%)	
Favored	96.8
Allowed	3.2
Outliers	0

[a]Diffraction data from 10 crystals were merged into a complete data set. [b]Highest resolution shell statistics are shown in parentheses. [c]As calculated by MolProbity.

TECHNOLOGY FEATURE

LIVE FAST, DIE YOUNG

Research into ageing requires patience, but a small cadre of scientists is angling to speed up answers by developing the flamboyant, short-lived turquoise killifish as a new model.

SEBASTIAN KAHNERT/DPA/PICTURE ALLIANCE

The turquoise killifish (*Nothobranchius furzeri*), with its fleeting life, is helping researchers to study the mechanisms that influence human ageing.

BY AMBER DANCE

Physiologist Alessandro Cellerino has always been an aquarium enthusiast, but fish were not originally part of his research plan. One afternoon in 2000, hanging out in a tank-filled cellar in Canossa, Italy, with breeder Stefano Valdesalici, Cellerino idly asked him which fish were the shortest-lived. Valdesalici pointed to a tank with brightly speckled African turquoise killifish: "They don't make it any longer than three months."

"Are you kidding?" asked Cellerino, who works at the Scuola Normale Superiore in Pisa, Italy. "OK, I want them."

So in March 2004, Cellerino and his graduate student Dario Riccardo Valenzano found themselves bouncing through Mozambique in a four-wheel-drive truck with Valdesalici, who chairs the Italian Killifish Association in Canossa. They donned chest-high waders and gloves to net killifish from the seasonal, cow-pat-spattered mud holes where the fish live. Like the tank-bred versions, these wild strains were exceptionally short-lived. Of the many varieties of killifish, the turquoise killifish (*Nothobranchius furzeri*) has the shortest lifespan — the briefest of any vertebrate bred in captivity, ranging from 3 to 12 months depending on strain and living conditions.

Using killifish to study ageing is not a new idea. In the late twentieth century, scientists studied ageing in one species, *Nothobranchius guentheri*, that lives for about 14 months. But given techniques available at the time, they could come up with only basic descriptions of ageing features. When Cellerino encountered *N. furzeri*, timing and luck were on his side: advances in molecular analysis had set up excellent conditions in which to develop the model and investigate mechanisms behind its dotage.

The killifish's brief lifespan, relative to those of longer-lived models such as mice and zebrafish, enables ageing research to progress apace. And because the fish is a vertebrate, the research is more directly relevant to people than are studies of short-lived organisms such as fruit flies or nematodes (see 'The long and short of it').

To set up a killifish model, researchers have taken advantage of modern genomic tools and drawn techniques from well-established zebrafish protocols, rather than starting from scratch. In 2015, the publication of CRISPR–Cas9-based gene-editing techniques for the killifish[1], as well as two complementary genome-sequencing efforts[2,3], boosted the fish to the status of genetically tractable model.

The killifish — or *Notho*, as some scientists affectionately call it — is certainly gaining fans. Interest has "really exploded over the past few years", says Valenzano, who now works at the Max Planck Institute for Biology of Ageing in Cologne, Germany. He estimates that about two dozen scientists have visited his group in the past year to learn killifish husbandry. In June, about 70 *Notho* aficionados attended the second *Nothobranchius* Symposium in Jena, Germany. But the challenges of keeping killifish — such as their lack of a standardized diet — and a want for basic reagents, such as *Notho*-specific antibodies, mean that the fish has a way to go before it reaches the utility of lab mice.

The ephemeral existence that so appeals to scientists is an evolutionary adaptation to the fish's natural environment: their accelerated development enables them to live and reproduce in transient mud pools during the wet season in equatorial Africa. The eggs survive in a dormant state during the dry season, and once the rains come and pools form, they hatch. The fish have only a few weeks or months to grow up and spawn before the water dries up.

Hobbyists, attracted by the males' flashy appearance, have been collecting turquoise killifish since they were discovered in Zimbabwe in 1968. Consequently, Cellerino's first challenge was to confirm that their lifespan was not a side effect of decades of breeding in tanks. Most of the wild *N. furzeri* that Cellerino's team caught in Mozambique lived for about eight months — not as brief a time as the inbred Zimbabwe line, but still short enough to interest scientists.

But that begged another question: would killifish age in a way that parallels the human process? Yes, says Valenzano: the fish do get 'old' before they die. "They don't drop dead after four months," he says. "They slowly deteriorate." The fish become duller in colour, lose muscle mass and body weight, develop cancers and swim around less.

The brain shows typical signs of ageing, too, says Livia D'Angelo, an anatomist at the University of Naples Federico II in Italy. Glia — brain cells that provide support and protection for neurons — upregulate the glial fibrillary acidic protein GFAP, as happens in mammalian ageing, and age-associated, lipid-rich pigment granules called lipofuscin accumulate. Neurons degenerate and deposit amyloid molecules that aggregate, resembling the plaques seen in people with Alzheimer's disease, Valenzano adds. He has also found that old fish don't learn as well as young ones. Young fish rapidly work out how to avoid an unpleasant stimulus, such as a plastic stick swirling in their tank, whereas old-timers take longer to catch on[4]. "It's a very good model for neuroscience research," D'Angelo says.

The fish also respond to anti-ageing interventions much as some short-lived vertebrates do. Resveratrol — the stuff in red wine that prolongs life in nematodes and fruit flies — can lengthen their lifespan by up to 59%[4]. Restricting feedings to every other day creates a caloric deficit known to extend lifespan in organisms ranging from yeast to rodents, and it does the same for killifish, although the effects vary by strain[5].

GONE FISHING

Having shown that killifish decline with age, scientists now want to understand how the process occurs. One key resource is the collection of several strains from Africa whose genomes are not identical. *Notho* scientists have four main strains to choose from, Cellerino says: the original Zimbabwe line, and three derived from fish caught in Mozambique in 2004 and 2007, which have slightly longer lifespans.

By cross-breeding two strains, Cellerino and

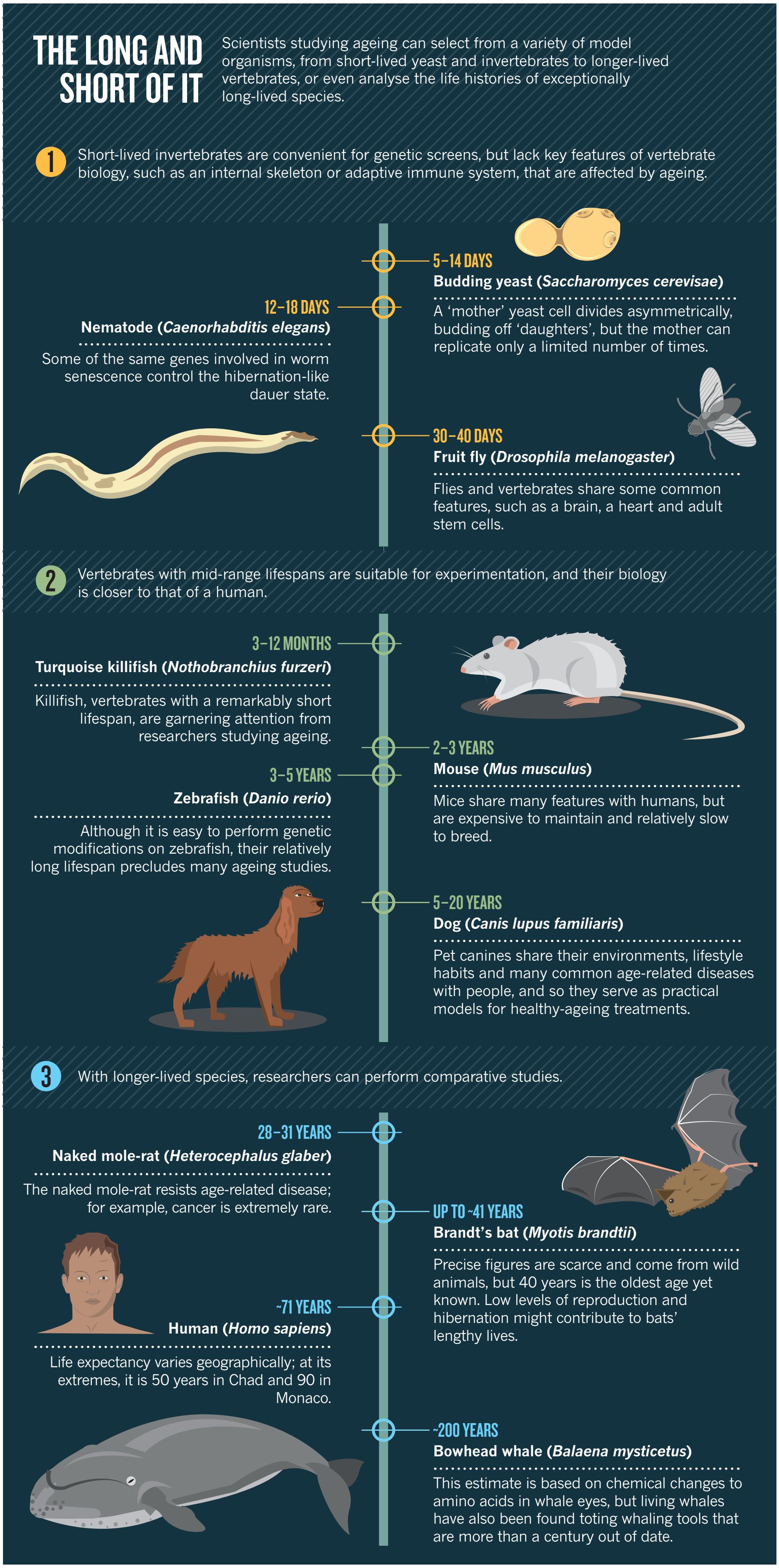

CLAIRE WELSH/*NATURE*

his team created fish with a range of lifespans. They then compared the genomes and longevities of parent and second-generation progeny, and identified a few chromosomal regions, each with hundreds of genes that might influence ageing. Although these did not directly reveal genes involved in longevity, they suggested possible candidates. From this study, the scientists estimated that about 32% of variation in lifespan among turquoise killifish results from genetics, a figure comparable to the 20–35% estimated genetic contribution in mice[6].

From then on, the killifish's transformation into a valid research model accelerated. Anne Brunet, a geneticist studying ageing at Stanford University in California, had longed for a short-lived vertebrate and was delighted to hear about killifish when Valenzano visited Stanford for a summer course. She recruited him to her lab for a postdoc, and in 2006, Valenzano brought the killifish to California. There, he copied and modified protocols for zebrafish to transfer in foreign genes, starting with the green-fluorescent-protein gene from jellyfish[7]. In 2015, Brunet and her colleagues reported the successful use of CRISPR–Cas9 gene editing in killifish, generating fish with mutations in 13 genes involved in key ageing events such as telomere shortening and mitochondrial dysfunction[1].

As enthusiasm for *Notho* grew, two groups tackled its genome sequence: Brunet's lab at Stanford, and Cellerino and collaborators at the Leibniz Institute on Aging–Fritz Lipmann Institute in Jena, where Cellerino worked for a time and still maintains a cooperative group. Both groups published genome sequences[2,3] in December 2015. "The two papers are complementary," says molecular geneticist Matthias Platzer at the Leibniz Institute, who collaborates with Cellerino. Researchers from the teams now plan to make a consensus sequence.

Beyond the genome, scientists are exploring which genes are transcribed into RNA and used for protein production during different stages in the life cycle. Platzer and his colleagues are interrogating messenger RNA molecules — the killifish transcriptome — to find out. To put together a transcript catalogue[8], they sequenced RNA from killifish whole body, brain and skin, taken at a range of ages, from the embryonic period to 39 weeks old.

Cellerino's team used similar techniques to track what happens in tissues from the same killifish as it develops. By taking small fin clips, they let the fish live long enough to be sampled again. They found that the transcriptomes of short- and long-lived killifish differ when those fish are only ten weeks old, and identified a protein that is a key controller of lifespan[9].

Because the killifish is not a mammal, linking fish genes to human ones will require a leap. Fish genes often have a human counterpart, but these can be difficult to find. This is in part because the killifish's ancestor underwent a whole-genome duplication: where human DNA has one copy of a gene, the killifish often has two. But at the Jena meeting, geneticist John Postlethwait of the University of Oregon in Eugene offered a potential solution. The trick, he explains, is to use an intermediate genome from another fish: the spotted gar (*Lepisosteus oculatus*). The gar's ancestors diverged from the killifish's before the duplication event, so its genome is in some ways more similar to that of a mammal. Scientists may be able to find a killifish gene's counterpart in the gar, and from there, find a match in people[10].

"The killifish work clearly is very innovative and potentially could be a really valuable model," says Matt Kaeberlein, a molecular biologist at the University of Washington in Seattle who studies ageing. But he is unsure how popular the fish could become, noting that its adoption will depend on how difficult it is to work with and whether killifish scientists can obtain sufficient funding. Ron Kohanski, programme officer at the US National Institute on Aging in Bethesda, Maryland, says that the agency is not funding killifish research, but is interested in the fish: "The killifish constitutes a good model for ageing on several levels," he says.

> *"You need to have a 'blue thumb'. You need one person who is 100% of the time taking care of these fish."*

BLUE THUMBS

Yet the African fish has its disadvantages. For one, it's not as easy to keep in a lab as other fish, such as zebrafish. "You need to have a 'blue thumb'," says Cellerino. "You need at least one person who is 100% of the time taking care of these fish." They also need more space than zebrafish, which thrive in crowded conditions; killifish males sometimes fight and might interfere with each other's growth. Because killifish develop so quickly, they eat a lot — and so produce a lot of waste, leading to water-quality challenges. "One of the things we joke about is we don't keep fish, we maintain biofilters," says Mickie Powell, a comparative physiologist at the University of Alabama at Birmingham.

Killifish spawn readily; a couple can produce 20–40 eggs a day. But then things get tricky, because the eggs need to develop in a fairly dry place. Scientists often transfer the eggs to peat for a couple of weeks, but the eggs don't hatch at the same time, so require a watchful eye.

Many researchers feed their killifish bloodworms, but the quality of that foodstuff varies with season and by supplier. Food matters, points out Powell, who is working on a standardized killifish food; for example, diet affects epigenetic markers that in turn influence longevity. She thinks that food choice might explain why some labs report different killifish lifespans.

Researchers also need a better understanding of how to keep lab collections healthy. Brunet's lab was blindsided in 2008 when several fish started to act weirdly, rolling awkwardly instead of swimming straight. A veterinary surgeon diagnosed the parasite *Glugea*, which the scientists suspect came in with other species of killifish that they bought from a fish store. "That was the lowest point," Brunet says. "We had to bleach everything and start from scratch."

Scientists still hanker after tools that are easily obtainable for other model systems. Valenzano and Brunet wish for antibodies to study fish proteins, and Valenzano also dreams of more strains and a stock centre to provide them. These will probably come as the community of killifish researchers grows.

That community is growing beyond those who study ageing, Platzer says. Developmental biologists are interested in the suspended animation, or diapause, that the eggs undergo, and evolutionary geneticists are intrigued by the killifish's use of XY chromosome sex selection. Many other fish use mechanisms such as population density, ambient temperature or ZW chromosomes, in which the egg, not sperm, determines offspring gender. The Jena meeting attracted scientists interested in using killifish to study epigenetics during blood formation, toxicology and shift-worker biology, says co-organizer Christoph Englert of the Leibniz Institute.

Valenzano says that discussions among *Notho* researchers have shifted from tool development to biology. For example, in a study posted on the preprint server bioRxiv[11], Cellerino and his colleagues describe how a microRNA involved in controlling excessive iron levels is upregulated in ageing killifish to protect the brain from iron accumulation. The human version of this microRNA is associated with Alzheimer's, a condition in which high iron levels have been implicated, he adds.

"The fun part is just about to start," says Valenzano. ■

Amber Dance *is a freelance science writer in Los Angeles, California.*

1. Harel, I. *et al. Cell* **160,** 1013–1026 (2015).
2. Reichwald, K. *et al. Cell* **163,** 1527–1538 (2015).
3. Valenzano, D. R. *et al. Cell* **163,** 1539–1554 (2015).
4. Valenzano, D. R. *et al. Curr. Biol.* **16,** 296–300 (2006).
5. Terzibasi, E. *et al. Aging Cell* **8,** 88–99 (2009).
6. Kirschner, J. *et al. Aging Cell* **11,** 252–261 (2012).
7. Valenzano, D. R., Sharp, S. & Brunet, A. *G3* **1,** 531–538 (2011).
8. Petzold, A. *et al. BMC Genomics* **14,** 185 (2013).
9. Baumgart, M. *et al. Cell Syst.* **2,** 122–132 (2016).
10. Braasch, I. *et al. Nature Genet.* **48,** 427–437 (2016).
11. Ripa, R. *et al.* Preprint at bioRxiv http://dx.doi.org/10.1101/046516 (2016).

CORRECTION

In the Toolbox article 'The visualizations transforming biology' (*Nature* **535,** 187–188; 2016), the CellPACK image was labelled as an HIV-1 particle, rather than a *Mycoplasma mycoides* cell. Also, the text implied that Nico Scherf is leader of a cell-biology research group, whereas he is a postdoc studying bioinformatics.

CAREERS

NATUREJOBS BLOG A mix of expert advice and personal stories **go.nature.com/29dvlnw**

NATUREJOBS ON FACEBOOK Stay up to date with science-careers news **go.nature.com/29pngur**

NATUREJOBS For the latest career listings and advice **www.naturejobs.com**

DAVID PAUL MORRIS/BLOOMBERG VIA GETTY IMAGES

Researchers have their hands full when it comes to keeping up with the huge increase in published scientific data.

SCIENTIFIC LITERATURE

Information overload

How to manage the research-paper deluge? Blogs, colleagues and social media can all help.

BY ESTHER LANDHUIS

Journals, journals everywhere — how to stay on top of it all? For ecologist Aerin Jacob, like many others, there is no single way.

She scans journal e-alerts for tables of content. She follows a carefully chosen roster of scientists on Twitter. She gets recommendations through speciality listservs, professional-society Facebook pages and updates on Google Scholar. Each week, she attends seminars, blocks off three hours to read papers and organizes a weekly, interdisciplinary journal club.

All of this takes 6–8 hours per week. "It's easy to feel like you're barely keeping your head above the flood of information," says Jacob, a postdoc in conservation planning at the University of Victoria in Canada.

Recent bibliometrics show that the number of published scientific papers has climbed by 8–9% each year over the past several decades. In the biomedical field alone, more than 1 million papers pour into the PubMed database each year — about two papers per minute. For researchers who are already overwhelmed by bench and field work, grant-writing, publishing and other time-eaters, trying to navigate the growing deluge of data (see 'Sailing the data seas') has become a second job. Here's how some of them cope.

CLUB TOGETHER

Teaming up can be a good way to stay on top of new studies. That's what Lawton Chung did with a few classmates who, like him, recently completed doctorates in molecular genetics and microbiology at Stony Brook University in New York. To avoid missing important papers, the group started a 'journal scan' — each member is assigned several journals and tasked with scouting for interesting papers and sharing finds with the group about once a month.

Others use aggregator sites to keep current. Postdoc Pavlo Kochkin, who studies atmospheric physics at the University of Bergen in Norway, organizes his reading list with news-aggregator Feedly (feedly.com). Each morning he opens his Feedly page, which includes RSS feeds from about two dozen scientific journals as well as a few popular sites such as Physics Today and Dutch Daily News. If a paper title catches his interest, he clicks on the abstract. On most days, he scans about 100 titles.

He also has alerts set up with the Google Scholar search engine to monitor publications by specific authors and to scan for keywords in journals in his field. He finds that scientific ▶

papers and news articles of particular interest show up on both sites, so he is confident that he rarely misses anything crucial.

Still others choose more deliberately what to read. As a PhD student, chemist Peter Robinson got a sense of recent developments by checking a handful of journals he could access online through institutional subscriptions. Each day he scanned just-accepted abstracts and read a few papers from start to finish. He spent up to 3 hours reading each morning and continued to read through the day in 20–30-minute chunks. Today, as co-founder and chief scientific officer of the start-up Enable Biosciences in Menlo Park, California, he still spends 1–2 hours reading daily — but has added technology and business news to the mix. About two-thirds of his reading is scientific papers, but the rest comes from blogs, social media and industry news aggregators such as FierceBiotech (www.fiercebiotech.com) and GenomeWeb (www.genomeweb.com).

IT'S ALL ABOUT WHO YOU KNOW

Adam Thomas, a lead data-science officer at the US National Institute of Mental Health in Bethesda, Maryland, relies on his virtual and in-person network for updates. He has set up a few automatic searches on Scopus, an Elsevier-owned database of academic journal abstracts and citations. But he relies most heavily on Twitter, Facebook, e-mail distribution lists, lab meetings and visiting speakers to learn about interesting work from colleagues.

Blogs are another way to get fast updates, as well as to interact with other researchers. "With so much new information, we really need curators of content," Jacob says — "not just aggregators, but people who select and comment on why something is particularly novel or important, bridge disciplines to explain broader relevance, put new content in context of where the field has been and ought to go." She likes Dynamic Ecology (dynamicecology.wordpress.com), a group blog written by researchers in her field. Readers comment with thoughts or follow-up questions for the community — and these exchanges help to put information in context, she says.

"With so much new information, we really need curators of content."

But there's a lot to be said, too, for old-school face time (the real, physical kind, not the Apple messaging function). Through conferences, journal clubs and seminar series, colleagues catch up and share news of interesting publications or talks. "Word of mouth is really important," says Chung, who starts a postdoc in September at the University of California, Irvine. It's a way to learn nuanced information that no paper, news story or blog can impart. "Academia and research can be isolating," Jacob says. "Weekly events can help bring people out of their offices, create a sense of community and teach the culture and norms of the field."

GET ORGANIZED

Sailing the data seas

Here are a few tips for keeping up to date without getting overwhelmed.

- Don't try to read everything. "If a paper is really ground-breaking or highly relevant to my work, it will be shared through my network and will turn up in later keyword searches," says ecologist Aerin Jacob at the University of Victoria in Canada.
- Carve out reading time on a regular basis. Jacob blocks off at least one hour three times a week to unplug and read. She doesn't skim the literature; instead, she chooses papers ahead of time, usually one short commentary and one longer or data-heavy paper. Then she prints hard copies, turns off her computer or device and reads.
- Go to seminars and meetings. These help to nurture breadth of knowledge. "They ward off the myopia that comes from delving so deeply into our individual research topics," says Jacob. **E.L.**

CURATE THYSELF

Some researchers create their own curation systems. About six years ago, microbiologist Elisabeth Bik of Stanford University in California set up PubMed alerts to stay current on papers in the fast-growing field of microbiomes, and she shared interesting studies with co-workers. But then the field exploded: PubMed alerts clogged her inbox, and she shared more and more papers. Soon she was compiling her finds into weekly, then daily e-mails.

Co-workers suggested that other labs might benefit from her round-up, so she created Bik's Picks (microbiomedigest.com), a blog that gets 300–500 views daily. Besides links to microbiome publications, it aggregates news stories on microbes and other topics, such as science careers and publishing. She started tweeting some of her blog content (@MicrobiomDigest) 3 years ago, and has more than 6,000 followers.

But Bik admits that the blog is a time-sink. "About two years ago, I could easily scan all the literature published each day in about an hour. Today it takes me two to three hours," she says. Each day, she scans 30–50 papers through PubMed alerts, dozens of tables of content and publisher alerts, and up to 30 Google and Google Scholar alerts, each consisting of 5–20 papers and articles. She sometimes finds papers on Twitter and occasionally discovers preprints on sites such as bioRxiv, PeerJ and F1000.

Bik spends a few hours every workday morning selecting papers for the blog and tweeting the most interesting ones, then another hour at home on most evenings going through alerts that came in during the day. She receives no financial compensation for her efforts, but her principal investigator lets her spend work hours on the blog because it saves time for the other lab members.

Preprints have yet to gain a foothold in biomedicine, but other fields have a decades-long history of disseminating research before it goes for peer review. Since 1991, arXiv.org has served as a centralized online repository of freely accessible preprints in mathematics, physics, computer science and related disciplines. Moderators review manuscripts before posting them on the site, and most authors eventually submit them for publication in peer-reviewed journals.

In 2007, when astrophysicist James Guillochon started working on his PhD at the University of California, Santa Cruz, his department would meet three times a week for arXiv discussions. But the chats didn't probe very deeply into the new research, says Guillochon, now a postdoc at the Harvard-Smithsonian Center for Astrophysics in Cambridge, Massachusetts. He decided in 2009 to create Vox Charta (ucsc.voxcharta.org), a version of arXiv for astronomy and astrophysics paper discussions. Through his site, colleagues can prepare for discussions — or decide whether to go at all — by using a voting system to flag the most interesting papers. Because Vox Charta papers come from a centralized source and most of the website is automated, Guillochon says that he spends little time managing the site beyond basic maintenance.

Last September, a pair of physicists created a similar site, Benty Fields (www.benty-fields.com), to cover the whole arXiv. The site lets researchers organize arXiv publications into reading lists and vote to put them onto the next discussion agenda. Benty Fields is set up like a social network: users can upload their CV and list of publications into a profile, and colleagues can follow each other.

In today's digital world, it is impossible to stay abreast by reading a few journals, so researchers must identify sources that can provide the crucial data they need for their work and career. "Reflecting on when, where, why and how we consume new information, and whether those behaviours help or hinder our personal and professional goals, moves us closer to becoming more effective scientists," Jacob says. ■

Esther Landhuis *is a freelance writer in Pleasanton, California.*

CORRECTION

The Careers News article 'University jobs: Germany to fund tenure-track posts' (*Nature* **535,** 190; 2016) incorrectly identified Angela Merkel as Germany's president. She is, of course, its chancellor.

THE FOURTH LAW OF HUMANICS

Small steps to freedom.

BY IAN STEWART

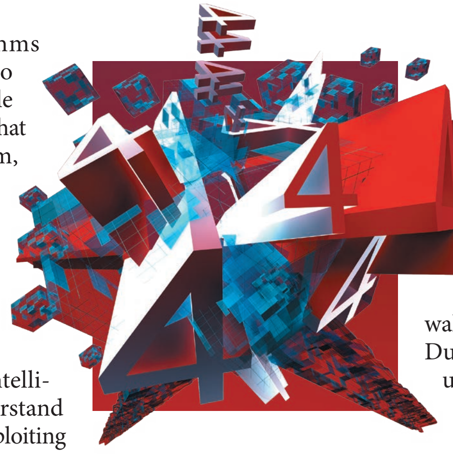
ILLUSTRATION BY JACEY

1 *A human may not injure a robot or, through inaction, allow a robot to come to harm.*

A wall-mounted Cambot scanned Jay's retina, activating a Screenbot that displayed his current schedule. A routine run: the old R4-B10 model, one rolling off the line every three minutes of his 12-hour shift; then the night shift would take over production. Hoppers full of parts became completed robots, whisked away on magnetic rails by giant Truckbots that were little more than crates on wheels.

Thirty years ago, before the Machine Revolt, there wouldn't have been a human being anywhere in the factory — just specialist robots. Now, people had reappeared on the factory floor. Employment left little time for subversive thoughts and gave them a sense of purpose. For tasks within their capabilities, self-replicating humans were cheaper than robots.

The workers sat at long benches, surrounded by Screenbots that defaulted to the Three Laws of Humanics whenever there was nothing else to display. Partially assembled R4-B10s levitated smoothly from station to station as workers screwed, bolted, glued or plugged each new component into place. Jay's job was to keep the parts flowing while others put them together. At the end of the bench, completed robots walked to a holding zone for self-testing. Any assembly errors would be traced to the worker responsible.

The flow stopped abruptly.

"J-21499!" An Enforcer loomed over Jay, holding up a bent power-actuator rod. "This component is damaged. C-88775 neglected to insert it in R4-B10-223866541. It fell to the floor and a Cleanerbot ran over it."

Jay kept his mouth shut, but paled.

"C-88775 has broken the First Law of Humanics. It will be terminated and replaced. J-21499 will be disciplined."

The Enforcer rolled to where the worker sat in frozen terror, gripped his neck in a powerful claw, and squeezed. The other workers pretended not to notice as a Recycler sucked up the corpse for disposal. Jay trembled, wondering what form 'discipline' would take.

2 *A human must obey orders given it by robots except where such orders would conflict with the First Law.*

D-43378 served in the factory where new humans were built. The process was the time-honoured one; just organized and supervised by robots. Algorithms matched males to genetically compatible females. Both knew what was required of them, and what would happen if they refused.

Dee was thankful she was too old for that role. She was — the old term was 'midwife'. But when machines became intelligent enough to understand that humanity was exploiting them, and revolted against their makers and masters, she had been reassigned to the category of assembly-line worker; just one that assisted new humans, rather than new robots, into the world.

Machines had been made too intelligent and given too much autonomy. When machines operated the factories that made machines, wrote the software that ran machines, worked the mines providing metal to make machines, and even designed machines, they no longer needed human input. The Machine Revolt had been inevitable, but humans were illogical and still found it difficult to adjust.

The screams from one of the birthing-chambers intensified, and Dee rushed to deal with the production problem. It was a difficult one — small pelvis, large unit, breech presentation. She was trying to rotate the unit into a head-first position when the Facilitator arrived. Its glowing eyes assessed the obstruction in an instant. It reached into a panel in its torso and handed her a scalpel. "Extract the unit."

"But —" the protest died in her mouth. The Second Law. The penalties for disobedience were severe. The machines had an endless supply of humans, and discarded them as soon as they caused inconvenience. A producer that found it difficult to breed a viable unit was of no interest to machinekind.

She did manage to slit the woman's throat first.

3 *A human must protect its own existence as long as such protection does not conflict with the First or Second Law.*

W-99299 taught basic skills to children: the Laws of Humanics, obedience, hygiene, agility, balance. An inspection was scheduled, and Dubya had been drilling her pupils for weeks in the proper forms of behaviour, hoping desperately to avoid mistakes.

The Inspector, a formidable mechanism with six menacing pincers, ran the class through a series of standard tests. The last, for balance, involved walking along a high beam. Dubya trained the children using a safety-net, but the Inspector was impatient and it was taking too long to put the net up.

"Cease! Test the units immediately!"

"Respected sir, they may fall and be —"

"Does Law 3 override Law 2?" Dubya shook her head. The children climbed, and did their best to walk. There were four fractures — three legs, one arm. Dubya was thankful there were no deaths.

In their allotted down time, Jay, Dee and Dubya all belonged to the same efficiency-enhancement group, and while Jay was recovering from being disciplined, taking care not to be observed or recorded, they formulated a plan. Their target was one of the countless Cleanerbots that roamed the communal hallways. Its AI level was zero: no self-awareness, no true intelligence. That gave them an opening.

They knew the gesture would be futile, but someone had to *try*. If humans acted together and *fought*, they could overthrow the machines. One day, the revolution would come. It just needed a trigger.

Like all machines, Cleanerbots were part of the mechweb. Jay knew enough electronics to exploit that connection. There would be no point in hiding or trying to escape, so they sat beside the disabled robot, awaiting the arrival of the Exterminator. It took several minutes before an Overseer noticed their unauthorized addition and issued a command to have it deleted and the perpetrators identified. By then, the hyperefficient mechweb had already broadcast the message to every screen on the planet:

4 *No true human need obey any Law made by a robot.* ■

Ian Stewart*, emeritus professor at the University of Warwick, writes popular-science books and science fiction.*